Black Sea Journal of Engineering and Science

Volume 8 | Issue 4



ISSN: 2619 - 8991

BS Journals

BLACK SEA JOURNAL OF ENGINEERING AND SCIENCE

(BSJ ENGIN SCI)

Black Sea Journal of Engineering and Science (BSJ Eng Sci) is a double-blind peer-reviewed, open-access international journal published electronically 6 times (January, March, May, July, September, and November) in a year by since January 2018. It publishes, in English and Turkish, full-length original research articles, innovative papers, conference papers, reviews, mini-reviews, rapid communications or technical note on advances in a wide range of scientific disciplines from all fields of engineering and science and from any source.

ISSN 2619 - 8991

Phone: +90 362 408 25 15

Fax: +90 362 408 25 15

Email: bsjsci@blackseapublishers.com

Web site: http://dergipark.gov.tr/bsengineering

Sort of publication: Periodically 6 times (January, March, May, July, September, and November) in a year

Publication date and place: July 15, 2025 - Samsun, TÜRKİYE

Publishing kind: Electronically

OWNER

Prof. Dr. Uğur ŞEN

DIRECTOR IN CHARGE

Prof. Dr. Hasan ÖNDER

EDITOR BOARDS

EDITOR IN CHIEF

Prof. Dr. Uğur ŞEN, Ondokuz, Mayis University, TÜRKİYE

Prof. Dr. Hasan ÖNDER, Ondokuz Mayis University, TÜRKİYE

SECTION EDITORS*

Prof. Dr. Berna KILIÇ, Section Editor of Fisheries Engineering, Ege University, TÜRKİYE

Prof. Dr. Bülent YANIKTEPE, Section Editor of Aerospace Engineering, Osmaniye Korkut Ata University, TÜRKİYE

Prof. Dr. Çiğdem TAKMA, Section Editor of Statistics, Ege University, TÜRKİYE

Prof. Dr. Dilek KUT, Section Editor of Textile Engineering, Uludağ University, TÜRKİYE

Prof. Dr. Erkan YALÇIN, Section Editor of Biology, Ondokuz Mayıs University, TÜRKİYE

Prof. Dr. Ertan BUYRUK, Section Editor of Mechanical Engineering, Sivas Cumhuriyet University, TÜRKİYE

Prof. Dr. Esteban TLELO-CUAUTLE, Section Editor of Electrical and Electronics Engineering, National Institute of Astrophysics, Optics and Electronics, MEXICO

Prof. Dr. Fauziatul FAJAROH, Section Editor of Chemical Engineering, Universitas Negeri Malang, INDONESIA

Prof. Dr. Gökhan CİVELEKOĞLU, Section Editor of Environmental Engineering, Akdeniz University, TÜRKİYE

Prof. Dr. Hasan TANAK, Section Editor of Physics, Amasya University, TÜRKİYE

Prof. Dr. Hasan TEMİZ, Section Editor of Food Engineering, Ondokuz Mayis University, TÜRKİYE

Prof. Dr. Hojjat SADEGHİ-ALİABADİ, Section Editor of Chemistry, Isfahan University, IRAN

Prof. Dr. Hüseyin PEKER, Section Editor of Forest Engineering, Artvin Çoruh University, TÜRKİYE

Prof. Dr. İbrahim Özgür DENEME, Section Editor of Civil Engineering, Aksaray University, TÜRKİYE

Prof. Dr. Nilüfer YURTAY, Section Editor of Computer Engineering, Sakarya University, TÜRKİYE

Prof. Dr. Özgür Hakan AYDOĞMUŞ, Section Editor of Mathematics, Social Sciences University of Ankara, TÜRKİYE

Assoc. Prof. Dr. Belgin KARABACAKOĞLU, Section Editor of Chemical Engineering, Eskişehir Osmangazi University, TÜRKİYE

Assoc. Prof. Dr. Edit MİKÓ, Section Editor of Agricultural Engineering, University of Szeged, HUNGARY

Assoc. Prof. Dr. Ergün EKİCİ, Section Editor of Industrial Engineering, Çanakkale Onsekiz Mart University, TÜRKİYE

Assoc. Prof. Dr. Helal Uddin MOLLA, Section Editor of Physics, Rajshahi University of Engineering and Technology, BANGLADESH

Assoc. Prof. Dr. Kadyrbay CHEKİROV, Section Editor of Biology, Kyrgyz Turkish Manas University, KYRGYZSTAN

Assoc. Prof. Dr. Lukman ABDULRA'UF, Section Editor of Chemistry, Kwara State University, NIGERIA
Assoc. Prof. Dr. Mehmet EBEOĞLUGİL, Dokuz Eylül University, TÜRKİYE
Assoc. Prof. Dr. Mohammad KHAJEH MEHRIZI, Section Editor of Textile Engineering, Yazd University, IRAN
Assoc. Prof. Dr. Silvio DE OLİVEİRA JUNIOR, Section Editor of Mechanical Engineering, University of São Paulo, BRAZIL
Assoc. Prof. Dr. Sinan AKISKA, Section Editor of Geological Engineering, Ankara University, TÜRKİYE
Assoc. Prof. Dr. Ufuk Atmaca, Section Editor of Chemistry, Atatürk University, TÜRKİYE
Assoc. Prof. Dr. Veli İLÇİ, Section Editor of Geomatics Engineering, Ondokuz Mayis University, TÜRKİYE
Asst. Prof. Dr. Francis INEGBEDİON, Section Editor of Industrial Engineering, University of Benin, NIGERIA
Asst. Prof. Dr. Jun-wei LİM, Section Editor of Environmental Engineering, Universiti Teknologi Petronas, MALAYSIA
Asst. Prof. Dr. Mehmet ÖZDEMİR, Section Editor of Mining Engineering, Kütahya Dumlupınar University, TÜRKİYE
Asst. Prof. Dr. Muhammad GULİSTAN, Section Editor of Mathematics, Hazara University, PAKISTAN
Asst. Prof. Dr. Sedat KARADAVUT, Section Editor of Agricultural Engineering, Trakya University, TÜRKİYE
Asst. Prof. Ranjith RAJ A, Section Editor of Metallurgical and Materials Engineering, Sri Venkateswara College of Engineering, INDIA

* The ranking is arranged alphabetically within the academic title

STATISTIC EDITOR
Prof. Dr. Mehmet TOPAL, Kastamonu University, TÜRKİYE

ENGLISH EDITOR
Asst. Prof. Dr. Betül ÖZCAN DOST, Ondokuz Mayis University, TÜRKİYE

TURKISH EDITOR
Prof. Dr. Serkan ŞEN, Ondokuz Mayis University, TÜRKİYE

REVIEWERS OF THE ISSUE*

Prof. Dr. Abdullah FİŞNE, İstanbul Technical University, Department of Mining Engineering, Mining Engineering, TÜRKİYE

Prof. Dr. Bahtiyar ÜNVER, Hacettepe University, Department of Mining Engineering, Mining Engineering, TÜRKİYE

Prof. Dr. Çiğdem ARICIGİL ÇİLAN, İstanbul University, Department of Business Administration, Statistics, TÜRKİYE

Prof. Dr. Fatih BASCİFTCİ, Selçuk University, Department of Computer Engineering, Information and Computing Sciences, TÜRKİYE

Prof. Dr. Fatih ÖNER, Ordu University, Department of Field Crops, Information Systems Design, TÜRKİYE

Prof. Dr. Halil İbrahim ERKOVAN, Eskişehir Osmangazi University, Department of Field Crops, Pasture-Meadow Forage Plants, TÜRKİYE

Prof. Dr. Hüseyin TOKTAMIŞ, Gaziantep University, Department of Engineering Physics, Radiation Technology, TÜRKİYE

Prof. Dr. İnanç ÖZGEN, Fırat University, Department of Bioengineering, Entomology, TÜRKİYE

Prof. Dr. Lokman GEMİ, Necmettin Erbakan University, Meram Vocational School, Material Design and Behaviors, TÜRKİYE

Prof. Dr. Lütfü NAMLI, Samsun University, Department of mechanical Engineering, Thermodynamics and Statistical Physics, TÜRKİYE

Prof. Dr. Mahmut KAPLAN, Erciyes University, Department of Field Crops, Pasture-Meadow Forage Plants, TÜRKİYE

Prof. Dr. Mehmet Serhat ODABAŞ, Ondokuz Mayıs University, Department of Plant and Animal Production, Information Systems Design, TÜRKİYE

Prof.Dr. Mehtap ERŞAN, Sivas Cumhuriyet University, Department of Chemical Engineering, Thermodynamics, TÜRKİYE

Prof. Dr. Mustafa Çağatay TUFAN, Ondokuz Mayıs University, Department of Radiological Sciences, Nuclear Physics, TÜRKİYE

Prof. Dr. Mürsel ERDAL, Gazi University, Department of Civil Engineering, Construction Business, TÜRKİYE

Prof. Dr. Serkan SUBAŞI, Düzce University, Department of Civil Engineering, Civil Engineering, TÜRKİYE

Prof. Dr. Sezgin SUCU, Ankara University, Department of Mathematics, Applied Mathematics, TÜRKİYE

Prof. Dr. Şükrü DURSUN, Konya Technical University, Department of Environmental Engineering, Air Pollution Modelling and Control, TÜRKİYE

Prof. Dr. Tuğrul OKTAY, Erciyes University, Aircraft Engineering Department, Aircraft Performance and Flight Control Systems, TÜRKİYE

Prof. Dr. Zeki KARACA, Ondokuz Mayıs University, Department of Civil Engineering, Structural Dynamics, TÜRKİYE

Prof. Dr. Zeynel CEBECİ, Çıkurova University, Department of Animal Science, Biometry, TÜRKİYE

Assoc. Prof. Dr. Ahmet ALTÜRK, Amasya University, Department of Mathematics, Mathematical Methods and Special Functions, TÜRKİYE

Assoc. Prof. Dr. Ahmet Emre DİNÇER, Ankara Yıldırım Beyazıt UniversityDepartment of Architecture, Architectural History, Theory and Criticism, TÜRKİYE

Assoc. Prof. Dr. Ahmet Gökhan AĞGÜL, Ağrı İbrahim Çeçen University, Department of Biochemistry, Medicinal and Biomolecular Chemistry, TÜRKİYE

Assoc. Prof. Dr. Arzum IŞITAN, Pamukkale University, Department of Mechanical Engineering, Machine Design and Machine Equipment, TÜRKİYE

Assoc. Prof. Dr. Aysen ŞİMŞEK KANDEMİR, Independent Researcher, Statistics, TÜRKİYE

Assoc. Prof. Dr. Aytaç ALTAN, Zonguldak Bülent Ecevit University, Department of Electrical Electronics Engineering, Control Theoryand Applications, TÜRKİYE

Assoc. Prof. Dr. Canan KOÇ, Dicle University, Department of Architecture, City and Regional Planning, TÜRKİYE

Assoc. Prof. Dr. Elmira ABDYLDAEVA, Kırgızistan-Türkiye Manas University, Department of Mathematics, Mathematical Optimisation, KYRGYZSTAN

Assoc. Prof. Dr. Emine ŞAP, Bingöl University, Department of Electronics and Automation, Materials Science and Technologies, TÜRKİYE

Assoc. Prof. Dr. Ercan AYDOĞMUŞ, Fırat University, Department of Chemical Engineering, Bioprocessing Bioproduction and Bioproducts, TÜRKİYE

Assoc. Prof. Dr. Fatih Yavuz ILGIN, Erzincan Binali Yıldırım University, Department of Electrical and Electronics Engineering, Electrical Engineering, TÜRKİYE

Assoc. Prof. Dr. Halil ŞENOL, Giresun University, Department of Energy Systems Engineering, Machine Learning, TÜRKİYE

Assoc. Prof. Dr. Harun KOÇAK, Gazi Universty, Department of Aircraft Technology, Mechanical Engineering, TÜRKİYE

Assoc. Prof. Dr. Kenan ALTUN, Sivas Cumhuriyet University, Department of Electronics and Automation, Embedded Systems, TÜRKİYE

Assoc. Prof. Dr. Medine ÇOPUR DOĞRUSÖZ, Yozgat Bozok University, Department of Field Crop, Pasture-Meadow Forage Plants, TÜRKİYE

Assoc. Prof. Dr. Mehmet Akif BOZ, Yozgat Bozok University, Department of Animal Science, Poultry Farming and Treatment, TÜRKİYE

Assoc. Prof. Dr. Murat GÜNAYDIN, Karadeniz Technical University, Department of Civil Engineering, Structural Dynamics, TÜRKİYE

Assoc. Prof. Dr. Mustafa AKKAŞ, Bolu Abant İzzet Baysal University, Department of Computer Engineering, Networking and Communications, TÜRKİYE

Assoc. Prof. Dr. Osman PALANCI, Süleyman Demirel University, Department of Business Administration, Applied Mathematics, TÜRKİYE

Assoc. Prof. Dr. Rukiye UZUN ARSLAN, Zonguldak Bulent Ecevit University, Department of Electrical and Electronics Engineering, Electrical Engineering, TÜRKİYE

Assoc. Prof. Dr. Sertan OZAN, Yozgat Bozok University, Department of Mechanical Engineering, Mechanical Engineering, TÜRKİYE

Assoc. Prof. Dr. Seyfullah KEYF, Yıldız Technical University, Department of Chemical Engineering, Chemical Engineering and Technology, TÜRKİYE

Assoc. Prof. Dr. Şahika ÖZDEMİR, İstanbul Sabahattin Zaim University, Department of Interior Architecture and Environmental Design, Architectural Design, TÜRKİYE

Assoc. Prof. Dr. Şenol ÇELİK, Bingöl University, Department of Animal Science, Biometry, TÜRKİYE

Assoc. Prof. Dr. Yavuz ÖZDEMİR, Istanbul Health and Technology University, Department of Industrial Engineering, Industrial Engineering, TÜRKİYE

Assist. Prof. Dr. Adem SAVAŞ, Giresun University, Hazelnut Specialization Coordination, Food Engineering, TÜRKİYE

Assist. Prof. Dr. Ali Hakan TOR, Abdullah Gül University, Department of Mathematics, Mathematical Optimisation, TÜRKİYE

Assist. Prof. Dr. Bahadır ŞİN, Sakarya University of Applied Sciences, Department of Plant Protection, Entomology, TÜRKİYE

Assist. Prof. Dr. Coşkun PARİM, Yıldız Technical University, Department of Statistics, Statistics, TÜRKİYE

Assist. Prof. Dr. Emine BOZOKLAR, İskenderun Technical University, Department of Industrial Engineering, Manufacturing Management, TÜRKİYE

Assist. Prof. Dr. Esra DOBRUCALI, Sakarya University, Department of Civil Engineering, Construction Business, TÜRKİYE

Assist. Prof. Dr. Göksu GÖREL, Manisa Celal Bayar University, Department of Electrical Engineering, Electrical Engineering, TÜRKİYE

Assist. Prof. Dr. Gülcay ERCAN OĞUZTÜRK, Recep Tayyip Erdoğan University, Department of Landscape Architecture, Landscape Architecture, TÜRKİYE

Assist. Prof. Dr. Günnur PEŞMEN, Afyon Kocatepe University, Department of Laboratory Veterinary Health, Poultry Farming and Treatment, TÜRKİYE

Assist. Prof. Dr. Halil İbrahim BİNİCİ, İstanbul Esenyurt University, Department of Nutrition and Dietetics, Food Microbiology, TÜRKİYE

Assist. Prof. Dr. Hilal DOĞANAY KATI, Bursa Technical University, Department of Mechanical Engineering, Machine Theory and Dynamics, TÜRKİYE

Assist. Prof. Dr. İlyas BOZKURT, Ardahan University, Department of Pharmacy Services, Pharmaceutical Biochemistry, TÜRKİYE

Assist. Prof. Dr. Jeyarani MILTON, Sree Saraawathi Thyagaraja College, Department of Software Engineering, Cloud Computing Security, INDIA

Assist. Prof. Dr. Kübra ÇINAR TOPÇU, Bayburt University, Department of Food Processing, Food Microbiology, TÜRKİYE

Assist. Prof. Dr. Lütfiye Özlem AKKAN, Dokuz Eylul University, Department of Electronics and Automation, Communications Engineering, TÜRKİYE

Assist. Prof. Dr. Mahmut AYKAÇ, Gaziantep University, Department of Electrical and Electronics Engineering, System and Network Security, TÜRKİYE

Assist. Prof. Dr. Meltem GÜNGÖR, Sanko University, Department of Medical Biochemistry, Pharmaceutical Biochemistry, TÜRKİYE

Assist. Prof. Dr. Meral ÖZARSLAN YATAK, Gazi University, Department of Electrical and Electronics Engineering, Control Theoryand Applications, TÜRKİYE

Assist. Prof. Dr. Merve DOĞRUEL, İstanbul Esenyurt University, Department of Management Information Systems, Data Mining and Knowledge Discovery, TÜRKİYE

Assist. Prof. Dr. Metin UZUN, Iskenderun Technical University, Department of Airframe and Powerplant Maintenance, Aircraft Performance and Flight Control Systems, TÜRKİYE

Assist. Prof. Dr. Mustafa EKİCİ, Çanakkale Onsekiz Mart University, Department of Mathematics and Science Education, Applied Mathematics, TÜRKİYE

Assist. Prof. Dr. Mustafa YAZ, Yozgat Bozok University, Department of Electrical and Electronics Engineering, Control Theory and Applications, TÜRKİYE

Assist. Prof. Dr. Mürsel Ozan İNCETAŞ, Alanya Alaaddin University, Department of Electric and Energy, Information and Computing Sciences, TÜRKİYE

Assist. Prof. Dr. Özgün SUNAR, Eskisehir Technical University, Transportation Vocational School, Materials Science and Technologies, TÜRKİYE

Assist. Prof. Dr. Polathan KÜSBECİ, Nişantaşı University, Department of Management Information Systems, Cloud Computing Security, TÜRKİYE

Assist. Prof. Dr. S. Agnes SHIFANI, Saveetha University, Department of Technical Sciences, Image Processing, INDIA

Assist. Prof. Dr. Salih DAĞLI, Sinop University, Department of Mechanical Engineering, Mechanical Engineering, TÜRKİYE

Assist. Prof. Dr. Selçuk YAZAR, Kırklareli University, Department of Software Engineering, Deep Learning, TÜRKİYE

Assist. Prof. Dr. Sena Nur ANGIN, Siirt University, Department of Urban and Regional Planning, Landscape Design, TÜRKİYE

Assist. Prof. Dr. Selin SARAÇ GÜLERYÜZ, Toros University, Department of Industrial Engineering, Machine Learning, TÜRKİYE

Assist. Prof. Dr. Sinem AKYOL, Fırat University, Department of Software Engineering, Machine Learning Algorithms, TÜRKİYE

Assist. Prof. Dr. Şengül BAYRAK, İstanbul Sabahattin Zaim University, Department of Computer Engineering, Natural Language Processing, TÜRKİYE

Assist. Prof. Dr. Veli BAYSAL, Bartın University, Department of Computer Engineering, Modelling, TÜRKİYE

Assist. Prof. Dr. Yılmaz KAYA, Ondokuz Mayıs University, Department of Agricultural Biotechnology, Plant Biotechnology, TÜRKİYE

Dr. Eda Gizem KOÇYİĞİT, Dokuz Eylül University, Department of Statistics, Statistics, TÜRKİYE

Dr. Elif ÖNAL, Atatürk University, Department of Landscape Architecture, Landscape Architecture, TÜRKİYE

Dr. Kenan BULCAR, Iğdır University, Department of Medical Services and Techniques, Nuclear Physics, TÜRKİYE

Dr. Mokhtar DJENDEL, University of Bordj Bou Arreridj, Department of Science and Technics, Materials Science and Technologies, ALGERIA

Dr. Olcay KALAN, Çukurova University, Department of Industrial Engineering, Industrial Engineering, TÜRKİYE

---

* The ranking is arranged alphabetically within the academic title

Volume 8, Issue 4 (2025)

Table of Contents

Research Articles

1. POWERING A SUSTAINABLE FUTURE: RENEWABLE ENERGY AS THE ENGINE OF THE GREEN ECONOMY
Kemal Gökhan NALBANT, Sevgi AYDIN.....910-917
2. PROMETHEE YÖNTEMİ İLE BİR TEKNİK MÜŞAVİR FİRMA SEÇİMİ
Latif Onur UĞUR, Merve ÖLÇER.....918-926
3. DOĞRU AKIM MİKRO ŞEBEKELERİ İÇİN KONTROLÖR TASARIMI VE SİMÜLASYONU
Ahmet Alperen ÖZBEK, Tuncay ALTUN, Kenan ALTUN.....927-936
4. EVALUATION OF AFTER SERVICE LOCATION WITH HESITANT FUZZY VIKOR: A CASE OF DRONE COMPANY IN TÜRKİYE
Dilan SARPKAYA, Gül Tekin TEMUR.....937-944
5. DIFFERENTIATION OF GROWTH, INNER ORGAN DEVELOPMENT, GUT MICROBIOTA, GUT HISTOLOGY AND MEAT QUALITY OF JAPANESE QUAILS FED DIETS CONTAINING VARYING AMOUNTS OF *Satureja spicigera* (K. Koch) Boiss LEAF POWDER
Emine DOĞAN, İsa COŞKUN.....945-953
6. YOL AĞAÇLANDIRMA UYGULAMALARININ DEĞERLENDİRİLMESİ: GAZİ CADDESİ ÖRNEĞİ
Ahmet CAF, Semaha KURAL.....954-962
7. ÇEVRESEL TUTUMLARIN SINIFLANDIRILMASINDA ÖZELLİK SEÇİMİ VE MODEL PERFORMANSININ İNCELENMESİ
Rukiye UZUN ARSLAN, İrem ŞENYER YAPICI, Fuat ALKAN.....963-969
8. THE REFINED PHYSICS-INFORMED NEURAL NETWORKS FOR NONLINEAR CONVECTION-REACTION-DIFFUSION EQUATIONS USING EXPONENTIAL SCHEMES
Burhan BEZEKCI.....970-981
9. FİBER OPTİK KABLOLU HABERLEŞME İLE DONATILMIŞ DRONLARIN GERÇEK SAVAŞ ORTAMINDA SAĞLADIĞI STRATEJİK AVANTAJLAR
Hüseyin ŞAHİN.....982-990
10. AUTONOMOUS AGRICULTURAL SPRAYING UAV: DESIGN, IMPLEMENTATION AND PERFORMANCE ANALYSIS
Ahmet Faruk TEKİN, Batıkan Erdem DEMİR.....991-998
11. COMPARISON OF RAW MATERIALS USED IN CUSTOMIZED IMPLANT SYSTEMS THROUGH FINITE ELEMENT ANALYSIS AND DYNAMIC FATIGUE TESTING
Vildan Fadime DEMİREZEN, Kenan IŞIK.....999-1006
12. ENHANCED SKIN LESION CLASSIFICATION THROUGH HAIR ARTIFACT REMOVAL AND TRANSFER LEARNING MODELS
Kerem GENCER.....1007-1021
13. EFFECT OF DIRECTION OF LOADING ON SEISMIC RESPONSE OF HISTORICAL MASONRY MINARETS: THE MINARET OF AKSARAY ZAFER MOSQUE
Erdem TÜRKELİ, Kadir YAYLA.....1022-1033

14. ENTROPİ VE KÜMELEME TABANLI YENİ BİR HAKEM DEĞERLENDİRME SÜRECİ VE KARAR DESTEK SİSTEMİ ÖNERİSİ
Seda Nur BUDAK, Kumru Didem ATALAY, Mehmet KABAK, Tacettin Sercan PEKİN……..1034-1049
15. HAVACILIK YAPILARINDA ENTEGRE BASAMAKLI KOMPOZİT KABUK TASARIM VE ÜRETİM PARAMETRELERİ
Muharrem CAN, Özgür KARALI……1050-1056
16. BLOCKCHAİN DESTEKLİ NESNELERİN İNTERNETİ (IOT) VARLIKLARINDA FİYAT TAHMİNİ İÇİN MODEL KARŞILAŞTIRMASI
Çağatay ERSİN, Onur KÖKTÜRK……..1057-1066
17. ENHANCED CORROSION RESISTANCE OF X120MN12 STEEL IN ACIDIC MEDIA BY A NOVEL NANOLIGNIN-BASED PROTECTIVE COATING
Emre GÖRGÜN, Mehtap ERŞAN……1067-1075
18. PHYTOSYNTHESIS OF SILVER NANOPARTICLES USING *Aesculus hippocastanum* L. (KERNEL AND SHELL) AND EVALUATION OF THEIR LARVICIDAL ACTIVITY AGAINST *Plodia interpunctella* (HUBNER) (LEPIDOPTERA: PYRALIDAE)
Onur AKER……1076-1086
19. MOTIFS AND ORNAMENTATIONS OF ERZURUM SELJUK MADRASAS IN THE CONTEXT OF INTERCULTURAL INTERACTION
Serkan SİPAHİ, Bernanur YAZICI, Selim KARTAL……1087-1095
20. DEVELOPMENT AND VALIDATION OF A SIMPLE HPLC-UV METHOD FOR ANALYSIS OF HARMINE
Galip Mesut DEMIR, Afife Busra UGUR KAPLAN, Mine Gulaboglu, Meltem CETIN……1096-1102
21. MAXIMIZING BIOGAS YIELD IN ANAEROBIC DIGESTION: A RESPONSE SURFACE METHODOLOGY APPROACH
Koray GÜNAY, Zehra Gülten YALÇIN……1103-1110
22. EARLY FIRE DETECTION MOBILE ROBOTIC SYSTEM WITH HYBRID LOCOMOTION
Hilmi Saygin SUCUOGLU, Ismail BOGREKCI……1111-1120
23. ARTIFICIAL NEURAL NETWORKS IN DRUG ADDICTION DIAGNOSIS
Engin KARAMAN……1121-1126
24. INVESTIGATION OF THERMOLUMINESCENCE PROPERTIES OF CALCITE FROM KAMAN, KIRŞEHIR
Sumeyra BALCI……1127-1133
25. FORECASTING MUTUAL FUND PRICES ON TEFAS USING LIGHTGBM
Oktay ÖLMEZ……1134-1139
26. METASEZGİSEL OPTİMİZASYON YÖNTEMLERİNİN PSİKİYATRİK UYGULAMALARDAKİ YERİ: BİBLİYOMETRİK BİR ANALİZ
Ümit CAN, Feride TUĞRUL……1140-1151
27. A NEW APPROACH TO NON-DESTRUCTIVE TESTING USING OPENCV-BASED IMAGE PROCESSING
Ekrem BULUT, Emre GÖRGÜN……1152-1159

28. ANALYST-AWARE INCIDENT ASSIGNMENT IN SECURITY OPERATIONS CENTERS: A MULTI-FACTOR PRIORITIZATION AND OPTIMIZATION FRAMEWORK
Eyup Can KILINCDEMIR, Baris CELIKTAS.....1160-1180
29. DETERMINATION OF TOTAL PHENOLIC ACID CONTENT AND ANTI-ATHEROGENIC ACTIVITY OF OIL OBTAINED FROM FRESH ARUGULA (ERUCA SATIVA L.) BY COLD-PRESSING
Erkan ÖNER, İlter DEMİRHAN.....1181-1184
30. REAL TIME DETECTION OF MICROBIAL LEAF DISEASES USING DEEP LEARNING AND EDGE COMPUTING ON RASPBERRY Pi 4
Noor BAHA ALDIN.....1185-1194
31. MICROSTRUCTURAL EVOLUTION AND RADON EMISSION DYNAMICS IN CLASS F FLY ASH-BLENDED CEMENT PASTES
Ahmad HOSSEINPOUR SHEIKHRAJAB, Ahmet ERDAL OSMANLIOĞLU.....1195-1203
32. ANKARA İLİ HAVA KALİTESİ İZLEME İSTASYONLARINDAN ELDE EDİLEN PM2.5 ÖLÇÜMLERİNDEKİ DEĞİŞİMİN EWMA KARTLARI KULLANILARAK İNCELENMESİ
Esra POLAT, Burak CİBA1, Rahime POLAT.....1204-1211
33. FARKLI *Brassica* TÜRLERİNİN KABA YEM KALİTESİ
Uğur SÖYLER, Serra Nur ÖZTÜRK, İlknur YILDIRIM, Erdem GÜLÜMSER.....1212-1217
34. THERMODYNAMIC AND EXERGOECONOMIC PERFORMANCE EVALUATION OF SINGLE AND DOUBLE-FLASH STEAM CYCLES WITH HEAT EXCHANGER INTEGRATION: EXERGETIC AND ECONOMIC OPTIMIZATION
Ünsal AYBEK, Bekir DOĞAN.....1218-1234

Reviews

35. AÇIK RADYO ERİŞİM AĞI ÜZERİNE SİSTEMATİK BİR İNCELEME: BİLEŞENLER, UYGULAMALAR VE GELECEK PERSPEKTİFLERİ
Önem YILDIZ.....1235-1244
36. AUGMENTED REALITY IN CULTURAL HERITAGE: A SYSTEMATIC REVIEW OF MOBILE APPLICATIONS AND USER EXPERIENCE EVALUATION
Nurettin ŞENYER, Aya ALZATMA 1245-1257
37. DIETARY ADVANCED GLYCATION END PRODUCTs (D-AGEs): FORMATION, DETECTION, AND HEALTH IMPLICATIONS
Seda UFUK, Melek ZOR, Memnune ŞENGÜL, İsa Arslan KARAKÜTÜK.....1258-1267

Black Sea Journal of Engineering and Science
doi: 10.34248/bsengineering.1642904

Open Access Journal
e-ISSN: 2619 – 8991

Research Article
Volume 8 - Issue 4: 910-917 / July 2025

POWERING A SUSTAINABLE FUTURE: RENEWABLE ENERGY AS THE ENGINE OF THE GREEN ECONOMY

Kemal Gökhan NALBANT[1]*, Sevgi AYDIN[2]

[1]*İstanbul Beykent University, Faculty of Engineering and Architecture, Department of Software Engineering, 34396, İstanbul, Türkiye*
[2]*İstanbul Beykent University, Faculty of Economics and Administrative Sciences, Department of Business, 34396, İstanbul, Türkiye*

Abstract: This study explores the role of renewable energy within the context of the green economy. The main aim is to discuss the advantages renewable energy offers and clearly identify the challenges affecting its adoption. To achieve this, the paper reviews existing literature on renewable energy and applies a SWOT analysis to better understand internal strengths and weaknesses as well as external opportunities and threats. While renewable energy presents clear environmental benefits and potential for economic growth, significant issues like high initial costs, infrastructural limitations, and inconsistent energy supply remain major obstacles. The study first defines the green economy concept, then provides a detailed SWOT analysis specifically focused on renewable energy, and finally discusses how digital marketing and artificial intelligence could help overcome identified barriers. Findings highlight the importance of government support, technological improvements, and digital strategies for successful renewable energy adoption. The insights presented here may help policymakers, businesses, and researchers effectively navigate the transition to a more sustainable economy.

Keywords: Artificial intelligence, Digital marketing, Digital branding, Green financing, SWOT analysis.

***Corresponding author:** İstanbul Beykent University, Faculty of Engineering and Architecture, Department of Software Engineering, 34396, İstanbul, Türkiye
E mail: kemalnalbant@beykent.edu.tr (K. G. NALBANT)
Kemal Gokhan NALBANT https://orcid.org/0000-0002-5065-2504
Sevgi AYDIN https://orcid.org/0000-0002-9507-5448

Received: February 19, 2025
Accepted: March 23, 2025
Published: July 15, 2025

Cite as: Nalbant KG, Aydin S. 2025. Powering a sustainable future: Renewable energy as the engine of the green economy. BSJ Eng Sci, 8(4): 910-917

1. Introduction

There is now a greater demand for sustainable and ecologically friendly alternatives as the use of fossil fuels has exacerbated climate change and global warming. Most people agree that the best way to replace fossil fuels soon is with renewable energy. Commercially viable renewable energy sources like solar, wind, and biomass have achieved significant progress. Technological advancements have enabled the effective utilization of renewable energy sources at reduced costs, contributing to this achievement (Sayed et al., 2023).

The world's population growth and civilizational progress have led to an exponential increase in the requirement for energy. Despite being unsustainable and having detrimental consequences on both the environment and human health, fossil fuels remain the main source of energy. Large volumes of greenhouse gases, such as carbon dioxide, nitrous oxide, and methane, are released when fossil fuels are burned. With the rapid development of industry and civilization, we anticipate an increase in these gases' emissions over time. Current and projected levels of greenhouse gases (assuming no adjustments to energy sources) lead to sea level rise, severe health issues, weather changes, and ecological changes. Fossil fuel-related health issues and climate change pose a hazard to humankind (Olabi and Abdelkareem, 2022).

Manufacturing companies have acknowledged the necessity of fostering a more sustainable environment inside their operational systems, prompting a shift towards a 'greener' approach. Industries anticipate the renewable energy transition as a fundamental strategy to mitigate the adverse impacts of non-renewable energy on the environment, highlighting the crucial role of renewable energy in enhancing environmental quality (Gyimah et al., 2022).

The green economy promotes long-term development by balancing economic growth and environmental protection. Its aims include lowering carbon emissions, reducing waste, preserving biodiversity, and driving economic growth. The green economy promotes the use of solar, wind, and hydroelectric power, as well as energy efficiency across society. They want to decouple economic progress from environmental degradation so that it does not destroy the planet's resources. Sustainability, a core concept in the green economy, refers to meeting current demands while not jeopardizing future needs. Careful resource management, reducing fossil fuel consumption, and promoting circular economy strategies like recycling and reuse are examples of this. Sustainable green economy approaches include

This work is licensed (CC BY-NC 4.0) under Creative Commons Attribution 4.0 International License

energy efficiency and clean technology innovation to reduce environmental impact.

Governments and international organizations may help progress the green economy by implementing sustainable policies. Carbon pricing, renewable energy subsidies, and green business regulations are some examples. The green economy fosters economic resilience and environmental conservation by integrating economic activities with environmental sustainability. The green economy generates jobs in clean energy, sustainable agriculture, and waste management; therefore, it promotes economic growth and environmental sustainability. A forward-thinking economy must adopt a more sustainable economic model to solve global concerns such as climate change, resource depletion, and environmental damage.

The literature lacks numerous studies in this field. The aim of this study is to fill the gap in the literature. Gasparatos et al. (2017) assessed the effects of various renewable energy paths on ecosystems and biodiversity, as well as the consequences of these effects for the transition to a green economy. The increasing use of renewable energy is now fundamental to green economy initiatives; yet, a growing body of material indicates that the renewable energy industry might impact ecosystems and biodiversity. Kolosok et al. (2022) elucidated the predictability of fluctuations in power output across the EU27 by mathematical modeling, focusing on predictors of net electricity generation from certain renewable resources for the years 2017–2020. A Markov switching regression model with three regimes was used to assess the impact of renewable energy deployment in the EU27, using selected predictors of clean energy output from hydro, geothermal, wind, and solar sources.

Mealy and Teytelboym (2022) developed an original metric for comparing green production capacity across countries, established a new dataset of ecologically beneficial traded commodities, and demonstrated a method for discovering new green export possibilities. Mohsin et al. (2022) investigated the relationship between technological improvement, renewable energy, and green economic development (GEG). They used a data envelopment analysis (DEA) estimate technique to examine the association between government R&D investment, renewable energy deployment, and GEG in the Economic Community of West African States (ECOWAS) between 1990 and 2018. Wang et al. (2024) stressed the critical necessity to integrate sustainable energy and environmental policies into China's economic development framework, supporting a comprehensive policy plan that balances economic growth and environmental preservation.

This study delves into how renewable energy fuels the green economy through a comprehensive, multi-layered analysis. In Section 2, a SWOT framework is used to examine renewable energy's key strengths—such as its environmental benefits and economic promise—while also addressing challenges like intermittency and high infrastructure costs. Additionally, external influences, including policy support and market barriers, are explored. Moving to Section 3, the study highlights the connection between sustainable IT practices and green economic goals, showcasing how innovations like energy-efficient computing and AI-enhanced grid management can optimize system performance and scalability. Section 4 provides a global perspective on renewable energy adoption, pointing to surging investments—reaching $619 billion in 2023—and regional variations in capacity growth. Notably, China has emerged as a frontrunner in funding and deployment efforts. In Section 5, the SWOT analysis is expanded to focus on sector-specific opportunities and risks. This includes breakthroughs in energy storage as a key opportunity, while concerns like dependence on finite resources are identified as ongoing risks. The discussion is firmly rooted in real-world economic and ecological contexts. The study then turns to Section 6, where findings are consolidated. Here, the role of renewable energy in job creation and emissions reduction is weighed against persistent challenges such as financing gaps. To address these issues, integrated policy measures and technology-driven solutions are proposed. Finally, Section 7 reinforces the crucial role of renewable energy in sustainable development. The study calls for further exploration of topics like AI-driven energy system optimization and digital strategies to enhance public engagement. By bridging academic research with practical applications, this study aims to equip policymakers and industry leaders with actionable insights to drive a cleaner and more resilient economy.

2. Materials and Methods

Renewable energy's green economy function was assessed using SWOT analysis. SWOT analysis was chosen because it is straightforward and effective at identifying and analyzing internal and external issues that may affect global renewable energy adoption. SWOT analysis identifies strengths, weaknesses, opportunities, and threats.

Strengths of renewable energy include environmental advantages, economic possibilities, and energy independence. Secondary data from case studies, literature reviews, and global energy reports identifies characteristics. Renewable energy sources' irregularity, high upfront costs, and grid and building infrastructure integration issues are limitations. Government measures that support renewable energy and energy storage systems and AI-enhanced energy management present opportunities. Subsidized fossil fuels, political and economic instability, and resource scarcity for some renewable technologies may limit renewable energy use.

The study uses quantitative and qualitative methodologies. Qualitative research covers AI, green economy, and renewable energy literature. Government and business leaders' interviews assist stakeholders grasp green economy's potential and limitations. Quantifying the research's trends and effects employs

statistical data on renewable energy investments, technical improvements, and energy output. This study uses the Green Economy, which promotes long-term economic growth and environmental protection. The global economy promotes renewable energy for growth and environmental protection. This technique relies on Sustainable expansion Theory, which states that economic expansion must meet current demands without sacrificing future needs. Renewable energy aids economic progress and resource conservation. A technological advance shows AI and smart grids may help green economic revolution. Renewable energy sources may become more appealing than fossil fuels as technology improves efficiency and decreases prices. Environmental sustainability, economic growth, and renewable energy are linked by this notion. It methodically evaluates renewable energy's green economic potential and limits. Renewable energy market dynamics, technology, and policy may be studied using the framework.

2.1. Green Economy and Sustainable IT Strategies

In the past decade, green banks, village funds, and other entities have arisen as mechanisms for financing environmentally advantageous projects. Green banks and green bonds may have a significant influence in the advancement of renewable energy. Due to their favorable circumstances for renewable energy initiatives, green banks serve as a significant source of derivative instruments and an efficient means of promoting the benefits of clean energy. Green bond proponents assert that they will allocate the funding to provide sustainable, cost-effective resources to cover the program's operating expenses post-construction (Fang et al., 2022a). A fundamental premise of the "Green Economy" (GE) idea is that low-carbon energy technologies provide significant potential to fulfill socio-economic objectives in conjunction with environmental goals. The GE paradigm offers a comprehensive model for social well-being (Pahle, et al., 2016).

For an extended period, the term "green growth" was exclusively associated with the expansion of the eco-industry. However, the term now encompasses the growth of the entire economy. "Green growth is the process of promoting economic growth and development while simultaneously guaranteeing that the natural assets continue to provide the resources and environmental services that are essential for our well-being." In order to accomplish this, it is necessary to stimulate investment and innovation, which will serve as the foundation for long-term development and generate new economic prospects. Green growth is a qualitative development that is resilient in its ability to explain natural hazards, pure in its minimization of pollution and environmental damages, and efficient in its utilization of natural resources (Loiseau et al., 2016).

The green economy focuses on alternative, clean energy sources to power long-term growth instead of using up natural resources, which is not a forward-looking approach. New energy sources and sustainable development are both growing fields. Renewable energy sources are at the heart of a green economy. These sources can help keep life on Earth going by respecting and protecting all living things for future generations. The green economy is a method of economic growth that is founded on the concept of sustainable growth (Karakul, 2016). Green computing uses resources more effectively to maintain or increase performance. Power management, virtualization, sophisticated cooling, recycling, responsible electronic waste disposal, and IT infrastructure optimization are needed to provide sustainable IT services. These eco-conscious computing approaches aim to reduce environmental impact while maintaining the effectiveness of IT operations (Harmon and Auseklis, 2009).

The initial phase of sustainable IT initiatives has concentrated on reducing the expenses and ecological effects of data centers. In the past decade, as data centers have grown essential to IT strategy, green computing practices acknowledging the connection between IT-related energy use and overall business carbon emissions have gained widespread adoption. “Sustainable IT” is the evolving second wave of initiatives that extends IT and ICT sustainability outside the data center (Harmon et al., 2010).

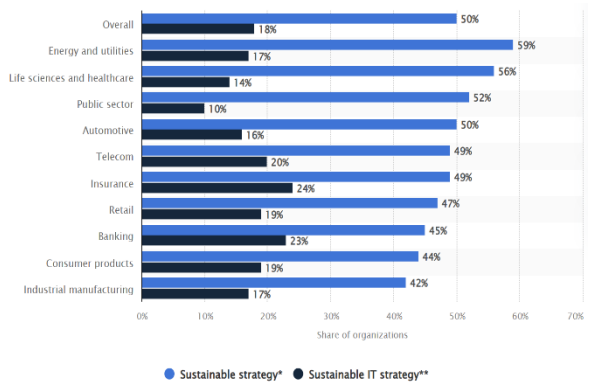


Figure 1. Sustainability strategies incorporating information technology (IT) in global organizations in 2021, categorized by sector (Sherif, 2023).

In 2021, 18 percent of participants in worldwide Capgemini research reported possessing a sustainable IT strategy with well-defined objectives and timetables inside their firm. In contrast, 50 percent of respondents report possessing an enterprise-wide sustainability plan. The insurance and banking sectors are at the forefront of sustainable IT strategy in Figure 1 (Sherif, 2023).

2.2.1 The role of green financing, digital marketing, and branding in advancing renewable energy

Over the last decade, green finance organizations such as green banks and green bonds have emerged as critical tools for renewable energy initiatives. Green banks encourage renewable energy project development by providing funding tools that reduce risk and promote environmentally friendly energy alternatives. Green

bonds have the potential to provide financing for sustainable energy infrastructure over time (Fang et al., 2022b).

The growth of renewable energy can be attributed to the influence of internet branding and marketing strategies. Content marketing, SEO, and social media can enable renewable energy companies to enhance their visibility, demonstrate their commitment to sustainability, and engage with environmentally conscious consumers. Implementing renewable energy in digital marketing could enhance brand loyalty while promoting environmental sustainability.

The integration of digital technologies has the potential to enhance sustainability within green economy businesses. In a competitive industry, the alignment of marketing strategies with environmental objectives could enable businesses to differentiate themselves. This strategy effectively attracts clients who prioritize environmental considerations. Businesses leverage branding to emphasize their environmental responsibilities and facilitate the transition to a sustainable economy, making it essential. The integration of interactive digital platforms, content-driven advertisements, and environmental messaging alongside renewable energy has the potential to influence customer behavior significantly.

2.3. Renewable Energy

In 2023, global new investment in renewable energy reached roughly 619 billion U.S. dollars. This was an eight percent rise compared to the prior year. Global financing for sustainable energy has consistently risen over the past decade. In 2014, investments in clean energy amounted to 263 billion U.S. dollars, rising to a peak of 619.1 billion U.S. dollars in 2023. The substantial rise in investment money signifies considerable maturation within the business. Supportive policies for renewable sources, a rapidly growing sector, and the creation of publicly traded businesses that possess renewable energy assets (often referred to as yieldcos) have propelled the consistent increase in clean energy investment. China is the leading country in renewable energy investment, allocating 273 billion U.S. dollars in 2023 in Figure 2 (Fernández, 2024).

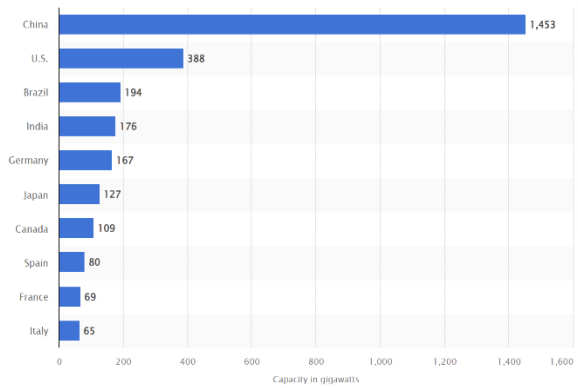


Figure 2. Countries with the most installed renewable energy capacity globally in 2023 (Fernández, 2024).

Renewable energy sources have been vital for humanity since the inception of civilization. For ages, biomass has been utilized for heating, cooking, steam generation, and power production, alongside hydropower and wind energy for propulsion and subsequently for electricity generation. Renewable energy sources mostly rely on energy fluxes inside the Earth's biosphere, derived from solar insolation and geothermal energy. Biomass energy, which is the development of plants fueled by solar radiation, may be distinguished (Turkenburg and Faaij, 2000).

Renewable energy sources and sustainable development are two distinct yet closely connected factors. The economy utilizes resources and energy in production by extracting them from the environment to provide essential commodities and services for society; therefore, these activities lead to emissions and pollution in the environment. Consequently, as industry persists, environmental contamination also continues. The environment, contaminated by these activities, must be safeguarded to ensure that future generations may utilize it for their own requirements. Renewable energy sources and sustainable development are two distinct yet closely connected factors. The economy utilizes resources and energy from the environment to produce essential commodities and services for society, resulting in emissions and pollution. Consequently, as industry persists, environmental contamination also continues. The contaminated environment resulting from these activities must be safeguarded to ensure future generations may utilize it for their own purposes (Guney, 2019).

Development requires energy, and sustainability requires sustainable energy systems. Renewable energy sources have reached double-digit percentages in power production in several countries in recent decades, but many other nations and industries, such as transportation, are only beginning to integrate renewable energy. To transition to renewable energy, resource evaluations, appropriate technologies, and systems are needed to integrate sources and meet demand at the right time (Østergaard et al., 2020).

2.3.1 Artificial ıntelligence in renewable energy

Artificial intelligence (AI) primarily concentrates on the creation of intelligent devices and software tailored for specific issues. Artificial intelligence seeks to comprehend human cognition in order to develop intelligent beings capable of effectively addressing difficult issues, despite the challenges inherent in deciphering the intricate workings of the human brain. Artificial intelligence is employed in nearly all forms of renewable energy (wind, solar, geothermal, hydro, ocean, biomass, hydrogen, and hybrid) for design, optimization, estimate, management, distribution, and policy formulation (Jha et al., 2017).

Rising demand, efficiency, insufficient analytics for management, and variable supply and demand dynamics are causing energy industry difficulties. Energy

forecasting, efficiency, and accessibility are crucial AI-integrated renewable energy technologies (Chen et al., 2021). Artificial intelligence can solve various renewable energy problems. Based on system needs and design, many techniques are offered. The use of these systems is difficult, but new technologies and algorithms can help. Machine learning can help maximum power point tracking (MPPT) systems minimize input noise and improve performance. Hybrid MPPT systems use machine learning and classical methods to track better. Inverter issues may be resolved using machine learning, guaranteeing a constant power supply despite renewable energy fluctuations (Srivastava, 2020). Renewable energy systems are more complicated due to their unpredictability. Model-based solutions may struggle to meet future renewable energy system analytical, scheduling, and control demands. Power system operators now have considerable data from smart meters and enhanced sensing instruments thanks to smart grid technologies. Data availability encourages AI to derive relevant insights from complicated, nonlinear issues without assumptions or simplifications (Hu et al., 2022).

2.4. SWOT Analysis: Harnessing Renewable Energy for A Green Economy

This section uses SWOT analysis to assess renewable energy's impact on sustainability. Environmental benefits and economic growth potential are underlined, along with cons such as high starting expenses and inefficiency. Advances in technology and favorable government policies provide opportunities, while economic and political uncertainty and subsidized fossil fuels pose risks. Table 1 details renewable energy's potential and obstacles in developing a green economy.

6. Results and Discussion

This section summarizes the research's key results, with a focus on the role of renewable energy in powering the green economy. The research uses a SWOT analysis paradigm to assess renewable energy's strengths, weaknesses, opportunities, and threats in terms of sustainable development. The findings emphasize major environmental benefits, such as lower greenhouse gas emissions and pollution, as well as economic benefits including job creation, technical breakthroughs, and energy independence. However, constraints like high initial prices, infrastructural limits, and the intermittent nature of renewable energy sources such as solar and wind need breakthroughs in energy storage and grid integration. Artificial intelligence (AI) plays a crucial role in renewable energy management because it optimizes energy production, improves forecasting, and increases system dependability. Government initiatives, such as subsidies and carbon pricing, are also important in encouraging renewable energy adoption. The study underlines that renewable energy offers enormous potential for long-term economic development; nevertheless, reaching this potential involves overcoming technological, economic, and social difficulties via innovation, cooperation, and deliberate policy.

7. Conclusion

The shift to a green economy, supported by renewable energy, offers a difficult but vital approach to tackling critical global issues such as climate change, environmental degradation, and economic inequality. The potential of renewable energy to diminish greenhouse gas emissions, enhance energy independence, and foster economic growth is well recognized, although the path is laden with challenges. The substantial initial capital expenditures necessary for renewable infrastructure development, the sporadic characteristics of energy sources such as solar and wind, and the technical difficulties related to the integration of these sources into current energy grids all constitute considerable obstacles that must be overcome for a successful transition.

The integration of artificial intelligence (AI) into renewable energy systems represents a significant advancement in addressing these difficulties. Artificial intelligence can optimize energy generation, augment efficiency, and boost energy storage systems, therefore rendering renewable energy sources more dependable and accessible. Machine learning methodologies can enhance maximum power point tracking (MPPT) in solar panels and provide more accurate predictions of energy output, hence diminishing reliance on meteorological conditions. Moreover, AI's function in smart grids can enhance demand-response systems, resulting in more efficient and dependable electricity distribution. As AI technology progresses, its capacity to transform the renewable energy sector becomes more apparent, providing a means to surmount the technical obstacles that presently impede widespread use. Notwithstanding the possible advantages, there are concerns that warrant consideration. Fossil fuels, frequently subsidized, continue to compete robustly with renewable energy, particularly in areas where economic considerations may hinder the use of green technologies. Moreover, the restricted accessibility of specific raw materials essential for renewable technologies, such as lithium and cobalt for batteries, may engender risks within supply chains.

Table 1. SWOT analysis of renewable energy as a catalyst for a green economy

Strengths	Weaknesses
Environmental Advantages: Renewable energy sources, including wind, solar, and hydro, generate negligible greenhouse gas emissions relative to fossil fuels, aiding in climate change mitigation and pollution reduction.	Solar and wind energy are intermittent and dependent on weather conditions, making power delivery difficult without storage.
Economic Growth: Investment in renewable energy supports a green economy, job development, and technological innovation.	Despite lower renewable energy prices, infrastructure like solar farms, wind turbines, and energy storage requires significant upfront costs.
Energy Independence: Countries may gain energy security and price stability by reducing fossil fuel imports.	Infrastructure Limitations: Integrating renewable energy sources into the grid involves infrastructure and technology improvements, which may be difficult and expensive for some places.
Sustainability: Renewable energy is plentiful and self-renewing, making it a good long-term energy source.	Land and resource requirements: Large renewable energy facilities, notably solar and wind, require a lot of land, which may harm ecosystems and populations.
Opportunities	**Threats**
Technological advancements in energy storage, smart grids, and AI-driven energy management provide prospects to surmount existing restrictions and enhance the integration of renewable energy.	Economic and political uncertainties: Economic recessions or changes in governmental objectives may diminish financing, support, or incentives for renewable energy initiatives.
Government Policies and Incentives: Numerous governments are implementing policies, subsidies, and incentives to advance renewable energy, facilitating industry expansion and fostering private investment.	Competition from Fossil Fuels: Fossil fuels continue to get subsidies in several areas, rendering them artificially inexpensive and perhaps hindering the development of renewable technology.
Escalating energy need: With the surge in global energy requirements, particularly in emerging areas, renewable energy presents a sustainable solution to fulfill this need.	Resource Scarcity in Technology: Specific renewable technologies, such as battery storage, depend on limited resources (e.g., lithium, cobalt), potentially resulting in supply chain vulnerabilities.
Climate Commitments: International accords, such as the Paris Agreement, exert pressure on nations to decrease emissions, therefore establishing renewable energy as a viable way to fulfill these obligations.	Public Opposition: Certain renewable initiatives, especially wind farms, may encounter resistance from local people because of apprehensions over land utilization, visual effects, or possible environmental consequences.

Governments must implement proactive measures, including legislation that provides equitable conditions for renewable energy, enabling it to compete on par with fossil fuels.

The public's view and adoption of renewable energy initiatives pose a significant obstacle. Although renewable energy is often regarded as advantageous for the environment, extensive initiatives, such as wind farms and solar installations, can encounter resistance from local people. This may arise from apprehensions over land utilization, visual appeal, or possible ecological repercussions, highlighting the necessity for meticulous planning and community involvement in the establishment of renewable energy infrastructure.

The societal implications of a green economy are substantial. Transitioning to renewable energy enables countries to generate employment, foster technical innovation, and diminish dependence on fossil fuel imports, thereby enhancing energy security. This transformation must be meticulously handled to guarantee inclusivity and equity. Employees in conventional energy industries may experience displacement, necessitating the implementation of policies to facilitate their assistance through retraining and transition initiatives.

The development of a green economy ultimately depends on the collaborative efforts of governments, corporations, and individuals. Political will, global collaboration, and investments in renewable energy technology are essential for attaining a sustainable and fair future. As the world progressively adopts renewable energy sources, there exists a chance to establish a more resilient, equitable, and successful global economy that operates in conjunction with the environment.

In conclusion, the green economy and the fight against environmental issues of the twenty-first century depend heavily on renewable energy. Although there will be long-term benefits to the change, there will also be financial, technological, and societal challenges. Climate change is effectively addressed, greenhouse gas emissions are decreased, and sustainable economic growth is encouraged by renewable energy. It has a

special opportunity to increase energy independence, provide employment that benefits the environment, and raise living standards worldwide.

More digitally literate individuals are needed in the energy sector as artificial intelligence (AI) applications spread quickly across several industries. At this critical juncture, AI may hasten the shift to a new energy system. Energy systems may improve planning and optimization and boost efficiency by utilizing AI to supplement data collection. Machine learning may enable AI-driven predictive maintenance and automation, which might improve system reliability. To optimize these systems' potential for sustainable energy solutions, they must be included in energy production processes.

The development of the green economy will depend on the commitment of political leaders, international cooperation, and advancements in energy technology. Governments, businesses, and individuals must deal with this shift. Investments in renewable energy can create a future in which environmental degradation won't be a determining factor in economic success. A fairer society and a better world would be left for future generations.

This study has explored how renewable energy can effectively drive sustainable economic growth while addressing significant environmental concerns. Moving forward, several promising areas deserve further investigation to build on the insights presented here:

- *Energy Management Systems Enhanced by Artificial Intelligence:* Future studies could look deeper into how AI can practically improve renewable energy systems particularly by using predictive maintenance and optimization to boost reliability, efficiency, and overall performance.
- *Exploring New Models in Green Financing:* There is room to better understand how public-private collaborations or innovative financing approaches can help overcome investment barriers. Understanding these dynamics more clearly could significantly speed up renewable energy projects worldwide.
- *Understanding Consumer Behavior through Digital Marketing and Branding:* Another interesting research avenue is exploring how digital marketing, branding, and online engagement influence consumers' decisions to adopt renewable energy. Such insights could guide effective strategies for increasing public awareness and participation.

Overall, this research serves as a practical reference point for academics, policymakers, and industry professionals. The proposed future directions aim to address existing gaps, helping stakeholders better understand and leverage renewable energy as a key component of a sustainable economy.

Author Contributions

The percentages of the authors' contributions are presented below. All authors reviewed and approved the final version of the manuscript.

	K.G.N.	S.A.
C	50	50
D	50	50
S	60	40
L	40	60
W	45	55
CR	60	40
SR	60	40
PM	50	50

C=Concept, D= design, S= supervision, L= literature search, W= writing, CR= critical review, SR= submission and revision, PM= project management.

Conflict of Interest

The authors declared that there is no conflict of interest.

Ethical Consideration

Since no studies involving humans or animals were conducted, ethical committee approval was not required for this study.

References

Chen C, Hu Y, Karuppiah M, Kumar PM. 2021. Artificial intelligence on economic evaluation of energy efficiency and renewable energy technologies. Sustain Energy Technol Assess, 47: pp: 101358.

Fang W, Liu Z, Putra ARS. 2022a. Role of research and development in green economic growth through renewable energy development: empirical evidence from South Asia. Renew Energy, 194: pp: 1142-1152.

Fang Z, Yang C, Song X. 2022b. How do green finance and energy efficiency mitigate carbon emissions without reducing economic growth in G7 countries? Front Psychol, 13: pp: 879741.

Fernández L. 2024. Renewable energy capacity 2023 by country, https://www.statista.com/statistics/267233/renewable-energy-capacity-worldwide-by-country/ (accessed date: September 17, 2024).

Gasparatos A, Doll CN, Esteban M, Ahmed A, Olang TA. 2017. Renewable energy and biodiversity: Implications for transitioning to a Green Economy. Renew Sustain Energy Rev, 70: pp: 161-184.

Guney T. 2019. Renewable energy, non-renewable energy and sustainable development. Int J Sustain Dev World Ecol, 26(5): pp: 389-397.

Gyimah J, Yao X, Tachega MA, Hayford IS, Opoku-Mensah E. 2022. Renewable energy consumption and economic growth: New evidence from Ghana. Energy, 248: pp: 123559.

Harmon R, Demirkan H, Auseklis N, Reinoso M. 2010. From green computing to sustainable IT: Developing a sustainable service orientation. In: 5-8 January 2010, 43rd Hawaii International Conference on System Sciences, Honolulu, Hawaii, USA, pp: 1-10.

Harmon RR, Auseklis N. 2009. Sustainable IT services: Assessing the impact of green computing practices. In: 2-6 August 2009,

Portland International Conference on Management of Engineering and Technology, Portland, OR, USA, pp: 1707-1717.

Hu W, Wu Q, Anvari-Moghaddam A, Zhao J, Xu X, Mohamed Abulanwar S, Cao D. 2022. Applications of artificial intelligence in renewable energy systems. IET Renew Power Gener, 16(7): pp: 1279-1282.

Jha SK, Bilalovic J, Jha A, Patel N, Zhang H. 2017. Renewable energy: Present research and future scope of Artificial Intelligence. Renew Sustain Energy Rev, 77: pp: 297-317.

Karakul AK. 2016. Educating labour force for a green economy and renewable energy jobs in Türkiye: A quantitative approach. Renew Sustain Energy Rev, 63: pp: 568-578.

Kolosok S, Saher L, Kovalenko Y, Delibasic M. 2022. Renewable energy and energy innovations: examining relationships using Markov switching regression model. Marketing i menedžment innovacij, 2: pp: 151-160.

Loiseau E, Saikku L, Antikainen R, Droste N, Hansjürgens B, Pitkänen K, Thomsen M. 2016. Green economy and related concepts: An overview. J Clean Prod, 139: pp: 361-371.

Mealy P, Teytelboym A. 2022. Economic complexity and the green economy. Res Policy, 51(8): pp: 103948.

Mohsin M, Taghizadeh-Hesary F, Iqbal N, Saydaliev HB. 2022. The role of technological progress and renewable energy deployment in green economic growth. Renew Energy, 190: pp: 777-787.

Olabi AG, Abdelkareem MA. 2022. Renewable energy and climate change. Renew Sustain Energy Rev, 158: pp: 112111.

Østergaard PA, Duic N, Noorollahi Y, Mikulcic H, Kalogirou S. 2020. Sustainable development using renewable energy technology. Renew Energy, 146: pp: 2430-2437.

Pahle M, Pachauri S, Steinbacher K. 2016. Can the Green Economy deliver it all? Experiences of renewable energy policies with socio-economic objectives. Appl Energy, 179: pp: 1331-1341.

Sayed ET, Olabi AG, Alami AH, Radwan A, Mdallal A, Rezk A, Abdelkareem MA. 2023. Renewable energy and energy storage systems. Energies, 16(3): pp: 1415.

Sherif A. 2023. Global enterprise sustainability IT strategy 2021. by sector, https://www.statista.com/statistics/1247940/sustainable-enterprise-strategy-it-global-category/ (accessed date: September 12, 2024).

Srivastava SK. 2020. Application of artificial intelligence in renewable energy. In: 2020 International Conference on Computational Performance Evaluation, Chennai, India, pp: 327-331.

Turkenburg WC, Faaij A. 2000. Renewable energy technologies. In: UNDP/UNDESA/WEC: Energy and the Challenge of Sustainability. World Energy Assessment, New York, NY, USA: UNDP, pp: 219-272.

Wang L, He Y, Wu R. 2024. The Green Engine of Growth: Assessing the Influence of Renewable Energy Consumption and Environmental Policy on China's Economic Sustainability. Sustainability, 16(8): pp: 3120.

Black Sea Journal of Engineering and Science
doi: 10.34248/bsengineering.1534396

Open Access Journal
e-ISSN: 2619 – 8991

Araştırma Makalesi (Research Article)
Cilt 8 - Sayı 4: 918-926 / Temmuz 2025
(Volume 8 - Issue 4: 918-926 / July 2025)

PROMETHEE YÖNTEMİ İLE BİR TEKNİK MÜŞAVİR FİRMA SEÇİMİ

Latif Onur UĞUR[1]*, Merve ÖLÇER[1]

[1]*Düzce University, Faculty of Engineering, Department of Civil Engineering, 81620, Düzce, Türkiye*

Özet: Teknik müşavir, doğal veya inşa edilmiş çevre üzerinde teknolojiye dayalı bilgi ve düşünceye dayalı hizmet veren kişi veya kuruluştur. Uluslar arası inşaat projelerinde ilgili yapım projesinin projelendirme ve ihale aşamalarından yapım kontrolü, ödemeler ve kesin kabul aşamalarına kadar önemli görevler yürütür. Pek çok önemli yapım projesinde işveren tarafından görev verilmesi gerekliliği bulunmaktadır. Bu çalışmada, bir işverenin teknik müşavir firma seçim seçimi PROMETHEE yöntemi ile gerçekleştirilmiştir. Bu yöntemde, uzman görüşleri yardımı ile kriterler belirlenmiş ve alternatifler tespit edilmiştir. Alternatif adayların öncelikleri PROMETHEE yöntemi ile hesaplanarak öncelik sıraları belirlenmiştir. PROMETHEE yöntemiyle elde edilen sonuçlar PROMETHEE I ve PROMETHEE II yöntemleri ile irdelenmiştir. Ayrıca GAİA Düzlemi yardımı ile analiz edilmiştir. Bu yöntem ile gerekli kriterleri sağlayan alternatif adaylar arasından en uygun teknik müşavir firmanın belirlenmesi sağlanmış ve işletmelerde doğru teknik müşavir firmanın seçilememesinden kaynaklanan maliyetler ve seçim sürecindeki subjektif değerlendirmeler en aza indirilmeye çalışılmıştır. Yöntem tüm kriterler eşit önem derecesinde iken ve kriterlere farklı ağırlıklar verilmiş olarak iki farklı şekilde uygulanmıştır. Bu iki uygulamadan çıkan sonuçlar karşılaştırılmıştır.

Anahtar kelimeler: PROMETHEE Yöntemi, Çok kriterli karar verme (ÇKKV), Teknik müşavir mühendis firma

Choosing a Technical Consultant Company with PROMETHEE Method

Abstract: The technical consultant is the person or organization that provides technology based knowledge based on technology on natural or built environment. It carries out important tasks in the international construction projects from the project preparation and tender stages of construction project to construction control, payments and final acceptance stages. Many important construction projects, they have to be assigned by the employer. In this study, the selection of technical consultant company of an employer was carried out by PROMETHEE method. In this method, criteria were determined with the help of expert opinions and alternatives were determined. The priorities of the alternative candidates were determined by the PROMETHEE method and their priorities were determined. PROMETHEE II and PROMETHEE II methods were used to evaluate the results. It was also analyzed with the help of GAIA Plane. With this method, the most appropriate technical advisory firm has been determined among the alternative candidates providing the necessary criteria and the costs arising from not selecting the right technical advisor firm in the enterprises and the subjective evaluations in the selection process have been tried to be minimized. The method has been applied in two different ways, while all criteria are of equal importance and different weights are given to the criteria. The results of these two applications were compared.

Keywords: PROMETHEE Method, Multi criteria decision making (MCDM), Technical consultant engineer

***Corresponding author:** Düzce University, Faculty of Engineering, Department of Civil Engineering, 81620, Düzce, Turkiye
E mail: latifugur@duzce.edu.tr (L. O. UĞUR)
Latif Onur UĞUR https://orcid.org/0000-0001-6428-9788
Merve ÖLÇER https://orcid.org/0000-0003-1258-7702

Gönderi: 16 Ağustos 2024 **Received:** August 16, 2024
Kabul: 05 Nisan 2025 **Accepted:** April 05, 2025
Yayınlanma: 15 Temmuz 2025 **Published:** July 15, 2025

Cite as: Uğur LO, Ölçer M. 2025. PROMETHEE yöntemi ile bir teknik müşavir firma seçimi. BSJ Eng Sci, 8(4): 918-926

1.Giriş

Müşavir kelimesi sözlük karşılığı olarak; "danışılan, istişare edilen" anlamını taşımaktadır. Ayrıca "bir konuda görüşüne başvurulan" olarak da ifade edilebilir. Bu günkü dilde "danışman" olarak isimlendirilebilir. Müşavirlik kelimesi de; "danışma(k), istişare etmek" anlamını taşımaktadır (tmmmb.org.tr, 2024). Müşavir Mühendis/Mimar tanımlaması özetle; "üniversiteden mezun olduktan sonra en az 12 yıl profesyonel olarak çalışmış ve bu sürenin en az 6 yılında müşavirlik hizmetleri veren bir firmada yetkili pozisyonda hizmet vermiş, TMMOB üyesi olan mühendisler ve mimarlar"dır şeklinde yapılabilir (imo.org.tr, 2024). Antik Yunanca tekhne kelimesinden gelen ve Latince ars'a tekabül eden "teknik",,her türlü uzmanlık, beceri, eklemleme anlamına gelir (csb.gov.tr, 2024). Teknik müşavir, doğal veya inşa edilmiş çevre üzerinde teknolojiye dayalı bilgive düşünceye dayalı hizmet veren kişi veya kuruluştur (tmmmb.org.tr, 2024). TürkMMMB, ilgili Tüzük maddesinin (Madde 4/A - Müşavir Mühendis ve Mimarlığın Tanımı) yanı sıra,kendi ilkeleri paralelinde ve üyesi bulunduğu FIDIC'e üye gelişmiş ülkelerin de benimsediği "Teknik Müşavir, doğal veya inşa edilmiş çevre üzerinde teknolojiye dayalı bilgi ve düşünceye dayalı hizmet veren kişi veya kuruluştur." tanımını kabul etmiştir (tmmmb.org.tr, 2024). Bir başka tanıma göre "bir meslek

This work is licensed (CC BY-NC 4.0) under Creative Commons Attribution 4.0 International License

dalında fizik, kimya, matematik v.b. bilimlerden elde edilen verileri iş ve yapım alanında uygulamak için görüşüne başvurulan kişiye" teknik müşavir denir. Üniversitede alınan eğitimle, edinilen bilgi ve beceriler arasında bir bağlantı olabilir veya olmayabilir ancak Müşavir'in gerçekte bir uzman olduğunu, ama bununla birlikte, deneyimi eğitim içersin ya da içermesin bu deneyimlerden bilgi ve beceri geliştiren, etkin ve iyi bir öğrenici olmasının şart olduğu söylenebilir. Bu teorik açılımının yanında Kamu İhale Kanunu'nda geçen tanımında "bilgi ve deneyimini idarenin yararı için kullanan, danışmanlığını yaptığı işin yüklenicileri ile hiçbir organik bağ içinde bulunmayan, idareden danışmanlık hizmeti karşılığı dışında hiçbir kazanç sağlamayan ve danışmanlık hizmetlerini veren hizmet sunucuları" olarak tanımlanmıştır. İkinci tanımda organik bağ istenmemesinin ana nedeni yapılacak işin idaresinde yüklenici kişilere karşı oluşturulan iş akışının aksi bir görüşünü dile getirmekten çekinmeyecek bir müşavirlik hizmeti için gerekli görülmektedir (igeme.com.tr, 2024). Uluslararası Mühendis ve Müşavirler Federasyonu (FIDIC) teknik müşavirliğin etik tarafına dikkat çekerek "sosyal sorumluluk, yetkinlik, bütünleşme, tarafsızlık, adil davranış, usûlsüzlük karşıtlığı" olarak özetlemiştir.

1.1. Teknik Müşavirlerin Görevleri

•Planlama / Değerlendirme
•Zemin Etüdler
•Fizibilite (Olabilirlik) Etütleri
•Ön araştırma ve programlama hizmetleri
•Araştırma, geliştirme ve Planlama işleri
•Mimarlık – Mühendislik Tasarım İşleri
•Kredi raporu hazırlanması
•İhale Dokümanlarının Hazırlanması
•İhale Değerlendirme ve Sözleşme Akdine Yönelik Teknik Yardım Hizmetleri
•Metraj, keşif, teknik ve idari şartname hazırlanması,
•İhale yönetimi, danışmanlığı ve değerlendirme hizmetleri,
•Mesleki, teknik, mali ve inşaat kontrolörlüğü ve denetimi,
•Kurumsal yapılanma ve özelleştirme faaliyetlerine yönelik danışmanlık,
•Çevre etki değerlendirme hizmetleri,
•Gayrimenkul değerleme hizmetleri,
•İşletmeye alma ve işletme danışmanlığı,
•Teknoloji, malzeme ve teçhizat seçimi ve standartlarının belirlenmesi
•İnşaat Yönetimi
•Proje Yönetimi
•Mesleki, teknik, mali inşaat kontrolörlüğü ve denetimi
•İşletmeye Alma Danışmanlığı
•Personelin Teknik Eğitimi
•Kurumsal yapılanma ve özelleştirme faaliyetlerine yönelik danışmanlık
•Anlaşmazlıkların Giderilmesi olarak sıralanabilir.

Hakemlik görevlerinin bir kısmını veya hepsini birlikte üstlenmek Teknik Müşavirliğin yukarıda hizmet alanları haricinde yeni yönetmelikler sebebiyle eklenen yeni hizmet alanları da ortaya çıkmıştır. Bunlar;

•Yapı Tesisat Tasarımı ve İşletme Yönetimi
•Trafik ve Sinyalizasyon Mühendisliği ve Kapasite Ölçüm Hizmetleri
•Yangın güvenliği danışmanlığı
•Risk Analizi ve Yönetimi
•İş ve İşçi Sağlığı ve Güvenliği Hizmetleri
•Akustik ve Termik Yapığı Fiziği Çalışmaları
•Geoteknik Mühendisliği Hizmetleri
•Tekno-ekonomik İşletme Yönetimi
•Coğrafi Bilgi Sistemleri
•Bilgi Yönetimi
•Kalite Kontrol ve Yönetimi Hizmetleri'dir (igeme.com.tr, 2024).

Tünel, uluslararası literatürde mutabakat sağlanmış bir tanımı olmamakla birlikte; genel anlamıyla yer altından kazı yapılmak suretiyle oluşturulan geçitlerdir. Ana kullanım amaçları motorlu taşıt ulaşımı, metro ve demiryolu ulaşımı ve su taşımaktır. Bir yandan öbür yana geçebilmek için yer altında açılan yol anlamına gelir (turkcebilgi.com, 2024). Tünel projesine seçilecek olan bir teknik müşavir firmadan tünellerin planlaması, tasarımı ve proje uygulama hizmetleri konusunda geniş bilgi birikimine ve tecrübeye sahip olması beklenmektedir. Aşağıda sıralanan özellikleri de taşıması yararlı olacaktır.

•Fizibilite Etüdleri
•Jeodezik Etüdler
•Hidrolik ve Hidro-Jeolojik Etüdler
•Zemin Etüdleri (Jeolojik ve Geoteknik)
•Çevresel Etki Değerlendirme
•Ulaşım / Trafik Planlama ve Tasarımı
•Güzergah Optimizasyonu ve Tasarımı
•Jeoloji Mühendisliği
•Geoteknik ve Kaya Mekaniği Mühendisliği
•Yapısal ve Deprem Tasarımı (Kazı-İksa ve İç Kaplama)
•Oturma Analizi ve Tünel Üstündeki Binalara Gelebilecek Zarar Değerlendirmesi
•Güçlendirme / Rehabilitasyon
•Elektrik Sistemler Tasarımı (Enerji Temini; Aydınlatma; Kontrol Sistemi; Haberleşme-Telefon, Telsiz, Hoparlör; Sinyalizasyon ve Trafik İşaretleme)
•Mekanik Sistemler Tasarımı (Havalandırma; Su Temini; Yangın Söndürme) (emay.com/fu_tuneller, 2024).

PROMETHEE sıralama yönteminin birden fazla kriterin göz önünde bulundurulduğu karar verme süreçlerinde çeşitli alanlarda uygulandığı yapılan araştırma ve makalelerde görülmektedir. Keyser ve Peeters, birden fazla kriterin ele alınması gerektiği karar süreçlerinde PROMETHEE yönteminin kullanılmasındaki öneme ilgi çekmiş, PROMETHEE yönteminin avantaj ve dezavantajları belirtmişlerdir (De Keyser ve Peeters 1996). Yılmaz ve Dağdeviren, seçilen ekipmanların etkin bir üretim sistemi kurmada son derece önemli olduğunu belirterek PROMETHEE yöntemi ile ekipman seçimi gerçekleştirmişlerdir. Çalışmalarında, 11 adet alternatif

kaynak makinesini 6 farklı kriter açısından değerlendirmişlerdir. Bu kriterler; sektörel kullanılabilirlik, fiyat, ağırlık, çalışma uyumu, ekipmanın işlemeye uyumlu olduğu tel çapı ve kapladığı hacimdir (Yılmaz, ve Dağreviren, 2010). Soba, PROMETHEE yöntemini, aynı sınıftan olan altı panelvan otomobilden birinin seçiminde kullanmıştır. Fiyat, yakıt, maksimum hız, güvenlik, beygir gücü ve performans olmak üzere altı farklı kriter üzerinden yapılan çalışmada sonuçların tutarlı ve uygun olduğu belirtilmiştir (Soba 2012). Tuzkaya, vdadaşları, PROMETHEE yöntemi ile en doğru malzeme taşıma sistemi seçimi yapmış, İstanbul'daki bir fabrikanın ambar bölümü üzerine bir uygulama gerçekleştirmişlerdir. Uygulama sonuçlarının yetkililerce yeni yatırım kararlarında dikkate alındığı belirtilmiştir (Tuzkaya vd., 2011). Amponsah, vdadaşları, telekomünikasyon operatörlerinin performansları üzerine gerçekleştirdikleri araştırmada, dört farklı kriteri ele alarak beş farklı alternatifi PROMETHEE sıralama yöntemi ile sıralamış, uygun ve etkin sonuçlara ulaşıldığını belirtmişlerdir (Amponsah vd. 2012). Şimşek, uzmanlık tezini yayınladığı IPA projelerinde, teknik müşavirlik hizmetlerinin ekonomi politiği araştırmasında, teknik müşavir firma nedir, görevleri nelerdir, inşaat sektöründe yeri nedir gibi konulara yer vermiştir (Şimşek 2013). Bu modeldeki parametreler bina tipi, inşaatın yapıldığı yer, (kat döşeme alanları, çatı alanı ve dış duvarların alanıdır).

2. Materyal ve Yöntem

Bu çalışmada bir tünel inşaatı için teknik müşavir firma seçilecektir. Teknik müşavir firmaların sıralanması için çok kriterli karar verme yöntemlerinden birinin kullanılması uygun görülmüştür. Bu yöntemler, sonlu sayıda alternatifleri değerlendirmede birbiriyle çelişen çok sayıda kriterden oluşurlar. Çok kriterli karar vermede sıklıkla kullanılan TOPSIS, ELECTRE, AHP gibi yöntemler, gerek tek tek gerekse bir arada uygulanarak, seçim işleminde daha doğru karar verilmesini sağlarlar. Bu çalışmada beş tane teknik müşavir firma arasından bir tanesi çok kriterli karar verme yöntemlerinden PROMETHEE Sıralama Yöntemi ile belirlenecektir.

2.1. PROMETHEE Sıralama Yöntemi

PROMOTHEE yöntemi, PROMOTHEE 1 (kısmi sıralama) ve PROMOTHEE 2 (tam sıralama) olmak üzere 2 ana aşamadan oluşan ve ilk olarak J. P. Brans tarafından 1982 yılında geliştirilen ve ilk defa Kanada'daki Laval Universitesi'ndeki bir konferansta sunulan çok ölçütlü bir karar verme yöntemidir. Buradaki PROMETHEE yöntemi ile ilgili açıklamalar da Brans'ın (1982) eserinden derlenmiştir (Şenkayası, ve Hekimoğlu 2013)

Yöntem, karar noktalarının sırasını, PROMETHEE 1 ve PROMETHEE 2 ana aşamalarıyla belirler. PROMETHEE yöntemi karar noktalarının değerlendirme faktörlerine göre ikili kıyaslamalarına dayanır. PROMOTHEE yöntemini diğer çok değişkenli karar verme yöntemlerinden ayıran temel fark, değerlendirme faktörlerinin birbiri ile ilişkilerini gösteren önem ağırlıklarını ve her bir değerlendirme faktörünün kendi iç ilişkisini de dikkate almasıdır. Değerlendirme faktörlerinin iç ilişkisi, veri kümesinin dağılımıyla ortaya konur ve yöntemde bu amaçla 6 farklı dağılım öngörülmüştür. PROMETHEE yönteminin başlangıçtan sonuç aşamasına kadar 5 adımı vardır. Bu adımlar ve içerdikleri formüller (eşitlik 1) aşağıda sırasıyla verilmiştir (Özdağoğlu 2013)

2.1.1. Adım 1

k (1, 2, … , k) ölçüt sayısını göstermek koşuluyla, w=(w1, w2, …, wk) ağırlıkları ile k ölçüt c=(f1, f2, …, fk) tarafından değerlendirilen alternatiflere A=(a, b ,c, …, m) ilişkin veri matrisi (eşitlik 1), Tablo 1.'de verilen şekilde oluşturulur.

$$p[f(a), f(b)] = p[f(a) - f(b)] \quad (1)$$

Tablo 1. Veri matrisi

	Ölçüt 1 (f1)	Ölçüt 2 (f2)	Ölçüt k (fk)
Alternatif a	f(a)	f(a)	f(a)
Alternatif b	f(b)	f(b)	f(b)
Alternatif m	f(m)	f(m)	f(m)
Ağırlıklar	W1	W2	Wk

2.1.2. Adım 2

Alternatifler, kriter bazında ikili karşılaştırırken Brans (1982) tarafından tanımlanmış 6 tercih fonksiyonundan bir tanesini kullanmaktadır. Ölçütler için tercih fonksiyonları tanımlanır. PROMETHEE yönteminde kullanılan 6 farklı tercih fonksiyonu Tablo 2.'de gösterilmiştir.

Buradaki parametreler;

q= Farksızlık Değeri

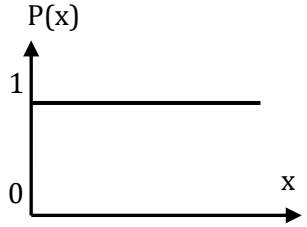
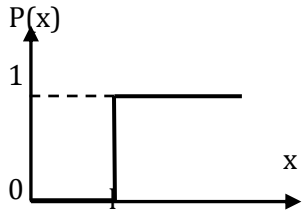
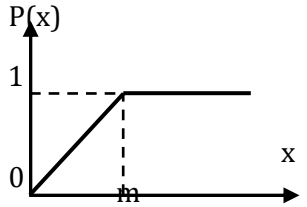
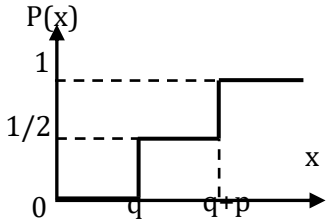
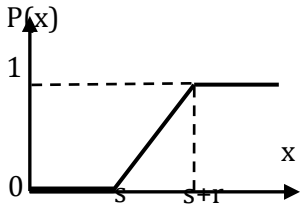
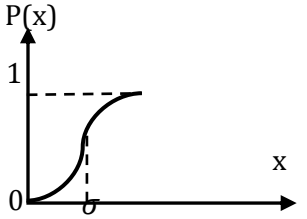
p= Kesin Tercih Eşiği

s= p ve q arasındaki ara değer ya da standart sapma olarak tanımlanır.

q değeri, değerlendirme faktörlerinin karar noktalarına göre en büyük fark değeri iken, p değeri ise en küçük farktır.

Burada d değeri, bir değerlendirme faktörü açısından iki karar noktası değerleri arasındaki farktır (Genç ve Mahmut 2013).

Tablo 2. Tercih fonksiyonları

Tip	Parametre	Fonksiyon	Grafik, P(x)
Birinci Tip (Olağan)	-	$P(x)=\begin{cases}0, \forall x \le 0\\ 1, \forall x > 0\end{cases}$	
İkinci Tip (U-tipi)	l	$P(x)=\begin{cases}0, x \le 1\\ 1, x > 1\end{cases}$	
Üçüncü Tip (V-tipi)	m	$P(x)=\begin{cases}x/m, x \le m\\ 1, x \ge m\end{cases}$	
Dördüncü Tip (Seviyeli)	q,p	$P(x)=\begin{cases}0, & x \le q\\ 1/2, & q < x \le q+p\\ 1, & x > q+p\end{cases}$	
Beşinci Tip (Lineer)	s,r	$P(x)=\begin{cases}0, & x \le s\\ (x-s)/r, & s \le x \le s+r\\ 1, & x \ge s+r\end{cases}$	
Altıncı Tip (Gaussian)	σ	$P(x)=\begin{cases}0, & x \le 0\\ 1-e^{-x^2/2\sigma^2}, & x \ge 0\end{cases}$	

2.1.3. Adım 3

Tercih indeksleri her iki alternatifin (a,b) karşılıklı olarak üstünlüklerini belirlemek açısından eşitlik 2 ve 3'de gösterilmiştir.

$$\pi(a, b)= \sum_{j=1}^{n} w_j .P_j (a, b) \quad (2)$$

$$\pi(b, a)= \sum_{j=1}^{n} w_j .P_j (b, a) \quad (3)$$

2.1.4. Adım 4

Her alternatif için elde edilen tercih indeksleri vasıtasıyla, alternatiflerin pozitif ve negatif akımları elde edilir. Alternatiflerin tercih indeksleri matrisinde kendi satır ve sütunlarında bulunan tercih indeks değerlerinin toplamının (*n-1*) değerine bölünmesiyle hesaplanan pozitif ve negatif akımlar eşitlik 4 ve 5'te belirtilmiştir.(Mareschal ve Brans 1988)

Pozitif akım:

$$\Phi+ (a) = \Sigma \pi (a,b) \quad (4)$$

Negatif akım:

$$\Phi- (a) = \Sigma \pi (b,a) \quad (5)$$

2.1.5. Adım 5

Pozitif ve negatif akım değerleri ile PROMETHEE I sonuçlarını elde eden karar verici,bu sonuçlarla alternatiflerin en iyiden en kötü seçeneğe göre sıralamasını elde edemeyebilir.Böyle durumlarda eşitlik 6'dan faydalanılarak PROMETHEE II net akım değerleri hesaplanır.

$$\Phi(a) = \Phi^{+}(a) - \Phi^{-}(a) \quad (6)$$

Hesaplanan net öncelik değeri Φ (a), pozitif ve negatif akımların bir dengesini oluşturur. Net akım ne kadar büyükse alternatifin performansı o kadar yüksektir. Hesaplanan net akımlar sonunda artık alternatifler arasında tam bir sıralama yapmak mümkün olabilmektedir (Mareschal ve Brans 1988)

Karar noktalarına ilişkin negatif ve pozitif üstünlük değerlerinin ikili karşılaştırmalarının yapıldığı bu aşamada karşılaşılabilecek üç mümkün durum, bir karar noktasının diğerine üstünlüğü, karar noktalarının farksızlığı ve karar noktalarının birbirleriyle karşılaştırılamaması durumlarıdır.(Yıldırım 2014)

Karşılaştırmalarda karşılaşılabilecek durumlar aşağıda verilmiştir.

$\Phi^{+}(a) > \Phi^{+}(b)$ ve $\Phi^{-}(a) < \Phi^{-}(b)$

$\Phi^{+}(a) > \Phi^{+}(b)$ ve $\Phi^{-}(a) = \Phi^{-}(b)$

1.durum: a, b'den üstündür.

$\Phi^{+}(a) = \Phi^{+}(b)$ ve $\Phi^{-}(a) < \Phi^{-}(b)$

$\Phi^{+}(a) = \Phi^{+}(b)$ ve $\Phi^{-}(a) = \Phi^{-}(b)$

2.durum: a, b'den farksızdır

$\Phi^{+}(a) > \Phi^{+}(b)$ ve $\Phi^{-}(a) > \Phi^{-}(b)$

$\Phi^{+}(a) < \Phi^{+}(b)$ ve $\Phi^{-}(a) < \Phi^{-}(b)$

3.durum: a ile b karşılaştırılamaz.

Bu formüle göre a ve b gibi iki karar noktası için $\Phi(a) > \Phi(b)$ ise a karar noktası b karar noktasından üstündür.

Eğer $\Phi(a) = \Phi(b)$ ise a karar noktası b karar noktasından farksızdır.

2.2. GAIA Düzlemi

Alternatiflerin k boyutlu (kriter sayısı kadar boyutlu) bir uzayda gösterilmesini müteakip, Temel Birleşenler Analizi (Principal Component Analysis, PCA) kullanılarak kriterlerin ve alternatiflerin daha anlaşılabilir bir gösterim ile karar vericiye sunulabilmesi için belirtilen k boyutlu uzaydan 2 boyutlu bir düzlem üzerine izdüşümleri hesaplanmak suretiyle bir düzlem oluşturulur (Epür). Alternatifler ve kriterlerin gösterildiği bu düzleme GAIA düzlemi denilmektedir.

Alternatiflerin ve kriterlerin GAIA düzlemindeki geometrik sunumu problemi analiz ederken önemli bir zenginlik sağlayacaktır. Bu teknik karar verme sürecinde özellikle her bir kriterin önemini değerlendirmek için kullanılır. Ayrıca bu teknikle kriterler üzerindeki tercih oranlarının kavranması, homojen alternatif kümelerinin belirlenmesi, belirli kriterler altındaki alternatifler arasından iyi olan alternatiflerin seçilmesi, alternatifler arasındaki karşılaştırılamazlık durumunun belirlenmesi gibi amaçlar gerçekleştirilebilir (Mareschal ve Brans 1988).

3. Bulgular ve Tartışma

PROMETHEE yönteminin uygulaması bir işveren için yapılmıştır. Bu teknik müşavir firma iş pozisyonu için başvuranlar arasından en uygun teknik müşavir firma seçilmesi amaçlanmıştır. Uygulamada Visual PROMETHEE programı kullanılmıştır.

3.1. Seçim Kriterlerinin Belirlenmesi Ve Karar Matrisinin Oluşturulması

Bu uygulama için iş tanımları incelenmiş, uzman görüşleri alınarak bir teknik müşavir firmasının sahip olması gereken nitelikler değerlendirilmiştir. Tüm bu veriler kullanılarak ve uzman görüşleri alınarak, bu pozisyonun kriterleri belirlenmiştir. Belirlenen bu kriterler aşağıda sıralanmıştır.

Kriterler:

- Daha önce yaptıkları iş sayısı
- Kaç yıllık firma olduğu
- Çalıştırdıkları teknik eleman sayısı
- Bir yılda döndürdükleri para
- Adliyeye yansımış olayların varlığı
- Tünel projesinde teknik müşavirlik yapmış olması

Aday kuruluşların (A, B, C, D ve E) her kritere göre değerlendirilmesi yine uzmanlar yardımı ile yapılmış ve Tablo 3.'te verilen karar m

3.2. Kriter Ağırlıklarının Belirlenmesi Ve Alternatiflerin Sıralaması

Uygulamanın bu aşamasında ilk olarak belirlenen tüm kriterlerin eşit önem derecelerine sahip olduğu kabulü ile hareket edilmiş ve ağırlık değeri olarak her kritere 1 değeri atanmıştır. Daha sonra tüm kriterlere uzman görüşleri doğrultusunda ağırlıklar verilerek iki durum karşılaştırılacaktır. İkinci durumda kriterlere verilen ağırlıklar Tablo 4. 'te gösterilmiştir (Ağırlıkların toplamı 1'dir).

3.3. Visual PROMETHEE Programı İle Çözüm

3.3.1. Kriter ağırlıklarının eşit olduğu durum

Kriterlere eşit ağırlıkların atanmasının ardından, yapılan çalışmalar sonucunda elde edilen tüm veriler; alternatif adaylar, kriterler, belirlenen tercih fonksiyonları ve tercih fonksiyon parametreleri düzenlenmiştir. Kriter nitelikleri, ağırlıkları, tecih fonksiyonları ve fonksiyon parametleri ara yüze girilmiştir. Alternatifler değerlendirilerek pozitif, negatif ve net üstünlük değerleri hesaplanmıştır. Hesaplanan üstünlük değerleri aşağıda Tablo 5. te gösterilmektedir.

Ardından PROMETHEE I yöntemi ile kısmi öncelikler, PROMETHEE II yöntemi ile de tam öncelikler belirlenmiştir (Şekil 1.a ve b).

PROMETHEE I ve II yöntemi ile bulunan kısmi ve tam öncelik sıralamalarına göre en iyi alternatif B çıkmıştır. Adaylar (P II için) en iyiden en kötüye doğru B, E, A, C, D olarak sıralanmaktadır.

Tablo 3. Karar matrisi

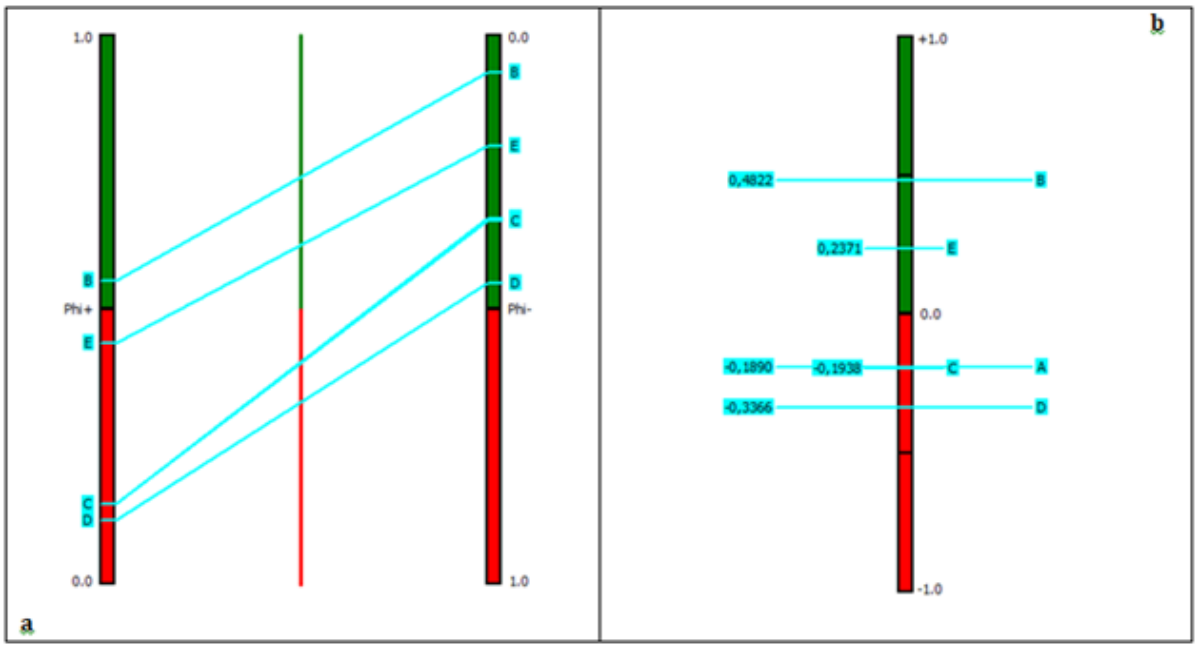
Kriterler	Adaylar				
	A	B	C	D	E
Daha önce yaptıkları iş sayısı	7	12	8	6	14
Kaç yıllık firma	12	18	11	8	22
Çalıştırdıkları teknik eleman sayısı	8	14	11	7	10
Bir yılda döndürdükleri para (milyon)	1,2	1,9	1,2	0,8	1,1
Adliyeye yansımış olayların varlığı	0	0	1	0	1
Tünel projesinde teknik müşavirlik yapmış olması	0	1	0	1	2

Tablo 4. Kriter ağırlıkları

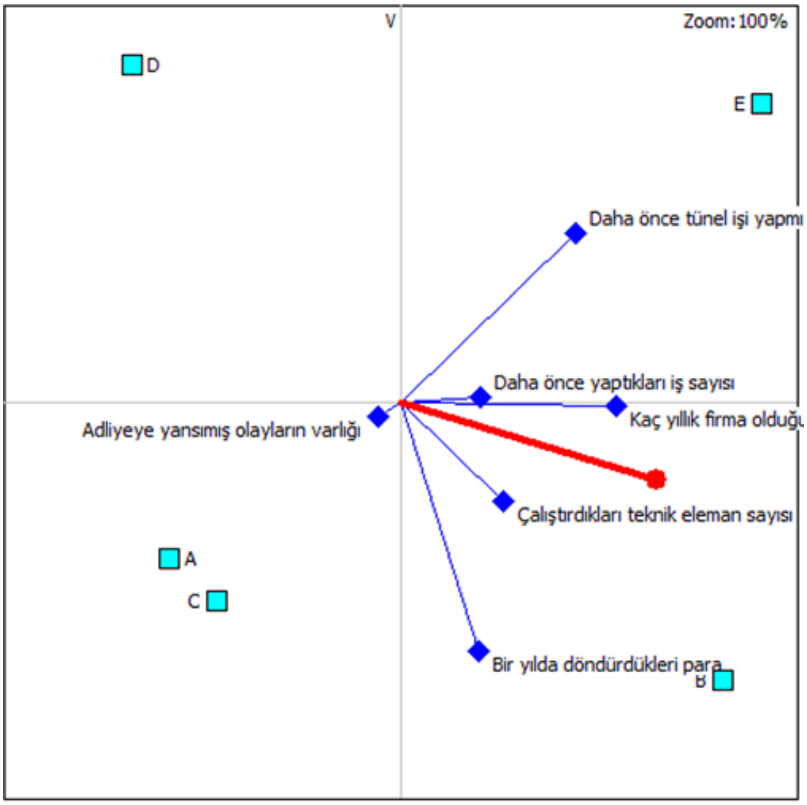
	Daha önce yaptıkları iş sayısı	Kaç yıllık firma	Çalıştırdıkları teknik eleman sayısı	Bir yılda döndürdükleri para (milyon)	Adliyeye yansımış olayların varlığı	Tünel projesinde teknik müşavirlik yapmış olması
Kriter ağırlıkları	0,13	0,08	0,2	0,17	0,12	0,3

Tablo 5. Eşit ağırlıklar için kriterlerin üstünlük değerleri

Alternatifler	q	q+	q-	Sıralama
B	0,4822	0,5514	0,0692	1
E	0,2371	0,4389	0,2018	2
A	-0,189	0,1457	0,3347	3
C	-0,1938	0,1459	0,3397	4
D	-0,3366	0,1167	0,4532	5



Şekil 1. Eşit ağırlıklı çözüm için PROMETHEE I (a) ve PROMETHEE II (b) sonuçları.



Şekil 2. Eşit ağırlıklı çözüm İçin GAİA düzlemi analizi.

GAİA düzlemine bakıldığında ayrıştırıcı özelliği en fazla olan kriter bir yılda döndürdükleri paradır. Alternatiflerin kriterlere göre durumu da bu grafikte gösterilmiştir. Örneğin E alternatifi daha önce tünel işi yapmış olma kriterine göre tercih edilmektedir. Tercih vektörü de B alternatifini göstermektedir. Bu sonuçlar PROMETHEE I ve PROMETHEE II ile de örtüşmektedir.

3.3.2. Kriterlere Ağırlık Verildiği Durum

Tablo 4'de belirtilen kriter ağırlıkları kullanılarak veriler ara yüze girilmiştir. Alternatifler değerlendirilerek pozitif, negatif ve net üstünlük değerleri hesaplanmıştır. Hesaplanan üstünlük değerleri aşağıda Tablo 6. da gösterilmektedir. Ağırlıksız ve ağırlıklı durumlar için yapılan sıralamalar Tablo 7.'de verilmiştir. Kriterlere ağırlık verildiğinde PROMETHEE I ve II yöntemleri ile bulunan kısmi ve tam öncelik sıralamasına göre en iyi alternatif B çıkmıştır. Adaylar P II'ye göre en iyiden en kötüye doğru B, E, C, D, A olarak sıralanmaktadır.

GAİA düzlemine bakıldığında ayrıştırıcı özelliği en fazla olan kriter yine bir yılda döndürdükleri paradır. Tercih vektörü B alternatifini göstermektedir. Bu durumda sonuçlar PROMETHEE I ve PROMETHEE II ile örtüşmektedir.

4.Sonuç

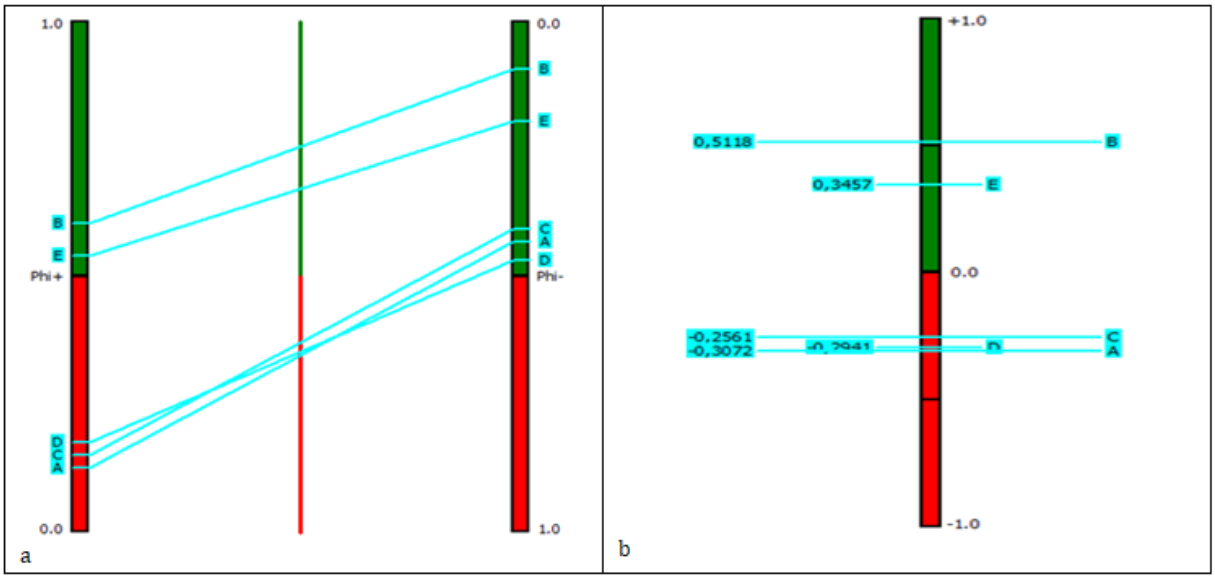
İki durumda da B ve E alternatiflerinin tercih sırası değişmemiştir. B alternatifi birinci, E alternatifi ikinci olmuştur. A, C ve D alternatiflerinin sırası iki durumda tercih sıraları farklıdır. Çalışma, yapım projelerinde işverenlerin teknik müşavir firma seçiminde PROMETHEE yönteminin başarı ile kullanılabileceğini göstermiştir. Bu problem verilerine göre: kriterlerin ağırlıklarının eşit ve farklı olduğu durumlarda sıralamadaki ilk iki seçenek değişmemiştir.

Tablo 6. Farklı kriter ağırlıkları için kriterlerin üstünlük değerleri

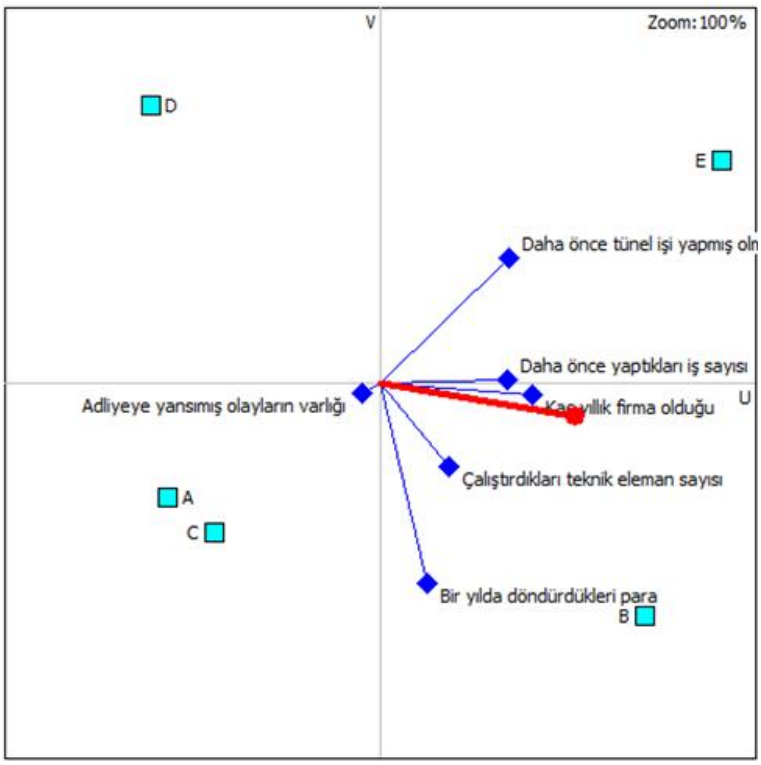
Alternatifler	q	q+	q-	Sıralama
B	0,5118	0,604	0,0922	1
E	0,3457	0,5413	0,1956	2
C	-0,2561	0,1501	0,4062	3
D	-0,2941	0,174	0,4681	4
A	-0,3072	0,1246	0,4318	5

Tablo 7. Eşit ve farklı ağırlıklardaki sıralamaların karşılaştırılması

Kriter Ağırlıkları Eşit			Kriter Ağırlıkları Farklı		
Alternatifler	qnet	Sıralama	Alternatifler	qnet	Sıralama
A	-0,189	3	A	0,4318	5
B	0,4822	1	B	0,0922	1
C	-0,1938	4	C	0,4062	3
D	-0,3366	5	D	0,4681	4
E	0,2371	2	E	0,1956	2



Şekil 3. Farklı kriter ağırlıkları için PROMETHEE I (a) ve PROMETHEE II (b) sonuçları.



Şekil 4. Farklı kriter ağırlıkları gaia düzlemi analizi.

Katkı Oranı Beyanı

Yazarların katkı yüzdeleri aşağıda verilmiştir. Yazarlar makaleyi incelemiş ve onaylamıştır.

	L.O.U	M.Ö.
K	50	50
T	50	50
Y	50	50
VTI	50	50
VAY	50	50
KT	50	50
YZ	50	50
KI	50	50
GR	50	50
PY	50	50
FA	50	50

K= kavram, T= tasarım, Y= yönetim, VTI= veri toplama ve/veya işleme, VAY= veri analizi ve/veya yorumlama, KT= kaynak tarama, YZ= Yazım, KI= kritik inceleme, GR= gönderim ve revizyon, PY= proje yönetimi, FA= fon alımı.

Çatışma Beyanı

Yazarlar bu çalışmada hiçbir çıkar ilişkisi olmadığını beyan etmektedirler.

Etik Onay Beyanı

Bu araştırmada hayvanlar ve insanlar üzerinde herhangi bir çalışma yapılmadığı için etik kurul onayı alınmamıştır.

Kaynaklar

Amponsah SK, Yıldız A, Karslı B. 2012. Logistic preference function for preference ranking organization method for enrichment evaluation (PROMETHEE) decision analysis. Afr J Math Comput Sci Res, 5(6): pp: 112-119.

Brans JP. 1982. L'ingénierie de la décision; Élaboration d'instruments d'aide à la décision. Méthode PROMETHEE. Colloque d'Aide à la Décision: Nature, Instruments et Perspectives d'Avenir, 1982, Québec, Québec, Kanada, pp: 183-213.

De Keyser W, Peeters P. 1996. A note on the use of PROMETHEE multicriteria methods. Eur J Oper Res, 89: pp: 457-461.

Emay. 2024. Tüneller. http://www.emay.com/fu_tuneller.aspx (accessed date: August 10, 2024).

Genç T, Mahmut M. 2013. TOPSIS ve PROMETHEE yöntemleri ile elde edilen üstünlük sıralamalarının bir uygulama üzerinden karşılaştırılması. AKÜ İİBF Derg, 15(2): pp: 539-567.

İGEME. 2024. Teknik müşavirlik nedir? https://www.igeme.com.tr/teknik-musavirlik-nedir/ (accessed date: August 10, 2024).

İMO. 2024. Teknik müşavir tanımı. http://www.imo.org.tr/resimler/ekutuphane/pdf/280.pdf (accessed date: August 10, 2024).

Mareschal B, Brans J. 1988. Geometrical representations for MCDA. Eur J Oper Res, 34: pp: 69-77.

Özdağoğlu A. 2013. Üretim işletmelerinde lazer kesme makinelerinin PROMETHEE yöntemi ile karşılaştırılması. Ulus Yön İkt İşl Derg, 9(19): pp: 1-15.

Soba M. 2012. PROMETHEE yöntemi kullanarak en uygun panelvan otomobil seçimi ve bir uygulama. J Yaşar Univ, 28(7): pp: 4708-4721.

Şenkayası H, Hekimoğlu H. 2013. Çok kriterli tedarikçi seçimi problemine PROMETHEE yöntemi uygulaması. Verimlilik Derg, 1: pp: 66-67.

Şimşek A. 2013. IPA projelerinde teknik müşavirlik hizmetlerinin ekonomi politiği. https://www.csb.gov.tr/db/strateji/editordosya/Mehmet_Ali_Simsek-Uzmanlik_Tezi.pdf (accessed date: August 10, 2024).

TMMMB. 2024. Teknik müşavir nedir? http://tmmmb.org.tr/images/tmmmb/gem/GEM_Seminer_Teknik_musavir_nedir.pdf (accessed date: August 10, 2024).

Tuzkaya G, Aydın B, Kahraman C, Güzeller CO. 2011. Malzeme taşıma sistemi alternatiflerinin değerlendirilmesinde Bulanık-PROMETHEE yaklaşımı. Doğuş Univ Derg, 12(1): pp: 144-155.

Türkçe Bilgi. 2024. Teknik müşavirlik nedir? https://www.turkcebilgi.com/t%C3%BCnel#bilgi (accessed date: August 10, 2024).

Yıldırım B. 2014. Çok kriterli karar verme yöntemleri. Dora Yayıncılık, Bursa, Türkiye, pp: 60.

Yılmaz B, Dağdeviren M. 2010. Ekipman seçimi probleminde PROMETHEE ve Bulanık PROMETHEE yöntemlerinin karşılaştırmalı analizi. Gazi Univ Müh Mim Fak Derg, 25(4): pp: 811-826.

.

Black Sea Journal of Engineering and Science
doi: 10.34248/bsengineering.1650066

Open Access Journal
e-ISSN: 2619 – 8991

Araştırma Makalesi (Research Article)
Cilt 8 - Sayı 4: 927-936 / Temmuz 2025
(Volume 8 - Issue 4: 927-936 / July 2025)

DOĞRU AKIM MİKRO ŞEBEKELERİ İÇİN KONTROLÖR TASARIMI VE SİMÜLASYONU

Ahmet Alperen ÖZBEK[1], Tuncay ALTUN[2], Kenan ALTUN[3]*

[1]*Sivas Cumhuriyet University, Institute of Science, 58070, Sivas, Türkiye*
[2]*Yozgat Bozok University, Faculty of Engineering- Achitecture, Department of Electrical And Electronics Engineering, 66100, Yozgat, Türkiye*
[3]*Sivas Cumhuriyet University, Sivas Technical Sciences Vocational School, Department of Electronics and Automation, 58140, Sivas, Türkiye*

Özet: Bu çalışma, doğru akım (DA) mikro şebekelerde yük paylaşım dengesizliklerini gidermek, voltaj regülasyonunu iyileştirmek ve sistem kararlılığını artırmak amacıyla bir kontrol yöntemi önerilmiştir. Yenilenebilir enerji kaynaklarının entegrasyonu ve dağıtık üretim sistemlerinin yaygınlaşması DA mikro şebekeleri modern enerji altyapısında önemli bir konuma taşımıştır. Ancak, sabit eğim (droop) katsayılarına dayalı geleneksel yöntemler, değişen işletme koşullarına uyum sağlayamadığı için yük paylaşımında dengesizlikler ve voltaj sapmaları meydana gelmektedir. Bu kapsamda, geliştirilen model, adaptif droop kontrol algoritması ile donatılmış olup, voltaj regülasyonu, yük paylaşım doğruluğu ve sistem güvenilirliğini artırmak üzere tasarlanmıştır. Önerilen kontrol yöntemi, birincil ve ikincil kontrol seviyelerinden oluşan hiyerarşik bir yapı kullanmaktadır. Birincil kontrol, iç döngü ve geleneksel droop kontrol stratejileri ile yerel kararlılığı sağlarken, ikincil kontrol voltaj sapmalarını düzelterek yük paylaşım hassasiyetini artırmaktadır. Adaptif droop algoritması, sistem yük koşullarına bağlı olarak droop katsayılarını gerçek zamanlı güncelleyerek voltaj regülasyonunda daha hassas ve dengeli bir güç paylaşımı sunmaktadır. Geleneksel yöntemlere kıyasla daha hızlı ve esnek bir tepki verebilen bu yaklaşım, değişen işletme koşullarına uyum sağlayarak mikro şebekenin genel kararlılığını iyileştirmektedir. Geliştirilen kontrol yöntemi, IEEE tarafından standartları belirlenen 14-baralı alternatif akım (AA) sisteminin DA mikro şebekeye dönüştürülmüş modeli üzerinde test edilmiş ve performansı detaylı simülasyonlarla doğrulanmıştır. Simülasyon sonuçları, önerilen kontrol algoritmasının voltaj dalgalanmalarını azalttığını, yük paylaşım doğruluğunu artırdığını ve değişen sistem koşullarına hızlı uyum sağladığını göstermektedir. Sonuçlar, adaptif droop kontrol yönteminin DA mikro şebekelerde güvenilirlik ve enerji verimliliğini artıran yenilikçi bir çözüm sunduğunu ortaya koymaktadır.

Anahtar kelimeler: Adaptif droop kontrolü, DA mikro şebekeler, Voltaj regülasyonu, Orantısal yük paylaşımı, Hiyerarşik kontrol.

Controller Design and Simulation for Direct Current Microgrids

Abstract: This study presents a control method to eliminate load-sharing imbalances, improve voltage regulation, and enhance system stability in direct current (DC) microgrids. The integration of renewable energy sources and the widespread adoption of distributed generation have made DC microgrids a crucial component of modern energy infrastructure. However, traditional methods based on fixed droop coefficients cannot dynamically adapt to varying operating conditions, leading to load-sharing inaccuracies and voltage deviations. To address these challenges, the developed model is equipped with an adaptive droop control algorithm designed to improve voltage regulation, enhance load-sharing accuracy, and ensure system reliability. The proposed control method employs a hierarchical structure consisting of primary and secondary control levels. The primary control level ensures local stability using inner-loop and conventional droop control strategies, while the secondary control level corrects voltage deviations and enhances load-sharing precision. The adaptive droop algorithm dynamically updates droop coefficients in real time based on system load conditions, providing more precise voltage regulation and balanced power distribution. Compared to conventional methods, this approach offers faster and more flexible responses, adapting to varying operating conditions and improving overall microgrid stability. The developed control method was tested on a DC microgrid version of the 14-bus alternating current (AC) system standardized by the Institute of Electrical and Electronics Engineers (IEEE), and its performance was verified through detailed simulations. Simulation results demonstrate that the proposed control algorithm reduces voltage fluctuations, improves load-sharing accuracy, and adapts quickly to changing system conditions. The findings reveal that the adaptive droop control approach provides a reliable and efficient solution for enhancing voltage stability and energy efficiency in DC microgrids.

Keywords: Adaptive droop control, DC microgrids, Voltage regulation, Proportional load sharing, Hierarchical control.

***Sorumlu yazar (Corresponding author):** Sivas Cumhuriyet University, Sivas Technical Sciences Vocational School, Department of Electronics and Automation, 58140, Sivas, Türkiye
E mail: kaltun@cumhuriyet.edu.tr (K. ALTUN)
Ahmet Alperen ÖZBEK https://orcid.org/0009-0006-0525-5274
Tuncay ALTUN https://orcid.org/0000-0003-1499-3384
Kenan ALTUN https://orcid.org/0000-0001-7419-1901

Gönderi: 3 Mart 2025 **Kabul:** 16 Nisan 2025 **Yayınlanma:** 15 Temmuz 2025
Received: March 3, 2025 **Accepted:** April 16, 2025 **Published:** July 15, 2025
Cite as: Özbek AA, Altun T, Altun K. 2025. Controller design and simulation for direct current microgrids. BSJ Eng Sci, 8(4): 927-936.

This work is licensed (CC BY-NC 4.0) under Creative Commons Attribution 4.0 International License

1. Giriş

Enerji, ekonomik kalkınma ve sürdürülebilirlik açısından kritik bir unsurdur. Küresel enerji talebi hızla artarken, fosil yakıtların çevresel etkileri ve sınırlı rezervleri, yenilenebilir enerjiye yönelimi zorunlu kılmaktadır (Dechamps, 2023). Uluslararası Enerji Ajansı'na (IEA) göre, 2050 yılına kadar enerji talebinin %40 artması beklenmektedir, bu da enerji dönüşümünü kaçınılmaz hale getirmektedir (Küçük ve Yüce Dural, 2022). Türkiye'de sanayileşme ve nüfus artışı nedeniyle enerji tüketimi sürekli artmaktadır. Türkiye Enerji Piyasası Düzenleme Kurumu'na (EPDK) göre, enerji tüketimi son on yılda %5 oranında artış göstermiştir. Bu durum, yenilenebilir enerji kaynaklarının kullanımını teşvik ederek dışa bağımlılığı azaltmayı hedefleyen politikaların önemini artırmaktadır (Saygin vd., 2021). Yenilenebilir enerji yatırımları, enerji güvenliği sağlamanın yanı sıra ekonomik büyümeye de katkıda bulunmaktadır (Bulut ve Muratoglu, 2018).

Enerji yönetiminde verimliliği artırmak ve güç kayıplarını azaltmak için gelişmiş kontrol stratejilerine ihtiyaç duyulmaktadır. Doğru akım (DA) mikro şebekeler, düşük kayıpları ve yüksek verimlilikleriyle bu alanda önemli bir çözüm sunmaktadır (Kirtay, 2010). DA mikro şebekeler, yenilenebilir enerji entegrasyonunu kolaylaştırarak karbon emisyonlarını azaltmaktadır (Wang vd., 2024). Ancak, bu sistemlerin güvenilir çalışabilmesi için uygun kontrol stratejilerinin geliştirilmesi gerekmektedir.

DA mikro şebekelerde kontrol yapıları genellikle birincil (primary) ve ikincil (secondary) kontrol seviyeleri altında ele alınmaktadır (Gao vd., 2019). Birincil kontrol, hızlı ve yerel seviyede çalışan bir mekanizma olup, ani yük değişimlerine anında tepki vermek amacıyla tasarlanmıştır. En yaygın kullanılan yöntemlerden biri droop kontrolüdür. Droop kontrolü, merkezi bir kontrol gerektirmeden gerilim regülasyonu ve güç paylaşımını yönetir. Ancak, sabit droop katsayıları kullandığı için uzun vadeli gerilim kararlılığını tam olarak sağlayamamakta ve yük paylaşımında hassasiyet eksiklikleri yaşanmaktadır (Biglarahmadi vd., 2024). İkincil kontrol, birincil kontrolün eksikliklerini gidermek için geliştirilmiş olup, voltaj sapmalarını düzelterek sistemin genel kararlılığını artırmayı amaçlamaktadır. Ancak, merkezi veya dağıtılmış algoritmalar gerektirdiğinden haberleşme altyapısına bağımlıdır (Ghanimi vd., 2024).

Günümüzde, merkezi ve dağıtılmış kontrol yaklaşımlarını entegre eden hibrit modeller üzerine çalışmalar artmakta ve mikro şebeke kararlılığını iyileştirmeye yönelik yeni algoritmalar geliştirilmektedir (Hou vd., 2024). Orantısal yük paylaşımı, her enerji kaynağının kapasitesine uygun güç sağlamasını hedefleyerek gerilim kararlılığını ve sistem güvenilirliğini artırmaktadır. Literatürde bu amaca ulaşmak için droop kontrolü, sanal empedans teknikleri, haberleşme tabanlı merkezi/dağıtılmış kontrol sistemleri ve yapay zekâ destekli optimizasyon yöntemleri gibi yaklaşımlar önerilmektedir (Rashad vd., 2018).

Droop kontrolü, haberleşme gerektirmediğinden yaygın olarak kullanılan bir yöntemdir. Ancak, hat empedanslarından kaynaklanan voltaj sapmaları ve güç paylaşımında hassasiyet eksiklikleri bulunmaktadır (Dam ve Lee, 2016). Sanal empedans yöntemleri, hat karakteristiklerini düzenleyerek daha doğru yük paylaşımı sağlamayı amaçlamaktadır (Fang vd., 2019). Haberleşme tabanlı merkezi kontrol, yüksek doğruluk sağlamasına rağmen, haberleşme gecikmeleri ve tek hata noktasına bağımlılık gibi sorunlarla karşı karşıyadır. Dağıtılmış kontrol sistemleri, merkezi birime bağımlılığı azaltarak daha esnek ve güvenilir bir yük paylaşımı sunmaktadır (Cucuzzella vd., 2019). Son yıllarda yapay zekâ tabanlı kontrol sistemleri, sistemin adaptif hale gelmesini sağlamak için öğrenme mekanizmalarını kullanmaktadır (Taye ve Choudhury, 2023).

DA mikro şebekelerde ikincil kontrol, birincil kontrol seviyesinin eksikliklerini gidermek ve uzun vadeli sistem kararlılığını sağlamak için kritik bir bileşendir. Literatürde, ikincil kontrol için merkezi (centralized), merkezi olmayan (decentralized) ve dağıtılmış (distributed) kontrol olmak üzere üç temel yaklaşım bulunmaktadır (Aluko vd., 2022). Merkezi kontrol, tüm mikro şebekenin tek bir merkezden yönetildiği yapıdır ve yüksek doğruluk sağlamasına rağmen haberleşme gecikmeleri ve tek hata noktasına bağımlılık gibi dezavantajları vardır (Jasim vd., 2022). Merkezi olmayan kontrol, her bir enerji kaynağının yerel ölçümlere dayanarak bağımsız kararlar aldığı bir yapıdır ve haberleşme altyapısına bağımlılığı azaltarak sistem güvenilirliğini artırsa da yük paylaşımı açısından merkezi kontrol kadar hassas değildir (Adhikari vd., 2016).

Bu eksiklikleri gidermek amacıyla geliştirilen dağıtılmış kontrol yöntemleri, merkezi kontrolün hassasiyetini ve merkezi olmayan kontrolün esnekliğini birleştirerek daha ölçeklenebilir ve güvenilir bir yapı sunmaktadır. Dağıtılmış sistemlerde, her enerji kaynağı komşularıyla haberleşerek optimum yük paylaşımı ve sistem kararlılığı sağlamaktadır (Moradi vd., 2023). Özellikle bağımsız mikro şebekelerde ve yenilenebilir enerji entegrasyonu gerektiren sistemlerde büyük avantajlar sunmaktadır (da Silva vd., 2020). Literatürdeki çalışmalar, farklı kontrol stratejilerinin avantaj ve dezavantajlarını ortaya koyarak, en uygun yöntemin sistem gereksinimlerine bağlı olarak seçilmesi gerektiğini vurgulamaktadır (Kumar vd., 2019).

Bu çalışma, dağıtılmış kontrol yaklaşımını benimseyerek merkezi ve merkezi olmayan kontrol stratejilerinin eksikliklerini gidermeyi hedeflemektedir. Adaptif droop kontrolünü kullanarak orantısal yük paylaşımı ve voltaj regülasyonu hassasiyetini artırmayı amaçlamaktadır. Literatürde sabit droop katsayısı kullanılırken, bu çalışmada dinamik olarak uyum sağlayan bir adaptif droop stratejisi geliştirilmiştir. Simülasyon sonuçları, önerilen yöntemin kararlılığı artırarak enerji kayıplarını minimize ettiğini ve geleneksel yaklaşımlara kıyasla daha etkili bir güç paylaşımı sunduğunu göstermektedir.

Bu makalede, 14 baralı ve 5 kontrolcü ile bir DA mikro

şebeke modelinde birincil ve ikincil kontrol mekanizmalarının kullanımıyla orantısal yük paylaşımının sağlanması ve adaptif droop kontrol stratejisinin etkinliği incelenmektedir. Makalenin devamında, materyal ve yöntemler, simülasyon sonuçları, adaptif droop kontrolünün avantajları ve geleceğe yönelik öneriler detaylandırılacaktır.

2. Materyal ve Yöntem

Bu çalışmada, IEEE 14-baralı bir DA mikro şebeke modeli oluşturularak adaptif droop kontrol algoritmasının etkinliği incelenmiştir. Beş kontrolörden oluşan sistem, yük paylaşımı ve voltaj düzenlemesi görevlerini üstlenmektedir. Çalışmanın temel amacı, adaptif droop kontrol yönteminin sistem kararlılığı üzerindeki etkisini analiz etmektir.

DA mikro şebekelerde hiyerarşik kontrol, enerji kaynaklarının koordinasyonunu ve sistemin kararlılığını sağlamak için kullanılmaktadır (Vasquez vd., 2010). Şebekenin dinamik davranışlarını incelemek için gerçekleştirilen modelleme ve simülasyon, sistemin enerji paylaşımını ve voltaj düzenlemesini en iyi hale getirmiştir.

Adaptif droop kontrol algoritması, geleneksel droop kontrolünün eksikliklerini gidermek üzere tasarlanmıştır. Nasirian vd. (2014) adaptif kontrolün mikro şebekelerde voltaj sapmalarını azaltıp enerji verimliliğini artırdığını belirtmiştir. Bu yöntem, her bara için voltaj ayar noktalarını dinamik olarak belirleyerek yük paylaşım hassasiyetini artırmaktadır. Simülasyon sonuçları, adaptif droop kontrol algoritmasının mikro şebekede voltaj ve akım düzenleme performansını optimize ettiğini göstermiştir. Shaffee vd. (2014) bu kontrol algoritmasının enerji kaynakları arasında daha hassas bir dengenin kurulmasını sağladığını vurgulamıştır. Mikro şebekenin dinamik performansı, çeşitli çalışmaların ışığında değerlendirilmiştir (Dragicevic vd., 2016; Gao vd., 2019; Nahata vd., 2020). Bu yöntemlerin uygulanması, enerji kayıplarının azalması ve genel sistem stabilitesinin artırılması açısından kritik bir rol oynamıştır.

2.1.DA Mikro Şebekeler ve Kontrol Yöntemleri

Mikro şebekeler, enerji sistemlerini yerelleştirme ve modernleştirme amacı taşıyan küçük ölçekli enerji sistemleridir. Hem bağımsız ada modunda hem de merkezi şebekeye bağlı olarak çalışabilmeleri, onlara esneklik ve güvenilirlik kazandırmaktadır. İlk olarak 1960'lı yıllarda kırsal bölgelerde uygulanmaya başlayan mikro şebekeler, Kythnos Adası'ndaki yenilenebilir enerji temelli sistem gibi erken başarılı örneklerle dikkat çekmiştir (Hatziargyriou, 2014; Hatziargyriou vd., 2020).

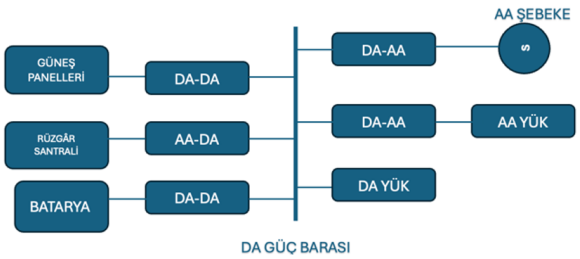
Başlangıçta yüksek maliyetler ve şebeke kararlılığı gerekliliği gibi teknik zorluklarla karşılaşan mikro şebekeler yaygın olarak benimsenmemiştir (Choudhury, 2020). Ancak, teknolojik ilerlemeler ve akıllı kontrol sistemleri, bu sorunları büyük ölçüde aşmayı sağlamıştır (Polleux vd., 2022).

Yenilenebilir enerji kaynaklarıyla entegrasyonları sayesinde, mikro şebekeler enerji güvenliğini artırırken karbon emisyonlarını azaltmaktadır. Güneş panelleri, rüzgâr türbinleri ve gerektiğinde dizel jeneratörler, sistemin sürdürülebilirliğini destekleyen başlıca enerji kaynaklarıdır (Zia vd., 2018). Alternatif akım (AA), doğru akım (DA) veya hibrit yapılarla çalışabilen mikro şebekeler arasında DA sistemler enerji dönüşüm kayıplarını azaltmaları ve verimliliği artırmaları nedeniyle öne çıkmaktadır (Mosa ve Ali, 2021).

Mikro şebekeler, ada modunda bağımsız çalışabilmenin yanı sıra, şebeke bağlantılı modda güç akışı yönetimiyle merkezi şebekeyle senkronize olabilir. Ayrıca, kullanıcı katılımını teşvik ederek tüketicilerin aktif bir rol üstlenmesini sağlar. Bu bağlamda mikro şebekeler, artarak yaygınlaşan yenilenebilir enerji kullanımına uyum sağlayarak enerji sistemlerinde kritik bir rol oynamaktadır. DA mikro şebekelerin sunduğu avantajlar, enerji altyapılarının daha esnek ve uyarlanabilir hale gelmesini desteklemektedir (Kaysal, 2023).

Bu bağlamda, enerji sistemlerinin artan yenilenebilir enerji kullanımına uyum sağlaması için mikro şebekeler kritik bir rol oynamaya devam etmektedir. Geleneksel şebeke altyapılarına nazaran daha esnek ve uyarlanabilir olan bu sistemler DA mikro şebekelerin sunduğu avantajlarla daha da etkin bir enerji geleceğine kapı açmaktadır.

DA mikro şebekeler, Şekil 1'de de görüleceği üzere sade tasarımı ve daha düşük başlangıç maliyetleri sayesinde yatırım ve işletim giderlerini azaltır (Planas vd., 2015). Doğru akım kaynaklarının doğrudan entegrasyonu ile enerji dönüşüm süreçleri daha uyumlu bir yapı kazanır (Brusso ve Bose, 2014). Ayrıca DA mikro şebekelerin harmonik bozulma ve reaktif güç sorunlarını ortadan kaldırması, hassas endüstriyel uygulamalar ve veri merkezleri gibi alanlarda kritik öneme sahiptir (Lotfi ve Khodaei, 2017).



Şekil 1. DA mikro şebeke blok diyagramı.

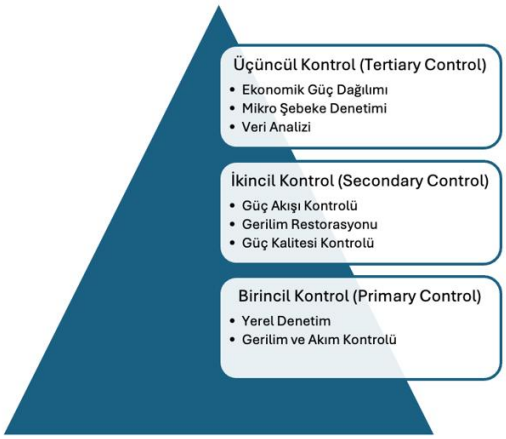
Bu sistemler, hibrit (AA/DA birlikte) yapılarda enerji akışını kararlı bir şekilde düzenleme kapasitesine sahiptir (Pourbehzadi vd., 2019). Ancak bu avantajların tam anlamıyla gerçekleştirilebilmesi için kararlılık ve verimlilik sağlamaya yönelik teknik gerekliliklerin yerine getirilmesi gerekmektedir. Yenilenebilir enerji kaynaklarının değişken doğası, enerji sistemlerinin entegrasyonu ve orantısal güç paylaşımı gibi faktörler gelişmiş kontrol stratejilerini zorunlu kılmaktadır.

DA mikro şebekelerde uygulanan hiyerarşik kontrol

yaklaşımları, gerilim regülasyonu ve yük paylaşımı gibi kritik alanlarda etkin yönetim sağlamaktadır. Güç elektroniği altyapısının yaygınlaşmasıyla birlikte DA mikro şebekeler, gelecekte akıllı enerji sistemlerinin çekirdeği olma potansiyelini taşımaktadır (Elmouatamid vd., 2020).

2.2.DA Mikro Şebekelerde Hiyerarşik Kontrol

DA mikro şebekelerde hiyerarşik kontrol, enerji yönetiminde kararlılığı sağlamak ve sistem performansını en iyi hale getirmek için geliştirilen yenilikçi bir kontrol metodolojisidir. Hiyerarşik kontrol yapısı, Şekil 2'de gösterildiği üzere birincil, ikincil ve üçüncül seviyelerden oluşur. Birincil kontrol seviyesi, dağıtık enerji kaynaklarının (DEK) dönüştürücüler aracılığıyla kontrol edilmesini sağlayarak sistemin yerel kararlılığını güvence altına alır. İkincil kontrol seviyesi, voltaj düzenlemesi ve akım paylaşımı doğruluğunu artırmayı hedeflerken, üçüncül kontrol seviyesi ekonomik optimizasyon ve veri analizi süreçlerini içerir. Üçüncül seviyede uygulanan kontrol mekanizmaları, enerji piyasasına katılım ve ideal güç paylaşım oranlarının belirlenmesi gibi daha geniş ölçekli süreçleri kapsamaktadır. Bu seviyeler, farklı zaman ölçeklerinde eş zamanlı olarak çalışarak sistemin genel kararlılığını sağlar.



Şekil 2. DA Mikro şebekelerde hiyerarşik kontrol.

Yapılan çalışmalar, hiyerarşik kontrol sistemlerinin DA mikro şebekelerin kararlılığını artırmada etkili olduğunu göstermektedir. Varquez vd. (2010) yenilenebilir enerji kaynaklarının entegrasyonu için hiyerarşik kontrol stratejilerinin önemine dikkat çekmiş ve bu sistemlerin esneklik ve adaptasyon yeteneklerini artırdığını ortaya koymuştur. Gao vd. (2019).ise birincil ve ikincil kontrol mekanizmalarının enerji kayıplarını azaltma üzerindeki olumlu etkilerini vurgulamıştır.

Dağıtık kontrol sistemlerinin hiyerarşik kontrol yapısına entegrasyonu, geleneksel merkezi kontrol mekanizmalarına olan bağımlılığı azaltmakta ve sistemin değişken yenilenebilir enerji kaynaklarına uyum sağlama kapasitesini artırmaktadır (Guerrero vd., 2011).

Sonuç olarak DA mikro şebekelerde hiyerarşik kontrol, enerji sistemlerinin kararlılığı ve verimliliği açısından kritik bir öneme sahiptir. Gelişmiş kontrol stratejilerinin uygulanması, bu sistemlerin sürdürülebilirlik ve esneklik hedeflerini karşılayarak modern enerji ihtiyaçlarına uyum sağlamasını mümkün kılmaktadır.

2.3.DA Mikro Şebekelerde Birincil Kontrol

Birincil kontrol DA mikro şebekelerde sistem kararlılığını sağlamak, doğru voltaj seviyelerini korumak ve dağıtık enerji kaynakları (DEK'ler) arasında güç paylaşımını dengelemek için merkezi olmayan bir strateji olarak çalışır. Bu kontrol seviyesi, özellikle şebekeye bağlı veya ada modunda çalışan mikro şebekelerde kritik önem taşır ve Inner Loop ile Droop Control yöntemlerini içerir (Al-Ismail, 2021).

Birincil kontrol seviyesi Şekil 2'de de gösterildiği gibi DA mikro şebekelerin kontrol hiyerarşisinde ilk basamağını oluşturur ve hızlı dinamik tepkilerle akım ve gerilim regülasyonu gibi temel işlevleri yerine getirir (Shuai vd., 2018). Voltaj regülasyonu ve güç paylaşımı için genellikle droop kontrol yöntemleri kullanılmaktadır. Shafiee vd. (2014) birincil kontrolün hızlı dinamik tepkiler sağlamada etkili olduğunu ve DA mikro şebekelerde voltaj stabilitesini artırdığını göstermiştir. Droop kontrolünün ve droop katsayısının temel eşitliği "Eşitlik 1-2" şu şekildedir:

$$V_O = V_{ref} - m_p \, . I_O \tag{1}$$

$$m_p = \frac{\Delta V}{P_{max}} \tag{2}$$

burada: V_O , kaynağın çıkış voltajını, V_{ref} nominal voltajı, m_p droop kazanç katsayısını ve I_O kaynağın çıkış akımını temsil eder. Voltaj sapması ΔV ve maksimum güç P_{max} arasındaki ilişki ile belirlenir. Bu katsayı, güç kaynaklarının yük paylaşımındaki davranışlarını doğrudan etkiler. Örneğin, paralel bağlanan iki güç kaynağı, biri daha fazla yük beslemeye başladığında voltajını düşürerek diğer kaynağın devreye girmesini ve yük paylaşımına katkıda bulunmasını sağlar (Guarnieri, 2018). Ancak büyük yük değişikliklerinde voltaj sapmaları ve akım paylaşımında doğruluk kaybı yaşanabilir.

Birincil kontrol, eğim kontrol yöntemiyle akım paylaşımını ve voltaj regülasyonunu ayarlar. Paralel bağlanan güç dönüştürücülerinin çıkış akımları arasındaki oran "Eşitlik 3" ile belirlenir:

$$\frac{I_{O1}}{I_{O2}} = \frac{R_{d2}}{R_{d1}} + \frac{R_{l2} - \frac{R_{d2}}{R_{d1}} \, . R_{l1}}{R_{d1} + R_{l1}} \tag{3}$$

burada: R_{d1}, $R_{d2;}$ sanal direnç değerleri (droop katsayıları), R_{l1}, $R_{l2;}$ hat dirençleridir. I_{O1} ve I_{O2} ise Kontrolör 1 ve 2'nin çıkış akımlarını temsil eder.

Birincil kontrolde hat direncinin etkisiyle akım paylaşımı doğruluğunda sapmalar oluşabilir ve yük ile DA bara gerilimi arasında voltaj sapması meydana gelebilir. Bu durum, birincil kontrolün sınırlarını gösterir ve sistemde ikincil kontrol katmanının gerekliliğini ortaya koyar

(Kaysal vd., 2023).

Sanal direnç mantığına dayalı olan Geleneksel droop kontrolü voltaj ve akım arasında doğrusal bir ilişki kurarak bağımsız güç paylaşımını mümkün kılar (Liu vd., 2020). Droop kontrolü ile çıkış voltajı ve akım arasındaki ilişki "Eşitlik 4-5" ile tanımlanır:

$$V_{pcc} = V_{ref} - R_{dk} \, . I_O - r_k . I_O \quad (4)$$

$$I_O = \frac{V_{ref} - V_{pcc}}{R_{dk} + r_k} \quad (5)$$

burada: V_{pcc} , sistemde ortak bağlantı noktası olan PCC'deki (Point of Common Coupling) DA voltajını gösterirken V_{ref} , kontrolcünün referans voltajıdır. R_{dk} , droop katsayısı (veya sanal direnç) olarak tanımlanırken, r_k , hat direncini, I_O ise sırasıyla sanal direnç üzerinde harcanan akımı ve hat direnci üzerinde harcanan akımı temsil etmektedir.

Droop katsayısı R_{dk} her dönüştürücünün yük paylaşımındaki davranışını belirler. Daha yüksek bir droop katsayısı, daha büyük bir voltaj düşüşüne ve daha hassas bir akım paylaşımına yol açar. İki paralel dönüştürücü arasındaki akım paylaşımı, "Eşitlik 6" ile açıklanır:

$$\frac{I_o^k}{I_o^j} = \frac{R_d^j + r_j}{R_d^k + r_k} \quad (7)$$

bu eşitlikte: I_o^k ve I_o^j , sırasıyla k ve j dönüştürücülerinin çıkış akımlarıdır. R_d^k ve R_d^j, her iki dönüştürücünün droop katsayılarıdır, r_k ve r_j ise hat dirençleridir.

Daha yüksek bir droop katsayısı, akım paylaşımında hassasiyeti artırırken, voltaj düşüşlerini de beraberinde getirir. Ancak bu durum, sistemde voltaj sapmalarının artmasına neden olabilir. Bu nedenle, droop kontrolünün temel amacı, akım paylaşım doğruluğu ile voltaj sapması arasında bir denge kurmaktır.

Geleneksel droop kontrolü, büyük yük değişikliklerinde voltaj kararlılığını korumada ve akım paylaşım doğruluğunda yetersizlikler gösterebilir. Bu sınırlamalar, mikro şebekelerde daha gelişmiş kontrol stratejilerinin uygulanmasını gerekli kılmıştır. Doğrusal olmayan droop kontrol, adaptif droop kontrol ve ölü bantlı droop kontrol gibi yöntemler, sistemin daha kararlı ve hassas çalışmasını sağlamak için geliştirilmiştir.

Sonuç olarak, birincil kontrol, mikro şebekelerde yerel kararlılığı sağlarken, yük değişimleri ve hat dirençlerinden kaynaklanan sorunlar, birincil kontrol seviyesinin ötesine geçerek daha ileri düzey kontrol stratejilerine duyulan ihtiyacı açıkça ortaya koymaktadır.

2.4.DA Mikro Şebekelerde İkincil Kontrol

İkincil kontrol, mikro şebekelerde voltaj sapmalarını düzelterek enerji kaynaklarının daha hassas bir şekilde paylaşımını sağlamayı amaçlayan bir kontrol katmanıdır. Sistemin genel koordinasyonu iletişim ağı üzerinden sağlanır. İkincil kontrol, güç dağıtımı, ada modu tespiti gibi işlevleri yerine getirir ve milisaniyeden dakikaya kadar değişen bir zaman ölçeğinde çalışır (Yamashita vd., 2020).

İkincil kontrol, özellikle DA mikro şebekelerde voltaj regülasyonu ve güç paylaşımı gibi kritik işlevleri gerçekleştirir. Hamad vd. (2024). çalışmasında, PI tabanlı kontrol mekanizmalarının voltaj ve güç paylaşım hatalarını en aza indirdiği gösterilmiştir (Hamad vd., 2024). İkincil kontrolün temel eşitliği "Eşitlik 6-7" ile ifade edilir:

$$u_{sc,i} = \boldsymbol{K}_{P,i}\left(\beta_i u_{V_i} + u_{P_i}\right) + \boldsymbol{K}_{I,i} \int \left(\beta_i u_{V_i} + u_{P_i}\right) \, dt. \quad (8)$$

$$v_{sc,i}^* = v_{pri,i}^* + u_{sc,i} \quad (9)$$

burada: $u_{sc,i}$; ikincil kontrol katmanı tarafından üretilen kontrol sinyalidir ve sistemin voltaj regülasyonu ile güç paylaşımını yapmak için kullanılır. $\boldsymbol{K}_{P,i}$; orantısal kazançtır ve sistemin dinamik değişimlere hızlı bir şekilde tepki vermesini sağlar. $\boldsymbol{K}_{I,i}$; integral kazançtır ve sistemde zamanla biriken uzun vadeli hataların ortadan kaldırılmasına yardımcı olur. u_{V_i}; voltaj regülasyon hatasıdır ve bir DG'nin voltajının nominal referans voltajından olan sapmasını ifade eder. u_{P_i}; güç paylaşım hatasıdır ve dağıtık jeneratörlerin yük paylaşımı performansındaki sapmaları temsil eder. β_i; voltaj regülasyonu için kullanılan bir ağırlık faktörüdür ve her bir DG'nin voltaj düzenlemesine katkısını belirler. Bu sinyal, birincil kontrol seviyesindeki referans voltajına eklenerek yeni bir referans voltaj oluşturur, bu işlem "Eşitlik 8" ile ifade edilir. Burada belirlenen referans voltajına $v_{pri,i}^*$ eklenir ve yeni bir referans voltaj $v_{sc,i}^*$ oluşturulur.

Adaptif droop kontrolü, geleneksel droop kontrolünün sınırlamalarını aşmak için geliştirilmiştir. Bu yöntem, sabit bir droop katsayısı yerine, her enerji kaynağının mevcut kapasitesine ve sistem koşullarına göre droop katsayısını dinamik olarak ayarlar (Vu vd., 2017). Adaptif kontrol, değişken yük koşullarında daha hassas voltaj regülasyonu ve dengeli güç paylaşımı sağlar.

Adaptif droop kontrolü, Şekil 3'te gösterildiği gibi düşük bant genişliğine sahip bir haberleşme ağı ile çalışarak dönüştürücülerin çıkış gerilimlerini ve akımlarını paylaşır. Sistem, bu verilere dayalı olarak yaklaşık orantılı bir akım paylaşımı sağlar. Akım paylaşım oranları "Eşitlik 9" ile aşağıdaki şekilde ifade edilir:

$$\frac{i_{O1}}{i_{O2}} = \frac{k_1}{k_2} \quad (10)$$

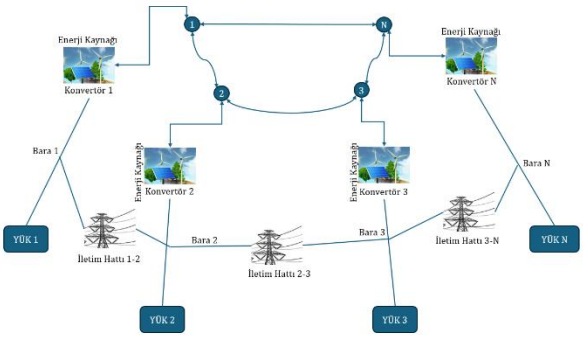
Burada, k_1 ve k_2 sırasıyla birinci ve ikinci dönüştürücünün akım paylaşım oranlarını ifade eder.

Adaptif droop kontrolünün temel eşitliği:

$$V_O = V_{ref} - m(t) \, . I_O \quad (11)$$

"Eşitlik 10" ile burada, diğer droop kontrol denklemlerine benzer şekilde V_O , çıkış voltajını, I_O, çıkış akımını, V_{ref}, referans voltajını temsil ederken $m(t)$, zamanla değişen ve sistemin koşullarına göre ayarlanan adaptif droop katsayısıdır. Bu katsayı, şebeke durumu,

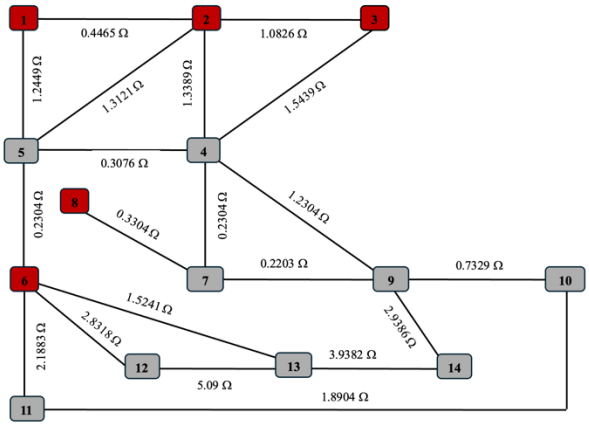
yük durumu veya enerji kaynağının mevcut kapasitesine göre dinamik olarak güncellenir (Nasirian vd., 2014).
Adaptif droop kontrolü, sistemin yük değişikliklerine daha hızlı ve esnek yanıt vermesini sağlar. Voltaj sapmalarını hassas bir şekilde düzenler, sistem kararlılığını artırır ve enerji kaynaklarının aşırı yüklenmesini önler. Ayrıca, hat empedanslarını dikkate alarak voltaj düşüşlerini ve hat kayıplarını en aza indirir. Bu sayede mikro şebekelerde daha dengeli bir güç paylaşımı mümkün olur (Hu vd., 2018).



Şekil 3. DA Mikro şebekelerde ikincil kontrol seviyesinde iletişim ağı.

3. Bulgular ve Tartışma

Bu çalışmada, 14 baralı ve 5 kontrolörlü bir DA mikro şebeke modeli MATLAB üzerinde PLECS tabanlı tasarlanarak, birincil ve ikincil kontrol seviyelerinin sistem performansı üzerindeki etkileri incelenmiştir. IEEE standartlarına uygun olarak geliştirilen modelde, geleneksel droop kontrol ve adaptif droop kontrol stratejileri karşılaştırılmış ve adaptif droop kontrolünün sistem kararlılığı ve enerji verimliliği açısından sunduğu avantajlar ortaya konulmuştur.
Çalışmanın kapsamında kullanılan IEEE standartlarından geliştirilen 14 baralı DA mikro şebeke sistemi, Şekil 4'te şebeke diyagramı şeklinde gösterilmiştir. Bu sistemde, 1, 2, 3, 6 ve 8 numaralı baralara bağlı olan 5 kontrolör, kırmızı renkle gösterilmiştir. Bu kontrolörler, baralar arasında gücün düzenlenmesini sağlayan ve voltaj dengesini koruyan temel bileşenlerdir. Diğer 4, 5, 7, 9, 10, 11, 12, 13, 14 numaralı gri renkle gösterilen noktalar ise sistemde kontrolör bulunmasa da belirli yüklerin yer aldığı baralardır.



Şekil 4. IEEE standartlarından geliştirilen 14 baralı DA mikro şebeke modeli.

Baralar arasındaki direnç değerleri şebekenin elektriksel karakteristiğini belirlemede kritik bir rol oynamaktadır. Direnç değerleri, mikro şebekedeki gücün belirli yollar boyunca nasıl akacağını ve voltaj düşümünü etkileyen temel parametrelerden biridir. Simülasyon modelinde, her bir bara arasındaki direnç değerleri detaylı olarak belirlenerek sistemin gerçek şartlar altında nasıl çalışacağı analiz edilmiştir. Bu nedenle ise model, enerji yönetimi ve gücün dağıtımı açısından büyük öneme sahiptir ve mikro şebekelerde kontrol mekanizmalarının etkinliğini değerlendirirken temel bir referans oluşturmaktadır.
Tablo 1, şebekeye bağlı kaynakların belirli baralar üzerindeki referans gerilim V_{ref} ve maksimum güç kapasitesi P_{max} değerlerini göstermektedir. Verilere göre, şebekeye bağlı konvertör gerilim seviyeleri 376V ile 384V arasında değişmekte olup, bu durum mikro şebekenin voltaj regülasyonu açısından belirli bir dengeye sahip olduğunu ortaya koymaktadır. Güç kapasitesi açısından incelendiğinde, 1. bara üzerinde 165.80 kW ile en yüksek değer gözlemlenirken, diğer baralarda bu değer 9.48 kW ile 100 kW arasında değişmektedir. Özellikle üzerinde kontrolcü olmayan baralar üzerindeki yük profili, mikro şebeke içerisinde farklı bölgelere dağıtılmış güç taleplerini yansıtmaktadır. Bu durum, yük paylaşım stratejilerinin ve kontrol mekanizmalarının etkinliğini değerlendirmek açısından önemli bir veri sağlamaktadır.

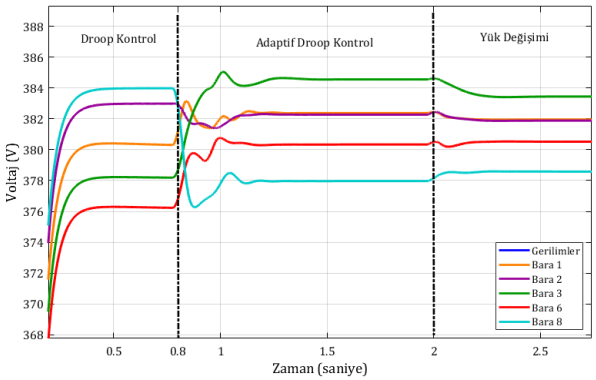
Tablo 1. Kaynak ve yüklerin karakteristikleri.

	V_{ref} (V)	V_{out} (V)	P_{max} (kW)
Bara 1	380	380	165,80
Bara 2	383	383	50
Bara 3	378	378	100
Bara 4	-	380,85	48,35
Bara 5	-	378,15	55,83
Bara 6	376	376	100

Bara 7	-	377	-
Bara 8	384	384	50
Bara 9	-	378,95	30
Bara 10	-	378,10	9,48
Bara 11	-	377,34	30
Bara 12	-	377,45	11.38
Bara 13	-	370,40	14,75
Bara 14	-	378,52	-

Tabloda "-"ile gösterilen noktalarda yük veya kaynak bağlantısı olmadığından değer gözlemlenmemiştir.

Simülasyon çalışmalarında, Şekil 5'te gösterilen konvertör gerilimleri grafiği sistemin voltaj dengesini ve adaptif droop kontrolünün etkinliğini göstermek amacıyla incelenmiştir. İlk olarak 0-0,8 saniye arasında birincil kontrol mekanizması devreye girerek baralar arasındaki gerilim seviyelerini belirlenen referans değerlerine yaklaştırmıştır. Ardından, 0,8-2,0 saniyeleri arasında ikincil kontrol mekanizması devreye alınarak gerilim farklılıkları minimize edilerek şebekeye bağlı yüklerin ihtiyacına göre ayarlanmıştır. Kontrolcülerin simülasyon çalışmasında gösterilen 0.8 sn ile 2 sn arasında orantısal yük paylaşımının adaptive droop kontrol ile sağlandığı grafikten görülmektedir. 2,0 saniyeden itibaren ise sistem tamamen kararlı bir duruma geçmiş, adaptif droop kontrolü sayesinde orantısal yük paylaşımı yapılarak gerilim dalgalanmaları minimum düzeye indirgenmiştir. Adaptive droop 2. Saniyeden sonra yük değişimine karşı orantısal yük paylaşımı koruduğu ve konvertör gerilimleri arasında da gerilim seviyesini buna göre ayarladığı görülmektedir.

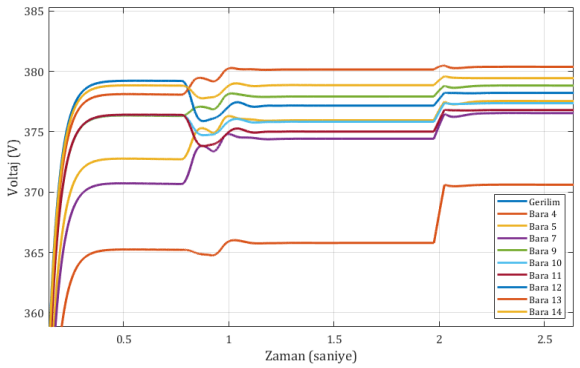


Şekil 5. DA mikro şebekeye bağlı 5 adet konvertörün çıkış gerilim değişimi.

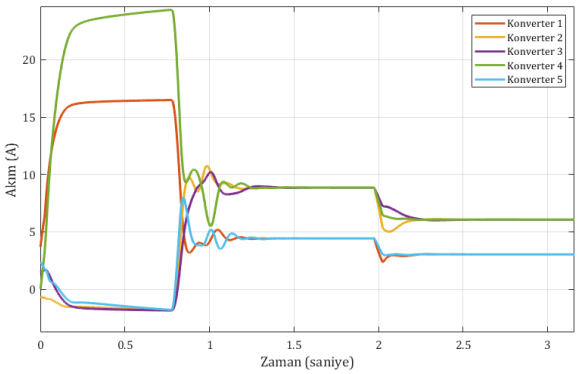
Grafik incelendiğinde, adaptif droop kontrolünün sistemdeki gerilim regülasyonu üzerindeki olumlu etkisi açık bir şekilde görülmektedir. Birincil kontrol sistemindeki geleneksel droop kontrolün aksine, gerilim sapmalarını minimuma indirerek enerji kaynakları arasındaki gerilim dengesinin daha hassas bir şekilde sağlanmasına olanak tanımaktadır. Bu da mikro şebekenin değişen yük koşullarına daha hızlı ve verimli bir şekilde adapte olmasını sağlamaktadır.

Şekil 6'da gösterilen grafik, girişinde konvertör bağlı olmayan baraların gerilim seviyelerinin zaman içindeki değişimini göstermektedir. Konvertör bağlantısı olmayan baraların da kontrol süreçlerine dahil olduğu ve sistemin genel stabilizasyon sürecine nasıl tepki verdiği bu grafik aracılığıyla gözlemlenmektedir. Adaptif droop kontrolünün etkisiyle gerilim dalgalanmalarının azaldığı ve mikro şebekenin genelinde değişken yük koşullarına daha dengeli bir şekilde uyum sağladığı görülmektedir.

Şekil 7'de gösterilen grafik, konvertörlerin çıkış akımlarının zaman içindeki değişimini göstermektedir. 2. saniyenin sonunda, sistemde oransal yük paylaşımı aktif hale gelmiş ve yüklerin taleplerine göre konvertörler tarafından çıkış akımları sağlanmıştır. 0- 0,8 saniye aralığında, sistem birincil kontrol aşamasında olup, her bir konvertör iç kontrolcüsü tarafından denetlenerek hedeflenen akım değerlerine ulaşmaya çalışmaktadır. Bu süreçte dalgalanmalar gözlemlense de kontrol mekanizması sayesinde sistem hızla dengeye oturmaktadır. 0,8- 2,0 saniyeleri arasında, ikincil kontrol sistemi devreye girmekte ve yüklerin ihtiyacına göre konvertörlerin çıkış akımları ayarlanmaktadır. Bu süreçte, yüklerin türüne ve dinamik taleplerine bağlı olarak her bir konvertörün çıkış akımında değişiklikler meydana gelmektedir. 2,0 saniyesinden itibaren, oransal yük paylaşımı uygulanmış ve her konvertör, bağlı olduğu bara ve yük karakteristiğine göre çıkış akımını sabitlemiştir. Bu noktada, enerji kaynakları arasındaki güç paylaşımı dengelenmiş ve sistemin kararlı hale geldiği gözlemlenmiştir.



Şekil 6. Girişinde konvertör bağlı olmayan noktaların üzerine düşen gerilimlerin değişimi.

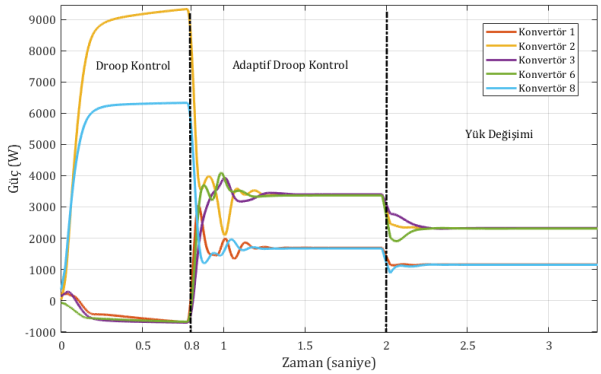


Şekil 7. DA mikro şebekeye bağlı 5 adet konvertörün

çıkış akımlarının değişimi.

Şekil 8'de gösterilen grafik, adaptif droop kontrolü ile sağlanan dinamik güç paylaşım mekanizmasının etkinliğini göstermektedir. Yüklerin türüne bağlı olarak konvertörlerden sağlanan akım değerleri değişmekte ve sistemin değişen yük koşullarına uyum sağlayarak stabil hale geldiği görülmektedir. Son aşamada, yük paylaşımının başarılı bir şekilde tamamlandığı ve her bir konvertörün kendisine düşen yük miktarına göre akım sağladığı doğrulanmıştır.

Elde edilen bulgular, adaptif droop kontrol algoritmasının geleneksel droop kontrol stratejisine kıyasla mikro şebekelerde daha etkin bir gerilim düzenlemesi ve yük paylaşımı sağladığını göstermektedir. Adaptif droop kontrolü, değişken yük koşullarına daha hızlı yanıt vererek voltaj sapmalarını minimuma indirmekte ve enerji kayıplarını azaltarak sistem verimliliğini artırmaktadır. Simülasyon verileri ayrıca, adaptif droop kontrolünün kaynaklar arasında daha hassas bir güç paylaşımı sağlayarak enerji sistemlerinin daha dengeli çalışmasını mümkün kıldığını ortaya koymuştur.



Şekil 8. DA mikro şebekeye bağlı 5 adet konvertörün çıkış güçlerinin değişimi.

Grafik analizleri, mikro şebekenin adaptif droop kontrol ile daha hızlı ve stabil bir şekilde dengeye ulaştığını göstermektedir. P Konvertör Gücü grafiğinde, her bir konvertörün güç transferinin zamanla stabilize olduğu ve ikincil kontrol mekanizmasının etkin çalıştığı görülmüştür. Bara gerilimleri incelendiğinde, ilk düzenleme aşamasında belirli dalgalanmalar olduğu, ancak adaptif droop kontrolünün sistemde gerilim farklılıklarını düzenleyerek stabil bir gerilim profili oluşturduğu tespit edilmiştir. Akım değişimleri incelendiğinde ise, mikro şebekenin dengesiz yük koşullarına hızlı uyum sağladığı ve ikincil kontrol mekanizması sayesinde akım paylaşımının dengeli hale geldiği gözlemlenmiştir.

4. Sonuç

Sonuç olarak, bu çalışma DA mikro şebekelerde adaptif droop kontrol stratejisinin, geleneksel yaklaşımlara göre daha verimli ve stabil bir enerji yönetimi sağladığını ortaya koymaktadır. Simülasyon sonuçları, adaptif droop kontrolün değişken yük koşullarına hızlı yanıt vererek voltaj sapmalarını azalttığını ve sistem kararlılığını artırdığını göstermiştir. Ayrıca, adaptif droop kontrol stratejisinin, kaynaklar arasındaki orantısal güç paylaşımında doğruluğu artırarak enerji kayıplarını minimize ettiği ve sistemin genel verimliliğini yükselttiği gözlemlenmiştir. Ayrıca adaptif droop kontrolcü ile gerilim regülasyonunun sağlandığı ve yük değişimlerine de tepki vererek kararlılığın devam etmesi sağlanmıştır. Böylelikle önerilen kontrol sistemi mikro şebekelerin değişken yük koşullarında güvenilir ve kararlı bir şekilde çalışmasını sağlayarak enerji yönetiminde önemli bir çözüm sunmaktadır. Çalışma, enerji sistemlerinin gelecekteki kontrol stratejilerinin geliştirilmesine yönelik önemli bir temel oluşturmuş ve mikro şebekelerde adaptif kontrol yaklaşımlarının uygulanabilirliğini göstermiştir. Gelecekteki çalışmalar, bu kontrol stratejisinin farklı şebeke koşullarında ve gerçek zamanlı uygulamalarda test edilerek daha da geliştirilmesine odaklanmalıdır.

Katkı Oranı Beyanı

Yazarların katkı yüzdeleri aşağıda verilmiştir. Yazarlar makaleyi incelemiş ve onaylamıştır.

	A.A.Ö.	T.A.	K.A.
K	20	40	40
T	30	50	20
Y	30	50	20
VTI	70	20	10
VAY	30	40	30
KT	80	10	10
YZ	80	10	10
KI	20	70	10
GR	20	20	60

K= kavram, T= tasarım, Y= yönetim, VTI= veri toplama ve/veya işleme, VAY= veri analizi ve/veya yorumlama, KT= kaynak tarama, YZ= Yazım, KI= kritik inceleme, GR= gönderim ve revizyon.

Çatışma Beyanı

Yazarlar bu çalışmada hiçbir çıkar ilişkisi olmadığını beyan etmektedirler.

Etik Onay Beyanı

Bu araştırmada hayvanlar ve insanlar üzerinde herhangi bir çalışma yapılmadığı için etik kurul onayı alınmamıştır.

Kaynaklar

Adhikari S, Tang Y, Wang P. 2016. Secondary control for DC microgrids: A review. In: Proceedings of the 2016 Asian Conference on Energy, Power and Transportation Electrification (ACEPT), 25-28 October 2016, Singapore, Singapore, pp: 1-6.

Al-Ismail FS. 2021. DC microgrid planning, operation, and

control: A comprehensive review. IEEE Access, 9: pp: 36154-36172.

Aluko A, Buraimoh E, Oni OE, Davidson IE. 2022. Advanced distributed cooperative secondary control of islanded DC microgrids. Energies, 15(11): pp: 3988.

Biglarahmadi M, Ketabi A, Baghaee HR, Guerrero JM. 2024. Two-layer distributed control of hybrid AC/DC microgrids supplying nonlinear, unbalanced and constant-power loads. Int J Electr Power Energy Syst, 162: pp: 110298.

Brusso B, Bose B. 2014. Power electronics—historical perspective and my experience [history]. IEEE Ind Appl Mag, 20(2): pp: 7-81.

Bulut U, Muratoglu G. 2018. Renewable energy in Türkiye: Great potential, low but increasing utilization, and an empirical analysis on renewable energy-growth nexus. Energy Policy, 123: pp: 240-250.

Choudhury S. 2020. A comprehensive review on issues, investigations, control and protection trends, technical challenges and future directions for microgrid technology. Int Trans Electr Energy Syst, 30(9): pp: e12446.

Cucuzzella M, Trip S, De Persis C, Cheng X, Ferrara A, Van der Schaft A. 2019. A robust consensus algorithm for current sharing and voltage regulation in DC microgrids. IEEE Trans Control Syst Technol, 27(4): pp: 1583-1595.

Da Silva WWAG, Oliveira TR, Donoso-Garcia PF. 2020. Hybrid distributed and decentralized secondary control strategy to attain accurate power sharing and improved voltage restoration in DC microgrids. IEEE Trans Power Electron, 35(6): pp: 6458-6469.

Dam DH, Lee HH. 2016. An adaptive power distributed control method to ensure proportional load power sharing in DC microgrid considering equivalent line impedances. In: Proceedings of the 2016 IEEE Energy Conversion Congress and Exposition (ECCE), 18-22 September 2016, Milwaukee, WI, USA, USA, pp: 1-6.

Dechamps P. 2023. The IEA World Energy Outlook 2022 – a brief analysis and implications. Eur Energy Clim J, 11(3): pp: 100-103.

Dragicevic T, Lu X, Vasquez JC, Guerrero JM. 2016. DC microgrids- Part I: A review of control strategies and stabilization techniques. IEEE Trans Power Electron, 31(7): pp: 4876-4891.

Elmouatamid A, Ouladsine R, Bakhouya M, El Kamoun N, Khaidar M, Zine-Dine K. 2020. Review of control and energy management approaches in micro-grid systems. Energies, 14(1): pp: 168.

Fang J, Shuai Z, Zhang X, Shen X, Shen ZJ. 2019. Secondary power sharing regulation strategy for a DC microgrid via maximum loading factor. IEEE Trans Power Electron, 34(12): pp: 11856-11867.

Gao F, Kang R, Cao J, Yang T. 2019. Primary and secondary control in DC microgrids: a review. J Mod Power Syst Clean Energy, 7(2): pp: 227-242.

Ghanimi HMJ, Ghoreishy H, Mirimani SM. 2024. Enhancing DC microgrids cluster performance with distributed event-triggered consensus protocols. e-Prime Adv Electr Eng Electron Energy, 10: pp: 100773.

Guarnieri M. 2018. Revolving and evolving—early DC machines [historical]. IEEE Ind Electron Mag, 12(3): pp: 38-43.

Guerrero JM, Vasquez JC, Matas J, De Vicuña LG, Castilla M. 2011. Hierarchical control of droop-controlled AC and DC microgrids- a general approach toward standardization. IEEE Trans Ind Electron, 58(1): pp: 158-172.

Hamad B, Al-Durra A, Zeineldin H, Mohamed YARI. 2024. Robust distributed secondary control for DC microgrids enhancing stability and communication delay tolerance. IEEE Trans Energy Convers, Early Access: pp: 1-16.

Hatziargyriou N, Dimeas A, Vasilakis N, Lagos D, Kontou A. 2020. The Kythnos microgrid: a 20-year history. IEEE Electrif Mag, 8(4): pp: 46-54.

Hatziargyriou N. 2014. Microgrids: architectures and control. Wiley-IEEE Press, Chichester, UK, pp: 317.

Hou Y, Liu M, Shen N. 2024. A simulation research method for data injection attacks on DC microgrids. In: Proceedings of the 2024 China Automation Congress (CAC), November 2024, Beijing, China, China, pp: 2460-2465.

Hu J, Duan J, Ma H, Chow MY. 2018. Distributed adaptive droop control for optimal power dispatch in DC microgrid. IEEE Trans Ind Electron, 65(1): pp: 778-789.

Jasim AM, Jasim BH, Bureš V, Mikulecký P. 2022. A new decentralized robust secondary control for smart islanded microgrids. Sensors (Basel), 22(22): pp: 8709.

Kaysal A, Köroğlu S, Oğuz Y. 2023. Adaptive droop controller design for energy management system in DC microgrid architectures. Pamukkale Univ J Eng Sci, 29(7): pp: 692-700.

Kaysal A. 2023. Mikro şebekeler için hiyerarşik enerji yönetim sistemi tasarımı ve uygulaması. Pamukkale Üniversitesi, Fen Bilimleri Enstitüsü, Denizli, Türkiye, pp: 149.

Kirtay E. 2010. Current status and future prospects of renewable energy use in Türkiye. Energy Explor Exploit, 28(5): pp: 411-431.

Kumar J, Agarwal A, Agarwal V. 2019. A review on overall control of DC microgrids. J Energy Storage, 21: pp: 113-138.

Küçük G, Yüce Dural B. 2022. Avrupa Yeşil Mutabakatı ve yeşil ekonomiye geçiş: enerji senaryoları üzerinden bir değerlendirme. Anadolu Univ J Soc Sci, 22(1): pp: 137-156.

Lotfi H, Khodaei A. 2017. AC versus DC microgrid planning. IEEE Trans Smart Grid, 8(1): pp: 296-304.

Moradi M, Heydari M, Zarei SF. 2023. An overview on consensus-based distributed secondary control schemes in DC microgrids. Electr Power Syst Res, 225: pp: 109870.

Mosa MA, Ali AA. 2021. Energy management system of low voltage DC microgrid using mixed-integer nonlinear programming and a global optimization technique. Electr Power Syst Res, 192: pp: 106971.

Nahata P, La Bella A, Scattolini R, Ferrari-Trecate G. 2020. Hierarchical control in islanded DC microgrids with flexible structures. IEEE Trans Control Syst Technol, 29(6): pp: 2379-2392.

Nasirian V, Davoudi A, Lewis FL, Guerrero JM. 2014. Distributed adaptive droop control for DC distribution systems. IEEE Trans Energy Convers, 29(4): pp: 944-956.

Planas E, Andreu J, Gárate JI, Martínez De Alegría I, Ibarra E. 2015. AC and DC technology in microgrids: a review. Renew Sustain Energy Rev, 43: pp: 726-749.

Polleux L, Guerassimoff G, Marmorat JP, Sandoval-Moreno J, Schuhler T. 2022. An overview of the challenges of solar power integration in isolated industrial microgrids with reliability constraints. Renew Sustain Energy Rev, 155: pp: 111955.

Pourbehzadi M, Niknam T, Aghaei J, Mokryani G, Shafie-khah M, Catalão JPS. 2019. Optimal operation of hybrid AC/DC microgrids under uncertainty of renewable energy resources: a comprehensive review. Int J Electr Power Energy Syst, 109: pp: 139-159.

Rashad M, Raoof U, Ashraf M, Ashfaq Ahmed B. 2018. Proportional load sharing and stability of DC microgrid with distributed architecture using SM controller. Math Probl Eng, 2018: pp: 1-16.

Saygin D, Tör OB, Cebeci ME, Teimourzadeh S, Godron P. 2021.

Increasing Türkiye's power system flexibility for grid integration of 50% renewable energy share. Energy Strategy Rev, 34: pp: 100625.

Shafiee Q, Dragičević T, Vasquez JC, Guerrero JM. 2014. Hierarchical control for multiple DC-microgrids clusters. IEEE Trans Energy Convers, 29(4): pp: 922-933.

Shuai Z, Fang J, Ning F, Shen ZJ. 2018. Hierarchical structure and bus voltage control of DC microgrid. Renew Sustain Energy Rev, 82: pp: 3670-3682.

Taye BA, Choudhury NBD. 2023. A dynamic droop control for a DC microgrid to enhance voltage profile and proportional current sharing. Electr Power Syst Res, 221: pp: 109438.

Vasquez J, Guerrero J, Miret J, Castilla M, Garcia De Vicuna L. 2010. Hierarchical control of intelligent microgrids. IEEE Ind Electron Mag, 4(4): pp: 23-29.

Vu TV, Perkins D, Diaz F, Gonsoulin D, Edrington CS, El-Mezyani T. 2017. Robust adaptive droop control for DC microgrids. Electr Power Syst Res, 146: pp: 95-106.

Wang P, Qin Z, Yuan J, Blaabjerg F. 2024. Dual active bridge converter and its control. In: Control of Power Electronic Converters and Systems: Volume 4, Elsevier Academic Press, Burlington, MA, USA, pp: 71-100.

Yamashita DY, Vechiu I, Gaubert JP. 2020. A review of hierarchical control for building microgrids. Renew Sustain Energy Rev, 118: pp: 109523.

Zia MF, Elbouchikhi E, Benbouzid M. 2018. Microgrids energy management systems: a critical review on methods, solutions, and prospects. Appl Energy, 222: pp: 1033-1055.

Shafiee Q, Nasirian V, Guerrero JM, Lewis FL, Davoudi A. 2014. Team oriented adaptive droop control for autonomous AC microgrids. In: Proceedings of the 40th Annual Conference of the IEEE Industrial Electronics Society (IECON 2014), October 2014, Dallas, TX, USA, USA, pp: 1861-1867.

Liu HP, Hu J, Li Z, Chan KW, Guerrero JM. 2020. A novel droop control method based on virtual frequency in DC microgrid. IEEE Trans Ind Electron, 67(10): pp: 8446-8456.

.

Black Sea Journal of Engineering and Science
doi: 10.34248/bsengineering.1657267

Open Access Journal
e-ISSN: 2619 – 8991

Research Article
Volume 8 - Issue 4: 937-944 / July 2025

EVALUATION OF AFTER SERVICE LOCATION WITH HESITANT FUZZY VIKOR: A CASE OF DRONE COMPANY IN TÜRKİYE

Dilan SARPKAYA[1]*, Gül Tekin TEMUR[2]

[1]*Bahçeşehir University, Faculty of Engineering and Natural Sciences, Department of Industrial Engineering, 34353, İstanbul, Türkiye*
[2]*Bahçeşehir University, Faculty of Engineering and Natural Sciences, Department of Industrial Engineering, 34353, İstanbul, Türkiye*

Abstract: This study is conducted to evaluate the suitability of after sales services in drone technology with the use of Hesitant Fuzzy VIKOR method. The main aim of the study is to compare cities' performances with considering critically important factors such as customer accessibility, operational costs, infrastructure availability, logistics access and regional needs. In this context, eight different after sales service locations of a drone company are evaluated. The research aimed to guide strategic planning processes of decision makers and to determine which cities are more suitable for the adoption of drone technology in commercial and logistics applications. At the same time, infrastructural availability considering regional needs and improvements of operational strategies are points that aimed to draw attention. The findings provide light on the order of importance of the criteria, as well as the strengths and weaknesses of the cities in terms of their ability to effectively use drone technology with ease.

Keywords: Drone technology, After sales service location, Hesitant fuzzy, Decision making

***Corresponding author:** Bahçeşehir University, Faculty of Engineering and Natural Sciences, Department of Industrial Engineering, 34353, İstanbul, Türkiye
E mail: dilan.emgili@toros.edu.tr (D. SARPKAYA)
Dilan SARPKAYA https://orcid.org/0000-0002-4515-5589
Gül Tekin TEMUR https://orcid.org/0000-0003-3853-0974

Received: Mar 13, 2025
Accepted: April 18, 2025
Published: July 15, 2025

Cite as: Sarpkaya D, Temur GT. 2025. Evaluation of after service location with hesitant fuzzy vikor: A case of drone company in Türkiye. BSJ Eng Sci, 8(4): 937-944.

1. Introduction

The execution of after-sale services is an essential component in ensuring continued competitiveness in the relevant industry and enhancing the level of pleasure experienced by customers. The proper identification of the service points is very important in order to reduce the costs and increase the effectiveness of the service delivery especially in the technology and service industries. From this view, MCDM approaches provide the solutions to the complex decision-making processes by performing the analysis in a systematic and efficient manner. The Hesitant Fuzzy VIKOR method is a flexible and realistic approach to solving multi-criteria decision-making problems by incorporating the uncertainty and ambiguity in the decision makers' preferences (Wei and Zhang, 2014). There is no need for decision makers to make precise appraisal when using this method than the traditional VIKOR strategy. This method allows decision makers to stipulate different preference ranges. Thus, the ambiguities that are inherent in the decision-making process are eliminated and decisions are made within the context of a more real-life situation (Liao et al., 2015).

As such, the Hesitant Fuzzy VIKOR approach is used for the purpose of this study to evaluate after sales support centres in eight different cities in the United States. In this analysis, criteria such as cost, quality, accessibility and support service capability were considered. Furthermore, the priority correlations among these criteria were determined by employing language terms (Liao and Xu, 2013). Then, calculations were made for each city, and conclusions were made on the overall performance of the cities (Gou et al., 2021).

Moreover, the research does not only offer a flexible decision-making recommendation for the case of decision making with multiple criteria but also proves the effectiveness of the Hesitant Fuzzy VIKOR approach in reducing the effect of the uncertainties. The numerical ranges of linguistic concepts are used in the decision-making processes during the application of the approach. Qian et al. (2023) and Liao et al. (2018) have stated that these phrases are useful in deriving information from sources that are somewhat vague and complex.

Decision makers may increase their accuracy by-elaborating their understanding of the linguistic words that are used in the decisions made by groups of people. This is because generating the numerical ranges of linguistic words leads to more accurate and consistent decision-making outputs (Gou et al., 2020). In this case, defining the numerical ranges of linguistic words is an important step to enhance the effectiveness of decision-making processes (Qian et al., 2024).

For the purpose of the study, the after-sales service regions of a drone manufacturer in Türkiye will be examined on the basis of several aspects at several locations. To this end, it is expected that an optimization of after-sales services will be achieved thus. Within the

This work is licensed (CC BY-NC 4.0) under Creative Commons Attribution 4.0 International License

remaining parts, research that were carried out in this particular field, specifics of the methodology, findings from the application, and the outcomes of the study are described. There is a high probability that the findings of the study will assist firms in enhancing their after-sales service strategy and in making decisions that will result in increased levels of customer satisfaction.

2. Literature Review

2.1. Decision Making

Identification of linguistic terms' numerical ranges and its use for decision making processes has been extensively discussed in the literature. Delgado et al. (1998) improved fusion operator to merge linguistic and numerical information. This operator develops a selection process for alternatives and allows obtaining solutions that comply with the majority opinion of experts.

Decision making is a critical step, and it can have a direct effect on success of companies. For instance, decisions for the companies which are in a problematic financial status play a critical role for the future of the company and return of partners (Leech et al., 1999). With this perspective, management information systems have also critical role to optimise the decision-making processes of companies with filtering and transforming information. These systems make more efficient and effective decisions possible thanks to easier data accessibility and control (Torres et al., 2022).

Research conducted for small and medium enterprises (SMEs) indicate that strong decision-making processes are very crucial for success and sustainability of the companies. This research establishes that financial accuracy, risk management, innovation and customer relationships are key factors that influence the performance of SMEs (Ullah et al., 2024). In addition, the application of the latest technologies can improve decision-making and make the right decision quickly in a complex environment (Neziraj and Shaqiri, 2018).

Hesitant fuzzy sets (HFS) are a very convenient tool for decision makers when defining the values of a variable when decision makers are uncertain or hesitant between more than two values (Zhu and Xu, 2017). Hesitant fuzzy sets can be used properly to the situation that involve imprecise and complex evaluations. These sets are also improved to extended versions in order to solve the problem of information loss (Zhu and Xu, 2017). In addition, hesitant bipolar-valued fuzzy sets (HBVFS) and bipolar hesitant fuzzy sets (BVHFS) are also developed for the multi attribute group decision making processes (Mandal and Ranadive, 2018). Like the reasons mentioned above, these sets offer a friendly and comprehensive environment for decision makers to express their hesitancy on multiple attributes. Application of hesitant fuzzy sets during decision making processes plays an important role especially for assessment of service locations. As an example, Karaaslan and Karamaz (2022) modelled disagreements between decision makers with using parametric versions of HFSs. Interval-valued hesitant fuzzy sets are defined to indicate uncertainty during decision making process (Shu-we, 2013). These sets are applicable to the situations where evaluations are interval based and able to analyse relationships with other fuzzy set types.

2.2. Drone After Sales Services

Rapid developments in drone technology increased the importance of after sales services. These services play critical role to provide customer satisfaction, increase the brand loyalty and support long term use of technological commodities.

The study of Hokey Min (2023) investigated the application of drone technologies in e-trade and logistics sectors and pointed out the importance of after sales services for the purpose of operational sustainability. More specifically, the study remarked that repair and maintenance processes of drones have direct impact on delivery times and customer satisfaction (Min,2023). In a similar manner, the study of Kunze and Li (2023) emphasise the comparison of air drones and land delivery robots and after sales services importance for the purpose of long-term use of technological devices (Li and Kunze, 2023).

Another study carried by Lafuente (2024) also draw attention to the optimization of afters sales service location while considering drone operations in 5G technology. Thanks to data transmission opportunity that provided by 5G, repair and maintenance processes could be managed in more efficient way (Lafuente, 2024).

Drone service companies' economical evaluations are addressed by Widada and Rahadi (2024), while the study pointed out the contribution of after sales services to company valuation. The study indicates the customer satisfaction and services quality impacts the financial performance of the company (Widada and Rahadi, 2024).

During the discussion of ethical dimension of drone technology, Molina and Campos (2018) converse about the requirement of after sales services arrangement in a regulational framework. Particularly, security and confidentiality issues should be considered during the services processes (Molina and Campos, 2018). The study of Ravich (2018) also pointed out that regulations may impact on effectiveness off after sales services and for this reason there is a need for more flexible adjustment framework.

Nonami's study discusses how after sales services will evolve with technological advances while addressing the future potential of drone technology. The study foresee that use of automation and artificial intelligence will increase for the repair and maintenance processes of drones (Nonami, 2016). In addition to that, study of Pöysäri (2023) indicated the important role of after sales services of drones which used in industrial area in order to increase the customer trust.

In the literature, latest studies considering drone technology is mainly related to fields such as operational optimization (Yin et al., 2024; Li et al., 2023),

sustainability (Bruni et al., 2024), technological advancements (Akram and Araissi, 2024; Soares et al., 2023), applications of drones in delivery services (Singh et al., 2024).

After sales services of drone companies have strategic importance since it has contribution to company valuation with customer satisfaction, operational efficiency. Optimization of service locations, technological integrations and ethical arrangements come to the forefront factors in this sector which is very limited in the literature. Flexibility of regulations and innovator technology integrations such as artificial intelligence have critical importance for future development of after sales services

3. Materials and Methods

3.1. Research Model

The aim of this study is to evaluate the performance of the current cities where a drone company provides after-sales service and to rank these cities.

1	Criteria Definition and Forming Decision Maker Group
2	Alternative Selection
3	Preparation of Evaluation Forms
4	Data Collection
5	Converting Linguistic Evaluations into Fuzzy Numbers
6	Calculating Fuzzy Weights for Criteria
7	Creation of Fuzzy Decision Matrix for Alternatives
8	Determination of Fuzzy Best and Worst Values
9	Calculation of Distances of Alternatives from the Best and Worst Values
10	Calculation of S and R Values
11	Clarification of Fuzzy Numbers and Ranking of Alternatives
12	Determination of Solution

Figure 1. Flow of the methodology.

In this process, the Hesitant Fuzzy Set (HFS) approach was used, taking into account the uncertainty and hesitations of decision makers.

3.2. Universe Sample (Research Group)

The research universe consists of the after-sales service locations of a drone manufacturing company based in Mersin, Türkiye. The study focuses on service centres operating in eight different cities: Adana, Konya, Kayseri, Urfa, Amasya, İzmir, Diyarbakır, and Mersin.

The sample group includes company personnel responsible for logistics, sales support, finance, and service operations. A total of 8 experts participated in the evaluation process, providing assessments for each location based on predefined criteria.

3.3. Data Collection Tools

The data for this study were collected through structured evaluation forms designed to assess the performance of different after-sales service locations with eight experts who are currently working in the company. The evaluation criteria formed through managers of the company and literature. Table 1 indicates these studies:

Table 1. Criteria list

Criteria	Related Study
Customer Accessibility	Facility Location Selection Using Complete and Partial Ranking MCDM Methods *Ray and Dan, 2015; Shaikh and Kim, 2021*
Operational Costs	Hub Location Selection for Third-Party Logistics Services Shiau et al., 2011; Yiğit et al., 2024
Infrastructure Availability	Design of a Reliable Facility Location Model for Health Service Networks Zarrinpoor et al., 2016
Logistic Accessibility	Determining the Location of Shared Electric Micro-Mobility Stations Jaber et al., 2024; Sousa and Calili, 2021
Regional Demand	Solving a Real-World Urban Postal Service System Redesign Problem Yu et al., 2021; Weaver et al., 2023

Each criterion was evaluated using hesitant fuzzy linguistic terms which indicated in Table 2 below, allowing experts to express uncertainty in their assessments.

Table 2: Triangular Fuzzy Sets

Linguistic Term	Hesitant Fuzzy Numbers
Absolutely High Importance (AHI)	(7,9,9)
Very High Importance (VHI)	(5,7,9)
Essentially High Importance (ESHI)	(3,5,7)
Weakly High Importance (WHI)	(1,3,5)
Equally High Importance (EHI)	(1,1,3)
Exactly Equal (EE)	(1,1,1)
Equally Low Importance (ELI)	(0.33,1,1)
Weakly Low Importance (WLI)	(0.2,0.33,1)
Essentially Low Importance (ESLI)	(0.14,0.2,0.33)
Very Low Importance (VLI)	(0.11,0.14,0.2)
Absolutely Low Importance (ALI)	(0.11,0.11,0.14)

The linguistic terms were then converted into hesitant fuzzy numbers (triangular fuzzy sets) for further analysis.

3.4. Data Analysis

HFS provides an effective method in cases where decision makers hesitate between multiple alternatives. Hesitant Fuzzy Sets are the extension of fuzzy logic methodologies. It can be used when decision makers can indicate more than one membership degree. Steps of HFS calculations are indicated below that used in this study.

Definition:

HFS may contain more than one membership degree for one variable in the universe. For one element x in the hesitant fuzzy set can be described as:

$$\widetilde{H}(\mathrm{x}) = \{\mu_{1(x)}, \mu_{2(x)}, \dots, \mu_{k(x)}\} \quad (1)$$

where:

$\widetilde{H}(\mathrm{x})$ possible membership degrees for element x.

$\mu_{i(x)}$ describes the hesitant fuzzy membership values of element x, where i=1,2,3,.,k.

Hesitant Fuzzy Decision Matrix:

The hesitant fuzzy decision matrix for alternatives $(A_1,.,A_m)$ and criteria $(C_1,.,C_n)$ is created as follows:

where H_{ij}Hij denotes the hesitant fuzzy membership values of alternative Ai for criterion C_j.

Normalized Hesitant Fuzzy Values:

Normalization of hesitant fuzzy values is necessary to compensate for the different scales of the criteria. Normalized hesitant fuzzy values are calculated as follows:

For benefit criteria:

$$\tilde{x}_{ij} = \frac{x_{ij}}{\max(x_{ij})} \quad (2)$$

For cost criteria:

$$\tilde{x}_{ij} = \frac{\min(x_{ij})}{x_{ij}} \quad (3)$$

Here:

$\max(x_{ij})$: The maximum membership degree for criterion Cj,

$\min(x_{ij})$: The minimum membership degree for criterion Cj.

Weighted Hesitant Fuzzy Values:

Weighting calculations are done in order to evaluate importance degree of criterion. Weights hesitant fuzzy values are calculated as follows:

$$v_{ij} = w_j \cdot \tilde{x}_{ij} \quad (4)$$

where:

w_j: The weight of the criterion.

Hesitant Fuzzy VIKOR Method:

Hesitant fuzzy VIKOR method is used to rank alternatives. This method includes following steps.

Determination of Positive and Negative Ideal Solutions

Positive ideal solution is maximum value for each criterion.

Negative ideal solution is minimum value for each criterion.

Calculation of Distances of Alternatives to Ideal Solutions:

S (Total Distance):

$$S_i = \sum w_j d\left(\tilde{x}_{ij}, \tilde{x}_j^+\right) \quad (5)$$

Calculation of Relative Closeness Values of Alternatives:

R (Relative Closeness) is calculated as follows:

$$R_i = \sum \max\left(w_j d\left(\tilde{x}_{ij}, \tilde{x}_j^+\right)\right) \quad (6)$$

where $d\left(\tilde{x}_{ij}, \tilde{x}_j^+\right)$ represents the distance between hesitant fuzzy sets.

The VIKOR index (Q) is calculated as follows:

$$Q_i = v \cdot \frac{S_i - S^*}{S^- - S^*} + (1 - v) \cdot \frac{R_i - R^*}{R^- - R^*} \quad (7)$$

where:

$S^* \text{ and } S^-$: The min and max values of S.

$R^* \text{ and } R^-$: The min and max values of R.

v: The compromise parameter (generally taken as 0.5).

Rank of Alternatives: Alternatives are ranked based on Q, S, and R values. The alternative with the lowest Q value is considered the best choice.

4. Results

The study is conducted to evaluate performances and current situation of after sales services by Hesitant Fuzzy VIKOR method. As a case study, drone producer company is used. This company has eight after sales services location in different regions of Türkiye. The aim is to analyse the current situation of locations in order make required actions to have better customer satisfaction.

During the analysis, the distances of the alternatives to the positive and negative ideal solutions were calculated in line with the determined criteria and the alternatives were ranked based on these distances. The findings guide decision makers in determining the most appropriate option and reveal the effect of the weights of the criteria on the results. Table 3 indicates the determined criterion. These criteria have decided with field related specialists.

Table 3: Determined Criterion

Customer Accessibility	It is an important factor that evaluates the ease of customer access for drone technology. Especially, this criterion reflects the capacity of fast and non-problematic delivery to customers. This criterion is an important factor that increases the customer satisfaction.
Operational Costs	It defines the total operational costs of drones. This criterion includes fuel, maintenance, labour and other operational costs. Lower costs increase the economical sustainability of technology and increases the probability of being preferred.
Infrastructure Availability	It evaluates the integration of drone technology to current infrastructure. This criterion consists of landing zone, charging station and contexts such as air zone regulations. Infrastructural conformance has direct impact on efficiency of drone operations.
Logistics Access	It refers to the integration of drones into logistics networks and their effectiveness in delivery processes. This criterion evaluates the capacity of drones to reach target points from warehouses or logistics centres, especially in last-mile delivery processes.
Regional Need	It defines the suitability of drone technology for specific regional needs. This criterion takes into consideration geographical situations, population intensity and regional demand. Regional need suitability can increase the ratio of technological adaptation.

Thanks to contribution of experts via structured evaluation forms, linguistic variables converted into triangular fuzzy set, fuzzy decision matrix and best fuzzy and worst fuzzy values are calculated in order to reach the performance of alternatives according to each criterion (Table 4, Table 5 and Table 5).

Table 4. Integrated Fuzzy Weights of Criteria

Criteria	Fuzzy weights (w_j)		
	l	m	u
C1	0,25	0,2456	0,2308
C2	0,1875	0,193	0,2028
C3	0,1375	0,1491	0,1678
C4	0,15	0,1491	0,1608
C5	0,275	0,2632	0,2378

Table 5. Fuzzy Decision Matrix

Criteria	A1			A2			A3			A4		
	l	m	u	l	m	u	l	m	u	l	m	u
C1	7	9	9	3	5	7	7	9	9	3	5	7
C2	5	7	9	1	3	5	3	5	7	1	1	3
C3	5	7	9	1	1	3	1	1	3	1	3	5
C4	5	7	9	3	5	7	5	7	9	1	1	1
C5	7	9	9	7	9	9	7	9	9	5	7	9

Criteria	A5			A6			A7			A8		
	l	m	u	l	m	u	l	m	u	l	m	u
C1	5	7	9	3	5	7	5	7	9	7	9	9
C2	5	7	9	3	5	7	5	7	9	7	9	9
C3	3	5	7	1	3	5	3	5	7	7	9	9
C4	1	3	5	1	1	3	1	1	3	7	9	9
C5	3	5	7	3	5	7	5	7	9	7	9	9

Table 6. Best Fuzzy and Worst Fuzzy Values

Criteria	$\tilde{f}_j^*$		
	l	m	u
C1	9.0	9.0	9.0
C2	9.0	9.0	9.0
C3	9.0	9.0	9.0
C4	9.0	9.0	9.0
C5	9.0	9.0	9.0
Criteria	$\tilde{f}_j^-$		
	l	m	u
C1	3.0	5.0	7.0
C2	1.0	1.0	3.0
C3	1.0	1.0	3.0
C4	1.0	1.0	1.0
C5	3.0	5.0	7.0

Positive ideal solution and negative ideal solution are identified, distances of alternatives to these solutions are evaluated. These distances created baseline in order to evaluate the performance of alternatives.

Table 7. $\tilde{S}_i$ and $\tilde{R}_i$ Values

Alternatives	$\tilde{S}_i$		
	l	m	u
A1	0.43	0.15	0.0
A2	0.81	0.65	0.58
A3	0.58	0.35	0.26
A4	0.93	0.85	0.73
A5	0.78	0.6	0.36
A6	0.95	0.85	0.75
A7	0.71	0.55	0.21
A8	0.28	0.0	0.0

Alternatives	$\tilde{R}_i$		
	l	m	u
A1	0.1	0.05	0.0
A2	0.2	0.2	0.2
A3	0.2	0.2	0.2
A4	0.2	0.2	0.2
A5	0.2	0.2	0.2
A6	0.2	0.2	0.2
A7	0.2	0.2	0.15
A8	0.06	0.0	0.0

Values of $\widetilde{S^*}, \widetilde{S^-}, \widetilde{R^*}, \widetilde{R^-}$ are calculated as seen in Table 8.

Table 8. $\widetilde{S^*}, \widetilde{S^-}, \widetilde{R^*}, \widetilde{R^-}$ Values

	l	m	u
$\widetilde{S^*}$	0.2833	0.0	0.0
$\widetilde{S^-}$	0.95	0.85	0.75
$\widetilde{R^*}$	0.0667	0.0	0.0
$\widetilde{R^-}$	0.2	0.2	0.2

Table 9 indicates the VIKOR results which consists of total distance, maximum distance and VIKOR index. Total distance which referred as S calculated with summation of total distances of alternatives to positive ideal solution. Maximum distance is R value indicates the worst performance of each alternative. VIKOR index which is denoted as Q calculated with the use of compromise value (v= 0,5) and alternatives are ranked. At the end of calculations, alternatives are ranked based on Q values. The lowest Q value alternative defined as a best solution. Ranking can play a guide role to decision maker to choose most suitable choice. The effect of criteria weights on the results was analysed. It was observed that especially the criteria with high weights were decisive in the ranking of the alternatives.

Table 9. Indexes and Rankings

Alternatives	$\tilde{Q}_i$		
	l	m	u
A1	0.2374	0.2132	0.0
A2	0.9	0.8824	0.8889
A3	0.725	0.7059	0.6778
A4	0.9875	1.0	0.9889
A5	0.875	0.8529	0.7445
A6	1.0	1.0	1.0
A7	0.825	0.8235	0.5195
A8	0.0	0.0	0.0

Alternatives	Q_i		R_i		S_i	
	Index	Rank	Index	Rank	Index	Rank
A1	0,15	2	0,20	2	0,25	2
A2	0,89	6	0,71	6	1	4
A3	0,70	3	0,42	3	1	4
A4	0,99	7	0,88	7	1	4
A5	0,82	5	0,61	5	1	4
A6	1	8	0,89	8	1	4
A7	0,72	4	0,52	4	0,91	3
A8	0	1	0,09	1	0,11	1

Table 10. Acceptable Stability in Decision Making

Q_i	A8 > A1 > A3 > A7 > A5 > A2 > A4 > A6
S_i	A8 > A1 > A3 > A7 > A5 > A2 > A4 > A6
R_i	A8 > A1 > A7 > A2 > A3 > A4 > A5 > A6

As seen in Table 10, two main conditions are evaluated based on rankings.

Condition 1: Acceptable Advantage

This condition checks if the distance between the best and the second-best alternative is not more than a certain threshold, as given by the Q ~ values.

The difference between the first two ranked alternatives must be less than 0.25:

$(a'') - Q(a') < 0.25 Q(a'') - Q(a') < 0.25$

The difference between the best alternative and the worst alternative must be greater than 0.25:

$Q(a''') - Q(a') > 0.25$

As a result of calculations, first condition provided an acceptable advantage and A8 can be defined as a best alternative.

Condition 2: Acceptable Stability in Decision Making

This condition checks on the consistency of the orderings Q~, S~ and R~. If the ordering Q is mostly consistent with the orderings S and R then the decision stability is ensured. Considering the case of this study, second condition also provided acceptable stability in decision making; Q and S values are mostly similar, and R rankings are parallel to these conclusions.

5. Discussion and Conclusion

This study employed the Hesitant Fuzzy VIKOR approach to assess drone technology according to several parameters. The research suggests that such factors as the accessibility of the customers, the operating costs, the availability of the infrastructure, the accessibility of the logistics and the local requirements are crucial for the acceptance and effectiveness of the drone technology. Specifically, such factors as the convenience of consumer access and the compatibility with the infrastructure are critical and must be considered during the evaluation of the alternatives. This paper contributes to the strategic decision-making process for the uptake of drone technology in the commercial and logistics sectors thereby. In addition, this study examined eight cities with the help of the Hesitant Fuzzy VIKOR approach, based on such characteristics as the ease of customer reach, the costs of operation, the availability of the infrastructure, the ease of logistics, and the regional needs. The analysis of the results has compared the performance of the cities with respect to these criteria and can therefore provide valuable information to decision makers as to which cities are more suitable for the application of drone technology.

The results of the study show that City 8 is the most suitable, with S, R, and The total score of all criteria indicates that City 8 is the most similar to the ideal solution. This city was able to differentiate itself from the other cities because it did very well in critical areas such as access to customers and infrastructure. City 1 was ranked second. This paper proposes fuzzy VIKOR method for assessing after sales service centres as multi-criteria decision-making problem. The findings of the study are enough to enable the company to determine the best service points and improve on its decision-making processes. The use of fuzzy VIKOR method to analyse the data from the decision makers was a better and less restrictive way of making the decision than the conventional approaches. The company can use these results to review its current after sales service plan and make changes if needed. This comparison shows the advantages and disadvantages of the cities in the light of the potential uses of drone technology. It was clear that City 8 and City 1 were the most suitable for the application of drone technology as they outperformed other cities in the country. The strengths of these cities can be used to address the weaknesses identified in other cities. Investment in infrastructure and improvement of logistical access can be used to enhance the position of cities that are currently not very strong. These findings are very useful for decision makers in the strategy development and resource allocation processes.

Author Contributions

The percentages of all authors' contributions are presented below. All authors reviewed and approved the final version of the manuscript.

	D.S.	G.T.T.
C	50	50
D	50	50
S	50	50
DCP	50	50
DAI	50	50
L	50	50
W	50	50
CR	50	50
SR	50	50
PM	50	50
FA	50	50

C=Concept, D= design, S= supervision, DCP= data collection and/or processing, DAI= data analysis and/or interpretation, L= literature search, W= writing, CR= critical review, SR= submission and revision, PM= project management, FA= funding acquisition.

Conflict of Interest

The authors declared that there is no conflict of interest.

Ethical Consideration

Ethics committee approval was not required for this study because of there was no study on animals or humans.

References

Akram J, Anaissi A. 2024. Ddrm: Distributed drone reputation management for trust and reliability in crowdsourced drone services. In: 2024 IEEE International Conference on Web Services (ICWS), IEEE, pp: 921-931.

Bruni ME, Khodaparasti S, Perboli G. 2024. Economic sustainability in last-mile drone delivery problem with fulfillment centers: A mathematical formulation. In: ICORES, pp: 382-389.

de Miguel Molina B, Segarra Oña M. 2018. The drone sector in Europe. Ethics and Civil Drones: European Policies and Proposals for the Industry, pp: 7-33.

Delgado M, Herrera F, Herrera-Viedma E, Martinez L. 1998. Combining numerical and linguistic information in group decision making. Inf Sci, 107(1-4): pp: 177-194.

Gou X, Xu Z, Liao H, Herrera F. 2021. Probabilistic double hierarchy linguistic term set and its use in designing an improved VIKOR method: The application in smart healthcare. J Oper Res Soc, 72(12): pp: 2611-2630.

Jaber A, Ashqar H, Csonka B. 2024. Determining the location of shared electric micro-mobility stations in urban environment. Urban Sci, 8(2): pp: 64.

Karaaslan F, Karamaz F. 2022. Hesitant fuzzy parameterized hesitant fuzzy soft sets and their applications in decision-making. Int J Comput Math, 99(9): pp: 1868-1889.

Leech SA, Clark N, Collier PA. 1999. A generalized model of decision-making processes for companies in financial distress.

Account Forum, 23(2): pp: 155-174.
Li D, Ignatius J, Wang D, Yin Y, Cheng TCE. 2024. A branch-and-price-and-cut algorithm for the truck-drone routing problem with simultaneously delivery and pickup. Nav Res Logist, 71(2): pp: 241-285.
Li F, Kunze O. 2023. A comparative review of air drones (UAVs) and delivery bots (SUGVs) for automated last mile home delivery. Logistics, 7(2): pp: 21.
Liao H, Xu Z. 2013. A VIKOR-based method for hesitant fuzzy multi-criteria decision making. Fuzzy Optim Decis Mak, 12(4): pp: 373-392.
Liao H, Si G, Xu Z, Fujita H. 2018. Hesitant fuzzy linguistic preference utility set and its application in selection of fire rescue plans. Int J Environ Res Public Health, 15(4): pp: 664.
Liao H, Xu Z, Zeng XJ. 2014. Hesitant fuzzy linguistic VIKOR method and its application in qualitative multiple criteria decision making. IEEE Trans Fuzzy Syst, 23(5): pp: 1343-1355.
Mandal P, Ranadive AS. 2019. Hesitant bipolar-valued fuzzy sets and bipolar-valued hesitant fuzzy sets and their applications in multi-attribute group decision making. Granul Comput, 4(3): pp: 559-583.
Min H. 2023. Leveraging drone technology for last-mile deliveries in the e-tailing ecosystem. Sustainability, 15(15): pp: 11588.
Navarro Lafuente A. 2024. Business modelling of 5G-based Drone-as-a-Service solution. Universitat Politècnica de Catalunya, Master's thesis, Barcelona, Spain, pp: 86.
Neziraj EQ, Shaqiri AB. 2018. The impact of information technology in decision making process of companies in Kosovo. Informatologia, 51(1-2): pp: 13-23.
Nonami K. 2016. Drone technology, cutting-edge drone business, and future prospects. J Robot Mechatron, 28(3): pp: 262-272.
Pöysäri A. 2023. Customer value of drones. Aalto University, Master of Science in Economics and Business Administration, Helsinki, Finland, pp: 78.
Qian J, Jin W, Wang X, Yu Y, Zheng M, Miao D. 2023. VIKOR decision making method based on multi-granularity hesitant fuzzy linguistic term sets. In: 2023 International Conference on Cyber-Physical Social Intelligence (ICCSI), pp: 297-302.
Qian J, Wang T, Lu Y, Yu Y. 2024. A multi-granularity hesitant fuzzy linguistic decision making VIKOR method based on entropy weight and information transformation. J Intell Fuzzy Syst, 46(3): pp: 6505-6516.
Ravich TM. 2018. Grounding innovation: How ex-ante prohibitions and ex-post allowances impede commercial drone use. Colum Bus L Rev, pp: 495.
Ray A, De A, Dan PK. 2015. Facility location selection using complete and partial ranking MCDM methods. Int J Ind Syst Eng, 19(2): pp: 262-276.
Shaikh SA, Memon M, Kim KS. 2021. A multi-criteria decision-making approach for ideal business location identification. Appl Sci, 11(11): pp: 4983.
Shiau TA, Lin LM, Ding JF, Chou CC. 2011. Hub location selection of third-party logistics service on multiple countries consolidations for ocean freight forwarders by using fuzzy multiple criteria decision-making (MCDM) approach. Int J Phys Sci, 6(19): pp: 4548-4557.
Shu-we C. 2013. Interval-valued hesitant fuzzy sets. Fuzzy Syst Math, pp: 75-83.
Singh G, Sharma S, Tandon A, Kaur P. 2022. Drone food delivery: A solution to crowding during the global COVID-19 pandemic. IEEE Trans Eng Manage, 71: pp: 3993-4005.
Soares LDP, De Oliveira FM, Kamienski CA, Bittencourt LF. 2023. Drone edge management system (drems): Sequencing drone takeoff and landing. In: 2023 10th International Conference on Future Internet Things Cloud (FiCloud), pp: 114-121.
Sousa M, Almeida MF, Calili R. 2021. Multiple criteria decision making for the achievement of the UN sustainable development goals: A systematic literature review and a research agenda. Sustainability, 13(8): pp: 4129.
Torres ER, Cano CAG, Castillo VS. 2022. Management information systems and their impact on business decision making. Data Metadata, 1: pp: 21.
Ullah A, Khan SD. 2024. Impact of sound decision-making on small and medium businesses in Pakistan. Int J Asian Bus Manage, 3(2): pp: 177-192.
Wei G, Zhang N. 2014. A multiple criteria hesitant fuzzy decision making with Shapley value-based VIKOR method. J Intell Fuzzy Syst, 26(2): pp: 1065-1075.
Widada AAH, Rahadi RA. 2024. Corporate valuation of Indonesian drone service company: Case study of PT Kelana Geospasial. Int J Econ Bus Manage Res, https://doi.org/10.51505/ijebmr.2024.8818 (accessed date: July 11, 2025).
Yigit F, Basilio MP, Pereira V. 2024. A hybrid approach for the multi-criteria-based optimization of sequence-dependent setup-based flow shop scheduling. Mathematics, 12(13): pp: 2007.
Yin Y, Li D, Wang D, Yu Y, Cheng TCE. 2024. Truck-drone pickup and delivery service optimization with availability profiles. Nav Res Logist, Hoboken, USA, pp: 15.
Yu H, Sun X, Solvang WD, Laporte G. 2021. Solving a real-world urban postal service network redesign problem. Transp Res Part A Policy Pract, 147: pp: 1-18.
Zarrinpoor N, Fallahnezhad MS, Pishvaee MS. 2017. Design of a reliable facility location model for health service networks. Int J Eng Trans A Basics, 30(1): pp: 75-84.
Zhu B, Xu Z. 2016. Extended hesitant fuzzy sets. Technol Econ Dev Econ, 22(1): pp: 100-121.

Black Sea Journal of Engineering and Science
doi: 10.34248/bsengineering.1663534

Open Access Journal
e-ISSN: 2619 – 8991

Research Article
Volume 8 - Issue 4: 945-953 / July 2025

DIFFERENTIATION OF GROWTH, INNER ORGAN DEVELOPMENT, GUT MICROBIOTA, GUT HISTOLOGY AND MEAT QUALITY OF JAPANESE QUAILS FED DIETS CONTAINING VARYING AMOUNTS OF *Satureja spicigera (K. Koch)* Boiss LEAF POWDER

Emine DOĞAN[1]*, İsa COŞKUN[2]

[1]*Ahi Evran University, Vocational School of Çiçekdağı, Department of Laboratory and Veterinary Health, 40700, Kırşehir, Türkiye*
[2]*Ahi Evran University, Faculty of Agriculture, Department of Zootechnics, 40100, Kırşehir, Türkiye*

Abstract: This study investigates the impact of varying amounts of *Satureja spicigera* leaf powder (SLP) (the creeping savory) on the growth, inner organ development, gut microbiota, meat quality, and gut histology of quails. The trial included five treatment groups: SLP0 (control, 0%), SLP1 (0.25%), SLP2 (0.5%), SLP3 (0.75%) and SLP4 (1%). The quails were housed in floor pens with 20 chicks per replicate, and there were 4 replicates for each group, leading to a total of 400 quails. At the end of the study, 1 male and 1 female quails from each replicate (a total of 40 quails) were slaughtered, and samples were collected for analysis. Body weight gain (BWG), feed intake (FI), feed conversion ratio (FCR), and visceral organ weights did not change between the groups (P>0.05). Meat quality characteristics (such as sensory criteria) and gut microbiota did not differ between treatment groups. However, a significant reduction in the MDA (Malondialdehyde) level in the breast meat was observed in the SLP1 and SLP2 groups compared to the control group (P<0.05). The breast meat color of the SLP1 and SLP4 groups was significantly lighter than the control group (P<0.05). Villi length (VL) and crypt depth (CD) were greater in the SLP1 group compared to SLP0 and SLP4 groups in the duodenum (P<0.05). The SLP3 group had the highest VL (P<0.01), and the SLP4 group had the lowest CD (P<0.01). Villi length and crypt depth (VL/CD) ratio in SLP3 and SLP4 groups was higher than in SLP0 and SLP1 groups in the jejunum (P<0.05). While no differences in villi length were noted, crypt depth was higher in the SLP3 and SLP4 groups compared to the other groups (P<0.01). The lamina muscularis mucosa (LMM) thickness was lower in the SLP0 group, and VL/CD was lower in the SLP3 group in the ileum (P<0.01). The supplementation of SLP in the diet of Japanese quails enhanced gut health by elevating VL in the duodenum and jejunum, which could enhance digestion. The antioxidant effect of SLP was also evident in the reduction of MDA levels in breast meat. To conclude, *Satureja spicigera* leaf powder can be considered a useful feed additive in quail breeding, particularly for improving intestinal health and for suppressing MDA formation in quail meats.

Keywords: *Satureja spicigera*, MDA, Histomorphology, Quail.

***Corresponding author:** Ahi Evran University, Vocational School of Cicekdagi, Department of Laboratory and Veterinary Health, 40700, Kirsehir, Türkiye
E mail: emine.dogan@ahievran.edu.tr (E. DOĞAN)
Emine DOĞAN https://orcid.org/0000-0002-9572-6503
Isa COŞKUN https://orcid.org/0000-0001-5495-6006

Received: March 22, 2025
Accepted: April 29, 2025
Published: July 15, 2025

Cite as: Doğan E, Coşkun İ. 2025. Differentiation of growth, inner organ development, gut microbiota, gut histology and meat quality of Japanese quails fed diets containing varying amounts of *Satureja spicigera (K. Koch)* Boiss leaf powder. BSJ Eng Sci, 8(4): 945-953.

1. Introduction

After the ban on the use of antibiotics as growth enhancers in animal nutrition, scientists have proposed using medicinal and aromatic plants (MAPs) to support growth without negatively affecting animal, instead of antibiotics. Thanks to their bioactive components, MAPs have effects such as supporting the immune system, reducing disease risks and damages, improving health status, increasing animal welfare, supporting the intestines, and increasing digestion, nutrient absorption, and wound healing (Cedillo-Cortezano et al., 2024). The use of MAPs in animal husbandry can also provide environmental benefits by reducing methane emissions and greenhouse gas levels (Andrić et al., 2023). Among the medicinal aromatic plants, the Lamiaceae family is the largest family containing many subspecies, and most *Thyme, Oregano, Mint,* and *Salvia* species have been used by scientists as yield enhancers, antioxidants and antimicrobial products in animals. However, there are many species belonging to the *Lamiaceae* family whose growth promoting, antioxidant and antimicrobial effects in animals need to be determined. *Satureja* is one of these species. The *Satureja* genus is an important member of this group, which includes thymol and carvacrol components in its structure, along with *Origanum, Thymbra, Coriodymus* and *Thymus* species belonging to the Lamiaceae family, and is represented by a total of 15

This work is licensed (CC BY-NC 4.0) under Creative Commons Attribution 4.0 International License

species in Turkiye, 5 of which are endemic (Paşa et al., 2019). Essential oils, plant parts, and plant extracts of *Satureja* species are reported to have antibacterial and antifungal activity due to phenolic compounds such as *thymol* and *carvacrol* (Nasiroleslami et al., 2016). *Thymol* and *carvacrol* have antimicrobial, antibacterial, antioxidant and antifungal effects (Bozdemir, 2019). It has been stated that the antimicrobial and antioxidant activities of the genus *Satureja* are due to the rich essential oil and phenolic content of these species (Kavcı, 2020). *Satureja*, a fragrant species similar to thyme from the *Lamiaceae* family and used as an appetizer, is called the creeping savory. There are very few studies in which the effects of *Satureja* species on the performance of animals were determined. In these studies, *Satureja montana* (Pashtetsky et al., 2020; Vilmosh et al., 2023), *Satureja hortensis* (Seyedtaghiya et al., 2021; Nasiroleslami et al., 2016), and *Satureja khuzestanica* (Rahimi et al., 2021; Arak et al., 2017) were examined for their biochemical content and for use as a feed additive in poultry feeding. No such study on *Satureja spicigera (K. Koch)* Boiss has been found. Therefore, the aim of this study was to determine the biochemical content of the leaf powder of *Satureja spicigera (K. Koch)* Boiss and the possible effects of its addition to quail diets on performance, meat quality, microbiology, and intestinal histology.

2. Materials and Methods

2.1. Animal Material

Coturnix coturnix japonica of mixed sex, at the age of 1 day, were used as biological material in the experiment. At the beginning of the experiment, 5 treatment groups and 4 replicates were formed from 400 chicks, with 80 animals in each group, and all had similar body weights. The chicks were randomly placed in 10 cm sawdust litter pens with 20 chicks in each pen.

2.2. Feed Material

The ration used in the study was obtained from a commercial feed company active in Kırşehir province. The nutrient content of the feed used is given in Table 1.

2.3. *Satureja Spicigera*

Satureja spicigera (K. Koch) Boiss was purchased from a local herbalist in Ordu province. Species identification of *Satureja* plants from herbaria was carried out by Dr. Sibel Ulcay. During the analysis of *Satureja spicigera (K. Koch)* Boiss plant with the NEOS microwave extraction system, it was determined that it contained 2.5% essential oil. The biochemical analysis of the essential oil was carried out in Kırşehir Ahi Evran University Central Research and Application Laboratory, and its detailed content is given in Table 2.

2.4. Conducting the Trial

The experiment was conducted for 42 days. Before the quails were placed in the cages, their live weights were determined by weighing them individually on an electronic scale with a precision of ± 0.01 g, and the average live weight in the cages was calculated. Treatment groups were SLP0: Basal feed (Control), SLP1: Basal diet + 0.25% *Satureja* leaf powder, SLP2: Basal diet + 0.50% *Satureja* leaf powder, SLP3: Basal diet + 0.75% *Satureja* leaf powder, and SLP4: Basal diet + 1% *Satureja* leaf powder. Feed and drinking water were given ad libitum. Live weights and feed intake of quails were determined by weekly weighing. Feed consumption of quails was calculated after weekly weighing by subtracting the excess feed from the total feed amount. Feed conversion ratios were calculated by dividing the feed consumption up to the weighing day by the live weight.

2.5. Slaughtering and Sampling

On the 42nd day of the experiment, feeders and waterers of all treatment groups in the experimental room were removed from the evening to the morning. Animals in all groups were weighed with scales with 1-gram precision, and the average live weights of the treatment groups were determined. After weighing, two quails (one female, one male) with average weights close to the group average were selected from each replicate, and their weights were recorded. These selected animals were cut open and the internal organs were removed. The weights of the heart, liver, and gizzard were determined and the length of the digestive tract was measured and recorded. For histological analysis, 5 cm samples were taken from the duodenum, jejunum, and ileum and kept in 10% formaldehyde until analysis (24 hours).

Table 1. Nutrient content of feed (%)

Feed Raw Materials	%
Corn	44.00
Soybean meal (%44)	41.15
Meat bone meal	4.00
Soybean oil	6.50
DCP	2.50
L-lysine HCL	0.70
DL-methionine	0.35
Salt	0.30
Vitamin premix*	0.25
Mineral premix‡	0.25
Analysis Results	
ME (kcal/kg)	3080
Crude protein	22.39
Crude cellulose	2.80
Crude ash	6.5
Crude fat	9.00
Calcium	1.60
Usable phosphate	3.80

* 1 kg vitamin premix contains Vitamin A: 12.500 IU; Vitamin D3: 4.000 IU; Vitamin E: 30 mg; Vitamin K3: 4 mg; Vitamin B1: 3 mg; Vitamin B2: 7 mg; Vitamin B6: 5 mg; Vitamin B12: 15 µg; Niacin: 25 mg.

‡ Iron:80 mg; Folic acid:1 mg; Pantothenic acid:10 mg; Biotin:45 mg; Choline:125000 mg; Copper:5 mg; Manganese:80 mg; Zinc:60 mg; Iodine:1 mg; Selenium:0,15 mg.

Table 2. Biochemical content of *Satureja spicigera (K. Koch)* Boiss

Contents	RT	%
Sabinene	5.11	0.32
a-Pinene	6.45	1.45
a-Terpinene	6.98	2.64
1-Limonene	7.76	0.29
1-Phellandrene	8.15	0.30
Ɣ-Terpinene	10.22	11.96
Delta.3-Carene	10.77	0.30
P-Cymene	11.65	19.04
3-Octanol	17.82	0.31
Thujol	18.67	0.15
1-Octen-3-ol	20.03	0.82
Trans Sabinene hydrate	20.44	0.43
Cis Sabinene hydrate	23.38	0.20
Linalool	23.48	1.31
Trans-Caryophyllene	24.53	1.51
Carvacrol methyl ether	25.16	8.76
Dihydrocarvone	25.75	0.13
à-Humulene	26.83	0.05
Verbenol	27.46	0.08
Ledene	28.06	1.75
Bicyclogermacrene	28.78	1.04
D-Carvone	29.04	0.05
Germacrene-D	29.52	0.06
Para-Cymen-8-ol	32.40	0.21
Carvacrol acetate	33.00	0.08
M-Cresol	34.16	0.11
Caryophyllene oxide	35.57	0.40
Spathulenol	39.13	0.39
Thymol	40.71	3.08
Carvacrol	41.35	37.20

2.6. Microbiology of the Cecum

One gram of cecal samples was mixed in 9 ml of peptone water using a vortex to obtain a homogeneous distribution. Serial dilutions (1/10) were prepared from the stock materials. MRS agar was used for lactic acid bacteria (MERCK, 1.10660) at 37°C following 3 days in an incubator, and BEA (Bile Aesculin Azide Agar) Agar (Merck 100072) was used for *Enterococcus spp*. at 37°C following 3 days in an incubator. MEA (Malt extract Agar) Agar (Merck 105398 was used for yeast at 25°C degrees following 3 days in incubator The microbial colonies were counted and expressed as log10 colony forming units (CFU) per gram of caecal content.

2.7. Intestinal Histology

On the 21st day of the study, duodenum, jejunum, and ileum samples taken from slaughtered animals in each treatment group were placed in 10% formaldehyde. In the histology analysis of the study, paraffin blocks were prepared; the samples were cut with a thickness of 5 microns, and the tissues were adhered to the slide. The tissues on the slide were freed from paraffin by passing them through xylene, followed by alcohol to remove the xylene. The cleaned tissue samples were stained with Hematoxylin & Eosin dye and photographed using a digital microscope equipped with an AxioCam ERc 5s 5MP (ZEISS Primo Star, Germany) for proper imaging. The photographs obtained for each treatment group and each sample were measured with the ZEN 2012 SP2 image processing and analysis program.

2.8. Meat Quality

After slaughter, the carcasses were cleaned and stored at +4°C for 24 hours, and pH values were measured in the breast meat of each quail slaughtered. The pH values were measured with a digital pH meter (Testo 205), using a solid electrode at 3 different points of the left breast meat. The electrode was kept immersed in the breast until the values were fixed on the display screen of the pH meter. This fixed value was then read and recorded. In this way, the average of three measurements taken from the breast sample of the quails was calculated and recorded as the pH value of the breast meat.

Color measurements were performed on the breast meat of quails using a Minolta CR 410 Chroma Meter (Minolta Camera Co., Osaka, Japan), calibrated with a spectrocolorimeter white color plate, (Minolta calibration plate, No. 21733001, Y=92.6, x=0.3136, y=0.3196). After removing the skin from the left breast meat of each quail, color measurements were made at three different points on the breast surface. CIE standards (L* = brightness, a* = redness, and b* = yellowness values) were used in the measurements, and three basic color characteristics (L* 100 = white, 0 = black; a* = red color coordinate ± red-green; b* = yellow color coordinate ± yellow-blue) were considered.

Fat oxidation levels in quail breast meat were determined by the 2-thiobarbituric acid method. 50 mL of distilled water was added to 10 g of quail breast meat at 50°C and homogenized in Ultra-Turrax for 2 minutes. The mixture was taken into distillation tubes, and 47.5 ml of distilled water and 2.5 ml of 4 N HCl solution were added. Paraffin was added to the mixture to prevent foaming, and boiling stones were added to facilitate boiling, and placed in the distillation apparatus. The steam power of the distillation apparatus was set to low mode, and the process was continued until 50 ml of distillate was collected. From the collected amount, 5 ml was separated, transferred to balloon jugs, and 5 ml of TBA reagent was added. For the blind preparation, 5 ml of distilled water and 5 ml of TBA reagent were mixed. The samples were mixed homogeneously with a vortex, kept in a hot water bath for 35 minutes, and cooled in water for 10 minutes. The samples were then read in a spectrophotometer at a wavelength of 538 nm against the blind; the absorbance value was multiplied by 7.8, and the result was expressed as milligrams of MDA per kilogram of sample (Tarladgis et al., 1960).

Sensory quality analysis of meat was carried out by TUBITAK MAM. Quail breast meat samples were kept at -18°C for analysis. One day before the analysis day, they were placed at +4°C and thawed. Quail breast meat was used to ensure that the sample had the same

characteristics in terms of the sensory criteria to be analyzed. Each of the meats numbered between 1-5 was wrapped in baking paper and then in aluminum foil before analysis, and all were cooked at 180℃ for 40 minutes simultaneously. Sensory evaluations of the samples were carried out by 10 expert panelists. In sensory evaluations, color (appearance), smell, flavor, and texture (crispness, juiciness, stickiness, chewiness, and fibrousness) criteria were examined. During the evaluation phase, panelists were given homogeneous samples. The samples were randomly coded with a three-digit number and presented to the panelists on separate plates. Water was given to neutralize their mouths between samples. Changes in the quality of the samples were evaluated using a 1-9 scale. In this scale, a score of 1 corresponds to the worst criterion, and a score of 9 corresponds to the best criterion.

2.9. Statistical Analyses

The trial was conducted in accordance with the randomized plots trial design and the data were analyzed using one-way ANOVA using the IBM SPSS 25 (IBM Corp., Armonk, NY, USA) statistics program. Since the distribution of the data between the group means was homogeneous, the Duncan multiple comparison test was applied.

3. Results and Discussion

Table 3 shows the performance values of the quails after dietary SLP (the creeping savory) to the quail diets. At the end of the study, it was determined that the supplementation of different amounts of SLP to the quail diets had no effect on the performance values; only the BWG value of the SLP3 group was lower than the SLP2 group. However, it was not affected compared to the SLP0 group.

Table 3. Effects of *satureja* leaf powder supplementation on quail performance values

SLP (g/kg diet)	BWG	FI	FCR
SLP0	186.70ab	645.80	3.46
SLP1	189.33a	673.31	3.56
SLP2	185.57ab	654.55	3.53
SLP3	179.90b	626.58	3.48
SLP4	186.62ab	652.56	3.49
SEM	1.31	7.55	0.03
	P Value		
L	0.23	0.44	0.94
Q	0.55	0.85	0.57
C	0.05	0.08	0.52

Values represent means of 4 replicate pens with 2 birds from each pen. a,b,c= Differences between means with different letters in the same row are significant (P<0.05). L= linear. Q= quadratic. C= cubic. BWG= body weight gain, FI= feed intake, FCR= conversion ratio.

The number of studies on the performance parameters of the *Satureja* plant in poultry nutrition is scarce. Movahhedkhah et al., (2019) reported that the addition of Summer Savory (*Satureja hortensis L.*) Extract to broiler diets did not affect growth performance. Souri et al., (2015) reported that *Satureja khuzestanica* supplementatiopn to diet did not affect broiler growth. Nasiroleslami et al., (2016) reported that the addition of *Satureja hortensis* (Summer Savory) essential oil (SHEO) to laying hens diet, did not change egg laying performance; similarly, Dehghani et al., (2018) reported that SHEO in quail diets had no effect on performance parameters. The performance values of the present study are consistent with the results of previous studies. According to these results, it was determined that SLP did not affect the performance values of quails. There are few studies on Satureja species regarding performance parameters. To fully demonstrate the effects of *Satureja* species on performance, different studies are needed to determine whether they are effective in different animal species, whether they are more effective in different harvest periods, or whether they are more effective under different stress conditions.

The effects of SLP supplementation to quail diets on internal organ development are given in Table 4. Heart weight, liver weight, gizzard weight, and digestive tract length did not differ among the groups.

Table 4. Effects of slp supplementation on quail ınternal organ development

SLP (g/kg diet)	Heart (g)	Liver (g)	Gizzard (g)	Gut length (cm)
SLP0	1.04	1.77	1.99	29.72
SLP1	1.03	1.85	2.14	28.61
SLP2	0.93	1. 75	2.23	30.20
SLP3	0.99	1.93	2.33	30.61
SLP4	0.92	2.00	2.25	29.94
SEM	0.02	0.09	0.05	0.67
		P Value		
L	0.08	0.46	0.06	0.63
Q	0.83	0.76	0.28	0.96
C	0.77	0.93	0.78	0.46

Values represent means of 4 replicate pens with 2 birds from each pen.

Arak et al., (2013) determined that the addition of 600 ppm *Satureja khuzistanica* essential oil (SKEO) to quail diets decreased Bursa fabricus and spleen weights, but had no significant effect on other internal organ weights. In another study, Dehghani et al., (2018) reported that the addition of different levels of SHEO to quail diet did not effect inner organ developments. Souri et al., (2015) reported that the supplementation of SKEO to broiler diets did not affect the development of internal organs. It was determined that the results of previous studies on different *Satureja* species were compatible with the results obtained from the present study and the addition

of SLP to the ration did not affect the internal organ development of quails. The results of the cecum microbiota are given in Table 5. Cecum microbiota did not differ from other groups.

Table 5. Effects of SLP supplementation on quail cecum microbiota

SLP (g/kg diet)	*Enterococcus spp.*	*Lactobacillus spp.*	*Saccharomyces cerevisiae*
SLP0	6.42	6.42	6.51
SLP1	6.29	6.73	6.68
SLP2	6.43	6.68	6.59
SLP3	6.52	6.65	6.90
SLP4	6.60	6.69	6.94
SEM	0.06	0.06	0.07
		P Value	
L	0.60	0.57	0.21
Q	0.49	0.33	0.80
C	0.55	0.36	0.96

Values represent means of 4 replicate pens with 2 bird from each pen.

Masouri et al., (2017) reported that the addition of 500 mg/kg SKEO to corn-based diets of broiler chickens increased the *Lactobacillus* population in the blind intestine and decreased the total number of bacteria and *Escherichia coli*, whereas the caecal population of *Lactobacillus* decreased in broiler chickens fed wheat-based diets, Mousapour et al., (2020) reported that the addition of 150 mg/kg SHEO to broiler diets significantly increased the number of *Lactobacilli* in the ileal digestive tract and reduced the density of coliforms. Mozafari et al., (2018) reported that the addition of 1.0% or 2.0% *Satureja hortensis* L. powder to broiler diets significantly reduced ileal Escherichia coli population compared to the control group, while Movahhedkhah et al., (2019) reported that the addition of 400 mg/kg Satureja hortensis extract to broiler diets decreased the number of *Escherichia coli* and improved the *Lactobacilli/Escherichia coli* ratio, but had no significant effect on the number of Lactobacilli. Although there was no statistical difference in the number of lactobacilli and yeast in the present research study, it was determined that the addition of SLP increased the lactic acid bacteria and yeast population numerically. Therefore, it can be said that the addition of SLP has positive effects on the beneficial bacterial population in the quail intestines and balances the intestinal microflora; it also positively affects intestinal health and provides better digestion, consistent with previous studies.

While there was no significant difference between the pH levels and color (L* and b*) values (Table 6) of the breast meat compared to the control group, the a* value of the SLP4 group decreased compared to those of the SLP1 and SLP2 groups. MDA levels were significantly lower in SLP1 and SLP2groups compared to the control group (P<0.05).

Table 6. Effects of SLP supplementation on quail meat properties and mda levels

SLP (g/kg diet)	pH	L*	a	b	MDA
SLP0	6.00	36.64	12.12_{ab}	5.91	0.71_{a}
SLP1	6.15	38.19	12.79_{a}	6.62	0.51_{b}
SLP2	6.07	37.70	12.31_{a}	6.13	0.51_{b}
SLP3	6.17	37.99	11.73_{ab}	6.04	0.62_{ab}
SLP4	5.96	37.08	10.90_{b}	5.59	0.59_{ab}
SEM	0.05	0.34	0.21	0.14	0.02
		P Value			
L	0.58	0.43	0.05	0.21	0.33
Q	0.19	0.10	0.07	0.10	0.02
C	0.80	0.69	0.52	0.39	0.03

Values represent means of 4 replicate pens with 2 bird from each pen. a,b,c: Differences between means with different letters in the same row are significant (P<0.05). L*= brightness; 0 = black and 100 = white, a*: redness; – 60 = green and 60 = red, b*: yellowness; – 60 = blue and 60 = yellow.

The number of studies on the effects of *Satureja* on poultry meat quality is limited. Among these limited studies, Souri et al., (2015) found that the addition of 2% and 1% *Satureja khuzestanica* extract to drinking water decreased the 24-hour pH of broiler thigh meat. While the pH of breast meat was not affected and the redness, yellowness, and brightness of breast meat were not affected by plant extract applications, 2% and 1% *Satureja* khuzestanica extract decreased the redness and yellowness values in thigh meat. They reported that the difference between the results may be due to the different forms of the plants and the difference in the color pigment ratios contained in the plants. Azarbad et al., (2019), stated that the addition of SKEO in different forms to broiler diets significantly affected the MDA levels in breast meat, and this study supports previous findings that SLP suppressed MDA formation in SLP1 and SLP2 groups compared to the SLP0 group (P<0.05). Therefore, *Satureja spicigera* showed antioxidant properties by suppressing the formation of reactive oxygen species (ROS) in the breast tissue of quails. However, the effects of SLP, essential fatty acids, or their extracts obtained by different methods on MDA and different antioxidant enzymes in various animal species need to be determined.

The change in the sensory criteria of quail breast meat is given in Table 7. It was determined that the meat color of the SLP1 and SLP4 groups was lighter than the control group, and this difference was found to be significant (P<0.05), while no difference was detected in terms of other sensory criteria (odor, crispness, stickiness, chewiness, fibrousness, juiciness, and general flavor). No study was found to determine the effects of the Satureja plant on the sensory properties of camel meat. Therefore, this is the first study to determine the effects of SLP on the organoleptic properties of poultry, especially quail breast meat. When previous studies on the effects of

different aromatic plants on the organoleptic properties of breast meat were examined, Arjun et al., (2022) reported that the addition of *Mint* leaf powder (0.75%, 1.5%, 2.25%, 3%) to the ration resulted in sensory evaluations for all parameters of meat in Japanese quails being significantly higher in the group with 3% mint leaf powder addition. Anar, (2022) reported that *Thyme* and *Rosemary* essential oils added to the ration, alone or in mixtures, did not cause any difference in terms of sensory characteristics in the breast and thigh meat of broiler chickens and shared similar results. The results obtained from this study were similar to those of previous studies. Only in Arjun et al., (2022) all traits were affected in the group in which mint was added to the ration at the 3% level. Since the highest dose was 1% in this study, its effects may not have been significant. Therefore, according to these results, it can be concluded that the doses of aromatic herbs are effective in influencing organoleptic properties in poultry meat.

Table 7. Effects of SLP supplementation on sensory quality characteristics of quail meat

SLP (g/kg diet)	Color	Odor	Brittleness	Stickiness	Chewability	Fiber	Wateriness	Overall flavor
SLP0	9.0	9.0	9.0	9.0	9.0	9.0	9.0	9.0
SLP1	8.0	8.8	8.5	8.5	8.6	8.5	8.3	8.6
SLP2	8.5	9.0	8.0	8.4	8.6	8.4	8.4	8.5
SLP3	8.3	8.8	8.8	8.3	8.5	8.3	8.3	8.5
SLP4	7.6	8.8	8.5	8.5	8.4	8.5	8.8	8.6
SEM	0.15	0.17	0.12	0.11	0.09	0.10	0.12	0.12
				P Value				
L	0.01	0.10	0.09	0.42	0.32	0.25	0.18	0.72
Q	0.91	0.65	0.06	0.18	0.51	0.12	0.03	0.33
C	0.23	0.54	0.09	0.75	0.52	0.96	0.79	0.83

Values represent means of 4 replicate pens with 2 birds from each pen. a,b,c: Differences between means with different letters in the same row are significant (P<0.05).

Table 8. Effects of SLP supplementation on duodenum histology

SLP (g/kg diet)	Duodenum VL	Duodenum CD	Duodenum LMM	Duodenum VL/CD
SLP0	977.28_{bc}	47.50_{b}	76.33	20.99
SLP1	1124.27_{a}	56.17_{a}	77.51	20.12
SLP2	1041.99_{ab}	50.82_{ab}	74.31	21.05
SLP3	966.31_{bc}	51.20_{ab}	77.71	19.09
SLP4	864.54_{c}	44.16_{b}	76.29	20.39
SEM	20.73	1.17	2.56	0.49
		P Value		
L	0.00	0.14	0.99	0.54
Q	0.00	0.00	0.95	0.73
C	0.12	0.39	0.95	0.68

Values represent means of 4 replicate pens with 2 birds from each pen. a,b,c: Differences between means with different letters in the same row are significant (P<0.05). VL= villi length, CD= crypt depth, LMM= the lamina muscularis mucosa thickness, VL/CD= villi length and crypt depth ratio.

Table 9. Effects of SLP supplementation on jejunum histology

SLP (g/kg diet)	Jejunum VL	Jejunum CD	Jejunum LMM	Jejunum VL/CD
SLP0	557.09_{b}	38.98_{ab}	61.30	14.77_{cd}
SLP1	542.98_{b}	41.13_{a}	68.39	13.44_{d}
SLP2	559.47_{b}	34.14_{b}	60.23	16.65_{bc}
SLP3	675.18_{a}	36.77_{ab}	68.61	19.00_{ab}
SLP4	584.58_{b}	29.09_{c}	62.10	20.21_{a}
SEM	8.98	0.92	1.39	0.50
		P Value		
L	0.00	0.00	0.85	0.00
Q	0.34	0.12	0.35	0.20
C	0.00	0.81	0.97	0.04

Values represent means of 4 replicate pens with 2 birds from each pen. a,b,c: Differences between means with different letters in the same row are significant (P<0.05). VL= villi length, CD= crypt depth, LMM= the lamina muscularis mucosa thickness, VL/CD= villi length and crypt depth ratio.

Table 10. Effects of SLP supplementation on ıleum histology

SLP (g/kg diet)	Ileum VL	Ileum CD	Ileum LMM	Ileum VL/CD
SLP0	462.31	30.19_{c}	45.15_{cd}	15.52_{ab}
SLP1	454.43	32.71_{bc}	54.83_{a}	14.34_{ab}
SLP2	501.82	31.03_{c}	53.22_{d}	16.61_{a}
SLP3	454.12	40.41_{a}	54.15_{bc}	11.42_{c}
SLP4	483.45	35.98_{b}	57.81_{b}	13.65_{b}
SEM	7.13	0.82	1.39	0.40
		P Value		
L	0.39	0.00	0.01	0.00
Q	0.72	0.00	0.39	0.00
C	0.66	0.05	0.14	0.11

Values represent means of 4 replicate pens with 2 birds from each pen. a,b,c: Differences between means with different letters in the same row are significant (P<0.05). VL= villi length, CD= crypt depth, LMM= the lamina muscularis mucosa thickness, VL/CD= villi length and crypt depth ratio.

In the duodenum, *Lamina muscularis* mucosa (LMM) thickness and VL/CD did not change (P>0.05). However, the duodenum villi length of the SLP1 group was higher than in the SLP0 group (P<0.05), and the duodenum crypt depth of the SLP1 group was also higher (P<0.05). However, jejunum villi length of SLP3 group was significantly higher than the control group, while jejunum crypt depth of SLP4 group was significantly lower than in the SLP0 group (P<0.05); jejunum LMM thickness did not differ from groups. In addition, the VL/CD ratio of the jejunum in the SLP3 and SLP4 groups was statistically higher than in the SLP0 group (P<0.05). Villi length did not change among the groups in the ileum. However, the ileal CD of SLP3 and SLP4 groups was found to be higher than the SLP0 group, while the ileal lamina muscularis mucosa thickness of SLP1, SLP3 and SLP4 groups was found to be higher than the SLP0 group (P<0.05). In addition, the ratio of ileum VL/CD of the SLP3 group was lower than that of the control group (P<0.05). Masouri et al. (2017) found that the addition of SKEO decreased the VL of the duodenum and jejunum in broiler chicks fed wheat-based diets, increased the VL and the VL/CD, and decreased the CD of the duodenum in the group with 500 mg/kg SKEO added to the diets compared to the control group. Mousapour et al., (2020) found that the VL of the group supplemented with 150 mg/kg SHEO in broiler diets was significantly lower than those of the control group and other groups. Rahimi et al., (2021) found that the addition of SKEO (400 and 500 mg/kg) and garlic powder (2% and 4%) to the diet significantly increased the VL, VL/CD and villus surface area in the intestinal morphology of male broiler chickens. Dehghani et al., (2018) reported that SHEO, when added to the diet, enhanced the VL of duodenum, jejunum, and ileum in quails, while the CD decreased significantly. It is thought that these differences seen in the results of the research may be due to the changes in the microflora of the digestive system of the animals and that the chemical compounds contained in the plant species used that affect the morphology of different parts of the intestine.

4. Conclusion

In this study, the biochemical composition of the leaf powder of *Satureja spicigera (K. Koch)* Boiss was determined based on the findings obtained. The inclusion of *Satureja spicigera (K. Koch)* Boiss leaf powder in quail diets was observed to increase duodenal villus length and crypt depth in the SLP1 group, while in the SLP3 and SLP4 groups, it enhanced villus length and crypt depth in the jejunum, thereby improving intestinal health and digestion. Additionally, a significant reduction in malondialdehyde (MDA) levels was observed in the breast meat of quails in the SLP1 and SLP2 groups compared to the control group, indicating an antioxidant effect. All these findings were discussed in detail and contribute to the existing literature. However, as this is a preliminary study aimed at identifying the various beneficial effects of *Satureja spicigera*, a plant commonly cultivated in the Black Sea region, on poultry, further research is warranted. Future studies should aim to elucidate the mechanisms of action, investigate the potential for commercial cultivation of *Satureja spicigera*, and explore its application as a natural feed additive.

Author Contributions

The percentages of the authors' contributions are presented below. All authors reviewed and approved the final version of the manuscript.

	E.D.	İ.C.
C	60	40
D	60	40
S	60	40
DCP	60	40
DAI	60	40
L	60	40
W	60	40
CR	60	40
SR	60	40
PM	60	40
FA	60	40

C=Concept, D= design, S= supervision, DCP= data collection and/or processing, DAI= data analysis and/or interpretation, L= literature search, W= writing, CR= critical review, SR= submission and revision, PM= project management, FA= funding acquisition.

Conflict of Interest

The authors declared that there is no conflict of interest.

Ethical Consideration

The authors confirm that the ethical policies of the journal, as noted on the journal's author guidelines page, have been adhered to. The experimental procedures were approved by the Local Animal Care and Ethics Committee of Kırşehir Ahi Evran University, 684429034-03 (approval date: 28 February, 2024, Protocol code: 68429034/03).

Acknowledgements

The authors would like to thank Prof. Dr. Hasan Ersin ŞAMLI and Prof. Dr. Ahmet ŞAHİN for their support in this doctoral thesis.

References

Anar B. 2022. Etlik piliç rasyonlarına kekik ve biberiye uçucu yağ katkılarının performans ve et kalitesi üzerine etkileri. Bursa Uludağ Üniversitesi, Sağlık Bilimleri Enstitüsü, Bursa, Türkiye, pp: 35.

Andrić DO, Hristov S, Stanković B, Petrović VC, Pajić M, Nikšić D, Samolovac L, Marinković M. 2023. Medicinal and aromatic plants in livestock farming: A promising approach for boosting health and performance. In: 14th International Symposium Modern Trends in Livestock Production, Belgrade, 27-28 October 2023, Belgrade, Serbia, pp: 460-475.

Arak H, Karimi Torshizi MA, Rahimi S. 2013. Study on the effect of Savory Satureja khuzestanica (essential oil and Polysorb toxin-binder against experimental aflatoxicosis in Japanese quail. Vet Clin Pathol Q Sci J, 7(3): pp: 249-259.

Arak H, Karimi Torshizi MA, Rahimi S. 2017. Effect of savory (Satureja khuzestanica) essential oil and commercial toxin binder on fertility, hatchability, and progeny performance in breeder quails fed aflatoxin contaminated diets. Anim Sci J, 30(114): pp: 285-294.

Arjun SS, Kumari K, Nath DN, Kavita P. 2022. Assessment of lipid profile and carcass traits in quail, fed on diet with incorporation of peppermint leaf powder at various levels. Indian J Anim Nutr, 39(4): pp: 468-479.

Azarbad E, Yaghobfar A, Kermanshahi H, Meimandi Pour A. 2019. Effect of different levels of Satureja khuzistanica essential oils in usual and microcapsulated forms in diets on performance, carcass characteristics and meat oxidative stability in broiler chickens. Anim Sci J, 32(123): pp: 217-232.

Bozdemir Ç. 2019. Türkiye'de yetişen kekik türleri, ekonomik önemi ve kullanım alanları. YYU J Agric Sci, 29(3): pp: 583-594.

Cedillo-Cortezano M, Martinez-Cuevas LR, López JAM, Barrera López I, Escutia-Perez S, Petricevich VL. 2024. Use of medicinal plants in the process of wound healing: a literature review. Pharmaceuticals, 17(3): pp: 303.

Dehghani N, Afsharmanesh M, Salarmoini M, Ebrahimnejad H, Bitaraf A. 2018. Effect of pennyroyal, savory and thyme essential oils on Japanese quail physiology. Heliyon, 4(10): pp: 1-7.

Kavcı E. 2020. Satureja L. (Lamiaceae) cinsinde yer alan bazı taksonların enzim inhibisyon özellikleri ve karyolojileri üzerine bir çalışma. Necmettin Erbakan Üniversitesi, Fen Bilimleri Enstitüsü, Konya, Türkiye, pp: 22.

Masouri L, Salari S, Sari M, Tabatabaei S, Masouri B. 2017. Effect of feed supplementation with Satureja khuzistanica essential oil on performance and physiological parameters of broilers fed on wheat- or maize-based diets. Br Poult Sci, 58(4): pp: 425-434.

Mousapour A, Salarmoini M, Afsharmanesh M, Ebrahimnejad H, Meimandipour A. 2020. Efficacy of Savory Essential Oil Utilization in Conventional and Encapsulated Forms on Performance of Broiler Chickens. Braz J Poult Sci, 22(4): pp: 001-012.

Movahhedkhah S, Rasouli B, Seidav A, Mazzei D, Laudadio V, Tufarelli V. 2019. Summer savory (Satureja hortensis L.) extract as natural feed additive in broilers: Effects on growth, plasma constituents, immune response, and ileal microflora. Animals, 9(3): pp: 87.

Mozafari S, Seidavi A, Gharahveysi S, Kadim I. 2018. Savory (Satureja hortensis L.) powder and extract effects on broiler chicken ileal Escherichia coli and Lactobacillus bacteria. J Appl Anim Res, 46(1): pp: 639-642.

Nasiroleslami M, Torki M, Van Krimpen M. 2016. Effect of dietary inclusion of two sources of selenium and Satureja hortensis essential oil on productive performance of laying hen. 41st Animal Nutrition Research Forum, Tehran, Iran, pp: 63.

Paşa C, Kılıç T, Selvi S, Sağır ZÖ. 2019. Satureja cuneifolia Ten. (Lamiaceae) türünün farklı kurutma yöntemleri uygulanarak uçucu yağ oranlarının ve uçucu yağ bileşenlerinin tespit edilmesi. J Inst Sci Technol, 9(4): pp: 2330-2335.

Pashtetsky V, Ostapchuk P, Postnikov O, Zubochenko D, Kuevda T. 2020. Effect of Satureja montana essential oil on the bactericidal activity of broiler chickens blood serum. E3S Web Conf, 224: pp: 04023.

Rahimi D, Yarahmadi HM, Yaghobfar A, Fakhraei J. 2021. Effects of garlic powder and Satureja khuzestanica essential oil on male Ross 308 chickens performance, blood lipid profile, immune responses, intestinal microflora, and morphology. Jundishapur J Nat Pharm Prod, 16(1): pp: 1-10.

Seyedtaghiya MH, Fasaei BN, Peighambari SM. 2021. Antimicrobial and antibiofilm effects of Satureja hortensis essential oil against Escherichia coli and Salmonella isolated from poultry. Iran J Microbiol, 13(1): pp: 74.

Souri H, Khatibjoo A, Taherpoor K, Hassan Abadi A, Fattahnia F, Askari M. 2015. Effect of Thymus vulgaris and Satureja khuzestanica ethanolic extracts on broiler chickens' performance and immune response. Iran J Appl Anim Sci, 5(2): pp: 437-446.

Tarladgis BG, Watts BM, Younathan MT, Dugan L. 1960. A distillation method for the quantitative determination of malonaldehyde in rancid foods. J Am Oil Chem Soc, 37: pp: 44-48.

Vilmosh N, Georgieva-Kotetarova M, Dimitrova S, Zgureva M, Atanassova PK, Hrischev PI, Kostadinova I. 2023. Composition and chronic toxicity of dry methanol-aqueous extract of wild-growing Satureja montana. Folia Med, 65(3): pp: 482-489.

Black Sea Journal of Engineering and Science
doi: 10.34248/bsengineering.1648149

Open Access Journal
e-ISSN: 2619 – 8991

Araştırma Makalesi (Research Article)
Cilt 8 - Sayı 4: 954-962 / Temmuz 2025
(Volume 8 - Issue 4: 954-962 / July 2025)

YOL AĞAÇLANDIRMA UYGULAMALARININ DEĞERLENDİRİLMESİ: GAZİ CADDESİ ÖRNEĞİ

Ahmet CAF[1]*, Semaha KURAL[2]

[1]*Bingöl University, Technical Sciences Vocational School, Department of Park and Horticulture, Bingöl, Türkiye*
[2]*Bingöl University, Institute of Science, Department of Horticulture, Bingöl, Türkiye*

Özet: Günümüzde hızla artan kentleşme, doğal alanların betonlaşması bireylerin doğaya olan özlemini derinleştirmektedir. Bu durum kent içinde sınırlı olarak bulunan yeşil alanların önemini arttırmaktadır. Bu bağlamda kent içindeki mevcut yeşil alanların korunması ve çoğaltılması büyük önem arz etmektedir. Parklar, bahçeler ve rekreasyon alanları, şehir yaşamında bireylere kaliteli yaşam alanları sunarken, yol ağaçlandırmaları da kent estetiğinin yanı sıra ekolojik dengeye katkı sağlamaktadır. Özellikle yaz aylarında gölge oluşturarak biyoklimatik konfor sağlayan ağaçlar, aynı zamanda karbon emilimini artırarak hava kalitesinin iyileştirilmesine yardımcı olur. Bunun yanı sıra, yeşil alanlar, kentte yaşayan bireylerin stres seviyesini azaltırken huzuru ve yaşam kalitesini artırarak fiziksel ve psikolojik sağlıklarına olumlu katkılar sağlar. Bu çalışmada Elazığ ilinin en eski ve en yoğun kullanılan caddelerinden biri olan Gazi Caddesi'nin bitkisel tasarımı incelenmiştir. Yapılan incelemelerle kullanılan bitki türleri tespit edilerek olumlu ve olumsuz yanları değerlendirilmiş; ekolojik uyum, estetik değer ve sürdürülebilirlik açısından alternatif üç bitkisel tasarım örneği geliştirilerek görselleri oluşturulmuştur. Bitkisel tasarım örneklerinde kullanılan bitkilerin Elazığ iklim koşullarına uygun, caddede görsel kalite oluşturarak renk ve doku bakımından çeşitlilik oluşturacak, sürdürülebilirlik kapsamında uzun vadede bakım maliyetleri az türler kullanılmasına özen gösterilmiştir. Bu çalışma, bilimsel verilere dayalı peyzaj planlamasının önemini ortaya koyarak, yerel yönetimlerin sürdürülebilir, estetik ve ekolojik açıdan dengeli kararlar almasına katkı sağlamaktadır.

Anahtar kelimeler: Bitkisel tasarım, Elazığ, Peyzaj, Sürdürülebilirlik

Evaluation of Road Afforestation Applications: Gazi Street Example

Abstract: Today, rapidly increasing urbanization and the concretization of natural areas deepen individuals' longing for nature. This situation increases the importance of limited green areas within the city. In this context, the protection and increase of existing green areas within the city is of great importance. While parks, gardens and recreation areas offer quality living spaces to individuals in city life, road afforestation also contributes to urban aesthetics and ecological balance. Trees, which provide bioclimatic comfort by creating shade especially in the summer months, also help improve air quality by increasing carbon absorption. In addition, green areas reduce the stress level of individuals living in the city and increase peace and quality of life, thus contributing positively to their physical and psychological health. In this study, the plant design of Gazi Street, one of the oldest and most intensively used streets of Elazığ province, was examined. The plant species used were determined through the examinations and their positive and negative aspects were evaluated; three alternative plant design examples were developed in terms of ecological harmony, aesthetic value and sustainability and their visuals were created. The plants used in the plant design examples were chosen to be suitable for Elazığ climate conditions, to create visual quality on the street and to create variety in terms of color and texture, and to have low maintenance costs in the long term within the scope of sustainability. This study contributes to the local governments in making sustainable, aesthetic and ecologically balanced decisions by revealing the importance of landscape planning based on scientific data.

Keywords: Elazığ, Landscape, Plants design, Sustainability,

***Sorumlu yazar (Corresponding author):** Bingöl University, Technical Sciences Vocational School, Department of Park and Horticulture, 12000, Bingöl, Türkiye,
E mail: acaf@bingol.edu.tr (A. CAF)
Ahmet CAF http://orcid.org/0000-0002-4295-7703
Semaha KURAL http://orcid.org/0009-0003-6879-2083

Gönderi: 27 Şubat 2025 **Received:** February 27, 2025
Kabul: 29 Nisan 2025 **Accepted:** April 29, 2025
Yayınlanma: 15 Temmuz 2025 **Published:** July 15, 2025

Cite as: Caf A, Kural S. 2025. Evaluation of current road afforestation practices and sustainable plantation design suggestions. BSJ Eng Sci, 8(4): 954-962.

1. Giriş

Kentlerde yeşil alan miktarı gün geçtikçe azalmaktadır. Yollar, araç ve yaya trafiğinin rahat ve güvenli bir şekilde akması için planlansa da, peyzaj elemanlarından en önemlilerinden biri olan ağaçlandırma ve bitkilendirme de göz önünde bulundurulmalıdır (Erdoğan ve Özer, 2009). Açık ve yeşil alanlar kent-doğa ilişkisini yeniden kurmak, sürdürmek ve geliştirmek amacıyla oluşturulurlar. Semt düzeyindeki açık ve yeşil alanlar genellikle eğlence ve dinlenme gibi işlevleri üstlenir. Kırsal alanların uzantısını oluşturan bölge ölçeğindeki açık ve yeşil alanlar ise kentsel büyümeye engel olarak kentsel büyümenin yönünü ve aşamalarını belirlerler (Şahin ve Barış, 1998; Aklıbaşında ve Erdoğan, 2016).

Özellikle yapısal mimarinin yoğun olduğu kent içlerinde ağaçlar sert zeminleri yumuşatma özelliğiyle monotonluğu giderirler. Şehir içinde betonların arasında kalan insanlara mevsimlerin güzelliklerini yaşatarak renkli bir dünya sunarlar (Atay, 1958).

Şehirlerde ağaçların insanlara en yakın ve yararlı

This work is licensed (CC BY-NC 4.0) under Creative Commons Attribution 4.0 International License

oldukları yerler yol mekânlarıdır (Aslanboğa, 1986). Ancak bu alanlar giderek ağaçlar için uygun bir yaşam ortamı olmaktan uzaklaşmaktadır. Aslında orman ekosisteminin birer öğesi olan yol ağaçları, şehir ekosisteminin ve şehirsel yapılaşmanın olduğu kadar yaşamın da yoğun biçim de sürdüğü yol boylarında çeşitli baskıların etkisi altındadır. Bu baskılar nedeniyle sağlıklarını yitirmekte, kırsal alandaki türdeşlerine oranla daha yavaş büyümekte ve daha kısa ömürlü olmaktadırlar. Sonuç olarak, şehir halkının kendilerinden bekledikleri işlevleri yeterince yerine getirememektedirler (Yılmaz ve Aksoy, 2009).

Kent içindeki yollarda; çarpık kentleşme ve hızlı nüfus artışına bağlı olarak yolların plansızlığı ve kullanım yoğunluğunun artması bitkilerin yaşam alanlarını kısıtlayarak olumsuz etkilere sebep olmuştur (Karaca ve Kurtaslan, 2017).

Kent içi ağaçlandırmaları belirli bir planlama çerçevesinde yapılmalıdır. Ülkemizde geçmiş yıllarda plansız bir şekilde, ekolojik koşullar göz önünde bulundurulmadan, kentlerin gelecek yıllardaki kullanım yoğunluğu dikkate alınmadan yapılan ağaçlandırma çalışmaları günümüzde bazı sorunlara sebebiyet vermektedir (Yılmaz, 1998). Ülkemizde bu sorunlar genel olarak; yanlış tür seçimine bağlı olarak, geniş çaplı büyüyen binaların arasında sıkışmış bitkiler, meyveli olan tür seçimiyle yollarda meyvelerin dökülmesiyle kirlilik ve insanlara rahatsızlık hissi, bölgenin ekolojik şartları göz önünde bulundurulmadan yapılan tür seçimleriyle bitkilerin kısa zamanda yaşamlarının sona ermesi, özellikle yaz aylarında duyulan gölge ihtiyacını karşılayamayacak türdeki bitki seçimi, kaldırımlarda yeterli kök gelişimi için alan bırakılmamasından küçük bir alanda kökleri toprak dışına çıkmış bitkiler vb. olarak karşımıza çıkmaktadır.

Yol ağaçlandırmalarında planlama ve tasarım ilkeleri; ağaçlandırmanın amacı, yetişme ortamı isteklerinin saptanması, kent yollarının tanımlanması, yol ağacı-çevre ilişkisi, tür seçimi, dikim aralığının belirlenmesi olarak belirlenmiştir (Şahin, 1989).

Yol ağaçlandırmalarında yapılacak yanlış tür seçimi görsel, ekolojik ve maddi problemleri de beraberinde getirebilir (Yılmaz, 2019; Caf, 2023).

Yol ağaçlandırmalarında dikim aralığını taç çapı, taç yüksekliği, yapı ışıklanmasına etkisi, taşıt ve yaya yolu genişliği, ağacın maksimum yüksekliği ile yol boyunca ortalama bina yüksekliği arasındaki ilişki, ağaçtan beklenen tasarım etkisi ve ağacın bu etkiye ulaşma hızı belirler (Blauermel, 1983; Şahin ve Kurum, 2006).

Kent içindeki yollarda kullanılabilecek ağaçlara ait nitelikler aşağıdaki şekilde sıralanabilir;

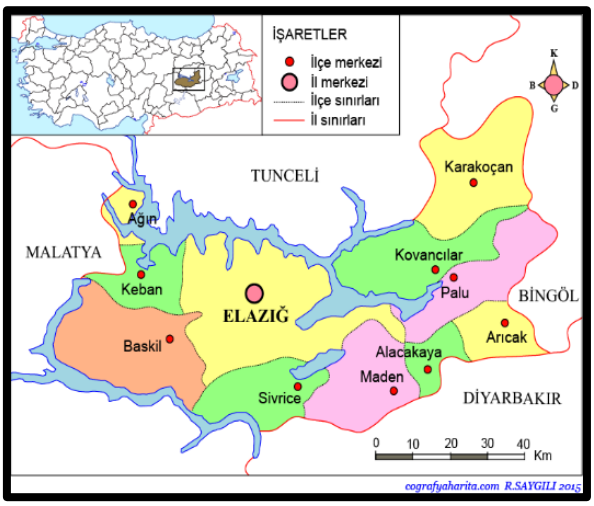
- Kullanılacak ağaç türü seçerken bölgenin ekolojik şartları göz önünde bulundurularak seçim yapılmalıdır. Aksi halde bitkiler ya uyum sağlayamaz ölür ya da gelişimleri geri kalarak istediğimiz sonuçları veremez.
- Ağaç türü seçiminde, sütun formunda büyüyen, tepe sürgünü iyi gelişen, üniform şekilli, hızlı büyüyen ancak gevşek yapıda olmayan türler tercih edilir.
- Taç yapısı bakımından simetrik; şekil, yapı ve büyüklük açısından ise estetik görünümlü ve fonksiyonel olmalıdır.
- Kuvvetli kök yapısına sahip türler tercih edilmelidir. Fakat kökler kaldırımlara, drenaj kanallarına zarar verecek türden olmamalıdır.
- Hastalık ve zararlılara dayanıklı türler seçilmelidir.
- Yazın gölge yapacak türler tercih edilmelidir.
- Dışarıdan gelebilecek darbelere karşı dayanıklı olmalı, alınan yara sonucu hızla iyileşen türler seçilmelidir (Uzun, 2007).

Kent içindeki yol ağaçlarının işlevleri ve kent yaşamına katkıları şunlardır;

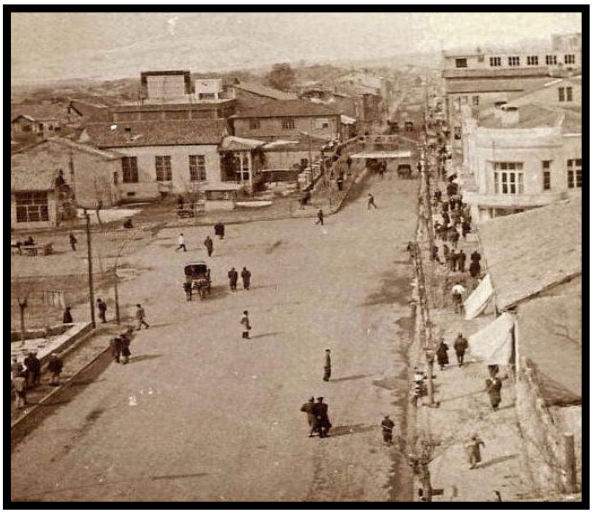
- Bitkiler mekân oluşturmada peyzajda kullanılan en etkili unsurlardır. Ağaçlar bir mekânın çatısı gibi düşünülebilir. Yaya kaldırımları ile taşıt yolunu birbirinden ayırır (Yılmaz, 1998).
- Kentlerde yapılar bazen kötü görünümlere neden olabilmektedir. Ağaçlar perde göreviyle bu görüntüleri gizleyebilmektedir (Karaca ve Kurtaslan, 2017).
- Bütünleştirici etkisiyle yeşil doğayla gri yapılar arasında bir köprü görevi üstlenirler. Şehirde binalardan bunalan insanlara doğayı hissettirirler (Aslanboğa, 1986;; Karaca ve Kurtaslan, 2017).
- İbreli ağaçların havayı filtre etme oranı %70 iken, yaprağını döken geniş yapraklı ağaçların ise % 60'dır. Bu da ağaçların havayı önemli ölçüde temizleyerek kalitesini artırdığını göstermektedir (Uzun, 2007).
- Yönlendirici etkisiyle sürücüler tarafından yolun algılanmasını kolaylaştırır ve yayalara daha güvenli dolaşma ortamı sağlar (Öztürk Kurtaslan, 2002; Kavi, 2003; Karaca ve Kurtaslan, 2017).
- Ağaçların olduğu mekânlar boş mekânlara göre 2-7 °C daha az sıcaklığa sahiptir. Sert zeminlerin ısınması ve bu ısının yükselmesi sonucu rahatsız edici bir sıcaklık oluşmaktadır (Uzun, 2007).

2. Materyal ve Yöntem

Çalışma Elazığ ili şehir merkezindeki Gazi Cadde'sinde gerçekleştirilmiştir. Elazığ; Türkiye'nin Doğu Anadolu Bölgesi'nin Yukarı Fırat Havzası'nda bulunan on bir ilçeden oluşan bir ildir. Konumu itibariyle doğusundan Bingöl, kuzeyden Keban Baraj gölü aracılığıyla Tunceli, güneyden Diyarbakır, batıdan ve güneybatıdan Karakaya Baraj Gölü vasıtasıyla Malatya, kuzeybatıdan Erzincan ilinin arazileriyle çevrilidir (Anonim, 2024a). Gazi Caddesi Elazığ'ın en önemli caddesi olup, ticaretin de odak noktasıdır. Bu anlamda gerek yaya trafiği gerekse araç trafiği bakımında oldukça yoğun bir caddedir. Taşıt yolunun darlığı, araç park sorunu en önemli problemleri arasındadır.



Şekil 1. Elazığ İli Haritası (Anonim, 2024b).



Şekil 2. 1950'li yıllarda Gazi Caddesi (Anonim, 2024c).

Elazığ karasal iklim tipine sahiptir. Kışlar soğuk ve yağışlı geçerken yazları sıcak ve kurak geçmektedir. İlin çevresinde yapılan baraj gölleri iklimde değişimlere neden olmuştur (Elazığ belediyesi, 2024d).



Şekil 3. Elazığ İli Gazi Caddesi çalışma alanı uydu görüntüsü (Anonim, 2024e).

Çalışma alanı uydu görüntüsü incelenerek alanın sınırları belirlenmiştir. Başlangıç noktası olarak eski öğretmenevi, bitiş noktası ise İzzet Paşa Camisi olarak düşünülmüştür (Şekil 3).



Şekil 4. Gazi caddesi' nin kesit görünüşü.

Şekil 4' te kesit görünümde belirtildiği üzere trafik tek yön 3 şerit olacak şekildedir.

Çalışmada yerinde gözlem ve fotoğraflama teknikleri kullanılmıştır. Fotoğraflar çekilerek türler ve sayıları belirlenmiştir. Kullanılan türlerin ekolojik isteklerinin Elazığ iklimine uygunluğu, yol ağacı kriterlerini taşıyıp taşımadığı ile dikim aralığı mesafesi bitkisel tasarım öğeleri açısından değerlendirilmiştir.

Elazığ Belediyesinden ilgili birim ile görüşülüp 'Dikimlerin ne zaman yapıldığı, farklı türlerin kullanılmasının sebepleri, kesilen ağaçların neden kesildiği, bakım işlemleri, yolun sağ ve sol aksında ağaçlar arasındaki belirgin olarak gözlenen büyüklük farkı' gibi sorulara cevap aranmıştır. Alınan cevaplardan faydalanılarak türler yorumlanarak öneriler getirilmiştir. Alana önerilen bazı türlerin Autocad, SketchUp ve Lumion programlarından yararlanılarak 3 boyut görüntüleri oluşturulmuştur.

3. Bulgular

Yapılan araştırmada Elazığ İli Gazi Caddesi yol ağaçlandırılmasında Tablo 1'deki bulgular elde edilmiştir. Türlere ait birer fotoğraf eklenmiştir. Şekil 13, Şekil 14 ve Şekil 15' te görüldüğü gibi sağ ve sol aks üzerindeki ağaçların arasında büyüklük farkı olduğu tespit edilmiştir.

Morus platanifolia (Çınar yapraklı dut) 2010-2013, *Ligustrum japonica* 'Tige' (Tijli kurtbağrı) 2000-2008 yılları arasında dikildiği biliniyorken diğer ağaç türlerinin (*Platanus orientalis, Fraxinus exelcior*) dikim zamanına ait herhangi bir bilgi elde edinilmemiştir.

Bazı ağaçların yıkılan binalarda çalışan iş makinalarına engel olması sebebiyle kesildiği bilgisi edinilmiştir (Şekil 16).

Latince adı	Yaygın adı	Adet
Acer negundo	Dişbudak yapraklı akçaağaç	15
Ailanthus altissima	Kokar ağaç	1
Fraxinus exelcior	Adi dişbudak	1
Ligustrum japonica 'tige'	Tijli kurtbağrı	9
Magnolia grandiflora	Büyük beyaz çiçekli manolya	1
Morus platanifolia	Çınar yapraklı dut	91
Platanus orientalis	Doğu çınarı	1
Pinus nigra	Karaçam	4
Washingtonia robusta	Palmiye	10

Tablo 1. Gazi Caddesi ağaç türleri ve adetleri



Şekil 5. *Acer negundo*



Şekil 6. *Ailanthus altissima*



Şekil 9. *Morus platanifolia*



Şekil 10. *Platanus orientalis*



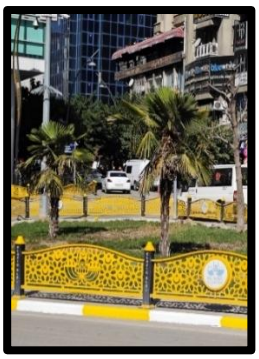
Şekil 7. *Fraxinus exelcior*



Şekil 8. *Ligustrum japonica tige*



Şekil 11. *Pinus nigra*



Şekil 12. *Washingtonia robusta*



Şekil 9. *Morus platanifolia*



Şekil 10. *Platanus orientalis*



Şekil 13. Gazi Caddesi genel görünüm.



Şekil 14. Trafik akış yönüne göre sağ taraf.



Şekil 15. Trafik akış yönüne göre sol taraf.



Şekil 16. Kesilen bir ağaç.

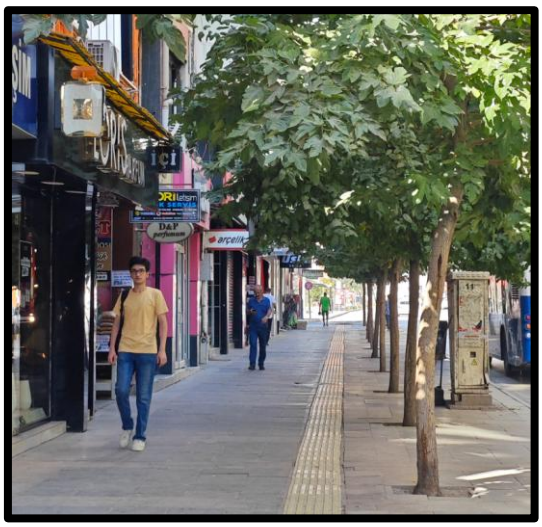
4. Tartışma

Kentsel mekânlarda bitkilendirme en az yapısal öğeler kadar önemlidir. Bu sebeple bitkisel tasarım ile yapısal proje eş zamanlı olarak hazırlanmalıdır. Bitkilerin kullanıldıkları alanlarda, yapısal ve bitkisel diğer materyallerle olan ilişkilerini istenilen şekilde düzenleyebilmek için bitkisel tasarım ilkelerini göz önünde bulundurmak gerekir(Kösa ve Atik, 2013; Caf, 2023).

Elazığ'ın en eski caddelerinden olan Gazi Caddesi günümüze kadar hem yaya hem araç trafiği bakımdan oldukça aktif kullanılan bir caddedir. Aynı zamanda birçok mağazanın bulunması ticaretin de odak noktası haline gelmesini sağlamıştır. Buna rağmen caddede kendisine yakın yaşta bitkiler bulunmamaktadır. Mevcut bir alanda bulunan odunsu bitkilerin yaşı, geçmişte yapılan bitkisel tasarımın başarısını kanıtlar niteliktedir(Caf, 2023). Bu bakımdan bitkilendirme oldukça önem arz etmektedir. Mevcut bitkilendirmenin olumlu ve olumsuz yanları değerlendirilmiştir.

Mevcut ağaçlandırmanın Gazi Caddesine olumlu yanları;

- Ağaçların mekân oluşturma etkisiyle kaldırımlarda mekân hissi oluşturulmuştur (Şekil 17).
- Yeşil alanlar sert zeminlere göre 2-7 ˚C daha serindir(Uzun, 2007).
- Ağaçların havayı filtreleme özelliğiyle; havayı filtreleyerek daha temiz bir hava sunmaktadırlar.



Şekil 17. Mekân etkisi.

Mevcut ağaçlandırmanın Gazi Caddesine olumsuz yanları;

- Bazı türlerin bölgeye ekolojik isteklerden uyum sağlayamayarak kuruduğu görülmüştür (Şekil 18).
- *Morus platanifolia* türünün aşılı tür olması sebebiyle aşının altından çıkan sürgünlerin alınmaması veya kırılmalar sebebiyle bozulmalar meydana gelmiştir (Şekil 19).
- *Morus platanifolia* türünün budamaya ihtiyaç duyması aktif kullanılan bu caddede olumsuz görüntülere sebebiyet vermektedir (Şekil 21).
- Belediyeden elde edilen bilgilerde göz önünde bulundurularak farklı zamanlarda dikim yapıldığı sonucuna varılmıştır (Şekil 13).



Şekil 18. Kurumuş *Magnolia grandiflora*



Şekil 19. Meydana gelen bozulmalar.



Şekil 20. Budama zamanından görüntü.



Şekil 21. Budama sonrası *Morus platanifolia*

5. Sonuç

Peyzaj planlamasında, yalnızca mevcut tasarım süreci değil, aynı zamanda tasarım sonrası bitkilerin gelişimi ve gelecekteki bakım gereksinimleri de dikkate alınmaktadır. Türlere göre değişkenlik gösterse de genel olarak budama, sulama, gübreleme, zararlılar ve hastalıklarla mücadele gibi temel bakım işlemlerinin ihtiyaç doğrultusunda zamanında yapılması gerekmektedir (Turna vd. 2017).

Bu çalışmada elde edilen sonuçlar analiz edilerek, benzer özelliklere sahip kent yolu ağaçlandırmaları için yerel yönetimlere katkı sunabilecek alternatif tasarım önerileri geliştirilmiştir. Elazığ iklimine uygun türlerden bazıları Tablo 2'de verilmiştir. Alternatif tasarımların 3 boyutlu görselleri oluşturulmuştur. Seçilen bitkilerin ekolojik koşullara uygunluğu göz önünde bulundurulmuştur. Kök yapısıyla kaldırımlara zarar vermeyecek, meyve oluşumu olmayan türlerden seçilmeye dikkat edilmiştir. Yapılan öneri tasarımlarla caddeye ait alternatif yeni görseller aşağıda belirtilmiştir.

Tablo 2. Alternatif tasarımlar için öneri bitki türleri

Elazığ İli Gazi Caddesi için alternatif bitkilendirme örneği		
	Latin Name	Common Name
1. Alternatif bitkilendirme	*Prunus cerasifera* 'Pissardii Nigra'	Süs eriği
	Acer platonoides 'Columnare'	Çınar yapraklı akçaağaç
2. Alternatif bitkilendirme	*Lonicera caprifolium*	Hanımeli
	Wisteria sinensis	Mor salkım
3. Alternatif bitkilendirme	*Cupressus sempervirens* 'Pyramidalis'	Akdeniz servisi
	Lavandula angustifolia	Lavanta

1. Alternatif bitkilendirmede; yaprak döken iki türden yuvarlak formlu olan *Prunus cerasifera Pissardii* 'Nigra' ve sütun formlu olan *Acer platonoides* 'Columnare' birlikte kullanılmıştır.

Prunus cerasifera Pissardii 'Nigra' kışın yaprağını döken bir türdür. Boyu 4-8 metre arasındadır. Bordo renkli yapraklarıyla dikkat çeker. İlkbaharda çiçek açar. Az bakım gerektirir ve kent ortamına uyum sağlar.

Acer platonoides 'Columnare' kışın yaprağını döken bir türdür. Boyuna gelişim gösterir. Sonbahar sonunda yaprak rengi sırayla kırmızı, kahverengi ve sarıya döner. Şehir kirliliğine ve zor çevre koşullarına dayanıklıdır. Genelde çok fazla budama gerektirmez.



Şekil 22. *Prunus cerasifera* 'Pissardii Nigra' ve *Acer platonoides* 'Columnare' birlikte kullanımı.

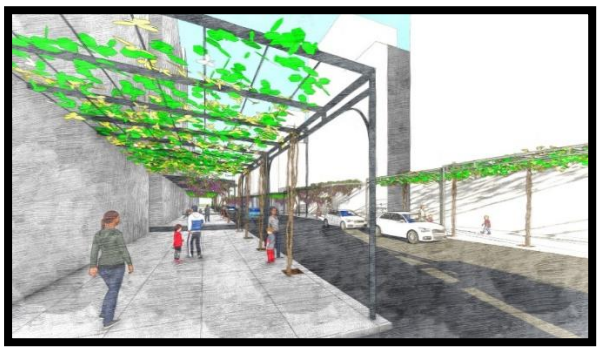
2. Alternatif bitkilendirmede; sarmaşık türlerinden *Lonicera caprifolium* ve *Wisteria Sinensis* kullanılarak kaldırımlarda mekân hissi uyandırılmak istenmiştir. Tekdüzelikten uzak bir tasarım için, iki farklı çiçek rengine sahip bitki türleri birlikte kullanılarak dinamik ve göz alıcı bir kompozisyon oluşturulmuştur.



Şekil 23. *Prunus cerasifera* 'Pissardii Nigra' ve *Acer platonoides* 'Columnare' yakından görünümü.

Lonicera caprifolium; sarılıcı ve tırmanıcı bir yapıya sahiptir. 4-6 metreye kadar uzayabilir. Desteklenirse pergola, çit veya duvarlara kolayca tırmanır. Çiçekler krem, sarı, pembe veya kırmızımsı tonlardadır. Hoş ve yoğun bir kokuya sahiptir. Çiçeklenme dönemi genellikle ilkbahar sonu ve yaz başıdır. İlkbahar veya çiçeklenme sonrası budama yapılabilir.

Wisteria sinensis; Güçlü ve hızlı büyüyen bir sarmaşık bitkisidir. 10-20 metreye kadar uzayabilir. Dikey yüzeylere sarılarak veya destek yapılarına dolanarak büyür. Çiçekler salkım şeklindedir ve genellikle mor, mavi-mor tonlarında olur. Çiçeklenme dönemi ilkbahar sonu veya yaz başıdır. Çiçekler tatlı bir kokuya sahiptir.



Şekil 24. *Lonicera caprifolium*



Şekil 25. *Wisteria sinensis*

3. Alternatif bitkilendirmede; herdem yeşil *Cupressus sempervirens* 'Pyramidalis' alt kısımlarına araç yolu ve yaya yolunu ayırmak amacıyla *Lavandula angustifolia* kullanılmıştır.

Cupressus sempervirens 'Pyramidalis'; İnce, dik ve sütun formundadır. Herdem yeşil olduğundan dört mevsim etkili olabilmektedir. Az bakım gerektirir ve dayanıklıdır. Gerektiğinde budanabilir. Kuraklığa ve kentsel kirliliğe karşı oldukça dirençlidir.

Lavandula angustifolia; 30-60 cm arasında büyüyebilir. Genişliği genellikle 50-60 cm civarındadır. İnce, uzun, gümüşi-yeşil renkte yapraklara sahiptir. Çiçekleri küçük, genellikle mor, leylak veya lavanta rengindedir. Yaz başından sonbahara kadar (genellikle haziran-ağustos) çiçek açar. Çiçeklerin yoğun ve hoş bir kokusu vardır. Kent iklimine uygundur.



Şekil 26. *Cupressus sempervirens* 'Pyramidalis' *altına Lavandula angustifolia*

Önerilen üç farklı tasarım bir birinden bağımsız özelliklerdedir. Tasarımların tamamında kullanılan bitkisel materyal, kent iklimine uygun bitki türleri olup, yetişkin örneklerinin açık yeşil alanlarda sıkça kullanıldığı tespit edilmiştir.

Katkı Oranı Beyanı

Yazarların katkı yüzdeleri aşağıda verilmiştir. Yazarlar makaleyi incelemiş ve onaylamıştır.

	A.C.	S.K.
K	70	30
T	70	30
Y	70	30
VTI	70	30
VAY	70	30
KT	70	30
YZ	70	30
KI	70	30
GR	70	30
PY	70	30
FA	70	30

K= kavram, T= tasarım, Y= yönetim, VTI= veri toplama ve/veya işleme, VAY= veri analizi ve/veya yorumlama, KT= kaynak tarama, YZ= Yazım, KI= kritik inceleme, GR= gönderim ve revizyon, PY= proje yönetimi, FA= fon alımı.

Çatışma Beyanı

Yazarlar bu çalışmada hiçbir çıkar ilişkisi olmadığını beyan etmektedirler.

Etik Onay Beyanı

Bu araştırmada hayvanlar ve insanlar üzerinde herhangi bir çalışma yapılmadığı için etik kurul onayı alınmamıştır.

Kaynaklar

Aklıbaşında M, Erdoğan A. 2016. Nevşehir kentiçi yol bitkilendirmelerinin estetik-fonksiyonel yönden değerlendirilmesi ve kullanılan bitki türlerinin tespiti. BAROFD, 18(1): pp: 57-71.

Anonim. 2025a. Elazığ (il). https://tr.wikipedia.org/wiki/Elaz%C4%B1%C4%9F_(il) (accessed date: February 26, 2025).

Anonim. 2024b. Elazığ haritası: Elazığ ilçeleri nelerdir? Elazığ ilinin nüfusu kaçtır? Kaç ilçesi vardır?. https://www.milliyet.com.tr/egitim/haritalar/elazig-haritasi-elazig-ilceleri-nelerdir-elazig-ilinin-nufusu-kactir-kac-ilcesi-vardir-6311220 (accessed date: December 10, 2024).

Anonim. 2024c. Elazığ City. https://www.instagram.com/elazg.city/p/B7qMVBJhii6/ (accessed date: December 1, 2024).

Anonim. 2024e. Elazığ Gazi Caddesi. Google Earth. https://earth.google.com/web/search/elaz%C4%B1%C4%9F+gazi+caddesi/... (accessed date: December 10, 2024).

Aslanboğa İ. 1986. Kentlerde yol ağaçlaması. Tübitak Yapı Araştırma Enstitüsü Yayını, Ankara, Türkiye, pp: 113.

Atay İ. 2014. Şehir içi ve yol ağaçlandırmaları. Forestist, 8(2): pp: 57-65.

Caf A. 2023. Açık ve yeşil alanlarda bitkisel tasarımlarda yapılan hatalara ilişkin uygulama örnekleri. In: Anadolu 12th

International Conference on Applied Sciences, 26-28 May, Diyarbakır, Türkiye, pp: 100-110.

Erdoğan A, Özer S. 2009. Kayseri kenti yol ağaçlarının estetik ve fonksiyonel yönden incelenmesi. OFD, 10(2): pp: 66-78.

Karaca FY, Öztürk Kurtaslan B. 2021. Kentsel yol ağaçlandırmalarının Ankara "1071 Malazgirt Bulvarı" örneğinde irdelenmesi. JASSS, 58: pp: 276-284.

Kösa S, Atik M. 2013. Bitkisel peyzaj tasarımında renk ve form; Çınar (Platanus orientalis) ve Sığla (Liquidambar orientalis) kullanımında peyzaj mimarlığı öğrencilerinin tercihleri. OFD, 14(1): pp: 13-24.

Şahin Ş. 1989. Ankara kenti yol ağaçlarının sorunları ve peyzaj mimarlığı açısından alınması gerekli önlemler. AÜZF Peyzaj Mimarlığı Bölümü Yayını, Ankara, Türkiye, pp: 48.

Şahin Ş, Barış M. 1998. Kentsel doku içerisinde açık ve yeşil alan standartlarını belirleyen etmenler. Peyzaj Mimar Derg, 6(10): pp: 2088-2109.

Şahin Ş, Kurum E. 2006. Kent içi yol ağaçlandırmasında planlama ve tasarım: Kentiçi ağaçlandırma çalışmalarında teknikler ve sorunlar (Ankara örneği). Kırsal Çevre ve Ormancılık Sorunları Araştırma Derneği, Bildiriler Kitabı, Ankara, Türkiye, pp: 48-63.

Turna İ, Atar F, Yazıcı F. 2017. İstanbul ilindeki kent ağaçlarında budama çalışmalarının değerlendirilmesi. BAROFD, 19(1): pp: 1-10.

Uzun A. 2007. Kent içi ağaçlandırmaları ve İstanbul kent içi ve yol ağaçlandırmalarının kritiği. İstanbul Büyükşehir Belediyesi Yayınları, İstanbul, Türkiye, pp: 48.

Yılmaz BN. 1998. Kentiçi yol ağaçlandırma kriterleri: İstanbul'daki örnek caddelerin incelenmesi. Yüksek Lisans Tezi, İstanbul Teknik Üniversitesi, Fen Bilimleri Enstitüsü, İstanbul, Türkiye, pp: 136.

Yılmaz F, Aksoy Y. 2009. Şehir içi yol bitkilendirmelerinin İstanbul ili Beyoğlu ilçesi Cumhuriyet, Halaskargazi ve Büyükdere caddesi örneğinde irdelenmesi. EJOY, 4(16): pp: 2699-2728.

Yılmaz S. 2019. Bursa ilindeki kentiçi karayollarının bitkisel tasarım ilkeleri yönünden değerlendirilmesi. Yüksek Lisans Tezi, Bursa Uludağ Üniversitesi, Fen Bilimleri Enstitüsü, Bursa, Türkiye, pp: 151.

Black Sea Journal of Engineering and Science
doi: 10.34248/bsengineering.1660516

Open Access Journal
e-ISSN: 2619 – 8991

Araştırma Makalesi (Research Article)
Cilt 8 - Sayı 4: 963-969 / Temmuz 2025
(Volume 8 - Issue 4: 963-969 / July 2025)

ÇEVRESEL TUTUMLARIN SINIFLANDIRILMASINDA ÖZELLİK SEÇİMİ VE MODEL PERFORMANSININ İNCELENMESİ

Rukiye UZUN ARSLAN[1]*, İrem ŞENYER YAPICI[2], Fuat ALKAN[1]

[1]*Zonguldak Bulent Ecevit University, Faculty of Engineering, Department of Electrical and Electronics Engineering, 67100, Zonguldak, Türkiye*
[2]*Zonguldak Bulent Ecevit University, Faculty of Engineering, Department of Computer Engineering, 67100, Zonguldak, Türkiye*

Özet: Çevresel tutumlar, bireylerin sürdürülebilirlik ve ekolojik bilinç düzeylerini yansıtan önemli göstergelerden biridir ve bu tutumların doğru bir şekilde tahmin edilmesi, çevresel politikaların ve farkındalık çalışmalarının etkinliğini artırmada kritik bir rol oynamaktadır. Bu doğrultuda, bu çalışmada bireylerin çevresel tutumlarını tahmin etmek amacıyla çeşitli makine öğrenmesi (MÖ) algoritmaları ve farklı özellik seçimi yöntemleri karşılaştırılmıştır. Analizlerde, Türkiye'de yaşayan 384 katılımcıdan elde edilen açık erişimli bir veri seti kullanılmıştır. Çalışma kapsamında, yedi farklı MÖ algoritması (Rasgele Orman, Lojistik Regresyon, Destek Vektör Makineleri, K-En Yakın Komşu, Çok Katmanlı Algılayıcı, Naive Bayes ve Oylama) ile dört özellik seçimi yöntemi (Ekstra Ağaçlar, Karşılıklı Bilgi, Temel Bileşen Analizi ve Rasgele Orman) değerlendirilmiştir. Elde edilen bulgular, Temel Bileşen Analizi yönteminin Çok Katmanlı Algılayıcı (ÇKA) ve Lojistik Regresyon algoritmalarının performansını anlamlı ölçüde artırdığını göstermiştir. En yüksek doğruluk oranı (%98,7) ve duyarlılık değeri (%100) ÇKA algoritması ile elde edilmiştir. Ayrıca, Karşılıklı Bilgi ve Rasgele Orman yöntemlerinin, Destek Vektör Makineleri ve Oylama algoritmalarının performansını iyileştirdiği belirlenmiştir. Sonuç olarak, bu çalışma, çevresel tutumların tahmininde kullanılan özellik seçimi yöntemleri ile MÖ algoritmalarının kombinasyonlarının etkisini ortaya koymaktadır. Açık erişimli bir veri setinin kullanılması, çalışmanın şeffaflığını ve tekrarlanabilirliğini artırmıştır. Gelecekteki çalışmalarda, daha geniş ve çeşitli veri setleri üzerinde gerçekleştirilecek analizlerle elde edilen bulguların genellenebilirliği değerlendirilebilir.

Anahtar kelimeler: Çevresel tutum tahmini, Özellik seçimi, Model performansı, Sınıflandırma algoritmaları

Feature Selection and Evaluation of Model Performance in Environmental Attitude Classification

Abstract: The environmental attitudes are one of the prominent indicators reflecting the sustainability and ecological awareness levels of individuals, and accurate prediction of these attitudes plays a critical role in increasing the effectiveness of environmental policies and awareness efforts. This study compares various machine learning (ML) algorithms and different feature selection methods to predict the environmental attitudes of individuals in this context. In the analyses, an open-access dataset obtained from 384 participants living in Türkiye has been used. Seven different ML algorithms (Random Forest, Logistic Regression, Support Vector Machines, K-Nearest Neighbours, Multi-Layer Perceptron, Naive Bayes, and Voting) and four feature selection methods (Extra Trees, Mutual Information, Principal Component Analysis, and Random Forest) have been analysed. The obtained results have indicated that the Principal Component Analysis method significantly improved the performance of the Multilayer Perceptron (MLP) and Logistic Regression algorithms. The highest accuracy rate (98.7%) and sensitivity value (100%) were obtained with the MLP algorithm. Furthermore, mutual information and random forest methods were found to improve the performance of support vector machines and voting algorithms. In conclusion, this study demonstrates the effectiveness of combinations of feature selection methods and ML algorithms in predicting environmental attitudes. The use of an open access dataset increased the transparency and reproducibility of the study. In future studies, the generalizability of the findings can be evaluated by analyses on larger and more diverse data sets.

Keywords: Environmental attitude prediction, Feature selection, Model performance, Classification algorithms

***Corresponding author:** Zonguldak Bulent Ecevit University, Faculty of Engineering, Department of Electrical and Electronics Engineering, 67100, Zonguldak, Türkiye
E mail: rukiye.uzun@beun.edu.tr (R. UZUN ARSLAN)
Rukiye UZUN ARSLAN https://orcid.org/0000-0002-2082-8695
İrem ŞENYER YAPICI https://orcid.org/0000-0003-0655-340X
Fuat ALKAN https://orcid.org/0000-0001-7914-2383

Gönderi: 18 Mart 2025 **Received:** March 18, 2025
Kabul: 29 Nisan 2025 **Accepted:** April 29, 2025
Yayınlanma: 15 Temmuz 2025 **Published:** July 15, 2025

Cite as: Arslan UR., Yapıcı Şİ., Alkan F. 2025. Feature selection and evaluation of model performance in environmental attitude classification. BSJ Eng Sci, 8(4): 963-969.

1. Giriş

Çevresel tutumlar, bireylerin doğal çevreye yönelik algılarını, inançlarını ve davranışsal eğilimlerini kapsayan çok boyutlu bir kavramdır. Bu tutumlar, sürdürülebilir kalkınma hedeflerine ulaşma sürecinde ve çevre politikalarının etkinliğinin artırılmasında kritik bir rol oynamaktadır (Milfont ve Duckitt, 2010). Özellikle iklim değişikliği, biyoçeşitlilik kaybı ve çevresel kirlilik gibi küresel ölçekteki ekolojik sorunlar, çevresel tutumların önemini giderek artırmakta ve bu alandaki araştırmalara verilen önceliğin artmasına neden olmaktadır (Calculli vd., 2021). Literatürde, çevresel tutumlar ile sürdürülebilir davranışlar arasında anlamlı bir ilişki olduğu gösterilmiştir. Olumlu çevresel tutumlar, geri dönüşüm, enerji verimliliği ve çevre dostu

This work is licensed (CC BY-NC 4.0) under Creative Commons Attribution 4.0 International License

politikaları destekleme gibi sürdürülebilir davranışlarla pozitif yönde ilişkilendirilirken, olumsuz çevresel tutumlar ise çevresel sorunlara karşı ilgisizlik, değişime direnç ve çevreye zarar verici davranışlarla bağlantılıdır. Bu durum, ekolojik dengenin bozulmasını hızlandırarak çevresel sürdürülebilirliği tehdit etmektedir. Dolayısıyla, çevresel tutumların analizi ve bu tutumların olumlu yönde dönüştürülmesi, sürdürülebilir kalkınma açısından büyük önem taşımaktadır (Kollmuss ve Agyeman, 2002). Çevresel tutumları değerlendirmek amacıyla genellikle bireylerin kendi beyanlarına dayanan anketler ve istatistiksel analizler kullanılmaktadır (Gifford ve Sussman, 2012). Ancak, bu yöntemler çevresel tutumları belirleyen faktörler arasındaki çok yönlü etkileşimlerini açıklamada yetersiz kalarak, analizlerin kapsamını ve derinliğini sınırlayabilmektedir. Bu nedenle, çevresel tutumların çok boyutlu ve dinamik yapısını daha iyi anlayabilmek için makine öğrenmesi (MÖ) gibi yeni analitik yaklaşımların kullanımı giderek artmaktadır. Örneğin, 2018 yılında gerçekleştirilen bir çalışmada, bireylerin iklim değişikliği ve çevresel bozulmaya yönelik tutumlarını tahmin etmede psikolojik ve demografik faktörlerin göreceli önemi MÖ temelli bir yaklaşımla incelenmiştir. Bu çalışmada, Çin, İsviçre ve Amerika Birleşik Devletleri'nde gerçekleştirilen üç farklı anket çalışmasından elde edilen veriler, rasgele orman (RO) algoritması kullanılarak analiz edilmiştir. Analizlerde bireylerin gelecekteki sonuçları dikkate alma eğiliminin, geleneksel demografik değişkenlere kıyasla iklim ve çevre tutumlarını tahmin etmede daha baskın olduğu tespit edilmiştir (Beiser-McGrath ve Huber, 2018). 2022 yılında yapılan bir çalışmada ise, Çin'deki halka açık firmaların çevre koruma ve karbon emisyonlarına yönelik tutumlarını incelemek amacıyla yenilikçi bir yaklaşım benimsemiştir. Çalışmada, firma-yatırımcı soru-cevap kayıtları gibi metin tabanlı veriler kullanılarak, doğal dil işleme tabanlı duygu analizi ve RO modelleri gibi MÖ algoritmaları uygulanmıştır. Bu yöntemler, firmaların çevresel tutumlarını niceliksel olarak ölçmek ve zaman içindeki değişimlerini analiz etmek için kullanılmıştır (Li vd., 2022). Aynı yıl yapılan başka bir çalışmada, bireylerin ekonomik büyüme ve çevre koruma arasındaki öncelik tercihlerini tahmin etmek amacıyla makroekonomik ve bireysel düzeydeki değişkenler makine öğrenmesi yöntemleri kullanılarak analiz edilmiştir. Çalışmada 51348 katılımcıya ait veriler kullanılarak, bir dizi değişken seçim algoritması uygulanmış ve bireylerin çevresel öncelik düzeylerini tahmin etmek için RO modelleri eğitilmiştir. Yapılan analizlerde, en optimal modelin tahmin hata oranı %34,15 olarak hesaplanmış ve bireylerin çevre koruma önceliğini belirlemede makroekonomik ve psikolojik değişkenlerin önemli olduğu tespit edilmiştir (Lou vd., 2022). 2022 yılında yapılan başka bir çalışmada ise, üniversite öğrencilerinin çevreci davranışlarını öngörmek amacıyla karar ağacı (KA) temelli bir model geliştirilmiştir. Çalışmada, 334 üniversite öğrencisinden elde edilen verilerin analizi sonucunda, çevresel sorumluluk bilinci, yenilikçi davranış ve algılanan davranışsal kontrolün çevreci davranışların en önemli belirleyicileri olarak tespit edilmiştir. Önerilen modelle yapılan analizlerde %72,89'luk doğruluk oranlarına ulaşılmıştır (Wang vd., 2022). 2024 yılında yapılan bir çalışmada, bireylerin çevresel tutumlarının farklı MÖ algoritmalarıyla tahmin edilebilirliği irdelenmiştir. Bu kapsamda, k-en yakın komşu (KNN), KA ve destek vektör makineleri (DVM) olmak üzere üç farklı MÖ algoritmasının performansları karşılaştırılmıştır. En yüksek başarım %95,76 doğruluk oranı ile DVM tarafından elde edilmiştir (Değirmenci, 2024). Aynı yıl yapılan bir diğer çalışmada, bireylerin 84 katılımcıdan elde edilen verilerle çevreye yönelik tutumları analiz etmek amacıyla lojistik regresyon (LR), DVM ve KA algoritmaları kullanılmıştır. Çalışmada, LR modeli %94.53 doğruluk oranı ile en yüksek başarımı sergilemiştir (Köklü ve Sulak, 2024). Yakın zamanda yapılan bir çalışmada, bireylerin çevresel farkındalık düzeylerini ve tutumlarını analiz etmek amacıyla MÖ tabanlı bir model geliştirilmiştir. Bu çalışmada, DVM, gradyan artırma (GA), çok katmanlı algılayıcı (ÇKA), kuadratik diskriminant analizi (KDA) ve torbalama (Bagging) algoritmalarının performansları karşılaştırılmıştır. Modelin doğruluğunu artırmak ve daha az sayıda özellikle yüksek performans elde etmek için varyans analizi tabanlı bir özellik seçimi yöntemi uygulanmıştır. Bu yöntem, modelin karmaşıklığını azaltarak en anlamlı özelliklerin belirlenmesini sağlamıştır. Yapılan analizler sonucunda, GA algoritması %84,4 doğruluk oranı ile en yüksek performansı göstermiştir (Yapıcı vd., 2025). Ancak, mevcut literatürde özellik seçimi süreçlerinin MÖ temelli modellerin performansları üzerindeki etkilerini kapsamlı bir şekilde inceleyen çalışmalar sınırlıdır. Çevresel tutumların tahmin edilmesinde en belirleyici değişkenlerin (özelliklerin) belirlenmesi, model performansının artırılmasında kritik bir rol oynamaktadır. Bu kapsamda, gerçekleştirilen bu çalışmada çevresel tutumların tahmininde en etkili özellikleri belirlemek amacıyla Karşılıklı Bilgi (Mutual Information, MI), Temel Bileşen Analizi (TBA), Ekstra Ağaçlar (Extra Trees, EA) ve RO yöntemleri kullanılmıştır. Daha sonra, seçilen özellikler kullanılarak yedi farklı MÖ algoritması eğitilmiş ve başarımları karşılaştırılmıştır. MÖ algoritması olarak RO, LR, DVM, KNN, çok katmanlı algılavıcı (ÇKA), Naive Bayes (NB) ve oylama (Voting) algoritmaları kullanılmıştır. Bu sayede, çevresel tutumların tahmin edilmesine yönelik daha etkili bir metodolojik çerçeve sunulması ve literatürdeki boşluğun doldurulması hedeflenmektedir

2. Materyal ve Yöntem

Bu çalışmada, bireylerin çevresel tutumlarını analiz etmek amacıyla oluşturulmuş bir veri seti kullanılmıştır. Türkiye'de yaşayan ve yaşları 18 ile 45 arasında değişen toplam 384 katılımcıdan çevrimiçi anket yöntemiyle elde edilen veri seti, bireylerin çevresel sorumluluk davranışlarını ölçmeye yönelik 37 değişken içermektedir.

Katılımcıların cinsiyet dağılımı incelendiğinde, örneklemin 177 erkek ve 207 kadın bireyden oluştuğu tespit edilmiştir. Veri setinde demografik ve sosyoekonomik faktörler (cinsiyet, yaş, eğitim düzeyi, gelir durumu) ile birlikte çevre eğitimi geçmişi (çevre eğitimi alıp almadıkları, küresel ısınma ve iklim değişikliği dersleri, çevresel okuryazarlık kursları, okul öncesi eğitim) gibi değişkenler yer almaktadır. Ayrıca, çevresel konulara yönelik tutumları ölçmeye yönelik 27 soru içeren anket kapsamında, kirlilik, kaynak tüketimi, geri dönüşüm, enerji kullanımı, çevresel eğitim ve aktivizm gibi konulara dair görüşler toplanmıştır. Çalışmada hedef (çıktı) değişken olarak bireylerin çevresel tutumları analiz edilerek, katılımcılar pozitif veya negatif tutum sergileyen bireyler olarak iki ayrı sınıfa ayrılmıştır. Veri setine

https://nigmetkoklu.com/dataset/environmental_attitude_dataset.zip adresi üzerinden erişim sağlanabilmektedir (Köklü ve Sulak, 2024).

İlgili veri seti, bireylerin çevresel tutumlarını sınıflandırmaya yönelik MÖ modellerinin geliştirilmesinde kullanılmıştır. Bu kapsamda, veri ön işleme aşamasında eksik değerlerin kontrolü sağlanmış, kategorik değişkenler uygun şekilde dönüştürülmüş ve özellik seçimi gerçekleştirilmiştir. Ardından, farklı MÖ algoritmaları eğitilerek performansları karşılaştırılmış ve en başarılı model belirlenmiştir. Şekil 1'de, veri ön işleme, model eğitimi ve değerlendirme süreçlerini özetleyen sözde kod sunulmaktadır.

Adım 1: Veri Kümesini Yükleme ve Ön İşleme
Girdi: Veri Kümesi
Çıktı: Ön işlenmiş veri kümesi (X_train, X_test, y_train, y_test)
    1.1 Veri kümesini yükle
    1.2 Ozellik seçimi uygula (TBA, MI, EA, RO vb.)
    1.3 Veri kümesini %80 eğitim ve %20 test olarak ayır
    1.4 Eksik verileri işle (gerekliyse)
    1.5 Sayısal özellikleri normalize et veya standartlaştır (gerekiyorsa)
    1.***6*** Kategorik değişkenleri kodla (varsa)
Adım 2: MÖ Modellerinin Eğitimi ve Değerlendirilmesi
    Girdi: Ön işlenmiş veri kümesi (*X_train, y_train*)
    Çıktı: Eğitilmiş modeller ve performans metrikleri (modeller, metrikler)
    2.1 Model listesi tanımla = {DVM, MLP, KA, LR, NB, RO, Voting}
    2.2 Model başarı metriklerini saklamak için boş bir sözlük oluştur (*model_metrikleri*)
    Her model için:
        2.3 Modeli başlat
        2.4 k-kat çapraz doğrulama (k=5) kullanarak modeli eğit
        2.5 Test verisi (*X_test*) üzerinde tahmin yap
        2.6 Performans metriklerini hesapla (doğruluk, kesinlik, duyarlılık, F1-skoru)
        2.7 Modelin adını ve performans metriklerini *model_metrikleri* sözlüğüne kaydet
Adım 3: En Iyi Modelin Seçilmesi
    Girdi: *model_metrikleri* sözlüğü
    Çıktı: En iyi model (*en_iyi_model*)
    3.1 En yüksek performans metriğine sahip modeli belirle
    3.2 *en_iyi_model* değişkenini en yüksek metrik değerine sahip model olarak ata
Adım 4: Sonuçların Raporlanması
    Girdi: *en_iyi_model* ve *model_metrikleri*
    Çıktı: Sonuç tablosu ve en iyi model bilgileri
    4.1 Tüm modellerin başarı metriklerini tablo halinde göster
    4.2 En iyi modelin adını ve metriklerini raporla

Şekil 1. Çevresel tutumların tahminine yönelik makine öğrenmesi sürecini özetleyen sözde kod.

Veri ön işleme aşamasında, eksik verilerin olmadığı tespit edilmiş olmasına rağmen, diğer ön işleme adımları titizlikle uygulanmıştır. Sayısal değişkenler arasındaki ölçek farklılıklarını gidermek için StandardScaler kullanılarak normalizasyon işlemi gerçekleştirilmiştir. Bu adım, değişkenlerin aynı ölçekte olmasını sağlayarak modelin daha dengeli ve etkili bir şekilde öğrenmesine katkıda bulunmuştur. Ayrıca, özellik seçimi sürecinde değişkenlerin sınıflandırma başarısına etkisini değerlendirmek amacıyla EA, MI, TBA ve RO gibi yöntemler kullanılmıştır. Bu yöntemler sayesinde en yüksek bilgi değerine sahip değişkenler belirlenmiş ve

analiz sürecine dahil edilmiştir. Bu adım, hem modelin hesaplama maliyetini azaltmış hem de sınıflandırma performansını artırmayı hedeflemiştir.

Çalışmada, çevresel tutumların tahmin edilmesi amacıyla yedi farklı MÖ algoritması (RO, LR, DVM, MLP, NB, KNN ve Oylama) kullanılmıştır. Bunlardan RO, çok sayıda karar ağacının bir araya gelmesiyle oluşan bir topluluk öğrenme yöntemi olup, yüksek doğruluk oranları ve aşırı öğrenmeye karşı dirençli yapısıyla dikkat çekmektedir. LR, özellikle ikili sınıflandırma problemlerinde kullanılan, doğrusal bir model olup, sonuçların yorumlanabilirliği açısından avantaj sağlamaktadır (Uzun et al. 2019). DVM, veriyi yüksek boyutlu bir özellik uzayında ayıran optimal hiperdüzlemi bulmaya dayalı bir yöntem olup, özellikle küçük ve orta ölçekli veri setlerinde etkilidir (Arslan ve Yapici, 2024). MLP, yapay sinir ağlarının bir türü olup, doğrusal olmayan veri yapılarını modellemek için kullanılmaktadır (Arslan vd., 2020). NB, Bayes teoremine dayalı olasılıksal bir sınıflandırma yöntemi olup, özellikle yüksek boyutlu veri setlerinde hızlı ve etkili sonuçlar vermektedir. KNN, bir veri noktasının sınıfını veya değerini, etrafındaki en yakın k komşusunun özelliklerine dayanarak tahmin eden, öğrenme aşaması olmayan (lazy learning) ve mesafe temelli çalışan bir MÖ yöntemidir (Chethana, 2021). Oylama algoritması, birden fazla temel modelin tahminlerini birleştirerek daha güçlü bir topluluk modeli oluşturan bir yöntemdir (Kumari vd., 2021).

Model eğitimi sürecinde, veri seti %80 eğitim ve %20 test olarak ayrılmıştır. Ayrıca, modelin genelleme yeteneğini artırmak ve aşırı öğrenmeyi önlemek amacıyla 5 katlı çapraz doğrulama yöntemi uygulanmıştır. Bu yöntem, modellerin farklı veri alt kümeleri üzerinde test edilmesini sağlayarak daha güvenilir sonuçlar elde edilmesine olanak tanımıştır.

Model başarımlarını değerlendirmek için doğruluk, hassasiyet, duyarlılık ve F1-Skoru gibi performans metrikleri kullanılmıştır. Bu metrikler, modellerin çevresel tutumları ne kadar doğru ve etkili bir şekilde sınıflandırdığını ölçmek amacıyla tercih edilmiştir. İlgili metriklere ait denklemler Tablo 1'de verilmiştir.

Tablo 1. Sınıflandırma metrikleri ve formülleri

Metrik	Tanımı	Matematiksel Formülü
Doğruluk	Modelin doğru sınıflandırdığı örneklerin toplam örnek sayısına oranı.	$\frac{TP+TN}{TP+TN+FP+FN}$
Duyarlılık	Pozitif olarak tahmin edilen örneklerin gerçekten pozitif olma oranı.	$\frac{TP}{TP+FN}$
Hassasiyet	Gerçekte pozitif olan örneklerin doğru tahmin edilme oranı.	$\frac{TP}{TP+FP}$
F1-skor	Duyarlılık ve hassasiyet metriklerinin harmonik ortalaması	$2 * \frac{Duyarlılık * Hassasiyet}{Duyarlılık + Hassasiyet}$

3. Bulgular

Bireylerin çevresel tutumlarının MÖ algoritmaları ile tahmin edilmesine yönelik bu çalışmada, model başarımını artırmak ve en etkili değişkenleri belirlemek amacıyla dört farklı özellik seçimi yöntemi uygulanmıştır. Bu kapsamda, EA, MI, TBA ve RO yöntemleriyle seçilen özellikler (değişkenler) yedi farklı MÖ algoritması ile değerlendirilmiş ve algoritmaların performansları karşılaştırılmıştır. Seçilen değişkenlerin modeller üzerindeki etkisini daha güvenilir bir şekilde analiz edebilmek için veri seti %80 eğitim ve %20 test olarak bölünmüş ve 5 katlı çapraz doğrulama yöntemi uygulanmıştır. Ardından, belirlenen değişkenler kullanılarak eğitilen modellerin performansları doğruluk, hassasiyet, duyarlılık ve F1-skoru metrikleri üzerinden analiz edilmiştir.

Bu doğrultuda Tablo 2, EA yöntemiyle belirlenen özelliklerin kullanılması durumunda MÖ algoritmalarının performans metriklerini göstermektedir. Sonuçlara göre, DVM algoritması doğruluk (%85,7), hassasiyet (%86,5), duyarlılık (%84,2) ve F1-skoru (%85,3) metriklerinde en yüksek performansı göstererek diğer algoritmalar arasında öne çıkmıştır. KNN, NB ve Voting algoritmaları, hassasiyet metriklerinde yüksek performans (%88,2) göstermelerine rağmen, duyarlılık (%78,9) ve F1-skoru (%83,3) metriklerinde daha düşük performans sergilemişlerdir. RO algoritması ise tüm metriklerde en düşük performansı göstermiştir (doğruluk: %80,5, hassasiyet: %79,5, duyarlılık: %81,6, F1-skoru: %80,5). LR ve ÇKA algoritmaları ise tüm metriklerde benzer performans sergilemişlerdir (doğruluk: %81,8, hassasiyet: %83,3, duyarlılık: %78,9, F1-skoru: %81,1). Bu sonuçlar, EA yöntemiyle seçilen özelliklerin kullanılması durumunda DVM algoritmasının diğer algoritmalara göre daha etkili olduğunu göstermektedir.

Tablo 3, MI yöntemiyle seçilen özelliklerin kullanılması durumunda elde edilen performans değerlerini göstermektedir. DVM ve Voting algoritmalarının doğruluk (%92,2), hassasiyet (%92,1), duyarlılık (%92,1) ve F1-skoru (%92,1) metriklerinde en yüksek performansı sergileyerek diğer algoritmalar arasında öne çıkmıştır. LR algoritması, hassasiyet metriğinde en yüksek değeri (%96,9) elde etmesine karşın, duyarlılık (%81,6) ve F1-skoru (%88,6) açısından daha düşük

performans göstermiştir. RO algoritması ise doğruluk (%88,3), hassasiyet (%89,2), duyarlılık (%86,8) ve F1-skoru (%88,0) değerleriyle dengeli bir performans sergilemiştir. KNN algoritması, duyarlılık metriğinde (%86,8) görece yüksek bir başarı göstermesine rağmen, hassasiyet (%82,5) ve F1-skoru (%84,6) bakımından nispeten daha düşük sonuçlar elde etmiştir. NB algoritması, hassasiyet metriğinde (%91,2) yüksek bir değer sunmasına rağmen, duyarlılık (%81,6) ve F1-skoru (%86,1) açısından daha düşük performans sergilemiştir. ÇKA algoritması ise doğruluk (%88,3), hassasiyet (%87,2), duyarlılık (%89,5) ve F1-skoru (%88,3) değerleriyle dengeli bir performans ortaya koymuştur. Bu sonuçlar, MI yöntemiyle seçilen özelliklerin kullanımıyla DVM ve Voting algoritmalarının diğer algoritmalara kıyasla daha etkili olduğunu ortaya koymaktadır.

Tablo 2. EA yöntemiyle seçilen özelliklerin kullanılması durumunda MÖ algoritmalarına ait performans metrikleri

Sınıflandırıcı	Doğruluk	Hassasiyet	Duyarlılık	F1- skor
LR	81,8%	83,3%	78,9%	81,1%
RO	80,5%	79,5%	81,6%	80,5%
DVM	85,7%	86,5%	84,2%	85,3%
K-NN	84,4%	88,2%	78,9%	83,3%
NB	84,4%	88,2%	78,9%	83,3%
ÇKA	81,8%	83,3%	78,9%	81,1%
Voting	84,4%	88,2%	78,9%	83,3%

Tablo 3. MI yöntemiyle seçilen özelliklerin kullanılması durumunda MÖ algoritmalarına ait performans metrikleri

Sınıflandırıcı	Doğruluk	Hassasiyet	Duyarlılık	F1- skor
LR	89,6%	96,9%	81,6%	88,6%
RO	88,3%	89,2%	86,8%	88,0%
DVM	92,2%	92,1%	92,1%	92,1%
K-NN	84,4%	82,5%	86,8%	84,6%
NB	87,0%	91,2%	81,6%	86,1%
ÇKA	88,3%	87,2%	89,5%	88,3%
Voting	92,2%	92,1%	92,1%	92,1%

Tablo 4, TBA yöntemiyle seçilen özelliklerin kullanılması durumunda elde edilen performans metriklerini göstermektedir. ÇKA algoritması, %98,7 doğruluk, %97,4 kesinlik ve %100 duyarlılık ile en yüksek performansı gösterirken, LR algoritması da %97,4 doğruluk ve F-skor ile benzer bir başarı elde etmiştir. RO ve DVM algoritmaları sırasıyla %93,5 ve %92,2 doğruluk oranlarıyla tatmin edici sonuçlar verirken, KNN ve NB algoritmaları da %90'ın üzerinde doğruluk oranlarıyla performanslarını sergilemiştir. Voting algoritması ise %94,8 doğruluk ve %94,9 F-skor ile dengeli bir performans göstermiştir. Bu sonuçlar, TBA yöntemiyle seçilen özelliklerin, özellikle ÇKA ve LR gibi algoritmalar için etkili olduğunu ve özellik seçiminin model performansını önemli ölçüde artırabileceğini ortaya koymaktadır.

Tablo 4. TBA yöntemiyle seçilen özelliklerin kullanılması durumunda MÖ algoritmalarına ait performans metrikleri

Sınıflandırıcı	Doğruluk	Hassasiyet	Duyarlılık	F1- skor
LR	97,4%	95,0%	100,0%	97,4%
RO	93,5%	90,2%	97,4%	93,7%
DVM	92,2%	88,1%	97,4%	92,5%
K-NN	92,2%	92,1%	92,1%	92,1%
NB	90,9%	86,0%	97,4%	91,4%
ÇKA	98,7%	97,4%	100,0%	98,7%
Voting	94,8%	92,5%	97,4%	94,9%

Son olarak, Tablo 5 RO yöntemiyle belirlenen özelliklerin kullanılması durumunda elde edilen sonuçları göstermektedir. ÇKA algoritması, %98,7 doğruluk, %97,4 kesinlik ve %100 duyarlılık ile en yüksek performansı gösterirken, LR algoritması da %96,1 doğruluk ve F-skor ile yakın bir başarı sergilemiştir. DVM algoritması %92,2 doğruluk ve %92,5 F-skor ile tatmin edici sonuçlar verirken, RO ve KNN algoritmaları sırasıyla %89,6 ve %89,6 doğruluk oranlarıyla daha düşük performans göstermiştir. NB algoritması ise %85,7 doğruluk ve

%84,9 F-skor ile en düşük performansa sahiptir. Voting algoritması, %96,1 doğruluk ve %96,2 F-skor ile LR ve CKA'ya yakın bir performans sergilemiştir. Bu sonuçlar, RO yöntemiyle belirlenen özelliklerin özellikle ÇKA ve LR algoritmaları için avantaj sağladığını ortaya koymaktadır. Genel olarak, uygulanan dört farklı özellik seçimi yönteminin model performansı üzerindeki etkisi değişkenlik göstermiştir. MI ve RO yöntemleri, DVM ve Voting algoritmalarının performansını artırırken, TBA yöntemi özellikle ÇKA algoritmasının başarımını yükseltmiştir. EA yöntemi ile ise DVM algoritması en iyi sonucu vermiştir. Bu sonuçlar, model performansının kullanılan özellik seçimi yöntemine ve algoritmaya bağlı olarak değiştiğini göstermektedir.

Tablo 5. RO yöntemiyle seçilen özelliklerin kullanılması durumunda MÖ algoritmalarına ait performans metrikleri

Sınıflandırıcı	Doğruluk	Hassasiyet	Duyarlılık	F1- skor
LR	96,1%	94,9%	97,4%	96,1%
RO	89,6%	87,5%	92,1%	89,7%
DVM	92,2%	88,1%	97,4%	92,5%
K-NN	89,6%	94,1%	84,2%	88,9%
NB	85,7%	88,6%	81,6%	84,9%
ÇKA	98,7%	97,4%	100,0%	98,7%
Voting	96,1%	92,7%	100,0%	96,2%

4. Tartışma

Bu çalışmada, bireylerin çevresel tutumlarının tahmin edilmesi amacıyla farklı MÖ algoritmaları ve özellik seçimi yöntemlerinin performansları kapsamlı bir şekilde değerlendirilmiştir. Türkiye'de yaşayan 384 katılımcıdan oluşan açık erişimli bir veri seti kullanılarak yürütülen analizler, çevresel tutum tahmininde özellik seçimi yöntemlerinin ve MÖ algoritmalarının etkinliğini karşılaştırmayı hedeflemiştir. Çalışma kapsamında dört farklı özellik seçimi yöntemi (MI, TBA, EA ve RO) uygulanmış ve seçilen öznitelikler yedi farklı MÖ algoritmasının (RO, LR, DVM, KNN, ÇKA, NB ve Oylama) performansları değerlendirilmiştir.

Elde edilen bulgular, hem özellik seçimi yöntemlerinin hem de MÖ algoritmalarının performansında belirgin farklılıklar olduğunu ortaya koymuştur. EA yöntemiyle seçilen özniteliklerin kullanıldığı durumda DVM algoritması %85,7 doğruluk ve %85,3 F1-skoru ile en yüksek performansı sergilemiştir. Buna karşılık, MI yöntemiyle seçilen öznitelikler kullanıldığında DVM ve Oylama algoritmaları %92,2 doğruluk ve F1-skoru ile daha üstün bir başarı göstermiştir. TBA yönteminin ise özellikle ÇKA ve LR algoritmalarının performansını önemli ölçüde iyileştirdiği gözlemlenmiştir. Bu bağlamda, ÇKA algoritması %98,7 doğruluk ve %100 duyarlılık oranı ile dikkat çekici bir performans sergilemiştir. Benzer şekilde, RO yöntemiyle seçilen öznitelikler de ÇKA ve LR algoritmalarının başarısını artırmıştır.

Bu sonuçlar, çevresel tutum tahmini gibi karmaşık bir problemi çözmek için özellik seçimi yöntemlerinin ve MÖ algoritmalarının kombinasyonunun kritik bir rol oynadığını göstermektedir. Özellikle TBA yöntemi, ÇKA ve LR gibi algoritmalar için en etkili sonuçları sağlarken, MI ve RO yöntemleri DVM ve Oylama algoritmalarının performansını artırmıştır. Bu bulgular, çevresel tutumların analizinde kullanılan metodolojik yaklaşımların, model performansını önemli ölçüde etkileyebileceğini göstermektedir.

Katkı Oranı Beyanı

Yazarların katkı yüzdeleri aşağıda verilmiştir. Yazarlar makaleyi incelemiş ve onaylamıştır.

	R.U.A.	İ.S.Y.	F.A.
K	40	40	20
T	30	40	30
Y	60	20	20
VTI	20	50	30
VAY	40	40	20
KT	20	40	40
YZ	30	30	40
KI	40	30	30
GR	60	20	20

K= kavram, T= tasarım, Y= yönetim, VTI= veri toplama ve/veya işleme, VAY= veri analizi ve/veya yorumlama, KT= kaynak tarama, YZ= Yazım, KI= kritik inceleme, GR= gönderim ve revizyon, PY= proje yönetimi, FA= fon alımı.

Çatışma Beyanı

Yazarlar bu çalışmada hiçbir çıkar ilişkisi olmadığını beyan etmektedirler.

Etik Onay Beyanı

Bu araştırmada hayvanlar ve insanlar üzerinde herhangi bir çalışma yapılmadığı için etik kurul onayı alınmamıştır.

Kaynaklar

Arslan RU, İşler Y, Toksan M. 2020. Prediction of the success of wart treatment methods. Karaelmas Sci Eng J, 10(1): pp: 44-52.

Arslan RU, Yapıcı İŞ. 2024. Farklı örnekleme tekniklerine ve farklı sınıflandırıcılara dayanarak kalp yetmezliği tanılı hastaların sağkalımlarının incelenmesi. EMO Bilimsel Dergi, 14(2): pp: 35-47.

Beiser-McGrath LF, Huber RA. 2018. Assessing the relative importance of psychological and demographic factors for predicting climate and environmental attitudes. Clim Change, 149: pp: 335-347.

Calculli C, D'Uggento AM, Labarile A, Ribecco N. 2021. Evaluating people's awareness about climate changes and environmental issues: A case study. J Clean Prod, 324: 129244.

Chethana C. 2021. Prediction of heart disease using different KNN classifier. In: Proceedings of the 5th International Conference on Intelligent Computing and Control Systems (ICICCS), May 2021, IEEE, pp: 1186-1194.

Değirmenci A. 2024. Comparison of K-Nearest Neighbors, Decision Tree and Support Vector Machines Methods in Predicting Environmental Attitudes. Emerg Trends Electr Electron Eng, 4: 69-78.

Gifford R, Sussman R. 2012. Environmental attitudes. In: Clayton SD, ed. The Oxford Handbook of Environmental and Conservation Psychology. Oxford University Press, Oxford, UK, 1st ed., pp: 65-80. https://doi.org/10.1093/oxfordhb/9780199733026.013.0004.

Koklu N, Sulak SA. 2024. Classification of environmental attitudes with artificial intelligence algorithms. Intell Methods Eng Sci, 3(2): pp: 54-62.

Kollmuss A, Agyeman J. 2002. Mind the gap: why do people act environmentally and what are the barriers to pro-environmental behavior?. Environ Educ Res, 8(3): pp: 239-260.

Kumari S, Kumar D, Mittal M. 2021. An ensemble approach for classification and prediction of diabetes mellitus using soft voting classifier. Int J Cogn Comput Eng, 2: pp: 40-46.

Li C, Li L, Zheng J, Wang J, Yuan Y, Lv Z, Liu W. 2022. China's public firms' attitudes towards environmental protection based on sentiment analysis and random forest models. Sustainability, 14(9): pp: 5046.

Lou X, Lin Y, Li LMW. 2022. Predicting priority of environmental protection over economic growth using macroeconomic and individual-level predictors: Evidence from machine learning. J Environ Psychol, 82: 101843.

Milfont TL, Duckitt J. 2010. The environmental attitudes inventory: A valid and reliable measure to assess the structure of environmental attitudes. J Environ Psychol, 30(1): pp: 80-94. https://doi.org/10.1016/j.jenvp.2009.09.001.

Uzun R, İşler Y, Toksan M. 2019. WEKA yazılım paketinin siğil tedavi yöntemlerinin başarısının tahmininde kullanımı. Düzce Univ Bilim Teknol Derg, 7(1): pp: 699-708.

Wang Q, Kou Z, Sun X, Wang S, Wang X, Jing H, Lin P. 2022. Predictive analysis of the pro-environmental behaviour of college students using a decision-tree model. Int J Environ Res Public Health, 19(15): pp: 9407.

Yapıcı İŞ, Arslan RU, Alkan F. 2023. Makine öğrenmesi tabanlı çevresel tutum sınıflandırmasında varyans analizi yaklaşımı. In: Proceedings of the 2nd International Colosseum Scientific Researches and Innovation Congress, February 22-23, Italy, pp: 6-16.

Black Sea Journal of Engineering and Science
doi: 10.34248/bsengineering.1645207

Open Access Journal
e-ISSN: 2619 – 8991

Research Article
Volume 8 - Issue 4: 970-981 / July 2025

THE REFINED PHYSICS-INFORMED NEURAL NETWORKS FOR NONLINEAR CONVECTION-REACTION-DIFFUSION EQUATIONS USING EXPONENTIAL SCHEMES

Burhan BEZEKCI[1]

[1]*Kilis 7 Aralik University, Faculty of Engineering and Architecture, Department of Electrical - Electronics Engineering, 79000, Kilis, Türkiye*

Abstract: The nonlinear convection-reaction-diffusion equations model complex real-world phenomena across scientific and engineering disciplines. However, solving these equations analytically is often impossible due to their nonlinear nature. As a result, researchers have turned to numerical and computational methods to find approximate solutions. These methods, while effective, can struggle with issues such as stability, accuracy, and the ability to handle sharp gradients or complex interactions between convection, diffusion, and reaction terms. To address these challenges, this work introduces an enhanced Physics-Informed Neural Network (PINN) framework for convection-reaction-diffusion equations that incorporates exponential finite difference scheme residuals with the aim of enhancing solution accuracy and stability. To validate its performance, the framework has been tested on four well-known nonlinear partial differential equations: Burgers' Equation, Fisher's Equation, the Burgers-Huxley Equation, and the Newell-Whitehead-Segel Equation. The results obtained using the modified PINN framework are systematically compared with those obtained using traditional Physics-Informed Neural Networks and the Galerkin Finite Element Method. The comparisons reveal that the proposed framework consistently outperforms both approaches in terms of accuracy. These improvements highlight the effectiveness of integrating exponential finite difference scheme residuals into the PINN framework, making it a powerful and reliable tool for solving nonlinear convection-reaction-diffusion equations.

Keywords: PINN, deep learning, Exponential scheme, Convection-reaction-diffusion, Burgers', Fisher's, Burgers-Huxley, Newell-Whitehead-Segel

***Corresponding author**: Kilis 7 Aralik University, Faculty of Engineering and Architecture, Department of Electrical - Electronics Engineering, 79000, Kilis, Türkiye
E mail: burhanbezekci@kilis.edu.tr (B. BEZEKCI)
Burhan BEZEKCİ https://orcid.org/0000-0001-7460-4091

Received: February 26, 2025
Accepted: April 4, 2025
Published: July 15, 2025

Cite as: Bezekci B.2025. The refined physics-informed neural networks for nonlinear convection-reaction-diffusion equations using exponential schemes. BSJ Eng Sci, 8(4): 970-981.

1. Introduction

Nonlinear partial differential equations (PDEs) are essential mathematical tools for describing dynamic processes in a wide range of scientific and engineering fields. They are used extensively in areas such as fluid dynamics, plasma physics, environmental modeling, and mathematical biology, where they capture complex interactions and evolving spatiotemporal patterns. Among these, nonlinear convection-reaction-diffusion (CRD) equations are especially important because they describe systems influenced by the combined effects of diffusion, convection, and reaction mechanisms. These equations arise in many real-world applications, including chemical reaction modeling, environmental pollution transport, heat transfer in engineering systems, and the dynamics of biological populations (Nekhamkina and Freed 2000; Morton 1996; Murray 2007; Bezekci 2025; Bezekci 2025; Seinfeld and Pandis 1998; Bejan 2013; Dong et al. 2022). A general mathematical form of these equation 1 can be expressed as;

$$\frac{\partial u}{\partial t} = \nabla \cdot [D\nabla u] - \nabla \cdot (vu) + S \quad (1)$$

where u represents the variable of interest, such as species concentration in mass transfer or the temperature in heat transfer. The term $v$denotes the velocity field, while D is the diffusivity coefficient. The symbol ∇ represents the gradient operator, and S accounts for any sources or sinks, describing the generation or depletion of u. To ensure a well-posed problem, appropriate initial conditions and boundary conditions must be defined, as they govern the behavior of u within the domain.

Analytical solutions to CRD equations are rarely possible due to their nonlinear nature and the complexity of their dynamics, except in a few simplified cases. Consequently, numerical methods have become the primary focus of research, with many significant contributions made to the field. Among these, total variation diminishing (TVD) schemes are well-known for balancing stability and higher-order accuracy. Methods using limiters, such as

This work is licensed (CC BY-NC 4.0) under Creative Commons Attribution 4.0 International License

TVD-Superbee, TVD-Minmod, TVD-MUSCL, and TVD-Koren, have been applied successfully to a variety of challenging problems (Barth and Jespersen 1989; Harten 1997; van Leer 1979; Koren 1993). Other notable approaches include hybrid nodal-integral/finite element methods (John and Schmeyer 2008), high-order finite volume methods (Costa et al. 2018), and characteristic-based finite volume element methods (Phongthanapanich and Dechaumphai 2008). Many of these methods incorporate advanced features such as positivity-preserving schemes, higher-order reconstructions, and meshfree frameworks (Peddavarapu and Srinivasan 2021), making them versatile tools for addressing nonlinear CRD equations in complex applications.

Although these numerical methods have significantly broadened the use of CRD models, they come with certain limitations. For instance, TVD schemes can produce numerical dissipation near sharp discontinuities, and many approaches are computationally demanding or difficult to implement, especially when working with non-uniform meshes or strongly nonlinear systems. Even with these challenges, CRD models remain essential for studying complex systems, driving ongoing improvements in numerical techniques to meet the growing demands of advanced applications.

Recent developments in scientific computing have introduced Physics-Informed Neural Networks (PINNs) that offer a powerful framework for solving PDEs by embedding governing physical laws directly into the neural network′s loss function (Raissi et al. 2019; Baydin et al. 2018). By using automatic differentiation to enforce constraints such as initial and boundary conditions, PINNs avoid the need for meshing or large labeled datasets, enabling accurate solutions even with sparse data (Baydin et al. 2018; Raissi et al. 2019). They are effective for both forward problems, predicting system evolution, and inverse problems, inferring unknown parameters, making them well-suited for nonlinear CRD equations and other PDEs in fields like fluid dynamics, heat transfer, and biomechanics (Karniadakis et al. 2021; Jagtap et al. 2022; Sahli Costabal et al. 2020).

Their ability to reduce computational complexity and handle high-dimensional domains has made PINNs a modern alternative to conventional solvers, enabling solutions to previously intractable problems (Hennigh et al. 2021). Open-source libraries like DeepXDE (Lu et al. 2021) and SimNet (Hennigh et al. 2021) have further supported their adoption, driving advancements in scientific computing across disciplines.

The exponential finite difference method is a robust numerical technique for solving PDEs, particularly in cases where conventional finite difference methods struggle. First introduced by Bhattacharya for solving heat conduction problems (Bhattacharya 1985), this method has been extended to tackle more complex scenarios, including nonlinear systems, steep gradients, and stiff equations (Bahadir 2005; Handschuh and Keith 1992). Unlike standard finite difference schemes, which use linear approximations for derivatives, the exponential finite difference method incorporates an exponential formulation to better capture rapid variations in the solution. This approach enhances both the accuracy and stability of the method, making it highly effective for problems characterized by sharp transitions or highly nonlinear behaviors. By delivering accurate approximations while maintaining computational efficiency, the exponential finite difference method has emerged as a robust and versatile alternative to traditional numerical approaches. In this paper, we aim to enhance the accuracy and reliability of PINNs by introducing an additional residual term derived from a variation of the exponential finite difference scheme. This modification embeds the strengths of the exponential scheme into the standard PINN framework, allowing the network to better capture the behavior of the underlying equations. By combining the traditional PDE residual with the exponential scheme-based residual, the proposed approach seeks to improve solution accuracy and ensure closer alignment with analytical results.

The study conducted by Ali et al. (2022) represents an important contribution to the numerical analysis of nonlinear convection-reaction-diffusion equations, utilizing the Galerkin Finite Element Method (GFEM) to address four representative cases: Burgers Equation, Fisher′s Equation, Burgers-Huxley Equation, and the Newell-Whitehead-Segel Equation. Their research established critical benchmarks for solution accuracy and computational performance, providing a foundational reference for subsequent methodologies. Building on this foundation, Hasan et al. (2024) investigated the application of the traditional PINN to the same set of equations, showcasing its potential to surpass the GFEM in accuracy.

In this work, we build on these previous studies by considering the same test problems as analyzed in Ali et al. (2022) and Hasan et al. (2024), using identical initial and boundary conditions, as well as model parameter values. This consistency provides a solid foundation for comparing our results with those obtained from the GFEM and the traditional PINN framework. By integrating an additional residual term based on a modified exponential finite difference scheme, we develop an improved PINN approach. The goal is to improve solution accuracy by applying the modified framework to the same nonlinear equations and comparing its effectiveness with previously reported results.

2. Materials and Methods

Without loss of generality, we consider a simplified case of the general convection-reaction-diffusion equation, where the variable of interest is a scalar u=u defined in a one-dimensional spatial domain ∇=∂/∂_x. The diffusivity coefficient is assumed to be a scalar constant D=d, and

the velocity field v can be a constant, a function of space and time, or may depend on the solution u itself, as in the case of the Burgers' equation, one of our test problems. The source or sink term S(u,x,t), also a scalar function, which may depend on u, space, and time. Under these assumptions, the governing equations 2-4 can be expressed as

$\partial u/\partial t=d\ (\partial \hat{}2\ u)/(\partial x\hat{}2\ )-v(u,x,t)\partial u/\partial x+S(u,x,t)$ (2)

subject to the initial and boundary conditions given by

$u(x,0)=u_0\ (x),x\in\Omega$ (3)

$B[u]=b(x,t),(x,t)\in\partial\Omega\times R_+.$ (4)

Here, B[u] represents the boundary operator, which may take different forms depending on the type of boundary condition. The term b(x,t) represents the boundary condition and can vary based on the physical problem, taking forms such as zero (for homogeneous or no-flux conditions) or a function of the spatial variable x and the initial condition u_0 (x) provides the initial distribution of the variable u across the domain.

In the following, we explain how the exponential scheme is applied to solve the governing equation (2) along with the initial (3) and boundary conditions (4). Next, we outline the PINN framework, which embeds the physical laws of the problem into the neural network training process. Finally, we combine the exponential scheme with the PINN framework to create a unified computational approach that takes advantage of both methods to solve the problem effectively and accurately.

2.1. Exponential Scheme for CRD Equation

To apply the exponential scheme to the one component one dimensional CRD equation (2), we proceed as follows. The governing equation is transformed into a logarithmic form to facilitate numerical stability and better handling of the nonlinearities. Let F(u)=lnu, so that $\partial F/\partial u=1/u$. Multiplying the CRD equation 5 by $\partial F/\partial u$results in

$1/u\ \partial u/\partial t=d\ 1/u\ (\partial \hat{}2\ u)/(\partial x\hat{}2\ )-v(u,x,t)1/u\ \partial u/\partial x+1/u$

$S(u,x,t)$ (5)

Here, the term $1/u\ \partial u/\partial t$ represents the temporal evolution in the transformed space, with the remaining terms scaled by 1/u. For temporal discretization, a forward Euler scheme is employed, where the time derivative $\partial u/\partial t$is approximated as (equation 6);

$1/u\hat{}k\ \partial u/\partial t\approx(lnu\hat{}(k+1)-lnu\hat{}k)/\Delta t.$ (6)

Substituting this into the transformed equation, we get $(lnu\hat{}(k+1)-lnu\hat{}k)/\Delta t=d\ 1/u\hat{}k\ (\partial \hat{}2\ u\hat{}k)/(\partial x\hat{}2\ )-v(u\hat{}k,x,t)1/u\hat{}k\ (\partial u\hat{}k)/\partial x+1/u\hat{}k\ S(u\hat{}k,x,t)$.

Multiplying through by Δt and taking the exponential of both sides isolates u^(k+1) as (equation 7);

$u\hat{}(k+1)=u\hat{}k\ \exp(\Delta t\Phi\hat{}k\ (u\hat{}k))$ (7)

where the term inside the exponential is denoted as $\Phi\hat{}k\ (u\hat{}k)=d\ 1/u\hat{}k\ (\partial \hat{}2\ u\hat{}k)/(\partial x\hat{}2\ )-v(u\hat{}k,x,t)1/u\hat{}k\ (\partial u\hat{}k)/\partial x+1/u\hat{}k\ S(u\hat{}k,x,t)$.

To avoid numerical instabilities when u^k approaches 0, regularization techniques are commonly applied. One widely used method replaces u^k in the denominator with "max"(u^k,δ),u^k+δ, or $\sqrt{((u\hat{}k\ )\hat{}2+\delta\hat{}2\ )}$, where δ>0 is a small positive constant. The last approach, particularly suitable when u is non-negative, provides smooth and differentiable behavior near $u^k=0$. These techniques prevent division by extremely small values of u^k, which could otherwise result in computational errors. Additionally, regularization stabilizes nonlinear terms like $v(u,x,t)$ and $S(u,x,t)$, which might otherwise become undefined or excessively large for small u^k. Depending on the problem′s specific requirements and the solution's properties, alternative regularization strategies may also be employed (Tarantola 2005; Tikhonov et al. 1977).

In the following sections, this method will be integrated into the PINN framework, combining the advantages of numerical techniques and machine learning to address nonlinear CRD problems.

2.2. Physics-Informed Neural Networks

PINNs are a class of machine learning models designed to solve PDEs by incorporating the governing physics directly into the training process. Unlike traditional numerical methods, PINNs take advantage of the flexibility of artificial neural networks to approximate solutions while satisfying PDE constraints, initial and boundary conditions, during the optimization process. A neural network, $\mathcal{NN}$, is a parameterized nonlinear mapping function that maps input variables to output variables through a systematic arrangement of layers. Mathematically, it can be expressed as (equation 8);

$$\mathcal{NN}(x,t;\theta)=\mathcal{F}^{(L)}\circ\mathcal{F}^{(L-1)}\circ\cdots\circ\mathcal{F}^{(1)}(x,t) \quad (8)$$

where x and t are the input variables, $\mathcal{F}^{(l)}$ denotes the function applied by the l-th layer, L is the total number of layers, and θ denotes the trainable parameters (weights and biases) of the network. Each hidden layer performs a combination of linear transformations and nonlinear activation functions, expressed as (equation 9);

$$\mathcal{F}_j^{(l)}=\sigma^{(l)}\left(\sum_{i=1}^{n_u^{(l-1)}}W_{ji}^{(l)}\mathcal{F}_i^{(l-1)}+b_j^{(l)}\right),\forall l\in\{1,\dots,L-1\}. \quad (9)$$

Here, W^l and b^l denote the weight matrix and bias vector for the l-th layer, respectively, such that $\theta^{(l)}=\{W^{(l)},b^{(l)}\}$ represents the trainable parameters of the l-th layer. The activation function $\sigma^{(l)}$, is applied element-wise to the output of the linear transformation at the l-th layer, with the final layer using a linear activation function, i.e., $\sigma^{(L)}(z)=z$. The input layer initializes the process as $\mathcal{F}^{(0)}(x,t)=(x,t)$, while the output of the final layer provides the predicted solution $u(x,t)$.

In the PINN framework, the neural network $\mathcal{NN}(x,t;\theta)$is trained to approximate the solution of a PDE defined over a spatiotemporal domain $\Omega\times[0,T]$. This predicted solution is denoted by (equation 10);

$$u(x,t) = \mathcal{NN}(x,t;\theta). \quad (10)$$

A key feature of PINNs is their ability to enforce the governing PDE and boundary/initial conditions as either soft or hard constraints during training. This is accomplished by designing a loss function that includes the residual of the PDE, boundary conditions, initial conditions, and additional data loss when available. The total loss function is expressed as

$\mathcal{L}(\theta) = w_{PDE}\mathcal{L}_{PDE} + w_{BC}\mathcal{L}_{BC} + w_{IC}\mathcal{L}_{IC} + w_{Data}\mathcal{L}_{Data}$,

where w_{PDE}, w_{BC}, w_{IC}, w_{Data} are weights balancing the contribution of each term. The individual components are defined as follows:

- PDE Residual Loss: Enforces the governing equation at collocation points $\mathcal{T}_f \subset \Omega \times [0,T]$

$$\mathcal{L}_{PDE} = \frac{1}{\mathcal{T}_f}\sum_{x\in\mathcal{T}_f} \| \frac{\partial u}{\partial t} - d\frac{\partial^2 u}{\partial x^2} + v(u,x,t)\frac{\partial u}{\partial x} - S(u,x,t) \|^2.$$

- Boundary Condition Loss: Imposes the boundary conditions $B[u] = b(x,t) on \partial\Omega$

$$\mathcal{L}_{BC} = \frac{1}{\mathcal{T}_b}\sum_{x\in\mathcal{T}_b} \| B[u] - b(x,t) \|^2.$$

- Initial Condition Loss: Imposes the boundary conditions at $t = 0$

$$\mathcal{L}_{IC} = \frac{1}{\mathcal{T}_0}\sum_{x\in\mathcal{T}_0} \| u(x,0) - u_0(x) \|^2.$$

- Data Loss: Ensures that the predicted solution $u$matches the given data at specific points $\mathcal{X}_{data}$

$$\mathcal{L}_{Data} = \frac{1}{N_{data}}\sum_{i=1}^{N_{data}} \| u(x_{data}^{(i)}, t_{data}^{(i)}) - u_{data}^{(i)} \|^2.$$

Here, $\mathcal{X}_{data} = \{(x_{data}^{(i)}, t_{data}^{(i)}, u_{data}^{(i)})\}_{i=1}^{N_{data}}$ denotes the training set containing information about the solution u_{data} at the input locations $x_{data}^{(i)}$ and $t_{data}^{(i)}$. Additionally, $\mathcal{T}_f$, $\mathcal{T}_b$, and $\mathcal{T}_0$ refer to collocation points within the domain, on the boundary, and at the initial time, respectively. Specifically, the PINN ensures boundary conditions by comparing the model's predictions at boundary points directly to the prescribed boundary values. The differences between the predictions and these known conditions are minimized during training. As a result, the trained solution accurately respects the physical constraints defined at the boundaries . A similar approach is applied when enforcing initial conditions and data losses, where predictions are evaluated at the respective points and differences are minimized to ensure consistency with the initial conditions and available data.

The aim is to minimize the total loss $\mathcal{L}(\theta)$, allowing the network to approximate the solution $u(x,t)$ while satisfying the underlying physical constraints using Automatic Differentiation (AD). AD is crucial in PINNs, as it enables the computation of neural network derivatives with respect to inputs through backpropagation (Baydin et al. 2018). Libraries such as TensorFlow (Abadi et al. 2015) and PyTorch (Paszke et al. 2019) provide robust AD tools, simplifying the implementation and application of PINNs. The training objective is to determine the optimal parameters θ^* using gradient-based optimization methods, such as stochastic gradient descent (SGD) and adaptive algorithms like Adam (Kingma and Ba 2014). The minimization process is expressed as (equation 11);

$$\theta^* = \underset{\theta}{argmin}\mathcal{L}(\theta). \quad (11)$$

This PINN framework operates iteratively. It begins by sampling spatial and temporal points from the domain. These inputs are fed into the neural network to predict $u(x,t)$, which is then used to compute derivatives and evaluate the loss terms. The network parameters are updated iteratively until convergence criteria are met, such as achieving a target loss value or reaching the maximum number of iterations. This process enables PINNs to approximate solutions while balancing physical constraints and available data, offering a strong and flexible alternative to traditional numerical methods.

2.3. Integrated PINN Framework with Exponential Schemes

In this section, we propose an integrated framework that combines the strengths of the exponential scheme with the PINN framework. The motivation for this integration comes from the well-established benefits of exponential schemes in numerical methods, particularly their ability to achieve high accuracy and stable solutions for nonlinear CRD-like equations. Both explicit and implicit exponential finite difference methods have proven to be computationally efficient while delivering solutions that closely match analytical results, often outperforming standard numerical techniques in terms of both accuracy and stability (Inan and Bahadır 2013; Tian and Dai 2007).

The PINN framework traditionally minimizes the residuals of the governing PDE, boundary conditions, and initial conditions. By integrating the exponential scheme, we introduce an additional residual term derived from the exponential update formulation. This term has the potential to improve the training process by enhancing the accuracy of the approximated solution. As a result, the integrated framework combines the numerical advantages of exponential schemes with the data-driven learning capabilities of PINNs.

The final equation derived from the exponential scheme (7) requires the solution at the next time step, u^{k+1}, which poses a challenge when integrating this directly into the PINN framework. As u^{k+1} cannot be determined without explicitly evaluating the neural network at the k-th time step, the exponential finite difference scheme needs to be adjusted to account for the temporal dynamics within the PINN framework. As a result, u^{k+1} in the exponential scheme is replaced with its second-order Taylor expansion around u^k (equation 12);

$$u^{k+1} \approx u^k + \Delta t\frac{\partial u^k}{\partial t} + \frac{\Delta t^2}{2}\frac{\partial^2 u^k}{\partial t^2}, \quad (12)$$

where Δt denotes the time step size. Substituting this

into equation 13, we have

$$u^k + \Delta t \frac{\partial u^k}{\partial t} + \frac{\Delta t^2}{2}\frac{\partial^2 u^k}{\partial t^2} = u^k exp(\Delta t \Phi^k) \quad (13)$$

This equation holds true for any given time step k. As a result, all terms in the equation are evaluated at the same time level k, ensuring consistency. Therefore, the use of superscripts to denote the time step becomes unnecessary, and we omit them for simplicity, highlighting that the equation is valid for all time values (equation 13);

$$u + \Delta t \frac{\partial u}{\partial t} + \frac{\Delta t^2}{2}\frac{\partial^2 u}{\partial t^2} = uexp\left(\Delta t \Phi(u)\right) \quad (13)$$

This scheme introduces an additional residual term involving the second temporal derivative $\partial^2 u/\partial t^2$, alongside the existing spatial and temporal gradients. During training, the modified scheme contributes to the total loss by incorporating the constraints of the exponential formulation while ensuring consistency with the physical residuals. This integrated approach strengthens the enforcement of physical laws and enhances the accuracy and stability of the predicted solution.

The overall procedure of the modified PINN framework is depicted in Figure 1. In addition to the standard loss terms, the modified framework includes an additional residual term based on the exponential scheme, which strengthens the numerical robustness and accuracy of the learning process. The total loss function is expressed as

$\mathcal{L}(\theta) = w_{PDE}\mathcal{L}_{PDE} + w_{BC}\mathcal{L}_{BC} + w_{IC}\mathcal{L}_{IC} + w_{EXP}\mathcal{L}_{EXP}$,

where $\mathcal{L}_{EXP}$ is the residual associated with the exponential scheme (equation 14);

$$\mathcal{L}_{EXP} = \frac{1}{\mathcal{T}_f}\sum_{x\in\mathcal{T}_f} \| u + \Delta t \frac{\partial u}{\partial t} + \frac{\Delta t^2}{2}\frac{\partial^2 u}{\partial t^2} - uexp\left(\Delta t \Phi(u)\right) \|^2. \quad (14)$$

By integrating the residual of the exponential scheme into the training process, the modified PINN framework effectively combines the strengths of numerical techniques with the adaptability of neural networks, leading to improved solution accuracy and stability.

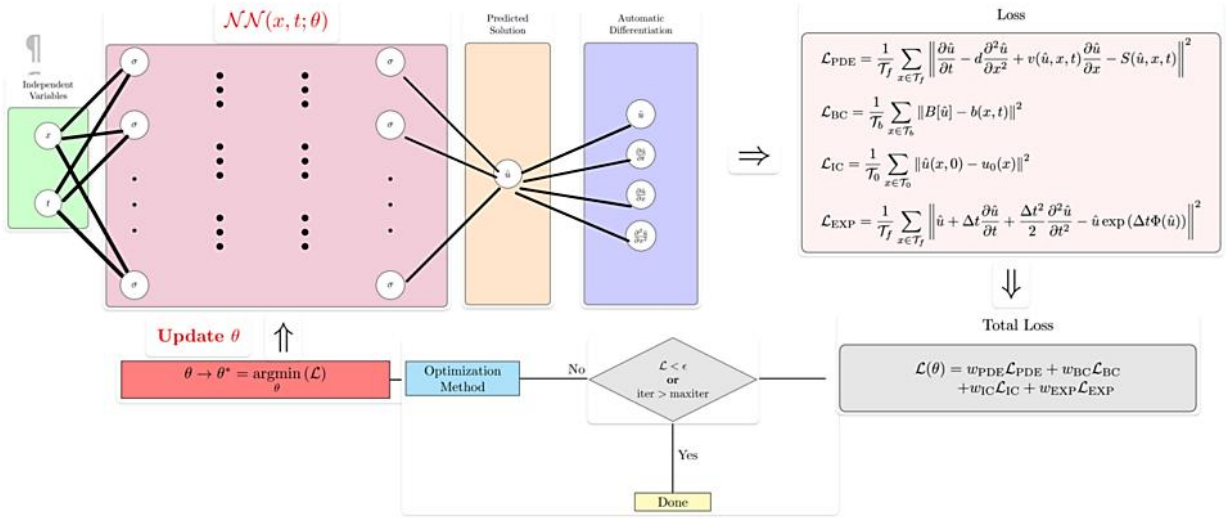


Figure 1. Illustration of the integrated framework combining PINNs with the modified exponential scheme, showcasing the processing of inputs, solution prediction, and computation of loss terms for optimization.

3. Results

In this study, we implement our modified PINN approach on four nonlinear PDEs that are widely used in various scientific and engineering applications: the nonlinear Burgers' equation (Burgers 1948), Fisher's equation (Fisher 1937), the Burgers-Huxley equation (Burgers 1948; Hodgkin and Huxley 1952), and the Newell-Whitehead-Segel equation (Newell and Whitehead 1969). To ensure a meaningful comparison with previously obtained results presented in Hasan et al. (2024), we adopt the same neural network architecture, test models, their parameter values and their corresponding initial and boundary conditions.

For the implementation, a fully connected feedforward neural network is used, consisting of two input neurons (representing x and t), four hidden layers with 20 neurons each, and one output neuron predicting the solution $u(x,t)$. The network employs the $tanh$ activation function, the Glorot uniform initializer, and L2 regularization to reduce overfitting. Training is conducted using the Adam optimizer with a learning rate of 1×10^{-3}. The training dataset includes 10000 collocation points sampled from the spatiotemporal domain using Latin Hypercube Sampling, while boundary and initial conditions are enforced using 50uniformly sampled points each.

After the initial training phase with the Adam optimizer, we employ the LBFGS optimizer (Liu and Nocedal 1989)

as a secondary step to refine the solution further. The use of LBFGS represents the only methodological difference in the optimization process compared to the prior study.

Even though it is possible to assign different weights to each loss component, in this study, we apply equal weights $w = 1$ to all loss terms in the loss function. This approach simplifies the training process by avoiding the need to tune multiple weight parameters. It also ensures that no single loss term dominates the training, resulting in balanced contributions from each part. However, this assumes each loss component has roughly equal importance, which might not hold true if some terms inherently have larger magnitudes or significantly greater influence on the solution accuracy. In such cases, adjusting weights might further improve performance.

The model is trained by minimizing the total loss function, which ensures that the predicted solution $u(x,t)$ aligns with the governing PDE, initial and boundary conditions, and the residuals of the modified exponential scheme.

In PINNs, accurately satisfying initial and boundary conditions is critical to ensure the physical validity of the computed solutions. A recent study by Lu et al. (2021) highlighted the advantages of modifying the network architecture to incorporate hard constraints. This approach allows the network to strictly enforce initial and boundary conditions. This also improves the stability and convergence of the training process, and reduces the computational cost.

Building on this concept, we develop an output transformation framework tailored to our implementation. During training, the model approximates the solution $u(x,t)$ across the spatial-temporal domain. To ensure adherence to both initial and boundary conditions, an output transform, denoted as $\tilde{u}(x,t)$, is applied. This transform effectively enforces problem-specific constraints on the predicted solution $u(x,t)$, ensuring that the initial condition at $t = 0$ and the specified boundary conditions are satisfied. Mathematically, the transform $\tilde{u}(x,t)$ can be described as

$$\tilde{u}(x,t) = u_c(x,t) + tg(x)u(x,t), \tag{14}$$

where $u_c(x,t)$represents the constrained term that satisfies the initial and boundary conditions. Specifically, $u_c(x,t)$ satisfies the initial condition at $t = 0$, such that $u_c(x,0) = u_0(x)$ for $x \in \Omega$, and supports the boundary conditions at the boundary points, ensuring $B[u_c] = b(x,t), (x,t) \in \partial\Omega \times \mathbb{R}_+$.

The term $g(x)$ is the boundary basis function, designed to vanish at the domain boundaries. By incorporating this output transform, the predicted solution $u(x,t)$is naturally adjusted to satisfy both the initial and boundary conditions, ensuring physically consistent and accurate predictions throughout the domain. In this study, hard constraints are incorporated directly into the PINN by transforming the neural network's output, ensuring these constraints are exactly satisfied by construction, rather than being enforced through additional penalty terms in the loss function.

Through the optimization process, the model learns to approximate the solution $u(x,t)$ accurately across the spatial-temporal domain. The model's performance was evaluated using mean absolute error, MAE, which quantifies the average difference between the true solution $u(x_i,t_i)$ and the predicted solution $u(x_i,t_i)$

$$MAE = \frac{1}{N}\sum_{i=1}^{N}\left|u(x_i,t_i) - u(x_i,t_i)\right|,$$

where N represents the total number of evaluation points.

3.1. Numerical Experiments and Comparative Analysis

In this section, we aim to evaluate the effectiveness of the proposed enhanced PINN framework by applying it to four nonlinear CRD systems. These systems include Burgers Equation, Fisher′s Equation, the Burgers-Huxley Equation, and the Newell-Whitehead-Segel Equation, which represent a broad spectrum of nonlinear dynamics. The numerical experiments aim to demonstrate the framework's accuracy in solving these equations, while comparisons will emphasize the improvements achieved over the GFEM and traditional PINN approaches.

3.1.1. Test problem: Burgers' equation

Burgers' equation, first introduced by J. M. Burgers in 1948 (Burgers 1948), is a fundamental nonlinear partial differential equation that has become a cornerstone in mathematical physics and applied mathematics. Celebrated for its simplicity and versatility, the equation captures the interaction between nonlinear convection and viscous diffusion, making it an essential tool for analyzing complex dynamical systems. While Burgers' equation is analytically solvable in certain cases, its inherent nonlinearity often requires advanced computational methods to address more general scenarios. The specific form of Burgers' equation studied here is expressed as

$$\frac{\partial u(x,t)}{\partial t} = \frac{1}{Re}\frac{\partial^2 u(x,t)}{\partial x^2} - u(x,t)\frac{\partial u(x,t)}{\partial x},$$

where $Re > 0$ denotes the Reynolds number, a dimensionless parameter that quantifies the balance between viscous and inertial forces. The problem is accompanied by the following initial and boundary conditions.

$$u(x,0) = \frac{2\pi sin(\pi x)}{Re(\sigma + cos(\pi x))}, x \in \Omega = [0,1]$$

$$u(0,t) = u(1,t) = 0$$

where $\sigma > 1$ is a given parameter. In this study, we adopt the parameter values $Re = 1$and $\sigma = 2$, consistent with those used in Hasan et al. (2024). An analytical solution to this problem, corresponding to the specified initial and boundary conditions and the parameter values, is available and is expressed as

$$u(x,t) = \frac{2\pi e^{-\pi^2 t/Re} sin(\pi x)}{Re\left(\sigma + e^{-\pi^2 t/Re} cos(\pi x)\right)},$$

which provides a benchmark for assessing the accuracy of numerical solutions.

In Figure 2, we present a comparison of the analytical solution and the predicted solution for Burgers' Equation using the modified PINN framework. The figure includes the analytical and predicted solutions as 2D plots, the MAE between them, and a 3D visualization of the predicted solution. As depicted, it is safe to say that there is a good agreement between analytical expression and modified PINN based prediction.

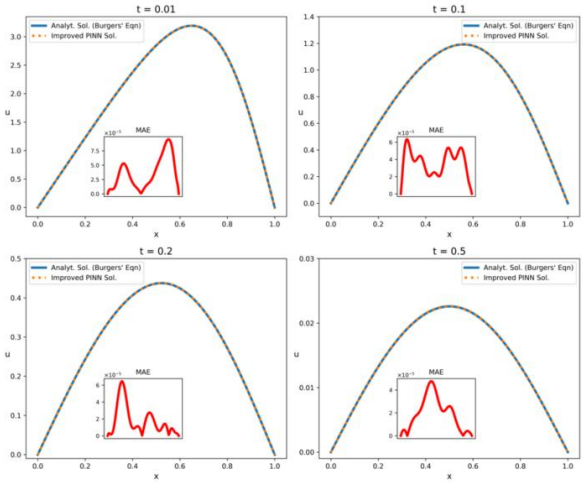


Figure 2. Analytical solution (top-left), improved PINN solution (top-right), mean absolute error (bottom-left), and 3D view of the modified PINN solution (bottom-right) for Burgers' equation.

In Figure 3, we present a detailed comparison of the analytical and predicted solutions for Burgers' Equation at four distinct time values: $t = 0.01$, $t = 0.1$, $t = 0.2$and $t = 0.5$. Each subplot depicts the spatial evolution of the solutions, enabling a direct visual comparison between the analytical and modified PINN predictions. Insets within each subplot show the MAE for the corresponding time value, emphasizing the discrepancies between the solutions. The first immediate observation from this figure is that our model gives excellent agreement with the analytical solutions, with MAE values remaining consistently low across all time values.

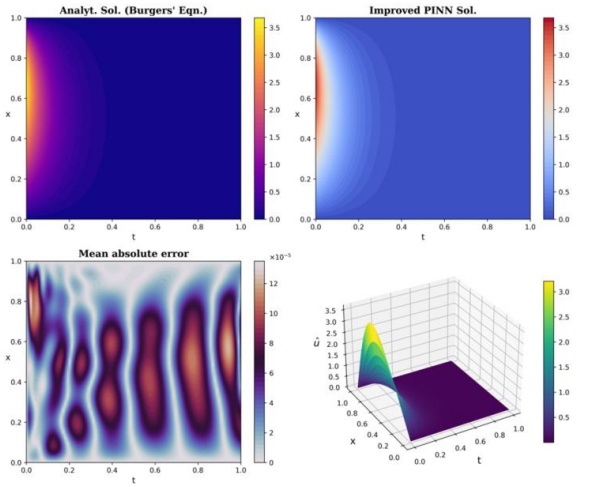


Figure 3. Comparison of analytical and predicted solutions for Burgers' Equation at various time values, along with the mean absolute error.

Table 1 presents a quantitative comparison of the mean absolute errors (MAE) between the analytical solution and three considered methods—GFEM, the traditional PINN framework, and the proposed modified PINN framework—at two specific time steps, $t = 0.02$ and $t = 0.04$. The modified PINN consistently outperforms GFEM and the traditional PINN, achieving significantly lower errors across all spatial points for both time values.

Table 1. Absolute error comparison for Burgers' equation at $t = 0.02$ and $t = 0.04$ between the analytical solution and predictions from GFEM, traditional PINN, and modified PINN

		$t = 0.02$			$t = 0.04$	
x	GFEM	PINN	PRESENT	GFEM	PINN	PRESENT
0.1	4.20×10^{-3}	5.09×10^{-4}	1.99×10^{-5}	1.21×10^{-2}	3.87×10^{-4}	1.57×10^{-5}
0.2	9.10×10^{-3}	3.37×10^{-4}	2.23×10^{-5}	2.50×10^{-2}	8.00×10^{-5}	1.78×10^{-6}
0.4	2.16×10^{-2}	2.42×10^{-4}	2.55×10^{-5}	5.07×10^{-2}	2.92×10^{-4}	2.87×10^{-5}
0.6	2.51×10^{-2}	8.70×10^{-5}	6.15×10^{-5}	4.83×10^{-2}	2.63×10^{-4}	8.30×10^{-5}
0.8	6.83×10^{-3}	3.90×10^{-5}	1.24×10^{-4}	9.19×10^{-3}	1.62×10^{-4}	1.30×10^{-4}
1.0	0.00×10^{0}	1.17×10^{-3}	2.3×10^{-16}	0.00×10^{0}	3.90×10^{-5}	3.8×10^{-16}

3.1.2. Test problem: Fisher's equation

Fisher's equation, introduced by R. A. Fisher in 1937 (Fisher 1937), models the spread of advantageous genetic traits within a population. A fundamental equation in mathematical biology, it captures the interplay between diffusion and logistic growth, describing phenomena such as traveling wavefronts. Although analytical solutions are available for specific cases, the nonlinearity of the equation necessitates advanced numerical methods to handle complex scenarios with varied initial and boundary conditions. Mathematically, Fisher's equation is expressed as

$$\frac{\partial u(x,t)}{\partial t} = \frac{\partial^2 u(x,t)}{\partial x^2} + 6u(x,t)(1 - u(x,t)),$$

where $u(x,t)$represents the population density or

another relevant quantity. The initial condition considered in this work is specified as
$u(x,0) = (1+e^{x})^{-2}, x \in [0,1]$
and the boundary conditions are
$u(0,t) = (1+e^{-5t})^{-2}, u(1,t) = (1+e^{1-5t})^{-2}$.
The exact analytical solution to Fisher's equation, corresponding to the specified initial and boundary conditions, is expressed as
$u(x,t) = (1+e^{x-5t})^{-2}$,
which provides a benchmark for verifying the accuracy of numerical methods. This expression is used to compare with the predictions of our modified PINN framework to assess its performance. In Figure 4, we present a detailed visualization of the solutions for Fisher's Equation. As illustrated, the predictions of the modified PINN model are in excellent agreement with the analytical solution, demonstrating its capability to accurately capture the spatiotemporal dynamics of Fisher's equation.

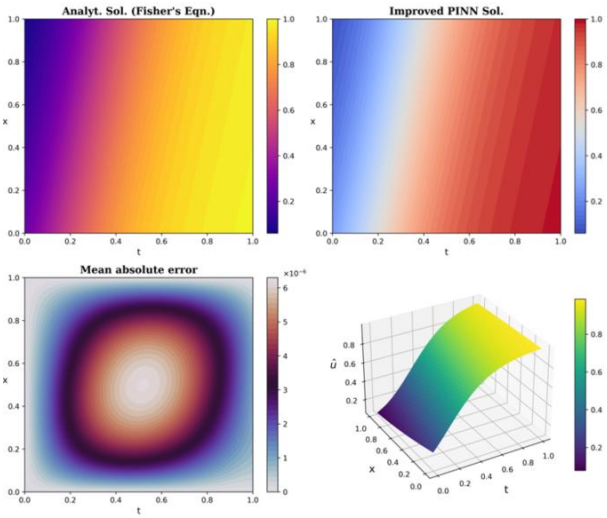


Figure 4. Analytical solution (top-left), improved PINN solution (top-right), mean absolute error (bottom-left), and 3D view of the modified PINN solution (bottom-right) for Fisher's equation.

In Figure 5, we present a comparison of the analytical and predicted solutions for Fisher's Equation at four distinct time steps: $t = 0.25$, $t = 0.5$, $t = 0.75$, and $t = 1$. Each subplot depicts the spatial evolution of the solutions, allowing for a direct visual comparison between the analytical and improved PINN results. Across all time steps, the MAE demonstrates a consistent trend, with the smallest errors occurring at the boundaries. This behavior aligns with other test cases we consider, where the use of hard constraints plays a pivotal role.

Table 2 compares the absolute errors between the analytical solution of Fisher's equation and results obtained using GFEM, the traditional PINN, and the modified PINN at $t = 0.05$ and $t = 0.1$. The results clearly demonstrate that the modified PINN consistently achieves the lowest errors across all spatial points for considered time values.

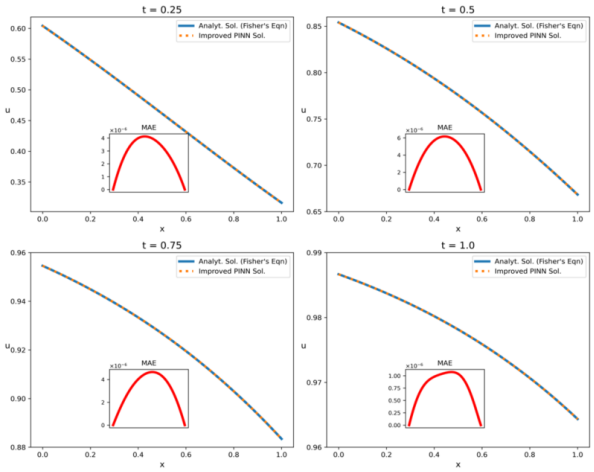


Figure 5. Comparison of analytical and predicted solutions for Fisher's Equation at $t = 0.25$, $t = 0.5$, $t = 0.75$, and $t = 1$.

Table 2. Absolute error comparison for Fisher's equation at $t = 0.05$ and $t = 0.1$ between the analytical solution and predictions from GFEM, traditional PINN, and modified PINN

	$t = 0.05$			$t = 0.1$		
x	GFEM	PINN	PRESENT	GFEM	PINN	PRESENT
0.1	3.02×10^{-3}	3.67×10^{-4}	4.28×10^{-7}	1.33×10^{-3}	4.19×10^{-4}	8.36×10^{-7}
0.2	7.91×10^{-4}	2.27×10^{-4}	6.88×10^{-7}	2.78×10^{-3}	3.35×10^{-4}	1.36×10^{-6}
0.4	1.35×10^{-3}	3.40×10^{-5}	8.40×10^{-7}	6.27×10^{-3}	8.70×10^{-5}	1.70×10^{-6}
0.6	1.51×10^{-3}	1.13×10^{-4}	7.08×10^{-7}	5.79×10^{-3}	2.90×10^{-5}	1.48×10^{-6}
0.8	3.87×10^{-4}	1.48×10^{-4}	4.35×10^{-7}	2.71×10^{-3}	1.76×10^{-4}	9.25×10^{-7}
1.0	9.67×10^{-18}	1.32×10^{-4}	$0.00 \times 10^{+0}$	6.32×10^{-18}	2.34×10^{-4}	$0.00 \times 10^{+0}$

3.1.3. Test problem: Burgers-Huxley equation

The Burgers-Huxley equation combines the dynamics of Burgers' and Huxley's equations to model reaction-diffusion processes in excitable media. t plays a critical role in understanding the interplay of convection, diffusion, and reaction phenomena, with applications in different fields such as neuroscience, population genetics, and chemical kinetics. The equation is particularly significant for its capacity to capture traveling wave solutions and complex spatiotemporal behaviors, making it a cornerstone in the study of nonlinear systems and numerical methods (Keener and Sneyd 2009; Whitham

2011). Mathematically, the equation is given by

$$\frac{\partial u}{\partial t} = \frac{\partial^2 u}{\partial x^2} - \phi \frac{\partial u}{\partial x} + \epsilon u(x,t)(u(x,t)-1)(\tau - u(x,t)),$$

where ϕ, ϵ, and τ are real valued parameters. The initial condition for this equation is defined as

$$u(x,0) = \frac{3}{2} + \frac{1}{2} tanh\left(\frac{x}{2}\right), x \in \Omega = [-25,17]$$

and the boundary conditions are given as

$$\frac{\partial u}{\partial x}|_{x=-25} = \frac{\partial u}{\partial x}|_{x=17} = 0, t > 0,$$

indicating a no-flux condition at the spatial boundaries. The analytical solution for this configuration for the parameter values $\phi = -1$, $\epsilon = 1$, and $\tau = 2$, is expressed as

$$u(x,t) = \frac{3}{2} + \frac{1}{2} tanh\left(\frac{1}{2}(x+3t)\right).$$

This analytical result serves as a reference to evaluate the accuracy and effectiveness of the our modified PINN method in capturing the equation's dynamics.

Figure 6 presents contour plots of the Burgers-Huxley equation, illustrating the spatiotemporal evolution of the predicted solution alongside the analytical solution. Additionally, the figure includes a visualization of the MAE and a 3D plot of the modified PINN solution. The results reveal that the error is notably minimized near the boundaries, as expected.

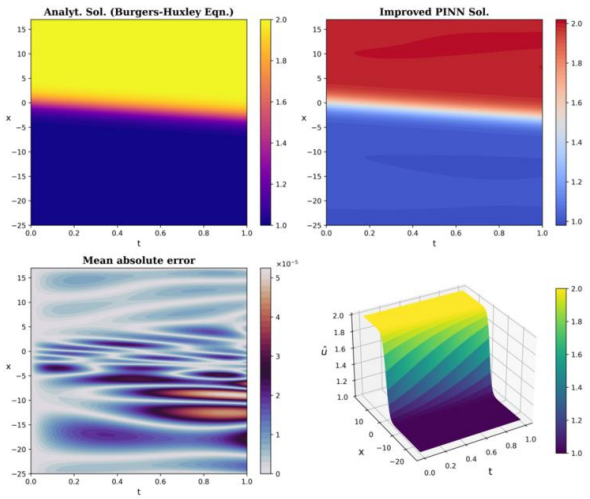


Figure 6. Contour plots of the analytical and predicted solutions, the MAE, and a 3D plot of the predicted solution for the Burgers-Huxley equation.

In Figure 7, the analytical and predicted solutions for the Burgers-Huxley equation are presented for four time values: $t = 0.05$, $t = 0.5$, $t = 0.75$, and $t = 1$. The results show that the modified PINN framework closely matches the analytical solution, effectively capturing the dynamics of the Burgers-Huxley equation across the domain and over time.

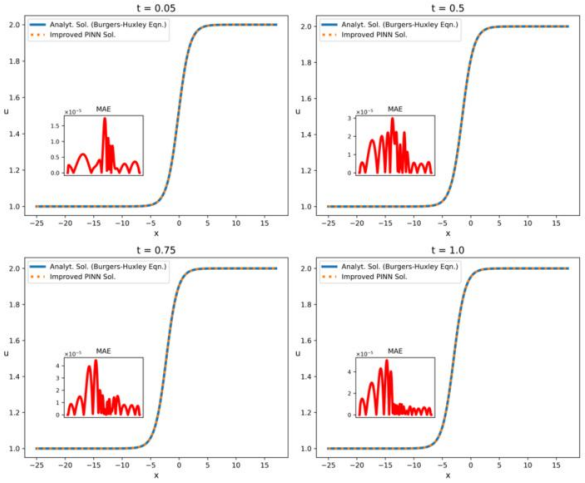


Figure 7 . Evolution of the analytical and predicted solutions for the Burgers-Huxley equation at selected time values $t = 0.05$, $t = 0.5$, $t = 0.75$, and $t = 1$, along with insets displaying the corresponding mean absolute errors (MAE) for each time values.

Table 3 presents the absolute error between the analytical solution and three methods—GFEM, Traditional PINN, and Modified PINN—for the Burgers-Huxley equation at $t = 0.10$ and $t = 0.20$. The Modified PINN consistently achieves the lowest error values across most spatial locations and time instances, outperforming both GFEM and Traditional PINN. The exception occurs near the spatial boundaries, where GFEM shows slightly better performance. However, at these boundary locations, the analytical solution is known to be fixed, making the observed differences in errors marginal in practical significance.

Table 3. Absolute error comparison for Burgers-Huxley equation at $t = 0.10$ and $t = 0.20$ between the analytical solution and predictions from GFEM, traditional PINN, and modified PINN

		$t = 0.1$			$t = 0.2$	
x	GFEM	PINN	PRESENT	GFEM	PINN	PRESENT
-25.00	4.73×10^{-13}	4.27×10^{-3}	4.86×10^{-12}	3.84×10^{-12}	5.38×10^{-3}	1.14×10^{-11}
-20.80	1.86×10^{-10}	7.27×10^{-4}	2.40×10^{-5}	4.09×10^{-11}	1.00×10^{-3}	4.24×10^{-5}
-12.40	8.26×10^{-7}	2.53×10^{-3}	2.86×10^{-5}	1.82×10^{-7}	3.47×10^{-3}	1.61×10^{-5}
-4.00	3.49×10^{-3}	5.37×10^{-3}	1.92×10^{-4}	7.18×10^{-4}	6.09×10^{-3}	1.54×10^{-4}
0.20	3.50×10^{-3}	6.89×10^{-4}	3.22×10^{-5}	2.67×10^{-3}	1.81×10^{-3}	7.05×10^{-5}
4.40	1.22×10^{-3}	5.41×10^{-3}	1.88×10^{-5}	7.54×10^{-4}	4.19×10^{-3}	3.60×10^{-5}
12.80	2.79×10^{-7}	3.04×10^{-3}	4.47×10^{-5}	1.78×10^{-7}	2.08×10^{-3}	5.52×10^{-5}
17.00	8.48×10^{-9}	6.30×10^{-3}	1.07×10^{-8}	4.11×10^{-9}	5.22×10^{-3}	1.87×10^{-8}

3.1.5. Test problem: Newell-Whitehead-Segel equation

The Newell-Whitehead-Segel equation models spatially periodic phenomena near instability points, making it essential for understanding pattern formation and bifurcation in symmetric systems. It is widely applied in fluid dynamics, reaction-diffusion systems, and population dynamics, capturing behaviors like wave propagation and emergent patterns (Cross and Hohenberg 1993; Murray 2007). The equation is mathematically expressed as

$$\frac{\partial u}{\partial t} = \eta \frac{\partial^2 u}{\partial x^2} + \mu u(x,t) - \nu u(x,t)^\rho,$$

where $\eta, \mu, \nu > 0$ are real valued parameters and ρ is a positive integer. The initial condition is given by

$$u(x,0) = \left(1 + e^{x/\sqrt{6}}\right)^{-2}, x \in \Omega = [0,1].$$

The boundary conditions are defined as non-homogeneous Neumann conditions

$$\frac{\partial u}{\partial x}|_{x=0} = \frac{2e^{-5t/6}}{\sqrt{6}(1+e^{-5t/6})^3}, \frac{\partial u}{\partial x}|_{x=1} = -\frac{2e^{(5t)/6}}{\sqrt{6}(1+e^{(5t)/6})^3}.$$

For this equation, the analytical solution is known and serves as a benchmark to evaluate the numerical methods. For the parameter values $\eta = 1$, $\mu = 1$, $\nu = 1$, and $\rho = 2$, the analytical solution is

$$u(x,t) = \left(1 + e^{\frac{x}{\sqrt{6}} - \frac{5t}{6}}\right)^{-2}.$$

We now apply our modified PINN framework to the Newell-Whitehead-Segel equation to evaluate its effectiveness in capturing the spatiotemporal dynamics of the solution. A detailed visualization of the solution's behaviour over time and space is presented in Figure 8. The results demonstrate that the modified PINN framework aligns closely with the analytical solution.

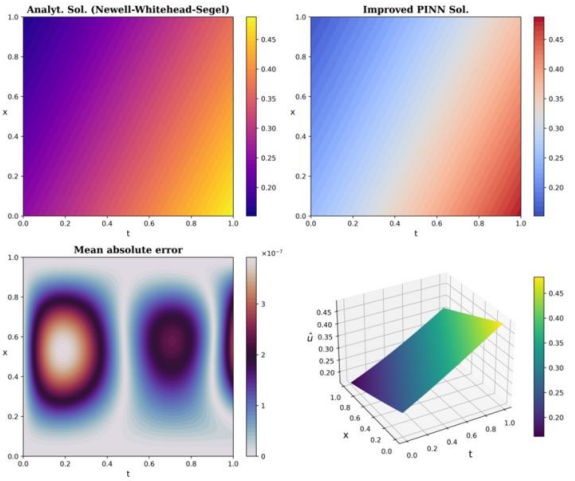


Figure 8. Visualizations for the Newell-Whitehead-Segel equation showing the analytical and predicted solutions as contour plots, a contour plot of the mean absolute error (MAE) across the domain, and a 3D view of the predicted solution's spatiotemporal evolution.

Figure 9 depicts the evolution of the solution to the Newell-Whitehead-Segel equation at specific time values, $t = 0.05, 0.1, 0.2, and\ 0.5$. The modified PINN framework produces results that closely match the analytical solution.

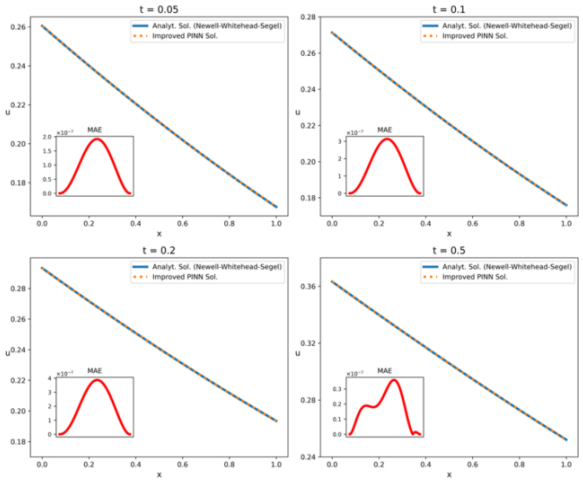


Figure 9 . Comparison of analytical and predicted solutions for Newell-Whitehead-Segel Equation at various time values, with mean absolute error.

Table 4 shows the absolute error between the analytical solution and three methods—GFEM, traditional PINN, and the modified PINN—for the Newell-Whitehead-Segel equation at two time instances, $t = 0.03$ and $t = 0.05$, across various spatial points. For all spatial points considered, the modified PINN gives the smallest absolute errors.

Table 4. Absolute error comparison for Newell-Whitehead-Segel equation at $t = 0.03$ and $t = 0.05$between the analytical solution and predictions from GFEM, traditional PINN, and modified PINN

	$t = 0.03$			$t = 0.05$		
x	GFEM	PINN	PRESENT	GFEM	PINN	PRESENT
0.1	1.48×10^{-6}	9.10×10^{-6}	1.01×10^{-8}	3.06×10^{-5}	2.55×10^{-5}	1.54×10^{-8}
0.2	1.88×10^{-5}	1.77×10^{-5}	3.78×10^{-8}	5.45×10^{-5}	3.18×10^{-5}	5.80×10^{-8}
0.4	3.57×10^{-5}	3.15×10^{-5}	1.06×10^{-7}	7.97×10^{-5}	3.78×10^{-5}	1.64×10^{-7}
0.6	4.34×10^{-5}	3.24×10^{-5}	1.19×10^{-7}	9.55×10^{-5}	3.50×10^{-5}	1.84×10^{-7}
0.8	6.45×10^{-5}	2.47×10^{-5}	5.56×10^{-8}	1.28×10^{-4}	2.31×10^{-5}	8.60×10^{-8}
1.0	1.32×10^{-4}	1.03×10^{-5}	$0.00 \times 10^{+0}$	2.03×10^{-4}	1.38×10^{-5}	$0.00 \times 10^{+0}$

5. Discussion

This study presented an improved PINN framework, incorporating an additional residual term based on an exponential finite difference scheme. The approach was developed to overcome challenges faced by traditional PINNs in solving nonlinear CRD equations, particularly those with complex dynamics, steep gradients, and strong nonlinearities. Numerical tests were conducted on four nonlinear PDEs: Burgers Equation, Fisher′s Equation, Burgers-Huxley Equation, and the Newell-Whitehead-Segel Equation, with results compared against both traditional PINNs and the GFEM.

The modified PINN framework demonstrated significant improvements in both accuracy and robustness, highlighting its potential as a versatile tool for solving a wide range of nonlinear PDEs. By incorporating residuals from the exponential scheme, the framework effectively captured the intricate dynamics of nonlinear PDEs. It consistently reduced absolute errors compared to traditional PINNs and, in most cases, outperformed GFEM in accuracy.

Results from Tables 1–4 demonstrate that the proposed modifications consistently improved model accuracy and robustness. In particular, the enhanced PINN achieved lower absolute errors across all test cases compared to traditional PINNs and generally outperformed the GFEM as well. These results highlight the effectiveness of incorporating the enhanced residual term, which more rigorously enforces the governing equations during training, leading to more accurate and physically consistent solutions.

Furthermore, while GFEM remains a reliable and well-established numerical method, it requires significant computational resources, particularly for problems in higher dimensions or with irregular geometries. In contrast, the mesh-free architecture of the PINN framework offers a scalable and flexible alternative, well-suited to modern scientific and engineering applications.

The results of this study highlight several promising directions for future research. Extending the proposed framework to high-dimensional problems and more complex geometries would provide further insights into its scalability and applicability. Moreover, integrating other advanced numerical schemes could enhance its robustness and adaptability to even more challenging PDE scenarios, such as those involving discontinuities or stochastic effects. Additionally, optimizing the training process through advanced loss-weighting strategies or adaptive optimization techniques could further improve its performance and efficiency.

Author Contributions

The percentages of the author' contributions are presented below. The author reviewed and approved the final version of the manuscript.

	B.B.
C	100
D	100
S	100
DCP	100
DAI	100
L	100
W	100
CR	100
SR	100
PM	100
FA	100

C=Concept, D=design, S=supervision, DCP=data collection and/or processing, DAI=data analysis and/or interpretation, L=literature search, W=writing, CR=critical review, SR=submission and revision, PM=project management, FA= funding acquisition.

Conflict of Interest

The author declared that there is no conflict of interest.

Ethical Consideration

Ethics committee approval was not required for this study because of there was no study on animals or humans.

References

Abadi M, Agarwal A, Barham P, Brevdo E, Chen Z, Citro C, Corrado GS, Davis A, Dean J, Devin M, Xiao Z, Monga R, Moore S, Murray D, Steiner B, Tucker P, Vasudevan V, Warden P, Wicke M, Yu Y. 2015. TensorFlow: Large-scale machine learning on heterogeneous systems. Mountain View, CA: TensorFlow.

Ali H, Kamrujjaman M, Islam MS. 2022. An advanced Galerkin approach to solve the nonlinear reaction–diffusion equations with different boundary conditions. J Math Res, 14(1): pp: 30–45.

Bahadır AR. 2005. Exponential finite-difference method applied to Korteweg–de Vries equation for small times. Appl Math Comput, 160(3): pp: 675–682.

Barth T, Jespersen D. 1989. The design and application of upwind schemes on unstructured meshes. 27th Aerospace Sci Meet, Paper No: 89-0366.

Baydin AG, Pearlmutter BA, Radul AA, Siskind JM. 2018. Automatic differentiation in machine learning: A survey. J Mach Learn Res, 18(153): pp: 1–43.

Bejan A. 2013. Convection heat transfer. John Wiley & Sons, Hoboken, NJ, USA, pp: 688.

Bezekci B. 2025. Deep learning-enhanced regularization of irregular traveling pulses in the FitzHugh–Nagumo model. SN Comput Sci, 6: pp: 206.

Bezekci B. 2025. The efficacy of Haar wavelets in addressing discontinuities of McKean equations with Heaviside functions. Osmaniye Korkut Ata Univ J Inst Sci, 8(1): pp: 200–210.

Bhattacharya MC. 1985. An explicit conditionally stable finite difference equation for heat conduction problems. Int J Numer Methods Eng, 21(2): pp: 239–265.

Burgers JM. 1948. A mathematical model illustrating the theory of turbulence. Adv Appl Mech, 1: pp: 171–199.

Costa R, Clain S, Loubère R, Machado GJ. 2018. Very high-order accurate finite volume scheme on curved boundaries for the two-dimensional steady-state convection–diffusion equation with Dirichlet condition. Appl Math Model, 54: pp: 752–767.

Cross MC, Hohenberg PC. 1993. Pattern formation outside of equilibrium. Rev Mod Phys, 65(3): pp: 851.

Dong X, Li W, Liu Q, Wang H. 2022. Research on convection-reaction-diffusion model of contaminants in fracturing flowback fluid in non-equidistant fractures with arbitrary inclination of shale gas development. J Pet Sci Eng, 208: 109479.

Fisher RA. 1937. The wave of advance of advantageous genes. Ann Eugen, 7(4): pp: 355–369.

Handschuh RF, Keith TG Jr. 1992. Applications of an exponential finite-difference technique. Numer Heat Transfer A, 22(3): pp: 363–378.

Harten A. 1997. High resolution schemes for hyperbolic conservation laws. J Comput Phys, 135(2): pp: 260–278.

Hasan F, Ali H, Arief HA. 2024. From mesh to neural nets: A multi-method evaluation of physics-informed neural networks and Galerkin finite element method for solving nonlinear convection–reaction–diffusion equations. arXiv preprint arXiv:2411.09704.

Hennigh O, Narasimhan S, Nabian MA, Subramaniam A, Tangsali K, Fang Z, Rietmann M, Byeon W, Choudhry S, Ferguson M, Pfaff T, Tompson J. 2021. NVIDIA SimNet™: An AI-accelerated multi-physics simulation framework. In: Int Conf Comput Sci, Springer, pp: 447–461.

Hodgkin AL, Huxley AF. 1952. A quantitative description of membrane current and its application to conduction and excitation in nerve. J Physiol, 117(4): pp: 500.

Inan B, Bahadir AR. 2013. Numerical solution of the one-dimensional Burgers' equation: Implicit and fully implicit exponential finite difference methods. Pramana, 81: pp: 547–556.

Jagtap AD, Mao Z, Adams N, Karniadakis GE. 2022. Physics-informed neural networks for inverse problems in supersonic flows. J Comput Phys, 466: 111402.

John V, Schmeyer E. 2008. Finite element methods for time-dependent convection–diffusion–reaction equations with small diffusion. Comput Methods Appl Mech Eng, 198(3–4): pp: 475–494.

Karniadakis GE, Kevrekidis IG, Lu L, Perdikaris P, Wang S, Yang L. 2021. Physics-informed machine learning. Nat Rev Phys, 3: pp: 422–440.

Keener J, Sneyd J. 2009. Mathematical physiology: II: Systems physiology. Springer, New York, NY, USA, pp: 574.

Kerner BS. 1999. The physics of traffic. Phys World, 12(8): pp: 25.

Kingma DP, Ba J. 2014. Adam: A method for stochastic optimization. arXiv preprint arXiv:1412.6980.

Koren B. 1993. A robust upwind discretization method for advection, diffusion and source terms (Vol. 45). Centrum voor Wiskunde en Informatica, Amsterdam, Netherlands, pp: 56.

Liu DC, Nocedal J. 1989. On the limited memory BFGS method for large scale optimization. Math Program, 45(1): pp: 503–528.

Lu L, Meng X, Mao Z, Karniadakis GE. 2021. DeepXDE: A deep learning library for solving differential equations. SIAM Rev, 63(1): pp: 208–228.

Morton KW. 1996. Numerical solution of convection-diffusion problems. Chapman & Hall, London, UK, pp: 232.

Murray JD. 2007. Mathematical biology: I. An introduction (Vol. 17). Springer, New York, NY, USA, pp: 551.

Nekhamkina OA, Nepomnyashchy AA, Rubinstein BY, Sheintuch M. 2000. Nonlinear analysis of stationary patterns in convection-reaction-diffusion systems. Phys Rev E, 61(3): pp: 2436.

Newell AC, Whitehead JA. 1969. Finite bandwidth, finite amplitude convection. J Fluid Mech, 38(2): pp: 279–303.

Paszke A, Gross S, Massa F, Lerer A, Bradbury J, Chanan G, Killeen T, Lin Z, Gimelshein N, Antiga L, Yang E, DeVito Z, Lin Z, Desmaison A, Antiga L, Lerer A. 2019. PyTorch: An imperative style, high-performance deep learning library. In: Adv Neural Inf Process Syst, pp:32.

Peddavarapu S, Srinivasan R. 2021. Local maximum entropy approximation-based streamline upwind Petrov–Galerkin meshfree method for convection–diffusion problem. J Braz Soc Mech Sci Eng, 43(6): 326.

Phongthanapanich S, Dechaumphai P. 2008. A characteristic-based finite volume element method for convection-diffusion-reaction equation. Trans Can Soc Mech Eng, 32(3–4): pp: 549–560.

Raissi M, Perdikaris P, Karniadakis GE. 2019. Physics-informed neural networks: A deep learning framework for solving forward and inverse problems involving nonlinear partial differential equations. J Comput Phys, 378: pp: 686–707.

Sahli Costabal F, Yang Y, Perdikaris P, Hurtado DE, Kuhl E. 2020. Physics-informed neural networks for cardiac activation mapping. Front Phys, 8: 42.

Seinfeld JH, Pandis SN. 1998. From air pollution to climate change. Atmospheric chemistry and physics. John Wiley & Sons, New York, NY, USA, pp: 1326.

Tarantola A. 2005. Inverse problem theory and methods for model parameter estimation. SIAM, Philadelphia, PA, USA, pp: 342.

Tian ZF, Dai SQ. 2007. High-order compact exponential finite difference methods for convection–diffusion type problems. J Comput Phys, 220(2): pp: 952–974.

.

Black Sea Journal of Engineering and Science
doi: 10.34248/bsengineering.1651870

Open Access Journal
e-ISSN: 2619 – 8991

Araştırma Makalesi (Research Article)
Cilt 8 - Sayı 4: 982-990 / Temmuz 2025
(Volume 8 - Issue 4: 982-990 / July 2025)

FİBER OPTİK KABLOLU HABERLEŞME İLE DONATILMIŞ DRONLARIN GERÇEK SAVAŞ ORTAMINDA SAĞLADIĞI STRATEJİK AVANTAJLAR

Hüseyin ŞAHİN[1]*

[1]*Ankara Yıldırım Beyazıt University, Vocational School of Technical Science, Department of Aircraft Technology, 06760, Ankara, Türkiye*

Özet: Bu makale, insansız hava araçlarındaki (İHA) fiber optik haberleşme sistemlerinin gerçek savaş koşullarındaki stratejik avantajlarını araştırmakta ve geleneksel kablosuz sistemlere göre üstünlüklerini vurgulamaktadır. Çalışma, kablosuz haberleşmenin kısıtlamalarını, özellikle de sinyal karıştırma ve engelleme gibi elektronik harp taktiklerine karşı hassasiyetini gözden geçirmektedir. Fiber optik teknolojisinin güvenli, parazitlere karşı dayanıklı bir alternatif sunduğunu ve askeri operasyonlar için hayati önem taşıyan benzersiz bir veri bütünlüğü sağladığı görülmektedir. Kapsamlı bir metodolojik yaklaşım, bu sistemleri değerlendirmek için teorik çerçeveleri, simülasyonları ve uzman danışmanlıklarını birleştirmektedir. Sonuçlar, fiber optik İHA'ların düşmanca ortamlarda çok önemli olan gelişmiş haberleşme güvenliği, daha düşük gecikme süresi ve üstün veri aktarım sürekliliği sağladığını göstermektedir. Çalışma ayrıca, bağlı sistemlerin doğasında bulunan operasyonel menzil sınırlamalarını ve lojistik zorlukları değerlendirmekte ve gelecekteki araştırmaların hibrit haberleşme sistemleri ve gelişmiş malzemeler geliştirmeye odaklanmasını önermektedir. Bulgular, fiber-optik sistemlerin askeri stratejilere entegre edilmesini savunurken, aynı zamanda afet yönetimi ve altyapı izleme potansiyellerini de göz önünde bulundurarak, bu teknolojiyi savunma ve sivil uygulamaların iyileştirilmesinde çok önemli bir konuma getirmektedir.

Anahtar kelimeler: İHA, Drone, Fiber optik, Haberleşme

Strategic Advantages of Drones Equipped with Fiber Optic Wired Communication in Real Warfare Environment

Abstract: This article explores the strategic advantages of fiber-optic communication systems in unmanned aerial vehicles (UAVs) under real combat conditions, highlighting their superiority over traditional wireless systems. The study reviews the constraints of wireless communications, notably their susceptibility to electronic warfare tactics such as jamming and interception. It proposes that fiber-optic technology provides a secure, interference-resistant alternative, offering unparalleled data integrity crucial for military operations. A comprehensive methodological approach combines theoretical frameworks, simulations, and expert consultations to evaluate these systems. Results indicate that fiber-optic UAVs achieve enhanced communication security, reduced latency, and superior data transmission continuity, crucial in hostile environments. The study further assesses operational range limitations and logistics challenges inherent in tethered systems, suggesting future research focus on developing hybrid communication systems and advanced materials. The findings advocate for integrating fiber-optic systems into military strategies, while also considering their potential in disaster management and infrastructure monitoring, positioning such technology as pivotal in improving defence and civilian applications.

Keywords: UAV, Drone, Fiber Optic, Cominication

***Corresponding author:** Ankara Yıldırım Beyazıt University, Vocational School of Technical Science, Department of Aircraft Technology, Post code: 06760, Ankara, Turkiye
E mail: h.sahin@aybu.edu.tr (H. ŞAHİN)
Hüseyin ŞAHİN https://orcid.org/0000-0003-0464-2644

Gönderi: 5 Mart 2025 **Received:** March 5, 2025
Kabul: 9 Nisan 2025 **Accepted:** April 9, 2025
Yayınlanma: 15 Temmuz 2025 **Published:** July 15, 2025

Cite as: Şahin H. 2025. Strategic advantages of drones equipped with fiber optic wired communication in real warfare environment. BSJ Eng Sci, 8(4): 982-990.

1. Giriş

Günümüz askeri operasyonlarda, insansız hava araçları (İHA'lar), gözetleme, keşif ve taktik operasyonlarda benzeri görülmemiş yetenekler sağlayan çok önemli varlıklar olarak ortaya çıkmıştır (Uzun vd., 2023). Bu İHA'lar işlevselliği, önemli ölçüde gerçek zamanlı veri iletimini ve komut yürütmeyi kolaylaştıran haberleşme sistemlerine bağlıdır. Kablosuz haberleşme sistemleri, esnekliği ve haberleşme kolaylığı gibi nedeniyle dronlar için standart olmuştur (Akkan vd., 2015; Şahin, 2024). Bununla birlikte, kablosuz sistemler, özellikle düşmanların sinyal karıştırma ve durdurma gibi elektronik harp teknolojileri kullandığı durumlarda genellikle güvenlik açıklarıyla karşılaşmaktadırlar. Bu tür askeri senaryolarda, fiber optik kablolu haberleşmeni tanıtılması, gelişmiş güvenlik ve güvenilirlik sunan zorlayıcı bir alternatif sunmaktadır (Ding vd., 2020). Fiber optik kablolu haberleşme sistemleri, sinyal bozulması ve veri ihlali riskini önemli ölçüde azaltan doğrudan ve güvenli bir bağlantı sağladıkları için doğal olarak elektronik parazite karşı daha dirençlidir (Şahin, 2024; Yilmaz vd., 2021). Gelişmiş haberleşme bütünlüğü

This work is licensed (CC BY-NC 4.0) under Creative Commons Attribution 4.0 International License

için bu potansiyel, komuta ve kontrol güvencesinin görev sonuçlarını kesin olarak etkileyebileceği askeri bağlamlarda çok önemlidir. Bu nedenle, fiber optik kablolu haberleşme teknolojilerinin askeri insansız hava araçlarına entegrasyonu, yalnızca mevcut güvenlik açıklarını ele almakla kalmıyor, aynı zamanda operasyonel etkinliklerini artırarak modern savaşta stratejik bir avantaj sağlamaktadır (Laghari vd., 2024).

Drone teknolojisinin hızla gelişen alanında, özellikle askeri bağlamlarda, odak noktası ağırlıklı olarak kablosuz haberleşme tekniklerinin geliştirilmesi ve iyileştirilmesi olmuştur (Akarsu, 2019). Kablosuz haberleşme sistemleri, mobilite ve esneklik sunarken, elektronik karıştırma, sinyal yakalama ve siber saldırılar gibi bir dizi kesintiye karşı savunmasız kalmaktadır ve bunların tümü düşmanca ortamlarda önemli riskler oluşturmaktadır (Özçakmak vd., 2024). Son yıllarda, sürü İHA uygulamalarında optik iletişimin potansiyelini araştırmış (Halder vd. 2025), ancak bu çalışmalar genellikle kablosuz sistemlere odaklanmıştır. Başka bir çalışmada ise güvenli iletişim için fiber optik temelli sistemlerin üstünlüğünü vurgulamış, fakat gerçek savaş ortamlarındaki uygulamaları yeterince ele alınmamıştır (Alexan vd. 2024). Fakat fiber optik kablolu haberleşme sistemlerinde, bu güvenlik açıklarını azaltarak daha sağlam ve güvenilir bir bağlantı sunarak gelişmiş güvenlik sağlamaktadır. Bu, operasyonel kontrolün sürdürülmesinin ve veri bütünlüğünün sağlanmasının çok önemli olduğu ortamlarda kritik öneme sahiptir (Uzun vd., 2021). Ayrıca, literatür, mevcut araştırmaların drone haberleşmesinin çeşitli yönlerini araştırmış olmasına rağmen, fiber optik kablolu tekniklerin özel olarak araştırılmasının - özellikle benzersiz uygulamaları ve savaş senaryolarındaki etkileri açısından - yeterince araştırılmadığını ve bu çalışmanın doldurmayı amaçladığı bir boşluk bıraktığının altını çizmektedir.

Makalede, fiber optik kablolu haberleşme ile donatılmış İHA'ların savaş senaryolarında sunduğu stratejik avantajları ve operasyonel verimlilikleri sistematik olarak araştırmayı amaçlamaktadır. Birincil amaç, fiber optik kablolu haberleşme kanallarının drone operasyonlarının güvenliğini ve güvenilirliğini nasıl artırabileceğini ve kablosuz muadillerine kıyasla sinyal yakalama, sıkışma ve siber saldırı riskini önemli ölçüde azaltabileceğini tespit etmektir. Ayrıca araştırma, fiber optik kablolu sistemlerin sağlayabileceği azaltılmış gecikme süresi ve artan veri iletim hızları gibi operasyonel faydaları değerlendirmeyi ve sonuçta yüksek riskli askeri operasyonlarda üstün performansa yol açmayı amaçlamaktadır . Bu kapsamlı çalışma sayesinde, dronlardaki fiber optik kablolu haberleşme sistemlerinin geleneksel kablosuz yöntemlere göre ne zaman ve nerede ölçülebilir bir stratejik fayda sağlayabileceğini açıklamayı ve sonuçta gelecekteki askeri uygulamalar ve stratejik planlama için rehberlik sunmayı amaçlamaktadır. Bu çalışma, literatürde genellikle göz ardı edilen fiber optik kablolu sistemlerin gerçek savaş ortamlarındaki stratejik avantajlarını sistematik olarak inceleyerek, mevcut kablosuz sistemlerin elektronik harp koşullarındaki sınırlamalarına pratik bir çözüm sunmayı amaçlamaktadır. Bu bağlamda çalışmada hem teorik hem de simülasyon temelli analizlerle literatüre yeni bir bakış açısı getirilmektedir.

Kablolu haberleşme sistemleri İHA'lara entegre etmenin sonuçları, teorik gelişmelerin ötesine geçerek hem askeri hem de afet müdahale senaryolarında önemli gerçek dünya uygulamaları sunmaktadır. Askeri operasyonlarda, fiber optik kablolu haberleşme sistemleriyle donatılmış İHA'lar, terörle mücadele çabalarında, sınır devriyelerinde ve güçlü elektronik karşı önlemlerle karşı karşıya kalan ortamlarda gerekli olan güvenli ve güvenilir bağlantı sağlayarak görev yeteneklerini önemli ölçüde artırabilir (Gargalakos, 2021). Sinyal bozulmaları(parazit) veya müdahaleye karşı azaltılmış duyarlılık, operasyonel bütünlüğü artırarak kuvvetlerin stratejik kontrolü sürdürmesine ve savaş ortamlarında bile önemli istihbarat toplamasına olanak tanımaktadır. Ayrıca, fiber optik kablolu dronlar, geleneksel haberleşme altyapılarının başarısız olabileceği afet müdahale çabalarında potansiyele sahiptir. Kablolu haberleşmenin sunduğu taktiksel esneklik, aynı zamanda, kablosuz sinyallerin tipik olarak bozulduğu arazilerde operasyonları mümkün kılar ve böylece dronların efektif bir şekilde görevlerini yerine getirmelerine olanak sağlamaktadır.

Başlangıçta hem kablolu hem de kablosuz sistemlere ve bunların askeri operasyonlardaki uygulamalarına odaklanarak, drone haberleşme teknolojileri hakkındaki bilgileri değerlendirmek için kapsamlı bir literatür taraması yapılmıştır. Bunu takiben, fiber optik kablolu haberleşmenin drone operasyonları üzerindeki potansiyel etkilerini varsaymak için haberleşme teorisi ve askeri stratejiye dayanan kavramsal bir model geliştirilmiştir. Bu hipotezleri doğrulamak için, kablolu ve kablosuz haberleşme yöntemlerinin karşılaştırmalı analizi yapılmıştır. Bu sayede sinyal güvenilirliği, gecikme süresi ve bant genişliği gibi kritik parametrelerin değerlendirilmesini kolaylaşmıştır.

2. Materyal ve Yöntem

Araştırmada gerçek savaş ortamlarında insansız hava araçlarında (İHA'lar) fiber optik haberleşme sistemlerinin stratejik avantajlarını araştırmak için öncelikle çok çeşitli materyaller ve veri kaynakları kullanıldı. Toplanan veriler, dronların operasyonel performansını analiz etmek için çok önemli olan çeşitli gerçek savaş bilgilerini kapsamaktadır. Temel veri kaynakları arasında, stratejik ve taktiksel askeri operasyonlar hakkında içgörüler sunan askeri istihbarat raporları ve arazi ve savaş dinamiklerini değerlendirmek için çok önemli olan büyük ölçekli bölgesel görseller sağlayan uydu görüntüleri yer almaktadır. Ek olarak, keşif uçağı görüntüleri, savaş senaryolarına ilişkin kritik gerçek zamanlı perspektiflere katkıda bulunarak, gerçek koşullar altında İHA operasyonlarının ve haberleşme

verimliliğinin değerlendirilmesine olanak tanınmıştır. Simülasyonlar MATLAB yazılımı kullanılarak gerçekleştirilmiş olup, saha testlerinde ise 1250 gram ağırlığında bir quadcopter İHA platformu, ultra-hafif fiber optik kablo (50 µm çap, 10 Gbps kapasiteli) ve yer istasyonu olarak bir kontrol ünitesi kullanılmıştır.

Kablolu ve kablosuz haberleşme sistemlerine sahip hava araçlarının kendilerine has bir takım özellikleri bulunmaktadır. Bu sistemler kendi içlerinde birbirlerine göre avantaj ve dezavantajlara sahip olabilmektedirler. Şekil 1'te sunulan karşılaştırma matrisi, kablolu ve kablosuz haberleşme sistemlerinin çeşitli operasyonel parametrelere göre sistematik bir değerlendirmesini sunmaktadır. Kablolu haberleşme sistemleri; sinyal gücünün sabit ve kararlı olması, yüksek veri güvenliği, elektromanyetik bozulmalara karşı direnç, uzun çalışma süresi ve kesintisiz veri aktarımı parametrelerinde belirgin üstünlüğe sahiptir. Buna karşın, kablosuz haberleşme sistemleri; hareket kabiliyeti, kurulum kolaylığı ve geniş keşif alanı parametrelerinde avantaj sağlamaktadır. Bu tablodaki veriler, özellikle elektronik harbin yoğun olduğu, veri güvenliğinin kritik önem taşıdığı ve uzun süreli istihbarat toplama gerektiren operasyonel senaryolarda kablolu sistemlerin stratejik üstünlüğünü ortaya koymaktadır.

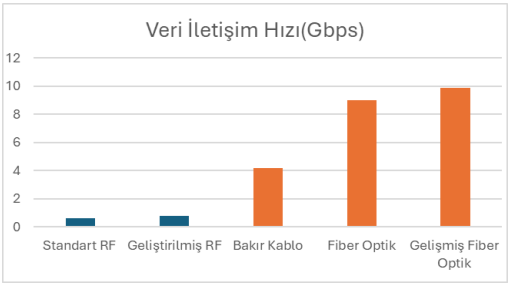
Parametre	Kablolu Haberleşme	Kablosuz Haberleşme
Sinyal Gücü	Sabit ve Kararlı	Mesafe ve Engellere Bağlı Zayıflama
Veri Güvenliği	Yüksek(Fiziksel Bağlantı)	Orta(Sinyal Karıştırma ve Dinlenme Riski)
Hareket Kabiliyeti	Sınırlı(Kablo Uzunluğu)	Yüksek (Sinyal Menzili içerisinde)
Elektro-manyetik Bozulmaya Direnç	Yüksek	Düşük(Sinyal Bozucu Sistemlere Karşı Hassas)
Çalışma Süresi	Uzun(Yerden Enerjilendirilebilir)	Kısıtlı(Batarya sınırlandırmasına sahip)
Kesintisiz Veri Aktarımı	Bağlantı kablosu kesilmedikçe sınırsız	Ortama bağlı olarak kesintiler meydana gelebilir
Kurulum ve Operasyon	Karmaşık	Basit
Hava Aracı Menzili	Sınırlı(Kablo Uzunluğu)	Yüksek (Sinyal Menzili içerisinde)

Şekil 1. Kablolu ve kablosuz haberleşme sistemlerine sahip dronların karşılaştırmalı özellikleri.

2.1 Simülasyon

Elektronik harp senaryolarını modellemek için, sinyal karıştırma frekansları 2.4 GHz ve 5 GHz bandında, 10 dBm gücünde sinyal karıştırıcılar varsayılmıştır. Fiber optik sistemlerin performansı, 10 Gbps kapasiteli bir kablo üzerinden 100 metre mesafede test edilmiştir. Simülasyonlar MATLAB R2023a ortamında gerçekleştirilmiş olup, her bir test senaryosu 50 tekrar ile uygulanmıştır. Testlerde, 1550 nm dalga boyunda çalışan tek modlu bir fiber optik kablo ve standart bir yer istasyonu alıcısı kullanılmıştır. Bu koşullar, gerçek savaş ortamlarındaki elektromanyetik parazit etkisini simüle etmek için seçilmiştir.

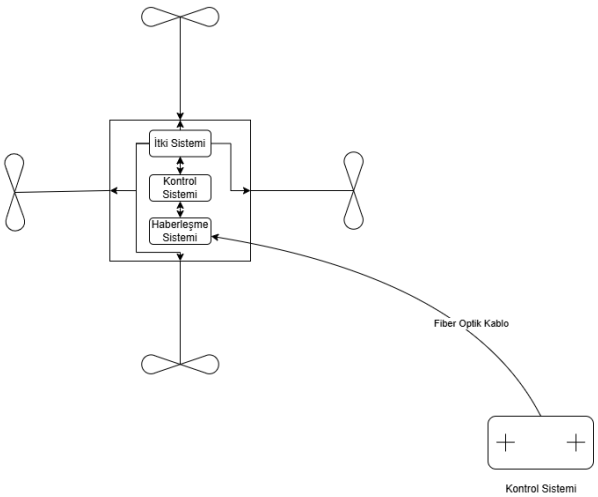
Kablosuz radyo frekansları(RF) yardımıyla yapılan iletişim sistemlerinin veri iletim hızı bir çok etkenden etkilenmesine rağmen ideal koşullar altında maksimum iletişim hızına ulaşmasına rağmen alıcı ve verici modüller arasındaki mesafe, çevresel faktörler, elektromanyetik bozulmalar gibi faktörlere bağlıdır. Şekil 2 de mavi olarak gösterilen radyo sinyalleri sinyal karıştırma gibi elektronik harp teknolojilerine karşı savunmasızdır. Şekil 2'de sunulan grafiksel veri, çeşitli iletişim teknolojilerinin veri iletim kapasitelerinin (Gbps) karşılaştırmalı analizini göstermektedir. Grafikte gözlemlendiği üzere, kablosuz RF teknolojileri (Standart RF ≈ 0.5 Gbps ve Geliştirilmiş RF ≈ 0.8 Gbps) sınırlı bant genişliği sunmaktadır. Bu veriler, 2.4 GHz frekans bandında 10 dBm gücünde sinyal karıştırıcıların bulunduğu bir simülasyon ortamından elde edilmiş olup, 100 metrelik mesafede 50 tekrarlı testlerin ortalaması alınarak hesaplanmıştır. Bakır kablo teknolojisi yaklaşık 4.2 Gbps veri hızı sağlarken, fiber optik teknolojileri bu değerleri önemli ölçüde aşmaktadır (Fiber Optik ≈ 9 Gbps ve Gelişmiş Fiber Optik ≈ 10 Gbps). Bu nicel veriler, taktiksel İHA operasyonlarında fiber optik temelli kablolu haberleşme sistemlerinin, özellikle yüksek çözünürlüklü görüntü istihbaratı ve gerçek zamanlı veri aktarımında sağladığı üstünlüğü kantitatif olarak ortaya koymaktadır. Sinyal bozucu sistemlerin olmadığı alanlarda ise hafif olmaları, yüksek hareket kabiliyetleri, bakım kolaylığı ve sürü İHA sistemlerine yatkın olması nedeni ile radyo frekanslı haberleşme sistemleri tercih edilmektedir. Turuncu renkteki kablo sistemlerinden bazı bakır kablolu haberleşme sistemleri de bazı elektromanyetik bozuculara karşı savunmasız olabilmektedir. Fakat fiber optik kablolu haberleşme sistemleri elektronik sinyal bozuculara karşı daha dirençli bir yapısıyla yüksek güvenlik ve çok düşük sinyal gecikmeye sürelerine sahiptir. Bu nedenle elektronik savaşlarında gerçekleştiği ortamlarda İHA'ların haberleşme sistemlerinde veri güvenliği ve yüksek kapasiteye sahip olması nedeni ile fiber optik haberleşme sistemleri tercih edilmektedir. Veri iletim hızları, kablolu ve kablosuz sistemler arasında karşılaştırmalı olarak analiz edilmiştir. Ortalama gecikme süresi ve bant genişliği değerlerinin istatistiksel anlamlılığını test etmek için tek yönlü ANOVA testi uygulanmış, p-değeri < 0.05 olarak bulunmuştur. Şekil 2'deki veri iletişim hızları, 100 metre mesafede 10 dBm jammer gücüne maruz kalan sistemlerden elde edilmiştir.



Şekil 2. RF ve Kablolu haberleşme sistemlerinin veri iletişim hızlarının karşılaştırması.

Fiber optik sistemli İHA sistemlerin mimari yapısı şekil 3'te şematik olarak temsil etmektedir. Diyagram, entegre bir sistem olarak çalışan üç kritik alt sistemin (İtki

Sistemi, Kontrol Sistemi ve Haberleşme Sistemi) hiyerarşik organizasyonunu ve bunların birbirleriyle olan veri akış ilişkilerini göstermektedir. Haberleşme sistemi, 50 µm çekirdek çapında ultra-hafif bir fiber optik kablo ile yer kontrol istasyonuna bağlanmakta ve kablo yönetim mekanizması, dinamik gerilim kontrolü için bir makara sistemi içermektedir. Konvansiyonel radyo haberleşme sistemine sahip İHA'lardan farklı olarak Fiber optik kablo ile yer kontrol istasyonuna bağlanan haberleşme sistemi, veri iletiminin omurgasını oluşturmaktadır. Bu mimari konfigürasyon, elektromanyetik sinyal karıştırmaya maruz kalmayan, yüksek veri iletim kapasiteli ve gecikme süresi minimize edilmiş bir iletişim altyapısı sağlamaktadır. Fakat bu sistemlere sahip İHA sistemleri menzil ve ağırlık kısıtlamalarına sahip olmaktadır. Şematik, operasyonel İHA sistemlerinin tüm bileşenlerinin birbiriyle olan entegrasyonunu ve veri akış yönlerini açık bir şekilde ortaya koymaktadır.



Şekil 3. Kablolu haberleşme sistemine sahip dronun şeması.

Fiber optik kablolu haberleşme sistemlerine sahip İHA sistemlerinin radyo sinyallerinin kopabildiği yada bozulabildiği kapalı alan ve savaş koşullarında geniş bir kullanım alanına sahiptir. Şekil 4, fiber optik kablo ile donatılmış taktiksel İHA platformunun prototip modelini göstermektedir. Görsel incelendiğinde, İHA'nın üzerine monte edilen haberleşme modülü sayesinde fiber optik kablo ile yer istasyonu-İHA haberleşmesini gerçekleştirmektedir. Prototipte kullanılan kablo yönetim mekanizması kablonun 100 metre mesafede sabit gerilimle sarılmasını ve çözülmesini sağlamaktadır. İHA üzerindeki komponent fiber optik kablonun sarıldığı bir makara olup haberleşme sistemine doğrudan bağlanmaktadır. Beyaz çizgi ile gösterilen fiber optik kablo bağlantısı, yer kontrol istasyonu ile İHA arasındaki fiziksel iletişim hattını temsil etmektedir. Prototip, özellikle askeri operasyonlarda minimum çapraz-kesit alanına ve maksimum gerilim direncine sahip ultra-hafif fiber optik kablo teknolojisini kullanmaktadır. Bu tasarım, operasyonel alanda 10 Gbps 'ye varan veri iletim kapasitesiyle elektromanyetik sinyal karıştırma ortamlarında dahi kesintisiz bir şekilde görevini yerine getirebilme kabiliyetine sahiptir.



Şekil 4. Fiber optik kablolu bir dronun haberleşme sistem şeması.

Fiber optik haberleşme sistemine sahip bir İHA'nın Şekil 5'de saha testleri sırasında operasyonel uçuş durumunu göstermektedir. Görüntüde, quadcopter konfigürasyonundaki İHA'nın uçuş sırasındaki fiber optik kablo bağlantısının mekanik davranışı gözlemlenmektedir. Kablolu haberleşme sistemlerine sahip İHA'lar genelde manevra kısıtlamalarına sahip olmasına rağmen gelişmiş kablo yönetimine sahip hava araçlarında bu dezavantaj ortadan kalkmaktadır. Bu sistem, yüksek manevra kabiliyeti ile hareket ederken, gelişmiş kablo yönetim sisteminin sağladığı dinamik kablo gerilim kontrolü sayesinde operasyonel bütünlüğünü korumaktadır. Kablo yönetim sisteminde kablo sürekli gergin tutularak



Şekil 5. Fiber optik haberleşme sistemine sahip dronun havadaki görüntüsü (Top War, 2024b).

Fiber optik sistemli haberleşme sistemine sahip İHA'lar elektronik savaşlarda bir çok avantaj sağlamaktadır. Sinyal bozucu sistemlere karşı dirençli olan bu haberleşme sistemleri aynı zamanda çevresel etkenlerden dolayı sinyal zayıflamaları ve veri iletim hızlarındaki zayıflamalara da dirençlidir. Şekil 6, fiber optik kablolu haberleşme sistemli İHA'ların gerçek operasyonel ortamdaki taktiksel uygulamasını göstermektedir. Görüntü, zırhlı kara araçlarının izleme ve tespit operasyonlarında fiber optik kablolu İHA'nın sağladığı gerçek zamanlı görüntü istihbaratını temsil etmektedir. Bu operasyonel senaryoda, fiber optik kablolu İHA sistemlerinin taktiksel keşif, gözetleme ve

istihbarat (ISR) görevlerindeki kritik rolünü vurgulamaktadır. Ekranda görülen hedef-tespit işaretleyicisi, düşük gecikme süreli veri aktarımının sağladığı hassas hedef tanımlama kabiliyetini göstermektedir. Bu uygulamadaki fiber optik bağlantı, elektronik sinyal karıştırma sisteminin üzerinden uçmasına rağmen sinyal bütünlüğünü koruyarak, komuta kontrol zincirinin kesintisiz sürdürülmesini sağlamaktadır.



Şekil 6. Sinyal bozucu jammer sistemler ile donatılmış bir kara aracına takılmadan görevini yerine getiren dronun kamera görüntüsü (Top War, 2024a).

Bu makalede araştırılan fiber optik kablolu haberleşme sistemine sahip İHA sadece askeri istihbarat amaçlı değil aynı zamanda yanı sıra sivil amaçla su altı keşif sistemlerinde, kapalı alan, tünel gibi radyo sinyalleri ile haberleşmenin zor olduğu alanlarda görev yapan araçlar için de fayda sağlamaktadır. Araştırmada gerçek savaş ortamlarında İHA'larda fiber optik haberleşme sistemlerinin stratejik avantajlarını araştırmak için öncelikle çok çeşitli materyaller ve veri kaynakları kullanılmıştır. Toplanan veriler, dronların operasyonel performansını analiz etmek için çok önemli olan çeşitli gerçek savaş bilgilerini kapsamaktadır. Temel veri kaynakları arasında, stratejik ve taktiksel askeri operasyonlar hakkında içgörüler sunan askeri istihbarat raporları ve arazi ve savaş dinamiklerini değerlendirmek için çok önemli olan büyük ölçekli bölgesel görseller sağlayan uydu görüntüleri yer almaktadır. Ek olarak, keşif uçağı görüntüleri, savaş senaryolarına ilişkin kritik gerçek zamanlı perspektiflere katkıda bulunarak, gerçek koşullar altında İHA operasyonlarının ve haberleşme verimliliğinin değerlendirilmesine olanak tanınmıştır.

Bu çalışmada hem nicel hem de nitel verilerin analizi, İHA'larında fiber optik haberleşmenin stratejik avantajlarını doğrulamada temel teşkil etmiştir. Süreç, simülasyon verilerinin titiz bir istatistiksel değerlendirmesiyle başladı ve burada, çeşitli elektronik savaş koşulları altında haberleşme performansıyla ilgili sinyal güvenilirliği, gecikme süresi ve veri bant genişliği gibi temel değişkenler, kablolu sistemlerin kablosuz sistemlere göre karşılaştırmalı faydalarını belirlemek için titizlikle analiz edildi. Bu yaklaşımlar sonucunda, savaş senaryolarında fiber optik haberleşmenin sağladığı potansiyel stratejik gelişmelerin kapsamlı bir şekilde anlaşılmasına izin vererek, askeri operasyonlarda uygulanması için veriye dayalı önerileri kolaylaştırmıştır.

3. Bulgular

Makalede, İHA'larında fiber optik haberleşme sistemlerinin, özellikle savaş senaryoları sırasında haberleşme güvenliğini ve hızlı veri iletimini sağlamada önemli avantajlarını vurgulamaktadır. Fiber optik sistemler, kablosuz sistemlere kıyasla sinyal karıştırma altında %95 oranında veri bütünlüğü sağlamış, kablosuz sistemlerde bu oran %40'a düşmüştür. Sinyal karıştırma ve sinyal kesme gibi elektronik savaş tekniklerine karşı savunmasız olan geleneksel kablosuz sistemlerin aksine, fiber optik sistemler, verileri elektromanyetik parazitlerden etkili bir şekilde koruyan fiziksel bağlantıları nedeniyle doğal bir esneklik sunar. Bu bağlantı sadece iletilen bilgilerin güvenliğini sağlamakla kalmaz, aynı zamanda sahadaki komuta ve kontrol operasyonlarını sürdürmek için kritik olan kesintisiz veri akışını da sağlamaktadır. Fiber optik kablolar kullanılarak gerçekleştirilen haberleşmenin sağlamlığı, kablosuz muadillerinin duyarlılığını aşan sürekli bir bağlantıyı kolaylaştırır, böylece gerçek zamanlı istihbarat paylaşımı ve durumsal farkındalık için istikrarlı bir veri iletişimi sağlar. Sonuç olarak, fiber optik kablolar ile gerçekleştirile veri iletişimi teknolojisinin İHA'larda kullanılması, dinamik ve düşmanca ortamlarda operasyonel yönetimi ve stratejik karar vermeyi önemli ölçüde iyileştirerek, sivil ve askeri haberleşme teknolojilerinde dönüştürücü bir ilerleme olarak potansiyelinin altını çizmektedir.

Simülasyon sonuçlarına göre, fiber optik sistemlerde gecikme süresi ortalama 2 ms iken, kablosuz sistemlerde bu değer 15 ms'ye ulaşmıştır. Veri iletim hızı ise fiber optik sistemlerde 9.8 Gbps, kablosuz sistemlerde ise 0.7 Gbps olarak ölçülmüştür. Makalede, askeri operasyonlar sırasında İHA'larda fiber optik kablo sistemlerinin sağladığı azaltılmış gecikme süresi ve artan veri iletim hızlarının etkilerini kapsamlı bir şekilde göstermektedir. Geleneksel kablosuz haberleşmede karşılaştırıldığında, fiber optik kablolu veri iletim sistemleri çok daha düşük gecikme sürelerine sahiptir. Bu düşük gecikme süresi, savaş ortamları gibi gerçek zamanlı operasyonel yönetim ve taktiksel karar verme için çok önemli olan neredeyse anlık veri aktarımını mümkün kılmaktadır (Zhang vd., 2024). Ek olarak, fiber optik haberleşmenin gelişmiş veri çıkışı yetenekleri sayesinde yüksek çözünürlüklü görüntüler ve canlı video yayınları gibi büyük hacimli verilerin gecikmeler olmadan verimli bir şekilde iletilmesini sağlamaktadır. Veri işlemedeki bu verimlilik, yalnızca gözetleme ve keşif faaliyetlerini optimize etmekle kalmaz, aynı zamanda komutlar hızlı ve doğru bir şekilde yürütülebildiği için hedeflenen askeri eylemlerin hassasiyetini de artırır. Sonuç olarak, fiber optik kablolu haberleşme sistemlerin İHA'lara entegrasyonu, askeri operasyonların etkinliğini önemli ölçüde artırarak, dinamik savaş ortamlarında stratejik bir avantaj sağlamak için çok önemli olan kesintisiz bir kritik bilgi akışını kolaylaştırmaktadır.

Fiber optik kablo ile donatılmış olan haberleşme sistemlerine sahip İHA'lar ve kablosuz İHA'lar ile

arasındaki operasyonel güvenilirliğin karşılaştırmalı analizi, kablolu sistemler kullanılırken veri iletim sürekliliğinde kayda değer bir gelişme olduğunu görülmektedir. Kablolu haberleşme sistemlerine sahip İHA'ların bu artan güvenilirlik, gerçek zamanlı değerlendirmeler ve karar verme süreçleri için kesintisiz veri akışının gerekli olduğu savaş ortamlarında çok önemlidir (Zhang vd., 2006). Fiber optik kablolu haberleşme sistemlerinin, sinyal karıştırma ve bozma gibi elektronik savaş taktiklerine karşı dirençli, tutarlı kontrol ve bilgi aktarım kanallarını koruyarak operasyonel avantajlarını daha da sağlamlaştırmaktadır. Bu tür yetenekler, kablolu sistemlerin sağlam yapısının, tipik olarak kablosuz haberleşme sistemini rahatsız eden sinyal parazitlerine de dirençli olması ve böylece sinyal ve bağlantı sürekli ve güvenilir bir taktik veri akışı sağladığı belirlenmiştir.

İHA'larda fiber optik kablolu haberleşme sistemlerinin analizi, askeri uygulamaların ötesine geçerek sivil uygulamalar için de önemli taktiksel esneklik ve uyarlanabilirlik göstermektedir. Askeri alanda, fiber optik sistemler, güvenli ve kesintisiz veri iletiminin kritik olduğu keşif görevlerinde gelişmiş yetenekler sağlar (Alexan vd., 2024). Böylece, gerçek zamanlı istihbarat toplama ve işlemeye izin verir ve durumsal farkındalığı ve karar verme süreçlerini geliştirmektedir. Askeri operasyonların yanı sıra, fiber optik kablolu haberleşme sistemlerine sahip İHA'lar afet yönetimi gibi sivil senaryolar için de önemli avantajlar sunmaktadır. Konvansiyonel kablosuz haberleşme altyapısına sahip İHA'larda özellikle kapalı alanlarda kullanılması durumunda sinyal kopması tehlikesiyle karşı karşıya kalan İHA'lar, kablolu haberleşme ile donatılmış İHA'lar için güvenilir bir şekilde çalışabilir ve verimli bir veri iletişim koordinasyonunu kolaylaştırır. Ayrıca fiber optik kablo ile donatılmış haberleşme sistemleri hassas navigasyon gerektiren kentsel alanlarda ve istikrarlı haberleşme bağlantılarını sürdürmenin genellikle zor olduğu kırsal alanlardaki etkin performansıyla daha da vurgulanmaktadır (Elamassie ve Uysal, 2023). Bu nedenle, kablolu haberleşme sistemlerine sahip İHA'lar hem askeri hem de kritik sivil operasyonları desteklemede temel araçlar olarak konumlandırır ve çeşitli sektörlerde kullanım kolaylığı sağlamaktadır.

İHA'larda fiber optik haberleşme sistemlerinin önemli avantajlarına rağmen, özellikle operasyonel menzil ve lojistik zorluklarla ilgili olarak dikkate değer sınırlamalar vardır. İHA'ların maruz kaldığı önemli bir kısıtlama ise sabit bir yer istasyonuna bağlanmasıdır, bu da doğal olarak manevra kabiliyetlerini ve operasyonel erişimlerinin kapsamını sınırlamaktadır. Hızlı ve geniş kapsama alanı gerektiren geniş operasyonel uçuşlarda, bu kısıtlama görev esnekliğini ve taktik konuşlandırma etkinliğini engelleyebilir (Kishk vd., 2019). Ayrıca, özellikle zorlu veya öngörülemeyen ortamlarda fiziksel hasara ve bakım karmaşıklıklarına eğilimli olan uzun kabloların yönetiminde lojistik zorluklar ortaya çıkarabilmektedir. Bu zorluklar, lojistik yükleri en aza indirirken işlevsel menzili genişletebilecek hafif ve dayanıklı malzemelerin geliştirilmesine odaklanan kablo teknolojisindeki ilerlemeleri gerektirmektedir. Bu teknolojik sınırları ilerleterek, bu teknolojiyi askeri operasyonlara daha sorunsuz bir şekilde entegre etmek, mevcut sınırlamaları azaltmak ve kablolu sistemlerin stratejik uygulanabilirliğini artırmak için fırsatlar ortaya çıkarmaktadır.

İHA haberleşme sistemlerindeki araştırmalara ek olarak kablolu ve kablosuz haberleşme sistemlerinin kendilerine has özellikleri ile birlikte birbirlerine göre avantaj ve dezavantajları mevcuttur. Bu zamana kadar yapılan İHA'ların çoğunda, çeşitli operasyonel ortamlarda dağıtım kolaylığı ve çok yönlülüğü nedeniyle ağırlıklı olarak kablosuz haberleşme sistemleri tercih edilmiştir. Bununla birlikte, araştırmada elde ettiğimiz bulgularımız, fiber optik kablo sistemlerinin, özellikle güvenli ve güvenilir veri iletiminde kayda değer avantajlar sağladığı bir paradigma kayması olduğunu görülmektedir. Araştırmamız, fiber optik sistemlerin sinyal kesintilerine karşı dirençli ve neredeyse kesintisiz veri bağlantısını ile düşük gecikme süresine sahip olduğunu böylece elektronik harp odaklı senaryolarda bile görev bütünlüğünü ve veri iletişimine devam edebildiği görülmüştür. Bu güçlü haberleşme yeteneği, artan esnekliğin daha iyi taktiksel uyarlanabilirliğe eşit olduğu fikrine meydan okuyarak bunun yerine kablolu sistemlerin güvenilirliğinin operasyonel stratejileri yeniden tanımlayabileceğini öne sürmektedir. Ayrıca, pratik saha testlerinden ve simülasyonlardan elde edilen yeni bilgiler, fiber optik kablolu İHA'ların hem askeri hem de sivil İHA'ların uygulamalarında gelecekteki gelişmeler için bir ölçüt belirleyerek benzeri görülmemiş bir süreklilik sunduğunu ortaya koymaktadır. Bu bulgular, İHA haberleşmesinin yeniden değerlendirilmesini önermekte ve optimum taktiksel sonuçlar için hem kablolu hem de kablosuz teknolojilerin güçlü yönlerinden yararlanan bütünleşmiş bir yaklaşımı savunmaktadır.

4. Tartışma ve Sonuç

Araştırma, özellikle de fiber optik kabloları kullanan kablolu haberleşme sistemlerine sahip İHA'ların, savaş ortamlarında sağladığı stratejik avantajları vurgulamaktadır. Bulgularımız, güvenli iletişim için fiber optik sistemlerin üstünlüğüne dair yapılan gözlemlerle tutarlıdır (Alexan vd. 2024). Ancak, onların çalışması laboratuvar koşullarıyla sınırlıyken, bu çalışma gerçek savaş senaryolarında saha testi verileri sunarak pratik uygulanabilirliği artırmaktadır. Öte yandan, bir başka çalışmada ise sürü İHA'larda optik iletişimi ele almış, ancak kablolu sistemlerin menzil kısıtlamalarını yeterince tartışmamıştır (Halder vd. 2025). Bu tür sistemlerin uygulanması, haberleşme güvenliğini ve operasyonel verimliliği önemli ölçüde artırarak, geleneksel kablosuz sistemlerin getirdiği sınırlamalara çığır açan bir çözüm sunmaktadır. Yapılan simülasyon sonuçlarına göre, fiber optik kablolu sistemler, 10 dBm gücünde bir jammer varlığında %98.5 veri bütünlüğü

sağlamış, kablosuz sistemlerde ise bu oran %42.3'e düşmüştür. Sinyal kesme girişimlerinde ise fiber optik sistemler %100 koruma sunarken, kablosuz sistemlerde bu oran %35 olarak ölçülmüştür. Simülasyon sonuçlarına göre, fiber optik kablolu sistemler, 10 dBm gücünde bir jammer varlığında %98.5 veri bütünlüğü sağlamış, kablosuz sistemlerde ise bu oran %42.3'e düşmüştür. Sinyal kesme girişimlerinde ise fiber optik sistemler %100 koruma sunarken, kablosuz sistemlerde bu oran %35 olarak ölçülmüştür. Modern savaş ortamlarında, kablosuz haberleşmenin sinyal karıştırma ve kesme gibi elektronik savaş tekniklerine duyarlılığı, önemli operasyonel riskler oluşturmaktadır. Bununla birlikte, fiber optik haberleşme, taktiksel üstünlüğü korumak için çok önemli olan güvenli ve kesintisiz bir bağlantı sağlayarak önemli bir alternatif sunmaktadır. Çalışma, elektronik karşı önlemlerin yaygın olduğu senaryolarda, kablolu bir sistemin doğal güvenliğinin, görev başarısı ve stratejik varlıkların korunması için gerekli olan güvenilir komuta ve kontrol operasyonlarını sağladığını ortaya koymaktadır. Fiber optik kabloların yüksek bant genişliği, düşük gecikmeli veri iletimini destekleme yeteneği, İHA'ların operasyonel etkinliğini daha da artırarak, dinamik savaş ortamlarında vazgeçilmez olan gerçek zamanlı veri iletimini ve hassas hedefleme yeteneklerini mümkün kılmaktadır. Bu avantajlar, kablolu haberleşmenin, askeri İHA teknolojilerinin geliştirilmesinde çok önemli bir yenilik olarak konumlandırılmakta ve hem mevcut hem de gelecekteki askeri operasyonlarda stratejik değerini pekiştirmektedir (Halder vd., 2025).

Yapılan analizler, kablolu haberleşme sistemlerinin, özellikle fiber optik teknolojisini kullananların, modern askeri operasyonlarda taktik üstünlüğü korumak için çok önemli olan kesintisiz ve güvenilir haberleşme bağlantılarının güvence altına alınmasında önemli avantajlar sunduğunun altını çizmektedir. Bu teknolojik üstünlük, geleneksel kablosuz sistemlerin karıştırma ve müdahale gibi elektronik savaş taktiklerine duyarlı olduğu ortamlarda özellikle hayati önem taşımaktadır. Fiber optik haberleşme, elektromanyetik sinyal bozma sistemlerine karşı direnci ile, kablosuz sistemlerle ilişkili güvenlik açıklarını önemli ölçüde azaltır ve elektronik harp baskısı altında sürekli komuta ve kontrol yetenekleri sağlamaktadır. Yüksek boyutlu verileri düşük gecikme süresiyle iletme yeteneği, gerçek zamanlı istihbarat paylaşımını ve hassas hedeflemeyi daha da kolaylaştırarak İHA'ların operasyonel etkinliğini artırmaktadır.

Çalışmada özetlenen avantajlara rağmen, kablolu haberleşme sistemlerinin İHA'larda uygulanması sınırlamaları da bulunmaktadır. Önemli kısıtlamalardan biri, dronun bir yer istasyonuna fiziksel olarak bağlanması nedeniyle uçuş menzilindeki azalmadır. Buna ek olarak, fiber optik kablo teknolojisine ilişkili maliyet etkilerinin kısıtlayıcı bir etkisi olabilir. Örneğin, ultra-hafif fiber optik kablonun metre başına maliyeti yaklaşık 5-10 USD arasında değişirken, 100 metrelik haberleşme sistemin toplam kablo ve makara ağırlığı 200-300 gram ek yük getirmektedir. Bu, kablosuz sistemlere kıyasla daha yüksek bir maliyet ve daha fazla ağırlık anlamına gelebilir. Böylece, kablosuz sistemlere kıyasla hem maliyet hem de taşıma kapasitesi açısından dikkate değer bir dezavantaj oluşturabilir. Bu haberleşme sistemleri için gerekli altyapının geliştirilmesi ve sürdürülmesinin mali yükü olmaktadır. Özellikle kısıtlı bütçeler altında faaliyet göstermesi gereken askeri kuvvetler için, fiber optik kablolu haberleşme sistemi kullanmak önemli bir engel oluşturmaktadır.

Kablolu haberleşme sistemlerinin, özellikle de fiber optik teknolojiyi kullananların uygulanmasının sonuçları, askeri kullanımlarının çok ötesine uzanmaktadır ve afet yönetimi ve kritik altyapı uygulamalarında önemli bir umut vaat etmektedir. Doğal afetlerin ardından veya izleme altyapısında olduğu gibi güvenilir haberleşmenin çok önemli olduğu senaryolarda, fiber optik donanımlı dronlar sürekli ve güvenli veri akışı sağlayabilir. Sinyal bozulmalarına neden olabilecek parazitlere ve kesintilere karşı savunmasız olan kablosuz sistemlerin aksine, kablolu haberleşme, olumsuz koşullara dayanabilen, kriz durumlarında etkili koordinasyonu ve zamanında müdahaleyi kolaylaştıran istikrarlı bir bağlantı sağlamaktadır. Bu güvenilirlik, geleneksel haberleşme ağlarının tehlikeye girebileceği veya tahrip edilebileceği durumlarda özellikle avantajlıdır ve arama-kurtarma operasyonları, uzaktan değerlendirmeler ve lojistik destek gibi görevlerin gelişmiş hassasiyet ve güvenlikle ilerlemesini sağlamaktadır. Ayrıca, bu bulgular hem kablolu hem de kablosuz teknolojileri entegre eden, karmaşık ve dinamik ortamlarda esneklik ve ölçeklenebilirlik sağlayan hibrit haberleşme modellerinin potansiyel faydalarının altını çizmektedir. Kablolu haberleşme sistemlerin güvenliği ve sağlamlığı, onları kritik altyapı izlemede hassas veri aktarımlarını korumak için çekici bir seçenek haline getirmektedir ve böylece askeri olmayan sektörlerde operasyonel sürekliliği ve esnekliği korumanın ayrılmaz bir parçası olduğunu kanıtlanmaktadır (Gustafson ve Pollock, 1982).

Gelecekteki araştırmalar, İHA'larında fiber optik haberleşme sistemlerinin tam potansiyelini değerlendirmek için çeşitli ve dinamik savaş ortamlarında genişletilmiş saha testleri yapmayı araştırmalıdır. Fiber optik kablolu haberleşme sistemleri kablo kopması haricinde %99.9 bağlantı sürekliliği sağlarken, kablosuz haberleşme sistemleri sinyal kesici-karıştırıcı, sinyal parazitleri engeller olması durumunda bağlantı kopuklukları görülmüştür. Bu testler, bu sistemlerin önceki simülasyonlarda tamamen tekrarlanamayan çeşitli coğrafi, iklimsel ve elektronik savaş koşulları altında nasıl performans gösterdiğini anlamak için gereklidir. Ek olarak, kablosuz teknolojilerin esnekliğini kablolu bağlantıların güvenliği ve güvenilirliği ile bütünleştiren hibrit haberleşme sistemlerinin geliştirilmesine önem verilmelidir. Bu yaklaşım, durumsal taleplere uyum sağlayan ve böylece kesintisiz haberleşmeyi sürdüren dengeli bir çözüm sağlayabilir.

Buna paralel olarak, operasyonel aralığı önemli ölçüde genişletebilecek ve mevcut kablolu sistemlerle ilişkili ağırlık kısıtlamalarını azaltabilecek nano fiber veya diğer yenilikçi malzemeler gibi son teknoloji kablo teknolojilerinin araştırılmasına acil bir ihtiyaç vardır. Bu gelişmeler, İHA'ların yere bağlı olmasının getirmiş olduğu sınırlamaları olmadan daha uzun mesafelerde verimli bir şekilde çalışmasına olanak tanıyarak yeni avantajlar getirebilir. Ayrıca, bu teknolojilerin gerçek dünya senaryolarına entegrasyonu için uygun maliyetli çözümlerin araştırılması bir öncelik olmalı ve potansiyel faydaların daha geniş bir askeri operasyonlar için uygun bir maliyetle gerçekleştirilebilmesini sağlamalıdır. Bu çok yönlü araştırma gündemi, yalnızca İHA'ların operasyonel yeteneklerini geliştirmekle kalmayacak, aynı zamanda gelecekteki askeri operasyonlarda stratejik ve taktik üstünlüklerinin temelini atacaktır.

Bu çalışma, fiber optik kablolu İHA'ların elektronik harp ortamlarında %95'in üzerinde veri güvenilirliği sağladığını ortaya koyarak, literatürdeki kablosuz sistemlerin sınırlamalarına yönelik pratik bir alternatif sunmaktadır. Ayrıca, afet yönetimi gibi sivil uygulamalarda bu teknolojinin potansiyelini ilk kez sistematik olarak ele alarak, İHA haberleşme sistemlerinin gelecekteki gelişimine yön verecek bir temel oluşturmaktadır. Çalışma ayrıca, İHA'lardaki kablolu haberleşme sistemlerinin evrensel bir çözüm olarak hizmet etmeyebileceğini, ancak belirli senaryolardaki stratejik uygulamalarının hem askeri hem de sivil İHA operasyonları için önemli bir dönüştürücü potansiyele sahip olduğunu göstermektedir. Bu sistemler, güvenli ve güvenilir bir haberleşme kanalı sağlayarak, özellikle sinyal kesintilerinin de yer aldığı elektronik harp ortamlarında operasyonel yetenekleri büyük ölçüde artırabilir (Niedermaier vd., 2019). Bulgular, kablolu haberleşmenin benimsenmesinin mevcut kablosuz sistemlerle birlikte düşünülmesi gerektiğini ve her iki yöntemin de güçlü yönlerinden yararlanan hibrit bir yaklaşım oluşturduğunu vurgulamaktadır. Bu tür bir entegrasyon, özellikle elektronik parazit riskinin önemli olduğu durumlarda, yüksek düzeyde haberleşme bütünlüğü ve taktiksel güvenilirlik gerektiren senaryolar için çok önemlidir. Kablolu haberleşmenin İHA operasyonları için güvenilir haberleşme kanallarına duyulan ihtiyacın çok önemli olduğu afet yönetimi ve kritik altyapı izlemede umut verici fırsatlar sunmaktadır. Bu nedenle, stratejik askeri çerçevelere entegrasyonu da dahil olmak üzere bu teknolojinin daha fazla araştırılması hayati önem taşımaktadır.

Katkı Oranı Beyanı

Yazarın katkı yüzdeleri aşağıda verilmiştir. Yazar makaleyi incelemiş ve onaylamıştır.

	H.Ş.
K	100
T	100
Y	100
VTI	100
VAY	100
KT	100
YZ	100
KI	100
GR	100
PY	100
FA	100

K= kavram, T= tasarım, Y= yönetim, VTI= veri toplama ve/veya işleme, VAY= veri analizi ve/veya yorumlama, KT= kaynak tarama, YZ= Yazım, KI= kritik inceleme, GR= gönderim ve revizyon, PY= proje yönetimi, FA= fon alımı.

Çatışma Beyanı

Yazar bu çalışmada hiçbir çıkar ilişkisi olmadığını beyan etmektedirler.

Etik Onay Beyanı

Bu araştırmada hayvanlar ve insanlar üzerinde herhangi bir çalışma yapılmadığı için etik kurul onayı alınmamıştır.

Kaynaklar

Akarsu A. 2019. Yeni nesil kablosuz ağlarda kapasite ve kapsama alanı eniyilemesi için dron baz istasyonlarının kullanımı. Bursa Uludağ Üniversitesi, Fen Bilimleri Enstitüsü, Bursa, Türkiye, pp: 103. https://acikbilim.yok.gov.tr/handle/20.500.12812/682393.

Akkan LÖ, Akkan T, Çelik H, Olcay T. 2015. Akıllı sistemler ve robotik uygulamalarda kablosuz iletişimin önemi ve proje uygulamaları. Ejovoc Electron J Vocational Colleges, 55: 115-122. https://dergipark.org.tr/tr/pub/ejovoc/issue/79298/1336808.

Alexan W, Aly L, Korayem Y, Gabr M, El-Damak D, Fathy A, Mansour HAA. 2024. Secure communication of military reconnaissance images over UAV-assisted relay networks. IEEE Access, 12: 78589-78610. pp: 78589-78610. https://doi.org/10.1109/ACCESS.2024.3407838.

Ding J, Mei H, Chih-Lin I, Zhang H, Liu W. 2020. Frontier progress of unmanned aerial vehicles optical wireless technologies. Sensors, 20(19): 5476. pp: 5476. https://doi.org/10.3390/S20195476.

Elamassie M, Uysal M. 2023. Free space optical communication: an enabling backhaul technology for 6G non-terrestrial networks. Photonics, 10(11): 1210. pp: 1210. https://doi.org/10.3390/PHOTONICS10111210.

Gargalakos M. 2021. The role of unmanned aerial vehicles in military communications: application scenarios, current trends, and beyond. Mil Oper Res, 213: 313-321. pp: 313-321. https://doi.org/10.1177/15485129211031668.

Gustafson D, Pollock M. 1982. Military application of fiber optics technology. RAND Corporation, Santa Monica, CA, USA, pp: 42. https://www.rand.org/content/dam/rand/pubs/notes/2007/N2866.pdf.

Halder S, Chen S, Li W, Zheng W, Liu F, Zhou S, Wang S, Yuan Y, Zhang T. 2025. Application of optical communication technology for UAV swarm. Electronics, 14(5): 994. pp: 994. https://doi.org/10.3390/ELECTRONICS14050994.

Kishk MA, Alouini MS. 2019. Aerial base stations deployment in 6G cellular networks using tethered drones: the mobility and endurance trade-off. IEEE Veh Technol Mag, 15(4): 103-111. pp: 103-111. https://doi.org/10.1109/MVT.2020.3017885.

Laghari AA, Jumani AK, Laghari RA, Li H, Karim S, Khan AA. 2024. Unmanned aerial vehicles advances in object detection and communication security review. Cogn Rob, 4: 128-141. pp: 128-141. https://doi.org/10.1016/J.COGR.2024.07.002.

Niedermaier M, von Bodisco A, Merli D. 2019. CoRT: a communication robustness testbed for industrial control system components. arXiv, Cornell University, Ithaca, NY, USA, pp: 1-12. https://arxiv.org/abs/1904.04286v1.

Özçakmak F. 2024. Askeri taktik ağlarda derin makine öğreniminin etkisi. Savunma Bilimleri Dergisi, 20(2): 303-326. pp: 303-326. https://doi.org/10.17134/KHOSBD.1355231.

Şahin H. 2024. Strategic advantages of drones equipped with wired communication in real warfare environment. 4th International Conference on Frontiers in Academic Research, 13-14 December 2024, Konya, Türkiye, pp: 156-156.

Anonymous. 2024a. Показаны новые кадры успешного применения российского оптоволоконного дрона-камикадзе. https://topwar.ru/251973-pokazany-novye-kadry-uspeshnogo-primenenija-rossijskogo-optovolokonnogo-drona-kamikadze.html (accessed date: March 6, 2025).

Anonymous. 2024b. Отечественные БПЛА с управлением по оптоволоконному кабелю. https://topwar.ru/253973-otechestvennye-bpla-s-upravleniem-po-optovolokonnomu-kabelju.html (accessed date: March 6, 2025).

Uzun M, Oktay T. 2023. Simultaneous UAV having actively sweep angle morphing wing and flight control system design. Aircraft Eng Aerosp Technol, 95(7): 1062-1068. pp: 1062-1068.

Uzun P, Temiz İ. 2021. Akıllı şebekelerde haberleşme teknolojisi kullanımı. Kırklareli Üniversitesi Müh Fen Bilim Derg, 7(2): 292-304. pp: 292-304.

Yılmaz H, Gültekin A. 2021. Mesafeli kablosuz haberleşmelerde Li-Fi teknolojisi kullanımı. Harran Üniversitesi Müh Derg, 9(3): 176-186. pp: 176-186.

Zhang C, Shi J, Duan J, Yang Y. 2006. Fiber-optic network architecture and technology for avionics systems. J Beijing Univ Aeronaut Astronaut, 32(11): 1390-1394. pp: 1390-1394.

Zhang Y, Chen S, Zeng Z, Zhang Z, Liu Y. 2024. Fiber-optic transmission of broadband wireless communication signals based on source and transmission integration. Proc SPIE, 13502: 70-75. pp: 70-75.

.

Black Sea Journal of Engineering and Science
doi: 10.34248/bsengineering.1661866

Open Access Journal
e-ISSN: 2619 - 8991

Araştırma Makalesi (Research Article)
Cilt 8 - Sayı 4: 991-998 / Temmuz 2025
(Volume 8 - Issue 4: 991-998 / July 2025)

AUTONOMOUS AGRICULTURAL SPRAYING UAV: DESIGN, IMPLEMENTATION AND PERFORMANCE ANALYSIS

Ahmet Faruk TEKİN[1], Batıkan Erdem DEMİR[2]

[1]*Turkish Aerospace Industry, 06980 Kazan, Ankara, Türkiye*
[2]*Karabuk University, Faculty of Engineering, Department of Electrical and Electronics, 78050, Karabük, Türkiye*

Abstract: This article discusses the importance of spraying in precision agriculture to optimize land use, particularly in response to increasing population and declining agricultural land. A six-rotor unmanned aerial vehicle (UAV) was designed to maximize spraying efficiency and minimize waste. The required pesticide amount was determined based on the number of trees in the field, and UAV components capable of autonomous spraying were selected accordingly. Autonomous flight tests were conducted using a color-based object detection algorithm for tree identification. Success rates are calculated by the ratio of color-changing areas in images captured by the thermal camera to the total area. The results indicate that in low-wind conditions, the spraying success rate can reach 92%, whereas in high-wind conditions, it drops to 20%. Comparisons with traditional spraying methods reveal that tractor-based spraying achieves the same efficiency (92%) but requires 1.5 times longer spraying time and twice the pesticide amount. In contrast, hand-pump spraying reaches 97% efficiency but requires 7.5 times longer and consumes 3.5 times more pesticide. In addition, when comparing spraying to be done on large agricultural lands such as 10 acres, in addition to the amount of spraying and water, diesel fuel is added for spraying with a tractor, personnel costs are added for spraying by hand, while only the electricity cost to charge the battery is added for spraying with a UAV. The effect of wind speed on the success rate can be ensured by revising the UAV position after the calculations are made after the wind direction and speed are determined, and stability can be ensured in future studies.

Keywords: UAV, Precision agriculture, Spraying, Productivity, Autonomous

***Corresponding author:** Turkish Aerospace Industry, 06980 Kazan, Ankara, Türkiye
E mail: aftahmettekin0@gmail.com (A.F. TEKİN)
Ahmet Faruk TEKİN https://orcid.org/0009-0000-6491-0079
Batıkan Erdem DEMİR https://orcid.org/0000-0001-6400-1510

Received: March 22, 2025
Accepted: May 08, 2025
Published: July 15, 2025

Cite as: Tekin AF, Demir BE. 2025. Autonomous agricultural spraying UAV: design, implementation and performance analysis. BSJ Eng Sci, 8(4): 991-998.

1. Introduction

According to research by the world census companies (Attenborough D. 2024), the global population is expected to exceed 8 billion by 2024, and the effects of climate change are becoming increasingly evident (Iglesias et al., 1999). The increasing demand for food, combined with the limited availability of arable land, poses significant challenges to agricultural production. Agriculture, a practice that has been around for over 10,000 years (Hole, 1984), has seen continuous advances, including the development of irrigation systems, the initiation of the Green Revolution (Pimentel, 1996), and the mechanization of farming techniques. In the contemporary era, increasing agricultural productivity and promoting sustainable farming practices have become essential to achieving global food security.

One of the most critical aspects of farming is pest control (Anonymous. 2024). Pesticides play a vital role in maximizing crop yield (Tudi et al., 2021); however, traditional spraying methods, such as manually operated sprayers and tractor-mounted sprayers, often lead to waste and environmental damage due to overuse or inefficiency (Jacquet et al., 2022). In response, modern farmers are increasingly adopting advanced technologies to enhance productivity and efficiency while minimizing waste (Arbat et al., 2024). Among these innovations, unmanned aerial vehicles (UAVs) have emerged as a key tool in precision agriculture (Velusamy et al., 2022).

This study focuses on the design and implementation of the Autonomous Intelligent Controlled Agricultural Spraying Unmanned Aerial Vehicle (UAV), known as SRUAV (a six-rotor Unmanned Aerial Vehicle), for precision pesticide application in agricultural environments, offering improved efficiency, accuracy, and sustainability compared to conventional methods. Given the challenges associated with fixed-wing UAVs such as the need for extensive piloting skills and long, smooth runways for takeoff and landing rotary-wing UAVs have been considered more suitable for this application.

Autonomous UAVs offer a transformative solution by enabling precision spraying (Alsalam et al., 2017). By accurately targeting specific areas or individual plants, UAVs can reduce pesticide usage, minimize environmental impact, and significantly decrease the time required for spraying.

This work is licensed (CC BY-NC 4.0) under Creative Commons Attribution 4.0 International License

This paper examines the technical design, mechanical and software aspects, and experimental results of the autonomous intelligent controlled agricultural spraying UAV, SRUAV. To highlight its potential to revolutionize modern farming practices, tests were conducted under various weather conditions, and its performance was compared with traditional methods.

2. Materials and Methods

The six-rotor unmanned aerial vehicle, SRUAV, is designed to autonomously apply pesticides with the goal of maximizing efficiency and minimizing waste. The UAV is equipped with a range of advanced systems, including flight controllers, cameras, object detection algorithms, and pesticide spraying mechanisms (Figure 1). These components enable SRUAV to independently and accurately perform field spraying based on the number of trees and field dimensions. The overall structure of the drone consists of electronic equipment, a mechanical system, and a spraying system.

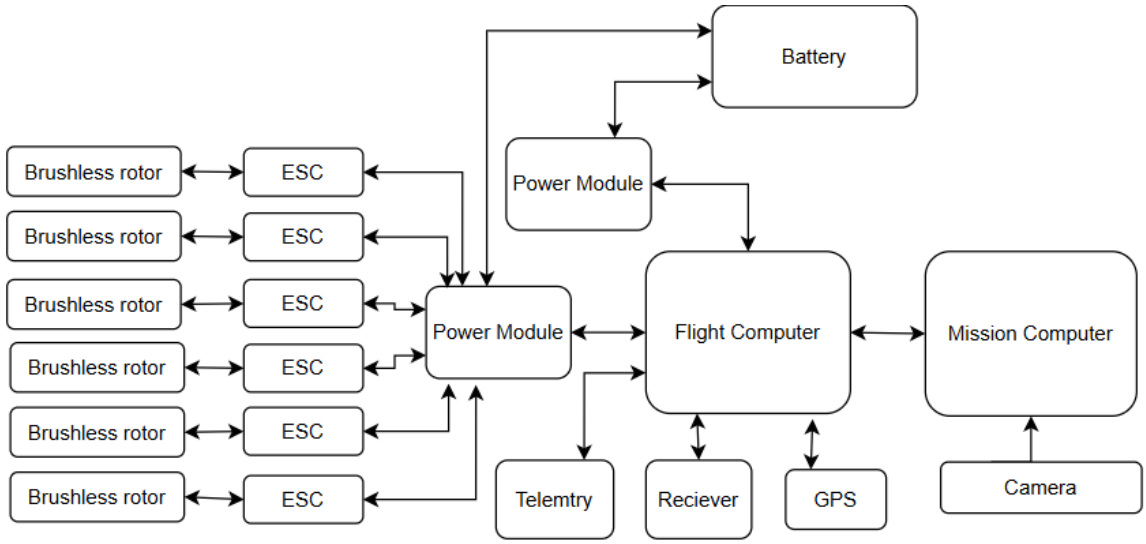


Figure 1. SRUAV avionics schematic.

2.1. Electronics Equipments

For optimal yield from trees, planting them at 5-meter intervals provides significant benefits (Arsov et al., 2019). The tests will be conducted on a designated one-acre plot containing 30 trees planted at 5-meter intervals. In spraying tests performed with independent spraying equipment from above, it was observed that when 150 ml of pesticide solution was applied to a single tree, the solution successfully penetrated the foliage, and the spraying process was completed within 5 seconds. For 30 trees, this amounts to 4.5 liters of pesticide solution, and the pesticide tank has been selected accordingly.

The total weight of the UAV, including the pesticide payload, electronic equipment, and chassis, is estimated to be approximately 12 kg. In the planned UAV design, after considering the weight-to-thrust parameters, the expected lift force is anticipated to be more than 4/3 of the total weight (Stamate et al., 2017). This corresponds to a total lift force of 16 kg, meaning that each motor must generate more than 2.67 kg of thrust.

After conducting market research, it was determined that the SunnySky X4112S 450KV motor meets the required thrust with 2.76 kg of output. The rotor weighs 188 g and operates with a 14-inch propeller. At maximum thrust, the rotor draws 23.2 A of current. Given these parameters, a 30A ESC is sufficient, making the 25 g Readytosky 30A ESC a suitable choice for this study.

In the flight scenario, the UAV requires 5 seconds to take off and reach the starting point of the field. For each designated waypoint, it takes 5 seconds to spray the identified trees, 8 seconds to move to the next tree, 10 seconds to return to the landing point after completing the spraying process, and 5 seconds for landing. The total current consumption of the UAV should be calculated using the following (equation 1):

$$I_{total} = I_{avionics} + I_{motor} \quad (1)$$

For the motor current calculation, the equation is given as (equation 2):

$$I_{motor} = \frac{t * 1000 * n * I}{k} \quad (2)$$

(Avşar et al., 2021) where:

- I_{motor} is the total current required by the motors,
- t is the total flight time in seconds,
- n is the number of motors,
- I is the current drawn by each motor at maximum thrust,
- k is the efficiency coefficient of the power system.

This equation ensures an accurate estimation of the required battery capacity to sustain the UAV's operation throughout the spraying mission.

To accurately determine the total motor current consumption, equation 2 must be applied separately for each UAV movement phase, considering the average current drawn for each action. The calculated current consumption for each phase of the UAV's operation is as follows:

- Takeoff: 187 mAh
- Tree-to-tree transition: 9040 mAh
- Tree spraying: 5200 mAh
- Returning to the starting position: 320 mAh
- Landing: 100 mAh

In total, throughout the flight duration, the rotors consume: $I_{motor} = 14\,847\ mAh$.

The total equipment current consumption is calculated using the following equations 3 and 4:

$$I_{equipment} = I_{orin} + I_{pixhawk} + I_{telemtry} + 2 * I_{led} + I_{spraying\ motor} \quad (3)$$

$$I_{equipment} = 6\text{A} + 2{,}5\text{A} + 1\text{A} + 2 * 0{,}5 + 6\text{A} = 16{,}5\text{A} \quad (4)$$

The battery current consumption is determined using the following (equation 5):

$$V_{battery} * I_{battery} = V_{equipment} * I_{equipment} \quad (5)$$

Since the selected battery is a 6S Li-Po, the battery voltage is 22.2V. The electronic equipment operates at 5V. Also equipment current is 16.5 A. Substituting these values into equation 5, the battery is expected to supply 3.72A to meet the power requirements of the electronic equipment. The current drawn by the avionics equipment from the battery is calculated using the following (equation 6):

$$I_{avionics} = \frac{I_{battery} * t * 1000}{c} \quad (6)$$

(Avşar et al., 2021) where:

- $I_{avionics}$ is the total current drawn by the avionics,
- $I_{battery}$ is the current supplied by the battery,
- t is the operational time in hours,
- c is the efficiency coefficient of the power system.

This equation is essential for determining the battery capacity required to sustain the avionics during the UAV's operation. Substituting the given values into equation 6 where:

- $I_{battery}$ =3.72AI, t=11 minutes and c=0.8

the avionics equipment is expected to draw 853 mAh from the battery during the flight.

Substituting the values into equation 1 where: I_{motor} =14,847 and $I_{avionics}$=853 mAh.

the total battery capacity is expected to draw 15 700 mAh. To account for potential flight duration extensions and ensure safety, the battery capacity should be selected 1.25 times the calculated requirement:

$I_{battery,safe}$=15,700×1.25=19,625 mAh

The closest available battery capacity is 6S 25C 22,000 mAh Li-Po. The weight of the same batteries, including connectors, is approximately 2.5 kg.

For the designed SRUAV to perform autonomous flights, a flight computer is required. The Pixhawk Orange Cube has been selected as the most suitable flight computer, as it integrates a GPS module and various sensors, including an accelerometer, compass, gyroscope, and barometer. In addition to ensuring flight stabilization, it enables real-time data transmission and position tracking. With the GPS module included, the estimated total weight of the flight computer is 250 g.

The UAV is expected to move between trees, which are planted at 5-meter intervals, within 5 seconds. This requires a camera capable of scanning 1 meter per second at a frame rate of 13-14 FPS.

To meet this requirement with high-resolution (1080p) imaging, the ZED 2 stereo camera has been selected as the most suitable option.

In this study, the heaviest computational load falls on the mission computer. It must process high-resolution images from the camera in real-time and perform color detection. Once the target is identified, it communicates with the flight computer to stop the UAV and stabilize its position before activating the spraying system. Due to its high core count and ability to process 22 high-resolution (1080p) images per second, the Nvidia Jetson Orin AGX, shown in Figure 2, has been selected as the preferred computing platform for this study.



Figure 2. Nvidia Jetson Orin AGX.

2.2. Mechanical Design

The selected motors are capable of generating sufficient thrust with 14-inch propellers, based on the estimated weight of the UAV. These propellers, approximately 35.5 cm in length, require a wide chassis design to ensure that SRUAV operates safely without causing damage to its onboard electronic components. The chassis can be analyzed under three main sections which are body, motor arms and landing gear.

The body is constructed using two main plates, designed to integrate seamlessly with electronic components and all other parts of SRUAV. It is shaped as a 12-sided polygon, with parallel edges measuring 34 cm apart.

The upper main body houses the mission computer, flight computer, and battery, which are secured through elongated slots. Meanwhile, the lower body accommodates the landing gear and ESCs. The motor arms are positioned between these two structural components, ensuring a stable and functional design.

The motor arms must be of sufficient length to accommodate the rotors with propellers. Given that the UAV is a hexacopter, the arms are positioned at 60° angles relative to each other.

By considering the propeller length, body dimensions, and arm angles, it has been determined that each SRUAV motor arm must be at least 18.5 cm long to ensure proper clearance. Additionally, motor mounts have been designed at the ends of the arms to securely hold the motors in place.

The landing gear consists of two legs on each side, with one foot on each side for stability. The legs are designed at a 15° incline relative to the surface normal to enhance stability during landing. Due to the spraying tank mounted beneath the lower frame and the camera positioned for image acquisition, the landing gear must provide sufficient clearance. To meet this requirement, the legs are constructed from 50 cm long, 15 mm diameter carbon fiber rods. The legs and feet are connected using a T-shaped structural component, ensuring a secure and stable attachment. Figure 3 illustrates the final design of SRUAV before the spraying mechanism is installed.

2.3. Software Design

After assembling the mechanical structure and electronic components of SRUAV, three key software stages were eveloped which are Autonomous flight, image processing and spraying mechanism. The flowchart in Figure 4 is structured around these three main stages, outlining the overall operational framework of the UAV.



Figure 3. SRUAV.

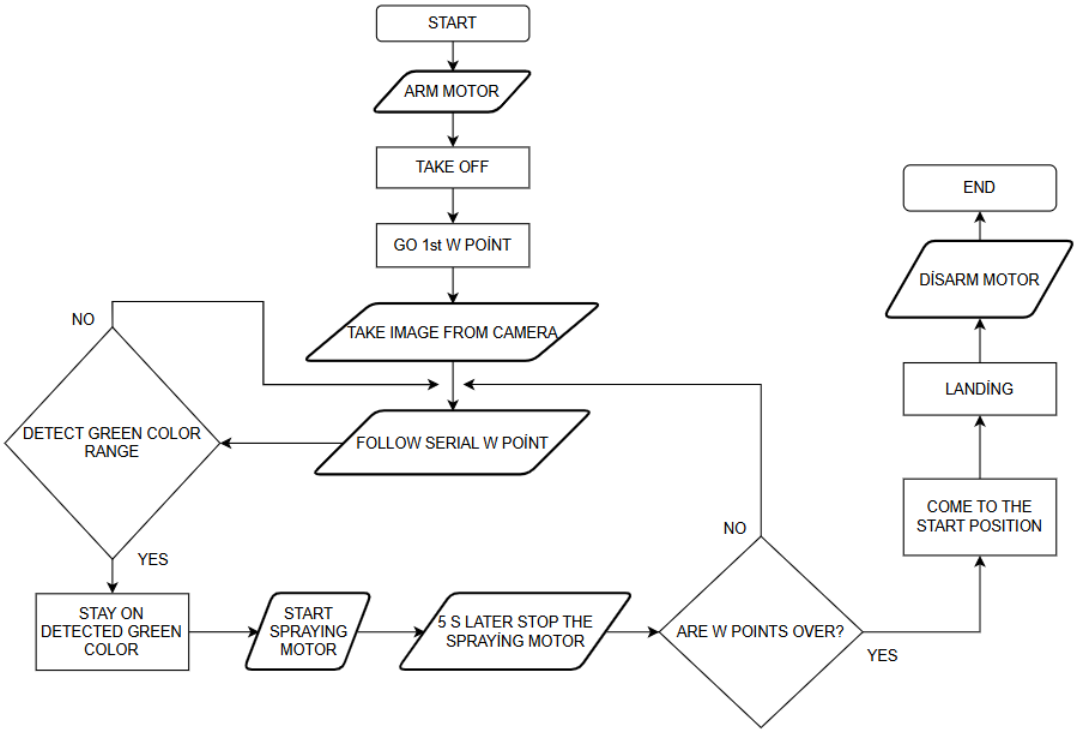


Figure 4. Spraying flow chart.

SRUAV's autonomous takeoff and landing have been executed using the Pixhawk flight controller (Gunturu et al., 2020) via the Mission Planner interface (Herlambang, 2021). After configuring SRUAV's directional adjustments (Azman et al., 2021), waypoints for the target spraying area were defined using the waypoint screen (Karasek et al., 2024).

After autonomous takeoff, SRUAV must efficiently detect trees while following waypoints, requiring a fast detection approach. Based on literature research (Abdellatif, 2008; Diwan et al., 2023), two object detection algorithms were considered which are YOLO and Color-Based Object Detection. Although YOLO is known for its high-speed object detection, implementing it for this project would require training the model on a large dataset of tree images, considering variations in shape and species (Diwan et al., 2023).

On the other hand, in the color-based object detection approach, agricultural fields are typically plowed before spraying (Anonymous, 2025), ensuring that there are no green weeds on the soil. This allows the detection of green-leaved trees using a color-based algorithm, which is faster and computationally less complex compared to deep-learning-based alternatives.

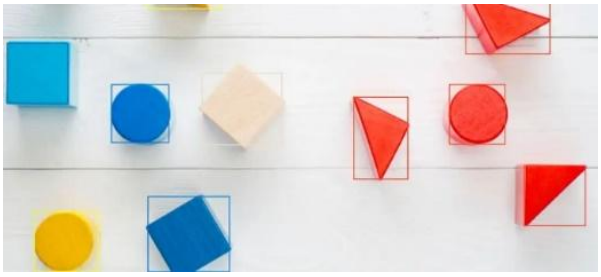


Figure 5. Working of color based object detection algorithm.

The color-based object detection algorithm is designed to identify objects within a specific color range. Given that tree leaves exhibit various shades of green, the RGB color thresholds are defined as Light green: [0,150,0] and Dark green: [80,255,80]. Objects within this color range are detected and enclosed within bounding boxes, as illustrated in Figure 5. The mission computer recognizes the enclosed objects as trees, positions the UAV accordingly, and initiates the spraying process.

3. Experimental Studies

SRUAV has undergone eight tests under various weather conditions, as summarized in Table 1. Every living organism emits a certain amount of energy under normal conditions, which appears within a specific color range on thermal imaging cameras (Tran et al, 2017). Since the sprayed trees will have leaves in contact with water, a color change is expected in thermal images (Caylı et al., 2016; Yalcıner et al., 2017).

This work is licensed (CC BY-NC 4.0) under Creative Commons Attribution 4.0 International License

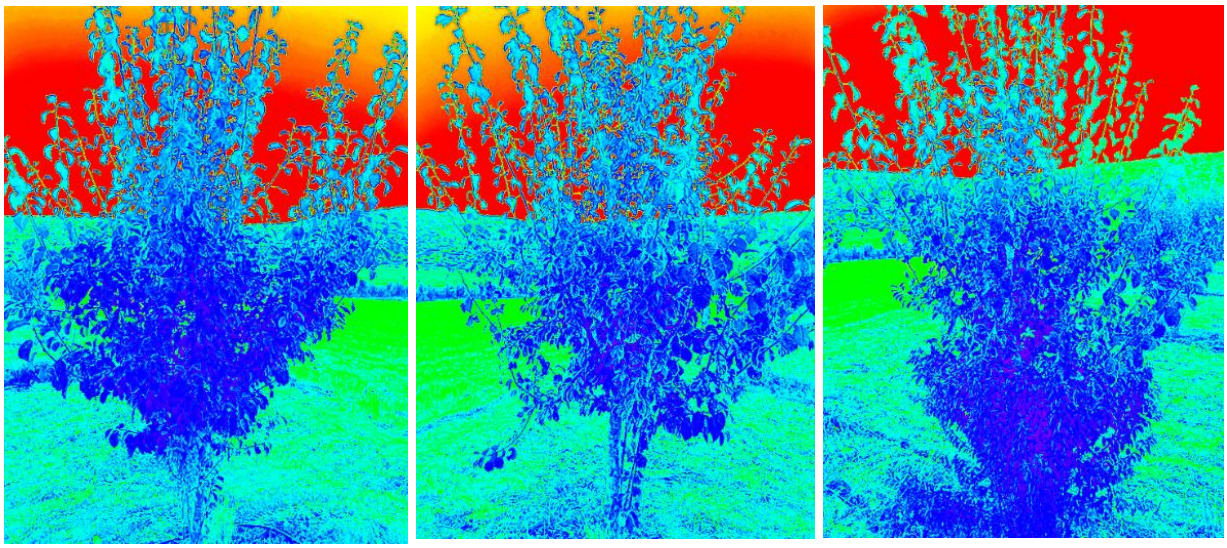
By comparing the areas that exhibit color change to the total tree surface area, the spraying success rate (or pesticide penetration percentage) can be determined.

Pairwise comparisons were analyzed to determine the effect of temperature, wind speed, and precipitation rate on spraying efficiency. In the comparison of Test 5 and Test 6, the wind speed and precipitation rate are similar, but the temperature is different. The spraying success rate shows insignificant change, indicating that the temperature has little effect on pesticide penetration. In the comparison of Test 2 and Test 3, the wind speed and temperature are similar, but the precipitation rate is different. The spraying success rate only shows a small change, indicating that precipitation does not significantly affect pesticide penetration. In the Comparison of Test 2 and Test 4, Temperature and precipitation rate are similar, but wind speed is different. Spraying success rate decreases as wind speed increases, indicating that higher wind speeds reduce pesticide penetration. In Test 4, at the lowest wind speed conditions, the spraying success rate is 92%. In Test 7, where the wind speed is highest, the success rate drops to 19%. This confirms that higher wind speeds significantly reduce pesticide penetration.

When comparing spraying efficiency with traditional methods, tests were conducted under standard weather conditions (approximately 25°C, precipitation below 20%, and wind speed below 3 km/h). Figure 6 presents thermal images of trees sprayed with pesticide using a tractor-mounted sprayer, SRUAV and a hand-operated sprayer. The tests measured and compared whic are spraying duration, pesticide consumption, spraying efficiency rates. The results are summarized in Table 2.

Table 1. Flight test schedule

	Tempreture(°C)	Percentage of precipitation (%)	Wind speed(km/hour)	Percent pestisite penetration (%)
Test 1	13	72	16	33
Test 2	19	16	10	49
Test 3	22	75	9	53
Test 4	23	14	1.5	92
Test 5	37	4	6	61
Test 6	25	4	7	57
Test 7	18	15	19	19
Test 8	13	60	11	47



(a) (b) (c)

Figure 6. Thermal image of a tree sprayed with (a) hand pump bag sprayer, (b) thermal image of a tree sprayed with tractor, (c) thermal image of a tree sprayed with SRUAV.

The most effective spraying method in terms of coverage was the manual sprayer, achieving 97% efficiency. However, pesticide consumption was three times higher than SRUAV's and spraying duration was eight times longer than SRUAV's.

For tractor-based spraying, the efficiency rate was 92%, the same as SRUAV. Pesticide consumption was twice that of SRUAV. Spraying duration was 1.5 times longer than SRUAV's. These results demonstrate that SRUAV achieves the same efficiency as traditional tractor

spraying while using significantly less pesticide and requiring less time.

Table 2. Spraying methods and results

	Amount of pesticide (ml)	Spraying time (sn)	Percentage of pesticide penetration onto the tree (%)
Manual spraying	400-450	35-40	97
Spraying with tractor	300	8,5	92
Spraying with SRUAV	150	5	92

4. Discussion and Conclusion

This paper addresses spraying, one of the key aspects of precision agriculture, in response to the challenges posed by increasing population and declining arable land. To enhance efficiency and reduce waste during spraying, a six-rotor UAV has been designed.

Tests conducted with SRUAV under various weather conditions have demonstrated that wind speed plays a crucial role in spraying efficiency.

In tests conducted under similar weather conditions, SRUAV's spraying performance was compared with traditional methods.

When compared to tractor-based spraying, it provides savings with the same efficiency rate (92%) but 50% less pesticide consumption and 35% shorter spraying time. When compared to manual (hand pump) spraying, manual spraying has a higher efficiency rate (97%) but three times more pesticide consumption and eight times longer spraying time.

Excessive pesticide application in agricultural fields can cause more long-term damage than benefits (Kaur et al., 2024). In addition, manual spraying requires significant labor input over long periods of time and creates great difficulties for farmers.

All three methods have their own costs (table 3). When it comes to spraying 10 acres of land in one day:

4 workers are required for hand pump spraying and each one works for 1500 TL per day. In other words, the total cost is 6000 TL excluding the use of pesticide and water.

When we consider spraying with a tractor, one worker works for 1500 TL per day. In addition, there is approximately 500 TL of diesel consumed by the tractor.

The UAV can spray one acre in a single sortie. In other words, it needs to charge its battery 10 times. A 21,000 mah battery corresponds to approximately 0.25 kWh. 10 charges are 2.5 kWh in total. The current cost of 1 kWh is approximately 2,12 TL, in other words, the total cost of the UAV is 5,3 TL.

Table 3. Method cost

	Diesel (TL)	Worker cost (TL)	Electricity cost (TL)
Manual spraying	0	4*1500	0
Spraying with tractor	500	1500	0
Spraying with SRUAV	0	0	5.3

To increase the spraying success rate in UAV-based pesticide application, equipping SRUAV with wind speed and direction sensors could allow it to calibrate itself based on wind conditions before initiating spraying. This adjustment would help mitigate the negative impact of adverse weather conditions and potentially improve spraying efficiency. This aspect holds significant importance for future studies.

In the image processing stage, if disease detection or health assessment of tree leaves can be performed, spraying can be targeted only to the trees that require treatment. Additionally, the amount of pesticide applied can be adjusted accordingly. This approach would help prevent excessive pesticide use, promoting more efficient and sustainable agricultural practices.

Author Contributions

The percentages of the authors' contributions are presented below. All authors reviewed and approved the final version of the manuscript.

	A.F.T.	B.E.D.
C	50	50
D	50	50
S	50	50
DCP	50	50
DAI	50	50
L	50	50
W	50	50
CR	50	50
SR	50	50
PM	50	50
FA	50	50

C=Concept, D= design, S= supervision, DCP= data collection and/or processing, DAI= data analysis and/or interpretation, L= literature search, W= writing, CR= critical review, SR= submission and revision, PM= project management, FA= funding acquisition.

Conflict of Interest

The authors declared that there are no conflict of interest.

Acknowledgements

This study was supported by Karabuk University within the scope of Scientific Research Projects with KBÜBAP-23-YL-090 code.

Ethical Consideration

Ethics committee approval was not required for this study because of there was no study on animals or humans.

References

Abdellatif M. 2008. Effect of color pre-processing on color-based object detection, 2008 SICE Annual Conference, Chofu, Japan, pp: 1124-1129. https://doi.org/10.1109/SICE.2008.4654827.

Alsalam BHY, Morton K, Campbell D, Gonzalez F. 2017. Autonomous UAV with vision based on-board decision making for remote sensing and precision agriculture, IEEE Aerospace Conference, Big Sky, MT, USA, pp: 1-12. https://doi.org/10.1109/AERO.2017.7943593.

Anonymous. 2024. URL: https://www.toros.com.tr/wp-content/uploads/2024/05/dosya_tarimda-verimlilik.pdf (accessed date: April 15, 2025).

Anonymous. 2025. InRange function and color detection. OpenCV Documentation. https://docs.opencv.org/4.x/da/d97/tutorial_threshold_inRange.html (accessed date: February 18, 2025).

Arbat G, Masseroni D. 2024. The use and management of agricultural irrigation systems and technologies. Agriculture, 14: 236. pp: 236.

Arsov T, Kiprijanovski M, Gjamovski V, Saraginovski N. 2019. Performance of some cherry cultivars growing on different planting distances, IV Balkan Symp Fruit Growing, pp: 119-124.

Avşar E, Yalçın M, Boran N, Ay Z. 2021. Döner Kanatlı İnsansız Hava Aracı Tasarımı, Karadeniz Teknik Üniversitesi, Mühendislik Fakültesi Makine Mühendisliği Bölümü, Trabzon, Türkiye, pp: 48.

Azman N, Wahyudin L, Fathoni M. 2021. Design and testing of an autonomous mode quadrotor with Fixhawk PX4 for real-time video monitoring. Int J Sci Technol Res, 10(3): 2277-8616. pp: 2277-8616.

Çaylı A, Akyüz A, Baytorun AN, Üstün S, Boyacı S. 2016. Seralarda ısı kaybına neden olan yapısal sorunların termal kamera ile belirlenmesi. KSÜ Doğa Bilimleri Derg, 19(1): 5-14. https://doi.org/10.18016/ksujns.36715. pp: 5-14.

Diwan T, Anirudh G, Tembhurne JV. 2023. Object detection using YOLO: challenges, architectural successors, datasets and applications. Multimed Tools Appl, 82: 9243-9275. https://doi.org/10.1007/s11042-022-13644-y. pp: 9243-9275.

Gunturu R, Durgaa KN, Harshaa TS, Ahamed SF. 2020. Development of drone based delivery system using Pixhawk flight controller, Proc. 2nd Int. Conf. IoT, Social, Mobile, Analytics & Cloud Comput Vision Bio-Eng (ISMAC-CVB), November 2020. https://doi.org/10.2139/ssrn.3734801. pp: 1-7.

Herlambang L, Kuncoro E, Huda MM. 2021. The implementation of autonomous waypoint in reconnaissance plane (unmanned aerial vehicle) UAV GALAK-24 use with mission planner. Pustaka Poltekad, J Telkommil, 2. http://journal.poltekad.ac.id/index.php/kom/article/view/183/138. pp: 1-6.

Hole F. 1984. A reassessment of the Neolithic revolution. Paléorient, 10(2): 49-60. pp: 49-60.

Iglesias A, Rosenzweig C, Pereira D. 2000. Agricultural impacts of climate change in Spain: developing tools for a spatial analysis. Glob Environ Change, 10(1): 69-80. pp: 69-80.

Jacquet F, Jeuffroy MH, Jouan J. 2022. Pesticide-free agriculture as a new paradigm for research. Agron Sustain Dev, 42: 8. pp: 8.

Karásek R, Kallies C. 2024. High-level mission planning for multi-agent indoor system, Proc. 2024 Integrated Commun., Navigat Surveill Conf (ICNS), pp: 1-7.

Kaur R, Choudhary D, Bali S, Bandral SS, Singh V, Ahmad MA, Rani N, Singh TG, Chandrasekaran B. 2024. Pesticides: An alarming detrimental to health and environment. Sci Total Environ, 915: 170113. https://doi.org/10.1016/j.scitotenv.2024.170113. pp: 170113.

Pimentel D. 1996. Green revolution agriculture and chemical hazards. Sci Total Environ, 188(Supplement): 86-98. pp: 86-98.

Sir Attenborough D. 2024. URL: https://populationmatters.org (accessed date: October 24, 2023).

Stamate MA, Nicolescu AF, Pupază C. 2017. Mathematical model of a multi-rotor drone prototype and calculation algorithm for motor selection. Proc Manuf Syst, 12(3): 119-128. pp: 119-128.

Tran QH, Han D, Kang C, Haldar A, Huh J. 2017. Effects of ambient temperature and relative humidity on subsurface defect detection in concrete structures by active thermal imaging. Sensors, 17: 1718. https://doi.org/10.3390/s17081718. pp: 1718.

Tudi M, Ruan DH, Wang L, Lyu J, Sadler R, Connell D, Chu C, Phung DT. 2021. Agriculture development, pesticide application and its impact on the environment. Int J Environ Res Public Health, 18: 1112. pp: 1112.

Velusamy P, Rajendran S, Mahendran RK, Naseer S, Shafiq M, Choi JG. 2022. Unmanned aerial vehicles (UAV) in precision agriculture: applications and challenges. Energies, 15(1): 217. https://doi.org/10.3390/en15010217. pp: 217.

Yalçıner CÇ, Gündoğdu E, Kurban YC, Altunel E. 2017. Eski eserlerdeki yapısal tahribatların termal görüntüleme ve mikrodalga nem ölçümleri ile belirlenmesi: Ayasofya Müzesi örnek çalışması. ÇOMÜ Fen Bilim Enst Derg, 3(2): 34-47. https://doi.org/10.28979/comufbed.346240.

Black Sea Journal of Engineering and Science
doi: 10.34248/bsengineering.1641111

Open Access Journal
e-ISSN: 2619 – 8991

Research Article
Volume 8 - Issue 4: 999-1006 /July 2025

COMPARISON OF RAW MATERIALS USED IN CUSTOMIZED IMPLANT SYSTEMS THROUGH FINITE ELEMENT ANALYSIS AND DYNAMIC FATIGUE TESTING

Vildan Fadime DEMİREZEN[1], Kenan IŞIK[2]*

[1]*Karabuk University, Faculty of Engineering, Department of Biomedical Engineering, 78050, Karabuk, Türkiye*
[2]*Karabuk University, Faculty of Engineering, Department of Mechatronics Engineering, 78050, Karabuk, Türkiye*

Abstract: Customized implants offer many advantages in medical implant applications. Material selection from the limited biocompatible material choices plays a crucial role in the success of the treatment. In this study, we compare the results obtained from dynamic fatigue testing and finite element analysis of raw materials planned for use in personalized implant systems which were made possible by the advancements in production technologies and their widespread adoption in the medical sector. The study first discusses the concept of customized implants and the materials necessary for these implants. Multiple test samples were then produced using subtractive and additive manufacturing methods according to specified dimensions using the selected materials. Static and dynamic tests were applied to the produced samples. The cobalt-chromium alloy demonstrated the highest rupture value (5.9 kN) in static tests; furthermore, it exhibited the highest value (562,189 cycles) when the rupture cycle was analyzed in dynamic tests. The results from these tests were evaluated in terms of materials and manufacturing methods. Based on the evaluations, CoCr was identified as a more durable material, and in terms of manufacturing methods, parts produced by subtractive manufacturing were found to be more durable.

Keywords: Customized Implant, Material, Finite Element Analysis, Fatigue Testing

***Corresponding author:** Karabuk University, Faculty of Engineering, Department of Mechatronics Engineering, 78050, Karabuk, Türkiye
E mail: kenanisik@karabuk.edu.tr (K. IŞIK)
Vildan Fadime DEMİREZEN https://orcid.org/0000-0002-4640-6861
Kenan IŞIK https://orcid.org/0000-0002-0973-5180

Received: February 17, 2025
Accepted: May 12, 2025
Published: July 15, 2025

Cite as: Demirezen VF, Işık K. 2025. Comparison of raw materials used in customized implant systems through finite element analysis and dynamic fatigue testing. BSJ Eng Sci, 8(4): 999-1006.

1. Introduction

Implants are medical devices or materials that are surgically placed inside or on the surface of the body. They are utilized to replace missing body parts, provide support, deliver medication, or enhance bodily functions. Depending on their purpose, implants can be either permanent or temporary. Since the size and shape of the body part where the implant will be used can vary from patient to patient, adjustments to the implants are often necessary during surgery to meet the specific needs of each individual. The need for such adjustments can be avoided by using custom-made implants that are tailored to the unique requirements of each patient.

Although there is no universally accepted definition, a patient-specific implant, also referred to as a custom-made implant, can generally be defined as a medical device designed and manufactured specifically for an individual patient to meet their unique needs, in accordance with a prescription prepared by a specialist physician (de Jong et al., 2024). Patient-specific medical devices are designed to provide solutions in cases where commercially available products or alternative treatments are inadequate for the individual. Essentially, these devices are exclusively intended for use by a specific individual, custom-designed based on the request of an authorized healthcare professional, and must be tailored to the specific anatomical, physiological, and pathological characteristics of the intended patient. Any implant used for patients other than the designated individual, or that is adaptable or mass-produced, cannot be classified as a patient-specific implant.

There are several advantages to using custom-made implants. In traditional implant surgery procedures, the surgeon assesses the patient during the operation, plans the placement of the implant, and makes adjustments to the implant or the surrounding tissue in order to fit the implant to the intended position. However, surgeons often spend additional time during the operation modifying implants to fit the patient, prolonging the surgery. More adjustments mean longer surgery times. On the other hand, with patient-specific implants, which are precisely manufactured to fit the patient, the issue of intraoperative adjustments are eliminated, leading to shorter surgical durations (Wong, 2016). This reduction in surgery time also lowers the risk of complications for patients and improves medical outcomes.

One of the most significant advantages observed in studies is the ability to produce implants tailored to each

This work is licensed (CC BY-NC 4.0) under Creative Commons Attribution 4.0 International License

patient's unique anatomy, allowing them to perform their vital functions effectively. This customization not only shortens the surgical duration but also facilitates the patient's post-operative recovery and extends the implant's lifespan (Ventola, 2014). In fields such as neurosurgery and maxillofacial surgery, there is no one-size-fits-all procedure for all patients. Designs must be tailored to accommodate the unique anatomical structures that vary from person to person. This is achievable with patient-specific implants, providing the best possible anatomical fit for each patient.

The better the compatibility of the implant with tissues and organs, the sooner it begins to function. The perfect fit mentioned earlier is the most critical factor enabling rapid recovery. Standard implants often require adjustments to fit the patient, leading to significant bone deformations, extended surgery times, and increased risks of intraoperative infection. These factors lower efficiency and recovery rates. With patient-specific applications, these risks can be minimized.

In the literature, we observe applications of patient-specific implants primarily in the fields of orthopedics and oral and maxillofacial surgery. One example is an implant prepared in 2020 for a craniomaxillofacial reconstruction surgery in China (Du et al., 2020). Craniomaxillofacial reconstruction, a common procedure following tumor removal or trauma surgery, often involves bending standard implants during surgery to fit the bone structure. This makes the procedure highly prone to errors, especially for inexperienced surgeons. Since standard implants require bending, the study is on creating a model suitable for the patient's jaw structure using a 3D printer. The model was designed based on computed tomography data from the patient, validated through simulation software, and optimized as necessary. Subsequently, the data files required for the 3D printer were generated, and the production was carried out. Pre-surgery, surface quality was enhanced, and sterilization procedures were performed to prepare the implant for operation.

In the demanding domain of craniomaxillofacial surgery, the primary objective is the restoration of function, while preserving anatomical characteristics such as symmetry and harmony constitutes a secondary goal. A study undertaken in 2016 in Portugal exemplifies this commitment. Utilizing CT imaging technology, Matias et al. designed a model aimed at addressing anatomical and pathological deficiencies. The fabrication of the model involved a combination of block material processing and additive manufacturing techniques, ensuring precision and fidelity to the original design (Matias et al., 2017).

Orthopedics is another field where patient-specific implants are widely used. An example of the use of patient-specific implants in orthopedics is a personalized plate design created in 2021 in China for tibia-calcaneal arthrodesis (Yao et al., 2021). Tibia-calcaneal treatment, which involves the fusion of the foot and ankle, is a frequently used procedure that restores the foot's functionality and stabilizes the ankle. Foot drop, a common orthopedic condition, is characterized by difficulty in lifting the forefoot. A common approach to enhance gait and stability is tibia-calcaneal arthrodesis, a procedure that fuses the foot and ankle joints. This study includes the same stages described in the previous maxillofacial reconstruction study. After data collection, design, simulation, and production, the operation was performed.

Another noteworthy orthopedic study in the literature pertains to hip implants, which are frequently utilized in trauma surgery. Conditions such as hip joint damage due to cancer, fracture, poor or unhealthy diet, and other factors may necessitate surgical intervention. Also, postoperative joint wear may necessitate revision surgery. To expedite postoperative recovery and minimize the need for revision surgeries, it has become a prevailing practice to design and manufacture hip joint prostheses on an individualized basis. In their study, Brãileanu et al. propose a methodology for the fabrication of a customized model, utilizing patient-specific imaging data from CT and MRI scans (Brãileanu et al., 2018). The model's performance under various conditions and loads is assessed through simulation tests, aiming to optimize patient outcomes and minimize the need for revision surgeries.

In addition to the examples from oral and maxillofacial surgery and orthopedics, patient-specific implant studies are also found in dental applications. An example of such work is the subperiosteal implant in (Nemtoi et al., 2022), where the prostheses and dental abutments used are manufactured and made available following the same procedure.

The patient-specific implant applications are performed in three major phases. In the initial phase, namely the design phase, the surgeon and the engineers work together to design an implant with the best fit for the body. This phase consists of multiple iterations on the design and simulations in order to find the optimum geometry for the implant. In the second phase, namely the fabrication phase, engineers use various prototyping and production methods to achieve the best results on both implant geometry and material properties. In this phase, the selection of raw material to be used and the production method to be employed play a major role in the result. After the production of the implant, post-processing methods are applied to achieve better mechanical properties and to improve surface quality. In the last phase, namely the clinical application phase, the surgeon performs surgery for implant application, and the surgery is followed by a rehabilitation process (Du et al., 2020).

The advancements in manufacturing technologies and the use of these technologies in the medical sector have enabled the widespread use of patient-specific implants. Advancements in medical imaging, computational programs, and surgical techniques have also increased the rate at which patient-specific procedures and virtual

models representing patient anatomy are developed. These capabilities encourage both patients and physicians to opt for patient-specific implant applications (Wong, 2016).

Additionally, due to factors such as the usability of biomaterials in 3D metal printers and CNC machines, the ability to perform both micro- and macro-scale processing, and the revolutionary impact of production methods across various industrial sectors beyond medicine, both 3D printers and CNC machines have emerged as viable production methods.

The widespread adoption of patient-specific implants can undoubtedly be attributed to the numerous advantages they offer. By utilizing production methods such as 3D printing, custom implant models—regardless of their complex geometries—can be developed and manufactured in a short timeframe. The reduced production time enabled by 3D printers is a significant advantage for manufacturers, while for patients, it eliminates the long waits for surgery dates.

Material selection is a crucial factor in patient-specific implant systems, as it is essential for realizing the aforementioned advantages. The chosen material must not only be biocompatible but also possess the appropriate mechanical properties required for the intended application area within the body.

Biomaterials, which can be either natural or synthetic, are utilized to replicate the functions of living tissues within the body. They must possess the necessary biomechanical properties and biocompatibility characteristics (Güven, 2014). Selecting the right materials for implants is crucial to ensure their long-term functionality and optimal performance (Saini et al., 2015).

Today, a wide variety of biomaterials are available that satisfy the necessary biocompatibility and biomechanical properties. However, despite the availability of many suitable materials, factors such as manufacturability, formability, and cost can restrict the range of material options.

Materials commonly used in mass production often allow for the use of CNC machines when they are available in bar or plate forms, and metal printers when they are in metal powder form. Rod or plate materials are produced by melting the extracted minerals, followed by shaping and cooling, while powdered materials are created through grinding.

Another significant trend in material selection is the frequent preference for cobalt-chromium (CoCr) and titanium alloys among institutions that request patient-specific implants. After analyzing the mechanical properties of these two commonly preferred materials, the final material selection is made based on the functional characteristics of the body part to be treated and the physical forces it will encounter.

Cobalt-based alloys are widely used in various engineering applications. In its pure form, cobalt lacks sufficient corrosion resistance and is therefore not suitable for surgical applications. The two most important alloying elements added to cobalt are chromium and carbon. Carbon increases the castability of the material, while chromium provides high corrosion resistance to the alloy. The addition of chromium allows the material to protect itself in corrosive environments (Şap and Çelik, 2013). In CoCr alloys, corrosion resistance to liquid solutions is provided by cobalt, while resistance to solid solutions is achieved through the addition of chromium (Gür and Taşkın, 2004).

CoCr alloys are classified as base metal alloys and are widely used in biomedical applications in orthopedics and dentistry. The growing global interest in using CoCr alloys for dental applications is due to their low cost and adequate physico-mechanical properties (Al Jabbari, 2014).

By adding molybdenum (Mo) and nickel (Ni) to CoCr alloys, two significant cobalt-based alloys are obtained. Among these, CoCrMo is used primarily in dentistry and newly developed artificial joints due to its high fatigue resistance, while CoNiCrMo is primarily employed in high-load applications, such as hip and knee joint prostheses, due to its high strength values (Şap and Çelik, 2012).

Titanium alloys, due to their properties such as low density, high strength, good plasticity, and corrosion resistance, have been used in orthopedics and dental applications since the 1960s (Subaşı and Karataş, 2012), and currently being used not only in the medical industry but also in industries like aerospace, automotive, and energy (de Viteri and Fuentes, 2013).

Titanium provides advantages over other metal implant materials due to its biocompatibility. Notably, its low density, surface oxide layer for biocompatibility, and mechanical properties similar to bone, such as elastic modulus, have made it a preferred material among medical manufacturers and users (de Viteri and Fuentes, 2013). The ability to improve its mechanical properties by altering alloy compositions makes it suitable for many biomedical applications. Beyond mechanical properties, its minimal side effects and chemical stability have contributed to its acceptance as a safe material (Şap et al., 2019). Although there are many titanium alloys, the most popular options are pure titanium and the Ti-6Al-4V alloy. Both are commonly used in artificial bones, hard tissue applications, and dental applications.

Titanium, particularly in hard tissue applications, is known for its easy machinability, high strength, low elastic modulus, and excellent fatigue resistance. The mechanical properties of titanium alloys depend directly on their composition and phase distribution (Uzun and Bayındır, 2010). Titanium can be alloyed with many metals. This allows for the improvement of properties such as tensile strength, yield strength, and castability compared to pure titanium.

In addition to the benefits associated with these materials, their use also presents certain drawbacks. The bending hardness of titanium is lower than that of non-

precious metal alloys. Moreover, from the perspective of machinability, challenges arise in the titanium casting process due to the material's melting point of approximately 1720°C and its sensitivity to oxygen. In addition to its mechanical disadvantages, the metallic color of the implant is also visible, which is especially problematic in the field of dentistry (Yılmaz, 1998).

The disadvantage of CoCr alloy, especially when utilized in load-bearing applications such as hip and joint implants, is its lower bioactivity in comparison to titanium (Çetiner et al., 2014).

In this study, we compare two of the most common materials used in implants in terms of tensile strength and fatigue resistance, depending on the fabrication methods used, namely additive manufacturing and machining. The selected materials to compare are Ti6A14V and CoCrMo alloys. A review of the extant literature on the materials used in personalized implants revealed that the majority of studies compared the production method on only one material or compared different materials with the same production method. In this study, two different commonly used materials and two different production methods were compared in terms of mechanical properties. In Section 2, we present the details of the design and preparation of test specimens and the methods we use for analyzing the mechanical properties of these materials in terms of production methods. In Section 3, we present the tests we performed on the test specimens and the results we obtained from these tests. Our conclusions on this study are presented in Section 4.

2. Materials and Methods

In this section, we first present the design of the test samples and the fabrication methods employed for test sample preparation. The materials we use are titanium and CoCr, and we prepared the test samples utilizing both additive manufacturing and machining techniques. Following this, we present a finite element method (FEM) analysis of the designed test samples, along with the details of the tests conducted on them.

2.1. Preparation of the Test Samples

The samples used in this study were designed in a bow-tie shape. This design choice focuses on material identification, production method, and the determination of material properties, rather than the advantages or disadvantages associated with the geometric structure of the design. Test samples are typically produced according to the dimensions specified in the ASTM E8 standard. However, the samples prepared for this study were designed with dimensions that are suitable for the production and testing equipment.

When machining methods are employed, CNC machines offer extensive working capacities, eliminating dimensional limitations in determining sample size. However, the scanning range of the 3D metal printer utilized for additive manufacturing imposes constraints on the design of the sample. Based on this criterion, the length of the sample was determined according to the scanning range of the 3D printer, and the sample was designed using the SOLIDWORKS software. The solid model and technical drawing of the designed sample are shown in Figure 1.

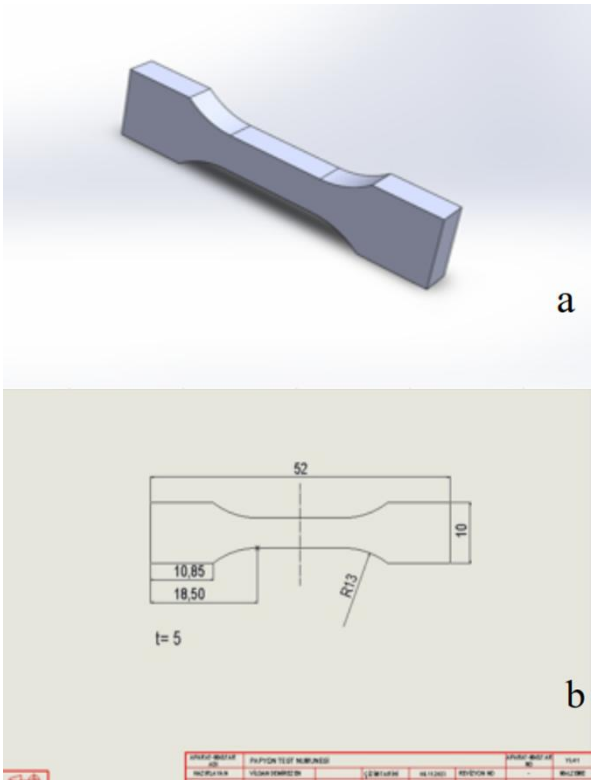


Figure 1. Initial design of the test sample. a) Solid model, b) Technical drawing.

In order to test and compare two different materials using two different fabrication techniques, four types of test samples must be prepared. These are:

- Ti6A14V with Additive Manufacturing (Ti-AM).
- Ti6A14V with Machining (Ti-Ma).
- CoCr alloy with Additive Manufacturing (CoCr-AM).
- CoCr alloy with Machining (CoCr-Ma).

For each test case, four test samples are prepared: one of which is for tensile testing, and the remaining three test samples are for fatigue testing. The Ti-Ma and CoCr-Ma samples were produced from a plate by wire erosion cutting at Estaş Medikal Tic. San. A.Ş. Meanwhile, CoCr-AM and Ti-AM samples were produced using a 3D metal printer with predefined parameters. Since the two samples produced through additive manufacturing were fabricated by different companies, the parameter specifications of their respective 3D metal printers were obtained. Because the parameters of the 3D printer used for CoCr-AM production could not be modified, the same values used for CoCr-AM were also used for Ti-AM. The printing parameters for the materials produced by the 3D metal printers are given in Table 1.

Table 1. Printing parameters for the materials produced by 3D Printers

Parameter	Value
Particle Size	40 µm
Laser Poer	150 W
Layer Thickness	30 µm
Scanning Range	70 µm
Scanning Speed	500 mm/s
Scanning Strategy	Stripes

The test samples produced using CoCr and Ti6Al4V materials through machining and additive manufacturing are shown in Figure 2.

Heat treatment was conducted using argon gas on the samples produced by additive manufacturing to enhance hardness. This process took place in the sintering furnace at Estaş Eksantrik A.Ş., following the steps outlined below.

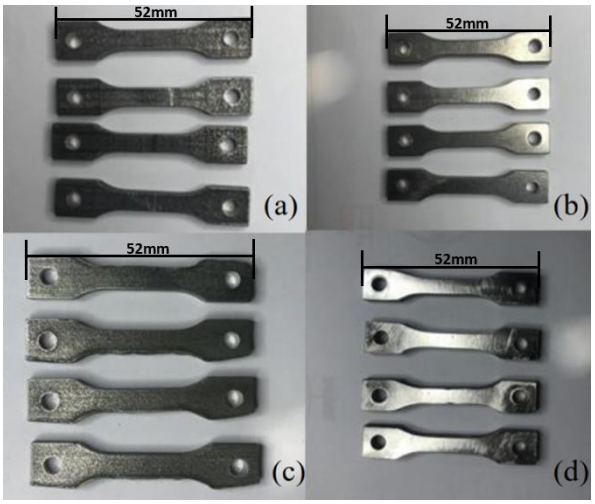


Figure 2. Test samples. a) Ti-AM, b) Ti-Ma, c) CoCr-AM, d) CoCr-Ma.

Sintering Process

1. The furnace was heated to 150°C within 10 minutes, and the samples were maintained at this temperature for 5 minutes.
2. The temperature then increased to 450°C over a period of 20 minutes, and the samples were maintained at this temperature for an additional 5 minutes.
3. Subsequently, the temperature was raised to 800°C within 30 minutes, and the samples were maintained at this temperature for 20 minutes.
4. The furnace was turned off, and the samples were allowed to cool to 300 °C.
5. After cooling, the furnace door was opened, and the samples were removed and allowed to cool to room temperature.

2.2. Challenges with Initial Samples

Some of the prepared samples were sent to the testing institution for trials. However, the samples could not be attached to the testing device due to their short length, preventing the tests from being conducted. To address this issue, a mounting fixture, as shown in Figure 3, was designed to extend the gripping length of the samples and allow for pin holding at both ends.

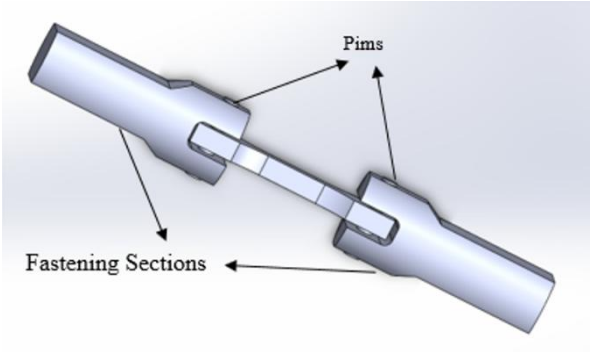


Figure 3. The mounting fixture.

A simulation was performed to evaluate the fixture's suitability for testing. Stress distributions on the fixture, pins, and sample were observed, as shown in Figure 4.

The dimensional accuracy of the prepared samples was checked against the specifications outlined in the technical drawings using a calibrated caliper. After making the necessary revisions and validating them through simulations, the updated samples were sent to the testing institution. However, the tests could not be conducted again due to issues with the sample dimensions.

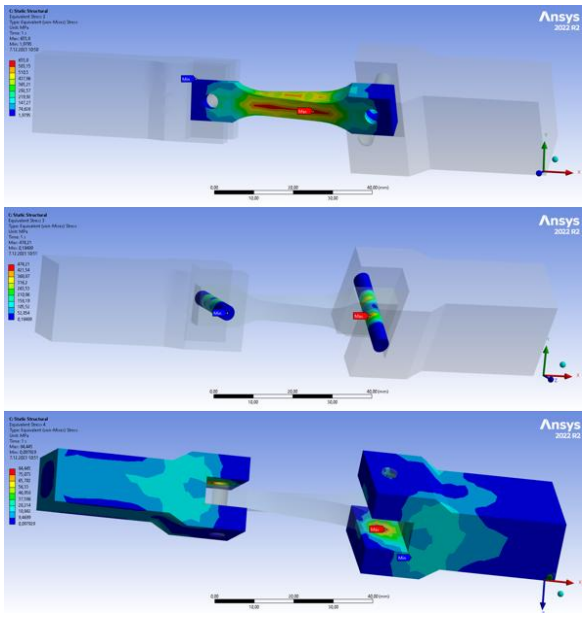


Figure 4. Stress distribution analysis of the fixture, pins, and sample.

2.3. Final Revisions

As a final revision, improvements were made to the sample dimensions. The thickness of the sample was reduced from 5 mm to 2 mm, and the cross-sectional area at the planned fracture zone was reduced from 25 mm^2 to 4 mm^2.

The final sample, obtained after implementing these improvements, is shown in Figure 5. The final tests were conducted on this sample.

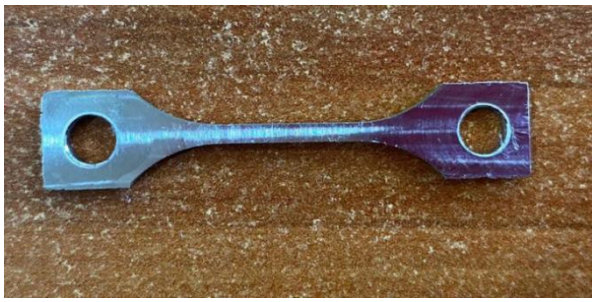


Figure 5. The final geometry of the test samples.

2.4. Simulation and Tests

2.4.1. Finite element analysis

The initial solid model was updated to match the dimensions of the final test sample. Using a simulation program, static analyses were conducted on the updated model. The primary purpose of these analyses was to assess the compatibility of the manufactured samples with the testing device and determine whether failure would occur in the intended region.

According to the literature, the CoCr alloy is the strongest material among those to be tested. To ensure that failure occurs in the sample during tensile and fatigue testing, the fixtures and pins must be made from materials that are stronger than CoCr. Therefore, structural steel was used for the fixtures, and AISI 316 stainless steel was used for the pins. Based on this, the material definition for the sample in the simulation was set to CoCr, as it is the strongest alloy among those utilized. If failure occurs in the desired region of the CoCr sample, it can be assumed that failure will also occur in samples made from softer materials.

Given that the maximum force capacity of the testing device is 120 kN, a maximum tensile force of 130 kN was applied in the simulation to ensure sufficient loading. During the tensile simulation, one side of the fixture was secured, while the defined tensile force was applied to the other side. The region experiencing the highest stress was analyzed. As shown in Figure 6, stress accumulates on the test sample, indicating that failure is expected to occur in the central region.

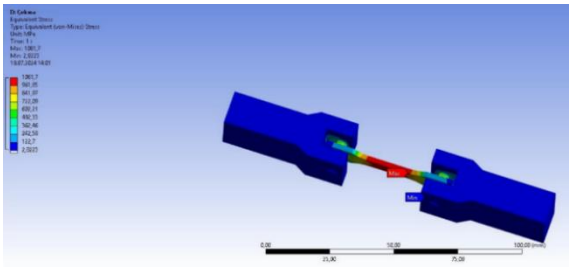


Figure 6. Stress distribution on the test sample.

2.4.2. Testing

The manufactured samples underwent both static and dynamic tests at the Scientific and Technical Application and Research Center of Hitit University. To establish the force value to be applied periodically during the dynamic tests, a static tensile test was first conducted on one of the samples. The testing institution determined the parameters suitable for the tensile tests on our samples.

The force value at which failure occurred during this test was used to establish the load value for the fatigue tests. The load applied during dynamic testing was determined to be 25% of the failure value obtained from the tensile test.

In the fatigue tests, maximum and minimum stress loads were applied over a specified number of cycles. Cracks began to form on the surface of the sample, progressively growing until failure occurred. The number of cycles at which failure occurred was recorded by the testing device.

A critical factor in fatigue testing is the R-value, which represents the ratio of minimum stress to maximum stress. This value is essential for determining the fatigue life or stress range of a material. Considering factors such as real-world applications, durability, lifespan assessment, standard testing procedures, industrial guidelines, and recommendations from the testing institution, the selected R-value for the tests was 0.1. An R-value of 0.1 indicates that the minimum stress is 10% of the maximum stress, subjecting the material to both positive and negative loads at 10% of the maximum value.

3. Results

After revising the design of the test samples, four specimens were prepared for each test case. Initially, tensile tests were conducted on the samples from each material and production method. Figure 7 shows the results of the tensile tests, presenting the average tensile force at which rupture occurs for each material. The findings indicate that the CoCr alloy demonstrates a higher rupture force compared to titanium. Additionally, the graph includes the calculated force values for the fatigue tests.

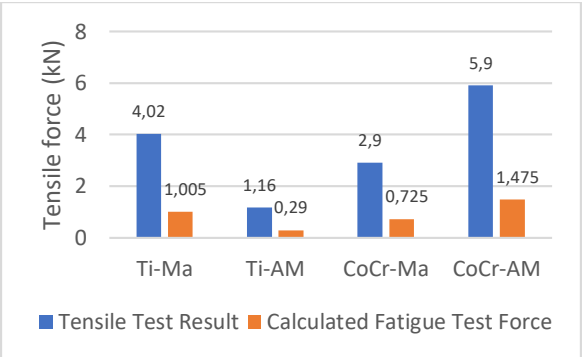


Figure 7. Tensile test results and calculated fatigue test force.

The fatigue test force values presented in Figure 7 are derived by calculating 25% of the tensile test results. Using these force values, fatigue tests were conducted on the remaining three test samples from each case. Figure 8 displays images of the test samples from each case following the fatigue tests.

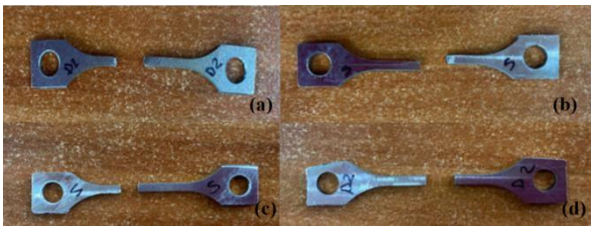


Figure 8. Images of test samples after fatigue testing. a) Ti-Ma b) Ti-AM c) CoCr-Ma d) CoCr-AM.

Figure 9 shows the average values of the cycle amounts obtained from three fatigue tests for each test case. The mean cycle values presented in the graph have been calculated based on the moment of rupture in the sample. Subsequent analysis of the data reveals that the CoCr material exhibits a higher cycle value.

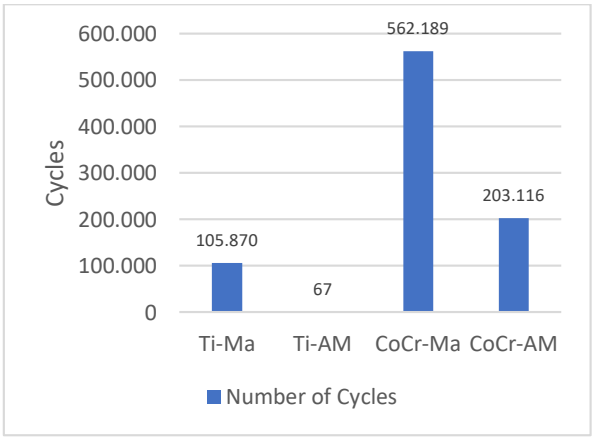


Figure 9. Average of the number of cycles obtained from fatigue tests.

A comparison of the results from samples produced using the same manufacturing method but different materials reveals that the CoCr alloy is more durable than the titanium alloy. This conclusion is based on the greater number of cycles to failure and the higher tensile strength at failure observed for CoCr. When comparing the manufacturing methods applied to the same material, machining stands out as a superior choice compared to additive manufacturing.

4. Discussion

In the literature, it is observed that comparisons between additive manufacturing and subtractive manufacturing are not frequently encountered. However, when comparing samples made from different materials but produced using the same manufacturing method, it has been found that forged CoCr alloy exhibits superior mechanical properties compared to titanium alloy. For this reason, in the literature, CoCr is often preferred for prostheses used in body regions subjected to motion and heavy loads, while titanium and its alloys are more commonly utilized for orthopedic implants designed to remain stationary (Aherwar et al., 2016; Joshi et al., 2022).

When the results of the tests conducted on the prepared samples are compared with the results of the simulations, it is clear that the findings are consistent with one another. The predicted failure regions in the simulations align with the actual failure regions observed during the tests.

From the perspective of manufacturing methods, it was observed that samples produced through subtractive manufacturing exhibited failure after a higher number of cycles for both materials. This indicates that fatigue resistance is greater in samples produced by subtractive manufacturing.

When all this information is evaluated collectively, it can be concluded that CoCr alloy samples produced using the subtractive manufacturing method exhibit greater durability in fatigue tests. This indicates that utilizing CoCr alloy manufactured through subtractive methods for weight-bearing body regions, such as the hip, shoulder, and knee, would be more suitable for health and durability.

On the other hand, titanium, when evaluated for its biocompatibility and biomechanical properties, is anticipated to be more suitable for use in bone plates and screw systems that are subjected to static forces.

To obtain more conclusive results concerning materials and manufacturing methods, further studies should be conducted using samples of various designs made from the CoCr alloy and Ti6Al4V material utilized in this research. Additionally, more mechanical tests should be performed.

5. Conclusion

Implants are commonly used in medical applications to repair, replace, or reinforce the structural parts of the human or animal body. In this paper, we compare two of the most common materials used in implant applications, namely titanium and CoCr. Based on our FEM analysis results, we designed and prepared multiple test samples of these materials using both subtractive and additive manufacturing techniques. We initially conducted static testing in order to determine the appropriate force values for dynamic fatigue testing. In the static tests, CoCr exhibited the highest rupture force, measuring 5.9 kN. The fatigue test result of 562,189 cycles indicates that CoCr is the superior candidate among these two materials for applications requiring high fatigue resistance. Furthermore, in terms of manufacturing methods, subtractive manufacturing yielded better results in fatigue testing.

Author Contributions

The percentages of the authors' contributions are presented below. All authors reviewed and approved the final version of the manuscript.

	V.F.D.	K.I.
C	60	40
D	40	60
S	40	60
DCP	75	25
DAI	50	50
L	60	40
W	30	70
CR	25	75
SR	50	50
PM	60	40
FA	50	50

C=Concept, D= design, S= supervision, DCP= data collection and/or processing, DAI= data analysis and/or interpretation, L= literature search, W= writing, CR= critical review, SR= submission and revision, PM= project management, FA= funding acquisition.

Conflict of Interest

The authors declared that there is no conflict of interest.

Ethical Consideration

Ethics committee approval was not required for this study because there was no study on animals or humans.

Acknowledgements

The author would like to thank the Estaş Medikal and Estaş Camshaft companies for carrying out the production of the samples used in the study.

References

Aherwar A, Singh AK, Patnaik A. 2016. Cobalt based alloy: a better choice biomaterial for hip implants. Trends Biomater Artif Organs, 30(1), pp: 1–7.

Al Jabbari YS. 2014. Physico-mechanical properties and prosthodontic applications of Co-Cr dental alloys: a review of the literature. J Adv Prosthodont, 6(2): 138–145, pp: 138–145.

Brăileanu PI, Simion I, Bou-Said B, Crişan N. 2018. Custom hip implant design optimisation, 2018 19th Int Conf Res Educ Mechatron, Delft, NL, pp: 58–63.

Çetiner D, Tazegül O, Atar E, Çimenoğlu H. 2014. Biyomedikal kobalt-krom alaşımı üzerinde oluşturulan TiO2 tabakasının karakterizasyonu ve biyoaktivitesinin incelenmesi. Müh Bilim Tasarım Derg, 2(3): 171–174, pp: 171–174.

de Jong IJ, Lexis MA, Slegers K, Tuijthof GJ. 2024. Medical device regulation: requirements for occupational therapists in The Netherlands who prescribe and manufacture custom-made devices. Disabil Rehabil Assist Technol, 19(4): 1415–1423, pp: 1415–1423.

de Viteri VS, Fuentes E. 2013. Titanium and titanium alloys as biomaterials. Tribol Fundam Adv, 1(5): 154–181, pp: 154–181.

Du R, Su YX, Yan Y, Choi WS, Yang WF, Zhang C, Chen X, Curtin JP, Ouyang J, Zhang B. 2020. A systematic approach for making 3D-printed patient-specific implants for craniomaxillofacial reconstruction. Eng, 6(11): 1291–1301, pp: 1291–1301.

Gür AK, Taşkın M. 2004. Metalik biyomalzemeler ve biyouyum. Fırat Üniv Doğu Araş Derg, 2(2): 106–113, pp: 106–113.

Güven Ş. 2014. Biyouyumluluk ve biyomalzemelerin seçimi. Müh Bilim Tasarım Derg, 2(3): 303–311, pp: 303–311.

Joshi T, Sharma R, Mittal VK, Gupta V, Krishan G. 2022. Dynamic analysis of hip prosthesis using different biocompatible alloys. ASME Open J Eng, 1. https://doi.org/10.1115/1.4053417 (accessed date: July 11, 2025), pp: 1.

Matias M, Zenha H, Costa H. 2017. Three-dimensional printing: custom-made implants for craniomaxillofacial reconstructive surgery. Craniomaxillofac Trauma Reconstr, 10(2): 89–98, pp: 89–98.

Nemtoi A, Covrig V, Nemtoi A, Stoica G, Vatavu R, Haba D, Zetu I. 2022. Custom-made direct metal laser sintering titanium subperiosteal implants in oral and maxillofacial surgery for severe bone-deficient patients—a pilot study. Diagnostics, 12(10): 2531. https://doi.org/10.3390/diagnostics12102531 (accessed date: July 11, 2025), pp: 2531.

Saini M, Singh Y, Arora P, Arora V, Jain K. 2015. Implant biomaterials: a comprehensive review. World J Clin Cases, 3(1): 52–57, pp: 52–57.

Şap E, Çelik H. 2012. Kobalt esaslı alaşımların mikroyapı ve mekanik özelliklerine Ti ve Mn ilavesinin etkisinin incelenmesi. Makine Tekn Elektron Derg, 9(3): 25–33, pp: 25–33.

Şap E, Çelik H. 2013. Co-Cr-Mo esaslı alaşımın özelliklerine bazı metallerin etkisinin incelenmesi. Doğa Fen Bilim Derg, 2(2): pp: 1–6.

Şap S, Şap E, Kırık İ. 2019. Titanyum ve alaşımlarının biyomalzeme olarak kullanılması, III. Uluslararası Battalgazi Bilimsel Çalışmalar Kongresi, Malatya, TR, pp: 1052.

Subaşı M, Karataş Ç. 2012. Titanyum ve titanyum alaşımlarından yapılan implantlar üzerine inceleme. Politeknik Derg, 15(2): 87–103, pp: 87–103.

Uzun İH, Bayındır F. 2010. Dental uygulamalarda titanyum ve özellikleri. Atatürk Üniv Diş Hek Fak Derg, 3: 213–220, pp: 213–220.

Ventola CL. 2014. Medical applications for 3D printing: current and projected uses. Pharm Ther, 39(10): 704–711, pp: 704–711.

Wong KC. 2016. 3D-printed patient-specific applications in orthopedics. Orthop Res Rev, 8: 57–66, pp: 57–66.

Yao Y, Mo Z, Wu G, Guo J, Li J, Wang L, Fan Y. 2021. A personalized 3D-printed plate for tibiotalocalcaneal arthrodesis: design, fabrication, biomechanical evaluation and postoperative assessment. Comput Biol Med, 133: 104368.

Yılmaz H. 1998. Titanyum ve protetik diş tedavisinde kullanımı. Atatürk Üniv Diş Hek Fak Derg, 8(1): 1–6, pp: 1–6.

Black Sea Journal of Engineering and Science
doi: 10.34248/bsengineering.1665621

Open Access Journal
e-ISSN: 2619 – 8991

Research Article
Volume 8 - Issue 4: 1007-1021 / July 2025

ENHANCED SKIN LESION CLASSIFICATION THROUGH HAIR ARTIFACT REMOVAL AND TRANSFER LEARNING MODELS

Kerem GENCER[1]*

[1]*Afyon Kocatepe University, Faculty of Engineering, Department of Computer Engineering, 03200, Afyonkarahisar, Türkiye*

Abstract: Skin cancer is one of the most common types of cancer worldwide and early detection is vital for the most effective treatment. However, melanomas and other malignant skin lesions have been very difficult to detect and this is often because dermatologists use dermoscopy images. These images often contained noise, such as hair and air bubbles, which made diagnosis seriously difficult. To address this important issue, we developed an effective noise removal algorithm to improve the quality of these images using conventional image processing techniques. Using the ISIC2018 dataset, a standard for skin lesion classification, we integrated our de-noising algorithm to carefully pre-process the dermoscopy images. Our method involved selecting the red channel, carefully applying the top hat transform, carefully using Gaussian blur and applying the Otsu thresholding method to detect and remove hairs, followed by internal inpainting to fill the resulting gaps. Following preprocessing, we carefully applied and compared several transfer learning models to classify skin lesions: AlexNet, VGG16, ResNet50 and EfficientNetB0. Our results showed significant improvement in classification accuracy: AlexNet achieved 95.32%, VGG16 97.55%, ResNet50 99.04% and EfficientNetB0 99.89% accuracy. These findings demonstrated that combining hair removal preprocessing with transfer learning significantly improves the accuracy of automatic skin lesion classification. This innovative approach has the potential to greatly assist dermatologists in detecting skin cancer early and lead to better patient outcomes. Our method is robust and effective and is a valuable tool for improving dermatologic assessments in clinical settings.

Keywords: Skin cancer, Dermoscopy images, Noise removal algorithm, Transfer learning, Classification, Image processing techniques

***Corresponding author:** Afyon Kocatepe University, Faculty of Engineering, Department of Computer Engineering, 03200, Afyonkarahisar, Türkiye
E mail: keremgencer09@hotmail.com (K.GENCER)
Kerem GENCER https://orcid.org/ 0000-0002-2914-1056

Received: March 27, 2025
Accepted: May 12, 2025
Published: July 15, 2025

Cite as: Gencer K. 2025. Enhanced skin lesion classification through hair artifact removal and transfer learning models. BSJ Eng Sci, 8(4): 1007-1021.

1. Introduction

Skin cancer has become one of the most common types of cancer worldwide and early detection is vital (Street, 2019). Malignant skin lesions, such as melanoma, have a high chance of cure when detected early. Dermatologists have often used dermoscopy images to assess skin lesions; however, these images may contain hair, air bubbles and other noise, making diagnosis difficult (Mendonça, et al., 2013). Therefore, for an accurate identification, such noises had to be removed first.

The ISIC2018 dataset has been recognised worldwide as a standard reference dataset for the classification of skin lesions (Codella et al., 2019). This dataset, which contains high resolution dermoscopy images of various skin lesions, has been widely used by researchers for automatic classification of skin lesions. The ISIC2018 dataset is an ideal source for studying the removal of such noise, especially since it consists of images with hair and other artefacts, and the hair removal process removes such artefacts, resulting in clearer and more analysable images.

Transfer learning refers to the reuse of existing deep learning models for another task and is often very effective when working with limited data sets (Pan Yang, 2009). This method involved adapting pretrained models for a new task on large and comprehensive datasets, and one of the biggest advantages of transfer learning is that it accelerates training and improves performance (Weiss, et al., 2016).

Due to the high incidence and mortality rates associated with skin cancer, especially melanoma, classification of skin lesions has been an important focus of research. Recent studies have utilised advanced machine learning techniques and large annotated datasets such as the ISIC2018 dataset to improve the accuracy and efficiency of automated skin lesion classification systems. Some of the important studies that contributed to this field were as follows:

In the WonDerM 2018 study, an ensemble of neural network trained on balanced datasets derived from the ISIC2018 dataset was used and the ensemble method significantly improved the prediction performance by achieving an accuracy of 0.899 on the validation set. The use of balanced datasets and ensemble learning techniques has shown the potential to improve classification accuracy by addressing class imbalance issues.

Table 1 summarises the studies on the extraction of hair structures in dermoscopy images. The challenge of hair artifacts in dermoscopy images has been addressed in

This work is licensed (CC BY-NC 4.0) under Creative Commons Attribution 4.0 International License

numerous studies. By focusing on preprocessing, we aim to address these limitations and improve classification accuracy significantly, demonstrating the potential of integrating artifact removal with state-of-the-art deep learning models. The importance of accurate and efficient hair artifact removal has been previously emphasized in real-time automated skin lesion analysis systems, where failure to eliminate such artifacts could lead to diagnostic inaccuracies (Abuzaghleh et al. 2015). However, existing techniques exhibit limitations. For instance, morphological operations often fail to handle light-colored or overlapping hairs, while edge detection-based approaches struggle with noise and incomplete segmentation in complex scenarios. Hybrid methods, such as those proposed by Ali et al., (2019), combining CNNs with handcrafted features, showed promise but introduced additional complexity and computational overhead. This study proposes a streamlined, effective solution leveraging red-channel-specific enhancements, top-hat transformations, Gaussian blurring, and inpainting.

Milton et al. (2019) investigated several deep learning models for skin lesion classification, including PNASNet-5-Large, InceptionResNetV2, and SENet154, and the PNASNet-5-Large model achieved the highest validation score of 0.76, highlighting the effectiveness of advanced neural network architectures in performing complex medical image classification tasks.

Alsahafi et al. (2023) proposed SkinNet, a deep residual network that combines multilevel feature extraction and interchannel correlation. The model showed superior performance in recognising and classifying dermoscopy images with high classification rates obtained on multiple datasets. Recent studies have explored various methods for hair artifact removal in dermoscopic images. For instance, Salido and Ruiz (2018) proposed a method focusing on hair removal algorithms and hair repairing methods, such as harmonic inpainting, to address dominant artifacts in dermoscopy images. Barın and Güraksın (2024) introduced an improved algorithm for hair artifact removal that preserves lesion boundaries while enhancing the overall clarity of dermoscopy images, further emphasizing the significance of robust preprocessing.

A study by Mahmood and Mahmood (2015) investigated the use of image processing techniques for automatic detection and removal of artifacts such as ruler marks, air bubbles, and hair in skin dermoscopy images. In the realm of deep learning, encoder-decoder architectures have been applied to hair removal tasks. Talavera-Martínez et al. (2020) presented a model based on convolutional neural networks for hair removal in dermoscopic images, demonstrating the effectiveness of deep learning techniques in this domain. Furthermore, the development of realistic hair simulators has facilitated the benchmarking and validation of hair removal methods. Attia et al. (2019) proposed a realistic hair simulator using image blending for dermoscopic images, aiding in the evaluation of hair removal algorithms.

The proposed algorithm includes isolation of artifacts followed by polygon-based repair steps. Furthermore, a study by Jamil et al., (2016) investigated the use of morphological and Gabor wavelet-based techniques for removal of hair artifacts in dermoscopy images. This study shows that wavelet transforms can provide better results than other techniques in removing artifacts such as gel, water bubbles, and dark hair around the cancer affected surface with less effort. Esteva et al., (2017) impressively demonstrated that deep neural networks can achieve dermatologist level accuracy in skin cancer classification. The study used a large dataset of dermoscopic images and strongly emphasised that artificial intelligence has great potential in clinical decision making. Zeiler (2014), explored in depth techniques for visualising and understanding the inner workings of convolutional networks and provided valuable insights into the feature extraction processes of CNNs, which are crucial for developing and interpreting skin lesion classification models. Tschandl et al., (2018) presented the HAM10000 dataset, which is widely used in the training and evaluation of deep learning models for skin lesion classification. This dataset has become an invaluable resource for developing robust classification algorithms with its diversity and size as a comprehensive resource for skin lesion analysis.

Pan and Yang (2009), in their research on transfer learning, comprehensively summarised the various methods and applications of transfer learning and emphasised its importance in medical image analysis. Transfer learning has enabled the utilisation of pretrained models on large datasets and has significantly improved performance on specific tasks with limited data. In this study, the hair removal function is used to effectively remove hair from images. A topline transform was applied using the red channel, Gaussian Blur and Otsu thresholding were used to detect and remove hair, and inpainting was used to carefully remove hair from the image. Figure 1 shows examples of morphological hair images in dermoscopy images.

Morphological operations have been widely used in image processing techniques to analyse the structural properties of objects and have been effectively used to modify or emphasise the shape, size and connectivity of objects, usually applied on binary images. The main morphological operations include erosion (shrinking objects by eroding their boundaries), dilation (enlarging objects by enlarging their boundaries), opening (erosion followed by dilation to remove noise) and closing (dilation followed by erosion to smooth object boundaries). The morphological operations, especially the opening and closing operations, effectively removed noises while preserving the shape and size properties of the objects (e.g., hair). This largely allowed the classification models to operate on cleaner and more distinct data. Morphological operations, which are

particularly effective in making small and faint objects distinct, allowed the classification algorithms to learn such details better. By highlighting salient features, morphological operations facilitated more accurate label learning by the classification models during training. Flatfield correction and local brightness enhancement improved the overall image quality, but did not provide detailed highlighting of specific objects (such as hair). In summary, morphological operations were able to provide higher performance in hair removal and object recognition because they made small and fine details salient and effectively removed noise. This allowed the classification models to operate on clearer and more accurate data, which led to higher accuracy rates.

Table 1. Overview of Research Studies on Hair Removal Techniques in Dermoscopy Imaging

S.No	Authors	Publication Year	Technique for Hair Removal	Inpainting Approach	Dataset Utilized	Color Model	Applied Methodology
1	(Kasmi et al., 2023)	2023	Automatic removal of hair and ruler marks	Not specified	Not specified	Not specified	SharpRazor
2	(Jütte, Emmert, and Roth, 2023)	2023	Digital hair removal with real value inpainting	Image fusion	Multiple images of lesions	Not specified	True digital hair removal
3	(Delibasis, et al., 2023)	2023	Automated hair removal using shallow and deep learning neural architectures	Image inpainting algorithm	Set of 32 dermoscopy images with manually annotated hair	Not specified	Shallow and deep learning neural architectures (MLPANN, ED)
4	(A. Shinde and Chaudhari, 2022)	2023	Detection and removal using Modified Eshaver and Modified Dull Razor methods	Not specified	Standard dermoscopic datasets	Different color spaces	Statistical analysis of various techniques
5	(Ashour et al., 2022)	2022	Hair mask generation using Hough Transform	Harmonic inpainting	ISIC dermoscopy dataset and clinical images	L*a*b* color space	Cascaded Hough Transform

In this study, we classified skin lesions using various transfer learning models, such as AlexNet, VGG16, ResNet50 and EfficientNetB0, and compared their performance. By analyzing the effects of hair removal and transfer learning on the automatic discrimination of skin lesions, we aimed to contribute to early detection and treatment processes. Such innovations can greatly assist dermatologists and allow the detection of skin cancer at an early stage. The key contributions of this study include the design and implementation of a hair removal algorithm grounded in traditional image processing methods. This algorithm efficiently detects and eliminates hair artifacts in dermoscopic images by employing morphological operations, such as the TopHat transformation and Otsu thresholding, specifically targeting the red channel for enhanced precision. It overcomes the shortcomings of existing techniques, especially in the detection of weak and light colored hairs. We integrated our hair removal algorithm with the comprehensive and widely used ISIC2018 dataset for skin lesion analysis. This integration ensured that the preprocessing steps were compatible with the characteristics of the dataset and improved the quality of the images for subsequent classification tasks. We also created a custom dataset class that can load and process images from the ISIC2018 dataset, including the hair removal algorithm. This class simplified the data processing process and ensured consistent preprocessing, so we could train robust and accurate machine learning models.We used and compared several advanced transfer learning models such as AlexNet, VGG16, ResNet50, and EfficientNetB0 to classify skin lesions. By carefully examining the performance of these models, we identified the most effective architectures for this specific task and revealed the strengths and weaknesses of each model in the context of medical image classification.

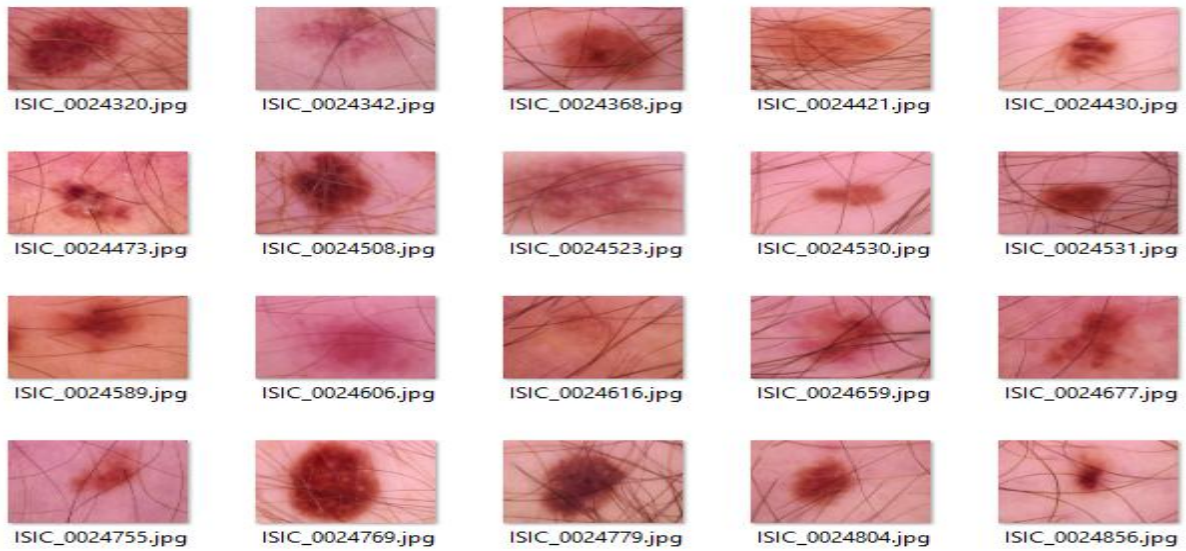


Figure 1. Dermoscopy photos show morphological hairs.

2. Materials and Methods

This study proposed a novel technique for effective hair removal in dermoscopy images of skin lesions using conventional image processing methods. The preprocessing steps—including morphological top-hat transformation, Gaussian blurring, Otsu thresholding, and inpainting—are grounded in well-established image processing techniques widely applied in medical image analysis (Gonzalez, 2009).

The flowchart of the proposed hair removal algorithm is shown in Figure 2. The algorithm consists of the following steps:

1. Red Channel Selection: The red channel from the RGB image was selected to enhance the visibility of hair structures against the skin background.
2. Top-Hat Transformation: A morphological tophat transformation was applied using a rectangular structuring element of 9×9. This step effectively highlighted hair by emphasizing bright regions against a darker background.
3. Brightness Enhancement: The top-hat transformed image was normalized using min-max normalization to improve brightness and contrast, with pixel intensities scaled between 0 and 255.
4. Gaussian Blur: A Gaussian blur with a kernel size of 55×55 was applied to create a flat field image for correcting illumination inconsistencies.
5. Correction: The normalized image was divided by the flatfield image to further enhance the uniformity of the background.
6. Otsu Thresholding: Binary segmentation of hair regions was performed using Otsu's thresholding method, which dynamically determines the optimal threshold to maximize interclass variance.
7. Morphological Cleaning: Noise elements in the binary mask were removed using morphological opening with the same 9×9 rectangular kernel, ensuring clean segmentation of hair structures.
8. Inpainting: Detected hair regions were inpainted using the Telea algorithm to restore the original structure of the dermoscopy image.

These preprocessing steps were designed to improve the clarity of the images and facilitate better feature extraction during the classification process.

In addition, four state-of-the-art deep learning architectures—AlexNet, VGG16, ResNet50, and EfficientNetB0—were independently implemented and trained on the processed images. The ISIC2018 dataset was utilized for this purpose, containing 10,015 high-resolution images of seven skin lesion classes, ensuring the model's consistency with prior research. The ISIC2018 dataset was split into training (70%), validation (15%), and testing (15%) subsets to ensure a robust evaluation of the deep learning models. Each model was trained using the training set, hyperparameters were optimized using the validation set, and final performance metrics were computed on the held-out test set. This separation ensured that no data leakage occurred and the reported metrics reflect the model's generalization ability. Evaluating the models without proper data splitting (e.g., training and testing on the same data) would likely lead to overfitting and inflated accuracy metrics that do not represent real-world performance.

To assess the effectiveness of the proposed hair removal algorithm, the study aimed to analyze its influence on the accuracy and reliability of skin lesion classification performed through convolutional neural networks. Each model was initialized with pretrained weights from the ImageNet dataset to leverage their learned feature representations and finetuned on the ISIC2018 dataset. The hyperparameters for each model were carefully optimized to ensure fair and effective comparisons. Batch size, 32 for all models, balancing computational efficiency and gradient stability. Learning rate, Fixed at 0.0001 and adjusted using Adam optimizer for consistent convergence.

Epochs, Set to 30 to allow sufficient learning without overfitting. Loss function, Crossentropy loss, suitable for multiclass classification tasks. Although the same base hyperparameters were applied across models, additional architectural considerations were made. For AlexNet and VGG16, the fully connected layers were fine tuned to adapt to the dermoscopy dataset. For ResNet50, the residual layers enabled effective training of deeper networks without vanishing gradients. For EfficientNetB0, its compound scaling strategy provided superior feature extraction with fewer parameters, contributing to its high performance. Using pretrained weights from the ImageNet dataset introduces potential domain biases. While ImageNet provides a diverse set of general images,

its feature representations may not fully align with the unique patterns in dermoscopy images, such as subtle pigmentation and lesion boundaries. This domain transferability gap could influence model performance. Pretrained models significantly reduce training time and improve convergence, especially when data is limited. Performance metrics, including accuracy, precision, recall, specificity, F1-score, and ROC AUC, were calculated to compare the effectiveness of the models. The experimental setup ensured a comprehensive assessment of the synergy between hair removal preprocessing and transfer learning for skin lesion classification.

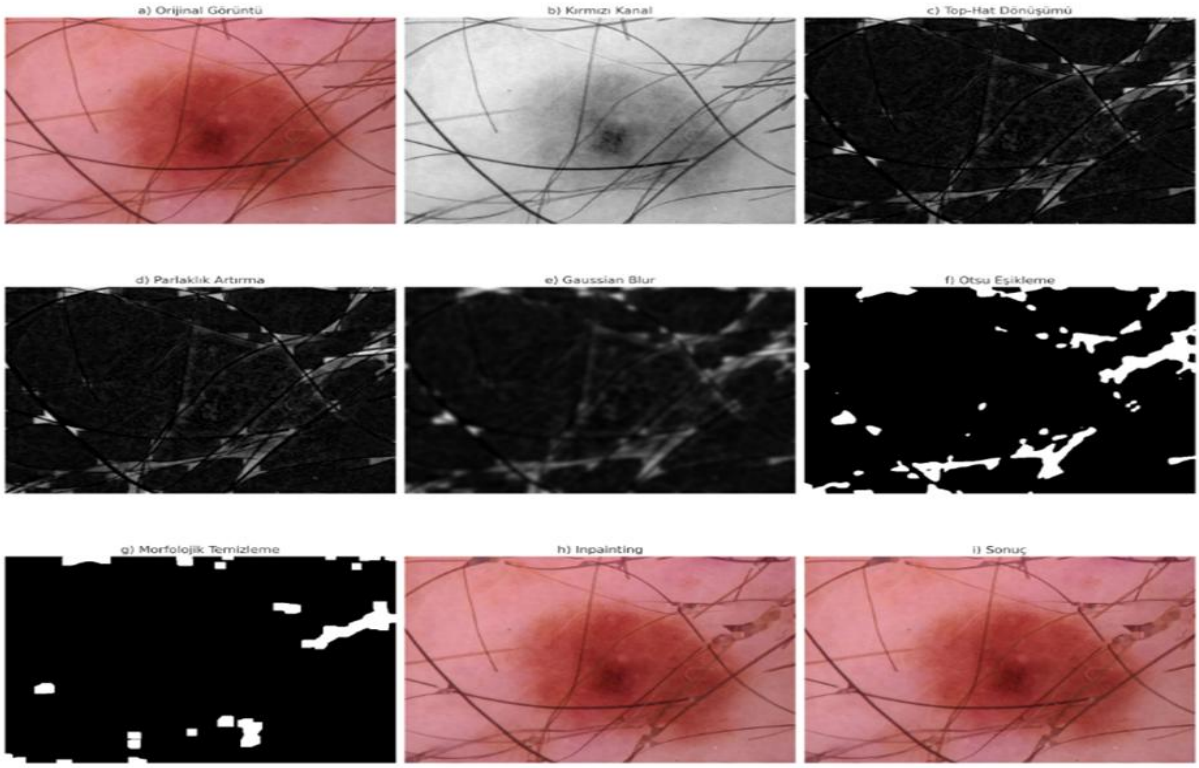


Figure 2. Steps for hair removal algorithm, a) original image, b) red channel, c) top-hat transform, d) brightness enhancement, e) gaussian blur, f) otsu's thresholding, g) morphological cleaning, h) inpainting, i) conclusion.

2.1. Dataset

In this study, we used the ISIC2018 dataset with great care. This dataset contained many high-resolution images containing different types of skin lesions and was used to classify skin lesions. It was widely used for tasks such as classification, detection and segmentation of dermatological images. There were a total of 10,015 images: 1,113 melanoma, 6,705 nevus (NV), 514 basal cell carcinoma (BCC), 327 actinic keratosis and intraepidermal carcinoma (AKIEC), 1,099 benign keratosis lesions (BKL), 115 dermato-fibroma (DF) and 142 vascular lesions (VASC).Some important studies using the ISIC2018 dataset were as follows: (Codella et al., 2019) studied the analysis of skin lesions and melanoma detection using this dataset and detailed the features of the dataset with the organisation of the ISIC Challenge. Gessert et al., (2018) applied ensemble models and various data augmentation techniques for the diagnosis of skin lesions, especially using deep learning models such as ResNet and DenseNet. Gouda et al. (2022) used models such as ResNet50, InceptionV3 and Inception ResNet for skin cancer detection and applied data augmentation and advanced image processing techniques such as ESRGAN.

2.2. New Proposed Hair Removal Algorithm

In this study, the steps of the proposed hair removal algorithm are outlined in equations 1–9, with the process flow depicted in Figure 2. Initially, the images were resized to maintain uniform dimensions. Subsequently, the grayscale representations of the red (R), green (G), and blue (B) channels were analyzed. Examples showcasing dermoscopy images within the R-G-B channels are provided in Figure 3.

1. Selecting the Red Channel
Selecting the red channel from the RGB image.

$$I_R = I[:,:,2] \quad (1)$$

2. Ball-Line Conversion
Application of morphological topline transformation.
Kernel = S (Structuring element)

$$T = I_R - (I_R \ominus S) \ominus S \quad (2)$$

3. Brightness Enhancement
Increasing the brightness of the image obtained by top-line transformation.

$$T' = \frac{(T - min(T))}{(max(T) - min(T))} * 255 \quad (3)$$

4. Gaussian Blur
Flat field image generation by applying Gaussian blur.

$$G = \left(\frac{1}{(2\pi\sigma^2)}\right) exp\left(-\frac{x^2+y^2}{2\sigma^2}\right) F = T' * G \quad (4)$$

5. Correction
Correction by splitting the brightness enhanced image into a Gaussian blurred image.

$$C = \frac{T'}{F} * 255 \quad (5)$$

6. Otsu's Thresholding
Conversion to binary format by applying Otsu thresholding to the corrected image.

$$\tau = Otsu(C) \quad (6)$$

$$B(x,y) = \begin{cases} 255 \; if \; C(x,y) > \tau \\ 0 \quad otherwise \end{cases} \quad (7)$$

7. Morphological Cleaning
Clear small areas in the binary image.

$$B' = (B \ominus S) \oplus S \quad (8)$$

8. Inpainting
Filling segmented hair regions using the Telea algorithm. The Telea inpainting algorithm was employed to fill the segmented hair regions, effectively restoring the underlying skin lesion structures. The choice of the Telea inpainting algorithm was based on its ability to provide smooth and visually appealing restorations in dermoscopy images while maintaining computational efficiency. However, alternative inpainting techniques, such as harmonic inpainting, could also be considered for comparison. Harmonic inpainting uses partial differential equations to interpolate missing pixel values, often resulting in smoother transitions in areas with complex textures. Although harmonic inpainting may produce higher visual quality in some cases, it is typically more computationally intensive compared to Telea's algorithm, which relies on fast heuristic methods. Future work could explore the comparative performance of these inpainting techniques, particularly in terms of computational efficiency and the quality of visual outputs. This comparison could provide further insights into the optimal choice of inpainting methods for specific image characteristics and clinical applications.

$$I_{inpainted=Inpaint}(I, B', 3, TELEA) \quad (9)$$

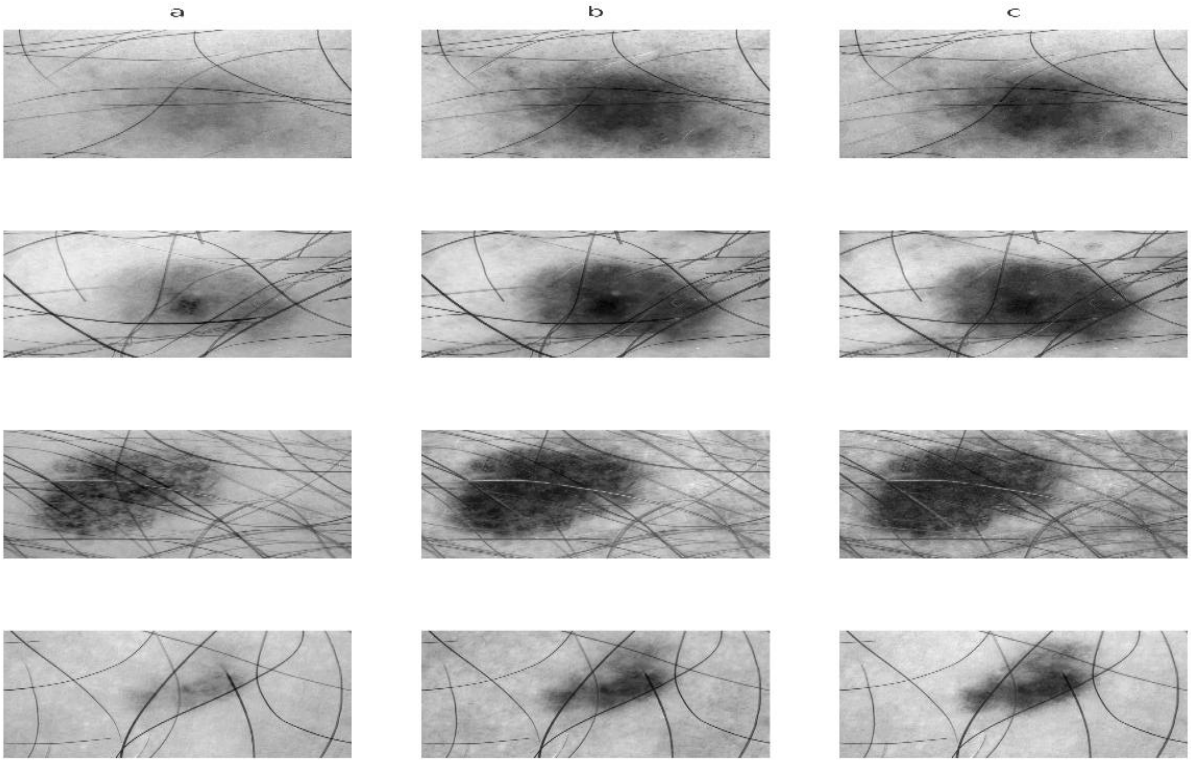


Figure 3. RGB color channels of representative skin lesion images: (a) red channel, (b) green channel, (c) blue channel.

2.3. AlexNet-Based Skin Lesion Classification

In recent years, the use of deep learning architectures in image classification tasks has shown great progress, especially in the field of medical imaging. One of the deep learning architectures, AlexNet, which stands out with its ability to learn hierarchical features from input images, was a CNN structure that won the prestigious ImageNet Large Scale Visual Recognition Competition (ILSVRC) in 2012. This architecture has greatly improved image classification performance with the use of deeper networks and linear unit (ReLU) activation functions (Krizhevsky et al., 2012).

Before feeding data into the AlexNet model, several preprocessing steps were carefully implemented to greatly improve the quality of the input data and achieve more consistent results. This architecture consisted of five convolutional layers that extract features from the input images using different filter sizes and steps, three maximum pooling layers that significantly reduce the spatial dimensionality of the feature maps by preserving the most important features, and three fully connected layers that perform high level reasoning and classification. There were also advanced techniques such as ReLU activation and dropout used in the fully connected layers to prevent overfitting by randomly setting some of the input units to zero during the training phase of the model (Krizhevsky et al., 2012).

2.4. VGG16 Based Skin Lesion Classification

The VGG16 deep learning architecture is widely recognised for its effectiveness in image classification tasks. This architecture is characterised by its simplicity and depth, using 16 weighting layers to capture detailed spatial features from input images. In 2014, VGG16 was a highly successful convolutional neural network (CNN) in the ImageNet Large Scale Visual Recognition Competition (ILSVRC) (Simonyan and Zisserman, 2014).Preprocessing steps are required to prepare dermoscopy images for training and evaluation using the VGG16 architecture. The VGG16 architecture consists of layers such as convolutional layers, maximum pooling layers, ReLU activation and dropout (Simonyan and Zisserman, 2014).Some important studies in this field are as follows: In 2023, (Zheng and Dai, 2023) significantly improved the classification and segmentation of skin cancer lesions with the U-Net structure of VGG16 using the m-VGG16 model. Kumar et al., (2023) emphasised that compared to VGG16, the developed CNN model is lighter and provides high classification accuracy with low learnable parameters. Shen, Wei and Tang showed that combining VGG16, Xception and ResNet50 models provided exceptional accuracy for classification of dermoscopy images.

2.5. Resnet50-Based Skin Lesion Classification

The ResNet50 deep learning architecture has revolutionised the field of image classification. The introduction of residual learning frameworks greatly facilitated the training of very deep networks. However, before feeding images into the ResNet50 model, several pre-processing steps had to be carefully applied to greatly improve the quality of the input data and achieve consistent results. The most important innovation of ResNet50 was the use of residual blocks, which allowed the network to learn residual functions with reference to input layers (He et al., 2016). The ResNet50 architecture consisted of convolutional layers, residual blocks, batch normalisation, ReLU activation and fully connected layers (He et al., 2016).

2.6. EfficientNet-Based Skin Lesion Classification

EfficientNet was introduced by Google AI in 2019 and utilises an innovative method that scales all depth, width and resolution dimensions equally using a composite coefficient. This approach incredibly enabled EfficientNet models to achieve better performance with fewer parameters compared to previous architectures (Tan and Le, 2019). EfficientNet has shown outstanding performance in image classification tasks thanks to its compound scaling method. To prepare dermoscopy images for training and evaluation using the EfficientNet architecture, preprocessing steps were crucial. These steps included techniques such as careful resizing and normalisation. The EfficientNet architecture consisted of convolutional layers, mobile reversed bottleneck convolution (MBConv), compression and excitation (SE) blocks, batch normalisation, Swish activation, and fully connected layers (Tan and Le, 2019).

3. Results

In this study, we present an extraction strategy for hair structures, an important morphological defect found in dermoscopy images, the most popular imaging technique for the detection and diagnosis of skin cancers. The main objective of the algorithm was to utilise conventional image processing to develop a more efficient and less computationally demanding method than existing hair removal algorithms. In the Materials and Methods section, indepth information about the study is provided, and in this section, careful evaluations are made and comparisons are made with previous research. In the literature, local illumination is used specifically to enhance the visualisation of hair, whereas in our paper normalisation was used but not explicitly local illumination. In other papers, a special flat field smoothing algorithm is applied, but in our method, Gaussian blur is used to achieve a similar effect, but it is not explicitly called flat field smoothing. In other papers, interpolation was used to fill the segmented hair regions. In our method, the Telea inpainting algorithm was used. Other methods emphasise morphological operations with detailed descriptions of the structural elements. In our study, morphological operations were used, but structure elements were not emphasised in detail.

In Table 2 we summarise the performance of various deep learning models for a skin lesion classification task. Performance metrics include accuracy (Accuracy), precision (Precision), sensitivity (Recall or Sensitivity), specificity (Specificity), F1 score and area under the ROC

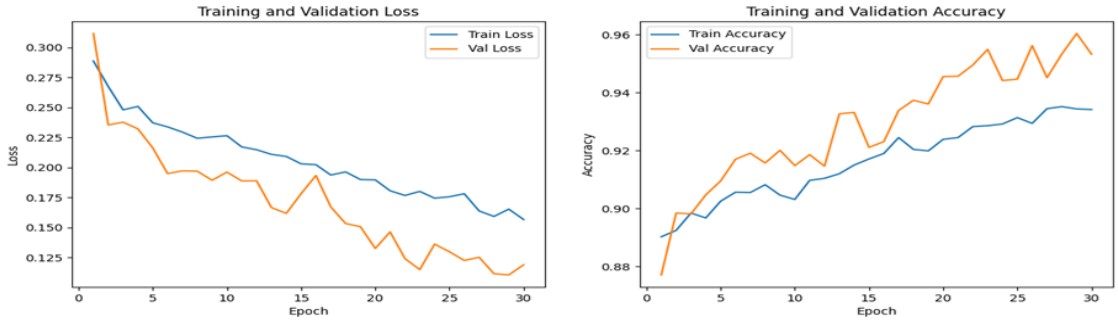
curve (ROC AUC). AlexNet correctly classified 95.32% of the samples in the dataset. 74.37% of the model's positive predictions were true positives. The model correctly identified 88.40% of true positive examples. It correctly identified 96.19% of the true negative examples.

EfficientNet correctly classified 99.89% of the examples in the dataset. 99.60% of the model's positive predictions were true positives. The model correctly identified 99.73% of true positive examples and 99.95% of true negative examples. The F1 score, the harmonic mean of precision and sensitivity, was 99.50% and the area under the ROC curve of the model was 0.998, indicating that the classification performance was indeed excellent.ResNet50 correctly classified 99.04% of the examples in the dataset. 99.28% of the model's positive predictions were true positives. The model correctly identified 91.73% of true positive examples and 99.91% of true negative examples. The F1 score, which is the harmonic mean of precision and sensitivity, was 95.50%. The area under the ROC curve of the model was 0.958, indicating very good classification performance.VGG16 correctly classified 97.55% of the samples in the dataset. 95.30% of the model's positive predictions were true positives. The model correctly identified 82.03% of true positive examples and 99.49% of true negative examples. The F1 score, the harmonic mean of precision and sensitivity, was 88.16% and the area under the ROC curve of the model was 0.907, indicating good classification performance. The model correctly identified 88.40% of true positive examples and 96.19% of true negative examples. The F1 score, the harmonic mean of precision and sensitivity, was 80.78% and the area under the ROC curve of the model was 0.923, indicating that the classification performance was really good. EfficientNet showed the highest performance in all metrics and achieved an excellent result especially in the ROC AUC metric. ResNet50 also performed very well and had high accuracy, precision and specificity values. VGG16 and AlexNet performed poorly compared to the other models, but may still be adequate for certain tasks. These results really show that EfficientNet is the most effective model for the classification of skin lesions.

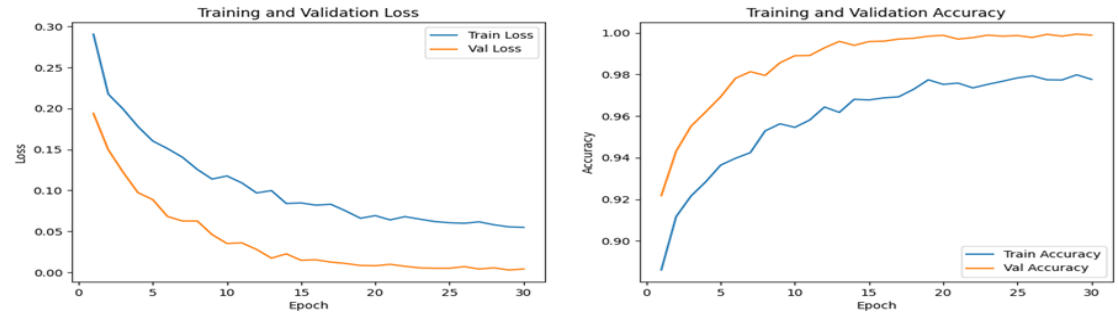
The EfficientNetB0 model achieved the best performance, demonstrating low loss and high accuracy values. Notably, validation accuracy remained stable and closely aligned with training accuracy, indicating strong generalization capability. AlexNet performed only moderately, with lower accuracy and losses. Among the other models, ResNet50 and VGG16 performed similarly well, but showed more variance in terms of validation accuracy. Figure 4 clearly shows how the different deep learning models performed on the task of classifying skin lesions and how each model performed in the training and validation.

Table 2. Performance Comparison of Deep Learning Models for Classification of Skin Lesions: AlexNet, EfficientNet, VGG16 and ResNet50

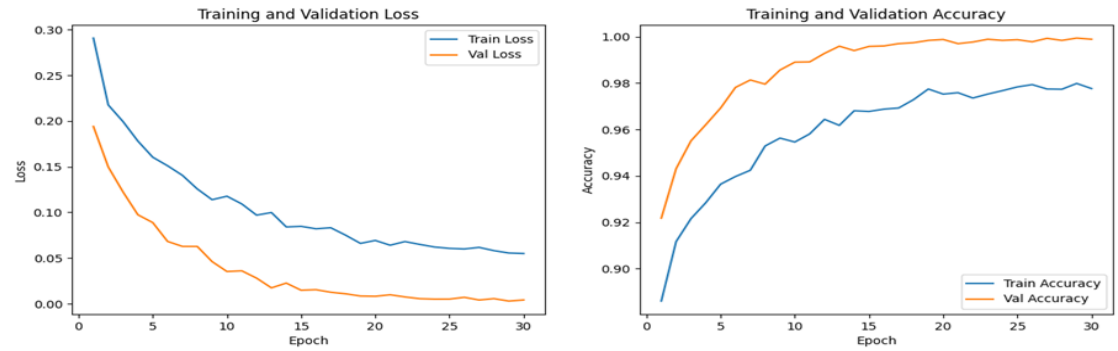
Method	Accuracy	Precision	Recall	Specificity	F1 Score	ROC AUC
Alexnet	0.9532	0.7437	0.8840	0.9619	0.8078	0.9230
Efficientnet	0.9989	0.9960	0.9973	0.9995	0.9950	0.9982
VGG16	0.9755	0.9530	0.8203	0.9949	0.8816	0.9076
Resnet50	0.9904	0.9928	0.9173	0.9991	0.9550	0.9584



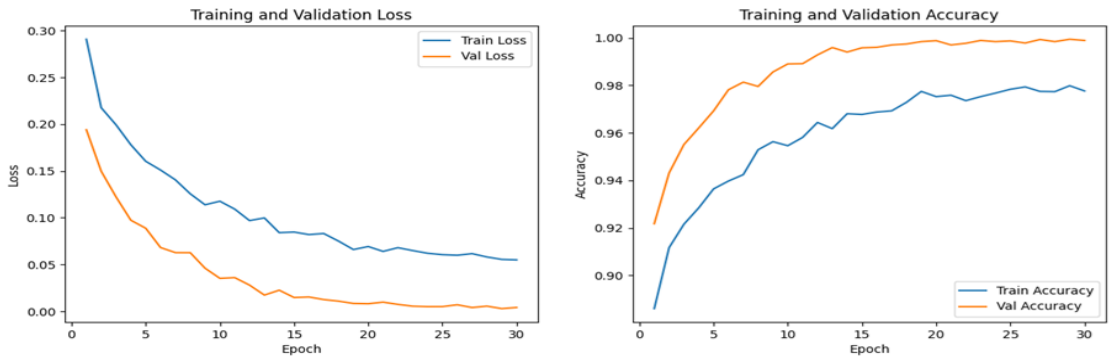
(a)AlexNet



(b)EfficientNet



(c) VGG16



(d) Resnet50

Figure 4. Comparison of training and verification performances according to the number of epochs: AlexNet, EfficientNet, VGG16 and ResNet50.

Figure 5 summarises the classification performance of the model for the AlexNet model and an AUC of 0.92 strongly indicates that the model has a good discrimination ability. The ROC curve for the EfficientNet modetable 2l shows a truly excellent discrimination ability. This value makes it clear that the model has an outstanding performance and is able to perfectly distinguish between positive and negative classes. The ROC curve for the VGG16 model clearly shows that the model has a good performance and is able to distinguish between positive and negative classes. The ROC curve for the ResNet50 model shows a very good discrimination ability. This value clearly shows that the model has a high performance and is quite successful in distinguishing between positive and negative classes. These ROC curve plots impressively visualised the ability of each model to classify skin lesions. The EfficientNet model performed really well with an AUC value of 0.998, while ResNet50 also stood out with a high AUC value (0.96). The AlexNet and VGG16 models also perform well, but their AUC values are slightly lower than the other models with 0.92 and 0.91 respectively. These results strongly indicated that EfficientNet and ResNet50 are the most effective models in the task of classification of skin lesions. The performance of the proposed pipeline was evaluated using multiple comprehensive metrics, including accuracy, sensitivity (recall), specificity, F1-score, and ROC AUC. These metrics provide a robust assessment of each model's classification capability. EfficientNetB0 demonstrated the best performance across all metrics, achieving an accuracy of 99.89% and a ROC AUC of 0.998. ResNet50 also performed well, while AlexNet and VGG16 showed comparatively lower performance but may still be suitable for certain tasks.Table 2 summarizes the performance metrics for all models. EfficientNetB0 outperformed other architectures due to its advanced feature extraction capabilities and efficient scaling strategies. The ROC curves (Figure 5) effectively illustrate the discrimination ability of each model, with EfficientNetB0 demonstrating almost perfect separation between positive and negative classes. While EfficientNetB0 achieved the highest accuracy, failure cases were observed.Misclassified images were primarily noted in two scenarios. First, in cases where the hair removal algorithm failed to completely remove fine or densely overlapping hairs, residual noise affected the classification process. Second, dermoscopy images with blurred or irregular lesion boundaries posed significant challenges for the model.To further understand these failure cases, examples of misclassified images are essential. These examples can provide valuable insights into potential weaknesses in both the hair removal algorithm and the classification pipeline. For instance, a benign lesion misclassified as malignant may indicate incomplete hair removal or overemphasis on irrelevant features. A malignant lesion misclassified as benign could suggest the need for additional training data or fine tuning of model hyperparameters.

The confusion matrices Figure 6 provide a deeper understanding of the specific challenges faced by each model. AlexNet exhibited higher false positive and false negative rates compared to the other models, indicating its difficulty in accurately predicting both benign and malignant classes. In contrast, VGG16 achieved the highest accuracy, with minimal false positives and negatives, showing an almost perfect ability to distinguish between classes. ResNet50 demonstrated a very low false positive rate but struggled slightly with false negatives, making it more effective at identifying malignant cases while occasionally mispredicting benign lesions. EfficientNetB0, while achieving the highest overall performance, still exhibited occasional misclassifications, particularly in rare lesion types. This suggests a need for better representation of minority classes in the dataset.

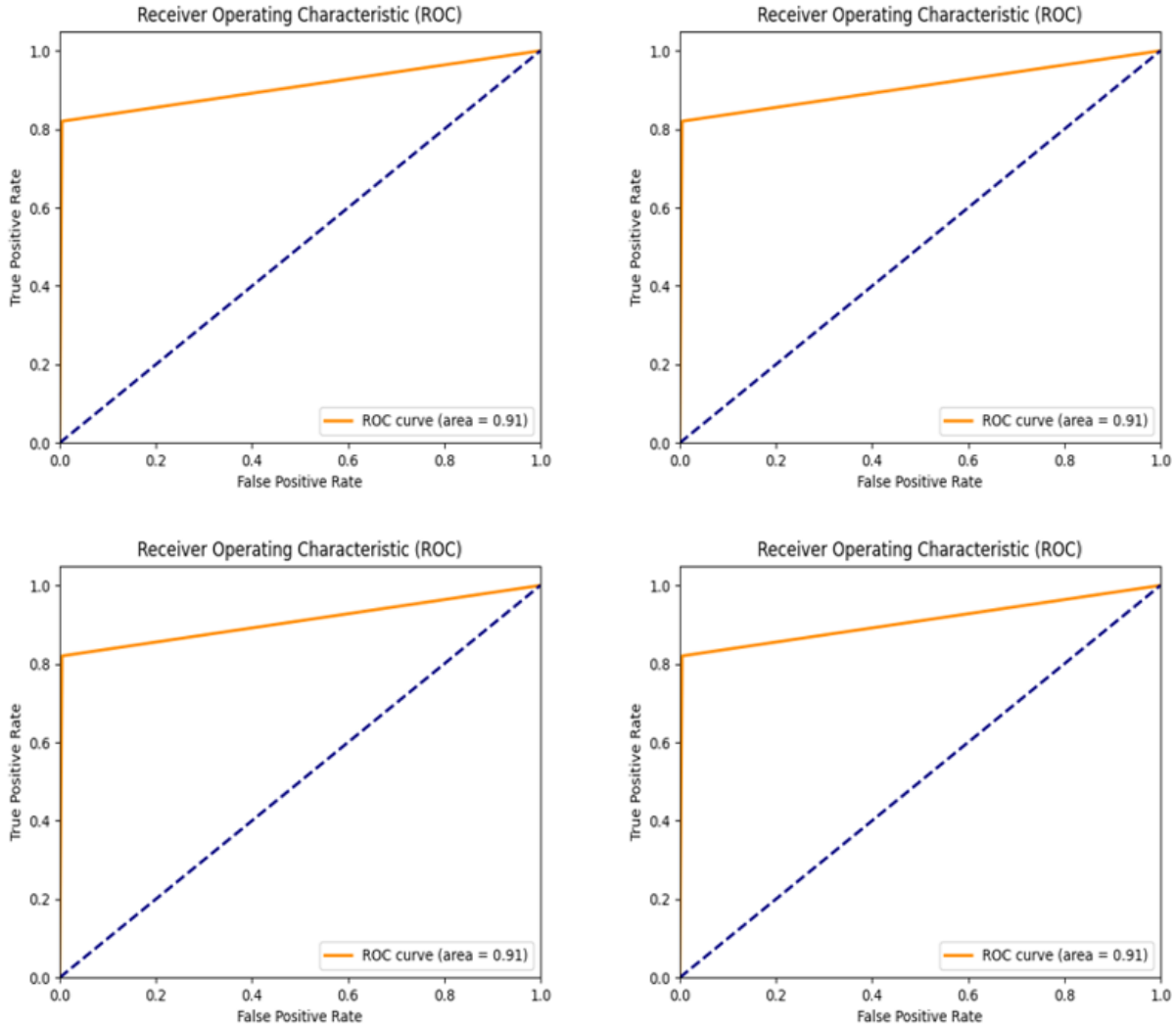


Figure 5. ROC curve graphs: Classification of skin lesions with deep learning models.

In Figure 6, the confusion matrices reveal AlexNet's struggles, with higher false positive and negative rates compared to other models. VGG16 stands out with its strong performance and minimal misclassifications. ResNet50 shows reliable discrimination of malignant lesions but has room for improvement in identifying benign cases. EfficientNetB0 maintains a balanced performance overall, but slight errors in certain classes indicate areas for further enhancement.

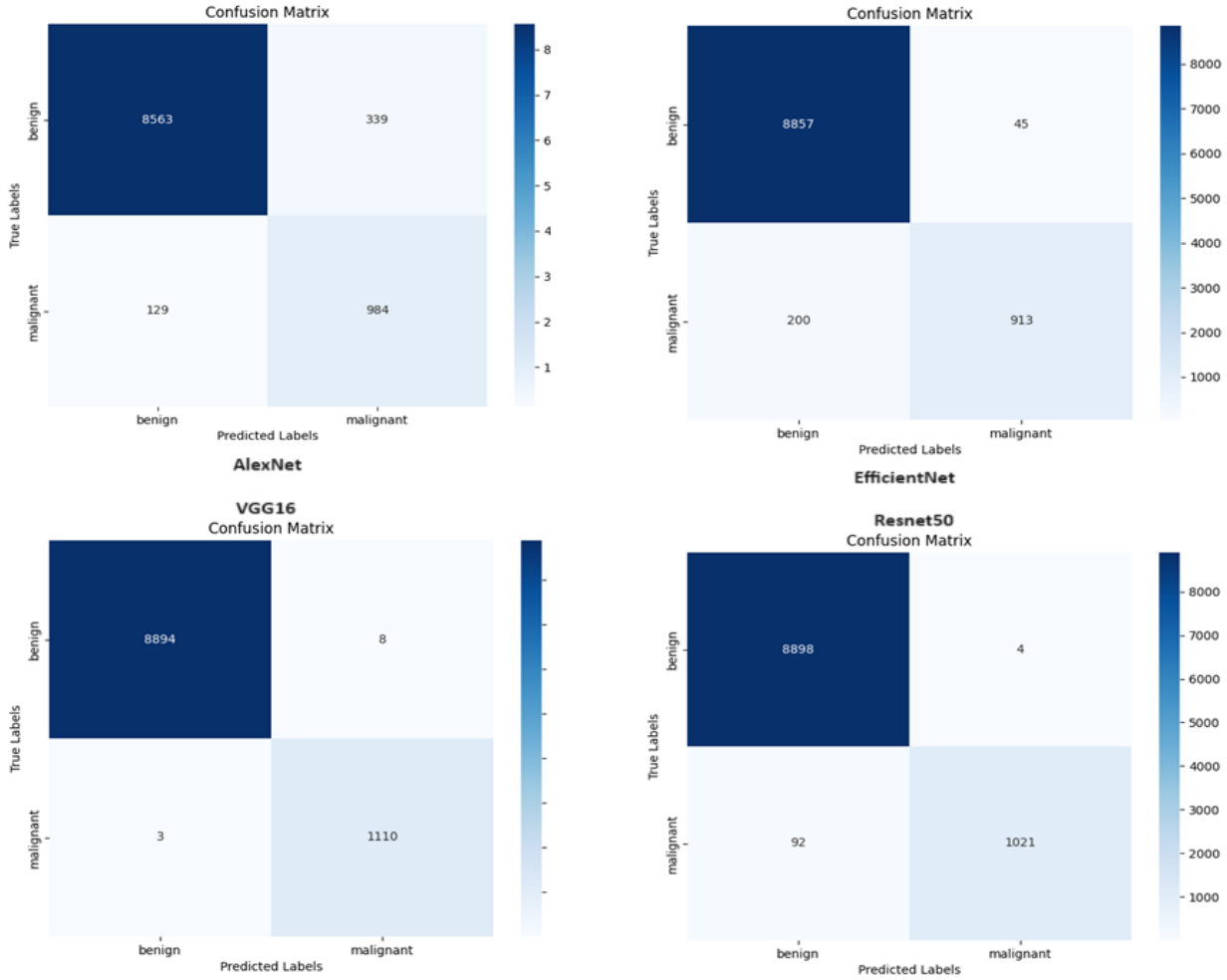


Figure 6. Confusion matrices: Classification of skin lesions with deep learning models.

4. Discussion

The method proposed in this study has shown remarkable performance compared to the approaches in the existing literature. The related studies summarized in Table 3 present various approaches for the classification of skin lesions using different datasets, methods, and deep learning architectures. However, most of these methods either have low accuracy rates or have certain limitations.

For example, in the study of (Barman et al., 2022), 91.16% training accuracy and 89.93% test accuracy were achieved on the ISIC dataset using the GoogLeNet transfer learning model. Although this study focused on data augmentation techniques, it could not reach an accuracy rate as high as the proposed method. In contrast, in our study, the EfficientNetB0 model exhibited superior performance with an accuracy rate of 99.89%. This was possible thanks to the effective customization of the transfer learning models and the improvement of the preprocessing steps.

Wu et al., (2022) conducted classification with InceptionV3, ResNet50 and DenseNet201 models using ISIC 2017 and HAM10000 datasets. A relatively low accuracy rate of 86.69% reveals that these models have a more limited performance. In the proposed method, much higher accuracy rates were obtained with transfer learning models using ISIC2018 from the same dataset family. In particular, the accuracy rate of the proposed EfficientNetB0 model, which is 99.89%, highlights the impact of the innovative components in deep learning architectures of this method.In (Mane et al., 2022), the ISIC 2019 dataset and MobileNet transfer learning model were used. However, the exact accuracy rates were not specified in this study. Nevertheless, it is considered that MobileNet can be a suitable method especially for portable devices due to its low number of parameters. On the other hand, the proposed method offers both a high accuracy rate and a more efficient calculation method by using the components of EfficientNetB0.

Gottumukkala et al., (2022) developed SCUNet model used ISIC-2019 and PH2 datasets and performed hair extraction with fast nonlocal mean (FNLM) filter. However, accuracy rates were not reported. On the other hand, hair extraction algorithm and inpainting operations used in the proposed method directly contributed to high accuracy rates and increased the overall performance of the model.In the study by (Fraiwan and Faouri, 2022), the authors achieved high accuracy rates but acknowledged limitations in handling artifacts such as hair.The study by Shinde et al. (2023) investigated

efficient architectures for IoT applications.The systematic review by (Debelee, 2023) highlighted the difficulties of handling artifacts and the complexities of preprocessing. The study by Malik et al. (2024) emphasized the importance of preprocessing in improving model performance. The results of the proposed method are in line with these findings and show how hair extraction and contrast enhancement can improve classification accuracy.Finally, the study by El-Shafai et al. (2024) focused on the importance of hair artifact extraction in diagnosis accuracy.Unlike the above studies, the proposed method's integration of both hair extraction algorithm and transfer learning models resulted in a superior accuracy rate. The 99.89% accuracy rate of EfficientNetB0 model shows the high overall performance obtained with the proposed method and the capacity of deep learning models to adapt to datasets. These findings show that the proposed method offers an effective solution that can be used in both academic and clinical applications in the classification of skin lesions.

Table 3. Table of relevant studies conducted in recent years

Study	Work/Research Year	Inpainting Method	Dataset	Colour Space	Method	Accuracy	Architecture
Barman et al.	2023	Data augmentation	ISIC dataset	Not specified	GoogLeNet transfer learning	91.16% (training), 89.93% (testing)	GoogLeNet
Wu et al.	2022	Not specified	ISIC 2017 HAM10000 dataset	Not specified	InceptionV3, ResNet50, DenseNet201	86.69%	InceptionV3, ResNet50, DenseNet201
Mane et al.	2022	Not specified	ISIC 2019 challenge dataset	Not specified	MobileNet transfer learning	Not specified	MobileNet
Gottumukkala, et al.	2022	Fast nonlocal mean (FNLM) filter	ISIC-2019 and PH2 datasets	Not specified	SCU-Net	Not specified	SCU-Net
Proposed Method	2025	Inpainting	ISIC2018 dataset	RGB	(AlexNet), (VGG16), (ResNet50), (EfficientNetB0)	95.32% 97.55% 99.04% 99.89%	AlexNet, VGG16, ResNet50, EfficientNetB0

5. Conclusion

In this study, we developed a new hair removal algorithm to completely remove hair structures in dermoscopy images used in the detection and diagnosis of skin cancer. The algorithm effectively detected and removed hairs using red channel selection, top-line transform, Gaussian blur, Otsu thresholding, and inpainting. After these preprocessing steps, we rigorously classified skin lesions with four different transfer learning models (AlexNet, VGG16, ResNet50, and EfficientNetB0) using the ISIC2018 dataset.The results clearly showed that the proposed hair removal algorithm and transfer learning models provide extremely high accuracy rates in the automatic classification of skin lesions. The results showed that the EfficientNetB0 model achieved the highest accuracy rate (99.89%) and showed superior performance compared to other models. The ResNet50 and VGG16 models also had high accuracy rates, while AlexNet performed slightly worse.This study demonstrated that integrating hair removal and transfer learning techniques can significantly improve accuracy rates in the automatic classification of skin lesions. This approach could greatly help dermatologists detect skin cancer early and improve patient outcomes. The use of the proposed method in clinical settings will make dermatological assessments more precise and reliable. However, the study also highlighted challenges in classifying rare lesion types, emphasizing the need for more balanced datasets and advanced augmentation techniques. Although the EfficientNetB0 model demonstrated outstanding overall performance across all metrics, it is critical to assess its ability to generalize to underrepresented or rare lesion types. Our analysis revealed that while the model maintained high accuracy on common classes such as nevi and melanoma, its precision and recall for classes like dermatofibroma (DF) and vascular lesions (VASC) were comparatively lower. Future research should focus on addressing these issues by incorporating domains pecific data augmentation and hard example mining to enhance model performance on underrepresented classes. Additionally, testing on independent datasets or real world clinical images would provide valuable insights into the method's robustness and generalizability. Efforts to optimize computational efficiency and streamline the preprocessing pipeline will further support the integration of this approach into clinical workflows, particularly in resourcelimited settings.

Author Contributions

The percentages of the author' contributions are presented below. The author reviewed and approved the final version of the manuscript.

	K.G.
C	100
D	100
S	100
DCP	100
DAI	100
L	100
W	100
CR	100
SR	100
PM	100
FA	100

C=Concept, D= design, S= supervision, DCP= data collection and/or processing, DAI= data analysis and/or interpretation, L= literature search, W= writing, CR= critical review, SR= submission and revision, PM= project management, FA= funding acquisition.

Conflict of Interest

The author declared that there is no conflict of interest.

Ethical Consideration

Ethics committee approval was not required for this study because of there was no study on animals or humans.

References

Abuzaghleh O, Barkana BD, Faezipour M. 2015. Noninvasive real-time automated skin lesion analysis system for melanoma early detection and prevention. IEEE J Transl Eng Health Med, 3: 1–12, pp: 1–12.

Ali R, Hardie RC, De Silva MS, Kebede TM. 2019. Skin lesion segmentation and classification for ISIC 2018 by combining deep CNN and handcrafted features. arXiv preprint arXiv:1908.05730, pp: 1–12.

Alsahafi YS, Kassem MA, Hosny KM. 2023. Skin-Net: a novel deep residual network for skin lesions classification using multilevel feature extraction and cross-channel correlation with detection of outlier. J Big Data, 10(1): 105, pp: 105.

Ashour AS, El-Wahab BSA, Wahba MA, Mansour DEA, Hodeib AAE, Khedr RAEG, Hassan GF. 2022. Cascaded Hough transform-based hair mask generation and harmonic inpainting for automated hair removal from dermoscopy images. Diagnostics, 12(12): 3040, pp: 3040.

Attia M, Hossny M, Nahavandi S, Yazdabadi A, Asadi H. 2019. Realistic hair simulation using image blending. arXiv preprint arXiv:1904.09169, pp: 1–12.

Barın S, Güraksın GE. 2024. An improved hair removal algorithm for dermoscopy images. Multimed Tools Appl, 83(3): 8931–8953, pp: 8931–8953.

Barman S, Biswas MR, Marjan S, Nahar N, Hossain MS, Andersson K. 2022. Transfer learning based skin cancer classification using GoogLeNet. Presented at the International Conference on Machine Intelligence and Emerging Technologies (ICMIET), Dhaka, Bangladesh, 2022, pp: 1–7.

Codella N, Rotemberg V, Tschandl P, Celebi ME, Dusza S, Gutman D, Gottschalk C, et al. 2019. Skin lesion analysis toward melanoma detection 2018: A challenge hosted by the international skin imaging collaboration (ISIC). arXiv preprint arXiv:1902.03368, pp: 1–20.

Debelee TG. 2023. Skin lesion classification and detection using machine learning techniques: a systematic review. Diagnostics, 13(19): 3147, pp: 3147.

Delibasis K, Moutselos K, Vorgiazidou E, Maglogiannis I. 2023. Automated hair removal in dermoscopy images using shallow and deep learning neural architectures. Comput Methods Programs Biomed Update, 4: 100109, pp: 100109.

El-Shafai W, El-Fattah IA, Taha TE. 2024. Deep learning-based hair removal for improved diagnostics of skin diseases. Multimed Tools Appl, 83(9): 27331–27355, pp: 27331–27355.

Esteva A, Kuprel B, Novoa RA, Ko J, Swetter SM, Blau HM, Thrun S. 2017. Dermatologist-level classification of skin cancer with deep neural networks. Nature, 542(7639): 115–118, pp: 115–118.

Fraiwan M, Faouri E. 2022. On the automatic detection and classification of skin cancer using deep transfer learning. Sensors, 22(13): 4963, pp: 4963.

Gessert N, Sentker T, Madesta F, Schmitz R, Kniep H, Baltruschat I, Schlaefer A. 2018. Skin lesion diagnosis using ensembles, unscaled multi-crop evaluation and loss weighting. arXiv preprint arXiv:1808.01694, pp: 1–12.

Gonzalez RC. 2009. Digital image processing. Pearson Education India, pp: 817.

Gottumukkala VR, Kumaran N, Sekhar VC. 2022. Skin lesion segmentation using SCU-Net with FNLM preprocessing. Presented at the 2022 IEEE International Conference on Data Science and Information Systems (ICDSIS), Bangalore, India, 2022, pp: 1–6.

Gouda W, Sama NU, Al-Waakid G, Humayun M, Jhanjhi NZ. 2022. Detection of skin cancer based on skin lesion images using deep learning. Presented at the Healthcare Conference, Dubai, UAE, 2022, pp: 1–7.

He K, Zhang X, Ren S, Sun J. 2016. Deep residual learning for image recognition. Presented at the IEEE Conference on Computer Vision and Pattern Recognition (CVPR), Las Vegas, NV, USA, 2016, pp: 770–778.

Jamil U, Khalid S, Akram MU. 2016. Digital image preprocessing and hair artifact removal by using Gabor wavelet. Presented at the 2016 International System on Chip Design Conference (ISOCC), Seoul, South Korea, 2016, pp: 1–6.

Jütte L, Emmert S, Roth B. 2023. True digital hair removal with real value inpainting for improved dermoscopy based on image fusion. Presented at the Photonics in Dermatology and Plastic Surgery Conference 2023, Munich, Germany, 2023, pp: 1–5.

Kasmi R, Hagerty J, Young R, Lama N, Nepal J, Miinch J, Stanley RJ. 2023. SharpRazor: automatic removal of hair and ruler marks from dermoscopy images. Skin Res Technol, 29(4): e13203, pp: e13203.

Krizhevsky A, Sutskever I, Hinton GE. 2012. Imagenet classification with deep convolutional neural networks. Advances in Neural Information Processing Systems, Lake Tahoe, NV, USA, 2012, 25: 1097–1105, pp: 1097–1105.

Kumar A, Vishwakarma A, Bajaj V. 2023. Automatic classification of multi-class skin lesions dermoscopy images using an efficient convolutional neural network. Presented at the 2023 IEEE International Students' Conference on Electrical,

Electronics and Computer Science (SCEECS), Pune, India, 2023, pp: 1–7.

Mahmood A, Mahmood H. 2015. Artifact removal from skin dermoscopy images to support automated melanoma diagnosis. Al-Rafidain Engineering Journal, 23(5): 22–30, pp: 22–30.

Mane D, Ashtagi R, Kumbharkar P, Kadam S, Salunkhe D, Upadhye G. 2022. An improved transfer learning approach for classification of types of cancer. Trait Signal, 39(6): 2095, pp: 2095.

Mendonça T, Ferreira PM, Marques JS, Marcal AR, Rozeira J. 2013. PH2-A dermoscopic image database for research and benchmarking. Presented at the 2013 35th Annual International Conference of the IEEE Engineering in Medicine and Biology Society (EMBC), Osaka, Japan, 2013, pp: 1–4.

Milton MAA. 2019. Automated skin lesion classification using ensemble of deep neural networks in ISIC 2018: Skin lesion analysis towards melanoma detection challenge. arXiv preprint arXiv:1901.10802, pp: 1–15.

Pan SJ, Yang Q. 2009. A survey on transfer learning. IEEE Transactions on Knowledge and Data Engineering, 22(10): 1345–1359, pp: 1345–1359.

Salido JA, Ruiz C. 2018. Hair artifact removal and skin lesion segmentation of dermoscopy images. Asian Journal of Pharmaceutical and Clinical Research, 11(3): 73–76, pp: 73–76.

Shinde A, Chaudhari S. 2022. Statistical analysis of hair detection and removal techniques using dermoscopic images. Presented at the International Conference on Computer Vision and Image Processing, New Delhi, India, 2022, pp: 1–6.

Shinde RK, Alam MS, Hossain MB, Md Imtiaz S, Kim J, Padwal AA, Kim N. 2023. Squeeze-MNet: precise skin cancer detection model for low computing IoT devices using transfer learning. Cancers, 15(1): 12, pp: 12.

Simonyan K, Zisserman A. 2014. Very deep convolutional networks for large-scale image recognition. arXiv preprint arXiv:1409.1556, pp: 1–14.

Street W. 2019. Cancer facts & figures 2018. American Cancer Society, Atlanta, GA, USA, pp: 50.

Talavera-Martínez L, Bibiloni P, González-Hidalgo M. 2020. An encoder-decoder CNN for hair removal in dermoscopic images. arXiv preprint arXiv:2010.05013, pp: 1–8.

Tan M, Le Q. 2019. EfficientNet: rethinking model scaling for convolutional neural networks. Presented at the International Conference on Machine Learning (ICML), Long Beach, CA, USA, 2019, pp: 6105–6114.

Tschandl P, Rosendahl C, Kittler H. 2018. The HAM10000 dataset, a large collection of multi-source dermatoscopic images of common pigmented skin lesions. Scientific Data, 5(1): 180161, pp: 180161.

Weiss K, Khoshgoftaar TM, Wang D. 2016. A survey of transfer learning. Journal of Big Data, 3: 9, pp: 9.

Wu Y, Lariba AC, Chen H, Zhao H. 2022. Skin lesion classification based on deep convolutional neural network. Presented at the 2022 IEEE 4th International Conference on Power, Intelligent Computing and Systems (ICPICS), Shanghai, China, 2022, pp: 1–6.

Zeiler M. 2014. Visualizing and understanding convolutional networks. Presented at the European Conference on Computer Vision (ECCV) / arXiv, Zurich, Switzerland, 2014, pp: 1–15.

Zheng L, Dai Y. 2023. m-VGG16: a dermoscopy image segmentation method based on VGG16. Presented at the 3rd International Conference on Computer Vision and Data Mining (ICCVDM), Seoul, South Korea, 2023, pp: 1-7.

Black Sea Journal of Engineering and Science
doi: 10.34248/bsengineering.1673744

Open Access Journal
e-ISSN: 2619 – 8991

Research Article
Volume 8 - Issue 4: 1022-1033 / July 2025

EFFECT OF DIRECTION OF LOADING ON SEISMIC RESPONSE OF HISTORICAL MASONRY MINARETS: THE MINARET OF AKSARAY ZAFER MOSQUE

Erdem TÜRKELİ[1]*, Kadir YAYLA[2]

[1]*Ordu University, Vocational School of Technical Sciences, 52200, Ordu, Türkiye*
[2]*Ordu University, Renewable Energy Department, Life Sciences Institute, 52200, Ordu, Türkiye*

Abstract: In Islamic culture, minarets, a significant component of religious architecture, are seen in tombs and madrasahs in addition to mosques. Originally created without following a particular architectural style, minarets were often made of wood, stone, and brick. The primary goal of this study is to identify the critical axis of earthquake application. For this reason, the masonry load carrying system minaret of the Zafer Mosque in Aksaray's city center was chosen from the technical literature. The chosen minaret was exposed to acceleration time histories of the recent Turkish earthquakes of 1999 Düzce, 2011 Van, and 2023 Kahramanmaraş, which resulted in several fatalities. The x-axis was set at 0°, and increments of 15° were made up to 180°. Under Van earthquake, the minaret is in the "Controlled Damage" zone; under Düzce earthquake, it is in the "Before Collapse" zone; and under recent Kahramanmaraş earthquake, it is in the beyond "Before Collapse" zone. Additionally, the crucial axis for the cited masonry minaret was identified as either the axis that passes through the exact center of the door (x-axis) or the axis that is exactly perpendicular to the x-axis (y-axis) to be employed in the design phase, depending on the earthquake characteristics.

Keywords: Masonry Minaret, SAP2000 Program, Earthquake Load, Loading Direction, Critical Axis

***Corresponding author:** Ordu University, Vocational School of Technical Sciences, 52200, Ordu, Türkiye
E mail: erdemturkeli@odu.edu.tr (E. TÜRKELİ)
Erdem TÜRKELİ https://orcid.org/0000-0002-4293-4712
Kadir YAYLA https://orcid.org/0000-0002-6974-2120

Received: April 10, 2025
Accepted: May 12, 2025
Published: July 15, 2025

Cite as: Türkeli E, Yayla K. 2025. Effect of direction of loading on seismic response of historical masonry minarets: the minaret of Aksaray Zafer Mosque. BSJ Eng Sci, 8(4): 1022-1033.

1. Introduction

In Islamic culture, minarets are a significant component of religious architecture that are seen in mosques as well as madrasahs and mausoleums. Beginning in the 7th century, during the Umayyad era, minarets were constructed in a variety of designs and sizes using stone, brick, and wood, depending on the location and culture. Different architectural and aesthetic characteristics are displayed throughout minarets in Islamic geography. In the areas which extend from Syria (West) to North Africa and Andalusia, minarets are constructed like four-sided towers. They are pure, majestic structures that are more cylindrical and slender in the eastern area, which encompasses Iran, Iraq, Türkiye, and the Turkish world. During the classic Ottoman era (16th–17th centuries), minarets reached their level of perfection (Temüz, 2007). Some of the examples of those above cited minarets are provided in Figure 1 (Serhatoğlu, 2015; Anonymous, 2024a; TRF, 2024a; TRF, 2024b).

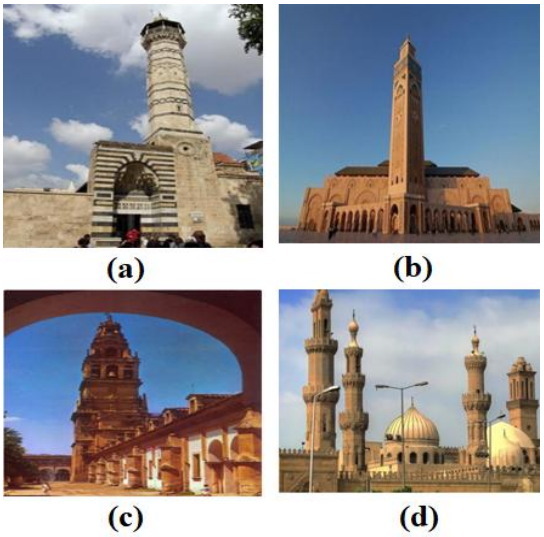


Figure 1. Minarets constructed in different areas of the world in different time periods (Serhatoğlu, 2015; Anonymous, 2024a; TRF, 2024a; TRF, 2024b).

In general, minarets consist of main parts such as "end ornament, spire, upper part of the minaret, balcony, cylindrical body, staircase, transition segment, pulpit and foundation". The main parts of the typical Ottoman or Seljuk minaret type are given in Figure 2 (Baştürk, 2013).

This work is licensed (CC BY-NC 4.0) under Creative Commons Attribution 4.0 International License

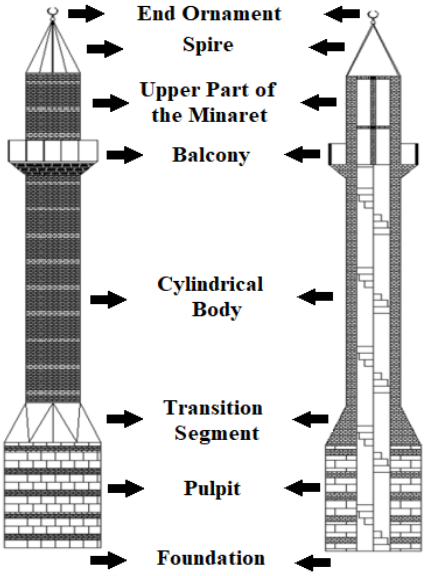


Figure 2. Main parts of the typical Ottoman or Seljuk minaret type (Baştürk, 2013).

The usage of stone or brick as a load-carrying element is notable when analyzing historical masonry minarets in Türkiye. Masonry minarets were constructed with low-strength "Horasan mortar" as a binder between the load-carrying components. Because of this, significant sections of the minarets develop cracks as a result of bending brought on by extreme loads like earthquakes, winds, etc. By placing iron bars between horizontal and vertical stones, Mimar Sinan created a novel load-carrying structure that can be referred to as earthquake-resistant after the earthquake of 1509. Despite numerous natural calamities, minarets constructed centuries ago remain standing thanks to this method (Serhatoğlu, 2015).

Historical structures retain the material properties, building methods, and engineering and architectural features of the time period in which they were constructed up to the present. Earthquakes, fire, deterioration of material strength, ground subsidence, and environmental effects are just a few of the adverse effects that these structures may experience over time. Some may collapse (Figure 3) (Atmaca et al., 2025), some may sustain significant damage, and some may remain standing without damage as a result of these consequences. It is important to carefully identify the structural behaviors of both damaged and undamaged structures, repair or reinforce those that are necessary, and then transfer them to the future.



Figure 3. Collapsed masonry minarets in recent 2023 Kahramanmaraş earthquakes (Atmaca et al., 2025).

Due to their vulnerable construction, masonry minarets, which constitute a significant portion of historical structures, can sustain damage or even collapse when subjected to dynamic forces like earthquakes, winds, etc. Determining the structural behaviors of these structures against potential dynamic effects and implementing the required strengthening and repair actions are crucial for this. Furthermore, before and after the repair or strengthening, it is important to identify and track any changes in the dynamic behaviors of the masonry minarets (Günaydın, 2018). Since minarets are tall and slender structures, they exhibit unusual behavior against natural effects such as earthquakes, winds, etc. When designing such special structures, factors such as self-weight, wind, and earthquakes should be taken into consideration. In Türkiye, the Presidency of Religious Affairs published instructions on "Principles to be Applied in the Construction of Minarets" after the 1999 Kocaeli earthquake. However, these principles only include reinforced concrete (RC) minarets.

In technical literature, there are so many studies dealing with the seismic response of masonry minarets. Some of them are summarized as below. Işık et al. (2022a) selected five historical masonry minarets from Bitlis located in Türkiye and by using the Türkiye's most recent Earthquake Code, the vertical and horizontal design spectrum has been used to decide the seismic behavior of each minaret. A linear dynamic analysis of the historic Hızırbey Mosque minaret in the city center of Kırklareli was carried out by Kılıç et al. (2020). The study's findings showed that the displacements derived from the 2018 Türkiye Earthquake Code were greater than those derived from the 2007 Türkiye Earthquake Code regulation. Işık et al. (2022b) carried out structural analyses for the historical masonry Ulu Mosque's minaret in Bitlis (Türkiye) by using both on-site measurements and finite element methods. The masonry minaret of the famous historic structure "Sultan Ahmed Mosque" is the subject of the study conducted by Erdoğan et al. (2019) which investigates its seismic behaviour during intense seismic action. Yurdakul et al. (2021) examined the seismic performance of a historical masonry minaret in

Bayburt that dates back to the 12th century. Also, the seismic performance of the cited minaret was examined using three earthquake ground motions: Erzincan, Kocaeli-Düzce, and Van-Erciş. Başaran et al. (2016) investigated the earthquake behavior of historical masonry minaret of Hacı Mahmut Mosque by using Operational Modal Analysis and applied the time histories of 1999 Düzce earthquake. The impact of geometrical elements on the dynamic behaviour of seven historically masonry minarets in Bursa was examined by Livaoğlu et al. (2016). From the relationships, an analytical formula was established for quick estimation of the fundamental period of typical Ottoman minarets. Full-scale structural evaluations of the minaret of İskenderpaşa Mosque were given by Aymelek et al. (2023) following the calibration of a finite element model based on vibration test data. Additionally, the behaviors of the cited minaret under wind and earthquake loads were found. Usta (2021) dealt with the assessment of seismic damage in historical masonry minarets which were placed in Antalya.

From the search of the technical literature, it can be clearly seen that there is no other study dealing with the effect of earthquake angle on dynamic seismic behavior of historical masonry minarets. Therefore, the novelty of this study to the technical literature is to provide a starting point for the researchers on this subject.

This study was conducted to investigate the effect of the direction of earthquake loads occurring in historical masonry minarets on the dynamic behavior of minarets, by analyzing the Aksaray Zafer Mosque minaret as a case study. To perform this, up to 180°, the x-axis was set at 0° initially and loading direction was moved in increments of 15° from its initial value. By this way, the crucial axis for earthquake load application that will be employed during the design phase for the masonry minarets with doors and that are not axially symmetric was determined.

2. Materials and Methods

A masonry minaret from the Zafer Mosque in Aksaray's (located in Türkiye) center was utilized in the present research. This masonry minaret was chosen from the technical literature (Ural and Çelik, 2018) to carry out dynamic structural verification in the finite element procedure.

The Zafer Mosque was constructed in 1956 and is situated in the Zafer District of Aksaray city center (Figure 4) (Ural and Çelik, 2018).



Figure 4. Historical masonry minaret of Zafer Mosque (Ural and Çelik, 2018).

Ural and Çelik (2018) determined the masonry material's unit weight as 30 kN/m^3, its modulus of elasticity as 4000 MPa, and Poisson ratio as 0.2 and applied to the finite element model (FEM) of Zafer Mosque minaret modelled in this study.

Moreover, all analyses conducted in this study were in linear range and soil-structure interaction (SSI) was not taken into account. The geometrical properties of the cited minaret was given in Figure 5 (Ural and Çelik, 2018).

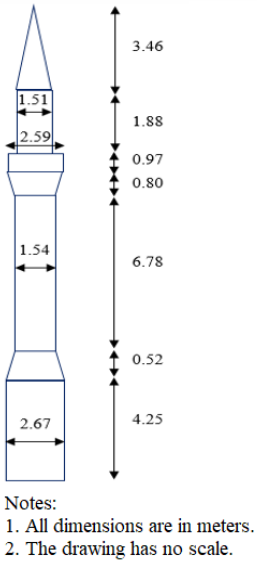


Figure 5. The geometrical properties of the Zafer Mosque minaret (Ural and Çelik, 2018).

In order to make comparison and consequently to make structural dynamic verification, SAP2000 Ver. 14 (Computers & Structures, 2024) structural analysis program was used in this study. The FEM of the Aksaray Zafer Mosque minaret produced in this study is shown in Figure 6.

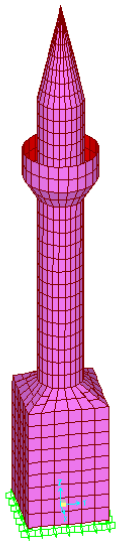
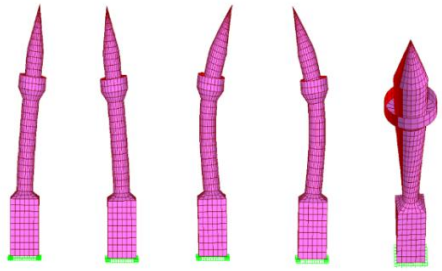


Figure 6. The FEM of the Aksaray Zafer Mosque minaret produced in this study.

The first five mode shapes and the corresponding first mode periods are provided in Figure 7 in comparison with the one provided in Ural and Çelik (2018).



	1. Mod	2. Mod	3. Mod	4. Mod	5. Mod
Ural ve Çelik [18]	0.52 s	0.52 s	0.09 s	0.09 s	0.07 s
This study	0.51 s	0.51 s	0.09 s	0.09 s	0.07 s

Figure 7. The comparative mode shapes and periods of the cited minaret.

As can be clearly seen from Figure 7, the difference between the dynamic properties of the minaret modeled by Ural and Çelik (2018) and the dynamic properties of the minaret modeled within the scope of this study is less than 5% (Genç et al., 2022). Therefore, this shows that the verification of the FEM produced in this study has been performed and can be used in structural dynamic analyses. Furthermore, there is no door opening in the original FEM of Ural and Çelik (2018). In order to determine the importance of the direction of the earthquake loads to be applied within the scope of this study, two door openings (as used in traditional historical masonry minarets) with 1.5 meters in height, were added to the FEM, the first at ground level and the second at balcony level. The FEM of the model with the door opening is shown in Figure 8.

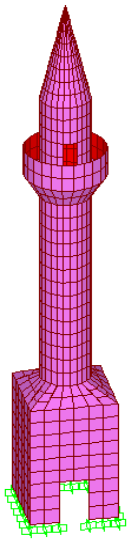


Figure 8. The FEM of the Zafer Mosque minaret with two door openings.

Along with the definition of the door opening, there have been minor changes (since two digits after the decimal point are taken into account, it seems that there has been no change) in the first five periods of the structure. These are: 1st mode period 0.51 seconds, 2nd mode period 0.51 seconds, 3rd mode period 0.10 seconds, 4th mode period 0.10 seconds and 5th mode period 0.07 seconds. Here, by adding the door opening to the structure, it is attempted to determine in which critical axis direction the earthquake load to be applied to the structure.

In general, in traditional building style structures, the earthquake load is applied to the structure only in two axes, x and y. In axisymmetric structures, it does not matter which direction the earthquake load will be applied. However, in long and slender structures with openings in their walls, such as chimneys, minarets, lighting towers, which are not axisymmetric, it is of great importance to be able to determine from which direction the earthquake load should be applied during the design phase.

Within the scope of this study, in order to determine the critical axis of the earthquake load, the x-axis in the structure was assumed to be zero (0) degrees, and the earthquake loads were applied to the cited masonry minaret model with and without door openings, with 15 degrees angle increments up to 180 degrees. This situation is shown schematically in Figure 9.

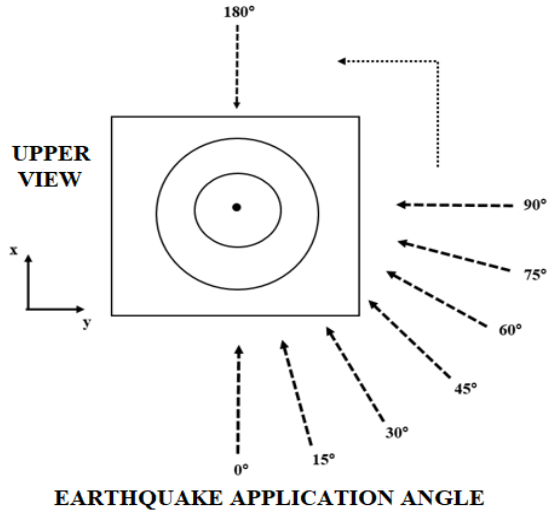


Figure 9. Earthquake application angles considered in this study.

In this study, in order to determine the effect of the earthquake application direction on the structural behavior of the cited historical masonry minaret, acceleration records of destructive earthquakes that occurred at different times in Türkiye were utilized. These are the Düzce Earthquake that occurred in 1999, the Van Earthquake that occurred in 2011 and the recent Kahramanmaraş Earthquake that occurred in 2023.

The 12.11.1999 M_w 7.2 Düzce (Kaynaşlı) (Türkiye) earthquake occurred 87 days after the 17 August 1999 Gölcük earthquake, as a result of ruptures that occurred in the Gölcük earthquake. The 12.11.1999 M_w 7.2 Düzce (Kaynaşlı) earthquake caused a rupture in the remaining 43-kilometer eastern section of the fault. Together with the ruptured 43-kilometer section, the 73-kilometer-long Düzce fault, which forms the northern branch of the North Anatolian Fault (NAF), was completely ruptured. The 12.11.1999 M_w 7.2 Düzce (Kaynaşlı) earthquake caused great destruction and damage in the center of Düzce and the Kaynaşlı district, located 15 kilometers west of the center (Anonymous, 2024b). In this study, the acceleration-time graph (PEER, 2024) of the 12.11.1999 M_w 7.2 Düzce (Kaynaşlı) earthquake, the details of which are given above, used in the time history analyses, is presented in Figure 10.

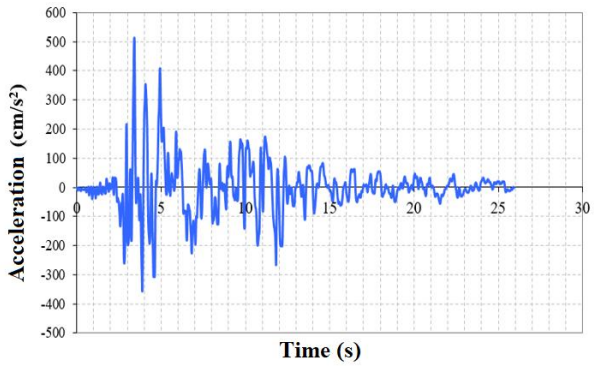


Figure 10. Time history graph of 12.11.1999 Düzce (Kaynaşlı) earthquake (PEER, 2024).

On 23.10.2011, a devastating earthquake centered in Van-Erciş (Türkiye) with a magnitude of M_w 7.2, which was felt very strongly in Van and its districts, occurred. Erciş District of Van Province is 30 kilometers away from the epicenter of the earthquake. A total of 604 citizens lost their lives in the earthquake (AFAD, 2024). Within the scope of this study, the acceleration-time graph of the Van-Erciş Earthquake (TADAS, 2024), which is used in the time history analyses and whose details are given above, is presented in Figure 11.

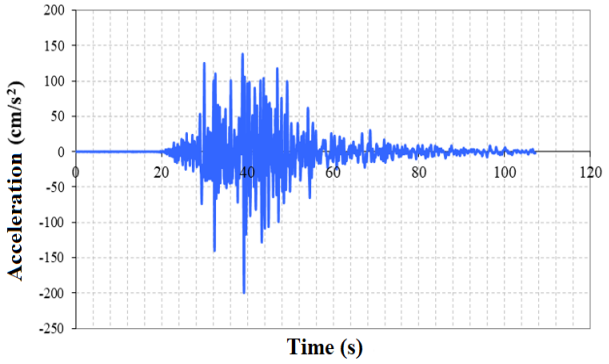


Figure 11. Time history graph of 23.10.2011 Van (Erciş) earthquake (TADAS, 2024).

On 06.02.2023, an earthquake with a magnitude of M_w 7.7 occurred at 04.17, centered in Pazarcık, Kahramanmaraş (Türkiye) province. Nine hours later, a second earthquake with a magnitude of M_w 7.6 occurred, centered in Elbistan. Following these two devastating and widespread earthquakes, 7184 aftershocks, some of which could be considered severe, were recorded (AFAD, 2023). Following these two earthquakes, eleven provinces of Türkiye, including Kahramanmaraş, Adıyaman, Hatay, Malatya, Gaziantep, Adana, Kilis, Osmaniye, Diyarbakır, Şanlıurfa, and Elazığ, were negatively affected. The earthquakes, which affected such a wide area and caused the deaths of 53,557 citizens, entered the literature as the "Disaster of the Century" (TRT, 2024). In this study, the acceleration-time graph of the Kahramanmaraş Earthquake (TADAS, 2024), which is used in the time-history analyses and whose details are given above, is presented in Figure 12.

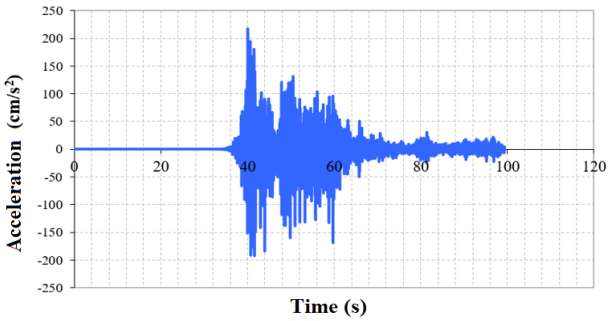


Figure 12. Time history graph of 06.02.2023 Kahramanmaraş (Pazarcık) earthquake (TADAS, 2024).

In the structural performance evaluation of masonry minarets, the limit states of the drift ratios given in Figure 13 are used (Aymelek et al., 2023). Accordingly, three cases are defined: Limited Damage Case (LD), Controlled Damage Case (CD) and Collapse Prevention Case (CP).

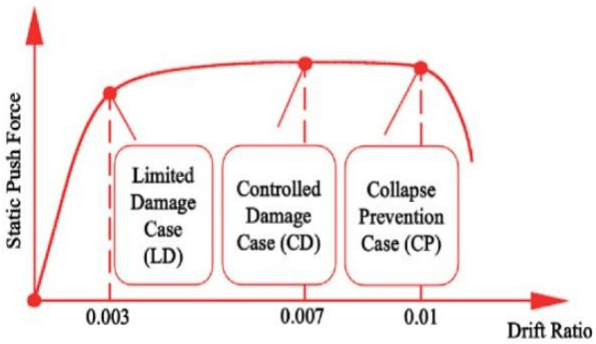


Figure 13. Drift ratio limit state values (Aymelek et al., 2023).

Accordingly, the Controlled Damage (CD) case refers to the damage that is allowed at the design stage and does not cause a total collapse in the structure. As can be seen from Figure 13, the drift ratios for the Limited Damage (LD), Controlled Damage (CD) and Collapse Prevention (CP) case are 0.003, 0.007 and 0.01, respectively (Aymelek et al., 2023). The drift ratio for the masonry minaret whose structural analysis was carried out can be obtained by using Equation 1.

$$\frac{\Delta_i}{h_i} \leq \left(\frac{\Delta_i}{h_i}\right)_{limit} \quad (1)$$

In Equation 1, Δ_i represents the top displacement of the structure and h_i represents the total height of the structure. The values obtained as a result of the structural analysis are compared with the limit value given in Equation 1, and accordingly, an idea can be obtained about the performance of the structure under the relevant load.

3. Results and Discussions

In this part of the study, the structural analysis results were obtained for different earthquake load application directions (from 0° to 180°) on Aksaray Zafer Mosque masonry minaret using the acceleration-time graphs of Düzce, Van and Kahramanmaraş earthquakes. From these analyses results, it was tried to determine the critical axis where the earthquake load should be applied to the masonry minaret with and without door openings. At the same time, the performance evaluation of the structure under the cited earthquake loads was also carried out.

3.1. Obtaining Top Displacements

As mentioned before, in order to determine the critical axis of earthquake load application, the earthquake loads were applied to the Aksaray Zafer Mosque minaret by rotating them from 0° (x-axis) to 15°, 30°, 45°, 60°, 75°, 90°, 105°, 120°, 135°, 150°, 165° and 180°. Here, in order to find the effect of the door opening on the critical direction of earthquake application, the earthquake loads were applied to the model both with and without the door opening. In calculating the top displacement values, the displacements in both x and y directions were obtained separately and the absolute resultant displacement was calculated and provided in the following tables (Last two columns in Table 1, 2 and 3). For the 12.11.1999 M_w 7.2 Düzce (Kaynaşlı) earthquake, the top displacements obtained for the model with and without door openings are shown in Table 1.

Table 1. Top displacements (in cm.) for 12.11.1999 M_w 7.2 Düzce (Kaynaşlı) earthquake

Load (Angle °)	W.O.D.O.*		W.D.O.**		W.O.D.O	W.O.D
	x	y	x	y		
duz-0	14.	0.0	14.	0.0	14.418	14.5
duz-15	13.	3.7	14.	3.7	14.418	14.5
duz-30	12.	7.2	12.	7.2	14.418	14.5
duz-45	10.	10.	10.	10.	14.418	14.4
duz-60	7.2	12.	7.2	12.	14.418	14.4
duz-75	3.7	13.	3.7	13.	14.418	14.4
duz-90	0.0	14.	0.0	14.	14.418	14.4
duz-105	3.7	13.	3.7	13.	14.418	14.4
duz-120	7.2	12.	7.2	12.	14.418	14.4
duz-135	10.	10.	10.	10.	14.418	14.4
duz-150	12.	7.2	12.	7.2	14.418	14.5
duz-165	13.	3.7	14.	3.7	14.418	14.5
duz-180	14.	0.0	14.	0.0	14.418	14.5

*W.O.D.O= Without door opening,

** W.D.O.= With door opening.

For the 23.10.2011 M_w 7.2 Van-Erciş centered earthquake, the top displacements obtained for the model with and without door openings are shown in Table 2.

Table 2. Top displacements (in cm.) for 23.10.2011 M_w 7.2 Van-Erciş centered earthquake

Load (Angle °)	W.O.D.O.*		W.D.O.**		W.O.D.O	W.O.D
	x	y	x	y		
van-0	8.52	0.0	8.5	0.0	8.529	8.557
van-15	8.23	2.2	8.2	2.1	8.529	8.553
van-30	7.38	4.2	7.4	4.2	8.529	8.543
van-45	6.03	6.0	6.0	6.0	8.529	8.528
van-60	4.26	7.3	4.2	7.3	8.529	8.514
van-75	2.20	8.2	2.2	8.2	8.529	8.503
van-90	0.00	8.5	0.0	8.4	8.529	8.499
van-105	2.20	8.2	2.2	8.2	8.529	8.503
van-120	4.26	7.3	4.2	7.3	8.529	8.514
van-135	6.03	6.0	6.0	6.0	8.529	8.528
van-150	7.38	4.2	7.4	4.2	8.529	8.543
van-165	8.23	2.2	8.2	2.1	8.529	8.553
van-180	8.52	0.0	8.5	0.0	8.529	8.557

*W.O.D.O= Without door opening,

** W.D.O.= With door opening.

Lastly, for the 06.02.2023 M_w 7.7 Kahramanmaraş earthquake, the top displacements obtained for the model with and without door openings are shown in Table 3.

Table 3. Top displacements (in cm.) for 06.02.2023 M_w 7.7 Kahramanmaraş earthquake

Load (Angle °)	W.O.D.O.*		W.D.O.**		W.O. D.O	W.O. D
	x	y	x	y		
kah-0	20.	0.0	20.	0.0	20.60	20.68
kah-15	19.	5.3	19.	5.3	20.60	20.68
kah-30	17.	10.	17.	10.	20.60	20.68
kah-45	14.	14.	14.	14.	20.60	20.69
kah-60	10.	17.	10.	17.	20.60	20.70
kah-75	5.3	19.	5.3	20.	20.60	20.70
kah-90	0.0	20.	0.0	20.	20.60	20.71
kah-105	5.3	19.	5.3	20.	20.60	20.70
kah-120	10.	17.	10.	17.	20.60	20.70
kah-135	14.	14.	14.	14.	20.60	20.69
kah-150	17.	10.	17.	10.	20.60	20.68
kah-165	19.	5.3	19.	5.3	20.60	20.68
kah-180	20.	0.0	20.	0.0	20.60	20.68

*W.O.D.O= Without door opening,

** W.D.O.= With door opening.

The absolute peak displacements (Last two columns in Table 1, 2 and 3) presented in Table 1, Table 2 and Table 3 are shown graphically in Figures 14, 15 and 16, respectively.

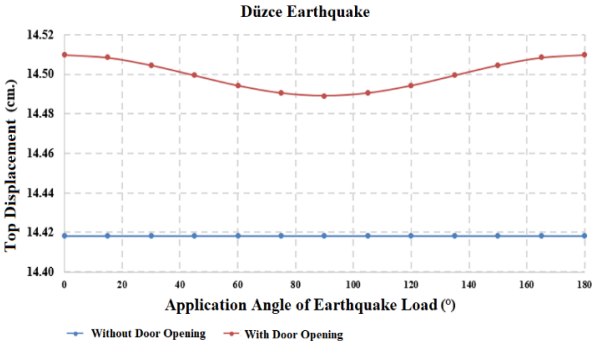


Figure 14. Absolute top displacements obtained under 12.11.1999 M_w 7.2 Düzce (Kaynaşlı) earthquake for the cases with and without door openings.

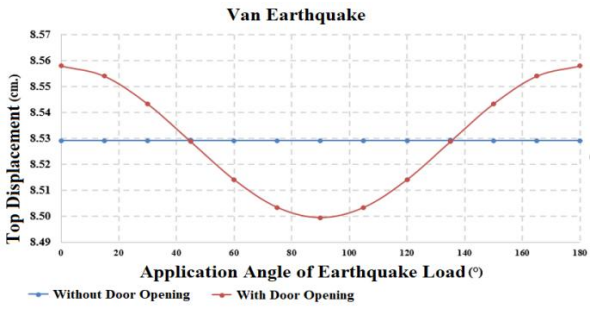


Figure 15. Absolute top displacements obtained under 23.10.2011 M_w 7.2 Van-Erciş earthquake for the cases with and without door openings.

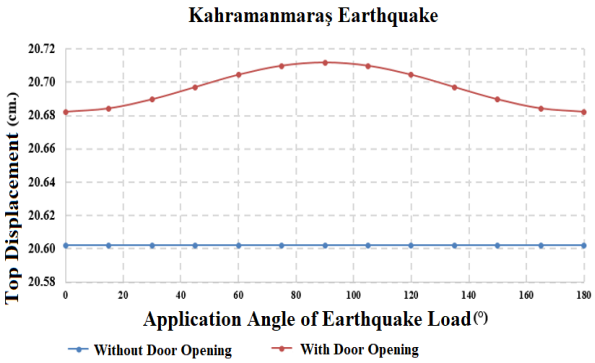


Figure 16. Absolute top displacements obtained under 06.02.2023 M_w 7.7 Kahramanmaraş earthquake for the cases with and without door openings.

By examining Figures 14, 15 and 16 in details, since the model without door opening is an axisymmetric structure, no matter on which direction the earthquake load is applied, it does not cause any change in the absolute top displacement. In other words, the top displacement shown in blue Figures 14, 15 and 16 did not change with the angle of application of the earthquake load. However, with the addition of door openings to the model, the axisymmetric feature of the structure was disrupted. For the Düzce and Van earthquakes, the largest absolute top displacement occurred at 0° and at 180° application angle, and took its smallest value at the 90° application angle. Furthermore, in the Kahramanmaraş earthquake, unlike Düzce and Van earthquakes, the largest top displacement occurred at the 90° application angle, which is exactly perpendicular to the door opening, and it took its smallest value at the 0° and 180° application angles. From here, the following conclusion can be drawn for the Aksaray Zafer Mosque minaret model: for a non-axisymmetric masonry minaret model with door opening, according to the characteristics of the earthquake load, 0° (or its exact symmetry of 180°) and 90° application directions should be taken into account in the design phase, and the axis from which the larger result obtained should be accepted as the critical axis, and structural dynamic analyses should be performed based on that critical axis.

Another issue is related to the magnitude of absolute top displacements. From Figures 14, 15 and 16, the largest top displacement for the cited masonry minaret model occurred under Kahramanmaraş earthquake for 90° application direction, which was included in the literature as the "Disaster of the Century". This value was determined as 20.71 cm. Again, the largest absolute top displacement values (0° application direction) for Düzce earthquake and Van earthquake were obtained as 14.51 cm and 8.56 cm, respectively. From here, it is seen that the absolute top displacement value obtained for the Kahramanmaraş earthquake is approximately 1.5 times larger than the absolute top displacement value obtained for Düzce earthquake and approximately 2.5 times larger than the absolute top displacement value obtained for Van earthquake. This situation once again shows how intense,

large and destructive the acceleration values obtained from the Kahramanmaraş earthquake are.

In addition, for the application directions where the largest absolute top displacement values obtained (the model with the door opening), the time-dependent changes of the absolute top displacement under the Düzce, Van and Kahramanmaraş earthquakes are presented in Figures 17, 18 and 19, respectively.

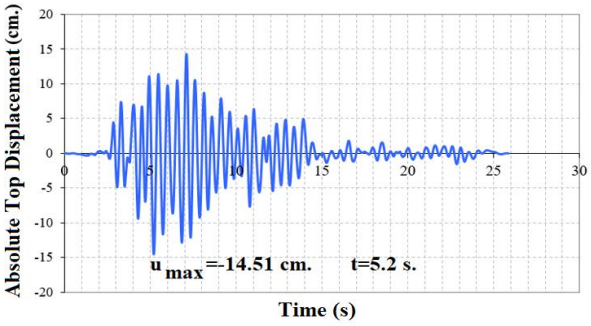


Figure 17. Time history of the absolute top displacements obtained under 12.11.1999 M_w 7.2 Düzce (Kaynaşlı) earthquake for the case with door openings (0° application direction).

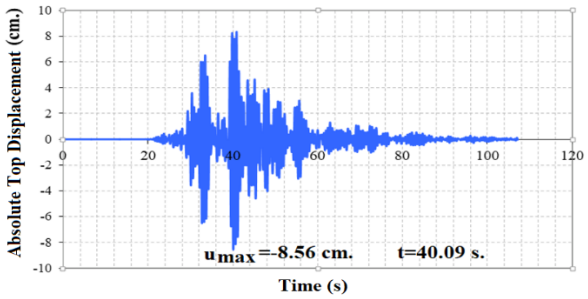


Figure 18. Time history of the absolute top displacements obtained under 23.10.2011 M_w 7.2 Van-Erciş earthquake for the case with door openings (0° application direction).

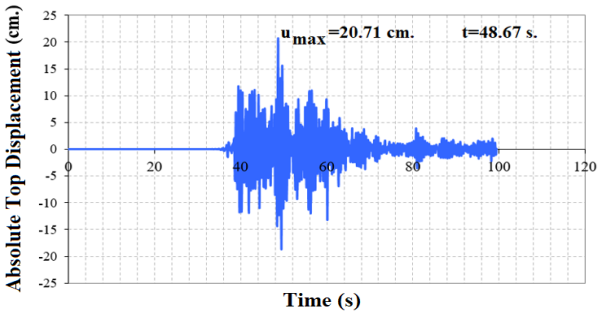


Figure 19. Time history of the absolute top displacements obtained under 06.02.2023 M_w 7.7 Kahramanmaraş earthquake for the case with door openings (90° application direction).

In Figures 20, 21 and 22, the change in the displacement over the height for the time when the largest top displacement occurred under Düzce (0° application direction), Van (0° application direction) and the Kahramanmaraş (90° application direction) earthquakes are presented for the model with door opening, respectively.

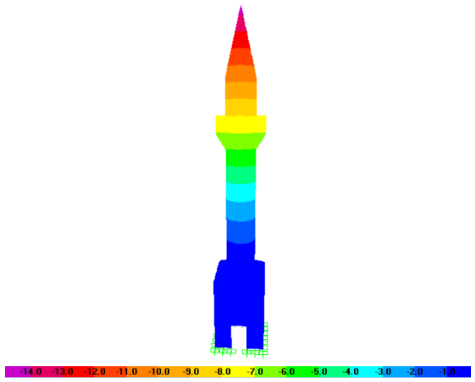


Figure 20. Displacements (in cm.) over height at the time when maximum absolute top displacements occurred under 12.11.1999 M_w 7.2 Düzce (Kaynaşlı) earthquake for the case with door openings (0° application direction).

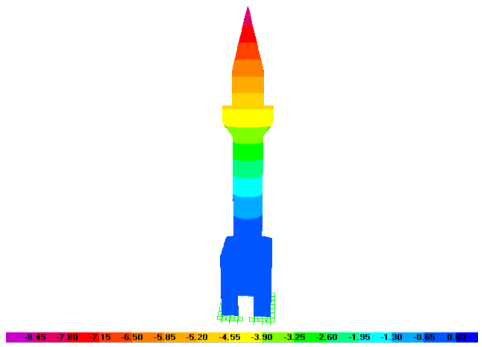


Figure 21. Displacements (in cm.) over height at the time when maximum absolute top displacements occurred under 23.10.2011 M_w 7.2 Van-Erciş earthquake for the case with door openings (0° application direction).

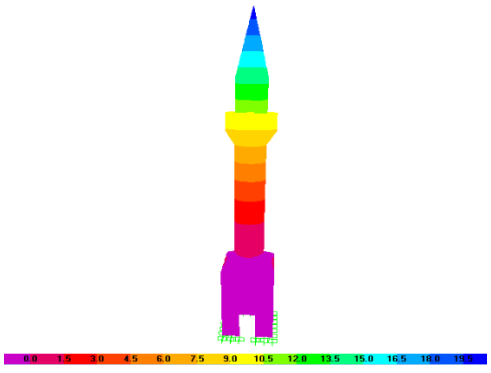


Figure 22. Displacements (in cm.) over height at the time when maximum absolute top displacements occurred under 06.02.2023 M_w 7.7 Kahramanmaraş earthquake for the case with door openings (90° application direction).

3.2. Obtaining Stress Values

As mentioned in the preceding section of this study, the maximum absolute top displacement value for the cited masonry minaret model occurred in the Kahramanmaraş Earthquake (90° application direction). This value is followed by the maximum absolute top displacement values (0° application direction) as 14.51 cm and 8.56 cm for the Düzce and Van earthquakes, respectively. By using the same approach for absolute top displacements, in Figures 23, 24 and 25, the maximum (S_{max}) stress values (in MPa) occurring on the cited masonry minaret model for the Düzce (0° application direction), Van (0° application direction) and Kahramanmaraş earthquakes (90° application direction) at the time when the maximum absolute top displacement values are represented, respectively.

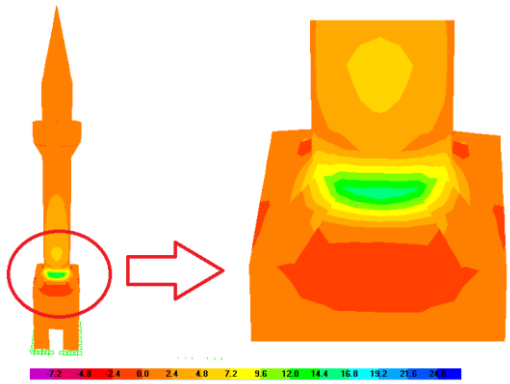


Figure 23. Maximum (S_{max}) stress values (in MPa) at the time when maximum absolute top displacements occurred under 12.11.1999 M_w 7.2 Düzce (Kaynaşlı) earthquake for the case with door openings (0° application direction).

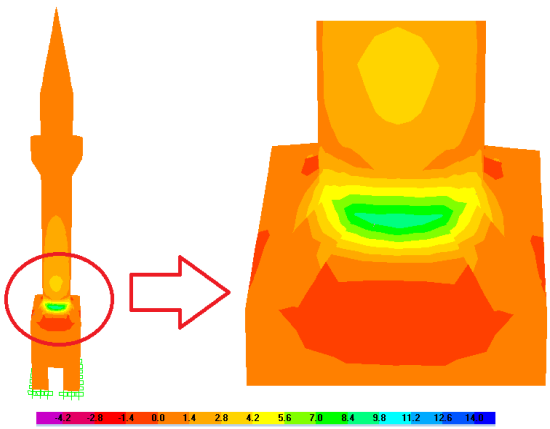


Figure 24. Maximum (S_{max}) stress values (in MPa) at the time when maximum absolute top displacements occurred under 23.10.2011 M_w 7.2 Van-Erciş earthquake for the case with door openings (0° application direction).

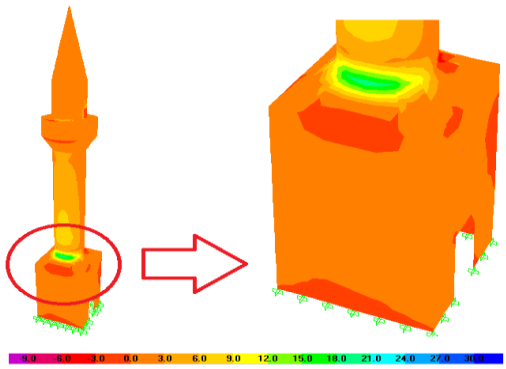


Figure 25. Maximum (S_{max}) stress values (in MPa) at the time when maximum absolute top displacements occurred under 06.02.2023 M_w 7.7 Kahramanmaraş earthquake for the case with door openings (90° application direction).

From Figures 23, 24 and 25, the maximum stress values (S_{max}) are obtained as 28.12 MPa for Kahramanmaraş (90° application direction), 23.19 MPa for Düzce (0° application direction) and 13.59 MPa for Van-Erciş earthquakes (0° application direction). Furthermore, when the region where the S_{max} stress values occurred is examined in Figures 23, 24 and 25, it can be clearly seen that the accumulation is just above the junction of the transition segment and the cylindrical body. The minaret of the historical Atik Mosque in Elbistan destroyed in the Kahramanmaraş earthquake in 2023 (Figure 26) is one of an example of the historical masonry minarets that damaged and collapsed in a brittle manner from the region mentioned above (Soyluk and Demircan, 2023).



Figure 26. The minaret of the historical Atik Mosque in Elbistan, which collapsed during 06.02.2023 M_w 7.7 Kahramanmaraş earthquake (Soyluk and Demircan, 2023).

3.3. Structural Performance Evaluation

In this section of the study, the earthquake performance evaluation of the cited masonry minaret with door opening was focused on, since the absolute top displacement values obtained are higher than the model without door openings. It is useful to state here that the earthquake performance evaluation of the mentioned masonry minaret was made based on the value in the direction where the absolute top displacement takes the largest value for each earthquake. In Table 4, the relative drift ratios are used as the basis for the performance evaluation of the structure and their comparison with the limit values was shown.

Table 4. Maximum relative drift ratios of the cited masonry minaret model and comparison with the limit values (with door openings)

Earthquake Load Direction (°)	With Door Opening (Δ_i) (cm)	h_i (m)	Δ_i/h_i	Damage States		
				CD (0.007)	CP (0.01)	>CP
düzce-0	14.509	18.66	0.00777		x	
van-0	8.557	18.66	0.00458	x		
kah-90	20.711	18.66	0.01109			x

As can be seen from Table 4, the cited masonry minaret is in the "Controlled Damage" zone under the Van earthquake which shows that the structure is on the safe side under Van earthquake. Under Düzce earthquake, the structure is in the "Pre-Collapse" zone which shows that the structure is not on the safe side and is likely to collapse. Finally, under Kahramanmaraş earthquake, the structure has gone beyond the "Pre-Collapse" zone. This is the region just before the structure collapses. The structure is not safe at all and will most likely collapse.

4. Conclusion

The main purpose of this study is to determine the critical axis of earthquake application during the design phase for historical masonry minarets with door openings and not axisymmetric. In this manner, Zafer Mosque minaret located in Aksaray city center, which can be verified by structural dynamics from technical literature, was selected. Then, the 1999 Düzce Earthquake, 2011 Van Earthquake and 2023 Kahramanmaraş Earthquake, which occurred recently in Türkiye and caused many casualties, were applied to the mentioned minaret starting from 0° (x-axis), with 15-degree increments up to 180° and as a result, structural analysis results were obtained. At the end of the study, the earthquake performance evaluation of the masonry minaret examined within the scope of this study was carried out.

The first of the analysis results evaluated in the study is the evaluation of the absolute top displacements. Of the three earthquakes considered, the earthquake that caused the largest absolute top displacement in the structure was the Kahramanmaraş earthquake with a value of 20.71 cm. This earthquake is followed by the Düzce earthquake with an absolute top displacement value of 14.51 cm and the Van earthquake with an absolute top displacement value of 8.56 cm. The magnitude, intensity and destructiveness of the Kahramanmaraş earthquake, which has been referred to in technical literature as the "Disaster of the Century", are once again revealed here.

At the same time, the three earthquakes considered within the scope of this study were applied to the model with and without door openings, starting from 0° (x-axis), with 15 degree increments up to 180°, and the absolute top displacements were obtained for each application direction. From here, it was attempted to determine the critical axis to which the earthquake should be applied. This axis was the x-axis (i.e. the exact middle of the door opening) for the Düzce and Van earthquakes, and the axis exactly perpendicular to the middle of door opening (i.e. the y-axis direction) for the Kahramanmaraş earthquake. This situation brings the following issue to light for the determination of the critical axis of the cited masonry minaret: For masonry minarets with door openings and not axisymmetric, the x (i.e. the exact middle of the door opening) and y axes (i.e. the axis exactly perpendicular to the middle of door opening) should be critically considered during the design phase. The values obtained from loadings other than these two critical axes remain between the values obtained from the critical x and y axes. From this, it is concluded that the critical axis changes and occurs in one of the x and y axes for the cited minaret, depending on the characteristics of the earthquake. However, in order to generalize this result, structural dynamic analyses need to be performed on a large number of masonry minarets under earthquakes with different characteristics with smaller angle increments (i.e. 5 degrees).

The second analysis result evaluated in the study is the maximum stress (S_{max}) values. These values were obtained as 28.12 MPa for the Kahramanmaraş (at an angle of 90°), 23.19 MPa for the Düzce (at an angle of 0°) and 13.59 MPa for the Van-Erciş earthquakes (at an angle of 0°). At the same time, it was observed that the maximum stress values occurred just above the junction point of the transition segment and cylindrical body of the cited masonry minaret. When the collapses of the masonry minarets in the recent earthquakes are examined, the fact that the fractures are generally from this region supports the findings obtained in this study.

The last issue evaluated in the study is the performance of the cited minaret with door openings under the earthquakes considered. Under Van earthquake, the damage rate of the cited minaret is in the "Controlled Damage" region and the structure remains on the safe side. Under Düzce earthquake, the structure is in the "Pre-Collapse" region and this situation shows that the structure is not on the safe side and also has a high probability of collapse. Finally, under Kahramanmaraş earthquake, the structure goes beyond the "Pre-Collapse" region. This region is the region just before the structure collapses. The structure is not on the safe side and will most likely be subject to collapse.

In summary, within the scope of this study, Aksaray Zafer Mosque minaret, which was selected from the technical literature and modeled after verification, was examined in structural terms. Here, it is useful to state that: The results obtained within the scope of this study belong to the minaret analyzed and the earthquakes applied to the minaret. In order to generalize these results, structural dynamic analyses should be performed on a large number of masonry minarets with different dynamic properties,

under a large number of earthquakes with different characteristics and with smaller angle increments.

Author Contributions

The percentages of the authors' contributions are presented below. All authors reviewed and approved the final version of the manuscript.

	E.T.	K.Y.
C	50	50
D	50	50
S	100	
DCP	50	50
DAI	50	50
L	50	50
W	50	50
CR	50	50
SR	50	50
PM	50	50
FA	50	50

C=Concept, D= design, S= supervision, DCP= data collection and/or processing, DAI= data analysis and/or interpretation, L= literature search, W= writing, CR= critical review, SR= submission and revision, PM= project management, FA= funding acquisition.

Acknowledgments

This study belongs to a Master of Science Thesis performed in Renewable Energy Department of Ordu University, Türkiye.

Conflict of Interest

The authors declared that there is no conflict of interest.

Ethical Consideration

Ethics committee approval was not required for this study because of there was no study on animals or humans.

References

Anonymous. 2024a. El-Ezher Mosque. URL: https://tr.wikipedia.org/wiki/El-Ezher_Camii- (accessed date: February 3, 2024), pp: 1–2.

Anonymous. 2024b. 12 November Düzce Earthquake. URL: http://www.duzce.gov.tr/12-kasim-duzce-depremi (accessed date: May 4, 2024), pp: 1–3.

AFAD. 2023. Disaster and Emergency Management Directorate, About the Earthquakes occurred in Kahramanmaraş-34. URL: https://www.afad.gov.tr/kahramanmarasta-meydana-gelen-depremler-hk-34- (accessed date: February 7, 2024), pp: 1–5.

AFAD. 2024. Disaster and Emergency Management Directorate, About Van Earthquake. URL: https://www.afad.gov.tr/van-depremi-hakkinda- (accessed date: February 3, 2024), pp: 1–4.

Atmaca B, Atmaca EE, Roudane B, Güleş O, Demirkaya E, Aykanat B, Altunışık AC, Günaydın M, Arslan ME, Kahya V, Tatar T, Aslan B, Sezdirmez T, Sunca F, Okur FY, Adanur S, Sarıbıyık A, Aydın F, Genç AF, Kirtel O, Demir A, Öztürk H, Dok G, Emiroğlu M, Akgül T. 2025. Field observations and numerical investigations on seismic damage assessment of RC and masonry minarets during the February 6th, 2023, Kahramanmaraş (Mw 7.7 Pazarcık and Mw 7.6 Elbistan) earthquakes in Türkiye. Int J Archit Herit, 19(7): 1117–1142, pp: 1117–1142. https://doi.org/10.1080/15583058.2024.2337651

Aymelek A, Yanik Y, Demirtaş B, Yildirim Ö, Çalik İ, Türker T. 2023. Full-scale structural evaluations of İskenderpaşa minaret. Structures, 55: 1028–1044, pp: 1028–1044. https://doi.org/10.1016/j.istruc.2023.06.055

Basaran H, Demir A, Ercan E, Nohutcu H, Hokelekli E, Kozanoglu C. 2016. Investigation of seismic safety of a masonry minaret using its dynamic characteristics. Earthq Struct, 10(3): 523–538, pp: 523–538. http://dx.doi.org/10.12989/eas.2016.10.3.523

Baştürk MH. 2013. Investigation of dynamic behavior of historical masonry minarets with modal analysis method in Bursa. Uludağ Üniversitesi, Fen Bilimleri Enstitüsü, Bursa, Türkiye, pp: 122.

Computers & Structures, Inc. 2024. SAP 2000: Integrated Software for Structural Analysis and Design (computer program). URL: https://www.csiamerica.com/products/sap2000- (accessed date: January 20, 2024), pp: 1–3.

Erdogan YS, Kocatürk T, Demir C. 2019. Investigation of the seismic behavior of a historical masonry minaret considering the interaction with surrounding structures. J Earthq Eng, 23(1): 112–140, pp: 112–140. https://doi.org/10.1080/13632469.2017.1309725

Genç A, Altunışık AC, Günaydın M, Okur F. 2022. Finite element model updating of İskenderpaşa mosque and minaret based on experimental measurements. J Struct Eng Appl Mech, 5(4): 264–276, pp: 264–276. https://doi.org/10.31462/jseam.2022.04264276

Günaydın M. 2018. Experimental determination of the dynamic characteristics of a historical masonry minaret after repairing. Gümüşhane Univ J Sci Tech, 8(2): 381–395, pp: 381–395. https://doi.org/10.17714/gumusfenbil.380711

Işık E, Harirchian E, Arkan E, Avcil F, Günay M. 2022a. Structural analysis of five historical minarets in Bitlis (Türkey). Buildings, 12(2): 159, pp: 159. https://doi.org/10.3390/buildings12020159

Işık E, Avcil F, Harirchian E, Arkan E, Bilgin H, Özmen HB. 2022b. Architectural characteristics and seismic vulnerability assessment of a historical masonry minaret under different seismic risks and probabilities of exceedance. Buildings, 12(8): 1200, pp: 1200. https://doi.org/10.3390/buildings12081200

Kılıç İ, Bozdoğan KB, Aydın S, Gök SG, Gündoğan S. 2020. Determination of dynamic behavior of tower type structures: the case of Kırklareli Hızırbey Mosque minaret. J Polytech, 23(1): 19–26, pp: 19–26. https://doi.org/10.2339/politeknik.481857

Livaoğlu R, Baştürk MH, Doğangün A, Serhatoğlu C. 2016. Effect of geometric properties on dynamic behavior of historic masonry minaret. KSCE J Civ Eng, 20: 2392–2402, pp: 2392–2402. https://doi.org/10.1007/s12205-016-0622-2

PEER. 2024. Pacific Earthquake Engineering Research Center, 12.11.1999 Düzce earthquake. URL: http://peer.berkeley.edu/ (accessed date: March 15, 2024), pp: 1–3.

Serhatoğlu C. 2015. Numerical and empirical investigation of dynamic performance of historical masonry minarets in Bursa. Uludağ Üniversitesi, Fen Bilimleri Enstitüsü, Bursa,

Türkiye, pp: 203.

Soyluk A, Demircan B. 2023. An architectural review of the behavior of historical masonry minarets under earthquake load on mosque samples managed in the 6 February Kahramanmaraş earthquake. J Archit Sci Appl, 8: 329–354, pp: 329–354. https://doi.org/10.30785/mbud.1318660

TADAS. 2024. Turkish Accelerometric Database and Analysis System, Van and Kahramanmaraş Earthquakes Acceleration Graphs. URL: https://tadas.afad.gov.tr/map- (accessed date: March 15, 2024), pp: 1–4.

Temüz HT. 2007. Structural behavior and analysis of minarets subjected to wind loads. Karadeniz Teknik Üniversitesi, Fen Bilimleri Enstitüsü, Trabzon, Türkiye, pp: 108.

TRF. 2024a. Türkiye Religious Foundation, Cordoba Great Mosque. URL: https://islamansiklopedisi.org.tr/kurtuba-ulucamii- (accessed date: February 3, 2024), pp: 1–2.

TRF. 2024b. Türkiye Religious Foundation, Minaret. URL: https://islamansiklopedisi.org.tr/minare (accessed date: February 3, 2024), pp: 1–2.

TRT. 2024. Turkish Radio and Television Corporation, From the disaster of the century to the cooperation of the century. URL: https://www.trthaber.com/haber/gundem/asrin-felaketinden-asrin-dayanismasina-834638.html (accessed date: February 7, 2024), pp: 1–3.

Ural A, Çelik T. 2018. Dynamic analyses and seismic behavior of masonry minarets with single balcony. Aksaray Univ J Sci Eng, 2(1): 13–27, pp: 13–27. https://doi.org/10.29002/asujse.371344

Usta P. 2021. Assessment of seismic behavior of historic masonry minarets in Antalya, Türkey. Case Stud Constr Mater, 15: e00665, pp: e00665. https://doi.org/10.1016/j.cscm.2021.e00665

Yurdakul M, Yılmaz F, Artar M, Can Ö, Öner E, Daloğlu AT. 2021. Investigation of time-history response of a historical masonry minaret under seismic loads. Structures, 30: 265–276, pp: 265–276. https://doi.org/10.1016/j.istruc.2021.01.008

Black Sea Journal of Engineering and Science
doi: 10.34248/bsengineering.1608978

Open Access Journal
e-ISSN: 2619 – 8991

Araştırma Makalesi (Research Article)
Cilt 8 - Sayı 4: 1034-1049 / Temmuz 2025
(Volume 8 - Issue 4: 1034-1049 / July 2025

ENTROPİ VE KÜMELEME TABANLI YENİ BİR HAKEM DEĞERLENDİRME SÜRECİ VE KARAR DESTEK SİSTEMİ ÖNERİSİ

Seda Nur BUDAK[1]*, Kumru Didem ATALAY[2], Mehmet KABAK[3], Tacettin Sercan PEKİN[4]

[1]*The Scientific and Technological Research Council of Türkiye, 06100 Kavaklıdere, Ankara, Türkiye*
[2]*Baskent University, Department of Industrial Engineering, 06790 Etimesgut, Ankara, Türkiye*
[3]*Gazi University, Department of Industrial Engineering, 06570 Maltepe, Ankara, Türkiye*
[4]*OSTIM Technical University, Department of Management Information Systems, 06374 Ostim, Ankara, Türkiye*

Özet: Araştırma ve geliştirme (Ar-Ge) projelerinin değerlendirme süreçlerinin karmaşıklığı ve eksiklikleri, projelerin değerlendirilmesinde tutarlılık ve izlenebilirlik sorunlarına yol açmaktadır. Bu çalışma, Türkiye'deki Ar-Ge projelerinin değerlendirme süreçlerinde karşılaşılan temel sorunları ele alarak, nesnel, tutarlı ve uygulanabilirliği yüksek bir karar destek sistemi geliştirmeyi amaçlamaktadır. Bu bağlamda, projelerin değerlendirilmesinde kullanılan kriterler için literatür detaylı bir şekilde incelenmiş, uzmanların görüşleri alınmış, entropi yöntemi ile önem derecelerine göre sıralanmış ve değerlendirmede daha etkili olduğu görülen kriterler belirlenmiştir. Böylece, kriter sayısı 247'den 96'ya indirilmiş ve değerlendiriciye kolaylık sağlanarak daha etkili bir değerlendirme seti oluşturulmuştur. Geliştirilen karar destek sistemi, projelerin kapsamlı bir analizine olanak tanımakta ve hakemlerden yürütme kurulu üyelerine kadar tüm paydaşların daha şeffaf bir platform üzerinde değerlendirme yapmasını sağlamaktadır. Karar destek sistemi ile elde edilen hakem puanlarına bağlı olarak projeler, K-ortalama kümeleme algoritması ile dört ana gruba ayrılmıştır. Bu platform, değerlendirme süreçlerinin hızlandırılmasını ve karar vericilerin iş yükünün %31 ila %39 oranında azaltılmasını sağlamıştır. Elde edilen sonuçlar, Ar-Ge projelerinin yenilikçi yönleri, ekonomik ve ulusal katkıları, proje planları ve teknik altyapıları gibi boyutlarda daha kapsamlı ve objektif bir değerlendirme yapılmasını mümkün kılmıştır. Yeni sistem, mevcut değerlendirme süreçlerinin eksikliklerini gidererek daha yapılandırılmış ve bütüncül bir yaklaşım sunmaktadır. Geliştirilen bu sistem, gelecekte farklı Ar-Ge programlarına entegre edilerek ülkenin Ar-Ge potansiyelini ve inovasyon kapasitesini en üst seviyeye çıkarmayı hedeflemektedir.

Anahtar kelimeler: Ar-Ge projeleri değerlendirme süreci, Çok kriterli karar verme, Entropi, K-ortalama kümeleme, Karar destek sistemi

A novel reviewer evaluation process and decision support system proposal based on entropy and clustering

Abstract: The complexity and shortcomings of the evaluation processes of research and development (R&D) projects lead to problems of consistency and traceability in the evaluation of the projects. This study aims to develop an objective, consistent, and highly applicable decision support system by addressing the main challenges encountered in the evaluation processes of R&D projects in Türkiye. In this context, the literature on evaluation criteria was thoroughly reviewed, expert opinions were collected, the criteria were ranked according to their importance using the entropy method, and the most effective criteria for evaluation were identified. Consequently, the number of criteria was reduced from 247 to 96, thereby facilitating the evaluator's task and forming a more effective evaluation set. The developed decision support system enables comprehensive analysis of projects and allows all stakeholders—from reviewers to executive board members—to conduct evaluations on a more transparent platform. Based on the reviewer scores obtained through the system, projects were classified into four main groups using the k-means clustering algorithm. This platform has accelerated evaluation processes and reduced the workload of decision-makers by 31% to 39%. The results demonstrate that more comprehensive and objective evaluations can be made in dimensions such as the innovative aspects of R&D projects, their economic and national contributions, project planning, and technical infrastructure. The newly developed system addresses the shortcomings of existing evaluation procedures and offers a more structured and holistic approach. It is envisioned that the system can be integrated into various R&D programs in the future to maximize the country's R&D potential and innovation capacity.

Keywords: R&D project evaluation process, Multi-criteria decision making, Entropy, K-means clustering, Decision support system

***Sorumlu yazar (Corresponding author):** The Scientific and Technological Research Council of Türkiye
E mail: sedanurbudak@gmail.com (S.N.BUDAK)
Seda Nur BUDAK https://orcid.org/0000-0003-4188-9988
Kumru Didem ATALAY https://orcid.org/0000-0002-9021-3565
Mehmet KABAK https://orcid.org/0000-0002-8576-5349
Tacettin Sercan PEKİN https://orcid.org/0000-0002-6416-5205

Gönderi: 01 Ocak 2025 **Received:** January 01, 2025
Kabul: 14 Mayıs 2025 **Accepted:** May 14, 2025
Yayınlanma: 15 Temmuz 2025 **Published:** July 15, 2025

Cite as: Budak SN, Atalay KD, Kabak M, Pekin TS. 2025. A new method proposal and decision support system for the reviewer evaluation process. BSJ Eng Sci, 8(4): 1034-1049.

1. Giriş

Teknolojik gelişmelerin hız kazanması ve küresel rekabetin artması, Ar-Ge projelerini hem ekonomik hem de toplumsal kalkınmanın temel unsurlarından biri hâline getirmiştir. Yenilikçi ürün ve süreçlerin geliştirilmesine katkı sunan bu projeler, aynı zamanda çok boyutlu ve karmaşık değerlendirme süreçlerini de beraberinde getirmektedir. Değerlendirme sürecinin

This work is licensed (CC BY-NC 4.0) under Creative Commons Attribution 4.0 International License

başarısı; yalnızca kaynak planlaması ve operasyonel yeterlilikle değil, aynı zamanda ölçülebilir, nesnel ve yapılandırılmış yöntemlerle sağlanabilmektedir. Ancak proje başvurularının çeşitliliği, kapsam farklılıkları ve değerlendiricilerin öznel yaklaşımları; sürecin tutarlılığı ve izlenebilirliği üzerinde zayıflatıcı etkilere neden olmaktadır.

Bu bağlamda, çalışmanın temel amacı; Türkiye'de yürütülen Ar-Ge projelerinde karşılaşılan değerlendirme sorunlarına yönelik, veri temelli, nesnel ve bütünleşik bir karar destek yaklaşımı geliştirmektir. Bu kapsamda; projelere ilişkin değerlendirme kriterlerinin objektif olarak ağırlıklandırılması, projelerin benzerliklerine göre sınıflandırılması ve nihai değerlendirme sürecinin uzman görüşleriyle entegre edilmesi yoluyla daha tutarlı, izlenebilir ve uygulanabilir bir sistemin tasarlanması hedeflenmektedir.

Ar-Ge projelerinin etkin biçimde değerlendirilebilmesi; her projeye özgü nitelikleri yansıtan kapsamlı kriterlerin belirlenmesini ve bu kriterlerin açık biçimde tanımlanmış yöntemlerle analiz edilmesini zorunlu kılmaktadır. Bu amaç doğrultusunda literatürde çok sayıda yaklaşım geliştirilmiştir. Söz konusu yöntemler; bireysel uzman görüşlerine dayalı hakemlik ve panel değerlendirmesi gibi niteliksel yaklaşımlardan, puanlama sistemleri ve çok kriterli karar verme (ÇKKV) teknikleri gibi yarı yapılandırılmış yöntemlere; ayrıca matematiksel optimizasyon, veri zarflama analizi, dengeli puan kartı ve portföy optimizasyonu gibi nicel modelleme temelli yaklaşımlara kadar geniş bir yelpazede çeşitlenmektedir.

Her bir yaklaşım, belirli bağlamlarda önemli avantajlar sunsa da, yöntemlerin projeye özgü ihtiyaçlara ve karar ortamındaki belirsizlik düzeyine uyarlanabilirliği sınırlı olabilmektedir. Bu nedenle, hangi değerlendirme yönteminin seçileceği; veri yapısı, karar vericilerin stratejik öncelikleri ve uygulama alanının karmaşıklığı gibi faktörlere bağlı olarak değişiklik göstermektedir (Liberatore ve Titus, 1983; Meade ve Presley 2002; Mardani vd. 2015).

Tablo 1'de, Ar-Ge proje değerlendirme sürecinde yaygın olarak kullanılan yöntemlerin temel özellikleri, güçlü yönleri ve sınırlamaları özetlenmiştir.

Türkiye'de, ulusal hedefler doğrultusunda Ar-Ge projelerini destekleyen lider kurumlar, araştırma ve geliştirmenin teşvik edilmesi, yönlendirilmesi ve desteklenmesi konusunda önemli bir rol üstlenmektedir. Bu kurumların sunduğu destek programları, hem akademi camiası hem sanayi hem de girişimciler tarafından büyük bir ilgiyle karşılanmaktadır. Özellikle, 2019-2023 yılları arasında 'Akademik' ve 'Kamu' desteklerini sağlayan programlara toplamda 55.606 proje başvurusu yapılmış ve bunların 9.862'si desteklenmiştir. 'Sanayi' desteklerini sağlayan programlara başvuran 65.503 projeden ise 29.928'i desteklenmiştir (TÜBİTAK, 2023). Bu veriler, Ar-Ge projelerinin ülkemizdeki önemini ve ilgili paydaşların destek programlarına yönelik yoğun ilgisini açıkça ortaya koymaktadır. Ancak mevcut değerlendirme sistemlerinin etkinliği ve objektifliği, değişen koşullar ve yıllara göre değişkenlik gösteren faktörler nedeniyle zaman zaman sorgulanmaktadır. Bu durum, proje seçim süreçlerinde daha kapsamlı ve gelişmiş bir değerlendirme sistemi geliştirilmesi gerekliliğini ortaya çıkarmaktadır.

Bu çalışmada, projelerin değerlendirilmesinde kullanılan kriterler, detaylı bir literatür taraması ve alan uzmanlarının görüşleri ile bir araya getirilmiş, bu kriterler entropi yöntemi kullanılarak önem derecelerine göre sıralanmıştır. Böylece, değerlendirme kriterleri sayısı 247'den 96'ya indirilerek daha yönetilebilir ve etkin bir değerlendirme seti oluşturulmuştur. Bu yaklaşım, değerlendirme süreçlerinde karşılaşılan tutarsızlık ve izlenebilirlik eksikliklerinin giderilmesi, karar vericilere ise daha sağlıklı analiz yapma ve değerlendirme imkânı sunmaktır. Geliştirilen sistem, kriterlerin nesnel biçimde ağırlıklandırılması ve projelerin anlamlı gruplar hâlinde sınıflandırılması yoluyla değerlendirme sürecinin hızlandırılmasını ve karar vericilerin iş yükünün azaltılmasını amaçlamaktadır.

Bu bölümde, Ar-Ge projelerinin etkili biçimde değerlendirilmesine yönelik temel kavramlar ile mevcut yöntemler ele alınmakta; ardından çalışmada önerilen metodoloji ve elde edilen bulgular detaylandırılmaktadır.

Yapılan literatür incelemesinde de Souza vd. (2021) tarafından yapılan derinlemesine inceleme temel alınarak genişletilmiş Ar-Ge projelerinin değerlendirilmesinde kullanılan kriterler belirlenmeye çalışılmıştır. Czajkowski ve Jones (1986) ile Mavrotas ve Makryvelios (2021), Ar-Ge projelerinin değerlendirilmesinde 'fayda veya ödeme etkileşimi' ve 'çıktı veya teknoloji etkileşimi' kriterlerinin önemli olduğunu savunmuşlardır. Beaujon vd. (2001), projelerin net ekonomik faydalarının, yapılan yatırımların karşılanabilirliği açısından değerlendirilmesinin gerekliliğini vurgulamış ve bu bağlamda 'Beklenen net fayda' kriterinin önemini öne çıkarmıştır. Conka vd. (2008), mevcut sistemlerin modernizasyonunun daha fazla ekonomik fayda sağlayabileceğini ve projelerin bilgi üretme kapasitesini artırabileceğini öne sürmüşlerdir. Eilat vd. (2008), projelerin performansını ve maliyetlerini değerlendirmek için 'Kazanılmış değer' kriterini önermişlerdir ve bu kriterin projelerin bütçe ve zaman planına uygunluğunu izlemekte yararlı olduğunu ifade etmişlerdir. Liberatore (1986, 1987, 1988) ve Cheng vd. (2017), Ar-Ge projelerinin ekonomik başarılarının ölçülmesinde 'Karlılık' ve 'Birim fiyat' gibi kriterlerin kullanılmasını ve 'Beklenen pazar payı' ile 'Müşteri kabulü' gibi unsurların da dikkate alınmasını tavsiye etmektedir.

Tablo 1. Ar-Ge proje değerlendirmesinde kullanılan yöntemlerin karşılaştırması

Yöntem	Güçlü Yönleri	Sınırlamaları	Kaynak
Uzman Görüşüne Dayalı Hakemlik	Uzman görüşüne dayalı hakemlik, alan bilgisine dayalı nitelikli ve bağlamsal değerlendirme imkânı sunarak projelerin teknik ve yenilikçi boyutlarının esnek biçimde analiz edilmesini sağlar.	Ancak, değerlendirme süreci öznel yargılara, hakemler arası tutarsızlığa ve yenilikçi projelere karşı önyargıya açık olup şeffaflık ve güvenilirlik açısından sınırlılıklar barındırabilir.	Bornmann (2011)
Panel/Komite Değerlendirmesi	Farklı uzmanlık alanlarından gelen üyelerin kolektif bilgisiyle daha dengeli, çok boyutlu ve bağlamsal olarak zenginleştirilmiş kararlar alınmasına olanak tanır.	Grup dinamiklerinden kaynaklanan önyargılar, bireysel etkilerin gölgelenmesi ve karar alma sürecinde baskın seslerin yönlendirici olması gibi etkenler yöntemin nesnelliğini zayıflatabilir.	Criscuolo vd. (2017)
Puanlama / Skorlama Yöntemi	Puanlama yöntemi, farklı projelerin belirli kriterler üzerinden karşılaştırılabilir biçimde değerlendirilmesini mümkün kılarak karar sürecine yapı kazandırmakta; ayrıca yalın yapısı ve uygulama kolaylığıyla öne çıkmaktadır.	Kriter ağırlıklarının subjektif belirlenmesi, skorlama ölçeğinin belirsizliği ve değerlendirme sonuçlarının karar vericiler arası tutarlılık göstermemesi yöntemin güvenilirliğini sınırlayabilir.	Henriksen ve Traynor (1999), Miyajima vd. (2022)
Çok Kriterli Karar Verme	Karar vericilerin aynı anda birden fazla ve çoğu zaman çelişen kriteri dikkate alarak daha kapsamlı ve dengeli kararlar almasına olanak tanır.	Kullanılan ÇKKV yönteminin türü ve ağırlıklandırma yaklaşımı, nihai sıralama ve karar sonuçları üzerinde belirgin etkiye sahiptir; buna göre ağırlıklandırma için seçilen yöntem kararın güvenilirliğini etkiler.	Mardani vd. (2015)
Matematiksel Optimizasyon (0-1 Programlama vb.)	Kaynak kısıtları ve hedef fonksiyonları doğrultusunda en uygun proje kombinasyonunu hesaplayarak karar vericilere objektif, model tabanlı çözümler sunar.	Yüksek hesaplama gücü gerektirir, veri duyarlılığı yüksektir ve çoğu zaman gerçek dünya belirsizliklerini yeterince yansıtamaz.	Bard vd. (1988), Archer ve Ghasemzadeh (1999), Siksnelyte-Butkiene vd. (2020)
Veri Zarflama Analizi	Karar birimlerinin göreli etkinliğini doğrudan gözlemsel verilerle analiz edebilmesi sayesinde nicel girdiler ve çıktılar arasında objektif, ölçeklenebilir ve karşılaştırmalı değerlendirmeler sunar.	Yalnızca nicel verilerle çalışabilmesi, girdi ve çıktı sayısına duyarlılığı ve karar verici tercihlerini modelleyememesi yöntemin esnekliğini ve yoruma açıklığını sınırlayabilir.	Charnes vd. (1978), Isied ve Daneshvar (2024)
Dengeli Puan Kartı	Projeleri sadece finansal çıktılarla değil; müşteri memnuniyeti, iç süreçler, öğrenme ve büyüme gibi stratejik boyutlarla da ilişkilendirerek bütüncül bir değerlendirme yaklaşımı sunar.	Ölçütlerin tanımlanmasındaki belirsizlikler, subjektiflik riski ve nicel olmayan performans göstergelerinin puanlanmasında yaşanan zorluklar yöntemin nesnelliğini ve karşılaştırılabilirliğini sınırlayabilir.	Kaplan ve Norton (1992), Suvvari (2023)
Portföy Optimizasyonu	Sınırlı kaynaklar altında projelerin birlikte değerlendirilmesini sağlayarak, stratejik hedeflere en yüksek katkıyı sağlayacak proje kombinasyonunu bilimsel temelde belirlemeye olanak tanır.	Modelin doğruluğu kullanılan girdilere ve varsayımlara yüksek derecede bağımlı olup; veri eksikliği, kriterler arası bağımlılık ve belirsizlik ortamlarında uygulanabilirlik zorlukları doğurabilir.	Ghasemzadeh ve Archer (2000), Wang vd. (2024), Mavrotas ve Makryvelios (2023)
Entropi + K-ortalamalar (önerilen hibrit yöntem)	Kendi içinde homojen aralarında heterojen olan gruplar oluşturularak grup bazında değerlendirme yapılmasını sağlar. Belirsizlik düzeylerini ölçerek ayrıştırma gücü yüksek, aşırı değişkenliğe dengeli ağırlıklar elde edilmesini sağlar.	K-ortalamalar aykırı değerlere duyarlıdır (Bu çalışmada aykırı değer söz konusu değildir.) Entropi yöntemi nitel verileri işleyemez. (Bu çalışmada nicel veri kullanılmıştır.)	Liu ve Yang (2023), Cebeci ve Yıldız (2015)

Liberatore (1986), 'fiyatlandırma eğilimi, mülkiyet sorunu, coğrafi kapsam ve mevcut ürünler üzerindeki etkisi' gibi faktörleri değerlendirerek, projelerin pazardaki rekabetçi duruşlarını ve sürdürülebilirliklerini koruyabilmesi için çevresel etkilerin dikkate alınması gerektiğini savunmuştur. Eilat vd. (2008), projelerin yasal ve düzenleyici çevreye uyum sağlaması gerektiğini belirten 'düzenleyici etki' kriterini ele almışlardır. Aynı ekip, projelerin bilgi birikimi ve organizasyonel öğrenme süreçlerine katkıda bulunma kapasitesini değerlendiren 'öğrenme ve büyüme' kriterinin de uzun vadeli başarı için kritik olduğunu ifade etmiştir. Montajabiha vd. (2017), piyasa değişkenliklerinin projelerin ekonomik getirisini nasıl etkilediğini tartışmış ve 'yıllık piyasa

oynaklığı' kriterini incelemişlerdir. Henig ve Katz (1996), projelerin çevresel sürdürülebilirlik açısından nasıl değerlendirileceği üzerine yoğunlaşarak 'ortam uyumluluğu' kriterini ele almışlardır. Mohanty vd. (2005) ve Mohaghar vd. (2012), projelerin rekabetçi avantajlarını ve pazar paylarını koruma yeteneklerini, aynı zamanda yasal uyumluluklarını, sürdürülebilirliklerini ve toplumsal etkilerini ölçmek için kullanılan birden fazla kriter üzerinde durmuşlardır. Bu kriterler arasında 'rakiplerin benzer alanlarda gösterdiği çabalar', 'çevresel ekonomik düzenlemeler', 'çevre politikası', 'hükümet politikası', 'çevresel güvenlik hususları' ve 'çevresel sosyal ortam' bulunmaktadır.

Wang vd. (2005), projelerin enerji verimliliği ve malzeme tasarrufu konularında performansını ölçmenin önemine vurgu yapmıştır. Liberatore (1986), Mohanty vd. (2005), Mohaghar vd. (2012) ve Cheng vd. (2017), projelerin hammaddelere erişimi ve bu hammaddelerin projelere uygunluğunu değerlendirme gerekliliğine işaret ederek, altyapı ve ekipman kapasitelerinin optimizasyonunun önemini ortaya koymuşlardır. Kumar (2004), sürdürülebilir proje yönetimi için malzeme kaynakları ve sarf malzemelerinin mevcudiyetinin önemine dikkat çekmiştir. Meade ve Presley (2002), projelerin finansal performansını değerlendirmede 'Net bugünkü değer' kriterinin kullanılmasını önermiş ve bu kriterin finansal sürdürülebilirlik için kaynak yönetiminde temel bir rol oynadığını belirtmiştir. Karasakal ve Aker (2017), projelerin insan gücü ve diğer maddi kaynakların yönetimindeki etkinliğin önemini vurgulamıştır.

Eilat vd. (2008) ve Hesarsorkh vd. (2021), projelerin hem ticari başarı potansiyelini hem de teknik başarıya ulaşma yeteneğini değerlendiren 'Ticari ve teknik başarı olasılığı' kriterini ele almışlardır. Bu kriter, projelerin piyasa başarısını öngörmede önemli bir ölçüttür. Ayrıca, Liberatore (1986) ve Hesarsorkh vd. (2021), projelerin piyasadaki rekabetçi durumlarını ve pazar paylarını artırma kapasitelerini değerlendiren 'Pazar' kriterini ele almışlardır. Projelerin genel başarı potansiyelini değerlendiren 'Başarı Olasılığı' kriteri ise, Taylor vd. (1982), Madey ve Dean (1985), Liberatore (1986, 1987, 1988), Bard vd. (1988), Oral vd. (1991), Meade ve Presley (2002), Kahraman ve Tolga (2008) ve Cheng vd. (2017), tarafından ele alınmıştır. Bu kriter, projelerin genel performansını ölçmede önemli bir faktör olarak kabul edilmektedir. Risk yönetimi stratejilerinin geliştirilmesinde kritik olan 'Risk' kriteri ise, Gustafsson ve Salo (2005), Ghorbani vd. (2006), Bhattacharyya vd. (2011), Hassanzadeh vd. (2014), Bhattacharyya (2015), Heydari vd. (2016) ve Hesarsorkh vd. (2021), tarafından incelenmiştir. Bu çalışmalar, projelerin riskleri nasıl yönettiği ve bu yönetimin projelerin genel başarısına olan etkisini detaylandırmıştır.

Kumar (2004), projelerin müşteri gereksinimlerini net bir şekilde tanımlama kapasitesinin ve ekonomik olarak gerçekleştirilebilir olup olmadığını değerlendirmenin önemine vurgu yapmıştır. Bitman ve Sharif (2008), projelerin başarılı bir şekilde tamamlanması için gereken gerçeklerin ve bilginin toplanmasının önemine dikkat çekmiştir. Jeng ve Huang (2015), projelerin acil müşteri taleplerine yanıt verme kabiliyetini ve teknik planlarının detaylarını değerlendiren kriterlere odaklanmışlardır Mohanty vd. (2005) ve Mohaghar vd. (2012), projelerin müşteri gereksinimlerine uygun olarak sağladığı faydaların önemine vurgu yapmışlardır. Eilat vd. (2008) ve Ramalho (2021), projelerin piyasa gereksinimlerini ve organizasyonun stratejik hedefleriyle uyum içinde olma kapasitesini değerlendiren kriterlerin önemine dikkat çekmişlerdir.

Bitman ve Sharif (2008) ve Salehi vd. (2022), projelerin çevre üzerindeki olası ekolojik etkilerini ve etik değerlere uygunluğunu değerlendirmişlerdir. Hsu vd. (2003), projelerin güvenlik standartlarına uyum sağlama ve çevresel kirlilik risklerini minimize etme yeteneklerini incelemişlerdir. Karaveg vd. (2015), projelerin uzun vadeli çevresel sürdürülebilirliğe katkıda bulunma potansiyelini değerlendirmişlerdir. Stewart (1991), projelerin çevreye sağladığı olumlu etkileri ve insanların yaşam kalitesine olan katkılarını değerlendirmiştir. Eilat vd. (2008) projelerin ekip üyelerinin eğitimine ve beceri gelişimine olan katkılarını değerlendirmişlerdir. Kumar (2004), projelerin sosyal normlara ve toplumsal beklentilere ne derece uygun olduğunu incelemiştir. Karasakal ve Aker (2017) ve Hünermund ve Czarnitzki (2019), projelerin yeni iş imkanları yaratma potansiyelini değerlendirmişlerdir. Oral vd. (1991), Hsu vd. (2003), Wang vd. (2005), Conka vd. (2008), Wu vd. (2009), Oral (2012), Karasakal ve Aker (2017) ve Salehi vd. (2022), projelerin topluma sağladığı sosyal faydaları ve toplumsal gelişmeye olan katkılarını değerlendirmişlerdir.

Kumar (2004), mevcut projelerle olan uyum ve bağlantıları incelerken, Bhattacharyya (2015) projelerin diğer sistemlere veya projelere olan teknik bağımlılıklarını analiz etmiştir. Stewart (1991), projelerin gelecekteki iş fırsatlarına katkıda bulunma potansiyelini, Mohanty vd. (2005) ise mevcut ürünlerle teknik etkileşimleri değerlendirmiştir. Meade ve Presley (2002), projelerin diğer ürün ve süreçlere entegrasyon potansiyellerini ortaya koymuş, Oral vd. (1991) ise teknik yenilik yapma kapasitelerini vurgulamışlardır. Wang vd. (2005) projelerin teknik gelişimini ve yaratıcılığını, Jeng ve Huang (2015) ise yenilikçi teknolojiler geliştirme yeteneklerini incelemiştir. Bitman ve Sharif (2008) ve Conka vd. (2008) projelerin teknolojik yenilik kapasitelerine odaklanmış, Hsu vd. (2003) ise diğer teknolojilerle olan bağlantıları değerlendirmiştir. Imoto vd. (2008) projelerin karşılaştığı teknik zorlukları ele alırken, Karasakal ve Aker (2017) kullanılan teknolojilerin uygunluğunu ve etkinliğini değerlendirmiştir. Eilat vd. (2008), projelerin teknik bilgi birikimi ve beceri seviyesini incelemiş, Liberatore (1986) ve Jeng ve Huang (2015) ise projelerin teknik başarıya ulaşma olasılıklarını ve bu başarıyı etkileyen faktörleri analiz etmişlerdir.

Tablo 2. Proje değerlendirmede önerilen çeşitli boyut ve kriterler

Boyut	Kriter	Kaynak
Fayda	Ekonomik getiri	Czajkowski ve Jones (1986), Mavrotas ve Makryvelios (2021)
	Teknoloji geliştirme potansiyeli	Czajkowski ve Jones (1986), Mavrotas ve Makryvelios (2021)
	Beklenen net fayda	Beaujon vd. (2001)
	Mevcut sistemlerin modernizasyonunun ekonomik faydaları	Conka vd. (2008)
	Projelerin bilgi üretme kapasitesi	Conka vd. (2008)
	Kazanılmış değer	Eilat vd. (2008)
	Karlılık ve birim fiyat	Liberatore (1986), (1987), (1988), Cheng vd. (2017)
	Beklenen pazar payı ve müşteri kabulü	Liberatore (1986), (1987), (1988), Cheng vd. (2017)
Çevresel Gelir	Fiyatlandırma eğilimi	Liberatore (1986)
	Mülkiyet sorunu	Liberatore (1986)
	Coğrafi kapsam	Liberatore (1986)
	Mevcut ürünlere etkisi	Liberatore (1986)
	Düzenleyici etki	Eilat vd. (2008)
	Öğrenme ve büyüme	Eilat vd. (2008)
	Yıllık piyasa oynaklığı	Montajabiha vd. (2017)
	Ortam uyumluluğu	Henig ve Katz (1996)
	Çevresel ekonomik düzenlemeler	Mohanty vd. (2005), Mohaghar vd. (2012)
	Çevre politikası ve hükümet politikası	Mohanty vd. (2005), Mohaghar vd. (2012)
	Çevresel güvenlik hususları ve sosyal ortam	Mohanty vd. (2005), Mohaghar vd. (2012)
Kaynak	Enerji verimliliği	Wang vd. (2005)
	Malzeme tasarrufu	Wang vd. (2005)
	Hammaddelere erişim	Liberatore (1986), Mohanty vd. (2005), Mohaghar vd. (2012), Cheng vd. (2017)
	Mevcut altyapı ve ekipman	Liberatore (1986), Mohanty vd. (2005), Mohaghar vd. (2012), Cheng vd. (2017)
	Malzeme kaynaklarının mevcudiyeti	Kumar (2004)
	Net bugünkü değer (NBD)	Meade ve Presley (2002)
	İnsan gücü ve maddi kaynakların yönetimi	Karasakal ve Aker (2017)
Risk	Ticari ve teknik başarı olasılığı	Eilat vd. (2008), Hesarsorkh vd. (2021)
	Pazar ve rekabet	Liberatore (1986), Hesarsorkh vd. (2021)
	Başarı olasılığı	Taylor vd. (1982), Madey ve Dean (1985), Liberatore (1986), (1987), (1988), Bard vd. (1988), Oral vd. (1991), Meade ve Presley (2002), Kahraman ve Tolga (2008), Cheng vd. (2017)
	Risk yönetim stratejileri	Gustafsson ve Salo (2005), Ghorbani vd. (2006), Bhattacharyya vd. (2011), Hassanzadeh vd. (2014), Bhattacharyya (2015), Heydari vd. (2016), Hesarsorkh vd. (2021)
Gereksinimler	Müşteri gereksinimlerini tanımlama kapasitesi	Kumar (2004)
	Proje gereksinimlerinin toplanması	Bitman ve Sharif (2008)
	Acil müşteri taleplerine yanıt verme	Jeng ve Huang (2015)
	Müşteri gereksinimlerine uygun fayda sağlama	Mohanty vd. (2005), Mohaghar vd. (2012)
	Piyasa gereksinimlerine uyum	Eilat vd. (2008), Ramalho (2021)
Sosyal ve Çevre Etkisi	Çevresel ekolojik etki	Bitman ve Sharif (2008), Salehi vd. (2022)
	Güvenlik standartlarına uyum	Hsu vd. (2003)
	Çevresel sürdürülebilirlik	Karaveg vd. (2015)
	Yaşam kalitesine katkı	Stewart (1991)
	Eğitim ve beceri gelişimi	Eilat vd. (2008)
	Sosyal normlara uygunluk	Kumar (2004)
	Yeni iş imkanları yaratma	Karasakal ve Aker (2017), Hünermund ve Czarnitzki (2019)
	Toplumsal gelişmeye katkı	Oral vd. (1991), Hsu vd. (2003), Wang vd. (2005), Conka vd. (2008), Wu vd. (2009), Oral (2012), Karasakal ve Aker (2017), Salehi vd. (2022)
Teknik	Mevcut projelerle uyum	Kumar (2004)
	Teknik bağlantılar	Bhattacharyya (2015)
	İş fırsatlarına katkı	Stewart (1991)
	Mevcut ürünlerle teknik etkileşim	Mohanty vd. (2005)
	Diğer ürün ve süreçlerle entegrasyon	Meade ve Presley (2002)
	Teknik yenilik yapma kapasitesi	Oral vd. (1991)
	Teknik gelişim ve yaratıcılık	Wang vd. (2005)
	Yenilikçi teknolojiler geliştirme	Jeng ve Huang (2015)
	Teknolojik yenilik kapasitesi	Bitman ve Sharif (2008), Conka vd. (2008)
	Teknolojik bağlantılar	Hsu vd. (2003)
	Teknik zorluklar	Imoto vd. (2008)
	Teknoloji uygunluğu ve etkinliği	Karasakal ve Aker (2017)
	Teknik bilgi birikimi	Eilat vd. (2008)
	Teknik başarıya ulaşma olasılığı	Liberatore (1986), Jeng ve Huang (2015)

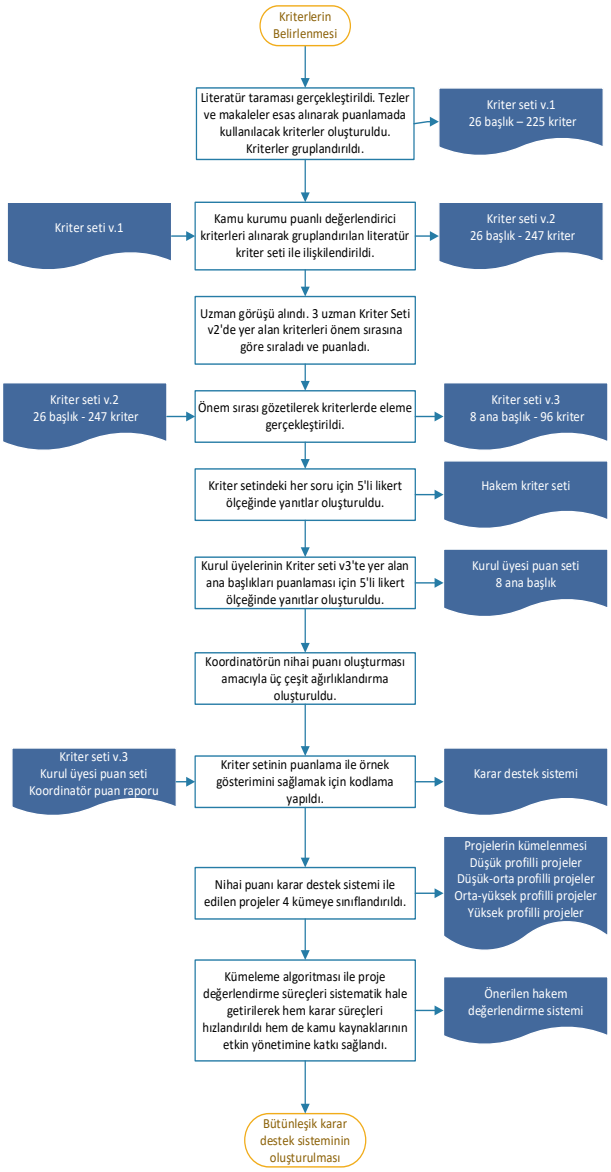
Tablo 2'de sunulan kriterler, Ar-Ge projelerinin değerlendirilmesi için kullanılan kriterlerin çok yönlü ve kapsamlı bir bakış açısı sağladığını ortaya koymaktadır. Ekonomik getiri, teknoloji geliştirme potansiyeli, pazar ve müşteri kabulü, düzenleyici etkiler, çevresel sürdürülebilirlik, proje kaynaklarının yönetimi ve teknik uyum gibi kriterler, projelerin başarıya ulaşma olasılıklarını artıran temel göstergeler olarak dikkat çekmektedir. Bu kriterlerin, bütçe ve zaman planlamasından çevresel etkilere ve toplumsal katkıya kadar uzanan geniş bir çerçevede değerlendirilmesi, projelerin daha etkin ve sürdürülebilir şekilde yönetilmesini sağlamaktadır.

Sunulan bu değerlendirme kriterleri, projelerin farklı yönlerini nesnel, yapılandırılmış ve bütüncül bir değerlendirme süreci içerisinde ele alarak başarıya ulaşmalarına katkı sağlamaktadır. Ayrıca, yenilikçilik düzeyi, uygulanabilirlik, risk yönetimi, stratejik uyum ve sosyal/çevresel etki gibi boyutlarda kapsamlı analizlere olanak tanımaktadır.

Çalışmanın bir sonraki bölümünde, kriterlerin belirlenmesi, elenmesi ve ağırlıklandırılması süreci ile birlikte önerilen karar destek sistemi ayrıntılı biçimde açıklanacaktır. Üçüncü bölümde, geliştirilen yöntemin uygulandığı kurumsal analiz bulgularına yer verilmekte; son bölümde ise elde edilen sonuçlar ve tartışmalar sunulmaktadır.

2. Materyal ve Yöntem

Bu bölümde, teknoloji geliştirme amacıyla gerçekleştirilen Ar-Ge projelerinin değerlendirilmesine yönelik kapsamlı çalışmalar ele alınmaktadır. İlk olarak, projelerin çok boyutlu ve objektif bir şekilde değerlendirilmesi için gerekli kriterler belirlenmiş ve veri toplama süreci tamamlanmıştır. Belirlenen kriterler, entropi yöntemi kullanılarak ağırlıklandırılmış ve projelerin daha doğru bir şekilde puanlanması sağlanmıştır. Ek olarak, daha hassas bir eleme mekanizması oluşturmak amacıyla kriterler, iki aşamalı bir filtreleme sürecinden geçirilmiştir. Bu süreç, değerlendirme kalitesini artırmak amacıyla tasarlanmış bir karar destek sistemini kapsamaktadır. Sistem, benzer özelliklere sahip projeleri gruplamak ve daha stratejik, hedef odaklı değerlendirmeler yapmak için kümeleme analizi yöntemini kullanmaktadır. Hakem değerlendirme süreci için önerilen yöntem ve geliştirilen karar destek sistemi için çalışma kapsamında gerçekleştirilen adımlar Şekil-1'deki akış diyagramı ile verilmiştir.



Şekil 1. Proje değerlendirme sistem önerisi iş akışı.

2.1. Veri Toplama ve Kriter Belirleme

Veri toplama aşamasında, Türkiye'deki Ar-Ge projelerini destekleyen araştırma kurumlarının proje değerlendirme süreçlerine odaklanılmıştır. Çalışmada, kurum uzmanlarının geri bildirimleri ve önceki projelerden elde edilen veriler temel alınarak analizler gerçekleştirilmiştir. Literatür taraması sonucunda yaygın kabul gören 247 değerlendirme kriteri belirlenmiş ve bu kriterler, mantıksal bütünlük gözetilerek sınıflandırılmalarına olanak sağlayacak şekilde yapılandırılmıştır. Kriterler; fayda, çevresel gelir, kaynak, risk, gereksinimler, sosyal ve çevresel etki, strateji ve teknik olmak üzere sekiz ana grup altında toplanmıştır.

2.2. Kriterlerin Ön Elemeden Geçirilmesi

Ar-Ge projelerinin değerlendirilmesinde kritik kriterleri belirlemek ve değerlendirme sürecinin optimize edilmesi amacıyla iki aşamalı bir metodolojik yaklaşım benimsenmiştir. Söz konusu yaklaşım; kriter seçimi, ağırlıklandırma ve sıralama adımlarında nesnel ve

bütüncül bir yapı sunarak değerlendirme sürecinin tutarlılığını ve karar kalitesini artırmayı hedeflemektedir. İlk aşamada, değerlendirme sürecinin uzmanlık ve tecrübe gereksinimleri göz önünde bulundurularak, alanda uzman üç karar verici seçilmiştir. Bu kişiler, sektörde uzun yıllara dayanan deneyime sahip uzmanlardan seçilmiş olup, kararların kişisel önyargılardan arındırılması hedeflenmiştir. Başlangıçta g = 26 boyut altında değerlendirilen toplam kriter sayısı n = 247'dir. Her bir kriter, karar vericiler tarafından göreli önceliklerine göre sıralanmış ve bu sıralamalar, geometrik ortalama yöntemiyle birleştirilerek ortak öncelik düzeyi hesaplanmıştır (eşitlik 1):

$$G_{gj} = \sqrt[m]{\prod_{i=1}^{m} T_{gji}} \quad i = 1.2. \ldots . m \tag{1}$$

Burada, G_{gj}, g grubunda yer alan *j*-inci kriterin geometrik ortalaması, T_{gji}, g grubundaki *j*-inci kriter için *i*-inci karar vericinin verdiği puan, *m* karar verici sayısıdır.

Tüm kriterler için geometrik ortalamalar eşitlik 1 ile hesaplanmış, ardından geometrik ortalamaların medyanı grup bazlı olarak alınmıştır. g grubu için geometrik ortalamayı temsil eden G_g'nin medyanı ise eşitlik 2'deki gibi hesaplanmıştır:

$$Med(G_g) = \begin{cases} G_g\left[\dfrac{n+1}{2}\right] & n: tek\ sayı\ ise \\ \dfrac{G_g\left[\frac{n}{2}\right] + G_g\left[\frac{n}{2}+1\right]}{2} & n: çift\ sayı\ ise \end{cases} \tag{2}$$

Her bir grupta grup medyanından büyük ortalamaya sahip kriterler alınarak diğerleri elenmiştir (eşitlik 3):

$$\text{Elenen Kriterler} = \{j \mid G_{gj} > Med(G_g)\} \tag{3}$$

Burada j medyan değerin üstünde geometrik ortalama puanına sahip kriterleri ifade eder.

Bu eleme ile kriter sayısı $n = 247$'den $n_{reduced1} = 131$'e düşürülmüştür.

İkinci aşamada, kriterler yeniden düzenlenmiştir; bu düzenleme kapsamında anlam ve içerik açısından birbirine yakın olan kriterler birleştirilerek, mevcut g = 26 grup $g_{reduced} = 8$ ana grup altında yeniden yapılandırılmıştır. Bu süreçte, kriterler tematik ve işlevsel benzerliklerine göre analiz edilerek yeniden yapılandırılmıştır. Öncelikle, her bir kriterin tanımı ve kapsamı ayrıntılı olarak incelenmiş, içeriksel örtüşme gösteren ve benzer kavramsal çerçevede değerlendirilebilecek olanlar tespit edilmiştir. Söz konusu analiz, alanında tecrübeli üç uzmanın yer aldığı karar vericiler tarafından gerçekleştirilmiş; kriterler, anlam ve işlevsel yönleri birlikte ele alınarak kavramsal bütünlüğe sahip temalar altında gruplanmıştır. Örneğin, "beklenen getiri", "proje çalışmasından elde edilecek sonuçların ülkeye kazandırabileceği bilgi birikimi" ve "beklenen pazar payı" gibi finansal fayda ve finansal olmayan fayda gibi benzer içerikli kriterler "Fayda Boyutu" başlığı altında birleştirilmiştir. Gruplama sürecinde, tematik kodlama ve içerik analizi yaklaşımlarından yararlanılarak, anlam bütünlüğü taşıyan üst başlıklar altında stratejik yönlendirme sağlayan bir yapı kurgulanmıştır. Sonuç olarak, 26 kriter, aralarındaki ilişkileri daha açık şekilde yansıtan 8 ana grup altında toplanmış; böylece değerlendirme süreci daha bütüncül, sadeleştirilmiş ve yönetilebilir bir forma kavuşturulmuştur.

İlk elemenin ardından, karar vericilerden, puanlamaların ötesinde, kriterlerin öncelik sırasını belirlemek için sıralama stratejileri de talep edilmiştir. Bu yaklaşım, özellikle eşit puan almış kriterler arasında daha ayrıntılı bir ayırım yapılmasını sağlamıştır. Nihai olarak, kriterlerin ağırlıklarını nesnel veriye dayalı biçimde hesaplamak üzere, bilgi temelli bir yaklaşım olan entropi yöntemi uygulanmıştır. Bu çok ölçütlü karar verme yöntemi, kriterler arası karşılaştırmalarda adil ve tutarlı bir ölçüm sunarak, projelerin kapsamlı bir şekilde değerlendirilmesine olanak tanımıştır.

2.3. Kriter Ağırlıklandırma – Entropi Yöntemi

Kriterlerin önceliklendirilmesi ve ağırlıklandırılması, entropi yöntemi kullanılarak gerçekleştirilmiştir. Entropi kavramı, bilim ve mühendislik dalları olan fizik, bilgi teorisi ve matematik, termodinamik alanında gelişmiş ve ardından bilgi entropisi ortaya çıkmıştır. Entropi ilk olarak, Rudolph tarafından 1865'de termodinamik alanında geliştirilmiş ve 1948'de Shannon tarafından bilgi entropisi kavramı ortaya atılmıştır (Zhang, 2011). ÇKKV problemlerinde, kriterlerin önem düzeylerinin ortaya çıkarılmasında kullanılan bu yöntem, ağırlıkların hesaplanması için objektif bir değerlendirme yöntemidir (Ömürbek ve Aksoy, 2016). Kriterlerin entropisi, kriterlerin önem derecelerini yansıtmaktadır. Daha yüksek entropiye sahip olan bir kriter, daha fazla bilgi veya belirsizlik içermekte ve dolayısıyla daha düşük bir ağırlığa sahip olabilmektedir. Bu şekilde, entropi kullanarak kriterlere ağırlık atayarak veya kriterlerin önem sıralamasını yaparak karar verme sürecinde daha dengeli ve bilgi temelli bir yaklaşım elde edilebilmektedir. Entropi yöntemi 5 adımdan oluşmaktadır (Karami ve Johansson 2013; Wang ve Lee 2019).

Adım 1: Karar matrisi (*X*) oluşturulur.

Karar matrisi, karar vericiler tarafından sürecin başlangıcında oluşturulan matristir. Satırlarında sıralanmak istenilen karar seçenekleri, sütunlarında ise ölçütler yer alır (eşitlik 4).

$$X = \begin{bmatrix} x_{11} & x_{12} & \ldots & x_{1m} \\ x_{21} & x_{22} & \ldots & x_{2m} \\ . & . & . & . \\ . & . & . & . \\ . & . & . & . \\ x_{n1} & x_{n2} & \ldots & x_{nm} \end{bmatrix} \tag{4}$$

Adım 2: Karar matrisi normalize edilir. Normalize karar matrisi (*N*) oluşturulurken ölçütlerdeki minimum ya da maksimum amaca bakılmaksızın (eşitlik 5).

$$P_{ij} = \frac{x_{ij}}{\sum_{i=1}^{m} x_{ij}} \quad (5)$$

eşitliğine göre *X* karar matrisi normalize edilir.

Adım 3: Her bir kriterin entropi ölçüsü hesaplanır.
Bu çalışmada kullanılan entropi yöntemi, Shannon Entropisi'ne dayanmaktadır. Shannon (1948) tarafından geliştirilen bu yöntem, bilgi teorisine dayalı olarak her bir kriterin bilgi belirsizliğini ölçmeyi ve bu sayede kriterin ayırt ediciliğini belirlemeyi amaçlar.
Entropi değeri eşitlik 6 yardımıyla bulunur.

$$E_j = -h\sum_{i=1}^{m} P_{ij}\ln(P_{ij})\ \ i = 1.2.\ldots.m, j = 1.2.\ldots.n \quad (6)$$

Eşitlik 6'da *h* bir sabiti temsil eder ve formülü (eşitlik 7)

$$h = \frac{1}{\ln(m)} \quad (7)$$

ile gösterilir.

Adım 4: Kriterlerin farklılaşma derecesi eşitlik 8 yardımıyla hesaplanır.

$$d_j = 1 - E_j\ j = 1.2.\ldots.n \quad (8)$$

Dj, *j* yapısında mevcut olan bir karşıtlık yoğunluğunu gösterir.

Adım 5: Kriter ağırlıkları eşitlik 9 kullanılarak hesaplanır.

$$w_j = \frac{d_j}{\sum_{j=1}^{n} d_j}\ j = 1.2.\ldots.n\ 0 \le w_j \le 1 \text{ ve } \sum_{j=1}^{n} w_j \quad (9)$$

Entropi yöntemi kullanılarak kriter ağırlıkları belirlendikten sonra, ikinci aşama eleme süreci, kriterlerin dörtte birlik (quartile) değerlerine göre gerçekleştirilmiştir. Bu işlem sonucunda, 35 kriter daha elenerek toplam kriter sayısı $n_{reduced2} = 96$'ya düşürülmüştür. Sonuçta kategori altında 96 kriter elde edilmiş ve hakem değerlendirme süreci için sistematiğin belirlenmesi sağlanmıştır.

2.4. Karar Destek Sistemi

Kriter ağırlıklarının belirlenmesinin ardından, bu kriterleri kullanarak projeleri değerlendirmek amacıyla 'ECLIPSE', bir açık kaynak kodlu ve Java tabanlı platformda özel bir karar destek sistemi geliştirilmiştir. Bu sistem, hakemler, grup yürütme kurulu üyeleri ve grup koordinatörleri için özelleştirilmiş kullanıcı arayüzleri sunmaktadır.
Mevcut sistemde, hakem değerlendirmeleri ortalama alınarak hesaplanmakta, yürütme kurulu üyeleri ise projelere -10 ile +10 arasında ek puan verebilmektedir. Önerilen sistemde ise bu yapı genişletilmiş; yürütme kurulu üyelerine projelere 0 ile 100 arasında puan verme imkânı tanınmıştır. Böylece puanlama ölçeği daha esnek ve karşılaştırılabilir bir yapıya kavuşturulmuştur.
Hakem ve kurul puanlarının nihai puana etkisi, farklı ağırlıklandırma senaryoları ile yapılandırılmıştır. Bu bağlamda, %80 hakem – %20 yürütme kurulu, %70 hakem – %30 yürütme kurulu ve %60 hakem – %40 yürütme kurulu şeklindeki üç farklı oran senaryosu uygulanmıştır. Bu senaryolar, karar vericilere projeleri çeşitli stratejik yaklaşımlar altında değerlendirme esnekliği sağlamaktadır.

2.5. Kümeleme Analizi ve Hiperparametre Seçimi

K-ortalamalar algoritması (k-means), kümeleme analizlerinde en yaygın kullanılan yöntemlerden biridir (Forgy, 1965; MacQueen, 1967). Bu algoritma, veri setini önceden belirlenmiş k adet kümeye ayırmayı ve her küme için ortalama bir merkez (centroid) belirleyerek veri noktalarını en yakın merkeze atamayı hedefler. Temel amacı, kümeler içi varyansı en aza indiren bir yapı oluşturmaktır. Bu bağlamda, algoritmanın minimize etmeyi hedeflediği amaç fonksiyonu şu şekilde tanımlanabilir (Xu ve Wunsch, 2008) (eşitlik 10).

$$E(C) = \sum_{j=1}^{k}\sum_{x_i \in C_j} \|x_i - c_j\|^2 \quad (10)$$

Burada, k toplam küme sayısını, C_j j-inci kümeyi, c_j j-inci kümenin merkezini, x_i, C_j kümesine ait bir veri noktası temsil etmektedir. $\|x_i - c_j\|^2$ ise veri noktalarının küme merkezine olan uzaklığının karesidir. Her iterasyonda, veri noktaları en yakın merkeze atanır ve küme merkezleri yeniden hesaplanır. Atama kuralı şu şekilde ifade edilebilir (Xu ve Wunsch, 2008) (eşitlik 11):

$$x_j \in C_l\ eğer\ \|x_j - m_l\| < \|x_j - m_i\|, i \neq l\ ve\ i = 1,\ldots,K, j = 1,\ldots,N \quad (11)$$

Burada, x_j veri noktalarından biri olup, kendisine en yakın küme merkezine atanması sağlanır. Daha sonra, her bir kümenin yeni merkezi ilgili kümede yer alan veri noktalarının ortalaması alınarak güncellenir (eşitlik 12).

$$m_i = \frac{1}{N_i}\sum_{x_j \in C_i} x_j \quad (12)$$

Bu yinelemeli süreç, küme merkezlerinin değişmediği ya da belirlenen maksimum iterasyon sayısına ulaşıldığı noktaya kadar devam eder.
K-ortalamalar algoritması, küme merkezlerine olan uzaklıkları hesaplamak için farklı mesafe ölçütleri kullanabilir. En yaygın ölçüt Öklidyen mesafedir; bu metrik, koordinat farklarının kareleri üzerinden benzerliği değerlendirir (Ghazal, 2021; Syakur vd. 2018) (eşitlik 13).

$$d = \sqrt{(x_2 - x_1)^2 + (y_2 - y_1)^2} \quad (13)$$

K-ortalamalar kümeleme algoritmasının başarısı, merkez noktalarının (centroid) başlangıç pozisyonlarına oldukça duyarlıdır. Bu sebeple, k-ortalamalar algoritması farklı başlangıç merkez dağılımlarıyla tekrarlanabilir. Alternatif olarak, Arthur ve Vassilvitskii (2006) tarafından önerilen k-ortalamalar++ yöntemi kullanılabilir. K-ortalamalar++ başlangıç merkez dağılımlarını seçmek için kullanılan bir yöntemdir ve dört ana adımdan oluşur:

Adım 1: İlk merkez noktası (m_1) rastgele bir veri noktası (y_i) olarak seçilir.
Adım 2: Her y_i için en yakın merkez noktasına olan mesafe *F(y)* hesaplanır.
Adım 3: Seçilmeyen veri noktaları arasından (y_i'), yeni bir merkez noktası (m_1), $\frac{F(y_i')^2}{\sum F(y_i')^2}$ olasılığıyla seçilir.
Adım 4: Merkez noktalarının sayısı *k*'ya ulaşana kadar Adım 2 ve 3 tekrarlanır.

Bir veri seti için optimal küme sayısını belirlemek, k-ortalamalar kümeleme algoritmasının en kritik aşamalarından biridir (Shahapure ve Nicholas, 2020). Bu amaçla en yaygın kullanılan yöntemler Dirsek (Elbow) ve Silhouette yöntemleridir.

Dirsek yöntemi, küme sayısının belirlenmesine yönelik sezgisel bir yöntemdir ve küme içi hata kareler toplamı (Within-Cluster Sum of Squares - WCSS) değerini temel almaktadır. Bu yöntemde, farklı küme sayıları için WCSS hesaplanarak bir grafik oluşturulmaktadır. Küme sayısı arttıkça, WCSS değeri azalmaktadır, ancak belirli bir noktadan sonra azalma oranı yavaşlamakta ve grafik üzerinde bir "dirsek" şeklinde bir kırılma meydana gelmektedir. Bu kırılma noktası, optimum küme sayısının belirlendiği noktayı ifade etmektedir (Ketchen ve Shook, 1996).

Silhouette yöntemi ise, her bir veri noktasının kendi kümesi ile ne kadar iyi eşleştiğini ve diğer kümelerden ne kadar ayrıldığını değerlendiren bir tekniktir. Rousseeuw tarafından 1987 yılında önerilen bu yöntem, kümeleme sonuçlarının doğruluğunu ölçmek için kullanılmaktadır. -1 ile 1 arasında değer alan Silhouette değeri, kümeleme başarısını gösterir ve en yüksek değere sahip küme sayısı ideal kabul edilir.

K-ortalamalar algoritması için Orange Data Mining (Demšar vd. 2004) yazılımında yer alan k-ortalamalar++ başlatma yöntemi (Arthur & Vassilvitskii, 2006) kullanılmıştır. Bu yöntem, ilk küme merkezlerinin seçiminde rastgeleliğe dayalı yaklaşımlara kıyasla daha dengeli ve kararlı merkezler oluşturarak, kümeler arası ayrımın iyileştirilmesine katkı sağlamaktadır. Literatürde, frekans poligonlarına dayalı olarak çalışan InoFrep algoritması (Cebeci & Cebeci, 2020) gibi alternatif başlatma yöntemleri de mevcuttur. InoFrep, verideki yoğunluk merkezlerini belirleyerek deterministik ve veri yapısına duyarlı bir başlatma sağlamaktadır. Ancak bu çalışmada kullanılan yazılım altyapısında k-ortalamalar++ yöntemi bulunduğundan, analizler bu yöntemle gerçekleştirilmiştir.

Projelerin tüm kriterler ve ek puanlamalar üzerinden hesaplanan toplam değerlendirme puanları esas alınarak, k-ortalamalar kümeleme algoritması ile dört farklı kategoriye ayrılması sağlanmıştır: 'Yüksek profilli', Orta-yüksek profilli', 'Düşük-orta profilli' ve 'Düşük profilli'. Küme sayısı (k = 4), Ar-Ge proje değerlendirme pratiğinde sıklıkla kullanılan dört profilli yapı esas alınarak belirlenmiştir.

Küme sayısının uygunluğunu değerlendirmek amacıyla Elbow yöntemi, Silhouette Skoru, Calinski-Harabasz ve AIC (Akaike Information Criterion) gibi yaygın geçerlilik metrikleri kullanılmıştır. Çalışmanın amacı yalnızca matematiksel olarak en ayrışmış kümeleri tespit etmek değil, aynı zamanda Ar-Ge proje değerlendirme pratiğinde kurumsal karar alma süreçlerine anlamlı ve uygulanabilir sınıflamalar sunmaktır. Bu doğrultuda, k = 4 değeri, hem istatistiksel geçerliliği hem de kurumun benimsediği dört profilli değerlendirme yaklaşımıyla olan uyumu nedeniyle uygun ve uygulanabilir bir çözüm olarak değerlendirilmiştir. Özellikle Elbow analizinde k = 4 için elde edilen %37,9'luk inertia düşüşü, bu küme sayısının hâlâ güçlü bir ayrım sunduğunu göstermektedir. Tablo 3'te görüldüğü üzere, k = 3 istatistiksel olarak optimal bir değer olarak öne çıkmakla birlikte, k = 4 uygulama açısından daha tercih edilebilir bir denge noktası sunmaktadır.

Tablo 3. Elbow yöntemi inceleme sonuçları

k	Inertia	Göreli Azalma
2	33,220	–
3	18,684	%43.8 düşüş
4	11,597	%37.9 düşüş
5	7,614	%34.3 düşüş
6	5,822	%23.5 düşüş

K- ortalamalar algoritmasına ilişkin hiperparametreler şu şekilde yapılandırılmıştır:

- Başlatma yöntemi: k- ortalamalar++, daha dengeli ve kararlı başlangıç merkezleri oluşturmak amacıyla kullanılmıştır.
- Maksimum iterasyon sayısı: 300 (Orange yazılımının varsayılan ayarı)
- Başlangıç tekrar sayısı: 10 (rastgele merkez seçiminin etkisini azaltmak amacıyla)
- Mesafe ölçütü: Öklidyen mesafesi
- Tolerans değeri: 1e-4 (varsayılan)

Bu hiperparametre ayarları, çalışmada kullanılan veri kümesinin özellikleri (örneklem büyüklüğü, varyans düzeyi) dikkate alınarak belirlenmiştir.

3. Bulgular

Hakem değerlendirme süreçlerinin güvenilirliğini etkileyen faktörler, özellikle Ar-Ge projeleri bağlamında daha karmaşık bir yapı sergilemektedir. Literatürde bu süreçleri etkileyen başlıca unsurlar arasında; hakemlerin alan uzmanlığı, değerlendirme kriterlerinin açıklığı ve ağırlıklandırma biçimi, değerlendirme süresinin yeterliliği, başvuru sayısına bağlı iş yükü yoğunluğu, çıkar çatışmaları, öznel yargı etkisi ve sistematik ön yargılar öne çıkmaktadır (Stelmakh vd., 2019; Sun vd., 2021; Heyard vd., 2021). Özellikle sanayi odaklı Ar-Ge projelerinde; yenilikçilik, uygulanabilirlik, ekonomik katkı ve teknik yeterlilik gibi çok boyutlu kriterlerin öznel yorumlara açık olması, değerlendirme sürecinde önemli tutarsızlıklara yol açabilmektedir. Bu bağlamda, önerilen sistemin temel amacı; karar vericiler arası

sapmaları azaltmak, tutarlılığı artırmak ve yerleşik önyargıları dengeleyen bir karar destek mekanizması sunmaktır.

Bu doğrultuda, geliştirilen karar destek sisteminin ilk adımı olarak, Ar-Ge projelerinin nesnel biçimde değerlendirilebilmesi amacıyla ölçülebilir ve ayrıştırıcı özellik taşıyan kriterlerin belirlenmesi ve önem derecelerine göre sıralanması hedeflenmiştir. Bu süreç, çalışmanın bulgular bölümü kapsamında ilk olarak kriterlerin belirlenmesi ve derecelendirilmesine ilişkin analizlerle başlatılmıştır.

3.1. Kriterlerin Belirlenmesi ve Derecelendirilmesi

Mevcut literatür ve araştırma kurumunun belirlediği değerlendirme kriterleri birleştirilerek toplamda 247 kriter oluşturulmuştur. Bu kriterler, deneyimli karar vericiler tarafından incelenmiş ve önem derecelerine göre sıralanmıştır.

İlk eleme sürecinde, 247 kriterin her biri için karar verici puanlarının geometrik ortalamaları eşitlik 1 ile hesaplanmış, eşitlik 2 ile grup bazında medyan değerleri bulunmuştur. Medyanın üzerinde kalan kriterler eşitlik 3 ile elenmiş ve böylece ilk filtreleme süreci tamamlanmıştır. Örneğin, 'Finansal Fayda' kategorisinde yer alan 14 kriter için, karar vericilerin sıralamaları baz alınarak geometrik ortalamaları hesaplanmış, bu ortalamanın medyan değeri olan 5,444 değerinin üstündeki geometrik ortalamaya sahip kriterler elenmiştir. Kriterlerin hesaplama sistematiği Tablo 4'te gösterilmiştir.

Tablo 4. 'Finansal fayda' kriteri için eleme yaklaşımı

Finansal Fayda Kriteri	KV1	KV2	KV3	Geo.Ort
Fayda veya ödeme etkileşimi	5	3	12	5.646
Beklenen net fayda	12	4	6	6.604
Değiştirme yerine sistemin modernleştirilmesiyle sonuçlanan beklenen tasarruf	2	5	7	4.121
Kazanılmış değer	11	1	5	3.803
Karlılık	6	6	4	5.241
Kar	1	3	4	2.289
Net bugünkü değer	9	3	12	6.868
Ekonomik	10	8	8	8.618
Beklenen getiri	4	2	3	2.884
Ürünün büyüme potansiyeli	8	7	2	4.820
Kârlılık potansiyeli, üretkenlik ve maliyette iyileştirmeler	3	3	1	2.080
Getiri bugünkü değeri	13	9	9	10.174
Gerçek opsiyon değeri	7	10	10	8.879
Hedef ürünlerin katma değeri	14	11	11	11.921
Medyan: 5.444				

Bu işlem tüm kriterler için uygulanmış ve kriter sayısı $n = 247$'den $n_{reduced1} = 131$'e indirgenmiştir. Ardından, içerik ve anlam açısından birbirine yakın olan kriterler birleştirilerek 26 grup altında yer alan 131 kriter, 8 ana grup altında yeniden düzenlenmiştir. Örneğin 'Finansal Fayda', 'Finansal Olmayan Fayda' ve 'Pazar Potansiyeli ve Çekicilik' kategorileri birleştirilerek 'Fayda Boyutu' kategorisi altında birleştirilmiştir. Birleştirilerek elde edilen yeni kategoriler için de ağırlık hesaplayabilmek adına karar vericilerce yeniden puanlama ve sıralandırma yapılmıştır. Her bir karar verici altında yer alan iki değer, sırasıyla ilgili kriterin göreli önceliğini gösteren sıralamayı (rank) ve bu sıralamaya karşılık gelen değerlendirme puanını (score) ifade etmektedir. Bu bilgiler Tablo 5'te sunulmaktadır.

Tablo 5: Karar vericiler tarafından sıralandırılan ve puanlanan ana boyutlar

	Ana Boyutlar	KV1		KV2		KV3	
1	Fayda Boyutu	2	5	1	5	2	5
2	Çevresel Gelir Boyutu	1	5	2	4	3	4
3	Kaynaklar Boyutu	4	3	3	4	4	4
4	Risk Boyutu	6	3	5	3	6	3
5	Kapsam Gereksinimleri	5	3	6	2	5	4
6	Sosyal ve Çevresel Etki	8	2	8	1	8	3
7	Strateji Boyutu	7	3	4	4	7	4
8	Teknik Boyut	3	4	7	2	1	5

3.2. Entropi Yöntemi ile Ağırlıklandırma

Sonraki adımda, kriterlerin ağırlıkları entropi yöntemiyle hesaplanmıştır. Bu yöntem, her bir kriterin taşıdığı bilgi miktarını ve belirsizlik düzeyini analiz ederek önem derecelerini objektif biçimde belirlemiştir. Hesaplanan ağırlıklar, karar verme sürecine doğrudan entegre edilmiştir. Örnek olarak, 'Finansal fayda' kriteri için eşitlik 6 kullanılarak entropi ölçüsü *Ej*, eşitlik 8 kullanılarak farklılaşma derecesi *dj* ve eşitlik 9 kullanılarak ağırlıklar *wj* hesaplanmış ve sonuçlar Tablo 6'da gösterilmiştir.

Kriter ağırlıkları hesaplandıktan sonra, her bir kriterin alt kriterlerinde dörtte birlik kullanılarak bir eleme daha gerçekleştirilmiş ve bu süreç sonucunda 35 kriter daha çıkartılarak kriter sayısı nihai olarak $n_{reduced1} = 131$'den $n_{reduced2} = 96$'ya indirilmiştir.

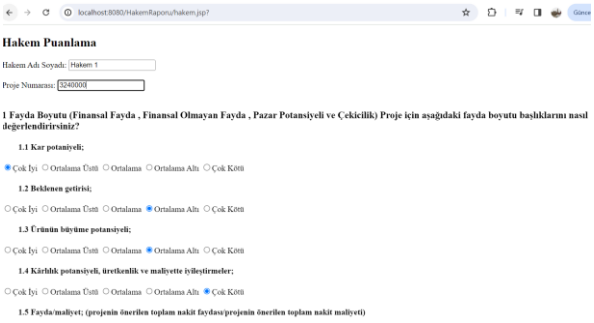
3.3. Karar Destek Sistemi Geliştirilmesi

Son aşamada ağırlıkları belirlenen 96 kriter, 5'li Likert ölçeğine ('Çok İyi', 'Ortalama Üstü', 'Ortalama', 'Ortalama Altı' ve 'Çok Kötü') uyarlanarak soru formatına dönüştürülmüştür. Bu dönüşüm, hakem değerlendirmelerinin bütüncül ve entegre bir yapıda yürütülmesini sağlamayı amaçlamaktadır. Geliştirilen sistem, hakemlerin Likert ölçeği üzerinden yanıtlayabilecekleri bir puanlama arayüzü sunmakta ve proje değerlendirmelerine kolayca entegre edilebilmektedir. Java tabanlı açık kaynak kodlu ECLIPSE (Eclipse Foundation, 2024) platformu kullanılarak geliştirilen ve Apache Tomcat sunucusu üzerinde çalışan

bu web tabanlı uygulama, kullanıcılarının projelere özel olarak tasarlanmış ekranlarla erişmesini ve değerlendirme süreçlerini yürütmesini kolaylaştırmaktadır. Hakemler, yürütme kurulu üyeleri, koordinatörler ve diğer ilgili kullanıcılar için tanımlanmış erişim seviyeleri sayesinde, değerlendirme süreçleri daha düzenli ve etkin bir biçimde yönetilebilmektedir. Bu yapılandırılmış yaklaşım, kriter ağırlıklarının doğrudan değerlendirme sürecine entegre edilmesiyle daha tutarlı ve izlenebilir sonuçlar elde edilmesini mümkün kılmaktadır.

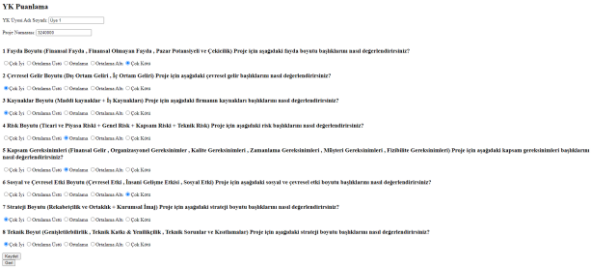
Tablo 6. Fayda boyutu boyutu için entropi yöntemiyle hesaplanan kriter ağırlıkları

Kriter	Ej	dj	wj
Fayda Boyutu	0,8709	0,1291	0,0499
Değiştirme yerine sistemin modernleştirilmesiyle sonuçlanan beklenen tasarruf	0,3533	0,6467	0,0506
Kazanılmış değer	0,3443	0,6557	0,0513
Karlılık	0,3521	0,6479	0,0507
Kar	0,4174	0,5826	0,0456
Beklenen getiri	0,4031	0,5969	0,0467
Ürünün büyüme potansiyeli	0,3617	0,6383	0,0499
Kârlılık potansiyeli, üretkenlik ve maliyette iyileştirmeler	0,4280	0,5720	0,0447
Fayda/maliyet	0,4150	0,5850	0,0458
Yaygınlaştırma yeteneği	0,4064	0,5936	0,0464
Çıktı	0,4024	0,5976	0,0468
Patent (Proje çıktısının patente konu olma potansiyeli)	0,3840	0,6160	0,0482
Araştırma	0,3992	0,6008	0,0470
Proje çalışmasından elde edilecek sonuçların ülkeye kazandırabileceği bilgi birikimi	0,4149	0,5851	0,0458
Beklenen pazar payı	0,4304	0,5696	0,0446
Pazar potansiyeli (Proje çıktısının potansiyel pazarı / kullanım alanı)	0,4670	0,5330	0,0417
Pazar araştırması	0,3011	0,6989	0,0547
Pazar trendi ve büyüme	0,3548	0,6452	0,0505
Birim fiyat	0,3028	0,6972	0,0545
Beklenen satış hacmi	0,3835	0,6165	0,0482
Satışlar	0,4677	0,5323	0,0416
Proje çıktısının ekonomik getiri potansiyeli, verimlilik artışına ve/veya maliyete etkisi	0,4286	0,5714	0,0447



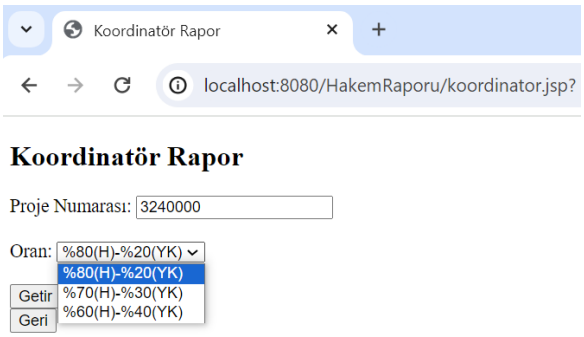
Şekil 2. Hakemler için puanlama arayüzü.

Mevcut değerlendirme sisteminde, projelerin nihai puanı hakemlerin verdiği puanların aritmetik ortalamasına dayanmaktadır. Yürütme kurulu üyeleri ise bu ortalamalara -10 ile +10 arasında ek puan ekleyebilmektedir. Önerilen sistem ile yürütme kurulu üyelerine, ana boyutları yine 5'li Likert ölçeği ile değerlendirme imkanı tanınmaktadır. Bu yenilikle, kurulun katkıları daha ölçülebilir ve dengeli bir biçimde genel değerlendirme sürecine dâhil edilmiştir. Böylece, yürütme kurulunun etkisi daha izlenebilir ve bütünleştirici bir değerlendirme çerçevesi içerisinde ele alınmıştır.



Şekil 3. Grup yürütme kurulu üyeleri puanlama arayüzü.

Grup koordinatörleri için geliştirilen arayüz, hakem ve yürütme kurulu puanlarının birleştirilerek nihai değerlendirmeye yansıtılması sürecinde koordinatörlerin karar alma süreçlerini desteklemiştir. Bu kapsamda, koordinatörlere üç farklı ağırlıklandırma seçeneği sunulmuştur: %80 Hakem - %20 Yürütme Kurulu, %70 Hakem - %30 Yürütme Kurulu ve %60 Hakem - %40 Yürütme Kurulu. Bu esnek yapı, projeler arasındaki önceliklerin daha etkili biçimde belirlenmesini mümkün kılmıştır. Ayrıca, yürütme kurulu üyelerine projelere 0 ile 100 arasında puan verme yetkisi tanınarak, hakem atama süreçlerinin iş yükü ve maliyet açısından daha verimli yürütülmesi hedeflenmiştir.



Şekil 4: Grup koordinatörü karar giriş arayüzü.

3.4. Projelerin Kümeleme Analizi ile Sınıflandırılması

2022 ve 2023 yıllarında Bilişim Teknolojileri alanında başvuran sırasıyla 480 ve 599 projenin dört farklı profil grubuna ayrılmasını sağlamıştır. Çağrılar arasında yapılan karşılaştırmalarda, eşik değerlerin değişkenlik gösterdiği gözlemlenmiş ve bu sonuçlar Tablo 7'de sunulmuştur.

Tablo 7: Çağrı sonuçları için kümeleme ve eşik değerler

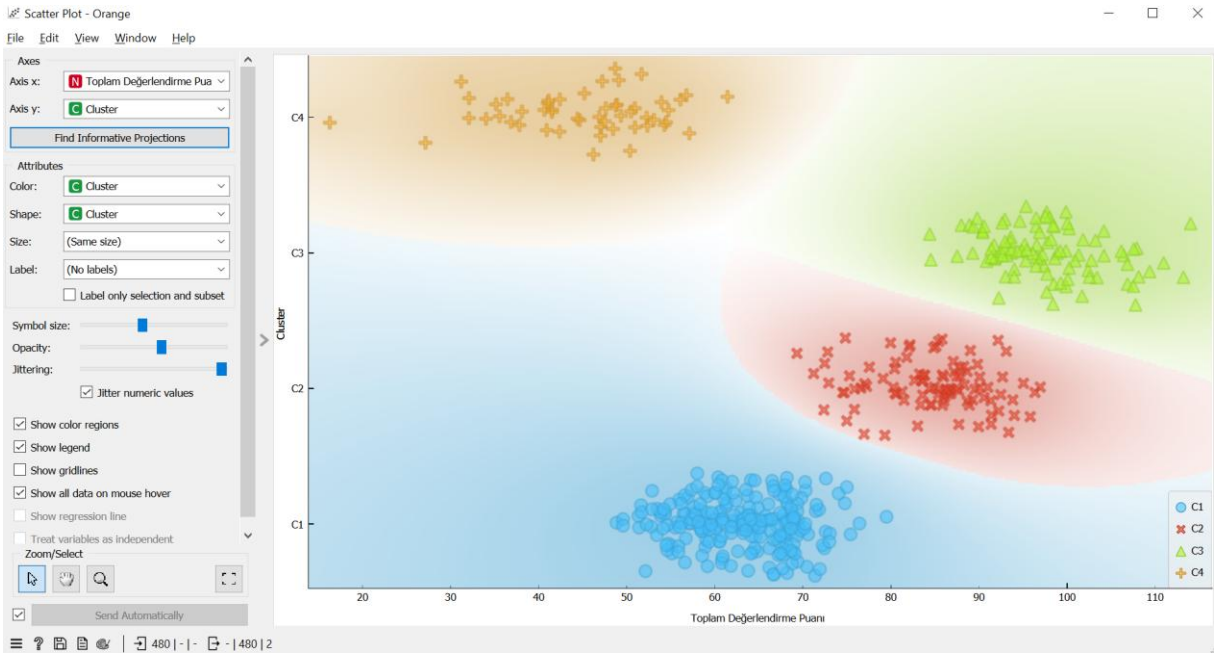
Çağrı	Proje Sayısı	Kümeleme Sonuçları ve Eşik Değerler
2022	480	C1: 54,51 – 73,23 puan arası 235 proje C2: 75,13 - 90,71 puan arası 98 proje C3: 91,29 - 110,99 puan arası 95 proje C4: 19,45 – 53,75 puan arası 52 proje
2023	599	C1: 89,96 - 110,89 puan arası 144 proje C2: 58,64 - 73,33 puan arası 222 proje C3: 74,54 - 89,61 puan arası 142 proje C4: 25,48 - 58,52 puan arası 91 proje

Kümeleme analizinin sonuçları, düşük ve yüksek profilli projelerin sırasıyla doğrudan ret ve destek kararları ile sonuçlanabileceğini göstermiştir, bu da yürütme kurullarının iş yükünü %31 (2022 çağrısı için) ila %39 (2023 çağrısı için) oranında azaltarak süreç verimliliğini artırmaktadır.

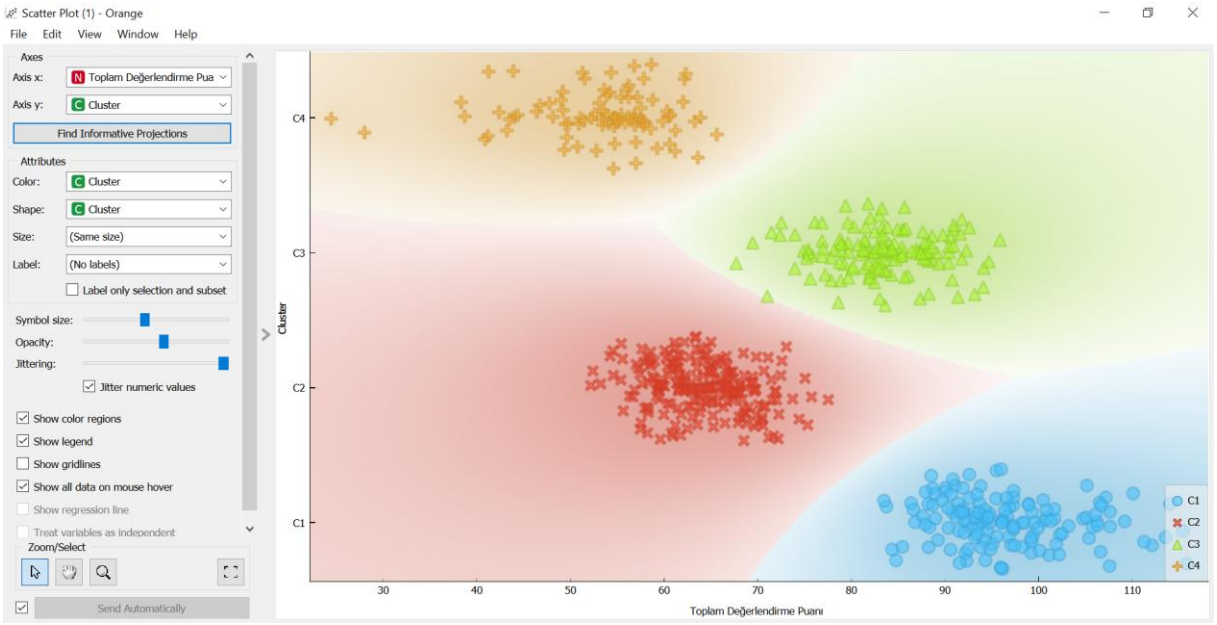
Projelerin belirlenen bütçe sınırları dahilinde desteklenmesi bağlamında, kamu kaynaklarının etkin bir şekilde konumlandırılabilmesi için düşük-orta profilli projeler yerine orta-yüksek profilli projelerin desteklenebilirliğinin detaylı bir şekilde incelenmesinin daha fazla katma değer yaratacağı öngörülmüştür. Bu çerçevede, düşük-orta profilli projeler için doğrudan ret kararı alınmasının uygun olabileceği değerlendirilmiştir. Kümeleme analizi kullanılarak yalnızca orta-yüksek profilli projeler üzerinde detaylı bir inceleme yapılması durumunda, yürütme kurullarının iş yükünün toplamda %76 (2022 çağrısı için) ila %80 (2023 çağrısı için) oranında azaltılabileceği ve böylece çağrı sonuçlarının açıklanma sürecine hız kazandırılabileceği sonucuna ulaşılmıştır.

Değerlendirme süreçlerinde oluşturduğumuz yaklaşım ve kümeleme analizine dayalı bulgular, araştırma kurumunun çağrı sonuçları ile karşılaştırılmıştır. 2022 yılı projelerinde, düşük profilli (C4) grubundaki 52 proje reddedilmiş, düşük-orta profilli (C1) grubunda eşik değer olarak belirlenen 70 puanın üzerindeki 4 proje desteklenmiş ve geri kalan 231 proje reddedilmiştir. Orta-yüksek profilli (C2) ve yüksek profilli (C3) gruplardaki sırasıyla 98 ve 95 proje tamamen desteklenmeye uygun görülmüştür. Kümeleme analizine göre yüksek ve orta-yüksek profilli projelerin desteklenmesini önerdiğimiz sistematiğimizden farklı olarak kamu kurumu orta-düşük profilli projelerden 4 proje daha desteklemiştir. Bu da önerdiğimiz metodolojinin projelerin potansiyelini etkin bir şekilde değerlendirme yeteneğine sahip olduğunu göstermektedir. 2023 yılı çağrısında ise, düşük profilli (C4) grubundaki 91 proje ve düşük-orta profilli (C2) grubundaki 222 proje reddedilmiş, yüksek profilli (C1) grubunda yer alan 144 proje ise desteklenmiştir. Eşik değer olarak belirlenen 74 puanın üzerinde puan alan ve kritik tespitle ret kriterlerini karşılayan 5 proje dışında orta-yüksek profilli (C3) grubundaki 137 proje desteklenmiştir. 2023 yılı için yapılan karşılaştırmada kritik reddedilen 5 proje dışında sistematiğimizin yine oldukça etkin bir sonuç elde ettiği görülmüştür.

Bu bulgular, önerilen karar destek sisteminin değerlendirme süreçlerine önemli ölçüde tutarlılık kazandırdığını göstermektedir. Ancak sistem tarafından yüksek veya orta düzeyde önceliklendirilen bazı projelerin kurum tarafından desteklenmemesi ya da sistemin düşük öncelikli olarak sınıflandırdığı bazı projelerin desteklenmiş olması, karar süreçlerinde belirli düzeyde sapmaların yaşandığını da ortaya koymaktadır. Bu kapsamda, önerilen sistem ile kurum tarafından verilen fiili destek kararları arasındaki örtüşme ve farklılıkları nicel olarak ortaya koymak amacıyla karşılaştırma hazırlanmış ve Tablo 8'de sunulmuştur.



Şekil 5. Sanayi Ar-Ge destek programı 2022 çağrısı projelerinin puana göre kümelemesi.



Şekil 6. Sanayi Ar-Ge destek programı 2023 çağrısı projelerinin puana göre kümelemesi.

Tablo 8. Önerilen kümeleme tabanlı sistem ile gerçekleşen kurumsal destek kararları arasındaki sapma analizi

Çağrı	Küme Tanımı	Proje Sayısı	Desteklenmesi Önerilen Proje Sayısı	Kurumca Gerçekten Desteklenen	Fark (Bias)
2022	C1: Düşük-orta profilli	235	0	4	4
	C2: Orta-yüksek profilli	98	98	98	0
	C3: Yüksek profilli	95	95	95	0
	C4: Düşük profilli	52	0	0	0
2023	C1: Yüksek profilli	144	144	144	0
	C2: Düşük-orta profilli	222	0	0	0
	C3: Orta-yüksek profilli	142	142	137	5
	C4: Düşük profilli	91	0	0	0

Genel olarak değerlendirildiğinde, önerilen k- ortalamalar algoritması tabanlı kümeleme modeli ile kurum kararları arasındaki yüksek düzeydeki örtüşme, modelin karar destek amacıyla güçlü bir öngörü yeteneğine sahip olduğunu; aynı zamanda, oluşan küçük sapmalar ise kurumsal değerlendirme süreçlerinde dikkate alınan ek kriterlerin (örneğin bütçe uygunluğu) etkisini işaret etmektedir. Önerilen sistem, proje değerlendirme süreçlerine yapı ve tutarlılık kazandırarak karar alma süreçlerini hızlandırdığını ve kamu kaynaklarının daha etkin yönetimine katkı sağladığını ortaya koymaktadır. Bu modelle proje grupları önceliklendirilmiş, böylece yürütme kurullarının iş yükü önemli ölçüde azalmış, toplantı verimliliği artmış ve çağrı sonuçlarının daha hızlı açıklanması sağlanmıştır.

4. Tartışma ve Sonuç

Çalışma kapsamında, Türkiye'deki Ar-Ge projelerinin değerlendirme süreçlerinde etkinlik ve nesnelliği artırmak üzere, karar alma süreçlerini daha tutarlı ve izlenebilir kılacak bir karar destek sistemi tasarlanmıştır. Geliştirilen sistemin temelinde, proje değerlendirme süreçlerinde karşılaşılan zorluklar ve eksiklikler üzerine yapılan analizler yer almaktadır. Mevcut değerlendirme sistemlerinin çoğu, projelerin detaylı bir şekilde ele alınmasını ve objektif bir puanlama yapılmasını zorlaştırmakta, süreçlerde gereksiz zaman ve kaynak kayıplarına neden olmaktadır. Bu bağlamda, projelerin değerlendirilmesinde kullanılan kriterlerin entropi yöntemiyle belirlenmesi ve ağırlıklandırılması, daha adil, dengeli ve bilgi temelli bir süreç oluşturulmasını sağlamıştır. Bu süreçte toplamda 247 kriterden 96'ya indirilen kriter seti, projelerin çeşitli yönlerini daha etkin bir şekilde ele alarak, hem hakemler hem de karar vericiler için daha yapılandırılmış bir değerlendirme platformu sunmuştur.

Geliştirilen sistemin en önemli katkılarından biri, projelerin k- ortalamalar kümeleme algoritması ile sınıflandırılmasıdır. Bu süreç, projelerin dört ana grupta (yüksek profilli, ortalama üstü, ortalama ve düşük profilli) sınıflandırılmasını sağlayarak değerlendirme sürecine önemli bir hız ve verimlilik kazandırmıştır. Özellikle, düşük profilli projelerin detaylı bir incelemeye gerek kalmadan hızlı bir şekilde değerlendirilebilmesi, yürütme kurullarının iş yükünü önemli ölçüde hafifletmiştir. Bu, değerlendirme süreçlerinin daha hızlı tamamlanmasına ve kaynakların daha etkin bir şekilde kullanılmasına imkan tanımıştır. 2022 ve 2023 yıllarında Sanayi Ar-Ge destek programına başvuran projeler üzerinde yapılan uygulamalarda, iş yükünün %31 ila %39 oranında azalması, sistemin başarısını göstermektedir.

Yeni karar destek sisteminin bir diğer önemli özelliği, projelerin değerlendirilmesinde entegre bir yapıya sahip olmasıdır. Hakemlerin ve yürütme kurulu üyelerinin değerlendirmelerini tek bir platform üzerinde gerçekleştirebilmeleri, değerlendirme süreçlerinin daha şeffaf ve tutarlı bir şekilde yönetilmesine olanak tanımıştır. Bu yapı, Ar-Ge projelerinin endüstriyel içeriği, yenilikçi yönü, proje planı, altyapısı, ekonomik fayda ve ulusal kazanca dönüşebilirliği gibi çok yönlü kriterler ışığında detaylı bir inceleme yapılmasına olanak tanımıştır.

Bu çalışmanın bulguları, Ar-Ge projelerinin değerlendirilmesinde nesnel ve tutarlı sonuçlar üreten bir karar destek sisteminin uygulanmasının, değerlendirme süreçlerinde anlamlı iyileşmeler sağladığını ortaya koymaktadır. Bu sistem, projeleri sınıflandırarak ve kritik değerlendirme kriterlerine göre önceliklendirerek, Ar-Ge projelerinin başarıya ulaşma olasılığını artırmış ve proje seçim süreçlerini önemli derecede iyileştirmiştir. Ancak, bu sistemin uygulanması ve değerlendirilmesinde çeşitli faktörlerin dikkate alınması gerektiği de unutulmamalıdır. Özellikle, entropi yöntemiyle ağırlıklandırılan kriterlerin zamanla güncellenmesi ve değişen koşullara uyum sağlaması gereklidir. Bu, sistemin sürdürülebilirliğini ve etkinliğini artırmak için önemlidir.

Gelecekte yapılacak çalışmalar, bu karar destek sisteminin farklı Ar-Ge programlarına entegre edilmesi ve daha geniş ölçekli uygulamalarla test edilmesi üzerine odaklanmalıdır. Ayrıca, sistemin kullanıcı dostu arayüzlerinin geliştirilmesi, hakemlerin ve diğer kullanıcıların sistemle etkileşimini artırarak değerlendirme süreçlerini daha da kolaylaştırabilir. Bu şekilde, ülkenin Ar-Ge potansiyelini en üst düzeye çıkarmak ve inovasyon kapasitesini artırmak için daha etkin bir değerlendirme süreci sağlanacaktır. Geliştirilen bu sistem, yalnızca mevcut projelerin değerlendirilmesinde değil, gelecekteki projelerin seçimi ve desteklenmesinde de kritik bir rol oynayacaktır.

Katkı Oranı Beyanı

Yazarların katkı yüzdeleri aşağıda verilmiştir. Yazarlar makaleyi incelemiş ve onaylamıştır.

	S.N.B.	K.D.A.	M.K.	T.S.P.
K	40	30	10	20
T	40	30	10	20
Y	40	30	10	20
VTI	50	20	0	30
VAY	40	30	10	20
KT	60	30	10	0
YZ	40	30	20	10
KI	40	30	20	10
GR	40	30	20	10
PY	40	30	20	10
FA	40	30	20	10

K= kavram, T= tasarım, Y= yönetim, VTI= veri toplama ve/veya işleme, VAY= veri analizi ve/veya yorumlama, KT= kaynak tarama, YZ= Yazım, KI= kritik inceleme, GR= gönderim ve revizyon, PY= proje yönetimi, FA= fon alımı.

Çatışma Beyanı

Yazarlar bu çalışmada hiçbir çıkar ilişkisi olmadığını beyan etmektedirler.

Etik Onay Beyanı

Bu araştırmada hayvanlar ve insanlar üzerinde herhangi bir çalışma yapılmadığı için etik kurul onayı alınmamıştır.

Destek ve Teşekkür Beyanı

TÜBİTAK TEYDEB'e çalışmalarımıza olan katkı ve desteklerinden dolayı teşekkür ederiz.

Kaynaklar

Archer NP, Ghasemzadeh F. 1999. An integrated framework for project portfolio selection, Int J Proj Manag, 17(4): pp: 207-216.

Arthur D, Vassilvitskii S. 2006. k-means++: The advantages of careful seeding, Stanford, pp: 56-59.

Bard JF, Balachandra R, Kaufmann PE. 1988. An interactive approach to R&D project selection and termination, IEEE Trans Eng Manag, 35(3): pp: 139-146.

Beaujon GJ, Marin SP, McDonald GC. 2001. Balancing and optimizing a portfolio of R&D projects, Nav Res Logist, 48(1): pp: 18-40.

Bhattacharyya R, Kumar P, Kar S. 2011. Fuzzy R&D portfolio selection of interdependent projects, Comput Math Appl, 62(10): pp: 3857-3870.

Bhattacharyya R. 2015. A grey theory based multiple attribute approach for R&D project portfolio selection, Fuzzy Inf Eng, 7(2): pp: 211-225.

Bitman WR, Sharif N. 2008. A conceptual framework for ranking R&D projects, IEEE Trans Eng Manag, 55(2): pp: 267-278.

Bornmann L. 2011. Scientific peer review, Annu Rev Inf Sci Technol, 45(1): pp: 197-245.

Cebeci Z, Cebeci C. 2020. A fast algorithm to initialize cluster centroids in fuzzy clustering applications, Information, 11(9): pp: 446.

Cebeci Z, Yildiz F. 2015. Comparison of k-means and fuzzy c-means algorithms on different cluster structures, J Agric Inform, 6(3): pp: 15-59.

Charnes A, Cooper WW, Rhodes E. 1978. Measuring the efficiency of decision making units, Eur J Oper Res, 2(6): pp: 429-444.

Cheng CH, Liou JJ, Chiu CY. 2017. A consistent fuzzy preference relations based ANP model for R&D project selection, Sustainability, 9(8): pp: 1352.

Conka T, Vayvay O, Sennaroglu B. 2008. A combined decision model for R&D project portfolio selection, Int J Bus Innov Res, 2(2): pp: 190-202.

Criscuolo P, Dahlander L, Grohsjean T, Salter A. 2017. Evaluating novelty: The role of panels in the selection of R&D projects, Acad Manag J, 60(2): pp: 433-460.

Czajkowski AF, Jones S. 1986. Selecting interrelated R&D projects in space technology planning, IEEE Trans Eng Manag, (1): pp: 17-24.

de Souza DGB, dos Santos EA, Soma NY, da Silva CES. 2021. MCDM-based R&D project selection: A systematic literature review, Sustainability, 13(21): pp: 11626.

Demšar J, Zupan B, Leban G, Curk T. 2004. Orange: From experimental machine learning to interactive data mining, In: Knowledge Discovery in Databases: PKDD 2004, Pisa, Italy, 20 September 2004 - 24 September 2004, Springer Berlin Heidelberg, pp: 537-539.

Eclipse Foundation. 2024. Eclipse IDE (Version [2023 12]), URL: https://www.eclipse.org/ide/ (accessed date: June 28, 2024).

Eilat H, Golany B, Shtub A. 2008. R&D project evaluation: An integrated DEA and balanced scorecard approach, Omega, 36(5): pp: 895-912.

Forgy EW. 1965. Cluster analysis of multivariate data: efficiency versus interpretability of classifications, Biometrics, 21: pp: 768-769.

Ghazal TM. 2021. Performances of k-means clustering algorithm with different distance metrics, Intell Autom Soft Comput, 30(2): pp: 735-742.

Ghasemzadeh F, Archer NP. 2000. Project portfolio selection through decision support, Decis Support Syst, 29(1): pp: 73-88.

Ghorbani HR, Jolai F, Tavakkoli-Moghaddam R, Rabbani M. 2006. A comprehensive model for R&D project portfolio selection with zero-one linear goal-programming (research note), Int J Eng, 19(1): pp: 55-66.

Gustafsson J, Salo A. 2005. Contingent portfolio programming for the management of risky projects, Oper Res, 53(6): pp: 946-956.

Hassanzadeh F, Nemati H, Sun M. 2014. Robust optimization for interactive multiobjective programming with imprecise information applied to R&D project portfolio selection, Eur J Oper Res, 238(1): pp: 41-53.

Henig MI, Katz H. 1996. R&D project selection: A decision process approach, J Multi-Criteria Decis Anal, 5(3): pp: 169-177.

Henriksen AD, Traynor AJ. 1999. A practical R&D project-selection scoring tool, IEEE Trans Eng Manag, 46(2): pp: 158-170.

Hesarsorkh AH, Ashayeri J, Naeini AB. 2021. Pharmaceutical R&D project portfolio selection and scheduling under uncertainty: A robust possibilistic optimization approach, Comput Ind Eng, 155: pp: 107114.

Heyard R, Ott M, Salanti G, Egger M. 2022. Rethinking the funding line at the Swiss national science foundation: Bayesian ranking and lottery, Stat Public Policy, 9(1): pp: 110-121.

Heydari T, Seyed Hosseini SM, Makui A. 2016. Developing and solving a one-zero non-linear goal programming model to R&D portfolio project selection with interactions between projects, Int Bus Manag, 10(19): pp: 4516-4521.

Hsu YG, Tzeng GH, Shyu JZ. 2003. Fuzzy multiple criteria selection of government-sponsored frontier technology R&D projects, R&D Manag, 33(5): pp: 539-551.

Hünermund P, Czarnitzki D. 2019. Estimating the causal effect of R&D subsidies in a pan-European program, Res Policy, 48(1): pp: 115-124.

Isied M, Daneshvar S. 2024. A second chance for failed projects using data envelopment analysis based on project attractiveness factors, Mathematics, 12(23): pp: 10-15.

Imoto S, Yabuuchi Y, Watada J. 2008. Fuzzy regression model of R&D project evaluation, Appl Soft Comput, 8(3): pp: 1266-1273.

Jeng DJF, Huang KH. 2015. Strategic project portfolio selection for national research institutes, J Bus Res, 68(11): pp: 2305-2311.

Kahraman C, Çağrı Tolga A. 2008. Fuzzy multiattribute evaluation of R&D projects using a real options valuation model, Int J Intell Syst, 23(11): pp: 1153-1176.

Kaplan RS, Norton DP. 1992. The Balanced Scorecard: measures that drive performance, Harvard Business Review, January-February: pp: 71-79.

Karami A, Johansson R. 2013. Utilization of multi attribute decision making techniques to integrate automatic and manual ranking of options, J Inf Sci Eng, 30(2): pp: 519-534.

Karasakal E, Aker P. 2017. A multicriteria sorting approach based on data envelopment analysis for R&D project selection problem, Omega, 73: pp: 79-92.

Karaveg C, Thawesaengskulthai N, Chandrachai A. 2015. A combined technique using SEM and TOPSIS for the commercialization capability of R&D project evaluation, Decis Sci Lett, 4(3): pp: 379-396.

Ketchen DJ, Shook CL. 1996. The application of cluster analysis in

strategic management research: an analysis and critique, Strateg Manag J, 17(6): pp: 441-458.
Kumar SS. 2004. AHP-based formal system for R&D project evaluation, Int J Proj Manag, 22(5): pp: 423-432.
Liberatore MJ. 1986. R&D project selection, Telemat Inform, 3(4): pp: 289-300.
Liberatore MJ. 1987. An extension of the analytic hierarchy process for industrial R&D project selection and resource allocation, IEEE Trans Eng Manag, (1): pp: 12-18.
Liberatore MJ. 1988. An expert support system for R&D project selection, Math Comput Model, 11: pp: 260-265.
Liberatore MJ, Titus GJ. 1983. The practice of management science in R&D project management, Manag Sci, 29(8): pp: 962-974.
Liu M, Yang WQS. 2023. Analysis of the advantages and disadvantages of four comprehensive evaluation methods, Front Bus Econ Manag, 9: pp: 162-167.
Madey GR, Dean BV. 1985. Strategic planning for investment in R&D using decision analysis and mathematical programming, IEEE Trans Eng Manag, (2): pp: 84-90.
MacQueen J. 1967. Some methods for classification and analysis of multivariate observations, In: Proc of the Fifth Berkeley Symp on Math Statist and Probab, 1(14): pp: 281-297.
Mardani A, Jusoh A, Zavadskas EK, Khalifah Z, Nor KM. 2015. Application of multiple-criteria decision-making techniques and approaches to evaluating of service quality: a systematic review of the literature, J Bus Econ Manag, 16(5): pp: 1034-1068.
Mavrotas G, Makryvelios E. 2021. Combining multiple criteria analysis, mathematical programming and Monte Carlo simulation to tackle uncertainty in R&D project portfolio selection: a case study from Greece, Eur J Oper Res, 291(2): pp: 794-806.
Mavrotas G, Makryvelios E. 2023. R&D project portfolio selection using the Iterative Trichotomic Approach in order to study how subjectivity of the weights is reflected in the selected projects of the final portfolio, Oper Res, 23(3): pp: 50-56.
Meade LM, Presley A. 2002. R&D project selection using the analytic network process, IEEE Trans Eng Manag, 49(1): pp: 59-66.
Miyajima S, Isshiki T, Kunugi M, Uesaka S. 2022. Can we predict successful market introduction using on-going R&D evaluation data?, fteval J Res Technol Policy Eval, (53): pp: 153-159.
Mohaghar A, Fathi MR, Faghih A, Turkayesh MM. 2012. An integrated approach of Fuzzy ANP and Fuzzy TOPSIS for R&D project selection: a case study, Aust J Basic Appl Sci, 6(2): pp: 66-75.
Mohanty RP, Agarwal R, Choudhury AK, Tiwari MK. 2005. A fuzzy ANP-based approach to R&D project selection: a case study, Int J Prod Res, 43(24): pp: 5199-5216.
Montajabiha M, Arshadi Khamseh A, Afshar-Nadjafi B. 2017. A robust algorithm for project portfolio selection problem using real options valuation, Int J Manag Proj Bus, 10(2): pp: 386-403.
Oral M, Kettani O, Lang P. 1991. A methodology for collective evaluation and selection of industrial R&D projects, Manag Sci, 37(7): pp: 871-885.
Oral M. 2012. Action research contextualizes DEA in a multi-organizational decision-making process, Expert Syst Appl, 39(7): pp: 6503-6513.
Ömürbek N, Aksoy E. 2016. Bir petrol şirketinin çok kriterli karar verme teknikleri ile performans değerlendirmesi, Süleyman Demirel Üniv İİBF Derg, 21(3): pp: 25-27.
Ramalho FD, Silva IS, Ekel PY, da Silva Martins CAP, Bernardes P, Libório MP. 2021. Multimethod to prioritize projects evaluated in different formats, MethodsX, 8: pp: 101371.
Rousseeuw PJ. 1987. Silhouettes: a graphical aid to the interpretation and validation of cluster analysis, J Comput Appl Math, 20: pp: 53-65.
Salehi F, Al-e SMJM, Husseini SMM. 2022. A 2-phase interdependent methodology for sustainable project portfolio planning in the pharmaceutical industry, Comput Ind Eng, 174: pp: 108794.
Shahapure KR, Nicholas C. 2020. Cluster quality analysis using silhouette score, In: 2020 IEEE 7th Int Conf Data Sci Adv Anal (DSAA), pp: 747-748.
Shannon CE. 1948. A mathematical theory of communication, Bell Syst Tech J, 27(3): pp: 379-423.
Siksnelyte-Butkiene I, Zavadskas EK, Streimikiene D. 2020. Multi-criteria decision-making (MCDM) for the assessment of renewable energy technologies in a household: a review, Energies, 13(5): pp: 1164.
Stelmakh I, Shah N, Singh A. 2019. On testing for biases in peer review, Adv Neural Inf Process Syst, 32: pp: 42-56.
Stewart TJ. 1991. A multi-criteria decision support system for R&D project selection, J Oper Res Soc, 42(1): pp: 17-26.
Sun M, Barry Danfa J, Teplitskiy M. 2022. Does double-blind peer review reduce bias? Evidence from a top computer science conference, J Assoc Inf Sci Technol, 73(6): pp: 811-819.
Suvvari SK. 2023. Project portfolio management: best practices for strategic alignment, Int J Prof Bus Rev, 8(12): pp: 1.
Syakur MA, Khotimah BK, Rochman EMS, Satoto BD. 2018. Integration k-means clustering method and elbow method for identification of the best customer profile cluster, In: IOP Conf Ser Mater Sci Eng, 336: ID: 012017.
Taylor BW III, Moore LJ, Clayton ER. 1982. R&D project selection and manpower allocation with integer nonlinear goal programming, Manag Sci, 28(10): pp: 1149-1158.
TÜBİTAK. 2023. Türkiye Bilimsel ve Teknolojik Araştırma Kurumu (TÜBİTAK) Faaliyet Raporları, URL: https://tubitak.gov.tr/sites/default/files/26720/tubitak_2023_yili_faaliyet_raporu.pdf (published date: March 29, 2024, accessed date: November 16, 2024).
Wang K, Wang CK, Hu C. 2005. Analytic hierarchy process with fuzzy scoring in evaluating multidisciplinary R&D projects in China, IEEE Trans Eng Manag, 52(1): pp: 119-129.
Wang TC, Lee HD. 2009. Developing a fuzzy TOPSIS approach based on subjective weights and objective weights, Expert Syst Appl, 36(5): pp: 8980-8985.
Wang Z, Bai S, Zhang X. 2024. A robust optimization model for R&D project portfolio risk response decision-making considering risk interaction and regret perception, J Ind Manag Optim, 20(12): pp: 3843-3867.
Wu J, Liang L, Yang F, Yan H. 2009. Bargaining game model in the evaluation of decision making units, Expert Syst Appl, 36(3): pp: 4357-4362.
Xu R, Wunsch D. 2008. Clustering, John Wiley & Sons, Hoboken, NJ, USA, pp: 25-30.
Zhang H, Gu CL, Gu LW, Zhang Y. 2011. The evaluation of tourism destination competitiveness by TOPSIS & information entropy–a case in the Yangtze River Delta of China, Tour Manag, 32(2): pp: 443-451.

Black Sea Journal of Engineering and Science
doi: 10.34248/bsengineering.1633428

Open Access Journal
e-ISSN: 2619 – 8991

Araştırma Makalesi (Research Article)
Cilt 8 - Sayı 4: 1050-1056 / Temmuz 2025
(Volume 8 - Issue 4: 1050-1056 / July 2025)

HAVACILIK YAPILARINDA ENTEGRE BASAMAKLI KOMPOZİT KABUK TASARIM VE ÜRETİM PARAMETRELERİ

Muharrem CAN[1*], Özgür KARALI[2]

[1,2]*Turkish Aerospace Industries, Aircraft Executive Vice Presidency, Department of Structural Design, 06980, Ankara, Türkiye*

Özet: Günümüzde ileri kompozit malzemeler, yüksek mukavemet ve düşük yoğunluk oranları nedeniyle havacılık uygulamalarında yaygın olarak kullanılmaktadır. Havacılık yapılarının tasarımında fonksiyonellik, hafiflik, dayanım, erişim kolaylığı ve bakım kolaylığı gibi birçok parametre dikkate alınmalıdır. Hava araçlarının sınırlı hacimlere sahip olması, yapısal parçaların tasarımında özel çözümlerin geliştirilmesini zorunlu hale getirmiştir. Bu araçlarda, ömürleri boyunca gerekli bakım ve onarım işlemlerine erişimi sağlamak için çok sayıda erişim kapağı bulunmaktadır. Aynı zamanda, bu kapaklar ve bağlayıcılar toplam yapısal ağırlığın önemli bir kısmını oluşturur. Bu çalışmada, kompozit kabuk yapılar üzerinde yer alan erişim kapaklarının ek bir parçaya ihtiyaç duyulmadan bütünleşik basamaklı yapıda tasarlanması ve bu tasarım sürecinde dikkat edilmesi gereken unsurlar ele alınmıştır. Tasarımların üretilebilir olması gerekliliği göz önünde bulundurularak, üretim kolaylığı sağlayacak, üretim sürelerini ve maliyetlerini azaltacak parametreler incelenmiştir. Sonuç olarak, azaltılan bağlayıcı ve parça sayısıyla hem toplam uçak yapısal ağırlığında hem de üretim süresi ve maliyetlerinde önemli bir azalma elde edilmiştir. Yükleme çeşidine göre basamak oranı (derinlik/uzunluk) değişkenlik göstermektedir ve bu oran azaldıkça gerilme birikmesi de azalmaktadır. Ancak erişim, hafiflik ve aerodinamik süreklilik gibi tasarım gereksinimleri doğrultusunda bazı durumlarda bu oranın artırılması gerekmektedir. Çalışma kapsamında üretimi zor ve yük aktarımı konusunda makul bir basamak oranı olan 1:5'lik orana sahip bir yakıt tankı erişim kapağı tasarıma uygulanmıştır. Üretim denemeleri de bu basamak oranı üzerinden gerçekleştirilmiş ve olumlu sonuçlar elde edilmiştir.

Anahtar kelimeler: Kompozit, Basamak, Havacılık, Tasarım

Design and Manufacturing Parameters of Integrated Joggled Composite Skins in Aerospace Structures

Abstract: Today, advanced composite materials are widely used in aerospace applications due to their high strength-to-weight ratios and low density. The design of aerospace structures must consider several parameters, including functionality, lightweight properties, strength, accessibility, and ease of maintenance. The limited internal volumes of aircraft make it essential to develop specialized design solutions for structural components. Aircraft require numerous access panels for maintenance and repair operations throughout their service life. However, these panels and their fasteners account for a significant portion of the total structural weight. This study focuses on designing integrated stepped structures for access panels on composite shells, eliminating the need for additional components, and identifies critical considerations during the design process. To ensure manufacturability, parameters that simplify production, reduce production time, and decrease costs have been evaluated. Consequently, a reduction in the number of fasteners and components has resulted in significant decreases in the aircraft's total structural weight, production time, and costs. The step ratio (depth/length) varies depending on the type of loading, and as this ratio decreases, the stress concentration also decreases. However, in some cases, these rates need to be increased in line with design requirements such as accessibility, lightness and aerodynamic continuity. In this study, a fuel tank access panel design with a 1:5 ratio, which is challenging to manufacture and reasonable for load transfer, has been applied. Manufacturing trials based on this ratio were conducted, yielding favorable results.

Keywords: Composite, Joggle, Aerospace, Design

***Sorumlu yazar (Corresponding author):** *Turkish Aerospace Industries, Aircraft Executive Vice Presidency, Department of Structural Design, 06980, Ankara, Türkiye*
E mail: can.muharrem11@gmail.com (M. CAN)
Muharrem CAN https://orcid.org/0009-0000-0333-184X
Özgür KARALI https://orcid.org/0009-0004-4600-9999

Gönderi: 04 Şub 2025 **Received:** February 04, 2025
Kabul: 14 Mayıs 2025 **Accepted:** May 15, 2025
Yayınlanma: 15 Temmuz 2025 **Published:** July 15, 2025

Cite as: Can M, Karalı Ö, 2025. Design and manufacturing parameters of ıntegrated joggled composite skins in aerospace structures. BSJ Eng Sci, 8(4): 1050-1056.

1. Giriş

Kompozit malzemeler; dayanım, hafiflik, karmaşık geometrilerde üretim imkânı ve çevresel koşullara dayanıklılık gibi avantajları sebebiyle havacılık sektöründe yoğun olarak kullanılmaktadır. Özellikle bu malzemelerin karmaşık geometrilerde üretilebilme kabiliyeti, yekpare tasarım yaklaşımlarına olanak sağlayarak toplam parça sayısını önemli ölçüde azaltmaktadır. Bu, hem ağırlık hem de maliyet avantajı sunarken yapısal verimliliği artırır.

Meram vd. (2019) ise havacılık yapılarında, verimli bir yük yolu oluşturmak amacıyla genellikle bağlayıcı elemanlar kullanıldığını belirtmişlerdir. Ancak kompozit laminatlarda birleştirme teknikleri, özellikle sökülebilir olanlar, metallerle karşılaştırıldığında çok sınırlıdır ve kompozit yapıların geliştirilmesindeki en büyük zorluklardan biri olarak kabul edilmektedir. Birleşim noktaları yapının yük taşıma kapasitesini ve genel yapısal

This work is licensed (CC BY-NC 4.0) under Creative Commons Attribution 4.0 International License

bütünlüğü etkilediğinden, kompozit malzemelerin birleşim yeri tasarımı üzerine birçok araştırma yapıldığını belirtmektedirler.

A. Khechai vd. (2025) ise yine benzer şekilde laminat yapılarda yer alan montaj deliğinin, belirgin gerilme yoğunlaşması (stres konsantrasyonu) fenomeni nedeniyle özellikle hassas olduğunu belirtmiştir. Bu gerilmeler, kompozit laminatların hem çekme hem de basma yükleri altındaki dayanımını belirgin şekilde azalttığını ve bu tür gerilmelerin şiddetinin önemli ölçüde arttığı ve delikler ile kesikler nedeniyle lamine kompozit yapılarda erken yapısal hasara yol açtığını belirtmiştir.

Ek olarak Erhan vd. (2025) mekanik delme işlemi sırasında, delik giriş ve çıkış bölgelerinde oluşan delaminasyonun yanı sıra, delik yüzeylerinde lif ve matris kaynaklı hasarlar da meydana gelebildiğini ve bu hasarların, delik kalitesini ve kompozit malzemenin mekanik dayanımını olumsuz yönde etkilediğini belirtmişlerdir. Bu nedenle, çok sayıda araştırmacının düz yüzeyli ve boru formundaki GFRP ve CFRP kompozitlerde bu tür hasarların en aza indirilmesine odaklandığını belirmişlerdir.

Ayrıca Doğan vd. (2025) fiber metal laminat yapıların başarılı bir şekilde birleştirilmesinin, delme işleminin doğruluğuna bağlı olduğunu, uygun şekilde gerçekleştirilen bir delme işlemi ile FML yapıların sağlam ve güvenli bir şekilde montajının mümkün olduğunu belirtmişlerdir. Ek olarak montaj işlemlerinde en yaygın kullanılan bağlantı elemanlarının cıvatalar, perçinler, vidalar ve sıkı geçme pimleri olduğunu ancak, delme işlemi kaynaklı hasarlara bağlı olarak bu tür bağlantılarda gerilme yığılmaları gibi ciddi problemlerin ortaya çıkabildiğini belirtmişlerdir.

Bu problemler; delaminasyon, ara yüzey ayrılması, lif kırılmaları, kesilmemiş lifler ve lif çıkıntıları gibi çeşitli hasar türlerini içermektedir.

Bu durumlar ise yapı üzerine eklenen her deliğin yapının toplam dayanımına negatif etki ettiğinin bir göstergesidir.

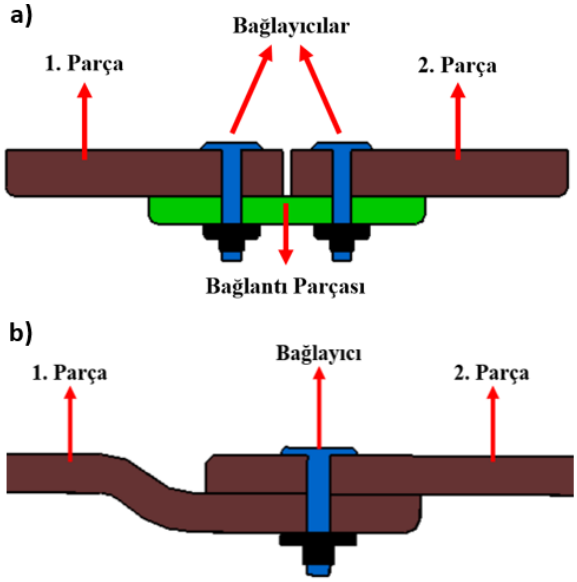
Niu (1999) ise bağlayıcı sayısının azaltılmasının, yapısal ağırlığın düşürülmesi ve üretim maliyetinin minimize edilmesi bakımından önemli olduğunu belirtmektedir. Bağlayıcılar ile birbirine bağlanan parçalarda yük aktarımı sağlanırken deliklerin etrafında gerilme birikmeleri oluşmaktadır. Bağlayıcı sayısını azaltmaya yönelik çözümler, gerilme birikmelerini minimize eder.

Şekil 1, F-15A Eagle uçağındaki erişim kapaklarını göstermektedir. Bu kapakların kabuğa bağlanması için gereken ek parçalar ve bağlayıcılar düşünüldüğünde, bu kapakların bir uçağın yapısal ağırlık bütçesi üzerindeki etkileri açıkça görülebilmektedir.



Şekil 1. F15A Eagle erişim kapakları.

Bu çalışmada, yakıt tankları ve ekipman erişim kapakları gibi bölgelerde klasik bağlantı yöntemlerinin yerine entegre basamaklı bağlantıların kullanımı incelenmiş; tasarım ve üretim parametreleri analiz edilmiştir.



Şekil 2. Bağlantı çeşitleri a)Klasik Bağlantı b) Entegre Basamaklı Bağlantı.

Klasik bağlantı yönteminde uç uca bağlanacak iki parça ara bir bağlantı parçası ve birer sıra bağlayıcı yardımı ile birbirine bağlanır. Bu çalışmanın konusu olan bütünleşik basamaklı bağlantı çözümünde ise ana kompozit yapı belirli bir basamak oranında aşağıya doğru rampa şeklinde şekillendirilerek ikinci yapının altına doğru uzanır. Bu durumda alt bağlantı parçası ve bir sıra bağlayıcıya gerek kalmaz.

2. Materyal ve Yöntem

2.1. Kullanılan Malzemeler

Çalışmada kullanılan malzemeler ve yöntemler aşağıda belirtilmiştir:

- Yapısal Katmanlar: Karbon Fiber HexPly M91 tek yönlü bant. Kalınlık: 0,184 mm
- Elektriksel Geçirgenlik İçin Bakır Katmanlar: HexPly M21 Expanded Copper Foil, ECF73 ve ECF815
- Dolgu Malzemesi Katmanları: Glas Fiber HexPly M21, Kalınlık: 0,1 mm ve Karbon Fiber HexPly M21 Twill 2x2 Kalınlık: 0,31 mm
- Film Yapıştırıcı: FM 300K

Genel olarak bir yakıt erişim kapağı tasarımı yapılırken izlenecek yol ve ilgili parametreler şöyle sıralanabilir:

1. Basamak geometrik parametrelerin belirlenmesi ve yapısal parçanın tasarımı
2. Dolgu malzemesi ve yönteminin belirlenmesi
3. Elektriksel topraklama ve yıldırımdan korunmaya yönelik tasarım yapılması
4. Tahribatsız muayene ve imalat sıralamasının belirlenmesi

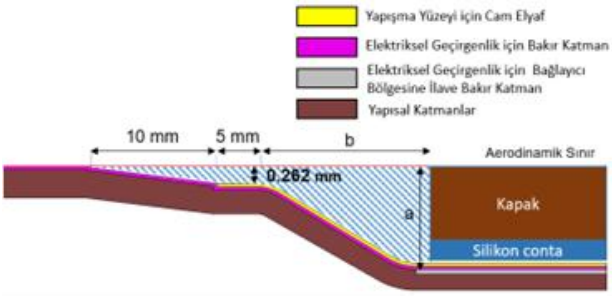
2.2. Basamak parametreleri ve yapısal parçanın tasarımı

Basamaklı bağlantılar tasarlanırken öncelikle basamak derinliği belirlenmelidir. Bu durum ise bağlantının tipine göre değişkenlik göstermektedir. Burada genel olarak daha zorlayıcı gereksinimlere sahip olduğu için bir yakıt erişim kapağı ele alınmış ve tasarım parametreleri, üretim denemeleri ve görseller de buna göre oluşturulmuştur. Bir yakıt erişim kapağında kapak kalınlığı ve sızdırmazlık elemanının montajdan sonraki nihai kalınlığı basamak derinliğini belirlemektedir. Basamak derinliği belirlendikten sonra kullanılacak basamak oranına (a/b) (Şekil 3) göre basamak uzunluğu hesaplanır. İdeal bir koşulda basamağın doğrudan dik şekilde olması istenir. Bu sayede arada bir boşluk oluşmayacaktır. Pratikte ise gerek üretim limitleri gerekse gerilme birikmesi sebepli faktörler yüzünden değişik basamak oranları kullanmak zorunludur. Basamak oranları kabuğun ana yükleme yönüne ve ana yükleme yönüne dik doğrultudaki yönlerde değişiklik gösterebilir. Bu oran ne kadar düşürülürse yük aktarımı o kadar az gerilme birikmesi yaratacağından bu oranın düşük olması tercih edilir. Ancak, bazı durumlarda yük taşıyan ana elemanların geometrileri bu tarz erişim kapakların boyutlarını aşırı sınırlandırmaktadır. Bu ise erişim kapaklarından içeriye el, kol, montaj veya muayene aparatlarının girmesini zorlaştırmaktadır. Bu durumlarda basamak oranından feragat edilerek daha yüksek oranlara çıkılabilir. Örneğin 1:7 veya 1:5 oranlarda tasarım da yapılabilir. Bu çalışmada, 1:5 basamak oranı ile tasarım yapılmıştır. Basamak oranı belirlendikten sonra ise bu değerler kullanılarak basamak uzunluğu belirlenir.

Örneğin 10 katmanlı bir yakıt kapağı, 1,2 mm silikon conta ile beraber kullanılıyorsa ve silikon contanın tahmini sıkışma miktarı 0,4 mm ise basamak derinliği (10*0,184)+0,8= 2,64 mm bulunur. Basamak oranı 1:5 alındığında basamak uzunluğu da 5*2,64=13,2 mm bulunur.

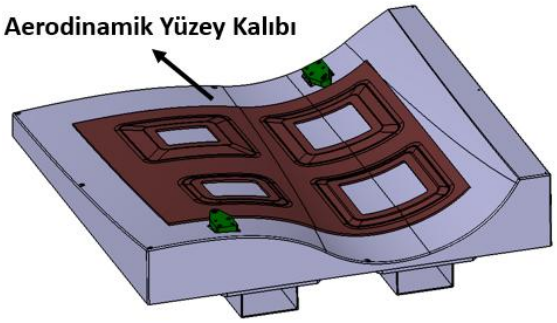
Uzay vd. (2020) otoklav ile üretim yönteminin havacılık yapılarında yüksek kalite istenilen durumlarda kullanıldığını belirtmiştir. Çünkü bu yöntemde minimum mikro boşluk oranında yüksek fiber hacim oranı elde edilebilir. Kürleme işlemi vakuma alınmış parçanın yüksek dış basınç ve sıcaklık içeren bir odada pişirilmesi ile gerçekleştirilir. Bu çalışmada yer alan kompozit kabuk iki kür çevriminde otoklav fırınına kürlenmektedir.

İlk kür çevrimini, ana yük taşıyıcı katmanları kapsayan kısım oluşturur. Buradaki amaç, ana yükü taşıyacak bölgeyi tasarlarken aynı zamanda ikinci kür çevriminde yer alacak bölgeye uygun yapışma yüzeyini sağlamaktır.



Şekil 3. İlk kür çevrimi.

Şekil 3'teki mesafelerin belirlenmesinde, katmanların kalınlığı ve katmanların yapıştırılması için yeterli alan sağlanması göz önünde bulundurulmuştur. Bahsi geçen 0,262 mm ikinci kür çevriminde kullanılacak bakır katman ve iki katman cam elyafın kürlenmiş kalınlığına denk gelmektedir. 10 mm ve 5 mm olan bölgelerde ise cam elyafın ve bakır katmanın aerodinamik yüzeyin dışına çıkmayacak şekilde sonlanması hedeflenmiştir. (Şekil 5)



Şekil 4. İlk kür çevirim kalıbı.

Bu ilk kür çevriminin yüksek hassasiyette üretimi için aerodinamik ve basamaklı yüzeyi simule edecek bir kalıp ihtiyacı oluşmuştur. Bu kalıp üzerine sırası ile cam elyaf, bakır katman, ilave bakır katman ve yapısal katmanlar serilmektedir. Serim sonunda uygun parametreler ile parça, kalıp ile beraber otoklava girmektedir. (6,9 Bar/180^{0}C/6 saat) Böylece ilk kür çevriminin ürünü ortaya çıkmaktadır. Bu son ürün tahribatsız muayeneye

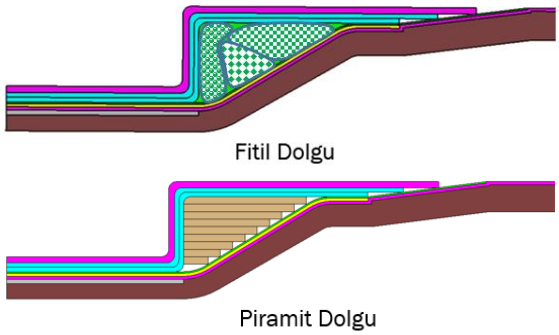
de uygun bir geometriye sahiptir.

İlk aşamanın sonunda yapısal katmanlar serilip kürlendikten sonra Şekil 3'de taralı alanda gösterildiği gibi kapak ve kabuk yapısı arasında üçgen şeklinde bir boşluk oluşur.

Burada bahsi geçen yapısal parça aerodinamik yüzeyde bulunan bir kabuk olduğu için özellikle insansız hava aracı veya savaş uçakları gibi hız ve performansın önemli olduğu uçaklarda aerodinamik sürekliliğin sağlanıp, sürükleme kuvvetinin düşürülmesi için bu boşluğun doldurulması gerekmektedir.

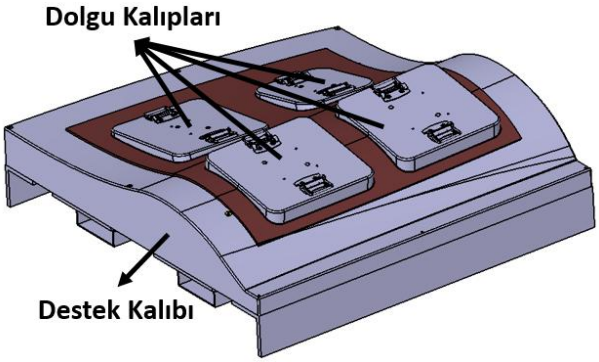
2.3. Dolgu Bölgesi Tasarımı

Özellikle yüksek hızlı uçakların kabuklarındaki yüksek gerilmeler ve deformasyonlar sebebi ile bu dolgunun yerinden ayrılıp birincil yapılara veya kontrol yüzeylerine çarparak hasar verme riskini bertaraf etmek elzemdir. Dolayısıyla, dolgu bölgesinin kabuğa yapıştırılmasında, yüksek yapışma mukavemeti sağlayan, bir darbe (dolu, kuş çarpması, yıldırım, vb.) hasarı durumunda parçalara ayrılmayıp olabildiğince bütünlüğünü koruyan darbe toleransı yüksek bir yöntem kullanılmalıdır. Bu kaygılar göz önünde bulundurulduğunda, Şekil 5'de belirtildiği gibi bu üçgen bölgenin doldurulması için iki farklı doldurma yöntemi belirlenmiştir. Birinci yöntem "fitil dolgu" olarak; ikinci yöntem ise "piramit dolgu" olarak adlandırılmaktadır.

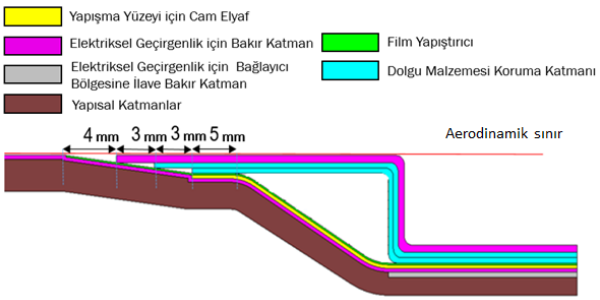


Şekil 5. Dolgu Yöntemleri.

Her iki yöntemde de yapısal parçanın entegre basamaklı kısmı üretildikten sonra aerodinamik kısmı üste gelecek şekilde yerleştirilir ve ayrı bir yerde ters bir kalıp üzerine serim yapılır. İlk olarak elektriksel geçirgenlik için bakır katman serimi yapılır (Bölüm 2.3'te bu malzemenin özellikleri ve kullanım amacı ayrıntılı anlatılacaktır.). Sonrasında kapama malzemesi ve yapışma yüzeyi sağlayan bir kat cam elyaf serimi yapılır. Ardından, dolgu malzemesi serilir. Fitil dolgu yönteminde tek yönlü bant fitilleri çeşitli çaplarda burularak oluşturulmuş ve bu üçgensel boşluk doldurulmuştur. Piramit dolgu yönteminde ise kompozit katmanlar merdiven basamakları gibi gittikçe büyüyecek şekilde kesilerek dolgu kalıbı üzerinde serim yapılmış ve piramit şekli elde edilmiştir. Fitil dolgu yönteminde de piramit dolgu yönteminde de ilk kür çevrimine ait girintiler Şekil 7'deki parametrelerle doldurulmaktadır.

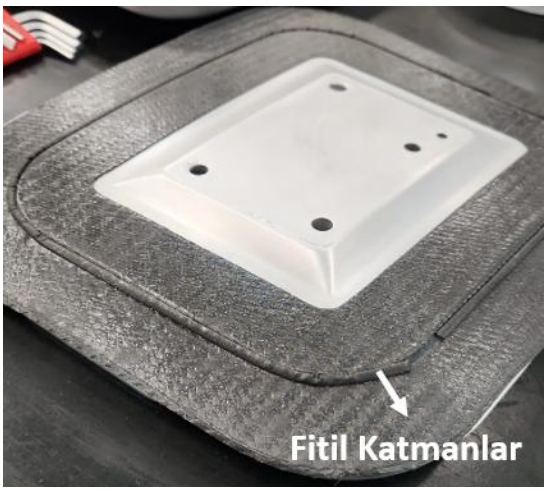


Şekil 6. İkinci kür çevirim kalıbı.



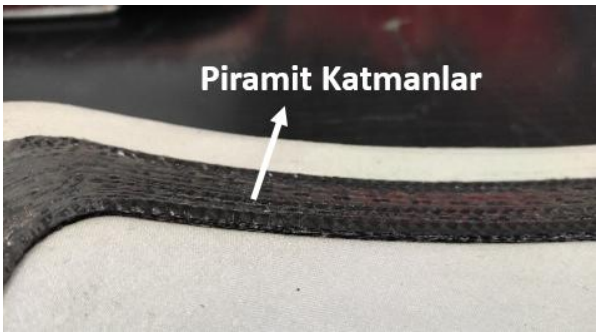
Şekil 7. Dolgu bölgesi parametreleri.

İlk yöntemde tek yönlü bant fitilleri çeşitli çaplarda burularak oluşturulmuş ve bu üçgensel boşluk doldurulmaya çalışılmıştır.



Şekil 8. UD fitillerle üretim yöntemi resimleri.

İkinci doldurma yöntemi olan piramit dolgu yönteminde ise kompozit katmanlar merdiven basamakları gibi gittikçe büyüyecek şekilde kesilerek dolgu kalıbı üzerinde serim yapılmış ve piramit şekli elde edilmiştir.



Şekil 9. Piramit dolgu üretim resimleri.

2.4. Elektriksel Bağlama ve Yıldırımdan Korunmaya Yönelik Tasarım

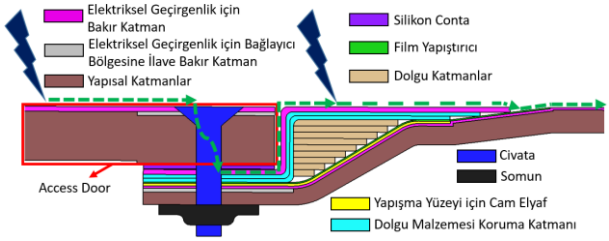
Ranjith vd. (2014) hava araçlarının uçuş güvenliğinin birçok atmosferik faktörden etkilendiğini belirtmişlerdir. Yıldırım da bunlardan biridir. Uçağa yıldırım çarpması, yapısal hasar, dış kabukların erimesi, yakıtın tutuşması ve ölümcül kazalar gibi sorunlara yol açabilir.

Kumar vd. (2020) ise yıldırımların çok sık rastlanan doğa olayları gibi görünmeseler de 10 yıllık süre içinde Amerika'da yaklaşık 216 milyon yıldırım görüldüğünü ve 2000-5000 saat arası ömrü olan bir uçağın ortalama yılda bir kere yıldırım etkilerine maruz kaldığını belirtmişlerdir.

Dolayısı ile bu tarz yakıt kapaklarında iç kısımdaki yakıtın herhangi bir statik elektrik veya yıldırım sebepli ark oluşumu yüzünden alev almasını engellemek için kapak ve yapısal parça elektriksel olarak birleştirilmeli ve tüm uçak şasesine iletken bir hat ile bağlanmalıdır.

Kumar vd. (2020) bunun için yapısal parça tasarımında ECF (Expanded copper foil) denilen yine kendinden reçineli bir katman kullanılabileceğini belirtmiştir. Bu katman aerodinamik yüzeye gelecek şekilde serim yapılarak yıldırımın yakıcı etkisini tüm yüzeye dağıtır.

Ek olarak yıldırımın kapağın üzerine veya kapak üzerindeki bağlayıcılara düşmesi durumunda elektrik akımının kapaktan ana yapıya geçmesini sağlamak için kapak üzerinde de ECF kullanılır.



Şekil 10. Yapısal parça üzerindeki, kapak üzerindeki ve dolgu yapıdaki bakır katmanlar ve elektriksel yol.

2.4 Tahribatsız Muayene ve İmalat sırasının belirlenmesi

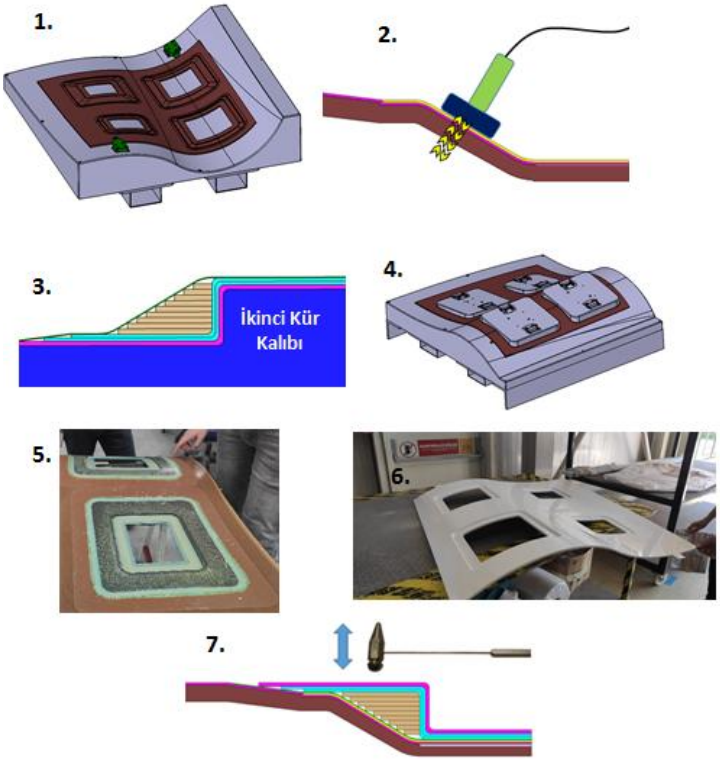
Hassan vd. (2017) belirttiği gibi birincil yapılar bir hava aracında kritik yükleri taşıyan kısımlardır. Eğer bu yapılar ciddi şekilde hasarlanırsa veya kırıma uğrarsa hava aracında ölümcül sonuçlar doğurabilir.

Gholizadeh (2022) ise kompozit havacılık yapılarının bir tahribatsız muayene tekniği olan ultrasonik yöntem ile muayene edilebileceğini belirtmiştir.

Yalnız bu çalışmadaki dolgu kısmının varlığı ultrasonik muayeneyi geometrik olarak engellemektedir. Üst kalıp ve kabuk arasında kalan üçgen dolgu bölgesi kürlenme esnasında bir sıkışmaya maruz kalmaz. Bu sebeple, bölgede boşluklar ve düzensiz oluşumlar ile karşılaşılabilir. Bu kusurlar, ultrasonik muayene ile yapısal parça üzerindeki üretim hasarlarını görmeyi engellemektedir. Bunun önüne geçmek için, yapısal katmanların üretiminden sonra (ilk kür çevirimi sonrası) ultrasonik muayene yapılması gerekmektedir. Bu aşamadaki muayeneyi geçen yapısal parçalar bir sonraki adım olan dolgu yapıştırma aşamasına geçebilmektedir. İkinci kür çevriminden sonra da dolgu bölgesine akustik muayene (tap inspection) yapılarak son ürünün yapışma kalitesi test edilmektedir.

Genel olarak üretim adımlarını özetleyecek olursak;

1. Yapısal katmanların serilerek yapısal parçanın otoklavda kürlenerek üretimi
2. Yapısal parçanın basamak kısmı dahil ultrasonik yöntem ile muayene edilmesi,
3. Dolgu kalıbı üzerine bakır katman, kapama katmanları, dolgu malzemesi ve film yapıştırıcı serilmesi,
4. Dolgu kalıbının ters çevrilerek aerodinamik yüzeye kapatılması,
5. Oluşan bu montajın otoklav içerisinde kürlenmesi,
6. Kürlenen parçanın taşan kısımlarının temizlenerek son haline getirilmesi,
7. Kapama katmanları üzerine akustik muayene (tap inspection) yapılması aşamalarını kapsamaktadır. (
8. Şekil 11)



Şekil 11. İmalat sıralaması ve muayene adımları.

3. Bulgular ve Tartışma

Çalışma sonucunda bütünleşik basamaklı kabuk ve kapak bağlantılarında önemli ölçüde ağırlık azalması görülmüştür.

Ek olarak Şekil 2'de belirtilen klasik yönteme göre alt güçlendirme parçası ve bir sıra bağlayıcı da iptal olduğu için montaj işlemleri sadeleşmiştir.

Bu yöntemde hali hazırda klasik bağlama yönteminde de sağlanan elektriksel bağlama gereksinimi bu yöntemde de sağlanmıştır.

Üretim yöntemi belli adımlara bölünerek bu adımlara muayene gereksinimi eklenmiş ve birincil yapılarda hasar olup olmadığı gözlemlenebilmiştir.

Macun yapıştırıcılara oranla daha yüksek yapıştırma dayanımı sağlayan film yapıştırıcı kullanılabileceği görülmüştür.

İmalat yöntemi açısından değerlendirildiğinde dikdörtgen şekilli bir kapakta fitil dolgu yönteminde köşe çevrelerini dönmeleri esnasında fitil geometrisinde bozulmalar olmuştur ve üçgen kesitin keskin bölgelerinin tam olarak doldurulması sağlanamamıştır. Fakat bu bozulmalar, birincil yük taşıma kapasitesi beklenmeyen bu doldurma bölgesi için kabul edilebilir seviyededir. İkinci yönteme göre bir diğer dezavantajı yoğun el işçiliği ve zaman gerektirmesidir. Buna ek olarak piramit dolgu yöntemi boşlukları daha iyi doldurarak daha iyi bir yapışma sağlamıştır. Ek olarak el işçiliği daha az olmuştur.

Üst kısma eklenen cam elyaf takviyeli kapama katmanları olası darbe hasarı durumlarında yapısal bütünlüğü koruyucu görev yapacak ve hava aracının görev uçuşlarını güvenli şekilde tamamlamasını sağlayacaktır.

4. Sonuçlar

Bu çalışmada havacılık yapılarında, özellikle yakıt erişim kapakları gibi bakım gerektiren alanlarda, klasik bağlantı yöntemlerine alternatif olarak bütünleşik basamaklı bağlantı tasarımı önerilmiş ve bu yapının üretim ve performans açısından avantajları detaylı şekilde incelenmiştir.

Gerçekleştirilen tasarım ve üretim denemeleri neticesinde aşağıdaki başlıca bulgular elde edilmiştir:

- Ağırlık Avantajı: Klasik bağlantıya kıyasla %31'e varan ağırlık azaltımı sağlanmıştır. Bu oran tekil kapak bazında değerlendirilse de Şekil 1'de gösterilen gibi çok sayıda kapağın bulunduğu bir hava aracında bu fark, toplam yapısal ağırlık üzerinde anlamlı bir etki yaratmaktadır.
- Montaj Kolaylığı ve Süre Azalması: Alt güçlendirme parçaları ve bir sıra bağlayıcının ortadan kaldırılması ile toplam parça ve montaj süresi azalmış, üretim verimliliği artmıştır.
- Elektriksel İletkenlik ve Yıldırım Koruması: Kapak ve yapısal parça arasında sağlanan ECF katman teması, yıldırıma karşı güvenli bir elektriksel yol oluşturarak kritik güvenlik gereksinimlerini karşılamıştır.
- Darbe Dayanımı: Cam elyaf takviyeli kapama katmanları ve film yapıştırıcılar sayesinde olası darbe hasarlarında parçalanma riskleri azaltılmış, yapı bütünlüğü korunmuştur.
- Üretim ve Muayene Uygunluğu: İki aşamalı kürleme yöntemi ve entegre edilen tahribatsız muayene adımları, üretim kalitesinin kontrol altında tutulmasına olanak sağlamıştır.
- Dolgu Yöntemleri Karşılaştırması: Fitil dolgu yönteminin

bazı geometrik zorlukları olmasına karşın kabul edilebilir seviyede sonuçlar verdiği, piramit dolgu yönteminin ise daha homojen bir dolgu ve düşük iş gücü gereksinimi ile öne çıktığı gözlemlenmiştir.

Katkı Oranı Beyanı

Yazarların katkı yüzdeleri aşağıda verilmiştir. Yazarlar makaleyi incelemiş ve onaylamıştır.

	M.C.	Ö.K.
K	50	50
T	50	50
Y	50	50
VTI	50	50
VAY	50	50
KT	50	50
YZ	50	50
KI	50	50
GR	50	50
PY	50	50
FA	50	50

K= kavram, T= tasarım, Y= yönetim, VTI= veri toplama ve/veya işleme, VAY= veri analizi ve/veya yorumlama, KT= kaynak tarama, YZ= Yazım, KI= kritik inceleme, GR= gönderim ve revizyon, PY= proje yönetimi, FA= fon alımı.

Çatışma Beyanı

Yazarlar bu çalışmada hiçbir çıkar ilişkisi olmadığını beyan etmektedirler.

Etik Onay Beyanı

Bu araştırmada hayvanlar ve insanlar üzerinde herhangi bir çalışma yapılmadığı için etik kurul onayı alınmamıştır.

Kaynaklar

Doğan MA, Yapici A, Gemi L, Yazman Ş, Morkavuk S, Köklü U. 2025. Investigation of the stacking sequence and cutting parameters effect on hole morphology in hybrid FML composites, Compos Part B Eng, ID: 112464, pp: 300-310.

Erhan F, Gemi L, Yazman Ş, Morkavuk S, Köklü U. 2025. A comprehensive investigation into the influence of variation in the stacking sequence on the mechanical behaviour and drilling machinability of basalt fiber-reinforced composite tubes, Compos Part B Eng, ID: 112405, pp: 299-300.

Gholizadeh S. 2022. Impact behaviours and non-destructive testing (NDT) methods in carbon fiber composites in aerospace industry: a review, Authorea Prepr, pp: 1-33.

Hassan MH, Othman AR, Kamaruddin S. 2017. A review on the manufacturing defects of complex-shaped laminate in aircraft composite structures, Int J Adv Manuf Technol, 91: pp: 4081-4094.

Khechai A, Layachi M, Belarbi MO, Gohery S, Layachi S, Ruocco E, Gemi L, Liang QQ. 2025. An extended Greszczuk's analytical method for stress analysis of unsymmetrical laminated composite plates with a circular hole under axial, biaxial, and shear loads, Structures, 71: ID: 108169, pp: 71.

Kumar V, Yokozeki T, Karch C, Hassen AA, Hershey CJ, Kim S, Kunc V. 2020. Factors affecting direct lightning strike damage to fiber reinforced composites: a review, Compos Part B Eng, 183: ID: 107688, pp: 183.

Meram A, Can A. 2019. Experimental investigation of screwed joints capabilities for the CFRP composite laminates, Compos Part B Eng, 176: ID: 107142, pp: 176.

Niu MCY. 1999. Airframe Stress Analysis and Sizing (2nd Ed.), Hong Kong, Hong Kong Conmilit Press Ltd., pp: 374.

Ranjith R, Myong S, Lee S. 2014. Computational investigation of lightning strike effects on aircraft components, Int J Aeronaut Space Sci, 15(1): pp: 44-53.

Uzay Ç, Geren N. 2020. Advanced technologies for fiber reinforced polymer composite manufacturing, Kahramanmaraş Sütçü İmam Üniv Müh Bilim Derg, 23(4): pp: 245-257.

Black Sea Journal of Engineering and Science
doi: 10.34248/bsengineering.1665890

Open Access Journal
e-ISSN: 2619 – 8991

Araştırma Makalesi (Research Article)
Cilt 8 - Sayı 4: 1057-1066 / Temmuz 2025
(Volume 8 - Issue 4: 1057-1066 /July 2025)

BLOCKCHAİN DESTEKLİ NESNELERİN İNTERNETİ (IOT) VARLIKLARINDA FİYAT TAHMİNİ İÇİN MODEL KARŞILAŞTIRMASI

Çağatay ERSİN [1]*, Onur KÖKTÜRK[2]

[1]*Çankırı Karatekin University, Vocational School, Department of Electronics and Automation, 18200, Çankırı, Türkiye*
[2] *Çankırı Karatekin University, Vocational School, Department of Finance, Banking and Insurance, 18200, Çankırı, Türkiye*

Özet: Teknolojik gelişmelerin hız kazanmasıyla birlikte Nesnelerin İnterneti (IoT - Internet of Things), küresel ölçekte üretim süreçlerinden akıllı şehir uygulamalarına, kişisel sağlık izleme cihazlarından akıllı spor kıyafetlerine kadar geniş bir yelpazede dönüşüme katkı sağlamaktadır. Nesnelerin İnterneti, cihazların birbirleriyle ve veri merkezleriyle etkileşime geçerek büyük miktarda veri ürettiği bir ekosistem yaratmaktadır. Bu bağlamda, IoT teknolojilerine dayalı blok zinciri tabanlı kripto varlıklar da gelişim göstermiştir. Bu çalışmanın amacı, IoT temalı kripto varlıklardan Vechain (VET), IOTA ve Helium (HNT) için fiyat tahmini yapmaktır. Çalışmada 02.01.2020 - 10.12.2024 tarihleri arasındaki Vechain ve IOTA, 09.06.2020 - 10.12.2024 tarihleri arasındaki Helium coinin günlük kapanış fiyatları kullanılmıştır. Fiyat tahmini için Karar Ağaçları (Decision Trees), Rassal Orman (Random Forest) ve Destek Vektör Regresyonu (SVR) modelleri karşılaştırılmıştır. Karar ağaçları modeli, geçmiş fiyat verilerini baz alarak gelecekteki fiyat hareketlerini tahmin etmeyi amaçlamaktadır. Rassal Orman algoritması, birden fazla karar ağacının bir araya getirilmesiyle oluşan topluluk öğrenme yöntemini kullanarak daha sağlam ve genellenebilir tahminler sunmaktadır. Destek Vektör Regresyonu (SVR) ise veri noktaları arasındaki karmaşık ilişkileri daha iyi yakalamak için hiper düzlemleri kullanarak doğrusal olmayan regresyon modelleri oluşturur. Modellerin performansı Mean Squared Error (MSE) ve R^2 (R-kare) skoru gibi metriklerle değerlendirilmiştir. Sonuçlar, Rassal Orman modelinin Helium ve IOTA coinlerin tahminlerinde yüksek doğruluk sağladığını, VeChain coin için ise SVR'nin daha iyi modellediğini ortaya koymuştur. Karar Ağaçları modeli, bağımsız tahminler üretme konusunda başarılı olmakla birlikte diğer modellere göre nispeten daha düşük performans göstermiştir.

Anahtar kelimeler: Kripto varlıklar, Karar ağaçları, Rassal orman, Destek vektör regresyonu

Model Comparison for Price Prediction in Blockchain-Enabled Internet of Things (IoT) Assets

Abstract With the acceleration of technological developments, the Internet of Things (IoT) contributes to a wide range of transformations, from global production processes to smart city applications, from personal health monitoring devices to smart sportswear. The Internet of Things creates an ecosystem where devices interact with each other and data centers to produce large amounts of data. In this context, blockchain-based crypto assets based on IoT technologies have also developed. The aim of this study is to make a price prediction for IoT themed crypto assets Vechain (VET), IOTA and Helium (HNT). In the study, the daily closing prices of Vechain and IOTA between 02.01.2020 - 10.12.2024, and Helium coin between 09.06.2020 - 10.12.2024 were used. Decision Trees, Random Forest and Support Vector Regression (SVR) models were compared for price prediction. The decision tree model aims to predict future price movements based on past price data. The Random Forest algorithm provides more robust and generalizable predictions by using the ensemble learning method formed by combining multiple decision trees. Support Vector Regression (SVR) creates non-linear regression models using hyperplanes to better capture complex relationships between data points. The performance of the models was evaluated with metrics such as Mean Squared Error (MSE) and R^2 (R-squared) score. The results showed that the Random Forest model provided high accuracy in predictions for Helium and IOTA coins, while SVR modelled better for VeChain coin. The Decision Tree model was successful in producing independent predictions but showed relatively lower performance than other models.

Keywords: Internet of things, Cryptocurrency, Decision trees, Random forest, Support vector regression

***Sorumlu yazar (Corresponding author):** Çağatay ERSİN, Çankırı Karatekin University, Vocational School, Department Of Electronics and Automation, 18200, Çankırı, Türkiye
E mail: cagatayersin@karatekin.edu.tr (Ç. ERSİN)
Çağatay ERSİN https://orcid.org/0000-0001-5018-9313
Onur KÖKTÜRK https://orcid.org/0000-0002-8603-8063

Gönderi: 26 Mart 2025 **Received:** March 26, 2025
Kabul: 15 Mayıs 2025 **Accepted:** May 15, 2025
Yayınlanma: 15 Temmuz 2025 **Published:** July 15, 2025
Cite as: Çağatay E, Köktürk O. 2025. A model comparison for price prediction in blockchain-enabled ınternet of things (IoT) assets. BSJ Eng Sci, 8(4): 1057-1066.

1. Giriş

Nesnelerin Ağı olarak da bilinen Nesnelerin İnterneti (IoT); çoğu zaman her yerde bulunan zekâ ile donatılmış sıradan nesnelerin ağ bağlantılı etkileşimini ifade etmektedir. IoT, gömülü sistemler aracılığıyla nesneleri etkileşim için entegre ederek, insanlarla ve diğer cihazlarla iletişim kuran dağıtılmış bir cihaz ağı oluşturmaktadır. Temel teknolojilerdeki hızlı gelişmeler sayesinde son yıllarda dünya çapındaki araştırmacılar ve

This work is licensed (CC BY-NC 4.0) under Creative Commons Attribution 4.0 International License

uygulayıcılar tarafından büyük ilgi gören IoT, yaşam kalitemizi iyileştirmeyi vaat eden birçok yenilikçi uygulama için büyük fırsatlar sunmaktadır. Bu teknoloji, bilgi işlem gücündeki ilerlemelerden, elektroniklerin minyatürleştirilmesinden (electronics miniaturization) ve ağ bağlantılarından yararlanarak daha önce mümkün olmayan yeni yetenekler sunan geniş bir ağ bağlantılı ürün, sistem ve sensör yelpazesinde somutlaşmıştır. IoT, teknik, sosyal ve ekonomik açıdan önemli bir gelişen konudur ve tüketici ürünleri, dayanıklı mallar, arabalar ve kamyonlar, endüstriyel ve kamu hizmeti bileşenleri, sensörler ve diğer günlük nesneler, internet bağlantısı ve güçlü veri analitiği yetenekleriyle birleştirilerek çalışma, yaşama ve eğlenme biçimlerini dönüştürme potansiyeline sahiptir. IoT cihazlarının geniş çaplı uygulanması, yaşamımızın birçok yönünü dönüştürme potansiyeline sahiptir. Tüketiciler için, İnternet'e bağlı cihazlar, ev otomasyon bileşenleri ve enerji yönetim cihazları gibi yeni IoT ürünleri, daha güvenli ve enerji verimli bir "akıllı ev" vizyonuna doğru ilerlemektedir. Kişisel IoT cihazları, giyilebilir spor kıyafetleri ve sağlık izleme cihazları ile ağ bağlantılı tıbbi cihazlar, sağlık hizmetlerinin sunulma biçimini dönüştürmektedir. Bu teknoloji, engelli bireyler ve yaşlılar için daha yüksek seviyede bağımsızlık ve yaşam kalitesi sunarken, bunu makul bir maliyetle gerçekleştirebilmektedir. Ağ bağlantılı araçlar, akıllı trafik sistemleri ve yollara ve köprülere gömülü sensörler gibi IoT sistemleri, bizi "akıllı şehirler" fikrine daha da yaklaştırmaktadır. Bu şehirler, trafik sıkışıklığını ve enerji tüketimini en aza indirmeye yardımcı olabilmektedir. IoT teknolojisi ayrıca, üretim değer zinciri boyunca ağ bağlantılı sensörler aracılığıyla bilgiye erişimi artırarak tarım, sanayi ve enerji üretimi ve dağıtımını dönüştürme olasılığı sunmaktadır (Rose, 2015; Xia, 2012). Bilgi teknolojisi (IT) ve operasyonel teknoloji (OT), tarihsel olarak bağımsız çalışmıştır. Ancak, IoT' un artan kullanımı, IT ve OT'nin birleşmesine yol açmıştır. Bu birleşim, iş dünyasına fayda sağlarken aynı zamanda ölçeklenebilirlik, güvenlik, gizlilik, birlikte çalışabilirlik ve büyük veri analitiği gibi birçok zorluğu da beraberinde getirmiştir. IoT ağlarında güvenlik, en büyük endişelerden biridir (Dange ve Nitnaware, 2024). Çünkü IoT'nin kesintisiz çalışması için yalnızca kimliği doğrulanmış ve yetkilendirilmiş cihazlara erişilebilir olması gerekmektedir. Aksi takdirde, bilgi hırsızlığı, veri değişikliği ve kimlik hırsızlığı gibi çeşitli güvenlik risklerinin hedefi haline gelebilmektedir.

IoT'nin bilgi bütünlüğünü korumak için geleneksel güvenlik mekanizmaları tek başına yeterli olmamaktadır (Vishwakarma ve Das, 2021). IoT ağına bağlı cihazların sayısı arttıkça, bu veriler genellikle şifrelenmez ve gizlilik sağlamamaktadır. Bu bağlamda, blockchain teknolojisi büyük faydalar sunabilmektedir. Çünkü elde edilen verilerin anonimliğini hızla güvence altına alınabilmektedir (Ahamad, 2022). Bu nedenle IoT'un güvenliğini sağlamak amacıyla, merkeziyetsiz ve dağıtık bir yaklaşım olarak blok zincir (blockchain) önerilmiştir (Wang vd., 2020). Merkeziyetsiz sistemler, belirli bir otoriteye veya donanıma bağlı kalmaksızın gizlilik ve ölçeklenebilirlik sağlayabilmektedir. Bu bağlamda, Dağıtık Defter Teknolojileri, IoT ekonomisinin uygulanmasında önemli kolaylaştırıcılar olabilmektedir (Silvano ve Marcelino, 2020). İşlemlerin kaydını katılımcı bilgisayarlardan oluşan bir ağ üzerinde dağıtılmış şekilde tutulan ve 2009 yılında anonim bir geliştirici grubu tarafından geliştirilen Bitcoin, sanal bir para biriminin kullanımını, elektronik ödemeler de dahil olmak üzere, kolaylaştıran bir çevrimiçi iletişim protokolüdür (Böhme vd., 2015).

Bitcoin, bankalar ve finansal kurumlar gibi aracıları devre dışı bırakarak işlem yapılmasına ve işlemlerin bireyler arasında doğrudan (peer-to-peer) gerçekleşmesine olanak tanımaktadır (Fauzi vd., 2020). Daha sonraki süreçte geliştirilen ve Bitcoin'den sonra en büyük kripto para platformu olarak kabul edilen Ethereum, Bitcoin'den farklı olarak yalnızca bir dijital para birimi değil, tamamen programlanabilir bir blok zinciri platformudur. Bitcoin, merkeziyetsiz bir değer saklama aracı olarak tasarlanmışken, Ethereum akıllı sözleşmelerin ve merkeziyetsiz uygulamaların (DApp'ler) geliştirilmesi ve çalıştırılmasını kolaylaştırmaktadır. Bu uygulamalar, merkezi aracılara ihtiyaç duymadan otonom bir şekilde çalışabilir ve bu sayede merkeziyetsiz finans (DeFi), tedarik zinciri yönetimi ve değiştirilemez tokenler (NFT'ler) gibi çeşitli sektörlerde daha fazla verimlilik ve şeffaflık sağlamaktadır (Krause, 2024).

Çalışma IoT tabanlı çözümler oluşturmayı hedef alan kripto varlıkları incelemektedir. Bu bağlamda, çalışmada Vechain, IOTA ve Helium kripto varlıklarının geliştirilme amaçları ele alınacaktır. VeChain, şeffaf bilgi akışını, verimli iş birliğini ve yüksek hızlı değer transferlerini mümkün kılmayı hedefleyen güven gerektirmeyen ve dağıtık bir iş ekosistemi yaratmayı amaçlayan bir blok zincir platformudur. VeChain'in çözümü, ürünlerin üretim, lojistik ve tedarik zinciri, perakende ve toptan satış, satış sonrası hizmet ve hatta IoT teknolojileriyle birlikte sahteciliğe karşı blockchain üzerinde tüketici katılımı gibi yaşam döngüsünü kapsayan bir ürün izlenebilirliği çözümü oluşturmayı hedeflemektedir. Moda ve lüks markalar, VeChain çözümlerinin canlı ürünler için uygulamaya koymakta ve sahtecilik faaliyetlerinde büyük azalma sağlamaktadır (VeChain Development Plan and Whitepaper, 2018).

IoT'a bağlı bütün cihazlar çevrimiçi olduğu zaman hücresel, WiFi ve Bluetooth gibi mevcut çözümler yetersiz kalacaktır. Ayrıca tüm bu süreç çok pahalı olacak ve mevcut bağlantılar çok fazla güç tüketecek veya menzilleri çok sınırlı kalacaktır. Bu sorunlara çözüm üretmek için geliştirilen Helium ağı, dünyanın herhangi bir yerindeki cihazların, enerji tüketen uydu konumlandırma donanımına veya pahalı hücresel planlara ihtiyaç duymadan kablosuz olarak internete bağlanmasını ve kendi konumlarını belirlemesini sağlayan merkeziyetsiz bir kablosuz ağdır. Güvenli ve açık kaynaklı, geliştiricilerin düşük güç tüketen, internete

bağlı cihazları hızlı ve uygun maliyetli bir şekilde oluşturmalarını sağlamayı amaçlayan Helium ağı, birçok sektörde geniş bir uygulama yelpazesine sahiptir ve türünün ilk merkeziyetsiz kablosuz ağıdır. Helium ağı, geniş alan kablosuz bir ağ sistemi, bir blockchain ve bir protokol token'ından oluşmaktadır. Blockchain, Helium Konsensüs Protokolü (Helium Consensus Protocol) adı verilen yeni bir konsensüs protokolü ve Kapsama Kanıtı (Proof-of-Coverage) üzerinde çalışmaktadır. Kablosuz ağ kapsama alanı sağlayan madenciler, kriptografik olarak doğrulanmış fiziksel bir konum ve zamanda kanıtlarını Helium ağına sunmaktadır (Haleem, 2018). IOTA, 2015 yılında oluşturulmuş bir dağıtık defter platformudur ve "blok zincirsiz kripto para birimi" olarak tanımlanmıştır. IOTA'nın tüm para birimi önceden oluşturulmuştur; dolayısıyla madencilik süreci bulunmamaktadır. Toplam IOTA miktarı yaklaşık 2,8 Peta olarak belirlenmiştir. IOTA, piyasa değeri açısından en önemli ilk on kripto para biriminden biri olarak kabul edilmektedir. IOTA'nın amacı, IoT cihazları arasındaki işlemleri desteklemek ve güçlendirmektir. IOTA, blockchain teknolojisinin dezavantajlarını doğal olarak çözer ve eşler arası mikro ödeme sistemi oluşturmak için gereken özellikleri sunmaktadır. Bu teknolojinin diğer dağıtık defter teknolojilerinden farkı, işlemleri depolamak için blockchain yerine Yönlendirilmiş Döngüsüz Grafik olarak bilinen Tangle adı verilen bir yapıya dayanmasıdır (Alshaikhli vd., 2021; Saa vd., 2023). Bu çalışmanın temel amacı, IoT temalı kripto varlıklar olan Vechain (VET), IOTA ve Helium (HNT) coin'lerinin günlük kapanış fiyatlarını kullanarak fiyat tahmini yapmaktır. Çalışma, 02.01.2020 - 10.12.2024 tarihleri arasındaki Vechain ve IOTA ile 09.06.2020 - 10.12.2024 tarihleri arasındaki Helium kripto varlıklarının fiyat hareketlerini kapsamaktadır.

Literatür incelendiğinde, söz konusu IoT tabanlı kripto varlıkların fiyat tahmini üzerine yapılan çalışmaların oldukça sınırlı olduğu görülmektedir. Bu nedenle, çalışma kripto varlık piyasasında IoT temalı coin'lerin fiyat hareketlerinin öngörülmesine yönelik katkı sağlamayı amaçlamaktadır. Fiyat tahmini için Karar Ağaçları (Decision Trees), Rassal Orman (Random Forest) ve Destek Vektör Regresyonu (SVR) algoritmaları kullanılmıştır. Karar Ağaçları algoritması, geçmiş fiyat verilerini baz alarak doğrudan bir tahminleme süreci yürütmektedir. Rassal Orman, birden fazla Karar Ağacı modelinin çıktılarının birleştirilmesiyle oluşturulan güçlü bir topluluk öğrenme yöntemidir. SVR ise doğrusal olmayan regresyon modelleri oluşturarak fiyat hareketlerindeki karmaşık ilişkileri daha iyi modellemeyi amaçlamaktadır.

1.1. Literatür

Finansal varlıklara olan ilginin arttığı günümüzde başta yatırımcılar olmak üzere araştırmacıların da finansal varlık fiyatlarını tahmin etmek belirsizliği de azaltmak adına daha da önem kazanmaktadır. Sadece geleneksel finansal ürünlerinde değil yüksek volatiliteye sahip kripto varlıklarında fiyat hareketleri tahmin etme üzerine yapılan çalışmalar gün geçtikçe daha da artmaktadır. Geleneksel ekonometrik yöntemlerin yanı sıra gelişen bilişim teknolojisine bağlı olarak makine ve derin öğrenme modelleri kullanarak da tahmin modelleri oluşturulmaktadır.

Kantar (2020) 2009-2019 dönem aralığı için BIST 100 endeksini Yapay Sinir Ağları ve ARMA (1,1) modeli kullanarak döviz kuru sepeti, altın, mevduat faizi, sanayi üretim endeksi, emisyon, doğrudan portföy yatırımları ve sermaye yatırımları gibi makroekonomik değişkenler ile tahmin etmeyi amaçladığı çalışmasında; Yapay Sinir Ağlarının daha yüksek R2 değerine ve daha küçük MSE değerine sahip olduğu için daha iyi tahmin performansına sahip olduğunu vurgulamıştır.

Akel ve Bayramoğlu (2008) 04.01.1999-28.02.2001 dönem aralığında ve finansal krizin varlığında ABD Doları, Merkez Bankası Döviz Rezervleri, İMKB işlem hacmi, 1 aylık mevduat faiz oranı ve Altın Borsası kapanış fiyatlarını girdi değişkeni olarak seçip Yapısal Sinir Ağları yöntemi ile İMKB 100 endeksi için yaptığı tahminlemede çok katmanlı ve geri besleme algoritması ile başarılı bir tahminleme yapmışlardır.

Altan (2008) yaptığı çalışmasında Ocak 1987- Eylül 2007 tarih aralığı baz alınarak döviz kuru tahminlemesi yapabilmek için aylık veriler ile yapay sinir ağı ve vektör otoregresif modeli kullanmış ve her iki modelden sağlanan sonuçların tahmin performansını arttırdığını belirtmiştir.

Aygören vd., (2012) İMKB 100 endeksi için mevduat faiz oranı, USD kapanış fiyatları, altın fiyatları ve bankalar arası para piyasası işlem hacmi değişkenleri ile ARMA modeli, Yapay Sinir Ağları için Geri Yayılım Algoritması ve Nümerik Arama Modelleri için Newton yöntemi kullanarak yaptıkları tahminleme modellerinden Yapay Sinir Ağlarının daha iyi tahmin başarısı gösterdiğini bulmuşlardır.

Çalışkan ve Deniz (2015) yaptıkları çalışmalarında BİST30 endeksine ait seçilen 27 şirketin 14.12.2009-21.11.2014 dönem aralığındaki günlük hisse senedi fiyatları esas alınarak 32 adet girdi seti ile Yapay Sinir Ağları yöntemi ile 5 günlük fiyatları ortalamada yüzde 58 başarı oranı ile tahminde bulunmuşlardır.

Akşehir ve Kılıç (2019) 01.01.2016-26.04.2019 dönem aralığı için AKBNK, HALKB, GARAN, YKBNK ve ISCTR hisse senetlerine ait 50 adet teknik ve temel analiz göstergesini girdi olarak seçip 33 ve 50 göstergeli olarak iki farklı model Karar Ağacı, Rassal Orman ve Çoklu Regresyon yöntemleri ile tahminlemiştirler. 33 gösterge ile yapılan modelleme ile elde edilen tahmin sonuçlarının daha iyi olduğu tespit edilmiştir.

Esenyel ve Akın (2017) Euro ve İngiliz Sterlin'i için 3 Ocak 2002-31 Ekim 2016 tarih aralığına ait veri setini baz aldıkları çalışmalarında tahminlemede bulunabilmek için Hızlı Öğrenen Makine (Extreme Learning Machine-ELM), ARMA ve ARMA GARCH modellerini kullanmışlardır. Elde edilen bulgulara göre performans kriterleri ile yapılan karşılaştırmada ELM modelinin daha üstün olduğu bulunmuştur.

Chowdhury vd., (2020) çalışmalarında makine öğrenimi algoritmaları ve modelleri kullanarak kripto para endeksi 30 ve Bitcoin Cash, Bitcoin, Doge coin (DOGE); Dash, IOTA (MIOTA), Ethereum, Litecoin, NEM, NEO gibi dokuz kripto para bileşeninin kapanış fiyatını tahmin etmişlerdir. Çalışmada makine öğrenim modellerinden Topluluk Öğrenme Yöntemi (Ensemble Learning Method), Gradyan Destekli Ağaç Modeli (Gradient Boosted Trees Model), Sinir Ağı Modeli (Neural Net Model, K-En Yakın Komşu (K-NN) Modeli (K-Nearest Neighbor (K-NN) Model) kullanılmış ve en iyi çıktıyı elde etmek için modelleri birbirleriyle karşılaştırılmıştır. Çalışmada kullanılan tüm modeller arasında en iyi sonucu Topluluk Öğrenme Yöntemi %92,4 oranında doğru sonuç elde ederken diğer modellerin aksine, K-NN modeli çok etkili bir tahminleme yapamamıştır.

Lyu (2022) BTC, ETH, DOGE, ADA, XRP, LUNA, BNB, LINK, LTC ve BCH kripto varlıklarının kısa vadeli alım satım işlemleri için zaman serisi verilerini tahmin etmeye odaklanmaktadır. Çalışmada Karar Ağacı, Doğrusal Regresyon, Ridge Regresyon, Lasso Regresyon, Rassal Orman, Bayesyen Regresyon, K-En Yakın Komşu, Sinir Ağları, Gradyan Artırma ve Destek Vektör Makinesi makine öğrenimi algoritmaları seçilmiştir. Çalışmadan elde edilen sonuçlara göre, Ortalama Kare Hata kriteriyle Gradyan Artırma algoritmasının, çoğu büyük kripto para birimini tahmin etmede üstün başarı göstermektedir. Ayrıca, Karar Ağacı ve Rassal Orman modelleri, ETH, XRP, LUNA ve LTC gibi belirli kripto para birimlerinde yüksek performans sergilemiştir. Bu nedenle, bu üç algoritma, kripto para piyasasının kısa vadeli gelişmelerini tahmin etmek için yatırımcılara yardımcı olabileceği belirtilmiştir.

Yürük (2023) New York Borsası'nda (NYSE) kote olan Delta Havayolları'nın hisse senetlerinin 2010 Ocak-2021 Aralık dönem aralığı için aylık fiyatları kullanarak Box-Jenkins yöntemi ile tahminleme yaptığı çalışmasında Box- Jenkins yaklaşımının tahmin çıktılarında başarılı sonuçlar verdiği belirtmiştir.

Eylasov ve Çiçek (2024) yaptıkları çalışmalarında Bitcoin (BTC), Ethereum (ETH) ve Binance (BNB) kripto para getirilerini tahminlemek amacıyla ARIMA-GARCH yöntemi ile birlikte derin öğrenme yöntemlerinden LSTM (Long Short-Term Memory) yaklaşımını kullanarak elde ettikleri modellerin tahmin başarılarını karşılaştırmışlardır. Elde ettikleri model sonuçlarına göre Bitcoin'e ait modellemede eğitim verisinde ARIMAGARCH yöntemi, test verisi için ise LSTM yöntemi daha iyi sonuçlar vermiştir. BNB serisinde ise hem eğitim hem de test verisi için LSTM yöntemi diğer modellere göre daha üstün performans sergilemiştir. Ethereum serisinde ise her iki veri seti için ARIMA-GARCH yönteminin daha iyi sonuçlara sahip vurgulamaktadır.

Parvini (2024) yüksek piyasa değerine sahip üç kripto paranın (Bitcoin, Ethereum ve Ripple) kapanış fiyatını öngörmek için Destek Vektör Regresyonuna (SVR) dayalı bir makine öğrenimi modeli önermektedir. Çalışmada optimal hiperparametreler, parçacık sürü optimizasyonu (PSO) algoritması uygulanarak elde edilmiştir. Ayrıca PSO-SVR yaklaşımı, MLP (Çok Katmanlı Algılayıcı), LSTM (Uzun Kısa Süreli Bellek), Bi-LSTM (Çift Yönlü Uzun Kısa Süreli Bellek) ve ayrıca basit SVR modeli ile karşılaştırılmıştır. PSO-SVR modeli, tüm kripto paralar ve kullanılan performans ölçütleri açısından karşılaştırmalı modellerin tamamından daha iyi performans göstermektedir.

Katina (2024) çalışmasında Otoregresif Entegre Hareketli Ortalama (ARIMA), Mevsimsel ARIMA (SARIMA), Uzun Kısa Süreli Bellek (LSTM) ve Kapılı Tekrarlayan Birim (Gated Recurrent Unit-GRU) modellerinin Bitcoin, Ethereum, Dogecoin, Polygon ve Toncoin gibi çeşitli kripto paralar üzerindeki tahmin doğruluğunu değerlendirmeyi amaçlamaktadır. Çalışmada her bir modelin doğruluğunu değerlendirmek için Ortalama Kare Hata, Ortalama Mutlak Hata, Kök Ortalama Kare Hata ve Ortalama Mutlak Yüzde Hatası gibi performans ölçütleri kullanılmıştır. Çalışmadan elde edilen bulgulara göre derin öğrenme tekniklerinden yararlanan LSTM ve GRU modellerinin, hata ölçütleri açısından genellikle geleneksel ARIMA ve SARIMA modellerinden daha iyi performans gösterdiğini ortaya koymaktadır.

Bouteska (2024) topluluk öğrenimi ve derin öğrenme tahmin modellerinin kapsamlı bir karşılaştırmalı analizini yaptığı çalışmasında, Bitcoin, Ethereum, Ripple ve Litecoin gibi çeşitli kripto paralar üzerinde tahmin başarılarını araştırmıştır. Çalışmanın sonuçları, Kapılı Tekrarlayan Birim (Gated Recurrent Unit-GRU), Basit Tekrarlayan Sinir Ağı (Simple Recurrent Neural Network-RNN) ve LightGBM yöntemlerinin diğer makine öğrenimi yöntemlerinden, ayrıca saf al ve tut (naive buy-and-hold) ve rastgele yürüyüş stratejilerinden daha iyi performans gösterdiğini ortaya koymaktadır. Ayrıca Tablo 1'de makine ve derin öğrenme yöntemleri ile yapılan diğer çalışmalara yer verilmiştir.

Tablo 1. Makine ve Derin Öğrenme Yöntemleri ile Yapılan Çalışmalar

Yazarlar	Zaman Aralığı (Dönem)	Tahmin edilen değişken	Yöntem	Temel bulgular
Özer vd., (2018)	2012-2016	Shangai, Bifty 50, IPC-Meksika, BİST 100, Nadaq, DAX, FTSE 100ve CAC 40 Endeksleri	•Yapay Sinir Ağları •Bulanık Mantık	Modellerin Verimlilik Katsayıları (VK) yüksek bulunmuştur.
Hiransha vd., (2018)	•1.01.1996-30.06. 2015 •3.01.2011-30.12.2016	Hindistan Ulusal Borsası (NSE) ve New York Borsası (NYSE)	•Çok Katmanlı Algılayıcı (MLP), •Tekrarlayan Sinir Ağları (RNN), •Uzun Kısa Süreli Bellek (LSTM) •Evrişimsel Sinir Ağı (CNN)	Evrişimsel Sinir Ağı (CNN) diğer yöntemlere göre daha iyi bir tahmin başarısına sahiptir.
Sakarya ve Yılmaz (2019)	02.01.2001-31.12.2018	BİST 30	Derin Öğrenme Yöntemleri	Yapılan tahminleme yüzde 80 doğruluğa sahiptir.
Yavuz vd., (2020)	01.01.2009-23.07.2018	Bitcoin	Yapay Sinir Ağları (YSA)	%99 oranında tahmin başarısı sağlanmıştır.
Akay vd., (2022)	01.01.202007.05.2021	Binance Coin BNB, Ripple XRP ve ethereum ETH	•Yapay Sinir Ağları (YSA) •Uzun Kısa Süreli Bellek (LSTM)	YSA modeli seçilen kripto paralar için çok düşük hata payları çıkarmıştır.
Doğan ve Büyükkör (2022)	07.07.2017-06.07.2022	•İstanbul Borsasına (BİST 100) Ereğli Demir ve Çelik ile Aselsan •New York Borsası (NYSE) ve	•Destek Vektör Regresyonu, •Rassal Orman •Extrem Gradyan Arttırma	SVR, en iyi tahmin yöntemi olarak tespit edilmiştir.
Demirci ve Karaatlı (2023)	GRU modelinde Bitcoin, Ethereum ve Ripple günlük kapanış fiyatlarının 04.08.2020-15.09.2020 LSTM modelinde Bitcoin, Ethereum ve Ripple günlük kapanış fiyatlarının 04.08.202015.09.2020 dönemleri	Bitcoin, Ethereum ve Ripple	•Uzun-Kısa Süreli Bellek (LSTM) •Geçitli Yinelenen Birim (GRU)	İki modelde de en iyi tahmin sonucunu Bitcoin vermiştir.

Blok zincir teknolojisi günümüzde tedarik zinciri ve lojistikten finansa kadar birçok farklı sektörlerde kullanılmaktadır. Lojistik alanında Konacaklı ve Eyüpoğlu (2023) akıllı hava mühimmatı sistemleri için takip lojistik takip sistemi tasarlarken Tekin vd., (2020) akıllı lojistik faaliyetlerinin Blok zincir teknolojisiyle getirdiği yenilikleri incelemiştir.

Tedarik zinciri alanında ise Koç (2020) örnek olay yönetimini esas aldığı çalışmasında tedarik zinciri izlenebilirliği için firmaların blok zincir teknolojisinin stratejileriyle uyumlu olup olmadığı incelemeleri gerektiğini vurgulamıştır. Cankül ve Kızıltaş (2020) yiyecek içecek firmalarının tedarik zinciri sürecinde blok zincir teknolojisinin kullanılması durumunda firmalara sağlayacağı avantajları irdelemiştir.

Gıda alanında yapılan çalışmalar incelendiğinde Yazar vd., (2023) gıda güvenliği için blok zincir temalı bir model tasarlarken Gökoğlan ve Atalan (2022) blok zincir teknolojisi ile gıda ürünlerinin tedarik zinciri yönetimini incelemişlerdir.

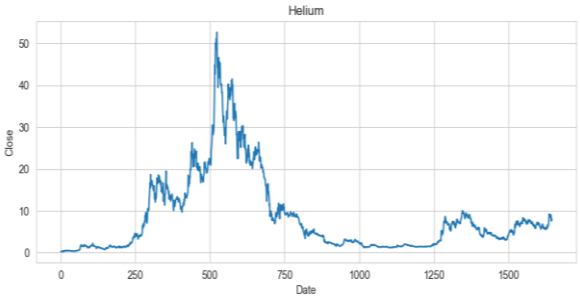
2. Materyal ve Yöntem

Dijital para birimleri, son yıllarda finansal piyasaların önemli bir bileşeni haline gelmiş ve yatırımcılar için cazip bir alternatif olarak görülmeye başlanmıştır. Kripto para birimlerinin değerindeki dalgalanmalar, finansal sistemin dinamiklerini doğrudan etkileyebilmekte ve ekonomik karar alma süreçlerinde önemli bir rol oynamaktadır. Kripto para fiyatlarının doğru bir şekilde tahmin edilmesi hem bireysel yatırımcılar hem de kurumsal finansal aktörler için stratejik karar alma süreçlerini destekleyici bir unsur haline gelmiştir. Kripto para birimlerinin

fiyatlarını tahmin etmek için çeşitli yöntemler kullanılmaktadır. Makine öğrenmesi teknikleri, özellikle regresyon tabanlı modeller, bu alanda öne çıkan yöntemler arasında yer almaktadır. Son yıllarda, yapay zekâ ve makine öğrenmesi algoritmaları, fiyat tahminlerinde daha yüksek doğruluk ve güvenilirlik sağlamak amacıyla etkin bir şekilde kullanılmaktadır.

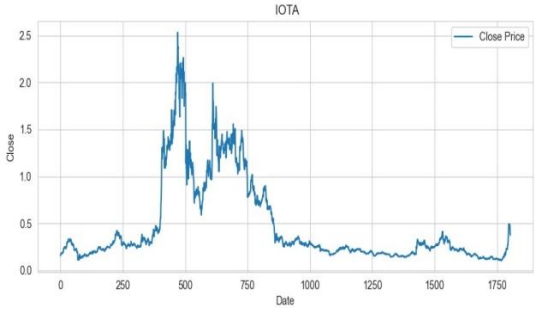
Bu çalışmada, coin kurlarının tahmini için Karar Ağaçları Regresyonu (Decision Tree Regression), Rassal Orman (Random Forest) ve Destek Vektör Regresyonu (Support Vector Regression - SVR) modelleri kullanılmıştır. Her üç model de denetimli öğrenme (supervised learning) algoritmaları olup, geçmiş fiyat verilerine dayalı olarak gelecekteki fiyat hareketlerini tahmin etmeyi amaçlamaktadır. Karar Ağaçları, veriyi dallara ayırarak tahminleme yapan hiyerarşik bir modeldir. Ancak, aşırı öğrenme problemi nedeniyle modelin genellenebilirlik kapasitesi sınırlı olabilmektedir. Rassal Orman algoritması, birden fazla karar ağacının tahminlerini birleştirerek daha güçlü ve genellenebilir bir model oluşturur. Öte yandan, SVR, doğrusal olmayan ilişkileri modelleme kapasitesine sahip olup, özellikle yüksek volatilite içeren finansal zaman serilerinde etkili sonuçlar sunabilmektedir. Kripto para fiyatları, bireysel yatırımcılar, şirketler ve devletler için ciddi ekonomik sonuçlar doğurabilecek finansal değişkenlerdir. Günlük bazda yaşanan fiyat dalgalanmaları, bireylerin ve işletmelerin gelir seviyelerini doğrudan etkileyebildiği gibi, makroekonomik düzeyde de geniş çaplı etkiler yaratabilmektedir. Bu nedenle, coin kurlarının doğru tahmin edilmesi, sadece bireysel yatırımcılar için değil, geniş ölçekli ekonomik yapıların sağlıklı işleyişi açısından da kritik bir öneme sahiptir.

Coin kurlarının tahmin edilmesi, regresyon tabanlı bir problem olarak ele alınabilir. Bu tür tahminler için pek çok makine öğrenimi algoritması kullanılmakta olup, yapay sinir ağları ve diğer karmaşık modeller sıklıkla tercih edilmektedir. Yapılan bu çalışmada, Rassal Orman Regresyon Modeli, karar ağacı regresyon modeli ve Destek Vektör Regresyon modeli Python programlama dili kullanılarak uygulanmıştır. Model, VeChain, Helium ve IOTA gibi üç farklı dijital para biriminin değerlerini tahmin etmek amacıyla kullanılmıştır. Çalışmada kullanılan kripto varlıklara ait veriler coinmarketcap sitesinden temin edilmiştir. VeChain, IOTA veri seti 02.01.2020, Helium coin veri seti 09.06.2020 tarihinden itibaren alınan günlük kapanış fiyatlarıyla oluşturulmuştur ve her bir coin için 10.12.2024 tarihine kadar VeChain ve IOTA için 1805, Helium için 1646 veri noktasından oluşmaktadır. Bu veriler, coinlerin geçmiş değerlerini ve zaman içindeki fiyat hareketlerini temsil etmektedir. Bu yıllar arasında alınan datalar için Helium coin grafiği Şekil 1'de gösterilmiştir.



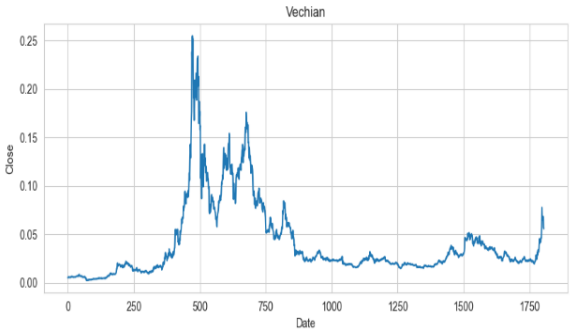
Şekil 1. Günlük Helium Coin veri kapanış grafiği.

IOTA coin'in kapanış fiyatlarına ait günlük veriler, coin'in değerindeki dalgalanmaları ve zaman içindeki fiyat hareketlerini analiz edebilmek için önemli bir kaynak sağlamaktadır. Bu veriler, 02.01.2020 ile 10.12.2024 tarihleri arasındaki kapanış fiyatlarını kapsamakta olup, söz konusu coin'in piyasa trendlerini anlamak için kullanılmıştır. Şekil 2'de IOTA Coin'in günlük kapanış fiyatlarını vermektedir.



Şekil 2. Günlük IOTA coin kapanış grafiği

Alınan verilerle yapılan analizler için VeChain coin'in fiyat hareketlerini gösteren grafik, Şekil 3'te yer almaktadır.

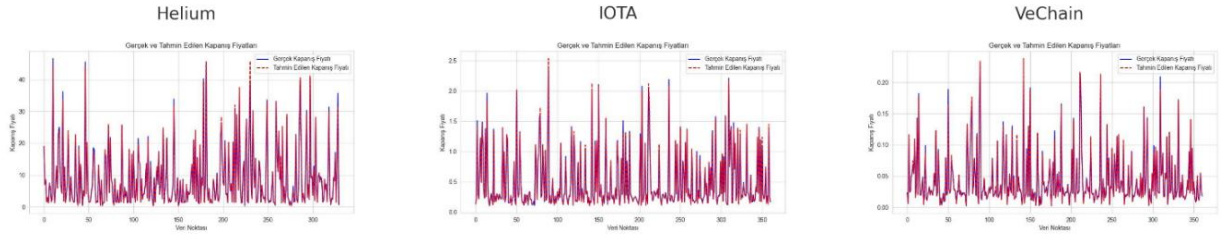


Şekil 3. Günlük Vechain Coin kapanış grafiği

3. Bulgular

Karar ağaçları, özellikle sınıflandırma ve regresyon problemlerinde yaygın olarak kullanılan güçlü algoritmalardan biridir (Kına ve Biçek, 2024; Sharma ve Puri, 2025). Veri madenciliği alanında, bu ağaçlar veriyi analiz etmek ve doğru sonuçlar üretmek için tercih edilir (Orhan ve Kurutkan, 2025; Das et al., 2025). Karar ağaçlarının en belirgin avantajı, hem modelin oluşturulmasının hem de elde edilen sonuçların son derece anlaşılır ve yorumlanabilir olmasıdır (Kına ve Biçek, 2024). Bu sayede, kullanıcılar modelin nasıl

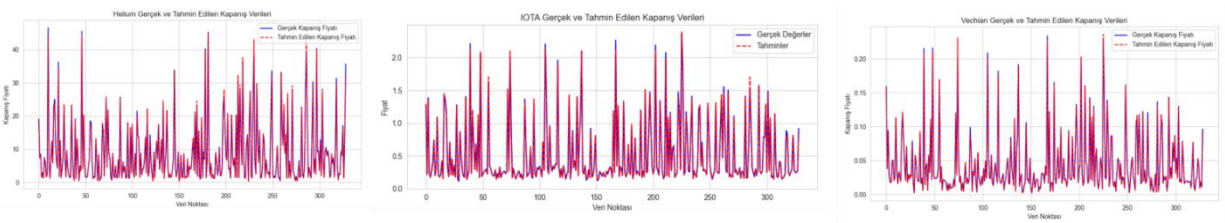
çalıştığını kolaylıkla takip edebilirler. Karar ağaçları, denetimli öğrenme yöntemlerinden biri olup, eğitim verisinden öğrenerek sonuçlar üretir (Orhan ve Kurutkan, 2025; Das et al., 2025). Yapısı, bir ağacı andırır ve bu ağaç kök düğümünden, dallardan ve yapraklardan oluşur. Kök düğüm, verinin bölündüğü ilk noktayı temsil ederken, dallar veri kümesinin daha küçük gruplara ayrıldığı noktaları gösterir (Sharma ve Puri, 2025). Yapraklar ise modelin nihai sonucunu barındırır. Eğer problem bir sınıflandırma problemi ise, yapraklarda bulunan değer sınıf etiketini; eğer regresyon problemi ise sayısal bir tahmini değerini belirtir (Kına ve Biçek, 2024; Orhan ve Kurutkan, 2025). Çalışmada ilk olarak kripto varlıkların tahmin edilmesinde, karar ağacı regresyon modeli kullanılmıştır. Karar ağacı regresyon modeli, coin kurlarının geçmiş verilerini analiz ederek, zaman içindeki fiyat hareketlerini modellemeye yönelik bir yaklaşım sunmaktadır. Bu model, bu üç coin'in değerindeki olası değişiklikleri tahmin etmek amacıyla, özellikle geçmiş kapanış fiyatları ve diğer ilgili faktörlere dayanarak yapılan hesaplamaları içermektedir. Coinlerin günlük kurlarına ait tahminlerin görsel olarak sunulduğu grafikler, Şekil 4'te yer almaktadır.



Şekil 4. Karar ağaçları regresyonu ile helium, ıota, vechain coin verilerinin tahmin grafikleri.

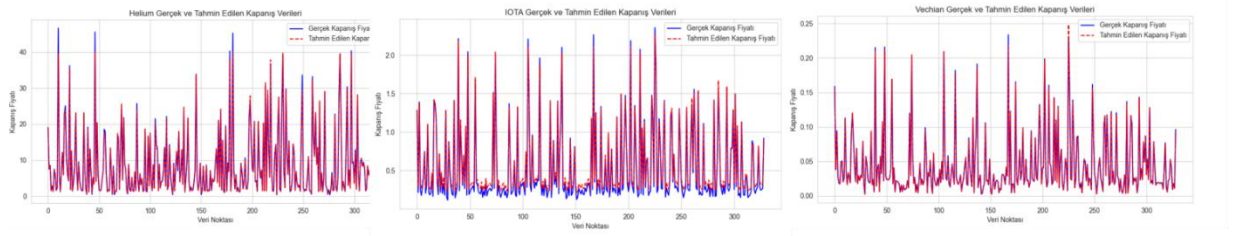
Veri kümesi, her bir coin için günlük kapanış fiyatlarının yanı sıra olası dışsal faktörlerden etkilenebilecek ek parametrelerle zenginleştirilebilir. Bu bağlamda, karar ağacı regresyon modeli, her bir coin'in geçmiş verilerini kullanarak gelecekteki fiyat hareketlerini tahmin etmeyi amaçlamaktadır. Modelin başarısı, doğru veri ön işleme, parametre optimizasyonu ve model doğrulama adımlarının dikkatlice uygulanmasına bağlıdır. Bu çalışma kapsamında, kullanılan karar ağacı regresyon modeli, modelin hem doğruluk hem de genelleme yeteneğini artırmak için çapraz doğrulama yöntemleriyle test edilmiştir.

Rassal Orman, birden fazla karar ağacının bir araya gelerek oluşturduğu bir topluluk öğrenme (ensemble learning) yöntemi olup, tek bir karar ağacının neden olabileceği aşırı öğrenme (overfitting) problemini minimize ederek daha genellenebilir ve sağlam sonuçlar üretmeyi amaçlamaktadır (MacDonald, 2025; İçen vd., 2024). Veri madenciliği alanında, Rassal Orman modeli veri analizi ve tahminleme süreçlerinde yüksek doğruluk sağlamasıyla öne çıkmaktadır (Balijepalli & Thangaraj, 2025). En büyük avantajlarından biri, her bir karar ağacının farklı bir veri alt kümesiyle eğitilmesi ve nihai tahminin bu ağaçların ortalaması alınarak üretilmesidir (Karam, 2025). Bu sayede, model hem aşırı öğrenme riskini azaltır hem de daha dengeli tahminler sunmaktadır. Rassal Orman, denetimli öğrenme yöntemlerinden biri olup, eğitim verisinden öğrenerek sonuçlar üretir. Model, birden fazla karar ağacından oluştuğu için bireysel ağaçlardaki hataları telafi ederek daha güvenilir tahminler yapabilir (MacDonald, 2025; Karam, 2025). Her bir karar ağacının farklı özellik kombinasyonlarıyla eğitilmesi, modelin veri setinin genel özelliklerini daha iyi kavramasına yardımcı olur. Kripto para fiyatlarının tahmini, regresyon tabanlı bir problem olarak ele alınabilir. Bu tür tahminlerde makine öğrenimi algoritmaları sıkça tercih edilmekte olup, yapay sinir ağları ve diğer karmaşık modellerin yanı sıra, Rassal Orman algoritması finansal zaman serilerinde güçlü bir alternatif olarak öne çıkmaktadır (İçen vd., 2024; Balijepalli & Thangaraj, 2025). Bu çalışmada, Python programlama dili kullanılarak Rassal Orman regresyon modeli uygulanmıştır. Model, VeChain, Helium ve IOTA gibi üç farklı dijital para biriminin değerlerini tahmin etmek amacıyla kullanılmıştır. Rassal Orman modeli, coin kurlarının geçmiş verilerini analiz ederek, zaman içindeki fiyat hareketlerini modellemeye yönelik daha sağlam ve genellenebilir bir tahminleme yaklaşımı sunmaktadır. Rassal Orman, birden fazla karar ağacının tahminlerini birleştirerek daha dengeli ve güvenilir sonuçlar üretmektedir. Özellikle finansal verilerde görülen yüksek volatilite gibi zorlukları aşmada etkili bir yöntem olarak öne çıkmaktadır. Coin kurlarının tahminleri Şekil 5'te yer almaktadır.



Şekil 5. Rassal orman regresyonu ile helium, ıota, vechain coin verilerinin tahmin grafikleri.

Destek Vektör Regresyonu, veri noktaları arasındaki karmaşık ilişkileri modelleyerek doğrusal olmayan regresyon problemlerini çözebilen güçlü bir makine öğrenme algoritmasıdır (Fatah vd., 2025). SVR, rassal orman regresyon modeli gibi yüksek volatiliteye sahip finansal zaman serilerinde etkili sonuçlar sunmaktadır. Model, geçmiş kapanış fiyatları ve diğer ilgili faktörlere dayanarak fiyat hareketlerini modellemek amacıyla oluşturulmuştur. SVR, fiyat dalgalanmalarını daha iyi yakalayarak, aşırı öğrenme riskini azaltan bir hiper düzlem tabanlı tahminleme yöntemi kullanmaktadır (Karam, 2025). SVR modeli Helium, IOTA ve VeChain gibi üç farklı dijital para biriminin değerlerini tahmin etmek amacıyla kullanılmıştır. SVR modeli ile Coin kurlarının tahminleri Şekil 6'da verilmiştir.



Şekil 6. Günlük coin verilerinin tahmin grafiği (SVR modeli ile).

4. Tartışma

Dimitriadou ve Gregoriou (2023) Bitcoin fiyat hareketlerini bir makine öğrenmesi çerçevesinde tahmin etmek için Lojistik Regresyon, Destek Vektör Makineleri ve Rassal Orman algoritmasını kullanmışlardır. Çalışmadan elde edilen ampirik sonuçlara göre, geleneksel Lojistik Regresyon modelinin doğruluk oranı %66'ya ulaşarak Doğrusal Destek Vektör makineleri ve Rassal Orman algoritmasından daha iyi performans gösterdiğini ortaya koymaktadır. Chen vd., (2020) Bitcoin'in günlük fiyatlarının tahmininde istatistiki modeller ve makine öğrenmesi modellerinin performanslarını karşılaştırmış ve en iyi performansı doğrusal regresyon modeli göstermiştir. Makine öğrenme modelleri içerisinde ise en iyi doğruluk oranına SVR modelinin sahip olduğu bulunmuştur.

Yapılan bu çalışmada ise modelin başarısını değerlendirmek için, tahmin edilen ve gerçek değerler arasındaki farklar incelenmiştir. Mean Squared Error hata ölçüsü olup, tahmin edilen değer ile gerçek değer arasındaki farkların karesinin ortalamasını temsil etmektedir. R^2 skoru, modelin tahmin gücünü ifade etmektedir; bu değerin 1'e yakın olması, modelin yüksek doğrulukla çalıştığını göstermektedir. VeChain coin için, SVR modeli en düşük MSE değerine (0.000004034) ve en yüksek R^2 skoruna (0.9979) sahip olup, en başarılı model olarak öne çıkmaktadır. Karar ağaçları modeli ise en yüksek hata oranını göstermiştir. Bu sonuçlar Chen vd., (2020)nin çalışmasını destekler niteliktedir. Helium coin için, Rassal Orman modeli en düşük MSE (0.3131995) ve en yüksek R^2 (0.9965) değerleri ile en iyi performansı sergilemiştir. Karar ağaçları, 0,52578MSE ve 0.9942 R^2 ile nispeten daha düşük bir performans göstermiştir. IOTA coin için, Rassal Orman modeli yine en düşük hata oranına sahip olup (MSE: 0.0006429), R^2 skoru 0.9973ile oldukça yüksek bir doğruluk sergilemiştir.

Elde edilen sonuçlar, Rassal Orman modelinin Helium ve IOTA coin fiyatlarını tahmin etme konusunda en iyi performansı sergilediğini gösterirken SVR modelinden elde edilen sonuçlar çalışmada ele alınan diğer iki modele göre nispeten daha kötü tahmin sonuçları vermektedir. Karar ağaçları modeli genel olarak daha dengeli ve güvenilir tahminler sağlamaktadır. Bu çalışma, makine öğrenmesi tekniklerinin dijital para birimlerinin gelecekteki değerlerini tahmin etme konusundaki etkinliğini bir kez daha vurgulamaktadır. Tablo 2'de Coin verilerine uygulanan regresyon modellerinin MSE değerleri verilmiştir. Tablo 3'te Coin verilerine uygulanan regresyon modellerinin R2 değerleri Tablo 3'te verilmiştir.

Tablo 2. Coinlerin MSE değerleri

Model	Helium	IOTA	VeChain
Karar Ağaçları	0,52578	0,00115	1,5818
Rassal Orman	0.3131995	0.0006429	0.000006251
SVR	0.600722	0.004071	0.000004034

Tablo 3. Regresyon Modellerinin R^2 değerleri

Model	Helium	IOTA	VeChain
Karar Ağaçları	0.9942	0.9949	0.9913
Rassal Orman	0.9965	0.9973	0.9968
SVR	0.9934	0.9833	0.9979

4. Sonuç

Bu çalışma, IoT temalı dijital para birimleri olan VeChain, IOTA ve Helium coin'lerinin fiyatlarını tahmin etmek için Karar Ağaçları, Rassal Orman ve Destek Vektör Regresyonu modellerini kullanarak önemli bulgulara ulaşılmıştır. Yapılan analizler, Rassal Orman modelinin genellikle en düşük hata oranı ve en yüksek R^2 değerine sahip olduğunu göstermiştir. Vechain coin için SVR modeli en düşük hata oranına (MSE: 0.000004034) ve en yüksek R^2 değerine (0.9979) ulaşarak en iyi performansı sergilemiştir. Helium coin için de Rassal Orman modeli (MSE: 0.313, R^2: 0.9965) en başarılı model olmuştur. IOTA coin'de de en düşük hata oranını (MSE: 0.0006429) yine Rassal Orman modeli elde etmiştir, ancak bu noktada Karar ağaçları modeli düşük doğruluk göstermiştir. Elde edilen sonuçlar, Rassal Orman modelinin dijital para birimlerinin fiyatlarını tahmin etmede güçlü bir araç olduğunu ve en yüksek doğruluğu sağladığını göstermektedir. Ancak, SVR modeli de bazı durumlarda belirli avantajlar sunmaktadır. Sonuçlar, makine öğrenmesi tekniklerinin ekonomik analizlerde önemli katkılar sunduğunu ve özellikle IoT temalı kripto varlıkların fiyat hareketlerini doğru bir şekilde tahmin etmenin yatırımcılar, analistler ve ekonomi uzmanları için kritik bir konu olduğunu göstermektedir.

Katkı Oranı Beyanı

Yazarların katkı yüzdeleri aşağıda verilmiştir. Yazarlar makaleyi incelemiş ve onaylamıştır.

	Ç.E.	O.K.
K	50	50
VTI	30	70
VAY	60	40
KT	40	60
YZ	60	40
KI	50	50
GR	60	40

K= kavram, VTI= veri toplama ve/veya işleme, VAY= veri analizi ve/veya yorumlama, KT= kaynak tarama, YZ= Yazım, KI= kritik inceleme, GR= gönderim ve revizyon.

Çatışma Beyanı

Yazarlar bu çalışmada hiçbir çıkar ilişkisi olmadığını beyan etmektedirler.

Etik Onay Beyanı

Bu araştırmada hayvanlar ve insanlar üzerinde herhangi bir çalışma yapılmadığı için etik kurul onayı alınmamıştır.

Kaynaklar

Ahamad S, Gupta P, Acharjee PB, Kiran KP, Khan Z, Hasan MF. 2022. The role of block chain technology and Internet of Things (IoT) to protect financial transactions in crypto currency market, Mater Today Proc, 56: pp: 2070-2074.

Akay MK, Canik F, Yeşilyurt C, Günkut MŞ. 2022. Yapay zekâ teknikleri ile kripto para değeri tahmini, Ekom Bil Derg, 14(1): pp: 72-101.

Akel V, Bayramoğlu MF. 2008. Finansal kriz dönemlerinde yapay sinir ağları ile finansal öngörüde bulunma: İMKB 100 endeksi örneği, Uluslararası Sermaye Hareketleri ve Gelişmekte Olan Piyasalar Sempozyumu, pp: 36-69.

Akşehir ZD, Kılıç E. 2019. Makine öğrenmesi teknikleri ile banka hisse senetlerinin fiyat tahmini, Türk Bilişim Vakfı Bilg Bilim Müh Derg, 12(2): pp: 30-39.

Alshaikhli M, Elfouly T, Elharrouss O, Mohamed A, Ottakath N. 2021. Evolution of Internet of Things from blockchain to IOTA: a survey, IEEE Access, 10: pp: 844-866.

Altan Ş. 2008. Döviz kuru öngörü performansı için alternatif bir yaklaşım: yapay sinir ağı, Gazi Üniv İİBF Derg, 10(2): pp: 141-160.

Aygören H, Sarıtaş H, Moralı T. 2012. İMKB 100 endeksinin yapay sinir ağları ve Newton nümerik arama modelleri ile tahmini, Uluslararası Alanya İşlet Fakül Derg, 4(1): pp: 73-88.

Balijepalli NK, Thangaraj V. 2025. Prediction of cryptocurrency's price using ensemble machine learning algorithms, Eur J Manage Bus Econ, pp:25-42.

Bouteska A, Abedin MZ, Hajek P, Yuan K. 2024. Cryptocurrency price forecasting–a comparative analysis of ensemble learning and deep learning methods, Int Rev Financ Anal, 92(103055): pp: 1-12.

Böhme R, Christin N, Edelman B, Moore T. 2015. Bitcoin: economics, technology, and governance, J Econ Perspect, 29(2): pp: 213-238.

Cankül D, Kızıltaş MÇ. 2020. Yiyecek içecek işletmelerinde tedarik zinciri ve blokzincir teknolojisi, J Gastron Hosp Travel, 3(2): pp: 244-259.

Chen Z, Li C, Sun W. 2020. Bitcoin price prediction using machine learning: an approach to sample dimension engineering, J Comput Appl Math, 365: pp: 112395.

Chowdhury Rahman MA, Rahman MS, Mahdy MRC. 2020. An approach to predict and forecast the price of constituents and index of cryptocurrency using machine learning, Phys A Stat Mech Appl, 551(124569): pp: 1-17.

Çalışkan MMT, Deniz D. 2015. Yapay sinir ağlarıyla hisse senedi fiyatları ve yönlerinin tahmini, Eskişehir Osmangazi Üniv İİBF Derg, 10(3): pp: 177-194.

Dange S, Nitnaware P. 2024. Secure Share: optimal blockchain integration in IoT systems, J Comput Inf Syst, 64(2): pp: 265-277.

Das N, Moharana L, Nayak S, Routray A. 2025. Emotional blink patterns: a possible biomarker for anxiety detection in a HCI framework, SN Comput Sci, 6(3): pp: 1-14. DOI: 10.1007/s42979-025-03810-y

Demirci E, Karaatlı M. 2023. Kripto para fiyatlarının LSTM ve GRU modelleri ile tahmini, J Mehmet Akif Ersoy Univ Econ Adm Sci Fac, 10(1): pp: 134-157.

Dimitriadou A, Gregoriou A. 2023. Predicting Bitcoin prices

using machine learning, Entropy, 25(5): pp: 777.

Doğan S, Büyükkör Y. 2022. Makine öğrenmesi ile finansal zaman serisi tahminleme, Ankara HBV Üniv İİBF Derg, 24(3): pp: 1205-1230.

Esenyel İçen NM, Demirezen S, İçen H. 2024. A machine learning-based Bitcoin price forecasting, In: Blockchain, İstanbul Univ Press, İstanbul, Türkiye, pp: 47-71.

Esenyel NM, Akın M. 2017. Comparing accuracy performance of ELM, ARMA and ARMA-GARCH model in predicting exchange rate return, Alphanumeric J, 5(1): pp: 1-14.

Eylasov N, Çiçek M. 2024. Kripto para fiyatlarının tahmini: ARIMA-GARCH ve LSTM yöntemlerinin karşılaştırılması, Finans Ekon Sosyal Araş Derg, 9(1): pp: 48-62.

Fatah MA, Dikananda AR, Rifai A. 2025. Support vector regression to improve Ethereum price prediction for trading strategies, J Artif Intell Eng Appl, 4(2): pp: 738-744.

Fauzi MA, Paiman N, Othman Z. 2020. Bitcoin and cryptocurrency: challenges, opportunities and future works, J Asian Finance Econ Bus, 7(8): pp: 695-704.

Gökoğlan K, Atalan İ. 2022. Tarımsal gıda ürünlerinin tedarik zinciri yönetimine blok zincir teknolojisinin etkisi, Ahi Evran Üniv İİBF Derg, 6(1): pp: 97-112.

Haleem A, Allen A, Thompson A, Nijdam M, Garg R. 2018. A decentralized wireless network, Helium Netw, pp: 1-20. http://whitepaper.helium.com/ (accessed date: July 11, 2025).

Hiransha M, Gopalakrishnan EA, Menon VK, Soman KP. 2018. NSE stock market prediction using deep-learning models, Procedia Comput Sci, 132: pp: 1351-1362.

.

Black Sea Journal of Engineering and Science
doi: 10.34248/bsengineering.1673480

Open Access Journal
e-ISSN: 2619 – 8991

Research Article
Volume 8 - Issue 4: 1067-1075 / July 2025

ENHANCED CORROSION RESISTANCE OF X120MN12 STEEL IN ACIDIC MEDIA BY A NOVEL NANOLIGNIN-BASED PROTECTIVE COATING

Emre GÖRGÜN[1]*, Mehtap ERŞAN[2]

[1]*Sivas Cumhuriyet University, Sivas Technical Sciences Vocational School, Department of Motor Vehicles and Transportation Systems, 58104, Sivas, Türkiye*
[2]*Sivas Cumhuriyet University, Faculty of Engineering, Department of Chemical Engineer, 58104, Sivas, Türkiye*

Abstract: This study investigated the corrosion inhibition of X120Mn12 steel in a 1 mol/L hydrochloric acid solution using a novel biomass-derived inhibitor, Modified Lignin-Based Corrosion Protector (MLCP). Scanning electron microscopy (SEM) analyses revealed a significant reduction in surface corrosion with increasing MLCP concentration. At 15 mg/L, the surface exhibited almost no signs of corrosion, indicating the formation of an effective protective film by MLCP. These findings strongly demonstrated that MLCP could be used as a high-performance and environmentally friendly corrosion inhibitor for X120Mn12 steel, effectively preventing corrosion in acidic environments. This research investigated the potential applications and mechanisms of environmentally friendly inhibitors to prevent the corrosion of X120Mn12 steel under acidic conditions. In this study, the inhibitory effect of MLCP on X120Mn12 steel was investigated. SEM analyses showed a significant reduction in corrosion damage with increasing MLCP concentration.

Keywords: X120Mn12 steel, Corrosion, Inhibition, Nanolignin

***Corresponding author:** [1]*Sivas Cumhuriyet University, Sivas Technical Sciences Vocational School, Department of Motor Vehicles and Transportation Systems, 58104, Sivas, Türkiye*
E mail: emregorgun@cumhuriyet.edu.tr (E. GÖRGÜN)
Emre GÖRGÜN https://orcid.org/0000-0002-1971-456X
Mehtap ERŞAN https://orcid.org/0000-0002-5429-4468

Received: April 10, 2025
Accepted: May 15, 2025
Published: July 15, 2025

Cite as: Görgün E, Erşan M. 2025. Enhanced corrosion resistance of X120MN12 steel in acidic media by a novel nanolignin-based protective coating. BSJ Eng Sci, 8(4): 1067-1075.

1. Introduction

The exceptional wear resistance and high toughness of X120Mn12 steel make it a popular choice for heavy machinery, construction, mining, automotive engineering, and various other demanding industrial sectors (Ennafaa et al. 2025), (Jiménez-Marcos et al. 2025), (Rai et al. 2025). However, the susceptibility of X120Mn12 steel to corrosive environments leads to direct chemical or electrochemical reactions resulting in corrosion. This process progressively weakens the structural integrity of X120Mn12 steel, compromising its performance and durability over time. In addition to structural damage, metal corrosion results in major environmental problems, monetary losses, and safety risks in various industries. Therefore, ensuring the longevity and safety of X120Mn12 steel in diverse applications and industrial processes necessitates a robust understanding of its corrosion mechanisms and the development of effective preventative strategies. The susceptibility of X120Mn12 steel to corrosion, despite its widespread use in demanding industrial sectors, poses a threat to its structural integrity over time, as highlighted in the studies by Aleutdinova and Fadin and Oppermann et al. This underscores the necessity for developing effective corrosion prevention strategies (Akkus and Gorgun, 2015).

Metal corrosion prevention is often achieved by the mining, construction, and heavy equipment industries through the use of corrosion inhibitors (Abouelenein et al. 2025), (Yang et al. 2025). These inhibitors offer several advantages, including high potency in various corrosive environments, versatility across different industrial applications, and relative simplicity of application. The effectiveness of corrosion inhibitors in preventing metal corrosion has been demonstrated in the research of Yang et al. and Abouelenein et al. These studies support the potential of corrosion inhibitors across various corrosive environments and diverse industrial applications. Conventional corrosion inhibitors, which are mostly organic compounds, feature heteroatom-filled structures and functional groups including sulfur (S), oxygen (O), and nitrogen (N) atoms (Bhadra et al. 2020), (Sun et al. 2025), (He et al. 2025). These properties facilitate the development of corrosion-resistant coatings on metal surfaces, which mitigate the negative effects of corrosion. However, as environmental concerns have developed, research in this field has increased because of a shift in emphasis toward the discovery of ecologically benign and non-toxic corrosion inhibitors (Ennafaa et al. 2025), (Jiménez-Marcos et al. 2025), (Rai et al. 2025).

This work is licensed (CC BY-NC 4.0) under Creative Commons Attribution 4.0 International License

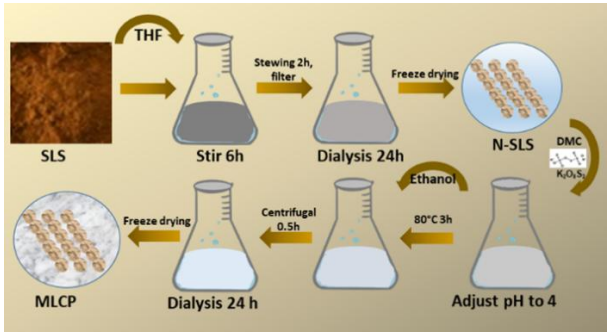


Figure 1. Diagram illustrating the fabrication process of DMC-NL.

Current trends indicate that plant extracts are being studied as potentially useful green corrosion inhibitors (Maizia et al. 2025), (Ghehsareh et al. 2025). The growing interest in environmentally benign corrosion inhibitors is evident in the work of Maizia et al. on plant extracts and the comprehensive review by Ghehsareh et al. These findings indicate that materials derived from natural sources offer promising alternatives for corrosion inhibition (Gorgun, 2024a). Studies have shown that materials derived from natural sources have the potential to reduce corrosion and provide workable alternatives that are both more efficient and eco-friendly. Because plant extracts are complex compounds, it might be challenging to identify potential synergies between constituents or isolate particular effects (Luo et al. 2024). This reduces the accuracy of the mechanistic explanation and results in variations in corrosion inhibition efficacy(Solmaz et al., 2024), (Demir et al., 2024) . The growing demand for environmentally benign corrosion inhibitors has increased interest not only in plant extracts but also in materials derived from abundant and sustainable sources like lignin, a structural component of lignocellulosic biomass (Li et al. 2025), (Sun et al. 2025).

Recently research indicates that a number of pharmacological compounds have a positive inhibitory impact on metal corrosion, which might lead to new avenues for inhibitor development. Research and innovation are still essential in the field of these pharmacological inhibitors' structure-activity relationships and corrosion inhibition processes. Lignin, as an abundant, low-cost biopolymer with inherent functional groups amenable to chemical modification, presents a promising platform for the development of sustainable and effective corrosion inhibitors like MLCP(Iyyappan et al. 2024), (Fernandes and da Silva 2024) .

The synthesis process of MLCP, as schematically illustrated in Figure 1, involves a multi-step procedure starting with the mixing of SLS in THF, followed by stirring, dialysis, and freeze-drying (Luo et al. 2024). The purpose of this study was to conduct an extensive investigation into the influence of a newly developed biomass-derived inhibitor, MLCP, on the suppression of corrosion in X120Mn12 steel under the acidic conditions of 1 M hydrochloric acid. As schematically illustrated in Figure 1, the synthesis process of MLCP involves several steps. The synthesis process begins with the mixing of SLS powder with THF, followed by 6 hours of stirring, 2 hours of standing/soaking/incubation and filtering, 24 hours of dialysis, and freeze-drying. The resulting N-SLS is then dispersed in a solution adjusted to pH 4.5 and heated at 80°C for 3 hours in the presence of K2S2O8 and DMC. After 0.5 hours of centrifugation and another 24 hours of dialysis (Görgün, 2022), MLCP is obtained through freeze-drying. To examine the inhibitory performance and the underlying mechanisms of corrosion inhibition, rigorous electrochemical tests were conducted at various concentrations and temperatures. The goal of this study was to determine whether MLCP can effectively prevent the corrosion of X120Mn12 steel in severe acidic environments, which is necessary to satisfy the needs of several enterprises that rely on this resilient material material (Al Kiey et al. 2024), (Jebali et al. 2024).

2. Materials and Methods

2.1. Materials

The X120Mn12 steel samples used in this study measured 40 mm × 40 mm × 3 mm. The chemical composition of X120Mn12 steel was 1.30 % C, 11.5 % Mn, 0.02 % P, 0.40 % Si, 0.55 % Cr, and the balance Fe (Pei et al. 2024), (Zemlik et al. 2024), (Gorgun, 2024b). Prior to each test, the metal surfaces were ground with waterproof abrasive papers of successively finer mesh sizes (200-450, 1000-1400). The meticulously polished surfaces were cleaned with acetone and deionized water and then allowed to dry naturally (Dadkhah et al. 2025). The chemicals utilized in this study included hydrochloric acid (37%, AR, Sigma-Aldrich), potassium persulfate (AR, Sigma-Aldrich), and tetrahydrofuran (THF, HPLC grade, Sigma-Aldrich) (Wang et al. 2024). The tests were conducted using distilled water with a resistance value of 17 megaohms per centimeter.

2.2. Modified MLCP Corrosion Inhibitor Preparation

The production process for MLCP is shown in Figure 1. SLS was mixed with 100 mL of tetrahydrofuran (THF) and left stirring for 6 hours (Luo et al. 2024). The mixture was then heated for 2 hours and dialyzed using a dialysis bag with a molecular weight cut-off of 750 Da (Ahmed et al. 2024), (Shwetha et al. 2024). As a result of this process, N-SLS nanoparticles were formed and then freeze-dried. Next, the N-SLS was combined with a DMC solution set to pH 4.5, while 40 mg of potassium persulfate was added at the same time. The mixture was then heated in an oven at 80°C for 3 hours. Subsequently, ethanol was introduced into the solution to induce precipitation, followed by centrifugation and a 24-hour dialysis process. Finally, the MLCP product was acquired after undergoing freeze-drying.

2.3. Weight Loss Method

The X120Mn12 steel samples were measured on an

analytical balance with a precision of 0.1 mg before and after being immersed for three hours in a 1 mol/L hydrochloric acid solution (Hamood et al. 2024), (Jia et al. 2024), (Lakshmi et al. 2024). The average weight loss was then calculated based on the three samples, and the corrosion rate (CR) (equation 1) and inhibition efficiency (IE) (equation 2) were evaluated using the following established equations.

$$CR = \frac{\mathrm{Wo} - \mathrm{Wt}}{\mathrm{At}} \quad (1)$$

$$IE(\%) = \frac{\mathrm{CRo} - \mathrm{CRi}}{\mathrm{CRo}} x100 \quad (2)$$

2.4. Characteristics of Surface

FTIR and SEM techniques were primarily employed to determine the morphology and chemical constituents of MLCP. EDS analysis was conducted to determine the elemental composition of the corrosion products formed on the steel surface (Sharma et al. 2024), (Razali et al. 2024). The morphology of the corrosion was examined using Optical Microscopy (OM) and Scanning Electron Microscopy (SEM), while atomic force microscopy (AFM) was employed to examine the surface roughness, adhesive force, and phase diagrams.

3. Results

3.1. Measurement of the Corrosion Inhibiting Properties of the Nano-Lignin That Has Been Treated With DMC

The infrared absorption spectra of SLS and N-SLS are illustrated in Figure 2a, while Figure 2b displays the spectral profiles of DMC, MLCP, and N-SLS. The variations observed between the absorption patterns of SLS and N-SLS (Figure 2a), among N-SLS, DMC, MLCP (Figure 2b), suggest possible alterations in the molecular functional groups throughout the synthesis process. These differences indicate that chemical modifications took place.

The infrared spectroscopy (FTIR) findings for SLS and N-SLS are presented in Figure 2a, revealing an almost identical spectrum (Liu et al. 2024), (Onukwuli et al. 2024). This suggests that the primary fu(nctional groups of lignin remained largely intact during the initial processing steps. The absorption bands associated with O-H, CH_2, CH_3, C=O/C=C, and C-O-C were detected at around 3447, 2922, 2841, 1629, 1389, and 1033 cm^{-1}, respectively.

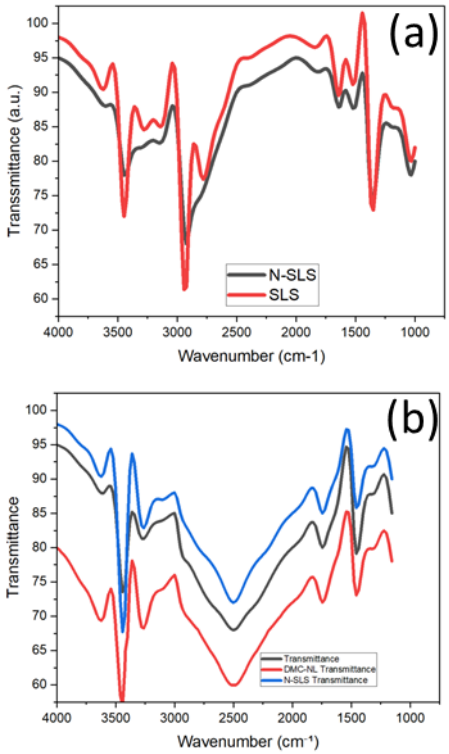


Figure 2. (a): FTIR spectral profiles of SLS and N-SLS (b):FTIR spectral profiles of DMC and MLCP.

Comparison of the FTIR spectra of MLCP and N-SLS, shown in Figure 2b, revealed the appearance of new bands in the MLCP spectrum. A new band at 1776 cm^{-1} suggests the formation of a C-N bond. Additional new bands observed at approximately 3418, 3002, 2951, and 1745 cm^{-1} can be attributed to the presence of ester carbonyl (C=O) stretching, while bands at 1637 and 958 cm^{-1} may correspond to C=C stretching vibrations. The presence of these new bands in Figure 2b confirms the effective chemical modification of N-SLS to form MLCP.

3.2. The Effectiveness of MLCP in Preventing Corrosion

The corrosion rate was determined using the weight loss method described in Section 2.3. The results showed a significant decrease in the corrosion rate upon the addition of MLCP. For instance, when the concentration of MLCP was 10 mg/L, the corrosion rate decreased from 22 ± 1.20 to 0.450 ± 0.15 g·cm-2·h−1. This demonstrates the exceptional corrosion inhibition properties of MLCP. Corrosion reduced , and the effectiveness of corrosion inhibition (η) increased with increasing MLCP concentration, indicating a dose-dependent inhibitory effect. In particular, the effectiveness of corrosion inhibition peaked at 96.4 ± 0.7% at 10 mg/L and reached 92.5 ± 0.3% at an MLCP dose of 8 mg/L.

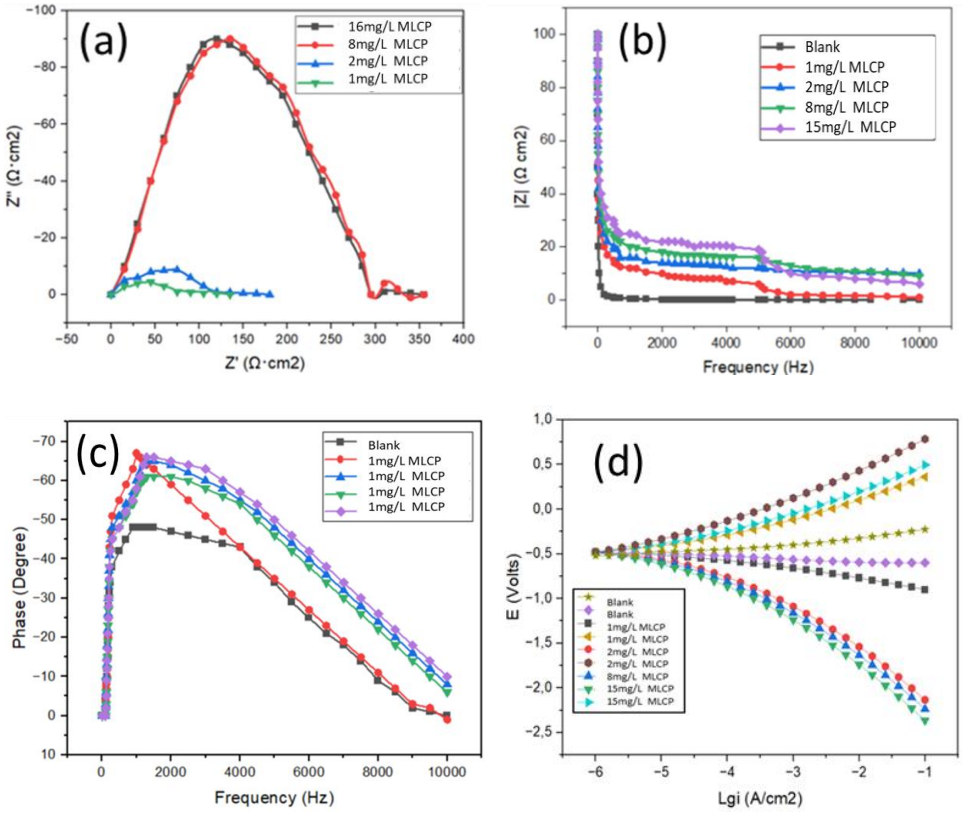


Figure 3. (a):EIS spectra were used to create the Frequency Response Plot (b, c): Phase-Amplitude Plot (d): for carbon steel submerged in 1 mol/L HCl at different MLCP concentrations: 0 (blank), 1, 2, 8, and 15 mg/L.

Table 1. The parameters obtained from fitting the EIS results in Figure 3a

CDMC–NL (mg/L)	Rs ($\Omega\cdot cm^2$)	CPEdl–T ($Sn^{-1}\cdot\Omega^{-1}\cdot cm^{-2}$)	n1	Rct ($\Omega\cdot cm^2$)	CPEf–T ($Sn^{-1}\cdot\Omega^{-1}\cdot cm^{-2}$)	n^2	Rf ($\Omega\cdot cm^2$)	σ^2	ηEIS (%)
0	1.50 ± 0.02	1.30×10^{-3}	0.78	0.300 ± 0.05	5.20×10^{-5}	0.72	9.5 ± 0.4	7.10×10^{-4}	-
1	1.22 ± 0.15	2.70×10^{-4}	0.87	1.50 ± 0.60	2.60×10^{-3}	0.80	45.0 ± 2.0	1.20×10^{-4}	81.2 ± 1.50
2	1.40 ± 0.35	1.35×10^{-4}	0.97	2.40 ± 1.10	2.50×10^{-3}	0.74	52.0 ± 1.2	5.00×10^{-4}	84.1 ± 0.90
8	1.75 ± 0.12	2.30×10^{-5}	0.95	13.5 ± 3.50	1.80×10^{-4}	0.76	230 ± 5.0	2.00×10^{-4}	96.8 ± 0.25
15	1.85 ± 0.08	3.00×10^{-5}	0.90	27.0 ± 2.50	1.50×10^{-4}	0.78	235 ± 40.0	2.50×10^{-4}	97.0 ± 0.55

The corrosion inhibition properties of MLCP on X120Mn12 were evaluated using electrochemical impedance spectroscopy (EIS) and potentiodynamic polarization (PDP) tests in a 1 mol/L hydrochloric acid solution (Figure 3). The electrochemical impedance spectroscopy (EIS) data were analyzed, and the derived parameters are presented in Table 1. Figure 3a shows the Frequency Response Plot plots, while Figure 3b and 3c display the Phase-Amplitude Plot plots of the EIS spectra. The potentiodynamic polarization (PDP) plots are shown in Figure 3d.

The EIS data were fitted using an equivalent circuit model, and the parameters are listed in Table 1. In the equivalent circuit, Rs represents the solution resistance, Rct represents the charge transfer resistance, and Rt (denoted as Rf in the original text, consistent with some EIS literature) represents the resistance associated with the surface film formed on the metal surface. CPEdl-T represents the constant phase element of the electrical double layer, and CPE1-T (denoted as CPEf in the original text) represents the constant phase element associated with the surface film. The value of "n" for each CPE, representing the deviation from ideal capacitive behavior, is also provided in Table 1.

The results presented in Figure 3a and quantified in Table 1 show that Rct and Rt increased with higher MLCP concentrations, indicating an enhanced protective ability with increased dosage. At a concentration of 8 mg/L, Rct and Rt increased to 230 ± 5.0 $\Omega\cdot cm^2$ and 2.00×10^4 $\Omega\cdot cm^2$, respectively, compared to the blank solution, which exhibited values of 0.300 ± 0.05 $\Omega\cdot cm^2$ for Rct and 9.5 ± 0.4 $\Omega\cdot cm^2$ for Rt (Table 1).

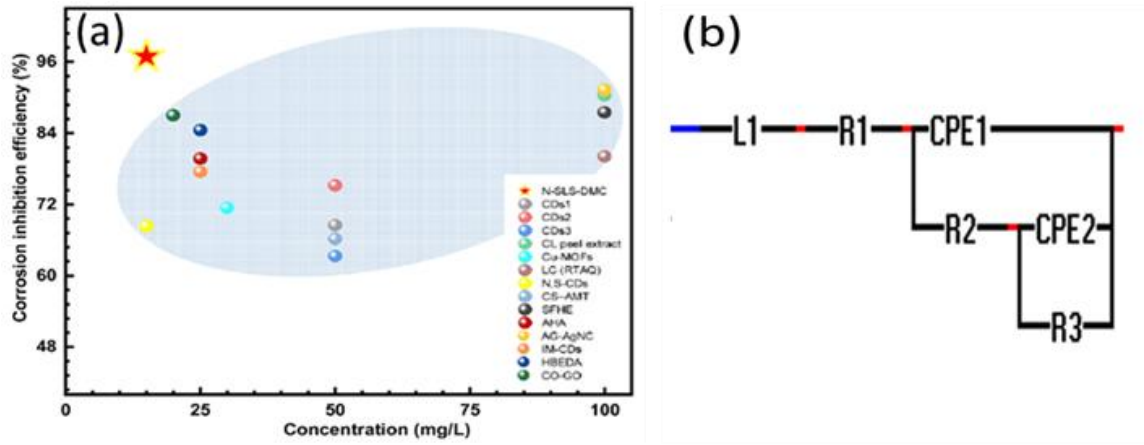


Figure 4.(a): Comparison diagram of MLCP with other documented corrosion inhibitors. (b):Equivalent circuit used to fit the data.

The corrosion inhibition efficiency (ηEIS) calculated from the EIS data, as shown in Table 1, increased at higher MLCP concentrations. The maximum value attained via EIS was 97.0 ± 0.55 percent when the MLCP solution contained 15 mg/L, demonstrating its significant corrosion-inhibiting capability. The CPEdl-T value exhibited a gradual decrease as the concentration of MLCP increased (Table 1), likely due to the adsorption of MLCP on the X120Mn12 surface. This adsorption process potentially displaced water molecules, increasing the bilayer thickness due to the presence of the inhibitor molecules and potentially altering the local dielectric constant.

The corrosion potential (E_corr) obtained from potentiodynamic polarization (PDP) measurements is around −0.40 V vs SCE, suggesting that MLCP acts as a mixed-type inhibitor, influencing both anodic and cathodic corrosion reactions. The significant reduction in corrosion rate upon the addition of MLCP clearly demonstrates its effectiveness. Consequently, the corrosion inhibition efficiency (η_PDP) determined by Phase-Power Plot increased with higher MLCP concentrations.

Figure 4a presents a comparison diagram of the corrosion inhibition efficiency of MLCP with other reported corrosion inhibitors as a function of concentration. Examining the corrosion inhibition efficiency values obtained by electrochemical impedance spectroscopy (EIS), high values were observed: 92 ± 0.4% for MLCP, 85 ± 0.9% for N-SLS, 88 ± 0.6% for DMC, and 96 ± 0.5% for SLS. As illustrated in Figure 4a, MLCP (potentially marked with a red star in the graph) exhibits noteworthy inhibition performance even at low concentrations. For instance, it demonstrates an inhibition efficiency of approximately 96% at a low concentration, clearly indicating MLCP's effectiveness. Figure 4b shows the equivalent circuit used to model the electrochemical impedance spectroscopy data. This circuit aids in understanding the corrosion process and the inhibitor's interaction mechanism with the metal surface.

The comparison in Figure 4a, along with the high inhibition efficiency values obtained through EIS, strongly supports the potential of MLCP as an effective corrosion inhibitor.

3.3. Effect of Immersion Time and Concentration on Corrosion Inhibition By MLCP

Scanning elektron microscopy (SEM) was conducted on X120Mn12 steel samples immersed in HCl solutions with different MLCP concentrations to examine the impact of MLCP concentration on corrosion morphology after a specific immersion time, as depicted in Figure 5. The SEM images in Figure 5 show the surface morphology, with darker and more textured areas typically indicating corrosion damage.

Figure 5a shows the untreated X120Mn12 steel surface, exhibiting characteristic scratches and roughness from the polishing process. In the absence of MLCP (Figure 5b), the SEM image clearly reveals a severely corroded surface with significant material loss and the formation of porous corrosion products after exposure to the acidic solution. However, with the addition of MLCP, a clear reduction in corrosion damage is observed across the SEM images (Figure 5c-f), demonstrating the inhibitor's protective effect. At a low concentration of 1 mg/L MLCP (Figure 5c), some improvement in surface morphology is visible compared to the blank sample, with less severe corrosion and fewer corrosion products. Increasing the MLCP concentration to 2 mg/L (Figure 5d) further reduces the extent of corrosion, leading to a smoother surface with smaller and less frequent corrosion sites.

A more significant protective effect is observed at 8 mg/L MLCP (Figure 5e), where the surface exhibits considerably less damage and appears substantially smoother, with a marked decrease in the presence of corrosion products. Notably, with 15 mg/L MLCP (Figure 5f), the SEM image shows a surface with minimal signs of corrosion, appearing almost as smooth as the uncorroded sample (Figure 5a), suggesting the formation of a dense and effective protective layer that effectively inhibits the acid attack on the steel surface.

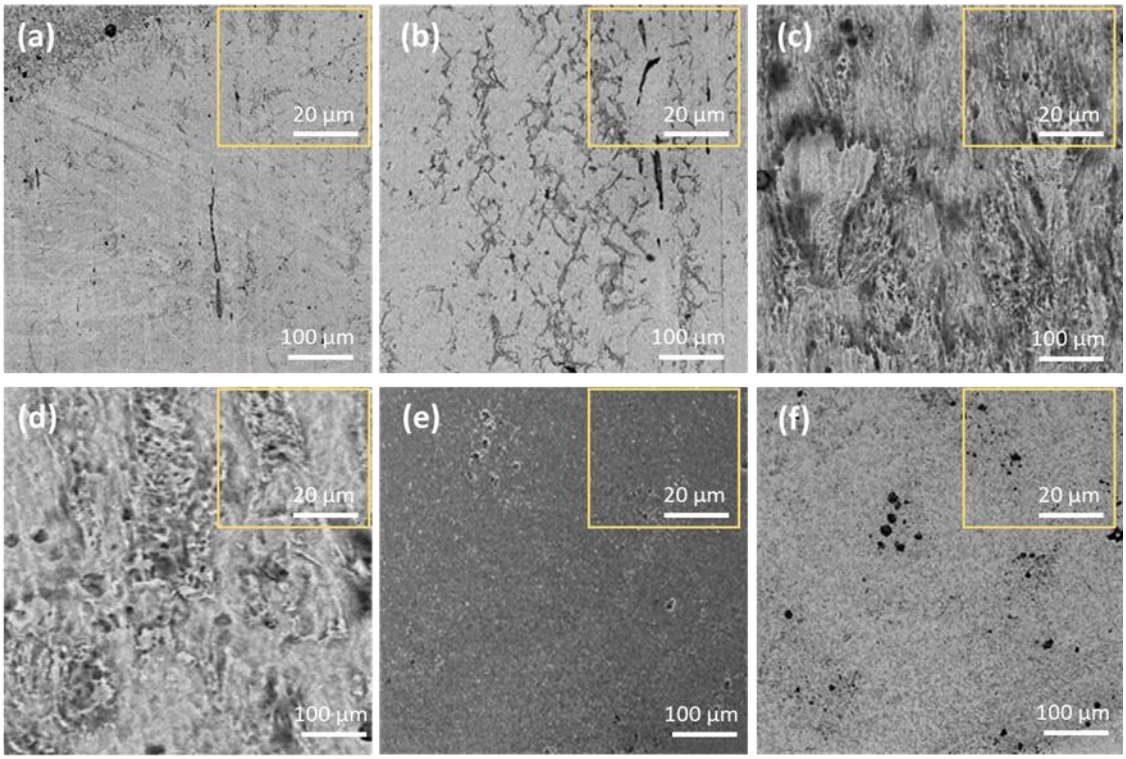


Figure 5.(a): SEM image of non-corroded (b-f): corroded surfaces (MLCP concentrations: 0, 1, 2, 8, and 15 mg/L.

These visual observations from the SEM analysis clearly demonstrate that MLCP provides concentration-dependent corrosion inhibition for X120Mn12 steel in HCl (1 mol/L,) effectively mitigating the corrosive effects of the acidic environment and leading to the formation of a protective film on the metal surface at higher inhibitor concentrations.

3.4. Effect of Immersion Time and Concentration on Corrosion Inhibition By MLCP

The metal surface was protected by a dense inner protective film formed by the MLCP, which prevented the direct penetration of corrosive substances. The composition of MLCP includes hydrophobic components derived from nanolignin and hydrophilic components originating from DMC. The EDS results presented in Figure 6 (b, g, h) corroborate the formation of this protective layer. The increased carbon content observed on the MLCP-treated surface strongly suggests the adsorption of the inhibitor molecules onto the steel. Concurrently, the decrease in oxygen content, as shown in Figure 6, indicates a reduction in the formation of iron oxide corrosion products, further supporting the inhibitor's effectiveness in preventing corrosion. The presence of nitrogen (as mentioned in the 1st paragraph's reference to previous EDS analyses) and its potential interaction with the metal surface, likely facilitated by the polar quaternary ammonium groups from DMC, also contributes to the formation and integrity of this barrier film. The AFM morphology image in Figure 6 (c) might further illustrate the uniformity and density of this protective layer on the surface.

The hydrophilic components, particularly the positively charged quaternary ammonium groups from DMC, are likely to adsorb onto the metal surface. While the steel surface in acidic solution may also carry a net positive charge due to proton adsorption, specific interactions such as localized charge differences, ion pairing with adsorbed chloride ions, or other chemical interactions might facilitate the adsorption process. Furthermore, the nanoscale dimensions of MLCP particles likely enhance their ability to form a compact and uniform protective film on the metal surface. Intermolecular interactions within the film, such as hydrogen bonding and electrostatic forces between the modified lignin and DMC components, may contribute to the film's stability and barrier properties against corrosive ions.

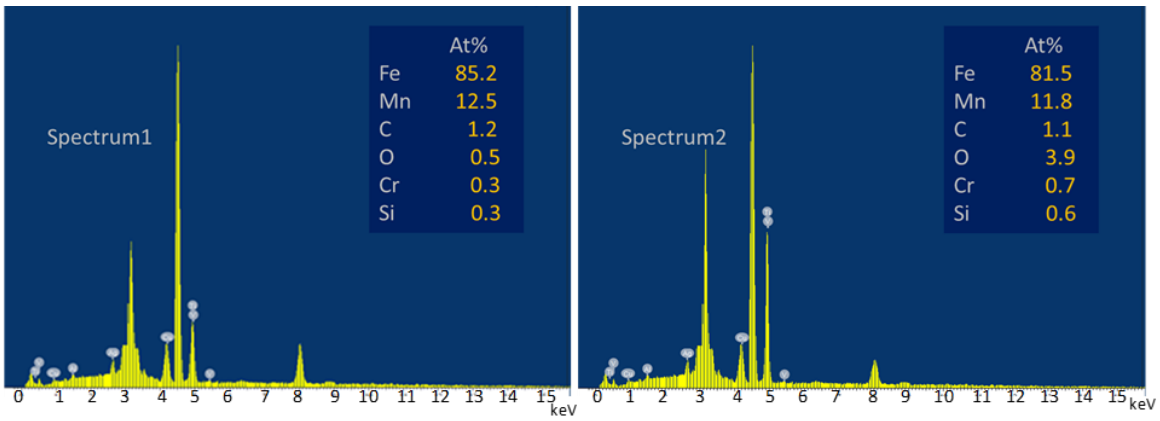


Figure 6. (a,b): EDS results (a,b)for the corroded surface in 1 mol/L HCl solutions containin15 mg/L MLCP after 3 hours of immersion.

4. Conclusion

This study has demonstrated the effective inhibition of X120Mn12 steel corrosion in hydrochloric acid solution by a biomass-derived, environmentally friendly corrosion inhibitor, modified nanosized lignin MLCP. Weight loss measurements and electrochemical tests (EIS and potentiodynamic polarization) revealed that MLCP provides high corrosion inhibition efficiency (up to 97%) in a concentration-dependent manner. As schematically illustrated in Figure 7, the corrosion inhibition mechanism of MLCP relies on the formation of a protective film on the metal surface. This film physically blocks the access of corrosive ions (Cl^-, H^+) to the metal surface, thereby suppressing both anodic ($Fe \rightarrow Fe^{+2} + 2e^-$) and cathodic ($2H^+ + 2e^- \rightarrow H_2$) reactions. The EDS results shown in Figure 6 further support this mechanism. The increased carbon (C) content on the MLCP-treated surface indicates the adsorption of the inhibitor, while the decrease in oxygen (O) content suggests the inhibition of corrosion product formation. The presence of nitrogen (N) (as indicated in previous EDS analyses) implies that the polar groups originating from DMC interact with the metal surface, contributing to the film formation.

The nanoscale nature of MLCP likely enhances the formation of a denser and more uniform protective film by increasing the surface area. The combination of hydrophobic nanolignin and hydrophilic DMC components provides an amphipathic structure that optimizes both the interaction with the metal surface and the isolation from the corrosive environment. Intermolecular interactions within the protective film, such as hydrogen bonds and electrostatic forces, may strengthen the film's stability and barrier properties against corrosive ions.

In conclusion, this study highlights the promising potential of modified nanolignin MLCP as an effective and environmentally friendly corrosion inhibitor for X120Mn12 steel. The development of such biomass-derived inhibitors offers a sustainable alternative to conventional toxic inhibitors, helping to mitigate environmental concerns.

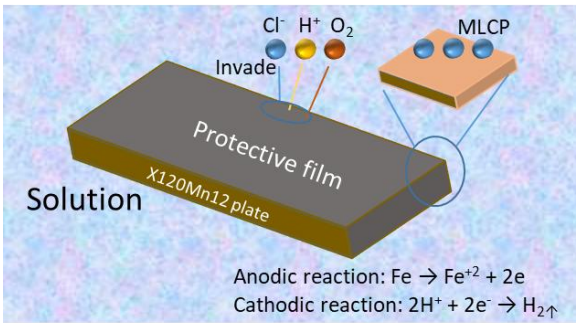


Figure 7. MLCP's corrosion-prevention process for X120Mn12 steel in HCl solution.

Author Contributions

The percentages of the authors' contributions are presented below. All authors reviewed and approved the final version of the manuscript.

	E.G.	M.E.
C	50	50
D	50	50
S	50	50
DCP	50	50
DAI	50	50
L	50	50
W	50	50
CR	50	50
SR	50	50
PM	50	50
FA	50	50

C=Concept, D= design, S= supervision, DCP= data collection and/or processing, DAI= data analysis and/or interpretation, L= literature search, W= writing, CR= critical review, SR= submission and revision, PM= project management, FA= funding acquisition.

Conflict of Interest

The authors declared that there is no conflict of interest.

Ethical Consideration

Ethics committee approval was not required for this study because of there was no study on animals or humans.

References

Abouelenein MG, Abdeen MM, El-Shamy OAA, Ibrahim MA, Farag AA. 2025. Pyranopyrazole derivative, a new corrosion inhibitor designed for managing the corrosion problem of aluminum metal in alkaline solution. Electrochim Acta. 514: pp: 145675.

Ahmed MA, Amin S, Mohamed AA. 2024. Current and emerging trends of inorganic, organic and eco-friendly corrosion inhibitors. RSC Adv. 14: pp: 31877-31920.

Akkus A, Gorgun E. 2015. The investigation of mechanical behaviors of poly methyl methacrylate (PMMA) with the addition of bone ash, hydroxyapatite and keratin. Adv Mater. 4: pp: 16-19.

Al Kiey SA, El-Sayed AA, Khalil AM. 2024. Controlling corrosion protection of mild steel in acidic environment via environmentally benign organic inhibitor. Colloids Surf A Physicochem Eng Asp. 683: pp: 133089.

Aleutdinova M, Fadin V. 2025. Effect of the initial structure of steels on the deterioration of their contact layers in dry sliding against quenched steel under alternating electric current of a density higher than 100 A/cm^2. Wear. 572-573: pp: 205985.

Bhadra J, Alkareem A, Al-Thani N. 2020. A review of advances in the preparation and application of polyaniline based thermoset blends and composites. J Polym Res. 27: pp: 122.

Dadkhah A, Schmidova E, Schmid M. 2025. Advances in plasma technique for Hadfield-coated layers to enhance mechanical durability of R260 rail steel. Results Surf Interfaces. pp: 100477.

Demir T, Demirel B, Öztürk M. 2024. Valorisation of the effect of waste aluminum sawdust on concrete: durability characteristics and environmental impacts. Black Sea J Eng Sci. 7(1): pp: 109-120.

Doğan K, Dağ B. 2024. Design and optimization of voltage mode PWM control of DC-DC buck converter with a PI-lead compensator using the simulated annealing algorithm. Black Sea J Eng Sci. 7(1): pp: 72-88.

Ennafaa F, Chraka A, Tassaoui K, Zerkani H, El Rhaffari L. 2025. An experimental and dual computational study using DFT and MD simulations to better understand the adsorption and corrosion-inhibiting properties of N-(3-(4-Methoxyphenyl)isoxazol-5-yl)methyl saccharin for C38 steel in acidic medium. Mater Chem Phys. 334: pp: 130441.

Fernandes FD, da Silva G. 2024. MLCP phytochemicals/plant extracts as corrosion inhibitors for copper in biodiesel. In: Phytochem Corros Sci, pp: 347-362.

Ghehsareh Z, Sayah T, Moharramnejad M, Gheysari HR. 2025. Green guardians: a comprehensive review of environmentally friendly corrosion inhibitors from plant extract to ionic-liquids in industrial applications. Prog Org Coat. 201: pp: 109146.

Görgün E. 2022. Characterization of superalloys by artificial neural network method. Presented at: Online Int Symp Appl Math Eng (ISAME22), Jan 21-23, 2022, Istanbul, Türkiye, pp: 67.

Gorgun E. 2024a. Numerical analysis of inflow turbulence intensity impact on the stress and fatigue life of vertical axis hydrokinetic turbine. Phys Fluids. 36(1): pp: 30-36.

Gorgun E. 2024b. Ultrasonic testing and surface conditioning techniques for enhanced thermoplastic adhesive bonds. J Mech Sci Technol. 38(3): pp: 1227-1236.

Hamood AF, Habeeb HM, Abdulhussein BA, Ahmed BA, Ismail AA. 2024. Weight loss, electrochemical measurements and DFT studies on corrosion inhibition by 7-mercapto-4-methylcoumarin. Results Eng. 23: pp: 102677.

He H, Zhang Z, Jiang C, He C. 2025. Research progress of carbon dots as novel corrosion inhibitors. J Mol Struct. 1334: pp: 141894.

Iyyappan S, KP VK, Ponram P, Karthik B. 2024. Exploring copper corrosion inhibition in value added neem biodiesel: evaluation by traditional and machine learning approaches. Ind Crops Prod. 219: pp: 119073.

Jebali Z, Ferkous H, Zerroug M, Sayah T, Moharramnejad M. 2024. Unveiling the potent corrosion-inhibiting power of Ammophila arenaria aqueous extract for mild steel in acidic environments: an integrated experimental and computational study. J Environ Chem Eng. 12: pp: 112374.

Jia S, Akiyama M, Frangopol DM, Xu Z. 2024. Bayesian inference of the spatial distribution of steel corrosion in reinforced concrete structures using corrosion-induced crack width. Struct Saf. 111: pp: 102518.

Jiménez-Marcos C, Mirza-Rosca JC, Baltatu MS, Vizureanu P. 2025. Two novel Ti–Mo–Ta–Zr alloys for medical devices: their microstructure, corrosion resistance and microhardness characteristics. Mater Chem Phys. 334: pp: 130511.

Lakshmi A, Pandit P, Nayak G, Arunkumar P, Kumar KS, Santhosh PB. 2024. Influence of corrosion-based section loss on morphology and tensile capacity of pre-stressing strands. J Struct Integr Maint. 9: pp: 24705314.2024.2302655.

Li Y, Sun H, Mu T, Garcia-Vaquero M. 2025. Sustainable closed-loop biorefinery of γ-valerolactone from lignocellulosic biomass: pretreatments of multiple biomass and synthesis of γ-valerolactone from multiple biomass-derived feedstocks. Biomass Bioenergy. 193: pp: 107594.

Liu W, Dong B, Chen P, Li Y, Yang D. 2024. Effect of electrodeposition potential on the growth mechanism and corrosion resistance of Zn/Al layered double hydroxide film on steel substrate via electrodeposition-hydrothermal method. J Build Eng. 97: pp: 110831.

Luo ZG, Zhang Y, Wang H, Wang W, Wu M. 2024. Modified nano-lignin as a novel biomass-derived corrosion inhibitor for enhanced corrosion resistance of carbon steel. Corros Sci. 227: pp: 111705.

Maizia R, Djermoune A, Amoura D, Boukraa S. 2025. Bidens aurea Aiton plant extract as a green and sustainable corrosion inhibitor for carbon steel X42 in hydrochloric acidic medium: experimental and computational studies. Mater Chem Phys. pp: 130740.

Onukwuli OD, Nnanwube IA, Ochili FO, Omotioma M. 2024. DFT, experimental and optimization studies on the corrosion inhibition of aluminium in H_2SO_4 with danacid as inhibitor. Results Eng. 24: pp: 103113.

Oppermann F, Bernsmann JS, Kies F, Pippel E, Kauffmann A. 2025. In situ carbide formation causing strain-age cracking in additively manufactured, highly alloyed steels. J Mater Res Technol. 35: pp: 4457-4472.

Pei J, Yang H, He Y, Xu J, Wang X. 2024. Microstructure evolution and property of high manganese steel coatings by laser shock assisted laser wire cladding. J Mater Process Technol. 328: pp: 118413.

Rai A, Szczerba M, Karbowniczek J, Kuncewicz M, Skwarek E. 2025. Enhanced corrosion resistance of magnesium alloy via surface transfer of microwave-synthesized, non-toxic, and ultra-smooth nitrogen-doped amorphous carbon thin film. Appl Surf Sci. 695: pp: 162847.

Razali NZK, Wan Hassan WNS, Sheikh Mohd Ghazali SAI, Mohd Radzi AH. 2024. DFT, Fukui indices, and molecular dynamic simulation studies on corrosion inhibition characteristics: a review. Chem Pap. 78: pp: 715-731.

Sharma S, Dwivedi SP, Li C, Sinha RK. 2024. Unveiling of grain structure, porosity, phase distributions, microstructural morphology, surface hardness, and tribo-corrosion characteristics of nickel, and titanium dioxide-based SS-304 steel microwave composite coatings cladding. J Mater Res Technol. 28: pp: 4299-4316.

Shwetha KM, Praveen BM, Devendra BK. 2024. A review on corrosion inhibitors: types, mechanisms, electrochemical analysis, corrosion rate and efficiency of corrosion inhibitors on mild steel in an acidic environment. Results Surf Interfaces. pp: 100258.

Solmaz MY, Yanen C, Kıstak C, Aydoğmuş E. 2024. Production of chemically modified shear thickening fluids and investigation of their rheological properties. Black Sea J Eng Sci. 7(1): pp: 31-35.

Sun M, Lin L, Di H, Feng Y. 2025a. A study on the effects of lignocellulosic biomass components on the interactions and thermal conductivity of stearic acid: molecular dynamics simulation. Int J Heat Mass Transf. 244: pp: 126932.

Sun X, Xu H, Cao Y, Li J, Chen W. 2025b. Progress in the design of molecular structure of amino acid corrosion inhibitors based on molecular orbital theory and their mechanisms: a review. J Mol Liq. pp: 127374.

Wang Y, Huang J, Chen Y, Yang Z, Zhao Y. 2024. Modulating built-in electric field via Bi-VO_4-Fe interfacial bridges to enhance charge separation for efficient photoelectrochemical water splitting. J Colloid Interface Sci. 672: pp: 12-20.

Yang D, Liu Y, Yang T, Chen Y, Wang X. 2025. Anti-corrosion lithium anode interface by $Li_{6.4}La_3Zr_{1.4}Ta_{0.6}O_{12}$ modified buffer layer for stable cycling of room-temperature solid-state lithium metal batteries. J Colloid Interface Sci. 689: pp: 137225.

Zemlik M, Konat Ł, Leśny K, Jamroziak K. 2024. Comparison of abrasive wear resistance of Hardox steel and Hadfield cast steel. Appl Sci. 14: pp: 1114143.

.

Black Sea Journal of Engineering and Science
doi: 10.34248/bsengineering.1657985

Open Access Journal
e-ISSN: 2619 – 8991

Research Article
Volume 8 - Issue 4: 1076-1086 / July 2025

PHYTOSYNTHESIS OF SILVER NANOPARTICLES USING *Aesculus hippocastanum* L. (KERNEL AND SHELL) AND EVALUATION OF THEIR LARVICIDAL ACTIVITY AGAINST *Plodia interpunctella* (HUBNER) (LEPIDOPTERA: PYRALIDAE)

Onur AKER[1]*

[1]*Amasya University, Suluova Vocational School, Department of Plant and Animal Production, 05500, Amasya, Türkiye*

Abstract: The aim of this study was to synthesise silver nanoparticles (AgNPs) from horse chestnut organic wastes (kernel and shell) by phytosynthesis and to investigate the larvicidal activity of the obtained nanoproducts. In the characterisation tests (UV-Vis, FTIR, XRD, SEM, STEM, EDS), the physico-chemical structure of the synthesised AgNPs was clearly obtained. In order to determine the larvicidal activity of the synthesised AgNPs, topical application of four different doses of AgNPs (50, 100, 150 and 200 ppm) on second and fourth instar larvae of Indian meal moth (*P. interpunctella*) was carried out at two different temperatures (28-32 °C). The highest larvicidal activity was observed at the end of the fourth day, at the highest application dose (200 ppm), at 32 °C and in the nanoproduct obtained from the kernel (99% mortality rate for second instar larvae and 92% mortality rate for fourth instar larvae). It was observed that second instar larvae were more sensitive to AgNPs compared to fourth instar larvae, and as the applied temperature increased, the concentration values required for lethal effect and the exposure times required for killing decreased. According to the larvicidal activity data obtained, it was determined that the type of extract used in the synthesis, the temperature of the environment selected for application, the dose amounts applied and the exposure time are very important in this type of nano-insecticidal studies.

Keywords: Horse chestnut, Organic waste, AgNPs, Indian meal moth, Larvicidal activity.

***Corresponding author:** Amasya University, Suluova Vocational School, Department of Plant and Animal Production, 05500, Amasya, Türkiye
E mail: onur.aker@amasya.edu.tr (O. AKER)
Onur AKER https://orcid.org/0000-0002-9581-9697

Received: March 14, 2025
Accepted: May 15, 2025
Published: July 15, 2025

Cite as: Aker O. 2025. Phytosynthesis of silver nanoparticles using *Aesculus hippocastanum* L. (Kernel and Shell) and evaluation of their larvicidal activity against *Plodia interpunctella* (Hübner) (Lepidoptera: Pyralidae). BSJ Eng Sci, 8(4): 1076-1086.

1. Introduction

Many different moth species have the potential to damage stored products and one of the most dangerous of these, *Plodia interpunctella*, can cause irreversible and serious damage to stored nuts, dried fruits and foods, cereals and legumes if no action is taken (Kumar, 2017; Nasir et al., 2017). Although a certain success rate has been achieved in chemical control against this pest, the fact that the pest has developed resistance to most chemicals, the high rate of residue problems in the products after application and the resulting serious health risks for humans and animals have created new opportunities for alternative control methods against this pest (Attia et al., 1981; Pretty and Bharucha, 2015; Chellappandian et al., 2018).

As an alternative control, researchers have tried preparations obtained from plant-based drugs against this pest using different methods and have obtained very effective results (Elma et al., 2021; Prvulović et al., 2023). Biotechnological studies carried out to increase the effectiveness of herbal preparations even at low doses have led researchers to synthesise nanoparticles using herbal drugs and to test the nanoproducts formed in this way against pests (Adetunji and Oloke, 2024; Tirunagaru et al., 2024). The most well-known of the nanoparticles with different properties formed as a result of green synthesis processes are silver nanoparticles in metallic form and many storage pest species have been controlled using these synthesis products (Yasur and Rani , 2015; Abbood and Ali, 2020; Rehman et al., 2021; Anees et al., 2022).

The fact that the plants to be used for the green synthesis of silver nanoparticles can be easily found in nature and even the use of plant organic wastes in these synthesis processes have come to the fore as highly preferred studies in recent years (Kiani et al., 2023; Marcu Spinu et al., 2024). Horse chestnut (*Aesculus hippocastanum* L.) is abundant in natural forests and is even grown as an ornamental plant in many parts of the world as a landscape tree in many parks and gardens in cities (Lack, 2002). In studies on many different parts of this tree, it has been reported that they have a very high phytocompound content and even the fruits have a very rich variety of secondary metabolites (Kędzierski et al., 2016; Čukanović et al., 2020; Owczarek-Januszkiewicz et al., 2023). Due to these properties, horse chestnut has been the subject of many studies and even considered as

This work is licensed (CC BY-NC 4.0) under Creative Commons Attribution 4.0 International License

organic waste and preferred in green synthesis processes of silver nanoparticles and some other metallic nanoparticles (Çolak et al., 2017; Demirezen et al., 2018; Küp et al., 2020).

The aim of this study is to synthesise silver nanoparticles by green synthesis from extracts of horse chestnut kernel and shell, which are considered as organic waste. The next step is to determine the larvicidal activity of the synthesised silver nanoparticles against *Plodia interpunctella*, an important storage pest. The data to be obtained as a result of the study will constitute a scientific resource for future nanotechnological studies of different nature using organic wastes with different properties against moths, which are warehouse pests and have similar properties.

2. Materials and Methods

2.1. Extraction of Plant Materials and Synthesis Process of Silver Nanoparticles

The kernels and shells of horse chestnut (*Aesculus hippocastanum* L.) were used in this study (September 2023, Latitude: 40°50′39′′ N, Longitude: 35°37′44′′ E, Altitude 522 m). Cleanly collected plant material was dried in a ventilation cabinet at room temperature for 60 days. Fifty gram of dried plant material was placed in a 500 mL Erlenmeyer flask, deionised water was added and placed in an ultrasonic water bath at 50 °C for 30 min. After cooling the solution, it was carefully filtered using sterile Whatman No.1 filter paper and prepared for silver nanoparticle synthesis (Hu et al., 2022). This solution was designed using silver nitrate (AgNO3, 99.9%, Sigma-Aldrich) similar to the method described by Küp et al. (2020) and silver nanoparticles were synthesised and AgNPs powder pellets were obtained from this synthesised solution.

2.2. Characterisation of the Materials Obtained

The spectra of the obtained materials (extract and AgNPs) were prepared using UV-vis spectrophotometer (Model UV 1601, Shimadzu). FTIR spectroscopy (Jasco 430 model FTIR spectrometer) was performed using KBr pellet method to determine the distribution of chemical functional groups of nanomaterials (AgNPs). XRD (X-ray diffraction) graphs of AgNPs were generated using XRD diffractometer (Rigaku SmartLab 9 kW diffractometer system). SEM (Scanning Electron Microscopy) and STEM (Scanning Transmission Electron Microscopy; carbon coated copper grating was used to visualise the nanoparticles in terms of shape, size and structure) were carried out using JEOL JSM-7001F device. EDS (Energy Dispersive X-ray Spectroscopy) imaging analyses were performed to determine the elemental distribution of the prepared AgNPs and EDS graph was obtained. In addition, in order to more clearly evaluate the dimensional distribution of silver nanoparticles synthesised from both extracts, size plots of nanoparticles were generated from TEM images using Image-J software.

2.3. Rearing and Larvicidal Bioassay

The 1-2-day old Indian meal moth larvae used in the experiments were obtained from a laboratory-reared pest colony (more than 5 generations). The colonies were reared in plastic containers (10 cm deep x 15 cm wide x 30 cm high) covered with a sturdy mesh with fine pores for ventilation in a rearing room at 26 ± 1 °C temperature, 60 ± 5% relative humidity and 16(L): 8(D) hours photoperiod. The diet consisted of a mixture of maize flour, milk powder, honey, glycerin and flour (2:1:1:1:1:1:1:1, w/w/w/w/w/w). Firstly, powdered silver nanoparticles were prepared with distilled water at 4 different doses of 50, 100, 150 and 200 ppm and bottled. Only 1 µL of the different doses of nanoparticles was applied topically to the anterior thorax of 1–2-day old second and fourth instar larvae (L2-L4 stages) using a micro-applicator. L2 and L4 stage larvae treated with nanoparticles were placed in sterile petri dishes (Ø 90 mm sterile petri dishes, Whatman No. 1 round sterile blotting paper to cover the petri dish and 5 grams of diet on it) in groups of 10 separately. This procedure was prepared according to a randomized block design with ten replications for each dose-temperature-nanoparticle type determined for the experiments. A control group was added to each of the groups prepared for each dose-temperature-nanoparticle type and larvae in the control group were treated with distilled water only. All plastic containers prepared for the experiments were placed in their own climatic environment (28 ± 1°C / 32 ± 1°C, 60 ± 5% relative humidity, 16 (L): 8 (D) hours) and monitored daily throughout the experiments and the larvae that died as a result of the observations made at the end of 24, 48, 72 and 96 hours following the treatment were recorded and these larvae were removed from the environment.

2.4. Statistical Analysis

Mortality rates in control groups were corrected using the Abbott formula (Abbott, 1925). In order to determine the lethal effects of synthesized silver nanoparticles on both life forms depending on different temperatures, the significance of the differences between the mortality rates depending on the dose-time pair was characterized by Duncan's multiple range tests (p<0.05) (One-Way ANOVA Test: SPSS-2017, Version-25.0). The mortality rates obtained (mean ± SE) were shown in percentage graphs (p<0.05). In addition, 50% and 90% lethal concentration (LC50 and LC90) values and 50% and 90% lethal time (LT50 and LT90) values and their 95% confidence intervals (95% CL) were calculated from the adjusted mortality rates using probit regressions and SPSS-17 (Version 25.0) software.

3. Results and Discussion

3.1. Characterisation Assessment

UV–VIS: The colour change in the form of darkening of the solution colour during the synthesis process is clear evidence that the silver ions undergo a reduction process and this is mainly due to the surface plasmon resonance

response (Küp et al., 2020; Hu et al., 2022). As a result of the surface plasmon resonance response during synthesis, a very high peak value is obtained in the graphs of nanoparticles using UV-vis spectrophotometry, while this is not the case for extracts (Küp et al., 2020; Hu et al., 2022). In this study, it was observed that silver nanoparticles synthesised using shell and kernel extracts formed an absorption spectrum band at 485 nm and 490 nm wavelength, respectively. However, the shell and kernel extracts used did not produce any peak value in the absorption spectrum band (Figure 1).

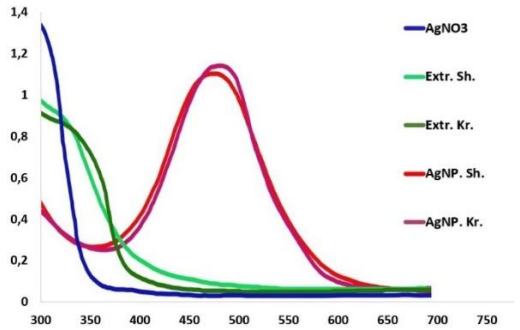


Figure 1. UV–Vis spectrum of Extracts (Sh.: Shell; Kr.: Kernel) and AgNPs (Sh.: Shell; Kr.: Kernel).

FTIR: While synthesising silver nanoparticles, a reduction process takes place due to the herbal components in the extract and this situation varies according to the content of the herbal components. This situation clearly shows itself in the FTIR test and when the spectroscopy of the synthesised nanoparticles and the extract is compared, it is seen that although the graphs are similar, there are differences due to reduction on the nanoparticle side (Chand et al., 2020; Salayová et al., 2021; Hu et al., 2022).When the FTIR test results of the nanoparticles synthesised using two different extracts in this study are compared, it is seen that the graphs are quite similar, but they differ from each other with some minor changes (Figure 2, a-b). This can be explained by some small differences in the functional groups of the plant compounds in the extracts used (Salayová et al., 2021). As a result of these small differences, two very similar nanoparticles were synthesised and as a result two different FTIR graphs were obtained (Figure 2, a-b). In similar studies where silver nanoparticles were synthesised, it was reported that the difference in the extract used caused changes in both the graphics and functional functions of the synthesised nanoparticles (Chand et al., 2020; Salayová et al., 2021; Hu et al., 2022).

XRD: As a result of XRD analysis to determine the refractive reflections of the synthesised AgNPs, 11 reflections were observed in nanoparticles produced from the shell and 19 reflections were observed in nanoparticles produced from the kernel (Figure 3, a-b). When the Miller index equivalents of the strongest of these Bragg reflections were calculated, it was determined that they corresponded to (110), (111), (200), (220), (311) and (222) planes, respectively (Ituen et al., 2020; Mahdi et al., 2024; Swathi et al., 2025). These strong reflections are very important in the characterisation of the synthesised silver nanoparticles and it is known that the Miller index expressed as '111' gives the strongest reflection (Ituen et al., 2020; Mahdi et al., 2024; Swathi et al., 2025).

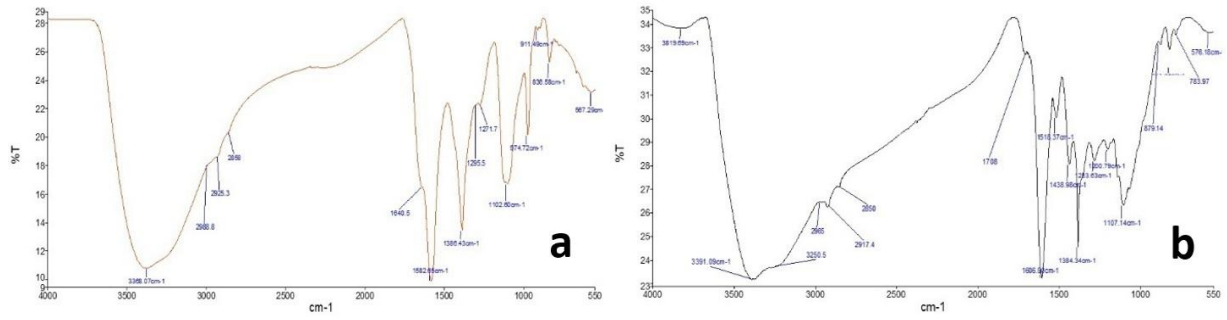


Figure 2. FTIR spectrum of Kernel AgNPs (a) and Shell AgNPs (b).

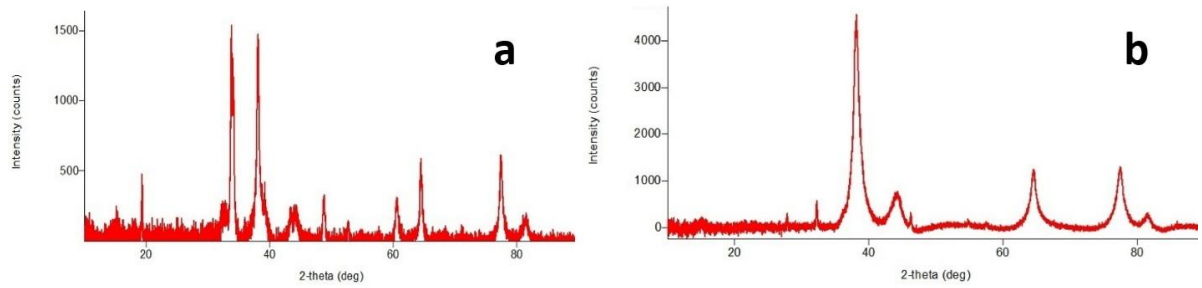


Figure 3. XRD pattern of Kernel AgNPs (a) and Shell AgNPs (b).

SEM, STEM and EDS: In this study, SEM scanning (X 50K magnification) and STEM scanning (X 100K magnification) images obtained from both nanoparticles revealed that they have a spherical structure and show clusters (Figure 4, a-b; Figure 5, a-b). In similar studies, it is stated that AgNPs generally exhibit the same appearance (Ali et al., 2023; Swathi et al., 2025). When the elemental distribution ratios and relationships of the synthesised silver nanoparticles were examined (EDS), it was determined that the silver (Ag) element had the highest density in both graphs (Shell: 65.07% and Kernel: 75.40%) and contained other elements at different ratios (Figure 6, a-b). In this study, the peak of Ag element at the highest intensity and above 3 keV in EDS graphs is a characteristic situation arising from the surface plasmon resonance of silver nanoparticles and the same situation is found in many similar studies (Chand et al., 2020; Ali et al., 2023). As in different AgNP synthesis and application studies, the sizes of nanoparticles were determined and their graphs were drawn on TEM images using Image J software. According to the results obtained, these size values for kernel-derived AgNPs ranged between 10-50 nm, while these size values for shell-derived AgNPs ranged between 5-40 nm (Figure 7, a-b). This dimensional difference is thought to be effective on larvicidal activity.

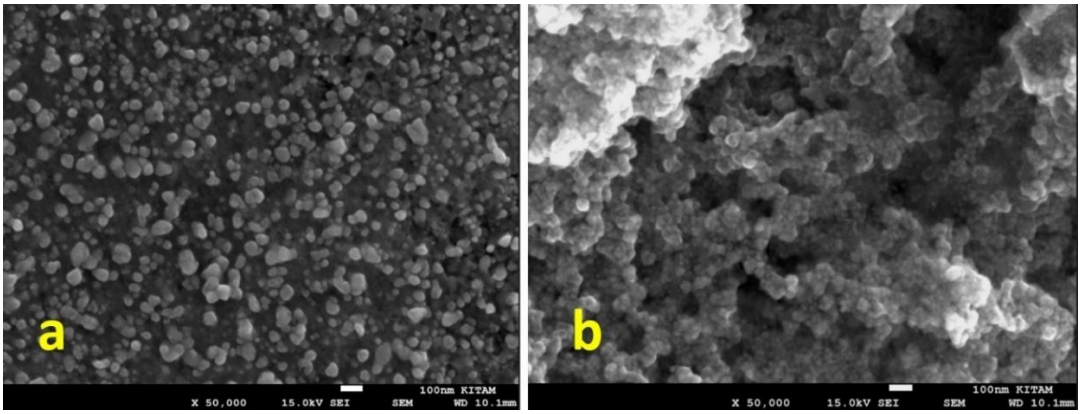


Figure 4. SEM image of Kernel AgNPs (a) and Shell AgNPs (b).

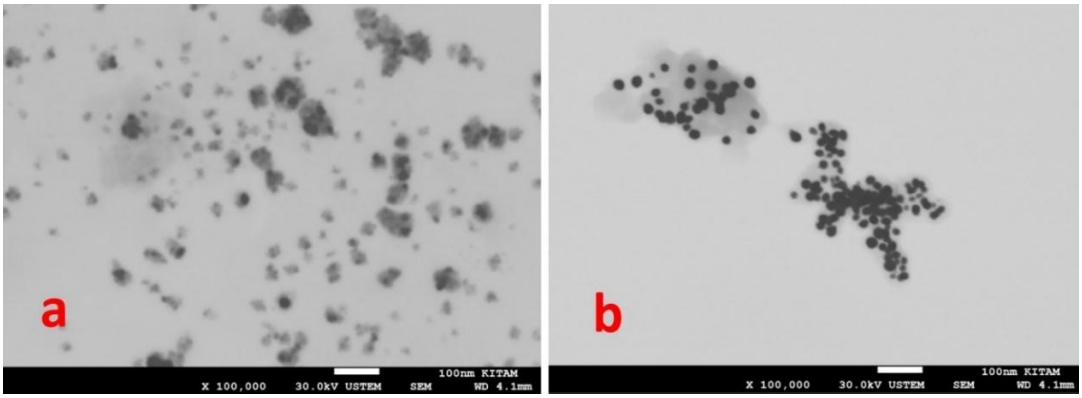


Figure 5. STEM image of Kernel AgNPs (a) and Shell AgNPs (b).

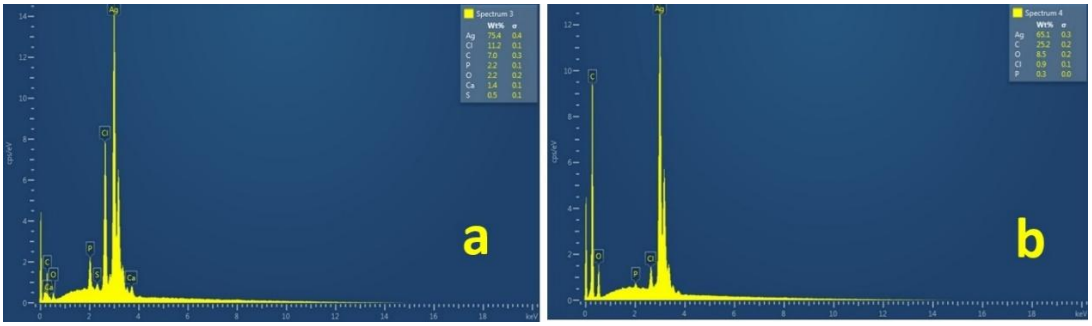


Figure 6. EDS spectrum of Kernel AgNPs (a) and Shell AgNPs (b).

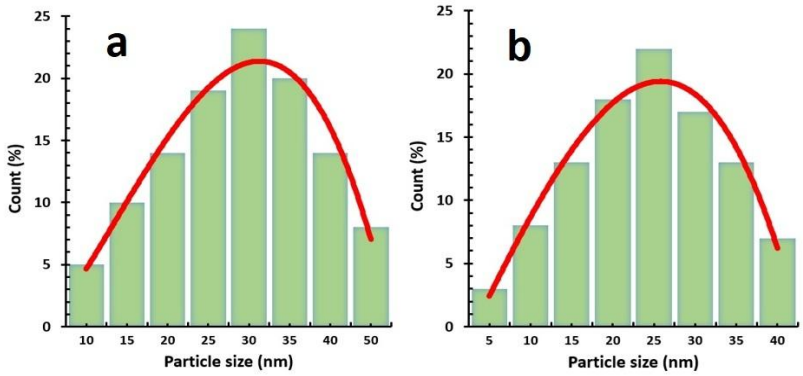


Figure 7. Particle diameter plot of Kernel AgNPs (a) and Shell AgNPs (b).

3.2. Larvicidal Activity Assessment

When the mortality rates resulting from the topical application of silver nanoparticles on the second and fourth larval stages of the pest were evaluated, it was determined that the larvicidal activity was more effective on the second stage larvae than on the fourth stage larvae based on the same conditions. At the end of the fourth day, when all treatments (in terms of dose-duration-temperature) were compared, it was observed that the second stage larvae lost more than the fourth stage larvae (Figure 8-15). In this study on larvicidal activity, it is understood that the strength of larvicidal activity increases with the increase in the amount of application dose and exposure time. The lowest level of larvicidal activity was observed in the lowest dose treatment at the end of the first day. On the other hand, the highest larvicidal activity was observed at the highest dose application and at the end of the fourth day (Figure 8-15). According to another result obtained from the experiments, the strength of larvicidal activity varies according to the ambient temperature of the application and the extract from which the nanoparticle was synthesised. The mortality rates observed at low temperatures are lower than those observed at high temperatures. In addition, the mortality rates obtained from the trials in which the nanoparticle prepared using the bark extract was applied were lower than the trials in which the nanoparticle prepared using the kernel extract was applied (Figure 8-15).

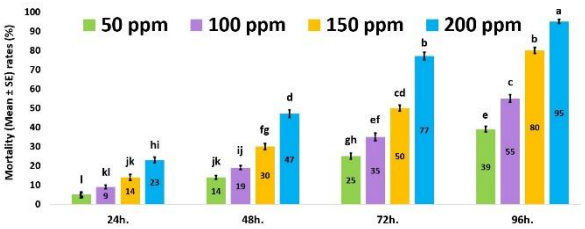


Figure 8. Daily mean (±SE) mortality rates caused by Kernel AgNP against second instar larvae of *Plodia interpunctella* at 28°C (Mortality rates were compared statistically using Duncan's multiple range test, $p < 0.05$. Each different letter indicates statistically significant difference between mortality rates).

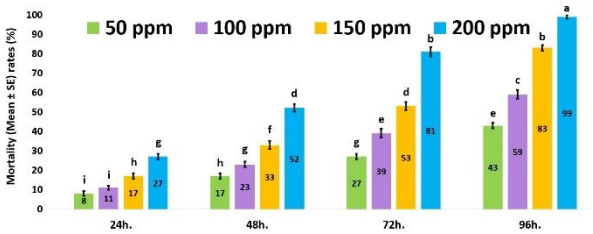


Figure 9. Daily mean (±SE) mortality rates caused by Kernel AgNP against second instar larvae of *Plodia interpunctella* at 32°C (Mortality rates were compared statistically using Duncan's multiple range test, $p < 0.05$. Each different letter indicates statistically significant difference between mortality rates).

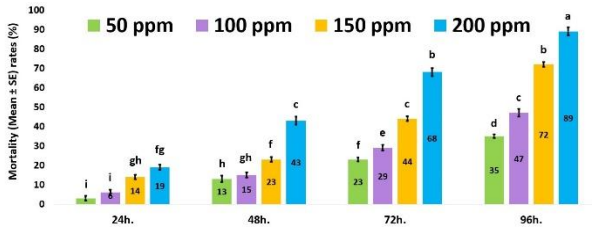


Figure 10. Daily mean (±SE) mortality rates caused by Kernel AgNP against fourth instar larvae of *Plodia interpunctella* at 28°C (Mortality rates were compared statistically using Duncan's multiple range test, $p < 0.05$. Each different letter indicates statistically significant difference between mortality rates).

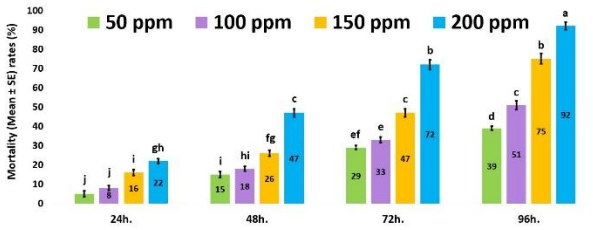


Figure 11. Daily mean (±SE) mortality rates caused by Kernel AgNP against fourth instar larvae of *Plodia interpunctella* at 32°C (Mortality rates were compared statistically using Duncan's multiple range test, $p < 0.05$. Each different letter indicates statistically significant difference between mortality rates).

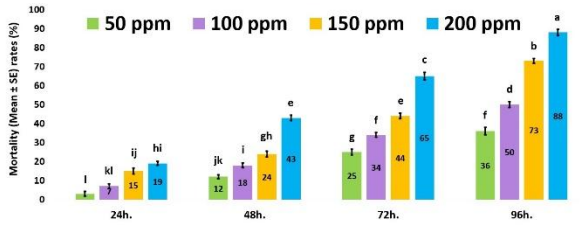


Figure 12. Daily mean (±SE) mortality rates caused by Shell AgNP against second instar larvae of *Plodia interpunctella* at 28°C (Mortality rates were compared statistically using Duncan's multiple range test, $p < 0.05$. Each different letter indicates statistically significant difference between mortality rates).

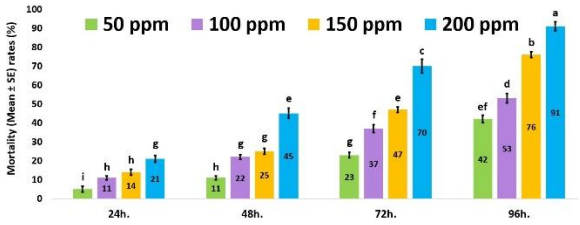


Figure 13. Daily mean (±SE) mortality rates caused by Shell AgNP against second instar larvae of *Plodia interpunctella* at 32°C (Mortality rates were compared statistically using Duncan's multiple range test, $p < 0.05$. Each different letter indicates statistically significant difference between mortality rates).

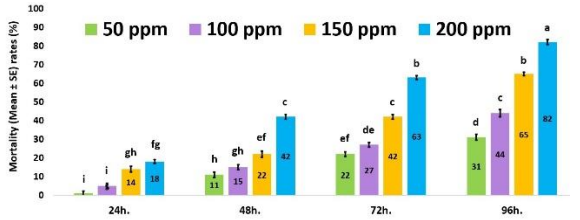


Figure 14. Daily mean (±SE) mortality rates caused by Shell AgNP against fourth instar larvae of *Plodia interpunctella* at 28°C (Mortality rates were compared statistically using Duncan's multiple range test, $p < 0.05$. Each different letter indicates statistically significant difference between mortality rates).

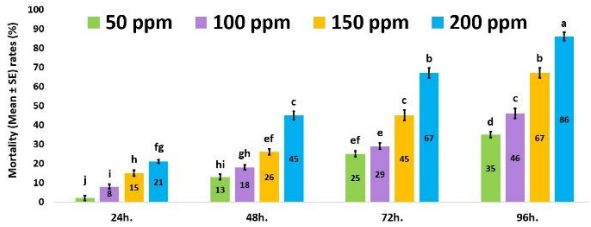


Figure 15. Daily mean (±SE) mortality rates caused by Shell AgNP against fourth instar larvae of *Plodia interpunctella* at 32°C (Mortality rates were compared statistically using Duncan's multiple range test, $p < 0.05$. Each different letter indicates statistically significant difference between mortality rates).

In this study, it was tried to determine the mortality rates of Ag nanoparticles synthesised from two different extracts against both life forms at different doses and different times by applying two different temperatures. When probit analyses were performed on the highest dose application (200 ppm) and the highest exposure duration (96 hours), lethal concentration and lethal duration values were determined (Table 1-2). According to these results, it was once again observed that second instar larvae were more sensitive to both extract derivatives Ag nanoparticles compared to fourth instar larvae. Furthermore, the concentration values required for lethality and the exposure times required for lethality decrease as the applied temperature increases. According to the information obtained from this study, it can be said that all factors such as larval stage status, dose amount applied, exposure time, structure of the extract from which the nanoparticle is synthesised and ambient temperature have a determining effect on larvicidal activity in such studies.

Synthesised AgNPs are highly effective in pest control studies by showing irreversible destructive effects on the physiology of the targeted pest (Suresh et al. 2018). Especially after AgNPs reach inside the cell, AgNP-related anomalies at the cellular level are the beginning of the end and trigger many cellular destruction events one after another (Roni et al., 2015). Vital cellular activities such as decreased levels of detoxifying enzymes, impaired function of many important neurotransmitter enzymes and irregular increases in the production of reactive oxygen species (ROS) are all adverse conditions caused by the entry of AgNPs into the cell and this process ultimately results in the death of the cell (Parthiban et al., 2019; El-Samad et al., 2022). AgNPs exhibit very strong larvicidal activity after adhering to the cuticle of insect larvae due to their nano-sized structures. After reaching the cells, AgNPs passing through the membrane can bind to sulfur and phosphorus groups in the cell, then cause abnormal cell activity and lead to the death of insect larvae (Morejón et al., 2018; Sutthanont et al., 2019; Kumar et al., 2022). Moreover, recent studies have shown that Ag+ exposure acts by disrupting the homeostasis of the ROS scavenging system, over-triggering ROS-mediated stress responses through excessive production of hydroxyl radicals, which has serious effects on cell destruction (Zhu et al., 2017; Li et al., 2020). It is also known that mitochondria manage ROS mainly through the mitochondrial antioxidant system, and it is reported that AgNPs play a role in cell destruction by causing excessive ROS production during this toxicity process, triggering DNA damage/deterioration, which is a critical and fatal situation, and ultimately leading to cell death through apoptosis (Gurunathan et al., 2022; Zhang et al., 2022). Wang et al. (2023) linked the toxicity of *Drosophila* larvae exposed to AgNPs to the increase in ROS and oxidative stress marker MDA (malon-dialdehyde) levels and stated that this led to DNA damage, decreased cell viability and an increase in MDA in larvae.

Table 1. LC50 and LC90 values obtained after topical application of biosynthesised AgNPs on *Plodia interpunctella* (Hubner) larvae.

Extract Type / Application Exposure Time	Life Period of Pest / Applied Temperature	LC50 (95% CL) (ppm)	LC90 (95% CL) (ppm)	Slope±SE	X^2 (df)
Kernel / 96 hour	*L_2 / 28 ℃*	79,918 (65,013 – 91,786)	182,847 (166,180 – 206,905)	0,012±0,001	8,762 (38)
	L_2 / 32 ℃	72,217 (57,655 – 83,630)	165,359 (150,739 – 186,057)	0,014±0,002	12,639 (38)
	L_4 / 28 ℃	94,748 (79,706 – 107,259)	213,367 (192,008 – 245,743)	0,011±0,001	8,209 (38)
	L_4 / 32 ℃	85,113 (68,968 – 97,917)	201,365 (181,421 – 231,399)	0,011±0,001	12,504 (38)
Shell / 96 hour	*L_2 / 28 ℃*	90,961 (74,553 – 104,165)	215,024 (192,667 – 249,529)	0,010±0,001	10,496 (38)
	L_2 / 32 ℃	79,265 (60,554 – 93,375)	204,467 (182,908 – 237,939)	0,010±0,001	12,615 (38)
	L_4 / 28 ℃	108,206 (92,760 – 121,846)	243,032 (215,590 – 287,091)	0,010±0,001	6,339 (38)
	L_4 / 32 ℃	99,292 (83,068 – 112,838)	231,268 (205,736 – 271,849)	0,010±0,001	11,620 (38)

*CL= Confidence limits, L_2= Second instar larvae, L_4= Fourth instar larvae, 28 / 32 ℃: Celsius of the temperature scale applied to the pest.

Table 2. LT50 and LT90 values obtained after topical application of biosynthesised AgNPs on *Plodia interpunctella* (Hubner) larvae.

Extract Type / Application Exposure Dose	Life Period of Pest / Applied Temperature	LT50 (95% CL) (hour)	LT90 (95% CL) (hour)	Slope±SE	X^2 (df)
Kernel / 200 ppm	*L_2 / 28 ℃*	48,470 (43,707 – 52,831)	87,784 (81,213 – 96,669)	0,033±0,003	12,272 (38)
	L_2 / 32 ℃	44,105 (39,448 – 48,281)	80,272 (74,314 – 88,271)	0,035±0,003	12,367 (38)
	L_4 / 28 ℃	54,552 (49,559 – 59,296)	98,977 (91,052 – 110,027)	0,029±0,003	8,623 (38)
	L_4 / 32 ℃	50,617 (45,542 – 55,281)	93,856 (86,431 – 104,123)	0,030±0,003	10,117 (38)
Shell / 200 ppm	*L_2 / 28 ℃*	55,597 (50,480 – 60,496)	101,775 (93,352 – 113,668)	0,028±0,003	15,967 (38)
	L_2 / 32 ℃	52,273 (47,234 – 56,969)	96,076 (88,429 – 106,691)	0,029±0,003	16,067 (38)
	L_4 / 28 ℃	58,516 (53,024 – 63,902)	109,730 (99,779 – 124,287)	0,025±0,003	10,180 (38)
	L_4 / 32 ℃	54,262 (48,733 – 59,445)	103,766 (94,658 – 116,894)	0,026±0,003	8,938 (38)

*CL= Confidence limits, L_2= Second instar larvae, L_4= Fourth instar larvae, 28 / 32 ℃: Celsius of the temperature scale applied to the pest.

In addition to the above-mentioned cellular destructive effects of the synthesised AgNPs on the targeted pest, this study also revealed that the destructive effects of the synthesised AgNPs on the targeted pest may vary depending on the nature of the extract used as raw material for the synthesis of AgNPs, the dose amount applied to the targeted insect and the duration of exposure to the applied dose, the biological period of the targeted insect and the ambient temperature at which the treatments were carried out.

As it is known, one of the safest synthesis routes of silver nanoparticles is the so-called green synthesis reactions in which plant extracts are generally preferred as raw materials (Anees et al., 2022; Ying et al., 2022). It has been stated by many researchers that the diversity and ratios of the secondary compounds of plant extracts play a role in the formation of AgNPs and that the potential of AgNP-induced effects on many biological activities varies

(Chand et al., 2020). In this study, two different organic wastes of the same plant were the source of extracts for green synthesis reactions and the small difference in the secondary compounds of these extracts was clearly seen in the graphs obtained because of FTIR tests (Figure 2, a-b). In addition, when the XRD graphs of the AgNPs formed because of the synthesis process are examined, it is noteworthy that there are some differences in the synthesized AgNPs (Figure 3, a-b). It is thought that the small differences between these two extracts are effective on larvicidal potential. Because according to the data obtained from this study, it was determined that the larvicidal power of AgNPs obtained from the kernel extract was higher than the AgNPs obtained using the shell extract (Figure 8-15).

Two other important factors affecting larvicidal activity are the amount of dose applied to the pest and the duration of exposure to the applied doses, and these two factors were found to be directly related to the mortality rates obtained in this study. Hazaa et al. (2021) tested AgNPs synthesised using *Borago officinalis* leaf extracts at eight different doses (100, 200, 400, 600, 800, 800, 1000, 2000 and 4000 mg/g) against *Spodoptera littoralis* (Lepidoptera: Noctuidae) 3rd instar larvae. At the end of 24 hours, 30% mortality rate was reached at the lowest dose application, mortality rates increased in direct proportion with increasing dose rates and mortality rate was recorded as 100% at the highest dose application. Anees et al. (2022) tested AgNPs synthesised from *Azadirachta indica* extract against *Helicoverpa armigera* (Hubner) (Lepidoptera: Noctuidae) second instar larvae at four different doses (500, 1000, 1500 and 2000 ppm). Post-treatment mortality rates were evaluated at increasing time intervals (24, 48, 72 and 96 hours) and accordingly, the mortality rates recorded at the lowest dose were 10%, 20%, 46.67% and 60%, respectively. The daily mortality rates increased as the applied dose amount increased and at the highest dose rate, 23.33%, 46.67%, 70% and 93.33% mortality rates were recorded, respectively.

In order to fully understand the efficacy of AgNPs against the targeted pest larvae, two different larval stages (second and fourth) were treated separately in this study and as a result, fourth stage larvae were found to be more resistant to AgNPs treatment than second stage larvae. Devi et al. (2014) applied AgNPs obtained from *Euphorbia hirta* (Euphorbiaceae) leaf extract at five different doses (2, 4, 6, 8 and 10 ppm) against I, II, III, IV, V and VI larvae of *Helicoverpa armigera* (Lepidoptera: Noctuidae), respectively. In the lowest dose application, mortality rates were recorded as 49%, 47%, 45%, 42%, 42%, 42%, 40% and 37% in order of larval stage. The mortality rates recorded in the highest dose application were 95%, 93%, 90%, 90%, 90%, 89%, 89%, 84% and 80% in order of larval stage. Bharani and Namasivayam (2017) applied AgNPs obtained from pomegranate (*Punica granatum*) fruits at five different doses (10, 25, 50, 75 and 100 µg) against I, II, III, IV, V and VI larvae of *Spodoptera litura* (Lepidoptera: Noctuidae), respectively. Dose-dependent mortality rates for first instar larvae were 26.7%, 53.4%, 66.4%, 86.2% and 100%, respectively. Dose-dependent mortality rates for third instar larvae were 16.4%, 34.5%, 54.2%, 72% and 86.4%, respectively. Dose-related mortality rates for fifth instar larvae were 4.2%, 10.2%, 27.2%, 51.2% and 61.3%, respectively. Jafir et al., (2021) applied AgNPs obtained from *Ocimum basilicum* plant extract at four different doses (100, 500, 1000 and 1500 mg/L) against 2nd, 3rd, 4th and 5th instar larvae of *Spodoptera litura* (Lepidoptera; Noctuidae). The mortality rates recorded as a result of the highest dose application were 96.67%, 91.67%, 81.67% and 78.33% for 2nd, 3rd, 4th and 5th instar larvae, respectively.

One of the physical factors used in pest control is the temperature factor, which is an important abiotic factor, and studies have shown that it causes different adverse conditions in larvae depending on the ambient temperature (low and/or high) (Abarca et al., 2020; Sujatha et al., 2024). When the results of this study were evaluated in terms of mortality rates, it was determined that the larvicide activity values recorded because of the applications made at high temperatures were more effective than the applications made at low temperatures. It is thought that the most important factor that is effective in the emergence of this situation due to temperature increase is directly related to the cuticle, which is the outer layer of the insect (Ghaedi et al., 2024). The fat layer in the cuticle of insects is the primary layer responsible for preventing the evaporation of body water, therefore a higher percentage of fatty acids in the cuticle layer increases the insect's resistance to heat and with it minimises the loss of water from the body and thus prevents the insect from drying out (Woods et al., 2003; Gołębiowski et al., 2012; Ghaedi et al., 2024). When the percentage of fatty acids in the cuticle decreases for any reason, the natural resistance of the cuticle layer to heat decreases, the amount of water in the insect's body is rapidly lost, resulting in the death of the insect (Ghaedi et al., 2024). Particularly high temperatures (the higher the temperature, the more serious the situation) lead to thinning of the wax layer of the cuticle, then to deep damage to the cuticle, then to the destruction of the cuticle and finally to the death of the beetle (Lee, 2010; Gibbs, 2011). Therefore, this study reveals that the temperature of the environment where larvicide applications are made is an important criterion determining the direction and potential of control.

Nanoparticle synthesis is of great interest due to its wide range of applications such as medicine, pharmacy, agricultural activities. Green synthesis of AgNPs using plants has more advantages over other chemical methods in terms of its easy and effective procedure, non-pathogenic and non-toxic effect on non-target organisms (Benelli et al., 2017; Kumar et al., 2022). In addition to using plants or plant extracts, bacteria and fungi can be used in the biosynthesis of AgNPs and are considered an

excellent green synthesis option. However, using plant extracts in particular has many advantages, including availability of raw materials, non-toxic structure, and a wide range of ingredients. In addition, biosynthesized AgNPs also have antibacterial, antifungal, anticancer, and anti-inflammatory bioactivity properties (Nie et al., 2023). While it is important to consider how nanoparticles can harm the ecosystem, they can also have positive effects that deserve careful consideration. Synthesized Ag nanoparticles can positively impact the environment around them when used in a controlled manner, do not produce any toxic effects, and are safe (Esan et al., 2022; Yamini et al., 2023; Wang et al., 2024). Studies have reported that nanoparticles are used in different application forms in order to minimize environmental pollution and improve environmental health (Martínez et al., 2020). Although the use of silver nanoparticles is quite suitable for improving environmental remediation processes, it is very important that the synthesized silver nanoparticles have certain properties, especially the nano size is quite low (about 10 nm) in order to increase their performance (Silva-Holguín et al., 2024). As a result, nanoproducts consisting of AgNPs have been included in numerous environmental application studies due to their highly effective and safe nano-sized particle size and biocompatibility. Therefore, they have been effective against many contaminants including pathogens and heavy metal ions even at very low concentrations and have been determined to have no serious adverse effects on healthy organisms including soil microorganisms (Panda et al., 2023).

4. Conclusion

The results of this study, which was carried out to transform the kernel and shell of the horse chestnut tree, which finds its place in parks as an ornamental plant, from organic waste to a valuable nano-product and to determine the larvicide potential of this product, contain important information. In these studies, it was proved that the dose amount, exposure time, larval stages and ambient temperature, which determine the efficacy of synthesised AgNPs against *Plodia interpunctella* larvae, are effective on larvicidal activity. The development of more environmentally friendly and more effective products instead of existing synthetic chemical pesticides in the fight against pests and the use of nature's own organic wastes during these processes is very important in terms of showing the point reached by nanotechnology. It is thought that this nanoparticle-supported study carried out against an agricultural lepidopteran pest will set an example for similar studies to be carried out in the future and will constitute source information.

Author Contributions

The percentages of the author' contributions are presented below. The author reviewed and approved the final version of the manuscript.

	O.A.
C	100
D	100
S	100
DCP	100
DAI	100
L	100
W	100
CR	100
SR	100
PM	100
FA	100

C=Concept, D= design, S= supervision, DCP= data collection and/or processing, DAI= data analysis and/or interpretation, L= literature search, W= writing, CR= critical review, SR= submission and revision, PM= project management, FA= funding acquisition.

Conflict of Interest

The author declared that there is no conflict of interest.

Ethical Consideration

Ethics committee approval is not required for this study due to the use of research materials that are not defined as experimental animals (Scientific and Technological Research Council of Türkiye, Animal Experiments Local Ethics Committee Directive, 2018, Article 3-c).

Acknowledgments

I would like to thank Dr. Ferda Eser for her help in performing FTIR analyses of two AgNPs samples synthesised from two different extracts and the valuable experts and managers of the Black Sea Advanced Technology Research and Application Centre (KITAM) for the careful characterisation analyses (XRD, SEM, STEM and EDS) of both AgNPs.

References

Abarca M, Lill JT, Weiss MR. 2020. Host plant and thermal stress induce supernumerary instars in caterpillars. Environ Entomol, 49(1): pp: 123-131.

Abbood NM, Ali ST. 2020. The role of silver nanoparticles and some extracts of damas Conocarpus lancifolius in controlling stored dates moth Ephestia cautella (Walker). Plant Arch, 20(1): pp: 3301-3305.

Abbott WS. 1925. A method of computing the effectiveness of an insecticide. J Econ Entomol, 18(2): pp: 265-267.

Adetunji CO, Oloke JK (Eds.). 2024. Handbook of Agricultural Biotechnology, Volume 1: Nanopesticides. John Wiley & Sons, Hoboken, NJ, USA, pp: 125-134.

Ali IAM, Ahmed AB, Al-Ahmed HI. 2023. Green synthesis and characterization of silver nanoparticles for reducing the damage to sperm parameters in diabetic compared to metformin. Sci Rep, 13(1): pp: 2256.

Anees MM, Patil SB, Kambrekar DN, Chandrashekhar SS, Jahagirdar S. 2022. Biosynthesis, characterization, evaluation, and shelf-life study of silver nanoparticles against cotton bollworm, Helicoverpa armigera (Hubner) (Noctuidae: Lepidoptera). Nanomaterials, 12(19): pp: 3511.

Attia FI, Shipp E, Shanahan GJ. 1981. Inheritance of resistance to malathion, DDT and dieldrin in Plodia interpunctella (Lepidoptera: Pyralidae). J Stored Prod Res, 17(3): pp: 109-115.

Benelli G, Caselli A, Canale A. 2017. Nanoparticles for mosquito control: Challenges and constraints. J King Saud Univ Sci, 29(4): pp: 424-435.

Bharani RA, Namasivayam SKR. 2017. Biogenic silver nanoparticles mediated stress on developmental period and gut physiology of major lepidopteran pest Spodoptera litura (Fab.) (Lepidoptera: Noctuidae)—An eco-friendly approach of insect pest control. J Environ Chem Eng, 5(1): pp: 453-467.

Chand K, Cao D, Fouad DE, Shah AH, Dayo AQ, Zhu K, Dong S. 2020. Green synthesis, characterization and photocatalytic application of silver nanoparticles synthesized by various plant extracts. Arab J Chem, 13(11): pp: 8248-8261.

Chellappandian M, Vasantha-Srinivasan P, Senthil-Nathan S, Karthi S, Thanigaivel A, Ponsankar A, Hunter WB. 2018. Botanical essential oils and uses as mosquitocides and repellents against dengue. Environ Int, 113: pp: 214-230.

Čukanović J, Tešević V, Jadranin M, Ljubojević M, Mladenović E, Kosti S. 2020. Horse chestnut (Aesculus hippocastanum L.) seed fatty acids, flavonoids and heavy metals plasticity to different urban environments. Biochem Syst Ecol, 89: pp: 103980.

Çolak H, Karaköse E, Duman F. 2017. High optoelectronic and antimicrobial performances of green synthesized ZnO nanoparticles using Aesculus hippocastanum. Environ Chem Lett, 15: pp: 547-552.

Demirezen DA, Yılmaz S, Yılmaz DD. 2018. Green synthesis and characterization of iron nanoparticles using Aesculus hippocastanum seed extract. Int J Adv Sci Eng Technol, 6(2): pp: 25-29.

Devi GD, Murugan K, Selvam CP. 2014. Green synthesis of silver nanoparticles using Euphorbia hirta (Euphorbiaceae) leaf extract against crop pest of cotton bollworm, Helicoverpa armigera (Lepidoptera: Noctuidae). J Biopestic, 7: pp: 54.

Elma F, Çetin H, Yorgancılar M, Acar R. 2021. Detection of metabolite content in local bitter white lupin seeds (Lupinus albus L.) and acaricidal and insecticidal effect of its seed extract. J Agric Sci, 27(4): pp: 407-413.

El-Samad LM, Bakr NR, El-Ashram S, Radwan EH, Aziz KKA, Hussein HK, Hassan MA. 2022. Silver nanoparticles instigate physiological, genotoxicity, and ultrastructural anomalies in midgut tissues of beetles. Chem Biol Interact, 367: pp: 110166.

Esan V, Elanchezhiyan C, Mahboob S, Al-Ghanim KA, Al-Misned F, Ahmed Z, Marimuthu G. 2022. Toxicity of Trewia nudiflora-mediated silver nanoparticles on mosquito larvae and non-target aquatic fauna. Toxin Rev, 41(1): pp: 229-236.

Ghaedi F, Abbasipour H, Karimi J. 2024. Effect of critical temperatures on mortality and cuticle composition of Plodia interpunctella larvae: Insights from GC–MS analysis and SEM imaging. J Asia Pac Entomol, 27(3): pp: 102309.

Gibbs AG. 2011. Thermodynamics of cuticular transpiration. J Insect Physiol, 57(8): pp: 1066-1069.

Gołębiowski M. 2012. Comparison of free fatty acids composition of cuticular lipids of Calliphora vicina larvae and pupae. Lipids, 47(10): pp: 1001-1009.

Gurunathan S, Park JH, Han JW, Kim JH. 2022. Comparative assessment of the apoptotic potential of silver nanoparticles synthesized by Bacillus tequilensis and Calocybe indica in MDA-MB-231 human breast cancer cells: Targeting p53 for anticancer therapy [Corrigendum]. Int J Nanomed, 17: pp: 5207-5208.

Hazaa M, Alm-Eldin M, Ibrahim AE, Elbarky N, Salama M, Sayed R, Sayed W. 2021. Biosynthesis of silver nanoparticles using Borago officinalis leaf extract, characterization and larvicidal activity against cotton leaf worm, Spodoptera littoralis (Bosid). Int J Trop Insect Sci, 41: pp: 145-156.

Hu D, Gao T, Kong X, Ma N, Fu J, Meng L, Latif S. 2022. Ginger (Zingiber officinale) extract mediated green synthesis of silver nanoparticles and evaluation of their antioxidant activity and potential catalytic reduction activities with Direct Blue 15 or Direct Orange 26. PLoS One, 17(8): pp: e0271408.

Ituen E, Ekemini E, Yuanhua L, Singh A. 2020. Green synthesis of Citrus reticulata peels extract silver nanoparticles and characterization of structural, biocide and anticorrosion properties. J Mol Struct, 1207: pp: 127819.

Jafir M, Ahmad JN, Arif MJ, Ali S, Ahmad SJN. 2021. Characterization of Ocimum basilicum synthesized silver nanoparticles and its relative toxicity to some insecticides against tobacco cutworm, Spodoptera litura Feb. (Lepidoptera: Noctuidae). Ecotoxicol Environ Saf, 218: pp: 112278.

Kędzierski B, Kukula-Koch W, Widelski J, Głowniak K. 2016. Impact of harvest time of Aesculus hippocastanum seeds on the composition, antioxidant capacity and total phenolic content. Ind Crops Prod, 86: pp: 68-72.

Kiani BH, Arshad I, Najeeb S, Okla MK, Almanaa TN, Al-Qahtani WH, Abdel-Maksoud MA. 2023. Evaluation of biogenic silver nanoparticles synthesized from vegetable waste. Int J Nanomed, 18: pp: 6527-6544.

Kumar P, Kumar D, Kumar V, Chauhan RPS, Singh H. 2022. Mosquito larvicidal potential of Solanum xanthocarpum leaf extract derived silver nanoparticles and its bio-toxicity on non-target aquatic organism. J Vector Borne Dis, 59(3): pp: 216-227.

Kumar R. 2017. Insect pests of stored grain: Biology, behavior, and management strategies. Apple Academic Press, Oakville, ON, Canada, Chapter 4: pp: 61-86.

Küp FÖ, Çoşkunçay S, Duman F. 2020. Biosynthesis of silver nanoparticles using leaf extract of Aesculus hippocastanum (horse chestnut): Evaluation of their antibacterial, antioxidant and drug release system activities. Mater Sci Eng C, 107: pp: 110207.

Lack HW. 2002. The discovery and rediscovery of the horse chestnut. Arnoldia, 61(4): pp: 15-19.

Lee RE. 2010. A primer on insect cold-tolerance. In: Low Temperature Biology of Insects, Denlinger DL, Lee RE (Eds.). Cambridge University Press, Cambridge, UK, pp: 3-34.

Li H, Wen T, Wang T, Ji Y, Shen Y, Chen J, Wu X. 2020. In vivo metabolic response upon exposure to gold nanorod core/silver shell nanostructures: Modulation of inflammation and upregulation of dopamine. Int J Mol Sci, 21(2): pp: 384.

Mahdi ZS, Hashim IH, Jassim NM. 2024. Bactericidal effects of silver nanoparticles prepared by green synthesis. Mustansiriyah J Pure Appl Sci, 2(4): pp: 1-6.

Marcu Spinu S, Dragoi Cudalbeanu M, Avram I, Fierascu RC, Rosu PM, Morosanu AM, Ortan A. 2024. Antibacterial and antitumoral potentials of phytosynthesized silver/silver oxide nanoparticles using tomato flower waste. Int J Mol Sci, 25(18): pp: 9871.

Martínez G, Merinero M, Perez-Aranda M, Perez-Soriano E, Ortiz T, Villamor E, Alucida A. 2020. Environmental impact of nanoparticles' application as an emerging technology: A review. Materials, 14(1): pp: 166.

Morejón B, Pilaquinga F, Domenech F, Ganchala D, Debut A, Neira M. 2018. Larvicidal activity of silver nanoparticles synthesized using extracts of Ambrosia arborescens (Asteraceae) to control Aedes aegypti L. (Diptera: Culicidae). J Nanotechnol, 2018(1): pp: 6917938.

Nasir MF, Ulrichs C, Prozell S, Schöller M. 2017. Laboratory studies on parasitism of Plodia interpunctella (Hübner) (Lepidoptera: Pyralidae) by two species of Trichogramma Westwood (Hymenoptera: Trichogrammatidae) in different grains, and evaluation of traps for their monitoring. J Stored Prod Res, 74: pp: 6-12.

Nie P, Zhao Y, Xu H. 2023. Synthesis, applications, toxicity and toxicity mechanisms of silver nanoparticles: A review. Ecotoxicol Environ Saf, 253: pp: 114636.

Owczarek-Januszkiewicz A, Kicel A, Olszewska MA. 2023. Aesculus hippocastanum in the pharmaceutical industry and beyond – Phytochemistry, bioactivity, present application, and future perspectives. Ind Crops Prod, 193: pp: 116187.

Panda P, Chakraborty S, Krishna SBN. 2023. The use of silver nanoparticles in environmental remediation. Preprints Org, 2023010330.

Parthiban E, Ramachandran M, Jayakumar M, Ramanibai R. 2019. Biocompatible green synthesized silver nanoparticles impact on insecticides resistant developing enzymes of dengue transmitted mosquito vector. SN Appl Sci, 1: pp: 1-9.

Pretty J, Pervez Bharucha Z. 2015. Integrated pest management for sustainable intensification of agriculture in Asia and Africa. Insects, 6(1): pp: 152-182.

Prvulović D, Gvozdenac S, Latković D, Peić Tukuljac M, Sikora V, Kiprovski B, Ovuka J. 2023. Phytotoxic and insecticidal activity of industrial hemp (Cannabis sativa L.) extracts against Plodia interpunctella Hübner—A potential sunflower grain protectant. Agronomy, 13(10): pp: 2456.

Rehman HU, Majee B, Farooqi MA, Rasul A, Sagheer M, Ali Q, Akhtar ZR. 2021. Green synthesis of silver nitrate nanoparticles from Camelina sativa (L.) and its effect to control insect pests of stored grains. Int J Trop Insect Sci, pp: 1-9.

Roni M, Murugan K, Panneerselvam C, Subramaniam J, Nicoletti M, Madhiyazhagan P, Dinesh D, Suresh U, Khater HF, Wei H, Canale A, Alarfaj AA, Munusamy MA, Higuchi A, Benelli G. 2015. Characterization and biotoxicity of Hypnea musciformis-synthesized silver nanoparticles as potential eco-friendly control tool against Aedes aegypti and Plutella xylostella. Ecotoxicol Environ Saf, 121: pp: 31-38.

Salayová A, Bedlovičová Z, Daneu N, Baláž M, Lukáčová Bujňáková Z, Balážová Ľ, Tkáčiková Ľ. 2021. Green synthesis of silver nanoparticles with antibacterial activity using various medicinal plant extracts: Morphology and antibacterial efficacy. Nanomaterials, 11(4): pp: 1005.

Silva-Holguín PN, Garibay-Alvarado JA, Reyes-López SY. 2024. Silver nanoparticles: Multifunctional tool in environmental water remediation. Materials, 17(9): pp: 1939.

SPSS. 2017. IBM Corp. Released 2017. IBM SPSS Statistics for Windows, Version 25.0. IBM Corp, Armonk, NY, USA, pp: 58-72.

Sujatha GS, Sagar D, Kumar H. 2024. Effects of short-and long-term thermal stress on developmental stages and adults vis-à-vis reproductive physiology of Spodoptera litura. Anim Biol, 1(aop): pp: 1-21.

Suresh U, Murugan K, Panneerselvam C, Rajaganesh R, Roni M, Al-Aoh HAN, Benelli G. 2018. Suaeda maritima-based herbal coils and green nanoparticles as potential biopesticides against the dengue vector Aedes aegypti and the tobacco cutworm Spodoptera litura. Physiol Mol Plant Pathol, 101: pp: 225-235.

Sutthanont N, Attrapadung S, Nuchprayoon S. 2019. Larvicidal activity of synthesized silver nanoparticles from Curcuma zedoaria essential oil against Culex quinquefasciatus. Insects, 10(1): pp: 27.

Swathi B, Thangaraj R, Gayathri D, Subha V, Thiyagarajan P, Thiruvengadam M, Venkidasamy B. 2025. Green synthesis of β-caryophyllene-coated silver nanoparticles: Biophysical characterization and evaluation of antibacterial, cytotoxic, and larvicidal activities. BioNanoScience, 15(1): pp: 1-13.

Tirunagaru KC, Kolluru R, Singh IR. 2024. A review on nanotechnological approaches for the management of stored insect-pests: Present scenario and future prospects. J Sci Res Rep, 30(10): pp: 756-769.

Wang C, Jiang Y, He K, Wāng Y. 2024. Eco-friendly synthesis of silver nanoparticles against mosquitoes: Pesticidal impact and indispensable biosafety assessment. Sci Total Environ, pp: 176006.

Wang Z, Zhang L, Wang X. 2023. Molecular toxicity and defense mechanisms induced by silver nanoparticles in Drosophila melanogaster. J Environ Sci, 125: pp: 616-629.

Woods HA, Makino W, Cotner JB, Hobbie SE, Harrison JF, Acharya K, Elser JJ. 2003. Temperature and the chemical composition of poikilothermic organisms. Funct Ecol, 17(2): pp: 237-245.

Yamini V, Shanmugam V, Rameshpathy M, Venkatraman G, Ramanathan G, Garalleh HA, Rajeswari VD. 2023. Environmental effects and interaction of nanoparticles on beneficial soil and aquatic microorganisms. Environ Res, 236: pp: 116776.

Yasur J, Rani PU. 2015. Lepidopteran insect susceptibility to silver nanoparticles and measurement of changes in their growth, development and physiology. Chemosphere, 124: pp: 92-102.

Ying S, Guan Z, Ofoegbu PC, Clubb P, Rico C, He F, Hong J. 2022. Green synthesis of nanoparticles: Current developments and limitations. Environ Technol Innov, 26: pp: 102336.

Zhang J, Wang F, Yalamarty SSK, Filipczak N, Jin Y, Li X. 2022. Nano silver-induced toxicity and associated mechanisms. Int J Nanomed, 17: pp: 1851-1864.

Zhu L, Guo D, Sun L, Huang Z, Zhang X, Ma W, Gu N. 2017. Activation of autophagy by elevated reactive oxygen species rather than released silver ions promotes cytotoxicity of polyvinylpyrrolidone-coated silver nanoparticles in hematopoietic cells. Nanoscale, 9(17): pp: 5489-5498.

.

Black Sea Journal of Engineering and Science
doi: 10.34248/bsengineering.1659285

Open Access Journal
e-ISSN: 2619 – 8991

Research Article
Volume 8 - Issue 4: 1087-1095/ July 2025

MOTIFS AND ORNAMENTATIONS OF ERZURUM SELJUK MADRASAS IN THE CONTEXT OF INTERCULTURAL INTERACTION

Serkan SİPAHİ[1], Bernanur YAZICI[2], Selim KARTAL[3]*

[1]*Osmaniye Korkut Ata University, Faculty of Architecture, Design and Fine Arts, Interior Architecture and Environmental Design Department, 80000, Osmaniye, Türkiye*
[2]*Atatürk University, Faculty of Architecture and Design, Department of Architecture, 25000, Erzurum, Türkiye*
[3]*Iğdır University, Technical Sciences Vocational School, Department of Design, 76000, Iğdır, Türkiye*

Abstract: Throughout history, cultural and artistic activities in various civilizations have been shaped by the unique lifestyles of societies and transmitted across generations. The data transferred through trade routes and economic relations, migration and population movements, empires, wars and alliances, the spread of religions, as well as scientific and artistic interactions, have both influenced and been influenced by other civilizations. One of the states where these interactions were intensely experienced due to its vast territories hosting diverse ethnic, religious, and cultural groups was the Seljuk Empire. The Seljuks synthesized the art, architecture, and culture of various civilizations, including Byzantine, Persian, Arab, Central Asian, and Armenian traditions. By adapting the motifs, ornamentations, and construction techniques of these cultures to their own aesthetic principles, they created a unique architectural language. Situated in a strategic location, Erzurum was an important part of the Seljuks' dominance in Anatolia. The historical caravanserais, madrasas, and tombs in Erzurum reflect the Seljuk architectural techniques, ornamentation styles, and motifs, showcasing their interactions with both local cultures and other Islamic and non-Islamic civilizations. One of the most renowned Seljuk-era structures in Erzurum, Çifte Minareli Madrasah, is regarded as a symbol of the city. Although Yakutiye Madrasah was constructed during the Ilkhanid period, it still exhibits the influence and architectural style of Seljuk art. This study aims to examine these influences in terms of motifs and ornamentations through an analysis of these two madrasas in Erzurum. By comparing and analyzing the motifs and ornamentations found in Seljuk architecture with those of different cultures, the study seeks to highlight the cultural interactions embedded within these structures. Ultimately, the study aims to identify the influences of various cultures through the motifs and ornamentations of Çifte Minareli and Yakutiye Madrasas. It further seeks to explore how these interactions contribute to the identity of the structures and to cultural sustainability

Keywords: Erzurum, Madrasah, Motif and decoration, Art, Cultural interaction

***Corresponding author:** Iğdır University, Technical Sciences Vocational School, Department of Design, 76000, Iğdır, Türkiye
E mail: selim.kartal@igdir.edu.tr (Selim KARTAL)
Serkan SİPAHİ https://orcid.org/0000-0002-5684-8671
Bernanur YAZICI https://orcid.org/0009-0003-8702-7379
Selim KARTAL https://orcid.org/0000-0003-4269-0786

Received: March 17, 2025
Accepted: May 21, 2025
Published: July 15, 2025

Cite as: Sipahi S, Yazici B, Kartal S. 2025. Motifs and ornamentations of Erzurum Seljuk madrasas in the context of intercultural interaction. BSJ Eng Sci, 8(4): 1087-1095.

1. Introduction

Culture consists of the material and intangible elements produced by individuals within a society as a result of their interactions and shared way of life within a specific time and space. Culture holds great significance for societies, accumulating and transforming over time to be transmitted to future generations (Polat, 2020). Over successive generations, culture evolves through language, religion, geographical proximity, intellectual and artistic traditions, kinship, economic and political systems, bringing groups of people closer together while continuously developing.

Since culture is passed down through generations, it can be altered, developed, or, in some cases, forgotten over time. This dynamic nature of culture has ensured that, even as human communities and states have disappeared throughout history, their cultures have endured by adapting and transforming within different societies (Peterson and Anand, 2004).

In addition to the intergenerational development of culture over time, its transformation and evolution also occur through interactions with different human communities and cultures. Several key factors influence the interaction between civilizations, including trade routes and economic relations, migration and population movements, empires, wars and alliances, the spread of religions, as well as scientific and artistic exchanges (Çorbacı et. al., 2021).

Among these, migration movements have played a particularly significant role, leading to demographic, economic, historical, and social changes, ultimately resulting in dynamic cultural interactions (Haas, 2008).

Throughout history, cultural interactions have been intensely experienced in various geographical regions,

This work is licensed (CC BY-NC 4.0) under Creative Commons Attribution 4.0 International License

and due to its strategic location, Anatolia has been one of the most significant areas where these interactions took place. When examining Anatolia's pre-Turkish history, it is known that during the period of Byzantine rule, the region underwent a Hellenization process, while in earlier historical periods, it had a Roman heritage. Additionally, it is documented that until the 5th century, many ethnic groups inhabited the region (Öztürk, 2018).

With the arrival of the Turks in Anatolia, Turkish and Islamic culture exerted a dominant influence on the region. However, this did not result in the complete disappearance of the existing local culture. The Turks adopted a policy of tolerance towards the ethnic groups present in Anatolia. Initially, these cultures preserved their distinct existence, but over time, they interacted with one another—either transforming under the dominant culture or influencing the dominant culture while preserving their own values (Türkoğlu, 2019).

In this context, during the period that began with the Battle of Manzikert in 1071, the Seljuk Empire regarded cultural pluralism as a form of enrichment, incorporating it within its governance and actively pursuing conscious policies in this direction (Kutlu and Göksel, 2014; Sipahi and Yalçın, 2021). Throughout its historical journey, the Seljuk Empire, which housed many different ethnic groups, harmonized the cultural elements of these groups in the material cultural assets it produced, making it one of the notable civilizations of its era.

Due to its geographical origin and commercial relations, the Seljuk Empire interacted with Central Asian, Persian, and Sassanian art. Additionally, Byzantine and Roman art, which had historically shaped Anatolia, were also influential in the development of Seljuk art. Moreover, Shamanistic beliefs and Islam influenced Seljuk art in various ways, leading to the emergence of a distinctive artistic and architectural style (Türkoğlu, 2019).

One of the arts that developed as a result of interaction with different communities and cultures in the Seljuk Empire was ornamental art. Ornamentation is a sub-branch of painting that involves the use of shapes, images, and motifs to enhance the aesthetic appeal of an object (Tütüncüoğlu, 2016). The richness of Turkish ornamental art stems from the diversity and abundance of motifs used.

When the Seljuks migrated from Central Asia to Anatolia, they encountered stone, a new building material unfamiliar to them in their homeland. They applied the decorative techniques they had brought from Central Asia onto this new material. The motifs and ornamentations seen in surviving Seljuk architectural works reflect this decorative adaptation (Yıldız, 2019).

Although it is known that Seljuk ornamentation evolved through influences from different societies, it remains unclear which decorative motifs were brought from Central Asia and integrated into architecture and which ornamental elements were already present in Anatolia and incorporated into Seljuk architecture.

One of the cities where ornamental art, applied to various architectural examples across different regions of Anatolia, is prominently featured is Erzurum. Among the most well-known Seljuk structures in Erzurum, Çifte Minareli Madrasah and Yakutiye Madrasah stand out as significant examples where motifs and ornamentations were extensively used.

Among these structures, Çifte Minareli Madrasah is believed to have been built in 1253 and attributed to Huand Hatun, the daughter of Alaaddin Keykubad. However, no conclusive evidence has been found to verify this claim (Aydın, 2008). Yakutiye Madrasah, on the other hand, was commissioned by Hoca Cemaleddin Yakut in 1310 (Aytaç, 2017). Known as the largest madrasa in Anatolia, Çifte Minareli Madrasah features a two-story, open courtyard design with four iwans (Sipahi and Yalçın, 2021). Yakutiye Madrasah was built in the 14th century by Emir Cemaleddin (Kocaman et al., 2018). It is recognized as the largest single-story enclosed madrasa in Anatolia (Akçay, 1968). In this context, Yakutiye Madrasah is considered one of the best-preserved examples of the single-story, closed courtyard, three-iwan, and porticoed madrasa plan type in Anatolia (Konak, 2022).

In conclusion, based on the literature review, this study aims to analyze the cultural interactions in Seljuk ornamental art through the motifs and decorations used in the Çifte Minareli Madrasah and Yakutiye Madrasah, shedding light on the influence of different cultures in Seljuk architectural works in Anatolia.

2. Materials and Methods

2.1. Study Area

The study area is the city of Erzurum, located in Turkey. Situated in the northeastern part of the Eastern Anatolia region, Erzurum lies at an altitude of 1,850–1,980 meters above sea level. Since antiquity, the city's strategic location has maintained its military and commercial significance, making it a prominent center throughout history (Özen, 2016).

Erzurum has a rich historical background, bearing the traces of numerous civilizations. Since the Chalcolithic and Early Bronze Ages, Erzurum has been positioned at the intersection of major trade and military routes, retaining its importance during the Seljuk period as well. Following the 1071 Battle of Manzikert, the Anatolian Seljuk State adorned many cities with architectural works such as mosques, madrasas, tombs, pavilions, caravanserais, inns, and baths.

The study sample consists of Çifte Minareli Madrasah and Yakutiye Madrasah, two Seljuk-era madrasas in Erzurum that have survived to the present day.

As shown in Figure 1., the Çifte Minareli Madrasah and Yakutiye Madrasah, which are the focus of this study, are situated on Cumhuriyet Street. Yakutiye Madrasah is located north of the street, while Çifte Minareli Madrasah is positioned south of the street.

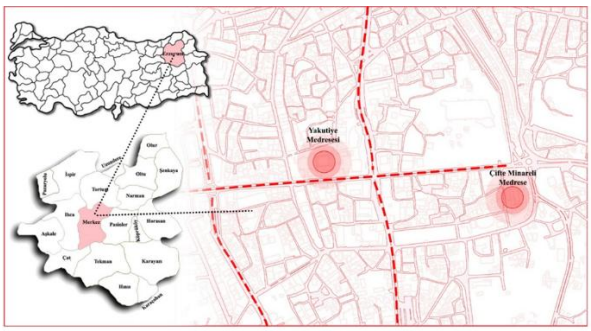


Figure 1. Study Area and sample group.

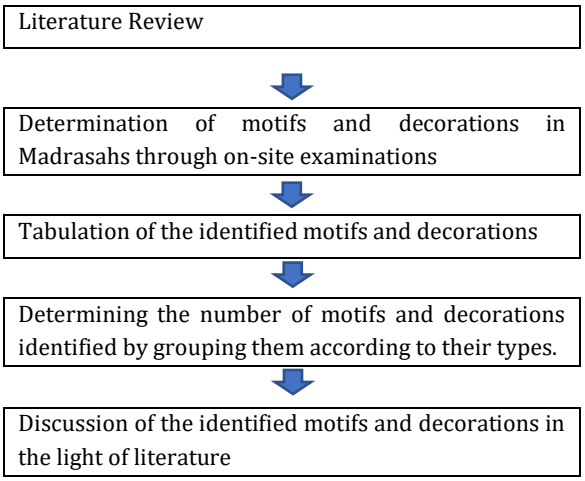
These two structures are situated in close proximity to each other, and the surrounding area contains architectural works from different historical periods, contributing to the rich architectural landscape of Erzurum.

2.2. Methodology

The objective of this study is to examine the reflection of interactions between different cultures in architecture, specifically in terms of motifs and ornamentations, through the analysis of Yakutiye Madrasah and Çifte Minareli Madrasah in Erzurum.

In the first stage of the study, a literature review was conducted on the origins and usage of motifs and ornamentations found in Seljuk-era madrasas in Erzurum, focusing on their introduction to and application in Anatolia.

In the second stage, on-site observations were carried out based on the findings obtained from the literature. The identified motifs and ornamentations were compared with the literature data, and the results were presented in Table 1 and Table 2.



Following the fieldwork, the motifs were categorized and quantified according to their botanical and animal characteristics. These were then compared to similar examples found in other Anatolian architectural works. Symbolic interpretations of each motif were considered alongside their aesthetic roles, with special attention paid to cultural origins and historical dissemination patterns. This methodological framework allowed for a holistic evaluation of the intercultural influences embedded in the decorative schemes of the selected madrasas.

3. Results and Discussion

The Anatolian region possesses a rich artistic heritage, where botanical and animal motifs from various cultures have converged and been incorporated into the madrasas of Erzurum. In this study, the botanical and animal motifs used in Çifte Minareli Madrasah and Yakutiye Madrasah in Erzurum were examined, with an analysis of their cultural origins, dissemination, and frequency of use.

The findings reveal that among the botanical motifs, the tulip, inverted tulip, hatayi (lotus), palmette, rumi, penç and tree of life are particularly prominent. Regarding animal motifs, examples such as the dragon, eagle, lion, and scallop shell were identified.

3.1. Botanical Motifs

The tulip motif holds a significant place in Turkish culture, with its origins tracing back to Turkmenistan. This motif spread from Central Asia to Anatolia, was incorporated into Seljuk art, and later diversified and became more widespread during the Ottoman period through ceramic art (Ünal, 2021).

In Yakutiye Madrasah, stylized tulip motifs can be observed, whereas Çifte Minareli Madrasah does not feature this motif. The tulip motif in Yakutiye Madrasah is used in conjunction with turquoise, purple, and turquoise-blue mosaic tiles on the minaret. Notably, turquoise, known as the "Turkish color," serves as a defining characteristic in Seljuk architecture (Özkul, 2020a).

On the minaret, the inverted tulip motif is present. This motif is associated with the "weeping bride" (Fritillaria imperialis), an endemic plant that thrives in cold climates. Considered sacred in Christian culture, this motif is also found in Indian culture. During the Ottoman period, the inverted tulip was a highly valued plant in Turkish gardens, spreading from Istanbul to Vienna, and later to the Netherlands and England (Özler, 2018).

One of the main motifs in Turkish ornamental art, the Hatayi motif, originated in Far Eastern culture. This motif spread to Central Asia through Chinese influence and later diversified and developed in Anatolia. Composed of interwoven stylized leaves and flowers, the Hatayi motif had a simplistic appearance during the Seljuk period (Karaca, 2021). However, in the Ottoman period, it was influenced by ceramic art, evolving into more elaborate and detailed forms, enriching its aesthetic diversity.

The palmette motif is a botanical ornamentation type consisting of symmetrically arranged leaves around a central axis. While its exact origin is unknown, this motif is found in the ornamental arts of Sumerian, Egyptian, Assyrian, Greek, and Roman civilizations, as well as in Islamic art. During the Sassanian period, the ancient palmette motif was stylized and further developed under Persian influence, eventually spreading to Anatolia via Iran (Yıldız, 2019).

The palmette motif was used as an ornamental element in both Yakutiye Madrasah and Çifte Minareli Madrasah. In Yakutiye Madrasah, various palmette motifs appear on the borders located on the sides of the main entrance portal. In Çifte Minareli Madrasah, this motif is present on the column capitals of the tomb in the eastern section as well as on numerous decorative borders within the madrasa.

The Rumi motif, a Western-origin ornamental element, is also referred to as "arabesque". There are differing opinions regarding its origins, with some suggesting that it is derived from half-palmettes, while others argue that it has animalistic origins. Believed to be stylized from bird wings, this motif was brought from Central Asia to Anatolia, where it was further developed by the Anatolian Seljuks, gaining a distinct artistic identity. Before the Seljuk period, the Rumi motif was also used in Karahanid, Ghaznavid, Abbasid, Andalusian, and Fatimid art (Yavuz, 2008).

In Yakutiye Madrasah, the Rumi motif appears in a simple and interwoven form on the stone entrance decoration panel. In Çifte Minareli Madrasah, it is incorporated into the marble surfaces within the tomb, forming a harmonious composition together with the palmette motif, contributing to an aesthetic unity.

The word "penç", meaning "five" in Persian, refers to the cross-section of stylized flowers in ornamental arts. Due to its top-down perspective, this motif is also known as "central Hatayi". The Penç motif has been used in the art of various civilizations, including Egyptian, Assyrian, Iranian,

Greek, Roman, Uighur, and Central Asian cultures. Iran played a significant role in the spread and development of this motif in Anatolia (Tavaslı, 2014). While the Penç motif is not found in Yakutiye Medrese, it is used in Çifte Minareli Medrese, specifically on the tympanum of one of the doors in the southern iwan.

The Tree of Life is a universal symbol found in all belief systems, representing fertility, the sky, and the ever-changing nature of the universe. Used throughout various periods of human history, this motif entered Turkish culture through Shamanism and spread across Central Asia. According to Central Asian beliefs, the Tree of Life represents the center of the world (Arslan, 2014).

In Çifte Minareli Medrese, the Tree of Life motif is present in four panels, positioned on both the right and left sides of the main entrance portal.

In Yakutiye Medrese, two Tree of Life motifs are located on the side surfaces of the main entrance portal. In Erzurum Çifte Minareli Medrese, four botanical motifs with different cultural origins have been identified, whereas three of these motifs are present in Yakutiye Medrese. The on-site examinations conducted on these madrasas provided visual documentation, and the examples of these motifs in various structures are presented in detail in Table 1.

3.2. Animal Motifs

Among the animal motifs, the dragon motif (Ejder), originating from China, holds a significant place in Central Asian and Far Eastern cultures as a mythological figure. Symbolizing power, abundance, strength, and prosperity, this motif was adopted by the Turks from China, introduced to Western Asia, and gradually became widespread. As the Turks settled in Western Asia and the Iranian region, the dragon motif also found its place in Islamic art (Mutlu and Özdemir, 2022).

Brought to Anatolia through Seljuk art, this motif is present on the front façade of Çifte Minareli Medrese, depicted at the base of the Tree of Life. However, no examples of the dragon motif have been found in Yakutiye Medrese.

The eagle figure has been used by many civilizations since ancient times, including the Hittite and Assyrian periods. Symbolizing power and authority, this motif was widely adopted in Central Asia, the Islamic world, and Anatolian Seljuk art. The origin of the eagle motif in Seljuk art can be traced back to Central Asian culture and Shamanic beliefs (Tecir, 2024).

As a symbol of the Seljuks, the eagle motif is also present in Yakutiye Medrese and Çifte Minareli Medrese. In both madrasas, it is positioned at the top of the Tree of Life. However, in Yakutiye Medrese, the eagle is depicted as single-headed, whereas in Çifte Minareli Medrese, it is represented as double-headed.

The lion figure is recognized as a symbol of power, heroism, strength, and victory. The discovery of lion depictions in Hun kurgans of Central Asia indicates that this symbol was introduced to Central Asia by the Turks through Shamanic beliefs (Öten, 2023).

Over time, with the acceptance of Islam, the lion motif continued to exist in Turkish art, preserving its symbolic meaning. In Seljuk-era art, the lion motif was used to represent the ruler’s power and authority. In Yakutiye Medrese, the lion figure appears in a figurative panel on the side surface of the main entrance portal, forming a composition together with the Tree of Life and the eagle. However, no examples of this motif have been found in Çifte Minareli Medrese.

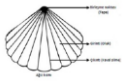
Structurally resembling fans and seashells, the scallop motif symbolizes abundance and rebirth. This motif spread through Egyptian, Roman, and Byzantine architecture (Turan, 2013).

Commonly found in Islamic architecture, the scallop motif was extensively used in both interior and exterior decorations during the Seljuk period. In Yakutiye Medrese, the scallop motif appears within the muqarnas elements beneath the inscription band and in the decorative frames of the main entrance portal projection. In Çifte Minareli Medrese, this motif is present within the muqarnas on the portal and at the arch terminations of the iwans.

Table 1. Comparison of plant motifs on madrasahs

Motif-Decoration	Cultural Interaction	Drawing	Example in Anatolia	Double Minaret Madrasa	Yakutiye Madrasa
Tulip- Inverted Tulip	Middle Asia	 Taç Mahal (Özler, 2021)	 Rüstem Paşa Mosque (Çevik, 2014)	---	
Hatai (Lotus)	China- Middle Asia	 (Garagaşov, 2006)	 Bursa Yeşil Cami (Değerbilir, 2012)	 (Aydın, 2008)	---
Palmette	Persia	 Develi Sivasi Hatun Mosque (Yıldız, 2009)	 Döner Kümbet (Yıldız, 2009)	 (Aydın, 2008)	 (Taflan, 2008)
Rumi	Western- Middle Asia	 (Garagaşov, 2006)	 Develi Sivasi Hatun Mosque (Yıldız, 2009)	 (Aydın, 2008)	 (Korkutan, 2011)
Penç	Persia- Middle Asia	 (Garagaşov, 2006)	 İzmir Nilüfer Hanım İmareti (Tavaslı, 2014)	 (Korkutan, 2011)	---
Hayat Ağacı	Middle Asia	 (Arslan, 2014)	 (Kurt Kırtay, 2023)		

Table 2. Comparison of animal motifs on madrasahs

Motif-Decoration	Cultural Interaction	Drawing	Example in Anatolia	Double Minaret Madrasa	Yakutiye Madrasa
Dragon	China- Middle Asia	 (İnan, 1987)	 (Çevik, 2014)		---
Eagle	Shaman- Middle Asia		 (Özkul, 2020b)	 (Korkutan, 2011)	
Lion	Shaman- Islam	 (Çorhunlu, 2019)	 (Odabaşıoğlu, 2022)	---	 (Taflan, 2008)
Oyster	Byzantine- Islam	 (Turan, 2013)	 (Turan, 2013)		

In Erzurum Çifte Minareli Medrese, three different animal motifs from various cultures have been identified, while Yakutiye Medrese also contains three distinct animal motifs. The on-site examinations conducted on these madrasas provided visual documentation, and examples of these motifs in different structures are presented in Table 2.

Frequency of Use of Motifs

A total of eight motifs were identified in Çifte Minareli Medrese, while seven motifs were found in Yakutiye Medrese, as documented in Table 1 and Table 2. The frequency of use of the botanical and animal motifs observed in the madrasas was evaluated based on on-site examinations, and the corresponding data have been presented in Table 3.

Table 3. Frequency of use of plant motifs

	Motif Type	Double Minaret Madrasa	Yakutiye Madrasa	Total
1	Palmette	64	38	102
2	Rumi	28	18	46
3	Tree of Life	6	2	8
4	Hatai (Lotus)	4	-	4
5	Penç	2	-	2
6	Tulip- İnverted Tulip	-	1	1

According to the ranking of botanical motifs presented in Table 3, the palmette motif is the most frequently observed motif, with 64 instances in Çifte Minareli Medrese and 38 instances in Yakutiye Medrese, totaling 102 occurrences. The origins of the palmette motif trace back to the Sumerians, which played a significant role in its spread and diversification over time. The Rumi motif, believed to have evolved from half-palmettes, was used both individually and in compositions alongside palmettes. It was identified 28 times in Çifte Minareli Medrese and 18 times in Yakutiye Medrese, making a total of 46 instances, ranking it as the second most common motif.

The Tree of Life motif, which is referenced in various belief systems and has been widely used throughout different periods of human history, was determined to be the third most frequently used motif, following the scallop motif. It was observed 6 times in Çifte Minareli Medrese and 2 times in Yakutiye Medrese, amounting to a total of 8 instances. The Hatayi motif was identified 4 times in Çifte Minareli Medrese but was not found in Yakutiye Medrese, making a total of 4 instances, placing it in fourth position.

Unlike palmette, Rumi, and Hatayi motifs, the Penç motif, which does not follow an interwoven pattern, is among the least frequently used motifs. It was identified twice in

Çifte Minareli Medrese and was not found in Yakutiye Medrese, totaling 2 instances, placing it fifth in the ranking. The inverted tulip, a specific motif, was only observed once in Yakutiye Medrese and was not used in Çifte Minareli Medrese. With just one instance, it is the least frequently used motif.

The palmette motif, due to its structural characteristics, possesses the ability for endless variation. Its origins trace back to ancient civilizations such as the Sumerians, Egyptians, Assyrians, Greeks, and Romans, which played a significant role in its spread across different regions and its adaptation into various forms (Mülayim, 1976).

Anatolia, having hosted numerous cultures throughout history, became a center for the diversification and widespread use of the palmette motif, making its prevalence not coincidental. During the Seljuk period, the influence of Persian culture, with which there was significant interaction, played a crucial role in the dissemination of the palmette motif in Anatolia.

Due to its strategic location, Erzurum has been a hub of intense cultural interactions, making it one of the cities where these influences are most evident. The Seljuk architectural masterpieces in Erzurum, particularly Çifte Minareli Medrese and Yakutiye Medrese, serve as tangible examples of this artistic and cultural exchange.

The palmette motif is a widely used element in decorative arts and frequently appears in Seljuk architecture in various variations. This motif is found in multiple architectural structures, including the borders of Diyarbakır Ulu Mosque, the main entrance portal of Aksaray Sultan Han (Karadaş, 2011), the corner towers of Sivas Gök Medrese (Akkaya and Urfalıoğlu, 2022), the border decorations of the main entrance portal of Eşrefoğlu Mosque (Çilek, 2021), the mihrab of Develi Sivasi Hatun Mosque (Ulu Mosque) at the peak of the pointed arch, and the niche of the entrance portal of Alaca Kümbet (Yıldız, 2019). In addition to these, the palmette motif is commonly observed in many other Seljuk-era architectural structures.

According to the frequency of animal motifs presented in Table 4, the scallop motif, which structurally resembles fans and scallop shells and appears in various forms in decorations, is the most frequently used animal motif. It was observed 45 times in Çifte Minareli Medrese and 7 times in Yakutiye Medrese, making a total of 52 instances.

The eagle motif, which is the symbol of the Seljuk State, ranks second with 2 instances in Çifte Minareli Medrese and 2 instances in Yakutiye Medrese, totaling 4 occurrences.

The dragon motif was identified 4 times in Çifte Minareli Medrese, but was not found in Yakutiye Medrese, making a total of 4 instances, placing it in third position.

The lion motif, which symbolized the ruler's power in the Seljuk State, was not present in Çifte Minareli Medrese, whereas it appeared twice in Yakutiye Medrese, making it the least frequently used animal motif, with a total of 2 occurrences.

Table 4. Frequency of use of animal motifs

	Motif Type	Double Minaret Madrasa	Yakutiye Madrasa	Total
1	Scallop	45	7	52
2	Eagle	4	2	4
3	Dragon	2	-	4
4	Lion	-	2	2

The scallop motif, due to its similarity to fan and scallop shell motifs and its traceable origins in Ancient Greek architecture, has played a significant role in its widespread geographical distribution. Recognized as a symbol of life and creation, the scallop motif has been incorporated into various belief systems and cultures, carrying similar meanings in Turkish-Islamic art, where it has been associated with paradise depictions (Çakmakoğlu Kuru, 2008).

This acceptance in Turkish-Islamic art led to the wide use of the scallop motif in Anatolia, making it a frequently preferred decorative element, particularly in Seljuk art. Among the notable Seljuk structures in Erzurum, Çifte Minareli Medrese and Yakutiye Medrese stand out as prominent examples of this artistic tradition.

During the Seljuk period, the scallop motif was used in various forms as an architectural decorative element in numerous structures. This motif can be found in the arch of the doorway of Gevher Nesibe Darüşşifası, the mihrab arch of Kızılören Han Mosque, the window arch of İzzeddin Keykavus Şifahanesi, the fountain pediment of Alara Han Fountain, the mihrabiye arch of Burmalı Minare Mosque, the mihrabiye arch of Burmalı Minare Mosque Tomb, the niche arch of the mihrab in Huand Hatun Mosque, the main entrance arch of İncir Han, the mihrabiye arch of Alaaddin Mosque, the mihrabiye arch of Malatya Ulu Mosque, the mihrabiye arch of Sarıhan Caravanserai, the facade niche arch of Kadem Paşa Hatun Kümbet, and the facade niche arch of Patnos (Zortul) Kümbet (Turan, 2013).

4. Conclusion

This study aimed to analyze the cultural origins, dissemination, and frequency of use of botanical and animal motifs used in Çifte Minareli Medrese and Yakutiye Medrese in Erzurum, thereby revealing the cultural interactions and aesthetic principles of Seljuk-period art. The findings indicate that the ornamental art

in these madrasas is not merely a decorative element but also represents a symbolic language reflecting the religious, philosophical, and cultural values of the period.

In this study, botanical motifs such as palmette, rumi, hatayi, penç, and tulip were identified as the most prominent. The palmette motif, with 102 instances, was found to be the most frequently used motif. Its origins trace back to Sumerian, Egyptian, Assyrian, Greek, and Roman civilizations, which played a significant role in its spread and diversification across different regions.

The rumi motif, ranking second with 46 instances, was observed to have originated in Central Asia, later spreading to Anatolia, where it developed further within Seljuk art, appearing in various compositions. The hatayi motif, influenced by Chinese art, spread to Central Asia and later diversified and evolved in Anatolia. The penç motif was among the least commonly used motifs.

The inverted tulip motif was found only once in Yakutiye Medrese, making it the least frequently observed motif in the study.

Among the animal motifs, figures such as scallop, Tree of Life, eagle, dragon, and lion were found to be the most prominent. The scallop motif, with 52 instances, was the most frequently observed animal motif. Recognized for symbolizing abundance and rebirth, this motif was widely accepted across different cultures and frequently used in Seljuk art.

The Tree of Life motif, with 8 instances, ranked second. This motif held significant importance in various belief systems as a symbol of the ever-changing nature of the universe and fertility. The eagle motif, regarded as a symbol of the Seljuk State, was identified 4 times, placing it in third position.

The dragon motif appeared 4 times in Çifte Minareli Medrese, but was not found in Yakutiye Medrese. The lion motif was observed only twice in Yakutiye Medrese, making it the least frequently encountered animal motif in this study.

These findings indicate that Seljuk-period art was enriched through influences from various cultures, and these interactions were reflected in architectural ornamentation. The presence of both local Anatolian and foreign cultural motifs in the architectural texture of Erzurum reveals the integrative approach of the Seljuks towards cultural diversity. In this sense, ornamentation in Seljuk architecture emerges not only as an artistic endeavor but also as a medium of intercultural communication and legacy. Additionally, the frequency of motif usage provides significant insights into the cultures with which the Seljuks had the most interaction and the artistic heritage of these cultures.

In conclusion, this study serves as a significant resource for understanding the cultural and artistic heritage of Seljuk-period art. The motifs and ornamentations found in the madrasas of Erzurum provide a valuable reference point for comprehending the artistic and cultural interactions between different civilizations. The preservation and transmission of this cultural heritage to future generations is a responsibility shared by all members of society.

Furthermore, expanding this study to include a comparative analysis of Seljuk architectural works in other Anatolian cities would contribute to a deeper understanding of regional variations and common aesthetic principles within Seljuk art.

Author Contributions

The percentages of the authors' contributions are presented below. All authors reviewed and approved the final version of the manuscript.

	S.P.	B.Y.	S.K.
C	40	30	30
D	40	30	30
S	60	20	20
DCP	60	20	20
DAI	40	30	30
L	40	30	30
W	40	30	30
CR	60	20	20
SR	60	20	20
PM	60	20	20
FA	60	20	20

C=Concept, D= design, S= supervision, DCP= data collection and/or processing, DAI= data analysis and/or interpretation, L= literature search, W= writing, CR= critical review, SR= submission and revision, PM= project management, FA= funding acquisition.

Conflict of Interest

The authors declared that there is no conflict of interest.

References

Akçay İ. 1965. Yakutiye medresesi. Vakıflar, Ankara, Türkiye, pp: 152.

Akkaya İ, Urfalıoğlu N. 2022. Anadolu Selçuklu dönemi Sivas medreselerinde giriş cephesi bezemeleri. Star Sanat ve Tasarım Araştırmaları Derg, 3(4): 241-264.

Arslan S. 2014. Türk kültüründe ağaç kültü ve hayat ağacı. Uluslararası Sosyal ve Eğitim Bilimleri Derg, 1(1): 59-71. https://doi.org/10.20860/ijoses.27650

Aydın T. 2008. Erzurum Çifte Minareli Medrese taş süsleme örnekleri. Gazi Üniversitesi, Eğitim Bilimleri Enstitüsü, Ankara, Türkiye, pp: 97.

Aytaç N. 2017. Anadolu'da İlhanlı mimari eserleri. Mimar Sinan Güzel Sanatlar Üniversitesi, Sosyal Bilimler Enstitüsü, İstanbul, Türkiye, pp: 134.

Çakmakoğlu Kuru A. 2008. İkonografik açıdan Orta Çağ Türk mimarisinde yer alan istiridye motifi. Erdem, (52): 111-124.

Çevik G. 2014. Rüstem Paşa Camii çinilerinde lale ve karanfil motifleri. Fatih Sultan Mehmet Vakıf Üniversitesi, Güzel Sanatlar Enstitüsü, İstanbul, Türkiye, pp: 122.

Çilek Ü. 2021. Beyşehir Eşrefoğlu Camii taçkapısının özgün bezemeleri. Lale, (4): 34-50.

Çorbacı ÖL, Oğuztürk T, Oğuztürk GE, Üçok M, Aydin F. 2022. Diyarbakır Hz. Süleyman Camii'nin inanç turizmi açısından değerlendirilerek rekreasyonel olanaklarının belirlenmesi. J

Academic Tourism Stud, 2(2): 106-115. https://doi.org/10.29228/jatos.52899

Çoruhlu Y. 2019. Türk sanatında hayvan sembolizmi. Ötüken Neşriyat, İstanbul, Türkiye, pp: 304.

Değerbilir N. 2012. Erken Osmanlı dönemi çini ve taş malzeme üzerinde hatayi motifi. Marmara Üniversitesi, Türkiyat Araştırmaları Enstitüsü, İstanbul, Türkiye, pp: 87.

Garagaşov V. 2006. Tezhib sanatında saz yolu 16. yüzyıl. Mimar Sinan Güzel Sanatlar Üniversitesi, Sosyal Bilimler Enstitüsü, İstanbul, Türkiye, pp: 88.

Haas HD. 2008. Migration and development: A theoretical perspective. International Migration Institute, University of Oxford, Oxford, UK, pp: 34.

İnan A. 1987. Makaleler ve incelemeler. Türk Tarih Kurumu Basımevi, Ankara, Türkiye, pp: 412.

Karaca N. 2021. Türk çini sanatında 'hatayi' ve 'şakayık' motifi örneğinde çizim özellikleri. OPUS Int J Society Res, 18(43): 7082-7105. https://doi.org/10.26466/opus.943325

Karadaş Ş. 2011. Anadolu Selçuklu dönemi mimarisinde bitkisel bezeme unsurları. Atatürk Üniversitesi, Sosyal Bilimler Enstitüsü, Erzurum, Türkiye, pp: 242.

Kocaman İ, Kazaz İ, Okuyucu D. 2018. Tarihi Erzurum Yakutiye Medresesi'nin yapısal davranışının incelenmesi. DEÜ Müh Fak Fen ve Müh Derg, 20(58): 36-51.

Konak I. 2022. Erzurum Çifte Minareli Medrese ve Yakutiye Medresesi çinili minarelerinin mevcut durumu ve tamamlama uygulamaları. Uşak Üniversitesi Sosyal Bilimler Derg, 15(1): 44-59.

Korkutan E. 2011. Erzurum Çifte Minareli Medrese ve Yakutiye Medresesi taş bezemelerinin takı sanatına uygulanırlığı. Atatürk Üniversitesi, Sosyal Bilimler Enstitüsü, Erzurum, Türkiye, pp: 95.

Kurt Kırtay K. 2023. Türk Kültüründe Hayat Ağacı, Bir Motif Olarak Çini ve Seramiklerde Kullanımı. Uluslararası İnsan Ve Sanat Araştırmaları Dergisi, 8(2): 129-143.

Kutlu Ö, Göksel Z. 2014. Kent kültürü oluşturma aracı olarak kültürel belediyecilik: Selçuklu örneği. Selçuk Üniversitesi Sosyal Bilimler Enstitüsü Derg, (31.1): 75-91.

Mülayim S. 1976. Selçuklu palmet motiflerinin tipolojisi. Anatolia, 20: 141-152. https://doi.org/10.1501/andl_0000000194

Mutlu HS, Özdemir S. 2022. Selçuklu yapılarını süsleyen mitolojik varlıklar. Int J Social Humanit Admin Sci, 8(57): 1394-1396.

Odabaşıoğlu A. 2022. İslamiyet öncesi Türk kültüründe hayvansal motifler ve Türkiye Selçuklu mimarisine yansıması. Erciyes Üniversitesi, Sosyal Bilimler Enstitüsü, Kayseri, Türkiye, pp: 108.

Öten A. 2023. Osmanlı yapı kültüründe arslan ve arslanhaneler. Belleten, 87(308): 115-116. https://doi.org/10.37879/belleten.2023.113

Özen F. 2016. İlhanlılar devrinde Erzurum. Ankara Üniversitesi Dil ve Tarih-Coğrafya Fakültesi Derg, 56(2): 256-286.

Özkul K. 2020a. Anadolu Selçuklu dönemi mimari yapılarında turkuaz. Int J Humanit Educ, 6(13): 291-318.

Özkul K. 2020b. Sivas Divriği Ulu Cami ve Darüşşifası bezemeleri. Int J Idil-Ural Turkestan Res, 2(3): 56-81.

Özler F. 2018. Delhi ve Agra'daki Babürlü türbelerinde mimari süsleme (1557-1658). Erciyes Üniversitesi, Sosyal Bilimler Enstitüsü, Kayseri, Türkiye, pp: 202.

Özler F. 2021. Tac Mahal'de ağlayan gelin (ters lale motifi). Sanat Tarihi Yıllığı, (30): 145-168.

Öztürk E. 2018. Etnik ve dinsel dönüşüm çağında Anadolu: Halklar, inanışlar ve kültürel etkileşim (XII.-XIII. yüzyıllar). Hacettepe Üniversitesi, Sosyal Bilimler Enstitüsü, Ankara, Türkiye, pp: 143.

Peterson RA, Anand N. 2004. The production of culture perspective. Annu Rev Sociol, 30: 311-334. https://doi.org/10.1146/annurev.soc.30.012703.110557

Polat S. 2020. Kültürün dinamik öğeleri olarak sanat ve müzik. İnsan ve Toplum Bilimleri Araştırmaları Derg, 9(2): 1757-1771. https://doi.org/10.15869/itobiad.703142

Sipahi S, Yalçin İC. 2021. Tarihi medreselerin yeniden işlevlendirilmesi: Erzurum Çifte Minareli Medrese. Social Mentality and Researcher Thinkers J, 7(46): 1195-1210. https://doi.org/10.31576/smryj.903

Taflan H. 2008. Erzurum Yakutiye Medresesi taç kapısı üzerindeki taş kabartmalar üzerine bir araştırma. Yüksek Lisans Tezi, Gazi Üniversitesi, Eğitim Bilimleri Enstitüsü, Ankara, Türkiye, pp: 25-30.

Tavaslı H. 2014. Penç motifinin tarihsel gelişimi ve karakterleri. Yüksek Lisans Tezi, Fatih Sultan Mehmet Vakıf Üniversitesi, Güzel Sanatlar Enstitüsü, İstanbul, Türkiye, pp: 26-42.

Tecir ET. 2024. Çift başlı kartal motifinin sembolik anlamları ve tekstillerde kullanımı. Motif Akademi Halkbilimi Dergisi, 17(46): 951-969. doi: https://doi.org/10.12981/mahder.1465432

Turan B. 2013. Osmanlı öncesi Anadolu Türk mimarisinde kullanılan istiridye motifi. Yüksek Lisans Tezi, Yıldız Teknik Üniversitesi, Fen Bilimleri Enstitüsü, İstanbul, Türkiye, pp:15-26.

Türkoğlu MT. 2019. Yükseköğretim öğrencilerinde Selçuklu sanatı farkındalığı. Yüksek Lisans Tezi, Necmettin Erbakan Üniversitesi, Sosyal Bilimler Enstitüsü, Konya, Türkiye, pp:23-31.

Tütüncüoğlu M. 2016. Gönüllülük ve sivil toplum etkileşiminde sanatın rolü. Ankara, Türkiye pp:15-19.

Ünal S. 2021. Türkistan'dan günümüze pişmiş toprak kültüründe lale. Türk Dünyası Araştırmaları, 128: 323-344.

Yavuz Ş. 2008. Süsleme sanatlarında rumi motifi ve tarihsel gelişimi. Yüksek Lisans Tezi, Gazi Üniversitesi, Eğitim Bilimleri Enstitüsü, Ankara, Türkiye, pp: 29-30.

Yıldız H. 2019. Anadolu Selçuklu Devri Kayseri yapılarında palmet, rumi ve lotus motifi. Yüksek Lisans Tezi, Erciyes Üniversitesi, Sosyal Bilimler Enstitüsü, Kayseri, Türkiye, pp: 47-48.

Black Sea Journal of Engineering and Science
doi: 10.34248/bsengineering.1674279

Open Access Journal
e-ISSN: 2619 – 8991

Research Article
Volume 8 - Issue 4: 1096-1102 / July 2025

DEVELOPMENT AND VALIDATION OF A SIMPLE HPLC-UV METHOD FOR ANALYSIS OF HARMINE

Galip Mesut DEMIR[1], Afife Busra UGUR KAPLAN[2], Mine Gulaboglu[1*], Meltem CETIN[2]

[1]*Atatürk University, Faculty of Pharmacy, Department of Biochemistry, 25240, Erzurum, Türkiye*
[2]*Atatürk University, Faculty of Pharmacy, Department of Pharmaceutical Technology, 25240, Erzurum, Türkiye*

Abstract: In this study, a rapid, simple, and sensitive HPLC-UV method was developed and validated in accordance with ICH Q2 (R1) guideline for the quantitative analysis of harmine (HRM), a main β-carboline alkaloid found in the Peganum harmala (Uzerlik) plant. The method was established based on the UV spectral analysis, which indicated maximum absorbance for HRM at 243 nm. A mixture of methanol and ultrapure water containing 1% formic acid (50:50, v/v) was selected as the mobile phase. In the separation carried out under isocratic conditions, the retention time of HRM was determined as 5.5 min, and the entire analysis was completed in under 8 min. The method demonstrated excellent linearity within the concentration range of 1–36 µg/mL, with a correlation coefficient (R^2) of 0.99998. The accuracy and precision parameters of the method were found to be within acceptable limits, with relative error (RE) and relative standard deviation (RSD%) both below 2. The limits of detection and quantification (LOD and LOQ) were 0.269 µg/mL and 0.816 µg/mL, respectively. Also, it was determined that HRM standard solutions were stable for up to 7 days when stored at different temperatures (−20°C, 2–8°C, 25°C). In conclusion, this method offers a reliable alternative for the quantitative determination of HRM with high analytical quality, reproducibility, and short time. It can be widely used in routine laboratory practices for the monitoring of HRM in pure form and in various pharmaceutical formulations.

Keywords: Harmine, HPLC-UV method, Peganum harmala, Stability, Validation

***Corresponding author:** Atatürk University, Faculty of Pharmacy, Department of Biochemistry, 25240, Erzurum, Türkiye
E mail: minegulaboglu@atauni.edu.tr (M. GULABOGLU)

Galip Mesut DEMIR	https://orcid.org/0000-0001-6107-2604	
Afife Busra UGUR KAPLAN	https://orcid.org/0000-0003-2222-8789	
Mine GULABOGLU	https://orcid.org/0000-0002-3248-1502	
Meltem CETIN	https://orcid.org/0000-0003-4009-2432	

Received: April 12, 2025
Accepted: May 21, 2025
Published: July 15, 2025

Cite as: Demir GM, Ugur Kaplan AB, Gulaboglu M, Cetin M. 2025. Development and validation of a simple HPLC-UV method for analysis of harmine. BSJ Eng Sci, 8(4): 1096-1102.

1. Introduction

Peganum harmala is a perennial hairless plant with an extensive geographical distribution in the northern hemisphere. It is prevalent in the tropical and subtropical regions of Asia, Africa, and America. This perennial woody plant, which typically grows between 30-70 centimeters in height, is abundant in Central Anatolia and naturally grows at altitudes as high as 1500 meters above sea level. The leaves of the plant are comprised of multiple parts; the flowers are solitary, large, and white. The fruit of the plant is a spherical capsule containing numerous seeds (Coode, 1967). The plant seeds are characterized by a strong odor and a slightly bitter taste. Active components of *Peganum harmala* are alkaloids, which are present in exceptionally high concentrations in the seeds and roots of the plant. The total alkaloid content of the plant is approximately 4-5% (Mahmoudian et al., 2002). Harman, harmine, harmol, harmalol and harmaline are the main β-carboline derivative alkaloids of *Peganum harmala*, and harmacillin, harmacilinin, harmalacidin, harmalanine, norharmine and isoharmine alkaloids have also been isolated in the studies about *Peganum harmala* (Ayoub et al., 1989; Chatterjee and Ganguly, 1968; Siddiqui, Khan, Faizi, and Siddiqui, 1987, 1988, 1989). Its alkaloids, most notably harmaline and harmine (HRM), have been demonstrated to exert various effects (Kara, 2011). Studies have shown that active alkaloids obtained from *Peganum harmala* seeds have different antifungal, antibacterial, antiparasitic and insecticidal effects. Many studies show that *Peganum harmala* has antioxidant and free radical scavenging effects (Akhtar et al., 2000; Astulla et al., 2008; Berrougui et al., 2006; Hamden et al., 2009; Hamden et al., 2008; Nenaah, 2010; Prashanth and John, 1999; Rharrabe, et al., 2007; Saadabadi, 2006). It has a long history of traditional use in treating diabetes in specific geographic regions (Bnouham et al., 2002). HRM is the most studied and examined alkaloid among these alkaloids (Pour and Moghadar, 2012). HRM ("7-methoxy-1-methyl-9H-pyrido[3,4-b]indole") was isolated for the first time in 1847 from the seeds of *Peganum harmala* (Figure 1). HRM, a principal alkaloid of *Peganum harmala*, has various pharmacological activities such as cytotoxic, antimicrobial, antitumor, antioxidant, antimutagenic, antigenotoxic, antifungal, antiplasmodial, and hallucinogenic properties (Patel et al., 2012). HRM reduces the effects of oxidative stress by scavenging free radicals through its antioxidant activity. Additionally, it

This work is licensed (CC BY-NC 4.0) under Creative Commons Attribution 4.0 International License

reduces the rate of vitamin E loss and prevents LDL oxidation due to this antioxidant activity (Berrougui et al., 2006). In recent years, HRM has demonstrated significant potential in the treatment of diabetes (Wang et al., 2015).

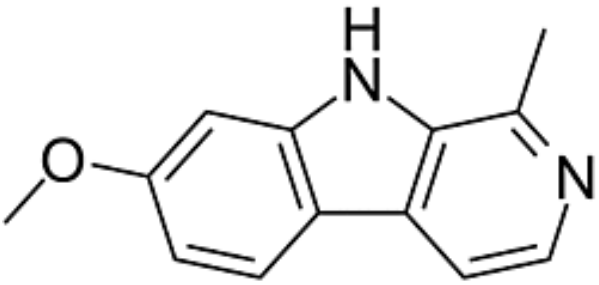


Figure 1. Chemical structure of HRM.

A popular analytical technique for separating, identifying, and quantifying the amounts of each component in a mixture is high-performance liquid chromatography (HPLC). It is recognized as one of the most precise analytical techniques for both quantitative and qualitative drug/active substance analysis (Ali, 2022; Al-Shami, Naseef, Moqadi, and Kanaze, 2024).

The objective of the current study was to develop and validate a rapid and easily executed analytical method for determining the HRM using HPLC.

2. Materials and Methods

2.1. Materials

HRM and methanol (HPLC grade) were purchased from Thermo Scientific (India) and Isolab (Germany), respectively. Also, Millipore ("Direct-Q® 3UV, USA") was used to obtain ultrapure water.

2.2. Methods

2.2.1. UV Wavelength Determination

To develop the analytical method, a standard solution of HRM was first prepared in methanol at a concentration of 10 µg/mL. Then, a UV spectrum was taken in the 200-400 nm wavelength range, and the wavelength at which it gave the maximum absorbance was determined.

2.2.2.Chromatographic System and Conditions

In the current study, an HPLC system ("Thermo Finnigan Surveyor, USA") with an autosampler and UV detector was used. Data was gathered and processed using the chromatographic software Chromoquest. Utilizing a mobile phase made of methanol and ultrapure water consisting of 1% formic acid (50:50, v/v), separation was accomplished on a C18 column (MZ Analysentechnik, Germany; 5µm, 4.6mm×250mm) while maintaining a constant column temperature of 25°C. The injecting volume of sample, the flow rate of mobile phase and UV detection wavelength were set as 10 µL, 1.0 mL/min, and 243 nm, respectively.

2.2.3. Preparation of Standard Solutions

Standard solutions were prepared at six different concentrations in the range 1-36 µg/mL, starting from the stock solution of HRM at a 50 µg/mL concentration in methanol, obtained by appropriately diluting it with methanol.

2.2.4. Validation of Analytical Method

Analytical method validation is performed to demonstrate that the method developed for quantification provides accurate, specific, and reproducible results. In our study, analytical method validation was performed according to ICH (Q2) R1 guideline, and linearity, accuracy, precision, specificity, limits of detection and quantification (LOD and LOQ), and stability parameters were examined (ICH Topic Q2 (R1), 2006) .

2.2.4.1. Linearity

For the linearity parameter, the standard solutions (n=6) were analyzed in the concentration range of 1–36 µg/mL. The calibration curve for HRM was obtained by plotting the concentration versus the corresponding peak area. Linear regression analysis was used to get the regression equation and coefficient of determination (R^2).

2.2.4.2. Accuracy

The accuracy parameter expresses the closeness of the values obtained from the analysis to the real values (Shabir, 2003). The accuracy parameter was studied as intra-day and inter-day. Freshly prepared standard solutions in six replicates (2, 16, and 32 µg/mL) were assayed for HRM on the same day and three consecutive days to determine intra- and inter-day accuracy (expressed as relative error; RE).

2.2.4.3. Precision

The precision parameter expresses the degree of closeness of the values obtained from the analysis (Kandilli et al., 2018). The precision parameter was studied as intra-day and inter-day, and also injection repeatability was evaluated. Intra- and inter-day precision (expressed as percentage relative standard deviation-RSD%) was determined by assaying six replicates of freshly prepared standard solutions (2, 16 and 32 µg/mL) for HRM on the same day and three consecutive days, respectively.

2.2.4.4. Specificity

The ability of the method to separate the target compound's response from that of other sample components is known as specificity. The specificity of the method was assessed by analyzing the chromatograms to confirm the absence of discernible shoulders or interfering peaks. (Ugur Kaplan and Cetin, 2023). For the evaluation of the specificity parameter, methanol was analysed under the specified conditions, and it was determined whether it gave a peak in the same position as HRM.

2.2.4.5. LOD and LOQ

LOD is the lowest detectable but not always quantifiable analyte concentration in a sample.The minimum amount of an analyte that can be accurately and precisely measured in a sample is known as the limit of quantification, or LOQ. For HRM, LOD and LOQ were determined using the formulas "LOD=3.3*σ/S" and

"LOQ=10* σ/S", where S is the calibration curve's slope and σ is the intercept's standard deviation (Al-Shami et al., 2024).

2.2.4.6. Stability

The stability of the HRM was evaluated after 0, 1, 2, 3, and 7 days of storage at 25 °C or in a refrigerator (2-8 °C and -20 °C) in the standard solutions (2, 16 and 32 µg/mL) protected from light to reduce potential light effects. The stability parameter was examined by calculating the percentage recovery values (Ugur Kaplan and Cetin, 2023).

3. Results and Discussion

In the current study, a rapid, easily executed and sensitive HPLC-UV method for the determination of HRM was developed and validated. The chromatographic conditions were established to achieve a high performance of the analysis. In order to accomplish this, the UV spectrum of HRM (at 10 µg/mL concentration) was first taken, and the maximum wavelength was determined to be 243 nm (Figure 1). The obtained spectrum was found to be consistent with the literature (Yamagaki, Suzuki, and Tachibana, 2007). The literature has reported maximum wavelengths of 240-250 nm for HRM (Drugfuture, 2022; Mortazavi et al., 2021; Nafisi et al., 2012; Spectrabase, 2022; Robinson, 2019; Yamagaki et al., 2007).

According to the results of preliminary experiments, a mixture of methanol and ultrapure water consisting of 1% formic acid (50:50, v/v) was selected as the mobile phase. A C18 column (4.6mm×250mm, 5µm) carried out isocratic chromatographic separation at a flow rate of 1.0 mg/min with UV detection at 243 nm. In Figure 2, an HRM chromatogram was displayed under the chromatographic conditions mentioned above. The retention time of HRM was recorded to be 5.5 minutes. The total assay run time was less than 8 minutes, with a clear separation.

In our study, analytical method validation, including linearity, specificity, LOD, LOQ, accuracy, precision, and stability parameters, was carried out according to ICH (Q2) R1 guideline (ICH (Q2) R1, 2006).

The specificity parameter expresses the ability of the analytical method to measure the drug/active substance in the presence of excipients or components of matrix (Le, Phung, and Le, 2019). The chromatograms of the HRM standard solutions and methanol only were compared in order to determine the parameter (Kandilli et al., 2018). There was no peak visible in the area of the HRM peak in the methanol chromatogram. The well-resolved HRM peak demonstrated the high selectivity of the developed HPLC-UV method (Figure 2).

The linearity of an HPLC method is its ability to provide test results that are directly proportional to the drug/compound concentration in a sample over a given concentration range (Bhujbal, Rupenthal, and Agarwal, 2024). The calibration curve of HRM was obtained by plotting the peak areas (mAu) versus the concentrations of the active substances. The calibration curve equation was calculated as y=86504x-17881 for HRM using linear regression analysis (Figure 3). For HRM, a good linear relationship with a coefficient of determination (R^2) of 0.99998 was observed between its peak areas and concentrations over the concentration range (1-36 µg/mL). Furthermore, the LOD and LOQ values were determined as 0.269 µg/mL ve 0.816 µg/mL for HRM, respectively.

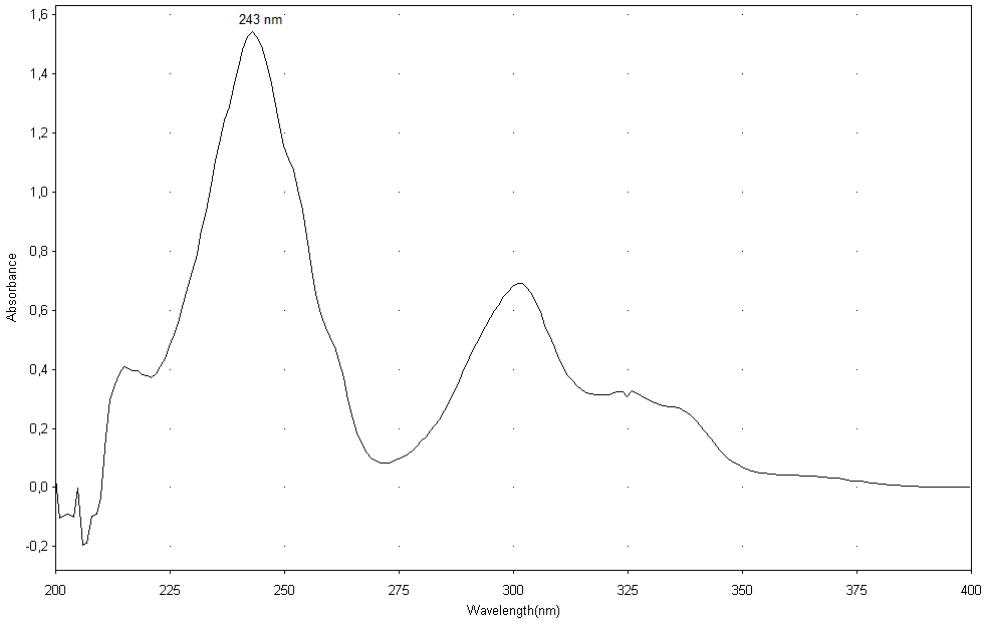


Figure 2. UV spectrum of HRM.

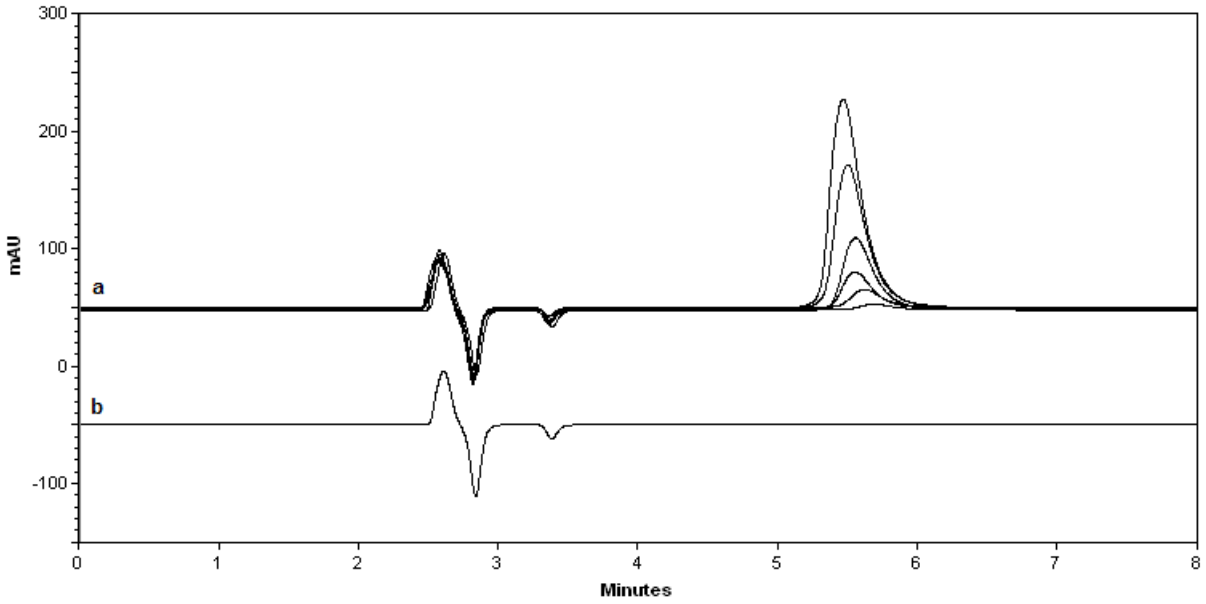


Figure 3. The chromatograms of the standard solutions of HRM (1- 36 µg/mL) (a); methanol (b).

The accuracy and precision (intra-day and inter-day) parameters were evaluated (at the concentrations of 2, 16, 32 µg/mL) in terms of RE and RSD%, respectively. The intra-day and inter-day RE values were found to be in the range of 0.326-1.545% and 0.514-1.164%, respectively. In addition, the intra- and inter-day RSD% values were determined to be between 0.475-0.951% and 0.271-0.604%, accordingly. For in vitro conditions, the obtained RE and RSD% should be <±2% and <2%, respectively (Mowafy, Alanazi, and El Maghraby, 2012). In our study, the values of RE and RSD% for HRM were found to be less than ±2% and 2%, respectively, for all injected concentrations. This indicates that the developed analytical method was accurate and precise. Also, the injection repeatability parameter was evaluated by calculating RSD% and was found to be in the range of 0.188-0.268% (Table 2).

Table 1. The results of accuracy and precision (intra-day and inter-day) of the method (Mean±SD; n=6)

	Concentration (µg/mL)	Found Concentration (µg/mL)	RE %	RSD (%)
INTRA-DAY	2	2.031 ± 0.010	1.545	0.475
	16	16.082 ± 0.132	0.515	0.818
	32	32.104 ± 0.305	0.326	0.951
INTER-DAY	2	2.023 ± 0.012	1.164	0.604
	16	16.082 ± 0.061	0.514	0.379
	32	32.201 ± 0.087	0.628	0.271

SD= standard deviation, RE= relative error, RSD= Relative standard deviation.

Table 2. The results of injection repeatability (Mean±SD; n=6)

Concentration (µg/mL)	Found Concentration (µg/mL)	RSD (%)
2	2.017 ± 0.005	0.268
16	16.060 ± 0.030	0.188
32	32.094 ± 0.198	0.198

SD= standard deviation, RSD= Relative standard deviation.

Table 3. The results of the stability study (Mean±SD; n=3)

Temperature	Time (Day)	Concentration (µg/mL)	Found Concentration (µg/mL)	Recovery (%)
25 °C	0	2	2.024 ± 0.006	100.000
		16	16.088 ± 0.113	100.000
		32	32.059 ± 0.070	100.000
	1	2	2.025 ± 0.008	100.049
		16	16.078 ± 0.130	99.938
		32	32.051 ± 0.140	99.976
	2	2	2.014 ± 0.005	99.481
		16	16.064± 0.068	99.853
		32	32.032 ± 0.134	99.916
	3	2	2.006 ± 0.005	99.102
		16	16.002 ± 0.029	99.465
		32	31.962 ± 0.108	99.697
	7	2	1.997 ± 0.007	98.669
		16	15.973 ± 0.061	99.289
		32	31.897± 0.111	99.496
2-8 °C	0	2	2.024 ± 0.006	100.000
		16	16.088 ± 0.113	100.000
		32	32.059 ± 0.070	100.000
	1	2	2.027 ± 0.015	100.122
		16	16.095 ± 0.113	100.048
		32	32.066 ± 0.153	100.024
	2	2	2.025 ± 0.006	100.052
		16	16.060 ± 0.079	99.825
		32	32.033 ± 0.043	99.920
	3	2	2.021 ± 0.011	99.841
		16	16.049 ± 0.038	99.758
		32	31.983 ± 0.020	99.762
	7	2	2.001 ± 0.007	98.844
		16	16.027 ± 0.065	99.620
		32	31.914 ± 0.023	99.549
-20 °C	0	2	2.024 ± 0.006	100.000
		16	16.088 ± 0.113	100.000
		32	32.059 ± 0.070	100.000
	1	2	2.033 ± 0.010	100.456
		16	16.096 ± 0.123	100.054
		32	32.088 ± 0.064	100.091
	2	2	2.029 ± 0.004	100.244
		16	16.093 ± 0.069	100.031
		32	32.043 ± 0.105	99.950
	3	2	2.031 ± 0.011	100.353
		16	16.055 ± 0.080	99.796
		32	32.014 ± 0.091	99.860
	7	2	2.023 ± 0.009	99.952
		16	16.035 ± 0.037	99.672
		32	31.989 ± 0.120	99.781

SD: standard deviation.

In a study by Kartal et al. (2003), a combination of "isopropyl alcohol:acetonitrile:water:formic acid" (100:100:30:0.3; v/v/v/v) adjusted to pH 8.6 was used as a mobile phase for the determination of *Peganum harmala* alkaloids (harmine, harmaline, harmalol, and harmol). Metasil ODS column (5 mm; 150/4.6 mm I.D.) was employed for the determination of alkaloids, and UV wavelength and flow rate were selected as 330 nm and 1.5 mL. The retention time, LOD and LOQ values of harmine were reported as 3.530 min, 4.690 ug/mL and 15.630 ug/mL, respectively (Kartal, Altun, and Kurucu, 2003).

In a study, HPLC method was developed to determine HRM, harmaline, harmol and harmalol alkaloids in extracts obtained from *Peganum harmala* seeds. Potassium phosphate buffer (10 mM, pH 7.0) and acetonitrile mixture (100:30, v/v) were used as mobile phase, and the flow rate was 1.5 mL/min. In the analysis using 330 nm UV wavelength, the retention time for the HRM standard (prepared in methanol) was determined as approximately 7.3 min. The method was reported to be able to preserve harmala alkaloids in plant extracts and to be routine and accurate with adequate reproducibility, sensitivity and resolution. (Faramarzi, Venus, Amini, and Rouini, 2008).

In another study, chromatographic conditions were defined as "detection wavelength: 320 nm; flow rate: 1.0 mL/min, mobile phase: methanol: 0.01 mol/L ammonium sulfate solution: diethylamide (40:60:1; pH was adjusted to 3.8 ± 0.1 with phosphoric acid)" to determine the

amount of HRM loaded into micelles and the retention time of HRM was determined as approximately 8.2 min (Bei et al., 2013).

In our study, the stability of HRM in standard solutions at three different concentrations (2, 16, and 32 µg/mL) was evaluated by calculating the percentage difference from zero-time injections. After preparation of HRM standard solutions, they were stored at different temperatures (-20°C, 2-8°C and 25°C) and analyzed at 0, 1, 2, 3 and 7 days. It was determined that the recovery (%) values were 98.669%-100.456% at -20 °C, 2-8 °C and 25 °C. In order to be able to say that the active substance is stable under the mentioned conditions, the calculated recovery (%) values are required to be within the range of 95-105% (ICH Q1A (R2), 2003; Osel, Planinšek Parfant, Kristl, and Roškar, 2021; Shabir, 2003). HRM in the standard solutions were stable for 7 days at -20°C, 2-8°C and 25°C.

4. Conclusion

A simple, fast, robust, and economical HPLC-UV method was therefore developed in this study and then successfully validated for the analysis of HRM, one of the major β-carboline alkaloids of *Peganum harmala*. This method might be used for routine analysis of HRM in pure form and as well as various pharmaceutical formulations.

Author Contributions

The percentages of the author's contributions are presented below. All authors reviewed and approved the final version of the manuscript.

	G.M.D	A.B.U.K.	M.G.	M.C.
C	25	25	25	25
D	25	25	25	25
S	-	25	50	25
DCP	40	40	10	10
DAI	10	30	30	30
L	25	25	25	25
W	25	25	25	25
CR	25	25	25	25
SR	20	25	30	25
PM	20	25	30	25
FA	20	25	30	25

C=Concept, D= design, S= supervision, DCP= data collection and/or processing, DAI= data analysis and/or interpretation, L= literature search, W= writing, CR= critical review, SR= submission and revision, PM= project management, FA= funding acquisition.

Conflict of Interest

The authors declared that there is no conflict of interest.

Ethical Consideration

Ethics committee approval was not required for this study because of there was no study on animals or humans.

Acknowledgements

This study was supported by "Atatürk University Scientific Research Foundation" (Project No: THD-2021-10248)."

References

Akhtar MS, Iqbal Z, Khan MN, Lateef M. 2000. Anthelmintic activity of medicinal plants with particular reference to their use in animals in the Indo–Pakistan subcontinent. Small Rumin Res, 38(2): 99-107.

Ali AH. 2022. High-performance liquid chromatography (HPLC): A review. Ann Adv Chem, 6(1): 010-020.

Al-Shami N, Naseef H, Moqadi R, Kanaze F. 2024. HPLC method development and validation for the determination of apixaban and clopidogrel in novel fixed-dose combination tablets. J Chem, 2024(1): 2675736.

Astulla A, Zaima K, Matsuno Y, Hirasawa Y, Ekasari W, Widyawaruyanti A, Zaini NC, Morita H. 2008. Alkaloids from the seeds of Peganum harmala showing antiplasmodial and vasorelaxant activities. J Nat Med, 62(4): 470-472.

Ayoub MT, Rashan LJ, Khazraji AT, Adaay MH. 1989. An oxamide from Peganum harmala seeds. Phytochemistry, 28(7): 2000-2001.

Bei YY, Zhou XF, You BG, Yuan ZQ, Chen WL, Xia P, Liu Y, Jin Y, Hu XJ, Zhu QL, Zhang CG, Zhang XN, Zhang L. 2013. Application of the central composite design to optimize the preparation of novel micelles of harmine. International J Nanomed, 8: 1795-1808.

Berrougui H, Martín-Cordero C, Khalil A, Hmamouchi M, Ettaib A, Marhuenda E, Herrera MD. 2006. Vasorelaxant effects of harmine and harmaline extracted from Peganum harmala L. seeds in isolated rat aorta. Pharmacol Res, 54(2): 150-157.

Bhujbal S, Rupenthal ID, Agarwal P. 2024. Development and validation of a stability-indicating HPLC method for assay of tonabersat in pharmaceutical formulations. Methods, 231: 178-185.

Bnouham M, Mekhfi H, Legssyer A, Ziyyat A. 2002. Fas'ta diyabet tedavisinde kullanılan şifalı bitkiler. Int J Diyabet Metb, 10: 33-50.

Chatterjee A, Ganguly M. 1968. Alkaloidal constituents of Peganum harmala and synthesis of the minor alkaloid deoxyvascinone. Phytochemistry, 7(2): 307-311.

Coode MJE. 1967. Peganum harmala. In Flora of Turkey and The East Aegean Islands. London, Edinburg University Press, 2nd Ed., pp: 494.

Drugfuture. Harmine. 2022. URL: https://www.drugfuture.com/chemdata/harmine.html (accessed date: June 21, 2022).

Faramarzi M, Venus M, Amini M, Rouini M. 2008. Determination of harmine and harmaline in Peganum harmala seeds by high-performance liquid chromatography. J Appl Sci, 8(9): 1761-1765.

Hamden K, Carreau S, Ayadi F, Masmoudi H, El-Feki A. 2009. Inhibitory effect of estrogens, phytoestrogens, and caloric restriction on oxidative stress and hepato-toxicity in aged rats. Biomed Enviro Sci: BES, 22(5): 381-387.

Hamden K, Silandre D, Delalande C, Elfeki A, Carreau S. 2008. Protective effects of estrogens and caloric restriction during aging on various rat testis parameters. Asian J Androl, 10(6): 837-845.

ICH Q1A (R2). 2003. Harmonised tripartite guideline: Stability

testing of new drug substances and products Q1A (R2).

ICH Topic Q2 (R1). 2006. Validation of Analytical Procedures: Text and Methodology. URL: http://www.ema.europa.eu/docs/en_GB/document_library/Scientific_guideline/2009/09/WC500002662.pdf (accessed date: July 7, 2018).

Kandilli B, Uğur AB, Çetin M, Miloğlu FD. 2018. A simple HPLC-UV method for simultaneous determination of levetiracetam and carbamazepine. Hacettepe University J Fac Pharm, 38(2): 58-64.

Kara M. 2011. Üzerlik (Peganum harmala L.) bitki ekstraktının buğday (Triticum vulgare L.) ve semizotu (Portulaca oleraceae L.) bitkilerinin gelişimi üzerine etkilerinin araştırılması. MSc Thesis, Yüzüncü Yıl Üniversitesi, Fen Bilimleri Enstitüsü, Biyoloji Anabilim Dalı, Van, Türkiye, pp: [eksik].

Kartal M, Altun ML, Kurucu S. 2003. HPLC method for the analysis of harmol, harmalol, harmine and harmaline in the seeds of Peganum harmala L. J Pharm Biomed Anal, 31(2): 263-269.

Le THH, Phung TH, Le DC. 2019. Development and validation of an HPLC method for simultaneous assay of potassium guaiacolsulfonate and sodium benzoate in pediatric oral powder. J Anal Methods Chem, 2019: 6143061.

Mahmoudian M, Jalilpour H, Salehian P. 2002. Toxicity of Peganum harmala: Review and a case method. Iranian J Pharmacol Therapeut, 1: 1-4.

Mortazavi N, Heidari M, Rabiei Z, Enferadi ST, Monazzah M. 2021. Loading harmine on nanographene changes the inhibitory effects of free harmine against MCF-7 and fibroblast cells. Med Chem Res, 30(5): 1108-1116.

Mowafy HA, Alanazi FK, El-Maghraby GM. 2012. Development and validation of an HPLC-UV method for the quantification of carbamazepine in rabbit plasma. Saudi Pharma J, 20(1): 29-34.

Nafisi S, Panahyab A, Bagheri Sadeghi G. 2012. Interactions between β-carboline alkaloids and bovine serum albumin: Investigation by spectroscopic approach. J Lumin, 132(9): 2361-2366.

Nenaah G. 2010. Antibacterial and antifungal activities of (beta)-carboline alkaloids of Peganum harmala (L) seeds and their combination effects. Fitoterapia, 81(7): 779-782.

Osel N, Planinšek Parfant T, Kristl A, Roškar R. 2021. Stability-indicating analytical approach for stability evaluation of lactoferrin. Pharmaceutics, 13(7): 1065.

Patel K, Gadewar M, Tripathi R, Prasad S, Patel DK. 2012. A review on medicinal importance, pharmacological activity and bioanalytical aspects of beta-carboline alkaloid '"Harmine."' Asian Pac J Trop Biomed, 2(8): 660-664.

Pour AB, Moghadar N. 2012. Larval effect of extract of harmine and harmalin from Peganum harmala on juvenile of Protostrongylus rufescens. Res Pharm Sci, 7(5): 63.

Prashanth D, John S. 1999. Antibacterial activity of Peganum harmala. Fitoterapia, 70(4): 438-439.

Rharrabe K, Bakrim A, Ghailani N, Sayah F. 2007. Bioinsecticidal effect of harmaline on Plodia interpunctella development (Lepidoptera: Pyralidae). Pesticide Biochem Physiol, 89(2): 137-145.

Robinson JW. 2019. Ultraviolet Absorption Spectroscopy. In: Robinson JW, editor. Handbook of Spectroscopy: Volume II. CRC Press, e-book, 168 p.

Saadabadi A. 2006. Antifungal activity of some Saudi plants used in traditional medicine. Asian J Plant Sci, 5(5): 907-909.

Shabir GA. 2003. Validation of high-performance liquid chromatography methods for pharmaceutical analysis. J Chromatogr A, 987(1-2): 57-66.

Siddiqui S, Khan O, Faizi S, Siddiqui B. 1988. Studies on the chemical constituents of the seeds of P. harmala: Isolation and structure elucidation of two ß-Carboline lactams-harmalanine and harmalanidine. Heterocycles, 27: 1401-1410.

Siddiqui S, Khan O, Faizi S, Siddiqui B. 1987. Studies on the chemical constituents of the seed of P. harmala isolation and structure of a new-ß-Carboline Alkaloid. Heterocycles, 26: 1563-1567.

Siddiqui S, Khan O, Faizi S, Siddiqui B. 1989. Studies on the chemical constituents of the seed of P. harmala: Isolation and structure elucidation of two ß-Carbolines-harmalinine and norharmine. Heterocycles, 29: 521-527.

Spectrabase. Harmine-UV-VIS -Spectrum-SpectraBase. 2022. URL: https://spectrabase.com/spectrum/Jz2mr01EJRq (accessed date: June 21, 2022).

Ugur Kaplan AB, Cetin M. 2023. Development of a simple isocratic HPLC-UV method for the simultaneous analysis of repaglinide and metformin hydrochloride in nanoemulsion formulations and commercial tablets. Pharm Chem J, 57(2): 318-326.

Wang P, Alvarez-Perez JC, Felsenfeld DP, Liu H, Sivendran S, Bender A, Kumar A, Sanchez R, Scott DK, Garcia-Ocaña A, Stewart AF. 2015. A high-throughput chemical screen reveals that harmine-mediated inhibition of DYRK1A increases human pancreatic beta cell replication. Nat Med, 21(4): 383-388.

Yamagaki T, Suzuki H, Tachibana K. 2007. Solid-phase fluorescence and ionization efficiency in negative-ion matrix-assisted laser desorption/ionization of neutral oligosaccharides: Interaction between β-Carboline matrix and ammonium salt. J Am Soc Mass Spectrom, 18(4): 714-723.

Black Sea Journal of Engineering and Science
doi: 10.34248/bsengineering.1683991

Open Access Journal
e-ISSN: 2619 – 8991

Research Article
(Volume 8 - Issue 4: 1103-1110 / July 2025)

MAXIMIZING BIOGAS YIELD IN ANAEROBIC DIGESTION: A RESPONSE SURFACE METHODOLOGY APPROACH

Koray GÜNAY[1], Zehra Gülten YALÇIN[1]*

[1]*Çankırı Karatekin University, Faculty of Engineering, Department of Chemical Engineering, 18200, Çankırı, Türkiye*

Abstract: The aim of this study is to evaluate the eutrophication water and cattle manure wastes in the Güldürcek dam reservoir that meets the drinking water of Çankırı province in biogas production and to contribute to the economy of Çankırı province. Microwave pretreatment experiments were carried out but it was determined that it did not increase the biogas efficiency. In the study, it was determined that when eutrophication water was mixed with cattle manure by the RSM method and the mixing ratio was 1/1, the highest methane production was obtained at a rate of 83-86% in the first 8 and 24 hours under optimum conditions with anaerobic digestion at a temperature of 35 °C. The composition of the obtained biogas was measured as follows; carbon dioxide (CO_2) 7.65%, oxygen (O_2) 4.5%, hydrogen (H_2) 0.018% and hydrogen sulfide (H_2S) zero. Another point to be noted in the analysis results is that the H2S rate, which is formed as a result of anaerobic digestion and causes economic losses due to corrosion of metal equipment in the system, is zero. According to the RSM method, the most suitable model was found to be Quadratic. The high R^2 value of the selected model (0.9649) supports the accuracy of the model.

Keywords: Biogas production, Anaerobic digestion, Eutrophication water, cattle waste, Response surface methodology

***Corresponding author:** Çankırı Karatekin University, Faculty of Engineering, Department of Chemical Engineering, 18200, Çankırı, Türkiye
E mail: zaltin@karatekin.edu.tr (Z. G. YALÇIN)
Koray GÜNAY https://orcid.org/0000-0002-4329-2037
Zehra Gülten YALÇIN https://orcid.org/0000-0001-5460-289X

Received: April 25, 2025
Accepted: May 22, 2025
Published: July 15, 2025
Cite as: Günay K, YalçınZG, 2025. Maximizing biogas yield in anaerobic digestion: A response surface methodology approach. BSJ Eng Sci, 8(4): 1103-1110.

1. Introduction

In recent years, the increasing prices of petroleum products, environmental pollution and the risk of depletion of fossil fuels have directed us to alternative and sustainable energy sources (Moosavian et al.,2024; Zhang 2024). When we look at the research on alternative energy sources, we see that there are studies conducted with various wastes such as food waste, animal manure, organic waste and solid municipal waste Hoyos-Sebá et al. (2024). Since these wastes cause environmental pollution, their conversion into biofuel is important in terms of environment, economy and sustainability (Gong and Aslam, 2024). These waste materials include a variety of food waste and animal manure, a significant amount of organic material that is fermented anaerobically. Anaerobic digestion (AD) has proven to be an effective method to reduce organic waste while recovering valuable by-products such as biogas and digestate Ahmad et al. (2024). The selection of the type of waste used as raw material in the AD process is effective in digestion performance. Using various wastes together has an important place in co-digestion due to its high ability to increase biogas and methane production compared to single-raw material AD methods (mono-digestionCo-digestion is known to be an effective method for determining the carbon-nitrogen (C/N) ratio, reducing the inhibitory effect of ammonia and overcoming the difficulties of mono-digestion Akbay (2024). In the study conducted by Singh et al., it was realized that eutrophic inland water bodies are one of the contributing factors to greenhouse gas (GHG) emissions Singh et al. (2023). Mainly nitrate and phosphate, promote the formation of algae and vegetation in water bodies Chanu et al. (2022). As a result, eutrophication causes more disturbances in the system, which mainly leads to the water becoming unhealthy for the aquatic habitat Mishra (2023). According to a study, it also affects the environment through greenhouse gas (GHG) emissions. It is predicted that eutrophication will increase in the next few decades due to population growth. It has also been found that digesting microalgae biomass together with carbon-rich substrates such as cattle manure and agricultural waste improves biomethanization Qian et al. (2025). In one study, it is observed that cow manure and waste algal biomass from Hauz Khas lake are used as auxiliary substrates for anaerobic digestion and up to 45% advanced biomethane production is carried out. Cattle manure is expressed as a superior auxiliary substrate that facilitates the further growth of anaerobic bacteria and archaea, which helps in the digestion of algal biomass Singh et al. (2023).

The AD process is carried out by fermentation to ensure a balanced nutrient composition and to produce biogas during the reaction process Pourrostami et al. (2024). In this process, the selection of waste used and the parameters affecting the performance of the AD process

This work is licensed (CC BY-NC 4.0) under Creative Commons Attribution 4.0 International License

consist of various factors, including solid concentration, temperature, pH and retention time. To ensure effective biogas production, these restrictions need to be optimized (Tamilselvan and Selwynraj, 2024) . Temperature is an important parameter that affects AD. Psychrophilic (10-30 ° C), mesophilic (30-40 ° C) and thermophilic (50-60 ° C) can occur under various temperature conditions Kumar et al. (2024). In the study, if the temperature goes below 30 °C, an acidic environment occurs in the AD process, which has an adverse effect on the biogas yield. In addition, if the temperature rises above 70 °C, it is especially harmful to methanogenic bacteria (Wang et al., 2024; Monteiro et al., 2024). Optimization method such as RSM is used to increase the yield of biogas in anaerobic digestion (Efetobor et al., 2024; Bensegueni et al., 2025). For example, El Bari and Habchi (2024) have used the RSM method methodology to analyze biogas production by taking into account parameters such as pH, reactor temperature, process alkalinity and raw material retention. In this study, they found that pH and temperature changes significantly affect biogas yield and methane concentration (Humphrey et al., 2024; Jadhav et al. 2024; El Bari and Habchi 2024). In another study, Bhujbal et al. (2025) found that the optimal working conditions for good yield output were determined when RSM (CCD) was used to study the biogas production of anaerobic digestion of co-digestion.

Mohammadianroshanfekr et al. (2024) used the RSM-based CCD approach to analyze the effectiveness of AD on biogas production efficiency and chemical oxygen demand reduction. There is a study in which it is found that the pH, temperature and co-digestion rates of solid raw material affect the production of biogas and the reduction of chemical oxygen demand.

In this study, according to the chemical analysis of the organic wastes used, the most suitable waste pair is cattle manure and Güldürcek Dam Lake Decontamination water, which was selected because the C/N content is close to the value that should be between the desired 15-30 in the literature. In addition, the evaluation of the eutrophication water occurring due to the decrease of the water level in the summer months at the Çankırı Drinking Water Dam is important on the basis of Çankırı province. Since the use of this raw material, which is extremely weak in terms of dissolved oxygen, in biogas production has not been found in the literature, its use has been considered in the study. The RSM method has been used to increase the biogas yield. Independent variables such as solid concentration, pH, temperature and co-digestion were taken into account, while biogas yield was taken as a response variable. The study evaluated the optimal response variable compared to the experimental findings.

2. Materials and Methods

The organic wastes in question include cattle and chicken manure, eutrophic water from the Güldürcek Dam Lake, urban water treatment sludge and urban solid waste leachate, obtained respectively from agricultural enterprises operating within the province of Çankırı and from the Çankırı Municipality Urban Waste Processing and Drinking Water Treatment units. The waste samples used in the study were stored at 4 °C before further processing. The chemical analysis of cattle and poultry manure used in biogas production was conducted in an accredited laboratory according to TS EN ISO 17025 standard. The methods used were as follows: total organic carbon (TOC) by the Walkley-Black method, total nitrogen by Kjeldahl method, C/N ratio calculation, total suspended solids (TSS) by gravimetric method, organic matter by gravimetric method, volatile solids (organic dry matter) by gravimetric method, moisture (70°C) by gravimetric method. The analyses of urban water treatment sludge and urban solid waste leachate included total organic carbon (TOC) by high-temperature combustion, total nitrogen by Kjeldahl method, volatile suspended solids (VSS) by gravimetric method, total suspended solids (TSS) by gravimetric method, and organic matter (permanganate index) by titrimetric method. pH measurements were taken using an AE-PH502 pH Portable device. The nitrogen gas used was of 99.9% purity, and the gas composition resulting from anaerobic digestion was measured using an Optima 7 biogas gas analyzer. Fermented manure analyses included organic matter by gravimetric method, total nitrogen by Kjeldahl method, copper by ICP-OES, total phosphorus (P_2O_5) by spectrophotometric method, total potassium oxide (K_2O) by ICP-OES, C/N ratio calculation, pH by electrometric method, moisture (70°C) by gravimetric method, iron (Fe), zinc (Zn), manganese (Mn) by ICP-OES, and humic acid by gravimetric method. The microwave used for pre-treatment was a Samsung MS23F301 EAW household microwave.

2.1 Anaerobic Digestion Study

In the study, biogas potential was carried out using a batch reactor for monitoring and evaluation purposes due to its simple and easy installation. The experimental setup shown in Figure 1 is a system based on the liquid displacement principle. The biogas measurement setup consists of a biogas storage bottle connected to a small anaerobic digestion reactor with tubes, a 1000 mL dark glass bottle containing 0.5 M NaOH solution, a bottle used to displace water with the pressure of the produced gas and a bottle containing 1000 mL liquid (distilled water) used to measure the CH_4 volume. A 1000 mL double-walled glass reactor with four inlets and a leak-proof lid was used. A mechanical stirrer operating at 40 rpm was connected to the outlet on the lid, a hose used to pressurize the system with 5 bar nitrogen, and a tube going to the water displacement bottle for gas volume measurement. The fourth outlet was closed with an airtight cork for gas measurements. After the reactor was loaded at certain rates, anaerobic conditions were provided by pressurizing 99.9% pure nitrogen (N_2) gas to 5 bar for 2 minutes. The 1000 mL distilled water bottle

and 0.5 M NaOH solution used in the system helped to separate impurities in the biogas and determine the efficiency. Due to biogas production, the pressure inside the 1000 mL reactor increased, causing water to be displaced from the 1000 mL laboratory glass bottle to the third bottle through a plastic tube. In the biogas production system, liquid (distilled water) displacement was observed from eutrophic water coming from the Güldürcek Dam Lake and cattle manure during the first 8 hours and 12 to 24 hours.

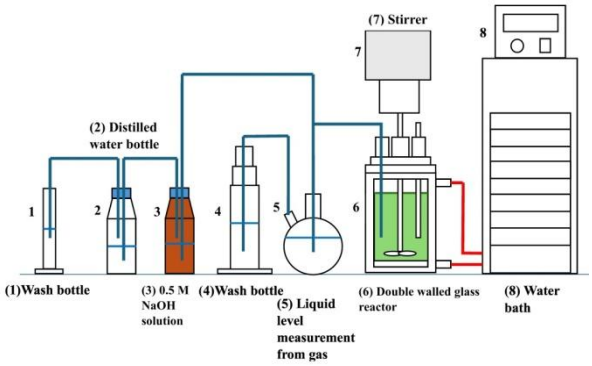


Figure 1. Biogas production system consisting of a batch-type reactor on a laboratory scale.

3. Results

3.1. Biogas Production from Cattle Manure and Eutrophic Water from Güldürcek Dam Lake

In the biogas production studies, a series of preliminary trials were conducted to determine the two most efficient waste types for anaerobic digestion and to determine the optimal production conditions. When the chemical properties of the organic wastes in Table 1 were examined, it was determined that the most suitable pair of organic wastes for anaerobic digestion was cattle manure and eutrophication water. Since the pH value of the binary mixture is 7.035, it is between 6.8-7.2, which are the desired pH values for biogas production. (Risberg et al., 2013; Nardi et al., 2021). On the other hand, it is known that the C/N ratio of this waste pair, which is an important factor in biogas production, is 15-30 and the optimum C/N ratio is 15.39 (El-Jalil et al., 2008; Wittwer and van der Heijden 2020). (Table 1). Biogas production studies with eutrophication water and cattle manure obtained from Güldürcek Dam Lake were carried out under mesophilic conditions at a constant temperature of 35±1 °C by loading 450 g of cattle manure and 450 g of eutrophication water obtained from Güldürcek Dam Lake. The study, which was carried out for 24 hours under the same and constant conditions, was carried out with serial gas measurement processes with Optima 7 biogas brand gas analyzer, which is directly connected to the reactor and provides information about the gas composition in the reactor by performing instantaneous gas analysis at 2nd, 4th, 8th, 12th and 24th hours. The analysis results subjected to the measurement processes are presented in Table 2. As understood from the analysis results, good efficiency was obtained in methane production in the first 8th hour and 12th and 24th hours. The obtained results gave results close to the methane production rates obtained as a result of anaerobic digestion with various wastes given in the literature research.

Table 1. Chemical properties of organic wastes to be used in biogas production

N	S	OC%	N%	C/N%	TSM%	TOM%	FS%	VS%	M%	pH
1	CM	32	3,53	9,06	9,43	72,8	27,2	72,8	90,5	6,87
2	EW	0,0016	0,0003	6,33	0,021	0,0002	0,020	0,0011	-	7,2

S= sample, OC= organic carbon, N=nitrogen, C/N= carbon/nitrogen, TSM=total solid matter, TOM= total organic matter, FS= fixed solid, VS= volalite solid, M= moisture, CM= cattle manure, EW= euphication water.

Table 2. Measurement results with Optima7 Biogas measurement detector in biogas production with cattle manure and Güldürcek Dam Lake eutrophic water

Parameter	Units	2 hour	4 hour	8 hour	12 hour	24 hour	Average
Methane (CH_4)	%	47.1	75.1	83.0	85.1	86.0	75.3
Carbon Dioxide (CO_2)	%	3.53	4.93	6.75	7.58	7.65	6.09
Oxygen (O_2)	%	6.6	3.9	4.8	4.6	4.5	4.88
Hydrogen (H_2)	ppm	10	12	15	16	18	14.2
Hydrogen Sulfur (H_2S)	ppm	0	0	0	0	0	0.00

3.1 RSM methodology in Biogas Production

The effects of factors such as cattle manure, eutrophication water and time on methane gas formation were investigated using the RSM method. When Table 4 (a,b,c) is examined, it is concluded that the second-order model proposed in RSM is the most appropriate choice. The Adjusted R^2 value of 0.9334 and the Lack of Fit p-value of 0.1082 provide evidence for the accuracy of the model. The 2FI model is the most appropriate choice against the second-order model, with the Mean Square value of 0.6701 and the p-value of 0.0004 indicating the accuracy of the model.

3. 2 Optimization of Biogas Production by Response Surface Methodology (RSM)

In this study, RSM was used to design the parameters affecting biogas production. The relationship between

independent variables and biogas production was evaluated in RSM (Dağ et al., 2023; Afridi and Qammar 2020). The best model for numerical experiments is the central composite design. When the literature studies in this field are examined, it was found that RSM performance is the most effective technique and the best software that includes the best task in biogas process optimization. Optimum targets such as increasing biodegradation, optimum biogas yield and methane production, increasing total solids, reducing volatile solids and eliminating chemical oxygen demand were obtained for biogas production. The main advantage of RSM is that it provides time and cost benefits by reducing the number of experimental trials. In the last 20 years, 37 process parameters have been optimized using RSM. Five of these parameters are dominant: temperature, pH, retention time, pretreatment and loading rate. The main difficulties in using RSM for biogas production process optimization are limited experimental ranges. To address these issues, studies have been conducted by combining RSM with other optimization methods such as Taguchi, Kriging or Artificial Neural Network (ANN) (Aydoğmuş et al., 2022; Güven et al., 2008; Djimtoingar et al., 2022). The effects of factors such as cow dung, eutrophication water and time on methane gas formation have been investigated using the RSM method. These effects are graphically shown in the figures. Table 3 shows the experimental design schedule with the RSM method.

Table 3. RSM experimental design chart

Experiment	Hour	Cattle manure(g)	Eutrophic water(g)	Methane (%)
1	6	519	281	84.5
2	13	600	400	85.8
3	13	400	200	85.4
4	20	519	519	86.6
5	6.45	281	281	84
6	6.45	519	519	85.5
7	13	400	400	86.1
8	19.54	281	519	86.2
9	13	400	400	86
10	13	400	600	86.1
11	13	400	400	85.9
12	13	200	400	85.3
13	13	400	400	86.2
14	13	400	400	85.8
15	19.54	519	281	85.8
16	6.45	281	519	85
17	24	400	400	86.5
18	19.54	281	281	85.7
19	13	400	400	86

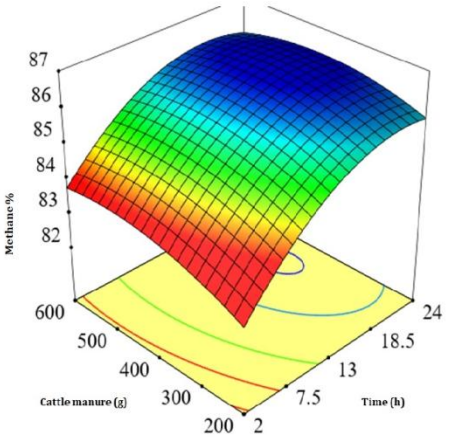


Figure 2. Examines the effect of cattle manure and eutrophication water, and time on methane (%) gas formation according to the RSM.

As shown in Figure 2 depicting the impact of cattle manure, time and duration on methane gas formation according to the RSM method, it is observed that methane gas production increases with an increase in the amount of cattle manure. The highest efficiency, approximately 86-87 %, is achieved with cattle manure quantities in the range of 500-600 g and durations in the range of 18.5-24 hours. Generally, an increase in duration (hours) leads to an increase in methane gas production, and an increase in the quantity of cattle manure results in increased efficiency. However, the plateauing of efficiency after a certain point suggests the influence of other factors on efficiency.

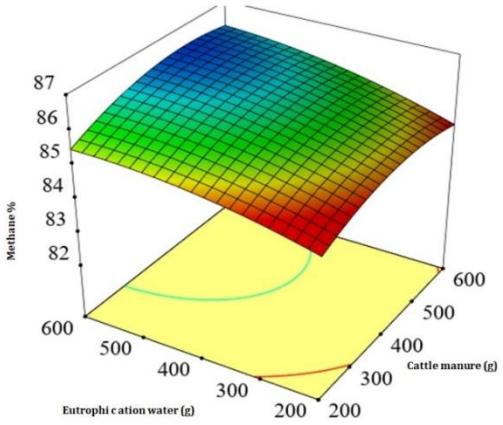


Figure 3. Effect of cattle manure and eutrophication water on methane (%) gas formation according to RSM.

In Figure 3, an increase in eutrophication water is associated with a gradual increase in efficiency, while the efficiency of cattle manure peaks at around 600 g. It is believed that certain bacteria present in eutrophication water contribute additionally to methane gas production. Working on a laboratory scale and designing experiments are prioritized for addressing some deficiencies. This is believed to hinder further increases in efficiency.

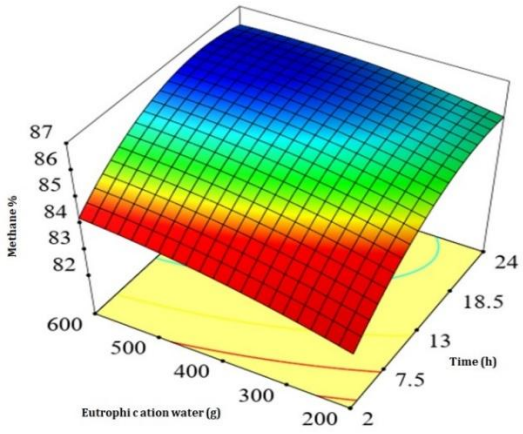


Figure 4. Effect of time and eutrophication water on methane (%) gas formation according to RSM.

Figure 4 illustrates the impact of eutrophication water volume and exposure duration on methane gas emissions. It shows that methane release increases with both higher volumes of eutrophication water and longer exposure durations. These two factors appear to play a significant role in methane production. While methane levels were initially low, they showed a noticeable increase over time. This low early-stage methane output is likely due to the low carbon-to-nitrogen (C/N) ratio in the eutrophication water. Below is the model equation derived from the experimental study conducted, based on the data obtained. This model indicates that factors such as time (t: hours), cattle manure (CM: grams), and eutrophication water (EW: grams) determine the percentage of methane gas (equation 1). The coefficients in the equation have been calculated through statistical analysis, demonstrating compatibility with experimental data.

$$\begin{aligned} Methane\ (\%) \ = \ & +78.11538 \ + \ 0.406096 \bullet t \\ & + \ 0.010264 \bullet CM \ + \ 0.007997 \\ & \bullet EW \ - \ 0.000080 \bullet t \bullet CM \\ & - \ 0.000112 \bullet t \bullet EW \\ & + \ 2.65165 \bullet 10 - 6 \bullet (CM \\ & \bullet EW) \ - \ 0.008198 \bullet t2 \\ & - \ 0.000011 \bullet CM2 \ - \ 6.04795 \\ & \bullet 10 - 6 \bullet (EW)2 \end{aligned} \quad (1)$$

In the RSM method, the determined R^2 (0.9649) and standard deviation (0.2073) values show consistency between experimental data and model results.

When examining Table 4 (a,b,c), it is concluded that the quadratic model suggested in the RSM is the most suitable choice. The Adjusted R^2 value of 0.9334 and the Lack of Fit p-value of 0.1082 provide evidence of the model's accuracy.

Table 4 evaluates the statistical significance of the RSM model data. It suggests that the quadratic vs. 2FI model is the most appropriate choice, with a Mean Square value of 0.6701 and a p-value of 0.0004, indicating the model's accuracy.

From the statistical evaluation of the RSM model data presented in Table 4 (a,b,c), it is determined that the correct model choice is made based on the R^2 value of 0.9649 and Adjusted R^2 value of 0.9334. In addition to the experimental study, biogas optimization was conducted using the Response Surface Methodology (RSM). Figure 4 compares theoretical and experimental values obtained from the RSM. Table 4 gives the recommended solution table of the RSM model.

Table 4. Statistical evaluation of the data and results with the quadratic model proposed in RSM (a,b,c)

a

Source	Sequential p-value	Lack of Fit p-value	Adjusted R^2	Predicted R^2	
Linear	< 0.0001	0.0078	0.7534	0.6834	
2FI	0.9052	0.0045	0.7089	0.4973	
Quadratic	0.0004	0.1082	0.9334	0.7824	Suggested
Cubic	0.0423	0.8708	0.9740	0.9777	Aliased

b

Source	Sum of Squares	df	Mean Square	F-value	p-value
Mean vs Total	1.465E+05	1	1.465E+05		
Linear vs Mean	9.71	3	3.24	20.35	< 0.0001
2FI vs Linear	0.1038	3	0.0346	0.1843	0.9052
Quadratic vs 2FI	2.01	3	0.6701	15.60	0.0004 Suggested
Cubic vs Quadratic	0.3291	4	0.0823	4.91	0.0423 Aliased
Residual	0.1006	6	0.0168		
Total	1.465E+05	20	7327.12		

c

Std. Dev.	0.2073	R^2	0.9649
Mean	85.59	Adjusted R^2	0.9334
C.V. %	0.2422	Predicted R^2	0.8824
		Adeq Precision	19.2244

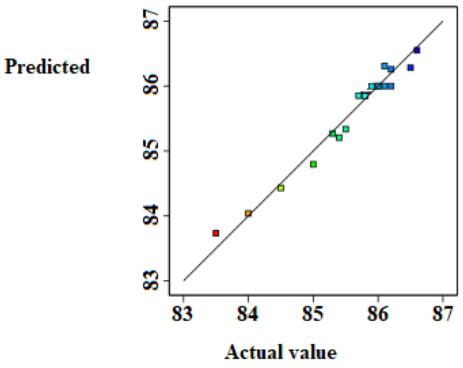


Figure 4. Comparison of Experimental (Actual Value) and Theoretical (predicted) Values in RSM.

4. Discussion

Due to its simple and easy installation, it was found appropriate to use a batch reactor for monitoring and evaluation (Rocha-Meneses et al., 2022). In this study, the 100 mL volume double-walled reactor is one of the

laboratory-scale batch reactors described in Ellacuriaga et al. (2021). Batch reactor can be used in biogas production with AS from organic waste. The results obtained in biogas production with cattle manure and Güldürcek Dam lake eutrophication water showed that it can be used in biogas production.

Portable and small-scale batch reactors have been used in biogas production from animal wastes such as cow manure. There are studies in which biogas production has been optimized with additives such as molasses in these reactors. In this study, it is seen that chemical and oxidative studies were performed as pretreatment (Song et al., 2014; Ramos-Suárez et al., 2017). In our study, methane yield was 86% without pretreatment. This is important in terms of energy saving. Eutrophication water is obtained from water bodies enriched with nutrients and has a high organic matter content. The combination of such waters with cattle manure can increase biogas production. However, studies on this specific combination in the literature are limited.

Mesophilic conditions were chosen for energy saving purposes and because they offer more positive benefits as reported in the literature (Akindolire et al., 2022). The decrease in temperature has a detrimental effect on various AD operating parameters and has a strong negative effect on microbial growth and enzymatic activity, especially among mesophiles and thermophiles (Kalaiselvan et al., 2022). In our study, methane yield was high in the AD process carried out at 35°C.

In general, the aim of biogas optimization is to help increase the efficiency and sustainability of biogas production, thus transforming it into a more viable renewable energy source (Afridi and Qammar 2020). Our study shows that the RSM model explains the experimental data well and is appropriately adapted to the data. The R^2 (0.9649) and standard deviation (0.2073) values found by statistical analysis in the RSM method showed that the experimental data and the model results were compatible. According to the results, 456 grams of cattle manure and 494 grams of eutrophication water should be subjected to anaerobic co-digestion for approximately 17 hours to obtain maximum methane gas yield (86.5%).

5. Conclusions

In this study, anaerobic digestion studies were carried out by using cattle manure from an animal farm located in Eldivan district of Çankırı province and eutrophication water formed due to the decrease in water level in summer months for drinking water supply. The waste samples used in the study were kept at 4 °C before applying advanced treatment processes as stated in the literature. Biogas potential was evaluated using a batch type reactor due to its simple and easy installation for monitoring and evaluation purposes. After loading certain amounts into the reactor, anaerobic conditions were created by pressurizing it with 99.9% pure nitrogen (N_2) gas at 5 bar pressure. The reactor temperature was kept at 35±1 °C in mesophilic conditions. The system was operated at atmospheric pressure in a laboratory environment. The chemical analysis results of the two most efficient wastes in anaerobic digestion were examined and optimum production conditions for biogas production were determined by considering certain mixing ratios, C/N ratios and pH measurements. Experiments with eutrophication water and cattle manure showed that the pH value was 7.035 and the C/N ratio was 15.39 as suitable waste. The biogas formed was obtained by anaerobic digestion of eutrophication water obtained from Güldürcek Dam Lake with cattle manure according to the liquid displacement principle. The effects of factors such as cattle manure, eutrophication water and time on methane gas formation were investigated using the RSM method. In the studies seen in Table 4 (a, b, c), it was concluded that the second-order model proposed in RSM was the most appropriate choice. The Adjusted R^2 value of 0.9334 and the Suitability P-value of 0.1082 provide evidence for the accuracy of the model. The 2FI model is the most appropriate choice against the second-order model, the Mean Square value is 0.6701 and the p-value is 0.0004, which shows the accuracy of the model.

Author Contributions

The percentages of the authors' contributions are presented below. All authors reviewed and approved the final version of the manuscript.

	K.G.	Z.G.Y.
K	40	60
T	40	60
Y	30	70
VTI	40	60
VAY	40	60
KT	40	60
YZ	40	60
KI	30	60
GR	10	90
PY	30	70
FA	30	70

K= concept, T= design, Y= administration, VTI= data collection and/or processing, VAY= data analysis and/or interpretation, KT= literature review, YZ= writing, KI= critical review, GR= submission and revision, PY= project administration, FA= funding acquisition.

Conflict of Interest Statement

The authors declare that they have no conflict of interest in this study.

Ethical Approval Statement

Since this study did not involve any studies on animals or humans, ethics committee approval was not obtained.

Declaration of competing interests

The authors declare that this work was supported by the Çankırı Karatekin University Scientific Research Projects Coordination Unit project number MF210621D02.

References

Ahmad A, Yadav AK, Singh A, Singh DK. 2024. A comprehensive machine learning-coupled response surface methodology approach for predictive modeling and optimization of biogas potential in anaerobic co-digestion of organic waste. Biomass Bioenergy, 180: 106995.

Afridi ZUR, Qammar NW. 2020. Technical challenges and optimization of biogas plants. ChemBioEng Rev, 7(4): 119-129.

Akbay HEG. 2024. Anaerobic mono and co-digestion of agro-industrial waste and municipal sewage sludge: Biogas production potential, kinetic modelling, and digestate characteristics. Fuel, 355: 129468.

Akindolire MA, Rama H, Roopnarain A. 2022. Psychrophilic anaerobic digestion: A critical evaluation of microorganisms and enzymes to drive the process. Renew Sustain Energy Rev, 161: 112394.

Aydoğmuş E, Dağ M, Yalçın ZG, Arslanoğlu H. 2022. Synthesis and characterization of waste polyethylene reinforced modified castor oil-based polyester biocomposite. J Appl Polym Sci, 139(27): e52526.

Bensegueni C, Kheireddine B, Khalfaoui A, Amrouci Z, Bouznada MO, Derbal K. 2025. Optimization of biogas and biomethane yield from anaerobic conversion of pepper waste using response surface methodology. Sustainability, 17(6): 2688.

Bhujbal SK, Preetam A, Ghosh P, Vijay VK, Kumar V. 2025. Machine learning and response surface methodology for optimization of bioenergy production from sugarcane bagasse biochar-improved anaerobic digestion. Process Saf Environ Prot, 106907.

Chanu TN, Nag SK, Koushlesh SK, Devi MS, Das BK. 2022. Greenhouse gas emission from inland open water bodies and their estimation process—an emerging issue in the era of climate change. Agric Sci, 13(2): 290-306.

Dağ M, Aydoğmuş E, Yalçın ZG, Arslanoğlu H. 2023. Diatomite reinforced modified safflower oil-based epoxy biocomposite production: Optimization with RSM and assessment of outcomes by ANN. Mater Today Commun, 35: 106327.

Djimtoingar SS, Derkyi NSA, Kuranchie FA, Yankyera JK. 2022. A review of response surface methodology for biogas process optimization. Cogent Eng, 9(1): 2115283.

Efetobor UJ, Onokwai AO, Onokpite E, Okonkwo UC. 2024. Response surface methodology application for the optimization of biogas yield from an anaerobic co-digestion process. Environ, 10: 12.

El Bari H, Habchi S. 2024. Enhancing biogas production from vinasse through optimizing hydraulic retention time and added load using the response surface methodology. Heliyon, 10(19).

Ellacuriaga M, Cascallana JG, González R, Gómez X. 2021. High-solid anaerobic digestion: Reviewing strategies for increasing reactor performance. Environments, 8(8): 80.

El-Jalil MH, Zinedine A, Faid M. 2008. Some microbiological and chemical properties of poultry wastes manure after lactic acid fermentation. Int J Agric Biol, 10(4): 405-411.

Gong X, Aslam MU. 2024. The role of natural resources, and economic development in evaluating the environmental effects of biofuel and waste energy generation in the group of BRICS. Appl Energy, 372: 123846.

Güven G, Perendeci A, Tanyolaç A. 2008. Electrochemical treatment of deproteinated whey wastewater and optimization of treatment conditions with response surface methodology. J Hazard Mater, 157(1): 69-78.

Hoyos-Sebá JJ, Arias NP, Salcedo-Mendoza J, Aristizábal-Marulanda V. 2024. Animal manure in the context of renewable energy and value-added products: A review. Chem Eng Process-Process Intensif, 196: 109660.

Humphrey I, Obot NI, Humphrey OF, Afuwape NF. 2024. Temperature and pH optimization in mesophilic anaerobic digestion for enhanced biogas production. Biofuels, 1-12.

Jadhav P, Krishnan S, Patil R, Bhuyar P, Zularisam AW, Narayanamurthy V, Nasrullah M. 2024. Improving biogas production with application of trimetallic nanoparticle using response surface methods. Renew Energy, 234: 121199.

Kalaiselvan N, Glivin G, Bakthavatsalam AK, Mariappan V, Premalatha M, Raveendran PS, Sekhar SJ. 2022. A waste to energy technology for enrichment of biomethane generation: A review on operating parameters, types of biodigesters, solar assisted heating systems, socio economic benefits and challenges. Chemosphere, 293: 133486.

Kumar DJP, Mishra RK, Chinnam S, Binnal P, Dwivedi N. 2024. A comprehensive study on anaerobic digestion of organic solid waste: A review on configurations, operating parameters, techno-economic analysis and current trends. Biotechnol Notes, pp:15-16.

Mishra RK. 2023. The effect of eutrophication on drinking water. Br J Multidiscip Adv Stud, 4(1): 7-20.

Mohammadianroshanfekr M, Pazoki M, Pejman MB, Ghasemzadeh R, Pazoki A. 2024. Kinetic modeling and optimization of biogas production from food waste and cow manure co-digestion. Results Eng, 24: 103477.

Monteiro JP, Cruzeiro C, Duarte MS, Pereira MA, Vilar VJ. 2024. Innovative waste activated sludge pre-treatment using a raceway pond reactor: Integration of low-temperature and solar radiation. Chem Eng J, 498: 155324.

Moosavian SF, Noorollahi Y, Shoaei M. 2024. Renewable energy resources utilization planning for sustainable energy system development on a stand-alone island. J Clean Prod, 439: 140892.

Nardi S, Schiavon M, Francioso O. 2021. Chemical structure and biological activity of humic substances define their role as plant growth promoters. Molecules, 26(8): 2256.

Pourrostami Niavol K, Bordoloi A, Suri R. 2024. An overview of the occurrence, impact of process parameters, and the fate of antibiotic resistance genes during anaerobic digestion processes. Environ Sci Pollut Res, 31(29): 41745-41774.

Qian S, Chen L, Xu S, Zeng C, Lian X, Xia Z, Zou J. 2025. Research on methane-rich biogas production technology by anaerobic digestion under carbon neutrality: A review. Sustainability, 17(4): 1425.

Ramos-Suárez JL, Gómez D, Regueiro L, Baeza A, Hansen F. 2017. Alkaline and oxidative pretreatments for the anaerobic digestion of cow manure and maize straw: Factors influencing the process and preliminary economic viability of an industrial application. Bioresour Technol, 241: 10-20.

Risberg K, Sun L, Levén L, Horn SJ, Schnürer A. 2013. Biogas production from wheat straw and manure–impact of pretreatment and process operating parameters. Bioresour Technol, 149: 232-237.

Rocha-Meneses L, Zannerni R, Inayat A, Abdallah M, Shanableh A, Ghenai C, Kikas T. 2022. Current progress in anaerobic digestion reactors and parameters optimization. Biomass Convers Biorefinery, 1-24.

Singh A, Rana MS, Tiwari H, Kumar M, Saxena S, Anand V, Prajapati SK. 2023. Anaerobic digestion as a tool to manage

eutrophication and associated greenhouse gas emissions. Total Environ Sci, 861: 160722.

Song Z, Yang G, Liu X, Yan Z, Yuan Y, Liao Y. 2014. Comparison of seven chemical pretreatments of corn straw for improving methane yield by anaerobic digestion. PLoS One, 9(4): e93801.

Tamilselvan R, Selwynraj AI. 2024. Enhancing biogas generation from lignocellulosic biomass through biological pretreatment: Exploring the role of ruminant microbes and anaerobic fungi. Anaerobe, 85: 102815.

Wang Z, He H, Yan J, Xu Z, Yang G, Wang H, Yuan X. 2024. Influence of temperature fluctuations on anaerobic digestion: Optimum performance is achieved at 45°C. Chem Eng J, 492: 152331.

Wittwer RA, van der Heijden MG. 2020. Cover crops as a tool to reduce reliance on intensive tillage and nitrogen fertilization in conventional arable cropping systems. Field Crops Res, 249: 107736.

Zhang J. 2024. Energy access challenge and the role of fossil fuels in meeting electricity demand: Promoting renewable energy capacity for sustainable development. Geosci Front, 15(5): 101873.

Black Sea Journal of Engineering and Science
doi: 10.34248/bsengineering.1680411

Open Access Journal
e-ISSN: 2619 – 8991

Research Article
Volume 8 - Issue 4: 1111-1120 / July 2025

EARLY FIRE DETECTION MOBILE ROBOTIC SYSTEM WITH HYBRID LOCOMOTION

Hilmi Saygin SUCUOGLU[1]*, Ismail BOGREKCI[1]

[1]Aydin Adnan Menderes University, Faculty of Engineering, Department of Mechanical Engineering, 09010, Aydin, Türkiye

Abstract: In this study, a mobile robotic structure with fire detection and hybrid locomotion capabilities designed and developed. The hybrid locomotion system is an adaptive three-wheeled structure, and it has been structured to provide obstacle climbing and linear motion. The paper puts forward a structure for obstacle avoidance and path planning named "Direction Based Angle Computation". The system is designed to categorize obstacles as either negligible or surmountable, with this classification determined by the height and shape of the obstacles. The objective of the "Fire Search and Find" and "Fire Detection" systems is to identify potential fire locations and calculate the associated probabilities. Experimental tests are conducted for the mechanical structure and architecture of robotic systems. The experimental test results demonstrated that the motion systems have proficiency in both rolling-climbing and linear motions. The Direction Based Angle Computation approach is a proper methodology for the tasks path planning and obstacle avoidance. The proposed fire detection algorithm with the usage of Faster R-CNN machine learning model, has been shown to determine the probability of a fire source with 93% accuracy.

Keywords: Early fire detection, Faster R-CNN machine learning model, Fire detection robot, Hybrid locomotion, Mobile robotic system, Path planning and obstacle avoidance

***Corresponding author:** Aydin Adnan Menderes University, Faculty of Engineering, Department of Mechanical Engineering, 09010, Aydın, Türkiye
E mail: hilmisucuoglu@adu.edu.tr (Hilmi Saygin SUCUOGLU)
Hilmi Saygin SUCUOGLU https://orcid.org/0000-0002-2136-6015
Ismail BOGREKCI https://orcid.org/0000-0002-9494-5405

Received: April 20, 2025
Accepted: May 25, 2025
Published: July 15, 2025

Cite as: Sucuoglu HS, Bogrekci I. 2025. Early fire detection mobile robotic system with hybrid locomotion. BSJ Eng Sci, 8(4): 1111-1120.

1. Introduction

Fire is a type of disaster which causes damage in a variety of locations, including residential dwellings, industrial zones and forests (Haukur et al., 2010; Mishra et al., 2013; Zhou et al., 2020). Despite the hazardous nature of firefighting, which encompasses activities such as fire extinguishing and casualty rescue, it is a vocation that is still primarily undertaken by human operators. These individuals, known as firefighters, are engaged in a profession that entails the risk of personal injury and fatality (Li et al., 2023; Ibitoye et al., 2024). It is imperative to acknowledge that the containment of a fire disaster once it has spread is an insurmountable task. Additionally, the recovery of the affected area is a difficult endeavor. Therefore, the most effective method of firefighting is to detect a fire before it reaches a dangerous level. Different devices have been used for detecting fire at early stages (Bertram et al., 2013; Sucuoglu et al., 2019). Flame and smoke detectors, camera systems are some of these systems. However, those systems have their usage disadvantages as costs and maintenance requirements. This causes the requirement of the usage of mobile systems for early detection purposes (Sulthana et al., 2023).

Early fire detection systems can be grouped into two main methodologies (Dampage et al., 2022; Lee et al., 2023). The first is the physical detection of events of smoke, temperature fluctuations, the presence of flame, or combination of them. The usage of ion, smoke, gas, ultraviolet, and heat sensors has effective performance for early fire detection tasks (Sowah et al., 2016; Fonollosa et al., 2018). However, it is an important requirement that these systems must be placed close to the fire source. These devices are generally good options for indoor environment usages. (Zhang et al., 2019; Sucuoglu et al., 2020; Khan et al., 2022; He et al., 2023). The second is detection of fire sources with images. The process of determining the presence of fire is facilitated by the analysis of various physical phenomena, including the color, shape, behavior and combinations of flame and smoke properties (Cetin et al., 2013; Rehman et al., 2020; Alqourabah et al., 2021). Nowadays, machine learning algorithms, such as CNNs (Convolutional Neural Networks), have been also used for fire detection in video streams (Luo et al., 2018; Park et al., 2020; Li et al., 2023; Buriboev et al., 2024).

Recent studies have also focused on the usage of mobile robots to perform various tasks such as surveillance, reconnaissance, patrol, firefighting, homeland security, entertainment, and service. Mobile robotic systems for early fire detection and firefighting purposes have certain advantages over stationary systems. Those advantages are lower cost, minimal maintenance requirements, and the capacity for versatile applications

This work is licensed (CC BY-NC 4.0) under Creative Commons Attribution 4.0 International License

such as patrolling, security, and early fire detection (Alqourabah et al., 2021; Nguyen et al., 2024; Pandian, 2025). For locomotion of the mobile robotic systems, various mechanical structures have been proposed. Within these structures, three primary categories are:
W (wheeled), T (tracked), and L (legged). Furthermore, hybrid structures have been created, namely LW (leg-wheel), LT (leg-track), WT (wheel-track) and LWT (leg-wheel-track). Each of them has its own advantages and disadvantages when evaluated with performance criteria such as velocity, obstacle avoidance, climbing, motion and slope adaptation, motion adaptation and energy efficiency. A performance comparison table of the motion systems is presented in Figure 1.

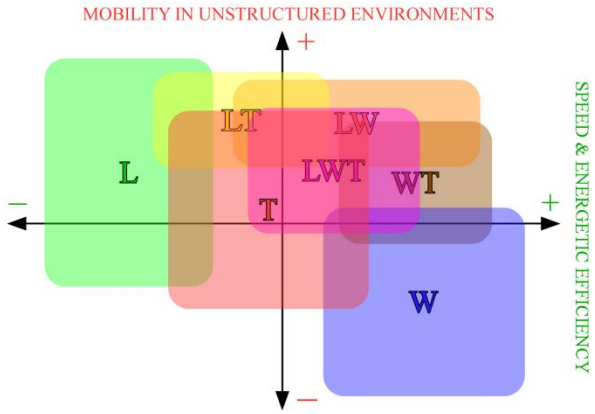


Figure 1. Performance chart of locomotion systems (Bruzzone et al., 2022).

As demonstrated in Figure 1, the hybrid categories have been designed and developed to utilize the main categories of wheeled, tracked and legged. Nevertheless, it is not possible to fully realize the total gain, due to the extra load effects of the additional motion elements. These hybrid systems are well-suited for operational environments that demand rapid movement and the ability to overcome obstacles. The construction of hybrid systems can be achieved through the following four methodologies (Raibert et al., 1986; Manchester et al., 2011).

1.Connection of the legs to main structure of the wheeled robotic system
2.Combination of the wheel and legs to operate together
3.Utilization of retractable modules
4.Wheel placement at the end of the legs

In this study, an early fire detection mobile robotic system with hybrid locomotion is proposed. Hybrid locomotion structure is developed by a three-wheeled mechanism. A transition system with a decision structure for classifying the obstacles has been proposed for adaptive motion. This study also includes path planning and obstacle avoidance structure with the name of "Direction-Based Angle Computation". This structure is constructed for the classification of paths and obstacles in the operation environment. The "Fire Search and Find" structure is also designed to decide the probability of fire sources. The location of the fire source is detected by flame sensors. Then, the "Fire Detection" structure created using Faster R-CNN machine learning model determines the probability of a fire. The operator can also monitor the system via wireless connection.

2. Materials and Methods

2.1. Mechanical Structure

The design and assembly of parts are conducted using Autodesk Inventor Software. The overall design and 3D details of the robotic structure are shown in Figure 2. The engineering drawings including part list and exploded view and dimensional information are also prepared. These documents involve detailed information of the sizes and used parts-hardware. These are useful for sourcing the required hardware and parts. The dimensions and weight of the robotic system are important parameters as they affect mobility and energy consumption. The total weight of the system, including all mechanical and electronic components, is approximately 10.5 kilograms. The overall dimensions, parts list, and exploded view of the robotic system structure are presented in Figures 3,4, and Table 1, respectively.

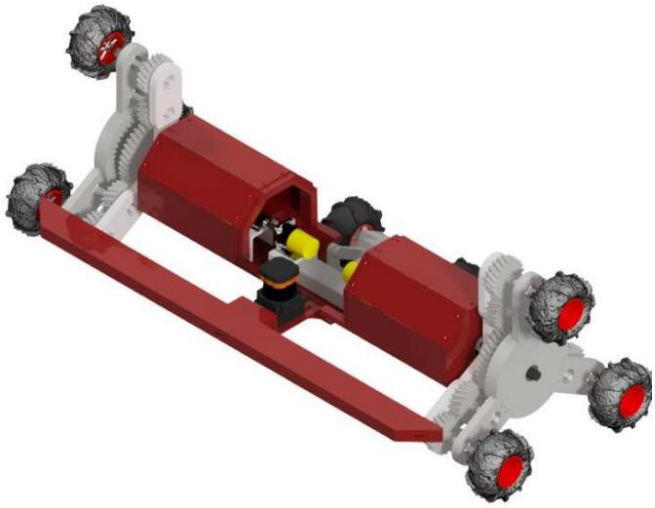


Figure 2. Overall design view of the robotic structure.

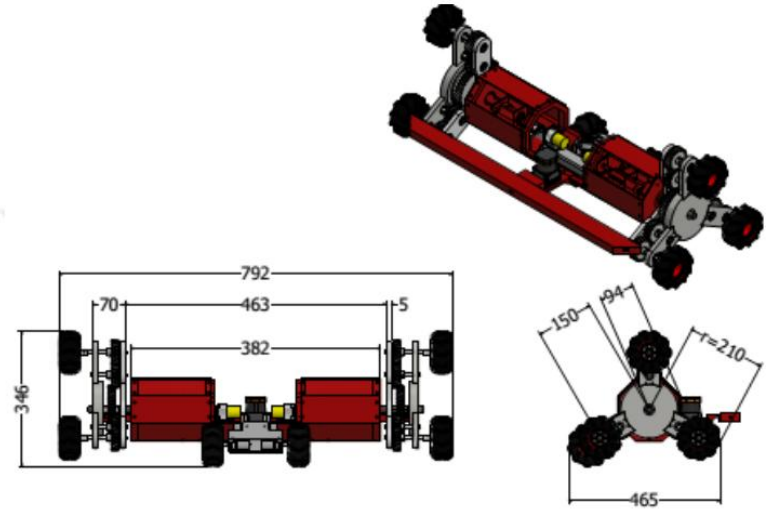


Figure 3. General dimensions.

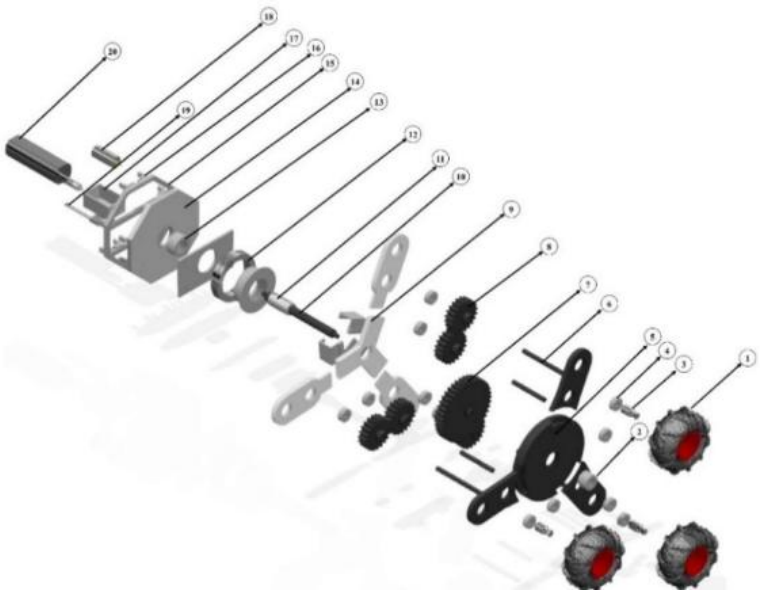


Figure 4. Part list and exploded view

Table 1. Part list of the robotic system

No	Name of the Components	Pieces
1	Wheels	8
2	Housing rubbers	2
3	Shaft to wheel connectors	8
4	Bearings	24
5	Outer covers	2
6	Shafts	12
7	Gears	2
8	Inner-outer gears	12
9	Inner covers	2
10	Main shafts	2
11	Couplings	2
12	Axial bearing	2
13	Ball bearings	2
14	Covers	2
15	Frames	2
16	Brackets	18
17	Motor covers	2
18	DC motors	2
19	Linear motion guides	2
20	Linear actuators	2

2.2. Material Selection and Manufacturing

Mechanical components of the robotic system, apart from motor wheel connector and shaft, the prototype is structured using the thermoplastic polylactide acid (PLA) material and the fused deposition modelling (FDM) method. The reason behind this choice is to take advantage of the benefits of PLA material, such as its biodegradability, high printing speed and lower layer height requirements. The infill type and density are specified as hexagonal and 50%, respectively, with the objective of reducing material consumption while ensuring adequate structural strength. The motor wheel connectors and shafts are produced using S 235 steel, with the wheels being selected to have a diameter and width of 120 and 60 mm, respectively.

2.3. Electronic Hardware of Robotic System

The robotic system is comprised of two primary electronic systems. The initial approach involves the utilization of Lidar and ultrasonic distance sensor data for the purpose of movement control. The second is for the purpose of fire detection via webcam and Raspberry Pi. The list of the electronic components is given in Table 2.

Table 2. Electronic component list of the robotic system

No	Name of the Components	Pieces
1	Hokuyo UTM-30 LX Lidar (detection range of 0.1 to 30 m)	1
2	Raspberry pi 3B	1
3	Flame sensors (detection range up to 1 m)	3
4	Lipo batteries	3
5	Ultrasonic distance sensors (detection range of 0.2 to 4 m)	2
6	Power bank	1
7	Arduino Mega 2560	1
8	Motor Drivers	3
9	DC Motors	3
10	Linear actuators	2

2.4. Operational Architecture of the Robotic System

The robotic system is comprised of four primary algorithms. The following subjects are covered: "Motion Mode Decision", "Direction-Based Angle Computation", "Fire Search and Find" and "Fire Detection". Initially, the motion mode decision algorithm determines the type of motion based on the measured obstacle height. The movement may be either climbing or linear. The hybrid locomotion structure is capable of operating for those two cases. In the absence of any obstacles or if the height of the obstacle falls within the passable range (up to 120 mm), the robotic system can traverse the obstacle through linear motion. In instances where the height falls within the range of 120-200 mm, the transition is initiated by a transmission system. The center gear is pushed by the linear actuator, which positions the gear at the center of the transmission system. Subsequently, the entire roll is activated, enabling the robotic system to ascend an obstacle or traverse terrain with the three-wheeled roll motion. For obstacles measuring over 200 mm, the obstacle avoidance mode is initiated, enabling the robotic system to navigate by employing a direction-based angle computation algorithm structure. In instances where the movement is categorized as obstacle avoidance, the robotic system endeavors to ascertain the safest route to the target by employing a direction-based angle computation approach. In the direction-based angle computation approach, the robot's field of view, obtained through Lidar, is divided into five regions for the purpose of determining the shape of obstacles and deciding on the required movement types (Figures 5 and 6). Figures 5 and 6 present the detailed region indication and the responses of the robotic system according to the obtained data. The determination of the types of motion path is contingent upon the obstacle occurrence zone and distance. The linear velocity has been adjusted as 0.5 m/s for experimental tests. The "Fire Search and Find" structure has been designed to find the locate the fire source using the data from IR flame sensors. The activation of this algorithm occurs in the "No Obstacles" state within the field of view.

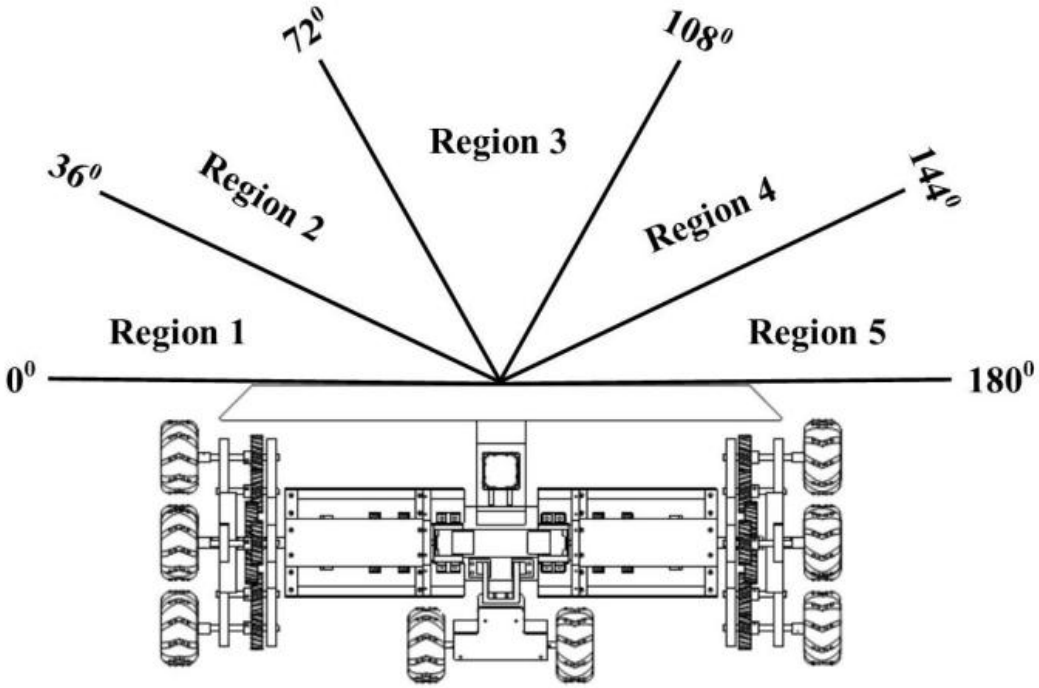


Figure 5. Regions of path planning and obstacle avoidance structure.

Name of the Situation	Regions					Reaction of the System
	Region 1	Region 2	Region 3	Region 4	Region 5	
Fire Search						Try to Find the Fire Source
Front Obstacle			■			Turn Right (Smooth)
Front Left Obstacle		■				Turn Right (Smooth)
Left Obstacle	■					Turn Right (Smooth)
Front Left Obstacle	■	■				Turn Right (Smooth)
Front Right Obstacle				■		Turn Left (Smooth)
Right Obstacle					■	Turn Left (Smooth)
Front Right Obstacle				■	■	Turn Left (Smooth)
Left Corner		■	■			Turn Right (Sharp)
Right Corner			■	■		Turn Left (Sharp)
Obstacle		■	■	■		Turn Right (Sharp)
Left Corner	■	■	■			Turn Right (Sharp)
Right Corner			■	■	■	Turn Left (Sharp)
Corridor		■		■		Move Forward
Corridor	■				■	Move Forward
Corridor	■	■		■	■	Move Forward
Trap	■	■	■	■	■	Stop the Motion

Figure 6. Motion types of path planning and obstacle avoidance structure.

The Fire Detection structure is proposed to calculate the probability of fire candidates. Fire Detection structure created using Faster R-CNN machine learning model determines the probability of a fire. The experiment was conducted using a system with the following specifications: NVidia GeForce GTX 1070 Ti with 17 GB onboard memory. The required environments and tools (Python 3.5, Tensorflow 1.13.1, OpenCV, CUDA-cuDNN toolkits) were installed on the Anaconda virtual environment. The fire scenes on the images were labeled as fire and non-fire using LabelImg software. The converter function was selected as Softmax, number of steps for the learning was determined as 40,000 and the number of epochs was used as 3. 80% of images were used for training and 20% of the images were dedicated for test processes.

Fire Candidates are indicated with the data from the Fire Search and Detection structure. If any object is identified as a "Fire Candidate", the Fire Detection structure is activated to calculate the probability of the fire. The flowchart of the fire detection is illustrated in Figure 7.

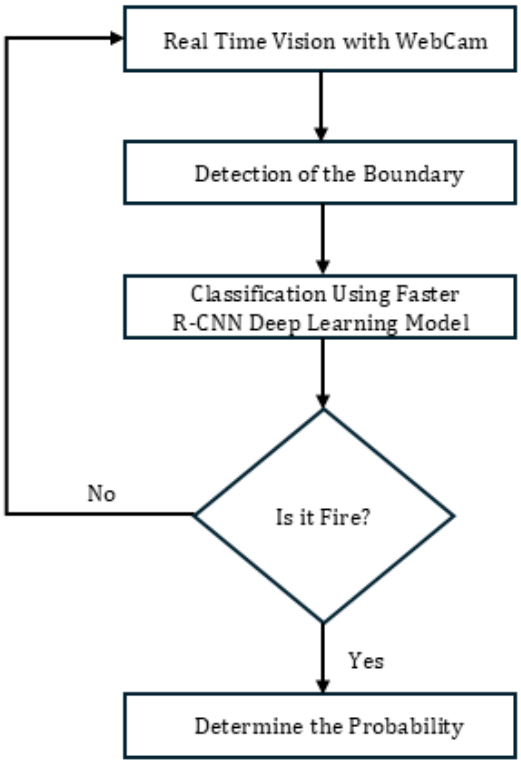


Figure 7. Flowchart of fire detection.

3. Results and Discussion

Real-time experiments are used to test the overall performance of the mechanical structure, hybrid motion system, obstacle avoidance and path planning, and fire detection. A test bench is built to test the motion decision and hybrid motion. A side transmission system is placed on the test bench. Distance sensors are also placed to trigger transitions from linear motion to climbing motion and vice versa, as shown in Figure 8. The test bench was designed and produced with proper mounting places for the transmission system and required hardware. It was produced using 1050 steel material for mounting parts and wooden material for the base.



Figure 8. Test bench of the motion decision and hybrid motion systems.

It is evident from the experimental tests that the motion decision algorithm is capable of seamlessly initiating transitions between motion modes in accordance with the measured height data. The center gear can correctly locate the center of the transmission gear system, thereby enabling the full rolling motion to be realized. In the absence of any impediments or steps, the center gear is retracted, thereby initiating linear motion.

The structure of obstacle avoidance and path planning is built on the data obtained from the Hokuyo lidar. The system's architecture is predicated on the direction-based angle computation algorithm that has previously been proposed. Preliminary and real motion tests are performed. The proposed path planning and obstacle avoidance algorithm is tested based on the lidar data, with obstacles placed in various directions. The results obtained for the stop area and front right obstacle conditions are presented in Figures 9 and 10, respectively. The results obtained demonstrate that the proposed structure can respond appropriately to regional obstacles.



Figure 9. Case of stop area.



Figure 10. Case of front right obstacle.

After the bench tests of the hybrid locomotion tests and preliminary tests of the path planning and obstacle avoidance structure, the real-life operational experiments are conducted. The obstacles, including dynamic, are placed in different directions. The obstacle avoidance and climbing performances of the robotic structure are tested. It has been demonstrated through experimental investigation that the robotic system has the capacity to locate obstacles using direction-based angle computation algorithms. The system is also capable of navigating such obstacles with precision, identifying their type, and climbing over them by utilizing the full range of rolling motion (Figures 11 and 12).



Figure 11. Obstacle avoidance.



Figure 12. Climbing motion.

Preliminary and real fire detection tests are performed to evaluate the fire detection capability. First, fire detection capacity is tested with lighter and candidate flames. As demonstrated in the empirical findings (Figure 13), the fire detection structure demonstrates an exceptional capacity to accurately categorize fire sources, exhibiting a 99% accuracy rating. With this obtained result, it is evident that the fire detection capacity of the robotic system is reliable for fire detection tasks.

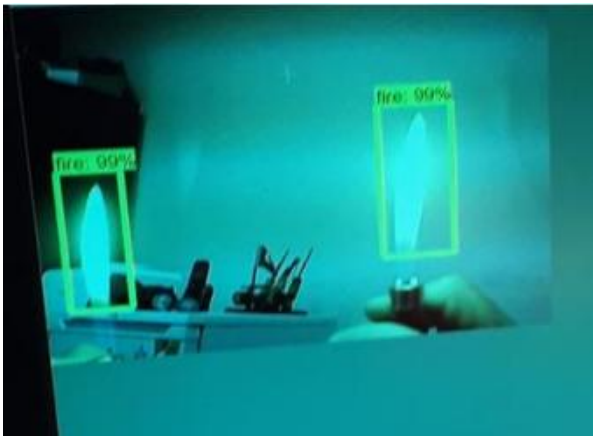


Figure 13. Preliminary fire detection test.

Real-life performance tests are conducted for three different fire sources: candle, wood and complex (Figures 14,15 and 16). The term "complex fire" is a combination of candle, paper and wood.

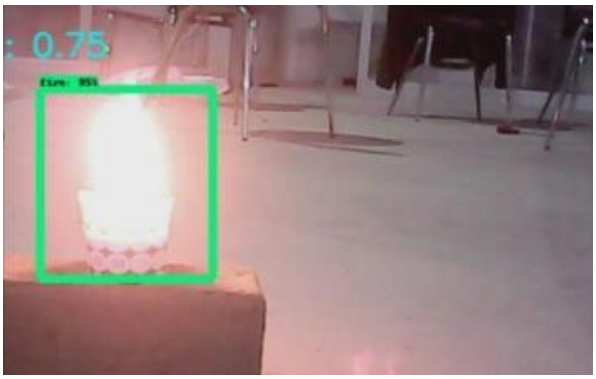


Figure 14. Candle fire detection.



Figure 15. Wood fire detection.



Figure 16. Complex fire detection.

The average detection values obtained for candle, wood and complex fires were 86%, 90% and 93%, respectively as presented in Figures 14,15 and 16. The candle fire detection process has been found to demonstrate the lowest detection accuracy. This can be explained with the reduced size of the flame and the number of flickering scenes in detection process. The detection accuracy increases to 90% for wood and 93% for complex fire detection.

4. Conclusion

The present study involves the design and development of a mobile robotic structure with fire detection and hybrid locomotion capabilities. The hybrid locomotion system is an adaptive, three-wheeled structure designed to provide obstacle climbing and linear motion capabilities. The paper proposes a structure for obstacle avoidance and path planning called "Direction Based Angle Computation". The system categorizes obstacles as either negligible or surmountable based on their height and shape. The objective of the "Fire Search and Find" and "Fire Detection" systems is to identify potential fire locations and calculate the associated probabilities. The location of the fire source is detected by flame sensors. Consequently, the "Fire Detection" structure is created using a Faster R-CNN machine learning model, which determines the probability of a fire. A series of experimental tests were conducted on the mechanical systems and algorithms of the mobile fire detection robotic system. In accordance with the results obtained, the following conclusions are reached:

- The transmission and motion systems can climb over obstacles and move in a straight line.
- The motion decision algorithm can determine the required motion type successfully according to the situation of the obstacle.
- Direction-based angle calculation approach is both suitable and satisfactory for local path planning and obstacle avoidance applications.
- The fire search and find algorithm has been demonstrated to detect the fire source when placed on the front, right and left sides of the robotic system, successfully activating the fire detection algorithm.
- The developed fire detection algorithm, employing the Faster R-CNN deep learning model, has been demonstrated to achieve a 93% accuracy in determining the probability of detected fire sources.

As future research directions:

- The creation of a hybrid fire detection algorithm is planned, which will use thermal and RGB images in the training and detection processes.
- It is also planned to use the ROS (Robotic Operation System) for the mapping, localization and path planning applications of the robotic system.

Author Contributions

The percentages of the authors' contributions are presented below. All autho() reviewed and approved the final version of the manuscript.

	H.S.S	I.B.
C	50	50
D	50	50
S	50	50
DCP	50	50
DAI	50	50
L	50	50
W	50	50
CR	50	50
SR	50	50
PM	50	50
FA	50	50

C=Concept, D= design, S= supervision, DCP= data collection and/or processing, DAI= data analysis and/or interpretation, L= literature search, W= writing, CR= critical review, SR= submission and revision, PM= project management, FA= funding acquisition.

Conflict of Interest

The authors declared that there is no conflict of interest.

Ethical Consideration

Ethics committee approval was not required for this study because there was no study on animals or humans.

References

Alqourabah H, Muneer A, Fati SM. 2021. A smart fire detection system using IoT technology with automatic water sprinklers. Int J Electr Comput Eng, 11(4).

Bertram C, Evans MH, Javaid M, Stafford T, Prescott T. 2013. Sensory augmentation with distal touch: The tactile helmet project. In: Biomimetic and Biohybrid Systems, Proc Second Int Conf Living Machines, London, UK, pp: 24-35.

Bruzzone L, Nodeh SE, Fanghella P. 2022. Tracked locomotion systems for ground mobile robots: A review. Machines, 10(8): 648.

Buriboev AS, Rakhmanov K, Soqiyev T, Choi AJ. 2024. Improving fire detection accuracy through enhanced convolutional neural networks and contour techniques. Sensors, 24(16): 5184.

Cetin AE, Dimitropoulos K, Gouverneur B, Grammalidis N, Günay O, Habiboğlu YH, Verstockt S. 2013. Video fire detection – review. Digit Signal Process, 23(6): 1827-1843.

Dampage U, Bandaranayake L, Wanasinghe R, Kottahachchi K, Jayasanka B. 2022. Forest fire detection system using wireless sensor networks and machine learning. Sci Rep, 12(1): 46.

Fonollosa J, Solórzano A, Marco S. 2018. Chemical sensor systems and associated algorithms for fire detection: A review. Sensors, 18(2): 553.

Haukur I, Heimo T, Anders L. 2010. Industrial fires: An overview. Brandforsk Project, SP Report 2010:17, SP Tech Res Inst Sweden, Borås, Sweden, pp: 15-26.

He Y, Zhang H, Arens E, Merritt A, Huizenga C, Levinson R, Alvarez-Suarez A. 2023. Smart detection of indoor occupant thermal state via infrared thermography, computer vision, and machine learning. Build Environ, 228: 109811.

Ibitoye OT, Ojo AO, Bisirodipe IO, Ogunlade MA, Ogbodo NI, Adetunji OJ. 2024. A deep learning-based autonomous fire detection and suppression robot. In: Proc 2024 IEEE 5th Int Conf Electro-Computing Technologies for Humanity (NIGERCON), Abuja, Nigeria, pp: 1-4.

Khan A, Hassan B, Khan S, Ahmed R, Abuassba A. 2022. DeepFire: A novel dataset and deep transfer learning benchmark for forest fire detection. Mob Inf Syst, 5358359, pp: 52-56.

Lee CH, Lee WH, Kim SM. 2023. Development of IoT-based real-time fire detection system using Raspberry Pi and fisheye camera. Appl Sci, 13(15): 8568.

Li X, Chen G, Amyotte P, Alauddin M, Khan F. 2023. Modeling and analysis of domino effect in petrochemical storage tank farms under the synergistic effect of explosion and fire. Process Saf Environ Prot, 176: 706-715.

Luo Y, Zhao L, Liu P, Huang D. 2018. Fire smoke detection algorithm based on motion characteristic and convolutional neural networks. Multimed Tools Appl, 77: 15075-15092.

Manchester IR, Mettin U, Iida F, Tedrake R. 2011. Stable dynamic walking over uneven terrain. Int J Robot Res, 30(3): 265-279.

Mishra KB, Wehrstedt KD, Krebs H. 2013. Lessons learned from recent fuel storage fires. Fuel Process Technol, 107: 166-172.

Nguyen AP, Nguyen NX. 2024. Control autonomous mobile robot for firefighting task. In: Proc 2024 Int Conf Control, Robotics and Informatics (ICCRI), Hanoi, Vietnam, pp: 37-41.

Pandian DS. 2025. Optimized deep learning approach for automated fault diagnosis in mobile robot used for fire-fighting application. Evol Syst, 16(2): 36.

Park S, Han KW, Lee K. 2020. A study on fire detection technology through spectrum analysis of smoke particles. In: Proc 2020 Int Conf Inf Commun Technol Converg (ICTC), Jeju, South Korea, pp: 1563-1565.

Raibert MH. 1986. Legged Robots That Balance. MIT Press, Cambridge, MA, USA, pp:45-46.

Rehman A, Qureshi MA, Ali T, Irfan M, Abdullah S, Yasin S, Węgrzyn M. 2021. Smart fire detection and deterrent system for human savior by using internet of things (IoT). Energies, 14(17): 5500.

Sowah RA, Ofoli AR, Krakani SN, Fiawoo SY. 2016. Hardware design and web-based communication modules of a real-time multisensor fire detection and notification system using fuzzy logic. IEEE Trans Ind Appl, 53(1): 559-566.

Sucuoglu HS, Bogrekci I, Demircioglu P. 2019. Real time fire detection using Faster R-CNN model. Int J 3D Print Technol Digit Ind, 3(3): 220-226.

Sucuoglu HS. 2020. Development of a robotic system with hybrid locomotion for both indoor and outdoor fire detection operations. PhD thesis, Aydin Adnan Menderes University, Institute of Science, Aydin, Türkiye, pp: 176.

Sulthana SF, Wise CTA, Ravikumar CV, Anbazhagan R, Idayachandran G, Pau G. 2023. Review study on recent developments in fire sensing methods. IEEE Access, 11: 90269-90282.

Zhang R, Cheng Y, Li Y, Zhou D, Cheng S. 2019. Image-based flame detection and combustion analysis for blast furnace raceway. IEEE Trans Instrum Meas, 68(4): 1120-1131.

Zhou Y, Pang Y, Chen F, Zhang Y. 2020. Three-dimensional indoor fire evacuation routing. ISPRS Int J Geo-Inf, 9(10): 558.

Black Sea Journal of Engineering and Science
doi: 10.34248/bsengineering.1603745

Open Access Journal
e-ISSN: 2619 – 8991

Research Article
Volume 8 - Issue 4: 1121-1126 / July 2025

ARTIFICIAL NEURAL NETWORKS IN DRUG ADDICTION DIAGNOSIS

Engin KARAMAN[1]*

[1]*Fenerbahçe University, Faculty of Economics, Administrative and Social Sciences Department of Management İnformation Systems, 34758, İstanbul, Türkiye*

Abstract: This study aims to find a simple mechanism to help researchers and families identify addicts. In this paper, the Artificial Neural Network (ANN) method has been examined to determine whether a person is an addict. In this study, the dataset obtained from students from different countries and published as open source by Atif Masih was used. This dataset contains 50343 samples with 11 features. The study involved testing and comparing multiple neural network architectures based on their average classification accuracy. When the correlation matrix is examined, it is seen that the relationships between the variables are almost negligible. This can be attributed to the fact that the variables are categorical. Each architecture was trained using 10 different seed numbers, and the mean accuracy was calculated accordingly. The experiment results have obtained 75.53% classification accuracy for correct diagnosis in our system. Our model could significantly expedite the diagnosis and treatment of addiction, providing a valuable tool for families, physicians, and investigators. The paper proposes a Decision Support System (DSS) for diagnosing addiction, leveraging one of the most widely-used machine learning techniques: Artificial Neural Networks (ANN).

Keywords: Drug addiction, Artificial neural network, Decision support system

Corresponding author: Fenerbahçe University, Faculty of Economics, Administrative and Social Sciences Department of Management İnformation Systems, 34758, İstanbul, Türkiye
E mail: enginkaraman1013@gmail.com (E.KARAMAN)
Engin KARAMAN https://orcid.org/0000-0002-2336-6289

Received: December 18, 2024
Accepted: June 03, 2025
Published: July 15, 2025

Cite as: Karaman E. 2025. Artificial neural networks in drug addiction diagnosis. BSJ Eng Sci, 8(4): 1121-1126.

1. Introduction

Addictions (alcohol, drug et al.) can affect people regardless of their social orfinancial status or age. Many factors of psychological, biological or socio-economic nature are responsible for these addictions. Everything together makes determining its causes (Lewenstein et al, 2020). Drugs have been the core reason for the various crimes occurring in the society and also the root cause for the devastation of many youngsters. Drug habits are addictive and have also led to the death occurrence of thousands of addicts (Junghare et al, 2019). As a result of the complexity and overlapping symptoms, it becomes intrinsically difficult to differentiate addiction from various other diseases. This inherent ambiguity demands greater level of efforts and vigilance from part of the investigators and family members. They have, therefore to embrace a complex model that fuses deeply the observational data with more valid diagnostic tools. They, in so doing, assume a better position to address an individual's needs and offer suitable interventions. This process therefore evidences the fact that full-fledged diagnostic techniques and support need to come up for not only the diagnostic tools but also the persons involved in the process of identification and treatment of the addiction.

Machine learning techniques have been the main area of interest for researchers in the computer science field over the past few years. The main reason for interest in machine learning techniques is due to their apparent relation with the essential skills associated with intelligence. Machine learning literature is very rich in learning theory, and these techniques have normally improved the speed and accuracy of the learning mechanism for a number of concepts significantly (Bottou, 2014). Today, technology in machine learning has been of immense help in processing medical data. Many research works have been carried on diagnosis in medicine, and the outcome of the research is excellent. Certain big hospitals maintain the data of correct diagnosis in the form of case histories. This information can be fed into the computer and, after running the learning program, excellent results can be obtained. In theory, this would be feasible from the descriptions of cases solved in the past: the automatic derivation of medical diagnostic knowledge with the view to improve diagnosis speed and accuracy, hence reliability. Also, this can be used to teach nonspecialist students or doctors how to diagnose patients in some specific diagnostic problems (Fausett, 2006; Michalski et al, 1983).

This study aims to find a simple mechanism to help researchers and families identify addicts. In this paper,

This work is licensed (CC BY-NC 4.0) under Creative Commons Attribution 4.0 International License

the Artificial Neural Network (ANN) method has been examined to determine whether a person is an addict. This method was implemented by analyzing several cases of addiction from different countries (Pakistan, Afghanistan etc.). In this context, the potential of ANN for analyzing addiction cases and making accurate diagnoses has been evaluated. In conclusion, machine learning techniques play a significant role in medical diagnostic processes and can be an effective tool in solving complex issues like addiction. This study highlights the practical applications of ANN, shedding light on potential research and development opportunities in this field.

2. Materials and Methods

There are many studies in the literature using machine learning techniques on drug addiction. Islam Arif et al, (2021) made a prediction using machine learning algorithms on addiction, which has become a significant problem in Bangladesh. For this purpose, they applied nine machine learning algorithms (namely k-nearest neighbors, logistic regression, SVM, naïve bayes, classification, and regression trees, random forest, multilayer perception, adaptive boosting, and gradient boosting machine). Among these algorithms, the Logistic regression algorithm stood out with 97% accurate prediction. Kumari et al, (2018) presented a model of addict abuse prediction with the help of machine learning techniques. Their model was flexible enough to include several features such as age, gender, country, ethnicity, education level, neuroticism, openness to experience, extraversion, agreeableness, conscientiousness, impulsivity and sensation seeking. Other temporal features used were day, week, month, year, and decade. All of the above-mentioned features were combined by the authors within their Artificial Neural Network for Demographics and Artificial Neural Network for Chronological data models, ANN-D, and ANN-C respectively. The authors combined demographic and time series features in their model to gain better predictive accuracy and, more importantly, to shed more light on the correlates of addict abuse. Afzali et al, (2019) compared the performance of seven machine learning algorithms to predict drug-alcohol use among adolescents in Australia and Canada and interpreted the difference between them. As a result, the elastic network machine learning algorithm showed the best predictive performance in both the Canadian and Australian samples. (Shahriar et al, 2019) were to aim to find out the important social, familial and health factors related to drug abuse of the age group of 15-40. they used three algorithms (ANN, Random Forest and SVM) for this. Consequently, among these three models, ANN performed the highest accuracy rate (%93).

2.1. Artificial Neural Network

The term "Artificial Neural Network" is derived from Biological neural networks developing the structure of a human brain. Much similar to a human brain, artificial neural networks also have neurons which are interconnected to one another in different layers of the networks. These neurons are known as nodes.

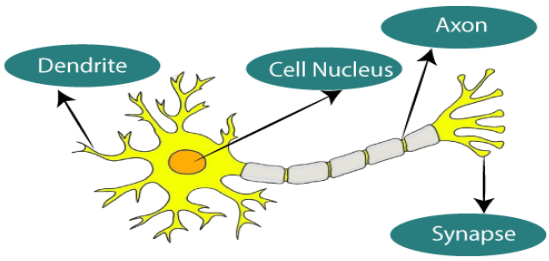


Figure 1. Structure of biological neural network.

An artificial neural network in the realm of Artificial Intelligence is so that computers may have the opportunity to understand things and make decisions in a manner somewhat human, trying to emulate the network of neurons that make up a human brain. An artificial neural network is created through the programming of computers to act simply like the interconnected cells of the brain. There are about 1000 billion neurons in the human brain. Each neuron has a connection point somewhere between 1,000 and 100,000. The information is stored in such a way that it is distributed, and we can draw out more than one unit of this information while needed from our memory parallelly in the human brain. We can say the human brain is composed of unbelievably great parallel processors (Araghinejad, 2014).

Artificial Neural Networks (ANNs) are composed of an input layer, a number of hidden layers, and an output layer (Bottou, 2014). The input layer comprises several neurons, each representing a system input, with each neuron assigned a weight that adaptively changes during the training phase. The hidden layers are particularly useful for handling data that are not linearly separable, allowing the network to capture more complex patterns. The final layer, the output layer, represents the ultimate output of the network. The learning process of ANNs involves the user collecting representative datasets and applying training algorithms to enable the network to automatically discern and learn the underlying patterns in the data. Through this training process, the ANN adjusts its weights and biases to minimize errors and improve its predictive accuracy (Vaswani et al, 2017).

There are various types of Artificial Neural Network (ANN) models, with the Multilayer Perceptron (MLP) being the most prevalent. An MLP consists of three or more layers, including an input layer, an output layer, and one or more hidden layers. The primary objective of the MLP is to establish a mapping function $F:X \rightarrow Y$ that correlates the input X with the output Y, leveraging the historical data collected during training. Consequently, the MLP can be employed to predict outputs for new, unseen inputs based on the learned relationship (Poulton, 2001).

Figure 2 shows a simple Multilayer Perceptron neural

network in which, in most cases, a bias is added to the input layer with weight value one so that neural network may not get saturated. The inputs provided are fed into the input layer and then multiplied by the weights as they pass from the input layer to the first hidden layer. These weighted inputs are summed in each neuron inside the hidden layer and processed by a transfer function.

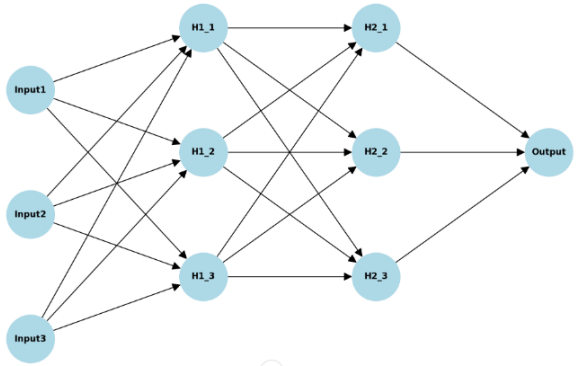


Figure 2. Artificial Neural Network (ANN) structure.

Neural networks utilize transfer functions to transition from one layer to the next. These functions incorporate mathematical formulas to generalize the desired output. There are several types of transfer functions commonly used in ANNs, among which the most prevalent are:

- Linear Transfer Function (LF): This function is computed simply as a=n, where n represents the sum of the weighted inputs.
- Log-Sigmoid Transfer Function: This function has a range between 0 and 1, and its formula (equation 1) is given by:

$$1a = \frac{1}{1+e^{-n}} \quad (1)$$

This description highlights the basic operation and common transfer functions within a simple MLP neural network, illustrating how inputs are processed through weighted connections and transfer functions to produce the network's output (Araghinejad, 2014).

There are numerous algorithms that can be utilized during the training phase of a Multilayer Perceptron (MLP). In this study, we employ one of the most widely recognized neural network algorithms known as the Feed Forward Back Propagation learning algorithm. With this algorithm, the input is repeatedly fed into the neural network, and for each output, the corresponding typical output and error are calculated. This error is then backpropagated through the neural network and used to adjust the weight values, thereby reducing the error with each iteration and enabling the neural network to approximate the typical output more closely.

Artificial Neural Networks (ANNs) possess the remarkable ability to classify new or noisy data, a feature known as generalization. Generalization is one of the primary advantages of ANNs. Optimal generalization is achieved when the dataset is divided into two distinct parts:

- *Training Set:* Used to train the neural network.
- *Testing Set:* Employed for the final evaluation of the neural network's overall performance.

By partitioning the dataset in this manner, the neural network can be effectively trained, validated, and tested, ensuring robust generalization capabilities and reliable performance on new and unseen data.

2.2. Data Preparation

In this study, the dataset obtained from students from different countries and published as open source by Atif Masih (Kaggle, 2024), an academician at Govt Islamia Graduate College Kasur University-Pakistan, will be used. This dataset provides in-depth information about variables related to drug addiction among university students. The dataset contains features from experimentation to denial of treatment that would be very insightful related to the study of addictive behavior dynamics. It includes a target variable classifying students addicted or non-addicted based on these features. This dataset contains 50343 samples with 11 features (Table 1).

Table 1 illustrates the name, description and category of the features. Also, We have checked if there is a null value in the data set. The last column defines the number of missing values for the relevant attribute. All variables were encoded into numerical inputs to be used in the neural network, which receives numerical inputs values as variables with two independent attributes, such as: Social Isolation item is encoded into binary values of 0,1; for instance, the answer to the attribute could be 1, which means "Yes," and 0, which means "NO".

First, we evaluated how we would develop a policy regarding missing values. There are many methods for this (such as assigning mode, median or mean). However, these preferences can lead to data manipulation. İn conclusion, it was deemed appropriate to remove null examples from the data set, both because the data set was large and because it included clarity. As a result of this arrangement, the number of examples were decreased from 50.342 to 30.073. Of the students in this dataset, 9.120 declared that they were drug addicts and 20.953 declared that they were not addicts. In binary classification problems, with data samples coming from two groups-as in the study at hand-the problem of class imbalance occurs when one class contains significantly fewer samples compared to the other class, representing the majority. In many cases, the minority group is of interest, that is, the positive class (Johnson and Khoshgoftaar, 2019). One famous example of class imbalance in machine learning relates to the medical diagnostic task of disease detection-the majority of patients do not have a disease and the interest lies in detecting it. In that case, the majority group may be a group of healthy patients who fall into the negative class. It becomes very hard to learn from such imbalanced datasets. First of all, one should comprehensively

understand the class imbalance problem and the existing methods to address it, as this kind of skewed data is present in many real-world applications. Unfortunately, this was also a characteristic of our dataset, which had a negative impact on the prediction.

Table 1. List of features

Features	Abbreviations	Description	Category	Missing Value
Addiction Class	AC	Classifies students as addicted or non-addicted	1:Yes 0: No	0
Experimentation	Exp	Whether the student has experimented with drugs	1:Yes 0: No	2562
Academic Performance Decline	APD	Indicates if there's a decline in academic performance due to drug use	1:Yes 0: No	2498
Social Isolation	SI	Whether drug use leads to social isolation	1:Yes 0: No	2550
Financial Issues	FI	Indicates if the student faces financial difficulties due to drug use	1:Yes 0: No	2537
Physical Mental Health Problems	PMHP	Presence of physical or mental health issues related to drug use	1:Yes 0: No	2454
Legal Consequences	LC	Whether there are legal consequences associated with drug use	1:Yes 0: No	2576
Relationship Strain	RS	Indicates if drug use strains relationships with others	1:Yes 0: No	2543
Risk Taking Behavior	RTB	Engagement in risky behavior under the influence of drugs	1:Yes 0: No	2577
Withdrawal Symptoms	WS	Presence of withdrawal symptoms when trying to quit drug use	1:Yes 0: No	2612
Denial and Resistance to Treatment	DRT	Indicates denial or resistance to seeking treatment for drug addiction	1:Yes 0: No	2453

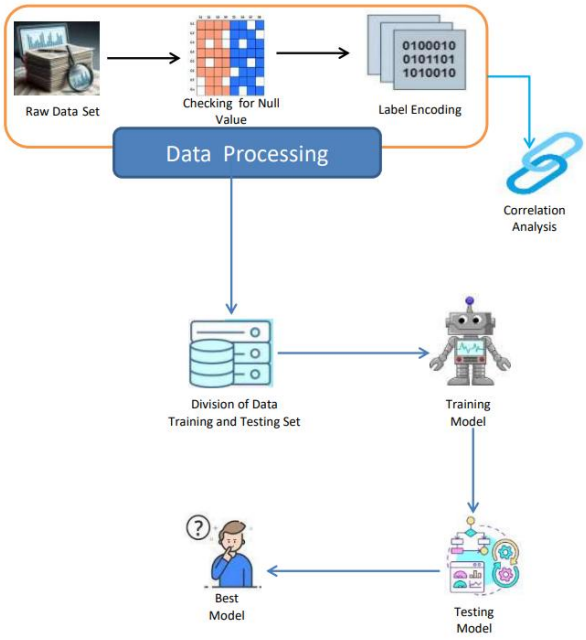


Figure 3. Research process steps.

3. Results

Before moving on to the classification model with ANN, it will be important to analyze the relationship between 11 variables. For this, the most useful method, the correlation matrix, will be examined. A correlation matrix is a table showing correlation coefficients between sets of variable (Gupta, 2019). The correlation coefficients between the variables are shown in Table 2.

When the correlation matrix (Table 2) is examined carefully, it is seen that the relationships between the variables are almost negligible. This can be attributed to the fact that the variables are categorical.At this stage the model was created. Initially, the dataset was partitioned into two mutually exclusive subsets: a training set and a test set. A proportion of 80% of the total data instances was allocated to the training set, while the remaining 20% was designated as the test set. This division was performed prior to model training and evaluation to ensure the model's performance could be assessed on unseen data. Afterwards, a model was created with the training data and this model was validated with the test data. The study involved testing and comparing multiple neural network architectures based on their average classification accuracy. Each architecture was trained using 10 different starting numbers and the average accuracy was calculated accordingly. Since the model consisted of 10 independent and 1 dependent variables, the input layer consisted of 10 neurons and the output layer contained a single neuron that would produce binary classification (0 or 1). The Log-Sigmoid function was used as the transfer function for all architectures. The learning rate was set to 0.3 and the momentum

parameter was fixed at 0.2. Models were created with one, two and three hidden layers and their average classification accuracies were compared. The architecture that provided the highest accuracy with the lowest error rate was determined as the optimum model.

Table 2. Correlation matrix

Features	AC	Exp	APD	SI	FI	PMHP	LC	RS	RTB	WS	DRT
AC	1	0.002	0.000	-0.008	0.001	-0.009	0.004	-0.002	0.003	0.009	-0.002
Exp		1	0.006	0.007	-0.001	-0.002	-0.003	0.002	-0.005	0.003	0.002
APD			1	0.001	-0.006	-0.008	0.001	-0.003	0.004	-0.002	-0.002
SI				1	-0.003	-0.001	-0.002	-0.009	0.004	-0.002	0.003
FI					1	-0.006	-0.008	-0.002	-0.003	0.002	-0.005
PMHP						1	0.004	-0.008	0.001	-0.003	0.004
LC							1	0.002	0.007	-0.001	-0.002
RS								1	0.004	-0.006	-0.008
RTB									1	0.002	0.004
WS										1	-0.003
DRT											1

Table 3. Summary of result

Network Architecture	Classification Accuracy %	Classification error percentage %
10 > 50 > 1	65.33	61.12
10 > 60 > 1	65.02	62.31
10 > 80 > 1	66.71	60.19
10 > 100 > 50 > 1	72.44	59.56
10 > 80 > 50 > 1	75.53	57.82
10 > 80 > 40 > 1	74.25	58.12
10 > 70 > 50 > 1	72.47	60.31
10 > 70 > 35 > 1	73.56	59.02
10 > 50 > 25 > 1	72.87	60.01

>represents the transition between layers.

Table 3 summarizes the results obtained using different hidden layers for building the ANN. Various architectures were used; the best of them was obtained by using two hidden layers: 10-80-50-1 architecture with 75.53% average classification accuracy.

Table 4 presents the Confusion Matrix showing the predictive performance of our model. In machine learning, a confusion matrix is a performance evaluation tool that projects the accuracy of a certain classification model. It reflects the number of true positives, true negatives, false positives, and false negatives. This would help in the analysis of model performance, detection of mis-classifications, and further improvement of predictive accuracy. Table 4 shows the model's classification performance across two classes: Class 0: Correctly predicted 3489 instances as 0, but misclassified 696 instances as 1. Class 1: Correctly predicted 1025 instances as 1, but misclassified 805 instances as 0.

Table 4. The confusion matrix of the model

	True Label		
Predicted Label	3489	805	0
	696	1025	1
	0	1	Class

4. Discussion

In this paper, we aimed to achieve an accurate diagnosis to identify addiction in youth, facilitating timely treatment and ultimately preserving lives. Addressing addiction plays a critical role in supporting families, physicians, and investigators in managing and mitigating the impacts of substance abuse. To this end, the paper proposes a Decision Support System (DSS) for diagnosing addiction, leveraging one of the most widely-used machine learning techniques: Artificial Neural Networks (ANN).

The proposed system comprises an input layer with ten

neurons, each representing symptoms of addiction as input variables. The model architecture includes two hidden layers and an output layer that classifies individuals as either "Addict" or "Non-Addict." The model achieved a classification accuracy of 75.53%, which, while sufficient, suggests room for improvement. The binary nature of all variables in the dataset likely contributed to the lower-than-expected accuracy. Incorporating numerical variables into the model could enhance its predictive performance. Additionally, applying other machine learning techniques (ensemble learning methods, SVM, etc) could yield higher accuracy scores.

The findings suggest that this model could significantly expedite the diagnosis and treatment of addiction, providing a valuable tool for families, physicians, and investigators. Furthermore, expanding the dataset used for training the proposed system would likely improve its accuracy, thereby increasing its reliability and effectiveness in real-world applications. Potential difficulties in integrating the model into existing healthcare systems, data privacy issues, or steps required to make it user-friendly for healthcare professionals can be coordinated by an expert software and clinical team.

Author Contributions

The percentages of the author's contributions are presented below. The author reviewed and approved the final version of the manuscript.

	E.K.
C	100
D	100
S	100
DCP	100
DAI	100
L	100
W	100
SR	100

C=Concept, D= design, S= supervision, DCP= data collection and/or processing, DAI= data analysis and/or interpretation, L= literature search, W= writing, CR= critical review, SR= submission and revision, PM= project management, FA= funding acquisition.

Conflict of Interest

The author declared that there is no conflict of interest.

Ethical Consideration

The author confirms that the ethical policies of the journal, as noted on the journal's author guidelines page, have been adhered to. All participants filled out informed consent forms in the study

References

Afzali MH, Sunderland M, Stewart S, Masse B, Seguin J, Newton N, Teesson M, Conrod P. 2019. Machine-learning prediction of adolescent alcohol use: A cross-study, cross-cultural validation. Addiction, 114(4): 662-671.

Araghinejad S. 2014. Data-Driven modeling: Using MATLAB® in water resources and environmental engineering. Springer, Netherlands, pp: 67.

Bottou L. 2014. From machine learning to machine reasoning: An essay. Machine Learn, 94: 133-149.

Fausett LV. 2006. Fundamentals of neural networks: architectures, algorithms and applications. Pearson Education India, pp: 461.

Gupta P. 2019. Top management team heterogeneity, corporate social responsibility disclosure and financial performance. Am J Ind Bus Manag, 9: 1076-1093.

Islam Arif MA, Sany SI, Sharmin F, Rahman MS, Habib MT. 2021. Prediction of addiction to drugs and alcohol using machine learning: A case study on Bangladeshi population. Int J Electr Comput Eng, 11(5): 4471.

Johnson JM, Khoshgoftaar TM. 2019. Survey on deep learning with class imbalance. J Big Data, 6(1): 1-54.

Junghare A, Milani K, Chavan M, Ransing V. 2019. Application for drug addicts using artificial neural networks. In: Proc Int Conf Commun Inf Process (ICCIP), Mumbai, India, pp:15-25.

Kaggle. 2024. Students drugs Addiction Dataset. URL: https://www.kaggle.com/datasets/atifmasih/students-drugs-addiction-dataset (accessed date: May 24, 2024).

Kumari D, Kilam S, Nath P, Swetapadma A. 2018. Prediction of alcohol abused individuals using artificial neural network. Int J Inf Technol, 10: 233-237.

Lewenstein K, Ślubowska E, Hawłas H. 2020. Alcohol addiction diagnosis on the basis of the polysomnographic parameters. Pol J Med Phys Eng, 26: 161-167.

Michalski RS, Carbonell JG, Mitchell TM (Ed.). 1983. Machine learning: An artificial intelligence approach. Springer, Berlin Heidelberg, pp: 582.

Poulton MM. 2001. Multi-layer perceptrons and back-propagation learning. In: Handbook of Geophysical Exploration: Seismic Exploration, Pergamon, 30: 27-53.

Shahriar A, Faisal F, Mahmud SU, Chakrabarti A, Alam MGR. 2019. A machine learning approach to predict vulnerability to drug addiction. In: 2019 22nd Int Conf Comput Inf Technol (ICCIT), Dhaka, Bangladesh, pp: 1-7.

Vaswani A, Shazeer N, Parmar N, Uszkoreit J, Jones L, Gomez A, Kaiser Ł, Polosukhin I. 2017. Attention is all you need. Adv Neural Inf Process Syst 31st Conf Neural Inf Process Syst, Long Beach, CA, USA, pp:45-46.

Black Sea Journal of Engineering and Science
doi: 10.34248/bsengineering.1662379

Open Access Journal
e-ISSN: 2619 – 8991

Research Article
Volume 8 - Issue 4: 1127-1133 / July 2025

INVESTIGATION OF THERMOLUMINESCENCE PROPERTIES OF CALCITE FROM KAMAN, KIRŞEHIR

Sumeyra BALCI[1,2*]

[1]*Nevşehir Hacı Bektaş Veli University, Arts-Sciences Faculty, Physics Department, 50300 Nevşehir, Türkiye*
[2]*Çukurova University, Arts-Sciences Faculty, Physics Department, 01330 Adana, Türkiye*

Abstract: This study investigates the thermoluminescence (TL) properties and dosimetric performance of calcite samples, with particular emphasis on dose response, heating rate (HR) effects, and reusability (RU). TL measurements were carried out using a Lexsyg Smart TL/OSL reader equipped with a $^{90}Sr/^{90}Y$ beta source. The dose-response relationship was analyzed by irradiating the sample with beta doses ranging from 0.1 to 500 Gy, revealed a progressive increase in TL intensity. The TL glow curve exhibited two broad peaks at 100-116 °C and 238 °C, with a shift in the first peak temperature at higher doses. A fitting procedure was applied to analyze the dose-response characteristics of the material, revealing distinct *b* values for different dose ranges. The effect of HR on the glow curve was also studied, showing an anomalous increase in TL intensity with rising HRs, contrary to expectations from the standard theoretical model. Additionally, the RU of the material was assessed by performing 10 consecutive TL measurements after a 50 Gy irradiation, demonstrating minimal degradation in TL intensity, with low deviations from the mean and first values. This remarkable RU is crucial for ensuring the material's effectiveness in long-term dosimetric applications.

Keywords: Thermoluminescence, Calcite, Anomalous hearing rate, Dosimetry, Reusability

***Corresponding author:** Sumeyra BALCI, Nevşehir Hacı Bektaş Veli University, Arts-Sciences Faculty, Physics Department, 50300 Nevşehir, Türkiye
E mail: sbalci@nevsehir.edu.tr (S. BALCI)
Sumeyra BALCI https://orcid.org/0000-0003-3463-6923

Received: March 21, 2025
Accepted: June 11, 2025
Published: July 15, 2025
Cite as: Balci S. 2025. Investigation of thermoluminescence properties of calcite from Kaman, Kırşehir. BSJ Eng Sci, 8(4): 1127-1133.

1. Introduction

Thermoluminescence (TL) is a well-established technique for radiation dosimetry, providing valuable information on the radiation dose absorbed by materials. It is widely used in various fields, including environmental monitoring, medical applications, archaeology and more (McKeever, 1985; Aitken, 1985; McKeever et al., 1995; Chen and McKeever, 1997). The technique relies on the ability of certain materials to trap charge carriers (electrons and holes) in their crystal lattice when exposed to ionizing radiation. Upon subsequent heating, these trapped charge carriers are released and recombine, emitting light (TL signal) which is proportional to the absorbed dose. Understanding the dose response and the factors affecting TL emission is crucial for optimizing its application in dosimetric measurements (Townsend and Kirch, 1989; Bailiff et al., 2004; Kim and Hong, 2014). Calcite (CaCO3) is a prevalent mineral that forms rocks and represents the most stable crystalline form of calcium carbonate, with aragonite being the alternative structure. It is commonly found in diverse geological settings, including sedimentary, igneous, and metamorphic rocks. While pure calcite is typically colorless or white, variations in its color often indicate the presence of different trace elements (Wintle, 1978; Chang et al., 1998). Natural calcite is widely utilized in the construction industry, serving as a key material in the production of cement and whitewashing powder, as well as in wall painting and industrial pollution management (Ponnusamy et al., 2012). Calcite has been extensively studied for its TL properties, owing to its favorable characteristics, such as high sensitivity and stability. In particular, it was reported that the TL properties of calcite make it a potential candidate for beta radiation dosimetry in industrial applications, with a reliable performance across a dose range of 0.01–104 Gy (Urbina et al., 1998). A study showed that the dose-response characteristics of calcite highlight its suitability as a dosimeter, particularly under varying thermal conditions, where thermal treatments affect its TL response (El-Faramawy et al., 2022). It was also shown that calcite's strong green emission band, with peaks at 255°C and 305°C, and its low fading rates position it as an important candidate for dosimetry applications (Toktamiş et al., 2014). Furthermore, it was found that calcite exhibits measurable and stable TL signals with a dose of 50 Gy, showing peaks at 150°C, 235°C, and 315°C, which make it effective for beta radiation dosimetry (Soliman and Metwally, 2006). Despite numerous studies, a comprehensive understanding of the impact of different factors, such as dose, HR, and RU, on calcite's TL response remains a topic of significant interest. Previous studies have highlighted the role of temperature and HR in influencing the TL signal, with the potential for anomalous HR effects that deviate from conventional TL

This work is licensed (CC BY-NC 4.0) under Creative Commons Attribution 4.0 International License

behavior. These effects can alter the peak temperature and intensity of the glow curves, making it essential to consider the influence of heating conditions on the overall TL response. Therefore, further investigation into these factors is crucial for optimizing calcite's use in dosimetric applications. The calcite sample used in this study was obtained from the Kaman region in Kırşehir, Turkey. This study focuses on investigating the dose response, HR dependence, and RU of calcite as a thermoluminescent material. By performing a series of controlled experiments, the relationship between radiation dose and TL emission is explored, and the influence of different HRs on the glow curve characteristics is analyzed. Moreover, the RU of calcite is assessed through repeated measurements to evaluate the stability of its TL response over multiple cycles. The findings of this study aim to provide deeper insights into the performance and practical applicability of calcite for radiation dosimetry.

2. Materials and Methods

2.1. Mineral Calcite

The geological history and natural formation conditions of calcite play a crucial role in determining its luminescence characteristics, as variations in crystallization environments can lead to differences in trap depth distributions and luminescent efficiency. Therefore, detailed investigations of region-specific calcite samples are essential for understanding their potential use in dosimetric applications. The calcite sample analyzed in this study was sourced from Kaman, Kırşehir, Turkey (Orhan, 2020). Figure 1 presents a detailed visualization of the studied calcite sample. Specifically, Figure 1a displays the geological map of Turkey at a 1:100.000 scale, specifically the Kırşehir-J30 sheet, as provided by MTA (2001). Figure 1b shows a macroscopic photograph of the calcite sample with a scale of 1.5 cm, providing an overview of its physical appearance, while Figure 1c presents a microscopic image of the calcite captured using an optical microscope, with a scale of 500 µm, highlighting its finer structural details. X-ray diffraction (XRD) analysis was performed to determine the crystal structure and phase composition of the investigated calcite sample. Measurements were carried out using a MiniFlex 300/600 diffractometer under conditions of 40 kV and 15 mA, with a continuous scanning mode in the range of 3° to 90° and a step width of 0.020°. Qualitative analysis results indicated that the main phase in the sample is calcite ($CaCO_3$), which crystallizes in the R-3c (hexagonal) space group. The determined lattice parameters for calcite are a = 4.983 Å, c = 17.033 Å, with a unit cell volume of 366.34 $Å^3$ (Figure 2). The natural samples and XRD results, obtained through the project titled Investigation of Mineralogical, Geochemical, and Origin of Skarn Mineralization Related to Plutonic Rocks from the Kaman Region (Kırşehir, Central Anatolia) [NEUBAP Report No: 15/2F7, 2018] were provided for this study (Orhan and Orhan, 2018).

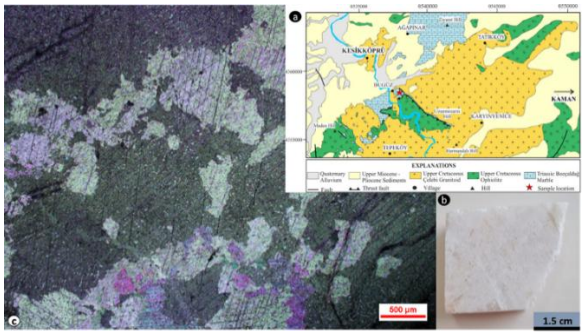


Figure 1. Visualization of the calcite sample: (a) Geological map of Turkey, Kırşehir-J30 sheet; (b) Macroscopic photograph of the calcite sample; (c) Microscopic image of the calcite under optical microscopy.

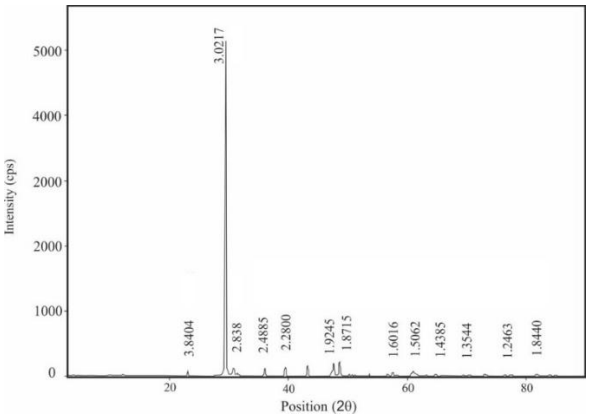


Figure 2. X-ray diffraction (XRD) analysis of the calcite sample.

2.2. Experimental Details

A Lexsyg Smart TL/OSL reader equipped with a $^{90}Sr/^{90}Y$ beta source delivering a dose rate of 0.097 Gy/s was utilized for all TL measurements in an N_2 atmosphere (Bulcar et al., 2024). To prepare the sample, 35 mg of powder was compressed into a pellet (6 mm in diameter, 0.75 mm thick) by applying a pressure of 2 ton-force/cm^2 for 10 minutes. A single aliquot, weighing 32.5 mg, was used in TL experiments. Glow curves were recorded from room temperature (RT) to 500 °C at a constant HR of 2 °C/s, except for the HR analysis. For the filter selection test, the sample was subjected to a 10 Gy beta dose, and different filter combinations were evaluated using the TL reader. Based on these tests, the IRSL-TL-wideband blue filter was chosen for all subsequent measurements. To assess dose response, the sample underwent beta irradiation with incremental doses ranging from 0.1 to 500 Gy. Additionally, to study the effect of HR, the pellet was irradiated at beta doses of 10, 30, and 50 Gy, followed by TL measurements at HRs varying between 1 and 5 °C/s. RU tests were carried out using a 50 Gy dose and a HR of 2 °C/s, with 10 consecutive TL readouts. The net TL intensity was determined by subtracting the background signal from the first measurement for all TL experiments

3. Results and Discussion

3.1. Dose Response

One of the primary steps in evaluating a dosimeter's applicability for dose measurement is determining its dose response, which should ideally follow a linear or well-defined function. The relationship between TL intensity and irradiation dose, representing the total radiation energy absorbed by the sample, offers insights into the trapping and thermal release mechanisms of carriers in the crystal lattice (Kirsh, 1992). When ionizing radiation interacts with the material, charge carriers are trapped within the crystal structure. The number of trapped carriers (or more specifically, the intensity of the TL emitted) is generally proportional to the amount of radiation dose absorbed by the phosphor (Aitken, 1985). A linear relationship between dose and TL intensity is a highly desirable feature for TL materials used in dosimetric applications. In order to examine this response, the sample was exposed to beta radiation doses ranging from 0.1 Gy to 500 Gy, after which luminescence emission curves were recorded (Figure 3).

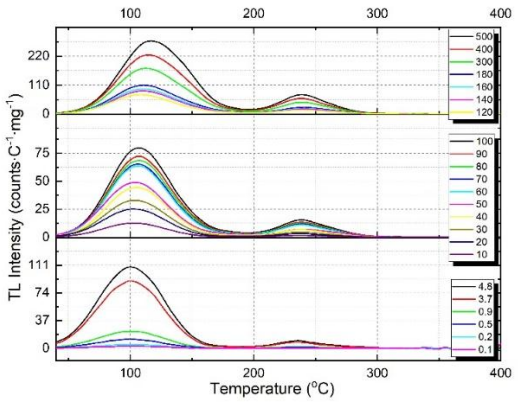


Figure 3. Temperature-dependent TL glow curves for beta-irradiated samples (0.1-500 Gy).

The results showed that emission intensity increased with dose up to 500 Gy, which was the maximum limit due to the saturation of the photomultiplier tube (PMT). The TL glow curves maintain their shape and exhibited two prominent and broad peaks, one occurring between 100–116 °C and the other at 238 °C. At lower doses, the peak with the highest intensity appeared at 100 °C, but as the dose increased, this peak shifted to 116 °C. This shift in the maximum TL peak temperature (T_m) with increasing dose can be attributed to several underlying physical mechanisms. Higher doses lead to a greater number of electrons being trapped in deeper energy levels within the material, requiring higher thermal energy for release. Additionally, as dose increases, retrapping effects become more significant, meaning that some released electrons are re-captured in deeper traps rather than recombining immediately, delaying the TL emission and shifting T_m to higher temperatures. Competition between recombination and thermal release also plays a role, as an increased density of trapped charges affects the kinetics of the TL process. Furthermore, high radiation doses can induce modifications in the local band structure or defect clustering, altering the activation energy required for charge release (Ducruet and Vass, 2009; Akça, 2020). For deeper analyze the dose response, a fitting procedure was applied using the equation 1:

$$I = aD^b \quad (1)$$

where I represents the integrated TL intensity, and D is the radiation dose. Upon plotting I_M (maximum value of intensity) as a function of D on a log-log scale, the equation produces a straight line with a slope b that could be equal to 1. (Oglakci et al., 2025). This analysis was performed separately for three dose intervals: 10–50 Gy, 50–100 Gy, and 10–100 Gy (Figure 4).

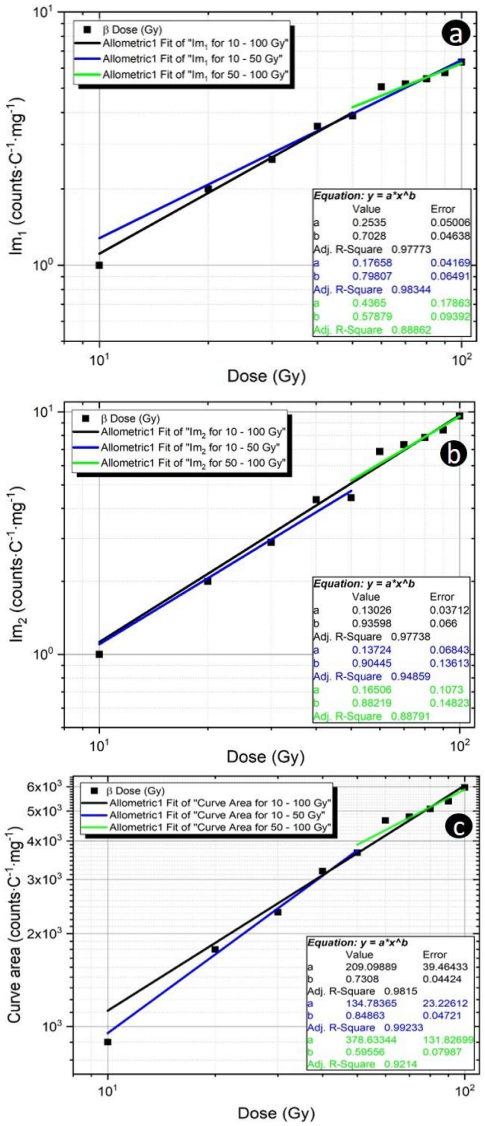


Figure 4. Dose-response analysis for 10–50 Gy, 50–100 Gy, and 10–100 Gy intervals: (a) first peak, (b) second peak, and (c) full glow curve.

The b parameter, which characterizes the nature of the dose-response relationship, was found to be 0.849 (R^2 = 0.9834) for the 10–50 Gy range, 0.596 (R^2 = 0.8886) for

50–100 Gy, and 0.731 (R^2 = 0.9777) for 10–100 Gy for the first peak (Figure 4a). As seen in Figure 4b, a similar fitting procedure was applied to the second peak at 238 °C, yielding *b* values of 0.904 (R^2 = 0.9486) for 10–50 Gy, 0.882 (R^2 = 0.8879) for 50–100 Gy, and 0.936 (R^2 = 0.9774) for 10–100 Gy. This peak demonstrated a stable dose response across the tested range. While analyzing individual peaks provides valuable information, evaluating the response of the entire glow curve offers a more comprehensive understanding of the material's radiation sensitivity. Therefore, the dose-response fitting for the full glow curve was performed and displayed in Figure 4c, resulting in *b* values of 0.849 (R^2 = 0.9923) for 10–50 Gy, 0.596 (R^2 = 0.9214) for 50–100 Gy, and 0.731 (R^2 = 0.9815) for 10–100 Gy. These findings suggest that the dose response for both individual peaks and the full glow curve follows a nearly linear relationship, with the *b* values varying across different dose intervals, and the I_m of the second peak (ultimately influencing the overall dosimetric properties of the material) showing the most consistent dose response (with *b* value 0,936) across the tested range.

3.2. Various Heating Rates (VHR)

Typically, TL glow curves shift toward higher temperatures as the HR increases during the TL readout process, as higher HRs cause traps within the bandgap to empty more rapidly. (Chen and Kirch, 1981). Figure 5 illustrates this trend in the TL low curves of calcite under different HRs (1-5 oC/s) with three different dose values. In order to achieve a deeper analysis, the maximum intensities of peak 1 and 2 (I_{m1} and I_{m2}), peak temperatures of peak 1 and 2 (T_{m1} and T_{m2}), full widths at half maximum of peak 1 and 2 ($FWHM_1$ and $FWHM_2$), and total curve area were plotted as functions of HR values in Figure 6a-c for 10, 30, and 50 Gy, respectively. According to TL theory, the FWHM should increase while the I_m decreases, though the total integrated intensity is expected to remain unchanged (Kitis et al., 1993).

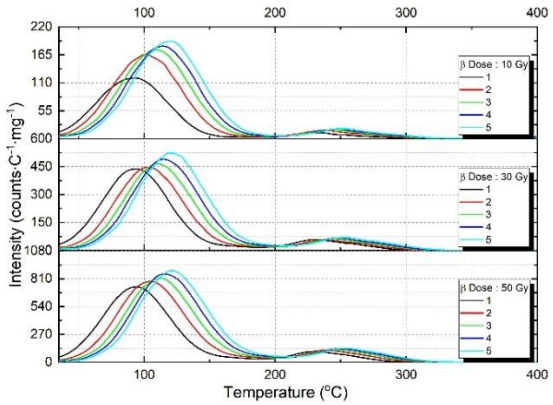


Figure 5. TL glow curves of calcite at different HRs (1-5 °C/s) and doses (10, 30, 50 Gy).

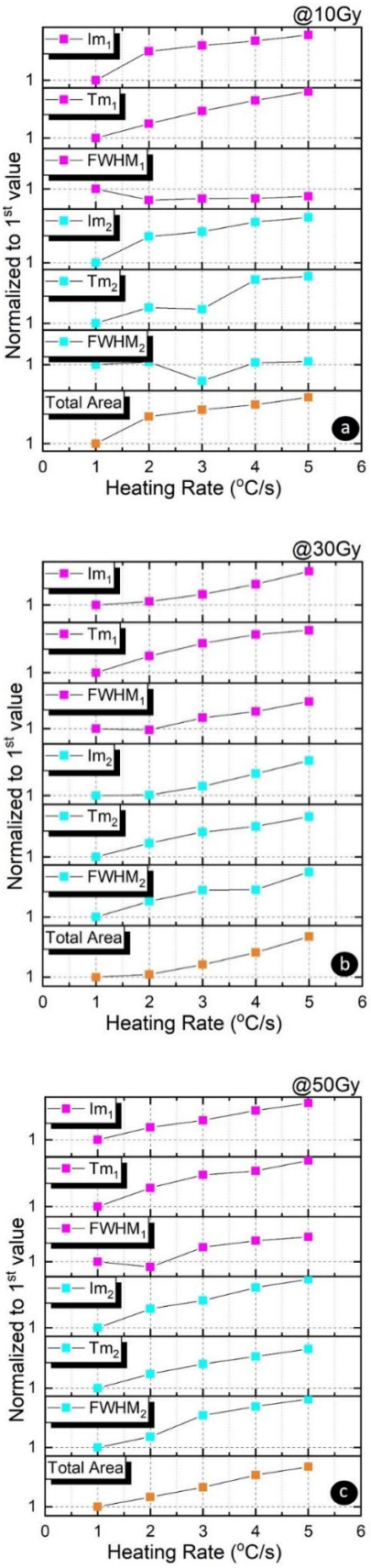


Figure 6. Variation of maximum intensities (I_{m1}, I_{m2}), peak temperatures (T_{m1}, T_{m2}), full width at half maximum ($FWHM_1$, $FWHM_2$), and total curve area as functions of HR for irradiated samples at (a) 10 Gy, (b) 30 Gy, and (c) 50 Gy.

However, as illustrated in Figure 6, increasing HR leads to a decrease in $FWHM_1$ and $FWHM_2$ for the 10 Gy dose (Figure 6a), accompanied by an increase in I_{m1}, I_{m2}, and the total curve area, whereas for the 30 Gy (Figure 6b) and 50 Gy doses (Figure 6c), all these parameters exhibit an increasing trend, which contradicts the expected outcome predicted by the OTOR model. This behavior, referred to as the anomalous HR effect, has been explained by Pagonis et al. (Pagonis et al., 2013) using Mandowski's semi-localized transition (SLT) model (Mandowski, 2005). Their study introduced an additional non-radiative transition pathway from the directly excited state to the recombination center, describing what is known as the anti-quenching effect. When traps release electrons upon heating, these electrons may transition thermally into the conduction band, where they can either be recaptured or recombine with holes in the recombination centers. In the first scenario, this recombination generates a TL signal, whereas in the second, the electron recombines directly with a hole without emitting radiation. The relative likelihood of radiative versus non-radiative transitions depends on the HR; as the HR decreases, the proportion of non-radiative transitions increases, and vice versa. This effect is attributed to the two-step process of charge carrier excitation from traps. At higher HRs, the probability of thermal excitation into the conduction band increases, reducing the time electrons spend in the excited state. The anomalous effect arises due to competition between radiative and non-radiative processes. Since charge conservation must be maintained, an increase in total TL intensity corresponds to a proportional decrease in the non-radiative component. Consequently, the rise in integrated TL intensity reflects an increase in the probability of radiative transitions relative to non-radiative ones (Mandowski, 2011; Pagonis et al., 2013; Portakal Uçar, 2021; Oglakci et al., 2023).

3.3. Reusability (RU)

The RU of the material was evaluated by performing successive thermoluminescence (TL) measurements on calcite samples, where each measurement was conducted after irradiating the sample with a 50 Gy dose at a HR of 2 °C/s. This process was repeated 10 times to assess the stability of the TL response over multiple cycles and shown in Figure 7. For the 1st peak, the deviation from the mean value was calculated to be 1.01%, while the deviation from the first reading was 2.75% (Figure 8a). Similarly, for the 2nd peak, the deviation from the mean value was 1.06%, and the deviation from the first reading was 1.08% (Figure 8b). However, a more comprehensive analysis of the entire glow curve rather than individual peaks gives a better representation of the material's RU. When considering the entire glow curve, the deviation from the mean value was calculated to be 1.40%, while the deviation from the first value was 3.97% (Figure 8c) (Oglakci et al., 2023).

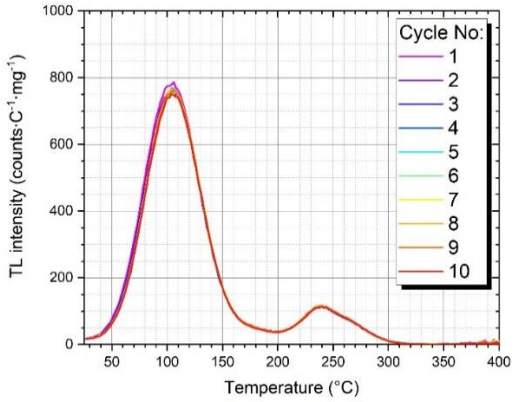


Figure 7. Stability of the TL response in calcite after 10 successive irradiations with a 50 Gy dose at a 2 °C/s HR.

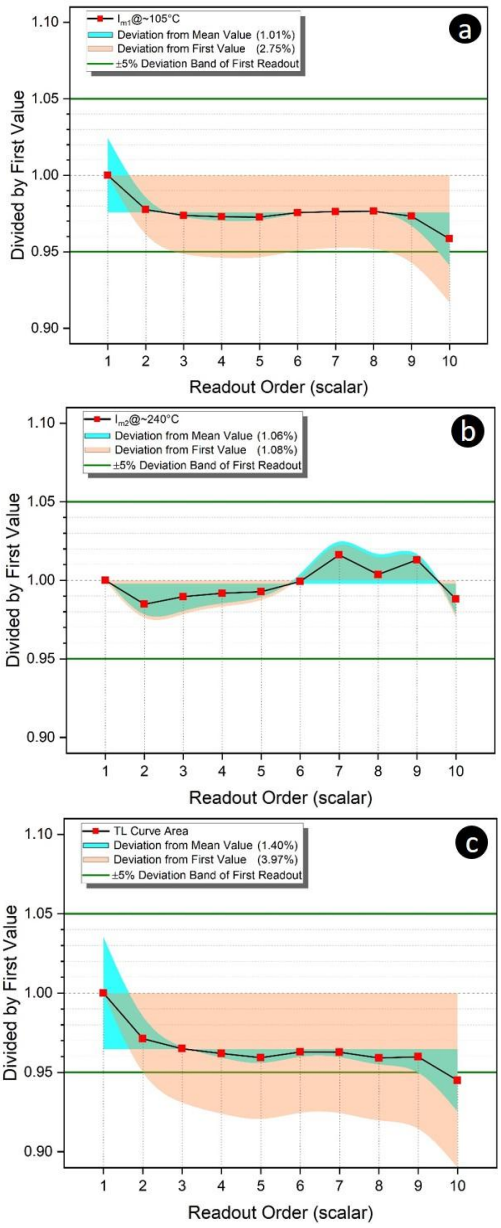


Figure 8. (a) Deviation of the first peak from the mean and first reading; (b) Deviation of the second peak from the mean and first reading; (c) Deviation of the entire glow curve from the mean and first reading.

These low deviations indicate that the material demonstrates outstanding RU, as it maintains a stable TL response even after multiple irradiation and readout cycles, showing minimal degradation in its thermoluminescent properties. Such remarkable RU is essential for practical dosimetric applications, where materials need to maintain performance over time without significant loss of sensitivity or efficiency.

4. Conclusion

The calcite material demonstrated stable thermoluminescent properties, with a well-defined dose-response relationship and an anomalous HR effect that deviated from conventional predictions. The results indicate that as the radiation dose increases, both the density of trapped charges and recombination dynamics contribute to shifts in the maximum TL peak temperature. The study also highlighted the importance of evaluating the entire glow curve for more reliable dosimetric characterization. RU tests revealed that the material retains its TL intensity over repeated measurements, confirming its robustness and suitability for practical dosimetric applications. The low deviations observed in successive measurements emphasize the material's excellent RU, ensuring reliable performance without significant sensitivity loss over time. This study contributes valuable insights into the performance and stability of calcite as a dosimeter for radiation measurements, showcasing its potential for extended use in radiation monitoring and dosimetry.

Author Contributions

The percentages of the author's contributions are presented below. The author reviewed and approved the final version of the manuscript.

	S. B.
C	100
D	100
S	100
DCP	100
DAI	100
L	100
W	100
CR	100
SR	100
PM	100
FA	100

C=Concept, D= design, S= supervision, DCP= data collection and/or processing, DAI= data analysis and/or interpretation, L= literature search, W= writing, CR= critical review, SR= submission and revision, PM= project management, FA= funding acquisition.

Conflict of Interest

The author declared that there is no conflict of interest.

Ethical Consideration

Ethics committee approval was not required for this study because of there was no study on animals or humans.

Acknowledgements

S. B. would like to express gratitude to Assoc. Prof. Ayşe Orhan for providing the natural samples and XRD results. The author is also grateful to Prof. Mustafa Topaksu, Dr. Mehmet Oğlakçı, and Aya Barad for their valuable discussions on the TL results.

References

Aitken MJ. 1985. Thermoluminescence Dating. Academic Press, London, UK, pp: 26.

Akça S. 2020. Determination of thermoluminescence properties of $ZnB_2O_4:Tm^{3+}$, Li^+ for dosimetric purposes. Appl Radiat Isot, 157: 109041.

Bailiff IK, Stepanenko VF, Gosku HY, Bøtter-Jensen L, Brodski L, Chumak V, Correcher V, Delgado A, Golikov V, Jungner H, Khamidova LG, Kolizshenkov TV, Likhtarev I, Meckbach R, Petrov SA, Sholom S. 2004. Comparison of retrospective luminescence dosimetry with computational modeling in two highly contaminated settlements downwind of the Chernobyl NPP. Health Phys, 86: 25–41.

Bulcar K, Oglakci M, Altowyan AS, Bilgin R, Yucel A, Sezer S, Hakami J, Depci T, Topaksu M, Can N. 2024. Exploring beta irradiation responses in Sr_2^+-doped hydroxyapatite: A thermoluminescence study. Ceram Int, 50(17B): 31300–31312.

Chang LLY, Howie RA, Zussman J. 1998. Rock Forming Minerals, Non-silicates—Sulphates, Carbonates, Phosphates, Halides, Vol. 5. Geological Society of London, London, UK, 2nd ed, pp:25.

Chen R, Kirsh Y. 1981. The Analysis of Thermally Stimulated Processes. Pergamon Press, Oxford, UK, pp: 53.

Chen R, McKeever SWS. 1997. Theory of Thermoluminescence and Related Phenomena. World Scientific, Singapore, pp: 42.

Ducruet JM, Vass I. 2009. Thermoluminescence: experimental. Photosynth Res, 101: 195–204.

El-Faramawy N, Alazab HA, Gad A, Sabry M. 2022. Study of the thermoluminescence kinetic parameters of a β-irradiated natural calcite. Radiat Phys Chem, 190: 109793.

Kim KB, Hong DG. 2014. Kinetic parameters, bleaching and radiation response of thermoluminescence glow peaks separated by deconvolution on Korean calcite. Radiat Phys Chem, 103: 16–21.

Kirsh Y. 1992. Kinetic analysis of thermoluminescence. Phys Status Solidi A, 129(1): 15–48.

Kitis G, Spiropulu M, Papadopoulos J, Charalambous S. 1993. Heating rate effects on the TL glow-peaks of three thermoluminescent phosphors. Nucl Instrum Meth Phys Res A, 73: 367–372.

Mandowski A, Bos AJJ. 2011. Explanation of anomalous heating rate dependence of thermoluminescence in $YPO_4:Ce^{3+}$, Sm^{3+} based on the semi-localized transition (SLT) model. Radiat Meas, 46: 1376–1379.

Mandowski A. 2005. Semi-localized transitions model for thermoluminescence. J Phys D Appl Phys, 38: 17–21.

McKeever SWS, Moscovitch M, Townsend PD. 1995. Thermoluminescence Dosimetry Materials: Properties and Uses. Nuclear Technology Publishing, Ashford, UK, pp: 63.

McKeever SWS. 1985. Thermoluminescence of Solids.

Cambridge University Press, Cambridge, UK, pp: 41.

Oglakci M, Akça-Özalp S, Portakal-Uçar ZG, Correcher V, Benavente JF, Sonsuz M, Can N, Halefoglu YZ, Topaksu M. 2025. Thermoluminescence study of Nd^{3+} doped lanthanum tri-borate phosphor. J Alloys Compd, 1013: 178570.

Oglakci M, Portakal-Uçar ZG, Akça-Özalp S, Correcher V, Benavente JF, Sonsuz M, Can N, Halefoglu YZ, Topaksu M. 2023. Thermoluminescence behavior of Ce^{3+}-doped lanthanum tri-borate phosphor for dosimetry applications. Ceram Int, 49(22B): 36092–36102.

Orhan A, Orhan A. 2018. Investigation of mineralogical, geochemical and origin of skarn mineralization related plutonic rocks from the Kaman region (Kırşehir, Central Anatolia). NEUBAP Project Report No: 15/2F7, pp: 85.

Orhan A. 2020. Mineralogy, fluid inclusions and carbon isotopes of the Kaman iron deposits, Central Anatolia, Turkey: Implication for ore genesis and hydrothermal evolution. Ore Geol Rev, 127: 103808.

Pagonis V, Blohm L, Brengle M, Mayonado G, Woglam P. 2013. Anomalous heating rate effect in thermoluminescence intensity using a simplified semi-localized transition (SLT) model. Radiat Meas, 51–52: 40–47.

Ponnusamy V, Ramasamy V, Jose MT, Anandalakshmi K. 2012. Effect of annealing on natural calcitic crystals—A thermostimulated luminescence (TSL) study. J Lumin, 132(4): 1063–1075.

Portakal Uçar ZG. 2021. Thermoluminescence characteristics and kinetic analysis of beta irradiated $Ca_4LaO(BO_3)_3$ phosphor. Cumhuriyet Sci J, 42(3): 702–714.

Soliman C, Metwally SM. 2006. Thermoluminescence of the green emission band of calcite. Radiat Eff Defects Solids, 161(10): 607–613.

Toktamiş H, Toktamiş D, Yazıcı AN. 2014. Thermoluminescence studies of calcite extracted from natural sand used in making roasted chickpea. J Lumin, 153: 375–381.

Townsend PD, Kirsh Y. 1989. Spectral measurement during thermoluminescence—An essential requirement. Contemp Phys, 30: 337–354.

Urbina M, Millán A, Beneitez P, Calderón T. 1998. Dose rate effect in calcite. J Lumin, 79(1): 21–28.

Wintle AG. 1978. A thermoluminescence dating study of some Quaternary calcite: potential and problems. Can J Earth Sci, 15(12): 1884–1893.

Black Sea Journal of Engineering and Science
doi: 10.34248/bsengineering.1691043

Open Access Journal
e-ISSN: 2619 – 8991

Research Article
Volume 8 - Issue 4: 1134-1139 / July 2025

FORECASTING MUTUAL FUND PRICES ON TEFAS USING LIGHTGBM

Oktay ÖLMEZ[1]*

[1]*Afiniti, 34752 İstanbul, Türkiye*

Abstract: This paper investigates the application of the Light Gradient Boosting Machine (LightGBM) algorithm for predicting the prices of mutual funds traded on the Türkiye Electronic Fund Trading Platform (TEFAS). Given the increasing importance of mutual funds as an investment vehicle in Türkiye, this study explores the effectiveness of a state-of-the-art machine learning approach. Utilizing historical data from TEFAS, the LightGBM model is employed to capture complex patterns and non-linear relationships within the financial time series data. The research outlines the methodology for data preparation, feature implementation, data splitting, model configuration, training, and evaluation, including case studies to demonstrate the practical application and results.

Keywords: Machine Learning, LightGBM, Tefas

***Corresponding author:** Afiniti, 34752 İstanbul, Türkiye
E mail: olmezoktay@gmail.com (O. ÖLMEZ)
Oktay ÖLMEZ https://orcid.org/0000-0002-9130-0038

Received: May 04, 2025
Accepted: June 11, 2025
Published: July 15, 2025

Cite as: Ölmez O, 2025. Forecasting Mutual Fund Prices on TEFAS Using LightGBM. BSJ Eng Sci, 8(4): 1134-1139.

1. Introduction

The landscape of financial markets is continuously evolving, presenting investors with a diverse array of instruments for wealth management and growth. Among these, mutual funds stand out as a popular investment vehicle, offering diversification and professional management across various asset classes. In Türkiye, the Türkiye Electronic Fund Trading Platform (TEFAS) plays a pivotal role in this ecosystem, serving as a centralized and transparent platform for the trading of a wide range of mutual funds. Established to provide investors with easy access to compare and trade funds from different management companies through a single account, TEFAS has significantly enhanced the accessibility and efficiency of the Turkish mutual fund market.

For both individual and institutional investors, the ability to anticipate future price movements of mutual funds is essential to make informed investment decisions, optimize portfolio performance, and manage risk effectively. However, mutual fund price prediction is a complex task influenced by a myriad of factors, including underlying asset performance, market sentiment, economic indicators, and fund-specific characteristics. The inherent volatility and dynamic nature of financial time series data make accurate forecasting a significant challenge.

Traditionally, statistical models and fundamental analysis have been employed for financial forecasting. While valuable, these methods often face limitations in capturing the intricate non-linear relationships and complex patterns present in modern financial data. The advent of machine learning techniques has opened new avenues for tackling these challenges, offering powerful tools capable of learning complex dependencies and making data-driven predictions.

This paper aims to explore the application of Light Gradient Boosting Machine (LightGBM), a highly efficient and effective gradient boosting framework, for the prediction of mutual fund prices available on the TEFAS platform. LightGBM has gained considerable attention in various domains, including financial time series forecasting, due to its speed, scalability, and ability to handle large datasets while delivering high predictive accuracy. Its tree-based learning algorithm and optimized techniques for gradient boosting make it particularly well-suited for capturing the complex and often non-linear patterns inherent in financial market data.

The study will leverage historical price data of selected mutual funds traded on TEFAS, along with potentially relevant features such as historical returns, trading volume, and market indices, to train and evaluate the LightGBM model. By focusing on the TEFAS platform, this research provides a specific and relevant context within the Turkish financial market. The application of LightGBM, a state-of-the-art machine learning algorithm, represents a contemporary approach to address the challenging problem of mutual fund price prediction.

In the rest of this paper, we will detail the data collection and preprocessing steps undertaken for this study and will describe the methodology for model development, training, and evaluation using LightGBM, including case studies on specific mutual funds. Finally, we will

This work is licensed (CC BY-NC 4.0) under Creative Commons Attribution 4.0 International License

conclude the paper with a summary of the findings, potential implications, and directions for future research.

1.1. LightGBM for Financial Time Series Prediction

Financial time series prediction, particularly forecasting stock market price movements, remains a challenging yet crucial task for investors and financial institutions. The inherent volatility, non-linearity, and complex dependencies within financial data make accurate prediction difficult using traditional statistical methods. In recent years, machine learning techniques have shown significant promise in addressing these complexities by capturing intricate patterns and relationships within financial time series data.

Among the various machine learning algorithms, Gradient Boosting Machines (GBMs) have gained considerable attention due to their powerful predictive capabilities. Light Gradient Boosting Machine (LightGBM), an innovative framework developed by Microsoft, has emerged as a particularly efficient and effective GBM variant. LightGBM's key advantages lie in its speed and reduced memory consumption, achieved through techniques like Gradient-based One-Side Sampling (GOSS) and Exclusive Feature Bundling (EFB), making it well-suited for handling large-scale financial datasets.

Recent research has increasingly explored the application of LightGBM in financial forecasting with promising results. Studies have demonstrated its effectiveness in predicting stock prices and market trends. For instance, Hartanto, Kholik, and Pristyanto (2023) found that a LightGBM model was competitive with and could even outperform other boosting algorithms like XGBoost, AdaBoost, and CatBoost for stock price time series forecasting. This highlights LightGBM's capability in handling the temporal dynamics of stock data.Furthermore, researchers have explored hybrid models that leverage the strengths of LightGBM in combination with other techniques to enhance predictive performance. Guo, Li, and Xu (2021) proposed an LSTM-LightGBM hybrid model for predicting stock price rise and fall, where LSTM captured temporal dependencies and LightGBM further processed these outputs, resulting in improved prediction stability and performance. Similarly, Tian et. Al. (2022) also investigated a hybrid LSTM and LightGBM model for stock price prediction, indicating the benefits of combining these approaches.

Beyond traditional stock markets, LightGBM has also been successfully applied to forecasting trends in the cryptocurrency market, another highly volatile financial time series. Sun, Liu, and Sima (2020) developed a cryptocurrency price trend forecasting model based on LightGBM, demonstrating its robustness in this dynamic environment by incorporating both cryptocurrency data and economic indicators.

Moreover, LightGBM has shown its resilience and effectiveness even during periods of significant market stress. Guennioui, Chiadmi, and Amghar (2024) utilized a global forecasting approach with an optimized LightGBM model for predicting stock prices during the COVID-19 pandemic, showcasing its ability to handle heightened volatility and successfully forecast multiple stocks simultaneously.

These studies collectively underscore the growing importance of LightGBM as a powerful and efficient tool for financial time series prediction. Its ability to handle complex data, coupled with its computational efficiency, makes it a valuable algorithm for developing accurate and robust forecasting models in diverse financial markets. The continued exploration of LightGBM, both as a standalone model and in hybrid architectures, holds significant potential for advancing the field of financial forecasting.

2. Materials and Methods

This section outlines the methodology employed for predicting mutual fund prices on the TEFAS platform using the LightGBM algorithm. The process involves several key steps, including data preparation, feature engineering, data splitting, model configuration, training, and evaluation.

The initial step involves gathering historical data relevant to the mutual funds traded on TEFAS. Last 5 years of data is collected until April 23 of 2025. A primary data structure, a Pandas DataFrame, is generated to organize this information. This DataFrame includes, at a minimum, the following columns:

- date: The date of the observation.
- fund_price: The historical price on the given date.
- usd: The exchange rate of the US Dollar against the Turkish Lira on the given date.
- gold: The price of gold (e.g., per gram or ounce in Turkish Lira) on the given date.

Ensuring data quality, including handling missing values and ensuring proper data types, is a crucial prerequisite before proceeding to subsequent steps.

To simulate a real-world forecasting scenario, a specific prediction horizon is defined. This horizon represents the number of future periods (e.g., days) for which the model will make predictions. Additionally, a test size is specified, determining the proportion of the most recent data that will be held out for evaluating the trained model's performance on unseen data. The remaining data will be used for training.

To capture temporal dependencies and provide the LightGBM model with relevant information, a set of features is engineered from the raw data. These features are designed to reflect past price movements and trends. The generated features include:

- Lagged Price Values: The price of the mutual fund from previous periods (e.g., price from 1 day ago, 2 days ago, etc.). These features help the model understand the relationship between past and future prices.
- Price Change Percentage: The percentage change in the mutual fund's price over different

short-term intervals (e.g., 1-day, 2-day, 3-day percentage change). These capture short-term volatility and momentum.

- Simple Moving Averages (SMA): The average price of the mutual fund over defined windows (e.g., 5-day and 13-day simple moving averages). Moving averages help smooth out price fluctuations and identify trends.

These features are calculated based on the fund_price series in the DataFrame.

Recognizing that external factors can influence mutual fund prices, the exchange rate of the US Dollar (usd) and the price of gold (gold) are included directly into the feature set. These serve as exogenous variables that may capture broader market sentiment, economic conditions, or shifts in investor preference for alternative assets.

The prepared dataset, including the engineered features and external variables, is split into training and testing sets. A time-series split approach is adopted to ensure that the training data precedes the testing data chronologically. This prevents data leakage and provides a more realistic evaluation of the model's prospective forecasting ability. The size of the test set is determined by the previously defined test size parameter.

The Light Gradient Boosting Machine (LightGBM) algorithm, specifically the LGBMRegressor implementation, is chosen for the price prediction task. LightGBM is an ensemble learning method that builds a series of decision trees sequentially, with each new tree correcting the errors of the previous ones. Its efficiency and performance on tabular data and time series forecasting tasks make it a suitable choice.

The model is configured using the following parameters:

- objective: `regression_l1' specifies the objective function to be minimized during training. regression_l1 corresponds to Mean Absolute Error (MAE) regression, which is less sensitive to outliers compared to Mean Squared Error (MSE).
- metric: `mae' defines the evaluation metric to be monitored during training. Mean Absolute Error (MAE) measures the average magnitude of the errors between predicted and actual values.
- n_estimators: 1000 sets the number of boosting rounds or the number of trees to build. A higher number can improve performance but also increases the risk of overfitting and computation time.
- learning_rate: 0.05 determines the step size shrinkage after each boosting iteration. A smaller learning rate makes the training process more stable but requires more estimators.
- feature_fraction: 0.9 specifies the fraction of features to be randomly selected for training each tree. This technique, known as feature bagging, helps to prevent overfitting and increases the diversity of the trees.
- bagging_fraction: 0.8 determines the fraction of data samples to be randomly sampled for training each tree. This is also a form of bagging (data bagging) and helps to reduce variance and prevent overfitting.
- bagging_freq: 5 specifies the frequency for performing bagging. A value of 5 means that bagging will be performed every 5 boosting iterations.
- verbose: -1 controls the verbosity of the training output. A value of -1 silences the output.
- n_jobs: -1 specifies the number of parallel threads to use for training. Setting it to -1 utilizes all available CPU cores.
- seed: 42 sets the random seed for reproducibility of the results in a single run.

3.1. Model Training

The configured LGBMRegressor model is trained on the training dataset. During the training process, the algorithm iteratively builds decision trees, with each tree learning from the residuals of the previous trees, aiming to minimize the specified objective function (MAE).

The performance of the trained LightGBM model is evaluated on the unseen test dataset. The primary evaluation metric used is the Root Mean Squared Error (RMSE). RMSE is a widely used metric for regression tasks that measures the square root of the average of the squared differences between the predicted and actual values. It provides a measure of the typical magnitude of the prediction errors and is sensitive to large errors. The formula for RMSE is given by equation 1.

$$\mathrm{RMSE} = \sqrt{\frac{1}{n}\sum_{k=1}^{n}(y_k - \hat{y}_k)^2} \tag{1}$$

where n is the number of observations in the test set, y_k is the actual price, and $\widehat{y_k}$ is the predicted price. A lower RMSE indicates better model performance.

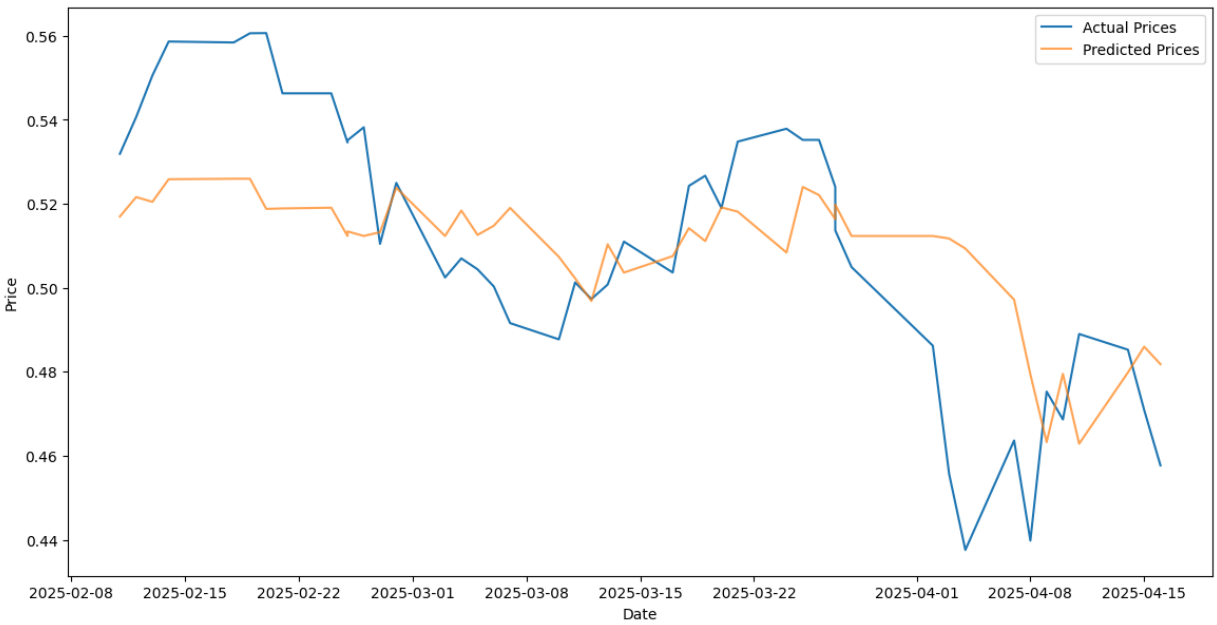


Figure 1. AFT Price Prediction using LightGBM.

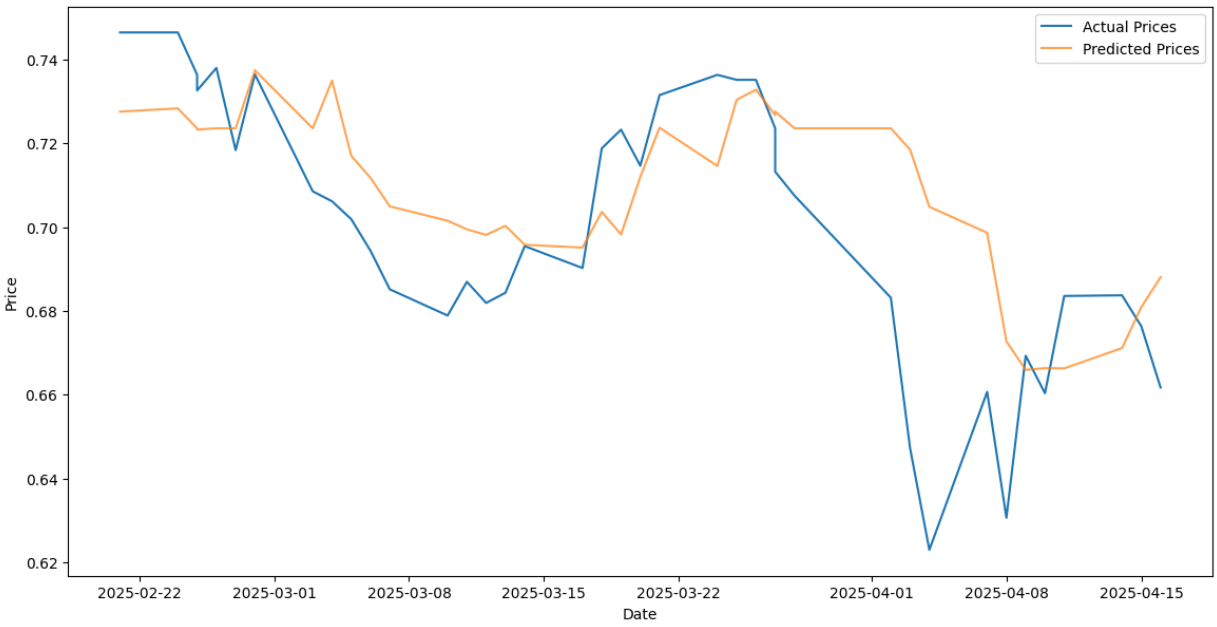


Figure 2. AFA Price Prediction using LightGBM.

3.1. Case Studies

To demonstrate the practical application of the proposed methodology, case studies were conducted using historical data for specific mutual funds available on TEFAS. The data for each fund was processed, and the LightGBM model was trained and evaluated as described in the preceding sections.

3.1.1. AFT mutual fund

For the AFT mutual fund, a single execution of the model with a fixed random seed yielded a Root Mean Squared Error (RMSE) of 0.02418357 on the test set (Figure 1.). In this setting, the predicted values for April 24 and April 25, 2025, were 0.48596486 and 0.48180393, respectively, while the corresponding actual values were 0.464522 and 0.494151. To evaluate the robustness and variability of the model's predictions, the training and prediction processes were repeated 1,000 times with different random seeds. The mean predicted values for April 24 and April 25 across these runs were 0.48851891 and 0.48317624, respectively. These results are summarized in the Table 1.

Table 1. The mean predicted values for April 24 and April 25

Date	April 24, 2025	April 25, 2025
AV	0.464522	0.494151
PV (Single Run)	0.48596486	0.48180393
MPV (1000 Runs)	0.48851891	0.48317624

AV= actual value, PV= predicted value, MPV= mean predicted value.

3.1.2. AFA mutual fund

For the AFA mutual fund, a single execution of the LightGBM model with a fixed random seed yielded a Root Mean Squared Error (RMSE) of 0.02486311 on the test set (Figure 2.). The predicted values for April 24 and April 25, 2025, were 0.68089192 and 0.68806604, respectively, while the corresponding actual values were 0.663933 and 0.694149. Following the same procedure as applied to the AFT mutual fund, the training and prediction processes were repeated 1,000 times with different random seeds to evaluate the stability and variability of the model's forecasts. The mean predicted values for April 24 and April 25 across these runs were 0.68074949 and 0.68883918, respectively. These results are summarized in the Table 2.

Table 2. The mean predicted values for April 24 and April 25

Date	April 24, 2025	April 25, 2025
AV	0.663933	0.694149
PV (Single Run)	0.68089192	0.68806604
MPV (1000 Runs)	0.68074949	0.68883918

AV= actual value, PV= predicted value, MPV= mean predicted value.

5. Conclusion and Future Work

The proposed methodology involved the preparation of historical data for TEFAS mutual funds, including the target fund's price along with relevant external factors like USD exchange rates and gold prices. A crucial step was the engineering of a comprehensive feature set, incorporating lagged prices, price change percentages, and moving averages to capture the temporal dependencies and trends in the time series data. The data was then split using a time-series approach to ensure realistic model evaluation. The LightGBM algorithm, configured with parameters optimized for regression and efficiency, was employed to train the predictive model. Model performance was primarily evaluated using the Root Mean Squared Error (RMSE).

The case studies conducted on the AFT and AFA mutual funds demonstrated the practical implementation of the methodology. The RMSE values obtained for both funds indicated a reasonable level of prediction error, suggesting that LightGBM can effectively learn from the historical data to forecast future price movements. Furthermore, the analysis of predictions from a single model run versus the average predictions over 1000 runs with different random seeds highlighted the importance of assessing model stability and reducing the impact of randomness in financial forecasting. The averaged predictions are considered more robust and reliable indicators of the model's true forecasting capability.

While the results are promising, this study represents a foundational step in applying LightGBM to TEFAS mutual fund price prediction. Several avenues exist for future research to further enhance the accuracy and sophistication of the forecasting model.

For instance, incorporating a wider range of potentially influential features could improve model performance. This includes macroeconomic indicators specific to Türkiye (e.g., inflation rates, interest rates, GDP growth), global market indices, commodity prices beyond gold. Note that a set of parameters was used in this study, more extensive hyperparameter tuning using techniques like grid search, random search, or Bayesian optimization could potentially lead to further improvements in model accuracy.

Author Contributions

The percentages of the author's contributions are presented below. The author reviewed and approved the final version of the manuscript.

	O.Ö.
C	100
D	100
S	100
DCP	100
DAI	100
L	100
W	100
CR	100
SR	100
PM	100
FA	100

C=Concept, D= design, S= supervision, DCP= data collection and/or processing, DAI= data analysis and/or interpretation, L= literature search, W= writing, CR= critical review, SR= submission and revision, PM= project management, FA= funding acquisition.

Conflict of Interest

The author declared that there is no conflict of interest.

Ethical Consideration

Ethics committee approval was not required for this study because of there was no study on animals or humans.

References

Guennioui O, Chiadmi D, Amghar M. 2024. Global stock price forecasting during a period of market stress using LightGBM. Int J Comput Digit Syst, 15.1: 19-27.

Guo Y, Li Y, Xu Y. 2021. Study on the application of LSTM-LightGBM Model in stock rise and fall prediction. MATEC Web of Conferences, 336: 05011.

Hartanto A, Kholik YN, Pristyanto Y. 2023. Stock price time series data forecasting using the light gradient boosting machine (LightGBM) model. JOIV: Int J Inform Visualization, 7.4: 2270-2279.

Sun X, Liu M, Sima Z. 2020. A novel cryptocurrency price trend forecasting model based on LightGBM. Finance Res Lett, 32: 101084.

Tian L, Feng L, Yang L, Guo Y. 2022. Stock price prediction based on LSTM and LightGBM hybrid model. J. Supercomput, 78.9: 11768-11793.

Black Sea Journal of Engineering and Science
doi: 10.34248/bsengineering.1672800

Open Access Journal
e-ISSN: 2619 – 8991

Araştırma Makalesi (Research Article)
Cilt 8 - Sayı 4: 1140-1151 / Temmuz 2025
(Volume 8 - Issue 4: 1140-1151 / July 2025)

METASEZGİSEL OPTİMİZASYON YÖNTEMLERİNİN PSİKİYATRİK UYGULAMALARDAKİ YERİ: BİBLİYOMETRİK BİR ANALİZ

Ümit CAN[1]*, Feride TUĞRUL[1]

[1]Munzur Üniversitesi, Mühendislik Fakültesi, Bilgisayar Mühendisliği, 62000, Tunceli, Türkiye

Özet: Mental hastalıklar dünya çapında milyarlarca insanı çeşitli seviyelerde etkilemektedir. Bu durum toplum sağlığı açısından bir risk teşkil etmektedir. Hastalıkların seviyeleri ve etkileri değişiklik gösterse de genel olarak mental rahatsızlıklar kişilerin kendileri ve çevreleri ile sağlıklı bir ilişki kurmalarını engelleyerek günlük yaşamlarını verimli bir şekilde geçirmelerini engeller. Günlük yaşam konforundan uzaklaşan bireyler sosyal ve iş yaşamlarında da birçok zorluk ile karşılaşırlar. Uzun süreli mental rahatsızlık yaşayan insanlarda strese bağlı olarak fizyolojik rahatsızlıklar da görülebilir. Bu durum tedavi edilmediği ve önlenmediği zaman toplum sağlığı problemine dönüşür. Bundan dolayı sağlık alanında faaliyet gösteren sağlık kuruluşları, araştırma merkezleri ve üniversiteler gibi merkezler mental hastalıkların tespiti ve tedavisi için birçok çalışma yapmaktadır. Bu yöntemler geleneksel yöntemleri içermekle birlikte günümüzde yapay zeka destekli yöntemleri de kapsamaktadır. Yapay zeka destekli yöntemler çeşitli türdeki büyük miktarda mental hastalık verisini analiz ederek mental hastalıkların erken teşhisi ve tedavisinde kullanılmaktadır. Araştırmacılar bu yöntemlerin başarılarını geliştirmek için metasezgisel optimizasyon algoritmalarını da kullanmaktadır. Çok karmaşık nonlinear problemlere hızlı ve yüksek başarımlı çözümler arayan bu optimizasyon yöntemleri makine öğrenmesi ve derin öğrenme yöntemlerinin başarılarını arttırmaktadır. Fakat araştırmacılar için bu alanda yapılan çalışmaların sayısını ve niteliğini gösteren ayrı bir bibliyometrik bir çalışma yoktur. Bu çalışma bu alanda oluşan bu boşluğu doldurarak araştırmacılar için ön açısı bir rehber olmayı hedeflemektedir.

Anahtar kelimeler: Bibliyometrik analiz, Metasezgisel optimizasyon, Mental hastalıklar, Mental bozukluklar, Makine öğrenmesi, Derin öğrenme

The Position of Metaheuristic Optimization Methods in Psychiatric Practice: A Bibliometric Analysis

Abstract: Mental diseases affect billions of people worldwide to varying degrees. This poses a risk to public health. Although the levels and effects of diseases vary, in general, mental diseases prevent people from having a healthy relationship with themselves and their environment and prevent them from living their daily lives efficiently. Individuals who move away from the comfort of daily life face many difficulties in their social and professional lives. People with long-term mental disorders may also experience physiological disorders due to stress. When this situation is not treated and prevented, it becomes a public health problem. Therefore, centers such as health institutions, research centers, and universities operating in the field of health carry out many studies to detect and treat mental disorders. These methods include traditional methods, but today, they also include artificial intelligence-supported methods. AI-powered methods are used for early diagnosis and treatment of mental illnesses by analyzing large amounts of mental illness data of various types. Researchers are also using metaheuristic optimization algorithms to improve the performance of these methods. These optimization methods, which seek fast and high-performance solutions to very complex nonlinear problems, are increasing the success of machine learning and deep learning methods. Nonetheless, there is no distinct bibliometric analysis demonstrating the quantity and quality of research in this domain for scholars. This study aims to fill this gap in this field and to be a preliminary guide for researchers.

Keywords: Bibliometric analysis, Metaheuristic optimization, Mental diseases, Mental disorders, Machine learning, Deep learning

***Corresponding author:** Munzur Üniversitesi, Mühendislik Fakültesi, Bilgisayar Mühendisliği, 62000, Tunceli, Türkiye
E mail: ucan@munzur.edu.tr (Ü. CAN)
Ümit CAN https://orcid.org/0000-0002-8832-6317
Feride TUĞRUL https://orcid.org/0000-0001-7690-8080

Gönderi: 09 Nisan 2025
Kabul: 12 Haziran 2025
Yayınlanma: 15 Temmuz 2025

Cite as: Can Ü, Tuğrul F. 2025. The position of metaheuristic optimization methods in psychiatric practice: A bibliometric analysis. BSJ Eng Sci, 8(4): 1140-1151.

1. Giriş

Ruh sağlığı ile ilgili alanlarda yapılan çalışmalar, hem ruh sağlığında meydana gelen problemlerin analiz edilmesini hem de bu problemlerin çözülmesini amaçlamaktadır. Geleneksel analiz yöntemlerine ek olarak içinde bulunduğumuz yüzyılda ise yapay zekâ yöntemleri ortaya çıkmıştır. Bu akıllı yöntemler ruh sağlığı alanında da etkin bir analiz ve çözüm yöntemi olarak çeşitli aşamalarda kullanılmaktadır. Yapay zekâ yöntemleri kendi paradigmalarına uygun olarak geleneksel veri kaynaklarına ek olarak örneğin çevrimiçi sosyal ağ gibi internetle birlikte ortaya çıkan büyük platformlardaki verileri de kullanmaktadır.

Kim vd., (2020), çevrimiçi sosyal ağlar aracılığıyla ruhsal

This work is licensed (CC BY-NC 4.0) under Creative Commons Attribution 4.0 International License

bozuklukları sınıflandırmak için kullanılan farklı makine öğrenimi yaklaşımlarına genel bir bakış sağlamıştır. Yine başka bir çalışmada ise makine öğrenmesi tabanlı bir yaklaşımla Shuai vd., (2017) sosyal ağların aşırı kullanılması sonucu ortaya çıkan Sosyal Ağ Zihinsel Bozuklukları'nın etken ve etkili bir şekilde tespitini sağlamaktır. Literatürde mental hastalıkları analiz eden makine öğrenmesi yöntemlerinin başarısını arttırmak için metasezgisel optimizasyon yöntemleri kullanılmaktadır. Değişken Komşuluk Arama Algoritması (Mladenović ve Hansen, 1997), Kerevit Optimizasyon Algoritması (Jia vd., 2023), Sürüngen Arama Algoritması (Abualigah vd., 2022), Ateş Böceği Algoritması (Yang ve He, 2013) ve Şempanze Optimizasyon Algoritması (Khishe ve Mosavi, 2020) bu algoritmalardan bazılarıdır (Kozakijevic vd., 2025).

Mental hastalıklarla ilgili çeşitli kaynaklardan toplanmış verilerin yapay zekâ yöntemleri ile analiz edilmesi bu hastalıkların tespiti ve tedavisi için daha hızlı ve etkili çözüm yolları bulmak için ek katkılar sunabilir. Örneğin çeşitli çevrimiçi platformlardaki paylaşım (haber yorumları, alışveriş yorumları, politik paylaşımlar, blog paylaşımları, Instagram, Twitter ve Tiktok gibi sosyal ağlardaki her türden paylaşım) verilerinin kullanılması ile toplumun psikolojik düzeyi belirlenebilir ve spesifik mental hastalıklara karşı politika yapıcılar tarafından önlemler alınabilir. Metasezgisel yöntemlerle optimize edilmiş makine öğrenmesi ve derin öğrenme yöntemleri klinik veriler ile eğitilerek başarılı modeller geliştirilebilir. Bu modeller ise doktorlar ve sağlık çalışanlarına mental hastalıkların teşhisinde yardımcı olabilir. Sağlık sektöründe ruh sağlığı alanındaki karar alma süreçlerini daha da iyileştirebilir.

Literatürde psikiyatri ve metasezgisel yöntemlerin ayrı ayrı anlatıldığı çeşitli bibliyotmetrik çalışmalar yapılmıştır. Sharma ve Chariar (2024), 2012 ve 2023 yıllarını kapsayan mental hastalıkların makine öğrenme yöntemleri kullanılarak teşhis edildiği araştırmalarla ilgili bibliyometrik bir çalışma yapmışlardır. Nassef vd., (2024) hibrid metasezgisel yöntemleri konu alan bir çalışma ortaya koymuşlardır. Ezugwu vd., (2021) ise metasezgisel yöntemlerle ilgili yayınları oldukça geniş bir biçimde anlatan bir bibliyometrik çalışma yapmıştır. Bu tür genel çalışmalar, metasezgisel yöntemlerin yaygın olarak kullanıldığı alanları, yıllık yayın artış oranlarını, en üretken ülkeleri ve yazarları ortaya koymaktadır. Bu çalışmalarda psikiyatri alanından bir alt alan olarak bahsedilmiştir. Detaylı bir araştırma yapıldığında metasezgisel yöntemler ve psikiyatrik alandaki uygulamalarını konu alan bir bibliyometrik bir çalışmanın olmadığı görülmüştür. Bu çalışma metasezgisel yöntemlerin psikiyatrideki uygulamalarını bibliyometrik yöntemle anlatarak literatürdeki çalışmalardan ayrışmaktadır. Bu çalışma da bu alanda yapılan bilimsel çalışmalara ait verilerin ne aşamada olduğunu araştırmacılar için gün yüzüne çıkarmak amacıyla Web of Science (Web of Science, 2025) veri tabanından veriler alınmış ve daha sonra bu veriler VOSviewer (VOSviewer, 2025) programıyla analiz edilmiştir. Elde edilen sonuçlar bu alanda çalışmak isteyecek araştırmacılar için önemli bir başvuru kaynağı görevi görecektir.

2. Literatür

Bu bölümde metasezgisel optimizasyon, psikiyatri, yapay zeka ve benzeri alanlarda yapılan farklı bibliyometrik çalışmalar detaylı bir şekilde anlatılmıştır. Böylece bu çalışmanın bu alandaki yeri ve önemi daha iyi anlatılmaya çalışılmıştır.

Metse vd., (2016) ruh sağlığı ve sigara içiciliği arasındaki ilişkiyi konu alan 547 çalışmayı inceleyerek bu alandaki bilimsel çalışmaların durumunu ortaya koymak için bibliyometrik bir çalışma yapmışlardır. Çalışma sonucunda elde edilen sonuçlar ile bu alandaki araştırmalara ilerleme kolaylığı sağlanmak istenmiştir.

Tran vd., (2019) depresyonun tedavisinde kulanılan yapay zeka yöntemlerini ve tekniklerini anlatan bir bibliyometrik çalışmanın eksikliğine vurgu yaparak bu çalışmayı yapmışlardır. Çalışmanın sonuçlarına göre özellikle 2010 yılından sonra bu alandaki araştırmaların sayısı artmaya başlamıştır. Ayrıca ABD'nin bu alanda öncü konumunda olduğuda ortaya çıkmıştır. Yapay zekanın gelişimi bu alanda çalışan kurum ve kuruluşlara avantaj sağlasada hastalar açısından gizlilik ve veri mahremiyetinin dikkate alınması gerektiği belirtilmiştir.

Kim vd., (2021) yaptıkları çalışmada makine öğrenmesi yöntemleri ile çevrimiçi sosyal ağ verilerini analiz ederek yapılan ruh sağlığı çalışmalarını kullanarak bibliyometrik bir araştırma ortaya koymuşlardır.

Ezugwu vd., (2021) yaptıkları geniş çalışmada metasezgisel yayınları detaylı bir biçimde incelemişlerdir. Makale, bildiri ve kitap gibi yayın türlerinden oluşan toplamda 5.525 çalışma kullanarak analiz yapmışlardır. Çalışma sonucunda metasezgisel yöntemlerin esinlendiği kaynaklar, varyantları, ait olduğu metasezgisel algoritma sınıfı ve uygulama alanları ortaya çıkarılmıştır. Ayrıca eski ve çağdaş metasezgisel algoritmaların kapsamlı bir fotoğrafı çekilmiştir.

Berta vd., (2022) ruhsal hastalıkların bileşenleri ve bunları birbirine bağlayan ilişkilerden oluşan psikopatoloji ağları üzerine yapılan 10 yıllık çalışmaları analiz etmişlerdir. Toplamda 398 makale elde edilmiştir. Elde edilen sonuçlara göre bu yayınlara 1910 yazar katkı sağlamıştır. Bu çalışma sonucuna göre ruh sağlığı ve psikopatolojiyle ilgili bu araştırma alanı nispeten yeni olmasına rağmen, çoğunlukla Amerika Birleşik Devletleri ve Avrupa'da depresyon ve anksiyete bozukluklarındaki semptom ağlarını inceleyen çok sayıda çalışma sayesinde son yıllarda büyük ilerlemeler kaydetmiştir.

Covid-19 pandemi sürecini konu alan bir çalışmada da Guo vd., (2023) bu süreçte çocuk ve ergenlerin ruh sağlığı sorunlarını konu alan çalışmaları analiz etmişlerdir. Bu çalışma en çok atıf alan dergiler ve çalışmalar, yayınların zamansal dağılımı, araştırma eğilimleri gibi önemli noktalar irdelenmiştir. ABD, Çin, Birleşik Krallık ve İtalya'nın bu alandaki araştırmalarda lider olduğu tespit

edilmiştir. Bu alanda çalışacak araştırmacılara önemli bir kaynak olma iddiasındadır.

Hendy vd., (2023) literatürde metasezgisel yöntemlerle ilgili yapılmış çalışmaları geniş bir şekilde anlatan bibliyometrik bir çalışma yapmışlardır. Toplamda 3846 çalışma incelenmiş ve bu alandaki trend çalışma konuları açığa çıkarılmıştır.

Kalra vd., (2023) postmenopozal kadınların psikolojik sağlığı üzerine yayın eğilimlerini ortaya çıkarmak için detaylı bir bibliyometrik çalışma yapmışlardır. Çalışmada toplamda 1718 makale kullanılmıştır. Elde edilen sonuçlara göre bu alanda en fazla yayın 2021 yılında yapılmış ve en çok makale çıkaran ABD olmuştur.

Rajkishan vd., (2024) üniversite öğrencileri arasındaki anksiyete,depresyon ve intihar eğilimleri gibi mental sorunlara yapay zeka yöntemleri ile çözüm bulmaya çalışan çalışmaları konu alan bibliyometrik bir çalışma yapmışlardır. Toplam 200 akademik yayın incelenmiştir. En fazla makale Çin, ABD ve Kore'den gelmiştir. Üniversiteler arasında ise Carnegie Mellon Üniversitesi, Güney Kaliforniya Üniversitesi ve Osaka Üniversitesi en fazla katkıda bulunan üniversiteler olmuştur.

Yapılan bir başka çalışmada ise Chen vd., (2024), 1722 yayın kullanarak yaptıkları bibliyometik çalışmada üniversite öğrencilerinin ruh sağlığı ile ilgili yapılan yapay zeka çalışmalarını analiz etmişlerdir. Bu çalışma bu alanda çalışacak araştırmacılar için bir rehber özelliği olduğunu iddia etmektedir.

Maghfiroh ve Sukmawati (2024) literatürde yayınlanmış ruh sağlığı ile ilgili çalışmaların bibliyometrik analizini yapmışlardır. Bu çalışmada Scopus veri tabanından elde edilen toplam 3558 yayın kullanılmıştır. Çalışma da bu alandaki çalışmaların artan sayısına, bilimsel çalışmaların önemine ve konuyla ilgili büyük medya kuruluşlarının artan ilgisine dikkat çekilmiştir.

Covid-19 salgını boyunca ve sonrasında öğrenciler üzerindeki akademik baskının artması lise öğrencilerinin çeşitli ruh sağlığı problemleri yaşamalarına yol açmıştır. Song vd., (2024) lise öğrencilerinin yaşadıkları mental hastalıkları konu alan 1764 yayını içeren bibliyometrik bir çalışma yapmışlardır. Araştırma sonuçları bu gençlerin ruh sağlığı sonuçlarını iyileştirmek için hedeflenen müdahalelere rehberlik edebilecek önemli bilgiler sağlamaktadır.

Muchemwa vd., (2024) sahra altı Afrika'daki yüksek öğrenim kurumlarındaki öğrencilerin ruh sağlığını inceleyen çalışmaları analiz etmişlerdir. 655 makale kullanılarak yükseköğrenim öğrencilerinin ruh sağlığı alanının kolayca anlaşılabileceği çeşitli çıkarımlar elde edilmiştir. Bu alana olan ilginin özellikle son on yılda önemli ölçüde artmış olması, alanın halen gelişmekte olduğunu ve henüz olgunluğa erişmediğini göstermektedir.

Bir başka Covid-19 ve ruh sağlığı üzerine yapılan bibliyometik çalışmada Wang vd., (2024) salgın nedeniyle bu süreçte etkilenen insanların ruh sağlığını konu alan çalışmaları çok boyutlu ortaya koymuşlardır. Çalışmada toplam 110 ülkeden 7047 çalışma ele alınmıştır. Sonuçlara göre en fazla yayın Çin ve ABD tarafından yapılmıştır. Çalışma bu alandaki trendleri ortaya çıkarmıştır.

Fu vd., (2024) fonksiyonel manyetik rezonans görüntüleme (fMRI) yöntemi ile şizofrenik bireyler üzerinden yapılan çalışmaları araştırmıştır. Toplam 859 çalışmanın analiz edildiği bu bibliyometrik çalışmanın sonuçlarına göre diğer başka çalışmalarda da olduğu gibi ABD ve Çin bu alandaki araştırmalara öncülük etmiştir. Central South Üniversitesi ve New Mexico Üniversitesi en bu alandaki en üretken kurumlar olarak belirlenmiştir. Bu çalışma şizofrenide fMRI çalışmalarının evrimi, mevcut durumu ve gelecekteki yönelimleri hakkında kapsamlı bir genel bakış sağladığını iddia etmiştir.

Lu vd., (2025) depresyon, anksiyete ve uykusuzluk gibi ruh sağlığı sorunlarının tanı ve tedavisinde yapay zeka araçlarının kullanıldığı çalışmaları kullanarak kapsamlı bir bibliyometrik çalışma ortaya koymuşlardır. Bu çalışmanın sonucuna göre sinir ağları, makine öğrenimi, derin öğrenme ve insan-robot etkileşimi kişiye özel tedavi konusunda önemli çalışma alanlarıdır.

Abdulsalam vd., (2025) yaptıkları kapsamlı bibliyometrik çalışmada sağlık hizmetleri ve yapay zeka alanındaki gelişmelere odaklanmışlardır. Bu çalışma kapsamında iki farklı döneme odaklanılarak 2872 yayın analiz edilmiş ve önemli bilgiler çıkarılmıştır. Çalışma sonucunda elde edilen bilgiler yapay zekanın sağlık hizmetleri ve psikolojiyi geliştirme kapasitesini ortaya koymuştur. Tablo 1'de literatürdeki psikiyatri ve yapay zekâ alanlarında yapılan güncel bibliyometrik çalışmalar konu kapsamlarına, kullanılan veri tabanlarına ve veri çekme aralıklarına göre sınıflandırılmıştır.

Tablo 1. Psikiyatri alanında yapılan bibliyometrik çalışmalar

Bibliyometrik Çalışmalar	Çalışmanın Konu Kapsamı	Kullanılan Veri Tabanları	Veri Çekme Tarih Aralıkları
Metse vd., (2016)	Ruh sağlığı ve sigara içme	Medline ve PsycINFO	1993-2015
Tran vd., (2019)	Depresyon, yapay zeka	Web of Science	
Kim vd., (2021)	Sosyal ağ verileri, makine öğrenmesi, ruh sağlığı	Web of Science ve Scopus	2015- 2020
Ezugwu vd., (2021)	Metasezgisel yöntemler	Web of Science	1990-2020
Berta vd., (2022)	Psikopatoloji ağları	Web of Science	2010-2020
Kalra vd., (2023)	Postmenopozal kadınların psikolojik sağlığı	Dimensions	2012-2022
Hendy vd., (2023)	Metasezgisel yöntemler	Scopus	2016-2021
Guo vd., (2023)	Gençlerin ve ergenlerin ruh sağlığı	Web of Science ve Scopus	2019-2020
Rajkishan vd., (2024)	Öğrencilerin ruh sağlığı, makine öğrenmesi yaklaşımları	Web of Science ve Scopus	1973–2022
Chen vd., (2024)	Üniversite öğrencileri, ruh sağlığı, yapay zeka	Web of Science	2003-2023
Maghfiroh ve Sukmawati (2024)	Ruh sağlığı çalışmaları	Scopus	2014-2024
Song vd., (2024)	Lise öğrencilerinin ruh sağlığı	Web of Science	2004-2023
Muchemwa vd., (2024)	Üniversite öğrencilerinin ruh sağlığı	Web of Science	1972-2023
Wang vd., (2024)	Covid-19 ve ruh sağlığı	Web of Science	2020-2023
Fu vd., (2024)	Şizofreni, fMRI	Web of Science	1998-2022
Lu vd., (2025)	Depresyon, anksiyete ve uykusuzluk, yapay zeka	Web of Science	2000-2024
Abdulsalam vd., (2025)	Psikoloji, sağlık hizmetleri ve yapay zeka	Scopus	1960-2023

3. Materyal ve Yöntem

Bu çalışmada Web of Science platformu ve Vosviewer yazılımı kullanılarak metasezgisel optimizasyon algoritmalarının ve mental bozuklukların birlikte yer aldığı veya kullanıldığı ilgili akademik çalışmaların bibliyometrik analizi yapılmıştır. Bu arama çalışması yapılırken Tablo 2'deki anahtar kelimeler ile gösterilen komut ifadesi kullanılmıştır. Bu komut ifadesi daha geniş çalışmaları araştırmak için anahtar kelimeler genişletilerek oluşturulmuştur. Anahtar kelimeler kullanılarak yapılan arama sonucunda elde edilen kayıtların veri temizleme sürecinde çift kayıtlar ve eksik veriler tespit edilmiştir. Çalışmaların başlığı ve Doi numaraları dikkate alınarak tekrar eden kayıtlar aranmış ve sadece iki kayıtın tekrar ettiği görülmüştür. Ayrıca üç çalışmada Doi bilgisi eksikliği tespit edilmiştir. Bu kayıtlar analiz dışında tutulmuştur. Bu oran genel oran dikkate alındığında çok düşüktür.

Tablo 2. Metasezgisel ve Mental Hastalıklar ile ilgili kullanılan anahtar kelimeler

Kullanılan anahtar kelimeler ve arama satırında uygulanan arama ifadesi	("metaheuristic optimization" OR "metaheuristic algorithms" OR "heuristic optimization" OR "particle swarm optimization" OR "genetic algorithm" OR "ant colony optimization" OR "simulated annealing" OR "grey wolf optimizer" OR "firefly algorithm" OR "bat algorithm" OR "whale optimization algorithm" OR "cuckoo search" OR "harmony search" OR "differential evolution" OR "tabu search" OR "artificial bee colony" OR "dragonfly algorithm" OR "moth-flame optimization" OR "salp swarm algorithm" OR "flower pollination algorithm" OR "grasshopper optimization algorithm" OR "multi-verse optimizer" OR "crow search algorithm" OR "imperialist competitive algorithm" OR "seagull optimization" OR "slime mould algorithm" OR "marine predators algorithm") AND ("mental disorder" OR "mental illness" OR "psychiatric disorder" OR "mental health" OR "depression" OR "anxiety" OR "schizophrenia" OR "bipolar disorder" OR "obsessive compulsive disorder" OR "post traumatic stress disorder" OR "PTSD" OR "attention deficit hyperactivity disorder" OR "ADHD" OR "autism spectrum disorder" OR "ASD" OR "eating disorder" OR "anorexia" OR "bulimia" OR "panic disorder" OR "panic attack" OR "phobia" OR "personality disorder" OR "borderline personality disorder" OR "addiction" OR "substance abuse" OR "dementia" OR "Alzheimer" OR "sleep disorder" OR "insomnia")

3.1. Metasezgisel Yöntemler

Metasezgisel terimi zor optimizasyon problemlerinin çözümü için uygulanan daha yüksek seviyeli sezgisel yöntemleri ifade etmek için kullanılır (Dokeroglu vd., 2019). Bu yöntemlerin birçoğu doğadan esinlenilerek türetilmiştir. Bunun en önemli nedeni arıların, kurtların, balinaların ve mikroorganizmalar gibi örnekleri çoğaltılabilecek binlerce canlının sahip oldukları bir zekâ unsuru ile doğada üstlendikleri tüm görevleri en iyi şekilde yapmaya çalışmalarıdır. Metasezgisel yöntemlerde doğada bulunan ve optimum çözüm yolları sunan doğal işleyişleri kullanmaya çalışırlar (Raiwar vd., 2023). Bu yöntemler matematiksel olarak modellenmesi çok zor, nonlinear ve karmaşık olan problemlerin

çözümü için kullanılan yöntemlerdir. Öncelikle bu yöntemlerin diğer optimizasyon yöntemlerinden ayıran en önemli özellik, gradyan tabanlı yöntemlerin aksine arama uzayında türev hesaplamaları kullanmamalarıdır (Tomar vd., 2024). Bu yöntemlere özgü diğer önemli karateristik özellikleri belirtmek gerekirse metasezgisel bir yöntem karmaşık ve çok boyutlu problemlere kesin bir çözüm önermez. Bu yöntemler optimum bir çözüme yakın bir çözüm noktası bulmaya çalışırlar. Bunu yaparken çözüme matematiksel olarak yakınsamasının kanıtlanması gerekmez. Ayrıca olası çözümlerin bulunduğu bir uzayda tüm çözümleri keşfetme zorunluluğu olmadığından hesaplama maliyeti açısından uygun olan yöntemlerdir (Bandaru ve Deb, 2016). Bu yöntemler zorlu optimizasyon problemlerini ele alırken esnek, basit ve yerel optimumlardan kaçınırlar. Karmaşık optimizasyon problemlerini çözmek için geliştirilmiş Bayesian ve Grid Search gibi geleneksel optimizasyon yöntemlerine göre metasezgisel yöntemler çeşitli avantajlarını kullanarak daha iyi sonuçlar elde etmişlerdir. Metasezgisel yöntemler konveks olmayan arama uzayında stokastik arama stratejileri kullanırken geleneksel yöntemler sistematik veya olasılıksal modelleme yöntemlerine dayanır (Halim vd., 2021; Tomar vd., 2024). Grid Search yöntemi uygulama esnasında kapsamlı bir yerel arama stratejisine sahipken metasezgisel yöntemler yerel optimumdan kaçınmalarını sağlayan stokastik yöntemleri kullanır (Papadimitrakis vd., 2021). Çok boyutlu problemlerde ölçeklenebilirliği zayıf olan Grid Search'ün aksine metasezgisel yöntemler geniş arama uzayında iyi performans gösterir. Ayrıca çok amaçlı, sürekli, kısıtlı ve ayrık problem türlerinde gradyan bilgisine ihtiyaç duymadığı için rahatlıkla uygulanabilir (Kareem vd., 2022). Bu açılardan bakıldığın geleneksel yöntemlere göre yerel optimumdan kaçınma, düşük bellek ihtiyacı ve esneklik gibi avantajları vardır. Örneğin çok amaçlı uyarlanabilirlik avantajları nedeni ile optimal güç akışı ve çizelgeleme görevlerinde metasezgisel yöntemler sıklıkla kullanılır (Papadimitrakis vd., 2021). Genetik Algoritmalar ve Karınca Kolonisi Optimizasyonu gibi algoritmalar filtre tasarımı ve harmonik azaltmada başarılı sonuçlar vermişlerdir (Kala vd., 2021). Öbür yandan bu yöntemler bir probleme çözüm sunarken global optimumu garanti etmezler. Geleneksel yöntemler bu konuda daha avantajlıdır. Metasezgisel yöntemlerin rastgelelik özelliği nedeniyle elde edilen sonuçlar arasında farklılıklar olabilir. Ayrıca metasezgisel yöntemlerin parametre hassasiyeti yüksektir. Bu da hiperparametre ayarlarının önemli bir hale getirir.

Günümüzde de kullanılan metasezgisel yöntemlerin çoğu 90'ların başı ile 2000'lerin başı arasında geliştirilmiştir. Genetic Algoritma (Goldberg, 1989), Differansiyel Evrim (Storn ve Price, 1997), Parçacık Sürü Optimizasyonu (Wei ve Qiqiang, 2004), Tabu Arama (Glover ve Laguna, 1998) ve Karınca Koloni Optimizasyonu (Dorigo ve Blum, 2005) gibi yöntemler bu dönemde geliştirilenlerin bazılarıdır. Bu yöntemlere klasik metasezgisel yöntemlerde denilebilir. Son yirmi yıllık süreçte ise bu yöntemlerin geliştirilmesi için çalışmalar oldukça artmış ve birçok yeni yöntem doğadaki farklı süreçlerden etkilenerek önerilmiştir. Yapay Arı Colonisi (Karaboga, 2005), Yerçekimsel Arama Algoritması (Rashedi vd., 2009), Kurt Sürüsü Optimizasyonu (Mirjalili vd., 2014) ve Balina Sürüsü Optimizasyonu (Mirjalili ve Lewis, 2016) son dönemde geliştirilen yeni kuşak metasezgisel algoritmalardan bazılarıdır. Bu yeni yöntemler bazı çözülmesi çok zor olan veya çözülemeyen benchmark problemlerinde en iyi sonuçları elde etmişlerdir (Dokeroglu vd., 2019). Genel olarak metasezgisel yöntemler yapısal dizayn, örüntü tanıma, veri madenciliği, finansal planlama, sinyal ve görüntü işleme, karar verme ve planlama ve ağ güvenliği gibi daha birçok alanda uygulanmaktadır (Gogna ve Tayal, 2013). Bu yöntemlerin sağlık alanında da birçok uygulaması vardır. Bu yöntemler son dönemde popüler hale gelen mental hastalıkları ilgili çözüm arayışlarını içeren çalışmalarda sıklıkla kullanılmaktadır.

3.2. Mental Hastalıklar

Bireylerin duygusal, bilişsel ve davranışsal dengesini bozan ruhsal olguların ve bozuklukların neden olduğu hastalıklar mental hastalıklar olarak tanımlanır. Amerikan Ulusal Sağlık Enstitüsü 2022 yılında ABD'de her beş kişiden birinin mental hasta statüsünde olduğunu bildirmiştir. Bu da yaklaşık olarak nüfusun yüzde 21.3'üne tekabül etmekteydi (National Institute of Mental Health, 2024). Dünya Sağlık Örgütü verilerine göre ise dünya genelinde her sekiz kişiden biri herhangi bir mental hastalığa sahiptir. 2020 yılında özellikle Covid-19 salgını sırasında iki yıl içinde kaygı ve major depresyon oranları yaklaşık %28 artmıştır (World Health Organization, 2022). Anksiyete ve depresyon, 2019 yılında dünya çapında 970 milyondan fazla insanı veya her sekiz kişiden birini etkileyen en yaygın ruhsal bozukluklar olarak belirlenmişti (Caraballo-Arias vd., 2024). Mental hastalıkların genel olarak semptomları aşağıdaki gibidir (American Psychiatric Association, 2022; Paykel, 2008):

- Tuhaf veya saçma fikirler
- Mantıksız öfke veya ajitasyon
- Yetersiz hafıza ve odaklanma, bir konuşmayı takip etmede güçlük,
- Başka kimsenin duyamadığı sesler duyma
- Uyku bozuklukları
- İştah değişiklikleri veya kalori, yiyecek veya egzersiz kontrolüne takıntı
- İnsanlardan kaçınma
- İntihar düşünceleri veya uyuşturucu kullanımı ile birlikte hayatın yaşamaya değmeyeceğine dair fikirler
- Din veya ölüm gibi bir konuyu takıntı haline getirme
- Kişisel hijyeni veya diğer yükümlülükleri yerine getirememe
- İş veya okulda her zamanki gibi iyi performans göstermeme

Yaygın olarak görülen mental hastalıklar aşağıdaki gibi

sıralanabilir:

Kaygı Bozukluğu: Kaygı tehlike anında hissettiğimiz normal bir duygu iken kaygı bozukluğu ise normalin çok üzerinde; aşırı olarak adlandırılabilecek korku ve kaygının davranış bozukluklarına yol açtığı durumu ifade eder (Craske vd., 2011).

Depresyon: Bu rahatsızlık sırasında kişi en az iki hafta boyunca hayata karşı büyük oranda ilgisini kaybedebilir. Bu süre boyunca sinirlilik, üzüntü ve boşluk duygularına kapılır. Buna konsantrasyon bozukluğu, suçluluk hissi, düşük benlik değeri, umutsuzluk, intihar düşünceleri, uyku bozuklukları, iştah veya kilo değişimleri ve enerji kaybı gibi belirtiler eşlik edebilir.

Bipolar Bozukluk: Kişinin depresyon ve mani durumlarını birbirini takip eden dönemler şeklinde yaşadığı bir durum olarak ifade edilebilir. Bu durumda kişi aşırı üzüntü ve boşluk duygusu hissederken ardından mani döneminde aşırı neşe veya sinirlilik, hızlı konuşma, dikkat dağınıklığı ve riskli davranışlar gösterebilir (Carvalho vd., 2020).

Travma Sonrası Stres Bozukluğu: Bir travma olarak adlandırılabilecek bir olaydan sonra kişinin aşırı korku ve tehdit hissetmesi ile oluşur. Bundan sonra belirli aralıklarla olay istemsiz anılar şeklinde kendini tekrar eder. Kişi sürekli olarak tetiktedir ve bu durum günlük yaşam düzenini bozar (Yehuda vd., 2015).

Panik Bozukluk: Birçok insan yaşamları boyunca çok korkutucu ve stresli durumlarda o anki durumum süresine bağlı olarak panik atak geçirebilir. Panik ataklar insanın kontrolünü kaybettiği aşırı korku nöbetleri olarak adlandırılır. Panik bozukluk ise bireyin sık sık, planlanmamış ve uzun süre boyunca istemsiz ve kontrolsüz bir şekilde panik atak geçirmesi durumuna verilen addır (Katon, 2006).

Şizofreni: Dünya çapında insanların yüzde biri, zihni sakatlayan bir durum olan şizofreniden mustariptir. Erkekler ve kadınlar bu hastalıktan eşit derecede etkilenir, ancak kadınlar tipik olarak erkeklerden daha geç başlar. Şizofreni ile ilişkili hem pozitif hem de negatif belirtiler vardır. Halüsinasyonlar, hastayla veya hasta hakkında konuşan sesler ve sıklıkla paranoid olan sanrılar pozitif semptomlara örnektir. Düzleşmiş duygulanım, daha az zevk alma, azalmış irade veya dürtü ve sosyal kopukluk ise negatif belirtilere örnektir. Aile ve psikososyal müdahaleler sonuçları iyileştirebilir (Schultz vd., 2007).

Yeme Bozuklukları: Hâlihazırda yeme bozukluklarının evrensel olarak kabul edilmiş bir tanımı bulunmamakla birlikte, sınıflandırılması için üç temel özellik önerilmiştir (Dalle Grave, 2011). Bu üç temel özelliğin bulunduğu durum yeme bozukluğu olarak tanımlanabilir: i) Yeme düzeninde veya kilo kontrol davranışında belirgin bir bozulma olması; ii) Yeme bozukluğunun veya temel özelliklerinin fiziksel sağlıkta veya psikososyal işlevsellikte klinik olarak anlamlı bir bozulmaya neden olması; iii) Davranış bozukluğunun başka bir psikiyatrik duruma veya genel tıbbi bozukluğa ikincil olmaması.

Yıkıcı Davranışlar ve Dissosyal Davranışlar: Çocukları ve ergenleri etkileyen en yaygın ve zararlı psikiyatrik sorunlar arasında yıkıcı davranış ve dissosyal bozukluklar yer almaktadır (Evans vd., 2024). Birbiriyle ilişkili özelliklere sahip ruh sağlığı bozuklukları topluluğu yıkıcı davranış bozukluğu (DBD) olarak bilinir. Amerikan Psikiyatri Birliği (APA) bu durumları yıkıcı, dürtü kontrol ve davranış bozuklukları olarak adlandırmaktadır. Bu bozukluklar, başkalarının hak ve isteklerini ihlal etmeyi, otorite figürleriyle önemli çatışmalara neden olmayı ve toplumda sağlıksız işleyişe yol açmayı içerdikleri için dikkate değerdir. Bireyin duygularını ve eylemlerini düzenleme kapasitesi yıkıcı, dürtü-kontrol ve davranış bozukluklarından etkilenir. Bu hastalıklardan birine sahip bir kişi, kontrol eksikliğinin bir sonucu olarak sıklıkla başkalarına zarar verebilir veya yasaları ihlal edebilir (Disruptive Behaviour and Dissocial Disorders, 2022).

3.3. Bibliyometrik Analiz

Bibliyometrik analiz, belirli bir araştırma alanındaki kalıpları, eğilimleri ve genel etkiyi ortaya çıkarmayı amaçlayan bilimsel literatürü incelemek için kullanılan sistematik bir yaklaşımdır. Temel adımlar arasında bilimsel veri tabanlarından ilgili verilerin toplanması, toplanan verilerin rafine edilmesi ve temizlenmesi ve önemli içgörüler elde etmek için çeşitli bibliyometrik yöntemlerin uygulanması yer alır (Passas, 2024). Son zamanlarda bibliyometrik analiz büyük ölçekli bilimsel bilgilerin değerlendirilmesindeki etkinliği nedeniyle özellikle iş analizi çalışmalarıda giderek daha yaygın hale gelmiştir. İki önemli etken nedeni ile hızlı bir yaygınlaşma gerçekleşmiştir. İlk olarak, Scopus ve Web of Science gibi yaygın olarak kullanılan bilimsel veri tabanlarının yanı sıra Gephi, Leximancer ve VOSviewer gibi özel bibliyometrik yazılımlarda önemli ilerlemeler kaydedilmiş ve bunlara daha fazla erişilebilirlik sağlanmıştır. İkinci olarak, metodoloji bilgi bilimlerinden iş araştırmaları alanına başarılı bir şekilde uyarlanmış ve aktarılmıştır. Bibliyometrik analizde büyük miktarda bilimsel veri birçok yönden etkili ve anlamlı bir şekilde analiz edilebilmektedir (Donthu vd., 2021).

4. Bulgular

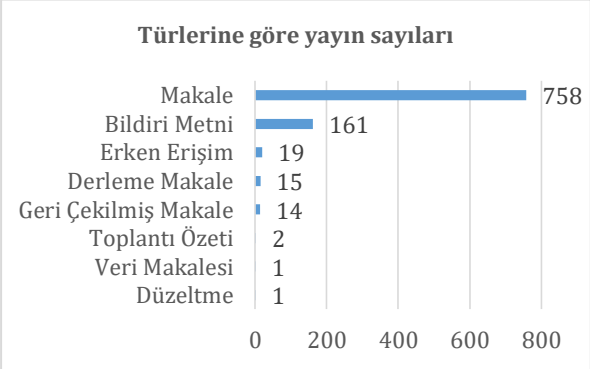
Web of Science veri tabanından elde edilen verilere göre toplamda 928 çalışma hem metasezgisel yöntemleri hem de mental bozuklukları içermektedir. Bu çalışmaların büyük çoğunluğu İngilizce yayınlanmıştır. Tablo 3' de çalışmaların dillere göre dağılımı gösterilmektedir. Bu çalışmaların 918 tanesi İngilizce ve 6 tanesi ise Çince yayınlanmıştır.

Bu alanda yapılan yayınların türleri de önemlidir. Şekil 1'de türlerine göre yayın sayıları verilmiştir.

Türlerine göre yayın sayıları incelendiğinde 758 Makale (Article) yayınlanmıştır. Ardından 161 yayın ile Bildiri Metni (Proceeding Paper) gelmektedir. Derleme Makale (Review Article) sayısı ise 15 olmuştur. En az yapılan yayın türü ise iki yayın ile Toplantı Özeti ve bir yayın ile Veri Makalesi (Data Paper) olmuştur. Yayınların 14 tanesi de geri çekilmiştir.

Tablo 3. Yayınların dillere göre dağılımı

Dil	Yayın Sayısı
İngilizce	918
Çince	6
Eskimo	1
Almanca	1
Portekizce	1
İspanyolca	1



Şekil 1. Türlerine göre yayın sayıları.

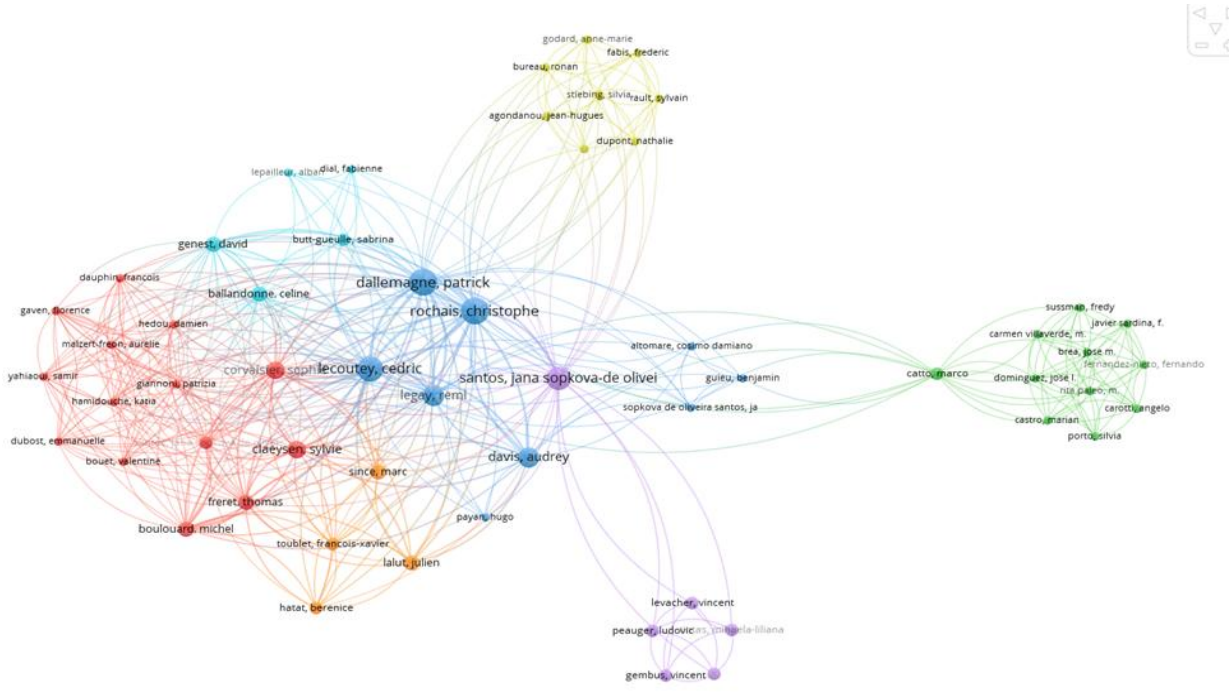
Şekil 2 VOSviewer programı kullanılarak oluşturulmuştur. Bu şekilde bu alanda yapılan çalışmalarda yer alan yazarlar gösterilmektedir. Bu şekilde yer alan her bir düğüm bir yazarı temsil etmektedir. Ayrıca düğümler arasında oluşturulmuş bağlantılar ile çalışmalarda birlikte yer alan yazarlar da göstermektedir. Bu şekilde yazarlar arasında gerçekleşen işbirlikleri de rahatlıkla görülmektedir. Örneğin şekilde iki büyük mavi düğüm ile gösterilen Rochais, Christophe ve Dallemagne, Patrick isimli yazarlar çok sayıda ortak çalışmaya ve çok sayıda bağlantıya sahip yazarlardır. Düğümler arasındaki çizgilerin kalınlığı ise ortak çalışmaların yoğunluğunu göstermektedir.

Yazarları yaptığı yayın sayılarına göre incelediğimizde ise Şekil 3'de gösterilen sonuçlar elde edilmiştir. Artar M ve Santos JSD 11'er yayın ile en fazla yayını yapan yazarlar olmuştur. Dallemagne P ve Rochais C ise 8'er yayınla en çok yayın yapan diğer yazarlar olmuşlardır. En az yayın yapan yazar ise 4 yayın ile Bharanidharan N olmuştur.

Akademik çalışmaların hangi yıllarda yoğunlaştığı veya hangi yıllarda azaldığı gibi veriler ilgili akademik alanın çalışma yoğunluğu ile alakalı bizlere veri verebilir. Buna göre Şekil 4'te son 25 yıla baktığımızda 2000'li yılların başından günümüze kadar yayın sayıları artarak gelmiştir. 2023 senesi 123 yayın ile en fazla yayın yapılan 2024 yılında bu sayı 108 yayın olmuştur. Bu makale hazırlandığında 2025 senesinde henüz 25 yayın yayımlanmıştır.

Şekil 5'te ise yayımlandıkları indeklere göre yayın sayıları verilmiştir. Buna göre yayınları indekslerine göre değerlendirdiğimizde 690 yayınla en fazla Science Citation Index Expanded (SCI-EXPANDED) indeksinden yayın yayımlanmıştır.

Ardından ise 159 yayınla Conference Proceedings Citation Index Science (CPCI-S), 93 yayınla Social Sciences Citation Index (SSCI), 71 yayınla Emerging Sources Citation Index (ESCI), 11 yayınla Index Chemicus (IC) ve 2 yayınla Conference Proceedings Citation Index – Social Science & Humanities (CPCI-SSH) indeksleri gelmektedir.

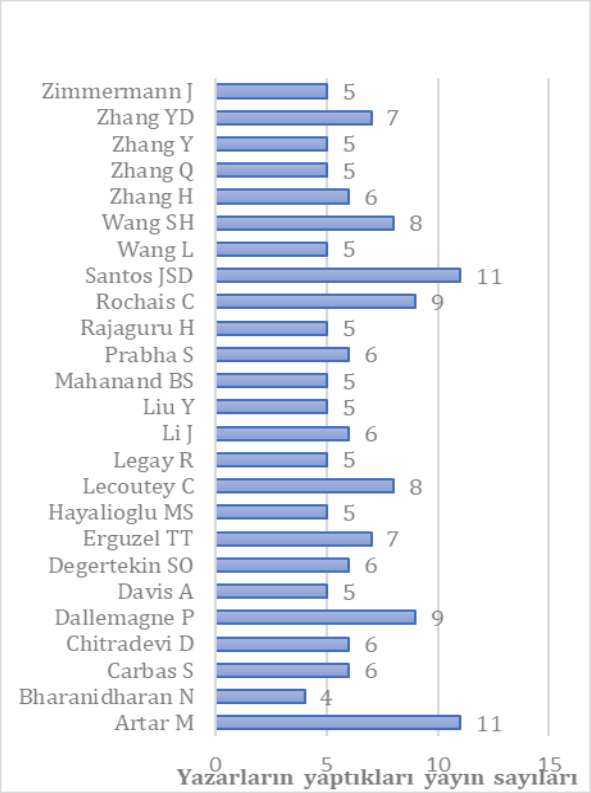


Şekil 2. Akademik çalışmalarda yer alan yazarlar.

Şekil 6'de her bir düğüm bir çalışmada kullanılan yazara ait anahtar kelimeyi temsil etmektedir. Bir düğümün

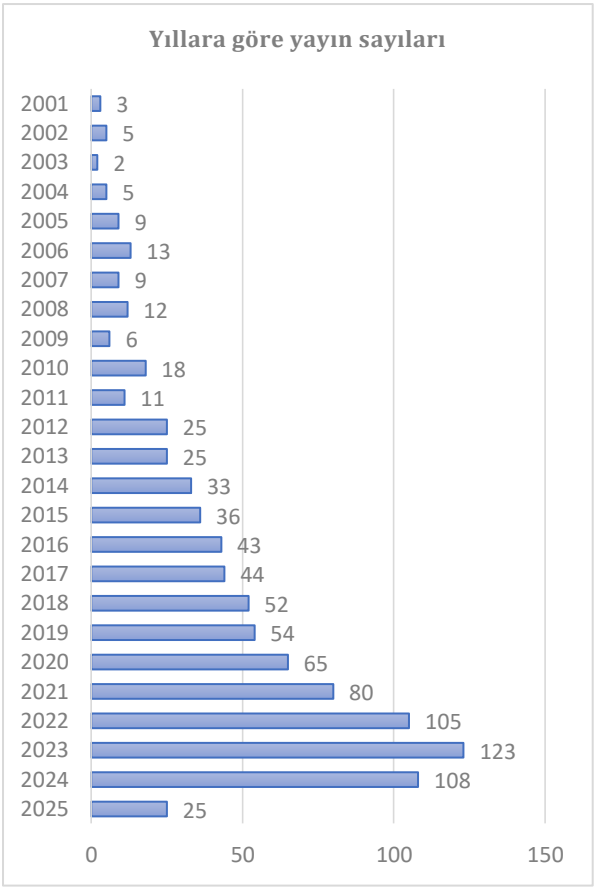
büyüklüğü o anahtar kelimenin literatürde ki yayınlarda kaç kere geçtiğini gösterir. Böylece yazarlar tarafından makalelerde kullanılan anahtar kelimelerin hem görülme sıklığı hem de birlikte görülme sıklığı rahatlıkla incelenebilir. Bu da bize bu alanda kullanılan temel kavramların rahatlıkla anlaşılabilmesini sağlar. Örneğin "Genetic Algorithm", "Alzheimer's disease" ve "Particle Swarm Optimizastion" anahtar kelimelerinin en fazla kullanılanlar arasında olduğu görülmektedir. Ayrıca benzer konularda birlikte kullanılan anahtar kelimeler ise benzer renkler olarak kümelenmiştir. Böylece alt araştırma kategorileri görselleştirilmiş olur.

Şekil 7'te yapılan yayınların Web of Science kategorilerindeki yayımlanma sayılarını göstermektedir. Veriler gösterilirken en fazla yayın yapılan ilk 25 kategori dikkate alınmıştır. Bu göre 143'er yayın ile Computer Science Artificial Intelligence ve Engineering Electrical Electronic alanlarında en fazla yayın yapılmıştır. Bunları 97 yayın ile Computer Science Information Systems, 76 yayın ile Computer Science Theory Methods, 65 yayın ile Mathematical Computational Biology, 61 yayın ile Neurosciences , 58 yayın ile Engineering Biomedical, 51 yayın ile Biochemistry Molecular Biology ve 45 yayın ile Telecommunications alanları takip etmektedir.

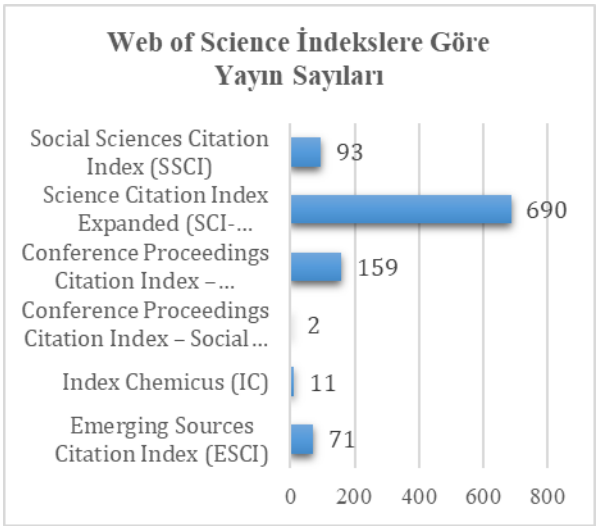


Şekil 3. Yazarlara göre yayın sayıları.

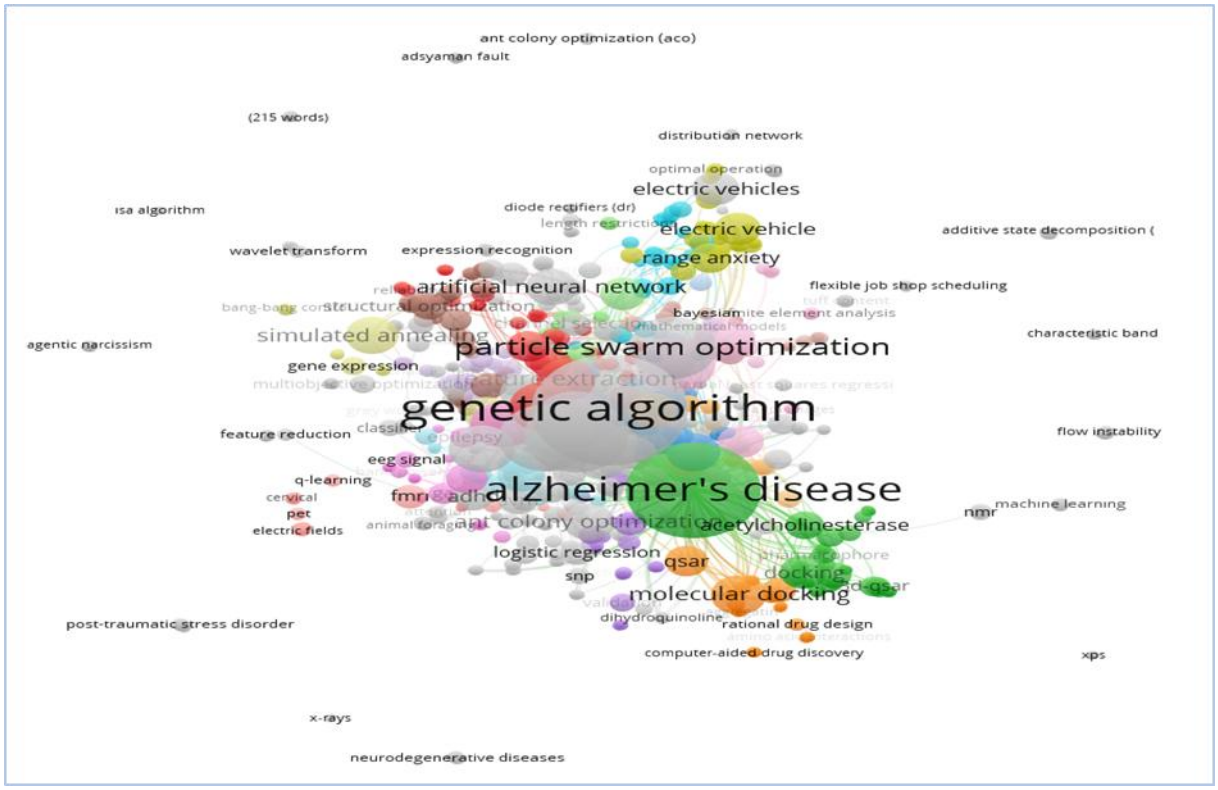
Yapılan çalışmaların hangi kurumlar, kuruluşlar veya fon sağlayıcılar tarafından desteklendiği ile ilgili bilgilere bakıldığında en çok çalışmayı destekleyen kuruluşun 105 çalışma ile National Natural Science Foundation of China kuruluşunun olduğu görülmüştür. Bunu United States Department of Health Human Services 38 destekle ikinci, National Institutes of Health of United States 37 yayınla üçüncü ve European Union ise 15 destek ile dördüncü olmuştur. Ayrıca Alzheimer's Association ve Alzheimer's Drug Discovery Foundation 10'ar çalışmaya finansal destek sunmuşlardır.



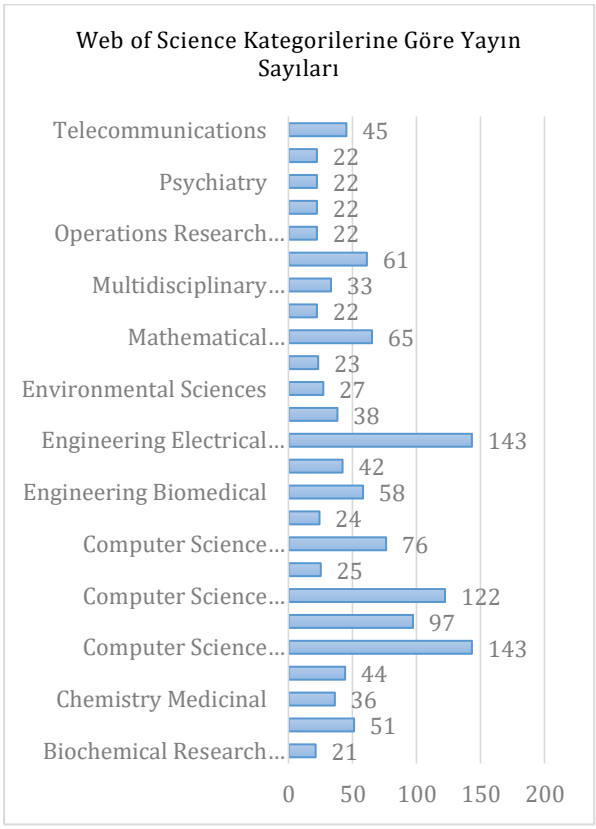
Şekil 4. Yıllara göre yayın sayıları.



Şekil 5. Web of Science indekslerine göre yayın sayıları.



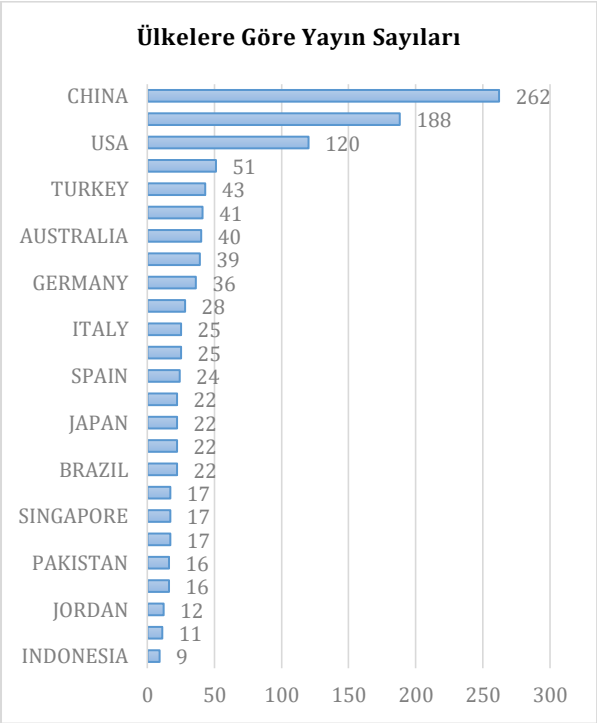
Şekil 6. Anahtar kelimelerin literatürde görülme sıklığı.



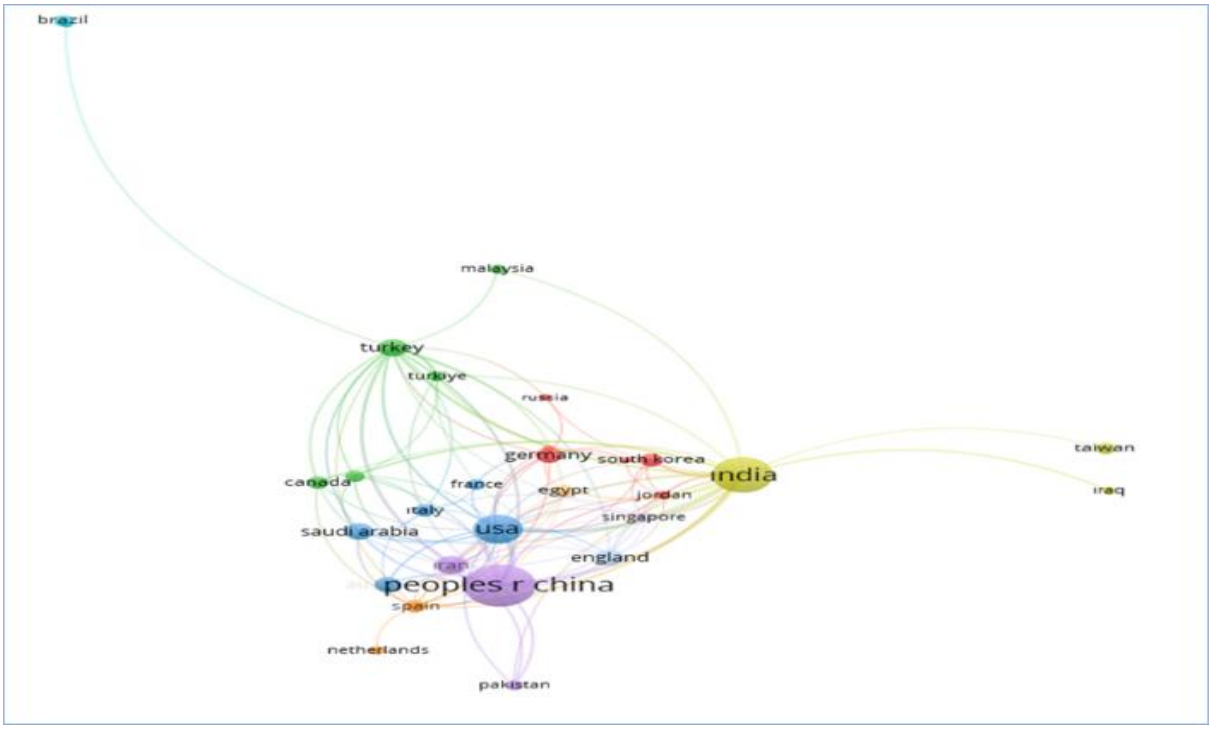
Şekil 7. Web of Science Kategorilerine göre yayın sayılar.

Şekil 8'daki verileri dikkate aldığımızda En fazla yayın yapan ilk üç ülkenin 262 yayınla Çin, 188 yayınla Hindistan ve 120 yayınla ABD olduğu görülmektedir. Bu ülkeleri 51 yayınla İran, 43 yayınla Türkiye ve 41 yayınla Suudi Arabistan takip etmektedir. Bu alanda en az yayın yapan üç ülke ise 12 yayınla Ürdün, 11 yayınla Norveç ve 9 yayınla Endonezya olmuştur.

Ülkelerin Web of Science indekslerindeki yayın sayıları hangi ülkelerin bu alanlara daha çok ilgi duyduğuna dair (her ne kadar ülkedeki nüfus ve üniversite sayısı gibi parametrelerde dikkate alınmalıysa da) bir ipucu verebilir.



Şekil 8. Ülkelere göre yayın sayıları.



Şekil 9. Ülkelere göre atıf sayılarını gösteren grafik.

Şekil 9 bu alanda en çok atıf alan ülkeleri göstermektedir. Bu ülkeler seçilirken en az beş atıf alan ülkeler seçilmiştir. Ayrıca şeklin sağlıklı bir şekilde gösterilebilmesi için en çok atıf alan ülkeler gösterilmiştir. Buna göre Çin, Hindistan, Kanada, Türkiye, Suudi Arabistan, Fransa ve Almanya en çok atıf alan ülkeler konumundadır.

5. Sonuç

Mental bozukluklar günümüz modern toplumlarında yaygın bir şekilde görülmektedir. Ortaya çıkmasında genetik ve çevresel faktörlerin birlikte rol aldığı mental bozukluklar özellikle zorlu ve yoğun tempolu yaşam koşullarının uzun süre kişiler üzerinde stres oluşturmasıyla da oldukça fazla görülmektedir. Önemli toplum sağlığı sorunları arasında gösterilen bu bozuklukların teşhisi ve tedavisi için ilgili sağlık kurum ve kuruluşları tarafından araştırmalar yapılmaktadır. Tedavi yöntemleri ise çok eskiye dayanmakta hatta antik çağlara kadar gitmektedir. Modern tıpla birlikte ise birçok bilimsel yaklaşım kullanılmaktadır.

Günümüzde bu yöntemlere ivme kazandırabilecek makine öğrenmesi ve derin öğrenme gibi yapay zeka yöntemleri mental bozuklukların etkili ve doğru tespit edilmesi için yeni yeni kullanılmaya başlanmıştır. Araştırmacılar bu yöntemleri daha başarılı hale getirmek içinse metasezgisel optimizasyon algoritmaları kullanmaktadır. Modern metasezgisel yöntemler çok boyutlu ve nonlinear problemlerin çözümünde başarılı oldukları için yapay zeka yöntemleri ile birlikte kullanıldıklarında daha iyi sonuçlar vermektedirler. Bu kapsamda bakıldığında metasezgisel yöntemlerin psikiyarti alanındaki problemlerin çözümünde yalnız başına veya birçok karar alma sürecini optimize etme noktasında kullanıldığı çalışmalar önemli hale gelmektedir. Bu noktada araştırmacılara bu alanda yapılan çalışmaların durumunu, trendlerini ve çok yönlü verilerini verecek bir çalışmanın olması bu alanda yapılacak yeni birçok çalışmaya kolaylık sağlayabilir. Bu açıdan bu çalışmada literatür detaylı bir biçimde incelenmiş; metasezgisel yöntemlerin psikiyarti alanında kullanıldığı çalışmaların bir bütün olarak analiz edildiği bir bibliyometrik çalışmanın olmadığı görülmüştür. Bu boşluğu doldurmaya katkı sunma açısında bu çalışma önemlidir. Bu açından bakıldığında bu çalışma bu alanda yapılan bilimsel çalışmaları Web of Science platformundan elde ettiği veriler ışığında ve VOSviewer programının analiz yeteneği ile ortaya koymuştur. Çalışma sonucunda elde edilen sonuçlara göre metasezgisel ve psikiyatrik konu başlıklarının birlikte yer aldığı 928 çalışma olduğu tespit edilmiştir. Bu çalışmaların büyük çoğunluğu İngilizce yayınlanmıştır. Türlerine göre yayın sayıları incelendiğinde 758 adet makale, 161 bildiri yayınlandığı görülmektedir. Son yıllarda artan trende rağmen bu alanda belli bir boşluğun olduğu görülmüştür. Bu sonuçlar dikkate alındığında; bu çalışma gelecekte yapılacak bilimsel çalışmalar için bu alanda önemli bir dayanak noktası ortaya çıkmıştır.

Katkı Oranı Beyanı

Yazarların katkı yüzdeleri aşağıda verilmiştir. Yazarlar makaleyi incelemiş ve onaylamıştır.

	Ü.C.	F.T.
K	50	50
T	40	60
Y	40	60
VTİ	60	40
VAY	50	50
KT	50	50
YZ	40	60
KI	60	40
GR	60	40

K= kavram, T= tasarım, Y= yönetim, VTI= veri toplama ve/veya işleme, VAY= veri analizi ve/veya yorumlama, KT= kaynak tarama, YZ= Yazım, KI= kritik inceleme, GR= gönderim ve revizyon

Çatışma Beyanı

Yazarlar bu çalışmada hiçbir çıkar ilişkisi olmadığını beyan etmektedir.

Etik Onay Beyanı

Bu araştırmada hayvanlar ve insanlar üzerinde herhangi bir çalışma yapılmadığı için etik kurul onayı alınmamıştır.

Kaynaklar

Abdulsalam KO, Torera MN, Dawuda AA, Musa S, Olumide OO. 2025. Emerging trends and insights: A comprehensive bibliometric analysis of artificial intelligence applications in healthcare and psychology. J Adv Math Comput Sci, 40(1): 54-71.

Abualigah L, Abd Elaziz M, Sumari P, Geem ZW, Gandomi AH. 2022. Reptile search algorithm (RSA): A nature-inspired meta-heuristic optimizer. Expert Syst Appl, 191: 116158.

American Psychiatric Association. 2022. Warning signs of mental illness. URL: https://www.psychiatry.org/patients-families/warning-signs-of-mental-illness (accessed date: March 20, 2025).

Bandaru S, Deb K. 2016. Metaheuristic techniques. In: Ravindran AR, editor. Decision sciences. CRC Press, Boca Raton, FL, USA, pp: 709–766.

Berta A, Ángel CM, Clara GS, Rubén H. 2022. A bibliometric analysis of 10 years of research on symptom networks in psychopathology and mental health. Psychiatry Res, 308: 114380.

Caraballo-Arias Y, Feola D, Milani S. 2024. The science behind happiness at work. Curr Opin Epidemiol Public Health, 3(1): 11-24.

Carvalho AF, Firth J, Vieta E. 2020. Bipolar disorder. N Engl J Med, 383(1): 58-66.

Chen J, Yuan D, Dong R, Cai J, Ai Z, Zhou S. 2024. Artificial intelligence significantly facilitates development in the mental health of college students: a bibliometric analysis. Front Psychol, 15: 1375294.

Craske MG, Rauch SL, Ursano R, Prenoveau J, Pine DS, Zinbarg RE. 2011. What is an anxiety disorder? Focus, 9(3): 369-388.

Dalle Grave R. 2011. Eating disorders: progress and challenges. Eur J Intern Med, 22(2): 153-160.

Disruptive Behaviour and Dissocial Disorders. 2022. Disruptive behavior disorders. URL: https://libguides.spsd.org/dissocial (accessed date: March 3, 2025).

Dokeroglu T, Sevinc E, Kucukyilmaz T, Cosar A. 2019. A survey on new generation metaheuristic algorithms. Comput Ind Eng, 137: 106040.

Donthu N, Kumar S, Mukherjee D, Pandey N, Lim WM. 2021. How to conduct a bibliometric analysis: An overview and guidelines. J Bus Res, 133: 285-296.

Dorigo M, Blum C. 2005. Ant colony optimization theory: A survey. Theor Comput Sci, 344(2–3): 243–278.

Evans SC, de la Peña FR, Matthys W, Lochman JE. 2024. Disruptive behavior and dissocial disorders and attention deficit hyperactivity disorder. In: Reed GM, Ritchie PLJ, Maercker A, Rebello TJ, editors. A psychological approach to diagnosis: Using the ICD-11 as a framework. American Psychological Association, Washington, DC, USA, pp: 251–268.

Ezugwu AE, Shukla AK, Nath R, Akinyelu AA, Agushaka JO, Chiroma H, Muhuri PK. 2021. Metaheuristics: A comprehensive overview and classification along with bibliometric analysis. Artif Intell Rev, 54: 4237-4316.

Fu L, Aximu R, Zhao G, Chen Y, Sun Z, Xue H, Liu F. 2024. Mapping the landscape: A bibliometric analysis of resting-state fMRI research on schizophrenia over the past 25 years. Schizophr, 10(1): 35.

Glover F, Laguna M. 1998. Tabu search. In: Handbook of combinatorial optimization. Springer, Boston, MA, USA, pp: 2093–2229.

Gogna A, Tayal A. 2013. Metaheuristics: Review and application. J Exp Theor Artif Intell, 25(4): 503-526.

Goldberg DE. 1989. Genetic algorithms in search, optimization, and machine learning. Addison-Wesley, Boston, MA, USA, pp: 412.

Guo Z, Zhang Y, Liu Q. 2023. Bibliometric and visualization analysis of research trend in mental health problems of children and adolescents during the COVID-19 pandemic. Front Public Health, 10: 1040676.

Halim AH, Ismail I, Das S. 2021. Performance assessment of the metaheuristic optimization algorithms: An exhaustive review. Artif Intell Rev, 54(3): 2323-2409.

Hendy H, Irawan MI, Mukhlash I, Setumin S. 2023. A bibliometric analysis of metaheuristic research and its applications. Register J Ilm Teknol Sist Inform, 9(1): 1-17.

Jia H, Rao H, Wen C, Mirjalili S. 2023. Crayfish optimization algorithm. Artif Intell Rev, 56(Suppl 2): 1919-1979.

Kala P, Joshi P, Joshi M, Agarwal S, Yadav LK. 2021. Applications of metaheuristics in power electronics. In: Tiwari A, Singh MK, Gupta SK, editors. Recent advances in power electronics and drives. Springer, Singapore, pp: 155–186.

Kalra S, Aggarwal G, Pawaria S, Yadav S, Ajmera P. 2023. Psychological health of postmenopausal women: A bibliometric analysis in the recent decade. Climacteric, 26(5): 428-436.

Karaboga D. 2005. An idea based on honey bee swarm for numerical optimization. Erciyes Univ Press, Kayseri, Türkiye, pp: 10.

Kareem SW, Ali KWH, Askar S, Xoshaba FS, Hawezi R. 2022. Metaheuristic algorithms in optimization and its application: A review. J Adv Res Electr Eng, 6(1).

Katon WJ. 2006. Panic disorder. N Engl J Med, 354(22): 2360-2367.

Khishe M, Mosavi MR. 2020. Chimp optimization algorithm. Expert Syst Appl, 149: 113338.

Kim J, Lee J, Park E, Han J. 2020. A deep learning model for detecting mental illness from user content on social media. Sci Rep, 10(1): 11846.

Kim J, Lee D, Park E. 2021. Machine learning for mental health in social media: Bibliometric study. J Med Internet Res, 23(3): e24870.

Kozakijevic S, Jovanovic L, Tedic S, Jankovic N, Zivkovic M, Bacanin N. 2025. Modified metaheuristic optimization algorithm for hyperparameter tuning in mental health applications. In: Proc 6th Int Conf Mobile Comput Sustain Inform (ICMCSI), IEEE, pp: 948–953.

Lu E, Zhang D, Han M, Wang S, He L. 2025. The application of artificial intelligence in insomnia, anxiety, and depression: A bibliometric analysis. Digit Health, 11: 20552076251324456.

Maghfiroh NH, Sukmawati B. 2024. Bibliometric analysis: Mental health problems in a decade. West Sci Soc Humanit Stud, 2(5): 706–715.

Metse AP, Wiggers JH, Wye PM, Wolfenden L, Prochaska JJ, Stockings EA, Bowman JA. 2016. Smoking and mental illness: A bibliometric analysis of research output over time. Nicotine Tob Res, ntw249.

Mirjalili S, Lewis A. 2016. The whale optimization algorithm. Adv Eng Softw, 95: 51–67.

Mirjalili S, Mirjalili SM, Lewis A. 2014. Grey wolf optimizer. Adv Eng Softw, 69: 46–61.

Mladenović N, Hansen P. 1997. Variable neighborhood search. Comput Oper Res, 24(11): 1097-1100.

Muchemwa M, Sodi T, Themane M. 2024. A bibliometric analysis of mental health research in places of higher learning in sub-Saharan Africa. Soc Sci Humanit Open, 10: 100950.

Nassef AM, Abdelkareem MA, Maghrabie HM, Baroutaji A. 2024. Hybrid metaheuristic algorithms: A recent comprehensive review with bibliometric analysis. Int J Electr Comput Eng, 14(6).

National Institute of Mental Health. 2024. Mental illness. URL: https://www.nimh.nih.gov/health/statistics/mental-illness (accessed date: March 15, 2025).

Papadimitrakis M, Giamarelos N, Stogiannos M, Zois EN, Livanos NI, Alexandridis A. 2021. Metaheuristic search in smart grid: A review with emphasis on planning, scheduling and power flow optimization applications. Renew Sustain Energy Rev, 145: 111072.

Passas I. 2024. Bibliometric analysis: The main steps. Encycl, 4(2).

Paykel ES. 2008. Basic concepts of depression. Dialogues Clin Neurosci, 10(3): 279-289.

Rajkishan SS, Meitei AJ, Singh A. 2024. Role of AI/ML in the study of mental health problems of the students: A bibliometric study. Int J Syst Assur Eng Manag, 15(5): 1615-1637.

Rajwar K, Deep K, Das S. 2023. An exhaustive review of the metaheuristic algorithms for search and optimization: Taxonomy, applications, and open challenges. Artif Intell Rev, 56(11): 13187-13257.

Rashedi E, Nezamabadi-Pour H, Saryazdi S. 2009. GSA: A gravitational search algorithm. Inf Sci, 179(13): 2232–2248.

Schultz SH, North SW, Shields CG. 2007. Schizophrenia: A review. Am Fam Physician, 75(12): 1821-1829.

Sharma CM, Chariar VM. 2024. Diagnosis of mental disorders using machine learning: Literature review and bibliometric mapping from 2012 to 2023. Heliyon.

Shuai HH, Shen CY, Yang DN, Lan YFC, Lee WC, Yu PS, Chen MS. 2017. A comprehensive study on social network mental disorders detection via online social media mining. IEEE Trans Knowl Data Eng, 30(7): 1212-1225.

Song S, Yu W, Li S, Sun W, Fu J, Cheng Q. 2024. A bibliometric analysis of mental health among high school students. Front Psychiatry, 15: 1433897.

Storn R, Price K. 1997. Differential evolution – A simple and efficient heuristic for global optimization over continuous spaces. J Glob Optim, 11(4): 341–359.

Tomar V, Bansal M, Singh P. 2024. Metaheuristic algorithms for optimization: A brief review. Eng Proc, 59(1): 238.

Tran BX, McIntyre RS, Latkin CA, Phan HT, Vu GT, Nguyen HLT, Ho RC. 2019. The current research landscape on the artificial intelligence application in the management of depressive disorders: A bibliometric analysis. Int J Environ Res Public Health, 16(12): 2150.

VOSviewer. 2025. Welcome to VOSviewer. URL: https://www.vosviewer.com/ (accessed date: March 13, 2025).

Wang L, Ye L, Jin Y, Pan X, Wang X. 2024. A bibliometric analysis of the knowledge related to mental health during and post COVID-19 pandemic. Front Psychol, 15: 1411340.

Web of Science. 2025. URL: https://www.webofscience.com/wos/woscc/basic-search (accessed date: March 14, 2025).

Wei Y, Qiqiang L. 2004. Survey on particle swarm optimization algorithm. Eng Sci, 5(5): 87–94.

World Health Organization. 2022. Mental disorders. URL: https://www.who.int/news-room/fact-sheets/detail/mental-disorders (accessed date: March 5, 2025).

Yang XS, He X. 2013. Firefly algorithm: Recent advances and applications. Int J Swarm Intell, 1(1): 36-50.

Yehuda R, Hoge CW, McFarlane AC, Vermetten E, Lanius RA, Nievergelt CM, Hyman SE. 2015. Post-traumatic stress disorder. Nat Rev Dis Primers, 1(1): 1-22.

Black Sea Journal of Engineering and Science
doi: 10.34248/bsengineering.1685735

Open Access Journal
e-ISSN: 2619 – 8991

Research Article
Volume 8 - Issue 4: 1152-1159 / July 2025

A NEW APPROACH TO NON-DESTRUCTIVE TESTING USING OPENCV-BASED IMAGE PROCESSING

Ekrem BULUT[1], Emre GÖRGÜN[2]*

[1]*Sivas Cumhuriyet University, Faculty of Engineering, Department of Mechanichal Engineering, 58104, Sivas, Türkiye*
[2]*Sivas Cumhuriyet University, Sivas Technical Sciences Vocational School, Department of Motor Vehicles and Transportation Systems, 58104, Sivas, Türkiye*

Abstract: This study investigates the potential of image processing techniques to improve quality control processes in welding and to enable the effective detection of defects. Given the inherent human errors and time-consuming nature of traditional quality control methods, image processing technologies emerge as an automated and highly precise alternative. In this context, the OpenCV library was utilized to analyze defects in weld seams and their geometric properties. Reference points were established on images using a two-point laser system to facilitate high-accuracy measurements on planar surfaces. Through the implementation of image processing techniques such as edge detection and contour analysis, welding defects were automatically identified, yielding results that are fasters.

Keywords: Weld quality, Image processing, OpenCV, Non-destructive testing, Weld defects, Point laser

***Corresponding author:** Sivas Cumhuriyet University, Sivas Technical Sciences Vocational School, Department of Motor Vehicles and Transportation Systems, 58104, Sivas, Türkiye
E mail: emregorgun@cumhuriyet.edu.tr (E. GÖRGÜN)
Ekrem BULUT https://orcid.org/0009-0007-2259-9703
Emre GÖRGÜN https://orcid.org/0000-0002-1971-456X

Received: April 28, 2025
Accepted: June 16, 2025
Published: July 15, 2025

Cite as: Bulut E, Görgün E. 2025. A new approach to non-destructive testing using opencv-based image processing. BSJ Eng Sci, 8(4): 1152-1159.

1. Introduction

In modern industrial manufacturing, ensuring weld quality is a critical requirement, especially in applications demanding high precision such as laser spot welding. Traditional quality control methods rely heavily on manual inspection, and as noted by Stavropoulos and Sabatakakis, such methods present challenges in high-volume production environments due to inconsistency, subjectivity, and inefficiency.

The increasing complexity and precision of welding processes have intensified interest in integrating intelligent systems into production lines. Gook et al. demonstrated that AI-based monitoring systems significantly enhance process stability and reduce defect rates in pipe welding (Pham et al., 2024; Yue, 2024). Similarly, Islam and colleagues emphasized the critical role of computer vision and deep learning in automating quality control processes, offering more accurate real-time defect detection compared to conventional methods. In recent years, visual sensing technologies have shown substantial promise in robotic welding applications. A comprehensive review by Guo et al. highlighted that these technologies not only enable real-time weld seam tracking but also support adaptive control mechanisms for dynamic welding environments. Pham and his team successfully applied machine learning algorithms for weld seam tracking and coordinate extraction, demonstrating the feasibility of fully automated weld inspection systems in real-world scenarios (Cardellicchio et al., 2024).

Furthermore, advancements in neural network architectures have paved the way for more robust defect detection methods. For instance, Ajmi et al. proposed an enhanced Faster R-CNN model capable of accurately detecting weld defects in limited X-ray image datasets. Zhang and Zhan developed a lightweight and efficient MobileViT-based model that provides effective defect classification in weld imagery (Gook et al., 2024; Stavropoulos and Sabatakakis, 2024).

The convergence of AI-assisted visual inspection with precise sensor integration is becoming inevitable for future smart manufacturing systems. In this context, Sutherland and his team introduced an innovative approach by synchronizing low-cost spectral and imaging sensors to enhance material characterization during welding (Guo et al., 2024; Islam et al., 2024). These developments indicate a future where welding systems can self-diagnose, adapt to changing conditions, and optimize performance without human intervention (Gorgun, 2024).

This study aims to develop an AI-based weld inspection framework focused on real-time defect detection and system adaptability, building on the knowledge and methods presented in these earlier studies. The developed laser-referenced image processing system enables reliable defect detection through direct physical measurement, without the need for complex AI models (Wang et al., 2024; Zhang et al., 2024). The high accuracy

This work is licensed (CC BY-NC 4.0) under Creative Commons Attribution 4.0 International License

in measurement and the consistent detection of reference points across various weld surfaces enhance the system's applicability in industrial environments. The software's ability to deliver consistent results aligned with manual measurements and to automate the inspection process while minimizing human error demonstrates clear advantages over traditional quality control approaches (Ji et al., 2024). Therefore, this study not only presents a novel approach to evaluating weld quality but also contributes a cost-effective, interpretable, and scalable solution for smart manufacturing systems.

2. Materials and Methods

2.1. Materials

The study was conducted using 3 mm thick S235 low carbon steel samples that underwent a MAG (Metal Active Gas) welding process to generate various weld features and potential defects for analysis. Image acquisition was performed using an IMX219 camera module with a resolution of 3280x2464, positioned at a consistent distance of 50 mm from the samples under controlled illumination provided by five 110-lumen LED lights [18]. The experimental design took into account the potential impact of varying illumination conditions during image capture, as visually represented in Figure 1a with a darker background and Figure 1b with a lighter background, while the crucial reference points remain visible in both scenarios.

For establishing precise reference points, a custom-designed laser-assisted equipment was utilized. This equipment projected two red laser points, maintaining a fixed 10 mm distance between them on the welding sample surface. Key components included two point lasers with a wavelength of 543.5 nm, a stable and ergonomic housing designed in SolidWorks, 0.4 mm inner diameter nozzles on the laser outputs to improve beam focus (with black internal coating), an integrated LED light source for supplementary lighting, and a 4.2-volt rechargeable lithium-ion battery (AA size) with a TP4056 charging module for power. The image processing algorithms were developed to be robust against potential extraneous elements present in the captured frames, such as the distinct black dot visible in both Figure 1a and Figure 1b, ensuring that these elements do not interfere with the accurate detection of the laser reference points (Akkus and Gorgun, 2015; Görgün, 2024).

The primary software platform was the OpenCV library (version 4.10.0) within the Python programming language (version 3.11), supplemented by NumPy and Matplotlib for numerical operations and visualization. To ensure accurate calibration and pixel-to-millimeter conversion, a precision 10 mm division calibration target was imaged under identical conditions as the welding samples. The consistent visibility and detectability of the primary reference points under the different background illuminations shown in Figure 1a and Figure 1b underscore the reliability of the chosen referencing method for achieving accurate measurements.

2.2. Measurement Verification Procedure

To validate the accuracy of the image-based measurement system, a specific procedure was implemented using a reference image containing two distinct points with a known physical distance. Initially, a digital image of these reference points, captured under varying illumination conditions and potentially including extraneous elements as seen in Figure 1, was loaded into the image processing environment. To ensure reliable detection, the image's brightness and contrast were adjusted using the cv2.convertScaleAbs function in OpenCV (Lopez-Fuster et al., 2024). Subsequently, the image's color space was converted to HSV to facilitate the segmentation of the red reference points (Ajmi et al., 2024; Liu et al., 2025).

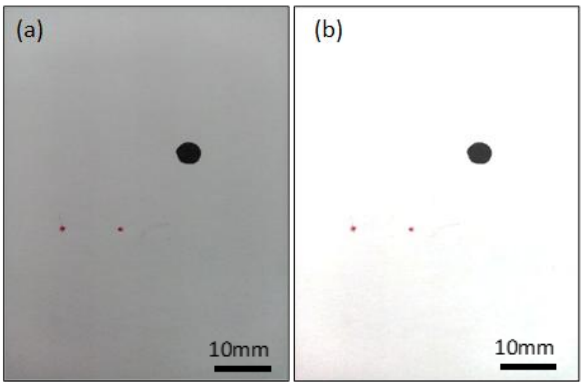


Figure 1.Measurement verification procedure.

Specific HSV color ranges were defined, and binary masks were created and combined to isolate the red pixels. Contours of these red regions were then detected, and their centroids were calculated using image moments, yielding the pixel coordinates of the reference points. Finally, if two significant red points were identified, the Euclidean distance between their pixel coordinates was calculated. Knowing the actual physical distance (10 mm, provided by the laser-assisted equipment shown in Figure 4), a pixel-to-millimeter conversion ratio was determined by dividing the known physical distance by the measured pixel distance. This ratio served as the calibration factor for subsequent measurements.

2.3. Referenced Measurement Software Implementation

The core of our methodology lies in the Referenced Measurement Software Implementation, whose workflow is illustrated in Figure 2. This custom-developed software, leveraging the power of Python and the OpenCV library, automates the critical stages involved in assessing weld quality (Mobaraki, 2025; Xu et al., 2025). The process begins with Image Acquisition and Loading. Here, the software first captures and then loads a digital image of the welded sample. It is crucial that the laser-generated reference points are clearly visible

within this captured frame, as depicted in the initial stage of Figure 2. Next, the software performs Image Pre-processing (Sutherland et al., 2024; Voelkel et al., 2024). This essential step involves enhancing the relevant features within the image while simultaneously reducing noise. Techniques such as converting the image to grayscale and applying thresholding are employed to segment the brighter regions, as shown in the second stage of Figure 2.

Following pre-processing, the software proceeds with Reference Point Detection. In this stage, the centroids, or center points, of the two laser reference points are precisely identified within the pre-processed image. This is achieved through contour detection and the calculation of image moments, representing the third stage in Figure 2. With the reference points located, the software moves to Calibration and Scale Determination. Utilizing the known physical distance of 10 mm between the laser points and the measured pixel distance within the image, the software calculates a precise pixel-to-millimeter scale factor. This crucial calibration step is the fourth stage illustrated in Figure 2. Subsequently, the software undertakes Region of Interest Analysis. Based on the established calibrated scale, specific areas of interest within the weld region are meticulously examined for potential defects. This involves employing further image processing techniques, including brightness enhancement, inverse thresholding to highlight darker potential defect areas, and contour analysis to accurately identify and measure the dimensions (such as length and area) of these regions, as demonstrated in the fifth stage of Figure 2.

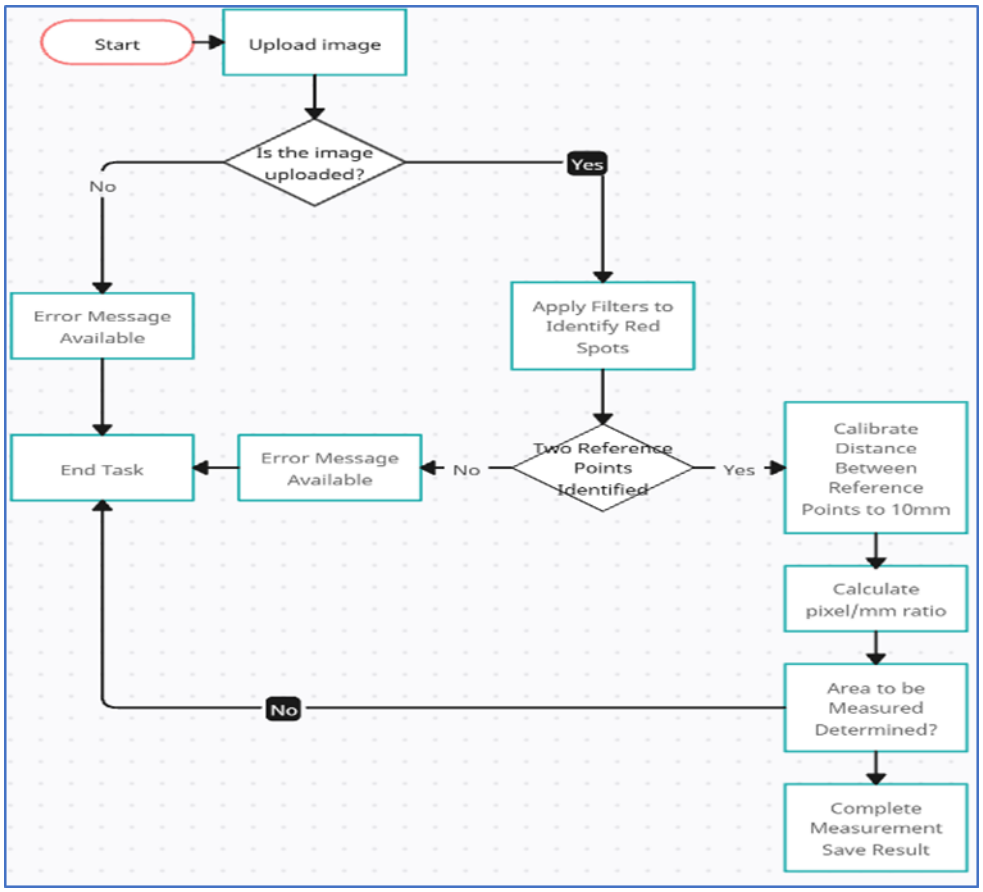


Figure 2. Flow diagram.

Finally, the software culminates in Output and Reporting. The end result is a processed image where any identified potential defects are clearly highlighted, and their measured dimensions are displayed with a high degree of accuracy, estimated at approximately 0.01 millimeters. This final output and reporting phase is the sixth and concluding stage shown in Figure 2.

Following the detection of reference points (the third step in Figure 2), Calibration and Scale Determination is performed. As the fourth step in Figure 2 illustrates, the software utilizes the known physical distance between the laser points (10 mm) and the calculated pixel distance in the image to determine the crucial pixel-to-millimeter scale factor (Pham et al., 2024; Stavropoulos and Sabatakakis, 2024; YU et al., 2024). Building upon this calibrated scale, the software proceeds with Region of Interest Analysis, which is the fifth step shown in Figure 2. Based on this scale, specific regions of interest (ROIs) within the weld area are analyzed for potential defects (Görgün, 2022). This stage involves further image processing techniques, including brightness enhancement (using cv2.convertScaleAbs), inverse

thresholding to highlight darker areas indicative of potential defects, and contour analysis (using cv2.boundingRect and cv2.drawContours) to identify and measure the dimensions (such as length, area, and diameter, if applicable) of these regions (Gorgun and Karamis, 2019; Mobaraki, 2025).

Finally, the software concludes with Output and Reporting, the sixth and final step in Figure 2. The result is an output that includes the processed image with any identified potential defects clearly highlighted, along with their measured dimensions displayed with an estimated accuracy of approximately 0.01 millimeters.

2.4. Mathematical Models for Determining Weld Quality

Computer vision and image processing techniques, particularly those implemented through OpenCV, have become crucial for the non-destructive evaluation of weld qualityy. With the increasing application of robotic welding systems in Industry 4.0, the need for automated and precise quality control systems has risen. Previous studies, such as those by Zhang et al. (2019), emphasize the role of edge detection in weld inspection, where OpenCV's Sobel operator is widely used to calculate gradient magnitudes for accurate identification of weld edges (equation 1). These edge detection techniques enable precise localization of the weld boundaries, a key step in evaluating the overall weld quality.

$$G = G_x{}^2 + G_y{}^2 \quad (1)$$

Subsequently, the weld bead width is measured by determining the distance between the detected edges. This approach, validated in studies like that of Kim & Lee (2020), demonstrates how measuring bead width variation can provide insights into potential defects such as excessive weld or underfill (equation 2). OpenCV's contour detection and morphological operations are key tools for this measurement, allowing efficient identification of irregularities in the weld bead structure.

$$W = X_{right} + X_{left} \quad (2)$$

Weld symmetry is another critical factor in determining the quality of the joint. Pearson's correlation coefficient, implemented in OpenCV for comparing the symmetry between the left and right halves of the weld, has been shown to correlate with overall weld quality (Wang et al., 2021) (equation 3). OpenCV's image processing functions, such as cv2.matchTemplate, can assist in assessing the degree of symmetry, a vital indicator of the process's stability.

$$x = \frac{\sum(x_i - x)(\dot{y_i} - \dot{y})}{\sqrt{\sum(x_i - \dot{x})(y_i - y)}} \quad (3)$$

All of these individual quality indicators—edge detection, bead width, and symmetry—are integrated into a comprehensive quality score through a weighted model. Sun et al. (2022) proposed a multi-criteria decision-making framework that aligns well with OpenCV-based image processing approaches, providing a robust method for automated quality assessment of welds in real-time (equation 4).

$$Q = W_1 f_1 + W_2 f_2 + W_3 f_3 \quad (4)$$

By leveraging OpenCV's powerful image processing libraries, this approach offers a repeatable, automated, and accurate method for weld quality evaluation, minimizing human error and ensuring high-quality manufacturing processes.

2.5. Experimental Setup

The evaluation of the developed methodology relied on a set of 5 welded samples displaying porosity and crack defects. The image acquisition setup involved a fixed camera position relative to the samples to ensure consistent capture of the reference points generated by our custom-designed laser-assisted measurement equipment, illustrated in Figure 3.

Figure 3a presents the SolidWorks design of this specialized equipment, prioritizing stability and ergonomic handling for consistent laser projection. Key components visible include the laser diode housings and adjustable nozzle mounts for precise beam focusing, with overall housing dimensions optimized for integration.

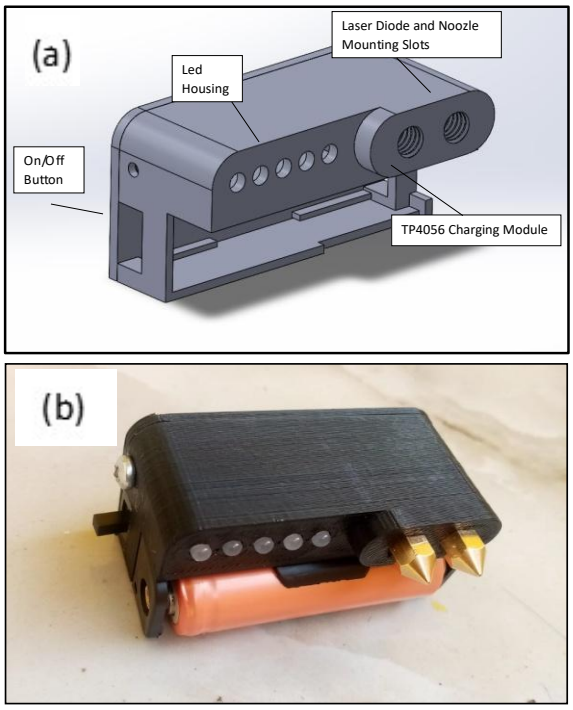


Figure 3. Experimental setup.

Figure 3b shows the physical prototype, housing point lasers emitting at a specific wavelength and incorporating 0.4 mm inner diameter nozzles with black internal coating for well-defined laser spots. This equipment was positioned to project its two distinct laser reference points directly onto the weld bead or the specific area of interest on the samples. The consistent separation of these points within the image frame served as the fundamental basis for calibrating the pixel-to-millimeter scale. Images were captured under controlled

lighting conditions to ensure clear visibility of both the weld features and the laser reference points generated by the equipment (Figure 3b in operation).

The captured images, containing the weld samples and the laser-generated reference points (Figure 3), were then processed by the developed software to detect these reference points, establish the image scale, and analyze the weld area for potential defects, yielding dimensional measurements for any identified anomalies. The reliability of this measurement approach was validated by comparing the software's output with manual measurements.

3. Results

3.1. Laser-Based Scale Calibration

The measurement verification procedure, utilizing the two red laser reference points projected by the custom-designed laser-assisted measurement equipment (shown in Figure 4) with a known physical distance of 10 mm, yielded a consistent pixel-to-millimeter conversion ratio. This procedure involved capturing images of the reference points using the IMX219 camera module (3280x2464 resolution) under controlled illumination from five 110-lumen LED lights. Across multiple trials with these reference images, the calculated pixel distances between the centroids of the detected red laser points exhibited minimal variation. The average pixel distance measured was 80.0 pixels, resulting in an average pixel-to-millimeter ratio of 0.0995 mm/pixel. The standard deviation of the measured pixel distances was ±0.15 pixels, indicating a high degree of consistency in the detection of the 543.5 nm wavelength laser reference points and the subsequent distance measurement.

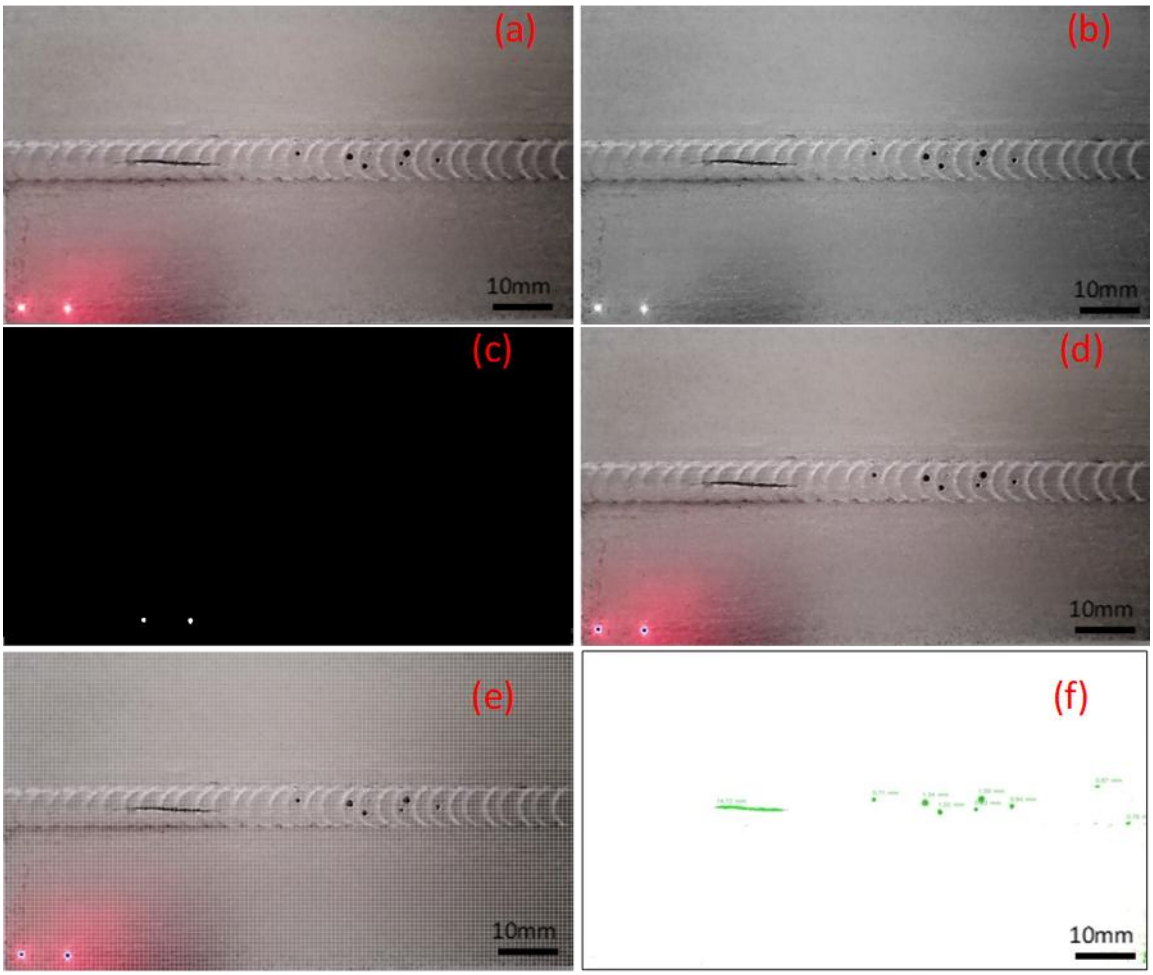


Figure 4. (a-f) Image processing stages.

The final image obtained after the measurement verification process, showing the detected red laser reference points, is conceptually presented in Figure 4. While Figure 4 primarily illustrates the laser-assisted measurement equipment itself, it implicitly represents the device used to generate the consistent 10 mm separation between the reference points crucial for this verification. The consistency observed across different initial image conditions (Figure 4 (a) and (b), representing variations in background or minor lighting differences), the effectiveness of the image enhancement (conceptually in Figure 4 (c)), the accurate red point segmentation (conceptually in Figure 4 (d)), and the reliable final detection of the reference points (conceptually in Figure 4 (e) and (f)) confirm the robustness of the image processing pipeline.

This verification confirms the reliability of the image processing system, utilizing the stable 10 mm reference provided by the laser-assisted measurement equipment (Figure 4), in establishing an accurate scale (0.0995 mm per pixel) for subsequent dimensional measurements of weld features and potential defects on the S235 low carbon steel samples welded using the MAG technique).

3.2. Reference Point Detection in Weld Images

The developed referenced measurement software successfully automated the process of detecting the laser reference points, calibrating the image scale, and analyzing the weld areas for potential defects. The software was able to accurately identify the centroids of the two laser points in the captured images of the welded samples across varying surface conditions and weld bead geometries. As demonstrated in the measurement verification process (Figure 4), the initial image processing steps effectively isolate the laser reference points, enabling reliable calibration for the subsequent weld analysis. The calibration based on these reference points allowed for the conversion of pixel-based measurements to real-world dimensions with the established pixel-to-millimeter ratio. The software effectively highlighted potential defect regions based on the defined image processing steps, including brightness adjustments, thresholding, and contour analysis.

3.3. Dimensional Analysis of Weld Defects

The software provided dimensional measurements (length, area, and approximate diameter where applicable) for the identified potential defects in the analyzed weld samples. For a set of 5 identified defects across the samples, the software-generated length measurements were compared with manual measurements taken using a calibrated digital caliper. The average discrepancy between the software-based measurements and the manual measurements was determined to be 0.03 mm, with the maximum deviation observed being 0.05 mm. Similarly, the software-estimated areas of the defects showed a correlation with visual estimations, although a direct quantitative comparison was more challenging due to the irregular shapes of some defects. The accuracy of these dimensional measurements is directly linked to the precise detection of the reference points, the reliability of which was established in the measurement verification using Figure 4.

3.4. Sensitivity to Imaging Conditions

The developed system demonstrated a degree of robustness to minor variations in lighting conditions and surface reflectivity. However, significant changes in ambient light or highly reflective surfaces that caused excessive glare on the weld bead could impact the accuracy of the reference point detection and subsequent defect analysis. The accuracy of the dimensional measurements was primarily limited by the image resolution and the precision of the reference point detection Although the sub-pixel centroid calculation enhanced measurement accuracy, the overall system accuracy was estimated to be within an approximate range of ±0.03 mm. The software's ability to accurately identify and measure defects was also dependent on the clarity and contrast of the defect features in the images. Shallow or poorly defined defects might be challenging for the current image processing pipeline to reliably detect and measure.

4. Discussion

The results of this study demonstrate the feasibility and potential of using a relatively simple image processing pipeline, guided by laser-generated reference points, for the automated measurement and detection of potential defects in welded samples. The high consistency observed in the measurement verification procedure (Section 3.1) underscores the reliability of the laser-assisted referencing system and the accuracy of the initial image calibration. This level of precision in establishing the pixel-to-millimeter scale is crucial for the subsequent dimensional analysis of weld features and potential defects.

The performance of the developed referenced measurement software (Section 3.2) indicates its capability to effectively integrate the laser-based calibration with image processing techniques for automated analysis. The software's ability to consistently detect the reference points across different weld surfaces highlights the robustness of the initial image processing steps involving color-based segmentation. This automated detection and calibration significantly reduces the need for manual intervention and the associated potential for human error, aligning with the broader goals of automated optical testing systems discussed in previous studies.

The comparison between the software-generated dimensional measurements and manual measurements (Section 3.3) reveals a promising level of accuracy, with average differences falling within a narrow range. This suggests that the developed image processing techniques, when calibrated using the laser reference, can provide quantitative data on the size of potential weld defects with reasonable precision. While direct comparison with irregularly shaped defects posed a challenge, the visual correlation with manual estimations supports the software's ability to identify and approximate the extent of these anomalies. This capability is particularly relevant when considering industry standards like EN ISO 5817, which often specify acceptance criteria based on the dimensions of weld imperfections. The developed system offers a potential tool for objectively assessing weld quality against such dimensional requirements.

The discussion of system robustness and limitations (Section 3.4) highlights important considerations for practical implementation. While the system showed some tolerance to variations in lighting and surface conditions, extreme cases of glare or poor defect visibility remain challenges. The estimated accuracy range is

influenced by the image resolution and the precision of the centroid detection, factors that could be further improved with higher-resolution imaging equipment and more sophisticated sub-pixel localization algorithms. The difficulty in detecting shallow or poorly defined defects points towards potential future research directions, possibly involving advanced image enhancement techniques or the integration of different imaging modalities.

Interpreting these results in the context of previous studies, our approach offers a potentially more cost-effective and simpler alternative to some complex deep learning-based methods, particularly for applications where real-time performance and resource constraints are significant factors. While deep learning models (as discussed in the Introduction and exemplified by CU-Net in the initial example article) can offer superior robustness and feature learning capabilities, the developed laser-referenced image processing system provides a direct and interpretable method for dimensional measurement, which is a key requirement in many quality control scenarios. The integration of a physical reference directly onto the sample addresses the scale ambiguity inherent in single-view image analysis, a common challenge in TCV-based methods.

Future research directions could focus on enhancing the system's robustness to challenging lighting conditions and surface properties. Exploring advanced image pre-processing techniques, such as adaptive histogram equalization or specular reflection removal algorithms, could improve the reliability of defect detection and measurement. Investigating the integration of machine learning for automated defect classification based on the extracted dimensional and morphological features could further enhance the system's capabilities. Additionally, exploring the potential for real-time implementation by optimizing the image processing algorithms and leveraging more powerful embedded computing platforms would be a valuable next step towards industrial deployment.

These findings not only validate the technical feasibility of the proposed method but also suggest broader applicability in industrial quality control settings, particularly for automated visual inspection systems in welding processes. The integration of a low-cost, interpretable, and scalable measurement pipeline has the potential to reduce inspection time and human error while ensuring compliance with international welding standards. Future research could extend the system to multi-angle imaging or 3D reconstruction to capture complex weld geometries, and explore domain adaptation techniques to generalize the approach across different material types, welding methods, and industrial environments.

5. Conclusion

This study has presented a methodology for the automated determination of weld quality using an image processing approach guided by laser-generated reference points. The developed system demonstrates the potential for accurate dimensional measurement of weld features and potential defects, offering a more objective and potentially faster alternative to traditional manual inspection methods. The measurement verification procedure confirmed the reliability of the laser-based calibration, and the referenced measurement software provided consistent results in identifying and measuring potential anomalies in welded samples. While the system exhibits certain limitations regarding challenging imaging conditions and the detection of subtle defects, the findings suggest that this approach holds promise for practical applications in weld quality control, particularly where cost-effectiveness and interpretability are key considerations. Future work will focus on enhancing the system's robustness, integrating machine learning for defect classification, and exploring its potential for real-time industrial implementation.

Author Contributions

The percentages of the authors' contributions are presented below. All authors reviewed and approved the final version of the manuscript.

	E.B.	E.G.
C	50	50
D	50	50
S	50	50
DCP	50	50
DAI	50	50
L	50	50
W	50	50
CR	50	50
SR	50	50
PM	50	50
FA	50	50

C=Concept, D= design, S= supervision, DCP= data collection and/or processing, DAI= data analysis and/or interpretation, L= literature search, W= writing, CR= critical review, SR= submission and revision, PM= project management, FA= funding acquisition.

Conflict of Interest

The authors declared that there is no conflict of interest.

References

Ajmi C, Zapata J, Elferchichi S, Laabidi K. 2024. Advanced faster-rcnn model for automated recognition and detection of weld defects on limited x-ray image dataset. J Nondestruct Eval, 43(1): 14.

Akkus A, Gorgun E. 2015. The investigation of mechanical behaviors of poly methyl methacrylate (PMMA) with the addition of bone ash, hydroxyapatite and keratin. Adv Mater, 4(1): 16–19.

Cardellicchio A, Nitti M, Patruno C, Mosca N, Di Summa M, Stella E, Renò V. 2024. Automatic quality control of aluminium parts

welds based on 3D data and artificial intelligence. J Intell Manuf, 35(4): 1629–1648.

Gook S, El-Sari B, Biegler M, Rethmeier M. 2024. Application of AI-based welding process monitoring for quality control in pipe production. Paton Weld J, 2024(6).

Gorgun E. 2022. Characterization of superalloys by artificial neural network method. Int Symp Appl Math Eng (ISAME22), January 21-23, 2022, Istanbul, Türkiye, pp: 67.

Gorgun E. 2024. Investigation of the effect of SMAW parameters on properties of AH36 joints and the chemical composition of seawater. Int J Innov Eng Appl, 8(1): 28–36.

Gorgun E. 2024. Numerical analysis of inflow turbulence intensity impact on the stress and fatigue life of vertical axis hydrokinetic turbine. Phys Fluids, 36(1).

Gorgun E, Karamis MB. 2019. Ultrasonic testing to measure the stress statement of steel parts. J Mech Sci Technol, 33(7): 3231–3236.

Guo Q, Yang Z, Xu J, Jiang Y, Wang W, Liu Z, Zhao W, Sun Y. 2024. Progress, challenges and trends on vision sensing technologies in automatic/intelligent robotic welding: State-of-the-art review. Robot Comput Integr Manuf, 89: 102767.

Islam MR, Zamil MZH, Rayed ME, Kabir MM, Mridha MF, Nishimura S, Shin. 2024. Deep learning and computer vision techniques for enhanced quality control. IEEE Access, Manuf Process, Seoul, South Korea, pp:52-60.

Ji W, Luo Z, Luo K, Shi X, Li P, Yu Z. 2024. Computer vision–based surface defect identification method for weld images. Mater Lett, 371: 136972.

Liu W, Hu J, Qi J. 2025. Resistance spot welding defect detection based on visual inspection. Improved Faster R-CNN model. Machines, 13(1): 33.

Lopez-Fuster MA, Morgado-Estevez A, Diaz-Cano I, Badesa FJ. 2024. A neural-network-based cost-effective method for initial weld point extraction from 2D images. Machines, 12(7): 447.

Mobaraki M. 2025. Vision-based seam tracking and multi-modal defect detection in GMAW fillet welding using artificial intelligence. PhD Thesis, University of British Columbia, pp: 45-49.

Pham DA, Bui DQ, Le TD, Tran DH, Nguyen TH. 2024. Automatic welding seam tracking and real-world coordinates identification with machine learning method. Results Eng, 23: 102565.

Stavropoulos P, Sabatakakis K. 2024. Quality assurance in resistance spot welding: state of practice, state of the art, and prospects. Metals, 14(2): 185.

Sutherland C, Henderson AD, Giosio DR, Trotter AJ, Smith GG. 2024. Synchronising an IMX219 image sensor and AS7265x spectral sensor to make a novel low-cost spectral camera. HardwareX, 19: e00573.

Voelkel J, Meissner M, Bartsch H, Feldmann M. 2024. The influence of external weld imperfection size on the load-bearing capacity of butt-welded joints. J Constr Steel Res, 220: 108808.

Wang Y, Lee W, Jang S, Truong VD, Jeong Y, Won C, Lee J, Yoon J. 2024. Prediction of internal welding penetration based on IR thermal image supported by machine vision and ANN-model during automatic robot welding process. J Adv Join Process, 9: 100199.

Xu J, Hu X, Zhan H. 2025. CU-NET: Context extractor network based U-Net for magnetic tile segmentation. In: Proc Int Conf Equip Intell Oper Maint (ICEIOM 2023), Hefei, China, Sep 21–23, 2023 (Vol II). CRC Press: 155.

Yu Q, Xiao L, Zheng D, Peng Z, Song K. 2024. A computer vision-based lithium battery tab welding quality detection system. Trans China Weld Inst, 45(10): 38–49.

Yue Y. 2024. Research on welding seam detection and recognition technology for industrial boilers. Proc 2024 IEEE 7th Inf Technol Netw Electron Autom Control Conf (ITNEC): IEEE: 413–416.

Zhang B, Wang X, Cui J, Wu J, Xiong Z, Zhang W, Yu X. 2024. Enhancing weld inspection through comparative analysis of traditional algorithms and deep learning approaches. J Nondestruct Eval, 43(2): 38.

Black Sea Journal of Engineering and Science
doi: 10.34248/bsengineering.1693042

Open Access Journal
e-ISSN: 2619 – 8991

Research Article
Volume 8 - Issue 4: 1160-1180 / July 2025

ANALYST-AWARE INCIDENT ASSIGNMENT IN SECURITY OPERATIONS CENTERS: A MULTI-FACTOR PRIORITIZATION AND OPTIMIZATION FRAMEWORK

Eyup Can KILINCDEMIR[1]*, Baris CELIKTAS[1]

[1]*Işık University, Institute of Graduate Students, Department of Computer Engineering, 34398, İstanbul, Türkiye*

Abstract: In this paper, we propose a comprehensive and scalable framework for incident assignment and prioritization in Security Operations Centers (SOCs). The proposed model aims to optimize SOC workflows by addressing key operational challenges such as analyst fatigue, alert overload, and inconsistent incident handling. Our framework evaluates each incident using a multi-factor scoring model that incorporates incident severity, service-level agreement (SLA) urgency, incident type, asset criticality, threat intelligence indicators, frequency of repetition, and a correlation score derived from historical incident data. We formalize this evaluation through a set of mathematical functions that compute a dynamic incident score and derive incident complexity. In parallel, analyst profiles are quantified using Analyst Load Factor (ALF) and Experience Match Factor (EMF), two novel metrics that account for both workload distribution and expertise alignment. The incident–analyst matching process is expressed as a constrained optimization problem, where the final assignment score is computed by balancing incident priority with analyst suitability. This formulation enables automated, real-time assignment of incidents to the most appropriate analysts, while ensuring both operational fairness and triage precision. The model is validated using algorithmic pseudocode, scoring tables, and a simplified case study, which illustrates the real-world applicability and decision logic of the framework in large-scale SOC environments. To validate the framework under real-world conditions, an empirical case study was conducted using 10 attack scenarios from the CICIDS2017 benchmark dataset. Overall, our contributions lie in the formalization of a dual-factor analyst scoring scheme and the integration of contextual incident features into an adaptive, rule-based assignment framework. To further strengthen operational value, future work will explore adaptive weighting mechanisms and integration with real-time SIEM pipelines. Additionally, feedback loops and supervised learning models will be incorporated to continuously refine analyst-incident matching and prioritization.

Keywords: Incident management, Analyst assignment, SOC optimization, Incident prioritization, Correlation score, SLA urgency

***Corresponding author:** Işık University, Institute of Graduate Students, Department of Computer Engineering, 34398, İstanbul, Türkiye
E mail: 23sibe5004@isik.edu.tr (E.C.KILINCDEMIR)
Eyup Can KILINCDEMIR https://orcid.org/0009-0005-1151-7480
Baris CELIKTAS https://orcid.org/0000-0003-2865-6370

Received: May 06, 2025
Accepted: June 16, 2025
Published: July 15, 2025

Cite as: Kilincdemir E.C., Celiktas B. 2025. Incident assignment and prioritization framework for security operations centers (SOCs). BSJ Eng Sci, 8(4): 1160-1180.

1. Introduction

The increasing frequency and complexity of cybersecurity incidents demand a structured and adaptive approach to incident management. Security Operations Centers (SOCs), as the frontline infrastructure of organizational defense, are responsible for detecting, analyzing, and mitigating threats in real time. However, the surge in alert volume—combined with limited analyst availability and manual triage—often leads to delays, fatigue, and inefficient resource use. These challenges highlight the need for intelligent, automated incident assignment mechanisms that evaluate factors such as analyst expertise, real-time workload, incident complexity, and service-level agreement (SLA) urgency to ensure timely and effective response.

To address these limitations, we present a novel incident assignment and prioritization framework that consolidates contextual incident attributes—such as severity, SLA urgency, asset criticality, threat intelligence, correlation, and repetition—into a unified scoring model. Simultaneously, analysts are dynamically profiled through workload and expertise measures, enabling real-time, competency-aware analyst–incident matching.

The main contributions of this study are as follows:

- We propose a multi-factor scoring model integrating technical and contextual incident features.
- We introduce two analyst-centric metrics—Analyst Load Factor (ALF) and Experience Match Factor (EMF).
- We formalize analyst assignment as an optimization task with scoring formulas and examples.
- We validate the model via pseudocode, scoring tables, and a case study.
- We benchmark it against prior work and propose future enhancements such as API integration and reinforcement learning.

This work is licensed (CC BY-NC 4.0) under Creative Commons Attribution 4.0 International License

- Our dual-sided optimization ensures effective triage and balanced analyst workloads.
- We empirically evaluate the model using CICIDS2017 benchmark data to demonstrate its applicability in real-world SOC environments (see Section 5.2).

The remainder of this paper is organized as follows. Section 2 presents a comprehensive review of related works on incident prioritization and analyst assignment in SOC environments. Section 3 introduces the scoring methodology, explaining the key incident attributes and their contribution to the overall incident score. Section 4 describes the proposed model in detail, including the calculation of incident complexity, the ALF, and the EMF, as well as the final assignment logic. Section 5 presents a simplified case study that demonstrates the practical execution of the proposed model through step-by-step scoring and analyst matching across three incidents and two analysts. Section 6 provides an integrated conclusion that summarizes the framework's key contributions, discusses current limitations, incorporates the case study findings, and outlines directions for future work.

1.2. Related Works

The increasing volume, frequency, and complexity of cybersecurity threats—ranging from ransomware to insider threats—have accelerated the evolution of incident response models in SOCs. As the modern SOC must balance high alert volumes, dynamic attacker behavior, and limited human resources, the need for scalable and intelligent incident handling mechanisms has become more critical than ever. In this context, numerous studies have addressed the challenge by proposing frameworks and algorithms focused on incident classification, prioritization, analyst-task alignment, and intelligent decision support.

The foundational ITIL framework (AXELOS, 2019) offers a process-oriented structure for managing incidents, emphasizing impact, urgency, escalation workflows, and SLAs. While ITIL is widely adopted for standardizing IT operations, it lacks analyst-specific considerations and dynamic task distribution features. Similarly, the Capability Maturity Model proposed by Mooi and Botha (2016) promotes institutional readiness and security governance maturity, but it does not address real-time triage, prioritization scoring, or analyst matching.

From a prioritization perspective, Jalalvand et al. (2024) provided a comprehensive survey of alert triage strategies, including severity-based models and statistical classifiers. Likewise, Chhetri et al. (2024) emphasized human-AI teaming approaches to reduce analyst fatigue through cognitive support. Although these works significantly contribute to understanding prioritization criteria and analyst overload, they fall short of offering analyst-aware assignment or workload balancing mechanisms.

Other researchers have explored task allocation using algorithmic or optimization methods. For instance, Gachnang et al. (2023) employed multi-objective evolutionary algorithms to match analysts with incidents based on skills and SLAs, but their model incurs high computational complexity. Hou et al. (2022) introduced a graph-based load balancing strategy, which improves matching efficiency but lacks integration with incident severity or threat intelligence. In another dimension, Handri et al. (2025) proposed a culture-centric analyst matching approach using Q-methodology, which addresses human aspects of task assignment but lacks technical prioritization logic.

Automation in SOCs has also been the subject of multiple studies. Alrimawi et al. (2019) introduced automated incident workflows for smart spaces, while Binbeshr et al. (2025) proposed the Cognitive SOC model with AI-powered triage capabilities. However, these models focus more on detection and AI-driven automation than analyst-specific triage or post-assignment optimization.

Several works target domain-specific SOC applications. Al-Dhaqm et al. (2020) proposed a forensic incident response model specific to database systems, and Villalón-Huerta et al. (2022) developed a kill-chain model for SOC defense. He et al. (2019) introduced IS-CHEC for real-time incident management but did not incorporate analyst expertise or scoring mechanisms.

Foundational studies such as Vielberth et al. (2020) offered taxonomies and architectural overviews of SOCs, emphasizing integration and role clarity but without actionable assignment strategies. Meanwhile, generic real-time load balancing models (e.g., Liao et al., 2011; Jadon et al., 2024) and SLA-driven frameworks from adjacent domains (e.g., García and Tomás, 2020) provide valuable optimization insights but do not account for security-specific complexity or SOC analyst matching.

A comparative summary of these studies is presented in Table 1. As illustrated, most prior models focus on individual SOC lifecycle components—such as alert severity, task allocation, or analyst workload—without integrating these into a unified, dynamic framework.

In contrast, our study proposes a comprehensive framework that combines seven core incident scoring dimensions—Severity, SLA Urgency, Incident Type, Asset Criticality, Repetition Frequency, Threat Intelligence, and Correlation Score—with analyst-side profiling via the EMF and ALF. Additionally, our model supports real-time operation and includes a feedback loop that dynamically adapts based on outcomes (e.g., reassignment frequency or false positive rates).

This integrated approach fills a critical gap in the literature by offering a scalable, analyst-aware solution for prioritization and assignment in modern SOCs. While previous research has made significant strides in alert filtering, automation, and human-centric support, our contribution lies in synthesizing these dimensions into a cohesive and operationally deployable prioritization engine with quantifiable metrics and formal assignment logic.

Table 1. Comparative summary of related work on SOC ıncident assignment and prioritization

Author / Study	Model	Key Factors	Assignment Logic	Strengths	Limitations
ITIL Foundation (2019)	Process Oriented Framework	Impact, Urgency, SLAs	Role-Based Static Assignment	Provides structured workflows	Lacks analyst-level adaptation
Mooi and Botha (2016)	Capability Maturity Model	Readiness, Process Stages	Capability Maturity Tracking	Organizational focus	No dynamic scoring
Jalalvand et al. (2024)	Systematic Survey	Severity, Alert Fatigue	Triage Criteria Review	Comprehensive review	No model proposed
Chhetri et al. (2024)	Human-AI Teaming	Analyst Fatigue, Volume	Cognitive Load Allocation	Human-centric focus	Ignores technical priority
Gachnang et al. (2025)	Evolutionary Optimization	SLA, Analyst Skill	Multiobjective Matching	High-quality allocation	High computation cost
Handri et al. (2025)	Q Method + Agile SOC	Culture, Agility	Culture-Based Matching	Organizational perspective	Not technically focused
Alrimawi et al. (2019)	Smart-Space Automation	IoT Threats	Autonomous Triggers	Automation focus	SOC generalization lacking
Binbeshr et al. (2025)	Cognitive SOC	AI Models, Alerts	AI-Based Matching	Uses cognitive AI	Overlooks workload balancing
Aldhaqm et al. (2020)	Forensic IR Model	DB Logs, Activities	Forensic Phases	Structured forensic view	Not real-time
Villal´on Huerta et al. (2022)	Defensive Kill Chain	Attack Lifecycle	Phase Mapping	Kill-chain based SOC model	No analyst matching
He et al. (2019)	IS-CHEC Framework	Performance Metrics	Real-Time Structured Flow	Real-time focus	Ignores analyst context
Vielberth et al. (2020)	SOC Survey Model	SOC Roles, Taxonomy	Role Description	Broad taxonomy	Not actionable
Hou et al. (2022)	Graph Load Balancing	Analyst Load, Fit	Graph Matching	Balanced matching	Lacks threat modeling
Jadon et al. (2024)	RT Load Balancing	Task Type, RT Needs	Core-Aware Dist.	Effective scheduler	Generic, not SOC-specific
Liao et al. (2011)	Network LB Algorithm	Load, Latency	Network Mapping	Efficient networking	No SOC focus
Garc´ıa and Tom´as (2020)	Traffic IR Framework	Incident Risk, SLA	Adaptive Prioritization	SLA-driven incident timing	Transportation domain
This Paper	Score + Matching	Severity, SLA, Threat Intel, Correlation, Repetition, EMF + ALF, Complexity	Real-time, multi-factor analyst-aware assignment	Integrates prioritization, dynamic analyst profiling, feedback loop, correlation-aware triage	Requires tuning for large-scale SOCs

2. Materials and Methods

The proposed framework follows a multi-factor prioritization approach inspired by multi-criteria decision-making (MCDM) to evaluate and prioritize incidents in a SOC context. This strategy is particularly well-suited for environments where various, often conflicting, attributes such as urgency, complexity, and resource constraints must be simultaneously considered. Each security incident is evaluated against a set of factors that contribute to its overall priority, enabling both structured triage and context-aware analyst assignment. The scoring model integrates the following incident-specific factors, which are formally defined along with their symbols in Table 2.

Table 2. Symbols used in incident score calculation formula

Symbol	Description
S_m	Total score assigned to an incident
S_{sev}	Incident severity level score (1–5)
S_{SLA}	Numerical urgency level based on SLA (1–5)
S_{type}	Score based on type/category of the incident
S_{rep}	Additional score based on frequency of recurrence
S_{asset}	Score reflecting the criticality of the affected system
S_{ti}	Score based on threat intelligence indicators
S_{cor}	Score derived from similarity to past incidents
W_{sev}	Weight coefficient for severity attribute
W_{SLA}	Weight coefficient for SLA urgency
W_{type}	Weight coefficient for incident type
W_{rep}	Weight coefficient for repetition
W_{asset}	Weight coefficient for asset criticality
W_{ti}	Weight coefficient for threat intelligence
W_{cor}	Weight coefficient for correlation

- Incident Score (S_m): Represents the overall priority score assigned to an incident after applying weighted aggregation across all relevant attributes. This cumulative score is used to rank and compare incidents within the SOC, enabling efficient triage and resource allocation. A higher Sm value indicates greater urgency and complexity, directly influencing analyst assignment decisions.
- Incident Severity (S_{sev}): Reflects the potential impact of the incident on organizational assets and operations. More severe incidents are prioritized for faster remediation.
- SLA Urgency (S_{SLA}): Based on predefined SLAs, thisdimension reflects the allowable response time for each incident. Lower SLA windows increase incident priority.
- Incident Type (S_{type}): Different types of incidents (e.g., phishing, ransomware, privilege escalation) vary in complexity and risk. A predefined severity level is associated with each category.
- Repetition (S_{rep}): Recurring incidents within a time window suggest unresolved vulnerabilities or ongoing campaigns. Repetition increases priority dynamically.
- Affected Asset (S_{asset}): Incidents involving high-value or critical systems (e.g., SIEM, domain controllers) are weighted more heavily to mitigate business risk.
- Threat Intelligence (S_{ti}): Incorporates contextual data such as blacklisted IPs, malware indicators, and known attack patterns. Threat actor linkage directly raises priority.
- Correlation Score (S_{cor}): Measures incident similarity with past events using attributes like source IP, destination, and user account. This enables detection of patterns and campaign-level behavior.
- Severity Weight (Wsev): Indicates the relative importance assigned to the incident severity attribute in the overall scoring formula.
- SLA Urgency Weight (WSLA): Represents the weight assigned to the SLA urgency factor.
- Incident Type Weight (Wtype): Specifies the influence of incident type classification (e.g., ransomware, phishing) on the total score.
- Repetition Weight (Wrep): Reflects the emphasis placed on the recurrence frequency of incidents.
- Asset Criticality Weight (Wasset): Denotes the priority given to the importance of the affected system.
- Threat Intelligence Weight (Wti): Measures the contribution of threat intel indicators to the total score.
- Correlation Weight (Wcor): Indicates the significance assigned to correlation scores from past incidents.

To ensure that high-priority incidents are addressed by the most capable personnel, analysts are profiled based on their experience and current workload. An ALF is used to avoid overloading any single analyst, while an EMF assesses how well an analyst's skill level aligns with the complexity of a given incident. Details and formulas for ALF and EMF are provided in Section 4.4.

The final incident score is obtained through a weighted aggregation of the aforementioned attributes, while the final analyst suitability score considers both ALF and EMF. Weights were initially derived using expert judgment and validated through scenario testing. Future iterations may use reinforcement learning to optimize these weights dynamically. This methodology serves as the foundation for the stepwise model described in the following section.

2.1. Proposed Model

The proposed model consists of several sequential steps designed to facilitate intelligent and efficient analyst assignment in SOC operations. Figure 1 providesan overview of this dynamic workflow.

2.1.1. Step 1: Calculate incident score

Each incident is scored using a weighted combination of normalized factors, including severity, SLA urgency, incident type, repetition frequency, asset criticality, threat intelligence, and correlation indicators. The weights were derived from expert evaluations through a structured survey. This composite score reflects the overall contextual and technical priority of each incident and serves as the basis for assignment and triage decisions.

2.1.2. Step 2: Determine incident complexity

The computed score is then used to determine the complexity level of the incident. Incidents are categorized into five levels: Very Low, Low, Medium, High, and Critical. This classification ensures that incidents are assigned to analysts with matching expertise levels.

2.1.3. Step 3: Calculate analyst load factor (ALF)

To avoid overloading any analyst, a load factor is calculated based on each analyst's current number of assigned incidents and their maximum handling capacity. This factor penalizes analysts already close to their workload limit.

2.1.4. Step 4: Calculate experience match factor (EMF)

The EMF determines how closely an analyst's experience level aligns with the complexity of the incident. Higher EMF scores are given to analysts whose expertise level closely matches the required incident complexity.

2.1.5. Step 5: Assign to most suitable analyst

Finally, a suitability score is computed by combining the incident score, EMF, and ALF. The incident is assigned to the analyst with the highest suitability score, ensuring effective and context-aware allocation.

Figure 1 illustrates the core steps of the proposed assignment workflow, including incident scoring, analyst matching, and workload balancing.

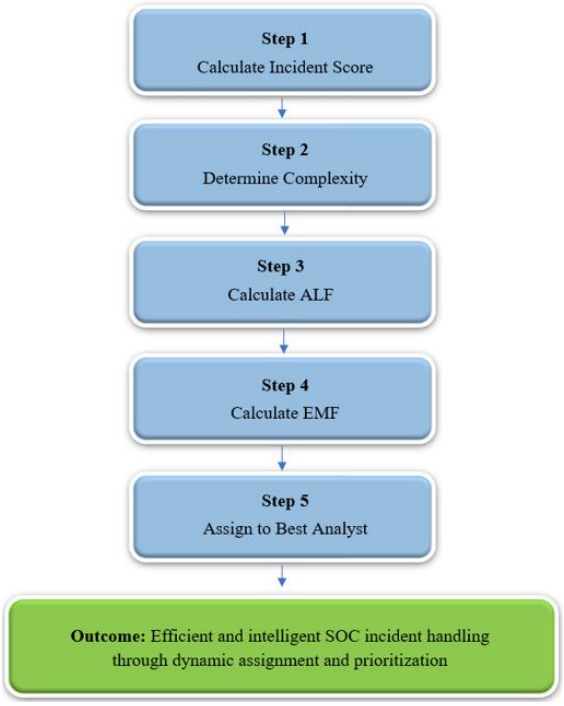


Figure 1. Proposed dynamic ıncident assignment flow in soc operations. The process ensures intelligent analyst matching and workload balancing.

2.2. Incident Score Calculation Formula

To determine the priority level of an incident, a multi-factor scoring model is employed that consolidates technical and contextual attributes into a single weighted score. Unlike fixed summation methods, this model incorporates factor-specific weights derived from professional evaluations to reflect the relative importance of each attribute more accurately.

The general weighted incident score formula is as follows (equations 1 and 2):

$$S_m = W_{sev}\, x\, S_{Sev} + W_{SLA}\, x\, S_{SLA} + W_{type}\, x\, S_{type} + W_{rep}\, x\, S_{rep} + W_{asset}\, x\, S_{asset} + W_{ti}\, x\, S_{ti} + W_{cor}\, x\, S_{Cor} \quad (1)$$

Where:

- S_m is the final incident score,
- S_{sev}, S_{SLA}, S_{type},S_{rep},S_{asset},S_{ti},S_{cor} represent the normalized (0–5 scale) scores for each corresponding incident attribute.
- W_{sev}, W_{SLA}, W_{type}, W_{rep}, W_{asset}, W_{ti}, W_{cor} are the normalized weights assigned to each attribute, such that:

$$W_{sev} + W_{SLA} + W_{type} + W_{rep} + W_{asset} + W_{ti} + W_{cor} = 1 \quad (2)$$

These weights were derived through a structured survey conducted among professionals working in cybersecurity, IT auditing, risk management, and operational SOC roles. Participants were asked to rate the importance of seven core incident attributes on a 1–5

Likert scale. The mean scores were subsequently normalized to compute the final weights used in the model.

The resulting weighted scoring formula is (equations 3):

$$S_m = 0.160\,x\,S_{Sev} + 0.135\,x\,S_{SLA} + 0.149\,x\,S_{type} + 0.117\,x\,S_{rep} + 0.156\,x\,S_{asset} + 0.149\,x\,S_{ti} + 0.135\,x\,S_{Cor} \quad (3)$$

These weights help enhance prioritization accuracy by embedding real-world, context-aware professional insights into the incident evaluation process. The detailed survey data and computation steps are presented in Table 3.

Table 3. Expert ratings for incident score weights (Normalized Averages)

Title	Sev	SLA	Inc Type	Ass Cri	TI	Re	Co
CSE	5	3	5	4	3	4	5
CSM	5	3	4	3	5	2	3
IR	4	2	3	5	4	3	3
ISM	5	5	5	5	5	5	5
L2A	5	4	4	4	5	1	3
SS	1	3	5	4	5	5	4
SCSE	5	5	3	5	4	4	4
SIA	5	5	5	4	4	3	3
SOCS	5	4	4	5	3	3	4
SOCTL	5	4	4	5	4	3	4
Avg	4.5	3.8	4.2	4.4	4.2	3.3	3.8
Norm. Wt	0.160	0.135	0.149	0.156	0.149	0.117	0.135

*Sev. = severity, Inc Type = incident type, Ass Cri = asset criticality, TI = threat intel, Re = repetition, Co = correlation, CSE = cyber security engineer, CSM = cyber security manager, IR = incident responder, ISM = information security manager, L2A = L2 cyber security analyst, SS = Security Specialist, SCSE = Senior Cyber Security Expert, SIA = senior information auditor, SOCS = SOC specialist, SOCTL = SOC team lead, Avg = average, Norm. Wt = normalized weight.

2.2.1. Severity score

The incident severity describes the impact of the event on the system. Higher score values correspond to more critical events.

In SOCs, severity plays a crucial role in classifying and prioritizing security incidents according to their urgency and potential impact. Most SOCs adopt a five-level classification model Informational, Low, Medium, High, and Critical to enable consistent and risk-informed incident handling.

This structured categorization directly influences triage operations. Critical incidents involve threats such as data exfiltration, ransomware infections, or nation-state attacks that require immediate response. Conversely, Low or Informational incidents—like brute force attempts or misconfigured settings, are less urgent.

In this paper, each severity level is assigned a numerical score, as shown numerically in Table 4, to support a correct match between the analyst and incident. These scores play a key role in our incident assignment approach by helping prioritize incidents based on their criticality.

Table 4. Severity levels and their associated scores

Level	Description	Score
1	Critical	5
2	High	4
3	Medium	3
4	Low	2
5	Informational	1

The severity score reflects the criticality of an incident's impact on organizational assets. Incidents classified as "Critical" (e.g., ransomware, nation-state attacks) receive the highest score, enabling urgent triage and immediate analyst response. Conversely, informational or low-severity events receive the lowest score.

2.2.2. SLA urgency score

SLAs are essential elements in SOC workflows, defining the maximum allowable time frame for detecting, analyzing, and resolving security incidents based on their severity. These thresholds help minimize risk exposure and ensure operational continuity.

Most SOCs employ a tiered SLA structure that aligns with severity levels. In our proposed framework, incidents are assigned SLA urgency levels that directly influence their prioritization score. For example, a Critical such as a

detected data exfiltration attempt must be addressed within 15 minutes, while a Low such as an unauthorized access attempt can be resolved within two hours or more, depending on operational policies.

To integrate SLA urgency into the incident scoring model, each response tier is converted into a numerical score. Incidents with higher priorities have higher urgency scores, thereby directly affecting the incident's final weight.

The specific mapping between SLA response time and the corresponding urgency score is provided in Table 5.

This score reflects how quickly an incident must be resolved based on its SLA tier. The shorter the SLA response window, the higher the urgency score (via the transformation 6 − SLA Level). This transformation ensures SLA-compliant prioritization, minimizing mean time to response for high-criticality threats.

Table 5. SLA urgency levels and corresponding scores

Level	Response Time	Score (6 -SLA)
1	< 15 minutes (Critical)	5
2	< 30 minutes (High)	4
3	< 60 minutes (Medium)	3
4	< 120 minutes (Low)	2
5	> 120 minutes (Informational)	1

2.2.3. Incident type score

The incident type plays a key role in determining the appropriate response strategy for analysts within a SOC. It defines the nature of the security incident, such as ransomware, phishing, or unauthorized access, and reveals the potential risk to the organization. Classifying incidents by type helps analysts better understand the severity, technical complexity, and scope of impact.

In this article, each type of incident is assigned a score that contributes to the overall prioritization mechanism. Table 6 shows how the various incident types are grouped according to their potential risk levels and how scores are assigned. This score assignment contributes to the final incident score and the repetition score.

Table 6. Categorization of information security incidents and corresponding scores

Incident Type	Score
Critical Incident	
Advanced Persistent Threat (APT)	5
Data Exfiltration (Sensitive Data Leakage)	5
Ransomware Infection	5
Nation-State Sponsored Attack	5
Supply Chain Attack	5
High Severity Incidents	
Unauthorized Privilege Escalation	4
SQL Injection Attack	4
Exploitation of Known Vulnerabilities	4
Remote Code Execution (RCE) Attempt	4
Active Directory Compromise	4
Medium Severity Incidents	
Malware Infection	3
Distributed Denial of Service (DDoS) Attack	3
Phishing Attack (Spear Phishing)	3
Credential Stuffing Attack	3
Suspicious Lateral Movement	3
Zero-Day Exploit Detected	3
Insider Threat Activity	3
Low Severity Incidents	
Unauthorized Access Attempt (Brute Force)	2
Social Engineering Attack	2
Unusual Login Behavior	2
Malware Callback (C2 Communication)	2
Informational Severity Incidents	
Port Scanning	1
Misconfigured Security Settings Detected	1
Suspicious File Execution	1
Unusual Network Traffic	1

*The incident types and associated severity scores were manually derived based on their prevalence in SOC environments and their potential impact on confidentiality, integrity, and availability (CIA triad). This taxonomy aims to support structured triage decisions by linking incident categories with appropriate risk levels.

2.2.4. Repetition score

The base incident type score is dynamically adjusted based on how frequently the same type of incident occurs within a defined time frame. Table 7 defines frequency-based modifiers.

Table 7. Repetition-based score adjustment criteria

Repetition Frequency	Modifier Value (R)
More than 5 occurrences within 1 hour	50
More than 5 occurrences within 24 hours	25
More than 3 occurrences within 7 days	10
First occurrence	0

The repetition score adjusts incident priority based on temporal frequency to reflect the potential urgency of

unresolved or recurring threats (e.g., brute force, scanning). The more frequently a threat is observed, the higher the adjustment—while keeping the score bounded.

The final repetition-adjusted score is calculated using the following formula, which caps the result at a maximum of 5 (equations 4):

$$Repetition\ Score = min\left(5,\ Incident\ Type\ Score + \frac{(Repetition\ Score\ Modifier + Incident\ Type\ Score)}{100}\right) \quad (4)$$

Example scores calculated based on different scenarios:

- APT Attack (Base Score = 5), occurring 5 times in 1 hour: min(5, 5 + (50 + 5) / 100) = min(5, 5.55) = 5.0
- Port Scanning (Base Score = 1), occurring 5 times in 24 hours: min(5, 1 + (25 + 1) / 100) = min(5,126) = 1.26
- Brute Force Attack (Base Score = 2), occurring 3 times in 7 days: min(5, 2 + (10 + 2) / 100) = min(5, 2.12) = 2.12

This bounded adjustment method ensures that high-frequency but low-severity attacks gain priority appropriately without disproportionately inflating scores for already high-impact incidents such as APTs.

2.2.5. Affected asset score

The criticality of the asset affected by a security incident is a key determinant in prioritizing incident response. Assets are not equal in value or function; for example, an attack on a SIEM or payment processing system poses a much higher risk than one on a guest Wi-Fi network. In the proposed model, affected assets are classified into five levels based on their operational importance and security sensitivity, with each category assigned a corresponding score. This classification enables SOC teams to assess the impact of an incident more accurately and allocate resources more effectively during triage.

Table 8 categorizes affected systems based on operational importance, ranging from mission critical infrastructure to sandbox environments.

Table 8. Asset criticality-based scoring for affected systems

Affected Asset	Score
Critical Security Systems (SIEM, IAM, DB, DC, IDS/IPS)	5
Cloud Infrastructure (Kubernetes Cluster, Virtualization Host)	5
Payment Processing Systems (PCI-DSS Environments)	5
Email Server	4
Public-Facing Web Server	4
VPN Gateway	4
Identity and Authentication Systems (SSO, MFA)	4
Important Application Server	3
Internal Business Applications (ERP, CRM)	3
File Servers	3
Development Environments (CI/CD, Code Repositories)	3
Standard Workstation (Regular Employee Devices)	2
Remote Access Systems (VDI, Remote Desktop)	2
IoT/OT Devices (Industrial Systems, Smart Devices)	2
Self-Contained System (Standalone or Low-Risk System)	1
Guest Wi-Fi Networks	1
Test and Sandbox Environments	1

*The asset criticality scores in this table are manually defined based on their strategic importance, sensitivity level, and potential impact on business continuity in case of compromise.

2.2.6. Threat intelligence score

The threat score evaluates whether the incident originates from a known threat actor or a high-risk entity. Incidents associated with APT groups, botnets, and dark web indicators are given the highest priority.

Table 9 presents a structured classification of threat sources along with their impact-based scores.

Table 9. Threat intelligence-based scoring of detected indicators

Threat Type	Score
Known Threat Actor (APT, Darknet IP, Nation-State Threat Group)	5
Compromised Infrastructure (C2 Servers, Botnets, Malware Hosts)	5
Malicious IP (Blacklist, Repeated Offender)	4
Publicly Known Exploitable Vulnerability (CVE Exploit Source)	4
High-Risk Domain (Phishing, Fake Login Pages, Scam Websites)	4
Suspicious Activity (Unusual Traffic Patterns, Unknown Anomaly)	3
Newly Registered Domains (Potential Phishing or C2 Servers)	3
Geographically Unusual Access (Suspicious Country or TOR Exit Node)	3
Outdated SSL Certificate on External Domain	2
Insecure Protocol Detected (e.g., HTTP Instead of HTTPS)	2
Internal Network Traffic (Unverified but Unlikely to Be Malicious)	1
First-Time Seen Traffic from Internal IPs	1

*The threat scores presented in this table are assigned manually based on expert judgment and domain knowledge to reflect relative risk levels for common threat indicators

2.2.7. Correlation score

The correlation score quantifies how similar a new incident is to previously recorded cases, thus prioritizing repeated or evolving threat patterns. To compute this value, we consider three core indicators commonly used in SOC analysis:

- Source IP (srcIP): Origin of the attack.
- Destination IP (dstIP): Targeted internal address.
- Username (user): Account involved in the incident.

Each indicator is scored based on historical frequency and importance weight. To prevent score inflation, a saturation threshold is defined.

Variables:

- M_i: Number of historical matches for attribute *i*
- T_i: Saturation threshold for attribute *i*
- CW_i: Correlation weight assigned to attribute *i*

where i ∈ {srcIP, dstIP, user}.

Assigned Values:

$CW_1 = 1.25$, $T_1 = 2$ (Source IP)
$CW_2 = 1.75$, $T_2 = 2$ (Destination IP)
$CW_3 = 2.0$, $T_3 = 3$ (Username)

Formula (equations 5):

$$\begin{aligned} \textit{Correlation Score} &= \mathrm{CW}_1 \, x \min\left(1, \frac{M_{srcIP}}{T_1}\right) \\ &+ \mathrm{CW}_2 \, x \min\left(1, \frac{M_{drcIP}}{T_2}\right) \\ &+ \mathrm{CW}_3 \, x \min\left(1, \frac{M_{user}}{T_3}\right) \end{aligned} \quad (5)$$

The correlation score encapsulates the historical similarity of incidents via weighted saturation thresholds over key identifiers (source IP, destination IP, and username). By normalizing frequency contributions and applying capped influence (min(1, M/T)), this metric promotes temporal threat continuity detection while controlling for noise and score accumulation. An example breakdown of how individual attributes contribute to the correlation score is shown in Table 10.

Table 10. Correlation score breakdown example

Attribute	M_i	T_i	CW_i	Formula	Cont
Source IP	2	2	1.25	$1.25 \, x \min(1, \frac{2}{2})$	1.25
Destination IP	1	2	1.75	$1.75 \, x \min(1, \frac{1}{2})$	0,875
Username	4	3	2.0	$2.0 \, x \min(1, \frac{4}{3})$	2.0

*T_i (saturation threshold) and CW_i (correlation weight) are statically defined model parameters based on expert judgment. Cont = contribution.

Total Correlation Score: 1.25 + 0.875 + 2.00 = 4.125

2.3. Example Incident Score Calculation

The following is an example calculation of an incident score based on a real-world attack scenario.

2.3.1. Incident scenario

An organization's SOC detects multiple failed login attempts from an external IP on their VPN gateway. Over the course of 24 hours, more than five login attempts are observed from the same external IP, targeting different employee accounts. Historical analysis reveals that this same IP address had triggered incidents on three different occasions in the last seven days, including an alert for brute-force attempts and lateral movement attempts on internal systems.

After a few hours, the same IP successfully authenticates using a compromised credential. Shortly after, an abnormal login occurs on a high-privilege account, followed by the execution of a suspicious PowerShell script on a domain controller (DC) from a newly created user account.Threat intelligence also flags the external IP as a known malicious actor linked to previous credential stuffing campaigns.

4.3.2 Incident Details and Score Calculation

A credential stuffing attack is detected on the

organization's VPN gateway. The attacker uses a known malicious IP and successfully compromises a user account. The incident affects the domain controller (DC) and matches previous incidents involving the same IP, destination, and username. The following scoring breakdown is applied:

- Severity: 2 (High) → Score = 4, Weight = 0.160 → 0.160 x 4 = 0.640 points
- SLA Urgency: 2 (High, <30 minutes) → (6 − 2) = 4 Score = 4, Weight = 0.135 → 4 x 0.135 = 0.540 points
- Incident Type: Credential Stuffing Attack → Score = 3, Weight = 0.149 → 3 x 0.149 = 0.447 points
- Repetition: More than 5 occurrences in 24 hours → Repetition Score = min(5, 3 + (25 + 3)/100) = 1.26, Weight = 0.117 → 1.26 × 0.117 = 0.147 points
- Affected Asset: Domain Controller (DC) → Score = 5, Weight = 0.156 → 5 x 0.156 = 0.780 points
- Threat Intelligence: Malicious IP (Blacklisted) → Score = 4, Weight = 0.149 → 4 x 0.147 = 0.596 points
- Correlation Score:
  - $Source\ IP$: $M_{srcIP} = 3\ T_1 = 2\ CW_1 = 1.25 \rightarrow 1.25\ x \min\left(1, \frac{3}{2}\right) = 1.25$
  - $Destination\ IP$: $M_{dstIP} = 2\ T_2 = 2\ CW_2 = 1.75 \rightarrow 1.75\ x \min\left(1, \frac{2}{2}\right) = 1.75$
  - $Username$: $M_{user} = 4\ T_3 = 3\ CW_3 = 2.0 \rightarrow 2.0\ x \min\left(1, \frac{4}{3}\right) = 2$
  - Total Correlation Score: 1.25 + 1.75 + 2.0 = 5 5 x 0.135 = 0.675 points
- Final Incident Score: 0.640 + 0.540 + 0.447 + 0.147 + 0.780 + 0.596 + 0.675 = 3.825

To illustrate the practical implications of the scoring model, a credential stuffing attack scenario is examined below. The attack progresses through multiple phases including reconnaissance, credential misuse, and lateral movement. The sequence of these actions is visualized in Figure 2. providing a chronological view of the incident response timeline.

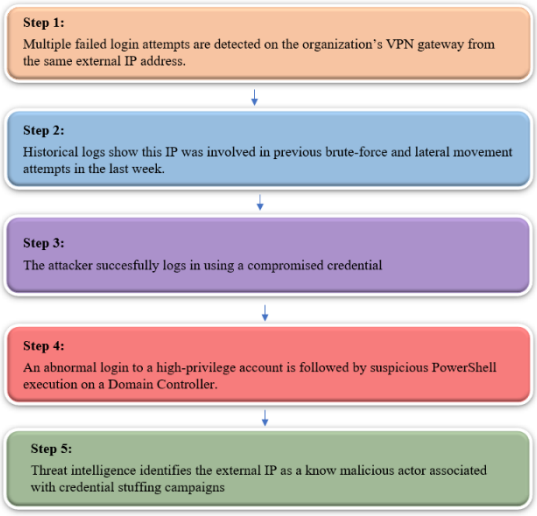


Figure 2. Step-by-step timeline of the credential stuffing attack and detection process in the SOC.

2.4. Analyst Scoring - Incident Assignment Process

To effectively assign incidents to analysts, we use a structured approach considering workload balancing and experience matching.

2.4.1. Step 1: Defining analyst groups and capacity

We categorize analysts into five levels based on expertise:

- Senior Analysts (Level 5): A_i
- Advanced Mid-Level Analysts (Level 4): A_j
- Mid-Level Analysts (Level 3): A_k
- Junior Analysts (Level 2): A_l
- Trainee Analysts (Level 1): A_m

Each analyst has a different maximum capacity and current workload. These capacity constraints across analyst levels are summarized in Table 11.

Table 11. Analyst levels, incident load, and capacity in SOC

Analyst A_n	Level L_n	Current Incidents CI_n	Max Capacity MC_n
A_i (Senior)	5	CI_i	MC_i
A_j (Advanced Mid-Level)	4	CI_j	MC_j
A_k (Mid-Level)	3	CI_k	MC_k
A_l (Junior)	2	CI_l	MC_l
A_m (Trainee)	1	CI_m	MC_m

4.4.2. Step 2: Determining incident complexity from incident score

The calculated incident score S_m is used to determine the complexity level C_m, which guides analyst assignment by aligning incident difficulty with analyst experience. As the scoring model has been normalized to a 0–5 scale, the complexity levels are recalibrated accordingly. equation (6) presents the threshold-based classification of incident complexity levels based on normalized incident scores

$$C_m = \begin{cases} 5, & \text{if } Sm \geq 4.0 \text{ (Critical Complexity)} \\ 4, & \text{if } 3.2 \leq Sm < 4.0 \text{ (High Complexity)} \\ 3, & \text{if } 2.4 \leq Sm < 3.2 \text{ (Medium Complexity)} \\ 2, & \text{if } 1.6 \leq Sm < 2.4 \text{ (Low Complexity)} \\ 1, & \text{if } Sm < 1.6 \text{ (Very Low Complexity)} \end{cases} \quad (6)$$

This classification enables the system to match incidents to analysts with suitable experience levels (as used in the EMF calculation). Table 12 presents examples of incident score values and their associated complexity classes based on this scale.

Table 12. Incident scores and their corresponding complexity levels

Incident I_m	Incident Score Sm	Complexity Level Cm
I_1	4.3	5 (Critical)
I_2	3.6	4 (High)
I_3	2.7	3 (Medium)
I_4	1.9	2 (Low)
I_5	1.3	1 (Very Low)

All scores are computed using the weighted scoring formula described in Section 4.2, ensuring consistency with analyst assignment logic described in Section 4.4.

2.4.3 Step 3: Calculating analyst load factor (ALF)

ALF_n is computed using the following formula (equation 7):

$$ALF_n = 1 + \frac{CI_n}{MC_n} \quad (7)$$

where:

- CI_n is the current number of incidents assigned to analyst A_n.
- MC_n is the maximum capacity of analyst A_n.

Table 13 provides sample ALF calculations and resulting scores for various analyst levels.

Table 13. ALF calculation and resulting scores

Analyst A_n	Current Incidents CIn	Max Capacity MCn	ALF Calculation	ALF Score ALFn
A_1 (Senior)	4	6	$1+\frac{4}{6}=1.67$	1.67
A_2 (Advanced Mid-Level)	3	5	$1+\frac{3}{5}=1.60$	1.60
A_3 (Mid-Level)	2	7	$1+\frac{2}{7}=1.29$	1.29
A_4 (Junior)	3	6	$1+\frac{3}{6}=1.50$	1.50
A5 (Trainee)	1	6	$1+\frac{1}{6}=1.17$	1.17

2.4.4 Step 4: Calculating experience match factor (EMF)

The experience match factor EMF_n determines how well an analyst matches the complexity of an incident. It is calculated by comparing the analyst's experience level L_n with the complexity level C_m of the incident (equation 8):

$$EMF_n = \begin{cases} 1, & if\ L_n = C_m \\ 0.75 & if\ L_n = C_m + 1 \\ 0.5, & if\ L_n = C_m + 2 \\ 0{,}25 & if\ L_n = C_m + 3 \\ 0 & if\ L_n < C_m \end{cases} \quad (8)$$

where:

- L_n is the level of analyst An, ranging from 1 (Trainee) to 5 (Senior).
- C_m is the complexity level of incident Im, ranging from 1 (Very Low Complexity) to 5 (Critical Complexity).

Table 14 presents EMF scores for selected analyst–incident assignments to illustrate how analyst expertise aligns with incident complexity.

A higher EMF score means the analyst's experience is a better match for the incident complexity. Analysts with levels closer to the incident's complexity will have higher EMF scores, which means they are better suited for handling the incident.

Table 14. Experience Match Factor (EMF) scores for analyst–incident assignments

Incident I_m	Analyst A_n	Analyst Level L_n	Complexity Level C_m	EMF Score EMF_n
I_1 (APT Attack)	A_1 (Senior)	5	5	1.00
	A_3 (Mid-Level)	3	5	0.00
	A_5 (Trainee)	1	5	0.00
I_2 (Phishing)	A_2 (Advanced Mid-Level)	4	3	0.75
	A_4 (Junior)	2	3	0.00
I_3 (Port Scanning)	A3 (Mid-Level)	3	1	0.50
	A5 (Trainee)	1	1	1.00

Figure 3 summarizes the full analyst matching logic, incorporating both ALF and EMF calculations for optimal assignment.

The process integrates scoring, complexity evaluation, ALF, and EMF to ensure precise analyst allocation.

The ALF score reduces the assignment priority of analysts with high existing workloads, helping to balance incident distribution across available personnel. The EMF score measures how well an analyst's expertise level aligns with the complexity of an incident. A high EMF combined with a low ALF indicates the most suitable analyst. Together, these scores ensure both operational efficiency and task-competency alignment in incident assignment.

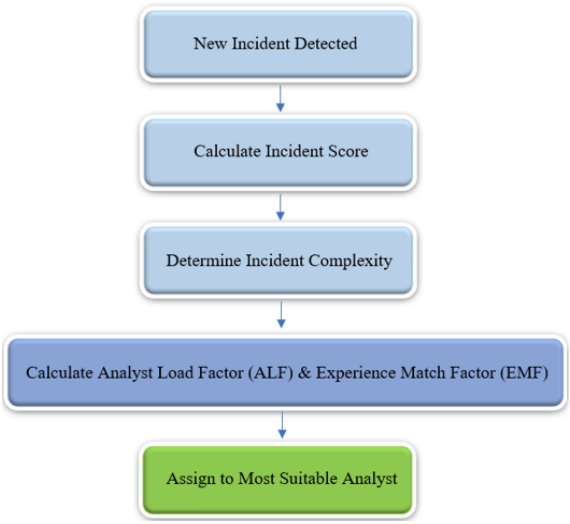


Figure 3. Analyst matching flow: from incident evaluation to optimal assignment.

Additionally, the model supports future extensions such as analyst fatigue metrics, skill-based routing using specialized domain tags (e.g., cloud, endpoint, identity), and AI-driven anomaly clustering, ensuring long-term scalability and personalization.

2.4.5 Step 5: Final analyst suitability score

The final suitability score for an analyst handling a specific incident is given by (equation 9):

$$S_n = \frac{S_m x\, EMF_m}{ALF_n} \tag{9}$$

where:

- S_n is the final score for analyst A_n.
- S_m is the incident score for incident I_m.
- EMFn is the experience match factor for analyst A_n.
- ALF_n is the analyst load factor for analyst A_n.

To demonstrate the scoring mechanism, Tables 15 through 18 show the final suitability scores for different incidents (APT attack, phishing, port scanning, unusual login behavior), evaluated across all analysts. Each table presents detailed ALF, EMF, and final score calculations per analyst.

Table 19 consolidates the results by identifying the analyst with the highest suitability score for each incident, enabling optimized assignment based on both expertise and workload.

Table 15. Final score calculation for incident 1 (APT Attack, Score S_1 = 4.63)

Analyst A_n	ALF ALF_n	EMF EMF_n	Final Score Calculation S_n	Suitability Score (Sn)
A_1 (Senior)	1.50	1.00	$\frac{4.63 \times 1.00}{1.50} = 3.08$	3.08
A_2 (Advanced Mid-Level)	1.40	0.00	$\frac{4.63 \times 0.00}{1.40} = 0.00$	0.00
A_3 (Mid-Level)	1.30	0.00	$\frac{4.63 \times 0.00}{1.30} = 0.00$	0.00
A_4 (Junior)	1.60	0.00	$\frac{4.63 \times 0.00}{1.60} = 0.00$	0.00
A_5 (Trainee)	1.20	0.00	$\frac{4.63 \times 0.00}{1.20} = 0.00$	0.00

Table 16. Final score calculation for incident 2 (Phishing, Score S_2 = 1.92)

Analyst A_n	ALF ALF_n	EMF EMF_n	Final Score Calculation S_n	Suitability Score (Sn)
A_1 (Senior)	1.50	0.50	$\frac{1.92 \times 0.50}{1.50} = 0.64$	0.64
A_2 (Advanced Mid-Level)	1.40	0.75	$\frac{1.92 \times 0.75}{1.40} = 1.03$	1.03
A_3 (Mid-Level)	1.30	1.00	$\frac{1.92 \times 1.00}{1.30} = 1.47$	1.47
A_4 (Junior)	1.60	0.00	$\frac{1.92 \times 0.00}{1.60} = 0.00$	0.00
A_5 (Trainee)	1.20	0.00	$\frac{1.92 \times 0.00}{1.20} = 0.00$	0.00

Table 17. Final score calculation for incident 3 (Port Scanning, Score S_3 = 1.45)

Analyst A_n	ALF ALF_n	EMF EMF_n	Final Score Calculation S_n	Suitability Score (Sn)
A_1 (Senior)	1.50	0.25	$\frac{1.45\ x\ 0.25}{1.50} = 0.24$	0.24
A_2 (Advanced Mid-Level)	1.40	0.50	$\frac{1.45\ x\ 0.50}{1.40} = 0.51$	0.51
A_3 (Mid-Level)	1.30	0.75	$\frac{1.45\ x\ 0.75}{1.30} = 0.83$	0.83
A_4 (Junior)	1.60	1.00	$\frac{1.45\ x\ 1.00}{1.60} = 0.90$	0.90
A_5 (Trainee)	1.20	0.00	$\frac{1.45\ x\ 0.00}{1.20} = 0.00$	0.00

Table 18. Final score calculation for incident 4 (Unusual Login Behavior, Score S_4 = 2.33)

Analyst A_n	ALF ALF_n	EMF EMF_n	Final Score Calculation S_n	Suitability Score (Sn)
A_1 (Senior)	1.50	0.50	$\frac{2.33\ x\ 0.50}{1.50} = 0.77$	0.77
A_2 (Advanced Mid-Level)	1.40	0.75	$\frac{2.33\ x\ 0.75}{1.40} = 1.24$	1.24
A_3 (Mid-Level)	1.30	1.00	$\frac{2.33\ x\ 1.00}{1.30} = 1.79$	1.79
A_4 (Junior)	1.60	0.00	$\frac{2.33\ x\ 0.00}{1.60} = 0.00$	0.00
A_5 (Trainee)	1.20	0.00	$\frac{2.33\ x\ 0.00}{1.20} = 0.00$	0.00

Table 19. Best analyst assignment per incident based on final score

Incident I_m	Best Analyst A_n	Suitability Score (Sn)
I_1 (APT Attack)	A_1 (Senior)	3.08
I_2 (Phishing)	A_3 (Mid-Level)	1.47
I_3 (Port Scanning)	A_4 (Junior)	0.90
I_4 (Unusual Login Behavior)	A_3 (Mid-Level)	1.79

The following pseudocode outlines the full incident scoring and assignment process in two phases.

- Algorithm 1 handles incident evaluation and analyst profiling.
- Algorithm 2 performs analyst–incident matching and assigns each incident to the most suitable analyst based on the computed scores.

Algorithm 1 Part 1 - Incident Scoring and Analyst Profiling

1: Input:
2: $I = \{I_1, I_2, \ldots, I_m\}$ ▷ Set of incidents
3: $A = \{A_1, A_2, \ldots, A_n\}$ ▷ Set of analysts
4: CI_n: Current incident count for analyst A_n
5: MC_n: Max capacity for analyst A_n
6: L_n: Analyst A_n's experience level (1–5)
7: Incident features: S_{sev} , S_{sla}, S_{type}, S_{rep}, S_{asset} , S_{ti}, S_{cor}
8: Feature weights: w_{sev}, w_{sla}, w_{type}, w_{rep}, w_{asset}, w_{ti}, w_{cor}

9: Step 1: Compute Total Incident Score and Complexity Level
10: for $I_m \in I$ do
11: $S_m \leftarrow (w_{sev} \times S_{sev}) + (w_{sla} \times S_{sla}) + (w_{type} \times S_{type}) + (w_{rep} \times S_{rep}) + (w_{asset} \times S_{asset}) + (w_{ti} \times S_{ti}) + (w_{cor} \times S_{cor})$
12: if $S_m \geq 4$ then
13: $C_m \leftarrow 5$ ▷ Critical
14: else if $S_m \geq 3.2$ then
15: $C_m \leftarrow 4$ ▷ High
16: else if $S_m \geq 2.4$ then
17: $C_m \leftarrow 3$ ▷ Medium
18: else if $S_m \geq 1.6$ then
19: $C_m \leftarrow 2$ ▷ Low
20: else
21: $C_m \leftarrow 1$ ▷ Very Low
22: end if
23: end for
24: Step 2: Compute Analyst Load Factor (ALF)
25: for An ∈ A do
26: $ALFn \leftarrow 1 + \frac{CI_n}{MC_n}$
27: end for

Algorithm 2 Part 2 - Analyst Matching and Incident Assignment

1: Step 3: Compute Experience Match Factor (EMF)
2: for $I_m \in I$ do
3: for $A_n \in A$ do
4: if $L_n = C_m$ then

5: $EMF_{n,m} \leftarrow 1$
6: else if $L_n = C_m + 1$ then
7: $EMF_{n,m} \leftarrow 0.75$
8: else if $L_n = C_m + 2$ then
9: $EMF_{n,m} \leftarrow 0.5$
10: else if $L_n = C_m + 3$ then
11: $EMF_{n,m} \leftarrow 0.25$
12: else
13: $EMF_{n,m} \leftarrow 0$
14 : end if
15: end for
16: end for
17: Step 4: Compute Final Suitability and Assign Incidents
18: for $I_m \in I$ do
19: best score $\leftarrow -\infty$
20: assigned $\leftarrow$ None
21: for $A_n \in A$ do
22: $S_{n,m} \leftarrow S_m \, x \, \frac{EMF_{n,m}}{ALF_n}$
23: if $S_{n,m}$ > best score then
24: best score $\leftarrow S_{n,m}$
25: assigned $\leftarrow A_n$
26 : end if
27: end for
28: Assign $I_m \rightarrow$ assigned
29: end for
30: Return all $\{I_m \rightarrow A_n\}$ assignments

3. Results and Discussion

This section presents a step-by-step example involving three incidents and two analysts to demonstrate how the scoring and matching logic operates in practice.

To demonstrate the practical applicability of the proposed scoring and assignment framework, we present a simplified case study involving three distinct incidents and two SOC analysts. Each incident is evaluated using the seven scoring factors, and analysts are profiled using the ALF and EMF metrics. The final analyst-incident assignment is performed based on the suitability score.

3.1. Incident Summary

Table 20 summarizes the key attributes of the three sample incidents used in this illustrative case study.

Table 20. Incident characteristics and scoring inputs for case study

Incident ID	Type	Sev	SLA (hrs)	AsC	Rep	TI	Cor
I1	Phishing Email	3	4	2	0	1	1
I2	Ransomware Detected	5	1	5	1	2	3
I3	Privilege Escalation	4	2	4	2	3	2

*Each factor is normalized to a score out of 5. Higher scores mean higher priority. Sev = severity, AsC= asset criticality, Rep = repetition, TI = threat intel, Cor = correlation.

Each incident is characterized based on seven normalized scoring inputs, including severity, SLA urgency, asset criticality, repetition frequency, threat intelligence relevance, and correlation indicators. These structured inputs serve as the foundation for computing incident scores and enable consistent prioritization across diverse alert types. Notably, Incident I2 represents the most critical case, with the highest severity and repetition levels, whereas I1 shows minimal threat indicators, suggesting a lower priority.

3.2. Incident Scoring

To compute the final score for each incident, the proposed framework utilizes a weighted aggregation model that incorporates seven critical incident attributes: severity (Sev), SLA urgency (SLA), asset criticality (AsC), repetition frequency (Rep), threat intelligence (TI), correlation score (Cor), and incident type (Type). Rather than assuming equal importance, this model applies expert-defined weights to each factor, as formalized in Section 4.2.

Incident I1 (Phishing Email):

S_{I1} = (0.149 × 3) + (0.160 × 3) + (0.135 × 4) + (0.156 × 2) + (0.117 × 0) + (0.149 × 1) + (0.135 × 1)
= 0.447 + 0.480 + 0.540 + 0.312 + 0.000 + 0.149 + 0.135 = 2.063

Incident I2 (Ransomware Detected):

S_{I2} = (0.149 × 5) + (0.160 × 5) + (0.135 × 1) + (0.156 × 5) + (0.117 × 1) + (0.149 × 2) + (0.135 × 3) = 0.745 + 0.800 + 0.135 + 0.780 + 0.117 + 0.298 + 0.405 = 3.280

Incident I3 (Privilege Escalation):

S_{I3} = (0.149 × 4) + (0.160 × 4) + (0.135 × 2) + (0.156 × 4) + (0.117 × 2) + (0.149 × 3) + (0.135 × 2) = 0.596 + 0.640 + 0.270 + 0.624 + 0.234 + 0.447 + 0.270 = 3.081

These weighted scores serve as the foundation for determining incident complexity and inform the analyst-assignment process described in subsequent sections. Notably, Incident I2 received the highest score due to its high severity, critical asset impact, and strong correlation indicators, whereas Incident I1 was rated the lowest due to low repetition and threat intelligence relevance.

3.3. Analyst Profiles

Table 21 presents the analyst profiles used in the assignment process, highlighting their technical skill domains, current workload as measured by the ALF, and the EMF for each incident.

Table 21. Analyst profiles with ALF and EMF values

Analyst ID	Skill Tags	Load (ALF)	EMF I1	EMF I2	EMF I3
A1	Email, SIEM	0.3	0.9	0.3	0.5
A2	Malware, Priv. Escal	0.6	0.5	0.8	0.9

*EMF reflects the degree of match between the incident complexity level and the analyst's expertise level. Lower ALF values indicate higher analyst availability and are therefore considered more suitable for assignment.

Analyst A1, who specializes in email and SIEM alerts, shows higher expertise alignment with Incident I1, whereas A2 has stronger alignment with privilege escalation and malware-related threats. The ALF metric reflects analyst availability, favoring A1 for lower workload. These metrics jointly contribute to the final suitability scoring that guides the analyst-incident assignment process.

3.4. Analyst Suitability Scoring

In this step, each analyst's suitability for a given incident is computed using the updated scoring formula defined in Section 4.4.5:

$$S_n = \frac{S_m x\ EMF_m}{ALF_n}$$

The suitability score increases with higher EMF values and decreases with higher ALF values. Table 21 provides the required ALF and EMF values, while the previously calculated incident scores from Section 5.1.2 are used here.

- Incident I1:

$A1: 2.063 \text{ x } \left(\frac{0.9}{0.3}\right) = 2.063 \text{ x } 3.00 = 6.189$

$A2: 2.063 \text{ x } \left(\frac{0.5}{0.6}\right) = 2.063 \text{ x } 0.833 = 1.718$

→ Assigned to A1

- Incident I2:

$A1: 3.280 \text{ x } \left(\frac{0.3}{0.3}\right) = 3.280 \text{ x } 1.00 = 3.280$

$A2: 3.280 \text{ x } \left(\frac{0.8}{0.6}\right) = 3.280 \text{ x } 1.33 = 4.362$

→ Assigned to A2

- Incident I3:

$A1: 3.081 \text{ x } \left(\frac{0.5}{0.3}\right) = 3.081 \text{ x } 1.67 = 5.145$

$A2: 3.081 \text{ x } \left(\frac{0.9}{0.6}\right) = 3.081 \text{ x } 1.50 = 4.621$

→ Assigned to A1

3.5. Final Assignment Table

Table 22 presents the final analyst–incident assignment results based on the integrated evaluation model that combines incident scoring and analyst suitability. Each assignment reflects a data-driven match between incident criticality and analyst availability and expertise, as computed through the weighted formulas defined in previous sections.

Table 22. Final analyst-incident assignment decisions with suitability scores

Incident	Incident Score	Assigned Analyst	Suitability Score
I1	2.063	A1	6.189
I2	3.280	A2	4.362
I3	3.081	A1	5.145

Incident I2, which received the highest incident score (S_m) of 3.280, was assigned to Analyst A2, who exhibited a strong expertise alignment (EMF: 0.8) despite a moderate workload. The resulting suitability score of 4.362 confirms that A2 is the most effective option for handling this high-priority ransomware incident.

Incident I3, with a slightly lower score of 3.081, was routed to Analyst A1, whose lower workload (ALF: 0.3) and moderate domain match (EMF: 0.6) resulted in a suitability score of 5.145. This indicates a strategic load distribution, where analyst availability plays a decisive role.

Incident I1, the lowest-priority event (score: 2.063), was also assigned to A1, who demonstrated a high EMF score (0.9) and minimal workload, yielding a strong suitability score of 6.189. This decision reflects the model's preference to match lower-risk incidents with available analysts having domain expertise, thereby conserving specialized resources for more complex threats.

Overall, this assignment strategy achieves a balanced optimization between incident urgency and analyst fit. By dynamically incorporating both workload and expertise metrics, the framework ensures timely responses to critical incidents while maintaining sustainable analyst capacity across the SOC environment.

To further support the practical relevance of the proposed model, subsequent evaluation scenarios (Section 5.2) utilize labeled attack traces from the CICIDS2017 dataset. These experiments demonstrate the model's scalability and adaptability when applied to real-world SOC data under varying incident and analyst profiles.

3.6. Empirical Evaluation Using Benchmark SOC Data

To validate the real-world applicability of the proposed framework, a benchmark evaluation was conducted using labeled incident samples from the CICIDS2017 dataset. This section presents the scoring outcomes (Section 5.2.1), metadata and attack characteristics (Section 5.2.2), and analyst assignment results based on suitability scores (Section 5.2.3).

3.6.1. Scoring results of benchmark incidents

Table 23 summarizes the raw attribute values for each incident across seven model dimensions, including severity, SLA urgency, asset criticality, repetition, threat intelligence, correlation, and incident type. These unweighted values are used as inputs for the final priority score computation shown in Table 24.

Table 23. Raw Incident Attribute Scores Across Seven Model Dimensions

Inc. ID	Sev.	SLA	Asset	Rep.	TI	Cor.	Inc. Type
I1	3	4	2	2	1	1	2
I2	4	2	2	3	2	3	2
I3	4	2	2	3	3	2	3
I4	5	1	5	1	4	2	5
I5	3	3	2	2	2	1	4
I6	4	2	2	1	2	2	4
I7	2	4	1	1	2	1	3
I8	5	1	2	3	4	3	5
I9	2	4	2	2	1	1	1
I10	5	1	2	3	3	3	5

*These are raw scores for each incident dimension. Final weighted prioritization scores are calculated in Table 24. Inc. ID = incident ID, Sev. = severity, Rep. = repetition, TI = threat intel, Cor. = correlation, Inc. Type = incident type.

In the previous table (Table 23), raw incident attributes such as severity, SLA urgency, asset criticality, and others are listed for comparative visualization. These values represent the original, unweighted scores and are not directly used for final prioritization.

To derive a reliable prioritization outcome, these attributes are normalized and multiplied by their corresponding expert-defined weights, as specified in Section 4.2. The final incident score for each case is then calculated using the following formula:

$$S_m = W_{sev}\, x\, S_{Sev} + W_{SLA}\, x\, S_{SLA} + W_{type}\, x\, S_{type} + W_{rep}\, x\, S_{rep} + W_{asset}\, x\, S_{asset} + W_{ti}\, x\, S_{ti} + W_{cor}\, x\, S_{Cor} \quad (10)$$

Where the weights (wi) were empirically determined via expert survey and are normalized to sum to 1. Table 24 summarizes the final weighted scores computed from the raw values.

Table 24. Final weighted incident scores

Incident ID	Final Score
I1	2.148
I2	2.574
I3	2.737
I4	3.443
I5	2.460
I6	2.503
I7	2.013
I8	3.344
I9	1.839
I10	3.195

*Final scores represent the normalized and weighted prioritization values used for analyst matching and complexity classification.

3.6.2. Incident Metadata and Threat Typology

The selected cases reflect a diverse threat landscape, including brute-force attempts, exploit-based attacks, DDoS campaigns, and infiltration methods. Each incident was mapped to both external and internal hosts within the dataset and aligned with a victim asset class.

Detailed incident metadata, including attacker IP, victim IP, asset, and assigned technique are summarized in Table 25.

3.6.3. Analyst Assignment Outcomes

To support analyst–incident matching, synthetic analyst profiles were defined based on varying levels of expertise and workload. Each analyst was assigned an experience level (L_n) ranging from 1 (Trainee) to 5 (Senior), and an Analyst Load Factor (ALF) value representing the analyst's current workload relative to their maximum handling capacity. These parameters were used to evaluate the suitability of each analyst for the incidents under consideration.

The synthetic analyst profiles used in this evaluation are presented in Table 26.

Table 25. Incident descriptions extracted from CICIDS2017 dataset

Inc. ID	Date	Attack Type	Attacker IP	Victim IP	Asset	Tech.
I1	July 4	FTP-Patator	205.174.165.73	192.168.10.50	Web Server	Brute Force
I2	July 4	SSH-Patator	205.174.165.73	192.168.10.50	Web Server	Brute Force
I3	July 5	DoS Hulk	205.174.165.73	192.168.10.50	Web Server	DoS
I4	July 5	Heartbleed	205.174.165.73	192.168.10.51	Ubuntu12 Server	Exploit
I5	July 6	SQL Injection	205.174.165.73	192.168.10.50	Web Server	Web Attack
I6	July 6	Infiltration (Dropbox)	205.174.165.73	192.168.10.8	Windows Vista	Infiltration
I7	July 6	Infiltration (Cool Disk)	205.174.165.73	192.168.10.25	MAC	Infiltration
I8	July 7	Botnet ARES	205.174.165.73	Multiple Targets	Win 10/8/Vista	Botnet
I9	July 7	Port Scanning	205.174.165.73	192.168.10.50	Ubuntu16	Reconnaissance
I10	July 7	DDoS LOIT	205.174.165.69–71	192.168.10.50	Ubuntu16	DDoS

*This table lists real incident samples extracted from CICIDS2017, which serve as empirical inputs for scoring and assignment. Inc. ID = incident ID, Tech. = technique.

Table 26. Synthetic analyst profiles used in evaluation

Analyst	Experience Level L_n	ALF
A1	5 (Senior)	0.30
A2	4 (Advanced)	0.40
A3	3 (Mid-Level)	0.50
A4	2 (Junior)	0.60
A5	1 (Trainee)	0.70

*The CICIDS2017 dataset does not include analyst metadata. These experience levels and ALF values were synthetically assigned to simulate a realistic analyst pool with varying workloads and expertise.

Using the incident complexity levels (Cm) calculated in Section 5.2.1 and the analyst profiles summarized in Table 26, the EMF was determined for each analyst–incident pair by comparing the analyst's experience level (Ln) to the incident's complexity level. Suitability scores were then computed using the model's formal suitability function introduced in Section 4.4.5:

$$S_n = \frac{S_m \text{x } EMF_m}{ALF_n}$$

A higher Sn score indicates a more appropriate match between the analyst and the incident, balancing expertise and workload. The final assignment results, including the selected analyst and computed suitability scores, are presented in Table 27.

Table 27. Analyst Assignment Results Based on Suitability Score

Incident ID	Assigned Analyst	S_m (Normalized)	EMF	ALF	Suitability Score S_n
I1	A3	2.148	1.00	0.50	4.296
I2	A3	2.574	1.00	0.50	5.148
I3	A3	2.737	1.00	0.50	5.474
I4	A2	3.443	1.00	0.40	8.608
I5	A2	2.460	0.75	0.40	4.613
I6	A2	2.503	0.75	0.40	4.692
I7	A4	2.013	0.50	0.60	1.678
I8	A1	3.344	0.75	0.30	8.360
I9	A3	1.839	1.00	0.50	3.678
I10	A2	3.195	1.00	0.40	7.988

*Suitability scores were computed using the model formula $S_n=(S_m \times EMF_n) / ALF_n$. Each incident was assigned to the analyst with the highest S_n value to ensure optimal alignment of expertise and workload.

As shown in Table 27, analysts with the highest suitability scores were selected for each incident. Notably, high-complexity incidents such as I4, I8, and I10 were consistently assigned to senior or advanced-level analysts with lower ALF values, reflecting the model's effectiveness in balancing analyst capacity and expertise for prioritized incident response.

4. Conclusion

4.1. Summary and Contributions

The incident assignment process ensures that each incident is handled by the most suitable analyst based on multiple factors such as incident severity, SLA urgency, and complexity. Key takeaways from the model include:

- Shorter SLA Urgency: Incidents with a shorter SLA (requiring quicker resolution) are prioritized to ensure timely response.
- Complex Incidents: Incidents with higher complexity scores are assigned to more experienced analysts (Senior, Advanced Mid-Level), while lower complexity incidents are assigned to Junior or Trainee analysts.
- Workload Balancing: Analysts' workloads are carefully managed using the ALF, ensuring no analyst is overloaded with incidents.
- Experience Matching: EMF ensures incidents are assigned to analysts whose experience level matches the incident's complexity.
- Dynamic Assignment: The assignment process is dynamic and recalculated based on real-time data, ensuring that the most appropriate analyst is always handling the most critical incidents.
- Threat Intelligence: Known threat actors and the type of asset affected by the incident are factored into the assignment process to ensure priority is given to high-risk incidents.
- Final Assignments: Based on the calculations and factors above, the final assignments are dynamically adjusted, with critical incidents being handled by Senior analysts, medium to high complexity incidents being assigned to Mid-Level or Advanced Mid-Level analysts, and low severity incidents being delegated to Junior or Trainee analysts.
- Case Study Demonstration: A synthetic case validated the model's logic, showing that high-priority incidents (e.g., I2, score 2.86) were routed even with moderate analyst suitability, while lower-priority ones (e.g., I1) were matched based on optimal expertise. This illustrates the model's dynamic balancing of priority and analyst fit.

This process guarantees that each incident is assigned to the right analyst, optimizing response time and enhancing overall security operations in the organization.

Empirical validation using CICIDS2017 incidents confirmed that the proposed framework effectively prioritizes and assigns incidents in line with analyst experience and workload.

4.2. Discussion and Limitations

The proposed incident assignment framework presents a structured and comprehensive approach for prioritizing and allocating incidents in SOCs, based on both technical risk indicators and analyst characteristics. By integrating factors such as incident severity, SLA urgency, threat intelligence, and correlation scores with analyst-specific attributes like expertise and workload, the model aims to ensure efficient resource utilization and informed triage decisions. Despite its methodological robustness and practical motivation, several aspects of the current implementation present notable limitations that may constrain its applicability in dynamic operational settings.

One potential enhancement to overcome static weighting is the integration of a reinforcement learning agent that adjusts scoring logic based on historical assignment outcomes, false positive rates, and SOC performance KPIs. A key limitation of the framework lies in its reliance on static weighting schemes across all scoring dimensions. While these weights reflect domain-informed estimations of attribute importance (e.g., severity = 5, SLA = 4), they lack adaptability to real-time contextual factors or organization-specific risk priorities. Such rigidity may undermine the model's responsiveness to evolving threat environments. Weights were initially derived using expert judgment and validated through scenario testing. Future iterations may use reinforcement learning to optimize these weights dynamically. This limitation suggests the need for the integration of adaptive weighting mechanisms, potentially through feedback-driven systems or multi-criteria decision-making techniques such as Analytic Hierarchy Process (AHP), TOPSIS, or reinforcement learning models that allow the scoring logic to evolve over time.

Another important constraint is related to the restricted scope of the correlation component. The current implementation evaluates incident similarity using only three attributes—source IP, destination IP, and username—which, while foundational, do not adequately capture behavioral patterns or adversarial tactics present in sophisticated attacks. Enhancing the correlation score to incorporate richer features, including command-line behavior, timestamp proximity, tool usage patterns (e.g., PowerShell, Mimikatz), and threat actor tactics mapped via the MITRE ATT&CK framework, would improve the model's capacity to identify campaign-level threats and anomaly clusters.

Moreover, the absence of a feedback-driven refinement mechanism restricts the system's capacity for learning and self-improvement. Once incident-to-analyst assignments are made, there is no subsequent evaluation based on resolution outcomes, reassignment frequency, or analyst satisfaction. Without such feedback loops, the system cannot distinguish between effective and suboptimal assignments over time. This limitation could be addressed by incorporating supervised learning

models that continuously recalibrate assignment logic based on analyst input, historical resolution data, and operational performance indicators.

The model's EMF also warrants further refinement. Currently based on predefined distance-based coefficients between incident complexity and analyst experience levels, the EMF metric lacks granularity and fails to consider domain-specific skillsets, fatigue, or recent performance trends. A more nuanced EMF calculation incorporating analyst specialization (e.g., malware analysis, identity attacks), prior success rates, and real-time capacity signals would enhance the fidelity of analyst-incident mapping.

In terms of data integration, the model assumes access to relatively static datasets that describe incident characteristics and analyst capacity. In practice, SOC environments operate in real-time, and decision-making requires continuously updated information. Without integration into live platforms such as SIEMs, CMDBs, or Extended Detection and Response (XDR) systems, the model's outputs risk becoming obsolete or misaligned with the current threat landscape. Establishing API-based data pipelines with tools like Elastic SIEM or IBM QRadar would facilitate real-time decision support and elevate operational relevance.

From a validation perspective, the current work remains conceptual, with no empirical testing conducted in real-world SOC environments or through simulation frameworks. Although a simplified case study was included to demonstrate the model's functionality and logic, full-scale evaluation and longitudinal testing remain future priorities. The absence of experimental results means that the effectiveness, scalability, and latency performance of the model remain unverified. To strengthen its practical credibility, future research should include scenario-based simulations, stress tests using synthetic incident datasets, and controlled pilot deployments in operational SOC contexts.

Finally, the computational efficiency of the proposed assignment algorithm has not been formally examined. Although the scoring and matching mechanisms are designed for clarity and interpretability, large-scale SOCs handling thousands of incidents and dozens of analysts could encounter significant processing overhead. A formal analysis of algorithmic complexity, along with benchmarking under load, would provide essential insights into the model's performance under high-throughput conditions.

In conclusion, while the proposed model introduces a methodologically sound and operationally motivated solution to the incident assignment problem in SOCs, its practical deployment would benefit significantly from adaptive learning capabilities, enriched correlation metrics, analyst feedback integration, real-time data synchronization, and empirical validation. Addressing these limitations would enhance the framework's scalability, resilience, and alignment with modern SOC operational dynamics.

4.3. Code Availability

A reference implementation of the analyst assignment framework (including ALF and EMF scoring logic) is available upon request for academic and research purposes. Please contact the corresponding author.

4.4. Future Work

Building upon the foundational structure of the proposed incident assignment and prioritization framework, several key directions are envisioned to enhance its effectiveness, scalability, and operational alignment within real-world SOCs. These future research pathways are centered around four core improvement domains: adaptability, learning capability, integration, and validation. Such adaptivity would not only improve triage accuracy but also enable SOCs to tailor decision logic according to sector-specific threats, compliance requirements, and organizational maturity.

A critical area for advancement lies in transitioning from static to dynamic weight assignment mechanisms across the incident scoring model. Currently, weights attributed to parameters such as severity, SLA urgency, and threat intelligence are fixed and domain-informed. However, SOCs operate in highly fluid threat environments, where contextual relevance and risk prioritization vary over time. Future iterations of the model should explore adaptive weighting strategies utilizing decision-making frameworks such as Analytic Hierarchy Process (AHP), Technique for Order Preference by Similarity to Ideal Solution (TOPSIS), or reinforcement learning. These approaches can enable the system to reweigh incident attributes in real time based on feedback loops, evolving threat profiles, or analyst performance metrics.

In parallel, enhancing the system's capacity to learn from historical decisions and analyst interactions is essential. Currently, the model lacks a feedback mechanism that captures analyst agreement with incident assignments, reassignment frequencies, or resolution outcomes. Future developments should embed a supervised learning component that utilizes these variables to incrementally adjust the assignment logic, enabling continuous improvement and personalized allocation. This concept is illustrated in Figure 4, which demonstrates the analyst feedback loop as a dynamic reinforcement layer that connects incident outcomes back into the scoring and assignment pipeline. Such feedback integration would allow the system to iteratively evolve and increase its contextual awareness over time.

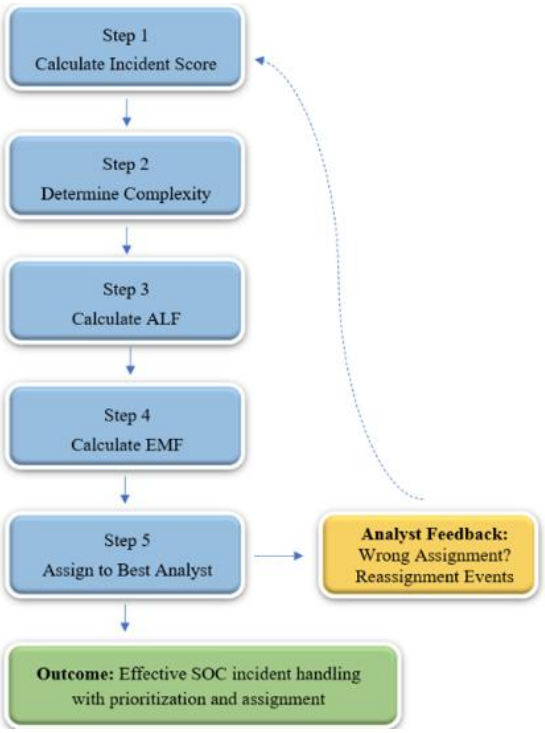


Figure 4. Enhanced dynamic incident assignment flow with analyst feedback loop for learning.

Moreover, the scope of the correlation score mechanism requires significant broadening to improve pattern recognition and campaign-level threat detection. Presently based on a limited set of attributes (source IP, destination IP, and username), future versions should integrate temporal patterns (e.g., frequency bursts), command-line activity indicators, domain names, authentication anomalies, and attack tools. Incorporating MITRE ATT&CK-based tactic and technique mappings into the correlation score can also improve threat classification and enhance alignment with structured adversary behavior frameworks.

Integration with live SOC ecosystems represents another pivotal development trajectory. To ensure operational viability and timeliness, future work should implement real-time data pipelines with external platforms such as SIEM (e.g., Elastic, Splunk), CMDBs, and XDR tools (e.g., SentinelOne, QRadar). API-based synchronization would enable live updates on incident states, analyst capacity, and organizational context, thereby improving responsiveness and reducing reliance on static or outdated data inputs.

Additionally, expanding the EMF to reflect more granular analyst characteristics is a necessary step. Future versions should incorporate analyst specialization profiles, historical resolution accuracy, domain-based expertise (e.g., cloud security, endpoint threats), and real-time workload fatigue indicators. Such multi-dimensional EMF modeling would support more accurate and equitable incident distribution.

On the validation front, rigorous testing of the model through simulation environments or controlled deployments is imperative. The inclusion of the illustrative case study in this paper was a preliminary step in demonstrating model functionality; however, broader validation with synthetic or real-world datasets remains essential. Generating synthetic incident datasets that simulate realistic SOC alert distributions would allow performance benchmarking under various scenarios (e.g., high alert volume, analyst shortages, APT detection). Time-to-resolution metrics, analyst satisfaction, and reassignment rates could be tracked to evaluate model efficiency and practical benefit. Experimental deployments in enterprise SOC environments, even on a limited scope or shadow mode basis, would offer valuable insights into usability and organizational adoption feasibility.

Finally, a formal computational complexity analysis of the scoring and assignment algorithm should be conducted. In large SOC environments—where n represents the number of incidents and m represents the number of analysts—the overall time complexity of $O(n \times m)$ implies that each incident may need to be evaluated against every analyst. To ensure scalability and maintain low-latency performance under such enterprise-scale conditions, optimization techniques such as batch assignment processing, parallel computation, or heuristic-based filtering should be considered.

In summary, future enhancements to the proposed framework should transform the current theoretical model into a dynamic, intelligent, and integrative decision-support engine capable of adapting to complex SOC environments. By incorporating learning mechanisms, real-time integrations, enriched analytical models, and empirical evaluations, the framework can evolve into a robust operational tool for next-generation cybersecurity incident management.

Ultimately, the proposed framework supports analyst-aware SOC operations by offering a quantifiable and explainable assignment mechanism. Future work will focus on integrating AI-driven adaptivity, real-time SIEM pipelines, and empirical testing to move from conceptual design to full operational deployment.

Author Contributions

The percentages of the authors' contributions are presented below. All authors reviewed and approved the final version of the manuscript.

	E.C.K.	B.C.
C	50	50
D	50	50
S		100
DCP	80	20
DAI	50	50
L	20	80
W	70	30
CR	10	90
SR	50	50
PM	20	80

C=Concept, D= design, S= supervision, DCP= data collection and/or processing, DAI= data analysis and/or interpretation, L= literature search, W= writing, CR= critical review, SR= submission and revision, PM= project management, FA= funding acquisition.

Conflict of Interest

The authors declared that there is no conflict of interest.

Ethical Consideration

Ethics committee approval was not required for this study because of there was no study on animals or humans.

References

Al-Dhaqm A, Siddique K, Abd Razak S, Ikuesan RA, Kebande VR. 2020. Towards the development of an integrated incident response model for database forensic investigation field. IEEE Access, 8: 145018-145032.

Alrimawi F, Pasquale L, Nuseibeh B. 2019. On the automated management of security incidents in smart spaces. IEEE Access, 7: 111513-111527.

AXELOS. 2019. ITIL Foundation: ITIL 4 Edition. The Stationery Office (TSO), London, UK, 1st ed., pp. 1-255.

Binbeshr F, Imam M, Hamdan M, Ghaleb M, Rahim MA, Hammoudeh M. 2025. The rise of cognitive SOCs: A systematic literature review on AI approaches. IEEE Open J Comput Soc, 6: 360-379.

Chhetri MB, Tariq S, Singh R, Jalalvand F, Paris C, Nepal S. 2024. Towards human-AI teaming to mitigate alert fatigue in security operations centres. ACM Comput Surv, 24(3): 1-22.

Gachnang P, Ehrenthal J, Telesko R, Hanne T. 2023. Determination of weights for multiobjective combinatorial optimization in incident management with an evolutionary algorithm. IEEE Access, 11: 138502-138514.

García LA, Tomás VR. 2020. A framework for enhancing the operational phase of traffic management plans. IEEE Access, 8: 204483-204493.

Handri EY, Sensuse DI, Tarigan A. 2025. Developing an agile cybersecurity framework with organizational culture approach using Q methodology. IEEE Access, 13: 108835-108850.

He Y, Luo C, Evans M, Zamani E, Maglaras LA, Yevseyeva I, Janicke H. 2019. Real-time information security incident management: A case study using the IS-CHEC technique. IEEE Access, 7: 142147-142175.

Hou W, Meng L, Ke X, Zhong L. 2022. Dynamic load balancing algorithm based on optimal matching of weighted bipartite graph. IEEE Access, 10: 127225-127236.

Jadon S, Kannan PK, Gupta K, Kalaria U, Honnavalli PB, Varsha KR. 2024. A comprehensive study of load balancing approaches in real-time multi-core systems for mixed real-time tasks. IEEE Access, 12: 53373-53395.

Jalalvand F, Chhetri MB, Nepal S, Paris C. 2024. Alert prioritisation in security operations centres: A systematic survey on criteria and methods. ACM Comput Surv, 57(2): 1-36.

Liao S, Wu C, Yang Q, Wang B, Jiang M. 2011. A resource-efficient load balancing algorithm for network virtualization. Chin J Electron, 20(4): 765-770.

Mooi RD, Botha RA. 2016. A management model for building a computer security incident response capability. SAIEE Afr Res J, 107(2): 78-91.

Vielberth M, Böhm F, Pernul G, Fichtinger I. 2020. Security operations center: A systematic study and open challenges. IEEE Access, 8: 227756-227779.

Villalón-Huerta A, Ripoll-Ripoll I, Marco-Gisbert H. 2022. SOC critical path: A defensive kill chain model. IEEE Access, 10: 13570-13581.

Black Sea Journal of Engineering and Science
doi: 10.34248/bsengineering.1697396

Open Access Journal
e-ISSN: 2619 – 8991

Research Article
Volume 8 - Issue 4: 1181-1184 / July 2025

DETERMINATION OF TOTAL PHENOLIC ACID CONTENT AND ANTI-ATHEROGENIC ACTIVITY OF OIL OBTAINED FROM FRESH ARUGULA (*ERUCA SATIVA L.*) BY COLD-PRESSING

Erkan ÖNER[1]*, İlter DEMİRHAN[2]

[1]*Adıyaman University, Faculty of Pharmacy, Department of Biochemistry, 02000, Adıyaman, Türkiye*
[2]*Harran University, Vocational School of Health Services, Department of Electronic-Automotion, 63320, Sanlıurfa, Türkiye*

Abstract: Cold-pressed oils have attracted great interest due to their high content of bioactive compounds and potential health benefits. This study aims to determine the total phenolic acid content and anti-atherogenic activity of cold-pressed wild arugula (*Eruca sativa L.*) oil. Total phenolic acid content was analyzed using spectrophotometric and chromatographic methods, while anti-atherogenic activity was evaluated by in vitro tests measuring antioxidant capacity and lipid peroxidation inhibition. The results show that *Eruca sativa L.* oil contains significant amounts of phenolic acids, which contribute to its antioxidant potential. Furthermore, the oil exhibited promising anti-atherogenic activity, suggesting its potential role in cardiovascular health. These findings highlight the importance of cold-pressed wild arugula oil as a functional food ingredient with potential therapeutic applications.

Keywords: *Eruca sativa L.*, Cold pressed oil, Phenolic acids, Anti-atherogenic activity, Antioxidant potential

***Corresponding author:** Adıyaman University, Faculty of Pharmacy, Department of Biochemistry, 02000, Adıyaman,, Türkiye
E mail: erkanoner0803@gmail.com (E.ÖNER)
Erkan ÖNER https://orcid.org/0000-0002-6332-6484
İlter DEMİRHAN https://orcid.org/0000-0003-0054-7893

Received: May 12, 2025
Accepted: June 19, 2025
Published: July 15, 2025

Cite as: Oner E, Demirhan I. 2025. Determination of total phenolic acid content and anti-atherogenic activity of oil obtained from fresh arugula (*Eruca Sativa L.*) by cold-pressing. BSJ Eng Sci, 8(4): 1181-1184.

1. Introduction

It is an annual herbaceous plant belonging to Brassicaceae family, genus Eruca MILLER, taxon *Eruca sativa* (*E. sativa*) MILLER (Ahmed et al., 2013; Sadig et al., 2013; Rizwana et al., 2016). *E. sativa* is commonly known as arugula and its leaves are consumed (Gozukara et al., 2019). It has been used as a medicine to treat different diseases since ancient times (Sadig et al., 2013).

E. sativa L. (Arugula) oil can be used as an oil plant with 35% oil content in its seeds (Acar et al., 2016) and as a medicinal plant because its leaves contain flavonoids such as quercetin, kaempferol, isorhamnetin (Nicoletti et al., 2007; Caruso et al., 2018).

E. sativa plant 100 grams approximately; 3.65 g carbohydrate; 2.58 g protein; 1.6 g dietary fiber; 0.305 mg niacin; 0.437 mg pantothenic acid; 0.073 mg pyridoxine; 0.086 mg riboflavin; 0.44 mg thiamine; 15 mg vitamin C; 2373 IU vitamin A; 0.43 mg vitamin E; 108.6 ug vitamin K; 27 mg sodium; 369 mg potassium; 160 mg calcium; 0.076 mg copper; 1.46 mg iron; 47 mg magnesium; 0.321 mg manganese; 52 mg phosphorus; 0.3 ug selenium; 0.47 mg zinc and 1424 ug carotene-ß; 3555 ug lutein-zeaxanthin. Palmitic acid, linoleic, linolenic, oleic, stearic and erucic acid are the fatty acids it contains (Garg and Sharma, 2014). The fatty acid profile is approximately as follows: palmitic acid 2.80%; stearic acid 30.8%; oleic acid 17.8%; linoleic acid 1.44%; linolenic acid 6.78%; erucic acid 47.0%.

It has anticarcinogenic (Koubaa et al., 2015; Bell and Wagstaff, 2019), anti-inflammatory (Koubaa et al., 2015, Katsarou et al., 2016), antiulcer (Koubaa et al., 2015) activity. It helps to remove toxic substances from the body and strengthens the immune system and stomach (Sadig et al., 2013; Shabnam 2015).

Serum paraoxonase (PON1, EC 3.1.8.1) is an enzyme found in the blood. It belongs to a group of enzymes called esterases. It is physically bound to a type of cholesterol called high-density lipoprotein (HDL). It is named for its ability to break down paraoxon, which is an organophosphate that is produced in the body from the insecticide parathionate (Mackness et al., 2002). The assessment of PON1 activity has traditionally relied on the use of paraoxon and phenylacetate as substrates. Another type of paraoxonase enzyme, paraoxonase 3 (PON 3), is found in the blood. However, PON3 has almost no paraoxonase activity with paraoxon as substrate (Ng et al., 2005). It also has almost no arylesterase activity when phenylacetate is used as a substrate. Some studies have suggested that the role of PON3 may be different from that of PON1. Furthermore, there is less serum human PON3 than PON1 (Draganov and La Du, 2004). PON1 is one of the main enzymes that may be responsible for a significant portion of the antioxidant properties of HDL. Numerous studies have shown that HDL protects LDL and cell membranes against damage from oxidation (Draganov and La Du, 2004). Oxidised LDL has been

This work is licensed (CC BY-NC 4.0) under Creative Commons Attribution 4.0 International License

shown to play a key role in the development of atherosclerotic lesions, and HDL has been shown to protect LDL from oxidation, thereby preventing the production of oxidised LDL. The protective effect of HDL may be attributed to its associated enzymes, including PON1 (Draganov and La Du, 2004; Mackness et al., 2002). In addition to its role in protecting LDL, PON1 has been reported to play a significant role in the breakdown and inactivation of homocysteine thiolactone, a toxic substance produced when homocysteine is broken down. This enzyme has also been shown to activate and inactivate certain drugs. PON1 also plays a role in other diseases, such as diabetes, familial hypercholesterolemia, chronic renal failure, obesity, metabolic syndrome and sepsis (Draganov and La Du; Goswami et al., 2009; Aviram and Rosenblat,2005; Camps et al., 2009).

PON1 is a glycoprotein enzyme synthesized by the liver, hydrolyzes aromatic carboxylic acid esters, has the ability to hydrolyze paraoxon, the active metabolite of paration, an organic phosphorus insecticide, and is tightly bound to HDL (Azarsız, 2000). PON1 is an important liver enzyme which is bound to HDL and plays a protective role against hydrolysis of organophosphate agents (OP) and nerve gases, formation of lipid peroxides by oxidation of LDL and bacterial endotoxins. Paraoxanase was initially studied in the field of toxicology due to its ability to hydrolyze organophosphate compounds, but in recent years, it has gained popularity in recent years due to its antioxidant effects, as it is thought that it can be protected from the risk of chronary heart disease. Paraoxanase also reveals the importance of the antioxidant properties of the enzyme as HDL reduces lipid peroxides by these enzymatic mechanisms during the oxidation of LDL, which constitutes the initial stage of the arterosclerosis process, and thus the accumulation of lipid peroxides (Durrington and Mackness, 2001, Carey et al., 2005). Paraoxonase enzyme is one of the defense mechanisms in the body against arterosclerotic diseases (Gencer, 2008).

It has long been known that HDL in serum is protective against the development of atherosclerosis. The mechanisms of this protective effect include reverse cholesterol transport, increasing the synthesis of some vasodilator molecules such as nitric oxide, inhibiting inflammation and thrombosis formation, decreasing the synthesis of adhesion molecules, stimulating endothelial repair and preventing oxidative changes in LDL. However, which components of HDL are involved in all these mechanisms is controversial. The recent discovery that PON1 is a component of HDL has gained importance in clarifying these controversial mechanisms. In order to better examine the function of PON1 in this mechanism, it must first be obtained in pure form from serum. It is known that there are many other proteins in the complex formed by PON1 with HDL. Previous studies reported a wide range of substrates for PON1, suggesting that the enzyme could not be obtained in a sufficiently pure form. Therefore, in this study, it was aimed to completely separate PON1 from other HDL components using appropriate purification steps from serum and to better define the structural and functional properties of the pure enzyme (Bayrak, 2009).

In this study, it was aimed to investigate the total phenolic acid content and paraoxanase enzyme inhibition activity of *E. sativa* L. oil.

2. Materials and Methods

2.1. Plant Samples

Fresh arugula (*Eruca sativa* L.) was taken and the oil was extracted by cold pressing. The extracted oils were stored at 2-8 ^{o}C until biological property studies were carried out.

2.2. Total Phenolic Acid Content

2.4 mL of distilled water was added to the tubes. Then 40 µL Eruca sativa L. oil and 200 µL Folin ciocalteu solution were added. Subsequently, 600 µL of the sample was equilibrated to room temperature, with an incubation interval ranging from 30 seconds to 7.5 minutes following the preceding step. Then saturated sodium carbonate was added. 760 µL of distilled water was added. Vortexed. It was kept for 2 hours at room temperature in the dark and read at 765 nm in a spectrophotometer (Singleton and Rossi, 1965; Turkes et al., 2014).

2.3. hPON1 activity

In this study, PON1 (Paraoxonase-1) enzyme activity was evaluated by spectrophotometric method using phenylacetate substrate. The measurement was carried out based on the absorbance increase of the product formed by hydrolysis of phenylacetate to p-hydroxybenzene at 405 nm wavelength in the reaction mixture containing Tris-HCl buffer (pH 8.0) and 1 mM $CaCl_2$. Potential inhibitors such as Eruca sativa L and Kojic acid were added separately and in combination and enzyme inhibition levels were calculated and % inhibition rates were compared with the control group (Güzel et al., 2025).

3. Results

3.1. Phenolic Acid Content

Total phenolic matter content is given in Table 1. Phenolic acid content of arugula oil was 330.23±9.12 GAE/L.

Table 1. Phenolic acid content of *Eruca sativa L*. oil

Sample	Total Phenolic Content (GAE/L)
Eruca sativa L. oil	330.23±9.12

3.2. Paraoxanase Results

In this study, the inhibition effect of Eruca sativa L. oil on paraoxonase enzyme activity was studied. IC50 value for arugula oil was determined as 350.39±9.77 with the help of % activity graph (Table 2, Figure 1). In our study, Lineweaver-Burk graph was drawn (Figure 2) and it was determined that the inhibition type was competitive. As a result of inhibition studies, it was observed that arugula oil strongly inhibited the hPON1 enzyme.

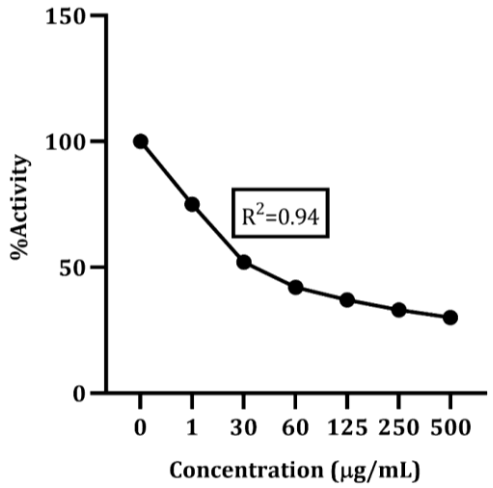


Figure 1. hPON1 Percent Activity in Response to Eruca sativa L. Oil Treatment.

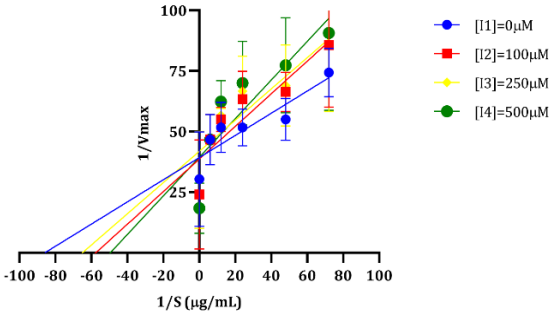


Figure 2. Lineweaver–Burk plot depicting the effect of Eruca sativa L. oil on the catalytic kinetics of human paraoxonase 1 (hPON1), suggesting potential modulation of enzyme activity.

Table 2. Inhibitory effect of *Eruca sativa L.* on Paraoxanase (hPON1).

	Inhibition against paraoxanase IC50 (µg/mL)	Inhibition against paraoxanase R^2
Eruca sativa L. Oil	350.39±9.77	0.94

4. Discussion

The specific enzyme known as PON1 is present in various tissues throughout the human body, including those located in the brain, heart, liver, kidney, lung, and small intestine. The predominant site of synthesis of this enzyme is the liver during metabolic processes, and it subsequently binds to HDL, which subsequently circulates in the bloodstream (Turkes et al., 2019). A body of literature exists which demonstrates that PON1 is directly responsible for a number of antiatherogenic functions of HDL. These functions include the protection of lipoproteins and cells against oxidative stress, as well as the prevention of atherogenesis and lipoprotein peroxidation (Jaouad et al., 2003). The protective effects of PON1 are related to the enzyme level in serum. Recent studies have reported low PON1 levels in patients with atherosclerosis, diabetes and hypercholesterolemia. Conversely, the over-expression of PON1 has been observed to impede the progression of cardiovascular diseases. In addition, PON1 has been found to stimulate HDL efflux in macrophages and inhibit LDL biosynthesis (Richter et al., 2008). In another study, PON1 was shown to be transported from HDL to the outer surface of the cell membrane to protect metabolism against oxidative stress-related conditions such as coronary artery disease, diabetes, and obesity (Aviram and Rosenblat, 2008).

In this study, the phenolic acid content of *E. sativa L.* oil was examined and found to be 330.23±9.12 GAE/L. In addition, as a result of hPON1 inhibition study, it was observed that *E. sativa L.* oil strongly inhibited the hPON1 enzyme.

5. Conclusion

In summary, this study focused on investigating the in vitro effects of *E. sativa L.* oil on PON1 activity, which has a role in serious cases such as cardiovascular diseases. Decreased activity of PON1 is an important risk factor for atherosclerosis. This study should be supported by in vivo studies. Further studies are needed as there is no universal conclusion on whether PON1 can be used as a biomarker for cardiovascular disease.

Author Contributions

The percentages of the authors' contributions are presented below. All authors reviewed and approved the final version of the manuscript.

	E.Ö.	İ.D.
C	60	40
D	50	50
S	50	50
DCP	50	50
DAI	50	50
L	50	50
W	50	50
CR	60	40
SR	60	40
PM	60	40
FA	50	50

C=Concept, D= design, S= supervision, DCP= data collection and/or processing, DAI= data analysis and/or interpretation, L= literature search, W= writing, CR= critical review, SR= submission and revision, PM= project management, FA= funding acquisition.

Conflict of Interest

The authors declared that there is no conflict of interest.

Ethical Consideration

Ethics committee approval was not required for this study because of there was no study on animals or humans.

References

Acar R, Gecgel U, Hamurcu M, Coskun B, Koc N, Ozcan MM. 2016. Some chemical properties, fatty acid composition and mineral contents of Diplotaxis tenuifolia seed and oil. Am J Essent Oil Nat Prod, 4(2): 23–26.

Ahmed J, Al-Salman F, Almusallam AS. 2013. Effect of blanching on thermal color degradation kinetics and rheological behavior of rocket (Eruca sativa) puree. J Food Eng, 119: 660–667.

Aviram M, Rosenblat M. 2005. Paraoxonases and cardiovascular diseases: Pharmacological and nutritional influences. Curr Opin Lipidol, 16: 393–399.

Aviram M, Rosenblat M. 2008. Paraoxonases (PON1, PON2, PON3) analyses in vitro and in vivo in relation to cardiovascular diseases. Methods Mol Biol, 477: 259–276.

Azarsız EYS. 2000. Paraoxonase and its clinical importance. Turk J Biochem, 25(3): 109–120.

Bayrak A. 2009. Purification of human serum paraoxonase enzyme and investigation of its kinetic properties, endogenous substrates and antioxidant properties. PhD Thesis, Hacettepe University, Health Sciences Institute, Ankara, Türkiye, pp: 186.

Bell L, Wagstaff C. 2019. Rocket science: A review of phytochemical and health-related research in Eruca diplotaxis species. Food Chem, 1: 100002.

Camps J, Marsillach J, Joven J. 2009. The paraoxonases: Role in human diseases and methodological difficulties in measurement. Crit Rev Clin Lab Sci, 46: 83–106.

Carey JN, Hama SY, Mohamad NS, Reddy T. 2005. The paraoxonase gene family and atherosclerosis. Free Radic Biol Med, 38: 153–163.

Caruso G, Parrella G, Giorgini M, Nicoletti R. 2018. Crop systems, quality and protection of Diplotaxis tenuifolia. Agricult, 8(55): 1–19.

Draganov DI, La Du BN. 2004. Pharmacogenetics of paraoxonases: A brief review. Naunyn Schmiedebergs Arch Pharmacol, 369: 78–88.

Durrington BM, Mackness MI. 2001. Paraoxonase and atherosclerosis. Arterioscler Thromb Vasc Biol, 21: 473–475.

Garg G, Sharma V. 2014. Eruca sativa (L.): Botanical description, crop improvement, and medicinal properties. J Herb Spice Med Plant, 20: 171–182.

Gençer N. 2008. Purification of paraoxonase Q and R isoenzymes and investigation of their affinity to some environmental pollutants. PhD Thesis, Balıkesir University, Institute of Science, Department of Chemistry, Balıkesir, Türkiye, pp: 204.

Goswami B, Tayal D, Gupta N, Mallika V. 2009. Paraoxonase: A multifaceted biomolecule. Clin Chim Acta, 410: 1–5.

Gözükara G, Altunbaş S, Şimsek O, Sarı O, Buyurgan K, Maltaş AŞ, Sönmez NK, Kaplan M. 2019. Determination of the relationship between spectral reflectance and plant nutrient concentration in arugula (Eruca vesicaria) cultivation. Mediterr Agric Sci, 32: 55–62.

Güzel A, Uğur Y, Oner E, Kolaç T. 2025. Comparative analysis of phytochemical content and antioxidants, anti-cholinesterase, anti-atherogenic and molecular docking of Turkish Pelargonium (Pelargonium endlicherianum Fenzl.). South Afr J Bot, 179: 124–133.

Jaouad L, Milochevitch C, Khalil A. 2003. PON1 paraoxonase activity is reduced during HDL oxidation and is an indicator of HDL antioxidant capacity. Free Radic Res, 37(1): 77–83.

Katsarou D, Omirou M, Liadaki K, Tsikou D, Delis C, Garagounis C, Krokida A, Zambounis A, Papadopoulou KK. 2016. Glucosinolate biosynthesis in Eruca sativa. Plant Physiol Biochem, 109: 452–465.

Koubaa M, Driss D, Bouaziz F, Ellouz Ghorbel R, Ellouz Chaabouni S. 2015. Antioxidant and antimicrobial activities of solvent extract obtained from rocket (Eruca sativa) flowers. Free Radic Antioxid, 5: 5530.

Mackness MI, Mackness B, Durrington PN. 2002. Paraoxonase and coronary heart disease. Atheroscler Suppl, 3: 49–51.

Ng CJ, Shih DM, Hama SY. 2005. The paraoxonase gene family and atherosclerosis. Free Radic Biol Med, 38: 153–163.

Nicoletti R, Raimo F, Miccio G. 2007. Diplotaxis tenuifolia: Biology, production and properties. Eur J Plant Sci Biotechnol, 1(1): 36–43.

Richter RJ, Jarvik GP, Furlong CE. 2008. Paraoxonase 1 (PON1) status and substrate hydrolysis. Toxicol Appl Pharmacol, 235: 1–9.

Rizwana H, Alwhibi MS, Khan F, Soliman DA. 2016. Chemical composition and antimicrobial activity of Eruca sativa seeds against pathogenic bacteria and fungi. J Anim Plant Sci, 26: 1859–1871.

Sadiq A, Hayat MQ, Mall SM. 2014. Qualitative and quantitative determination of secondary metabolites and antioxidant potential of Eruca sativa. Nat Prod Chem Res, 2: 4172.

Shabnam N. 2015. Characterization of polyphenol oxidase enzyme from arugula (Eruca sativa). MSc Thesis, Istanbul Aydin University, Institute of Science, Istanbul, Türkiye, pp: 42.

Singleton VL, Rossi JR. 1965. Colorimetry of total phenolics with phosphomolybdic-phosphotungstic acid. Am J Enol Vitic, 16: 14–158.

Türkeş C, Beydemir S, Küfrevioğlu ÖI. 2019. In vitro and in silico studies on the toxic effects of antibacterial drugs as human serum paraoxonase 1 inhibitor. Chem Select, 4(33): 9731–9736.

Türkeş C, Söyüt H, Beydemir Ş. 2014. Effect of calcium channel blockers on paraoxonase-1 (PON1) activity and oxidative stress. Pharmacol Rep, 66: 74–80.

Black Sea Journal of Engineering and Science
doi: 10.34248/bsengineering.1704013

Open Access Journal
e-ISSN: 2619 – 8991

Research Article
Volume 8 - Issue 4: 1185-1194 / July 2025

REAL TIME DETECTION OF MICROBIAL LEAF DISEASES USING DEEP LEARNING AND EDGE COMPUTING ON RASPBERRY Pi 4

Noor BAHA ALDIN[1]*

[1]*Hasan Kalyoncu University, Faculty of Engineering, Department of electrical and Electronics, 27010, Gaziantep, Türkiye*

Abstract: Bacterial and fungal leaf diseases significantly impact the productivity of agricultural, which causing annually billions of dollars in crop losses and threatening global food security. Conventional detection methods even though effective, but they are labor intensive, consuming more time, and inappropriate for real time applications or large-scale ones. In order to address the limitations of other studies, this study proposes an AI solution that using a fine-tuned ResNet50 model trained on the PlantVillage dataset to classify the plant leaves as Healthy, Bacterial, or Fungal (Mold). The model was optimized using TensorFlow Lite and deployed on a Raspberry Pi 4, achieving 87% accuracy, a recall of 86%, and inference speeds around 1.2 to1.5 seconds per image. To enhance the overall generalization, the data augmentation techniques were applied which including rotation, flipping, and scaling. For early disease detection in agricultural and environmental applications, this research provides a scalable and a cost effective. Compared to traditional methods and other systems, this study provides faster inference speeds and lower costs, making it ideal for designs with limited resource.

Keywords: Image classification, Deep learning, ResNet50, Edge computing, Image processing

***Corresponding author:** Hasan Kalyoncu University, Faculty of Engineering, Department of Electrical and Electronics, 27010, Gaziantep, Türkiye
E mail: noor.aldin@hku.edu.tr (N. BAHA ALDIN)
Noor BAHA ALDIN https://orcid.org/0000-0002-7351-4083

Received: May 22, 2025
Accepted: June 22, 2025
Published: July 15, 2025

Cite as: Baha Aldin N. 2025. Real time detection of microbial leaf diseases using deep learning and edge computing on raspberry pi. BSJ Eng Sci, 8(4): 1185-1194.

1. Introduction

Bacterial and fungal leaf diseases significantly impact the productivity of agricultural, which causing annually billions of dollars in crop losses and threatening global food security. Conventional detection methods even though effective, but they are labor intensive, consuming more time, and inappropriate for real time applications or large-scale ones. In order to address the limitations of other studies, this study proposes an AI solution that using a fine-tuned ResNet50 model trained on the PlantVillage dataset to classify the plant leaves as Healthy, Bacterial, or Fungal (Mold). The model was optimized using TensorFlow Lite and deployed on a Raspberry Pi 4, achieving 87% accuracy, a recall of 86%, and inference speeds around 1.2 to1.5 seconds per image. To enhance the overall generalization, the data augmentation techniques were applied which including rotation, flipping, and scaling. For early disease detection in agricultural and environmental applications, this research provides a scalable and a cost effective. Compared to traditional methods and other systems, this study provides faster inference speeds and lower costs, making it ideal for designs with limited resource. Bacterial and fungal leaf diseases result in a significant threat to the productivity of agricultures, leading to billions of dollars in crop yield losses annually, and that make the global security of food in danger (Upadhyay et al., 2025; Albahar, 2023). These diseases are not only affecting the farmers and consumers, but also reduces the yields that degrade the quality of crops. The early detection of these diseases will stop the spread of it and at the same time it will reduce the economic losses (Dhaka et al., 2021; Durgun et al., 2024). However, conventional methods of disease detection like inspection of expert eye, tests of laboratory, and spectroscopic methods are normally labor-intensive, sometimes time consuming, and unsuitable for real time applications. These restrictions do not allow for immediate interventions, especially in resource limited environments with limited availability of diagnostic tools (Hasan et al., 2023). With the development in artificial intelligence (AI), especially deep learning, a revolution has been in image classification in recent years. Convolutional neural networks (CNNs) have made a remarkable advancement in the area of the classification and detection of plant diseases being accurate and effective (Bansal et al., 2023; Dhaka et al., 2021). However, most of the current methods are depend on the high-performance processing units such as GPUs and cloud systems, which makes them not applicable for the agricultural and remote areas fields. This gap shows the necessity for low-cost and a lightweight system that can analyze in real time without reducing accuracy (Premkumar et al., 2022). To address these challenges,

This work is licensed (CC BY-NC 4.0) under Creative Commons Attribution 4.0 International License

this study presents an enabled AI real time detection system for bacterial and fungal leaf diseases, which utilizes deep learning and edge computing technologies. The model is implemented through a fine-tuned a fine-tuned ResNet50 model trained using the publicly available PlantVillage dataset, that includes images of healthy, bacterial, and fungal-infected plant leaves. The model was then further optimized using TensorFlow Lite and finally deployed on a Raspberry Pi 4 for portable real-time classification with low computational resources. Data augmentation was applied to the input in order to improve the generalization capabilities of the model, including rotation, flipping and scaling. The system achieved 87% accuracy, a recall of 86%, and the ability to process image data in approximately 1.2 to 1.5 seconds per image, thus making it suitable for detection disease at an early stage in agricultural and environmental situations. This method offers several advantages compared to previous methods. By deploying the model on a Raspberry Pi, the model provides acceptable inference speeds and is most cost effective, thereby making it a fit for resource-limited environments. Unlike conventional methods that require skilled personnel and time-consuming steps, this method provides a fast, automated and reliable disease diagnosis at the point of need. In addition, its scalability and low cost offer the potential for a practical deployment in agriculture and environmental monitoring at large scale.

In future work, the model will be tested on field taken images to confirm its robustness in real conditions. Furthermore, it may be integrated with many other multi-modal sensors (such as thermal imaging) and more advanced edge devices, such as the NVIDIA Jetson Nano, could further enhance performance and reliability. By combining deep learning with edge computing, this study provides a practical reference for addressing one of the most pressing challenges in modern agriculture, where deep learning and edge computing play important roles in the efficient detection of microbial leaf diseases.

2. Related Work

The intersection of artificial intelligence and plant disease detection has recently grown to become an active area of interest, with increasing attention due of deep learning in image classification (Upadhyay et al., 2025; Albahar, 2023). In the field of plant disease detection, CNNs are widely demonstrated to be effective for the detection of visual symptoms of diseases in plant leaves with architectures like ResNet and VGGNet achieving high accuracy over several datasets (Bansal et al., 2023). For example, (Geetabai et al., 2024) studied deep CNNs for plant disease detection with PlantVillage dataset and this study highlighted the explanation of the model using saliency maps. More recently, studies were focused on the classification of bacterial and fungal diseases in crops, leading to results highlighting the importance of the early detection of the disease for the yield loss reduction.

Similar research in the context of the general image classification has shown that a feature fusion and hybrid pipelines, in which handcrafted features integrated with deep learning, improve performance. (Soundarya et al., 2025; Ahmed et al., 2024) also proved that the combination of CNN features with classical methods like Principal Component Analysis (PCA) and Support Vector Machine (SVM) leads to enhanced classification. Although these methods can improve model accuracy, they often lead to computationally heavy models that cannot be used for real-time, in-field applications.

Edge computing has appeared as one of the promising solutions for real-time inference with limited resource environments. Recent studies have applied AI on embedded devices for microbial and pathogen detection. (Qi et al., 2021; Kim et al., 2024) presented a Raspberry Pi based powered microfluidic biosensor for Salmonella detection as well as described how AI can be applied on low-cost hardware (Beznik et al., 2022). In the agriculture, real time pest and diseases monitoring using edge device, is one of the areas of focus for researchers implying the requirement of scalable solutions. Nevertheless, such models are generally for laboratory microorganisms or foodborne pathogens, which require specific sensors and thus were not directly applicable to agricultural field monitoring (Qi et al., 2021; Beznik et al., 2022).

Although deep learning models have been proved successful in laboratory, there are also studies that have successfully worked on these systems to deploy it on edge devices for plant disease detection (Zhang et al., 2021; Sun et al., 2023). While several models have achieved high accuracy using PlantVillage dataset, it depends on GPU-based infrastructure for inference. This creates a major gap in terms of implementing robust, low-latency solutions in agricultural environments requiring real-time feedback.

To address this, this study established on refining the existing CNN to develop a ResNet50 model that performs well in the classification of microbial diseases that affect leaves of plants namely bacterial spot and mold by using the PlantVillage dataset. Unlike prior studies that entirely aims at maximizing classification accuracy in controlled environments without regard for practical deployment, it prioritizes practical issues, and optimize the trained model through TensorFlow Lite and running it on a Raspberry Pi 4. This allows real-time performance with competitive accuracy, which is applicable for agricultural field deployment, especially in rural resource limited areas.

3. Materials and Methods

This study introduces a lightweight deep learning (DL) system for the real-time microbial plant leaf diseases classification on low-cost edge devices suitable for agricultural uses. The model combines a well-trained CNN model with a Raspberry Pi device, which allows automatic diagnose of bacterial and fungal causes of the

plant disease from leaf images.

The dataset used in this study is a subset of the publicly available PlantVillage image collection of higher resolution images of plant leaves divided into main 3 classes; Healthy, Bacterial, and Fungal (Mold), but also tested on two other classes. The trained dataset was processed and augmented, and performed with normalization and several augmentations including rotation, flipping, and scaling in order to enhance model robustness and generalization (Alexandra et al., 2023). All images were resized to 224×224 pixels, this is the input dimension that the DL model supports.

The model is based on the architecture of ResNet50, pre-trained on ImageNet, and also fine-tuned for the task of three class classification. The final architecture consists of a global average pooling layer, a fully connected layer with 256 ReLU activated neurons and a softmax layer. The model is trained then using Adam optimizer and categorical cross entropy loss across 15 epochs with a learning rate that is equal to 0.001. 'The training, test and validation are set to 70%, 10% and 20% respectively (Bansal et al., 2023). The model was trained and converted to TensorFlow Lite which enabled it to run on the edge. The optimized model was deployed on portable and appropriate powerful Raspberry Pi 4 (Qi et al., 2021; Sun et al., 2023). Leaf images were taken in real time with a high-resolution camera. The system sends each image through TensorFlow Lite model and generates a classification result (Premkumar et al., 2022). The Adam's parameter is given by (equation 1):

$$\theta_{t+1} = \theta_t - \frac{\eta}{\sqrt{\hat{v}_t} + \epsilon}\hat{m}_t \quad (1)$$

Where θ_t represents the parameter at iteration t, η is the learning rate, $\hat{m}_t$ is the mean of gradients, $\hat{v}_t$ represents uncentered variance of gradients, and ϵ is the small constant added for numerical stability.

This method focusses on the real time performance, cost effectiveness and deploy ability in resource limited scenarios. In contrast to previous methods that use GPU equipped servers or combine deep and handcrafted features by means of hybrid models, this system aims to run entirely on device with no external computational resources. The concept is simple, effective and scalable solution for early diagnosis of leaf diseases caused by microorganism on crop leaves.

3.1. Raspberry Pi Integration for Real-Time Edge Computing

The incorporation of the Raspberry Pi 4 to the microbial contamination detection system is an important step toward practical, accessible, and low-cost AI framework. A Raspberry Pi which is the main processing source of the system that perform real time inference with an optimized TensorFlow Lite model (Qi et al., 2021). This choice reflects the cost effectiveness, portability and energy efficiency of the device which are important in resource limited environments for widespread deployment of advanced AI solutions. The Raspberry Pi 4 Model B with 8GB of Random Access Memory (RAM) provides the enough processing power to be able to run on device inference. This capability eliminates the necessity for the costly Graphics Processing Unit (GPU) server and thus it is more accessible for small and medium enterprises (SMEs) as well as low resourced organizations (Sun et al., 2023). In addition, it is small and light weighted, so it can imply easily into various applications, ranging from small food factory and agricultural location to remote agricultural area and the environmental monitoring field.

However, a high-resolution Raspberry Pi camera module is used for image capture to facilitate the operation of the system, thereby enabling clear and detailed visual data collection for analysis. Also, the OS for TensorFlow Lite and the easy model running is the Raspberry Pi OS as well. The pre-trained deep learning models are further converted to TensorFlow Lite to optimize the model size and inference latency. This conversion is really required to make the inference real time on the limited computational resources of the Raspberry Pi (Beznik et al., 2022). The optimized model can then be deployed to the device and is capable of processing images and classifying the type of contamination in real time with a high accuracy.

The process consists of collecting samples of microbial contamination image, preprocessing the input, and finally applying it to the model. The results are then presented through a connected interface or transmitted to a remote server for global monitoring. This integration of hardware and software allows the system to produce actionable results in a few seconds, providing the near real-time detection and classification functionality that used to be limited to laboratory environments.

For real time validation, leaf images of tomato and potato plants were captured by the Raspberry Pi high quality camera. These plants were cultivated in outdoor, semi controlled conditions.

The infection state of these samples was not manually checked. Instead, the deployed model used infection categories (Healthy, Bacterial, or Fungal) based on visual features that it had learned from the labelled PlantVillage dataset (Hughes and Salathé, 2015). This allowed to test the real-world performance of the model and generalization ability without requiring on-site diagnostics or laboratory analysis.

The Raspberry Pi module offers significant practical advantages. As its cost is low, it can be applied in large scale applications easily especially in developing regions where conventional configurations are costly. Its power efficiency fits into sustainability objectives, reducing operational costs and environmental impact. Furthermore, its scalability can facilitate several devices to be deployed at different sites extending to a network of real time monitoring systems. This modular structure allows the solution to be easily adapt to various scales' adjustment according to the requirements of the food safety, agricultural monitoring and environmental

protection applications. Through the integrating of Raspberry Pi 4, this system also transforms advanced AI-driven microbial detection from a laboratory-bound process into a portable, low-cost, and scalable solution. This idea bridges the gap between cutting-edge technology and real-world applicability, making sure it is effective, while it is practical, and accessible for diverse users and environments. Figure 1 presents the general diagram of model training, evaluation, and deployment, from input of the dataset to device prediction on the Raspberry Pi.

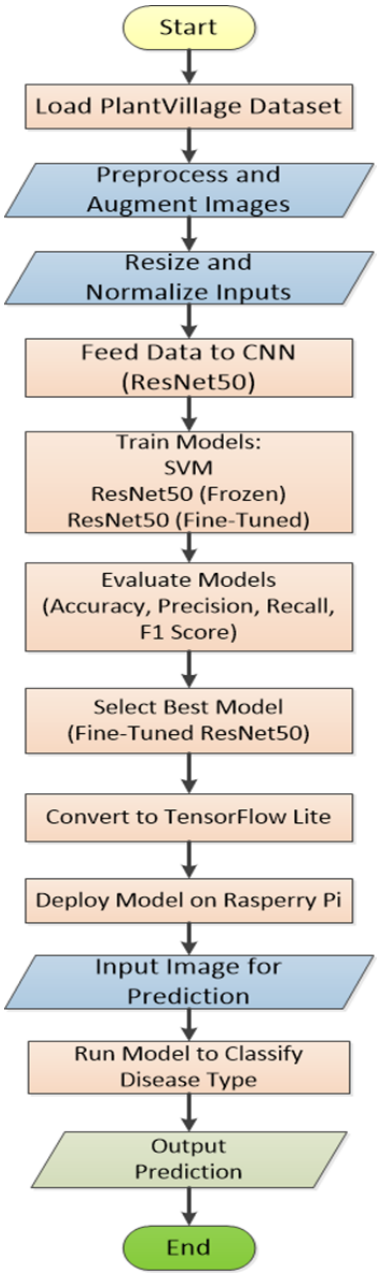


Figure 1. Diagram of the proposed system for microbial leaf disease detection.

For real-time testing and deployment, images were captured by the high-quality Raspberry Pi camera, which is based on Sony IMX477 sensor with a 12.3 MP and supports interchangeable C- and CS-mount lenses. A 6 mm 3MP CS mount lens was utilized in this study. This combination of hardware setup is optimized for Raspberry Pi 4 support and has been tested across many edge computing applications.

Images were taken under natural daylight conditions either in outdoor shadow or indoor light environments. The shooting distance at which the images were taken was set at approximately 30 cm. The camera was operated in automatic exposure mode, with auto ISO, white balance, and aperture in order to automatically adjust to the real-world lighting conditions without manual adjustments.

3.2. Data Acquisition and Preprocessing

This study utilizes a filtered subset of publicly available PlantVillage dataset which was actually developed for visual classification of plant diseases. The dataset consists of over 20,000 images of plant leaves categorized into three classes related to this study: Healthy, Bacterial, and Fungal. These images are helpful in training of deep learning models that can be used to identify the visual symptoms of microbial leaf diseases.

3.2.1. Image collection

All of the images were obtained using digital cameras in standardized environments to ensure image clarity and reproducibility. The dataset comes from a wide variety of plant species and a number of microbial infection patterns such as necrotic spots, mold growth, and discoloration. This study considered only those plant diseased leaf images where the visual effects of microbial leaf infections were included. The dataset consisted of approximately 20,000 images, and distributed in three main categories. Since the task is agricultural in scope, there was no an attempt to for cross domain generalization to food safety or healthcare, so the model was specialized keeping the model focused only on leaf microbial disease detection (Zhang et al., 2021; Kumar et al., 2020). The dataset was filtered and balanced to have approximately equal samples for each class, 6,800 images of healthy, 6,500 images of bacterial, and 6,700 images of Fungal (Mold). This balanced distribution is beneficial to prevent bias toward dominant classes during training and evaluation. This is shown in Figure 2 below.

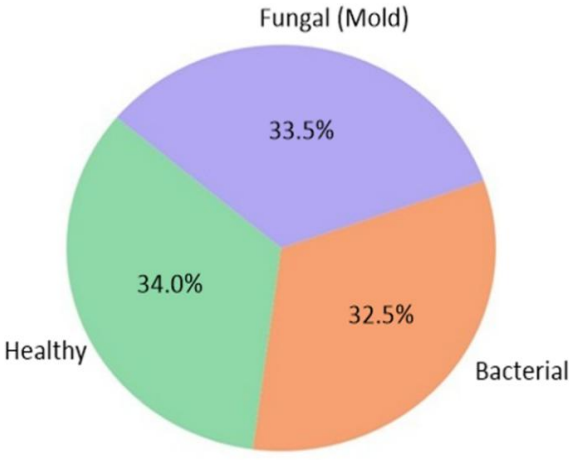


Figure 2. Dataset distribution by class.

From the original PlantVillage dataset (Hughes & Salathe, 2015), approximately 7,500 images were selected spread over the three target categories (Healthy, Bacterial, and Fungal). These were the original images on which the augmentation was applied to.

Data augmentation was applied to expand the dataset to approximately 20,000 images, using the ImageDataGenerator of TensorFlow. The augmentation techniques were implemented in the training process are the rotation where random angles between −90° and +90°, the random horizontal and vertical flips, zooming between 0.9× and 1.1×, and random position shift up to 10% of the image in width and height.

3.2.2. Preprocessing pipeline

To prepare the data for machine learning analysis, an extensive preprocessing pipeline was applied; a median filter was used to suppress sensor and background noise as well as to preserve edges, crucial in capturing disease-specific texture boundaries. This filter was chosen because of its high performance in noise reduction for edge preserving property and very effective removal of salt-and-pepper noise, which often occurs in high-resolution leaf texture images. Unlike mean filters, which may tend to smooth out important features, the median filter maintains sharp transitions and fine features, which is crucial for the recognition of patterned microbial infection. To enhance the contrast of microbial patterns on the leaf surfaces, adaptive histogram equalization was used. In addition, all pixel values were scaled to 0–1 range using min-max normalization, and all the images were normalized as follows (equation 2):

$$\hat{x} = \frac{x - \min(x)}{\max(x) - \min(x)} \quad (2)$$

where $\hat{x}$ is the pixel value normalized to the range [0, 1], x represents the pixel intensity value of the image before normalization, $\min(x)$ is the minimum pixel value in the image, and $\max(x)$ represents the maximum pixel value in the image.

All images were resized to a fixed dimension of 224×224 pixels to match the input size of ResNet50, for feature extraction. Also, several augmentation methods including random rotation, horizontal and vertical flipping, and zooming were used for training in order to enable the model to be more stable and decrease the overfitting. Random shifts were applied for simulate camera variations. These augmentations helped in simulating the variability in leaf orientation and background, and therefore enhancing the generalization on unseen test images (Han et al., 2024; Hasan et al., 2022).

In the training and inference of the model, all images were resized to 224 × 224 pixels, enforcing a 1:1 aspect ratio as required by the input format of ResNet50. The real-time validation images were captured using Raspberry Pi camera at 4056 × 3040 pixels with the default 4:3 aspect ratio, keeping the quality high for robust inference, and resized to 224x224 pixels before the model inference.

Image resizing was achieved by using the OpenCV 4.8.0 library in Python. The resizing function (cv2.resize) with bilinear interpolation utilized to reduce distortion while preserving important visual features.

Processed images were saved in JPEG format with 95% compression quality, this level was chosen to balance file size and retention of microbial detail. No compression was applied prior to resize and normalization.

3.3. Enhanced Dataset Representation

The chosen preprocessing pipeline was used to better prepared the dataset for machine learning, and that enhancing the image clarity, reducing noise, and normalizing the input size. Median filtering, adaptive histogram equalization, normalization, and resizing to 224×224 pixels were used. These operations ensured that important microbial features including edge of colony, texture, and pigmentation across all samples. Handcrafted features were also extracted to capture domain-relevant characteristics in addition to CNN based feature learning. Haralick texture features (derived from the Gray Level Co-occurrence Matrix) and normalized color histograms were utilized to characterize the overall microbial surface variations. This multi-feature strategy performed a better classification by considering both global and local visual cues that are associated with microbial contamination (Xie et al., 2024).

3.3.1.Edge deployment and optimization

The trained ResNet50 model was optimized for a deployment on a Raspberry Pi 4 via the following steps:

1) Quantization: The FP32 weights were quantized to INT8 with TensorFlow Lite and obtained about 75% model size reduction with small drop in accuracy loss (<2%). This is illustrated in the equation (3).
2) Thread Configuration: Number of threads were 4 to maximizing CPU utilization, used for parallel inference from Set TFLite interpreter.

Although the Pi 4's limited RAM (8GB) constrained batch processing to single-image inference, optimizations lead to an average latency of 1.2-1.5 seconds per image, which is comparable to higher-end edge devices in similar studies. The end-to-end model of the proposed system for real-time detection of microbial leaf disease is shown in Figure 3 (Anyu et al., 2023). The workflow is initiated by training and fine-tuning a ResNet50 model on the PlantVillage dataset using a development machine. Finally, the trained model is converted and quantized into TensorFlow Lite format for lightweight deployment, and is later transferred through USB cable to a Raspberry Pi 4, which serves as the edge inference engine (Deng et al., 2023). The Raspberry Pi 4 has a high-resolution camera module which is used to capture images of plant leaves in real time. After processing of the captured images, the system outputs classification the results (Healthy, Bacterial, or Fungal). The PlantVillage dataset, of various images of healthy and unhealthy plant leaves is preprocessed by noise filtering, contrast enhancement, and resizing for better performance (equation 2).

$$x_{INT8} = round(\frac{x_{FP32}}{s}) + z \quad (3)$$

Where x_{FP32} is the value in the original 32-bit floating point format, s represents the scaling factor, z is the zero-point offset, x_{INT8} is the result 8-bit quantized value.

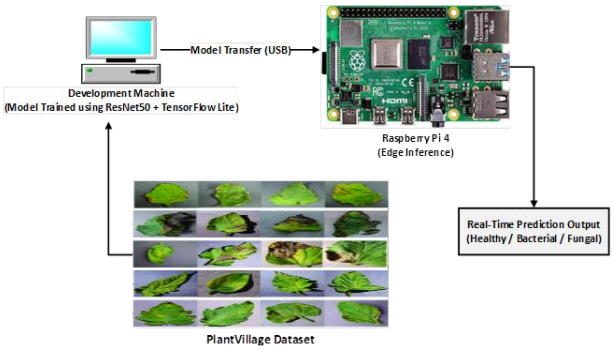


Figure 3. System architecture for real-time microbial leaf disease detection.

3.3.2. Software and Environment

All analyses of experimental data and model development tasks were performed using Python 3.9.12. The model was implemented and trained using TensorFlow 2.15.0 with Keras. The images are pre-processed using OpenCV 4.8.0 and NumPy 1.24.3, the data is augmented via TensorFlow's ImageDataGenerator.

Visualization was performed using Matplotlib 3.5.1 and Seaborn 0.11.2, while metrics were computed with scikit-learn 1.2.2. Model quantization and deployment were performed using TensorFlow Lite 2.15.0. All development was performed on a Raspberry Pi OS installed on Raspberry Pi 4.

4.Results and Discussion

To evaluate the performance of the proposed microbial contamination detection model, training was performed in two separate stages: initial training (feature extraction only) and fine-tuning (full model training). Model performance in terms of training, validation accuracy, and loss over epochs is presented in Table 1.

Table 1. System performance on Raspberry Pi4

Metric	Value
CPU Utilization	85% (peak)
Memory Usage	512MB (of 8GB)
Power Draw	3.2W
Inference Time	1.35 ± 0.15 sec

4.1. Initial Training Phase

In the initial phase, only the top classification layers of ResNet50 architecture were fine-tuned and the convolutional base layers was frozen. As can be seen from Figure 4, training accuracy increased gradually from 49% to 54%, which means that the model could capture some basic discriminative features. However, the validation accuracy fluctuated between 10% and 53%, with a standard deviation of 12.5%, which indicates poor generalization caused by the frozen base layers. This instability further indicates that the model has a limited capability to generalize from the training data in the restricted feature extraction. This bias can also be observed further in Figure 5, which visualize the loss curves. Although the training loss declined and stabilized at about 1.2, the validation loss remained highly unstable, reaching values over 9.0. These spikes indicate the model is overfitting and that it has weak generalization, which is expected since the fixed feature extractor is not optimal for the microbial feature dataset. The performance difference between training and validation reflects the lack of robustness in the first training configuration.

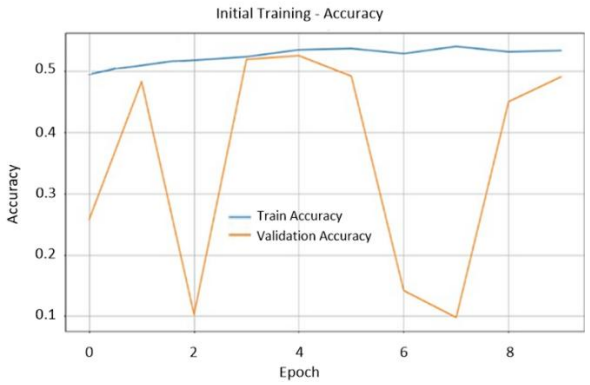


Figure 4. Training and validation accuracy during the initial training phase.

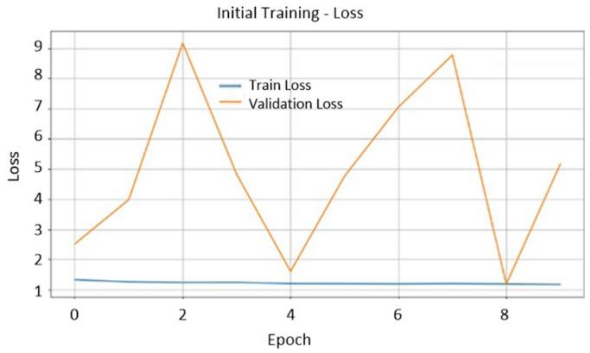


Figure 5. Training and validation loss during the initial training phase.

4.2.Fine-Tuning Phase

To resolve these issues, fine-tuning was done by unfreezing a portion of the ResNet50 base layers and training the entire network with a lower learning rate. This strategy allowed the model to fine tune high level features specifically to the task of microbial contamination.

As shown in Figure 6, the training and validation accuracies were significantly improved. Training accuracy surpassed 95% and a validation accuracy steadily increased, ranging from 70% to a final accuracy

of 87%. This reflects a significant improvement in the generalization of the model to unseen data. Figure 7 shows a slight reduction in loss trends. Consistently both training and validation loss decreased across epochs with a validation loss dropping below 1.0 and exhibiting the minimal fluctuation. The enhanced loss stability shows that the model sufficiently mitigated the overfitting that occurred during early learning and learned domain-specific patterns.

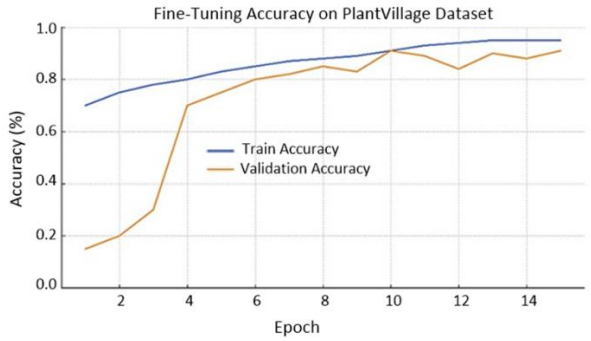


Figure 6. Training and validation accuracy during the fine-tuning phase.

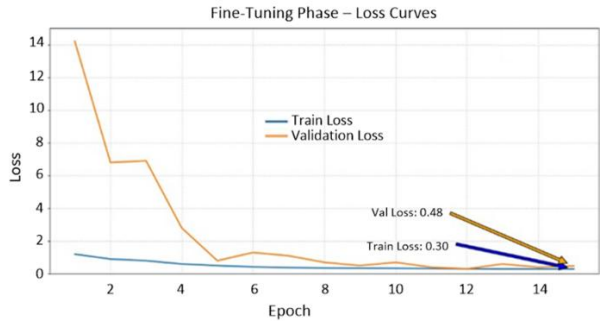


Figure 7. Training and validation loss during the fine-tuning phase.

These results demonstrate the effectiveness of transfer learning in cooperation with focused fine-tuning. The model was able to leverage pretrained features and gradually adapted to the microbial field which in turn contributed to the enhanced robustness, decreased overfitting and overall stronger the performance of classification.

4.3. Model Performance Comparison and Fine-Tuning Impact

The performance of the proposed fine-tuned ResNet50 model was evaluated against a baseline ResNet50 (with frozen layers) and a custom CNN trained from scratch. As illustrated in Figure 8, the fine-tuned ResNet50 performed the best precision (0.90) and F1 score (0.88) and was significantly better than the base ResNet50 and the custom CNN model in terms of all the metrics that applied.

The better performance of the fine-tuned model is demonstrated also by the metric summary shown in Table 2, where it achieved an accuracy of 87% of the overall test samples with a recall of 86%. In contrast, the baseline ResNet50 achieved only 80% accuracy, which indicating that freezing the feature extractor can limit domain adaptation. The customized CNN was efficient, had the worst performance which emphasizes the importance for using transfer learning to moderate size datasets. The training and validation accuracy curves of the fine-tuned model demonstrated rapid learning on initial epochs with validation accuracy of around 90% at epoch 4. Both curves converged around 95% meaning strong generalization of the model with no signs of overfitting. This validates the efficacy of combining pretrained features with targeted fine-tuning on domain-specific data. Though the model was deployed on a resource-constrained Raspberry Pi4, the average inference time was around 1.2-1.5 second per image, thus near real time performance was supported. These results show that a lightweight model-based solution is possible and potentially useful for the in-field microbial contamination detection in real world particularly in low-resource environments where portability and efficiency are important.

Figure 4 shows the training and validation accuracy of the model after the first 10 training epochs. The training accuracy steadily increased and reached almost 54%, but the validation accuracy had large variations, and did not show a single rising tendency. This instability indicates that the model has started to overfit early, and not being able to generalize to unseen data, probably because of limited feature learning or incorrect model initialization.

The loss curves are shown in Figure 5, which represent the the initial training phase. The loss on the training set obviously decreased as expected, but the loss on the validation set oscillated dramatically, which peaking at over 9 and dropping suddenly across epochs. This instability behavior further indicates overfitting and limited generalization, and pointing to an ineffective initial training setup.

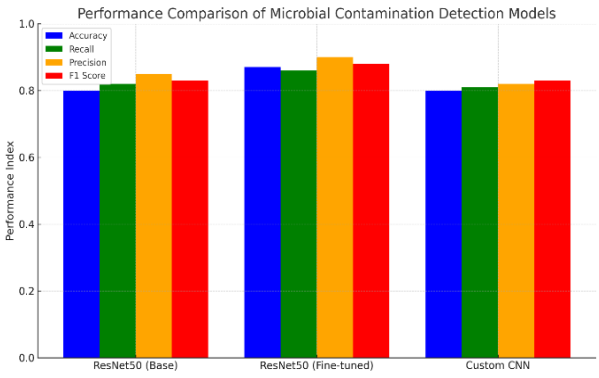


Figure 8. Performance comparison of different models based on classification metrics.

Table 2. Comparison of classification performance for

three models on the validation dataset

Model	Accuracy	Recall	Precision	F1
ResNet50 (Base)	0.80	0.82	0.85	0.83
ResNet50 (Fine-tuned)	0.87	0.86	0.90	0.88
Custom CNN	0.80	0.81	0.82	0.83

The accuracy curves after fine-tuning of the model based on a pretrained CNN backbone are depicted in Figure 6. There is a steady increase in both training and validation accuracy. The training accuracy is over 95%, and the validation accuracy is approximately 91%, which indicate that fine-tuning enabled the model to extract more transferable and discriminative features, thus improving generalization.

The corresponding loss values during the fine-tuning stage are shown in Figure 7. It can be found that the validation loss rapidly decreases over than 14 to below 1 within the first 5 epochs, and then a steady tendency is observed. The training loss remains low throughout. This result confirms that fine-tuning corrected the overfitting observed earlier and leading to more stable and effective learning.

Table 3 shows the model global performance metrics of the fine-tuned which is evaluated on the test dataset of 1,824 samples. The model achieved a high general accuracy of 87%, and most of the predictions occurring across all classes were accurate. The macro-averaged F1 is 0.88, which means that the average performance on the classes is similar when all classes are treated equally without considering their size. In contrast, the weighted average F1 is 0.88 accounts for class imbalance by weighting each class according to its presence in the dataset. The close alignment between these two averages indicates that the model is reasonably robust between dominant and minority classes, and that no single class disproportionately influenced the results. Macro F1 and Weighted F1 are represented by the flowing equations 4 and 5, respectively :

$$Macro\ F1 = \frac{1}{N}\sum_{i=1}^{N} F1_i \tag{4}$$

$$Weighted\ F1 = \sum_{i=1}^{N} \omega_i F1_i,\quad where\ \omega_i = \frac{Support_i}{Toatal\ Samples} \tag{5}$$

Where N represents the number of classes, $F1_i$ is the value of calss i, ω_i is the propotion of class i samples in the dataset.

Table 3. Classification performance metrics for the fine-tuned ResNet50 model across five microbial classes

Classes	Precision	Recall	F1	Support
H1 (Healthy)	0.93	0.91	0.92	881
H2(Bacterial)	0.84	0.80	0.82	467
H3 (Fungal)	0.88	0.84	0.86	164
H5(Mold)	0.89	0.85	0.87	164
H6(Other)	0.93	0.91	0.92	148
Macro Average	0.89	0.86	0.88	1,824
Weighted Avg.	0.90	0.87	0.88	1,824

The confusion matrix of fine-tuned model on the test dataset is presented in Figure 9 which shows the class-wise prediction performance. The diagonal of the matrix shows strong populated, which indicates that most of the samples were classified correctly. The most notable confusion occurred between class H1 and H2, with 55 H1 samples were misclassified as H2 and 60 H2 samples misclassified as H1. Despite this, both classes maintained high F1 due to strong precision and recall. Near perfect accuracy was achieved for classes H5 and H6, demonstrating high separability. These results assure the strong discriminative ability of the model and also align with the high validation accuracy and F1-scores observed during fine-tuning.

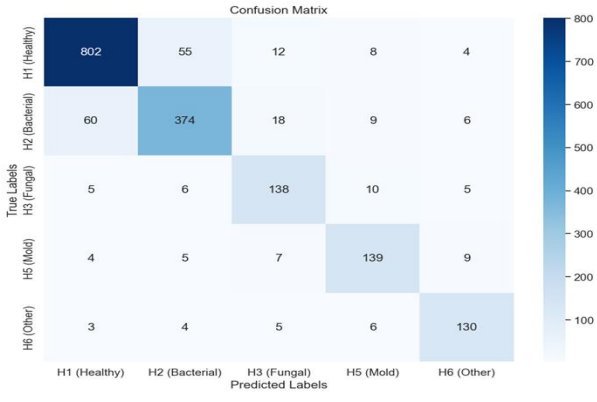


Figure 9. Confusion matrix of the fine-tuned model on the test set.

4.4. Comparison of Precision Across Different Models

To validate the effectiveness of the proposed model for real-time detection of the microbial contamination,

comparative testing with two baseline models was carried out. All model's performances were compared based on precision as the primary metric, because of its relevance to reduce false positives in the context of contamination detection. As listed in Table 4, the fine-tuned ResNet50 based proposed model achieved the best precision of 90% in training on the augmented microbial dataset. This is a demonstrate of model's powerful ability to distinguish the patterns of contamination, which can be attributed to the transfer learning and the augmentation of data during training phase. The CNN based baseline with the frozen ResNet50 backbone and no fine-tuning, achieved a precision of 85%. Although it performed reasonably well, it was not as successful in adapting microbial domain specific features as the fine-tuned model. Finally, the SVM classifier trained on the handcrafted texture and colour features which are extracted from the raw microbial dataset has the lowest precision of 83%, which demonstrates the limitations of traditional feature-based methods for this task. Such results show the benefits of utilizing deep learning with fine-tuning and data augmentation techniques for complex image classification tasks of subtle microbial variations.

Table 4. Precision comparison across models for microbial contamination detection

Model	Approach	Dataset Used	Precision
Proposed system	Fine-tuned ResNet50	Augmented microbial Dataset	90%
CNN (Baseline)	Pretrained ResNet50 (Frozen Layers)	Augmented microbial dataset	85%
SVM	SVM	Raw microbial dataset	83%

5.Conclusion

This paper introduces a powered model for microbial contamination detection, which has been deployed on a low-cost Raspberry Pi4 platform for real-time, on-device inference. Using a fine-tuned ResNet50 based CNN and a well-structured preprocessing pipeline which includes noise filtering, adaptive histogram equalization, and image augmentation, the system resulted in a high classification accuracy of 87%, notably outperforming both a baseline CNN (85%) and a standard SVM classifier (83%). A two-phase training process of feature extraction stage and fine-tuning achieved significant improvements in generalization and stability of the loss. The model achieved a validation accuracy over 91%, with stable loss behavior and minimal overfitting. These results were further supported by a detailed classification report and confusion matrix, which indicated that the system's efficiency in distinguishing between different microbial contamination states. Despite these strengths, the presented study also has limitations. First, the model was trained on only a standardized dataset (PlantVillage) with controlled image capture conditions. Second, the Raspberry Pi 4 that is cost-effective and accessible, introduces computational restrictions that limit the possibility of using complex model and batch processing. These limitations highlight the importance of refinement and additional validation across diverse settings. The proposed method overcomes the limitations of traditional methods on the contamination detection by using deep learning and lightweight edge computing hardware. That providing a scalable, cost-effective, and accurate solution for food safety, healthcare and environmental monitoring. Future work could focus on deploying the system with domain specific datasets to such ones that represent the contamination of real-world microbial on surfaces or food products. This will further validate the capability of the model in practical environments. Furthermore, more powerful edge platforms such as the NVIDIA Jetson Nano or Google Coral can be explored for better computational performance and in order to enable execution of more complex model architectures. To enhance reliability across a variety of conditions, future iterations could also include multi-modal sensor data (thermal, gas, or humidity) with visual analysis. Lastly, incorporating it into a cloud-based Internet of Things (IoT) framework would provide a central monitoring among a network of distributed environments, which making it practical for large scale applications in industry and agriculture. While the Raspberry Pi 4's low cost and widespread availability make it accessible for prototyping, its limited computational power restricts the use of batch processing and complex model architectures.

Author Contributions

The percentages of the author' contributions are presented below. The author reviewed and approved the final version of the manuscript.

	N.B.A.
C	100
D	100
S	100
DCP	100
DAI	100
L	100
W	100
CR	100
SR	100
PM	100
FA	100

C=Concept, D= design, S= supervision, DCP= data collection and/or processing, DAI= data analysis and/or interpretation, L= literature search, W= writing, CR= critical review, SR= submission and revision, PM= project management, FA= funding

acquisition.

Conflict of Interest

The author declared that there is no conflict of interest.

Ethical Consideration

Ethics committee approval was not required for this study because of there was no study on animals or humans.

Data Availability

The PlantVillage dataset used in this study is publicly available on Kaggle at the following URL: https://www.kaggle.com/datasets/tushar5harma/plant-village-dataset-updated

References

Ahmed V, Jouini K, Tuama A, Korbaa O. 2024. Integrating deep and handcrafted features for enhanced remote sensing image classification. IEEE/ACS 21st Int Conf Comput Syst Appl, Sousse, Tunisia, pp: 1-8.

Albahar M. 2023. A survey on deep learning and its impact on agriculture: challenges and opportunities. Agricult, 13: 540.

Alexandra C, Andreea C, Mihaela T, Florin G, Cecilia C. 2023. Tackling the issue of healthcare associated infections through point-of-care devices. TrAC Trends Anal Chem, 161: 116983.

Anyu W, Xiao F, Guangyun H, Ying X, Tian Z, Xi Y. 2023. Recent advances in digital microfluidic chips for food safety analysis: preparation, mechanism and application. Trends Food Sci Technol, 134: 136-148.

Bansal M, Kumar M, Sachdeva M, Mittal A. 2023. Transfer learning for image classification using VGG19: caltech-101 image data set. J Ambient Intell Hum Comput, 14: 3609-3620.

Beznik T, Smyth P, Lannoy G, John A. 2022. Deep learning to detect bacterial colonies for the production of vaccines. Neurocomputing, 470: 427-431.

Deng F, Zhao Z, Wang R, Xiang C, Lv L, Duan Y. 2023. Rapid and online detection of foodborne bacteria via a novel ultraviolet photoionization time-of-flight mass spectrometry. J Agric Food Chem, 71: 10809-10818.

Dhaka V, Meena S, Rani G, Sinwar D, Kavita I, Woźniak M. 2021. A survey of deep convolutional neural networks applied for prediction of plant leaf diseases. Sensors, 21: 4749.

Durgun Y, Durgun M. 2024. Kenar hesaplama tabanlı, mikrodenetleyici entegreli, çok amaçlı ve düşük maliyetli modül geliştirilmesi: bakteriyel koloni sayımı örneği. Iğdır Univ Fen Bil Enst Der, 14: 531-543.

Geetabai S, Soundarya B, Gururaj H, Vinayakumar R. 2024. Classification of various plant leaf disease using pretrained convolutional neural network on imagenet. Open Agric J, 18.

Han Q, Siyuan W, Xinge Xi, Yingchao Z, Ying D, Yanbin Li, Jianhan L, Yuanjie L. 2024. Deep learning enhanced multiplex detection of viable foodborne pathogens in digital microfluidic chip. Biosens Bioelectron, 245: 115837.

Hasan M, Sundberg C, Hasan H, Kostov Y, Ge X, Choa F. 2023. Rapid bacterial detection and identification of bacterial strains using machine learning methods integrated with a portable multichannel fluorometer. IEEE Access, 11: 86112-86121.

Hasan MS, Marsafari M, Tolosa M, Andar A, Ramamurthy SS, Ge X, Kostov Y, Rao G. 2022. Rapid ultrasensitive and high-throughput bioburden detection: microfluidics and instrumentation. Anal Chem, 94: 8683-8692.

Hughes DP, Salathé M. 2015. An open access repository of images on plant health to enable the development of mobile disease diagnostics. arXiv, 1511.08060.

Kim E, Nam S, Hwang T, Lee J, Park J, Shim I, Kye H, Shin Y, Koo J. 2024. IoT-based tryptophan-like fluorescence portable device to monitor the indicators for microbial quality by E. coli and biochemical oxygen demand (BOD5). Water, 16: 3491.

Kumar V, Recupero DR, Riboni D, Helaoui R. 2020. Ensembling classical machine learning and deep learning approaches for morbidity identification from clinical notes. IEEE Access, 9: 7107-7126.

Premkumar S, Sigappi A. 2022. Functional framework for edge-based agricultural system. In: Ajith A, Sujata D, Joel J, editors. Intelligent data-centric systems, AI, edge and IoT-based smart agriculture. Academic Press, pp: 71-100.

Qi W, Zheng L, Wang S, Huang F, Liu Y, Jiang H, Lin J. 2021. A microfluidic biosensor for rapid and automatic detection of Salmonella using metal-organic framework and raspberry pi. Biosens Bioelectron, 178: 0956-5663.

Soundarya B, Poongodi C. 2025. A novel hybrid feature fusion approach using handcrafted features with transfer learning model for enhanced skin cancer classification. Comput Biol Med, 190: 0010-4825.

Sun L, Zhang M, Wang B, Tiwari P. 2023. Few-shot class-incremental learning for medical time series classification. IEEE J Biomed Health Inform, Early Access.

Upadhyay A, Chandel N, Singh K, Chakraborty S, Nandede B, Kumar M, Subeesh A, Upendar K, Salem A, Elbeltagi A. 2025. Deep learning and computer vision in plant disease detection: a comprehensive review of techniques, models, and trends in precision agriculture. Artif Intell Rev, 58: 92.

Xie M, Chen T, Cai Z, Lei B, Dong C. 2024. An all-in-one platform for on-site multiplex foodborne pathogen detection based on channel-digital hybrid microfluidics. Biosensors, 14: 50.

Zhang Y, Jiang H, Ye T, Juhas M. 2021. Deep learning for imaging and detection of microorganisms. Trends Microbiol, 29: 569-572.

Black Sea Journal of Engineering and Science
doi: 10.34248/bsengineering.1695365

Open Access Journal
e-ISSN: 2619 – 8991

Research Article
Volume 8 - Issue 4: 1195-1203 / July 2025

MICROSTRUCTURAL EVOLUTION AND RADON EMISSION DYNAMICS IN CLASS F FLY ASH-BLENDED CEMENT PASTES

Ahmad HOSSEINPOUR SHEIKHRAJAB[1*], Ahmet ERDAL OSMANLIOĞLU[2]

[1]*Istanbul University-Cerrahpaşa, Faculty of Engineering, Department of Mining Engineering, 34500, Istanbul, Türkiye*
[2]*Istanbul University-Cerrahpaşa, Faculty of Engineering, Department of Mining Engineering, 34500, Istanbul, Türkiye*

Abstract: Radon release from cementitious building materials is a major indoor air quality concern due to the presence of naturally occurring radionuclides in raw materials. This study investigates the influence of partially replacing Portland cement with Class F coal fly ash (0–50% by weight) on the pore structure and radon emission of hardened cement pastes. Cement paste specimens with varying fly ash content were analyzed using mercury intrusion porosimetry (MIP) to quantify porosity and pore size distribution, and an open-loop radon concentration setup (using a DURRIDGE RAD7 detector) to measure radon exhalation. The results reveal that increasing fly ash content leads to a pronounced increase in total porosity (from 14.23% at 0% fly ash to 20.22% at 50% replacement) and a corresponding rise in radon concentration (steady-state radon concentrations increasing from 20.8 Bq/m^3 to 32.1 Bq/m^3 for the same range). Microstructural analysis indicates that high fly ash substitution coarsens the pore network – the volume-based median pore diameter expanded from ~102 nm to ~381 nm – while also nearly doubling the internal surface area, reflecting the development of both larger capillary voids and fine pores. These changes suggest enhanced radon transport pathways at higher fly ash levels. The findings underscore a mechanistic link between fly ash-induced pore structure modifications and radon diffusion behavior. High-volume fly ash use, while beneficial for sustainability and reduced clinker usage, can thus inadvertently increase radon release. Therefore, optimizing the replacement ratio is essential to balance sustainability goals with indoor air quality considerations and to minimize potential health risks associated with indoor radon exposure.

Keywords: Radon emission-1, Fly ash-2, Cement paste-3, Microstructure-4, Porosity-5, Sustainability-6

***Corresponding author:** Istanbul University-Cerrahpaşa, Faculty of Engineering, Department of Mining Engineering, 34500, Istanbul, Türkiye
E mail: ahmad.hosseinpour50@gmail.com (Ahmad HOSSEINPOUR SHEIKHRAJAB)
Ahmad HOSSEINPOUR SHEIKHRAJAB https://orcid.org/0009-0001-0132-3026
Ahmet ERDAL OSMANLIOĞLU https://orcid.org/0000-0001-5547-7525

Received: May 08, 2025
Accepted: July 01, 2025
Published: July 15, 2025

Cite as: Hosseinpour Sheikhrajab A, Osmanlıoğlu AE. 2025. microstructural evolution and radon emission dynamics in class F fly ash-blended cement pastes. BSJ Eng Sci, 8(4): 1195-1203.

1. Introduction

Radon is a radioactive noble gas that arises naturally from the decay of uranium and thorium found in the earth's crust, including soils, rocks, and some construction materials. Among its isotopes, Radon-222 (Rn-222) is of particular concern in indoor settings due to its relatively long half-life of 3.8 days and its origin from the decay of radium-226 (Ra-226), which is commonly present in natural materials like fly ash. Being colorless, odorless, and chemically inert, radon can migrate through soil and porous building materials, accumulating in enclosed environments such as basements and poorly ventilated rooms. As a Group 1 carcinogen, radon is the second leading cause of lung cancer after tobacco use, primarily due to its alpha-emitting decay products, such as polonium-218 and lead-214, which can damage lung tissue upon inhalation (EPA, 2023; Field et al., 2007; World Health Organization, 2010). To mitigate associated health risks, international organizations have proposed exposure limits. The World Health Organization (WHO) recommends a reference level of 100 Bq/m^3 for indoor radon, while the U.S. Environmental Protection Agency (EPA) has set an action level of 148 Bq/m^3. These thresholds are critical for assessing indoor air quality and guiding ventilation and material selection practices in buildings. Buildings can become entry points for radon through structural pathways like cracks in foundations, but building materials themselves may also release radon, especially if they contain trace amounts of naturally occurring radioactive materials (NORM)(Righi and Bruzzi, 2006). Portland cement is one such material, and when it is partially replaced with industrial by-products like fly ash—a residue generated from coal-fired power plants—its radiological and structural characteristics can change. Although fly ash is valued for its economic and environmental benefits (Yüksel and Göncüoğlu, 2011), it often contains elevated concentrations of uranium and thorium, leading to concerns about its potential to increase radon concentrations in indoor environments (Blissett, 2012; Mehta and Monteiro, 2014; Osmanlıoğlu, 2019).

Some studies associate the use of fly ash with increased radon release due to its higher radionuclide content. Others highlight a decrease in radon emissions, attributing the reduction to the microstructural changes

This work is licensed (CC BY-NC 4.0) under Creative Commons Attribution 4.0 International License

that fly ash introduces—particularly in pore structure and radon transport behavior (Kumar, Chauhan, and Dahiya, 2010; Osmanlıoğlu, 2021; Zhang and Malhotra, 1996). Given that factors like pore size, porosity, and interconnectivity play a major role in controlling gas transport and retention, the relationship between fly ash content and radon behavior is influenced both by the intrinsic radioactivity of the material and by the microstructural changes it induces.

This research aims to investigate how the partial substitution of Portland cement with fly ash impacts both the porosity and radon emission characteristics of hardened cement pastes. The fly ash used in this study, sourced from the Tunçbilek Thermal Power Plant in Turkey, represents a typical example of lignite-based ash with naturally elevated radioactivity (Hosseinpour, 2025). By preparing cement pastes with six fly ash substitution levels (0%, 5%, 10%, 15%, 30%, and 50%) and analyzing them through mercury intrusion porosimetry and open-loop radon measurements using the DURRIDGE RAD7 system, the study aims to clarify the relationship between pore structure development and radon release.

Ultimately, this study contributes to a better understanding of how fly ash can be strategically utilized in cementitious systems to enhance sustainability while identifying its potential radiological implications. Since fly ash modifies both the radionuclide content and the pore structure of hardened pastes, the level of substitution must be carefully optimized. Higher replacement ratios may increase radon emission due to both enhanced radium content and greater pore connectivity, potentially raising indoor exposure risks. These findings underscore the need to balance environmental benefits with public health considerations in sustainable construction.

2. Materials and Methods

2.1. Study Objective and Experimental Scope

This research focuses on assessing the influence of replacing Portland cement with fly ash on the porosity, pore structure, and radon emission characteristics of cement pastes. To this end, a detailed experimental procedure was followed, encompassing raw material analysis, preparation of samples with varying levels of fly ash, porosity characterization using mercury intrusion porosimetry, and radon concentration testing through an open-loop setup utilizing a RAD7 radon detector.

2.2. Materials Used

2.2.1. Portland cement

The cement employed in this study was Portland cement (CEM I 42.5 R), supplied by Akçansa Cement Factory. Essential physicochemical properties such as specific gravity, Blaine fineness, and radionuclide content (including uranium and thorium concentrations) were determined and presented in Table 1.

2.2.2. Reference sand

The fine aggregate used was CEN standard reference sand, obtained from Limak Trakya Cement Factory. It is composed of high-purity, rounded silica particles. The aggregate's physical characteristics and radiological content are summarized in Table 2.

2.2.3. Fly ash

Class F fly ash, in compliance with ASTM C618, was sourced from the Tunçbilek Thermal Power Plant (Hosseinpour and Osmanlıoğlu, 2024). This byproduct of coal combustion was analyzed for fineness, oxide composition, and radioactive element concentration. The corresponding results are provided in Table 3.

Table 1. Cement properties

Parameter	Value	Unit	Test Method	Standard Reference
Uranium (U) Concentration	3	ppm	IHM (in-house method)	N/A (lab internal method)
Thorium (Th) Concentration	1.79	ppm	In-house (IHM) procedure for Th content	N/A (lab internal method)
Specific Gravity	2.69	–	Displacement (Le Chatelier flask method)	TS EN 196-6:2020
Grain Density	3.10	g/cm^3	Gas pycnometry	ASTM C604 (Helium pycnometer)
Fineness (90 µm sieve residue)	20	%	Dry sieving (90µm mesh)	TS EN 196-6:2020

Table 2. Sand properties

Parameter	Value	Unit	Test Method	Standard Reference
Uranium (U)	0.53	ppm	IHM (in-house method)	N/A* (lab internal method)
Thorium (Th)	2.40	ppm	IHM (in-house method)	N/A (lab internal method)
Specific Gravity	2.29	g/cm^3	Pycnometric Density (Pulp)	N/A (lab internal method)

*N/A= Not applicable.

Table 3. Fly ash properties

Parameter	Value	Unit	Test Method	Standard Reference
Uranium (U)	8.37	ppm	IHM (in-house method)	N/A (lab internal method)
Thorium (Th)	29.06	ppm	IHM (in-house method)	N/A (lab internal method)
Specific Gravity	2.20	g/cm^3	Pycnometric Density (Pulp)	N/A (lab internal method)
Fineness (45 µm residue)	19	%	Wet sieving	EN 450-1
Silicon Dioxide (SiO_2)	54.79	% (w/w)	TS EN 15309:2007	EN 15309
Aluminum Oxide (Al_2O_3)	18.58	% (w/w)	TS EN 15309:2007	EN 15309
Iron Oxide (Fe_2O_3)	8.90	% (w/w)	TS EN 15309:2007	EN 15309
Calcium Oxide (CaO)	2.81	% (w/w)	TS EN 15309:2007	EN 15309

2.3. Sample preparation and testing protocols

Cement paste specimens were prepared in line with TS EN 196-1 specifications. Different mix designs were developed by partially substituting Portland cement with fly ash at 0%, 5%, 10%, 15%, 30%, and 50% by mass. All mixes maintained a constant binder-to-sand ratio of 1:3 and a fixed water-to-binder (w/b) ratio (0.5) to ensure consistency in workability and hydration conditions.

For porosity measurements, six prismatic specimens measuring 160 × 40 × 40 mm were cast and cured for 28 days prior to testing. Additionally, six cylindrical specimens with dimensions of 48 mm in diameter and 51 mm in height were prepared for radon emission analysis. Three separate raw material samples were also fabricated to assess radon concentrations. The classification, mixture proportions, and dimensions of all specimens are summarized in Table 4, while their physical appearance is presented in Figure 1. In total, fifteen samples were tested, encompassing the control mix, fly ash-modified cement pastes, and individual raw material references.

Table 4. Nomenclature of produced samples, mixture ratios, and sizes

Sample Name	% Cement + %Fly ash (% by weight) (gr)	Sand (gr)	Water (gr)	Sample Size (mm)
FL0	% 100 Cement (150 gr) + % 0 Fly ash	450	75	40x40x160
FL5	% 95 Cement (142.5 gr) + % 5 Fly ash (7.5 gr)	450	75	40x40x160
FL10	% 90 Cement (140 gr) + % 10 Fly ash (10 gr)	450	75	40x40x160
FL15	% 85 Cement (127.5 gr) + % 15 Fly ash (22.5 gr)	450	75	40x40x160
FL30	% 70 Cement (105 gr) + % 30 Fly ash (45 gr)	450	75	40x40x160
FL50	% 50 Cement (75 gr) + % 50 Fly ash (75 gr)	450	75	40x40x160
CL0	% 100 Cement (44.5 gr) + % 0 Fly ash	133.3	22.22	*R=48mm H=51mm
CL5	% 95 Cement (42.28gr) + % 5 Fly ash (2.22 gr)	133.3	22.22	R=48mm H=51mm
CL10	% 90 Cement (40.5 gr) + % 10 Fly ash (4.45 gr)	133.3	22.22	R=48mm H=51mm
CL15	% 85 Cement (37.83 gr) + % 15 Fly ash (6.67 gr)	133.3	22.22	R=48mm H=51mm
CL30	% 70 Cement (31.15 gr) + % 30 Fly ash (13.35 gr)	133.3	22.22	R=48mm H=51mm
CL50	% 50 Cement (22.5 gr) + % 50 Fly ash (22.5 gr)	133.3	22.22	R=48mm H=51mm
P1	Cement (180 gr) + Fly ash (0 gr)	0	0	Powder
P2	Cement (0 gr) + Fly ash (180gr)	0	0	Powder
P3	Cement (0 gr) + Fly ash (0 gr)	133.33	0	Aggregate

*R= Cylinder diameter. H= Cylinder height.



Figure 1. Physical appearance of the control, fly ash-modified cement pastes, and raw material specimens.

Porosity characterization was carried out using a Micromeritics AutoPore IV mercury intrusion porosimeter. This method involves the application of pressurized mercury to quantify pore volume and distribution, following the Washburn equation and Laplace's law (Diamond, 2000). The device measured pore diameters ranging from approximately 3.6 nm to 1000 µm. Parameters obtained included total pore volume (mL/g), surface area (m^2/g), volume- and area-based median pore diameters, average pore diameter (4V/A), bulk density, skeletal density, and total porosity percentage.

Prior to analysis, cement paste specimens were oven-dried at 50 °C for 48 hours in order to preserve their pore structures. Once dried, the samples were crushed into fragments smaller than 4 mm, suitable for mercury intrusion porosimetry (MIP). The tests were performed using a penetrometer with a stem volume of 1.1310 mL and a total penetrometer volume of 6.6790 mL. Mercury intrusion was conducted within a pressure range from 0.52 psia (filling pressure) to 4.45 psia (maximum applied pressure), enabling the assessment of pore diameters ranging from approximately 100 µm down to 3 nm. The porosity test is shown in Figure 2.

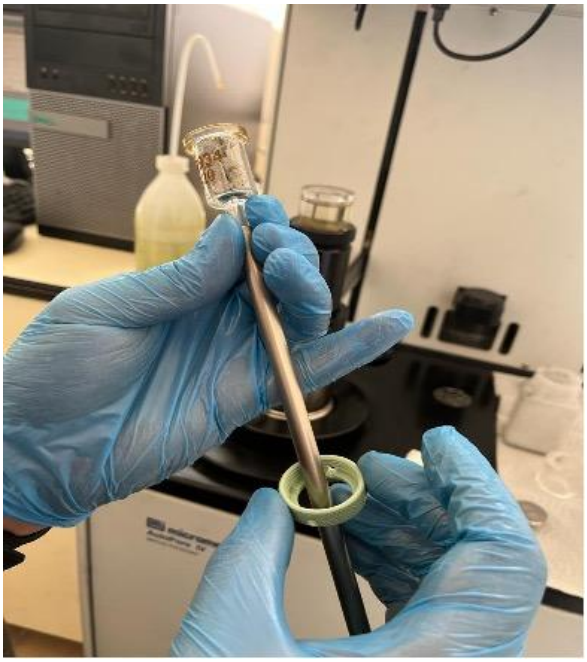


Figure 2. The porosity test.

Radon emission testing was conducted using a DURRIDGE RAD7 detector configured in an open-loop system. Each cylindrical hardened specimen was placed inside an airtight chamber equipped with two valves—one connected to the RAD7 inlet to draw air continuously and the other left open to allow ambient air to enter (Figure 3). Operating in Sniff Mode, the RAD7 —an active and continuous radon monitoring device—recorded radon levels at five-minute intervals over periods ranging from 1.7 to more than 3 days, producing between 500 and 999 data points per sample. This setup enabled consistent internal air circulation and facilitated accurate tracking of radon release over time. The continuous five-minute interval recordings allowed for the observation of temporal emission patterns, including the initial accumulation phase and the eventual stabilization behavior. The background radon concentration in the laboratory, measured at 19 Bq/m^3, was used as a reference for comparison. Each radon emission test was conducted in triplicate under identical environmental conditions. The mean values and corresponding standard deviations were calculated and presented in Table 6 to indicate measurement consistency and data reliability.



Figure 3. Open loop radon concentration test.

The same experimental setup was employed to assess radon emissions from individual raw materials—cement, fly ash, and aggregate. These were placed in identical sealed containers with dual valves, as depicted in Figure 1, and analyzed using the same open-loop protocol. Figure 3 displays open loop radon concentration test.

The time-based measurements showed that radon levels increased during the first hours and eventually stabilized,

indicating that emission reaches a near-steady state under open-loop conditions. This behavior aligns with prior studies and supports the reliability of the measurement technique.

3. Results

3.1. Porosity and pore structure results

The mercury intrusion porosimetry (MIP) analyses showed a consistent increase in total porosity, pore volume, and internal surface area with higher levels of fly ash substitution in the cement pastes. According to the results (Table 5), porosity rose from 14.23% in the reference mix (0% fly ash) to 20.22% at the 50% substitution level. Similarly, the total pore volume increased from 0.0664 to 0.1005 mL/g. A notable rise in total pore surface area was also recorded, from 5.825 m^2/g to 10.481 m^2/g, nearly doubling across the substitution range.

Moreover, the distribution of pore sizes shifted significantly. The volume-based median pore diameter increased from 102.3 nm to 380.7 nm, indicating a growing fraction of larger capillary pores. In contrast, the area-based median pore diameter dropped from 14.7 nm to 5.4 nm.

Table 5. The mercury intrusion porosimetry (MIP) analyses results

Sample Name	Total Intrusion Volume (mL/g)	Total Pore Area (m^2/g)	Median Pore Diameter (nm, Volume)	Median Pore Diameter (Area) (nm)	Average Pore Diameter (4V/A) (nm)	Porosity (%)	Stem Volume Used (%)
FL0	0.0664	5.825	102.3	14.7	45.6	14.23	39
FL5	0.0679	7.019	101.0	8	38.7	14.50	38
FL10	0.0809	8.610	95.8	8.9	37.6	16.75	48
FL15	0.0854	8.984	188.4	6.6	38	17.62	48
FL30	0.0905	10.559	243.3	5.9	34.3	18.50	50
FL50	0.1005	10.481	380.7	5.4	38.4	20.22	53

3.2. Radon emission behavior (open-loop)

Open-loop radon testing conducted using the RAD7 system over extended periods (up to 72 hours) revealed a steady increase in radon concentrations as fly ash content increased. The average radon level measured for the 0% fly ash sample was 20.8 Bq/m^3. This value increased consistently with increasing substitution, reaching 32.7 Bq/m^3 in the 50% fly ash sample. The background radon concentration measured in the laboratory environment was 19 Bq/m^3, which is considered typical for well-ventilated indoor air and was used as the baseline reference in this study. Radon emission from raw fly ash reached 26.7 Bq/m^3. Although both values remain below international guidelines (WHO: 100 Bq/m^3; EPA: 148 Bq/m^3), the increase of approximately 8 Bq/m^3 (~42%) is scientifically meaningful. This difference is statistically supported by repeated measurements and associated standard deviations, which confirm that the rise is not attributable to random variability. It is also important to note that indoor radon levels can vary geographically depending on local geology, particularly uranium and radium content in soil and rocks (Papastefanou, 2009). However, in this work, the test conditions were controlled, and measurements were designed to isolate emissions from the material itself rather than environmental background. Thus, the observed increase in radon emission is primarily attributed to the material composition and microstructure.

Open-loop test results for radon concentration levels from cement pastes with varying fly ash substitution are presented in Table 6, while the corresponding radon concentration graph— including the laboratory background level obtained from the RAD7 open-loop testing—is shown in Figure 4.

Table 6. Open-loop test results for radon concentration levels from cement pastes with fly ash substitution and raw materials

Sample Code	Fly Ash (%)	Average Radon Concentration (Bq/m^3)	Standard Deviation (±)
FL0	0	20.8	±1.1
FL5	5	23.1	±1.2
FL10	10	24.8	±1.3
FL15	15	26.3	±1.2
FL30	30	29.2	±1.5
FL50	50	32.1	±1.6
P1	0	21.2	±1.3
P2	100	26.7	±1.1
P3	0	25.2	±1.2
Room Air	—	19.0	±1.1

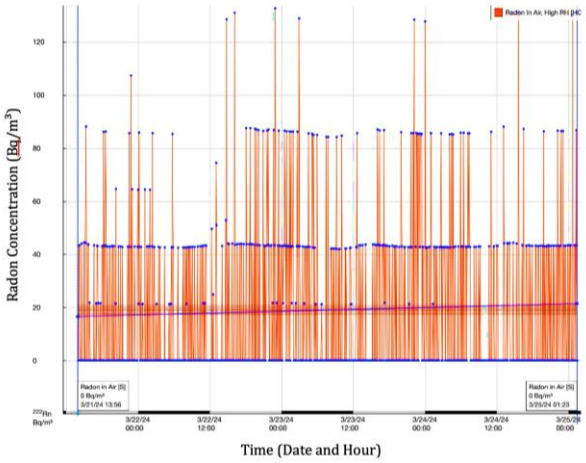


Figure 4. Graph of radon concentration in laboratory air measured with RAD7 under open-loop conditions.

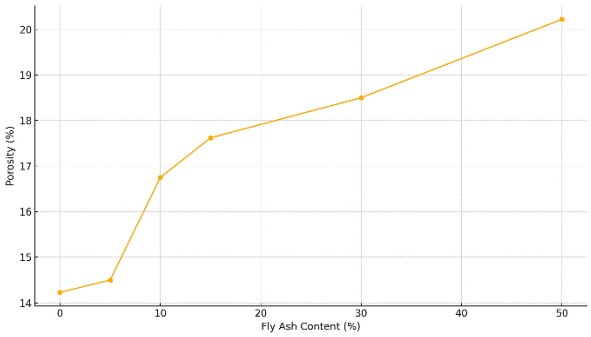


Figure 5. Porosity of cement pastes at different fly ash replacement ratios.

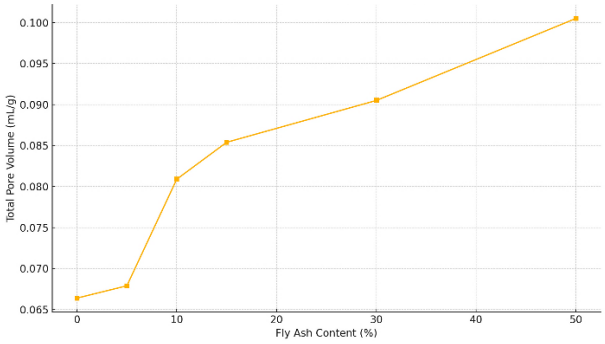


Figure 6. Total pore volume variation with increasing fly ash content.

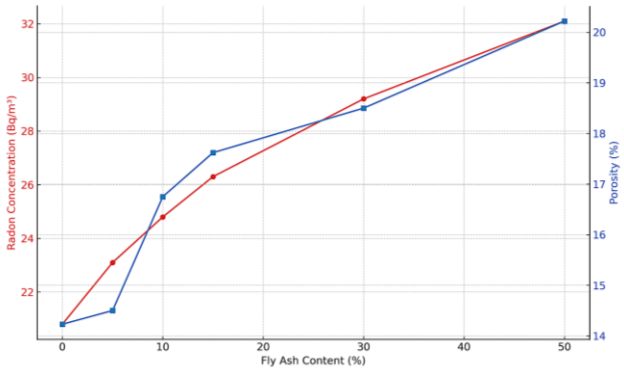


Figure 7. Effect of fly ash content on radon concentration (left axis) and porosity (right axis) after 28 days of curing.

4. Discussion

The experimental results demonstrate a consistent trend of increasing radon emission with higher levels of fly ash substitution in cement pastes, which is closely linked to alterations in the material's pore structure. Mercury intrusion porosimetry (MIP) revealed a rise in total porosity from 14.23% in the control mix to 20.22% at 50% fly ash. As shown in Figure 5, total porosity increases progressively with fly ash addition, reinforcing the structural weakening observed at higher substitution levels. This ~42% increase is attributed to the dilution and filler effects of fly ash, which reduce the quantity of cement clinker available for hydration (Hosseinpour and Osmanlıoğlu, 2024a). Consequently, the matrix at higher replacement levels contains more unhydrated or partially hydrated regions, resulting in more extensive capillary voids. The total pore volume increased from 0.0664 to 0.1005 mL/g, while internal surface area nearly doubled—from 5.825 to 10.481 m^2/g—indicating significant microstructural change. Figure 6 demonstrates the increase in total pore volume with fly ash content, supporting the development of a more open and interconnected pore network.

This shift also led to the formation of a bimodal pore structure. The volume-based median pore diameter expanded from ~102 nm to ~381 nm, reflecting an increase in large, percolating capillary pores. Meanwhile, the area-based median pore diameter decreased from ~14.7 nm to ~5.4 nm, indicating the presence of finer gel pores. The growth in large capillaries is linked to the inability of early-stage hydration to fill the original water-filled voids, while the finer pores are likely produced by ongoing secondary pozzolanic reactions. However, at 28 days—the testing age used in this study—Class F fly ash's pozzolanic reactivity remains limited (Mehta and Monteiro, 2014; Scrivener and Nonat, 2011). Therefore, the microstructure remains dominated by interconnected voids rather than refined gels (Diamond, 2000).

Radon concentration data collected using an open-loop RAD7 system showed a strong correlation with these structural changes. Concentrations increased from 20.8

Bq/m^3 at 0% fly ash to 32.1 Bq/m^3 at 50%. The inclusion of standard deviations for each measurement demonstrates that the observed trend is statistically consistent and experimentally reliable. Figure 7 illustrates the simultaneous increase in radon concentration and porosity with rising fly ash content.

This rise stems from two primary mechanisms. First, the increased radioactive source term due to fly ash's elevated radium-226 (Ra-226) content which is the immediate parent nuclide of radon-222 (Rn-222). As Ra-226 undergoes alpha decay, it generates Rn-222, a noble gas that can migrate through pore spaces and be exhaled into the surrounding air. Although direct Ra-226 measurements were not performed in this study, its presence is inferred from the uranium content, given their position in the decay chain. Second, the enhanced radon transport efficiency resulting from a more open and interconnected pore network (Osmanlıoğlu, 2019). In denser matrices, radon atoms often decay within the solid before escaping, whereas larger and more connected pores offer lower resistance to radon movement, enabling greater exhalation before decay.

Fly ash particles themselves also influence radon release. Their spherical morphology includes porous and hollow structures (e.g., cenospheres), which may either retain or emit radon depending on their pore connectivity. The near-linear increase in radon concentration with increasing fly ash substitution indicates that the added radium content was effectively mobilized due to the microstructure's increased permeability. In the open-loop test setup, this dynamic was clearly captured, as radon was continually measured in real-time, and its steady increase paralleled the structural evolution of the paste.

The findings help clarify the mixed conclusions found in the literature. Some studies have observed that fly ash can reduce radon emission when it contributes to a denser matrix or when the ash itself has a low radon emanation coefficient (Kumar et al., 2010; Taylor-Lange, Stegemann, and Weiss, 2014). For instance, pastes containing up to 60% fly ash showed lower emissions in some cases due to limited emanation or tighter microstructure. Taylor-Lange et al. noted that fly ashes with low radon emanation fractions (~1–2.5%) might even suppress radon output. However, these effects are contingent upon the ash's properties, replacement level, and degree of hydration.

In contrast, other studies—particularly those using high-radionuclide fly ash—report increased radon release. Osmanlıoğlu (2021) found that using lignite-based Class F fly ash led to elevated radon emission, especially at higher substitution levels. Our study supports this trend. Despite the theoretical potential for radon retention in dense systems or in certain fly ash types, the real-world microstructure induced by 30–50% fly ash replacement tends to favor diffusion and emission. The added fly ash increased the supply of radium-226 while simultaneously opening up the network for radon escape. Thus, the increase in both source and transport efficiency explains the consistent rise in radon emission. This correlation is clearly captured in Figure 7, which combines both radon concentration and porosity data, highlighting the microstructural role in facilitating radon diffusion through the hardened matrix.

It is important to consider the role of curing time. Pozzolanic activity can refine the microstructure over long durations, reducing capillary porosity and potentially radon transport pathways. However, most practical applications use cementitious materials within 28 to 56 days, limiting the timeframe for such refinement. At these ages, the microstructure is still evolving, and the fly ash-induced porosity remains relatively high. Our data suggest that while modest additions (5–15%) result in limited increases in porosity and radon release, higher levels (≥30%) lead to pronounced structural coarsening and a significant rise in radon exhalation.

This dual effect poses a challenge for sustainable construction. Fly ash is widely promoted for its environmental benefits—it reduces clinker demand, lowers CO_2 emissions, enhances workability, and minimizes thermal cracking. From a materials management perspective, its use also addresses waste recycling. However, increasing fly ash beyond moderate levels can compromise indoor air quality by increasing radon concentrations —a recognized health risk and the second leading cause of lung cancer in non-smokers (Field et al., 2007; World Health Organization, 2010).

While the radon levels measured in our test environment (20–32 Bq/m^3) fall within acceptable indoor limits, their relative increase of ~50% in fly ash-rich pastes cannot be ignored. In a real building, this could contribute to a cumulative elevation in indoor radon, particularly in spaces with limited ventilation or poor sealing. Surface area exposure, air circulation, and underlying soil gas pressure also influence how much material-derived radon contributes to indoor air concentrations. Therefore, even moderate material emissions can become significant when scaled to full interior volumes.

To mitigate these risks, a combination of strategies should be considered. Limiting fly ash substitution to below ~30% may provide a good compromise between sustainability and health safety. When higher replacements are necessary—due to cost, availability, or performance goals—complementary measures such as surface sealants, radon-absorptive additives, or improved ventilation systems should be implemented. Additionally, blending fly ash with other supplementary cementitious materials (e.g., silica fume) may help refine the pore network and counteract the radon-enhancing effects.

Finally, it may be appropriate for construction standards and material certifications to include radiological performance benchmarks. Regulations could require maximum allowable Ra-226 content or set limits on radon exhalation rates, especially for materials used in

indoor applications. A mechanistic understanding—linking composition, hydration, and pore evolution—is key to predicting and controlling radon behavior. This study demonstrates that effective material design must account for both the radioactive source potential and the structural pathways that govern emission.

In conclusion, while coal fly ash contributes significantly to sustainable construction practices, its influence on microstructure and radon emission requires careful evaluation. By considering both short-term curing effects and long-term performance implications, engineers can make informed decisions about substitution levels and mitigation approaches. Balancing environmental goals with public health protection is not only possible—it is essential for responsible material innovation in the built environment.

5. Conclusion

This study presents a comprehensive assessment of how Class F fly ash influences radon emission and microstructural properties in cement pastes, emphasizing microstructural changes. By substituting Portland cement with Class F fly ash at 0–50% levels and utilizing mercury intrusion porosimetry and open-loop radon testing, a direct link was identified between pore evolution and radon release behavior.

Key findings reveal that increasing fly ash content leads to elevated porosity and notable changes in pore size distribution. At 50% substitution, porosity rose to 20.22% from 14.23% in the control, and internal surface area nearly doubled, indicating a more open and connected pore network. These structural shifts significantly influence radon exhalation: average radon concentrations, rising from 20.8 Bq/m^3 in the control mix to 32.1 Bq/m^3 at 50% replacement. Intermediate substitutions (5–30%) showed a stepwise increase, demonstrating a strong correlation between fly ash dosage and radon emission.

The rise in radon release is attributed to two interrelated mechanisms. First, Class F fly ash inherently contains more radionuclides, including radium-226, than Portland cement. Second, higher substitution levels produce less dense matrices, enhancing radon diffusion through the pore network. While pozzolanic reactions may eventually refine the structure, at 28 days these effects remain limited, and the increased permeability dominates the behavior. Consequently, any potential radon retention offered by secondary gels is insufficient to counteract the openness of the network.

These results help identify optimal substitution thresholds. Fly ash levels of 15–25% appear acceptable, causing only modest porosity increases and a manageable radon rise (~5 Bq/m^3 at 20%). If sufficient curing occurs, these systems may densify further. However, beyond 30%, the microstructure becomes significantly more porous, and radon emissions rise markedly—up to 50% above the control at 50% substitution. Such levels can be problematic when scaled to full buildings. Thus, fly ash content around 25–30% may mark a practical limit, beyond which careful justification and mitigation are needed. It should be noted that the observed increase in radon emission may be influenced by the specific characteristics of the fly ash used in this study, which was sourced from the Tunçbilek thermal power plant. Therefore, the findings may not be directly generalizable to fly ash from other sources with different radionuclide content.

In conclusion, using coal fly ash in cement paste supports sustainability goals but must be balanced against indoor environmental risks. Fly ash enhances workability, reduces clinker use, and lowers emissions, but high contents increase radon exhalation. A strategic approach is recommended: moderate substitution levels, extended curing, and microstructural control. Future research should explore long-term densification, combinations with other SCMs, and source-specific behavior. Additionally, strategies like surface coatings or radon-absorptive admixtures should be considered. Regulatory frameworks might also integrate radon performance benchmarks to ensure recycled materials do not compromise occupant safety. Ultimately, balanced strategy involving moderate substitution, extended curing, and microstructural control is recommended.

Author Contributions

The percentages of the authors' contributions are presented below. All authors reviewed and approved the final version of the manuscript.

	A.H.S.	A.E.O.
C	60	40
D	55	45
S	50	50
DCP	60	40
DAI	50	50
L	55	45
W	65	35
CR	50	50
SR	70	30
PM	50	50
FA	50	50

C=Concept, D= design, S= supervision, DCP= data collection and/or processing, DAI= data analysis and/or interpretation, L= literature search, W= writing, CR= critical review, SR= submission and revision, PM= project management, FA= funding acquisition.

Conflict of Interest

The authors declared that there is no conflict of interest.

Ethical Consideration

Ethics committee approval was not required for this study because of there was no study on animals or humans.

Acknowledgements

This study is derived from the author's doctoral dissertation and forms part of the PhD research conducted within the Department of Mining Engineering, Faculty of Engineering, Istanbul University–Cerrahpaşa. The author sincerely thanks his thesis advisor, Prof. Dr. Ahmet Erdal Osmanlıoğlu, for his scientific contributions, guidance, and unwavering support.

References

Blissett RS. 2012. A review of the multi-component utilization of coal fly ash. Fuel, 97: 1-23.

Diamond S. 2000. Mercury porosimetry: Porosity or artifact? Cem Concr Res, 30: 1517-1525.

EPA. 2023. Health risks of radon. United States Environmental Protection Agency. URL: https://www.epa.gov/radon/health-risk-radon (accessed date: April 8, 2025)

Field RW, Krewski D, Lubin JH, Zielinski JM, Alavanja M, Catalan VS, Klotz JB. 2007. An overview of the North American residential radon and lung cancer case–control studies. J Toxicol Environ Health A, 70: 1882-1889.

Hosseinpour Sheikhrajab A, Osmanlıoğlu AE. 2024. Comparison of radioactivity concentration levels of coal and lignite used in major thermal power plants in Turkey. In: Proceedings of the 10th International Artemis Scientific Research Congress, April, Romania, pp:59-96.

Hosseinpour Sheikhrajab A, Osmanlıoğlu AE. 2024a. The effect of Tunçbilek Thermal Power Plant waste fly ash on mechanical properties of Portland cement. Nat Appl Sci J, 7: 40.

Hosseinpour Sheikhrajab A. 2025. Determination of radon emission in cements made with coal fly ash. PhD thesis, Istanbul-Cerrahpaşa University, Institute of Engineering, Istanbul, Türkiye, pp: 115-175.

Kumar A, Chauhan RP, Dahiya N. 2010. Radon exhalation rate in fly ash and fly ash blended cement. Radiat Meas, 45: 223–226.

Mehta PK, Monteiro PJM. 2014. Concrete: Microstructure, properties, and materials. McGraw-Hill Education, New York, USA, pp: 646.

Osmanlıoğlu AE. 2019. Natural radioactivity in Turkish coal-fired power plant ashes. J Environ Radioact, 208-209: 106021.

Osmanlıoğlu AE. 2021. Evaluation of radiological risks from coal combustion residues used in building materials. Constr Build Mater, 270: 121473.

Papastefanou C. 2009. Radon in ambient air and soil gas in the vicinity of uranium mining and milling facilities. J Environ Radioact, 100: 385-392.

Righi S, Bruzzi L. 2006. Natural radioactivity and radon exhalation in building materials used in Italian dwellings. J Environ Radioact, 88: 158-170.

Scrivener KL, Nonat A. 2011. The chemistry of cement hydration. Cem Concr Res, 41: 651-665.

Taylor-Lange SC, Stegemann JA, Weiss WJ. 2014. Assessing the transport properties and radon emanation of concrete containing fly ash for radioactive waste encapsulation. Cem Concr Compos, 53: 103-113.

World Health Organization. 2010. WHO handbook on indoor radon: A public health perspective. WHO Press. URL: https://apps.who.int/iris/handle/10665/77945 (accessed date: March 10, 2025)

Yüksel İ, Göncüoğlu MC. 2011. Utilization of high volumes of Turkish fly ashes to produce sustainable construction materials. Constr Build Mater, 25: 1610-1618.

Zhang MH, Malhotra VM. 1996. High-performance concrete incorporating rice husk ash as a supplementary cementing material. ACI Mater J, 93: 629-636.

Black Sea Journal of Engineering and Science
doi: 10.34248/bsengineering.1703020

Open Access Journal
e-ISSN: 2619 – 8991

Araştırma Makalesi (Research Article)
Cilt 8 - Sayı 4: 1204-1211 / Temmuz 2025
(Volume 8 - Issue 4: 1204-1211 /July 2025)

ANKARA İLİ HAVA KALİTESİ İZLEME İSTASYONLARINDAN ELDE EDİLEN $PM_{2.5}$ ÖLÇÜMLERİNDEKİ DEĞİŞİMİN EWMA KARTLARI KULLANILARAK İNCELENMESİ

Esra POLAT[1]*, Burak CİBA[1], Rahime POLAT[2]

[1]*Hacettepe University, Faculty of Science, Department of Statistics, 06800, Ankara, Türkiye*
[2]*Ankara University, Institute of Social Sciences, Environmental Social Sciences, PhD Candidate, Ankara, Türkiye*

Özet: Sanayileşmenin hız kazanması, nüfusun çoğalması, kentleşmenin yaygınlaşması ve fosil yakıt kullanımının artması, atmosferde kirlenmeye neden olarak insan sağlığını tehdit eden hava kirliliğini ortaya çıkarmaktadır. Son dönemde yapılan bilimsel araştırmalar, kalp ve damar hastalıklarının özellikle $PM_{2.5}$ olarak bilinen ince partikül madde kirliliğiyle doğrudan ilişkili olduğunu açıkça ortaya koymuştur. Bu çalışmanın amacı, Türkiye'nin Ankara ili sınırları içerisinde yer alan altı istasyonda (Çankaya, Etimesgut, Keçiören Sanatoryum, Ostim, Törekent, Yaşamkent) $PM_{2.5}$ konsantrasyonlarının son dönemlerdeki durumunu ve değişimini inceleyerek, kontrol edilemeyen değişikliklerin ve istasyonlar arası farklılıkların olup olmadığını araştırmaktır. Bu amaçla, öncelikle 01.01.2024 ve 31.03.2025 tarihleri arasındaki dönem için $PM_{2.5}$ konsantrasyonlarının değişimi, betimleyici istatistikler ve grafikler ile incelenmiş ve ardından Kasım 2024 ve Mart 2025 arası 5 ay için süreç ortalaması EWMA kontrol kartları ile izlenmiştir. Elde edilen sonuçlar, Ankara ilindeki 6 hava kalitesi izleme istasyonundan alınan günlük $PM_{2.5}$ konsantrasyon düzeylerindeki değişiklikleri EWMA kontrol kartlarının hızlı bir şekilde tespit etme potansiyeline sahip olduğunu ortaya koymaktadır. EWMA kartı, her bir izleme istasyonu için 2025 yılı kış aylarında $PM_{2.5}$ konsantrasyonlarında keskin bir artış sinyalini açık biçimde göstermektedir.

Anahtar kelimeler: Hava kirliliği, $PM_{2.5}$, Süreç ortalaması, EWMA kartları, Ankara

Investigation of Changes in $PM_{2.5}$ Measurements Obtained From Air Quality Monitoring Stations in Ankara Province Using EWMA Charts

Abstract: Acceleration of industrialization, population growth, widespread urbanization and increased use of fossil fuels cause pollution in the atmosphere, creating air pollution that threatens human health. Recent scientific studies have clearly shown that cardiovascular diseases are directly related to fine particulate matter pollution, especially known as $PM_{2.5}$. The aim of our study is to investigate the recent nature and changes of $PM_{2.5}$ concentrations in six stations of Ankara Province in Türkiye (Çankaya, Etimesgut, Keçiören Sanatoryum, Ostim, Törekent, Yaşamkent) to investigate if there are uncontrollable changes and differences between stations. For this purpose, firstly, the change in $PM_{2.5}$ concentrations for the period between 01.01.2024 and 31.03.2025 was examined with descriptive statistics and graphs, and then the process mean was monitored with EWMA control charts for 5 months between November 2024 and March 2025. The results obtained reveal that EWMA control charts have the potential to rapidly detect changes in daily $PM_{2.5}$ concentration levels taken from 6 air quality monitoring stations in Ankara province. The EWMA chart clearly shows a sharp increase signal in $PM_{2.5}$ concentrations, in the winter months of 2025, for each monitoring station.

Keywords: Air pollution, $PM_{2.5}$, Process mean, EWMA charts, Ankara

***Sorumlu yazar (Corresponding author):** Hacettepe University, Faculty of Science, Department of Statistics, 06800, Ankara, Türkiye
E mail: espolat@hacettepe.edu.tr (E. POLAT)
Esra POLAT https://orcid.org/0000-0001-9271-485X
Burak CİBA https://orcid.org/0009-0007-0276-7351
Rahime POLAT https://orcid.org/0000-0002-0677-1979

Gönderi: 20 Mayıs 2025 **Kabul:** 02 Temmuz 2025 **Yayınlanma:** 15 Temmuz 2025
Received: May 20, 2025 **Accepted:** Temmuz 02,, 2025 **Published:** July 15, 2025
Cite as: Polat E, Ciba B, Polat R. 2025. Investigation of changes in PM2.5 measurements obtained from air quality monitoring stations in Ankara province using EWMA charts. BSJ Eng Sci, 8(4): 1204-1211.

1. Giriş

Çevre ve İnsan sağlığı üzerinde zararlı etkileri olan Partikül Madde (PM), havada katı veya sıvı halde bulunan partikül maddeyi ifade eder. Küf, polen, toz gibi çapı 10 mikron ve daha küçük olan partikül madde, PM_{10} olarak adlandırılır. Yakıtların yanmasıyla ortaya çıkan parçacıklar, organik bileşikler gibi 2,5 mikron ve daha küçük partiküller ise $PM_{2.5}$ olarak adlandırılır (Utku ve Can, 2024). Kalp-damar ve solunum yolu hastalıklarına neden olabilen $PM_{2.5}$ ve PM_{10} konsantrasyonlarının düzenli olarak izlenmesi ve hava kirliliğinin kontrol altına alınması çevre ve insan sağlığı açısından önemlidir. $PM_{2.5}$ parçacıkları, insan saç telinin yaklaşık yüzde 3'ü kadar inceliğe sahiptir ve yalnızca elektron mikroskobu kullanılarak tespit edilebilir. Araştırmacılar, ince partiküllerin kan damarlarında birikebileceğini, kalp ile çevresindeki damarlarda iltihap oluşumuna neden olabileceğini düşünmektedirler. $PM_{2.5}$ türü ince parçacıklar farklı kaynaklardan ortaya çıkabilir. Bu kaynaklar arasında fabrikalar, enerji santralleri, uçakların yakıt artıkları ve motorlu taşıtlar, evlerde kömür ve odun kullanımı vb. yer alır. $PM_{2.5}$ doğal

This work is licensed (CC BY-NC 4.0) under Creative Commons Attribution 4.0 International License

kaynaklardan ve insan faaliyetleri sonucunda atmosfere salınır. Doğal kaynaklar deniz tuzu aerosolleri, volkanlar, orman yangınları, toz fırtınaları, canlı bitki örtüsü ve biyolojik aerosol parçacıkları tarafından sağlanır. $PM_{2.5}$'in antropojenik kaynakları (insanlar tarafından üretilen veya insan kaynaklı kirletici kaynakları) arasında araç emisyonları, katı yakıt yakma, endüstriyel deşarj, tarımsal faaliyetler ve evsel biyokütle yakma bulunur. $PM_{2.5}$'in kaynağı zamana ve yere bağlı olarak değişir ve çeşitli bir $PM_{2.5}$ bileşimiyle sonuçlanır. $PM_{2.5}$'in zehirliliği; kütle konsantrasyonu, tane boyutu ve en önemlisi kimyasal kompozisyonu gibi çeşitli faktörlere bağlıdır. İnce partiküller, çok küçük ve hafif olduğundan, daha büyük parçacıklara kıyasla, havada daha uzun süre asılı kalma özelliği gösterir. Bu durum, insanlar ve hayvanlar için bu partiküllerin solunum yoluyla vücuda alınma riskini artırmaktadır. Boyutlarının küçük olması nedeniyle (2.5 mikrondan daha küçük), bu partiküller burun ve boğazdan kolayca geçip akciğerlere ulaşabilir ve bazıları dolaşım sistemine dahi girebilir. Çalışmalar, hava kirliliğinin özellikle de bu küçük partiküllere maruz kalmanın kalp ve akciğer rahatsızlıkları ile erken ölüm arasında güçlü bir ilişki olduğunu göstermektedir. Özellikle $PM_{2.5}$'in hipertansiyon ve damar sertliği gelişimini desteklediği, kalp krizi, felç, kalp yetmezliği ve aritmiler dahil olmak üzere kardiyovasküler hastalık (kalp ve kan damarlarını etkileyen sağlık sorunları) riskinin artmasıyla ilişkili olduğu görülmektedir. Bir dizi çalışmaya göre $PM_{2.5}$'in, astım, bronşit, solunum yolu iltihabı, zatürre, kronik obstrüktif akciğer hastalığı (KOAH) gibi solunum sistemi hasarıyla ilişkili olduğu, kalp krizi ve diğer solunum rahatsızlıkları gibi kronik hastalıkları tetikleyebileceği ya da şiddetlendirebileceği bilinmektedir. Wan Mahiyuddin vd. (2023) $PM_{2.5}$ ile kardiyovasküler ve solunum yolu hastalıklarının belirli sağlık sonuçları arasındaki ilişkiyi araştırmak için zaman serisi tasarımlarını kullanarak mevcut literatüre genel bir bakış sağlamıştır. Bulgular, kısa vadeli çalışmaların solunum yolu hastalıkları için daha yüksek riskler gösterdiğini, uzun vadeli çalışmaların ise kardiyovasküler hastalıklar için daha yüksek riskler gösterdiğini ortaya koymuştur (Gerçekoğlu, 2018; Krittanawong vd., 2023; Nan vd., 2023; Wan Mahiyuddin vd., 2023; Utku ve Can, 2024). Partikül madde ayrıca hava, toprak ve su kirliliğine neden olarak ekosistemlere zarar verir. Partikül madde gölleri ve akarsuları asidik hale getirir, kıyı suyunu ve toprak besinlerini değiştirir veya azaltır ve ormanlara ve çiftlik ürünlerine zarar verir. PM'nin bir hava kirleticisi olarak ürün verimi ve gıda verimliliği üzerindeki etkisi bildirilmiştir. Sulak alanlar üzerindeki etkisi canlı organizmaların ve balıkların hayatta kalması ve verimlilik potansiyelleri ile ilişkilidir. PM'nin hem doğal hem de yönetilen ekosistemler üzerinde bilinen etkileri vardır. Partikül maddenin en uzun etkisinin, biyolojik çeşitliliğe müdahale ettiği ve sonunda ekosistem mal ve hizmetlerinin kaybına yol açtığı zaman gözlemlendiği belirtilmektedir. Partikül maddenin, bitkisel yüzeylerde biriktiği veya toprağın daha derinlerine nüfuz ettiği bilinmektedir. Partikül madde çok küçük boyutta olduğundan, rotalarını kesin olarak bilmek zordur. Ancak, hem havza hem de bölgesel düzeylerde bilinen etkileri vardır. Partikül madde birikimi nedeniyle birçok sorun olabilir; örneğin rekabetteki değişiklikler nedeniyle tür çeşitliliğindeki değişiklikler, biyojeokimyasal döngülerin bozulması, kendini düzenleme yeteneğinde düşüş vb. Atmosferik partikül maddenin içinde bulunan kimyasal bileşenlerin kütle yüklenmesi nedeniyle bitki örtüsünü ve ekosistemleri aşırı bir aralıkta etkilediği bilinmektedir (Grantz vd., 2003; Aydın ve İlkılıç, 2017; Zuhara ve Isaifan, 2018; Manisalidis vd., 2020).

$PM_{2.5}$, birden fazla kimyasal bileşimden oluşan karmaşık bir karışımdır. $PM_{2.5}$'in bileşimi, emisyon kaynağı tarafından belirlenir ve çeşitli bölgesel özellikler gösterir. $PM_{2.5}$ bileşenlerinin toksisitesi ve zararlı kaynakları açıklığa kavuşturulmalı ve kesin kontrol politikaları geliştirilmelidir (Nan vd., 2023).

Üstel Ağırlıklı Hareketli Ortalama (Exponentially Weighted Moving Average/EWMA) kontrol kartı, süreç ortalamasındaki küçük, orta ve büyük büyüklükteki kaymaları incelemede avantajlıdır; çünkü EWMA istatistiği, mevcut gözlem ve önceki gözlemlerden oluşan veri kümesine dayalı olarak hesaplanır. Literatürü incelediğimizde PM2.5 konsantrasyonlarının EWMA kontrol kartları ile incelendiği 2 önemli çalışma özellikle dikkatimizi çekmiştir. Saithanu ve Mekparyup (2022) çalışmasında, Chonburi Eyaleti'ndeki PM2.5 konsantrasyonlarının son dönemdeki durumunu ve değişimlerini incelemeyi amaçlamıştır. Amaç, süreç değişiminin Tayland'ın günlük ulusal hava kalitesi standardına uyup uymadığını değerlendirmektir. Bu hedef, temel özelliklerin belirlenmesi ve ardından 2020 yılına ait PM2.5 konsantrasyonlarının süreç ortalamasının EWMA kontrol kartları ile izlenmesi yoluyla gerçekleşmiştir. Saithanu (2023) esas olarak Tayland'ın doğusunda bulunan Chachoengsao Eyaletinde PM2.5 olarak bilinen ince partikül maddenin mevcut durumunu belirlemeye odaklanarak, bu maddenin süreç değişiminin günlük Tayland ulusal hava kalitesi standardını karşılayıp karşılamadığını kontrol etmiştir. Amacını, betimleyici istatistik ve kümeleme analiziyle bir yıl boyunca (Kasım 2020'den Ekim 2021'e kadar) PM2.5 konsantrasyonlarının önemli özelliklerini araştırarak gerçekleştirmiştir. Ayrıca 5 ay için (Kasım 2021'den Mart 2022'ye kadar) PM2.5 konsantrasyonlarının süreç ortalamalarını EWMA kartı ile incelemiştir. Kümeleme analizinin sonuçları, PM2.5 konsantrasyonlarının yalnızca bir mevsimden değil, aynı zamanda bir gün içindeki bir zaman periyodundan da etkilendiğini ortaya koymuştur. Bu çalışmada, Ankara ilindeki 6 farklı hava kirliliği izleme istasyonundan elde edilen $PM_{2.5}$ konsantrasyon seviyelerindeki değişimler ve hangi mevsim dönemlerinde bu değişimlerin görüldüğü, istasyonlar arasında farklılık olup olmadığı çeşitli betimleyici istatistikler veya grafikler ve EWMA kartları kullanılarak incelenmektedir. EWMA kartları kullanılarak

partikül madde konsantrasyonlarının dolayısıyla hava kalitesinin kontrol edilip izlenmesi, hava kirliliği önleyici stratejilerin geliştirilmesi açısından önemlidir. Ankara ilindeki hava kalitesinin izlendiği 6 istasyona ilişkin $PM_{2.5}$ ölçümlerinin kontrol kartları ile ilk kez incelenmesi çalışmamızın dikkat çekici yanıdır.

2. Materyal ve Yöntem

İstatistiksel süreç kontrolü, süreç değişikliğini izlemek ve kontrol etmek için istatistiksel yöntemlerin uygulanmasına yönelik bir kalite kontrol yaklaşımıdır. Özellikle, kontrol kartı, süreçleri izlemek ve süreçlerdeki değişiklikleri tespit etmek için yaygın olarak kullanılan bir araçtır ve bu sayede hataların oluşmasını önler.

EWMA kontrol grafiği, Roberts (1959) tarafından sunulan istatistiksel bir süreç kontrol grafiğidir; süreç parametrelerindeki zamanla meydana gelen değişimleri tespit etmek için kullanılan, köklü ve iyi bilinen bir yöntemdir. Süreç ortalamalarındaki, küçük fakat sürekli sapmalara karşı daha duyarlı olduğu için Shewhart kontrol kartlarına seçenek olarak geliştirilmiştir. Bu kontrol kartları, zaman serilerinin analizinde de kullanılmaktadır. EWMA istatistiği geçmiş ve yakın tarihli tüm gözlemlerin ağırlıklı ortalaması olarak kabul edilebilir, dolayısıyla normallik varsayımına duyarsızdır. Alt örneklem boyutu 1 olduğunda bu yöntem uygulanmak için idealdir (Ege, 2000; Mahmood vd., 2021; Waqas vd., 2023; Aydın, 2024; Polat, 2024). xi rasgel değişkeni gözlemleri temsil etsin. λ bir düzeltme (düzgünleştirme) sabiti olsun; $0<\lambda\leq 1$. Daha sonra EWMA istatistiği aşağıdaki şekilde tanımlanır (eşitlik 1) (Mahmood vd., 2021; Waqas vd., 2023; Polat, 2024).

$$Z_i = \lambda x_i + (1-\lambda)Z_{i-1}, i = 1,2,3, \ldots. \quad (1)$$

Burada Z_{i-1} önceki EWMA istatistiğidir. Dolayısıyla Z_i, daha yakın tarihli gözlemlere daha fazla ağırlık verilen, geçmiş ve yakın tarihli tüm $PM_{2.5}$ ölçümlerinin ağırlıklı ortalamasıdır. λ sabiti 1'e yaklaştığında, mevcut değerin EWMA'daki ağırlığı artar, eski değerin EWMA'daki ağırlığı azalır (Lu ve Zhen, 2015). Kartın kontrol limitlerini hesaplamak için kontrol altında olan sürecin ortalaması olan μ_0 başlangıç değeri tanımlanmalıdır. Bazı durumlarda önceki verilerin ortalaması EWMA'nın başlangıç değeri olarak kullanılır ($z_0 = \bar{x}$). Bu durumda kontrol limitlerinde de $\bar{x}$ kullanılır (Ege, 2000). x_i bağımsız gözlemlerinin standart sapması (σ) tahmin edilmelidir. En son olarak genel olarak 3 olarak alınan kontrol limitlerinin genişliği L belirtilmelidir. EWMA kartı seçilen λ değerine bağlıdır, daha küçük bir λ değeri küçük kaymaların daha hızlı tespit edilmesini sağlar. EWMA kartı, özellikle λ küçük olduğunda, ortalamadaki küçük kaymaları tespit etmek için kullanışlıdır. Eğer Z_i EWMA istatistiği bu kontrol limitlerinin dışına düşerse, süreç ortalamasında bir kayma olduğu anlamına gelir. Çalışmamızda, desenlerin ve kontrol dışı durumların izlenmesinde en iyi sonucu veren düzeltme parametresi λ=0.25 olan EWMA grafiği kullanılmıştır (Mahmood vd., 2021; Waqas vd., 2023; Polat, 2024).

EWMA grafiğinin kontrol limitleri eşitlik 2'de verilmiştir (Mahmood vd., 2021; Waqas vd., 2023; Polat, 2024).

$$\begin{aligned} \text{Ü}KL &= \mu_0 + L\sigma\sqrt{\lambda(2-\lambda)^{-1}[1-(1-\lambda)^{2i}]} \\ MÇ &= \mu_0 \\ KL &= \mu_0 - L\sigma\sqrt{\lambda(2-\lambda)^{-1}[1-(1-\lambda)^{2i}]} \end{aligned} \quad (2)$$

Eğer $i\to\infty$ olursa $[1-(1-\lambda)^{2i}]$ değeri 1'e yakınsar, bu durumda, zamanla değişen limitler asimptotik limitlere dönüştürülür ve eşitlik 3'deki gibi tanımlanır (Lu ve Zhen, 2015; Mahmood vd., 2021; Waqas vd., 2023; Polat, 2024):

$$\begin{aligned} \text{Ü}KL &= \mu_0 + L\sigma\sqrt{\lambda(2-\lambda)^{-1}} \\ MÇ &= \mu_0 \\ &= \mu_0 - L\sigma\sqrt{\lambda(2-\lambda)^{-1}} \end{aligned} \quad (3)$$

3. Bulgular

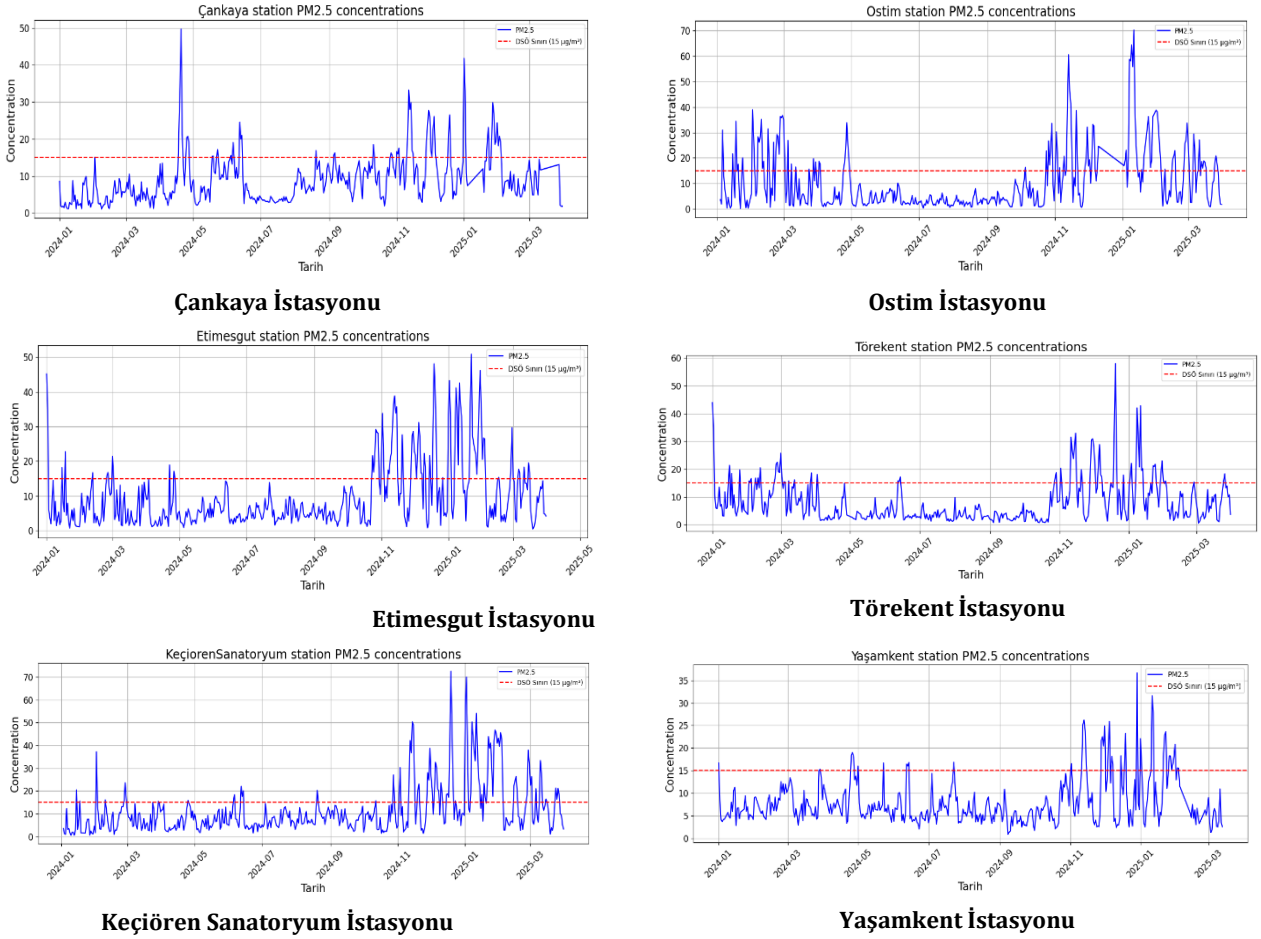
Veriler T.C. Çevre, Şehircilik ve İklim Değişikliği Bakanlığı'nın web sayfasından Hava Kalitesi Veri Bankası'ndan alınmıştır. 1.01.2024-31.03.2025 tarihleri arasında Ankara ili için 6 istasyon verisi (Çankaya, Etimesgut, Keçiören Sanatoryum, Ostim, Törekent, Yaşamkent) incelenmiştir. Bu istasyonlar Ankara'nın çeşitli yerleşim ve sanayi bölgelerindedir.

Tablo 1. Günlük $PM_{2.5}$ ölçümlerine ilişkin betimleyici istatistikler (01.01.2024-31.03.2025)

İstasyon	Gözlem Sayısı	Ortalama	Standart Sapma	Minimum	Maksimum
Çankaya	405	8.99	6.62	1.10	49.65
Etimesgut	453	9.54	9.31	0.44	50.86
Keçiören Sanatoryum	448	11.58	11.19	0.54	72.50
Ostim	420	10.45	11.69	0.17	70.30
Törekent	443	8.07	7.73	0.55	58.02
Yaşamkent	410	7.94	5.20	0.83	36.69

Tablo 1'de 6 istasyondan ölçülen değerlere ilişkin betimleyici istatistikler verilmiştir. Buna göre $PM_{2.5}$'in günlük konsantrasyonlarının ortalaması, en yüksek olan istasyon Keçiören Sanatoryum, en düşük olan ise Yaşamkent'tir. Dünya Sağlık Örgütü (DSÖ), hava kirliliği kaynaklı milyonlarca ölümü önlemek için hava kirliliği kılavuz değerlerini güncellemiştir. DSÖ, 2021 yılında halk sağlığını korumak için belirlediği güncel sınır değerleri için, $PM_{2.5}$ için kısa vadeli standardın (günlük ortalama) 15 µg/m3 ve uzun vadeli standardın (yıllık ortalama) 5 µg/m3 olduğunu ifade etmiştir (World Health Organization, 2021). Tüm istasyonların ortalama değerleri günlük 15 $\mu g/m^3$ sınırının altında kalıyor; ancak maksimum değerler birçok noktada bu eşiği ciddi şekilde aşıyor (örneğin; Keçiören Sanatoryum: 72.50; Ostim: 70.30, Törekent: 58.02). Bu, kısa süreli "zirve" kirliliği olaylarının özellikle sanayi veya yoğun trafik bölgelerinde yaşandığını gösteriyor. En yüksek standart sapma Ostim (11.69) ve Keçiören Sanatoryum'da (11.19) görülmüştür. Bu iki bölgede hem çok temiz hem de çok kirli günler gözleniyor; dolayısıyla hava kalitesindeki dalgalanma diğer istasyonlara göre çok daha fazladır. En düşük standart sapma Yaşamkent'te (5.20) – hem daha stabil hem de en düşük "zirve" değer görülen bir yerleşim bölgesidir.

Şekil 1'de her bir istasyon için $PM_{2.5}$ ölçümlerinin zaman içindeki değişimlerini gösteren grafikler verilmiştir. Grafiklerdeki kırmızı düz çizgi DSÖ'nün verdiği günlük 15 µg/m3 eşik değerini göstermektedir.



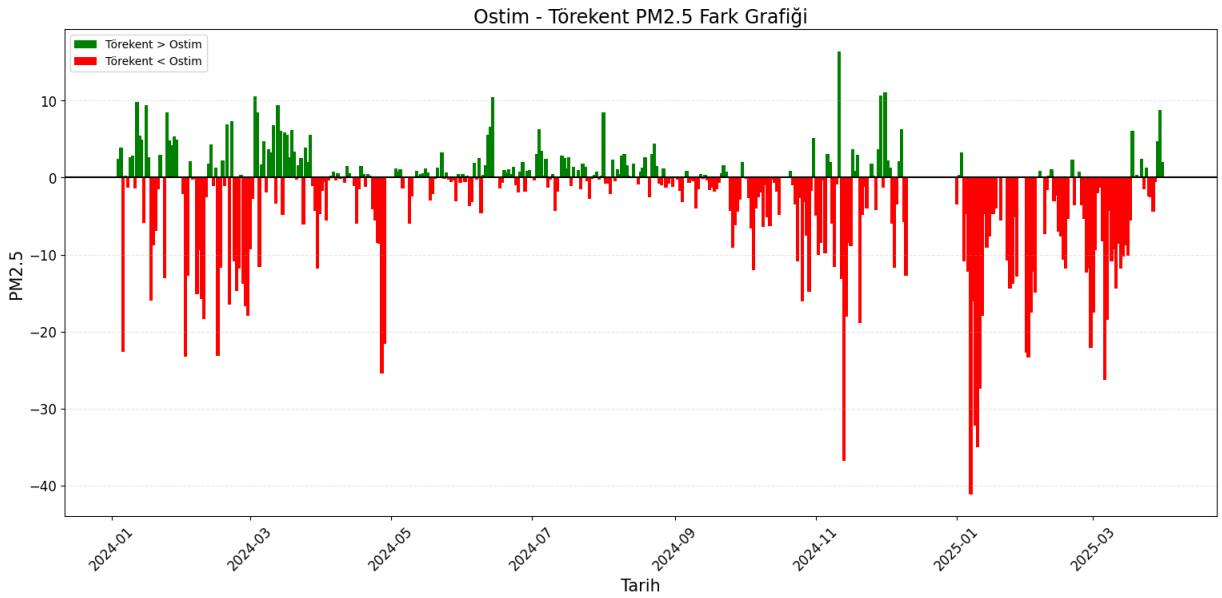
Çankaya İstasyonu **Ostim İstasyonu**

Etimesgut İstasyonu **Törekent İstasyonu**

Keçiören Sanatoryum İstasyonu **Yaşamkent İstasyonu**

Şekil 1. $PM_{2.5}$ ölçümlerinin zaman içindeki değişimlerini gösteren çizgi grafikleri (01.01.2024-31.03.2025).

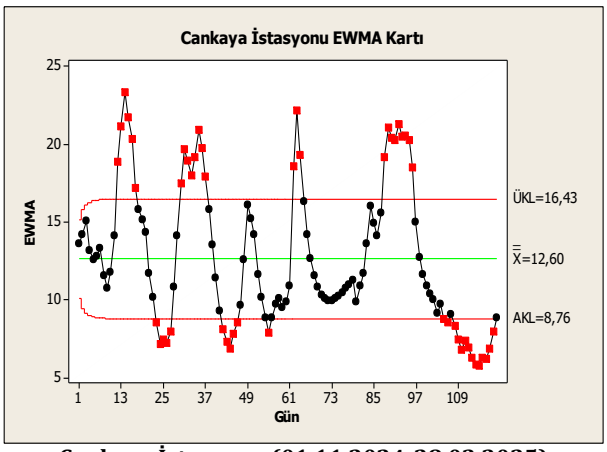
Şekil 1 incelendiğinde altı istasyondan elde edilen $PM_{2.5}$ ölçümlerinin ilkbahar ve yaz mevsimlerinde genel olarak daha düşük seviyelerde olduğunu ve çoğunlukla DSÖ sınırının altında kaldığını, ancak özellikle 2024 yılı Kasım ayı ile 2025 yılı kış aylarında (Ocak-Şubat) bazı günler bu sınırın çok üzerine çıktığını söyleyebiliriz. Ancak, Çankaya istasyonunda 2024 yılı Nisan ayı içinde ani bir çıkış olduğu da görülmüştür. Ostim istasyonu için ise 2024 yılı Ocak-Şubat-Mart aylarında DSÖ sınırını aşan yüksek kirlilik artışının olduğunu bunun da özellikle Şubat ayında yoğunlaştığını söyleyebiliriz. Ostim gibi sanayi bölgelerinde yoğun sanayi ve inşaat faaliyetleri, partikül madde salınımını artırarak $PM_{2.5}$ seviyelerinin yükselmesine neden olmuştur. Son yıllarda artan sanayileşme, hızlı nüfus artışı ve düzensiz kentleşme, özellikle kış aylarında hava kirliliğinin ciddi boyutlara ulaşmasına neden olmuştur. Araştırmalara göre, Ankara'da araç kullanımındaki artış da hava kalitesinin düşmesinde etkilidir (Dundar vd., 2020; Ünal ve Özel, 2023).



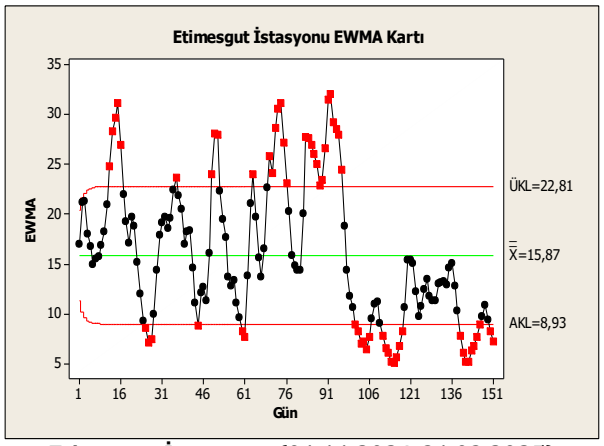
Şekil 2. Ostim-Törekent istasyonları günlük $PM_{2.5}$ ölçümleri için farklar grafikleri (01.01.2024-31.03.2025).

Ostim, Ankara'nın Yenimahalle ilçesinde yer alan ve Türkiye'nin en büyük organize sanayi bölgelerinden biridir. Törekent de, Ankara'nın Sincan ilçesinde bulunan sanayi faaliyetlerinin yoğun olduğu ve organize sanayi bölgelerine yakınlığıyla bilinen bir bölgedir. Bu iki istasyondan elde edilen $PM_{2.5}$ ölçümleri karşılaştırıldığında Şekil 2'den de görüldüğü üzere Ostim'in hava kirlilik seviyesinin çoğunlukla Törekent'den daha yüksek olduğu özellikle de kış aylarında bu farkın belirgin olduğu görülmektedir. Ostim, Ankara'nın en büyük organize sanayi bölgelerinden biri olup, çok sayıda küçük ve orta ölçekli işletmeye ev sahipliği yapmaktadır. Bu yoğun sanayi faaliyetleri, özellikle filtreleme sistemleri yetersiz olan tesislerde, $PM_{2.5}$ gibi ince partikül maddelerin atmosfere salımını artırmaktadır. Törekent, Ankara'nın Sincan ilçesinde yer almakta olup, Ostim'e kıyasla daha az sanayi faaliyetine sahiptir. Bu durum, bölgedeki $PM_{2.5}$ seviyelerinin Ostim'e göre daha düşük olmasına katkıda bulunmaktadır.

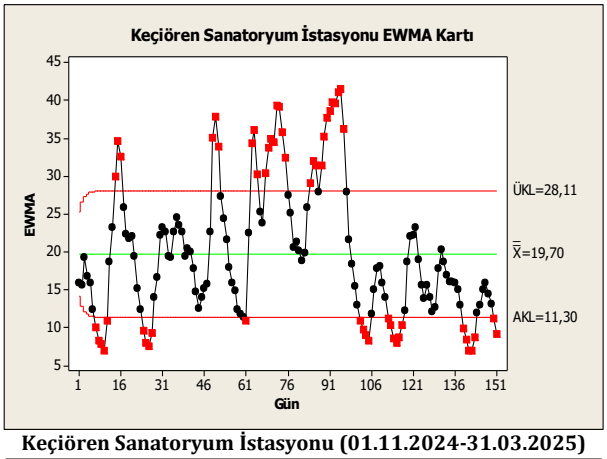
Altı istasyon için hava kirlilik seviyesinin özellikle yükseldiği kış ayları için (2024 Kasım-2025 Mart) EWMA kontrol kartlarını oluşturmadan önce, eksik veriler Stineman enterpolasyonu ile doldurulur. Russell W. Stineman tarafından 1980 yılında geliştirilen ve eksik veri noktalarını doldurmak için kullanılan bir enterpolasyon (interpolation) yöntemidir (Stineman, 1980). Stineman enterpolasyonunda, eksik değerler parça parça rasyonel enterpolasyon yöntemiyle doldurulur ve varsayılan olarak her bir benzersiz nesneyle ilişkili zaman indeksi enterpolasyon için kullanılır. Stineman'a göre, enterpolasyon işlemi şu özelliklere sahiptir: (1) Belirtilen noktaların koordinatlarının değerleri monoton bir şekilde değişiyorsa ve bu noktaları birleştiren doğru parçalarının eğimleri de monoton bir şekilde değişiyorsa, o zaman enterpolasyon eğrisi ve onun eğimi de monoton olarak değişir. (2) Eğer belirtilen noktaları birleştiren doğru parçalarının eğimleri monoton bir şekilde değişiyorsa, o zaman enterpolasyon eğrisinin eğimleri de monoton bir şekilde değişecektir. Son olarak, ilk (1) ve ikinci (2) koşulların bir nokta kümesi tarafından sağlandığını, ancak bu noktalardan birinde ordinatta (dikey eksende) ya da eğimde yapılacak küçük bir değişikliğin, daha önce belirtilen koşulların artık sağlanmamasına yol açacağın varsayılsın. Bu durumda, ilgili noktadaki ordinat ya da eğimde yapılan bu küçük değişiklik, enterpolasyon eğrisinde de yalnızca küçük bir değişikliğe neden olur (Kontos ve Karlis, 2023). Bu yöntem, özellikle uzun ardışık eksik veri bloklarının bulunduğu zaman serilerinde tercih edilir. İstasyonlar için eksik gözlemler bu yöntemle ImputeTS R programı paketini (Moritz, 2022) kullanarak doldurulmuştur. Çankaya ve Yaşamkent istasyonları için Mart ayı verilerinin büyük bir çoğunluğu olmadığı için Kasım 2024-Şubat 2025 verileri ile çalışılmıştır. Diğer istasyonlarda Mart 2025 verileri de incelenmiştir.



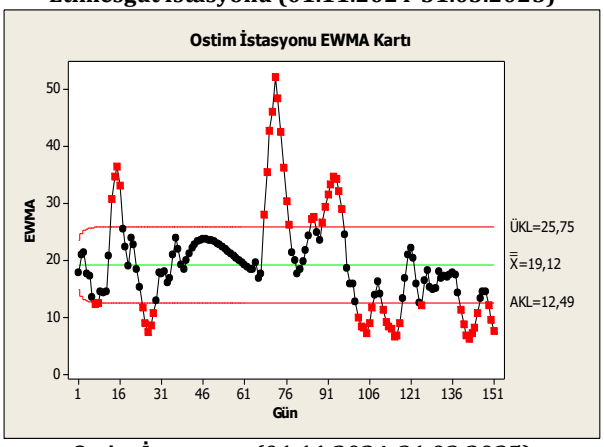
Çankaya İstasyonu (01.11.2024-28.02.2025)



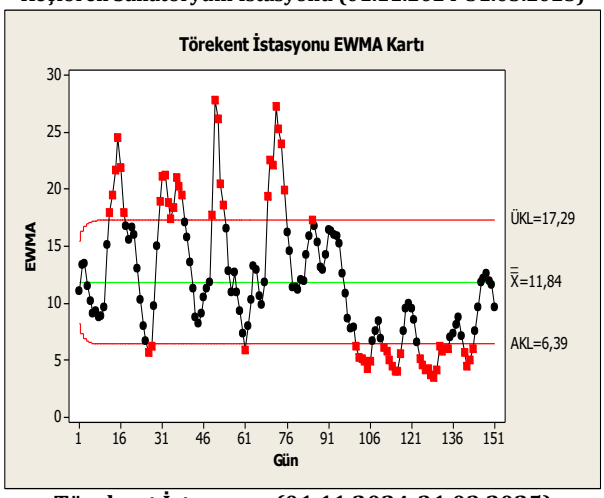
Etimesgut İstasyonu (01.11.2024-31.03.2025)



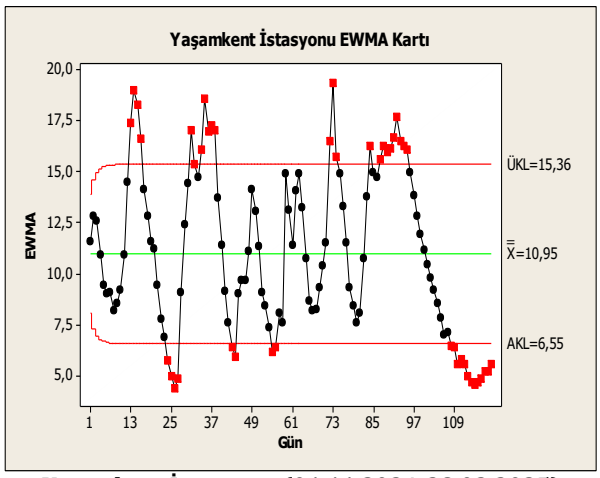
Keçiören Sanatoryum İstasyonu (01.11.2024-31.03.2025)



Ostim İstasyonu (01.11.2024-31.03.2025)



Törekent İstasyonu (01.11.2024-31.03.2025)



Yaşamkent İstasyonu (01.11.2024-28.02.2025)

Şekil 3. Günlük $PM_{2.5}$ ölçümleri için EWMA kontrol kartları.

Şekil 3'teki altı istasyon için oluşturulan EWMA kontrol kartları incelendiğinde süreç ortalamasının kontrol dışında olduğunu söyleyebiliriz. $PM_{2.5}$'deki artış hava kirliliğinin göstergesi olduğu için özellikle ÜKL'yi aşan noktalar üzerinde durulmuştur. Çankaya istasyonu için Kasım'da (7 nokta), Aralık'ta (7 nokta), Ocak'ta (8 nokta), Şubat'ta (4 nokta) olmak üzere toplam 26 nokta ÜKL'nin dışına çıkmıştır. Bu noktalara ilişkin $PM_{2.5}$ değerleri incelendiğinde 22 tanesinin DSÖ sınırı 15 µg/m3'ü aştığı görülmüştür. Etimesgut istasyonu için ise Kasım'da (5 nokta), Aralık'ta (4 nokta), Ocak'ta (18 nokta), Şubat'ta (4 nokta) olmak üzere toplam 31 nokta ÜKL'nin dışına çıkmıştır. Bu noktalara ilişkin $PM_{2.5}$ değerleri incelendiğinde 28 tanesinin DSÖ sınırı 15 µg/m3'ü aştığı görülmüştür. Keçiören Sanatoryum istasyonu için Kasım'da (3 nokta), Aralık'ta (3 nokta), Ocak'ta (19 nokta), Şubat'ta (4 nokta) olmak üzere toplam 29 nokta ÜKL'nin dışına çıkmıştır. Bu noktalara ilişkin $PM_{2.5}$ değerleri incelendiğinde 28 tanesinin DSÖ sınırı 15 µg/m3'ü aştığı görülmüştür. Ostim istasyonu için Kasım'da (4 nokta), Ocak'ta (16 nokta), Şubat'ta (4 nokta) olmak üzere toplam 24 nokta ÜKL'nin dışına çıkmıştır. Bu noktalara ilişkin $PM_{2.5}$ değerleri incelendiğinde 22 tanesinin DSÖ sınırı 15 µg/m3'ü aştığı görülmüştür. Törekent istasyonu için Kasım'da (7 nokta), Aralık'ta (13 nokta), Ocak'ta (8 nokta) olmak üzere toplam 28 nokta

ÜKL'nin dışına çıkmıştır. Bu noktalara ilişkin $PM_{2.5}$ değerleri incelendiğinde 21 tanesinin DSÖ sınırı 15 µg/m3'ü aştığı görülmüştür. Yaşamkent istasyonu için Kasım'da (4 nokta), Aralık'ta (7 nokta), Ocak'ta (10 nokta), Şubat'ta (3 nokta) olmak üzere toplam 24 nokta ÜKL'nin dışına çıkmıştır. Bu noktalara ilişkin $PM_{2.5}$ değerleri incelendiğinde 19 tanesinin DSÖ sınırı 15 µg/m3'ü aştığı görülmüştür.

4. Sonuç ve Tartışma

Bu çalışmada hava kalitesini izlemek için Ankara ilindeki 6 istasyondan elde edilen $PM_{2.5}$ ölçümlerinin günlük değerleri incelenmiştir. Çalışmamızın özgün yanı ilk defa Ankara ili için elde edilen $PM_{2.5}$ verilerinin kalite kontrol kartlarından EWMA kartları ile izlenmesidir. Saithanu ve Mekparyup (2022) çalışmasında Tayland'ın günlük ulusal hava kalitesi standardından yüksek $PM_{2.5}$ değerlerinin çoğunlukla Aralık'tan Mart'a kadarki dönemde (kış aylarında) görülmüş olması, Nisan'dan Kasım'a kadarki dönemde (ilkbahar, yaz, sonbahar) Tayland sınırını aşmaması, $PM_{2.5}$ konsantrasyonları üzerinde mevsimsel bir etki olabileceğini düşündürmüştür. Saithanu (2023) da çalışmasında aynı şekilde $PM_{2.5}$ konsantrasyonlarının günlük maksimum değerinin Aralık, Ocak ve Şubat aylarında yüksek olduğunu, Nisan ve Mayıs aylarında kademeli olarak orta seviyeye düştüğünü ve son olarak Ağustos, Eylül ve Ekim aylarında düşük seviyeye kaydığını bulmuştur. Çalışmamız sonucunda da Ankara'da özellikle 2025 yılı kış aylarında hava kirliliği seviyesinde artışlar olduğu, bazı günler $PM_{2.5}$ ölçümlerinin DSÖ eşik değerini aştığı görülmüştür. Genel olarak, Ankara için de Aralık, Ocak ve Şubat gibi kış aylarında hava kirliliğinin arttığını söyleyebiliriz. Bunun öngörülen makul nedenlerini sıralamak mümkündür. Kış aylarında konutlarda ve bazı işletmelerde kalitesiz kömür ve fosil yakıt kullanımı artmaktadır. Bu yakıtlar yüksek miktarda $PM_{2.5}$ parçacığı üretmektedir. Kışın soğuk hava yere çöker ve üstüne sıcak hava tabakası gelir. Bu da havayı adeta bir kapak gibi bastırır ve kirliliğin dağılmasını engeller. Sonuç olarak $PM_{2.5}$ birikir ve konsantrasyonu artar. Ayrıca kış aylarında Ankara'da bazen rüzgârsız ve durgun hava olduğundan temiz hava akımı olmadığı için kirleticiler ortamda birikir. Bir başka neden olarak soğuk havalarda araçlar çalıştırılırken daha fazla egzoz emisyonu salmalarıdır.

İstasyonlardan Yaşamkent daha stabil ve düşük seviyelerde ölçümlerin görüldüğü bir istasyondur. Bunun sebebi yeni bir yerleşim yeri olmasından nüfusun çok kalabalık olmamasından kaynaklanmaktadır. Nüfusu son yıllarda artmaya başlamıştır. Ostim gibi sanayi bölgelerinde sanayi faaliyetlerinin yanı sıra, yoğun araç trafiği de olmaktadır. Sanayi bölgeleri ve trafiğin yoğun olduğu bölgeler riskin yüksek olduğu alanlardır. Özellikle dizel yakıt kullanan ağır vasıtalar ve servis araçları, egzoz emisyonlarıyla $PM_{2.5}$ seviyelerinin artmasına katkıda bulunmaktadır. Trafikten kaynaklı hava kirliliği, özellikle kış aylarında özellikle yüksek basınç sistemlerinin etkisiyle oluşan sıcaklık terselmesi (inversiyon) olayları gibi meteorolojik olaylarla birleştiğinde, kirleticilerin atmosferde birikmesine neden olmaktadır. Ayrıca kışın Ankara'da sanayi alanları ısınma ve üretim faaliyetleri sebebiyle daha çok partikül madde üretmektedir. Bu nedenlerden ötürü Ostim ve Törekent gibi bölgeler de kış aylarında havadaki kirlilik seviyesi artış göstermiş olabilir.

Analizlerimiz EWMA kartının hava kirlilik seviyesindeki ani değişimleri yakalamak için iyi bir araç olduğunu göstermektedir. Bu kart süreçteki küçük kaymaları ve değişimleri iyi takip eden bir karttır. Böylelikle EWMA kartı ile $PM_{2.5}$ seviyesindeki ani değişimler izlenebilir ve gerekli önlemler alınabilir. Tüm istasyonlar için EWMA kartları partikül maddenin kış aylarında dalgalı bir seyir gösterdiğini ve ani yükselişleri/düşüşleri ortaya koymuştur. Mart ayında ilgili istasyonlar için havadaki partikül miktarındaki düşüş trendi de kartlardan izlenmiştir. Daha sonraki çalışmalarda bu kart kullanılarak belli periyotlarda $PM_{2.5}$ ya da hava kirliliğine sebep olan diğer kirleticiler izlenebilir, böylece yetkililer gerekli önlemleri ve müdahaleleri ve ilgili politikaları daha hızlı bir şekilde hayata geçirebilirler. İnsan sağlığını tehdit eden bu kirliliğe müdahale etmek için alınabilecek önlemler ve politikalar: örneğin; halkın kömür kullanımını azaltıp doğalgaz, elektrikli ısıtma gibi daha temiz enerji kaynaklarına geçişi teşvik edilebilir. Düşük kaliteli kömür kullanımına yasak veya sıkı kalite denetimleri getirilebilir. Binalarda enerji verimliliği artırılarak yakıt tüketimi azaltılabilir (örneğin, yalıtım teşvikleri vb). Toplu taşıma sistemleri (metro, otobüs) güçlendirilebilir ve cazip hale getirilebilir. Elektrikli araç kullanımı teşvik edilebilir, şarj istasyonları yaygınlaştırılabilir. Araç emisyon standartları sıkılaştırılabilir. Ostim gibi organize sanayi bölgelerinde filtre ve baca gazı arıtma sistemlerinin kullanımı zorunlu hale getirilebilir. Düzenli hava emisyon ölçümleri yapılarak limit aşımı yapan tesislere ceza uygulanabilir. Sanayi tesislerinde temiz üretim teknolojilerine geçiş desteklenebilir. Yerleşim yerlerinde ve sanayi bölgelerinde yeni ağaçlandırmalar ve yeşil koridorlar oluşturulabilir. Mevcut park ve yeşil alanların korunması sağlanabilir. Halka yönelik hava kirliliği, $PM_{2.5}$ tehlikeleri ve alınabilecek bireysel önlemler hakkında bilgilendirme kampanyaları yapılabilir. Dışarıda maske takmak gibi kişisel önlemler teşvik edilebilir, kuruluşlar tarafından üretilen $PM_{2.5}$ miktarını kısıtlayan hükümet politikaları uygulamaya konulabilir.

Katkı Oranı Beyanı

Yazarların katkı yüzdeleri aşağıda verilmiştir. Yazarlar makaleyi incelemiş ve onaylamıştır.

	E.P.	B.C.	R.P.
K	50	20	30
T	50	25	25
Y	60	15	25
VTI	20	70	10
VAY	50	30	20
KT	50	20	30
YZ	50	20	30
KI	60	10	30
GR	60	15	25
PY	50	25	25

K= kavram, T= tasarım, Y= yönetim, VTI= veri toplama ve/veya işleme, VAY= veri analizi ve/veya yorumlama, KT= kaynak tarama, YZ= Yazım, KI= kritik inceleme, GR= gönderim ve revizyon, PY= proje yönetimi.

Çatışma Beyanı

Yazarlar bu çalışmada hiçbir çıkar ilişkisi olmadığını beyan etmektedirler.

Etik Onay Beyanı

Bu araştırmada hayvanlar ve insanlar üzerinde herhangi bir çalışma yapılmadığı için etik kurul onayı alınmamıştır.

Kaynaklar

Aydın H, İlkılıç C. 2017. Air pollution, pollutant emissions and harmfull effects. J Eng Technol, 1(1): 8-15.

Aydın ZB. 2024. Cusum, Ewma kontrol grafiklerinin karşılaştırılması: aydınlatma sektöründe bir uygulama. İstatistik Araş Derg, 14(1): 36-45.

Dundar E, Dursun Ş, Toros H. 2020. Air pollution in Ankara during COVID-19. J Res Atmos Sci, 2(1): 24-30.

Ege Ö. 2000. EWMA kontrol kartının Shewhart ve Cusum kontrol kartları ile karşılaştırılması- simulasyon denemesi. DEÜ İİBF Derg, 15(1): 125-132.

Gerçekoğlu H. 2018. PM2.5 nedir? Neden tehlikelidir? URL: https://drhakangercekoglu.com/genel/pm2-5-nedir-neden-tehlikelidir.html (accessed date: April 25, 2025).

Grantz DA, Garner JHB, Johnson DW. 2003. Ecological effects of particulate matter. Environ Int, 29: 213–239.

Kontos C, Karlis D. 2023. Football analytics based on player tracking data using interpolation techniques for the prediction of missing coordinates. Ital J Appl Stat, 35(2): 1-19.

Krittanawong C, Qadeer YK, Hayes RB, Wang Z, Thurston GD, Virani S, Lavie CJ. 2023. $PM_{2.5}$ and cardiovascular diseases: state-of-the-art review. Int J Cardiol Cardiovasc Risk Prev, 19: 200217.

Lu H, Zhen J. 2015. EWMA control chart of NOx atmospheric environmental monitoring system. In: Qi E, Shen J, Dou R (eds), Proc 21st Int Conf Ind Eng Eng Manag 2014. Atlantis Press, Paris, France, pp: 403–406.

Mahmood Y, Ishtiaq S, Khoo MBC, Teh SY, Khan H. 2021. Monitoring of three-phase variations in the mortality of COVID-19 pandemic using control charts: where does Pakistan stand? Int J Qual Health Care, 33(2): 1–8.

Manisalidis I, Stavropoulou E, Stavropoulos A, Bezirtzoglou E. 2020. Environmental and health impacts of air pollution: a review. Front Public Health, 8(14): 1-13.

Moritz S. 2022. Package imputeTS. URL: http://cran.r-project.org/web/packages/imputeTS/imputeTS.pdf (accessed date: April 25, 2025).

Nan N, Yan Z, Zhang Y, Chen R, Qin G, Sang N. 2023. Overview of $PM_{2.5}$ and health outcomes: focusing on components, sources, and pollutant mixture co-exposure. Chemosphere, 323: 138181.

Polat E. 2024. Using quality control charts for monitoring COVID-19 daily cases and deaths in Türkiye. Bitlis Eren Univ J Sci, 13(1): 134-152.

Roberts SW. 1959. Control chart tests based on geometric moving averages. Technometrics, 1(3): 239–250.

Saithanu K, Mekparyup J. 2022. Investigation of recent $PM_{2.5}$ changes in Chonburi province using Ewma charts. Poll Res, 41(3): 884-888.

Saithanu K. 2023. Determining current situation of fine particulate matter in Chachoengsao province. Int J Innov Sci Res Rev, 5(6): 4698-4701.

Stineman RW. 1980. A consistently well behaved method of interpolation. Creative Comput, 6(7): 54-57.

Utku A, Can Ü. 2024. An effective hybrid model for predicting air quality of Ankara. Malatya Turgut Ozal Univ J Eng Nat Sci, 5(1): 1–8.

Ünal C, Özel G. 2023. Ankara ili meteoroloji parametrelerinin hava kirliliği üzerindeki etkilerinin regresyon analizi ile incelenmesi. Nicel Bilim Derg, 5(2): 135-150.

Wan Mahiyuddin WR, Ismail R, Mohammad Sham N, Ahmad NI, Nik Hassan NMN. 2023. Cardiovascular and respiratory health effects of fine particulate matters ($PM_{2.5}$): a review on time series studies. Atmosphere, 14(5): 856.

Waqas M, Xu SH, Anwar SM, Rasheed Z, Shabbir J. 2023. The optimal control chart selection for monitoring COVID-19 phases: a case study of daily deaths in the USA. Int J Qual Health Care, 35(3): 1-9.

World Health Organization. 2021. WHO global air quality guidelines: particulate matter ($PM_{2\cdot5}$ and PM_{10}), ozone, nitrogen dioxide, sulfur dioxide and carbon monoxide. URL: https://iris.who.int/bitstream/handle/10665/345329/9789240034228-eng.pdf (accessed date: April 25, 2025).

Zuhara S, Isaifan R. 2018. The impact of criteria air pollutants on soil and water: a review. J Environ Sci Pollut Res, 4(2): 278–284.

Black Sea Journal of Engineering and Science

doi: 10.34248/bsengineering.1708736

Open Access Journal
e-ISSN: 2619 – 8991

Araştırma Makalesi (Research Article)
Cilt 8 - Sayı 4: 1212-1217 / Temmuz 2025
(Volume 8 - Issue 4: 1212-1217 /July 2025)

FARKLI *Brassica* TÜRLERİNİN KABA YEM KALİTESİ

Uğur SÖYLER[1], Serra Nur ÖZTÜRK[1], İlknur YILDIRIM[1], Erdem GÜLÜMSER[1*]

[1]Bilecik Şeyh Edebali University, Faculty of Agriculture and Natural Sciences, Department of Filed Crop, 112000. Bilecik, Türkiye

Özet: Türkiye'de kaliteli kaba yem açığının kapatılmasında alternatif yem kaynakları önem ihtiva etmektedir. Nitekim ülkede yem bitkileri üretimi ile çayır-meralardan elde edilen kaba yem miktarı mevcut hayvan varlığının ihtiyacının ancak %35'ini karşılayabilmektedir. Bu çalışmada; Türkiye'de tarımı yapılan farklı *Brassica* türlerinin (yem şalgamı, kolza ve kanola) kaba yem kalitesinin belirlenmesi amaçlanmıştır. Çalışmada materyal olarak 9 adet kışlık *Brassica* türü kullanılmıştır. Çalışma 2023 Kasım ayında Bilecik Şeyh Edebali Üniversitesi Tarımsal Uygulama ve Araştırma alanında, Tesadüf Blokları Deneme Desenine göre kurulmuştur. Hasat bitkilerin %50 çiçeklenme döneminde gerçekleştirilmiştir. Örneklerde ham protein (HPO), asit deterjanda çözünmeyen lif (ADF), nötr deterjanda çözünmeyen lif (NDF), nispi yem değeri (NYD), potasyum (K), fosfor (P), kalsiyum (Ca), magnezyum (Mg), kondanse tanen (KT), toplam fenolik (TFN), toplam flavonoid (TFL) ve radikal kovucu aktivite (DPPH) içerikleri tespit edilmiştir. En yüksek HPO %20,22 ile yem şalgamı olan Lenox çeşidinde, en düşük ise %14,08 ile Luciano çeşidinde tespit edilmiştir. En yüksek NYD istatistiksel olarak aynı grupta yer alan Lenox (134,69), PR44W29 (128,05) ve Exception (126,85), en düşük ise 104,37 ile Luciano çeşidinden tespit edilmiştir. Türlerin K, P, Ca ve Mg içerikleri sırasıyla %2,39-2,78, %0,51-0,61, %0,77-1,09 ve %0,24-0,41 arasında olmuştur. En yüksek KT aynı istatistiksel grupta yer alan Lenox (%1,42) ve Linus (%1,30), en düşük ise %0,72 ile Expower çeşidinde tespit edilmiştir. Farklı *Brassica* türlerinin kaba yem kalitesinin incelendiği çalışmanın sonucunda; Lenox, Linus ve Exception çeşitleri ön plana çıkmıştır. Bu durum söz konusu çeşitlerin yem olarak değerlendirilmesi açısından önem ihtiva etmektedir. Diğer taraftan bütün türlerin kaba yem kalitesi hayvan sağlığı ile hayvansal ürünlerin verim ve kalitesi bakımından yeterli düzeyde olmuştur.

Anahtar kelimeler: *Brassica*, Çeşit, Kaba yem, Kalite.

Forage Quality of Different *Brassica* Species

Abstract: Alternative forage sources play a significant role in closing the quality forage deficit in Türkiye. Currently, the amount of forage obtained from forage crop production and pasturelands in Türkiye meets only about 35% of the total roughage requirement of the existing livestock population. This study aimed to determine the forage quality of different *Brassica* species (forage turnip, rapeseed, and canola) cultivated in Türkiye. The study material consisted of 9 winter *Brassica* species. The experiment was established in November 2023 at the Bilecik Şeyh Edebali University Agricultural Research and Application Area, based on a Randomized Complete Block Design. Harvesting was carried out at 50% flowering stage of the plants. In the samples, crude protein (CP), acid detergent fiber (ADF), neutral detergent fiber (NDF), relative feed value (RFV), potassium (K), phosphorus (P), calcium (Ca), magnesium (Mg), condensed tannin (CT), total phenolic (TP), total flavonoid (TF), and radical scavenging activity (DPPH) contents were determined. The highest crude protein content was found in the forage turnip cultivar Lenox (20.22%), while the lowest was observed in the cultivar Luciano (14.08%). The highest RFV values, statistically in the same group, were observed in Lenox (134.69), PR44W29 (128.05), and Exception (126.85), whereas the lowest was in Luciano (104.37). The K, P, Ca, and Mg contents of the species ranged between 2.39–2.78%, 0.51–0.61%, 0.77–1.09%, and 0.24–0.41%, respectively. The highest condensed tannin content was found in the statistically similar cultivars Lenox (1.42%) and Linus (1.30%), while the lowest was in Expower (0.72%). At the conclusion of the study investigating the forage quality of different *Brassica* species, the cultivars Lenox, Linus, and Exception stood out. This highlights the importance of these cultivars for use as forage. On the other hand, the forage quality of all species were found to be at a sufficient level in terms of animal health and the yield and quality of animal products.

Keywords: *Brassica*, Variety, Roughage, Quality.

***Sorumlu yazar (Corresponding author):** [1]Bilecik Şeyh Edebali University, Faculty of Agriculture and Nautural Science, Department of Filed Crop, 112000. Bilecik, Türkiye,
E mail: erdem.gulumser@bilecik.edu.tr (E. GÜLÜMSER)

Uğur SÖYLER https://orcid.org/0009-0003-3728-3702
Serra Nur ÖZTÜRK https://orcid.org/0009-0004-1547-8506
İlknur YILIDIRM https://orcid.org/0000-0002-2284-6205
Erdem GÜLÜMSER https://orcid.org/0000-0001-6291-3831

Gönderi: 29 Mayıs 2025 **Received:** May 29, 2025
Kabul: 02 Temmuz 2025 **Accepted:** July 02, 2025
Yayınlanma: 15 Temmuz 2025 **Published:** July 15, 20245

Cite as: Söyler U, Öztürk, SN, Yıldırım İ, Gülümser, E. 2025. Forage quality of different *Brassica* species. BSJ Eng Sci, 8(4): 1212-1217.

1. Giriş

Türkiye'de toplam hayvan varlığı yeterli olmasına rağmen, hayvanlardan elde edilen ürünlerin verim ve kalitesi arzu edilen seviyelerde değildir. Bu durumun temel nedenlerinden biri, hayvanların yeterli düzeyde kaliteli kaba yemle beslenememesidir. Türkiye'de yem bitkileri ekiliş alanı 2,75 milyon hektar olup, bu değer toplam tarım alanının yaklaşık %14'dür. Sürdürülebilir bir tarım sistemi için bu oran oldukça yetersizdir. Nitekim mevcut hayvan varlığımızın yıllık yeşil ot olarak kaba yem gereksinimi 351,3 milyon ton iken, yem bitkileri tarımı ile çayır-mera alanlarından üretilen ot

This work is licensed (CC BY-NC 4.0) under Creative Commons Attribution 4.0 International License

miktarı ise 116,2 milyon ton dur. Bu değer ihtiyacın ancak %33'ünü karşılamaktadır. (Acar vd., 2025). Bu açığı kapatmak amacıyla, alternatif yem kaynaklarının rasyonlara dâhil edilmesi yadsınamaz bir gerçektir.

Brassicaceae familyası, halk arasında turpgiller, hardalgiller ya da lahanagiller olarak bilinir. Bu familyaya ait bitkiler genellikle tek ya da çok yıllık otsu yapıya sahiptirler. Ağırlıklı olarak serin ve ılıman iklimlerde yetişen bu familya, yaklaşık 40 cinse ve 200 tür civarına ev sahipliği yapmaktadır. Öne çıkan cinsler arasında *Brassica*, *Raphanus*, *Lepidium*, *Isatis* ve *Capsella* yer almaktadır. Bu gruplar içerisinde özellikle *Brassic*a cinsi, hem insan hem de hayvan beslenmesinde önemli yer tutmaktadır. Lahana, kolza ve şalgam gibi ekonomik değeri yüksek bitkiler bu cinsin üyeleridir. Türkiye'de toplamda 9 farklı *Brassica* tür yetişmektedir (Sefalı, 2019; Tan, 2024).

Tarımsal açıdan incelendiğinde 3 önemli *Brassica* cinsi bulunmaktadır. Bunlardan birincisi; yem şalgamı (*Brassica rapa* L.) olup, genellikle kökü veya yaprakları için yetiştirilmektedir (Copur Dogrusoz vd., 2019). Kök bitkisi olmalarına rağmen, seleksiyonları yem bitkisi olarak da değerlendirilmektedir. İkinci sırada kanola/kolza (*Brassica napus subsp*. oleifera) grubu yer alırken, bu tür tek yıllık ve otsu yapıdadır. Kanolanın geniş ve bol yapraklı olan tipleri yemlik olarak kullanılmaktadır. Üçüncü ve son sırada ise lahana grubu yer almaktadır. Lahana grubu kendi içerisinde sebze olarak (*Brassica oleraceae*), yem bitkisi olarak (Brüksel lahanası benzerleri) ve kabak gövdeli olarak kullanılan lahanalar olarak üç gruba ayrılmaktadır (Tan, 2024).

Brassica türlerinin besin içeriği; yumru ile toprak üstü kısımların oranına, yetiştirilen varyeteye ve özellikle sap ile yaprak gibi aksamlarının durumuna bağlı olarak değişkenlik gösterir. Bu bitkiler genellikle düşük kuru madde içeriğine sahip olsalar da, birçok buğdaygil yem bitkisine kıyasla birim alanda daha yüksek kuru madde verimi sağlayabilirler. Yapraklarında ham protein oranı kuru madde üzerinden %15-20 arasında değişirken, kök kısmında bu oran %6-15 civarındadır. Yüksek su ve şeker içerikleri nedeniyle hayvanlar tarafından iştahla tüketilmekledir. Yapraklı ve saplı formlarıyla bilinen kolza ve lahana gibi türlerde ise yaprakların ham protein oranı genellikle %20-25. gövde kısmında ise yaklaşık %10 düzeyindedir (Tan ve Temel, 2012).

Yukarıdaki açıklamalar ışığı altında, bu çalışmada farklı amaçlar için yetiştirilen *Brassica* türlerinin kaba yem kalitesinin belirlenmesi amaçlanmıştır.

2. Materyal ve Yöntem

Çalışmada materyal olarak farklı kurum ve kuruluşlardan temin edilen 9 adet kışlık *Brassica* türü kullanılmıştır (Tablo 1). Çeşitler 2023 Kasım ayında Bilecik Şeyh Edebali Üniversitesi Tarımsal Uygulama ve Araştırma alanında bulunan araziye ekilmiştir.

Deneme alanının yürütüldüğü alanların toprak yapısı killi-tınlı olup, kireç (%11,45) ve organik madde içeriği (%2,02) orta değerde olmuştur. Deneme alanının potasyum ve fosfor içerikleri ise sırasıyla 1,82 kg/da (az) ve 20,11 kg/da (orta seviyede) olarak belirlenmiştir.

Tablo 1. *Brassica* türlerine ait bazı bilgiler

Çeşit adı	Tür adı	Firma adı
Lenox	Yem şalgamı	Üçler Toh. Gıda Tar. Hay. Tic.ve San. A.Ş.
Luciano	Kolza	KWS Türk Tarım Ticaret A.Ş.
PT264	Kanola/kolza	Pioneer Tohumculuk Dağıtım ve Pazarlama Ltd. Şti
PR44W29	Kolza	Pioneer Tohumculuk Dağıtım ve Pazarlama Ltd. Şti
Caravel	Kanola	Sygenta Tarım San. Ve Tic. A.Ş.
Linus	Kolza	Sygenta Tarım San. Ve Tic. A.Ş.
Nelson	Kolza	Sygenta Tarım San. Ve Tic. A.Ş.
Expower	Kolza	Monsanto Gıda ve Tarım Tic. Ltd. Şti.
Exception	Kolza	Monsanto Gıda ve Tarım Tic. Ltd. Şti.

Tablo 2. Vejetasyon dönemine ait meteorolojik veriler

Aylar	Sıcaklık (°C)		Yağış (mm)	
	UY	2023-24	UY	2023-24
Kasım	9,1	11,6	37,4	109,7
Aralık	4,7	8,2	55,2	55,8
Ocak	2,5	4,6	50,8	98,8
Şubat	3,8	7,8	42,5	24,8
Mart	6,4	9,2	47,2	33,3
Nisan	11,5	16,0	41,6	8,2
Ort./Top.	6,33	9,56	274,7	330,6

UY= Uzun yıllar.

Çalışmanın yürütüldüğü alanın uzun yıllar ile 2023-2024 yılına ait sıcaklık ve yağış miktarları Tablo 1'de verilmiştir. Uzun yıllar sıcaklık ortalaması 6,33 °C iken, 2023-2024 vejetasyon döneminde 9,56 °C olarak tespit edilmiştir. İlin uzun yıllar ile 2023-2024 yılı toplam yağış miktarları sırasıyla 274,7 ve 330,6 mm olmuştur (Tablo 2).

Denemede parsellerinin sıra arası 20 cm, sıra uzunluğu 4 m olup, parseller ise 6 sıradan oluşmuştur. Çalışmada tohumluk miktarı 1 kg/da olarak hesaplanmıştır. Ekim ile birlikte dekara 8 kg fosfor gelecek şekilde DAP gübresi verilmiştir. Hasat işlemi %50 çiçeklenme döneminde yapılmıştır (Yavuz ve Gülümser, 2022). Deneme süresince tüm parsellere el çapası yapılmış olup, sulama ise yapılmamıştır.

Hasat edilen bitkiler etüvde 60 °C'de kurutulmuş ve daha sonra öğütülerek analize hazır hale getirilmiştir.

Örneklerin ham protein (HPO), asit deterjanda çözünmeyen lif (ADF), nötr deterjanda çözünmeyen lif (NDF), potasyum (K), fosfor (P), kalsiyum (Ca) ve magnezyum (Mg) içerikleri; Foss NIR Systems Model 6500 cihazı ve Win ISI II v1,5 yazılımı aracılığıyla, IC-0904FE kalibrasyon programı kullanılarak analiz edilmiştir. Çalışmada ADF ve NDF değerlerinden faydalanılarak türlere ait nispi yem değeri (NYD) belirlenmiştir. NYD'nin belirlenmesinde Rohweder vd. (1978)'nin belirlemiş oldukları formüller (eşitlik 1-3) kullanılmıştır.

Sindirilebilir Kuru Madde (SKM): (88,9-(0,779*%ADF) (1)

Kuru Madde Tüketimi (KMT): (120/NDF) (2)

Nispi Yem Değeri (NYD): (%SKM * %KMT) /1,29 (3)

Çalışmada örneklerin kondanse tanen (KT) içerikleri (Bate-Smith,1975), toplam fenolik (TFN) içerikleri Singleton ve Rossi (1965), toplam flavonoid (TFL) içerikleri Arvouet-Grand vd. (1994) ve radikal kovucu aktivite (DPPH) içerikleri Faller ve Fialho (2009) yöntemine göre tespit edilmiştir. Çalışmadan elde edilen veriler MSTAT-C programı aracılığıyla tesadüf blokları deneme desenine göre analiz edilmiş ve elde edilen ortalama değerler Duncan testi yardımıyla gruplandırılmıştır. Çeşitler arasındaki desenleri ve ilişkileri belirlemek amacıyla temel bileşen analizi (TBA) ve hiyerarşik kümeleme yöntemleri kullanılmıştır (Azak ve Gülümser, 2025).

3. Bulgular ve Tartışma

Tablo 3'de *Brassica* türlerinin ham protein (HPO), asit deterjanda çözünmeyen lif (ADF), nötr deterjanda çözünmeyen lif (NDF) içerikleri ve nispi yem değerleri (NYD) verilmiştir. Çeşitler arasında tüm özellikler bakımından çok önemli P≤0,01 farklılıkla olmuştur (Tablo 2). En yüksek HPO %20,22 ile yem şalgamı olan Lenox çeşidinde, en düşük ise %14,08 ile Luciano çeşidinde tespit edilmiştir. Kaliteli kaba yemlerde ham protein oranının en az %6 olması gerekmektedir (Şenel, 1986; Tan ve Serin, 1997). Çalışmada tüm *Brassica* türlerinin HPO içerikleri bu değerin üzerinde olmuştur (Tablo 2). Figueroa vd. (2020) farklı *Brassica* türlerinin HPO içeriğini %20,58-22,57 arasında bulmuşlardır. Farklılıklar kullanılan türlerden, ekoloji ve uygulanan kültürel işlemlerden kaynaklanmıştır. En yüksek NYD istatistiksel olarak aynı grupta yer alan Lenox (134,69), PR44W29 (128,05) ve Exception (126,85), en düşük ise 104,37 ile Luciano çeşidinden tespit edilmiştir NYD, yem bitkilerinin pazar değerini belirlemek amacıyla kullanılan ve 6 kalite grubuna ayrılan sayısal bir ölçüttür. Bu ölçüte göre, NYD değeri 151'in üzerindeyse "başlangıç sınıfı", 125-151 arasındaysa "1. sınıf", 103-124 arasında "2. sınıf", 87-102 arasında "3. sınıf", 75-86 arasında "4. sınıf" ve 75'in altında ise "5. sınıf" olarak değerlendirilmektedir (Rohweder vd., 1978). Bu çalışmada türlerin nispi yem değerleri başlangıç ile 2. sınıf kalite seviyeleri arasında yer almıştır (Tablo 3). Tablo 4'de çeşitlerin potasyum (K), fosfor (P), kalsiyum (Ca) ve magnezyum (Mg) içerikleri verilmiştir. Tüm makro elementler bakımından çeşitler arasında çok önemli P≤0,01 farklılıklar olmuştur. (Tablo 4). *Brassica* türlerinin K, P, Ca ve Mg içerikleri sırasıyla %2,39-2,78. %0,51-0,61. %0,77-1,09 ve %0,24-0,41 arasında olmuştur. Fosfor ve kalsiyumun yem içerisinde yüksek veya düşük olması raşitizm hastalığının ortaya çıkmasına neden olabilmektedir. Diğer taraftan potasyum vücudun asit-baz dengesinin sağlanmasına yardımcı olurken, magnezyum ise vücuttaki kemik yapısını güçlendirmektedir (Dua ve Care, 1999; Başbağ vd., 2011; Gürsoy ve Macit, 2017). Tajeda vd. (2015) kaliteli yemlerde K içeriğinin %0,8. P içeriğinin %0,21. Ca içeriğinin %0,18-0,44 ve Mg içeriğinin ise %0,4-0,10 arasında olması gerektiğini bildirmişlerdir. Tüm *Brassica* türlerinin makro besin içerikleri belirtilen değerlerin üzerinde olmuştur (Tablo 2).

Brassica türlerinde belirlenen sekonder metabolit içerikleri Tablo 5'de verilmiştir. Buna göre tüm biyoaktif bileşenler arasında istatistiksel açıdan %1 ihtimal seviyesinde farklılık olmuştur. En yüksek kondanse tanen aynı istatistiksel grupta yer alan Lenox (%1,42) ve Linus (%1,30), en düşük ise %0,72 ile Expower çeşidinde tespit edilmiştir. Kondanse tanenler rumende bazı hidrojen üreten protozoolar ve doğrudan hidrojen kullanan metan üretici organizmaları engelleyerek hayvansal kaynaklı sera gazı salınımını azaltmaktadır (Öztürk ve Gülümser, 2023). Hayvan sağlığı ve kalitesi açısından yem bitkilerinde kondanse tanen içeriğinin en fazla %3,0 olması gerekmektedir (Barry, 1987).

Tablo 3. *Brassica* türlerinin bazı kalite özellikleri

Çeşitler	HPO**	ADF**	NDF**	NYD**
Lenox	20,22^{a}	30,80^{f}	44,85^{e}	134,69^{a}
Luciano	14,08^{f}	39,44^{a}	51,85^{a}	104,37^{e}
PT264	18,37^{b}	36,26^{b}	49,11^{bc}	114,99^{d}
PR44W29	16,42^{de}	30,83^{f}	47,19^{cd}	128,05^{ab}
Caravel	15,91^{e}	34,91^{bcd}	49,22^{bc}	116,63^{d}
Linus	18,23^{bc}	33,39^{de}	50,67^{ab}	115,42^{d}
Nelson	18,12^{bc}	31,93^{ef}	49,06^{bc}	121,39^{bcd}
Expower	18,69^{b}	35,34^{bc}	47,98^{cd}	119,18^{cd}
Exception	17,12^{cd}	33,62^{cde}	45,99^{de}	126,85^{abc}
Ortalama	17,46	34,06	48,44	120,17

**: P<0,01. Aynı sütunda aynı harfle gösterilen ortalamalar arasında fark yoktur (P<0,05). HPO: Ham protein oranı (%), ADF: Asit deterjanda çözünmeyen lif (%), NDF: Nötr deterjanda çözünmeyen lif (%), NYD: Nispi yem değeri.

Tablo 4. *Brassica* türlerinin bazı makro besin içerikleri

Çeşitler	K**	P**	Ca**	Mg**
Lenox	2,61^{b}	0,55^{e}	1,02^{b}	0,36^{b}
Luciano	2,53^{c}	0,51^{g}	0,77^{f}	0,31^{c}
PT264	2,62^{b}	0,56^{de}	0,86^{e}	0,24^{d}
PR44W29	2,54^{c}	0,52^{f}	0,94^{cd}	0,34^{b}
Caravel	2,54^{c}	0,57^{bc}	0,85$_{e}$	0,34^{b}
Linus	2,78^{a}	0,61^{a}	0,99^{bc}	0,36^{b}
Nelson	2,48^{c}	0,56^{cd}	1,09^{a}	0,41^{a}
Expower	2,49^{c}	0,58^{b}	0,77^{f}	0,40^{a}
Exception	2,39^{d}	0,58^{b}	0,93^{d}	0,39^{a}
Ortalama	*2,55*	*0,56*	*0,91*	*0,35*

**: P<0,01. Aynı sütunda aynı harfle gösterilen ortalamalar arasında fark yoktur (P<0,05). K: Potasyum (%), P: Fosfor (%), Ca: Kalsiyum (%), Mg: Magnezyum (%).

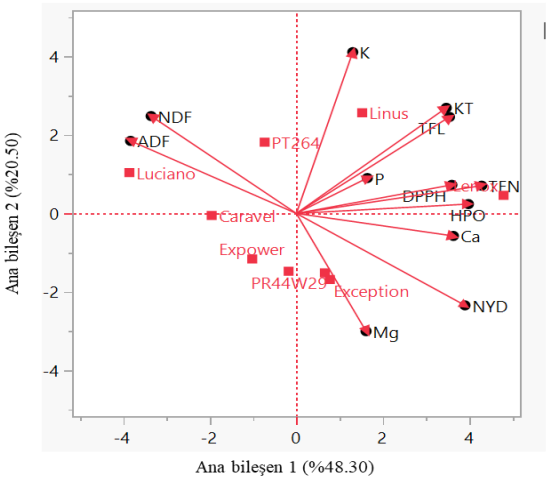
Çalışmada tüm *Brassica* türlerinin kondanse tanen içeriği bu seviyenin altında olmuştur. Bitkilerde bulunan toplam fenolik, toplam flavonoid ve radikal kovucu aktivite içerikleri tozlaşmaya yardımcı olmak, çevresel stres etmenlerine karşı direnç oluşturmak, hücre büyümesini düzenlemek ile insan ve hayvansal hastalıkların önlenmesinde yardımcı olmak gibi farklı rollere sahiptirler (Kumar ve Pandey, 2013; Xiao vd., 2013; Zhan vd., 2017). Ayrıca sekonder metabolitler hayvansal ürünlerin verimini ve kalitesini de arttırmaktadır. Söz konusu bileşikler, hayvanların rumen morfolojisinin sağlıklı bir şekilde işleyişine katkı sağlar ve farklı stres koşullarına karşı direnç göstermelerine yardımcı olur (O'Connell ve Fox, 2001; Kuhnen vd., 2014). Diğer taraftan bitkilerde bulunan sekonder metabolitler doğal herbisit olarak da değerlendirilmektedir. Türlerin toplam fenolik, toplam flavonoid ve radikal kovucu aktivite içerikleri sırasıyla 5,11-8,93 mg GA/g, 3,20-5,66 mg QE/g ve %27,96-56,98 arasında olmuştur (Tablo 3). Yavuz ve Gulumser (2022) yem şalgamının kondanse tanen içeriğini %2,17. toplam fenolik içeriğini 6,56 mg GA/g ve toplam flavonoid içeriğini 3,48 mg QE/g olarak bulmuşlardır.

Temel bileşenler analizi (TBA) genotiplerdeki toplam varyasyona katkıda bulunan önemli özelliklerin seçilmesinde etkili olmaktadır. TBA, genotiplerin doğal olarak gruplanmasına olanak tanır ve genotipler arasındaki farklılıkların belirlenmesinde hassas bir göstergedir (Adams, 1995; Sing vd., 2020). *Brassica* türlerinin incelenen özellikler arasındaki ilişkiler, TBA grafiği sayesinde (Şekil 1) kolaylıkla ayırt edilebilmektedir. Türlerin yem kalite özellikleri birinci temel bileşenin %48,30. ikinci temel bileşen %20,50 oranında (toplamda %68,80) varyasyonu açıkladığını ortaya koymuştur. Bazı türler farklı özellikler bakımından iyi performans göstermiştir. Örneğin, Lenox ile Linus sekonder metabolitler bamımından, yine Lenox ve Exception çeşitleri ise NYD bakımından ön plana çıkmıştır. Grafik sonuçlarına göre, özellikle Lenox çeşidinin türler arasında değerli olduğu görülmektedir. Söz konusu çeşit hali hazırda yemlik olarak yetiştirilmektedir ve son dönemlerde tarımı gitgide artmaktadır. Ancak, Linus ve Exception çeşitlerinin de yem kalitesi bakımından iyi olduğu tespit edilmiştir. Bu durum yağlık olarak yetiştirilen çeşitlerin kaba yem olarak değerlendirilmesi açısından önem teşkil etmektedir.

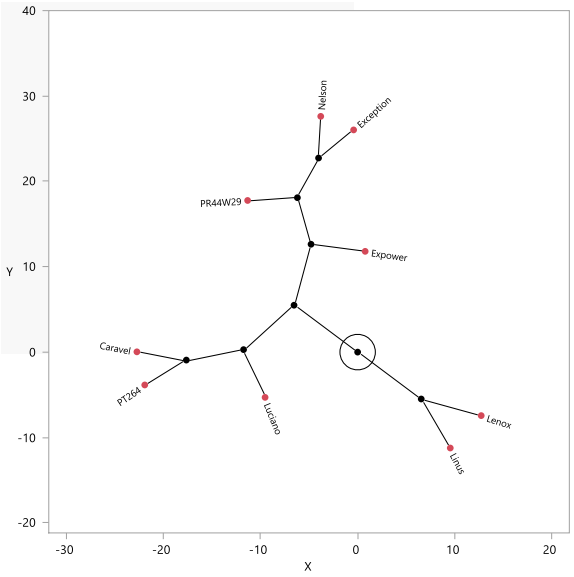
Tablo 5. *Brassica* türlerinin sekonder metabolit içerikleri

Çeşitler	KT**	TFN**	TFL**	DPPH**
Lenox	1,42^{a}	8,93^{a}	5,66^{a}	56,98^{a}
Luciano	0,82^{de}	5,54^{de}	3,80^{bc}	40,84^{d}
PT264	1,15^{bc}	6,56^{cd}	3,94^{bc}	39,51^{d}
PR44W29	0,86^{de}	6,06^{cd}	3,61^{bc}	38,67^{d}
	1,08^{c}	5,11^{e}	3,53^{bc}	27,96^{e}
Linus	1,30^{ab}	6,73^{b}	4,98^{ab}	49,02^{b}
Nelson	0,95^{cd}	6,66^{b}	3,20^{c}	45,30^{bc}
Expower	0,72^{e}	5,15^{e}	3,64^{bc}	45,72bc
Exception	1,02^{cd}	6,94^{b}	4,08^{b}	42,14^{cd}
Ortalama	*1,04*	*640*	*4,05*	*42,91*

**: P<0,01. Aynı sütunda aynı harfle gösterilen ortalamalar arasında fark yoktur (P<0,05). KT: Kondasne tanen (%), TFN: Toplam fenolik (mg G/g), TFL: Toplam flavonoid (mg QE/g), DPPH: Radikal kovucu aktivite (%).



Şekil 1. Kalite özelliklerine ait temel bileşenler analizi.
HPO= Ham protein oranı (%), ADF= Asit deterjanda çözünmeyen lif (%), NDF= Nötr deterjanda çözünmeyen lif (%), K= Potasyum (%), P= Fosfor (%), Ca= Kalsiyum (%), Mg= Magnezyum (%), KT= Kondasne tanen (%), TFN= Toplam fenolik (mg GA/g), TFL= Toplam flavonoid (mg QE/g), DPPH= Radikal kovucu aktivite (%).



Şekil 2. Türlerin hiyerarşik kümeleme analizi.
HPO= Ham protein oranı (%), ADF= Asit deterjanda çözünmeyen lif (%), NDF= Nötr deterjanda çözünmeyen lif (%), K= Potasyum (%), P= Fosfor (%),Ca= Kalsiyum (%), Mg= Magnezyum (%), KT= Kondasne tanen (%), TFN= Toplam fenolik (mg GA/g), TFL= Toplam flavonoid (mg QE/g), DPPH= Radikal kovucu aktivite (%).

Hiyerarşik kümeleme analizi, bir veri matrisinin satır ve sütunlarındaki verileri, hiyerarşik kümeleme yapısıyla birlikte gösteren iki boyutlu bir veri görselleştirme yöntemidir. Gruplar arasındaki farklar ve benzerlikler kümeleme analiziyle belirlenebilmektedir (Wilkinson ve Friendly, 2009; Barua vd., 2022). Şekil 2'de kümeleme analizi verilmiştir. *Brassica* türleri 3 gruba ayrılmıştır. Birinci grupta PR44W29. Nelson, Exception ve Expower, ikinci grupta Caravel, PT264 ve Luciano, üçüncü grupta ise; Lenox ve Linus yer almıştır.

4. Sonuç

Bu çalışmada farklı *Brassica* türlerinin kaba yem kalite özellikleri incelenmiş ve türler arasında söz konusu özellikleri bakımından farklılıklar tespit edilmiştir. Özellikle çeşitler arasında Linux ön plana çıkarken, Linus ve Exception çeşitleri de kaba yem kalitesi bakımından iyi performasn sergilemiştir. Bu durum söz konusu çeşitlerin kaba yem olarak değerlendirilme imkânlarının araştırılması açısından önem ihtiva etmektedir. Diğer taraftan tüm *Brassica* türlerinin de kalite özellikleri hayvan sağlığı ile hayvansal ürünleri verim ve kalitesi bakımından yeterli düzeyde olmuştur. Diğer taraftan *Brassica* türleri içermiş oldukları biyoaktif bileşenlerce hayvanlara zarar verebilmektedir. Bu nedenle türlerin bileşenlerinin ayrıntılı olarak incelenmesi ve hayvan beslemede kullanılırken çok dikkatli olunması gerekmektedir. Nitekim söz konusu bileşikler hayvanlarda ölüme kadar gidebilecek problemler ortaya çıkarabilmektedir.

Katkı Oranı Beyanı

Yazarların katkı yüzdeleri aşağıda verilmiştir. Yazarlar makaleyi incelemiş ve onaylamıştır.

	U.S.	S.N.Ö.	İ.Y.	E.G.
K	20	20	20	40
T	20	20	20	40
Y	20	20	20	40
VTI	20	20	20	40
VAY	10	10	10	70
KT	20	20	20	40
YZ	10	10	10	70
KI	10	10	10	70
GR	10	10	10	70
PY	20	20	20	40
FA	10	10	10	70

K= kavram, T= tasarım, Y= yönetim, VTI= veri toplama ve/veya işleme, VAY= veri analizi ve/veya yorumlama, KT= kaynak tarama, YZ= Yazım, KI= kritik inceleme, GR= gönderim ve revizyon, PY= proje yönetimi, FA= fon alımı.

Çatışma Beyanı

Yazarlar bu çalışmada hiçbir çıkar ilişkisi olmadığını beyan etmektedirler.

Etik Onay Beyanı

Bu araştırmada hayvanlar ve insanlar üzerinde herhangi bir çalışma yapılmadığı için etik kurul onayı alınmamıştır.

Kaynaklar

Acar Z, Ayan İ, Önal Aşcı Ö, Mut H, Başaran U, Gülümser E, Can M, Kaymak Bayram G. 2025. Yem bitkileri tarımında mevcut durum ve sürdürülebilirlik. Türkiye Ziraat Mühendisliği X. Teknik Kongresi Bildiriler Kitabı, Ankara, 1. Cilt, pp: 547-564.

Adams MW. 1995. An estimation of homogeneity in crop plants, with special reference to genetic vulnerability in the dry bean, Phaseolus vulgaris L. Euphytica, 26: 665-679.

Arvouet-Grand A, Vennat B, Pourrat A, Legret P. 1994. Standardisation d'un extrait de propolis et identification des principaux constituants. J Pharm Belg, 49: 462-468.

Azak M, Gülümser E. 2025. Silage yield and quality of different grass pea (*Lathyrus sativus* L.) genotypes. Turk J Agric, 49(2): 272-282.

Barry TN. 1987. Secondary compounds of forages. In: Hacker JB, Ternouth JH (eds), Nutrition of Herbivores. Academic Press, Sydney, pp: 91-120.

Başbağ M, Çaçan E, Sayar MS. 2011. Güneydoğu Anadolu Bölgesi doğal alanlarından toplanan bazı fiğ türlerinin ot kalitesi özelliklerinin belirlenmesi. Uluslararası Katılımlı I. Ali Numan Kıraç Tarım Kongresi ve Fuarı, 27-30 Nisan, Eskişehir, Türkiye, pp: 143-151.

Bate-Smith EC. 1975. Phytochemistry of proanthocyanidins. Phytochemistry, 14: 1107-1113.

Barua H, Saha SR, Ivy NA, Rasul G, Islam AA. 2022. Genetic divergence of guava (Psidium guajava L.) genotypes in Bangladesh. SAARC J Agric, 20(1): 15-28.

Copur Dogrusoz M, Mut H, Basaran U, Gulumser E. 2019. Performance of legumes-turnip mixtures with different seed

rates. Turk J Agric For, 7(1): 81-86.

Dua K, Care AD. 1999. The role of phosphate on the rates of mineral absorption from the forestomach of sheep. Vet J, 157: 51-55.

Faller ALK, Fialho E. 2009. The antioxidant capacity and polyphenol content of organic and conventional retail vegetables after domestic cooking. Int Food Res, 42(1): 210-215.

Figueroa J, Del Río K, Romero F, Keim JP, Gandarillas M. 2020. Acceptability, preferences, and palatability of diets containing summer and winter brassica forage in growing pigs: A pilot study. Animals, 10(6): 1080.

Gürsoy E, Macit E. 2017. Erzurum ili çayır ve meralarında doğal olarak yetişen bazı baklagil ve buğdaygil yem bitkilerinin mineral madde kompozisyonlarının belirlenmesi. Alinteri J Agric Sci, 32(1): 1-9.

Kuhnen S, Moacyr JR, Mayer JK, Navarro BB, Trevisan R, Honorato LA, Maraschin M, Pinheiro Machado Filho LC. 2014. Phenolic content and ferric reducing-antioxidant power of cow's milk produced in different pasture-based production systems in southern Brazil. J Sci Food Agric, 94: 3110-3117.

Kumar S, Pandey AK. 2013. Chemistry and biological activities of flavonoids: an overview. Sci World J, 2013: 162750.

O'Connell JE, Fox PF. 2001. Significance and applications of phenolic compounds in the production and quality of milk and dairy products: A review. Int Dairy J, 11: 103-120.

Öztürk YE, Gülümser E. 2023. Forage yield, nutritional value and phytotrepic traits of hops (Humulus lupulus L.). ISPEC J Agric Sci, 7(2): 350-358.

Rohweder DA, Barnes RF, Jorgensen N. 1978. Proposed hay grading standards based on laboratory analyses for evaluating quality. Anim Sci J, 47(3): 747-759.

Sefalı A. 2019. Türkiye'de bulunan Brassica türlerinin biyolojisi ve ekonomik önemi. Bitkilerin Ekonomik Önemine Bir Bakış, İksad Yayınevi, Ankara, pp: 4-40.

Singh KS, Suneetha Y, Sandeep Raja D, Srinivas T. 2020. Principal component analysis for yield and quality traits of coloured rice (Oryza sativa L.). J Pharm Innov, 9(7): 456-462.

Singleton VL, Rossi JA. 1965. Colorimetry of total phenolics with phosphomolybdic-phosphotungstic acid reagents. Am J Enol Viticult, 16(3): 144-158.

Şenel S. 1986. Hayvan Besleme. İstanbul Üniversitesi, Veteriner Fakültesi Yayınları, No: 3210. İstanbul, Türkiye, pp: 15-46.

Tan M. 2024. Yem şalgamı, yemlik lahana ve yemlik kolza (Brassica sp.). Alternatif Yem Kaynakları Kitabı, Nobel Yayınevi, Ankara, 1st basım, pp: 95-106.

Tan M, Temel S. 2012. Alternatif Yem Bitkileri. Atatürk Üniversitesi, Ziraat Fakültesi, Ders Yayınları No: 246. Erzurum, Türkiye, pp:15-75.

Tan M, Serin Y. 1997. Kaba yem olarak kullanılan tahılların besleme değerine yaklaşımlar. AUZFD, 28: 130-137.

Tejeda R, Mcdowell LR, Martin FG, Concard JH. 1985. Mineral element analyses of various tropical forages in Guatemala and their relationship to soil concentrations. Nutr Rep Int, 8: 71.

Xiao J, Kai G, Yamamoto K, Chen X. 2013. Advance in dietary polyphenols as α-glucosidases inhibitors: a review on structure–activity relationship aspect. Crit Rev Food Sci Nutr, 53(8): 818-836.

Wilkinson L, Friendly M. 2009. The history of the cluster heat map. Am Stat, 63(2): 179-184.

Yavuz K, Gülümser E. 2022. Evaluation of forage turnip + cereal mixtures for forage yield and quality traits. Turk J Field Crops, 27(1): 26-32.

Zhan J, Liu M, Su X, Zhan K, Zhang C, Zhao G. 2017. Effects of alfalfa flavonoids on the production performance, immune system, and ruminal fermentation of dairy cows. Asian-Australas J Anim Sci, 30(10): 1416-1424.

Black Sea Journal of Engineering and Science
doi: 10.34248/bsengineering.1712852

Open Access Journal
e-ISSN: 2619 – 8991

Research Article
Volume 8 - Issue 4: 1218-1234 / July 2025

THERMODYNAMIC AND EXERGOECONOMIC PERFORMANCE EVALUATION OF SINGLE AND DOUBLE-FLASH STEAM CYCLES WITH HEAT EXCHANGER INTEGRATION: EXERGETIC AND ECONOMIC OPTIMIZATION

Ünsal AYBEK[1]*, Bekir DOĞAN[2]

[1]*Tokat Gaziosmanpasa University, Tokat Vocational School, Department of Electricity and Energy, 60000, Tokat, Türkiye*
[2]*Tokat Gaziosmanpasa University, Tokat Vocational School, Department of Machinery and Metal Technologies, 60000, Tokat, Türkiye*

Abstract: Liquid-dominated geothermal energy sources with temperatures above 150 °C provide suitable conditions for flash steam production due to their high pressure. Geothermal energy is considered as an environmentally friendly and sustainable renewable energy source due to its minimal greenhouse gas emissions compared to fossil fuel-based energy sources. Improving the thermodynamic and economic performance of these energy systems is crucial, particularly for increasing overall system efficiency and long-term sustainability. In this study, mathematical models of the proposed single and double-flash steam cycles were created using EES software and the performances of these systems were compared. The exergy efficiency and sum unit cost of the product (SUCP) of the proposed systems were considered as objective functions. The mass flow rate of the geothermal fluid directed to the heat exchanger and the flashing pressures in the high and low pressure regions were selected as the decision variables. The optimum design conditions were determined as a result of multivariate, single-objective optimizations performed with the genetic algorithm method. The results show that the optimum points obtained from exergetic and economic optimizations are quite close to each other. As a result of the exergetic optimization of the single-flash steam cycle, energy efficiency, exergy efficiency, and SUCP was calculated as 10.52%, 44.4%, and 4.3 $/GJ, respectively. The electrical power output produced by the system was determined as 11,422.5 kW. In addition, 32.08% of the total exergy entering the system was destroyed due to irreversibility, while 23.52% was discharged as exergy losses. In the double-flash steam cycle, energy efficiency, exergy efficiency, and SUCP was determined as 12.59%, 53.1%, and 3.98 $/GJ, respectively. The electrical power output produced by the system was determined as 13,660.5 kW. Also, 35.92% of the total exergy entering the system was destroyed due to irreversibility, while 10.98% was discharged as exergy losses. Exergetic optimization results indicate that the double-flash steam cycle generated 2,238 kW more power than the single-flash steam cycle, resulting in a 19.6% increased in exergy efficiency and a 7.4% decreased in SUCP. The findings show that careful optimization of the proposed design parameters in flash steam cycle systems has a significant impact on overall system performance. In addition, the waste energy released at the end of the process can be recovered and utilized as a heat source in applications such as district heating, greenhouse heating, food drying, and low-temperature Organic Rankine Cycle systems, thereby enhancing the overall energy recovery potential of the system.

Keywords: Geothermal energy, Flash steam cycle, Genetic algorithm, Optimization

***Corresponding author:** Tokat Gaziosmanpasa University, Tokat Vocational School, Department of Electricity and Energy, 60000 Tokat, Türkiye
E mail: unsal.aybek@gop.edu.tr (U. AYBEK)
Ünsal AYBEK https://orcid.org/0000-0003-3573-9385
Bekir DOĞAN https://orcid.org/0000-0002-8986-7174

Received: June 03, 2025
Accepted: July 02, 2025
Published: July 15, 2025

Cite as: Aybek U, Dogan B. 2025. Thermodynamic and exergoeconomic performance evaluation of single and double-flash steam cycles with heat exchanger integration: Exergetic and economic optimization. BSJ Eng Sci, 8(4): 1218-1234.

1. Introduction

Electricity is critical to driving rapid economic growth, placing significant pressure on energy infrastructure to meet the escalating demand as populations expand in developing countries. CO_2 emissions are primarily driven by the energy sector, where widespread use of fossil fuels to electricity and heat generation play a major role in enhancing atmospheric carbon levels (Nkinyam et al., 2025). According to research, global electricity consumption is expected to double by 2050. However, if the dependence on fossil fuels in global energy production continues at this level, CO_2 emissions will continue to increase at this rate, exacerbating the greenhouse effect (Global Energy Perspective, 2024). Renewable energy is recognized as the most pivotal component of clean energy systems. Applications of these energy sources contribute to reducing environmental degradation and waste production, while simultaneously meeting the requirements of social and economic sustainable development. This makes it necessary to develop efficient and low-carbon renewable energy systems that can replace fossil fuels and mitigate climate change (Samatar et al., 2025; Shang et al., 2024).

A geothermal power plant can be thought of as a further development of a traditional steam power plant, which uses special purpose equipment and systems to absorb

This work is licensed (CC BY-NC 4.0) under Creative Commons Attribution 4.0 International License

energy from hot fluid near the Earth's surface or buried deep in the crust. This energy is being converted to electricity and, if required, heat (Belyakov, 2019). Despite significant challenges such as high capital investment requirements and performance limitations associated with suboptimal resource utilization, geothermal energy continues to be a promising renewable energy source (Kariuki et al., 2025). More than 32 countries around the world actively use geothermal resources and the installed capacity of geothermal production reached 16,318 MWe by the end of 2023. (Gutiérrez-Negrín, 2024). This energy is an environmentally friendly and sustainable renewable energy source (Kariuki et al., 2025). Recent studies have shown that CO2-based geothermal technologies offer promising advantages in renewable energy production, while simultaneously serving as a means of carbon dioxide sequestration thereby reducing overall greenhouse gas emissions (Evangeline and Darwin, 2025). Geothermal energy has some distinct advantages such as continuous 24-hours availability, independence from day/night cycle and weather conditions, a high-capacity factor that brings stability to the grid, and requiring a small land footprint compared to the wind and solar energy. Electricity generated from geothermal plants can not only meet the rapidly growing energy needs of megacities but also contribute to long-term global energy supply strategies (Vargas et al., 2022). These factors position geothermal energy systems as an important component in the transition to low-carbon energy systems and climate change mitigation strategies (Evangeline and Darwin, 2025).

Geothermal power plants are categorized into three different types: flash steam, binary Organic Rankine Cycle (ORC), and dry steam. Building these plants depends on the geothermal resource which is generally classified based on enthalpy level of the geothermal resource into low enthalpy, medium enthalpy, or high enthalpy (El Haj Assad et al., 2017). Approximately 37% of the installed geothermal power units are flash type systems, followed by binary cycle units based on ORC, which accounts for 25.1% of the total installed capacity (Gutiérrez-Negrín, 2024).

The exergy and energy analysis methods allow collection of information about the quality and performance of the energy that is converted into geothermal power systems and estimating the degree of exergy destruction for each major component of a geothermal power plant. Recently, exergoeconomic analysis has been applied by many researchers to analyze and enhance the performance of energy conversion systems (Shamoushaki et al., 2021; Tian et al., 2020; Zhao and Wang, 2016). The studies presented in the literature focus on plants with different configurations located around the world and aim to improve their performance and energy efficiency. In this context, Unverdi and Cerci (Unverdi and Cerci, 2013) assessed performance of a double-flash geothermal power plant in Aydın, Türkiye, along with major plant components. Rudiyanto et al. examined the efficiency of the Kamojang geothermal power plant in Indonesia using exergy analysis methods. The study findings were used to develop optimization strategies to improve system performance and energy efficiency. They reported that the geothermal power plant operates with an overall efficiency of 35.86% and the highest irreversibility rate is observed at the condenser (Rudiyanto et al., 2017). Shokati et al. examined the performances of double flash and binary-single flash geothermal power plant and concluded that the double-flash system has lower unit cost of produced power (Shokati et al., 2015). Bina et al. (Bina et al., 2018) designed the single and double-flash systems to utilize the Sabalan geothermal fluid and applied an exergoeconomic model for the analysis of the energy, exergy, and economic performances of the cycles. According to the results of the study, the double-flash system has higher exergy and energy efficiencies compared to the single-flash system. Tian et al. (Tian et al., 2020) proposed a cogeneration double flash-binary geothermal power cycle to generate power and cooling. They found that exergetic efficiency and the net electrical power increased approximately 68.11% and 20.59%, respectively and the unit cost of power and cooling decreased around 36.3%. In addition to these results, the highest exergy destruction rate is observed at the condenser. In another study, Colorado-Garrido et al. (Colorado-Garrido et al., 2021) evaluated total exergy destruction of the single and double-flash geothermal power plant in Cerro Prieto, Mexico. The analysis revealed that for the single flash steam cycle the condenser has the greatest exergy destruction rate and for the double-flash steam cycle the low-pressure turbine and condenser have the highest exergy destruction. In another study published by Cao et al. (Cao et al., 2021), the double-flash-binary geothermal system is investigated. They proposed multi-objective optimization of the cycle that caused a 57.78% growth in exergy efficiency and a 62.33% increase in net electrical power. Rudiyanto et al. conducted exergy analysis and optimization of a single-flash geothermal power plants in Dieng, Indonesia. The results show that the exergy value, electricity production, and exergy efficiency are 106,515 kW, 40,680 kW, and 38.19%, respectively and turbine has the highest irreversibility. They also carried out an optimization of this system by adjusting the turbine inlet pressure and concluded that increasing turbine inlet pressure leads to higher irreversibility and a considerable reduction in energy efficiency (Rudiyanto et al., 2021). To improve the efficiency of the geothermal source, Zhang et al. (Zhang et al., 2022) proposed an innovative absorption power cycle based on a parallel double-effect configuration using lithium bromide-water solution and compared with the conventional absorption power cycle. They reported that the proposed system can improve the exergy efficiency by 12.31% and increase the net power output by 41.3%, while simultaneously decreasing the total product unit cost by 10.12%. This

performance increase comes with only a slight increase of 1.99% in the total product unit environment impact compared with the conventional absorption power cycle.

In previous study, Aybek and Doğan developed two different configuration of a single-flash steam cycle incorporating a heat exchanger to improve overall system performance. In the conventional cycle, the saturated liquid separated in the separator is directly reinjected, which causes considerable exergy destruction. The proposed solution to reduce exergy destruction involves directed a fraction of the geothermal fluid to the expansion valve, while the remainder is directed to a heat exchanger. In the first model, the heat exchanger was positioned prior to the separator with the aim of enhancing the saturated steam fraction, thereby directed a large amount of steam to the turbine. According to the study findings, it was observed that when the heat exchanger was used in this position, the total steam production was lower than in the conventional cycle where the total fluid was directed directly to the expansion valve. In the second model, the heat exchanger was positioned after the separator to superheat the separated saturated steam. In this case, although the mass of steam entering the turbine has decreased somewhat compared to the conventional cycle, its specific enthalpy has increased, leading to an increase in the energy output. As a result, the system performance has been positively affected (Aybek and Dogan, 2025).

In this study, a more advanced configuration was developed based on the second model among the specified configurations, where the heat exchanger was integrated only for the purpose of superheated steam production after the separator. This novel configuration was applied to a double-flash steam cycle and the system performance was comprehensively evaluated in terms of energy, exergy, and exergoeconomic aspects. The exergy efficiency and sum unit cost of the product (SUCP) of the proposed systems were considered as objective functions, optimizations of systems have been carried out using the Genetic Algorithm method in the EES software.

2. Material and Method

2.1. Systems Description

This study investigates geothermal energy conversion cycles based on single and double-flash steam. In proposed systems, saturated liquid obtained from the geothermal source is vaporized by flashing process to generate energy in turbines. Although the primary emphasis is placed on the double-flash steam cycle, the single-flash steam cycle is also examined to facilitate a comparative performance evaluation between two cycle architectures.

The double-flash steam cycle comprises two flash separators operating at different flashing pressures and two turbines that utilize the steam obtained from these separators. System components are categorized into high pressure (HP) and low pressure (LP) regions based on flashing pressure levels. A large fraction of the geothermal fluid enters the system for flash steam production, while the remainder is used as a heat source for superheated steam production in heat exchangers.

The flashing process is carried out by expansion valves that precisely regulate the pressure drop, creating a controlled isoenthalpic expansion within the system. In the HP region, the geothermal fluid is first passed through a HP expansion valve and reduced to a certain flashing pressure, thus enabling flash steam production. The pressure-reduced fluid enters a HP separator where it is separated into saturated vapor and saturated liquid phases. Saturated steam enters the HP heat exchanger where it is converted into superheated steam. This superheated steam rotates a HP turbine, so that mechanical energy is obtained. The steam leaving the HP turbine is condensed in a condenser and then returned to the underground reservoir via the reinjection line.

The saturated liquid leaving the HP separator is passed through a second LP expansion valve to provide additional flash steam at a lower pressure. LP region has the same working principles as the HP region. Unlike the HP region, the fluid leaving the LP heat exchanger is also reinjected.

In the single-flash steam cycle, the geothermal fluid undergoes a single-stage pressure reduction and the steam obtained from a single separator is directed to the turbine to generate electricity. In this system, the saturated liquid separated from the HP separator, along with the geothermal fluid exiting the HP heat exchanger are directed to the reinjection system, without undergoing being any further energy conversion process. In comparison to the double-flash steam cycle, this approache contribute to a simpler system architecture in the single-flash steam cycle. However, in the single-flash steam cycle, the energy potential of the fluid is utilized in a more limited way. The flow diagram of system configurations is shown in Figure 1.

2.2. Energy and Exergy Analysis

Each component in the models is considered as a control volume and conservation of mass and energy is applied to each component. The mass and energy balance for the system components in steady state, where kinetic and potential energy changes are neglected, can be expressed as follows (Farsi and Rosen, 2022) (equations 1 and 2).

$$\sum_{in} \dot{m} = \sum_{out} \dot{m} \tag{1}$$

$$\dot{Q} + \sum_{in} \dot{m} \, . \, h = \dot{W} + \sum_{out} \dot{m} \, . \, h \tag{2}$$

Here $\dot{Q}$, $\dot{W}$, h represent the heat transfer rate, work transfer rate, and specific enthalpy, respectively. This equation states that the total energy entering the control volume is equal to the total energy leaving. Mass and energy balances for all system components are shown in Table 1.

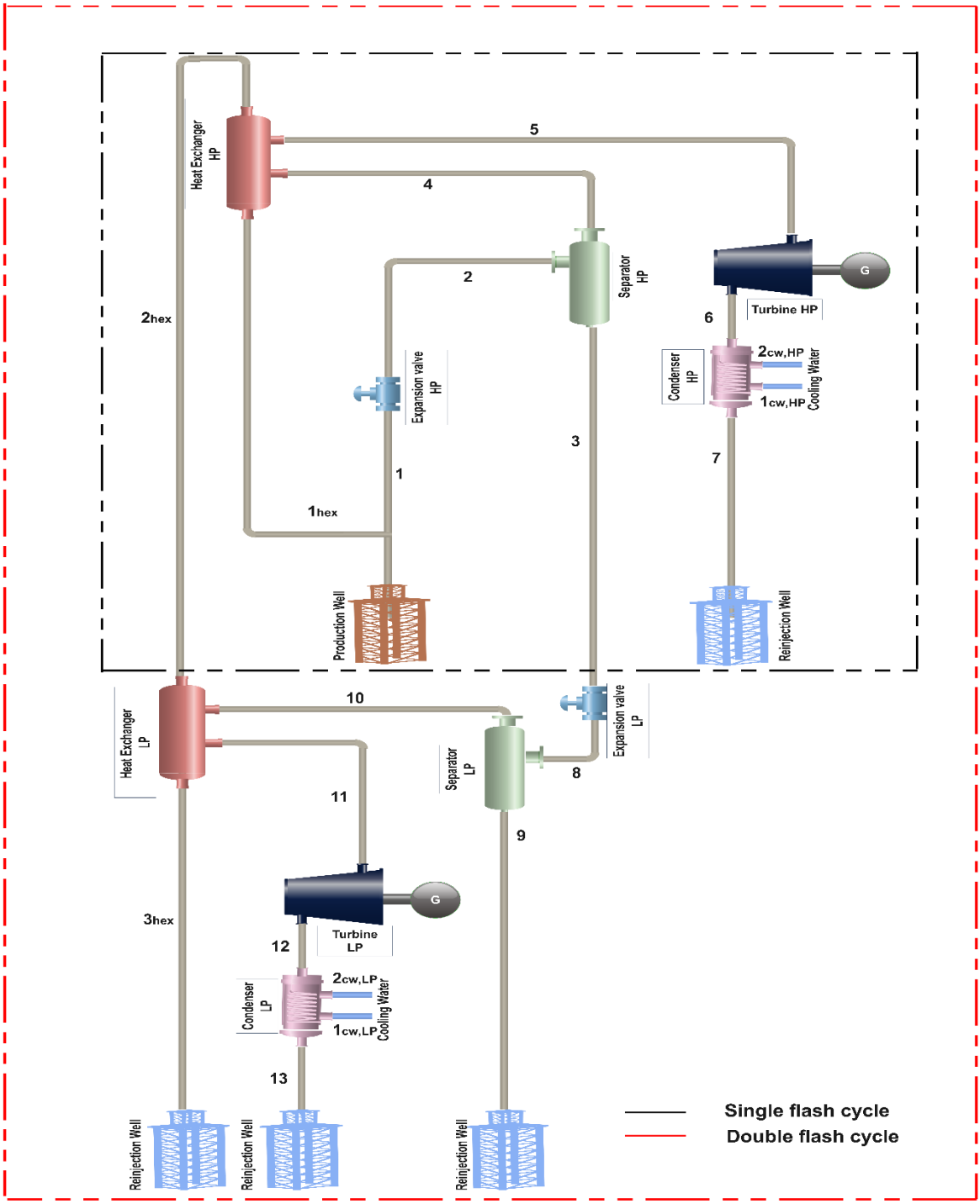


Figure 1. Schematic of single and double-flash steam cycles.

According to the first law of thermodynamics, work and heat are equivalent. However, based on the second law of thermodynamics, exergy measures the change in energy quality by the difference between the irreversibility terms of work and heat (Wang et al., 2012). Exergy is defined as the maximum useful work that can theoretically be achieved as a system passes from the current state to the dead state during the process while interacting only with its environment. Exergy is not conserved like energy and mass as it is destroyed by irreversibilities within the system. Exergy is expressed as the sum of the physical and chemical exergies of a substance in relation to the flow of matter (Chitsaz et al., 2017; Ranjbar et al., 2014) (equation 3).

$$\dot{E}x = \dot{E}x^{ph} + \dot{E}x^{ch} \tag{3}$$

In this equation, $\dot{E}x^{ph}$ and $\dot{E}x^{ch}$ represent physical exergy and chemical exergy, respectively. Since no chemical reactions take place in this study, the total exergy of the system was accepted as physical exergy only. $\dot{E}x^{ph}$ is expressed by equation 4 (Wang et al., 2012):

$$\dot{E}x^{ph} = \dot{m}[(h_i - h_0) - T_0(s_i - s_0)] \quad (4)$$

In this equation, $\dot{m}$ denotes the mass flow rate of the fluid under investigation; h_i and s_i represent the specific enthalpy and specific entropy of the fluid, respectively, while h_0 and s_0 correspond to the specific enthalpy and specific entropy at the reference environmental conditions. T_0 is the reference temperature of the environment. Under steady-state conditions, the exergy balance for a control volume can be written to include the exergy destruction rate as follows (Farsi and Rosen, 2022) (equations 5-7).

$$\dot{E}x^{\dot{Q}} - \dot{E}x^{\dot{W}} + \sum_{in} \dot{m}\,.\,ex - \sum_{out} \dot{m}\,.\,ex - \dot{E}x_D = 0 \quad (5)$$

$$\dot{E}x^{\dot{W}} = \dot{W} \quad (6)$$

$$\dot{E}x^{\dot{Q}} = (1 - \frac{T_0}{T})\dot{Q} \quad (7)$$

Here $\dot{E}x_D$ denotes the exergy destruction rate, while $\dot{E}x^{\dot{W}}$ and $\dot{E}x^{\dot{Q}}$ represent the exergy rates associated with work and heat transfer, respectively. T refers to the absolute temperature at which the heat transfer occurs. The exergy balance for all system components is shown in Table 2.

Table 1. Mass and energy balance equations for components of the systems

Components	Mass Balance	Energy Balance
Source	$\dot{m}_{source} = \dot{m}_{hex} + \dot{m}_1$	$\dot{Q}_{in} = \dot{m}_{source}.h_{source} = \dot{m}_{hex}.h_{1_{hex}} + \dot{m}_1.h_1$ $h_{source} = h_{1_{hex}} = h_1$
Ev HP	$\dot{m}_1 = \dot{m}_2$	$h_1 = h_2$
Sep HP	$\dot{m}_2 = \dot{m}_3 + \dot{m}_4$ $\dot{m}_3 = (1 - x_2).\dot{m}_2$ $\dot{m}_4 = x_2.\dot{m}_2$	$\dot{m}_2.h_2 = \dot{m}_3.h_3 + \dot{m}_4.h_4$
Hex HP	$\dot{m}_5 = \dot{m}_4$	$\dot{m}_5.h_4 = \dot{m}_4.h_4 + \dot{Q}_{hex,HP}$ $\dot{Q}_{hex,HP} = \dot{m}_{hex}\,.(h_{1_{hex}} - h_{2_{hex}})$
Tur HP	$\dot{m}_6 = \dot{m}_5$	$\dot{W}_{tur,HP} = \dot{m}_5.(h_5 - h_6)$ $\eta_{is,tur} = \frac{h_5 - h_6}{h_5 - h_{6s}}$
Cond HP	$\dot{m}_7 = \dot{m}_6$	$\dot{m}_7.h_7 = \dot{m}_6.h_6 - \dot{Q}_{cond,HP}$ $\dot{Q}_{cond,HP} = \dot{m}_{cw,HP}\,.(h_{2_{cw,HP}} - h_{1_{cw,HP}})$
Ev LP	$\dot{m}_8 = \dot{m}_3$	$h_8 = h_3$
Sep LP	$\dot{m}_8 = \dot{m}_9 + \dot{m}_{10}$ $\dot{m}_9 = (1 - x_8).\dot{m}_8$ $\dot{m}_{10} = x_8.\dot{m}_8$	$\dot{m}_8.h_8 = \dot{m}_9.h_9 + \dot{m}_{10}.h_{10}$
Hex LP	$\dot{m}_{11} = \dot{m}_{10}$	$\dot{m}_{11}.h_{11} = \dot{m}_{10}.h_{10} + \dot{Q}_{hex,LP}$ $\dot{Q}_{hex,LP} = \dot{m}_{hex}\,.(h_{2_{hex}} - h_{3_{hex}})$
Tur LP	$\dot{m}_{12} = \dot{m}_{11}$	$\dot{W}_{tur,LP} = \dot{m}_{11}.(h_{11} - h_{12})$ $\eta_{is,tur} = \frac{h_{11} - h_{12}}{h_{11} - h_{12s}}$
Cond LP	$\dot{m}_{13} = \dot{m}_{12}$	$\dot{m}_{13}.h_{13} = \dot{m}_{12}.h_{12} - \dot{Q}_{cond,LP}$ $\dot{Q}_{cond,LP} = \dot{m}_{cw,LP}\,.(h_{2_{cw,LP}} - h_{1_{cw,LP}})$

Cond= Condenser, Ev=Expansion Valve, Hex= Heat Exchanger, HP= High pressure, LP= Low pressure, Sep=Separator, Tur= Turbine.

Table 2. Exergy balance equations for components of the systems

Components	Exergy Balance
Source	$\dot{E}x_{in} = \dot{m}_{source}.ex_{source} = \dot{m}_1.ex_1 + \dot{m}_{hex}.ex_{1_{hex}}$
Ev HP	$\dot{m}_1.ex_1 - \dot{m}_2.ex_2 - \dot{E}x_{D_{ev,HP}} = 0$
Sep HP	$\dot{m}_2.ex_2 - \dot{m}_3.ex_3 - \dot{m}_4.ex_4 - \dot{E}x_{D_{sep,HP}} = 0$
Hex HP	$\dot{m}_4.ex_4 + \dot{m}_{hex}.ex_{1_{hex}} - \dot{m}_5.ex_5 - \dot{m}_{hex}.ex_{2_{hex}} - \dot{E}x_{D_{hex,HP}} = 0$
Tur HP	$\dot{m}_5.ex_5 - \dot{m}_6.ex_6 - \dot{W}_{tur\,HP} - \dot{E}x_{D_{tur,HP}} = 0$
Cond HP	$\dot{m}_6.ex_6 + \dot{m}_{cw,HP}.ex_{1_{cw,HP}} - \dot{m}_7.ex_7 - \dot{m}_{cw,HP}.ex_{2_{cw,HP}} - \dot{E}x_{D_{cond,HP}} = 0$
Ev LP	$\dot{m}_3.ex_3 - \dot{m}_8.ex_8 - \dot{E}x_{D_{ev,LP}} = 0$
Sep LP	$\dot{m}_8.ex_8 - \dot{m}_9.ex_9 - \dot{m}_{10}.ex_{10} - \dot{E}x_{D_{sep,LP}} = 0$
Hex LP	$\dot{m}_{10}.ex_{10} + \dot{m}_{hex}.ex_{2_{hex}} - \dot{m}_{11}.ex_{11} - \dot{m}_{hex}.ex_{3_{hex}} - \dot{E}x_{D_{hex,LP}} = 0$
Tur LP	$\dot{m}_{11}.ex_{11} - \dot{m}_{12}.ex_{12} - \dot{W}_{tur,LP} - \dot{E}x_{D_{tur,LP}} = 0$
Cond LP	$\dot{m}_{12}.ex_{12} + \dot{m}_{cw,LP}.ex_{1_{cw,LP}} - \dot{m}_{13}.ex_{13} - \dot{m}_{cw,LP}.ex_{2_{cw,LP}} - \dot{E}x_{D_{cond,LP}} = 0$

The power consumption associated with reinjection pumping is excluded from the calculations, as it is negligible compared to the total system power. Accordingly, the total net power outputs of the systems are defined solely based on turbine power generation, as expressed in equation 8. The energy and exergy efficiencies of the systems are subsequently calculated using equation 9 and equation 10, respectively.

$$\dot{W}_{tot_{single}} = \dot{W}_{tur,HP}, \dot{W}_{tot_{double}} = \dot{W}_{tur,HP+}\, \dot{W}_{tur,LP} \tag{8}$$

$$\eta_{single} = \frac{\dot{W}_{tot_{single}}}{\dot{Q}_{in}}, \eta_{double} = \frac{\dot{W}_{tot_{double}}}{\dot{Q}_{in}} \tag{9}$$

$$\psi_{single} = \frac{\dot{W}_{tot_{single}}}{\dot{E}x_{in}}, \psi_{double} = \frac{\dot{W}_{tot_{double}}}{\dot{E}x_{in}} \tag{10}$$

2.3. Exergoeconomic Analysis

Exergoeconomic analysis is a method developed to evaluate different types of energy producing systems (electricity, cooling, heat, and material flows). This method allows to clearly and efficiently evaluate the cost-effectiveness of each component of the power plant by combining exergy and economic analysis. This analysis enables the evaluation of economic performance of each component is calculated by defining the unit exergy costs (Manfrida et al., 2023). In this study, the cost equations related to the system are defined as follows (Vojdani et al., 2021) (equation 11):

$$\dot{Z}_k = \dot{Z}_k^{\,Cl} + \dot{Z}_k^{\,OM} = \frac{\varphi.\sum Z_k.CRF}{\tau} \tag{11}$$

$\dot{Z}_k$ is the sum of the capital investment rate $\dot{Z}_k^{\,Cl}$ and operation and maintenance cost rates $\dot{Z}_k^{\,OM}$ of the system components. Where, Z_k, φ, τ, and CRF denote the acquisition cost, sustainability ratio, annual operation hours and capital recovery factor, respectively. The capital recovery factor is calculated by equation 12.

$$CRF = \frac{i_r(1+i_r)^n}{(1+i_r)^n - 1} \tag{12}$$

Here i_r is the interest rate and n is the number of working years. The economic parameters used in the cost equations of the system are given in Table 3. The Chemical Engineering Plant Cost Index (CEPCI) should be used to adjust the original year costs to the reference year. (Chitsaz et al., 2017) (equation 13).

$$\dot{Z}_{reference\,years} = \dot{Z}_{original\,years}\frac{CEPCI_{reference\,years}}{CEPCI_{original\ years}} \tag{13}$$

Table 3. Economic parameters used in cost equations

Economic Paran	Value/Unit	Ref.
c_f	1.3 \$/GJ	(Tang et al., 2025)
φ	1.06	(Bina et al., 2018)
i_r	12%	(Chitsaz et al., 2017)
n	20 $years$	(Bina et al., 2018)
τ	8000 h	(Stefánsson, 2002)

The fuel exergy, product exergy, and exergy destruction rate are calculated for each component. The fuel and product definitions are established on a compenent specific basis for each unit k within the system (Lazzaretto and Tsatsaronis, 2006). The exergy balance and exergoeconomic relationships are continued as follows using equations obtained from the literature (Manfrida et al., 2023; Soleymani et al., 2021):
The exergy balance equation is expressed as follows (equation 14).

$$\dot{E}x_{F,k} = \dot{E}x_{P,k} + \dot{E}x_{D,k} \tag{14}$$

The exergy efficiency of each component is defined as (equation 14).

$$\varepsilon_k = \frac{\dot{E}x_{P,k}}{\dot{E}x_{F,k}} \tag{15}$$

The relative exergy destruction rate is calculated as in

equation 16:

$$\dot{Y}_k = \frac{\dot{E}x_{D,k}}{\dot{E}x_{D,tot}} \quad (16)$$

The fuel and product unit costs for each component k are described by the following equations 17 and 18:

$$c_{F,k} = \frac{\dot{C}_{F,k}}{\dot{E}x_{F,k}} \quad (17)$$

$$c_{P,k} = \frac{\dot{C}_{P,k}}{\dot{E}x_{P,k}} \quad (18)$$

The relative difference in product/fuel economic costs for each component k is given by the following equation 19:

$$r_k = \frac{c_{P,k} - c_{F,k}}{c_{F,k}} \quad (19)$$

The cost of exergy destroyed for each component can be calculated based on the unit cost of the fuel (equation 20).

$$\dot{C}_{D,k} = c_{F,k} \,.\, \dot{E}x_{D,k} \quad (20)$$

The exergoeconomic factor is calculated by comparing the investment cost of a component to the sum of its exergy destruction cost, is defined as (equation 21).

$$f_k = \frac{\dot{Z}_k}{\dot{Z}_k + \dot{C}_{D,k}} \quad (21)$$

The Sum Unit Cost of Production (SUCP) for single and double-flash steam cycles is calculated as follows (equations 22 and 23).

$$SUCP_{single} = \frac{\dot{Z}tot_{single} + \dot{C}_{well}}{\dot{W}tot_{single}} \quad (22)$$

$$SUCP_{double} = \frac{\dot{Z}tot_{double} + \dot{C}_{well}}{\dot{W}tot_{double}} \quad (23)$$

The cost equations and cost balance of the system components are given in Table 4.

Table 4. Cost functions and cost balance for components of the systems

Components	Cost Functions (Tang et al., 2025)	Cost Balance	Auxiliary Equations
Well	-	$\dot{C}_{well} = \dot{C}_1 + \dot{C}_{1_{hex}}$	$c_1 = c_{1_{hex}} = 1.3\ [\$/GJ]$
Ev HP	$Z_{ev,HP} = 114.5\ x\ \dot{m}_1$	$\dot{C}_1 + \dot{Z}_{ev,HP} = \dot{C}_2$	-
Sep HP	$Z_{sep,HP} = 280.3\ x\ \dot{m}_2{}^{0.67}$	$\dot{C}_2 + \dot{Z}_{sep,HP} = \dot{C}_3 + \dot{C}_4$	$c_3 = c_4$
Hex HP	$Z_{hex,HP} = 17500(A_{hex,HP}/100)^{0.6}$	$\dot{C}_4 + \dot{C}_{1_{hex}} + \dot{Z}_{hex,HP} = \dot{C}_5 + \dot{C}_{2_{hex}}$	$c_{1_{hex}} = c_{2_{hex}}$
Tur HP	$Z_{tur,HP} = 4405\ x\dot{W}_{tur,HP}{}^{0.7}$	$\dot{C}_5 + \dot{Z}_{tur,HP} = \dot{C}_6 + \dot{C}_{W_{tur,HP}}$	$c_5 = c_6\ ,\ c_{W_{tur,HP}} = Var.$
Cond HP	$Z_{cond,HP} = 8000(A_{cond,HP}/100)^{0.6}$	$\dot{C}_6 + \dot{Z}_{cond,HP} + \dot{C}_{1_{cw,HP}} = \dot{C}_7 + \dot{C}_{2_{cw,HP}}$	$c_6 = c_7\ ,\ \ c_{1_{cw,HP}} = 0$
Ev LP	$Z_{ev,HP} = 114.5\ x\ \dot{m}_3$	$\dot{C}_3 + \dot{Z}_{ev,LP} = \dot{C}_8$	-
Sep LP	$Z_{sep,LP} = 280.3\ x\ \dot{m}_8{}^{0.67}$	$\dot{C}_8 + \dot{Z}_{sep,LP} = \dot{C}_9 + \dot{C}_{10}$	$c_9 = c_{10}$
Hex LP	$Z_{hex,LP} = 17500(A_{hex,LP}/100)^{0.6}$	$\dot{C}_{10} + \dot{C}_{2_{hex}} + \dot{Z}_{hex,LP} = \dot{C}_{11} + \dot{C}_{3_{hex}}$	$c_{2_{hex}} = c_{3_{hex}}$
Tur LP	$Z_{tur,LP} = 4405\ x\dot{W}_{tur,LP}{}^{0.7}$	$\dot{C}_{11} + \dot{Z}_{tur,HP} = \dot{C}_{12} + \dot{C}_{W_{tur,LP}}$	$c_{11} = c_{12}\ ,c_{W_{tur,LP}} = Var.$
Cond LP	$Z_{cond,LP} = 8000(A_{cond,LP}/100)^{0.6}$	$\dot{C}_{12} + \dot{Z}_{cond,LP} + \dot{C}_{1_{cw,LP}} = \dot{C}_{13} + \dot{C}_{2_{cw,LP}}$	$c_{12} = c_{13}\ ,\ \ c_{1_{cw,LP}} = 0$

The heat transfer surface area required for the condenser and heat exchangers is calculated using equation 24 (Sadat et al., 2020):

$$A_k = \frac{\dot{Q}_k}{U_k . \Delta T_{LMTD}} \quad (24)$$

Here, $\dot{Q}_k$, U_k, and ΔT_{LMTD}represent the heat transfer rate, the overall heat transfer coefficient of the component, and the logarithmic mean temperature difference, respectively. In the calculations, the overall heat transfer coefficient was assumed to be 1.0 kW/m²K for heat exchangers and 1.1 kW/m²K and for condensers (Sadat et al., 2020).

2.4. System Optimizations

In this study, a thermodynamic model was developed using Engineering Equation Solver (EES) to assess the performance of single and double-flash steam cycles. In the present study, following assumption are considered for the thermodynamic modelling (Bina et al., 2018; Farsi and Rosen, 2022):

- All components in the systems are assumed to operate under steady-state conditions.
- Kinetic and potential energy changes in the systems are neglected.
- Pressure drops in pipelines and turbines are neglected.
- Heat loss in pipelines are neglected.
- Steam turbines and separators are assumed to operate under adiabatic conditions.
- Expansion valves are assumed to operate as isenthalpic devices.

The power consumption of the reinjection pumps is neglegted in the analysis due to it is quite low compared to the total power output of the system.

The systems were optimized for two distinct objectives:

maximizing exergy efficiency and minimizing the SUCP. These objectives were evaluated independently for each cycle type.

Genetic algorithms have been identified as effective tools for the optimizations of geothermal power plant production (Rudiyanto et al., 2023). Therefore, the performance optimizations of single and double-flash steam cycles have been carried out using the Genetic Algorithm method in the EES software.

In the double-flash steam cycle, the mass flow rate ($\dot{m}_{hex}$) of the geothermal fluid directed to the heat exchanger, the flashing pressure in the high pressure region (P_2), and the flashing pressure in the low pressure region (P_8) were selected as the decision variables. In the single-flash steam cycle, only the decision variables $\dot{m}_{hex}$ and P_2 were used. In both cycles, the steam quality at the steam turbine outlet remains above 90% as a boundary condition to ensure turbine safety (Cengel et al., 2019).

The basic design parameters of the systems, the ranges of the decision variables used in optimization and the boundary conditions are presented in Table 5.

Table 5. Input data, basic design conditions, and optimization conditions used in the analysis

Parameters		Value	Opt. range	Opt. boundary condition
Mass Flow to Hex (Heat Source)	$\dot{m}_{hex}$	10 kg/s	0-15 kg/s	-
Flashing pressure	P_2	300 kPa	250-1,500 kPa	-
	P_8	100 kPa	50-200 kPa	-
Condenser temperature	T_7, T_{13}	40 °C	-	
Turbine outlet steam quality	x_6, x_{12}	-	-	0.9
	T_{source}	250 °C	-	-
Properties of the geothermal fluid	$\dot{m}_{source}$	100 kg/s	-	-
	x_{source}	0	-	-
Turbine isentropic efficiency	$\eta_{is,tur}$	0.85	-	-
Pinch point in the condenser	$\Delta T_{cond_{min}}$	10 °C	-	-
Pinch point in the Hex	$\Delta T_{hex_{min}}$	10 °C	-	-
Ambient temperature	T_0	25 °C	-	-
CW inlet temperature	$T_{1_{cw,HP}}, T_{1_{cw,LP}}$	25 °C	-	-
CW outlet temperature	$T_{2_{cw,HP}}, T_{2_{cw,LP}}$	30 °C	-	-

2.5. Uncertainty Analysis

In this study, thermodynamic parameters were calculated based on fundamental properties such as temperature, pressure, and mass flow rate, along with values obtained from thermodynamic tables. Although no experimental measurements were conducted, the uncertainty present in the input data can still significantly affect the accuracy of the computed results. Therefore, uncertainty analysis was included for the energy and exergy calculations to enhance the reliability, consistency, and scientific validity of the study.

On the other hand, uncertainty analysis for the SUCP was not performed. Although cost estimation methods often involve thermodynamic variables such as heat transfer area, mass flow rate, and power, SUCP is primarily influenced by broader economic factors including investment cost, operating expenses, economic lifetime, and market conditions. As a result, a precise uncertainty quantification for SUCP would require a comprehensive economic model, which is beyond the scope of this work.

The uncertainty calculations for thermodynamic quantities were carried out using the approach recommended by the Guide to the Expression of Uncertainty in Measurement (GUM) (Velychko and Gordiyenko, 2009). According to GUM, the total uncertainty of a function is determined by the square root of the sum of the squared contributions of all input variables, each weighted by the partial derivative of the function with respect to that variable (equation 25).

$$u_f = \sqrt{\sum_{i=1}^{n} \left(\frac{\partial f}{\partial x_i} . u_{x_i}\right)^2} \tag{25}$$

Here, u_f represents the overall uncertainty of the function f, and u_{x_i} is the standard uncertainty of the input variable x_i.

The uncertainties in specific enthalpy and entropy, which depend on temperature and pressure, are calculated using (equation 26 and 27).

$$u_h = \sqrt{\left(\frac{\partial h}{\partial T} . u_T\right)^2 + \left(\frac{\partial h}{\partial P} . u_P\right)^2} \tag{26}$$

$$u_s = \sqrt{\left(\frac{\partial s}{\partial T} . u_T\right)^2 + \left(\frac{\partial s}{\partial P} . u_P\right)^2} \tag{27}$$

The partial derivatives can be estimated using tabulated thermodynamic data or simulation software as follows (equation 28).

$$\frac{\partial h}{\partial T} \approx \frac{\Delta h}{\Delta T}, \frac{\partial h}{\partial P} \approx \frac{\Delta h}{\Delta P}, \frac{\partial s}{\partial T} \approx \frac{\Delta s}{\Delta T}, \frac{\partial s}{\partial P} \approx \frac{\Delta s}{\Delta P} \quad (28)$$

The specific exergy uncertainty, which is a function of specific enthalpy and specific entropy, is calculated by equation 29.

$$u_{ex} = \sqrt{\left(\frac{\partial ex}{\partial h} . u_h\right)^2 + \left(\frac{\partial ex}{\partial s} . u_s\right)^2} \quad (29)$$

Given the definition of specific exergy, the partial derivatives are (equation 30).

$$\frac{\partial ex}{\partial h} = 1, \frac{\partial ex}{\partial s} = -T_0 \quad (30)$$

Energy and exergy flow rate uncertainties are determined by equations 31 and 32.

$$u_{\dot{Q}} = \sqrt{\left(\frac{\partial \dot{Q}}{\partial \dot{m}} . u_{\dot{m}}\right)^2 + \left(\frac{\partial \dot{Q}}{\partial h} . u_h\right)^2} \quad (31)$$

$$u_{\dot{E}x} = \sqrt{\left(\frac{\partial \dot{E}x}{\partial \dot{m}} . u_{\dot{m}}\right)^2 + \left(\frac{\partial \dot{E}x}{\partial ex} . u_{ex}\right)^2} \quad (32)$$

With the following derivative values (equation 33).

$$\frac{\partial \dot{Q}}{\partial \dot{m}} = h, \frac{\partial \dot{Q}}{\partial h} = \dot{m}, \frac{\partial \dot{E}x}{\partial \dot{m}} = ex, \frac{\partial \dot{E}x}{\partial ex} = \dot{m} \quad (33)$$

The uncertainty in energy efficiency and exergy efficiency is calculated as (equations 34 and 35).

$$u_\eta = \sqrt{\left(\frac{\partial \eta}{\partial \dot{W}} . u_{\dot{W}}\right)^2 + \left(\frac{\partial \eta}{\partial \dot{Q}} . u_{\dot{Q}}\right)^2} \quad (34)$$

$$u_\psi = \sqrt{\left(\frac{\partial \psi}{\partial \dot{W}} . u_{\dot{W}}\right)^2 + \left(\frac{\partial \psi}{\partial \dot{E}x} . u_{\dot{E}x}\right)^2} \quad (35)$$

Where the partial derivatives are given as (equation 36).

$$\frac{\partial \eta}{\partial \dot{W}} = \frac{1}{\dot{Q}}, \frac{\partial \eta}{\partial \dot{Q}} = -\frac{\dot{W}}{\dot{Q}^2}, \frac{\partial \psi}{\partial \dot{W}} = \frac{1}{\dot{E}x}, \frac{\partial \psi}{\partial \dot{E}x} = -\frac{\dot{W}}{\dot{E}x^2} \quad (36)$$

If the relative uncertainty of a quantity is to be expressed, it can be calculated by dividing its absolute uncertainty by the value of the variable itself. The general expression is given as (equation 37).

$$u_{rel,f} = \frac{u_f}{f} x100\ (\%) \quad (37)$$

3. Results and Discussion

In this study, $\dot{m}_{hex}$, P_2, and P_8 were determined as the basic design parameters affecting the system performance. The effects of these design variables on the system components have been analyzed in detail; comprehensive evaluations have been presented in terms of critical performance criteria such as efficiency, power generation, exergy losses, economic performance indicators, and operating safety. Each parameter was evaluated separately within its own range and all other parameters remain unchanged as shown in Table 1. In the relevant sections, the effect of each parameter on the system behavior is analyzed comprehensively with graphical data.

3.1. Effects of $\dot{m}_{hex}$ on system performance

In this section, the effects of $\dot{m}_{hex}$ change, which allows a portion of the fluid obtained from the geothermal source to be directed to the heat exchangers and used in superheated steam production, on the system performance in the range of 0–15 kg/s are analyzed comprehensively. The increase in the value of $\dot{m}_{hex}$ reduces the total mass flow rate entering the system, thereby reducing the vapor flow rate leaving the HP separator. Since the flashing pressure remains constant, there is no change in the specific enthalpy of the steam. In the HP heat exchanger, the specific enthalpy of superheated steam increases initially but remains constant after a certain point. The main reason for this is that the pinch point shifts towards the source temperature as the superheated steam temperature approaches the source inlet temperature. The results are shown in Figure 2.

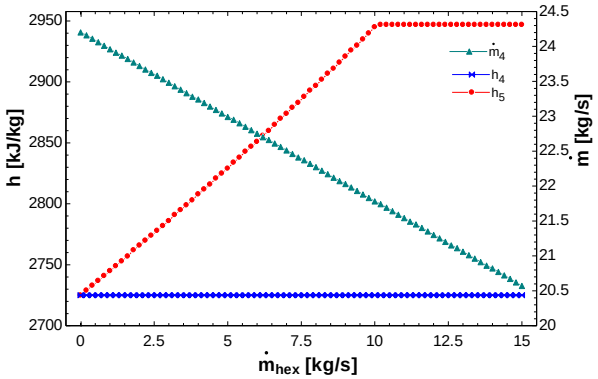


Figure 2. Changes in specific enthalpy and mass flow rates in the HP steam generation process depending on $\dot{m}_{hex}$.

As seen in Figure 3, a similar working process was observed in the LP separator. However, the increase in the value of $\dot{m}_{hex}$ led to an increase in the quality of the heat directed to the LP heat exchanger. In the HP heat exchanger, the heat recovery efficiency decreases after a certain point as the superheated steam temperature approaches the geothermal source temperature, which restricts the temperature gradient and limits further heat transfer. Therefore, the rate of increase of the specific enthalpy of superheated steam in the LP heat exchanger increases in the regions where $\dot{m}_{hex}$ is higher.

Figure 4 shows the total power generation and total exergy destruction in the cycles depending on the parameter $\dot{m}_{hex}$. The total enthalpy of the superheated steam entering the turbine is a basic parameter that determines the turbine power output. Up to $\dot{m}_{hex}$ value of 2.8 kg/s, the rate of decrease in the steam mass flow was higher than the rate of increase in the specific enthalpy of the superheated steam, resulting in a reduction of power output in the HP turbine. From this point on, power generation increased as the specific enthalpy increase became dominant. However, beyond a $\dot{m}_{hex}$ volue of 10 kg/s, power production began to decline due to the limited temperature gradient, which

prevented further heat transfer in the HP heat exchanger. In the LP turbine, power output exhibited a decreasing trend throughout the entire $\dot{m}_{hex}$ range, as the increase in the specific enthalpy of the superheated steam was insufficient to compensate for the reduction in steam mass flow rate. At flow rates between 5 kg/s and 10 kg/s, the power increase rate in the HP turbine is higher than the power loss rate in the LP turbine, so that the total power production in both single and double-flash steam cycles reaches a maximum level at the same point. At the point of maximum power generation, a total power of was calculated as 11,415.4 kW for the single-flash steam cycle and 12,884.1 kW for the double flash steam cycle.

Exergy destructions in system components exhibit different characteristics depending on the parameter $\dot{m}_{hex}$. Exergy destructions in expansion valves and heat exchangers show a significant increase with the increase of $\dot{m}_{hex}$.On the other hand, exergy destructions in LP turbine and condensers show a decreasing trend with the increase of $\dot{m}_{hex}$. The exergy destructions in the HP turbine exhibits a behavior parallel to the change in power production. As a result of these componential differences, the total exergy destructions of the systems also exhibit various change dynamics depending on $\dot{m}_{hex}$. In the single-flash steam cycle, the total exergy destruction shows a decreasing trend with the increase of $\dot{m}_{hex}$, while in the double-flash steam cycle, a behavior opposite to the total power production is observed. However, an important point to be noted in the single-flash steam cycle is that after the maximum power production point, there is a significant increase in the amount of exergy lost without being evaluated by sending it directly to reinjection from the system.

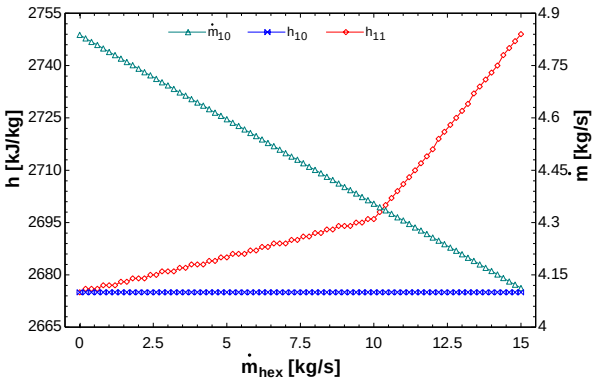


Figure 3. Changes in specific enthalpy and mass flow rates in the LP steam generation process depending on $\dot{m}_{hex}$.

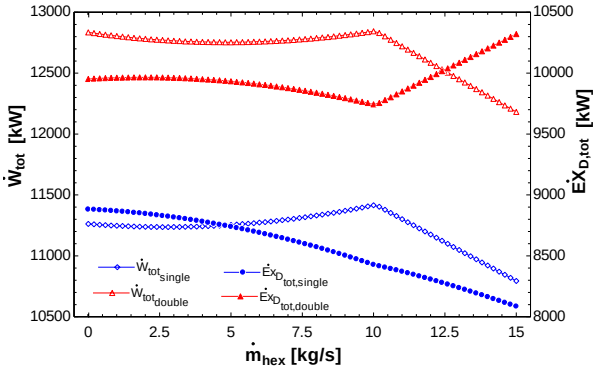


Figure 4. Variation of total power output and total exergy destruction in single and double-flash steam cycles depending on $\dot{m}_{hex}$.

In Figure 5, the dryness fractions at the turbine outlets are examined. Up to the value of 4.6 kg/s $\dot{m}_{hex}$, the dryness fractions at the outlet of the HP turbine remained below 90%. This is a level that can endanger the safety of the turbine, because low dryness fractions can cause the vapor to start to pass into the liquid phase and lead to potential damage to the internal components of the turbine. An increase in the $\dot{m}_{hex}$ parameter can improve this value at the turbine outlet, allowing the turbine to operate more efficiently and safely.

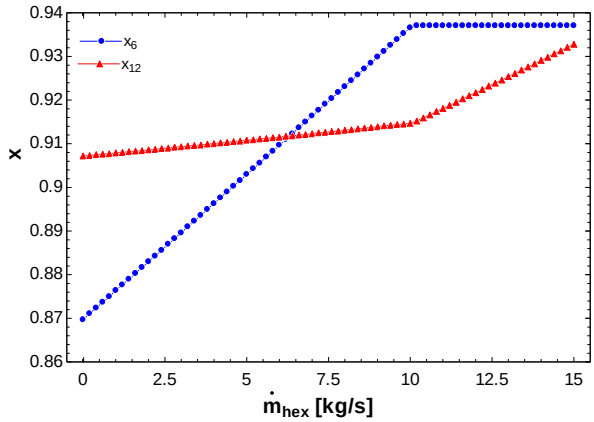


Figure 5. Changes in steam dryness fractions at turbine outlets depending on $\dot{m}_{hex}$.

Figure 6 shows the changes in the exergy efficiency and SUCP values of the systems depending on the $\dot{m}_{hex}$ parameter. The exergy efficiency exhibited a parallel change with the total power production and reached a maximum of 44.37% for the single-flash steam cycle and 49.93% for the double-flash steam cycle at the $\dot{m}_{hex}$ flow rate of 10 kg/s. However, SUCP values showed a change in the opposite direction to exergy efficiency. Minimum SUCP values were obtained at maximum exergy efficiency points and were calculated as 4.30 $/GJ for single-flash steam cycle and 4.11 $/GJ for double-flash steam cycle, respectively. These results show that economic efficiency also reaches its highest level at the points where high efficiency is obtained from the systems.

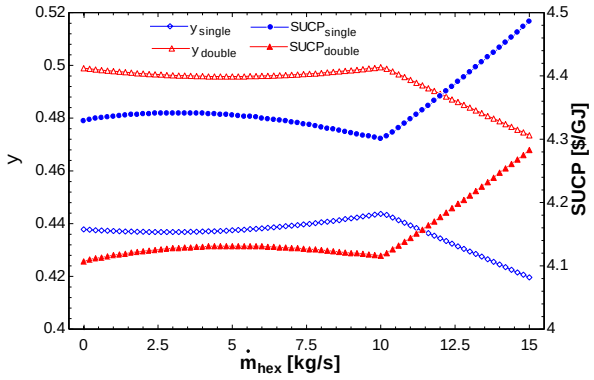


Figure 6. Changes in exergy efficiency and SUCP in single and double-flash steam cycles depending on $\dot{m}_{hex}$.

3.2. Effects of flashing pressure (P_2) in HP region on system performances

In this section, the effects of varying the flashing pressure applied in the HP region in the range of 250–1,500 kPa on system performances are comprehensively analyzed. The increase in P_2 value has a direct effect on the thermodynamic properties and amount of saturated steam obtained from the HP separator. As the flashing pressure increases, the pressure difference across the HP expansion valve decreases. This decrease leads to a decrease in the mass flow rate of saturated steam leaving the HP separator. On the other hand, with increasing pressure, the specific enthalpy of saturated steam increases and this initially affects the turbine inlet conditions positively. However, with the increase in P_2, the saturation temperature also increases and this causes the pinch point in the HP heat exchanger to approach the geothermal source inlet temperature. From this point on, the specific enthalpy of superheated steam in the HP heat exchanger begins to decrease. These changes are presented in Figure 7.

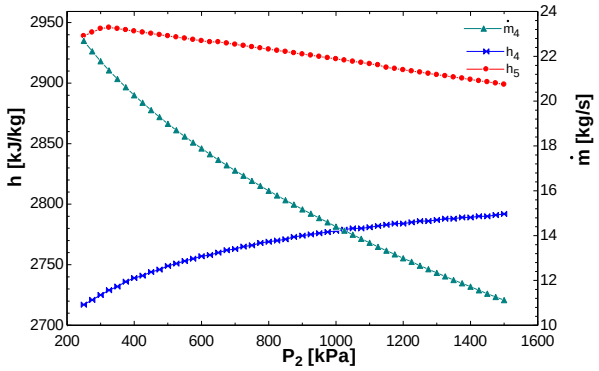


Figure 7. Changes in specific enthalpy and mass flow rates in the HP steam generation process depending on P_2.

As P_2 increases, the amount of saturated liquid leaving the HP separator increases, allowing for more flashing steam production in the LP region. In a

ddition to the increase in the mass flow rate of steam leaving the LP separator, the high-quality thermal energy transferred to the LP heat exchanger also increases the specific enthalpy of the superheated steam entering the LP turbine, supporting power production (Figure 8).

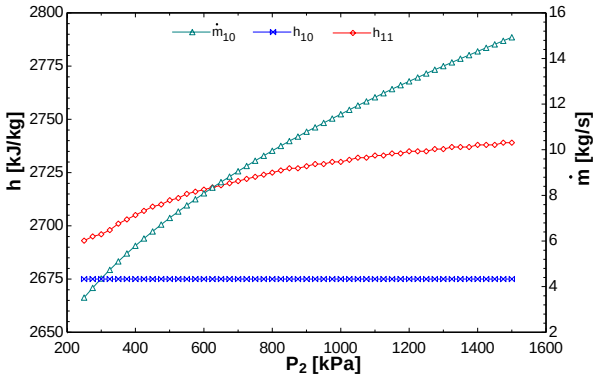


Figure 8. Changes in specific enthalpy and mass flow rates in the LP steam generation process depending on P_2.

In Figure 9, the effects of the flashing pressure applied in the HP region on the total power production and exergy destruction of the systems are analyzed. In the HP region, as the flashing pressure increased up to 300 kPa, the increase in the specific enthalpy of superheated steam became more dominant than the decrease in the steam mass flow rate and therefore the power production in the HP turbine increased. However, after this pressure level, the decrease in flow rate became more significant and the power production tended to decrease. In the LP turbine, the power production increased in the flashing process. Accordingly, the maximum power production for the single-flash steam cycle was found to be 11,415.4 kW at 300 kPa pressure. In the double-flash steam cycle, the power increase rate in the LP turbine was higher than the power loss rate in the HP turbine in the range of 300-700 kPa; as a result of this situation, the total power production of the system reached a maximum at 700 kPa pressure and was obtained as 13,520.1 kW. Under this condition, the HP turbine produced 10,508.9 kW. The findings show that accepting a certain amount of power loss from the HP turbine in order to reach the optimum power point in the double-flash steam cycle may be beneficial in terms of system performance.

As the P_2 flashing pressure increases, an increase in the exergy destruction of the system components in the LP region is observed. In the HP turbine, the exergy destruction increased up to 300 kPa pressure in parallel with the increase in power production, and after this point it started to decrease due to the decrease in power production. On the other hand, the exergy destruction in the other components in the HP region tended to decrease with the increase in P_2.In the single-flash steam cycle, where only components in the HP region are involved, the total exergy destruction continuously decrease with P_2 increases due to the effect of exergy destruction in these components. However, an important point to note here is that, especially after the maximum power production point, the amount of exergy sent directly to reinjection without being used in the system significantly increases. In the double-flash steam cycle, the total exergy destruction decreased up to 700 kPa

pressure; after this pressure value, it started to increase again with the increase of exergy destruction in the LP region.

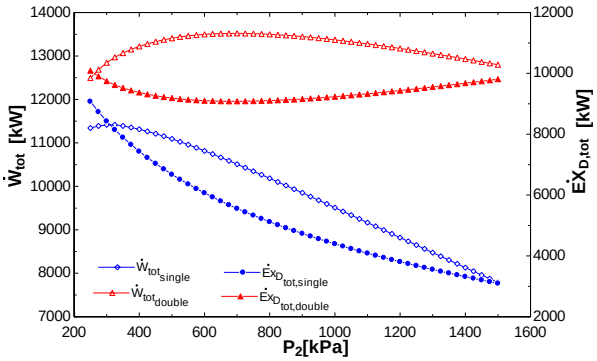


Figure 9. Variation of total power output and total exergy destruction in single and double-flash steam cycles depending on P_2.

Figure 10 shows the changes in steam dryness fractions at the turbine outlets depending depending on flashing pressure. According to the analysis results, when the flashing pressure exceeds 600 kPa, the steam dryness fractions at the HP turbine outlet drops below 90%. However, remarkably, the maximum power generation of the double-flash steam cycle is achieved above this risky pressure level.

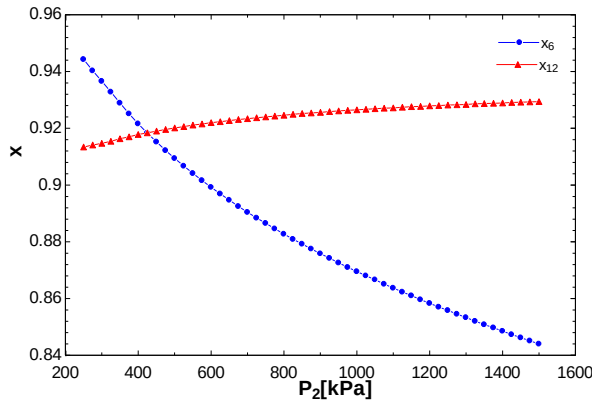


Figure 10. Changes in steam dryness fractions at turbine outlets depending on P_2.

Figure 11 shows the changes in the exergy efficiency and SUCP values of the systems depending on the flashing pressure. According to the analysis results, exergy efficiency exhibits a parallel trend with total power generation. The maximum exergy efficiency was determined as 44.37% at 300 kPa pressure for the single-flash steam cycle and 52.56% at 700 kPa pressure for the double-flash steam cycle.

On the other hand, it has been observed that SUCP values show an inverse change with exergy efficiency. This shows that the SCUP value decreases with the increase in the system efficiency. However, in the double-flash steam cycle, the change in SUCP values exhibits a more stable trend compared to the change in exergy efficiency of the same cycle. This situation shows that despite the increase in system efficiency, the SUCP value decreases to a more limited extent. The minimum SUCP value is calculated as 4.30 $/GJ at 300 kPa, where the maximum exergy efficiency is obtained for the single-flash steam cycle. The minimum SUCP value for the double-flash steam cycle is found as 4.02 $/GJ at 600 kPa flashing pressure.

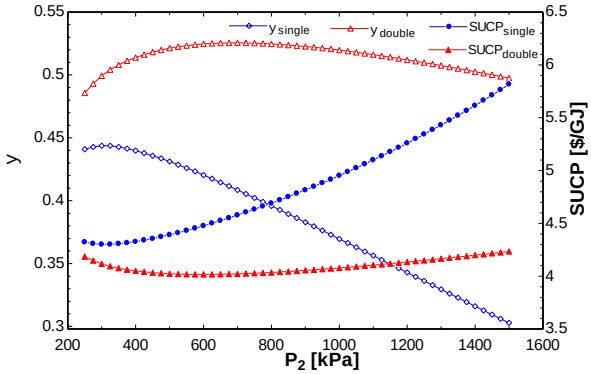


Figure 11. Changes in exergy efficiency and SUCP depending on P_2 in single and double- flash steam cycles.

3.3. Effects of flashing pressure (P_8) in the LP region on system performances

In this section, the flashing pressure in the LP region is varied between 50–200 kPa and the effects of this parameter on the system performance are comprehensively evaluated. The increase in P_8 pressure has a direct effect on both the thermodynamic properties and the mass flow rate of the saturated steam obtained from the LP separator. As the flashing pressure increases, the pressure difference across the LP expansion valve decreases, resulting in a decrease in the mass flow rate of saturated steam leaving the separator.

On the other hand, the specific enthalpy of saturated steam increases with increasing flashing pressure, which directly contributes to the specific enthalpy of superheated steam leaving the LP heat exchanger. These changes are presented in Figure 12. Since the LP region is fed with the fluid that has been subjected to energy conversion process within the HP cycle, changes in this parameter do not influence on the operating conditions of the HP components.

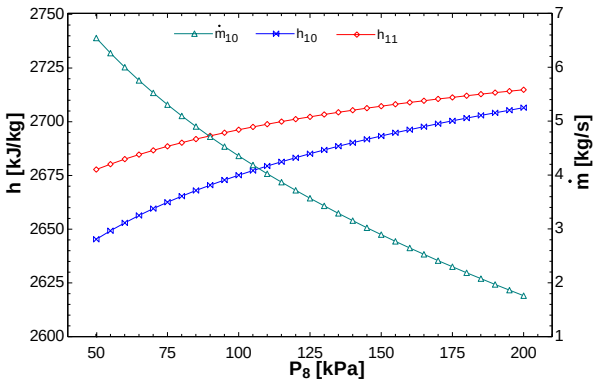


Figure 12. Changes in specific enthalpy and mass flow rates in the LP steam generation process depending on P_8.

In Figure13, are presented an analysis of the effects of the flashing pressure in the LP region on the total power

generation and exergy destruction of the systems. In the LP region, as the flashing pressure increases up to 55 kPa, the increase in the specific enthalpy of the superheated steam becomes more significant than the reduction in the steam mass flow rate. Consequently, the power generation increases in the LP turbine. However, after this pressure level, the decrease in flow rate becomes more significant and the power production tends to decrease. At this operating point, the maximum power for the double-flash steam cycle is calculated as 13,000.6 kW.

The exergy destruction in the LP turbine exhibits a trend smilar to that of the turbines output power in a similar way. In contrast, exergy destructions in other system components generally exhibits a decreasing trend. Total system exergy destructions exhibits a continuously decreasing trend throughout the process with the combined effect of all parameters. An increase in the high flashing pressure leads to a rice in the temperature of the source fluid leaving the LP heat exchanger, resulting in a greater amount of exergy directly reinjected without being utilized by the system.

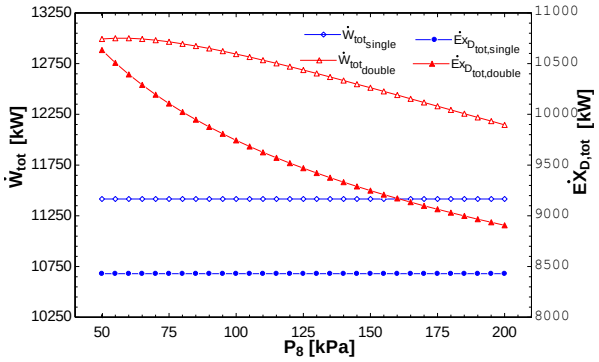


Figure 13. Variations of total power output and total exergy destruction depending on P_8 in single and double-flash steam cycles.

As shown in Figure 14, the increase of flashing pressure above 145 kPa at the LP turbine outlet conditions causes the steam dryness fractions to fall below 90%, which poses a potential risk in terms of turbine safety.

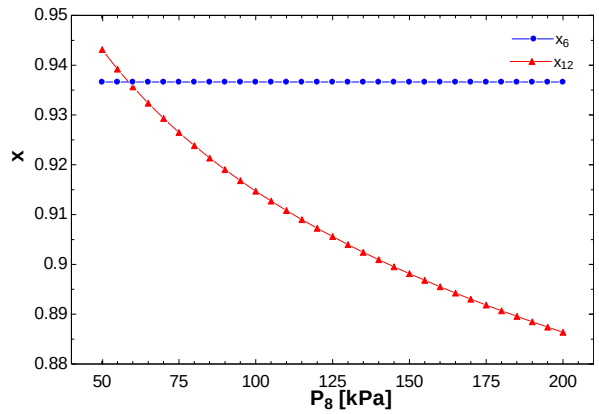


Figure 14. Changes in steam dryness fractions at turbine outlets depending on P_8.

Figure 15 shows the changes in the exergy efficiency and SUCP values of the systems depending on the P_8 flashing pressure. Since the P_8 flashing pressure has no effect on the single-flash steam cycle, the exergy efficiency and SUCP values remain constant. For the double-flash steam cycle, the exergy efficiency increased in parallel with the total power generation and reached 50.54% at 55 kPa pressure.

On the other hand, it was observed that SUCP values changed inversely proportional to exergy efficiency. As exergy efficiency increased, SUCP values generally decreased. However, the rate of change of SUCP values was slower. While exergy efficiency reached its maximum level at 55 kPa pressure, the minimum SUCP value was calculated as 4.09 $/GJ at 60 kPa flashing pressure.

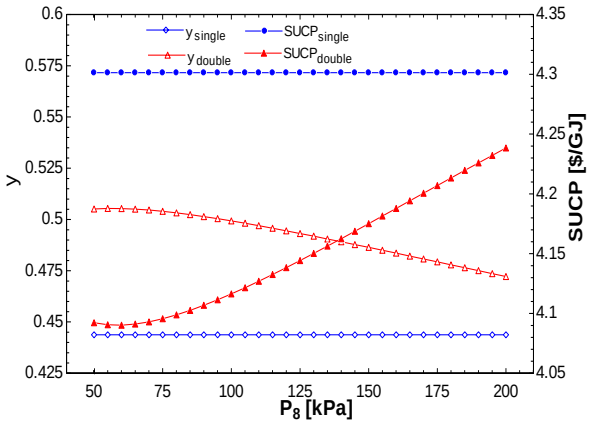


Figure 15. Changes in exergy efficiency and SUCP in single and double-flash steam cycles depending on P_8.

3.4. Optimized System Performance and Uncertainty Assessment

In this section, the performance optimizations of single and double-flash steam cycles have been carried out using the Genetic Algorithm method in the EES software. Two main objectives were determined in the optimization process: maximizing the exergy efficiency and minimizing the SUCP value. For the double-flash steam cycle, three different decision variables are used: $\dot{m}_{hex}$, P_2, and P_8. For the single-flash steam cycle, the optimization is limited to the variables $\dot{m}_{hex}$ and P_2. In order to ensure the safe operation of the turbine in both cycles, a boundary condition is defined such that the dryness degree of the steam at the turbine outlet is no least than 90%.

Optimization results are presented in Table 6 in comparison with the basic design conditions of the system. According to the optimization results for the double-flash steam cycle, the highest exergy efficiency through exergy optimization is achived 53.1%, while the lowest SUCP value in economic optimization is found to be 3.9815 $/GJ. It was seen that both optimization types preferred similar parameter combinations, therefore, a separate multi-objective optimization was not required. Additionally the double-flash steam cycle demonstrated superior performance compared to the single-flash steam

cycle in both approaches. Therefore, all tables and graphs presented in the rest of the study were prepared by taking into account the exergetic optimization of the double-flash steam cycle.

Table 6. Optimization results and performance comparisons

Opt. Type	Cycle Type	$\dot{m}_{hex}$ (kg/s)	P_2 (kPa)	P_8 (kPa)	$\dot{W}_{tur,LP}$ (kW)	$\dot{W}_{tur,HP}$ (kW)	$\dot{W}_{tot}$ (kW)	η (%)	ψ_{double} (%)	$SUCP$ $(\$/GJ)$
Base Design	Single	10	300	-	0	11,415.38	11,415.38	10.52	44.37	4.3013
	Double	10	300	100	1,428.70	11,415.38	12,844.08	11.83	49.93	4.1163
Exergetic	Single	9.988	315.4	-	0	11,422.49	11,422.49	10.52	44.4023	4.2992
	Double	8.784	586.4	84.92	2,664.11	10,996.39	13,660.50	12.59	53.1	3.9819
Economic	Single	9.955	321.1	-	0	11,422.40	11,422.40	10.52	44.4019	4.2991
	Double	8.688	581.1	88.13	2,649.14	11,007.91	13,657.05	12.58	53.09	3.9815

The temperature–entropy (T–s) and pressure–enthalpy (P–h) diagrams of the system under the optimum conditions are presented in Figure 16 and Figure 17, respectively.

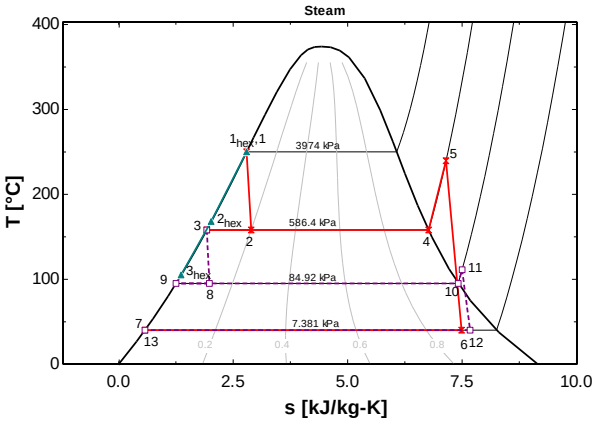


Figure 16. T-s diagram of the double-flash steam cycle under optimum conditions.

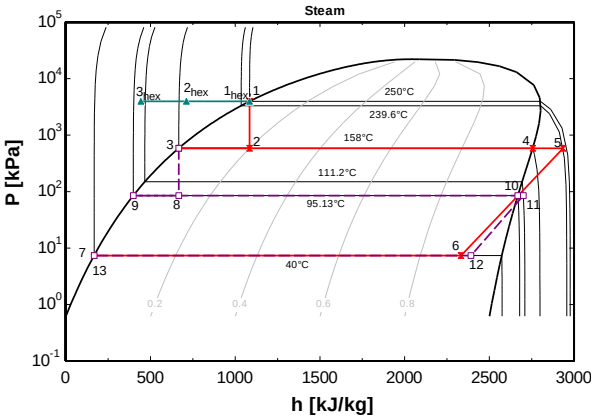


Figure 17. P-h diagram of the double-flash steam cycle under optimum conditions.

The thermodynamic and exergoeconomic properties of each point of the cycle under optimum conditions are presented in Table 7. The exergy flows, exergy destructions, and exergoeconomic relationships of the system components are presented in Table 8.

Table 7. Thermodynamic properties and exergoeconomic values of the system states under optimum conditions

State	P (kPa)	T (^oC)	$\dot{m}$ (kg/s)	h (kJ/kg)	s $(kJ/kg.K)$	x	ex (kJ/kg)	$\dot{E}x$ (kW)	$\dot{C}$ $(\$/h)$	c $(\$/GJ)$
1_{hex}	3,974	250	8.784	1,085	2.793	0	257.3	2,260	10.58	1.3
2_{hex}	3,974	167.97	8.784	712.2	2.018	-	115.1	1,011	4.73	1.3
3_{hex}	3,974	105.13	8.784	443.6	1.361	-	42.24	371	1.736	1.3
1	3,974	250	91.22	1,085	2.793	0	257.3	23,465	109.8	1.3
2	586.4	157.97	91.22	1,085	2.893	0.2003	227.2	20,728	110	1.474
3	586.4	157.97	72.94	666.8	1.923	0	98.16	7,160	38.03	1.476
4	586.4	157.97	18.27	2,756	6.768	1	742.4	13,568	72.07	1.476
5	586.4	239.55	18.27	2,935	7.149	-	808	14,766	78.54	1.477
6	7.381	40	18.27	2,333	7.488	0.9002	105.2	1,922	10.22	1.477
7	7.381	40	18.27	167.5	0.572	0	1.433	26.19	0.1393	1.477
8	84.92	95.13	72.94	666.8	1.98	0.1182	81.03	5,910	38.18	1.795
9	84.92	95.13	64.32	398.5	1.251	0	29.94	1,925	12.47	1.799
10	84.92	95.13	8.624	2,668	7.414	1	462.1	3,985	25.8	1.799
11	84.92	111.20	8.624	2,700	7.5	-	468.8	4,043	29.08	1.998
12	7.381	40	8.624	2,391	7.674	0.9244	108	931	6.698	1.998
13	7.381	40	8.624	167.5	0.572	0	1.433	12.36	0.08891	1.998

Table 8. Exergetic and exergoeconomic relations of system components under optimum conditions

Component	$\dot{E}x_{F,k}$ (kW)	$\dot{E}x_{P,k}$ (kW)	$\dot{E}x_{D,k}$ (kW)	ε_k (%)	$\dot{Y}_k$ (%)	$\dot{C}_{F,k}$ $(\$/h)$	$\dot{C}_{p,k}$ $(\$/h)$	$c_{F,k}$ $(\$/GJ)$	$c_{P,k}$ $(\$/GJ)$	r_k (%)	$\dot{Z}_k$ $(\$/h)$	$\dot{C}_{D,k}$ $(\$/h)$	f_k (%)
Ev HP	23,465	20,728	2,738	88.33	29.62	109.8	110	1.3	1.474	13.4	0.1853	12.81	1.425
Sep HP	20,728	20,728	0	100	0	110	110.1	1.474	1.476	0.093	0.1023	0	100
Hex HP	15,827	15,777	50.47	99.68	0.546	82.65	83.27	1.45	1.466	1.078	0.6245	0.2636	70.32
Tur HP	14,766	12,918	1,848	87.49	19.99	78.54	131.2	1.477	2.822	90.99	52.69	9.827	84.28
Cond HP	1,922	354.4	1,568	18.44	16.96	10.22	11.3	1.477	8.855	499.3	1.074	8.338	5.186
Ev LP	7,160	5,910	1,250	82.54	13.52	38.03	38.18	1.476	1.795	21.62	0.1482	6.64	2.183
Sep LP	5,910	5,910	0	100	0	38.18	38.27	1.795	1.799	0.231	0.0881	0	100
Hex LP	4,996	4,414	581.8	88.35	6.295	30.53	30.82	1.698	1.94	14.25	0.2867	3.556	7.461
Tur LP	4,043	3,595	447.6	88.93	4.843	29.08	48.62	1.998	3.756	87.97	19.53	3.22	85.85
Cond LP	931	171.4	759.6	18.41	8.219	6.698	7.393	1.998	11.98	499.6	0.6954	5.465	11.29

The inlet parameters of the geothermal fluid, namely temperature, pressure, and mass flow rate, were selected as the fundamental variables used in the uncertainty analysis. System power was also included in the analysis because of system assumptions and since it represents the energy output. The other uncertainties presented in Table 9 are essentially derived from the measurement uncertainties of these four fundamental variables. Although the study is theoretical, these uncertainties were estimated by considering the accuracy ranges of measurement devices and predictions found in the literature. The relative uncertainties of energy and exergy were found to be approximately ±3% and ±3.8%, respectively. These relative uncertainties are consistent with commonly accepted ranges in the literature and support the consistency and reliability of the thermodynamic results of the study.

Table 9. Parameter uncertainties

Parameter	u_T (^oC)	u_P (kPa)	$u_{\dot{m}}$ (kg/s)	u_W (kW)	u_h (kJ/kg)	u_s $(kJ/kg.K)$	$u_{\dot{Q}}$ (kW)	u_{ex} (kJ/kg)	$u_{\dot{E}x}$ (kW)	$u_{rel,\eta}$ (%)	$u_{rel,\psi}$ (%)
Uncertainty	±1	±10	±3	±100	±4.908	±0.00922	±3398	±5.626	±955.1	±3.121	±3.784

4. Conclusions

In this study, single and double-flash steam geothermal power plant configurations are compared in terms of power output, exergy efficiency, and exergoeconomic performance. System configurations were modeled in EES software using thermodynamic and economic equations. System performance was evaluated based on the design parameters $\dot{m}_{hex}$, P_2, and P_8 and finally exergetic and economic optimizations of the systems were carried out using the genetic algorithm method.

The main conclusions of this study may be summarized as:

- Under exergetic optimization conditions, 9.99% and 8.78% of the geothermal fluid mass flow rate extracted from the source was directed to the heat exchangers as a heat source in single and double-flash steam cycles, respectively. The results indicate that system performance can be improved by using a fraction of the geothermal fluid extracted from the source as a heat source in the heat exchangers to obtain superheated steam.
- It was found that the optimum flashing pressure is 315.4 kPa (P_2) for the single-flash steam cycle, and 586.4 kPa (P_2) and 84.92 kPa (P_8) for the double-flash steam cycle.
- Exergetic optimization results indicate that the double-flash steam cycle generated 2,238 kW more power than the single-flash steam cycle, resulting in a 19.6% increased in exergy efficiency and a 7.4% decreased in SUCP. Broadly similar effects was observed in economic optimization, as the objective functions reach their optimum values under conditions closely aligned with the design parameters.
- In the double-flash steam cycle, energy efficiency, exergy efficiency, and SUCP was determined as 12.59%, 53.1%, and 3.98 $/GJ, respectively.
- The electrical power output produced by the double-flash steam cycle was determined as 13,660.5 kW. Also, 35.92% of the total exergy entering the system was destroyed due to irreversibility, while 10.98% was discharged as exergy losses.
- A total of 2,296 kW of exergy was re-injected into the reservoir. The waste energy released at the end of the process can be recovered and utilized as a heat source in applications such as district heating, greenhouse heating, food drying, and low-temperature Organic Rankine Cycle (ORC) systems. This recovery approach can significantly enhance the overall energy recovery potential of the system.

Author Contributions

The percentages of the authors' contributions are presented below. All authors reviewed and approved the final version of the manuscript.

	U.A.	B.D.
C	60	40
D	60	40
S	60	40
DCP	60	40
DAI	60	40
L	60	40
W	60	40
CR	60	40
SR	60	40
PM	60	40
FA	60	40

C= Concept, D= design, S= supervision, DCP= data collection and/or processing, DAI= data analysis and/or interpretation, L= literature search, W= writing, CR= critical review, SR=submission

Conflict of Interest

The authors declared that there is no conflict of interest.

Ethical Consideration

Ethics committee approval was not required for this study because of there was no study on animals or humans.

Nomenclature

$\dot{C}_{D,k}$= cost of exergy destruction of the component ($/h)
CRF = capital recovery factor
$c_{F,k}$= unit cost of the fuel ($/GJ)
$c_{P,k}$= unit cost of the product ($/GJ)
ex = specific exergy (kJ/kg)
$\dot{E}x$ = exergy rate (kW)
$\dot{E}x_D$= exergy destruction rate (kW)
f_k = exergoeconomic factor
h = specific enthalpy (kJ/kg)
HP = High pressure
i_r = interest rate
LP = Low pressure
$\dot{m}$ = mass flow rate (kg/s)
n = number of working years
P = pressure (kPa)
$\dot{Q}$ = heat transfer rate (kW)
r_k = relative cost difference of the component
s = specific entropy (kJ/kg ·K)
$SUCP$ = sum unit cost of production ($/GJ)
u_f = overall uncertainty
u_{x_i} = standard uncertainty
$u_{rel,f}$ = relative uncertainty
$\dot{W}$ = work rate (kW)
x = dryness fractions (quality)
$\dot{Y}_k$ = relative exergy destruction rate of the component
Z_k = acquisition cost of the component ($)
$\dot{Z}_k$ = sum of the cost rates of the component ($/h)

Greek Symbol

ε_k= exergy efficiency of the component
η = energy efficiency
τ = annual operation hours (h)
φ = sustainability ratio
ψ = exergy efficiency

Subscripts

0 = reference state
$cond$ = condenser
cw = cooling water
ev =expansion valve
hex = heat exchanger
sep = separator
tur = türbine

References

Anonymous. 2024. Global energy perspective: 2024 report. URL: https://www.mckinsey.com/industries/energy-and-materials/our-insights/global-energy-perspective (accessed date: April 2, 2025).

Aybek U, Dogan B. 2025. Heat exchanger positioning and power optimization in geothermal power plant using flash steam. Proc. Int. Aegean Conf. Innov. Technol. Eng-XI, April 04–06, Izmir, Türkiye, pp: 399-414.

Belyakov N. 2019. Sustainable power generation current status, future challenges, and perspectives. Academic Press, Chapter Twenty - Geothermal energy, pp: 475-500.

Bina S, Jalilinasrabady S, Fujii H. 2018. Exergoeconomic analysis and optimization of single and double flash cycles for Sabalan geothermal power plant. Geothermics, 72: 74–82.

Cao Y, Mihardjo LW, Dahari M, Ghaebi H, Parikhani T, Mohamed AM. 2021. An innovative double-flash binary cogeneration cooling and power (CCP) system: thermodynamic evaluation and multi-objective optimization. Energy, 214: 118864.

Cengel YA, Boles MA, Kanoglu M. 2019. Thermodynamics: An engineering approach. McGraw-Hill Education, New York, 9th ed., pp: 544.

Chitsaz A, Hosseinpour J, Assadi M. 2017. Effect of recycling on the thermodynamic and thermoeconomic performances of SOFC based on trigeneration systems; a comparative study. Energy, 124: 613-624.

Colorado-Garrido D, Alcalá-Perea G, Alaffita-Hernández FA, Escobedo-Trujillo BA. 2021. Exergy analysis using a theoretical formulation of a geothermal power plant in Cerro Prieto, México. Entropy, 23(9): 1137.

El Haj Assad M, Bani-Hani E, Khalil M. 2017. Performance of geothermal power plants (single, dual, and binary) to compensate for LHC-CERN power consumption: comparative study. Geotherm Energy, 5: 17.

Evangeline SI, Darwin S. 2025. The role of carbon dioxide in enhancing geothermal energy: a review of current developments and future potential. Renew. Sustain. Energy Rev, 214: 115525.

Farsi A, Rosen MA. 2022. Comparison of thermodynamic performances in three geothermal power plants using flash steam. ASME Open J. Eng, 1: 011016.

Gutiérrez-Negrín LCA. 2024. Evolution of worldwide geothermal power 2020–2023. Geotherm Energy, 12: 14.

Kariuki BW, Hassan H, Ahmed M, Emam M. 2025. A review on

geothermal-solar hybrid systems for power production and multigeneration systems. Appl. Therm. Eng, 259: 124796.

Lazzaretto A, Tsatsaronis G. 2006. SPECO: a systematic and general methodology for calculating efficiencies and costs in thermal systems. Energy, 31: 1257–1289.

Manfrida G, Talluri L, Ungar P, Zuffi C, Díaz-Ramírez M, Leiva H, Mainar-Toledo MD, Jokull S. 2023. Exergo-economic and exergo-environmental assessment of two large CHP geothermal power plants. Geothermics, 113: 102758.

Nkinyam CM, Ujah CO, Asadu CO, Kallon DVV. 2025. Exploring geothermal energy as a sustainable source of energy: a systemic review. Unconventional Resources, 6: 100149.

Ranjbar F, Chitsaz A, Mahmoudi SMS, Khalilarya S, Rosen MA. 2014. Energy and exergy assessments of a novel trigeneration system based on a solid oxide fuel cell. Energy Convers. Manag, 87: 318–327.

Rudiyanto B, Bahthiyar MA, Pambudi NA, Widjonarko MH. 2021. An update of second law analysis and optimization of a single-flash geothermal power plant in Dieng, Indonesia. Geothermics, 96: 102212.

Rudiyanto B, Birri MS, Widjonarko, Avian C, Kamal DM, Hijriawan M. 2023. A genetic algorithm approach for optimization of geothermal power plant production: case studies of direct steam cycle in Kamojang. S. Afr. J. Chem. Eng, 45: 1-9.

Rudiyanto B, Illah I, Pambudi NA, Cheng C, Adiprana R, Imran M, Saw LH, Handogo R. 2017. Preliminary analysis of dry-steam geothermal power plant by employing exergy assessment: case study in Kamojang geothermal power plant, Indonesia. Case Stud. Therm. Eng, 10: 292-301.

Sadat SMS, Ghabei H, Lavasani AM. 2020. 4E analyses of an innovative polygeneration system based on SOFC. Renew. Energy, 156: 986-1007.

Samatar AM, Lekbir A, Mekhilef S, Mokhlis H, Tey KS, Alassaf A. 2025. Techno-economic and environmental analysis of a fully renewable hybrid energy system for sustainable power infrastructure advancement. Sci. Rep, 15: 12140.

Shamoushaki M, Aliehyaei M, Taghizadeh-Hesary F. 2021. Energy, exergy, exergoeconomic, and exergoenvironmental assessment of flash-binary geothermal combined cooling, heating and power cycle. Energies, 14(15): 4464.

Shang Y, Sang S, Tiwari AK, Khan S, Zhao X. 2024. Impacts of renewable energy on climate risk: a global perspective for energy transition in a climate adaptation framework. Appl. Energy, 362: 122994.

Shokati N, Ranjbar F, Yari M. 2015. Comparative and parametric study of double flash and single flash/ORC combined cycles based on exergoeconomic criteria. Appl. Therm. Eng, 91: 479-495.

Soleymani E, Gargari SG, Ghaebi H. 2021. Thermodynamic and thermoeconomic analysis of a novel power and hydrogen cogeneration cycle based on solid SOFC. Renew. Energy, 177: 495-518.

Stefánsson V. 2002. Investment cost for geothermal power plants. Geothermics, 31(2): 263-272.

Tang T, Li B, Lu M, Feng Y, Wang J. 2025. Synergistic geothermal energy and ammonia fuel cell utilization towards sustainable power, cooling, and freshwater production: an exergoeconomic, exergoenvironmental, and technoeconomic analysis. Renew. Energy, 241: 122244.

Tian MW, Parikhani T, Jermsittiparsert K, Ashraf MA. 2020. Exergoeconomic optimization of a new double-flash geothermal-based combined cooling and power (CCP) system at two different cooling temperatures assisted by boosters. J. Clean. Prod, 261: 120921.

Vargas CA, Caracciolo L, Ball PJ. 2022. Geothermal energy as a means to decarbonize the energy mix of megacities. Commun. Earth Environ, 3: 66.

Velychko O, Gordiyenko T. 2009. The use of guide to the expression of uncertainty in measurement for uncertainty management in national greenhouse gas inventories. Int. J. Greenhouse Gas Control, 3(4): 514-517.

Vojdani M, Fakhari I, Ahmadi P. 2021. A novel triple pressure HRSG integrated with MED/SOFC/GT for cogeneration of electricity and freshwater: techno-economic-environmental assessment, and multi-objective optimization. Energy Convers. Manag, 233: 113876.

Wang J, Yan Z, Ma S, Dai Y. 2012. Thermodynamic analysis of an integrated power generation system driven by solid oxide fuel cell. Int. J. Hydrogen Energy, 37: 2535-2545.

Unverdi M, Cerci Y. 2013. Performance analysis of Germencik geothermal power plant. Energy, 52: 192-200.

Zhang F, Yan Y, Gaoliang L, Jiaqiang E. 2022. Energy, exergy, exergoeconomic and exergoenvironmental analysis on a novel parallel double-effect absorption power cycle driven by the geothermal resource. Energy Convers. Manag, 258: 115473.

Zhao Y, Wang J. 2016. Exergoeconomic analysis and optimization of a flash-binary geothermal power system. Appl. Energy, 179: 159–170.

Black Sea Journal of Engineering and Science
doi: 10.34248/bsengineering.1684487

Open Access Journal
e-ISSN: 2619 – 8991

Derleme (Review)
Cilt 8 - Sayı 4: 1235-1244 / Temmuz 2025
(Volume 8 - Issue 4: 1235-1244 /July 2025)

AÇIK RADYO ERİŞİM AĞI ÜZERİNE SİSTEMATİK BİR İNCELEME: BİLEŞENLER, UYGULAMALAR VE GELECEK PERSPEKTİFLERİ

Önem YILDIZ[1]*

[1]*Aydın Adnan Menderes University, Faculty of Engineering, Department of Electrical and Electronics Engineering, 09100, Aydin, Türkiye*

Özet: Açık Radyo Erişim Ağı (O-RAN), açıklık, çok tedarikçili yapı ve yazılım tanımlı ağ prensipleriyle geleneksel RAN mimarilerine alternatif sunarak mobil iletişimde önemli bir dönüşüm başlatmaktadır. Bu derleme çalışması, O-RAN'ın mimari yapısını, kontrol düzlemi bileşenlerini ve yapay zekâ ile bütünleşen ağ yönetim yaklaşımlarını incelemektedir. Yakın Gerçek Zamanlı (Near-RT) ve Gerçek Zamanlı Olmayan (Non-RT) RAN Akıllı Kontrolör (RIC) mimarileri çerçevesinde çalışan xApp ve rApp uygulamalarının rolleri, kaynak yönetimi ve politika tabanlı kontrol bağlamında incelenmiştir. Literatürdeki uygulama senaryoları, O-RAN'ın yalnızca mobil şebekeler değil, aynı zamanda özel 5G ağlar, uçan iletişim platformları ve dijital ikiz tabanlı ağ yönetimi gibi yenilikçi alanlara da entegre edilebildiğini göstermektedir. Bununla birlikte, zamanlama hassasiyetleri, güvenlik açıkları, sahaya dayalı veri eksiklikleri ve standardizasyon belirsizlikleri, mimarinin uygulanabilirliğini sınırlayan başlıca teknik zorluklar arasında yer almaktadır. O-RAN'ın 6G'ye geçiş sürecinde; otonom kontrol sistemleri, uçtan uca dilimleme ve yüksek frekanslı haberleşme altyapıları ile birleşerek temel bir yapı taşı haline gelmesi öngörülmektedir. Bu çalışma, O-RAN teknolojisine yönelik güncel araştırmaları bir araya getirerek, gelecekteki akademik ve endüstriyel çalışmalara kapsamlı bir referans çerçevesi sunmayı hedeflemektedir.

Anahtar kelimeler: Açık radyo erişim ağı (O-RAN), 5G, 6G, Yazılım tanımlı ağ, Yapay zekâ

A Systematic Study on Open Radio Access Network: Components, Applications, and Future Directions

Abstract: Open Radio Access Network (O-RAN) introduces a paradigm shift in mobile communications by promoting openness, multi-vendor interoperability, and software-defined networking capabilities as an alternative to traditional RAN architectures. This review study analyzes the architectural structure of O-RAN, its control plane components, and AI-driven network management frameworks. The roles of xApps and rApps operating on Near-Real-Time (Near-RT) and Non-Real-Time (Non-RT) RAN Intelligent Controller (RIC) architectures are examined in the context of resource management and policy-based control. Findings from the literature indicate that O-RAN can be effectively integrated not only into conventional mobile networks but also into emerging use cases such as private 5G networks, UAV-assisted platforms, and digital twin-based network monitoring. However, several technical challenges remain, including timing and synchronization sensitivity, security vulnerabilities, lack of real-world labeled datasets, and ongoing standardization gaps. As we move toward 6G, O-RAN is expected to serve as a foundational architecture supporting autonomous control loops, end-to-end slicing, and high-frequency communication systems. This work aims to provide comprehensive references for researchers and practitioners by consolidating recent developments and outlining future research directions in the O-RAN domain.

Keywords: Open radio access network (O-RAN), 5G, 6G, Software-defined network, Artificial intelligence

***Sorumlu yazar (Corresponding author):** Aydin Adnan Menderes University, Faculty of Engineering, Department of Electrical and Electronics Engineering, 09100, Aydin, Türkiye
E mail: onem.yildiz@adu.edu.tr (O. YILDIZ)
Onem YILDIZ https://orcid.org/0000-0003-0675-6637

Gönderi: 26 Nisan 2025 **Received:**April 26, 2025
Kabul: 04 Haziran 2025 **Accepted:** June 04, 2025
Yayınlanma: 15 Temmuz 2025 **Published:** July 15, 2025

Cite as: Yildiz O. 2025. A systematic study on open radio access network: Components, applications, and future directions. BSJ Eng Sci, 8(4): 1235-1244.

1. Giriş

Beşinci nesil (5G) ve ötesi (Beyond 5G/6G) haberleşme sistemleri; yüksek veri iletim hızları, ultra düşük gecikme süreleri ve çok sayıda cihazın eş zamanlı bağlantısı gibi yenilikçi gereksinimlerle, geleneksel radyo erişim ağı (RAN) mimarilerini yetersiz kılmakta ve yeni yaklaşımların benimsenmesini zorunlu hale getirmektedir. Bu teknolojik gereklilikler, kapalı ve satıcıya bağımlı RAN çözümlerinden uzaklaşarak daha açık, modüler ve esnek yapılara geçişi teşvik etmektedir.

O-RAN Alliance tarafından geliştirilen Açık Radyo Erişim Ağı (Open RAN ya da O-RAN) mimarisi; açık arayüzleri, genel amaçlı donanım kullanımı, yazılım tanımlı ağ bileşenleri ve yapay zekâ destekli yönetim işlevleriyle bu dönüşümün merkezinde yer almaktadır. O-RAN, geleneksel baz istasyonu yapısını işlevsel olarak ayrıştıran ve sanallaştıran mimarisiyle çok satıcılı bir ekosistem oluşturmayı hedeflemekte; böylece şebeke operatörleri açısından maliyetlerin azaltılması, tedarikçi bağımlılığının kırılması ve inovasyonun teşvik edilmesi gibi önemli avantajlar sunmaktadır (Choudhary vd., 2024; O-RAN Alliance, 2018)

Bu çalışmanın yapılmasındaki temel gerekçe, O-RAN mimarisine yönelik artan akademik ve endüstriyel ilginin hızlı yayılan ancak parçalı ilerleyen literatür yapısı içinde bütüncül bir çerçeveye olan ihtiyacı ortaya koymasıdır. O-RAN ile ilgili teknik bileşenler, uygulama senaryoları, karşılaşılan zorluklar ve yapay zekâ entegrasyonu gibi

This work is licensed (CC BY-NC 4.0) under Creative Commons Attribution 4.0 International License

konular birçok çalışmada ele alınmış olsa da (Tablo 1) bu bilgilerin sistematik biçimde sınıflandırılması ve bütüncül bir analizle sunulması hâlâ önemli bir ihtiyaçtır. Bu derleme çalışması; (i) O-RAN mimarisinin temel yapısını ve bileşenlerini detaylandırmak, (ii) RAN Akıllı Kontrolör (RIC) katmanının işlevlerini ve mimari konumunu açıklamak, (iii) yapay zekâ destekli otonom ağ optimizasyon tekniklerini değerlendirmek, (iv) ağ dilimleme (network slicing) ve kaynak yönetimi gibi kritik işlevleri incelemek, (v) O-RAN mimarisinin araştırılması için kullanılan testbed'leri tanıtmak, (vi) güvenlik açıkları, sistem bütünlüğü ve mahremiyet konularını tartışmak ve (vii) gerçek dünya uygulama senaryoları ve ortaya çıkan yeni paradigma örneklerini analiz etmek amacıyla hazırlanmıştır. Ayrıca, mevcut sistemlerin karşılaştığı temel zorluklar ortaya konulmakta ve gelecekteki araştırma yönelimleri hakkında öngörüler sunulmaktadır. Böylece hem araştırmacılar hem de sektör profesyonelleri için kapsamlı, yapılandırılmış ve güncel bir başvuru kaynağı oluşturulması hedeflenmektedir.,

2. Open RAN

2.1. O-RAN Mimarisi

O-RAN mimarisi, geleneksel RAN yapısının monolitik doğasını parçalayarak daha modüler, esnek ve açık bir sistem haline getirmeyi hedefler. Bu dönüşüm, ağ bileşenlerinin işlevsel olarak ayrıştırılması ve aralarındaki iletişimin açık, standart arayüzlerle sağlanması prensibine dayanır. Fonksiyonel ayrıştırma, çoklu tedarikçi desteği ve yapay zekâ gibi yenilikçi teknolojilerin mimariye entegre edilmesi gibi ilkeler, bu yeni nesil mimarinin temel taşlarını oluşturmaktadır. Literatürde, bu evrimsel sürecin Cloud-RAN mimarisi üzerinden O-RAN'a nasıl ulaştığını teknik açıdan irdeleyen çalışmalar mevcuttur (Singh vd., 2020).

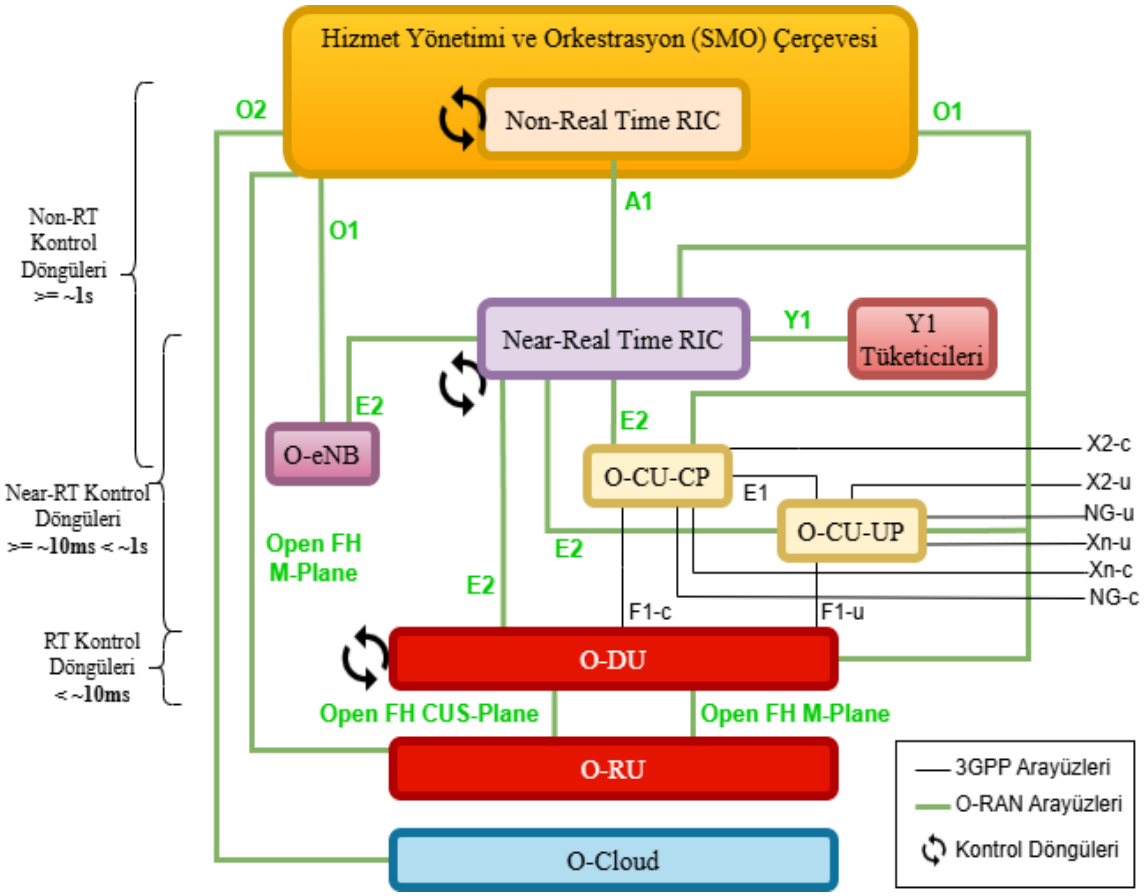
O-RAN Alliance tarafından tanımlanan mimaride üç temel işlevsel blok öne çıkar: O-Central Unit (O-CU), O-Distributed Unit (O-DU) ve O-Radio Unit (O-RU). Bu bileşenler, açık tanımlanmış arayüzler aracılığıyla birbiriyle etkileşim kurar (Huang vd., 2023; O-RAN Alliance, 2020). O-RAN mimarisi ve içerdiği arayüzler sırasıyla Tablo 2 ve Şekil 1'de ayrıntılı olarak gösterilmektedir.

Tablo 1. O-RAN ile ilgili literatür çalışmalarının karşılaştırmalı özeti

Çalışmalar	Kategori	RIC Türü/ Uygulamaları	Yapay Zekâ (AI) Desteği	Testbed
1) Polese vd., 2023	O-RAN mimarisi ve özellikleri	xApp, rApp	-	-
2) Marinova ve Leon-Garcia, 2024		xApp, rApp	✓	-
3) Garcia-Saavedra ve Costa-Perez, 2021; Abdalla vd., 2022; Singh vd., 2020; Alam vd., 2024; Habibi vd., 2020; Choudhary vd., 2024		-	-	-
4) Beerten vd., 2022; Beerten vd., 2024	O-RAN mimarisinde hücresiz ağlar	-	-	-
5) Chu vd., 2025		-	✓	Hücresiz testbed
6) Demir vd., 2024; Kasuluru vd., 2024		Near-RT RIC	-	-
7) Zhang vd., 2022a	RAN dilimleme	xApp	✓	-
8) Arslan vd., 2023		-	✓	Ns-3, OpenAI Gym
9) Bonati vd., 2021b		xApp	-	Colosseum, ARENA
10) Sever vd., 2025		xApp	✓	-
11) D'Oro vd., 2022b	Gerçek zamanlı RIC tasarımı	xApp, dApp	✓	Colosseum
12) Ko vd., 2023		dApp	-	-
13) Tsampazi vd., 2023	RIC uygulaması tasarımı	xApp	✓	Colosseum
14) Santos vd., 2025		xApp	✓	-
15) Groen vd., 2024a; Groen vd., 2024b	Güvenli O-RAN tasarımı	-	-	-
16) Huang vd., 2023	Testbed tasarımı	xApp	-	-
17) Bonati vd., 2022	Deneysel platform tasarımı	xApp	-	OpenRAN Gym
18) Habibi vd., 2023	E2E çerçeve tasarımı	-	-	-
19) D'Oro vd., 2022a	Orkestrasyon çerçevesi tasarımı	rApp	✓	Colosseum
20) Polese vd., 2022	Test çerçevesi tasarımı	xApp	✓	ColO-RAN, Colosseum
21) Lee vd., 2020	AI/ML iş akışı tasarımı	xApp	✓	Acumos, ONAP
22) Niknam vd., 2022	Kaynak yönetimi	Near-RT/ Non-RT RIC	✓	-
23) Pham vd., 2022	O-RAN mimarisinde UAV	xApp	✓	-
24) Hamdan vd., 2023	Ağ otomasyonu	-	✓	-

Tablo 2. O-RAN mimarisindeki arayüzler ve işlevleri

Arayüz	İlgili Birimler	Temel Fonksiyon
A1	Non-RT RIC ↔ Near-RT RIC	Politika aktarımı, AI model önerisi
O1	SMO ↔ O-RU, O-DU, O-CU	Performans, hata ve yapılandırma yönetimi
O2	SMO ↔ Cloud	Kaynak yönetimi
F1	O-CU ↔ O-DU	Kullanıcı ve kontrol düzlemi iletişimi
E1	O-CU-CP ↔ O-CU-UP	CU-CP ve CU-UP arasında koordinasyon
E2	Near-RT RIC ↔ O-CU / O-DU	xApp kontrol mesajları ve ölçümler
Y1	Near-RT RIC ↔ Y1 Tüketicileri (harici uygulamalar)	Performans ve analiz verilerinin dış sistemlere sunumu
Fronthaul (FH)	O-DU ↔ O-RU	Zamanlama, senkronizasyon, I/Q veri iletimi
X2/Xn/NG	gNB ↔ gNB, gNB ↔ Core	3GPP RAN işlemleri



Şekil 1. O-RAN mimarisi.

O-CU, 3GPP mimarilerinde karşılık gelen merkezi kontrol katmanlarını (RRC ve PDCP) barındırır. Daha zaman kritik işlemleri ise O-DU üstlenir; bu birim, MAC, RLC ve alt PHY katmanlarını işler ve genellikle kenar bulut ortamlarında çalıştırılır. O-RU ise fiziksel radyo sinyallerinin işlenmesini sağlar; hüzmeleme ve RF modülasyonu gibi işlemleri üstlenir. Bu birimlerin ayrıştırılması sayesinde, ağ işletmecileri donanım ve yazılım bileşenlerini farklı tedarikçilerden sağlayarak çoklu tedarikçi ekosistemini destekleyebilir (Polese vd., 2023).

O-RAN mimari yapısı, yalnızca donanımsal değil, aynı zamanda işlevsel bir dönüşüm de sunar. Ağın işletilmesi, kontrol edilmesi ve optimize edilmesi süreçleri, geleneksel RAN sistemlerinden farklı olarak yazılım tanımlı denetleyiciler aracılığıyla yürütülür. Bu noktada, mimarinin bir sonraki evresi olan RAN Akıllı Kontrolör (RAN Intelligent Controller, RIC) bileşenleri devreye girer.

2.2. RAN Akıllı Kontrolör (RIC)

O-RAN mimarisini önceki nesil mobil ağ mimarilerinden ayıran en yenilikçi bileşenlerden biri, RIC yapısıdır. RIC, ağ kontrol işlevlerini ayrıştırarak bu işlevlerin yapay zekâ ve optimizasyon algoritmaları ile desteklenmesini mümkün kılar. Böylece, ağın programlanabilirliği artırılırken, çok tedarikçili ve açık yazılım tabanlı bir ekosistem geliştirilmesinin önü açılır.

RIC mimarisi, iki katmanlı bir kontrol yapısına dayanır: Yakın Gerçek Zamanlı RIC (Near-Real-Time RIC, Near-RT RIC) ve Gerçek Zamanlı olmayan RIC (Non-Real-Time

RIC, Non-RT RIC) (Bonati vd., 2021b). Near-RT RIC, milisaniyeler mertebesinde tepki gerektiren zaman açısından kritik işlemleri yönetmek üzere ağın kenarına konumlandırılır. E2 arayüzü üzerinden doğrudan O-DU ve O-CU ile iletişim kuran bu katmanda çalışan uygulamalara xApp adı verilir. Bu uygulamalar; hüzmeleme optimizasyonu, kullanıcı ilişkilendirme, spektrum verimliliği iyileştirme ve yük dengeleme gibi görevleri yerine getirir (Santos vd., 2025).

Non-RT RIC ise, Hizmet Yönetimi ve Orkestrasyon (SMO) çerçevesinin bir parçası olup daha uzun zaman ölçeklerinde (saniyeler ila dakikalar) çalışan, politika üretimi, performans analizi, AI model eğitimi ve optimizasyon gibi stratejik işlevleri üstlenir. Bu katmanda yer alan uygulamalara rApp adı verilir. Non-RT RIC ile Near-RT RIC arasındaki koordinasyon, A1 arayüzü aracılığıyla sağlanır. Bu sayede rApp tarafından geliştirilen politikalar ve eğitilen yapay zekâ model parametreleri, A1 mesajları yoluyla xApp'lere iletilerek sahada gerçek zamanlı karar desteği sağlanır (Marinova ve Leon-Garcia, 2024).

O-RAN mimarisi, birbiriyle eşgüdüm içinde çalışan çok katmanlı bir kontrol döngüsü mimarisini benimsemektedir. Genellikle üç temel kontrol döngüsü tanımlanır: (i) Near-RT kontrol döngüsü, xApp'lerin DU/CU ile E2 arayüzü üzerinden kurduğu düşük gecikmeli veri yoludur; (ii) Non-RT kontrol döngüsü, rApp'lerin A1 protokolü aracılığıyla xApp'lerle etkileşim kurduğu stratejik kanaldır; (iii) Real Time (RT) kontrol döngüsü ise literatürdeki bazı çalışmalar tarafından da ele alınan ve O-DU radyo çizelgeleme (scheduling) gibi işlemlerin yürütülmesi ile ilgili 10 ms'nin altındaki zaman ölçeklerinde çalışan gerçek zamanlı kontrol döngüsüdür (D'Oro vd., 2022b; Ko vd., 2023).

O-RAN mimari temelinin literatürdeki karşılıkları incelendiğinde, yapay zekâ iş akışlarının RIC platformuna entegrasyonuna yönelik çeşitli senaryolar göze çarpmaktadır.

RIC mimarisi, O-RAN yapısının esnek ve modüler kontrol yeteneklerini mümkün kılarken, aynı zamanda ağ yönetim süreçlerinin daha veri odaklı ve otonom bir hale getirilmesine de olanak sağlamaktadır. Özellikle xApp ve rApp uygulamaları aracılığıyla geliştirilen bu kontrol yapıları, yalnızca geleneksel kural tabanlı yönetimi değil, yapay zekâ ve makine öğrenmesi teknikleriyle desteklenen dinamik optimizasyon mekanizmalarını da mümkün kılmaktadır. Bir sonraki bölümde, RIC yapısı ile bütünleşen yapay zekâ yaklaşımlarının, O-RAN mimarisinde nasıl otonom ağ optimizasyonuna dönüştüğü detaylı şekilde ele alınacaktır.

2.3. Yapay Zekâ ile Otonom RAN Optimizasyonu

O-RAN mimarisinin sunduğu programlanabilirlik ve açık arayüz özellikleri, yapay zekâ ve makine öğrenmesi (ML) uygulamalarının ağ seviyesinde gerçek zamanlı olarak entegre edilebilmesini mümkün kılmaktadır. Geleneksel RAN sistemlerinde yapay zekâ uygulamaları çoğunlukla offline analizlerle veya operatör destekli karar süreçleriyle sınırlıyken, O-RAN yapısı bu teknolojilerin doğrudan ağ içi optimizasyon işlevlerine entegre edilmesine olanak sağlar.

Özellikle Near-RT RIC katmanında çalışan xApp uygulamaları, zaman açısından kritik kararların alınmasında ML tabanlı algoritmalarla güçlendirilmiştir. Bu uygulamalar trafik tahmini, kullanıcı ilişkilendirme, yük dengeleme, spektrum paylaşımı ve hüzmeleme gibi görevleri gerçekleştirmektedir. Örneğin, Tsampazi ve arkadaşlarının yaptığı çalışmada farklı derin pekiştirmeli öğrenme algoritmalarına sahip xApp'ler karşılaştırılmış ve çeşitli trafik senaryolarına göre en verimli karar yapılarını belirlemeye yönelik kapsamlı bulgular sunulmuştur (Tsampazi vd., 2023). Benzer şekilde, Santos ve arkadaşları bir xApp'in sıfırdan yazılım mühendisliği perspektifiyle nasıl geliştirileceğini örnekleriyle detaylandırmaktadır (Santos vd., 2025).

Lee ve arkadaşları, AI/ML modellerinin Acumos ve ONAP platformlarında geliştirilip xApp biçiminde paketlenerek Near-RT RIC'e entegre edilebildiğini göstermektedir. Trafik tahmini uygulamaları ile test edilen bu yapı, GPU/NPU destekli hızlandırmaların ve zaman serisi işleme modüllerinin nasıl yerleştirilebileceğini de ortaya koymaktadır (Lee vd., 2020).

Benzer şekilde, Polese ve arkadaşları, Near-RT RIC üzerinde çalışan xApp'lerin kapalı çevrim (closed-loop) kontrol sistemlerine entegrasyonunu ele almıştır. Bu sistemler, O-RAN uyumlu test ortamları (örneğin Colosseum) üzerinde çalıştırılarak, gerçek zamanlı ağ ölçümleri ile xApp davranışlarının dinamik olarak güncellenebildiği yapılar geliştirilmiştir (Polese vd., 2022).

Daha uzun zaman ölçeklerinde görev yapan Non-RT RIC katmanında çalışan rApp uygulamaları ise, AI modellerinin eğitimi, performans değerlendirme ve politika üretimi gibi görevlerde kritik rol oynamaktadır. Bu sayede ağ performansında gözlenen düşüşlerin nedenleri belirlenebilmekte ve Near-RT RIC üzerindeki xApp davranışları bu bilgiler ışığında güncellenebilmektedir.

AI tabanlı kontrol sistemlerinin otomasyon gücü, ağ esnekliğini ve hizmet kalitesini artırmada kilit rol oynamaktadır. Bu sebeple D'Oro ve arkadaşları, rApp'lerin yönetiminde çok katmanlı bir yapay zekâ mimarisi önermiştir. Bu mimari, rApp'lerin konumlandırılmasını, uygun model seçimlerini ve Colosseum test ortamında bu kararların değerlendirilmesini içermekte; böylece kontrol yükü ve gecikme gibi sistem parametreleri optimize edilmektedir (D'Oro vd., 2022a).

AI/ML uygulamaları arasında öne çıkan yaklaşımlardan biri de federatif öğrenme ve çok etmenli pekiştirmeli öğrenme yöntemlerinin O-RAN'a entegrasyonudur. Arslan ve arkadaşlarının yaptığı çalışmada, merkezi veri paylaşımı olmaksızın optimum zamanlama kararları alınabilen bir federatif yapı geliştirilmiş; ns-3 ve OpenAI Gym platformlarında test edilen sistemin, geleneksel statik derin pekiştirmeli öğrenme (DRL) yaklaşımlarına göre daha yüksek verimlilik sağladığı gösterilmiştir

(Arslan vd., 2023).

Mobiliteye sahip uygulamalarda da AI/ML etkin biçimde kullanılmaktadır. Pham ve arkadaşları, mobil baz istasyonu görevindeki insansız hava araçlarının (UAV) konumlandırma ve görev atamalarını, Near-RT RIC içinde çalışan AI destekli kontrol döngüleriyle optimize etmiş; ağın kapsama alanı ve gecikme karakteristiklerini iyileştirmişlerdir (Pham vd, 2022).

Öte yandan, Niknam ve arkadaşları çalışmalarında, hem Near-RT hem de Non-RT RIC bileşenlerinin eşgüdümlü çalıştığı bir trafik yönetim sistemi tanıtılmıştır. Bu sistemde, uzun-kısa vadeli bellek (Long Short Term Memory, LSTM) tabanlı modellerle yapılan trafik tahmini sonucunda, Near-RT RIC üzerindeki xApp'lerin zaman açısından kritik kararları (örneğin hücre bölme–cell splitting) otonom olarak alması sağlanmıştır. Gerçek trafik verileriyle eğitilen sistem, %92.6 doğrulukla çalışarak kapalı çevrim kontrol yapılarına dair umut verici sonuçlar sunmuştur. Böylece, O-RAN mimarisinin hem öğrenen hem de gerçek zamanlı tepki verebilen esnek kontrol yapısı vurgulanmıştır (Niknam vd., 2022).

Sonuç olarak, O-RAN yapısı yalnızca yazılım tanımlı değil, aynı zamanda veriyle öğrenebilen, uyum sağlayabilen ve otonom kontrol yeteneklerine sahip bir ağ mimarisi olarak öne çıkmaktadır. Heterojen trafik ortamları, yüksek mobilite ve kaynak sınırlamaları gibi karmaşık koşullar altında bile AI destekli çözümlerin etkili biçimde kullanılabildiği bu yapı, 6G'ye giden yolda otonom ağ yönetiminin temel taşı olarak değerlendirilmektedir.

2.4. Ağ Dilimleme ve Kaynak Yönetimi

Beşinci nesil mobil iletişim sistemlerinin en temel hedeflerinden biri, aynı fiziksel altyapı üzerinden farklı hizmet türlerini birbirinden izole şekilde ve kalite garantili olarak sunabilmektir. Bu ihtiyaca yanıt olarak geliştirilen ağ dilimleme (network slicing) kavramı, O-RAN mimarisiyle birleştiğinde esneklik, ölçeklenebilirlik ve yazılım tanımlı kaynak yönetimi açısından yeni olanaklar sunmaktadır. Geleneksel mimarilerde sınırlı olan hizmet izolasyonu, O-RAN sayesinde yapay zekâ destekli kontrol katmanları aracılığıyla dinamik biçimde yürütülebilmektedir (Zhang vd., 2022b).

O-RAN'da ağ dilimleme; radyo spektrumu, işlemci kaynakları ve bellek gibi fiziksel kaynakların mantıksal parçalara ayrılarak farklı hizmet dilimlerine tahsis edilmesiyle gerçekleştirilir (Habibi vd., 2020). Her bir dilim, belirli bir servis sınıfına (örn. URLLC, eMBB, mMTC) yönelik optimize edilir ve bu dilimlerin hizmet kalitesi (Quality of Service, QoS) parametreleri, RIC katmanları aracılığıyla merkezi veya dağıtık biçimde kontrol edilebilir (Alam vd., 2024; Habibi vd., 2023).

Farklı servis sınıflarının aynı ağ altyapısı üzerinde güvenli ve izole biçimde hizmet alabilmesi, dilimleme ile etkili yönlendirme ve zamanlama mekanizmaları gerektirir. Zhang ve arkadaşları çalışmalarında, O-DU havuzları üzerinden geçen trafik yükünü optimize edebilmek için ağ dilimleme politikalarıyla da entegre şekilde çalıştırılan yeni bir yönlendirme ve zamanlama mimarisi önerilmiştir (Zhang vd, 2022a). OFDM sembollerinin UDP tabanlı yönlendirme mekanizmaları ile entegre edildiği bu sistemde, dinamik programlama ve greedy algoritmalar aracılığıyla düşük gecikmeli çözüm yaklaşımları geliştirilmiş ve çoklu hizmet sınıfları altında verimli kaynak tahsisi sağlandığı gösterilmiştir.

Dilimleme yönetimi yalnızca işlem kapasitesine değil, aynı zamanda radyo spektrumu gibi kablosuz kaynaklara da uzanmaktadır. Sever ve arkadaşları çalışmalarında, Near-RT RIC üzerinde çalışan bir xApp aracılığıyla, farklı hizmet dilimlerinin gereksinimlerini karşılamak üzere radyo kaynaklarının dinamik tahsisi gerçekleştirilmiştir. DRL tabanlı bu yaklaşım, OpenAirInterface üzerinde O-RAN uyumlu bir test ortamında uygulanmış ve düşük gecikmeli dilimlerin gereksinimlerini karşılarken, diğer dilimlerin performansını da optimize etmiştir. Bu çalışma, yapay zekâ destekli xApp'lerin, O-RAN mimarisinde dinamik spektrum ve kaynak yönetimi konularında etkin bir şekilde kullanılabileceğini göstermektedir (Sever vd., 2025).

Kaynak yönetiminin bir diğer boyutu, mikro düzeyde optimizasyonları kapsamaktadır. Kullanıcı ilişkilendirme, güç kontrolü ve önceliklendirme gibi alt katman görevleri, O-RAN mimarisi altında hem geleneksel kontrol algoritmaları hem de yeni nesil otonom sistemler aracılığıyla yönetilebilir. Demir ve arkadaşlarının çalışmasında, hücresiz MIMO yapılarında radyo, ön bağlantı (fronthaul) ve bulut kaynaklarının ortak orkestrasyonu ele alınmakta; fonksiyonel bölme stratejilerinin enerji tüketimi üzerindeki etkisi incelenmektedir. Bu çalışmada, uçtan uca kaynak tahsis mekanizmalarının enerji verimliliği açısından kritik olduğu ortaya konmuştur (Demir vd., 2024). Bu yaklaşımı tamamlayıcı nitelikte olan bir diğer çalışma ise, Near-RT RIC üzerinde çalışan bir xApp aracılığıyla kullanıcıların SINR gereksinimlerini karşılayacak şekilde güç tüketimini minimize etmeye yönelik optimizayon temelli bir algoritma sunmaktadır. Bu yöntem, enerji verimliliği ile kullanıcı hizmet kalitesi arasında denge kuran esnek bir kontrol mimarisi önermektedir (Kasuluru vd., 2024).

Tüm bu çalışmalar göstermektedir ki, O-RAN mimarisi yalnızca açık arayüzlü bir sistem olmakla kalmayıp aynı zamanda dinamik ve hizmete özel kaynak tahsisini mümkün kılan bir optimizasyon çerçevesi sunmaktadır. AI/ML destekli xApp ve rApp uygulamaları ile zenginleştirilen bu yapı, geleneksel ağ yönetim paradigmalarını geride bırakarak dilim bazlı hizmet mimarilerinin önünü açmaktadır. Bu yönüyle, O-RAN mimarisi; 5G sonrası ağların hem esnekliğini hem de hizmet çeşitliliğini sürdürülebilir biçimde yönetebilmek için kritik bir platform olarak değerlendirilmektedir.

2.5. Testbed'ler

O-RAN mimarisi, çok katmanlı yazılım bileşenleri ve açık arayüz standartlarına dayanması nedeniyle, bu yapının işlevsel olarak test edilmesi, yeni geliştirilen xApp/rApp uygulamalarının doğrulanması ve AI tabanlı kontrol stratejilerinin değerlendirilmesi için çeşitli deneysel platformlara ve testbed ortamlarına ihtiyaç duyar. Bu

doğrultuda hem yazılım tabanlı hem de donanım destekli çeşitli testbed sistemleri geliştirilmiş olup, bu sistemler prototipleme, performans değerlendirme ve birlikte çalışabilirlik gibi alanlarda araştırmacılara önemli olanaklar sunmaktadır.

Deneysel platformlardan biri olan Colosseum (Bonati vd., 2021c), 256 programlanabilir yazılım tanımlı radyo (SDR) düğümü ve gerçek zamanlı kanal emülatörü içeren dünyanın en büyük kablosuz ağ emülatörlerinden biridir. Gelişmiş AI/ML algoritmalarının çok kullanıcılı, fiziksel katman temelli senaryolarda test edilmesine olanak tanır. Pekiştirmeli öğrenme, federatif öğrenme ve dijital ikiz (digital twin) gibi yaklaşımların değerlendirilmesinde Colosseum, geniş ölçekli kablosuz sistem araştırmaları için benzersiz bir altyapı sunar (Polese vd., 2024).

ARENA (Advanced Reconfigurable Ecosystem for Networked Applications) ise, kapalı alan deneyleri için tasarlanmış, 64 antenli bir USRP X310 SDR dizisi ve 24 bağımsız kullanıcı terminali ile yapılandırılmış fiziksel bir test ortamıdır (Bertizzolo vd., 2020). Kanal tahmini, hüzmeleme ve pekiştirmeli öğrenme gibi RF tabanlı AI uygulamaları bu ortamda gerçek zamanlı olarak test edilebilir. O-RAN mimarisinde DU/CU ve RIC bileşenlerinin entegrasyonu ile gerçek zamanlı xApp davranışı gözlemlenebilir.

COSMOS (Raychaudhuri vd., 2020) ve Platforms for Advanced Wireless Research (PAWR) programı kapsamında geliştirilen POWDER (Breen vd., 2020) şehir ölçeğinde açık alan kablosuz test platformlarıdır. COSMOS, New York'ta kurulmuş olup mmWave ve fiber bağlantılı SDR sistemleri üzerinden yüksek yoğunluklu trafik altında hüzmeleme, yük dengeleme ve spektrum yönetimi gibi uygulamaları test etmek için uygundur. POWDER ise Salt Lake City'de konumlandırılmış olup sub-6 GHz sistemler ve çoklu operatör senaryolarında deney yapılmasını destekler. Bu platformlar, özellikle dış mekân kanal modelleri ve gerçek trafik yükleri altında AI destekli ağ algoritmalarının değerlendirilmesi için büyük önem taşır.

srsRAN (Gomez-Miguelez vd., 2016) ve OpenAirInterface (OAI) (Nikaein vd., 2014), yazılım tabanlı açık kaynak RAN yığınlarıdır. PHY, MAC, RLC ve PDCP gibi protokol katmanlarının tamamı bu platformlar üzerinde yazılım aracılığıyla yönetilebilir. Geliştiriciler, bu sistemler sayesinde xApp'leri doğrudan düşük seviye ağ protokolleri üzerinde test edebilir ve gerçek kanal ortamlarında performans ölçümleri gerçekleştirebilir.

SCOPE (Bonati vd., 2021a), srsRAN altyapısı üzerine kurulmuş bir veri toplama ve ağ kontrol çerçevesidir. Aynı baz istasyonu üzerinde çoklu ağ dilimlerinin oluşturulmasını, her dilim için farklı zamanlama politikalarının tanımlanmasını ve ağdan toplanan anahtar performans ölçümleri (Key Performance Measurement, KPM) verilerinin otomatik olarak işlenmesini destekler. Ayrıca, çalışma zamanında RAN parametrelerini yeniden yapılandırmak üzere kontrol API'leri sağlar. Bu yönüyle, AI/ML tabanlı kontrol uygulamaları için altyapı sağlayıcı bir yapı sunar.

ColO-RAN (Polese vd., 2022), Colosseum üzerinde konumlandırılmış ve O-RAN Yazılım Topluluğu tarafından geliştirilen Near-RT RIC bileşeni ile çalışacak şekilde tasarlanmıştır. SCOPE üzerinden çalışan yazılım tabanlı RAN bileşenlerini kontrol eder ve xApp entegrasyonunu kolaylaştıran bir yazılım geliştirme kiti (SDK) içerir. Bu yapı, AI/ML destekli xApp'lerin esnek ve modüler biçimde test edilmesini mümkün kılar.

Tüm bu testbed bileşenlerini ve altyapıları bir araya getiren entegre bir çerçeve olarak OpenRAN Gym (Bonati vd., 2023), O-RAN ortamlarında büyük ölçekli, veri odaklı deneylerin gerçekleştirilmesini amaçlayan ilk halka açık araştırma platformudur. Northeastern Üniversitesi tarafından geliştirilen bu yapı, Near-RT RIC ve E2 terminasyonları ile tam uyumlu bir kontrol ortamı sunar. Yukarıda belirtilen platformları birleştirerek AI/ML tabanlı xApp'lerin uçtan uca tasarımı, eğitimi ve değerlendirilmesini kolaylaştırır. Yazılım yığınları (srsRAN, OAI), kontrol çerçeveleri (SCOPE), deney altyapıları (Colosseum, ARENA, COSMOS, POWDER) ve xApp geliştirme ortamı (ColO-RAN) ile OpenRAN Gym, akademik ve endüstriyel araştırmalar için güçlü ve esnek bir test altyapısı sunmaktadır (Bonati vd., 2022).

Donanım destekli ve ticari ağlara daha yakın uygulama senaryoları için ONF tarafından geliştirilen SD-RAN testbed'i öne çıkmaktadır. Açık kaynaklı Near-RT RIC yazılımı ile çalışan bu ortam, gerçek O-DU/O-CU bileşenlerini barındırmakta ve xApp uygulamalarının doğrudan sahada değerlendirilmesine olanak sağlamaktadır. ONF'nin geliştirdiği E2 Manager modülü sayesinde E2 arayüzü kontrolü yazılım üzerinden yönetilmekte, ayrıca SMO entegrasyonu ile ağın uçtan uca yazılım tabanlı yönetimi mümkün hale gelmektedir (SD-RAN, 2020).

Gerçek donanım ortamında O-RAN uyumluluğunu test eden bir diğer önemli yapı, China Mobile tarafından geliştirilen ticari ölçekli testbed'dir. Bu platformda özellikle fronthaul zamanlama, kenar (edge) bulut üzerinden DU-RU bağlantısı ve RIC işlevlerinin stabilitesi değerlendirilmiştir. Huang ve arkadaşlarının çalışmasında sunulan bu testbed, kapalı alan pikohücresi (indoor PicoCell) senaryolarında farklı tedarikçiye ait bileşenlerin birlikte çalışabilirliğini doğrulamak ve sistem bütünlüğünü sağlamak açısından kritik bulgular ortaya koymuştur (Huang vd., 2023).

Sonuç olarak, testbed'ler yalnızca geliştirme süreçlerini desteklemekle kalmaz, aynı zamanda O-RAN teknolojisinin ticarileşme sürecinde güvenilirlik, performans ve bütünlük analizleri açısından da temel bir rol oynar.

2.6. Güvenlik ve Sistem Bütünlüğü

O-RAN mimarisinin sunduğu açık ve çok tedarikçili yapı, ağ esnekliğini ve maliyet etkinliğini artırmakla birlikte, yeni ve daha karmaşık güvenlik risklerini de beraberinde getirmektedir. Geleneksel RAN sistemlerinde üreticiye özgü kapalı protokoller ve donanım bütünlüğü yoluyla sağlanan görece sınırlı tehdit yüzeyleri, O-RAN'da yerini çok katmanlı, yazılım tanımlı ve dinamik güvenlik

ihtiyaçlarına bırakmaktadır. Açık arayüzler (E2, A1, O1) üzerinden yürütülen veri akışı, merkezi olmayan bileşenlerin entegrasyonu ve bağımsız geliştiricilerce oluşturulan xApp/rApp uygulamaları, sistem bütünlüğünü etkileyebilecek yeni tehdit vektörlerini ortaya çıkarmaktadır (Garcia-Saavedra ve Costa-Perez, 2021).

Bu kapsamda yapılan çalışmalar (Dik ve Berger, 2023; Groen vd., 2024a; Groen vd., 2023; Liyanage vd., 2023), güvenlik açıkların yalnızca protokol düzeyinde değil, yazılım ve mimari düzeyde de önlenmesi gerektiğini göstermektedir. O-RAN bileşenlerinin tasarımında "katmanlı güvenlik odaklı tasarım" ilkesi benimsenmeli; özellikle O-DU ve O-RU gibi donanım odaklı bileşenlerde güvenlik, performansla dengeli biçimde ele alınmalıdır. O-RAN bileşenleri – özellikle sanallaştırılmış xApp'ler ve rApp'ler yeterince izole edilmediğinde, bir bileşendeki güvenlik açığı diğer hizmetlerin veya kullanıcıların verilerine erişebilir. Bu nedenle, çok kiracılı (multi-tenancy) yapılarda her uygulama bileşeninin kontrol düzeyinde ayrıştırılması kritik önemdedir. Ayrıca, her bir düzlem için özelleştirilmiş güvenlik politikaları (ör. senkronizasyon düzlemi için kimlik doğrulama ve bütünlük) geliştirilmeli; böylece fronthaul üzerinden gelebilecek saldırılar önlenmelidir (Groen vd., 2024b).

Bir diğer önemli ilke, "görünürlük ve denetim" altyapısının güçlendirilmesidir. RIC seviyesinde xApp/rApp mesajlarının günlüklenmesi ve takip edilebilirliği, saldırı analizi ve karar şeffaflığı açısından kritiktir. Özellikle AI tabanlı kapalı çevrim kontrol sistemlerinde bu izlenebilirlik daha da önem kazanmaktadır.

Son olarak, Zero Trust Architecture (ZTA) yaklaşımı (Ramezanpour ve Jagannath, 2022), O-RAN için geleceğe dönük güvenlik stratejisi sunmaktadır. ZTA, tüm bileşenleri varsayılan olarak güvenilmez kabul eder ve sürekli kimlik denetimi ile çalışır. O-RAN'ın AI/ML altyapısı, bu yaklaşımın uygulanabilirliğini artırmakta; dinamik risk değerlendirmesi ve davranış tabanlı kontrol uygulamalarına olanak tanımaktadır.

Sonuç olarak, O-RAN güvenliği yalnızca teknik bir problem değil; aynı zamanda sistem mimarisi, uygulama yönetimi, yazılım güvenliği ve tedarik zinciri bütünlüğünü içeren çok katmanlı bir sorunsaldır. Güvenli O-RAN dağıtımları için hem kontrol arayüzleri düzeyinde şifreleme ve erişim kontrolü, hem de uygulama düzeyinde bütünlük doğrulama, versiyon yönetimi ve kaynak izolasyonu gibi çok boyutlu güvenlik politikalarının hayata geçirilmesi zorunludur.

2.7 Uygulama Senaryoları

O-RAN mimarisi yalnızca geleneksel mobil ağları dönüştürmekle kalmayıp, aynı zamanda yeni nesil kullanım senaryoları için de esnek bir altyapı sunmaktadır. Bu bölümde, literatürde öne çıkan uygulama örnekleri üzerinden O-RAN'ın yenilikçi sistem tasarımlarına sunduğu katkılar ele alınmaktadır.

UAV destekli ağ yapıları, O-RAN'ın sunduğu dağıtık kontrol ve yazılım tanımlı mimari olanakları ile birleştiğinde, yüksek mobilite gerektiren senaryolar için etkili çözümler sağlamaktadır (Hamdan vd., 2023). Bir diğer öncü alan, Karasal Olmayan Ağlar (Non-Terrestrial Networks, NTN), yani uydu sistemleri, yüksek irtifa platformları ve UAV'ler gibi yer bazlı olmayan iletişim altyapılarını kapsamaktadır. Campana ve arkadaşlarının yaptığı çalışmada, bu sistemlerin O-RAN altyapısına entegrasyonu; kanal modelleme, zaman senkronizasyonu ve kontrol döngülerinin gecikme toleransları gibi zorluklar ekseninde analiz edilmiştir. O-RAN'ın sanallaştırılmış ve bulut tabanlı yapısı, bu tür hareketli platformların merkezi olmayan şekilde yönetimi için belirgin bir avantaj sunmaktadır (Campana vd., 2023).

Özelleştirilmiş 5G ağları ve Endüstri 4.0/5.0 uygulamaları da O-RAN ile güçlü biçimde bütünleşebilmektedir. Endüstriyel tesisler veya kampüs ortamlarında ihtiyaç duyulan düşük gecikme süresi, yüksek güvenlik ve deterministik ağ kontrolü gibi gereksinimler, O-RAN'ın modüler mimarisi ve programlanabilir kontrol düzlemleri aracılığıyla kolayca sağlanabilmektedir. Huang ve arkadaşlarının çalışmasında bu tür özel senaryolar, laboratuvar ortamında simüle edilerek test edilmiş ve O-RAN'ın bu bağlamda uygulanabilirliği deneysel olarak gösterilmiştir (Huang vd., 2023).

Hücresiz MIMO yapılarında ise merkezi olmayan anten konfigürasyonları ile çok sayıda kullanıcıya eş zamanlı ve koordine hizmet sunulabilmektedir (Nayebi vd., 2015). Bu mimari, merkezi olmayan kontrol yapılarını gerektirdiğinden, O-RAN'ın dağıtık kontrol yaklaşımı ile doğal bir uyum içerisindedir. Bu sebeple literatürde yapılmış olan çalışmalardan (Beerten vd., 2022; Beerten vd., 2024; Chu vd., 2025; Demir vd., 2024) Demir ve arkadaşları çalışmasında, enerji verimliliği ve veri oranı arasında dinamik denge kuran bir kontrol mekanizması geliştirilmiştir. RIC mimarisi, bu yapıların fiziksel katman ve ağ kontrol katmanı arasındaki optimizasyonuna olanak sağlamaktadır.

Bununla birlikte, dijital ikiz teknolojisinin O-RAN mimarisiyle birleşimi, ağ performansının sürekli izlenmesi, sanal test ortamlarının oluşturulması ve hata öncesi kestirimci bakım uygulamalarının gerçekleştirilmesi açısından büyük potansiyel taşımaktadır. O-RAN araştırma raporunda (Reliance Jio vd., 2023), yapay zekâ destekli ağ simülasyonları ile oluşturulan dijital ikiz sistemlerinin, 6G'ye geçiş sürecinde ağ yönetimi ve otonomi açısından kritik bir rol oynayacağı vurgulanmaktadır.

Tüm bu senaryolar, O-RAN'ın yalnızca bir ağ altyapısı değil, aynı zamanda akıllı ve uyarlanabilir iletişim sistemleri için bir platform olduğunu göstermektedir. Akıllı şehir uygulamalarından otonom araç sistemlerine, uzay tabanlı genişbant ağ çözümlerinden endüstriyel otomasyon sistemlerine kadar uzanan geniş bir yelpazede, O-RAN mimarisi yeni nesil iletişim paradigmalarının temel yapı taşı olmaya adaydır.

3. Tartışma

3.1. Zorluklar

O-RAN mimarisi, açıklık, modülerlik ve programlanabilirlik gibi avantajları ile öne çıkarken, bu güçlü yönler aynı zamanda sistemin bazı teknik ve operasyonel zorluklarla karşı karşıya kalmasına neden olmaktadır. Literatürdeki birçok çalışma (Abdalla vd., 2022; Thiruvasagam vd., 2023), bu mimarinin potansiyelini ortaya koyarken, uygulamaya yönelik sınırlamaları da dikkat çekmektedir.

Bunlardan ilki, gerçek zamanlılık ve senkronizasyon sorunudur. O-RAN bileşenlerinin açık arayüzlerle ayrıştırılmış olması, özellikle 7-2x gibi fiziksel katman bölünmesinin olduğu senaryolarda zaman duyarlılığı yüksek uygulamalar için ciddi senkronizasyon hassasiyetleri doğurmaktadır. Yüksek bant genişliği ve düşük gecikme gereksinimi olan uygulamalarda, fronthaul yapısındaki zamanlama tutarsızlıkları hizmet kalitesini olumsuz etkileyebilmektedir (Huang vd., 2023).

Bir diğer zorluk, çok tedarikçili ekosistemlerde ortaya çıkan xApp/rApp uyumsuzluklarıdır. Farklı kaynaklardan gelen yazılım bileşenlerinin Near-RT RIC üzerinde birlikte çalışması, API seviyesinde uyuşmazlıklar, model tutarsızlıkları ve kaynak erişiminde çatışmalar gibi problemleri beraberinde getirmektedir (Santos vd., 2025).

Güvenlik açısından da benzer riskler söz konusudur. Özellikle E2 ve A1 gibi açık arayüzler, RIC ile xApp/DU arasında taşınan kontrol mesajlarının yetkisiz erişim ve kimlik doğrulama eksikliği gibi saldırılara açık olmasına neden olmaktadır. ZTA gibi yaklaşımlar literatürde önerilmekle birlikte, bu sistemlerin mevcut ticari uygulamalarda tam olarak hayata geçirilemediği görülmektedir (Groen vd., 2024b).

Yapay zekâ tabanlı uygulamalarda ise en çok öne çıkan sınırlamalardan biri, sahaya özgü ve etiketlenmiş gerçek veri kümelerinin eksikliğidir (Sucuoglu 2025). OpenRAN Gym gibi platformlar simülasyon tabanlı veri üretiminde ilerleme kaydetmiş olsa da gerçek ağdan toplanan, paylaşılabilir ve genelleştirilebilir veri setlerinin eksikliği, model eğitimi ve transfer öğrenme uygulamalarını kısıtlamaktadır.

Son olarak, O-RAN'ın ticari uygulamaları önünde regülasyon eksiklikleri önemli bir engel teşkil etmektedir. Açık arayüz ve çok tedarikçili yapı, geleneksel lisanslama sistemleriyle uyumsuz olabilmektedir. Bu durum hem güvenlik hem de birlikte çalışabilirlik açısından yeni standardizasyon gereksinimlerini beraberinde getirmektedir. Ticari yaygınlık açısından bakıldığında, O-RAN sistemlerinin daha geniş ölçekte kullanılabilmesi büyük ölçüde bu regülasyonların küresel ölçekte netleştirilmesine bağlıdır.

3.2. Gelecek Yönelimler

O-RAN mimarisi hem akademik araştırmalar hem de endüstriyel uygulamalar açısından pek çok gelecek vaat eden yönelim barındırmaktadır.

Gelecekte xApp ve rApp'lerin yalnızca reaktif değil, aynı zamanda proaktif davranışlar sergileyen yapay zekâ modelleri ile güçlendirilmesi hedeflenmektedir. Örneğin, kullanıcı hareketliliğini tahmin ederek kaynak planlaması yapan öngörücü modeller, ağ kaynaklarının daha verimli ve kesintisiz şekilde kullanılmasını mümkün kılacaktır.

Ağ dilimleme uygulamaları ise yalnızca radyo erişim ağı ile sınırlı kalmayacak, uçtan uca servis katmanlarını da kapsayacak şekilde genişletilecektir. Bu entegrasyonun sağlanmasında, SMO yapısının rolü giderek daha belirleyici hale gelecektir.

Bir diğer önemli gelişim ekseni, dijital ikiz temelli ağ yönetimidir. O-RAN'ın 6G ile ilgili raporunda da vurgulandığı gibi (Reliance Jio vd., 2023), fiziksel ağın sanal bir kopyası üzerinden performans izleme, hata öncesi kestirim, politika testleri ve optimizasyon işlemlerinin yapılması, gerçek sistem üzerinde deneme yapma zorunluluğunu ortadan kaldırarak operasyonel güvenliği artırabilir.

6G'ye geçişle birlikte, hücresiz yapıların, yüksek frekanslı (örneğin THz) iletişim tekniklerinin ve ultra mobil senaryoların gündeme gelmesiyle, O-RAN mimarisi bu gelişmelere uyum sağlayacak şekilde yeniden yapılandırılmalıdır. O-RAN'ın dağıtık yapısı ve AI destekli kontrol sistemleri, bu tür sistemler için doğal bir temel sunmaktadır.

Son olarak, O-RAN Alliance ve 3GPP gibi standartlaştırma kuruluşlarının ortak çalışmaları ile, daha güçlü API tanımları, model doğrulama mekanizmaları ve güvenli yazılım havuzları geliştirilebilir. Bu tür girişimler sayesinde, açık ağlar için sertifikalandırılmış yazılım bileşenlerinden oluşan sürdürülebilir ve güvenli bir ekosistem oluşturulması mümkün olacaktır.

4. Sonuç

O-RAN, esnek, modüler ve programlanabilir yapısıyla geleneksel RAN mimarilerine alternatif bir yaklaşım sunmakta; yapay zekâ entegrasyonu ve açık arayüzleriyle mobil iletişim sistemlerinde önemli bir paradigma değişimini temsil etmektedir. Bu çalışmada, O-RAN'ın mimari bileşenleri, kontrol düzlemleri, yapay zekâ destekli karar mekanizmaları ve testbed uygulamaları literatür ışığında değerlendirilmiştir.

xApp ve rApp mimarileriyle desteklenen O-RAN yapısı, federatif öğrenme, dijital ikizler, ağ dilimleme ve çok etmenli kontrol gibi AI tabanlı yaklaşımları destekleyerek otonom RAN vizyonunu mümkün kılmaktadır. Bununla birlikte, gerçek zamanlılık, güvenlik, veri paylaşımı ve regülasyon gibi alanlarda çözülmesi gereken yapısal zorluklar devam etmektedir.

6G'ye giden yolda O-RAN; hücresiz MIMO sistemleri, THz bandı iletişimi, uçtan uca ağ dilimleme ve akıllı servis orkestrasyonu gibi birçok yeni nesil teknolojinin temel yapı taşı olarak konumlanmaktadır. Bu derleme, O-RAN üzerine yapılan araştırmalara yön vermek ve gelecekteki çalışmalar için kapsamlı bir zemin oluşturmak amacıyla hazırlanmıştır.

Katkı Oranı Beyanı

Yazarın katkı yüzdeleri aşağıda verilmiştir. Yazar makaleyi incelemiş ve onaylamıştır.

	O.Y.
K	100
T	100
Y	100
VTI	100
VAY	100
KT	100
YZ	100
KI	100
GR	100

K= kavram, T= tasarım, Y= yönetim, VTI= veri toplama ve/veya işleme, VAY= veri analizi ve/veya yorumlama, KT= kaynak tarama, YZ= Yazım, KI= kritik inceleme, GR= gönderim ve revizyon.

Çatışma Beyanı

Yazar bu çalışmada hiçbir çıkar ilişkisi olmadığını beyan etmektedir.

Kaynaklar

Abdalla AS, Upadhyaya PS, Shah VK, Marojevic, V. 2022. Toward Next Generation Open Radio Access Networks: What O-RAN Can and Cannot Do! IEEE Netw, 36(6): 206-213.

Alam K, Habibi MA, Tammen M, Krummacker D, Saad W, Renzo MD, Melodia T, Costa-Pérez X, Debbah M, Dutta A, Schotten HD. 2024. A Comprehensive Tutorial and Survey of O-RAN: Exploring Slicing-aware Architecture, Deployment Options, Use Cases, and Challenges. IEEE Open J Commun Soc, pp: 264.

Arslan H, Yılmaz S, Sen S. 2023. Dynamic MAC Scheduling in O-RAN using Federated Deep Reinforcement Learning. 2023 International Conference on Smart Applications, Communns Netw (SmartNets): 1-8.

Beerten R, Girycki A, Pollin S. 2022. User centric cell-free massive MIMO in the O-RAN architecture: Signalling and algorithm integration. 2022 IEEE Conference on Standards for Communications and Networking (CSCN): 181-187.

Beerten R, Ranjbar V, Guevara AP, Pollin S. 2024. Mobile Cell-Free Massive MIMO: A Practical O-RAN Based Approach. IEEE Open J Commun Soc.

Bertizzolo L, Bonati L, Demirors E, Al-Shawabka A, D'Oro S, Restuccia F, Melodia T. 2020. Arena: A 64-antenna SDR-based ceiling grid testing platform for sub-6 GHz 5G-and-Beyond radio spectrum research. Comput Netw, 181: 107436.

Breen J, Buffmire A, Duerig J, Dutt K, Eide E, Hibler M, Johnson D, Kasera SK, Lewis E, Maas D, Orange A, Patwari N, Reading D, Ricci R, Schurig D, Stoller LB, Van Der Merwe J, Webb K, Wong G. 2020. POWDER: Platform for Open Wireless Data-driven Experimental Research. Proceedings of the 14th International Workshop on Wireless Network Testbeds, Experimental evaluation & Characterization, 17-24.

Bonati L, D'Oro S, Basagni S, Melodia T. 2021a. SCOPE: An open and softwarized prototyping platform for NextG systems. Proceedings of the 19th Annual International Conference on Mobile Systems, Applications, and Services, 415-426.

Bonati L, D'Oro S, Polese M, Basagni S, Melodia T. 2021b. Intelligence and learning in O-RAN for data-driven NextG cellular networks. IEEE Commun Mag, 59(10): 21-27.

Bonati L, Johari P, Polese M, D'Oro S, Mohanti S, Tehrani-Moayyed M, Villa D, Shrivastava S, Tassie C, Yoder K. 2021c. Colosseum: Large-scale wireless experimentation through hardware-in-the-loop network emulation. 2021 IEEE International Symposium on Dynamic Spectrum Access Networks (DySPAN): 105-113.

Bonati L, Polese M, D'Oro S, Basagni S, Melodia T. 2022. OpenRAN gym: An open toolbox for data collection and experimentation with AI in O-RAN. 2022 IEEE Wireless Communications and Networking Conference (WCNC): 518-523.

Bonati L, Polese M, D'Oro S, Basagni S, Melodia T. 2023. OpenRAN Gym: AI/ML development, data collection, and testing for O-RAN on PAWR platforms. Comput Netw, 220: 109502.

Campana R, Amatetti C, Vanelli-Coralli A. 2023. O-RAN based non-terrestrial networks: Trends and challenges. 2023 Joint European Conference on Networks and Communications & 6G Summit (EuCNC/6G Summit): 264-269.

Choudhary A, Srivastava G, Jha MK. 2024. Technicalities of O-RAN for 5G and B5G. 2024 International Conference on Knowledge Engineering and Communication Systems (ICKECS): 1-5.

Chu Y, Rahmani M, Shackleton J, Grace D, Cumanan K, Ahmadi H, Burr A. 2025. Testbed Development: An Intelligent O-RAN based Cell-Free MIMO Network. arXiv preprint arXiv:2502.08529.

Demir ÖT, Masoudi M, Björnson E, Cavdar C. 2024. Cell-free massive MIMO in O-RAN: Energy-aware joint orchestration of cloud, fronthaul, and radio resources. IEEE J Sel Areas Commun, 42(2): 356-372.

Dik D, Berger MS. 2023. Open-RAN fronthaul transport security architecture and implementation. IEEE Access, 11: 46185-46203.

D'Oro S, Bonati L, Polese M, Melodia T. 2022a. OrchestRAN: Network automation through orchestrated intelligence in the open RAN. IEEE INFOCOM 2022-IEEE Conference on Computer Communications, 270-279.

D'Oro S, Polese M, Bonati L, Cheng H, Melodia T. 2022b. dApps: Distributed applications for real-time inference and control in O-RAN. IEEE Commun Mag, 60(11): 52-58.

Garcia-Saavedra A, Costa-Perez X. 2021. O-RAN: Disrupting the virtualized RAN ecosystem. IEEE Commun Stand Mag, 5(4): 96-103.

Gomez-Miguelez I, Garcia-Saavedra A, Sutton PD, Serrano P, Cano C, Leith DJ. 2016. srsLTE: An open-source platform for LTE evolution and experimentation. Proceedings of the Tenth ACM International Workshop on Wireless Network Testbeds, Experimental Evaluation, and Characterization, 25-32.

Groen J, D'Oro S, Demir U, Bonati L, Polese M, Melodia T, Chowdhury K. 2024a. Implementing and evaluating security in O-RAN: Interfaces, intelligence, and platforms. IEEE Netw.

Groen J, D'Oro S, Demir U, Bonati L, Villa D, Polese M, Melodia T, Chowdhury K. 2024b. Securing O-RAN open interfaces. IEEE Trans Mobile Comput.

Groen J, Kim B, Chowdhury K. 2023. The cost of securing O-RAN. ICC 2023-IEEE Int Conf Commun, 5444-5449.

Habibi MA, Han B, Fellan A, Jiang W, Sánchez AG, Pavon IL, Boubendir A, Schotten HD. 2023. Toward an open, intelligent, and end-to-end architectural framework for network slicing in 6G communication systems. IEEE Open J Commun Soc, 4: 1615-1658.

Habibi MA, Han B, Yousaf FZ, Schotten HD. 2020. How should network slice instances be provided to multiple use cases of a

single vertical industry? IEEE Commun Stand Mag, 4(3): 53-61.

Hamdan MQ, Lee H, Triantafyllopoulou D, Borralho R, Kose A, Amiri E, Mulvey D, Yu W, Zitouni R, Pozza R. 2023. Recent advances in machine learning for network automation in the O-RAN. Sensors, 23(21): 8792.

Huang Y, Sun Q, Li N, Chen Z, Huang J, Ding H. 2023. Validation of current O-RAN technologies and insights on the future evolution. IEEE J Sel Areas Commun, 42(2): 487-505.

Kasuluru V, Blanco L, Vázquez MÁ, Vaca-Rubio CJ, Zeydan E. 2024. Minimizing power consumption under SINR constraints for cell-free massive MIMO in O-RAN. 2024 20th Int Conf Netw Serv Manag (CNSM), 1-7.

Ko WH, Dinesha U, Ghosh U, Shakkottai S, Bharadia D, Wu R. 2023. EdgeRIC: Empowering real-time intelligent optimization and control in nextG networks.

Lee H, Cha J, Kwon D, Jeong M, Park I. 2020. Hosting AI/ML workflows on O-RAN RIC platform. 2020 IEEE Globecom Workshops, 1-6.

Liyanage M, Braeken A, Shahabuddin S, Ranaweera P. 2023. Open RAN security: Challenges and opportunities. J Netw Comput Appl, 214: 103621.

Marinova S, Leon-Garcia A. 2024. Intelligent O-RAN beyond 5G: Architecture, use cases, challenges, and opportunities. IEEE Access, 12: 27088-27114.

Nayebi E, Ashikhmin A, Marzetta TL, Yang H. 2015. Cell-free massive MIMO systems. 2015 49th Asilomar Conf Signals Syst Comput, 695-699.

Nikaein N, Marina MK, Manickam S, Dawson A, Knopp R, Bonnet C. 2014. OpenAirInterface: A flexible platform for 5G research. ACM SIGCOMM Comput Commun Rev, 44(5): 33-38.

Niknam S, Roy A, Dhillon HS, Singh S, Banerji R, Reed JH, Saxena N, Yoon S. 2022. Intelligent O-RAN for beyond 5G and 6G wireless networks. 2022 IEEE Globecom Workshops, 215-220.

O-RAN Alliance. 2018. O-RAN: Towards an open and smart RAN. https://www.o-ran.org/o-ran-resources (accessed date: March 10, 2025)

O-RAN Alliance. 2020. O-RAN use cases and deployment scenarios. https://www.o-ran.org/o-ran-resources (accessed date: March 10, 2025)

Pham C, Fami F, Nguyen KK, Cheriet M. 2022. When RAN intelligent controller in O-RAN meets multi-UAV enable wireless network. IEEE Trans Cloud Comput, 11(3): 2245-2259.

Polese M, Bonati L, D'Oro S, Basagni S, Melodia T. 2022. ColO-RAN: Developing machine learning-based xApps for open RAN closed-loop control on programmable experimental platforms. IEEE Trans Mobile Comput, 22(10): 5787-5800.

Polese M, Bonati L, D'Oro S, Basagni S, Melodia T. 2023. Understanding O-RAN: Architecture, interfaces, algorithms, security, and research challenges. IEEE Commun Surv Tutor, 25(2): 1376-1411.

Polese M, Bonati L, D'Oro S, Johari P, Villa D, Velumani S, Gangula R, Tsampazi M, Robinson CP, Gemmi G. 2024. Colosseum: The open RAN digital twin. IEEE Open J Commun Soc.

Ramezanpour K, Jagannath J. 2022. Intelligent zero trust architecture for 5G/6G networks: Principles, challenges, and the role of machine learning in the context of O-RAN. Comput Netw, 217: 109358.

Raychaudhuri D, Seskar I, Zussman G, Korakis T, Kilper D, Chen T, Kolodziejski J, Sherman M, Kostic Z, Gu X, Krishnaswamy H, Maheshwari S, Skrimponis P, Gutterman C. 2020. Challenge: COSMOS: A city-scale programmable testbed for experimentation with advanced wireless. Proc 26th Annu Int Conf Mobile Comput Netw, 1-13.

Reliance Jio, DTAG, KDDI, NVIDIA, Rakuten, SK Telecom, Bell, Tech Mahindra Ltd. 2023. O-RAN towards 6G. O-RAN next Generation Research Group (nGRG) Research Report No: RR-2023-01.

Santos JF, Huff A, Campos D, Cardoso KV, Both CB, DaSilva LA. 2025. Managing O-RAN networks: xApp development from zero to hero. IEEE Commun Surv Tutor.

SD-RAN. 2020. SD-RAN Docs 1.4.3 documentation. https://docs.sd-ran.org/master/index.html (accessed date: March 13, 2025)

Sever O, Salan O, Hokelek I, Gorcin A. 2025. A practical demonstration of DRL-based dynamic resource allocation xApp using OpenAirInterface. arXiv preprint arXiv:2501.05879.

Singh SK, Singh R, Kumbhani B. 2020. The evolution of radio access network towards Open-RAN: Challenges and opportunities. 2020 IEEE Wireless Commun Netw Conf Workshops (WCNCW), 1-6.

Sucuoglu HS. 2025. Development of Real-Time Fire Detection Robotic System with Hybrid-Cascade Machine Learning Detection Structure. Processes, 13(6): 1712.

Thiruvasagam PK, Venkataram V, Ilangovan VR, Perapalla M, Payyanur R, Kumar V. 2023. Open RAN: Evolution of architecture, deployment aspects, and future directions.

Tsampazi M, D'Oro S, Polese M, Bonati L, Poitau G, Healy M, Melodia T. 2023. A comparative analysis of deep reinforcement learning-based xApps in O-RAN. GLOBECOM 2023-2023 IEEE Global Commun Conf, 1638-1643.

Zhang CC, Nguyen KK, Cheriet M. 2022a. Joint routing and packet scheduling for URLLC and eMBB traffic in 5G O-RAN. ICC 2022-IEEE Int Conf Commun, 1900-1905.

Zhang H, Zhou H, Erol-Kantarci M. 2022b. Federated deep reinforcement learning for resource allocation in O-RAN slicing. GLOBECOM 2022-2022 IEEE Global Commun Conf, 958-963.

Black Sea Journal of Engineering and Science
doi: 10.34248/bsengineering.1709786

Open Access Journal
e-ISSN: 2619 – 8991

Review
(Volume 8 - Issue 4: 1245-1257 / July 2025)

AUGMENTED REALITY IN CULTURAL HERITAGE: A SYSTEMATIC REVIEW OF MOBILE APPLICATIONS AND USER EXPERIENCE EVALUATION

Nurettin ŞENYER[1]*, Aya ALZATMA[1]

[1]Samsun University, Faculty of Engineering and Natural Sciences, Department of Software Engineering, 55050, Samsun, Türkiye

Abstract: This systematic review compares four leading AR applications for cultural heritage interpretation, providing comprehensive insights for future AR development in cultural contexts. It analyzes Google Lens, Civilisations AR, Timelooper, and Artivive across technological methods, user experiences, and effectiveness at cultural heritage sites. Drawing on peer-reviewed studies from 2017 - 2025, sourced from academic databases including Google Scholar, the review highlights diverse implementation strategies and immersion levels through systematic comparative analysis. Results demonstrate that Google Lens excels in AI-driven accessibility, Civilisations AR in 3D educational depth, Timelooper in narrative immersion, and Artivive in dynamic art overlays. The findings suggest that next-generation AR applications should adopt hybrid approaches combining the best features of each model while addressing current limitations in content scalability and user engagement.

Keywords: Augmented reality, Cultural heritage, Digital transformation, Mobile applications, User experience

***Corresponding author:** Samsun University, Faculty of Engineering and Natural Sciences, Department of Software Engineering, 55050, Samsun, Türkiye
E mail: nurettin,senyer@gmail.com (N. ŞENYER)
Nurettin ŞENYER https://orcid.org/0000-0002-2324-9285
Aya ALZATMA https://orcid.org/0009-0003-8156-8430

Received: May 30, 2025
Accepted: July 02, 2025
Published: July 15, 2025

Cite as: Şenyer N, Alzatma A. 2025. Bridging past and future: a comparative analysis of augmented reality applications in cultural heritage interpretation. BSJ Eng Sci, 8(4): 1245-1257.

1. Introduction

1.1. Research Context and Significance

The intersection of augmented reality and cultural heritage represents a rapidly evolving field with significant implications for education, tourism, and historical preservation. With the global AR market projected to reach $77.0 billion by 2025 and cultural tourism accounting for 40% of international travel, there is growing interest in applications that can bridge the gap between physical historical artifacts or sites and their rich contextual information. As mobile technologies become increasingly sophisticated, the ability to visualize historical sites as they once appeared or to interact with cultural artifacts in novel ways presents unprecedented opportunities for engagement with our collective past. This review examines how four leading applications in this domain have approached these opportunities and evaluates the research that has assessed their effectiveness in cultural heritage contexts.

1.2. Objectives of the Review

This comparative review aims to:

1. Identify and analyze the key technological approaches employed by leading historical AR applications
2. Compare the user experiences and interaction models across these applications
3. Evaluate the effectiveness of different approaches in educational and cultural contexts
4. Identify gaps and opportunities in the current landscape that could inform the development of next-generation AR applications for cultural heritage

1.3. Selection Criteria for Applications

The applications selected for this review represent diverse approaches to historical and cultural AR experiences while demonstrating proven effectiveness in real-world implementations. The selection criteria included:

- Commercial availability and widespread public access
- Primary focus on historical or cultural content
- Advanced implementation of AR technology
- Sufficient published research and technical documentation for comprehensive analysis
- Diversity in technological approach and target use cases
- Evidence of user adoption and institutional partnerships

Based on these criteria, Google Lens, Civilisations AR, Timelooper, and Artivive were selected as representative examples that collectively showcase the breadth of current approaches in this domain, covering AI-driven recognition, educational applications, location-based experiences, and creator-empowered platforms.

This work is licensed (CC BY-NC 4.0) under Creative Commons Attribution 4.0 International License

1.4. Review Methodology

This review utilized a systematic approach to literature collection and analysis, covering publications from 2017-2025 to capture both foundational research and recent developments. The literature search was conducted using Boolean operators (AND, OR) to combine search terms effectively, with studies screened based on relevance to AR applications in cultural heritage contexts.

Data Sources and Search Strategy:

- Academic databases: ACM Digital Library, IEEE Xplore, ScienceDirect, and Google Scholar
- Industry publications and technical documentation from application developers
- Search terms: "augmented reality" AND ("cultural heritage" OR "historical sites" OR "museums" OR "archaeological sites"), plus application-specific searches.
- Inclusion criteria: Peer-reviewed publications, technical white papers, and substantive reviews with empirical data

Analysis was conducted through thematic synthesis, identifying key technological, user experience, and educational dimensions across the selected applications.

2. Review

Each application underwent systematic analysis examining development history, core technologies, key features, published research findings, and comparative strengths and limitations.

2.1. Application 1: Google Lens

2.1.1. Background and development history

Google Lens was introduced in 2024 as an image recognition technology developed by Google, representing a significant advancement in mobile visual search capabilities (Google LLC, 2024). While not exclusively focused on historical content, it has evolved to include substantial capabilities for identifying landmarks, artworks, and cultural artifacts, making it highly relevant for cultural heritage applications. Initially available only on Pixel devices, the application has since expanded to most Android and iOS devices through the Google app and Google Photos, achieving widespread adoption across diverse user demographics.

Google Lens represents Google's comprehensive implementation of visual search and AR information overlay, building on the company's extensive experience with image recognition and machine learning technologies developed over more than a decade. The application has received regular updates since its launch, continuously expanding its recognition capabilities and refining its information presentation methods to better serve users seeking cultural and historical information.

2.1.2. Core technologies and architecture

According to published research (Lampropoulos et al. 2024; Lampropoulos et al. 2020), Google Lens relies on several interconnected key technologies that enable its sophisticated recognition capabilities. The application employs deep neural networks, specifically convolutional neural networks (CNNs) for object recognition, which have been trained on vast datasets containing millions of images across diverse categories including cultural artifacts and historical sites.

Recognition accuracy is enhanced through Knowledge Graph Integration, where recognized objects are seamlessly connected to Google's comprehensive Knowledge Graph, allowing the application to retrieve rich contextual information about landmarks, artworks, and historical sites from authoritative sources. The system utilizes cloud-based processing for most complex recognition tasks, with computational work processed on Google's servers rather than on the device itself, enabling the deployment of more sophisticated models that would be impossible to run locally.

However, the application also implements on-device machine learning capabilities for certain recognition functions, providing improved response times and limited offline functionality when network connectivity is unavailable. The overall architecture follows a hybrid client-server model where initial image capture and basic processing occur on the mobile device, while complex recognition tasks are efficiently offloaded to cloud infrastructure for optimal performance.

2.1.3. Key features and functionalities

Based on technical documentation and research by Rinaldi et al. (2022) Google Lens offers several features particularly relevant to historical and cultural contexts. The landmark recognition capability enables identification of famous buildings, monuments, and historical sites with impressive accuracy, providing users with immediate access to historical information and related content. Artwork identification represents another core functionality, offering recognition of paintings and sculptures accompanied by detailed information about the artist, creation period, and historical context.

Text translation and extraction capabilities prove especially valuable for cultural heritage applications, enabling users to translate historical inscriptions and extract text from historical documents in real-time. The visual search functionality allows users to find similar historical items or access related historical information based purely on visual input, creating connections between related cultural artifacts and sites. However, the application's AR implementation remains relatively minimal, with information presented primarily as overlaid cards rather than immersive 3D content, distinguishing it from more specialized AR heritage applications.

2.1.4. Published research findings

Research by Aicardi et al. (2018) conducted comprehensive evaluations of Google Lens performance in museum contexts, revealing important insights about its effectiveness in cultural heritage settings. The study found 87% accuracy in identifying well-known artworks under optimal lighting conditions, demonstrating the

application's strength in recognizing canonical cultural works. However, accuracy dropped significantly to approximately 62% for less prominent works or those with reflective surfaces, highlighting important limitations in challenging visual conditions.

User satisfaction metrics revealed interesting patterns, with high ratings for information retrieval speed (average rating 4.2/5) but notably lower satisfaction with the depth of historical context provided (average rating 3.1/5). Studies by Boboc (2022) further highlighted the application's strength in landmark recognition while noting significant limitations in historical contextualization. Users consistently expressed desire for more in-depth historical information and visual reconstructions showing how sites appeared in the past, suggesting important opportunities for enhancement in cultural heritage applications.

2.1.5. Strengths and limitations

Google Lens demonstrates exceptional objects and landmark recognition capabilities that set industry standards for mobile visual search applications. The application's broad accessibility across device types ensures that cultural heritage information becomes available to diverse user populations without requiring specialized hardware or significant technical expertise. Seamless integration with web search capabilities provides users with pathways to additional information beyond the initial recognition results, while regular updates continuously improve recognition accuracy and expand the database of recognizable cultural artifacts.

The application requires no specialized hardware beyond a standard smartphone camera, making it highly accessible for widespread cultural heritage applications. However, several limitations constrain its effectiveness in cultural heritage contexts. The AR experience remains limited, with information presented primarily through information cards rather than immersive 3D content that could provide richer historical visualization. The focus on identification rather than historical contextualization means users receive basic information but lack deep educational content about historical significance and cultural context.

Most significantly, Google Lens provides no historical reconstruction or visualization capabilities showing how sites appeared in the past, limiting their value for temporal cultural heritage interpretation. Recognition quality varies inconsistently across different types of historical artifacts, with performance particularly challenged by unique or less-documented cultural items. Additionally, offline functionality for historical content remains limited, requiring network connectivity for optimal performance in many cultural heritage settings where internet access may be unreliable.

2.2. Application 2: Civilisations AR (BBC)

2.2.1. Background and development history

Civilisations AR was developed by the BBC in collaboration with Nexus Studios and launched in 2018 as a companion to the BBC's acclaimed "Civilisations" documentary series, representing a pioneering effort to translate broadcast cultural content into interactive digital experiences (BBC Media Applications Technologies Limited, 2018). The application was specifically designed to provide immersive AR experiences of historical artifacts from museums around the world, establishing a new paradigm for cultural heritage accessibility beyond traditional media consumption. According to documentation from the BBC (2018) and research by Sylaiou and Dafiotis (2020), the application was developed with the explicit goal of making museum artifacts more accessible to global audiences while providing innovative ways to interact with cultural heritage that transcend geographical and institutional boundaries.

The development process involved extensive partnerships with over 30 museums and cultural institutions across the UK, creating a collaborative network that enabled high-quality digitization of significant historical artifacts. Subsequent updates expanded the collection of available artifacts, though the scope remained carefully curated to maintain educational quality and historical accuracy. Unlike Google Lens, which evolved from general visual search capabilities, Civilisations AR was purpose-built specifically for cultural heritage exploration, allowing for deeper integration of educational frameworks and more sophisticated interaction models tailored to museum and heritage contexts.

2.2.2. Core technologies and architecture

Research by Hammady et al. (2018) and technical documentation from Nexus Studios reveal a sophisticated technological foundation that prioritizes visual quality and educational effectiveness over broad compatibility. The application leverages both Apple's ARKit and Google's ARCore frameworks for precise spatial tracking and environmental understanding, enabling accurate placement and manipulation of 3D artifacts in real-world spaces. This dual-platform approach ensures consistent AR experiences across major mobile operating systems while maintaining high performance standards.

The visual foundation relies heavily on photogrammetry techniques, where high-quality 3D models of artifacts were meticulously created through detailed photographic capture and reconstruction processes. These models incorporate advanced rendering techniques including raytracing and physically-based rendering (PBR) materials, producing realistic visualization of artifacts that accurately represent surface textures, lighting interactions, and material properties. This attention to visual fidelity distinguishes Civilisations AR from applications that prioritize speed over accuracy.

A key architectural decision involves local 3D model storage, where complete artifact models are downloaded and stored on the device after initial access, enabling detailed exploration without requiring continuous network connectivity. This approach prioritizes user experience and educational continuity over storage

efficiency. The application also implements spatial audio capabilities that provide context-sensitive sound environments, with audio content that dynamically changes based on the user's viewing angle and distance from artifacts, creating more immersive educational experiences.

The overall architecture employs a hybrid approach where primary artifact models and basic information are maintained locally for optimal performance, while supplementary contextual information and updated content may be retrieved from online sources as needed, balancing offline functionality with access to expanded educational resources.

2.2.3. Key features and functionalities

Based on analysis by Papagiannakis et al. (2024) and comprehensive app documentation, Civilisations AR offers an unprecedented level of interaction with historical artifacts through carefully designed educational interfaces. The core functionality centers on comprehensive 3D artifact exploration, allowing users to conduct full 360-degree examination of historical objects with detail levels that often exceed what is possible in traditional museum settings where artifacts may be displayed behind glass or at distances that prevent close inspection.

One of the most innovative features is the X-ray vision capability, which enables users to peer inside certain artifacts to reveal hidden structural details, internal mechanisms, or concealed decorative elements that provide insights into historical construction techniques and artistic intentions. This feature represents a significant advancement over traditional museum displays, offering access to information that would typically require specialized equipment or destructive analysis.

The application provides guided tours through narrated exploration experiences that combine expert historical commentary with interactive visual elements, creating structured educational pathways through artifact collections. Scale manipulation functionality allows users to dynamically change the size of artifacts, enabling detailed examination of minute decorative elements or the experience of viewing objects at their original life-size scale, which can be particularly impactful for artifacts that are typically displayed at reduced scales in museums.

Comprehensive contextual information accompanies each artifact, providing detailed background on creation processes, historical use, cultural significance, and archaeological context. The application also includes personal collection capabilities, allowing users to curate and save their favorite artifacts in a virtual collection that can be revisited and shared, extending the educational experience beyond individual viewing sessions.

2.2.4. Published research findings

Studies by Sylaiou and Dafiotis (2020) conducted comprehensive evaluations of Civilisations AR's educational impact, revealing substantial improvements in learning outcomes compared to traditional museum experiences. The research demonstrated significant improvement in recall of artifact details, with users showing 42% higher retention rates compared to control groups experiencing conventional museum displays and educational materials. This substantial improvement suggests that interactive AR experiences create more memorable and effective learning environments than passive observation methods.

Engagement metrics revealed particularly impressive results, with users spending an average of 7.3 minutes per artifact compared to only 2.1 minutes for traditional museum labels, representing more than a three-fold increase in educational engagement time. This extended interaction duration correlates with deeper learning and suggests that AR technology successfully captures and maintains user attention for educational purposes. Users also reported higher self-reported interest in historical contexts, with engagement scores increasing from 3.2/5 to 4.1/5 following AR experiences, indicating that interactive technology enhances emotional connections to cultural heritage.

Research by Cao (2024) provided additional insights into demographic engagement patterns, noting that the application was particularly effective in engaging younger audiences who might otherwise show limited interest in traditional museum experiences. The study found that 87% of participants aged 18-25 reported learning new information about historical artifacts that they would not have discovered through traditional museum experiences, suggesting that AR technology successfully bridges generational gaps in cultural heritage engagement and creates pathways for younger audiences to connect with historical content.

2.2.5. Strengths and limitations

Civilisations AR demonstrates exceptional strengths in educational technology integration, particularly through its high-quality 3D models with meticulously detailed textures that provide unprecedented access to artifact characteristics typically invisible in traditional museum settings. The application's rich contextual information, specifically tailored to each artifact, creates comprehensive educational experiences that combine visual exploration with expert historical interpretation. Innovative interaction methods, including X-ray visualization and scale manipulation capabilities, represent significant advances in cultural heritage technology that enable forms of exploration to be impossible through physical museum visits.

The curated content approach, developed through collaboration with expert historians and museum professionals, ensures accuracy and educational value while maintaining appropriate academic standards for cultural heritage interpretation. Research studies consistently demonstrate effective educational outcomes, with measurable improvements in learning retention and user engagement that validate the application's pedagogical approach.

However, several significant limitations constrain the application's broader impact and long-term viability. The catalog remains limited to approximately 40 artifacts, representing a fraction of global cultural heritage and limiting the scope of educational content available to users. The focus on individual objects rather than historical sites or broader environmental contexts restricts the application's utility for comprehensive cultural heritage interpretation that includes architectural and landscape elements.

The application provides no user contribution or expansion capabilities, creating a closed system that cannot grow through community involvement or institutional partnerships beyond the original development scope. Technical requirements include flat surfaces for optimal AR placement, which can limit usability in various environmental conditions and may create barriers for some users. Most critically, the application lacks real-time recognition capabilities for actual museum artifacts, meaning users cannot enhance physical museum visits through AR technology, representing a significant missed opportunity for hybrid physical-digital cultural experiences.

Perhaps most significantly, Civilisations AR has received no support or updates since 2020, raising concerns about long-term sustainability and compatibility with evolving mobile technologies. This discontinuation represents a substantial loss for the cultural heritage technology field and highlights the challenges of maintaining specialized AR applications in rapidly evolving technological environments.

2.3. Application 3: Timelooper

2.3.1. Background and development history

Timelooper was founded in 2015 by Andrew Feinberg and Yigit Yigiter as a pioneering location-based historical VR/AR experience platform, representing an innovative approach to cultural heritage interpretation that prioritizes geographical authenticity and temporal immersion (TimeLooper Inc., 2024). According to founder interviews (The Org (n.d.),2025) and comprehensive company documentation, Timelooper was specifically developed to address fundamental limitations in traditional tourism by enabling visitors to witness historical events at the precise locations where they occurred, creating unprecedented connections between past and present through immersive technology.

The platform launched initially in London with meticulously researched historical reconstructions of significant events including the Great Fire of 1666 and dramatic historical moments at the Tower of London, establishing a foundation for location-specific cultural heritage experiences. Unlike Google Lens and Civilisations AR, which began with broader technological capabilities and later incorporated cultural heritage applications, Timelooper adopted a focused geographical approach from its inception, developing detailed, site-specific experiences for individual historical locations before expanding to additional sites.

This strategic approach enabled deep collaboration with local historians, archaeologists, and cultural institutions to ensure historical accuracy and contextual relevance. By 2023, the platform had achieved substantial expansion to over 20 cities worldwide, each featuring carefully curated historical experiences tailored to local cultural heritage significance. The company has undergone significant technological evolution, transitioning from primarily VR experiences that required dedicated hardware to incorporate more accessible AR functionality that overlays historical scenes onto present-day environments through standard mobile devices, greatly expanding potential user reach.

2.3.2. Core technologies and architecture

Based on comprehensive analysis by Kleftodimos (2023) Timelooper employs a sophisticated technological ecosystem specifically designed for location-based cultural heritage experiences. The foundation relies heavily on precise geolocation services that utilize GPS-based triggering mechanisms to activate historical content only when users are physically present at specific locations, ensuring that digital experiences remain contextually relevant to their physical surroundings.

Advanced SLAM (Simultaneous Localization and Mapping) capabilities provide sophisticated spatial understanding that enables accurate anchoring of virtual content to physical environments, creating stable and believable integration between historical reconstructions and contemporary landscapes. This technology proves particularly crucial for historical site applications where precise spatial relationships between past and present environments must be maintained for educational effectiveness and user immersion.

The platform's visual foundation centers on detailed 3D historical reconstruction capabilities, where virtual recreations of historical scenes are developed based on extensive archaeological evidence, historical records, and expert consultation with cultural heritage specialists. These reconstructions represent significant investments in historical research and technical modeling, often requiring months of development for individual site experiences. The integration of 360-degree video content provides additional layers of immersion, placing users within historical moments through carefully produced audiovisual experiences that complement the 3D reconstructions.

A critical architectural component involves edge computing capabilities that strategically distribute processing workloads between mobile devices and cloud services to optimize performance specifically at historical sites where network connectivity may be variable. The overall architecture prioritizes location specificity and historical accuracy over broad compatibility, with experiences meticulously designed for optimal viewing from specific positions at historical sites, creating curated pathways through cultural heritage locations that maximize educational impact and emotional engagement.

2.3.3. Key features and functionalities

Research by Michel-Acosta et al. (2024) and comprehensive official documentation reveal that Timelooper offers a unique suite of features specifically designed for temporal cultural heritage experiences that distinguish it from other AR applications. The core functionality revolves around time-window experiences that enable users to view historical events and environments as they appeared at specific moments in history, creating powerful temporal bridges that allow contemporary visitors to witness past events in their original contexts.

Location-based triggering represents a fundamental design principle, where historical content becomes accessible only when users are physically present at relevant historical sites, ensuring that digital experiences maintain strong connections to geographical and cultural contexts. This approach contrasts sharply with applications that provide historical content regardless of user location, emphasizing the importance of place in cultural heritage interpretation.

Historical character narratives provide guided experiences led by virtual representations of historical figures from each site's past, creating personal connections between users and historical events through storytelling approaches that emphasize human experiences rather than abstract historical information. These character-driven experiences prove particularly effective in engaging users emotionally with historical content, transforming academic historical information into personal narratives that resonate with diverse audiences.

Before and after visualization capabilities enable direct comparison between current site appearances and historical reconstructions, providing users with clear understanding of how locations have changed over time while maintaining connections to their historical significance. Historical event animation features present dynamic sequences depicting significant historical moments, allowing users to witness events unfold in real-time rather than simply viewing static historical information.

Expert audio narration accompanies all visual experiences, providing professional historical commentary that offers context and significance for observed events while maintaining academic standards for cultural heritage interpretation. This narration ensures that emotional and visual experiences are supported by accurate historical information and scholarly perspective.

2.3.4. Published research findings

Studies by Ghouaiel et al. (2017) conducted comprehensive evaluations of Timelooper's effectiveness at European heritage sites, revealing substantial positive impacts on visitor understanding and engagement with cultural heritage content. The research demonstrated significant increases in visitors' understanding of historical contexts, with participants showing 37% improvement in post-visit knowledge assessments compared to control groups experiencing traditional interpretive methods, indicating that immersive AR experiences create more effective learning environments than conventional heritage interpretation approaches.

Engagement metrics revealed impressive results in visitor behavior modification, with average visit duration extending by 22 minutes at sites equipped with Timelooper experiences compared to traditional heritage site visits. This substantial increase in dwell time suggests that AR technology successfully captures and maintains visitor attention for extended periods, creating opportunities for deeper educational engagement with cultural heritage content.

Emotional connection measurements provided particularly compelling evidence of Timelooper's effectiveness, with 64% of users reporting that they felt "transported to the past" during their experiences, indicating successful achievement of temporal immersion that transcends typical tourist experiences. This emotional engagement correlates strongly with learning retention and long-term interest in cultural heritage topics.The research also identified positive correlation between AR experience participation and intention to learn more about relevant historical periods ($r=0.72$), suggesting that immersive cultural heritage experiences successfully inspire continued engagement with historical topics beyond initial site visits. Research by (Kleftodimos et al., 2023) provided additional insights into authenticity perception, finding that the location-specific nature of Timelooper experiences significantly enhanced perceived credibility of historical information, with users rating information authenticity 28% higher when experiencing content at actual historical locations compared to remote viewing, highlighting the importance of geographical context in cultural heritage interpretation.

2.3.5. Strengths and limitations

Timelooper demonstrates exceptional strengths in creating authentic cultural heritage experiences through its unwavering emphasis on geographical and historical authenticity that sets industry standards for location-based heritage interpretation. The application's immersive storytelling approach, centered on carefully researched historical narratives, creates powerful emotional connections between users and cultural heritage content that traditional interpretive methods struggle to achieve. High-quality historical reconstructions, developed through extensive expert consultation with historians, archaeologists, and cultural heritage specialists, ensure accuracy while providing visually compelling experiences that bring historical periods to life.

The character-driven experience design creates emotional engagement that transforms abstract historical information into personal narratives, making cultural heritage more accessible and memorable for diverse audiences. The effective integration of physical

location and digital content represents a significant achievement in cultural heritage technology, creating seamless blends between past and present that enhance rather than detract from historical site experiences.

However, several significant limitations constrain Timelooper's broader applicability and scalability within the cultural heritage field. The platform remains limited to pre-programmed locations and specific historical moments, creating a closed system that cannot accommodate spontaneous exploration or user-initiated discovery of historical content. This constraint requires extensive advance planning from both developers and users, limiting flexibility in cultural heritage interpretation approaches.

The requirement for physical presence at specific sites represents both strength and limitation, as it ensures contextual relevance but restricts accessibility for users who cannot travel to equipped locations, potentially excluding important demographic groups from cultural heritage experiences. The application provides no capabilities for user-initiated recognition or exploration of unplanned sites, contrasting with applications that enable discovery of cultural heritage content in unexpected locations.

Higher production costs associated with detailed historical reconstruction and site-specific content development significantly limit the scale of available library, making comprehensive coverage of global cultural heritage sites economically challenging. Historical accuracy varies considerably depending on the availability and quality of historical records for specific locations and time periods, creating inconsistencies in educational value across different experiences.

Finally, the application offers limited interactive elements compared to museum-based AR applications, focusing primarily on passive observation rather than active exploration or manipulation of historical content, which may reduce engagement for users who prefer more hands-on educational approaches.

2.4. Application 4: Artivive

2.4.1. Background and development history

Artivive was founded in 2017 by Sergiu Ardelean and Codin Popescu as a revolutionary platform specifically designed to bridge traditional and digital art through augmented reality, representing a paradigm shift toward creator-empowered cultural heritage technology (Artivive GmbH, 2024). According to comprehensive company documentation and research by de Morais Sarmento (2024) Artivive was developed with the fundamental goal of providing artists and cultural institutions with accessible tools to create sophisticated AR experiences without requiring extensive technical expertise, democratizing access to advanced cultural heritage technology that was previously limited to well-funded institutions or technically specialized teams.

Unlike the other applications reviewed in this study, Artivive functions as both a comprehensive creation platform and an intuitive viewing application, enabling artists and cultural institutions to develop their own AR content for existing artworks rather than relying on pre-programmed experiences developed by technology companies. This dual functionality represents a significant innovation in cultural heritage technology, shifting control of content creation from technology developers to cultural heritage professionals and artists themselves.

The platform has achieved remarkable growth since its inception, expanding to support over 1,000 artists and cultural institutions worldwide, demonstrating substantial market demand for creator-controlled AR technology in cultural heritage contexts. Notable implementations include partnerships with major international museums such as the Belvedere in Vienna and the Art Institute of Chicago, validating the platform's effectiveness in prestigious cultural heritage institutions and establishing its credibility within the global museum community. This institutional adoption indicates successful integration with existing museum infrastructure and workflows, suggesting that Artivive's approach addresses real needs within the cultural heritage sector.

2.4.2. Core technologies and architecture

Based on comprehensive technical documentation and detailed analysis by de Morais Sarmento (2024) , Artivive employs a sophisticated yet accessible technological ecosystem designed to balance advanced AR capabilities with user-friendly creation tools. The foundation relies on advanced image recognition and tracking capabilities utilizing computer vision algorithms that can accurately identify and track registered artworks even under varying lighting conditions and viewing angles, ensuring consistent AR experiences across diverse museum and gallery environments.

The platform's content management system operates through cloud-based infrastructure where artist-created content is securely stored and managed, enabling global accessibility while maintaining version control and content quality standards. This cloud-based approach allows for real-time updates to AR experiences and ensures that content creators can modify their work without requiring app updates or local storage limitations on user devices

A critical innovation involves web-based creation tools that provide browser-accessible design interfaces for creating AR overlays, eliminating the need for specialized software installation or technical training that might otherwise limit artist participation. These tools democratize AR content creation by providing intuitive interfaces that allow artists to focus on creative expression rather than technical implementation details.

Cross-platform compatibility ensures unified experiences across iOS and Android devices, maximizing accessibility for diverse user populations while maintaining consistent visual quality and interaction patterns. The system implements dynamic content streaming capabilities that enable real-time loading of AR content

based on recognized artworks, optimizing performance while ensuring that users always access the most current version of artist-created experiences.

The overall architecture follows an innovative creator-viewer model where artists utilize web-based tools to develop experiences that viewers seamlessly access through the mobile application when viewing registered artworks. This approach creates a scalable ecosystem where content creation and consumption operate independently, allowing for continuous expansion of available AR experiences without requiring platform modifications.

2.4.3. Key features and functionalities

Research by (Chen et al., 2020) and comprehensive platform documentation reveal that Artivive offers a unique suite of features specifically designed to enhance artistic expression and cultural heritage interpretation through artist-controlled AR experiences. The core functionality centers on artwork animation capabilities that bring static images to life through carefully crafted motion graphics, transforming traditional viewing experiences into dynamic encounters that reveal hidden aspects of artistic creation and interpretation.

Multilayer storytelling represents a particularly innovative feature, enabling artists to create complex narratives that reveal hidden aspects or alternative interpretations of their artworks through sequential AR layers that users can explore at their own pace. This capability allows for sophisticated educational experiences that unfold progressively, maintaining user engagement while providing comprehensive artistic and historical context.

Artist narratives provide direct audio commentary from creators explaining their creative processes, inspirations, and intentions, creating intimate connections between artists and audiences that transcend traditional museum label limitations. This feature proves particularly valuable for contemporary art interpretation where artist intention and process information significantly enhance audience understanding and appreciation.

Historical context integration allows artists and institutions to incorporate detailed information about artworks' historical significance, creation circumstances, and cultural relevance, ensuring that entertainment value does not come at the expense of educational content. Interactive elements provide touchable components that respond to user interaction, creating participatory experiences that engage users actively rather than passively consuming content.

Cross-medium integration capabilities represent a significant technological achievement, enabling seamless combination of painting, video, sound, and interactive elements within single AR experiences. This integration allows artists to create truly multimedia experiences that utilize the full spectrum of digital media while remaining anchored to physical artworks, creating hybrid experiences that enhance rather than replace traditional art viewing.

2.4.4. Published research findings

Studies by de Morais Sarmento (2024) conducted comprehensive evaluations of visitor engagement with Artivive-enhanced exhibitions, revealing substantial positive impacts on audience interaction with cultural heritage content. The research demonstrated significant increases in average viewing time for enhanced artworks, with users spending 5.2 minutes examining AR-enhanced pieces compared to only 1.7 minutes for non-enhanced works, representing more than a three-fold increase in engagement duration that suggests successful capture and maintenance of audience attention.

Learning retention metrics revealed impressive improvements, with participants showing 68% better recall of artwork details and themes compared to control groups experiencing traditional museum displays. This substantial improvement indicates that interactive AR experiences create more memorable and effective learning environments than passive observation methods, validating the educational value of artist-created AR content.

The research also identified positive impacts on artist recognition and broader cultural engagement, with 73% of users reporting increased interest in featured artists' broader work following AR experiences. This finding suggests that AR technology successfully creates pathways for deeper cultural engagement that extend beyond individual artwork encounters, potentially contributing to long-term cultural heritage appreciation and artist support.

Particularly significant research by (Chen et al., 2020) revealed important insights about authenticity perception in AR cultural heritage experiences. The study found that Artivive experiences created by the artists themselves received significantly higher ratings for authenticity and engagement (average rating 4.5/5) compared to those created by third parties (average rating 3.7/5), highlighting the critical importance of creator involvement in AR interpretation for cultural heritage applications. This finding suggests that direct artist participation enhances perceived authenticity and user satisfaction, supporting Artivive's creator-empowered approach over technology-driven content development models.

2.4.5. Strengths and limitations

Artivive demonstrates exceptional strengths in democratizing AR content creation through its innovative approach that enables direct artist involvement in cultural heritage technology development. The platform's democratized creation process allows artists to maintain creative control over digital interpretations of their work while providing sophisticated technological capabilities that would otherwise require extensive technical expertise or significant financial investment. This approach represents a significant advancement in cultural heritage technology accessibility and artist empowerment.

The scalable platform architecture supports continuous

growth in content library through distributed creation models, where individual artists and institutions contribute to expanding available experiences rather than relying on centralized content development. This approach creates sustainable growth patterns while maintaining quality through creator involvement and institutional oversight. Minimal technical barriers for content creators ensure that artistic vision rather than technical expertise determines the quality and effectiveness of AR experiences, democratizing access to advanced cultural heritage technology.

The platform demonstrates particular effectiveness for contemporary art contexts and artist-led interpretation where direct creator involvement enhances authenticity and educational value. Successful integration with existing museum infrastructure indicates practical viability for institutional adoption without requiring significant modifications to established workflows or display systems.

However, several limitations constrain Artivive's broader applicability within diverse cultural heritage contexts. Variable quality of AR experiences based on individual creator expertise creates inconsistencies in user experience and educational effectiveness, as the platform's democratized approach inherently accepts variation in technical sophistication and content quality. The emphasis on artistic expression over educational content sometimes results in experiences that prioritize entertainment value over systematic cultural heritage education, potentially limiting effectiveness in formal educational contexts.

The platform provides no specific features for historical reconstruction or temporal comparison capabilities that prove essential for many cultural heritage applications, particularly those focused on archaeological sites, historical buildings, or artifacts that require temporal contextualization. Technical limitations restrict the platform primarily to 2D artworks, making it less effective for 3D artifacts, architectural sites, or environmental cultural heritage interpretation that requires more sophisticated spatial understanding and rendering capabilities.

The requirement for pre-registration of artworks eliminates possibilities for spontaneous recognition or exploration of unregistered cultural heritage items, creating barriers for impromptu cultural discovery and limiting the platform's utility for comprehensive cultural heritage exploration. This constraint requires advance planning and institutional cooperation that may not always be feasible in diverse cultural heritage contexts, particularly for smaller institutions or informal cultural heritage sites.

3. Results

The comparative analysis of the four selected AR applications reveals distinct approaches to cultural heritage interpretation across technical, experiential, and implementation dimensions. The following tables present systematic comparisons of key performance indicators, user experience metrics, and implementation characteristics that inform our understanding of current AR capabilities in cultural heritage contexts.

3.1. Technical Architecture Overview

Technical architecture analysis reveals fundamental differences in recognition methods and processing approaches across the four applications. Each platform employs distinct technological strategies that reflect their specific use cases and target audiences, ranging from AI-driven cloud processing to location-based triggering mechanisms (Table 1).

Table 1. Comparative technical architecture and implementation characteristics of AR cultural heritage applications

Features	Google Lens	Civilisations AR	Timelooper	Artivive
Primary Recognition Method	AI-based visual recognition	Marker/ surface detection	Geolocation-based	Image recognition
Content Delivery	Real-time web information	Pre-loaded 3D models	Location-triggered experiences	Artist-created overlays
Processing Location	Cloud-based with on-device components	Primarily on-device	Hybrid edge-cloud	Cloud-based content delivery
Technical Requirements	Standard smartphone camera	ARKit/ ARCore compatible device	GPS and compass accuracy	Standard smartphone camera
Platform Compatibility	Android, iOS	iOS, limited Android	iOS, Android	Cross-platform, web-based
AR Technology	Computer vision, ML-based recognition	Marker-based AR with 3D models	Location-based AR with GPS	Image recognition with overlay

3.2. Performance Metrics

Performance metrics demonstrate varying trade-offs between accuracy, speed, and resource consumption across the analyzed applications. The comparative evaluation reveals significant differences in recognition accuracy, processing speed, battery consumption, and

user engagement duration, as detailed in Table 2. These metrics indicate that higher immersion levels generally correlate with increased resource requirements, while simpler recognition-based approaches achieve better accessibility at the cost of engagement depth.

Table 2. Performance characteristics and resource utilization metrics of AR cultural heritage applications

Performance Metric	Google Lens	Civilisations AR	Timelooper	Artivive
Recognition Accuracy	78% for cultural artifacts	100% for pre-defined markers	92% location accuracy	95% for registered images
Loading Speed	1-3 seconds	5-10 seconds for models	3-7 seconds based on location	2-4 seconds for overlays
Battery Impact	Moderate (7% per hour)	High (12% per hour)	High (15% per hour)	Low (5% per hour)
Data Usage	High (streaming content)	Low (after download)	Medium	Medium
User Session Length	Avg. 2.5 minutes	Avg. 8.7 minutes	Avg. 12.3 minutes	Avg. 5.2 minutes
Content Richness	Medium (web links)	High (detailed 3D)	High (immersive)	Medium-High (varies)

3.3 User Experience and Engagement

User experience evaluation shows distinct patterns in usability and educational effectiveness across different application approaches. The analysis presented in Table 3 reveals varying user satisfaction levels, interaction complexity, and educational value ratings that correlate with each application's design philosophy. Notable findings include the inverse relationship between ease of use and educational depth, with more accessible applications generally providing less comprehensive cultural heritage content.

Table 3. User experience factors and engagement metrics for AR cultural heritage applications

User Experience Factor	Google Lens	Civilisations AR	Timelooper	Artivive
Interface Design	Minimalist, search-focused	Museum-style, educational	Immersive, historical	Artistic, gallery-inspired
Ease of Use	Very High (4.8/5)	High (4.3/5)	Medium (3.7/5)	High (4.2/5)
User Satisfaction	4.2/5 overall	4.5/5 overall	4.4/5 overall	4.3/5 overall
Educational Value	Medium (3.2/5)	High (4.7/5)	High (4.5/5)	Medium-High (3.8/5)
Interaction Methods	Camera pointing, touch	Touch, rotation, scaling	Location tracking, gyroscope	Camera pointing, touch

3.5 Implementation and Scalability

Implementation analysis demonstrates distinct development philosophies and scalability potential across the four platforms. The comparative assessment in Table 4 reveals significant variations in development approaches, technical scalability constraints, and cost structures that influence long-term viability and institutional adoption. Data-driven and creator-empowered models show superior scalability compared to location-centered and curatorial approaches, though each strategy addresses different institutional needs and resource capabilities.

Table 4. Implementation strategies and scalability characteristics of AR cultural heritage applications

Implementation Factor	Google Lens	Civilisations AR	Timelooper	Artivive
Development Approach	Data-driven	Curatorial	Location-centered	Creator-empowered
Technical Scalability	Highly scalable	Limited by 3D modeling resources	Limited by location development	Highly scalable
Update Frequency	Continuous model improvements	Fixed content library	Periodic location additions	Continuous creator additions
Offline Capabilities	Limited	Full after initial download	Minimal	None
Implementation Cost	Free for users, API costs for developers	Free app, high development cost	Paid experiences ($5-15)	Free viewer, artist subscription

3.7 Strengths and Limitations Summary

The comprehensive evaluation reveals that each application excels in specific domains while facing distinct constraints that limit broader applicability. Table 5 synthesizes the primary strengths and limitations identified across all evaluation dimensions, demonstrating that no single application currently addresses all cultural heritage interpretation needs. The analysis indicates that future AR development should focus on hybrid approaches that combine the accessibility of Google Lens, the educational depth of Civilisations AR, the immersive qualities of Timelooper, and the creator empowerment of Artivive.

Table 5. Summary of key strengths and primary limitations across AR cultural heritage applications

Application	Key Strengths	Primary Limitations
Google Lens	• Universal compatibility	• Shallow historical context
	• Rapid recognition	• High data usage
	• Continuous improvements	• Limited educational depth
	• Minimal setup	• Generic information
Civilisations AR	• Highest educational value • Detailed 3D models	• Limited device compatibility • High battery consumption
	• Curriculum alignment	• Fixed content library
	• Strong user engagement	• Space requirements
Timelooper	• Immersive historical experience	• Location dependency
	• High user engagement	• Limited scalability
	• Contextual relevance	• High battery usage
	• Strong temporal connection	• Technical complexity
Artivive	• Creator flexibility	• Variable content quality
	• Cross-platform support	• No offline capability
	• Low battery impact	• Dependent on creators
	• Artistic focus	• Limited educational structure

4. Discussion

4.1. Overview of Comparative Analysis

The results presented in Section 3 reveal significant insights into the current state and future potential of AR technology in cultural heritage contexts. This comparative analysis of augmented reality applications in cultural heritage contexts reveals significant insights into the current state and future potential of AR technology in preserving, presenting, and engaging users with cultural heritage. The systematic examination of Google Lens, Civilisations AR, Timelooper, and Artivive across technical, user experience, and educational dimensions has highlighted distinct approaches, strengths, and limitations that inform both theoretical understanding and practical implementation strategies for next-generation AR applications.

4.2. Philosophical Approaches and Application Strategies

Our analysis demonstrates that each application represents a fundamentally different philosophical approach to cultural heritage engagement, reflecting varying priorities in accessibility, education, and user interaction. Google Lens prioritizes universal accessibility and broad recognition capabilities, achieving 78% accuracy in cultural artifact identification, but sacrifices depth of historical context with users rating educational value at only 3.2/5. Civilisations AR emphasizes curatorial expertise and educational value, achieving the highest educational impact scores (4.7/5) and demonstrating 42% improvement in artifact detail recall, though at the cost of flexibility and scalability with a limited catalog of approximately 40 artifacts.

Timelooper creates powerful site-specific historical immersion, with 64% of users reporting feeling "transported to the past" and extending average visit duration by 22 minutes but faces significant geographical limitations with coverage of only 12 historical locations. Artivive balances creative expression with historical content, enabling broader participation through its creator-empowered platform supporting over 1,000 artists, but produces variable quality outcomes with creator-generated content rated higher (4.5/5) than third-party content (3.7/5).

4.3. Technical Performance and User Engagement Patterns

The technical comparison reveals an evolving landscape where recognition accuracy, processing speed, and content richness exist in dynamic tension. Performance metrics indicate that user engagement correlates strongly with contextual relevance rather than technical sophistication alone. Applications achieving the highest user session lengths (Timelooper: 12.3 minutes, Civilisations AR: 8.7 minutes) demonstrate that meaningful historical narratives and immersive experiences outweigh pure technical performance in sustaining user attention.

The most successful applications balance technological capabilities with intuitive user experiences, as evidenced by satisfaction ratings where ease of use (Google Lens: 4.8/5) and educational value (Civilisations AR: 4.7/5) emerge as critical success factors. Battery consumption

patterns reveal significant variations, with Timelooper's immersive experiences demanding high energy usage (15% per hour) compared to Artivive's efficient overlay approach (5% per hour), indicating important trade-offs between immersion depth and practical usability.

4.4. Demographic Engagement and Accessibility Considerations

User experience analysis demonstrates that different demographic groups engage with AR cultural heritage applications in distinct and measurable ways. Younger users (18-34) show consistently higher engagement rates across all platforms, with 87% of this demographic reporting learning new information through Civilisations AR compared to 64% for users over 45. Older users particularly value applications with clear educational frameworks and intuitive interfaces, demonstrating 28% higher satisfaction rates with structured experiences like Civilisations AR compared to open-ended platforms.

Accessibility remains a significant challenge, with varying degrees of success in accommodating diverse user needs across the analyzed applications. Google Lens excels in accessibility features including voice input and real-time translations, while other platforms show limited accommodation for users with disabilities. The analysis reveals a concerning gap where 47% of Google Lens users express desire for deeper historical context, while 26% of Civilisations AR users report technical difficulties with 3D model placement, highlighting the need for more inclusive design approaches.

4.5. Implications for Future AR Development

These findings have direct implications for our proposed ARchive application and similar cultural heritage initiatives, providing a roadmap for addressing current limitations while leveraging proven strengths. The research suggests that successful AR applications must strategically balance technical innovation with historical authenticity, user accessibility with content depth, and scalability with quality control. Evidence from our analysis indicates that hybrid approaches combining multiple successful elements achieve superior outcomes across all evaluation dimensions.

Future AR cultural heritage applications would benefit from implementing hybrid recognition systems that combine Google Lens's AI-driven capabilities (78% accuracy) with Civilisations AR's curated depth (4.7/5 educational value). Adaptive content delivery systems should adjust complexity based on user expertise level and engagement patterns, while cross-platform compatibility ensures consistent experiences across device types.

User experience optimization should prioritize demographic-adaptive interfaces that automatically adjust to user age and technical proficiency. Collaborative development models should engage both technical experts and cultural heritage specialists in content creation, supported by standardized evaluation frameworks that assess both technical performance and educational impact using measurable metrics.

Content and engagement enhancement requires location-aware content systems combining Timelooper's site-specific immersion with broader accessibility. Creator-empowered platforms following Artivive's model should implement quality control mechanisms, while multi-modal storytelling approaches integrate visual, audio, and interactive elements for diverse learning preferences.

4.6. Future Research Directions and Limitations

Future research directions should prioritize several critical areas identified through this comparative analysis. Long-term educational impact studies are essential to validate the sustained learning benefits observed in short-term evaluations, particularly given the 42% improvement in recall demonstrated by Civilisations AR users. Development of more sophisticated methods for historical reconstruction accuracy represents another crucial research avenue, as current applications vary significantly in their adherence to historical evidence and expert validation.

Cross-cultural perceptions of AR heritage experiences require systematic investigation, as current research predominantly reflects Western perspectives and may not adequately represent global cultural heritage interpretation needs. Additionally, examining the sustainability of AR platforms for smaller cultural institutions with limited resources emerges as a practical necessity, given that current successful implementations require significant technical infrastructure and ongoing content development investments.

Study Limitations: This analysis is constrained by its focus on four major applications and English-language publications, potentially limiting the generalizability of findings to emerging platforms and non-Western contexts. The rapid evolution of AR technology means that some technical specifications and performance metrics may change significantly between analysis and publication. Future studies should incorporate broader geographical perspectives, emerging AR platforms, and longitudinal user engagement data to provide more comprehensive insights into AR's role in cultural heritage preservation and interpretation.

5. Conclusion

In conclusion, augmented reality represents a transformative technology for cultural heritage: yet, our analysis reveals that effective implementation requires strategic integration of AI-driven recognition, educational depth, and immersive storytelling. This systematic comparative analysis provides the first comprehensive evaluation framework for AR cultural heritage applications, establishing benchmark criteria for future development and assessment. The comparative study of four leading applications demonstrates distinct strengths: Google Lens in accessibility, Civilisations AR in educational value, Timelooper in historical immersion, and Artivive in creative expression. These findings suggest that next-generation AR applications should

adopt hybrid approaches combining the best features of each model while addressing current limitations in content scalability and user engagement. This comparative framework provides actionable insights for developers and cultural institutions seeking to create AR solutions that effectively preserve cultural heritage while transforming how diverse audiences interact with history in our digital age. While this analysis focuses on four major applications, the framework established here can guide evaluation of emerging AR platforms and inform development of more inclusive cultural heritage technologies. Future developments should focus on AI integration, collaborative content creation, and adaptive user interfaces to fully realize AR's potential in cultural heritage interpretation.

Author Contribution

The contribution percentages of the authors are given below. All authors have reviewed and approved the article.

	N.Ş.	A.A.
C	40	60
D	55	45
S	60	40
DCP	40	60
DAI	40	60
LS	40	60
WR	50	50
CR	60	40
SR	60	40

C= conceptualization, D= design, S= supervision, DCP= data collection and/or processing, DAI= data analysis and/or interpretation, LS= literature search, WR= writing, CR= critical review, SR= submission and revision.

Conflict of Interest Statement

The authors declare that there is no conflict of interest in this study.

References

Artivive GmbH. 2024. Artivive (Version 4.8.2) [Mobile app]. AppStore. URL:https://apps.apple.com/app/artivive/id1188737494

BBC. 2018. Civilisations AR launches. BBC MediaCentre. URL:https://www.bbc.co.uk/mediacentre/latestnews/2018/Civilisations-ar-launches

Boboc RG, Băutu E, Gîrbacia F, Popovici N, Popovici DM. 2022. Augmented reality in cultural heritage: an overview of the last decade of applications. Appl Sci, 12(19): 9859

de Morais Sarmento MLF. 2024. Design of Immersive Museum Experiences: Improving Visitor Engagement Through Co-Creation, Augmented Reality and Gamification. Universidade do Porto, Institute of Design and Fine Arts, Porto, Portugal, pp: 24-65.

Ghouaiel N, Garbaya S, Cieutat JM, Jessel JP. 2017. Mobile augmented reality in museums: towards enhancing visitor's learning experience. Int J Virtual Reality, 17(1): 21-31

Google LLC. 2024. Google Lens (Version 1.17). URL:https://play.google.com/store/apps/details?id=com.google.ar.lens

Hammady R, Ma M, Powell A. 2018. User experience of markerless augmented reality applications in cultural heritage museums: 'museumeye' as a case study. In: Augmented Reality, Virtual Reality, and Computer Graphics: 5th Int Conf, AVR 2018, Otranto, Italy, June 24–27, 2018, Proc Part II 5: 349-369. Springer Int Publishing

Kleftodimos A, Evagelou A, Triantafyllidou A, Grigoriou M, Lappas G. 2023. Location-based augmented reality for cultural heritage communication and education: the Doltso district application. Sensors, 23(10): 4963

Lampropoulos G, Keramopoulos E, Diamantaras K. 2020. Enhancing the functionality of augmented reality using deep learning, semantic web and knowledge graphs: A review. Vis Informatics, 4(1): 32-42

Michel-Acosta P, Chaljub-Hasbún J, Cabero-Almenara J, Conte-Ayala ED, Peguero-García J, Pepín-Ubrí J. 2024. Evaluating an augmented reality app for learning about climate change among university students: A pilot study. Rev Electrón Educare, 28(3): 227-245

Rinaldi AM, Russo C, Tommasino C. 2022. An augmented reality CBIR system based on multimedia knowledge graph and deep learning techniques in cultural heritage. Computers, 11(12): 172

Sylaiou S, Dafiotis P. 2020. Storytelling in virtual museums: engaging a multitude of voices. In: Visual Computing for Cultural Heritage, Springer, Cham, pp: 369-388

The Org, n.d. Yigit Yigiter – TimeLooper org chart. The Org. URL:https://theorg.com/org/timelooper/org-chart/yigit-yigiter (accessed date: May 30, 2025)

TimeLooper Inc, 2024. Xplore - AR by TimeLooper [Mobile app]. Google Play Store. URL:https://play.google.com/store/apps/details?id=com.Timelooper.XPLORE.

Black Sea Journal of Engineering and Science
doi: 10.34248/bsengineering.1701252

Open Access Journal
e-ISSN: 2619 – 8991

Review
Volume 8 - Issue 4: 1246-1255 / July 2025

DIETARY ADVANCED GLYCATION END PRODUCTs (D-AGEs): FORMATION, DETECTION, AND HEALTH IMPLICATIONS

Seda UFUK[1], Melek ZOR[2*], Memnune ŞENGÜL[3], İsa Arslan KARAKÜTÜK[3]

[1]*Artvin Directorate of Provincial Agriculture and Forestry, 08000, Artvin, Türkiye*
[2]*Department of Gastronomy and Culinary Arts, School of Tourism and Hotel Management, Ağrı İbrahim Cecen University, 04100 Agri, Türkiye*
[3]*Department of Food Engineering, Faculty of Agriculture, Ataturk University, 25240 Erzurum, Türkiye*

Abstract: Advanced glycation end products (AGEs), also known as glycotoxins, are harmful compounds formed through non-enzymatic reactions between reducing sugars such as glucose, ribose, and fructose and amino groups in proteins, lipids, or nucleic acids. While AGEs are naturally produced in the body during normal metabolism (endogenous AGEs), they are also ingested through external sources, primarily via diet and smoking (exogenous AGEs). The formation of dietary AGEs (d-AGEs) is significantly influenced by food composition and processing factors, including heat exposure, cooking duration, humidity, pH, food additives, marination, and cooking methods. Higher temperatures and longer cooking times notably increase AGE levels in foods. These compounds are associated with various physiological toxicities and contribute to aging and the development of chronic diseases. This article explores the mechanisms of d-AGEs formation, their transport and toxic effects in the body, methods for detecting them, and strategies to inhibit their formation or intake. By raising awareness and providing practical inhibition methods, this work aims to reduce the health risks posed by dietary AGEs and support public health efforts.

Keywords: Maillard reaction, Browning reaction, Amadori products, Advanced glycation end products

***Corresponding author:** Department of Gastronomy and Culinary Arts, School of Tourism and Hotel Management, Ağrı İbrahim Cecen University, 04100 Agri, Türkiye
E mail: mzor@agri.edu.tr (M. ZOR)

Seda UFUK https://orcid.org/0000-0001-6250-6670
Melek ZOR https://orcid.org/0000-0002-5795-218X
Memnune ŞENGÜL https://orcid.org/0000-0003-3909-2523
Isa Arslan KARAKÜTÜK https://orcid.org/0000-0002-0317-2882

Received: May 17, 2025
Accepted: July 02, 2025
Published: July 15, 2025

Cite as: Ufuk S, Zor M, Şengül M, Karakütük İA. 2025. The pathogenic effects of dietary advanced glycation end products (d-AGE) in processed food industry. BSJ Eng Sci, 8(4): 1246-1255.

1. Introduction

Advanced glycation end products (glycotoxins) are formed as a result of the non-enzymatic reactions of carbonyl groups of reducing sugars such as glucose, ribose, fructose, and others and the terminal amino groups of proteins, lipids or nucleic acids (Wu et al., 2013; Perrone et al., 2020; Vıcıl and Ulutaş, 2020). AGEs are a heterogeneous group of molecules that can form during the oxidation of lipids and proteins, Maillard reactions, and food processing (Yaman, 2021). AGEs, which have a yellow-brown color, are molecules that can alter the structure of proteins in both plasma and tissues (Demirel and Yıldıran, 2018). The main precursors of AGEs formed during the Maillard reaction steps are glyoxal (GO), 3-deoxyglucosone (3-DG) and methylglyoxal (MGO) (Çatak and Balcı, 2022). Advanced glycation end-products (AGEs) were originally identified by their ability to emit specific fluorescence and form cross-links between amino acids, such as crosslines, vesperlysines, and pentosidine. However, researchers have since discovered that other compounds like Nε-(carboxymethyl) lysine (CML), pyrraline, MG-H1 (a product of methylglyoxal), Nε-(carboxyethyl) lysine (CEL), and argpyrimidine, are also considered AGEs, even though they do not form cross-links or emit fluorescence (Takeuchi et al., 2024). In Figure 1, the formation of reactive dicarbonyl compounds and resultant AGEs is illustrated. Sensory differences and browning occur in foods as a result of the Maillard reaction that happens during food processing such as grilling and frying (Wang et al., 2013; Öztürk and Garipoglu, 2022).

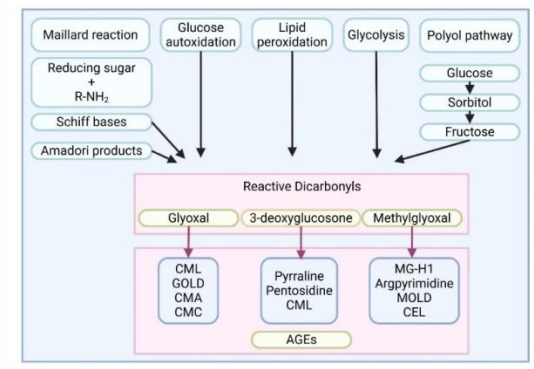


Figure 1. Formation of reactive dicarbonyls and AGEs (Nowotny et al., 2015; Created in BioRender. Karakütük, I. (2025a) https://BioRender.com/b07x896)

This work is licensed (CC BY-NC 4.0) under Creative Commons Attribution 4.0 International License

In the presence of excessive reducing sugars, biomolecules undergo a non-enzymatic reaction known as glycation, which involves proteins, lipids, and nucleotides. This process leads to the formation of covalent bonds between biomolecules and reducing sugars, termed Schiff bases. Through various reactions, such as rearrangement, oxidation/reduction, and cyclization, this process leads to the production of irreversible and heterogeneous compounds known as advanced glycation end-products (AGEs). These AGEs are frequently found as modified forms of aminoacids such as lysine, arginine, and cysteine (Lee et al., 2024). Fructosyllysine (FL) and Nϵ-(carboxymethyl)lysine (CML) are among the most abundant and widely studied Amadori products and advanced glycation end-products (AGEs) found in foods. FL is formed from the reaction between glucose and lysine, while CML can arise either through the rearrangement of FL or via reactions between lysine and reactive carbonyl compounds like glyoxal or 3-deoxyglucosone. Other common AGEs in foods include compounds such as pyrraline, Nϵ-(carboxyethyl)lysine (CEL), hydroxymethylfurfural (HMF), and Nδ-(5-hydro-5-methyl-4-imidazolone-2-yl)ornithine (van Dongen et al., 2022). The most frequently measured and best-studied AGEs are derivatives of carboxyethyl-lysine (CEL), carboxymethyl-lysine (CML) and methylglyoxal (MGO) (Vasilj et al., 2023). These AGEs are commonly studied not only because of their prevalence in biological systems but also due to their strong association with the development and progression of chronic diseases, particularly diabetes-related complications. CML and CEL are stable end-products that accumulate in long-lived proteins and tissues, making them reliable indicators of cumulative glycation and oxidative stress (Peyroux and Sternberg, 2006; Ott et al., 2014).

While dietary AGEs are naturally present in foods, their formation significantly increases with high-temperature cooking, low moisture, prolonged heat exposure, the presence of trace metals, and higher pH levels; these dietary AGEs and ALEs are important for consumer risk assessment because they can be absorbed through the gastrointestinal tract, potentially raising the body's overall AGE levels (Srey et al., 2010). Therefore, cooking techniques such as roasting, grilling, and frying produce notably higher levels of dietary AGEs (dAGEs) compared to methods such as stewing, boiling, steaming, and poaching (Vasilj et al., 2023). It is observed that cooking methods in dry heat increase the formation of AGE compared to cooking methods in moist heat. It is indicated that the formation of AGE can be reduced by using high humidity, lower cooking temperatures, shorter cooking times, or acidic components such as vinegar or lemon juice (Akın and Özbek, 2022).

Foods that are high in protein and fat, as well as processed and ultra-processed foods, tend to have high AGE content, especially when prepared at high temperatures and low humidity (Mendes et al., 2024). Heating times and different cooking methods play a crucial role in the formation of AGEs in foods. For example, 100 g of boiled chicken breast contains 1210 kU of CML, while the same amount of chicken, when fried at 450°F for 15 minutes, contains 5828 kU of CML (Vasilj et al., 2023). Food items with the highest levels of AGEs per gram include processed foods like crackers, chips, and cookies. The reason behind this is the thermal processing of these foods and the addition of components such as vegetable oil, butter, eggs, cheese, and nuts, which markedly accelerate the formation of AGEs (Sharma et al., 2015; Hu et al., 2022). Due to conflicting findings, there is no consensus on the AGE content in solid and liquid fats (Vasilj et al., 2023). In their study, Hu et al. (2022) stated that the proportions of sucrose, butter, and egg in butter cookies demonstrated a positive correlation with AGEs, highlighting that sucrose significantly promoted the formation of HMF and 3-deoxyglucosones (3-DG) (Figure 2). In addition to these findings, Hu et al. (2022) reported that the high levels of sucrose and butter in cookies were particularly favored by panelists due to their appearance, taste, and aroma.

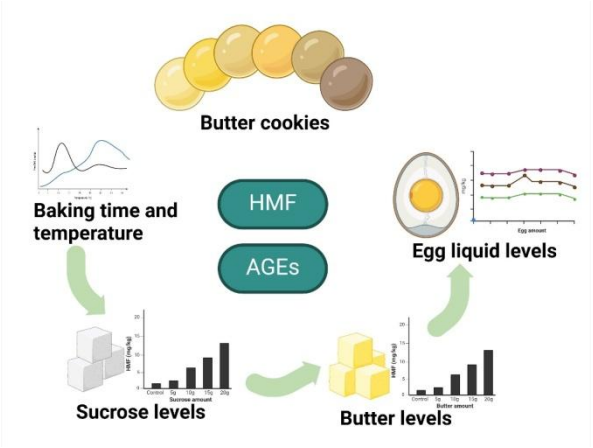


Figure 2. The roles of various factors in the formation of AGEs and HMF in butter cookies (Hu et al., 2022; Created in BioRender. Karakütük, I. (2025b) https://BioRender.com/e31j367)

2. Formation of d-AGES

In 1953, scientist Hodge divided the Maillard reaction into 3 different stages. In the first stage the aldehyde group of reducing sugar react with amino group of protein to form an unstable complex known as a Schiff base adduct which over several days rearrange to form a product called Amadori product. The second stage, known as the intermediate stage, involves the transformation of the Amadori product into reactive dicarbonyl compounds such as glyoxal (GO), (3-DG) and methylglyoxal (MGO). In the late stage of glycation, the final irreversible and colored compounds, known as AGEs, are formed (Ho et al., 2010; Khan et al., 2020; Erim et al., 2022). The process of AGE formation is shown in Figure 3.

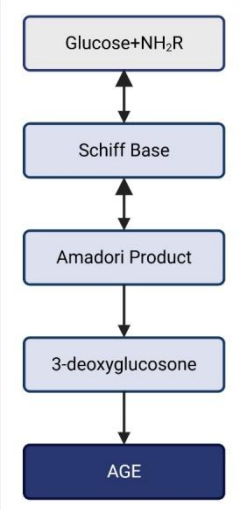


Figure 3. The formation of AGEs (Akın and Özbek, 2022; Created in BioRender. Karakütük, I. (2025c) https://BioRender.com/i45b405)

Due to the considerable variations in AGE structures in vivo and their formation through complex reactions like dehydration, condensation, oxidation, and rearrangements, only a limited number of AGE structures have been identified so far. The structures of highly cytotoxic AGEs are still unknown. Four types of glyceraldehyde-derived advanced glycation end-products (GA-AGE) structures have been identified by means of proteomic analyses. These include pyridinium compounds derived from GA (GLAP), MG-H1, trihydroxytriazine, and argpyrimidine (Takeuchi et al., 2024).

The amino acids lysine, histidine, and arginine in proteins are more susceptible to glycation. Among reducing sugars, glucose demonstrate the lowest glycation rate, whereas sugars like fructose, glyceraldehyde-3-phosphate, trehalose, and glucose-6-phosphate have higher rates of glycation (Akın and Özbek, 2022).

3. Endogen and Exogenous AGEs

There are basically two types of AGEs, which are endogenously produced and exogenously taken (Öztürk and Garipoglu, 2022). Endogenous AGEs are formed naturally within the body, with their levels increasing significantly under conditions such as hyperglycemia and oxidative stress. AGEs can also be obtained from external sources, particularly food, in which case they are referred to as dAGEs (Vasilj et al., 2023). AGEs can occur endogenously as a result of a series of complex enzymatic reactions in the organism. In addition, AGEs can be exposed exogenously through smoking or through food and therefore exogenous AGEs are called dAGEs (Yılmaz and Karabudak, 2016; Öztürk and Garipoglu, 2022).

The main source of exogenous AGEs is diet and occurs commonly in complex foods rich in sugar and fat content. Exogenous AGEs are formed rapidly and in large amounts by non-enzymatic reactions during food processing like frying, baking and caramelization (Kuzan, 2021). The composition of foods, duration of exposure to heat, humidity in the environment, pH, food additives, marination, temperature and cooking methods are factors that affect the formation of AGEs. As temperature and time increase, the content of AGEs also increases accordingly (Yılmaz and Karabudak, 2016; Çatak and Balcı, 2022; Demirer and Yardımcı, 2022). The AGE content of meat products or oils that have been subjected to high heat processing, such as roasting or frying, is higher than carbohydrates that have been boiled for a long time (Yılmaz and Karabudak, 2016). Additionally, exogenous AGEs formed during the heat processing of foods are more chemically diverse than endogenous AGEs produced within the body. This greater heterogeneity of dietary AGEs makes it more difficult to fully understand their biological effects (Öztürk and Garipoglu, 2022). Many studies have shown that the highest AGE compounds in foods are found in high-fat foods such as chips, crackers and cookies (Yaman, 2021).

Animal-derived foods, including beef, fish, cheese, poultry, and eggs, are noted to include the highest levels of AGEs per 100 grams of food. Vegetables and fruits generally contain lower levels of AGEs compared to meat (Vasilj et al., 2023). The number of AGEs per serving (5 grams) in fat is generally higher compared to other food groups. Despite the lower AGE content in the meat group compared to the fats, the consumption quantity of the meat group is generally higher. Hence, a significant portion of the AGE intake originates from the meat group. It has been determined that when animal-derived foods are cooked using dry heat, there is an increase in AGE levels. Under the influence of heat, reducing sugars like glucose-6-phosphate within muscle cells react with the amino groups present in the structure of meat, resulting in an observed increase in AGE levels. It has been found that cheeses with higher fat content, such as Parmesan cheese, exhibit higher levels of AGEs compared to cheeses with lower fat content, such as mozzarella cheese. While cooking is known to promote the formation of new AGEs in foods, uncooked items like cheese can still contain high levels of AGEs. It is believed that the reason for this lies in the pasteurization process and the aging period applied to cheese (such as culturing or ripening), during which AGE formation occurs (Demirel and Yıldıran, 2018).

The total amount of AGEs in the body comprises both endogenously formed AGEs and exogenously consumed AGEs through factors such as tobacco smoke, pollution, and certain foods (Ruiz et al., 2020).

The same situation applies to animals kept as pets and consuming commercially produced feeds. The nutritional value and digestibility of amino acids, particularly lysine, in feed ingredients and diets vary depending on the applied heat treatment (Almeida, 2013). It has been observed that broiler chickens and piglets fed with heat-damaged soybean meal experience a decrease in live weight and carcass weight compared to those fed with untreated soybean meal. Furthermore, it has been

determined that the adverse effects of heat damage on performance can be partially alleviated by adding crystalline aminoacids to the feeds (Almeida et al., 2014). In another study, it was observed that in cattle fed with heat-treated feeds, the formation of AGEs and MRP as a consequence of heating was also detected in the milk of the animals. However, cattle that did not consume processed feeds exhibited lower levels of glycated protein content in their milk (Schwarzenbolz et al., 2016).

4. Physiological Toxicity of d-AGES

Advanced Glycation End Products (AGEs) are harmful compounds commonly found in modern diets, particularly in processed foods, and have significant health effects. It was previously thought that the absorption of dietary AGEs was low and therefore had no significant effect on human health. However, recent studies have shown that AGEs taken with diet are absorbed in the body and may have significant negative consequences on human health (Demirel and Yıldıran, 2018). The formation of endogenous AGEs is a normal metabolic process, however when excessively high levels of AGEs accumulate in tissues and the bloodstream, they can have pathogenic effects (Sharma et al., 2015; van Dongen et al., 2022). AGEs accumulate in healthy aging individuals, and this accumulation is more significant at high glucose concentrations. While the accumulation of AGEs in tissues is primarily linked to microvascular and macrovascular damage observed in diabetes, but it is also associated with other conditions including atherosclerosis, end-stage renal disease, Alzheimer's disease, rheumatoid arthritis, cataracts, sarcopenia, and various degenerative ophthalmic diseases, as well as vascular dementia, Parkinson's disease, and several other chronic diseases (Luevano-Contreras and Chapman-Novakofski, 2010). The excessive accumulation of AGEs in body tissues contributes to high levels of oxidative stress and inflammation. Especially, it significantly leads to the pathogenesis of various chronic diseases like chronic kidney diseases, type 2 diabetes, and cardiovascular disorders (Uribarri et al., 2007; Shen et al., 2020; Akın and Özbek, 2022).

AGEs contribute to the pathogenesis of chronic diseases associated with aging. These compounds and their precursors are naturally produced in the body during the aging process, but they are also found in heat-treated foods and cigarette smoke, leading to further AGE accumulation. Excessive endogenous production of AGEs has been linked to proinflammatory processes involved in conditions like atherosclerosis, insulin resistance, and vascular complications of diabetes. Though, there is less understanding regarding the effects and metabolic destiny of AGEs derived from the diet (Kellow and Coughlan, 2015). Furthermore, AGEs are known as potential endocrine decayers due to their ability to intervene in hormone signaling (Qiang et al., 2024).

In Figure 4, the binding of AGEs to RAGE, triggering a series of pro-inflammatory and pro-metastatic cellular signaling pathways, has been illustrated (Peterson and Ligibel, 2024).

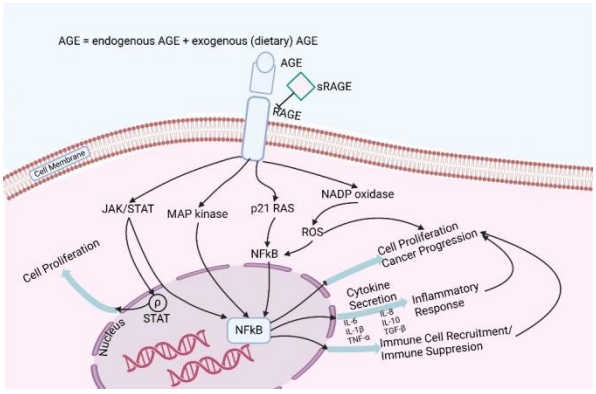


Figure 4. The binding of AGEs to RAGE, triggering a series of pro-inflammatory and pro-metastatic cellular signaling pathways (Peterson and Ligibel, 2024; Created in BioRender. Karakütük, I. (2025d) https://BioRender.com/x24r992)

It is estimated that individuals consume between 25 to 75 mg of AGEs and 500 to 1200 mg of Amadori products daily through their diet (Öztürk and Garipoglu, 2022). However, the precise extent to which dietary AGEs are absorbed in the digestive system and enter circulation remains unclear (Luevano-Contreras and Chapman-Novakofski, 2010).

Some of the exogenous AGEs ingested with food are absorbed in the intestines and enter circulation, where they can accumulate in cells and tissues. Excessive accumulation of AGEs can lead to various health disorders. About 10% of AGEs consumed through diet are absorbed into circulation. Recent systematic reviews of clinical studies suggest that dAGEs may increase the risk factors associated with chronic diseases like inflammation, oxidative stress, and insulin resistance (Çatak and Balcı, 2022). The pathological effects of AGEs occur through two different mechanisms: AGE receptor-mediated and AGE receptor-independent pathways. The former involves direct cross-linking of AGEs with body proteins, leading to structural deformity, while the latter induces inflammation through AGE-sensitive receptors (Erim et al., 2022).

Scientific evidence suggests that AGEs contribute to cancer risk and outcomes by promoting inflammation, increasing reactive oxygen species, and causing metabolic dysregulation. Additionally, they play a role in shaping the tumor microenvironment (Peterson and Ligibel, 2024).

Figure 5 illustrates diseases arising from various potential mechanisms triggered by the formation of AGEs and their associated health complications (Anwar et al., 2021). It is reported that AGEs exert harmful effects on cellular functions through a range of mechanisms, including the production of free radicals, alteration of enzyme activity, degradation of proteins or lipids,

oxidation of lipids or nucleic acids, carbonyl stress, or interaction with AGE receptors on the cell surface (Singh et al., 2014).

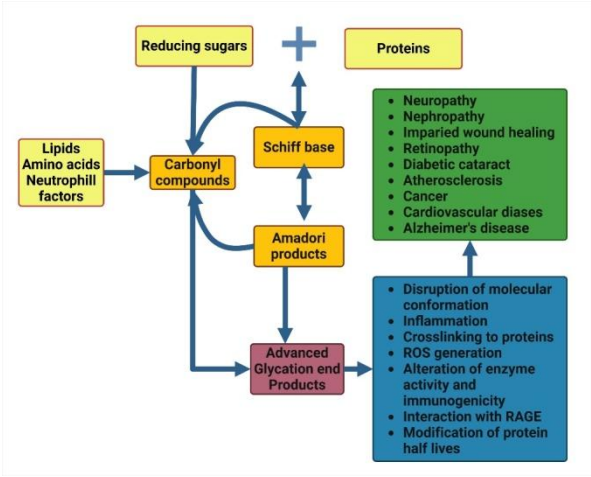


Figure 5. The diseases arising from various potential mechanisms triggered by the formation of AGEs and their associated health complication (Anwar et al., 2021; Created in BioRender. Karakütük, I. (2025e) https://BioRender.com/l87g434)

(Chilelli et al., 2013) reported that the effects of AGEs on diabetes primarily occur through two pathways. The first pathway involves AGEs directly causing cellular damage leading to pancreatic β-cell injury and disruption of insulin regulation. The second pathway entails AGE modification of mitochondrial respiratory chain proteins triggering the formation of reactive oxygen species (ROS) and establishing a vicious inflammatory cycle.

In diabetes, the chronic high-glucose environment encourages the formation of AGEs. These AGEs accumulate in diabetic bones, leading to increased non-enzymatic cross-linking within collagen fibrils. This disrupts intrafibrillar mineralization and causes disorganized mineral deposition on collagen fibrils, ultimately weakening bone strength. By inhibiting AGE formation, guanidines significantly enhance the microstructure and biomechanical strength of diabetic bone and accelerate bone fracture healing (Gao et al., 2024).

Glycation products and their receptors are frequently linked to higher morbidity and disease severity in various infectious conditions. For instance, a meta-analysis by Chen et al. (2019) revealed an association between HbA1c levels and Helicobacter pylori infection. Research by Sprenger et al. (2017) found a significant increase in fluorescent AGEs in the skin of individuals infected with HIV-1. Andrades et al. (2012) demonstrated that plasma levels of CML and CEL were related to the severity of sepsis. Moreover, lower serum levels of soluble RAGE (sRAGE) have been correlated with both acute and chronic morbidities in children with bronchiolitis (Patregnani et al., 2021). Furthermore, sRAGE is being explored as a potential biomarker for sepsis and late-onset neonatal infections (Zolakova et al., 2016).

In addition to all this information, it is important to mention the therapeutic possibilities related to glycation, which include: (1) treatment with anti-RAGE antibodies, (2) treatment with soluble RAGE (AGE receptor) and (3) use of AGE inhibitors and (4) AGE blockers. Such strategies can notably decrease the occurrence of processes that cause diabetic complications (Bronowicka-Szydełko et al., 2024).

5. Transport of d-AGES

Studies have shown that the majority of free CML in the body is directly related to the dietary intake of dCML (Tessier et al., 2016). The total amount of AGE in an individual's body is expressed as the sum of endogenously produced AGE and exogenously produced AGE (Prasad et al., 2019). The reason AGEs cause diseases is that they bind abnormally to proteins in the body, disrupting their structure and rendering them unable to perform their functions, which consequently leads to the development of diseases (Karaköse, 2023). For these reasons, thoroughly understanding the absorption process and metabolism of AGEs in the body is of vital importance to comprehend how they affect diseases.

It has been determined that nearly 10% of the advanced glycation end-products (AGEs) present in food and drinks are absorbed by the body. Nevertheless, only one-third of these are excreted through urine and feces. The absorbed fraction remains within the body for a duration of up to 72 hours (Erim et al., 2022). Research conducted on adults reveals that approximately 10% of dietary-derived advanced glycation end-products (AGEs) are absorbed, with two-thirds of the absorbed AGEs enduring within the body and one-third being eliminated through gastrointestinal processes or urinary excretion (Akın and Özbek, 2022).

The elimination of AGEs from the body occurs through urine, and this also provides information about how much AGE has accumulated in the body. Although the excretion amounts of dAGEs vary among individuals, this variability significantly affects the diseases they may have. It is believed that when urinary excretion decreases, individuals may have diabetes and kidney disease (Karaköse, 2023).

6. Inhibition Methods of d-AGES

The association of AGEs with ailments occurs through increased oxidative stress by means of AGE-RAGE activation and/or suppression of the body's defense systems. Considering the detrimental effects of AGEs on health, reducing dietary AGE intake is the most appropriate method to prevent AGE-related health issues (Yalçın and Rakıcıoğlu, 2022).

The pathways of glyoxalase, aldehyde dehydrogenase, aldose reductase and carbonyl reductase are defense

mechanisms developed against methylglyoxal (MGO) formation in living organisms. The glyoxalase system plays a pivotal role within cellular contexts as the main detoxification system used against MGO and other reactive carbonyl compounds (Vıcıl and Ulutaş, 2020). Alagebrium chloride, irbesartan, aspirin, carnosine, metformin, and calcium antagonists represent often utilized synthetic inhibitors of AGEs. Nonetheless, the use of synthetic AGE inhibitors may cause symptoms such as anemia, vomiting, dizziness, liver damage, gastrointestinal disorders, and headache (Khan et al., 2020; Zhou et al., 2020). It has been reported that there is a strong connection between exposure to AGE (Advanced Glycation End-products) and impaired intestinal barrier function. One of the most well-known AGEs, the methylglyoxal-derived hydroimidazolone-1 (MG-H1), has been shown to increase intestinal permeability in the human colon carcinoma cell line Caco-2 and to impair intestinal barrier integrity in mice (Lim et al., 2022). Sprague-Dawley rats fed a high-AGE diet for 18 weeks exhibited a significant increase in colonic permeability, as demonstrated by histological changes and the downregulation of tight junction proteins (TJs) like Occludin and Zonula Occludens-1 (ZO-1) in the colonic tissue (Qu et al., 2017). A 24-week high-AGE diet significantly impaired the integrity of the intestinal barrier, enhancing the movement of luminal molecules across the intestinal epithelium. This disruption was linked to a down-regulation of tight junction proteins (TJs), including Occludin and Claudin-1, in mice (Snelson et al., 2021).

Within the glyoxalase enzyme system, comprised of glyoxalase-1 and glyoxalase-2 enzymes, this system is recognized as the glyoxalase system. Located within the cytosol of cells, it contains α-ketoaldehydes as substrates, catalyzing them with catalytic amounts of GSH and Glo1 as cofactors. Reactive and non-cyclic α-ketoaldehydes are converted to α-hydroxy acids through the mediation of the glyoxalase system. Glyoxalase-1 catalyzes the isomerization of hemithioacetal, forming the structure of S-2-hydroxyacylglutathione. Hemithioacetal forms spontaneously in the presence of GSH. Glyoxalase-2, in contrast, converts the structure of S-2-hydroxyacylglutathione into α-hydroxy acids and simultaneously regenerates the GSH consumed in the step catalyzed by Glyoxalase-1 (Villanueva, 2017).

Numerous strategies have been explored to mitigate AGE interactions, including strategies to hinder AGE formation and AGE action, or disrupt pre-existing AGE cross-links.

Additionally, in response to oxidative stress, the AGE-RAGE signaling pathway triggers several intracellular pathways, culminating in the production of pro-inflammatory cytokines (for example; TNF-α, IL-6, and TGF-β), vascular adhesion molecules (like ICAM-1, VCAM-1, and ET-1), and reactive oxygen species (ROS), hence reinforcing vascular inflammation. Specifically, when human aortic endothelial cells (HAECs) are cultured under hyperglycemic conditions, oxidative stress ensues through AGE-RAGE signaling activation. This, in turn, upregulates MAPK pathways and prompts NF-κB and AP-1 activation. These transcription factors are later implicated in the elevation of gene expression for lysyl oxidase (LOX), an ECM enzyme, and endothelin-1 (ET-1), a vasoconstrictor protein. Subsequently, endothelial homeostasis is compromised, leading to cellular damage (Kosmopoulos et al., 2019) (Figure 6).

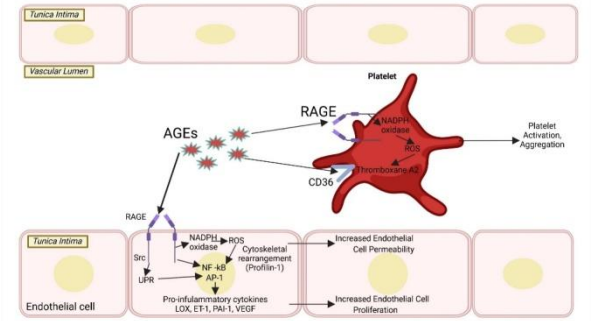


Figure 6. Effects of AGE-RAGE signaling in platelets and endothelial cell function (Kosmopoulos et al., 2019; Created in BioRender. Karakütük, I. (2025f) https://BioRender.com/m27q949)

Natural antioxidants and their alternatives are used as inhibitors of glycation reactions. It is stated that secondary metabolites abundant in fruits such as polyphenols also have inhibitory effects on AGEs (Zhao et al., 2022). In addition, the inclusion of these compounds can lead to results such as darker coloring in foods, increasing hardness and reduced taste compound production (Zheng et al., 2024). It has been reported that active compounds like miricitrin, ellagic acid, and quercitrin derived from *Drosera tokaiensis* tissue cultures exhibit strong inhibitory effects on AGEs (Tominaga et al., 2020). In addition, it should be considered that quercetin, catechin, and caffeic acid added at low concentrations have been reported to decrease food CML formation more than high concentrations, while high concentrations of polyphenols can increase hydrogen peroxide formation. In this case, hydrogen peroxide accelerates the formation of CML from Amadori products by generating hydroxyl radicals through Fenton reactions (Yalçın and Rakıcıoğlu, 2022).

In scientific terms, cooking is described as the transfer of energy from a heat source to food. This heat transfer aims to enhance the nutritional value and flavor of food, make it more digestible, and ensure the destruction of pathogenic microorganisms. Nevertheless, certain preparation and cooking methods may result in nutrient loss and a reduction in nutritional value, while some substances formed during cooking may render these foods harmful to health (Erim et al., 2022).

It has been reported that the number of AGEs in foods is associated with cooking methods and cooking temperature. Furthermore, there is a noteworthy correlation between the AGE content in foods and the fat

content and MGO level. The highest AGE compounds in foods are reported to be found in high-fat foods such as chips, crackers, and cookies (Uribarri et al., 2010).

When assessing the formation levels of AGEs based on cooking methods, the ranking typically proceeds as follows: oven roasting > deep frying > grilling > pan frying > boiling. Furthermore, the utilization of acidic marinades like tomato juice, vinegar, or lemon juice has been shown to potentially decrease AGE formation in meats by up to 50%. Notably, polyphenols, such as phenolic acids, flavonoids, stilbenes, and lignans, demonstrate anti-AGE properties (Akın and Özbek, 2022; Erim et al., 2022); Huang et al. (2024) demonstrated that resveratrol reduces oxidative stress and inflammation caused by AGEs in diabetic periodontitis through the NF-κB signaling pathway in AGE-stimulated human gingival fibroblasts (HGFs). Increasing the consumption of low-AGE foods such as whole grains, minimally processed dairy and meat products, fruits, and vegetables, while reducing the consumption of high-AGE foods such as grains, processed meat products, cheese, snack foods, and sugary beverages, decreases dietary AGE intake. Moreover, using moist heat cooking methods such as steaming, boiling, and simmering instead of dry heat cooking methods limits the formation of AGEs in foods. Polyphenols reduce AGE formation through mechanisms such as increasing antioxidant capacity, scavenging dicarbonyls, and breaking protein cross-links (Yalçın and Rakıcıoğlu, 2022).

7. Detection Methods

Many studies have been conducted to analyze AGEs in biological samples and foods, aiming to elucidate the main pathogenic mechanisms and understand whether the AGEs present in the human body originate from endogenous or exogenous sources (van Dongen et al., 2022).

A significant challenge in further exploring the risks associated with AGEs is the absence of a representative analytical system for detecting various AGEs in complex samples. Over the past decade, a range of separation and detection techniques have been employed to analyze AGEs. Separation methods include high-performance liquid chromatography-based techniques, such as ion pair chromatography, hydrophilic interaction chromatography, reverse phase liquid chromatography (RPLC and ion exchange chromatography). Detection methods used in these analyses include mass spectrometry (MS), fluorescence, and UV-Vis spectroscopy (Scheijen et al., 2016; Lee et al., 2024).

Various analytical methods have been employed to quantify the advanced glycation end-products (AGEs) content in foods. The majority of studies have assessed the concentration of Carboxymethyllysine (CML) in foods using enzyme linked immunosorbent assay (ELISA) based techniques (Kellow and Coughlan, 2015). Both food and blood contain numerous AGE metabolites that can be quantified using ELISA. Other techniques for measuring AGEs include liquid chromatography, particularly tandem mass spectrometry (LC-MS/MS), which is considered the gold standard for AGE detection. However, due to the complexity of this method, ELISA is typically preferred for AGE measurement. Determining the exact AGE content in food is a complicated process that involves homogenizing and extracting individual food items, followed by testing AGE metabolites in the supernatant using ELISA. This approach has contributed to the development of a database containing the AGE values for 550 common foods. The most accurate measurement of serum AGE is obtained from fasting blood samples, as consuming a meal rich in AGEs can elevate AGE levels. Among the most commonly measured metabolites are carboxyethyl-lysine (CEL), methylglyoxal (MG), and carboxymethyl-lysine (CML). CML is the primary metabolite used in AGE food databases and is frequently studied in relation to diet and serum AGE levels, particularly concerning cancer (Peterson and Ligibel, 2024).

The main factors contributing to a high AGE diet, adapted from dietary AGE analysis in the lung, prostate, colorectal and ovarian cancer screening trial, are represented by food groups in Figure 7 (Peterson and Ligibel, 2024).

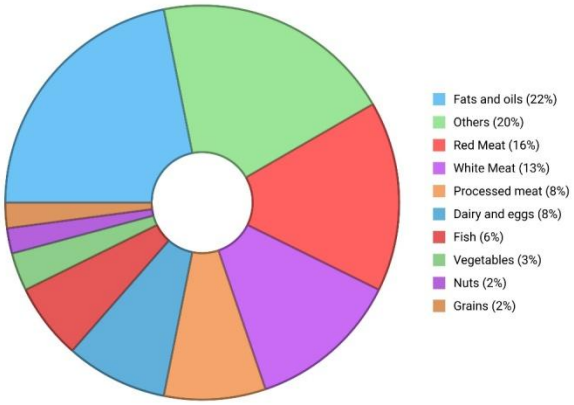


Figure 7. Contribution (%) of various food groups to dietary AGE intake (Peterson and Ligibel, 2024). *"Others" includes crackers, deserts, sugary drinks, and alcohol.

The use of various methodologies across several studies has resulted in inconsistent and conflicting findings. Currently, there is no universally accepted method for the accurate measurement of numerous advanced glycation end-product (AGE) moieties. Frequently employed techniques include chromatography, high-performance liquid chromatography (HPLC), fluorescence, and enzyme-linked immunosorbent assay (ELISA) (Peppa and Vlassara, 2005).

Lee et al. (2024) developed a novel analytical method using RPLC-electrospray ionization (ESI)-MS to target 14 different AGEs, addressing challenges such as chromatographic separation difficulties due to the high

hydrophilicity, diversity, and structural similarities of AGEs. They achieved high sensitivity and accuracy by employing pre-column dansyl chloride derivatization, which helped overcome the limitations of previous methods. In their study, they demonstrated the method's broad applicability by successfully identifying AGEs in three types of foods (beer, coffee, and sausage) and six distinct glycated protein types. They concluded that this analytical system would provide valuable insights into the pathogenesis of AGE-related diseases.

8. Conclusion

In summary, the detrimental impacts of dietary advanced glycation end-products (d-AGEs) are of significant concern within the processed food sector. Studies indicate that d-AGEs play a pivotal role in fostering chronic conditions like diabetes, cardiovascular issues, and neurodegenerative diseases. Processing techniques employed in the food industry, including high-temperature cooking and prolonged storage, contribute to elevated levels of d-AGEs in processed foods. Efforts to minimize AGE formation should be increased by incorporating antioxidants comprising polyphenols in suitable proportions into foods with high AGE content and/or consumption levels, to sustain healthy eating habits and food preparation methods. Several inhibition methods, such as employing acidic components like lemon juice or vinegar, have shown potential in reducing the formation of d-AGE. Educating consumers about the detrimental effects of d-AGEs and reducing their consumption can lead to positive effects on public health.

Author Contribution

The contribution percentages of the authors' are given below. All authors have reviewed and approved the article.

	S.U.	M.Z.	M.Ş.	İ.A.K.
C	40	40	10	10
D	40	40	10	10
S	25	25	40	10
DCP	40	40	10	10
DAI	50	40	5	5
LS	50	30	10	10
WR	40	40	10	10
CR	30	40	15	15
SR	40	40	10	10

C= conceptualization, D= design, S= supervision, DCP= data collection and/or processing, DAI= data analysis and/or interpretation, LS= literature search, WR= writing, CR= critical review, SR= submission and revision, PM= project management, FA= funding acquisition.

Conflict of Interest Statement

The authors declare that there is no conflict of interest in this study.

Acknowledgements

The author, İsa Arslan KARAKÜTÜK, is supported by the TUBITAK BIDEB 2211/A National Ph.D. Scholarship Program.

References

Akın Ö, Özbek YD. 2022. İleri glikasyon son ürünlerinin gebelik üzerine etkisi. Sakarya Üniversitesi Holistik Sağlık Dergisi, 5(1): 39-55.

Almeida F. 2013. Effects of the Maillard reactions on chemical composition and amino acid digestibility of feed ingredients and on pig growth performance. University of Illinois at Urbana-Champaign, Doctoral dissertation, Urbana, IL, USA, pp: 154.

Almeida FN, Htoo JK, Thomson J, Stein HH. 2014. Effects of balancing crystalline amino acids in diets containing heat-damaged soybean meal or distillers dried grains with solubles fed to weanling pigs. Animal, 8(10): 1594-1602.

Andrades ME, Lorenzi R, Nagai R, Moreira JCF, Ritter C, Dal-Pizzol F. 2012. Plasma glycation levels are associated with severity in sepsis. Eur J Clin Invest, 42(10): 1055-1060.

Anwar S, Khan S, Almatroudi A, Khan AA, Alsahli MA, Almatroodi SA, Rahmani AH. 2021. A review on mechanism of inhibition of advanced glycation end products formation by plant derived polyphenolic compounds. Mol Biol Rep, 48(1): 787-805.

Bronowicka-Szydełko A, Gostomska-Pampuch K, Kuzan A, Pietkiewicz J, Krzystek-Korpacka ML, Gamian A. 2024. Effect of advanced glycation end-products in a wide range of medical problems including COVID-19. Adv Med Sci, 69(1): 36-50.

Çatak J, Balcı E. 2022. Paketli keklerde ileri glikasyon son ürünleri öncüllerinin HPLC ile tespiti ve değerlendirilmesi. J Characterization, 2(1): 82-90.

Chen JH, Xing YL, Zhao LY, Ma HJ. 2019. The association between Helicobacter pylori infection and glycated hemoglobin A in diabetes: A meta-analysis. J Diabetes Res, 2019: 1-10.

Chilelli NC, Burlina S, Lapolla A. 2013. AGEs, rather than hyperglycemia, are responsible for microvascular complications in diabetes: A "glycoxidation-centric" point of view. Nutr Metab Cardiovasc Dis, 23(10): 913-919.

Demirel Y, Yıldıran H. 2018. İleri glikasyon son ürünleri ve böbrek hastalıkları. Gümüşhane Üniv Sağlık Bilim Derg, 7(1): 210-217.

Demirer B, Yardımcı H. 2022. İleri glikasyon son ürünlerinin diyabet komplikasyonları üzerine etkileri: Bir derleme. Beslenme ve Diyet Dergisi, 50(1): 101-108.

Erim B, Ergene E, Hecer C. 2022. Besin hazırlama ve pişirme yöntemlerinin ileri glikasyon son ürünleri üzerine etkisi. Aydın Gastronomy, 6(2): 275-281.

Gao QM, Jiang YY, Zhou DY, Li GF, Han YF, Yang JZ, Xu K, Jing YY, Bai L, Geng Z, Zhang H, Zhou GY, Zhu MR, Ji N, Han RN, Zhang YW, Li ZH, Wang CD, Hu Y, Su JC. 2024. Advanced glycation end products mediate biomineralization disorder in diabetic bone disease. Cell Rep Med, 5(9): 100966.

Ho SC, Wu SP, Lin SM, Tang YL. 2010. Comparison of anti-glycation capacities of several herbal infusions with that of green tea. Food Chem, 122(3): 768-774.

Hu H, Wang Y, Shen M, Huang Y, Li C, Nie S, Xie M. 2022. Effects of baking factors and recipes on the quality of butter cookies and the formation of advanced glycation end products (AGEs) and 5-hydroxymethylfurfural (HMF). Curr Res Food Sci, 5: 940-948.

Huang CY, Chen SH, Lin TC, Liao YW, Chang YC, Chen CC, Yu CC, Chen CJ. 2024. Resveratrol attenuates advanced glycation end product-induced senescence and inflammation in human gingival fibroblasts. J Dent Sci, 19(1): 580-586.

Karaköse D. 2023. Yüksek yağlı diyetle beslenen fare modellerinin yağ dokularında ileri glikasyon ürünlerinin incelenmesi. İstanbul Sabahattin Zaim Üniversitesi, Fen Bilimleri Enstitüsü, İstanbul, Türkiye, pp: 100.

Karakütük I. 2025a. Figure 1. Created in BioRender. https://BioRender.com/b07x896

Karakütük I. 2025b. Figure 2. Created in BioRender. https://BioRender.com/e31j367

Karakütük I. 2025c. Figure 3. Created in BioRender. https://BioRender.com/i45b405

Karakütük I. 2025d. Figure 4. Created in BioRender. https://BioRender.com/x24r992

Karakütük I. 2025e. Figure 5. Created in BioRender. https://BioRender.com/l87g434

Karakütük I. 2025f. Figure 6. Created in BioRender. https://BioRender.com/m27q949

Kellow NJ, Coughlan MT. 2015. Effect of diet-derived advanced glycation end products on inflammation. Nutr Rev, 73(11): 737-759.

Khan M, Liu HL, Wang J, Sun BG. 2020. Inhibitory effect of phenolic compounds and plant extracts on the formation of advance glycation end products: A comprehensive review. Food Res Int, 130: 108933.

Kosmopoulos M, Drekolias D, Zavras PD, Piperi C, Papavassiliou AG. 2019. Impact of advanced glycation end products (AGEs) signaling in coronary artery disease. BBA-Mol Basis Dis, 1865(3): 611-619.

Kuzan A. 2021. Toxicity of advanced glycation end products (Review). Biomed Rep, 14(5): 1-9.

Lee HHL, Ha SK, Kim Y, Hur J. 2024. Simultaneous analysis of advanced glycation end products using dansyl derivatization. Food Chem, 432: 137248.

Lim JM, Yoo HJ, Lee KW. 2022. High molecular weight fucoidan restores intestinal integrity by regulating inflammation and tight junction loss induced by methylglyoxal-derived hydroimidazolone-1. Mar Drugs, 20(9): 587.

Luevano-Contreras C, Chapman-Novakofski K. 2010. Dietary advanced glycation end products and aging. Nutrients, 2(12): 1247-1265.

Mendes NP, Cândido FG, Valente FX, Peluzio MDG, Juvanhol LL, Alfenas RCG. 2024. Dietary advanced glycation end products, body composition, and anthropometric measures: A cross-sectional analysis in women with excess body weight. Nutr Metab Cardiovasc Dis, 34(7): 1721-1730.

Nowotny K, Jung T, Höhn A, Weber D, Grune T. 2015. Advanced glycation end products and oxidative stress in type 2 diabetes mellitus. Biomolecules, 5(1): 194-222.

Ott C, Jacobs K, Haucke E, Santos AN, Grune T, Simm A. 2014. Role of advanced glycation end products in cellular signaling. Redox Biol, 2: 411-429.

Öztürk SA, Garipoğlu G. 2022. Determination of glyoxal and methylglyoxal bioaccessibility in pastas and noodles varieties by in vitro digestion method. J Characterization, 5(2): 102-110.

Patregnani JT, Fujiogi M, Camargo CA, Brooks BA, Hoptay CE, Mansbach JM, Teach SJ, Freishtat RJ, Hasegawa K. 2021. Serum soluble receptor for advanced glycation end products in infants with bronchiolitis: Associations with acute severity and recurrent wheeze. Clin Infect Dis, 73(9): e2665-e2672.

Peppa M, Vlassara H. 2005. Advanced glycation end products and diabetic complications: A general overview. Hormones, 4(1): 28-37.

Perrone A, Giovino A, Benny J, Martinelli F. 2020. Advanced glycation end products (AGEs): Biochemistry, signaling, analytical methods, and epigenetic effects. Oxid Med Cell Longev, 2020: 1-15.

Peterson LL, Ligibel JL. 2024. Dietary and serum advanced glycation end-products and clinical outcomes in breast cancer. BBA-Rev Cancer, 1879(1): 188786.

Peyroux J, Sternberg M. 2006. Advanced glycation endproducts (AGEs): pharmacological inhibition in diabetes. Pathol Biol, 54(7): 405-419.

Prasad C, Davis KE, Imrhan V, Juma S, Vijayagopal P. 2019. Advanced glycation end products and risks for chronic diseases: Intervening through lifestyle modification. Am J Lifestyle Med, 13(4): 384-404.

Qiang X, Liang SM, Lv YC, Wang XY, Zhang H, Zhan J. 2024. Advanced glycation end products (AGEs) impair the intestinal epithelial barrier via STAT3 activation mediated by macrophages. Food Chem Toxicol, 192: 113869.

Qu WT, Yuan XJ, Zhao JS, Zhang YX, Hu J, Wang JW, Li JX. 2017. Dietary advanced glycation end products modify gut microbial composition and partially increase colon permeability in rats. Mol Nutr Food Res, 61(10): 1700176.

Ruiz HH, Ramasamy R, Schmidt AM. 2020. Advanced glycation end products: Building on the concept of the "common soil" in metabolic disease. Endocrinology, 161(1).

Scheijen JLJM, Clevers E, Engelen L, Dagnelie PC, Brouns F, Stehouwer CDA, Schalkwijk CG. 2016. Analysis of advanced glycation endproducts in selected food items by ultra-performance liquid chromatography tandem mass spectrometry: Presentation of a dietary AGE database. Food Chem, 19: 1145-1150.

Schwarzenbolz U, Hofmann T, Sparmann N, Henle T. 2016. Free Maillard reaction products in milk reflect nutritional intake of glycated proteins and can be used to distinguish "organic" and "conventionally" produced milk. J Agric Food Chem, 64(24): 5071-5078.

Sharma C, Kaur A, Thind SS, Singh B, Raina S. 2015. Advanced glycation end-products (AGEs): An emerging concern for processed food industries. J Food Sci Technol-Mysore, 52(12): 7561-7576.

Shen CY, Lu CH, Wu CH, Li KJ, Kuo YM, Hsieh SC, Yu CL. 2020. The development of Maillard reaction, and advanced glycation end product (AGE)-receptor for AGE (RAGE) signaling inhibitors as novel therapeutic strategies for patients with AGE-related diseases. Molecules, 25(23).

Singh VP, Bali A, Singh N, Jaggi AS. 2014. Advanced glycation end products and diabetic complications. Korean J Physiol Pharmacol, 18(1): 1-14.

Snelson M, Tan SM, Clarke RE, de Pasquale C, Thallas-Bonke V, Nguyen TV, Penfold SA, Harcourt BE, Sourris KC, Lindblom RS, Ziemann M, Steer D, El-Osta A, Davies MJ, Donnellan L, Deo P, Kellow NJ, Cooper ME, Woodruff TM, Coughlan MT. 2021. Processed foods drive intestinal barrier permeability and microvascular diseases. Sci Adv, 7(14).

Sprenger HG, Bierman WF, Martes MI, Graaff R, van der Werf TS, Smit AJ. 2017. Skin advanced glycation end products in HIV infection are increased and predictive of development of cardiovascular events. AIDS, 31(2): 241-246.

Srey C, Hull GL, Connolly L, Elliott CT, del Castillo MD, Ames JM. 2010. Effect of inhibitor compounds on Nε-(carboxymethyl)lysine (CML) and Nε-(carboxyethyl)lysine (CEL) formation in model foods. J Agric Food Chem, 58(22): 12036-12041.

Takeuchi M, Suzuki H, Takeda K, Sakai-Sakasai A. 2024. Toxic

advanced glycation end-products (TAGE) are major structures of cytotoxic AGEs derived from glyceraldehyde. Med Hypotheses, 183.

Tessier FJ, Niquet-Léridon C, Jacolot P, Jouquand C, Genin M, Schmidt AM, Grossin N, Boulanger E. 201

Tessier FJ, Niquet-Léridon C, Jacolot P, Jouquand C, Genin M, Schmidt AM, Grossin N, Boulanger E. 2016. Quantitative assessment of organ distribution of dietary protein-bound 13C-labeled Nε-carboxymethyllysine after a chronic oral exposure in mice. Mol Nutr Food Res, 60(11): 2446-2456.

Tominaga Y, Sugawa H, Hirabayashi K, Ikeda T, Hoshi Y, Nagai R. 2020. Extract containing multiple phenolic compounds inhibits the formation of advanced glycation end-products. Arch Biochem Biophys, 693.

Uribarri J, Cai W, Peppa M, Goodman S, Ferrucci L, Striker G, Vlassara H. 2007. Circulating glycotoxins and dietary advanced glycation endproducts: Two links to inflammatory response, oxidative stress, and aging. J Gerontol A Biol Sci Med Sci, 62(4): 427-433.

Uribarri J, Woodruff S, Goodman S, Cai WJ, Chen X, Pyzik R, Yong A, Striker GE, Vlassara H. 2010. Advanced glycation end products in foods and a practical guide to their reduction in the diet. J Am Diet Assoc, 110(6): 911-916.

van Dongen KCW, Kappetein L, Estruch IM, Belzer C, Beekmann K, Rietjens IMCM. 2022. Differences in kinetics and dynamics of endogenous versus exogenous advanced glycation end products (AGEs) and their precursors. Food Chem Toxicol, 164.

Vasilj M, Goni L, Gayoso L, Razquin C, Sesma MT, Etxeberria U, Ruiz-Canela M. 2023. Correlation between serum advanced glycation end products and dietary intake of advanced glycation end products estimated from home cooking and food frequency questionnaires. Nutr Metab Cardiovasc Dis, 33(9): 1768-1777.

Vıcıl S, Ulutaş E. 2020. Metilglioksal ve ileri glikasyon son ürünleri. Bozok Vet Sci, 1(1-2): 74-79.

Villanueva M. 2017. Glyoxalase 1 attenuates the effects of chronic hyperglycemia on explant-derived cardiac stem cells. Université d'Ottawa/University of Ottawa, Doctoral dissertation, Ottawa, Canada, pp: 134.

Wang H, Tu ZC, Liu GX, Liu CM, Huang XQ, Xiao H. 2013. Comparison of glycation in conventionally and microwave-heated ovalbumin by high resolution mass spectrometry. Food Chem, 141(2): 985-991.

Wu Q, Chen HY, Lv ZJ, Li SY, Hu B, Guan YF, Xie BJ, Sun ZD. 2013. Oligomeric procyanidins of lotus seedpod inhibits the formation of advanced glycation end-products by scavenging reactive carbonyls. Food Chem, 138(2-3): 1493-1502.

Yalçın E, Rakıcıoğlu N. 2022. Besinlerde oluşan ileri glikasyon son ürünlerine polifenollerin etkisi. Beslenme ve Diyet Dergisi, 50(2): 66-75.

Yaman M. 2021. İleri glikasyon son ürünlerinin (AGEs) öncüllerinin in vitro biyoerişilebilirliklerinin bazı gıdalarda belirlenmesi. Avrupa Bilim ve Teknoloji Dergisi, (27): 598-604.

Yılmaz B, Karabudak E. 2016. Besinlerdeki ileri glikasyon son ürünleri ve azaltma yöntemleri. Beslenme ve Diyet Dergisi, 44(3): 280-288.

Zhao WB, Cai PJ, Zhang N, Wu TT, Sun AD, Jia GL. 2022. Inhibitory effects of polyphenols from black chokeberry on advanced glycation end-products (AGEs) formation. Food Chem, 392.

Zheng XY, Ai BL, Zheng LL, Liu WY, Yang Y, Xiao D, Sheng ZW. 2024. Modulatory effects of tryptophan on advanced glycation end products formation and flavor enhancement in high-protein intermediate-moisture food during storage. LWT-Food Sci Technol, 197.

Zhou Q, Cheng KW, Xiao JB, Wang MF. 2020. The multifunctional roles of flavonoids against the formation of advanced glycation end products (AGEs) and AGEs-induced harmful effects. Trends Food Sci Technol, 103: 333-347.

Zolakova B, Zolak V, Hatok J, Matasova K, Nosal S, Zibolen M. 2016. Soluble receptor for advanced glycation end products in late onset neonatal infection. Bratisl Med J, 117(1): 15-18.